Mechanical Design of Electric Motors

Wei Tong

CRC Press
Taylor & Francis Group

Mechanical Design of **Electric Motors**

Mechanical Design of **Electric Motors**

Wei Tong
Kollmorgen Corporation, Danaher Corporation
Radford, Virginia

CRC Press
Taylor & Francis Group
Boca Raton London New York

CRC Press is an imprint of the
Taylor & Francis Group, an **informa** business

CRC Press
Taylor & Francis Group
6000 Broken Sound Parkway NW, Suite 300
Boca Raton, FL 33487-2742

© 2014 by Taylor & Francis Group, LLC
CRC Press is an imprint of Taylor & Francis Group, an Informa business

No claim to original U.S. Government works
Version Date: 20140131

International Standard Book Number-13: 978-1-4200-9144-1 (eBook - PDF)

This book contains information obtained from authentic and highly regarded sources. Reasonable efforts have been made to publish reliable data and information, but the author and publisher cannot assume responsibility for the validity of all materials or the consequences of their use. The authors and publishers have attempted to trace the copyright holders of all material reproduced in this publication and apologize to copyright holders if permission to publish in this form has not been obtained. If any copyright material has not been acknowledged please write and let us know so we may rectify in any future reprint.

Except as permitted under U.S. Copyright Law, no part of this book may be reprinted, reproduced, transmitted, or utilized in any form by any electronic, mechanical, or other means, now known or hereafter invented, including photocopying, microfilming, and recording, or in any information storage or retrieval system, without written permission from the publishers.

For permission to photocopy or use material electronically from this work, please access www.copyright.com (http://www.copyright.com/) or contact the Copyright Clearance Center, Inc. (CCC), 222 Rosewood Drive, Danvers, MA 01923, 978-750-8400. CCC is a not-for-profit organization that provides licenses and registration for a variety of users. For organizations that have been granted a photocopy license by the CCC, a separate system of payment has been arranged.

Trademark Notice: Product or corporate names may be trademarks or registered trademarks, and are used only for identification and explanation without intent to infringe.

Visit the Taylor & Francis Web site at
http://www.taylorandfrancis.com

and the CRC Press Web site at
http://www.crcpress.com

To my wife, Zhangqing Zhuo, and daughter, Winnie Tong,

for their love, support, and patience

Contents

Preface xxi
Author xxv
List of Symbols xxvii

1. Introduction to Electric Motors 1
1.1 History of Electric Motors 1
1.2 Motor Design Characteristics 2
1.2.1 Motor Torque 2
1.2.1.1 Static and Dynamic Torque 2
1.2.1.2 Motor Torque in Motor-Load System 4
1.2.1.3 Continuous Torque 6
1.2.1.4 Peak Torque 6
1.2.1.5 Stall Torque 7
1.2.1.6 Cogging Torque and Reduction Methods 8
1.2.1.7 Torque Ripple 13
1.2.2 Motor Speed 14
1.2.2.1 Continuous Speed 15
1.2.2.2 Peak Speed 15
1.2.2.3 Speed Ripple 15
1.2.3 Torque Density 15
1.2.4 Motor Power and Power Factor 16
1.2.5 Torque–Speed Characteristics 17
1.2.6 Mechanical Resonance and Resonant Frequency 20
1.2.7 Load-to-Motor Inertia Ratio 25
1.2.8 Duty Cycle 26
1.2.9 Motor Efficiency 29
1.2.9.1 Definition of Motor Efficiency 29
1.2.9.2 IEC Standards on Efficiency Classes of AC Electric Motors 30
1.2.10 Motor Insulation 31
1.2.11 Motor Operation Reliability 36
1.3 Classifications of Electric Motors 36
1.3.1 DC and AC Motors 38
1.3.2 Single-Phase and Three-Phase Motors 39
1.3.3 Induction and Permanent Magnet Motors 40
1.3.4 Synchronous and Asynchronous Motors 44
1.3.5 Servo and Stepper Motors 45
1.3.6 Gear Drive and Direct Drive Motors 49
1.3.7 Brush and Brushless Motors 53
1.3.8 Reluctance Motors 54
1.3.9 Radial-Flux and Axial-Flux Motors 55
1.3.10 Rotary and Linear Motors 56
1.3.11 Open and Enclosed Motors 57
1.3.12 Motor Classification according to Power Rating 57

1.4 Motor Design and Operation Parameters 58
1.4.1 Back EMF Constant, K_e 58
1.4.2 Torque Constant, K_t 59
1.4.3 Velocity Constant, K_v 60
1.4.4 Motor Constant, K_m 60
1.4.5 Mechanical Time Constant, τ_m 61
1.4.6 Electrical Time Constant, τ_e 63
1.4.7 Thermal Time Constant, τ_{th} 64
1.4.8 Viscous Damping, K_{vd} 65
1.5 Sizing Equations 66
1.6 Motor Design Process and Considerations 67
1.6.1 Design Process 68
1.6.2 Design Integration 73
1.6.3 Mechatronics 74
1.7 Motor Failure Modes 74
1.8 IP Code 76
References 78

2. Rotor Design 83
2.1 Rotor in Induction Motor 83
2.1.1 Wound Rotor 83
2.1.2 Squirrel Cage Rotor 85
2.1.2.1 Factors Impacting Resistance of Squirrel Cage Rotor 86
2.1.2.2 Double-Cage Rotor 87
2.1.2.3 Casting Squirrel Cage Rotor 88
2.1.2.4 Skin Effect 91
2.1.3 Induction Motor Design Types and Their Performing Characteristics 91
2.2 Permanent Magnet Rotor 92
2.2.1 Discovery of Phenomenon of Magnetism 92
2.2.2 Permanent Magnet Characteristics 93
2.2.3 Permanent Magnet Materials 95
2.2.3.1 Ferrite Permanent Magnets 96
2.2.3.2 Rare-Earth Permanent Magnets 96
2.2.3.3 New Developments of Permanent Magnets 97
2.2.4 Magnetization 98
2.2.5 Factors Causing Demagnetization 99
2.2.6 Maximum Operation Temperature 102
2.2.7 Permanent Magnet Mounting and Retention Methods 102
2.2.8 Corrosion Protection of Permanent Magnets 107
2.3 Rotor Manufacturing Process 109
2.3.1 Lamination Materials 109
2.3.2 Lamination Cutting 111
2.3.3 Lamination Surface Insulation 112
2.3.4 Lamination Annealing 113
2.3.5 Lamination Stacking 113
2.3.6 Rotor Casting for Squirrel Cage Motor 113
2.3.7 Heat Treatment of Casted Rotor 114
2.3.8 Rotor Assembly 115

2.3.9 Rotor Machining and Runout Measurement 115
2.3.10 Rotor Balancing 115
2.3.10.1 Types of Unbalance 118
2.3.10.2 Rotor Balancing Machine 120
2.3.10.3 Balancing Operation 121
2.4 Interference Fit 122
2.4.1 Press Fit 124
2.4.2 Shrink Fit 128
2.4.3 Serration Fit 131
2.4.4 Fitting with Adjustable Ringfeder® Locking Devices 132
2.4.5 Fitting with Tolerance Rings 132
2.5 Stress Analysis of Rotor 135
2.6 Rotordynamic Analysis 137
2.6.1 Rotor Inertia 137
2.6.2 Motor Critical Speed and Resonance 139
2.7 Rotor Burst Containment Analysis 143
2.7.1 Rotor Burst Speed 143
2.7.2 Energy in Rotating Rotor 145
2.7.2.1 Kinetic Energy in Rotor 145
2.7.2.2 Elastic Potential Energy in Rotor 146
2.7.2.3 Ratio of Potential Energy to Kinetic Energy of Rotor 147
2.7.3 Rotor Burst Containment Design 147
References 150

3. Shaft Design 155
3.1 Shaft Materials 155
3.2 Shaft Loads 159
3.3 Shaft Design Methods 160
3.3.1 Macaulay's Method 160
3.3.2 Area–Moment Method 161
3.3.3 Castigliano's Method 162
3.3.4 Graphical Method 163
3.4 Engineering Calculations 163
3.4.1 Normal Stress for Shaft Subjected to Axial Force 164
3.4.2 Bending Stress for Shaft Subjected to Bending Moment 165
3.4.3 Torsional Shear Stress and Torsional Deflection 168
3.4.4 Lateral Deflection of Shaft 172
3.4.4.1 Lateral Deflection due to Bending Moment 173
3.4.4.2 Lateral Deflection due to Transverse Force 174
3.4.4.3 Lateral Deflection due to Shear Force 176
3.5 Shaft Design Issues 176
3.5.1 Shaft Design Considerations 176
3.5.2 Shaft Rigidity 178
3.5.3 Critical Shaft Speed 178
3.5.3.1 Shaft with Uniform Diameter 179
3.5.3.2 Stepped Shaft 179
3.5.4 Dimensional Tolerance 179
3.5.5 Dynamic Shaft Runout 180
3.5.6 Shaft Eccentricity 180

3.5.7 Heat Treatment and Shaft Hardness 180
3.5.8 Shaft Surface Finishing 182
3.5.9 Shaft Lead 184
3.5.10 Shaft Seal 186
3.5.10.1 O-Ring Seal 186
3.5.10.2 Universal Lip Seal 188
3.5.10.3 V-Shaped Spring Seal 189
3.5.10.4 Brush Seal 189
3.5.10.5 PTFE Seal 191
3.5.10.6 Noncontact Seal 191
3.5.11 Diametrical Fit Types 193
3.6 Stress Concentration 193
3.7 Torque Transmission through Mechanical Joints 194
3.7.1 Keyed Shafts 194
3.7.1.1 Selection of Key Material 194
3.7.1.2 Stress Analysis of Key and Keyseat 195
3.7.1.3 Key Fitting 198
3.7.1.4 Stress Concentration Factors of Keyed Shafts 199
3.7.2 Spline Shafts 200
3.7.2.1 Advantages of Spline Shafts 201
3.7.2.2 Spline Types 202
3.7.2.3 Stress Concentration Factors of Spline Shafts 203
3.7.3 Tapered Shafts 203
3.8 Fatigue Failure under Alternative Loading 205
3.9 Shaft Manufacturing Methods 206
3.9.1 Machined Shaft 206
3.9.2 Forged Shaft 207
3.9.3 Welded Hollow Shaft 207
3.9.4 Shaft Measurement 210
3.10 Shaft Misalignment between Motor and Driven Machine 210
3.10.1 Types of Misalignment 211
3.10.2 Correction of Shaft Misalignment 212
3.11 Shaft Coupling 213
3.11.1 Rigid and Semirigid Couplings 213
3.11.2 Flexible Couplings 216
References 216

4. Stator Design 219
4.1 Stator Lamination 219
4.1.1 State Lamination Material 219
4.1.2 Stator Lamination Patterns 219
4.1.2.1 One-Piece Lamination 219
4.1.2.2 T-Shaped Segmented Lamination 220
4.1.2.3 Connected Segmented Lamination 224
4.1.2.4 Two-Section Stator Lamination 224
4.1.2.5 Stator Lamination Integrated by Individual Teeth and a Yoke Section 225
4.1.2.6 Slotless Stator Core 226
4.1.2.7 Slinky Lamination Stator Core 227

4.2 Magnet Wire 230
4.2.1 Regular Magnet Wire 230
4.2.2 Self-Adhesive Magnet Wire 230
4.2.3 Litz Wire 231
4.3 Stator Insulation 232
4.3.1 Injection Molded Plastic Insulation 233
4.3.2 Slot Liner 233
4.3.3 Glass Fiber–Reinforced Mica Tape 234
4.3.4 Powder Coating on Stator Core 235
4.4 Manufacturing Process of a Stator Core 236
4.4.1 Stator Lamination Cutting 237
4.4.2 Lamination Fabrication Process 238
4.4.3 Lamination Annealing 239
4.4.4 Lamination Stacking 240
4.4.5 Stator Winding 242
4.4.5.1 Random Winding by Hand 243
4.4.5.2 Coil Formation: Distributed Winding 243
4.4.5.3 Coil Formation: Concentrated Winding 243
4.4.5.4 Coil Formation: Conductor Bar 243
4.5 Stator Encapsulation and Impregnation 245
4.5.1 Encapsulation 245
4.5.1.1 Encapsulation Materials 245
4.5.1.2 Encapsulation Process 248
4.5.2 Varnish Dipping 249
4.5.3 Trickle Impregnation 250
4.5.4 Vacuum Pressure Impregnation 250
4.6 Stator Design Considerations 253
4.6.1 Cogging Torque 253
4.6.2 Air Gap 253
4.6.3 Stator Cooling 254
4.6.4 Robust Design of Stator 254
4.7 Mechanical Stress of Stator 254
References 256

5. Motor Frame Design 259
5.1 Types of Motor Housing 259
5.1.1 Wrapped Housing 259
5.1.2 Casted Housing 260
5.1.2.1 Casting Materials 261
5.1.2.2 Casting Process 264
5.1.2.3 Pressure Casting 268
5.1.2.4 Heat Treatment 268
5.1.3 Machined Housing 269
5.1.4 Stamped Housing 269
5.1.5 Extruded Aluminum Motor Housing 269
5.1.6 Motor Housing with Composite Materials 270
5.1.7 Motor Housing Fabricated by 3D Printing Technology 270
5.1.8 Frameless Motor 271
5.2 Testing Methods of Casted Motor Housing 273

5.3 Endbell Manufacturing 276
5.3.1 Casted Endbell 277
5.3.2 Stamped Endbell 277
5.3.3 Iron Casting versus Aluminum Casting 278
5.3.4 Machined Endbell 279
5.3.5 Forged Endbell 279
5.4 Motor Assembly Methods 279
5.4.1 Tie Bar 279
5.4.2 Tapping at Housing End Surface 279
5.4.3 Forged Z-Shaped Fastener 280
5.4.4 Rotary Fasteners 282
5.4.4.1 Triangle-Base Rotating Fastener 283
5.4.4.2 Square-Base Rotating Fastener 285
5.4.4.3 Butterfly-Base Rotating Fastener 286
5.4.5 Other Types of Fasteners 286
5.4.5.1 Cylinder-Base Fastener Locked with Retaining Ring 287
5.4.5.2 Cylinder-Base Fastener with Self-Locking Aperture 287
5.4.5.3 Fastener Engaged with Housing from Housing Interior 289
5.5 Fastening System Design 290
5.5.1 Types of Thread Fasteners 290
5.5.2 Thread Formation 290
5.5.3 Fastener Preload 290
5.5.4 Fastener-Tightening Process 291
5.5.5 Tightening Torque 294
5.5.6 Thread Engagement and Load Distribution 297
5.6 Anticorrosion of Electric Motor and Components 298
5.6.1 Surface Treatment Methods 298
5.6.1.1 Electroplating 299
5.6.1.2 Electroless Plating 299
5.6.1.3 Physical Vapor Deposition 299
5.6.1.4 Inorganic Coating 300
5.6.1.5 Phosphate Coating 300
5.6.1.6 Electropolishing 300
5.6.2 Anticorrosion Treatment of Electric Motor 301
5.6.3 Hydrogen Embrittlement Issues 302
References 305

6. Motor Bearing 309
6.1 Bearing Classification 309
6.1.1 Journal Bearing 309
6.1.2 Rolling Bearing 313
6.1.2.1 Ball Bearing 313
6.1.2.2 Roller Bearing 319
6.1.3 Noncontact Bearing 320
6.1.4 Sensor Bearing 322
6.2 Bearing Design 323
6.2.1 Bearing Materials 323

6.2.2 Bearing Internal Clearances 324
6.2.3 Allowable Bearing Speed 328
6.2.4 Bearing Fitness 328
6.2.5 Prevention of Bearing Axial Movement 329
6.2.6 Bearing Load 331
6.2.6.1 Bearing Preload Arrangement 331
6.2.6.2 Radial and Axial Bearing Load 332
6.2.6.3 Load Distribution 332
6.3 Bearing Fatigue Life 335
6.3.1 Calculation of Bearing Fatigue Life 335
6.3.2 Bearing Failure Probability Distribution 336
6.3.3 Influence of Unbalance on Bearing Fatigue Life 338
6.3.4 Influence of Wear on Bearing Fatigue Life 341
6.3.5 Influence of Internal Radial Clearance on Bearing Fatigue Life 341
6.4 Bearing Failure Mode 343
6.4.1 Major Causes of Premature Bearing Failure 344
6.4.2 Lubricant Selection 344
6.4.3 Improper Bearing Lubrication 347
6.4.4 Lubricant Contamination 347
6.4.5 Grease Leakage 348
6.4.6 Bearing Sealing 349
6.4.7 Excessive Load 350
6.4.8 Internal Radial Interference Condition 351
6.4.9 Bearing Current 354
6.4.10 Impact of High Temperature on Bearing Failure 355
6.4.11 Bearing Failure Associated with Motor Vibration and Overloading 356
6.4.12 Improper Bearing Installation and Bearing Misalignment 357
6.4.13 Vertically Mounted Motor 358
6.5 Bearing Noise 359
6.6 Bearing Selection 360
6.6.1 Bearing Type Selection Based on Load 362
6.6.2 Bearing Type Selection Based on Speed 363
6.6.3 Selection of Bearing Size 363
6.7 Bearing Performance Improvement 364
References 365

7. Motor Power Losses 369
7.1 Power Losses in Windings due to Electric Resistance in Copper Wires 370
7.2 Eddy-Current and Magnetic Hysteresis Losses 373
7.2.1 Eddy-Current Loss 373
7.2.2 Magnetic Hysteresis Loss 374
7.2.3 Calculations of Eddy-Current and Magnetic Hysteresis Losses 374
7.2.4 Losses in Stator and Rotor Iron Cores 378
7.2.5 Losses in PMs 379
7.2.6 Power Losses in Other Core Components 381
7.3 Mechanical Friction Losses 381
7.3.1 Bearing Losses 381

7.3.2 Sealing Losses 385
7.3.3 Brush Losses 385
7.4 Windage Losses 386
7.4.1 Windage Loss due to Rotating Rotor 388
7.4.1.1 Taylor Vortex 388
7.4.1.2 Friction Factor 391
7.4.1.3 Prediction of Windage Loss due to Rotating Rotor 392
7.4.2 Windage Loss due to Entrance Effect of Axial Air-Gap Flow 393
7.4.3 Windage Loss due to Stator Surface Roughness 393
7.4.4 Fan Losses 395
7.4.5 Ventilating Path Losses 399
7.4.6 Methods for Reducing Windage Losses 399
7.5 Stray Load Losses 404
References 405

8. Motor Cooling 409
8.1 Introduction 409
8.1.1 Passive and Active Cooling Techniques 410
8.1.2 Heat Transfer Enhancement Techniques 411
8.2 Conductive Heat Transfer Techniques 412
8.2.1 Conductive Heat Flux and Energy Equations 412
8.2.2 Encapsulation and Impregnation of Electric Motor 414
8.2.3 Enhanced Heat Transfer Using High-Thermal-Conductivity Material 415
8.2.4 Using Self-Adhesive Magnet Wire for Fabricating Stator Winding 417
8.3 Natural Convection Cooling with Fins 417
8.3.1 Cooling Fin 418
8.3.2 Fin Optimization 418
8.3.3 Applications of Various Fins in Motor Cooling 421
8.3.4 Pin-Fin Heat Sink 425
8.3.5 Thermal Interface Materials 429
8.4 Forced Air Cooling Techniques 432
8.4.1 Thermophysical Properties of Air 432
8.4.2 Direct Forced Air Cooling Techniques 433
8.4.2.1 Forced Air Cooling at End-Winding Regions 434
8.4.2.2 Forced Air Flowing through Internal Cooling Channels across the Motor 434
8.4.2.3 Forced Air Flowing over Motor Outer Surfaces 438
8.4.2.4 Forced Air Flowing through Both Motor Outer and Inner Surfaces 439
8.4.2.5 Air Jet Impingement Cooling 440
8.4.3 Indirect Forced Air Cooling Techniques 441
8.4.3.1 Indirect Forced Air Cooling with Heat Exchangers 442
8.4.3.2 Indirect Forced Air Cooling via Indirect Evaporative Air Cooler 443
8.4.4 Fan and Blower 444
8.4.4.1 Fan Types 444
8.4.4.2 Forward-Curved, Backward-Curved, and Straight Blades of Centrifugal Fans 446

8.4.4.3 Fan Performance Curve and Operation Point 447
8.4.4.4 Fan Selection 448
8.5 Liquid Cooling Techniques 448
8.5.1 Thermophysical Properties of Coolants 449
8.5.2 Direct Liquid Cooling Techniques 450
8.5.2.1 Direct Liquid Cooling of Bundled Magnet Wires 451
8.5.2.2 Spray Cooling 452
8.5.2.3 Liquid Jet Impingement Cooling 456
8.5.3 Liquid Immersion Cooling 457
8.5.4 Indirect Liquid Cooling Techniques 458
8.5.4.1 Indirect Liquid Cooling via Cold Plates Attached to Motor Walls 458
8.5.4.2 Indirect Liquid Cooling via Helical Copper Pipes Casted in Motor Housing 458
8.5.4.3 Indirect Liquid Cooling with Cooling Channels on Casted Motor Housing 462
8.5.4.4 Indirect Liquid Cooling via Copper Pipe in Spacer 462
8.5.4.5 Indirect Liquid Cooling through Stator Winding Slots 463
8.5.4.6 Indirect Liquid Cooling through Microscale Channels 463
8.6 Phase-Change Cooling Techniques 465
8.6.1 Cooling with Heat Pipes 465
8.6.2 Cooling with Vapor Chambers 467
8.6.3 Evaporative Cooling 468
8.6.4 Mist Cooling 471
8.7 Radiative Heat Transfer 471
8.8 Other Advanced State-of-the-Art Cooling Methods 472
8.8.1 Microchannel Cooling Systems 472
8.8.2 Metal Foams 473
8.8.3 Heat Transfer Enhancement with Nanotechnology 474
8.8.3.1 Nanofluid 475
8.8.3.2 Carbon Nanotube 475
8.8.3.3 NanoSpreader™ Vapor Cooler 475
8.8.3.4 CarbAl™ Heat Transfer Material 476
8.8.3.5 Ionic Wind Generator 477
References 477

9. Motor Vibration and Acoustic Noise 481
9.1 Vibration and Noise in Electric Motor 481
9.2 Fundamentals of Vibration 483
9.2.1 Simple Harmonic Oscillating System 483
9.2.2 Damped Harmonic Oscillating System 485
9.2.3 Forced Vibration with Damping 487
9.2.4 Forced Vibration due to Mass Unbalance 492
9.2.5 Vibration Induced by Support Excitation 495
9.2.6 Directional Vibration 497
9.3 Electromagnetic Vibrations 498
9.3.1 Unbalanced Forces/Torques Caused by Electric Supply 498
9.3.2 Broken Rotor Bar and Cracked End Ring 499
9.3.3 Unbalanced Magnetic Pull due to Asymmetric Air Gap 500

9.3.3.1 Electromagnetic Force at Air Gap 500
9.3.3.2 Asymmetric Air Gap due to Nonconcentric Rotor and Stator 502
9.3.3.3 Asymmetric Air Gap due to Elliptic Stator 504
9.3.3.4 Asymmetric Air Gap due to Elliptic Rotor 505
9.3.3.5 Asymmetric Air Gap due to Rotor Misalignment 508
9.3.3.6 Asymmetric Air Gap Resulting from Shaft Deflection 508
9.3.4 Nonuniform Air Gap due to Stator Slots 508
9.3.5 Mutual Action Forces between Currents of Stator and Rotor 509
9.3.6 Vibration due to Unbalanced Voltage Operation 510
9.4 Mechanical Vibrations 510
9.4.1 Misaligned Shaft and Distorted Coupling 510
9.4.2 Defective Bearing 510
9.4.3 Self-Excited Vibration 511
9.4.4 Torsional Vibration 511
9.5 Vibration Measurements 512
9.6 Vibration Control 514
9.6.1 Damping Materials 514
9.6.2 Vibration Isolation 515
9.6.3 Tuned Mass Damper 518
9.6.4 Double Mounting Isolation System 521
9.6.5 Viscoelastic Bearing Support 522
9.6.6 Active Vibration Isolation and Damping 522
9.6.7 Measurements of Motor Vibration 525
9.7 Fundamentals of Acoustic Noise 526
9.7.1 Tonal Noise and Broadband Noise 527
9.7.2 Sound Pressure Level and Sound Power Level 527
9.7.3 Octave Frequency Bands 528
9.7.4 Three Sound Weighting Scales 530
9.7.5 Averaged Sound Pressure Level 531
9.7.6 Types of Noise 531
9.7.6.1 Structure-Borne Noise 532
9.7.6.2 Airborne Noise 532
9.7.6.3 Aerodynamic Noise 532
9.8 Noise Types and Measurements for Rotating Electric Machines 532
9.8.1 Noise Types in Rotating Electric Machines 533
9.8.1.1 Mechanical Noise 533
9.8.1.2 Electromagnetic Noise 534
9.8.1.3 Aerodynamic Noise 535
9.8.2 Acoustic Anechoic Chamber 535
9.8.3 Measurement of Motor Noise 536
9.8.4 Acoustic Noise Field Measurement 537
9.9 Motor Noise Abatement Techniques 537
9.9.1 Active Noise Reduction Techniques 538
9.9.2 Passive Noise Reduction Techniques 539
9.9.2.1 Blocking Noise Propagation Paths and Isolating Noise Sources 539
9.9.2.2 Using Noise-Absorbing Materials 540
9.9.2.3 Motor Suspension Mounting 543

9.9.2.4 Noise-Attenuating Structure 543
9.9.2.5 Smoothing Ventilation Paths 546
9.9.2.6 Selecting Low Noise Bearings 547
9.9.3 Innovative Noise Abatement Methods 548
References 548

10. Motor Testing 553
10.1 Motor Testing Standards 553
10.2 Testing Equipment and Measuring Instruments 554
10.2.1 Dynamometer 554
10.2.2 Thermocouples and Other Temperature Measuring Devices 559
10.2.3 Control System 560
10.2.4 Data Acquisition System 561
10.2.5 Torque Transducer 561
10.2.6 Power Supply 562
10.2.7 Motor Testbed 562
10.3 Testing Load Level 563
10.4 Testing Methods 564
10.4.1 Mechanical Differential Testing Method 564
10.4.2 Back-to-Back Testing Method 564
10.4.3 Indirect Loading Testing Method 564
10.4.4 Forward Short-Circuit Testing Method 567
10.4.5 Variable Inertia Testing Method 568
10.5 Off-Line Motor Testing 569
10.5.1 Winding Electrical Resistance Testing 570
10.5.2 Megohm Testing 570
10.5.3 Polarization Index Testing 571
10.5.4 High-Potential Testing 572
10.5.5 Surge Testing 572
10.5.6 Step-Voltage Testing 573
10.5.7 Determination of Rotor's Moment of Inertia 573
10.6 Online Motor Testing 576
10.6.1 Locked Rotor Testing 576
10.6.2 Motor Heat Run Testing 577
10.6.3 Motor Efficiency Testing 578
10.6.4 Impulse Testing 580
10.6.5 Cogging Torque Testing 580
10.6.6 Torque Ripple Measurement 583
References 585

11. Modeling, Simulation, and Analysis of Electric Motors 589
11.1 Computational Fluid Dynamics and Numerical Heat Transfer 589
11.1.1 Strategies in Modeling and Performing CFD Analysis 590
11.1.2 Rotating Flow Modeling 590
11.1.3 Porous Media Modeling 592
11.1.4 Numerical Simulation of Motor Cooling 595
11.1.4.1 Mathematical Formulations 596
11.1.4.2 Numerical Method 599
11.1.4.3 CFD Results 601

11.2 Thermal Simulation with Lumped-Circuit Modeling 607
11.3 Thermal Analysis Using Finite Element Method 610
11.4 Rotordynamic Analysis 614
11.4.1 Problem Description 614
11.4.2 Bearing Support's Stiffness and Damping 615
11.4.3 Rotordynamic Modeling 617
11.4.4 Results of Rotordynamic Analysis 618
11.5 Static and Dynamic Stress/Strain Analysis 621
11.5.1 Static Analysis 622
11.5.2 Dynamic Analysis 623
11.5.2.1 Centrifugal Force–Induced Stress on PMs 623
11.5.2.2 Structural Analysis Using Finite Element Method 625
11.5.3 Shock Load 626
11.6 Fatigue Analysis 627
11.7 Torsional Resonance Analysis 627
11.8 Motor Noise Prediction 629
11.9 Buckling Analysis 630
11.10 Thermally Induced Stress Analysis 632
11.11 Thermal Expansion and Contraction Analysis 632
References 635

12. Innovative and Advanced Motor Design 637
12.1 High-Temperature Superconducting Motor 637
12.2 Radial-Flux Multirotor or Multistator Motor 640
12.2.1 Radial-Flux Multirotor Motor 640
12.2.2 Radial-Flux Multistator Motor 642
12.2.3 Radial-Flux Brushless Double-Rotor Machine 643
12.2.4 Radial-Flux Double-Stator PM Machine 645
12.3 Axial-Flux Multirotor or Multistator Motor 646
12.3.1 Single-Sided and Double-Sided Axial-Flux Motors 646
12.3.2 Multistage Axial-Flux Motor 649
12.3.3 Yokeless and Segmented Armature Motors 650
12.4 Hybrid Motor 651
12.4.1 Hybrid Excitation Synchronous Machine 651
12.4.2 Hybrid Hysteresis PM Synchronous Motor 651
12.4.3 Hybrid Motor Integrating Radial-Flux Motor and Axial-Flux Motor 652
12.4.4 Hybrid-Field Flux-Controllable PM Motor 654
12.4.5 Hybrid Linear Motor 654
12.5 Conical Rotor Motor 655
12.6 Transverse Flux Motor 656
12.7 Reconfigurable Permanent Magnet Motor 660
12.8 Variable Reluctance Motor 661
12.9 Permanent Magnet Memory Motor 664
12.9.1 Variable Flux PM Memory Motor 664
12.9.2 Pole-Changing PM Memory Motor 664
12.9.3 Doubly Salient Memory Motor 665
12.10 Adjustable and Controllable Axial Rotor/Stator Alignment Motor 667
12.11 Piezoelectric Motor 669

12.12 Advanced Electric Machines for Renewable Energy 671
12.13 Micromotor and Nanomotor 672
12.13.1 Micromotor 672
12.13.2 Nanomotor 675
References 676

Index 679

Preface

Electric motors are extensively used in industrial, commercial, and military applications such as automobiles, elevators, electronic devices, robots, appliances, medical equipment, energy-conversion systems, machine tools, aircraft carriers, and satellites. Along with the rapid growth in energy demand all over the world in recent years, it has become a challenge for the motor industry to design and manufacture high-efficiency, high-reliability, low-cost, and quiet electric motors with superior performance.

Kollmorgen Corporation, a subsidiary of Danaher Corporation, is the global leader in the design, development, manufacture, and service of innovative and reliable products in the motion control industry. As the chief engineer of Kollmorgen, I have long been eagerly awaiting a modern book on the mechanical design of electric motors. However, most available books on electric motors in the market focus primarily on electromagnetic design rather than mechanical design. After a long unsuccessful search, one day I was suddenly struck with a thought: Why not write this book myself? This thought has inspired me to embark on the arduous task of compiling recent developments and advances in the mechanical design of electric motors into one book.

Despite significant advances in the last decades, the design, development, and implementation of modern electric motors still pose challenges for motor engineers and designers. This is because they involve a wide variety of disciplines, such as mechanics, electromagnetics, electronics, fluid and solid dynamics, heat transfer, material science, tribology, acoustics, control theory, manufacturing technology, and engineering economics, to name a few. In order to meet customer-specific requirements, today's motor manufacturers must effectively provide customized premium efficient products and services for accommodating multiple markets.

The ultimate goal of this book is to provide readers an in-depth knowledge base of designs, techniques, and developments of modern electric motors. The text is suitable for engineers, designers, and manufacturers in the motor industry, as well as maintenance personnel, graduate and undergraduate students, and academic researchers. This book has addressed in detail many aspects of motor design and performing characteristics, including motor classification, design of motor components, material selections, power losses, cooling, design integration, vibration, and acoustic noise. It also covers motor modeling, simulation, and engineering analysis. To reflect state-of-the-art electric motors, innovative and advanced motors developed in recent decades are reviewed in the book.

The book consists of a total of 12 chapters that cover electric motor fundamentals, practical design, engineering analysis, model setup, material and bearing selection, manufacturing processes, testing methods, and other design issues/practical considerations of electric motors. Chapter 1 presents the overview of the basic knowledge and fundamental principles of electric motors. Attempts have been made to introduce to readers motor operating characteristics, design parameters, manufacturing processes, and design methodologies.

Chapters 2 through 5 sequentially address design details of the most important components or subsystems of electric motors, including rotor, shaft, stator, and motor frame. In each of these chapters, design and manufacturing activities are addressed in detail to

cover material selection, manufacturing process, assembly method, engineering analysis, etc. The potential applications of some newly developed manufacturing technologies on electric motors are also discussed.

Statistical data have revealed that the majority of electric motor failures are attributed to premature bearing failures. Thus, it is critical to understand bearing operating characteristics, determine bearing failure modes, identify bearing failure root causes, and evaluate the effects of some factors (e.g., temperature, lubrication condition, contamination, bearing current, excessive loading, misalignment, etc.) on bearing life. All these are addressed in Chapter 6.

When a motor operates under load conditions, a certain portion of the input power does not convert into the mechanical power to do useful work. Most of the wasted energy is converted into heat, which must be effectively dissipated into the environment. This results in a decrease in motor efficiency. As a matter of fact, motor efficiency varies widely with the technology used. In order to improve motor efficiency, it is highly desirable to minimize these power losses. The analysis and calculation of each type of power loss are discussed in Chapter 7.

Motor cooling plays a major role in ensuring optimum performance, operating reliability, and cost-effectiveness of electric motors. The adoption of high-efficiency cooling techniques can significantly increase in the power density and overall motor efficiency. A variety of cooling techniques, including air cooling, liquid cooling, mist cooling, and phase change cooling, are reviewed in Chapter 8. The selection of cooling techniques depends on many factors, such as cooling load, cooling effectiveness, thermophysical properties of coolant, complexity of cooling system, type of motor application, and others. State-of-the-art cooling techniques that have been successfully used in electronics cooling are also reviewed, and these have been suggested for application in motor cooling.

Chapter 9 describes vibration and noise issues of electric motors. Motor vibration can not only cause high noise and high fatigue stress of motor, but also deteriorate the performance of motor and, in the worst-case scenario, lead to premature motor failure. High acoustic noise is prohibited by many legislative regulations. For some special motor applications, acoustic sound pressure levels are restricted by law.

Computer technology has become a key component in motor development and design processes over recent decades. Computer-aided design (CAD), computer-aided manufacturing (CAM), and computer-aided engineering (CAE) techniques today are widespread in their application to motor design. However, no matter how perfect the engineering design and how precise the theoretical calculations, motor testing is a necessary step to validate the conceptual design, ensure normal and safe operation of the motor, and further optimize the motor design. Chapter 10 presents the motor testing methods and procedures for both component and system levels. The important testing equipment is also addressed.

A variety of engineering modeling, simulation, and analysis that are frequently encountered during motor design processes are addressed in Chapter 11. The successful integration of the engineering analysis into the product design cycle can significantly enhance the design quality, improve design standards, and accelerate the design process. In this chapter, some important engineering analyses are discussed in detail, including CFD analysis, rotordynamic analysis, and stress/strain analysis.

With the rapid strides made in computer technology, material science, manufacturing process, control technology, and other fields, the motor industry has developed immensely in recent years. In fact, sustainable growth of the motor industry requires innovation. In the age of globalization, motor manufacturers tend to aim at high-efficiency, high-precision,

durable, and energy-saving products. Chapter 12 reviews and discusses some innovative and advanced motors.

Electric motors and generators are commonly referred to as electric machines. While electric motors convert electrical energy to mechanical energy, electric generators convert mechanical energy into electrical energy. Due to the similarities between electric motors and generators in many aspects such as mechanical construction, electromagnetic operating principles, power losses, cooling methods, etc., some contents in this book can also be applied in generator design and serve as a reference for generator design engineers. Similarly, a few generator design practices covered in this book can also benefit motor design engineers.

"The details determine success or failure"—this is true not only for industrial production but also for many aspects of human society. As a consequence, engineers and designers should pay special attention to details in designing and manufacturing electric motors.

I am greatly indebted to the excellent reviewers of this book. Their valuable and pertinent comments have greatly enhanced the quality of the book. The experts who have kindly read different parts of this book include the following:

Jeff Farrenkopf	Kollmorgen Corporation, USA
John Keesee	Kollmorgen Corporation, USA
Lih-Wu Hourng	Department of Mechanical Engineering, National Central University, Taiwan, Republic of China
Chen Fang	Heavy Oil Recovery Research Program, Exxon Mobil Corporation, USA
Igor V. Shevchuk	MBtech Group GmbH & Co. KGaA, Germany
Shanshan Conway	Remy International Inc., USA
Kamlesh Suthar	Argonne National Laboratory, USA
Shijun Ma	School of Mechanical Engineering, Southwest Jiaotong University, China
Zhangqing Zhuo	Power & Water Group, General Electric Company, USA

I wish to acknowledge my colleagues at Kollmorgen Corporation for their constructive discussions, suggestions, and comments during the preparation of the book, including, but not limited to, John Boyland, Jeff Farrenkopf, John Keesee, Todd Brewster, David Coulson, Lee Stephens, Gary Hodge, Jerry Brown, Mark Fields, Brad Trago, Denny Hu, Steve VanAken, James Davison, Tony Nozzi, Ron Bishop, David Guy, Stephen Funk, Brad Monday, Tommy Bunch, Ethan Filip, Amber Hollins, Kevin Garrison, and many others. It has been a great pleasure and honor working with them.

From November 2010 to May 2013, I was sent to Shanghai, China, for building up an engineering team. I wish to acknowledge all the engineers in the team for offering me some useful information. While providing training to these engineers, I have also learned a lot from them.

I am especially grateful to Jonathan Plant, Jennifer Ahringer, and Jennifer Stair of CRC Press for their valuable advice and guidance. Vijay Bose as the project manager at SPi Global has done an excellent job in editing and proofreading the manuscript with splendid efficiency.

I deeply miss my parents. Their imperceptible influence in my growing years helped me set my own life goals. At the most difficult time of my life (during a special historical period), they encouraged me to look forward and keep my faith and hope for the future. My biggest regret is that they cannot see this published book.

Finally, I wish to express my sincere gratitude to my lovely wife, Zhangqing Zhuo, and daughter, Winnie Tong, for their love and patience. Without their continuous support and encouragement, this book could have only been published in my dreams.

I welcome and greatly appreciate feedback, corrections, and suggestions from the readers for improving the technical contents. The readers can directly contact me via e-mail at motor.mechanical.design@gmail.com.

Wei Tong
Radford, Virginia

Author

Dr. Wei Tong's career started as a mechanical technician in the early of 1970s. He currently serves as Chief Engineer at Kollmorgen Corporation, a subsidiary of Danaher Corporation, and is responsible for the development, design, analysis, and implementation of electric motors. He has made significant contributions in developing innovations in motor cooling, structure, and manufacturing.

Prior to joining Kollmorgen, Dr. Tong worked at GE Energy at Schenectady, New York, where he conducted designs of high-efficiency, high-powered generators and steam turbines. He was the project leader of a number of design and R&D projects, such as the advanced cooling system, hydrogen sealing system, noise attenuation system, dynamic thrust control system, steam turbine axial clearance design, and thermodynamic operation design. All these projects had been led to great technical and commercial success. Prior to GE, he worked at Babcock & Wilcox carrying out design and analysis for the superconducting magnetic energy storage system, solar-powered satellite, and medical isotope production reactor.

Dr. Tong received his PhD from the University of Minnesota in 1989 and MBA from State University of New York at Albany in 1999. He has served as an Associate Editor of the *ASME Journal of Heat Transfer* for two terms (2009–2012 and 2012–2015) and of the *International Journal of Rotating Machinery* (2008–).

Dr. Tong currently holds 28 US patents and 16 foreign patents. He has been a licensed Professional Engineer in Virginia since 1996. He is an internationally recognized expert on mechanical–electrical–thermal systems.

As a fellow (2006–) of the American Society of Mechanical Engineering (ASME), Dr. Tong has served on several ASME committees, including Heat Transfer under Extreme Conditions (K-18), Heat Transfer in Energy Systems (K-6), Aerospace Heat Transfer (K-12), and Long Range Directions and Issues in Heat Transfer (K-2). He was the chair of the K-18 Committee during 2006–2009.

In 2006, Dr. Tong was appointed as an adjunct professor in the Department of Mechanical Engineering, Virginia Polytechnic Institute and State University, where he taught an undergraduate course on mechanical engineering design.

List of Symbols

A	area, m^2
a	acceleration, m/s^2
B	magnetic flux density, T (Tesla)
C_e	electric time constant, s
C_m	mechanical time constant, s
c	viscous damping coefficient, Ns/m
c	sound speed, m/s (Chapter 9)
c_p	specific heat, J/(kg-K) or J/(kg-°C)
D	outer diameter, m (Chapter 1)
d	diameter, m
d_e	effective diameter, m
E	modulus of elasticity or Young's modulus, Pa, MPa or GPa
E	energy, J (Chapters 2 and 9)
E_k	kinetic energy, J
E_p	potential energy, J
E_r	radiative energy, J
E_t	total energy, J
e	mass eccentricity, m
e	emissivity (Chapter 8)
e	specific internal energy, J/kg (Chapter 11)
F	force, N
F_{bt}	bolt axial tensile force, N
F_m	magnetomotive force, A (Ampere)
F_{mc}	fastener clamping force, N
F_u	unbalanced force resulting from unbalanced mass, N
f	frequency, Hz
f_c	centrifugal force, N
f_d	damping force, N
f_s	shape factor (Chapter 3)
f_R	resonant frequency, Hz
f_{tr}	torsional resonant frequency, Hz
G	shear modulus of elasticity, Pa, MPa or GPa
g	acceleration due to gravity, m/s^2
H	magnetic field strength, A/m (ampere per meter)
h	heat transfer coefficient, $W/(m^2\text{-K})$
h	specific enthalpy, J/kg (Chapter 11)
I	electric current, A
I	moment of inertia, $kg\text{-}m^2$
I_a	second moment of area, m^4 (Chapter 3)
I_p	peak current, A
I_r	rated current, A
i	electric AC current, A
J	second polar moment of area, m^4
J	current density in conductor, A/m^2 (Chapter 2)

Ja Jakob number
J_c coupling inertia, kg-m^2
J_{gb} gearbox inertia, kg-m^2
J_l load inertia, kg-m^2
J_m motor inertia, kg-m^2
J_o current density at conductor surface, A/m^2 (Chapter 2)
J_p polar moment of inertia, kg-m^2
J_{rl} reflected load inertia, kg-m^2
K tightening factor (Chapter 5)
K_ϕ ratio of electrical loading on rotor and stator
K_a loss coefficient for actual winding, $K_a = 2\Delta p_a / \rho u_a^2$ (Chapter 11)
KE kinetic energy, J
K_e back EMF constant, V/(rad/s) or V/rpm
K_i current waveform factor
K_m motor constant, N m/W$^{1/2}$ (Chapter 1)
K_p loss coefficient for porous media system, $K_p = 2\Delta p_p / \rho u_p^2$ (Chapter 11)
K_p electrical power waveform factor (Chapter 1)
K_t torque constant, N m/A (Chapter 1)
K_t normal stress concentration factor (Chapter 2)
K_{ts} shear stress concentration factor
K_v motor velocity constant, (rad/s)/V or rpm/V
K_{vd} viscous damping, N m/rpm or N m/(rad/s) (Chapter 1)
k stiffness, N/m
k shape parameter (Chapter 6)
k thermal conductivity, W/(m-K) (Chapters 8 and 11)
k spring coefficient, N-s/m (Chapter 9)
k radius of gyration, m (Chapter 11)
k_b bearing support stiffness, N/m
k_{eff} effective thermal conductivity, W/(m-K) (Chapters 11)
k_l linear stiffness, N/m
L inductance, H
L_e effective stack length, m
L_p sound pressure level, dB (Chapter 9)
L_w sound power level, dB (Chapter 9)
l length, m
l_g grid length, m
M bending moment, N m
M_a angular momentum, J · s or N m s
M_r rotor mass, kg
m mass, kg
m number of motor phases (Chapter 1)
m_c correction mass, kg
m_u unbalance mass, kg
$\dot{m}_a$ mass flowrate through actual winding, kg/s
$\dot{m}_p$ mass flowrate through porous media, kg/s
N_{phase} phase number
N_{slot} number of stator slots
n revolutions per minute, rpm
n_c factor of safety

n_s synchronous speed, rpm (Chapter 1)
n_{slot} slot number per pole
P_a apparent power, W
P_b bearing power loss, W
P_b brake power loss, W (Chapter 10)
PE potential energy, J
PF power factor
P_g gearbox power loss, W
P_{in} motor input power, W
P_{out} motor output power, W
P_p preload of fastener, N
P_r rated power of motor, W (Chapter 1)
P_r power loss due to electric resistance, W (Chapter 7)
P_{react} reactive power, W
P_{real} real power, W
P_s stator I^2R loss, W
P_{sc} stator iron core loss, W
P_s sealing power loss, W
P_w windage power loss, W
p pressure, Pa (Chapter 11)
p thread pitch, m (Chapter 5)
p_r number of pole pair per phase
Q_θ directivity factor (Chapter 9)
q'' heat flux, W/m^2
q''' volumetric heat generation, W/m^3
R electric resistance, Ohm
R supporting force of shaft, N (Chapter 3)
R_c room constant, m^2 (Chapter 9)
Re Reynolds number
R_m magnetic flux path, A(Ampere)/Wb(Weber)
R_{th} thermal resistance, °C/W or K/W
r radius, m
r_c radius from the center of correction mass to rotation axis, m
r_u radius from the center of unbalance mass to rotation axis, m
S material strength, Pa or MPa
S_h volumetric heat source, W/m^3
St Stribeck number (Chapter 6)
S_t torsional stiffness, N m/rad (Chapters 2 and 3)
S_{ut} ultimate tensile strength, Pa or kPa
S_y yield tensile strength, Pa or kPa
s slip
T torque, N m
T oscillating period, s (Chapter 9)
T temperature, °C or K (Chapter 8)
T_a ambient temperature, C or K
T_d damping torque, Nm
T_{dyno} dynamometer torque, N m
T_f final temperature, °C or K
T_{hs} hot spot allowance, °C or K

T_o mean motor torque, N m (Chapter 1)
T_p peak torque, N m
$T_p(t)$ periodic motor torque, as a function of time, N m (Chapter 1)
T_r continuous rated torque, N m
T_s stall torque, N m
t service time, s or h (Chapter 6)
t_f lubricant film thickness, m
U total strain energy, J (Chapter 3)
U unbalance, kg-m (Chapter 2)
u velocity, m/s
V voltage, V
v phase velocity of wave, m/s
W_{def} work done by friction of bolt head, J
W_f work done by friction of nut, J
W_t work done by fastener tightening torque, J
W_{th} work done by fastener thread friction, J

Greeks

α angular acceleration, rad/s^2
α half thread angle, radian or degree (Chapter 5)
α temperature coefficient of resistance, 1/°C or 1/K (Chapters 1, 7, and 10)
α thermal diffusivity ($= k/\rho c_p$), m^2/s (Chapter 8)
$\bar{\alpha}$ average sound absorption coefficient (Chapter 9)
β bearing contact angle, radian or degree (Chapter 6)
β coefficient of thermal expansion, 1/K or 1/°C (Chapter 8)
β frequency ratio, $\beta = \omega/\omega_n$ (Chapter 9)
β thread lead angle, radian or degree (Chapter 5)
Δp_a pressure drop through actual winding, Pa
Δp_p pressure drop through porous media, Pa
δ clearance, m (Chapter 2)
δ change in bolt length, m (Chapter 5)
δ interference, m (Chapter 6)
δ logarithmic decrement (Chapter 11)
ε strain, mm/mm or μm/mm (Chapter 11)
ε material elongation (%)
ε_h hoop strain
Φ magnetic flux, Wb (Weber)
φ torsional deflection angle, radian or degree (Chapter 3)
φ dissipation function, Pa-s^{-1} (Chapter 11)
γ shear strain
γ_g gear ratio
η efficiency (%)
η porosity in porous media, $\eta = A_a/A_p$ (Chapter 11)
φ phase angle, radian or degree (Chapters 2 and 9)
λ sound wavelength, m (Chapter 9)

λ coefficient of bulk viscosity (or expansion viscosity), Pa-s or N s/m^2 (Chapter 11)
λ scale parameter (Chapter 6)
μ dynamic viscosity, Pa-s or N s/m^2 (Chapter 11)
μ permeability, m^2 (Chapter 9)
μ_{eff} effective viscosity, Pa-s or N s/m^2
μ_h friction coefficient under bolt head
μ_n friction coefficient under nut
μ_h friction coefficient under bolt head
μ_{th} fastener thread friction coefficient
μ_r relative permeability
ρ density, kg/m^3
ρ electric resistivity, Ω·m (Chapters 7 and 10)
σ stress, N/m^2 or Pa
σ_h hoop stress, N/m^2
σ_{rad} radiation efficiency (Chapter 9)
τ shear stress, N/m^2
τ_e electrical time constant, s
τ_m mechanical time constant, s
τ_{th} thermal time constant, s
ω annular rotating speed, rad/s (Chapter 1)
ω oscillating frequency, Hz (Chapter 9)
ω_{dyno} dynamometer annular speed, rad/s
ω_n natural frequency, Hz
ω_p peak annular rotating speed, rad/s
ω_r rated annular speed, rad/s
ξ load-to-motor inertia ratio
ξ porous media inertial resistance factor, $\xi = K_p/\Delta L$, m^{-1} (Chapter 11)
ζ damping ratio, $\zeta = c/2(mk)^{1/2}$

Abbreviations

AC alternative current
AF axial flux
BDRM brushless double-rotor machine
CAD computer-aided design
CDF cumulative distribution function
CFD computational fluid dynamics
CFM cubic feet per minute
CMM coordinate measuring machine
CNC computer numerical control
CS-PMSM compound-structure permanent magnet synchronous machine
CTE coefficient of thermal expansion
CVD chemical vapor deposition
DC direct current
DDR direct drive rotary
DIR direction of rotation

DSP	digital signal processor
DSPM	doubly salient permanent magnet
DVA	dynamic vibration absorber
EDM	electrical discharge machining
EMF	electromotive force
EPC	evaporative pattern casting
EVS	electric vehicle system
FCPM	flux-controllable permanent magnet
FC-TFM	flux concentrated transverse flux machine
FEA	finite element analysis
FFT	fast Fourier transform
FNM	flow network modeling
FS	factor of safety
FVM	finite volume method
HDD	hard disk drive
HESM	hybrid excitation synchronous machine
HNS	high nitrogen steel
HSM	hysteresis synchronous motor
HTS	high-temperature superconductor
ICE	internal combustion engine
IGBT	insulated gate bipolar transistor
IM	induction motor
IP	international protection rating
IPM	interior permanent magnet
LDV	laser Doppler vibrometer
LHM	linear hybrid motor
LIM	linear induction motor
LPM	lumped parameter model
LSM	linear synchronous motor
MF	magnification factor
MMF	magnetomotive force
MPM	mixing plane model
MRF	multiple reference frame
Nd-Fe-B	neodymium-iron-boron
NEMS	nano-electromechanical system
NSM	negative stiffness mechanism
OEM	original equipment manufacturer
PCB	printed circuit board
PCMM	pole-changing memory motor
PDF	probability density function
PF	power factor
PI	polarization index
PM	permanent magnet
PMHS	permanent magnet hysteresis synchronous
PMM	permanent magnet motor
PMSM	permanent magnet synchronous motor
PMW	pulse width modulation
PVD	physical vapor deposition
RF	radial flux

RMS	root mean square
RNG	renormalization group
RDT	rim-driven thruster
RTD	resistance temperature detector
rpm	revolutions per minute
rps	revolutions per second
Sm-Co	samarium-cobalt
SPL	sound pressure level
SPM	surface-mounted permanent magnet
SPM-TFM	surface permanent magnet transverse flux machine
SRF	single reference frame
SRM	switched reluctance motor
STL	sound transmission loss
TEFC	totally enclosed fan-cooled
TF	transverse flux
TFM	transverse flux machine
TFRM	transverse flux reluctance motor
TMD	tuned mass damper
UMP	unbalanced magnetic pull
VCA	voice coil actuator
VCM	variable-capacitance micromotor
VFMM	variable flux memory motor
VPI	vacuum pressure impregnation
VRM	variable reluctance motor
YASA	yokeless and segmented armature

1

Introduction to Electric Motors

Electric motors are devices that convert electric energy into magnetic energy and finally into mechanical energy. Electromagnetism is the basis of electric motor operation by generating magnetic forces necessary to produce either rotational or linear motion. For rotating electric motors, it is the interaction between the stator and rotor magnetic fields that creates motor torque to drive external loads.

Today, electric motors come in a wide variety of types, sizes, operating characteristics, and configurations to suit different applications. They are used almost everywhere in the world, including industrial drives, household appliances, medical devices, electronic products, robots, electric vehicles, machine tools, spacecrafts, and military equipment. As one of the fastest growing industrial sectors, electric motor manufacturing represents a major industry worldwide. Today, electric-motor-driven systems account for approximately 45% of total global electricity consumption. By 2030, energy consumption from electric motors is expected to rise to 13,360 terawatt hour (TWh) per year. End users now spend USD 565 billion per year on electricity used in electric-motor-driven systems; by 2030, that could rise to almost USD 900 billion [1.1]. In the United States, motor-driven equipment accounts for 64% of the electricity consumed in the manufacturing sector. That is approximately 290 billion kilowatt hours (kWh) of power per year [1.2]. There are more than 40 million electric motors used in manufacturing operation [1.3]. In addition, more than 95% of an electric motor's life-cycle cost is the energy cost. In China, it is estimated that about 60% of the annual power generation is consumed through motor-driven systems. All these clearly show how important it is to take a variety of measures to promote electric motor efficiency for the energy saving and carbon emission reduction.

1.1 History of Electric Motors

The discoveries of phenomena of static electricity can be traced back in ancient Greece about 2600 years ago. However, there was little real progress until the English scientist William Gilbert in 1600 described the electrification of many substances and coined the term *electricity*, the Greek word for amber.

Hans Oersted discovered electromagnetism in 1820 and additional works were made by a number of other scientists such as William Sturgeon, Joseph Henry, Ander Marie Ampere, Michael Faraday, and Thomas Davenport. In 1831, Michael Faraday discovered electromagnetic induction, the principle behind the electric motor and generator. This discovery was crucial in allowing electricity to be transformed from a curiosity into a powerful new technology.

Using a broad definition of *motion* as meaning any apparatus that converts electric energy into motion, it is widely accepted that Michael Faraday invented the first direct

current (DC) electric motor in 1821. This motor was basically used to confirm his concept of electric motor and had no actual value in application. He succeeded in building the practical electric motor 10 years later. Following his groundbreaking work, many scientists had contributed to the developments of electric motors. William Sturgeon invented the first practical electric motor in the United Kingdom in 1832 [1.4]. The first US patent on electric motor was granted in 1837 to Thomas Davenport [1.5]. In 1887, Nikola Tesla introduced the world's first alternating current (AC) motor and gained a US patent in the next year [1.6]. Three-phase *cage-rotor* induction motors (IMs) were invented by Mikhail Dolivo-Dobrovolsky during 1889–1890 [1.7]. Even today, this type of motors is still in service for the vast majority of commercial applications.

1.2 Motor Design Characteristics

Electric motors are manufactured in a variety of types and configurations. Typically, an electric motor assembly is formed from a collection of parts, including a stator, a rotor, a shaft, a pair of end bells, bearings, and a motor housing supporting and enclosing the various components. In addition to these primary motor components, some motors may include electronic components that are used to modify operating characteristics for particular applications.

Motor design characteristics are the essential elements in the motor design and manufacturing processes. To select appropriate motors for specific applications, these design characteristics must be well understood.

1.2.1 Motor Torque

Torque is a measurement of the turning force acting on an object to cause that object rotating or twisting about an axis or pivot. Torque, like *work*, is measured as Newton meter (N-m) in the International System of Units (SI system) or pound-foot (lb_f-ft) in the English system. However, unlike *work* that only occurs during displacement, torque may exist even though no displacement or rotation occurs. A typical example is the static holding torque.

1.2.1.1 Static and Dynamic Torque

Torque can be divided into two major categories, either static or dynamic torque. From the standpoint of physics, the system is considered static if it has no angular or linear acceleration. Static torque refers to the amount of torque that an electric motor produces at zero speed (i.e., the motor is in a real static state) with the power output $P_{out} = 0$. By contrast, dynamic torque refers to the amount of torque that an electric motor produces at variable speeds of rotation with load applied (i.e., the motor is in a dynamic state) with $P_{out} > 0$. Simply, static torque is associated with forces that do not involve angular acceleration/deceleration, and dynamic torque is associated with dynamic forces that arise from acceleration/deceleration, following Newton's second law.

Some motor manufacturers may provide the information of continuous static torque rating for customers, indicating the motor is capable of supplying that static torque at zero speed of rotation continuously. However, this information may be not very useful in motor

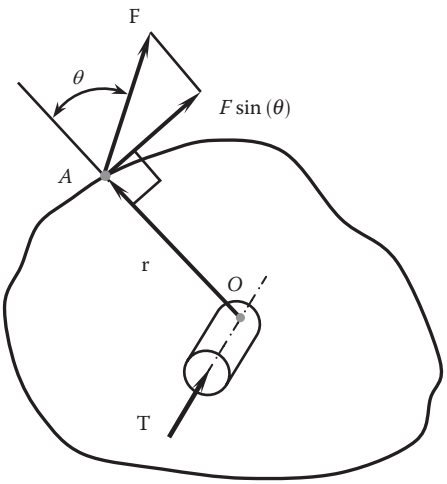

FIGURE 1.1
Torque vector ***T*** acting on a solid body to make it rotate.

selection because it does not define the continuous torque available from the motor at a specific speed (or in a range of speeds) to drive external load.

As a continuous torque rating is provided at a specific rated speed (or in a range of speeds), the torque is thus the dynamic torque, indicating the capability of the motor to provide up to a corresponding rated torque continuously. Furthermore, the maximum torque appearing on the motor nameplate refers to the highest dynamic torque for the motor at rated motor speed.

As shown in Figure 1.1, when a force vector **F** acts on a solid body at the point *A* to make the body rotate about its axis through the point *O*, the torque vector **T** around the point *O* is obtained by crossing product of the radial displacement vector **r** and the force vector **F**:

$$\mathbf{T} = \mathbf{r} \times \mathbf{F} \tag{1.1}$$

The direction of the torque vector **T** is determined by the right-hand rule, that is, it is perpendicular to both **r** and **F**. Correspondingly, the magnitude of the torque acting on the body is

$$T = rF\sin(\theta) \tag{1.2}$$

where the moment arm $r = \overline{OA}$, defined as the distance from the axis to the point where the force is applied, and θ is the measure of the smaller angle between the displacement vector **r** and the force vector **F**. It is worth to note that torque calculated from Equation 1.2 can be either static or dynamic torque depending on whether *F* is static or dynamic force.

For a rotating system with a fixed axis, the dynamic torque on the rotating system along axis of rotation is determined by the rate of change of the system angular momentum:

$$T = \frac{dM_a}{dt} \tag{1.3}$$

where M_a is the angular momentum of the rotating system, measured in N-m-s. M_a can be expressed as the product of the polar moment of inertia of the rotating system J_p and the rotating speed ω, that is,

$$M_a = J_p \omega \tag{1.4}$$

As a result, the torque on the rotating system can be expressed as

$$T = \frac{d(J_p \omega)}{dt} = J_p \frac{d\omega}{dt} = J_p \alpha \tag{1.5}$$

where α is the angular acceleration of the rotating system, measured in rad/s^2. This equation indicates that for electric motors, the less the motor inertia, the less torque the motor needs to produce to meet a desired acceleration rate. As a result, it is advantageous to minimize motor inertia to the greatest extent to maximize acceleration.

Servomotors are typically expected to accelerate loads from a stop to a given velocity and then decelerate the loads once again to a stop at precise position. Accordingly, to move or stop loads as fast as possible, the angular acceleration/deceleration α must be maintained high enough. As a result, the motor's polar moment of inertia J_p has to be kept at very low levels. For this reason, the motor inertia must be taken into account in the earlier stage of motor design.

1.2.1.2 Motor Torque in Motor-Load System

When a motor drives a load machine to perform work, it usually connects with some power transmission components such as coupling and gearbox. For demonstration purpose, a two-shaft gearbox is shown in Figure 1.2. The gear ratio γ_g is defined as the rotating speed of the gearbox input shaft that is directly coupled with the rotor shaft to the rotating speed of the gearbox output shaft, which is directly coupled with the load machine, that is,

$$\gamma_g = \frac{\omega_i}{\omega_o} = \frac{\omega_m}{\omega_l} \tag{1.6}$$

where

ω_i and ω_o are the rotating speeds of the input and output shaft of the gearbox
ω_m and ω_l are the rotating speeds of the motor and load, respectively

Unlike other components, because the input and output shaft of a gearbox have different rotating speeds, the inertia of each shaft must be calculated separately.

To determine the motor torque required for the system, a concept of reflected load inertia is introduced as the equivalent inertia of the load seen by the motor:

$$J_{rl} = J_c + J_{i,gb} + \frac{J_{o,gb} + J_l}{\gamma_g^2} \tag{1.7}$$

where J_c and J_l are the inertias of the coupling and load machine, respectively. This equation indicates that load inertia is reduced by the square of the gear ratio, which can be

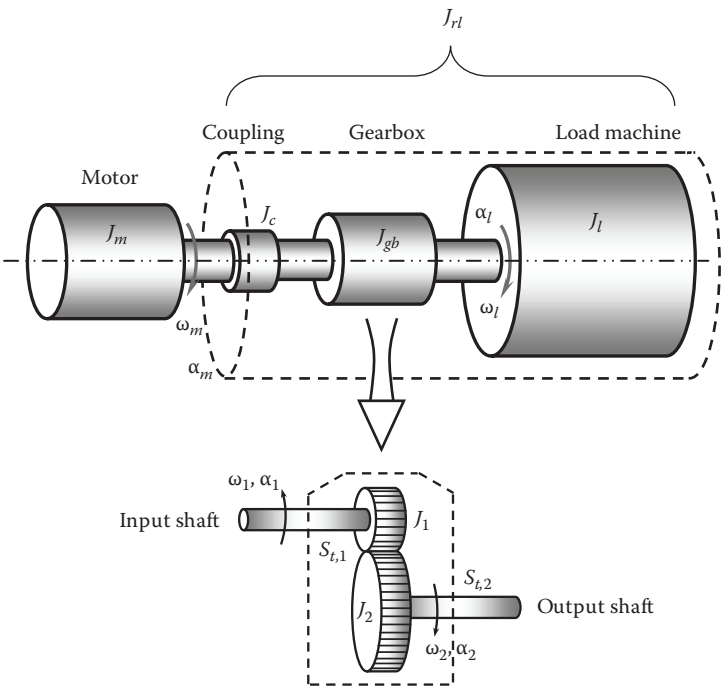

FIGURE 1.2
A motor is connected with a driven load machine via a coupling and a gearbox. The reflected load inertia is the equivalent inertia of the load seen by the motor.

derived from conservation of energy or power in a set of rotating components. In this resultant equation, it is assumed that the inertias of the coupling and gearbox are considered part of the load inertia.

The torque required at the motor thus becomes

$$T_m = \left(J_m + J_{rl}\right)\alpha_m = \left(J_m + J_c + J_{i,gb} + \frac{J_{o,gb} + J_l}{\gamma_g^2}\right)\alpha_m \tag{1.8}$$

The motor angular acceleration α_m has the relationship with the load angular acceleration α_l [1.8]:

$$\alpha_m = \alpha_l \gamma_g \tag{1.9}$$

Combining the aforementioned equations yields

$$\alpha_l = \frac{\alpha_m}{\gamma_g} = \frac{T_m}{\gamma_g}\left(J_m + J_c + J_{i,gb} + \frac{J_{o,gb} + J_l}{\gamma_g^2}\right)^{-1} \tag{1.10}$$

Taking the derivative of α_l with respect to γ_g, it follows that

$$\frac{d\alpha_l}{d\gamma_g} = T_m \frac{\left(J_l + J_{o,gb}\right) - \left(J_m + J_c + J_{i,gb}\right)\gamma_g^2}{\left[\left(J_l + J_{o,gb}\right) + \left(J_m + J_c + J_{i,gb}\right)\gamma_g^2\right]^2} \tag{1.11}$$

Let $d\alpha_l/d\gamma_g = 0$; thus,

$$\left(J_l + J_{o,gb}\right) = \left(J_m + J_c + J_{i,gb}\right)\gamma_g^2 \tag{1.12}$$

Thus, the optimum gear ratio is found at

$$\gamma_g = \sqrt{\frac{J_l + J_{o,gb}}{J_m + J_c + J_{i,gb}}} \tag{1.13}$$

The torque on a motor shaft can be measured using a number of strain gages to the shaft in a proper orientation. This allows directly measuring torsional shear strains that can be calibrated to output torque.

1.2.1.3 Continuous Torque

It is the interaction of the stator revolving field and the rotor induced field that produces the motor torque to drive load machines. Consequently, the motor torque is a function of both the field and armature currents and acts on both the rotor and stator simultaneously. The continuous rated torque T_r (in N-m) of a motor can be determined from its rated power P_r (in W) and rated rotor angular speed ω_r (in rad/s):

$$T_r = \frac{P_r}{\omega_r} \tag{1.14}$$

At normal operation, a motor provides a continuous torque, known as nominal torque, to drive an external load device smoothly. It can be seen from the previously mentioned equation that for a given motor power, the continuous torque is inversely proportional to the motor rotating speed. In practice, the continuous torque generated in a motor commonly has a cyclic variation as a result of the cyclic permeance variation that occurs as the rotating member moves with respect to the stationary member. The instantaneous torque of a motor can be expressed as (Figure 1.3)

$$T(t) = T_o + T_p(t) \tag{1.15}$$

where T_o and $T_p(t)$ are the mean component and the periodic component of the motor torque, respectively.

1.2.1.4 Peak Torque

The motor peak torque, which is always associated with the peak current, is the maximum torque a motor can produce for short periods of time without exceeding the motor

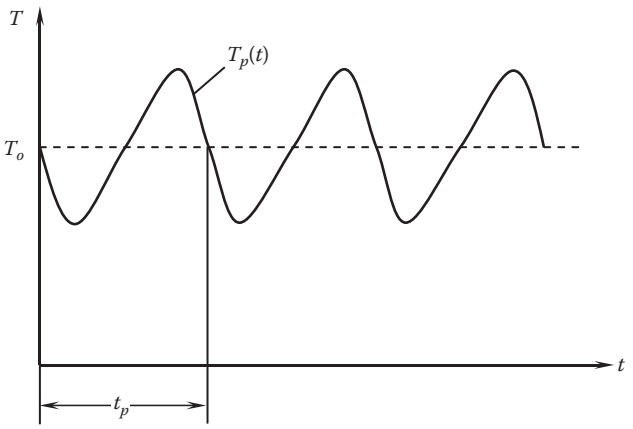

FIGURE 1.3
Mean component and periodic component of motor torque.

temperature limit or safe operating torque. A motor that operates under a peak torque condition is typically associated with a quick temperature rise. When the motor temperature exceeds the allowable value, it will cause degradation of insulation materials, irreversible demagnetization of permanent magnets (PMs) in PM motors (PMMs), and winding damage and, in turn, lead to the degradation of motor performance or even motor failure.

Peak torque contains two components [1.9]: (1) acceleration torque as inflicted by inertia forces with the maximum angular acceleration and (2) constant torque due to all other non-inertial forces such as gravity, friction, preloads, and other push–pull forces.

The continuous torque and peak torque curves are usually determined through motor testing and provided by motor manufacturers.

1.2.1.5 Stall Torque

The stall torque is the torque that a motor produces at zero rotating speed where $P_{\text{out}} = 0$. The stall torque, also known as locked rotor torque (LRT), can be measured with the rotor being locked. For a DC motor, the motor torque has a linear relationship with the motor rotating speed. The maximum torque occurs at zero rotating speed and zero torque occurs at maximum rotating speed. For an IM, the stall torque can be calculated as [1.10]

$$T_s = \frac{C_1 k_2 \left(P_{in,s} - P_s - P_{sc} \right)}{n_s} \tag{1.16}$$

where

C_1 is a reduction factor ($0.9 \le C_1 \le 1.0$) to account for nonfundamental losses
$k_2 = 9.549$ for torque in the unit of N-m
$P_{in,s}$ is the input power to stator (in W)
P_s is the stator I^2R loss (in W)
P_{sc} is the stator iron core loss (in W)
n_s is the synchronous speed in the unit of rpm

1.2.1.6 Cogging Torque and Reduction Methods

The torque generated from a PMM usually consists of two components: the effective driving torque, which is basically proportional to the supplied electric current, and the *no-current torque*, which is independent of the current, such as cogging torque.

Cogging torque originates from the interaction between rotor-mounted PMs and the stator teeth, which produces reluctance variations depending on rotor position [1.11]. As depicted in Figure 1.4, when the rotor rotates, the magnets attached to the rotor successively pass through the stator teeth and slot openings, resulting in the periodic variations of the magnetic field. During the process, the PM rotor tends to lock onto the position where the permeability reaches the largest. When the rotor deviates from this equilibrium position, tangential forces are produced between the magnets and stator teeth, either to return the rotor back to the old equilibrium position or to push the rotor to the next equilibrium position, leading to cogging torque.

Cogging torque is highly undesirable because it is the major cause of motor vibration and acoustic noise, particularly at light loads and low speeds. Even for high-speed applications, lower cogging torque always benefits smooth operation. For instance, in a servo system, the motor may come to a stop and then accelerate to another high speed after the stop. As the motor approaches zero speed, it is often to use settling time or settling error to measure how smoothly the motor approaches zero speed. This can definitely be impacted by cogging torque.

Because the rotor always tends to lock onto a position where it is aligned with the stator poles, it makes precise positioning of the rotor difficult. In addition, cogging torque is also an important source of torque ripples that have adverse effects in many demanding motion control applications.

Motor manufacturers often adopt the cogging torque ratio to quantitatively describe the level of cogging torque. This torque ratio is defined as the absolute cogging torque, which is characterized as peak-to-peak cogging torque, to the rated continuous torque. It is widely accepted that for regularly controlled servo systems, the maximum cogging torque ratio should keep under 5%. More ideally, for precisely controlled servo systems, the cogging torque ratio is 2% or less. Cogging torque below 1% really requires special design. For example, in some high-precision film roller systems that need super smooth operation at

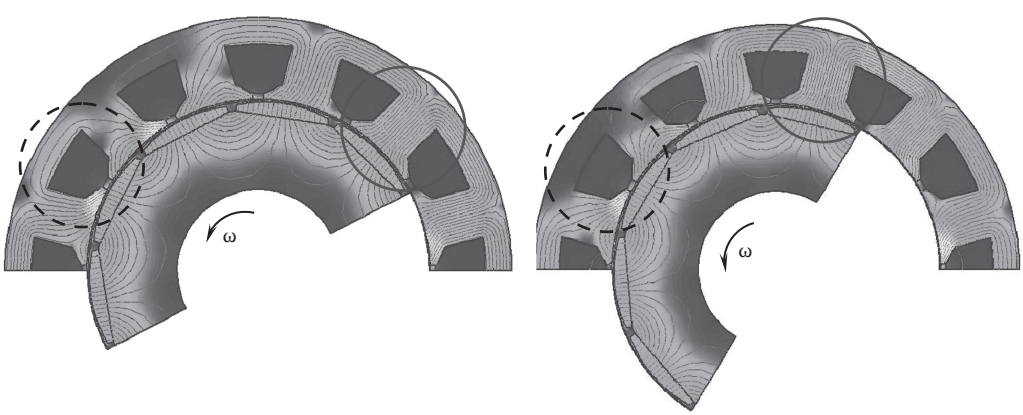

FIGURE 1.4
As a rotor rotates, magnets successively pass through stator teeth and slot, leading to different magnetic flux distributions, as shown earlier for magnet-teeth (solid circle) and magnet-slot (dashed circle) conditions.

very low speeds, an effective solution is to use DC torque motors for excellent operation. Three-phase brushless motors have been designed for very smooth telescope azimuth motion, that rotate at extremely slow earth rates of rotation of one revolution in 24 h. It is worth to note that each application may allow for different extremes of cogging torque.

Though cogging torque can be calculated accurately using numerical approaches such as finite element methods (FEMs), with simplified motor models, analytical methods may provide greater physical insight into the mechanism of cogging torque production. This is especially useful at the initial stage of the motor design. One approach to predict cogging torque is represented by [1.12]

$$T_{cog} = -\frac{\phi_g^2}{2}\frac{dR}{d\theta} \tag{1.17}$$

where
- ϕ_g is the air gap flux
- R is the air gap reluctance
- θ is the position of the rotor

This equation indicates that in order to reduce cogging torque, either the air gap flux ϕ_g or the rate of change of the air gap reluctance $dR/d\theta$ must be minimized. In practice, cogging torque is reduced by forcing the air gap reluctance R as close as possible to constant with respect to rotor position.

Another method for calculating cogging torque in PMMs was proposed by Lu et al. [1.13]:

$$T_{cog} = -\frac{p_r B_r}{2}\frac{l_m}{\mu_o \mu_r}\frac{d\Phi}{d\theta} \tag{1.18}$$

where
- p_r is the number of magnet pole pairs
- B_r is the remanent magnetic flux density at $H = 0$
- Φ is the magnetic flux calculated over a surface perpendicular to its direction of magnetization
- l_m is the magnet length along the magnetization direction
- μ_o and μ_r are the permeability of free space and the relative permeability of the magnet material, respectively

This equation shows that the magnitude of cogging torque is proportional to the number of magnet pole pairs, the remanent flux density value, the magnet length in the direction of magnetization, and the variation of the magnetic flux with respect to the rotor position. It has shown a good agreement of the predicted cogging torque with the cogging torque calculated using Maxwell stress method and measured results.

There are a number of techniques available for reducing cogging torque:

a. The most effective way in practice to reduce cogging torque is to skew either the stator teeth relative to the rotor centerline (Figure 1.5) or rotor magnets relative to the stator teeth, where Figure 1.6 is for step-skewing of segmented magnets

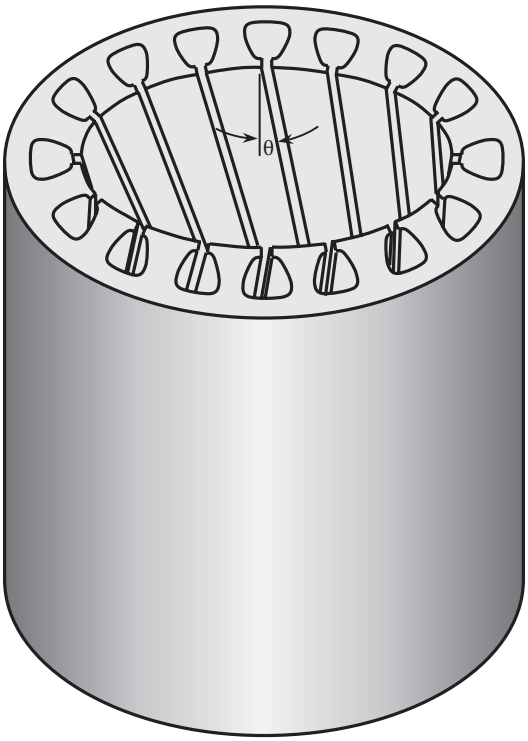

FIGURE 1.5
Skewed stator teeth with respect to its centerline for reducing cogging torque, where θ is the skew angle.

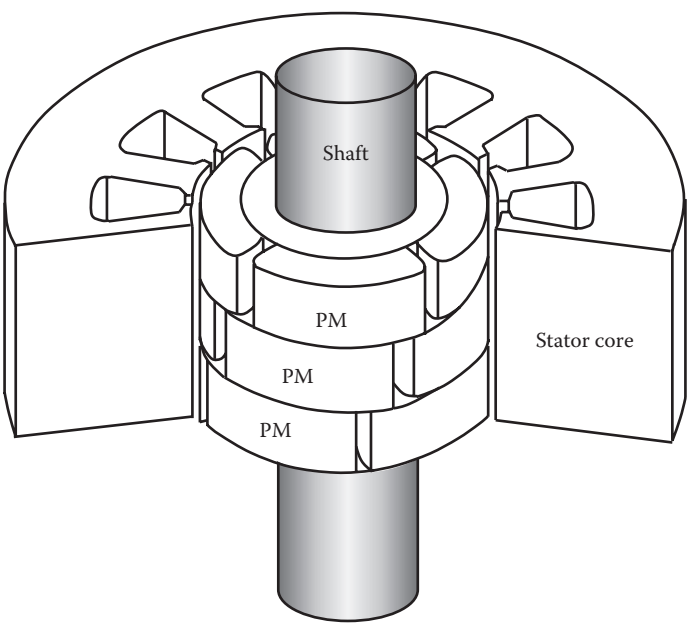

FIGURE 1.6
Step-skewed permanent magnets relative to stator teeth for reducing cogging torque.

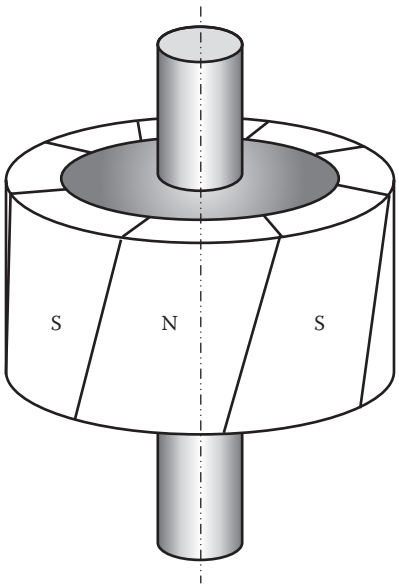

FIGURE 1.7
Skewed PMs on rotor core for reducing cogging torque.

and Figure 1.7 [1.14] is for skewing whole magnets. More detailed descriptions can be found in reference [1.15]. Skewing stator teeth needs special care in stacking steel laminations. Skewing whole magnets may have smoother rotor performance than step-skewing segmented magnets. However, it is to be noted that rotor skewing may also decrease the rotor saliency and thus reduces the back electromotive force (EMF) and motor effective torque. All forms of skewing will reduce the back EMF and motor effective torque as skewing affects total flux linkage to the coils.

b. Another technique is to use a fractional number of slots per pole. The use of this method not only reduces the amplitude of the cogging torque but also increases the fundamental order. This is because the stator slots are located at different relative circumferential positions with respect to the edges of the magnets [1.16–1.18]. To address the problem, the parameter q, which is defined as the slot number per pole n_{slot} divided by the phase number N_{phase}, is introduced as

$$q = \frac{N_{slot}}{2p_r N_{phase}} = \frac{n_{slot}}{N_{phase}} \tag{1.19}$$

where
p_r is the number of pole pair
N_{slot} is the number of the stator slots

The fractional slot winding arrangement with $q < 1$ is attractive for lower cogging torque. The investigations have shown that the cogging torque of the fractional slot motors can be less than 1% of the rated torque. In the case of multipole machines, the cogging torque of 0.05% could be estimated [1.19].

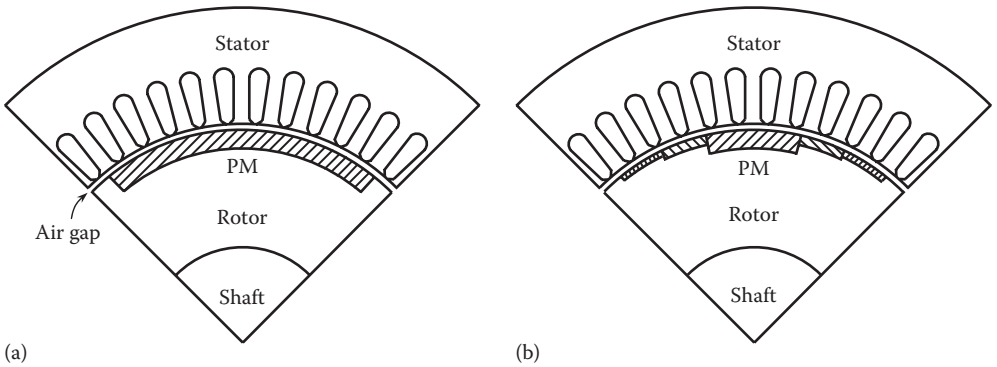

FIGURE 1.8
Rotors with surface-inset single PM (a) and stepped PMs (b).

c. The reduction in cogging torque can be also achieved by modulating drive current waveform [1.20].

d. It is a well-established fact that the magnet pole arc can have a large effect on the magnitude of the cogging torque [1.21,1.22]. The optimization of the magnet pole arc can reduce the harmonics of the air gap flux wave and the permeance wave [1.23].

e. Another technique is called magnet segmentation in which a pole magnet consists of several elementary magnet segments with the same polarities [1.24]. Furthermore, as shown in Figure 1.8, the segmented magnets may be selected with different thickness and lengths to obtain more sinusoidal flux density waves [1.25].

f. The shape of the magnetic pole has a strong impact on the uniformity of the stator–rotor air gap. A comparison of uniform and nonuniform air gap with different pole shapes of magnets is illustrated in Figure 1.9. It has been reported that the nonuniform pole shape of magnets can reduce cogging torque as high as 50% [1.25]. The normalized cogging torque to the peak torque between uniform air gap and nonuniform air gap is given in Figure 1.10. The simulation studies of the pole surface effect on cogging torque were performed by Lao et al. [1.26].

g. Other mechanical factors can affect cogging torque. Geometry factors such as rotor or magnet concentricity of the magnetic air gap can create eccentric magnet to stator teeth flux linkage. These variations in flux linkage can cause variations in cogging torque and torque ripple.

h. In order to achieve decreasing torque ripple, iron losses, and cogging torque for interior PM (IPM) synchronous machines, Soleimani et al. [1.27] proposed a novel structure of rotor. In their design, three layers of PM have been used and each layer has a fragmental trapezoid structure, as shown in Figure 1.11. With the optimized dimensions and shapes of the buried rotor magnets, the cogging torque ratio of 1.82% is achieved, comparing with torque ratio of 5% in conventional IPM machines.

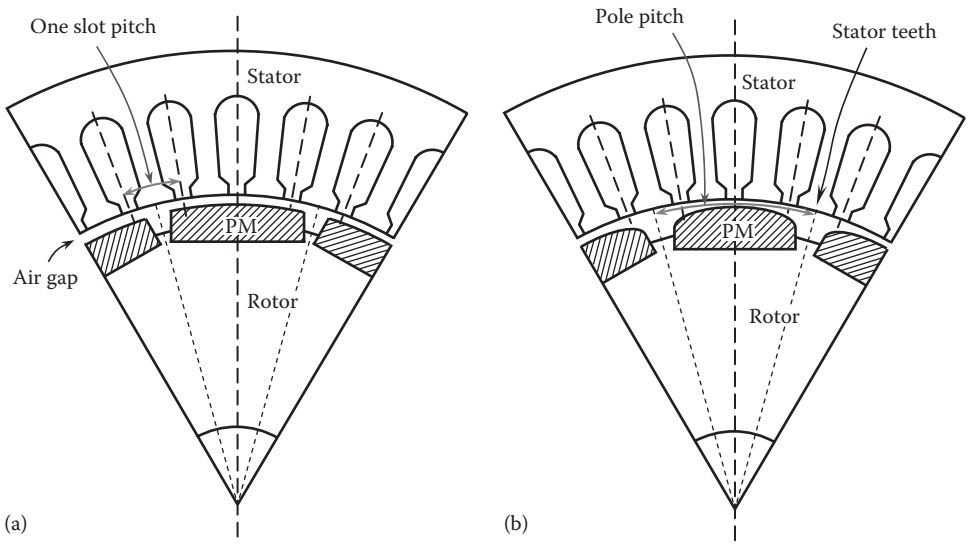

FIGURE 1.9
Surface-mounted PMs with different shapes for (a) uniform air gap and (b) nonuniform air gap.

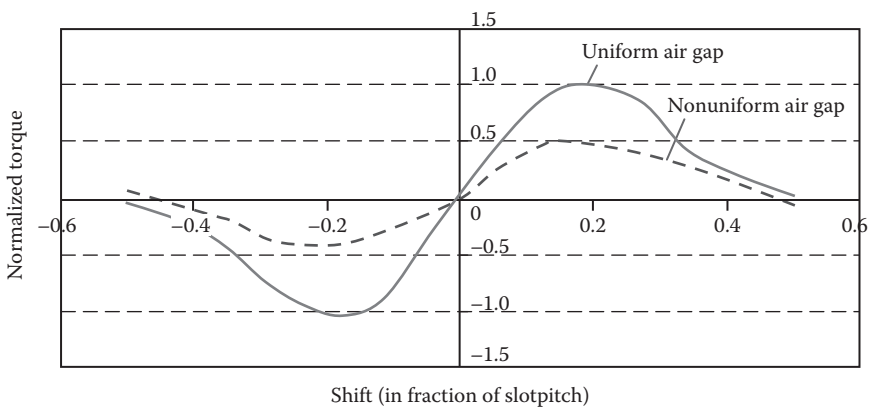

FIGURE 1.10
Comparison of cogging torque for uniform and nonuniform air gap (bread-loaf magnet shape).

1.2.1.7 Torque Ripple

PM synchronous motors usually generate torque ripple during their normal operation. The studies of Hsu et al. [1.28] have revealed that torque ripple can be classified into four types depending on the nature of their origin:

- Pulsating torque, which is inherently produced by the trapezoidal back EMF. The torque ripples caused by pulsating torque may be reduced by purposely produced fluctuating counter torques.
- Fluctuating torque, which is produced by altering the magnitudes of phase current in the same ratio.

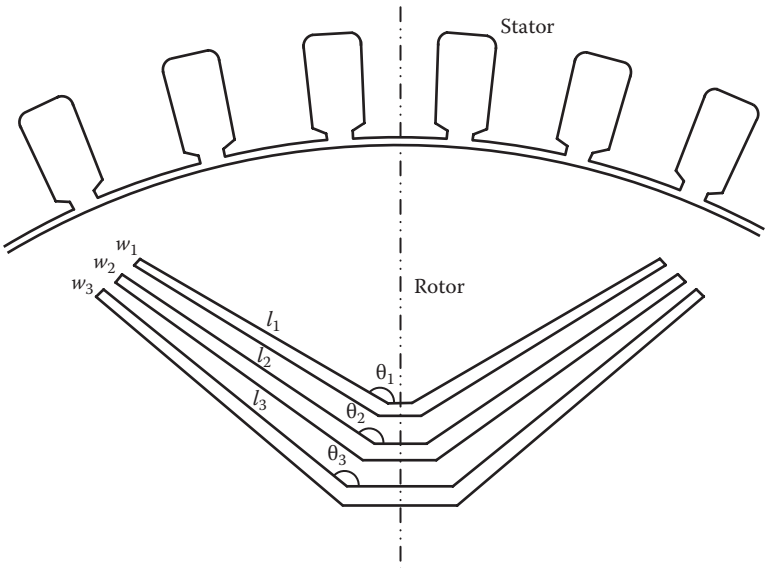

FIGURE 1.11
Novel structure of rotor for minimizing cogging torque for IPM synchronous motors.

- Reluctance cogging torque, which is produced by nonuniformly distributed air gap permeance associated with the teeth and PMs. Actually, this type of torque exists even when the motor is not energized.
- Inertia and mechanical system torques, which are generated by the dynamic motions of the mechanical components of motor. They are affected by the driven device.

Later, Holtz and Springob [1.29] have investigated the different sources of torque ripple in PM machines, including the distortion of the stator flux linkage distribution, variable magnetic reluctance at the stator slots, and secondary phenomena. In addition, the feeding power converter also contributes to torque ripple due to the time harmonics in the current waveform's time-varying delays between the commanded and the actual current.

1.2.2 Motor Speed

There are a few terms to describe rotational motion. Angular speed represents the change in angle per unit of time, typically measured in radians per second (rad/s) in the SI system and in degrees per second in the English system. Rotational speed is the measurement of revolutions per unit of time, expressed as either revolutions per second (Hz) or revolutions per minute (rpm). It is to be noted that speed is a scalar quantity and velocity is a vector. Thus, the difference between angular (or rotational) speed and angular (or rotational) velocity is that the latter contains the information of the rotational direction. Angular speed ω (in rad/s) and rotational speed n (in rpm) can be converted into each other:

$$\omega = \frac{\pi n}{30} \tag{1.20}$$

1.2.2.1 Continuous Speed

The continuous speed of a motor is an important design parameter, defining the nominal speed at which the motor continuously operates at the rated voltage and current to drive the full motor load. It depends on the number of the motor pole, the frequency of AC, and the amount of torque.

1.2.2.2 Peak Speed

The peak speed is the maximum speed a motor can reach during operation. It must be noted that at the peak rotating speed, all rotating components are subject to high centrifugal forces. Even a tiny unbalance in a high rotating speed system can cause severe motor vibration or serious damage of rotating components. Therefore, the motor peak speed needs to be carefully determined during motor design phase.

1.2.2.3 Speed Ripple

Speed or velocity ripple refers to the variations in steady-state speed in time. Velocity ripple values are usually defined as a percentage (%) of deviation from the ideal value. In practice, torque ripple has the tendency to cause speed ripple.

There are a large number of factors that affect motor velocity ripple and torque ripple [1.30], including

- Load-to-rotor inertia ratio
- Motor pole count—higher pole count leads to lower ripple
- Encoder resolution
- Commanded velocity
- System bandwidth (different between an analog and a digital drive)
- Commutation type (sinusoidal vs. trapezoidal commutation)
- System trajectory update rate (when using a digital drive)
- Natural (harmonic) frequencies of the system as a whole
- Mechanical resonance of motor components
- Mechanical friction in the system
- Physical alignment of mechanical components
- Inherent performance variances between two like components
- Load damping
- Consistency of the AC supply voltage to the drive (i.e., power supply integrity)
- Sampling rate/resolution of the tachometer (or velocity-measuring device)

1.2.3 Torque Density

Torque density is defined as the ratio of the nominal continuous torque T to the motor volume V, as the measure of the torque-carrying capability per unit volume. High torque density and high efficiency are two of the most desirable features for electrical motors. Torque density is a measure of the torque-carrying capability per unit volume of a motor, expressed in units of N/m^2 or lb_f/ft^2. Torque density is a system property since it depends

on the design of motor components and their interconnections. One of the main design goals in motor design is to improve torque density of motors.

1.2.4 Motor Power and Power Factor

The power output P_{out} of rotary motors is expressed as the product of the motor torque and the angular rotating speed, that is,

$$P_{out} = T\omega \tag{1.21}$$

Since the angular rotating speed ω (in rad/s) is related to the rotating speed n (in rpm) as $\omega = \pi n/30$, Equation 1.21 can be also expressed as

$$P_{out} = \frac{\pi n T}{30} \tag{1.22}$$

When an IM is connected to a power supply but still at rest, it appears just like a short-circuited transformer, drawing a very high current known as the locked rotor current (LRC). The torque corresponding the LRC is defined as the LRT. A motor that exhibits a high starting current will generally produce a low starting torque, and vice versa. Both the torque and current of the locked rotor are a function of the terminal voltage of the motor. Under a constant voltage, the torque and current vary with the rotor speed during the motor acceleration/deceleration process.

The most important two parameters for motor performance are motor efficiency and power factor. In the electric power industry, power factor PF is defined as the ratio of real power P_{real} to apparent power P_a. As shown in Figure 1.12, power factor PF (where $0 \le PF \le 1$) can be also expressed as the cosine of the impedance phase angle ϕ:

$$PF = \cos\phi = \frac{P_{real}}{P_a} \tag{1.23}$$

The power supply system provides both real and reactive power to operate the motor. Useful mechanical work is developed from real power P_{real} and is measured in watts (W)

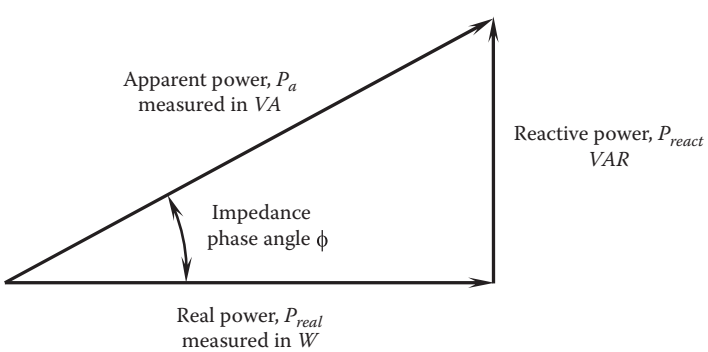

FIGURE 1.12
The power triangle: the relationship of real power, reactive power, and apparent power.

or kilowatts (kW). For AC motors, reactive power P_{react} is to develop magnetic fields. It is worth to note that reactive power does not provide any mechanical work. From the power triangle in Figure 1.12, apparent power P_a can be expressed as

$$P_a = \sqrt{P_{real}^2 + P_{react}^2} \tag{1.24}$$

Power factor depends upon motor load. When a motor is in normal operation, the electric current drawn by the motor varies with the external load. Under a no-load condition such as the motor start, the power factor is minimum, typically 0.1–0.25. As the shaft load increases, the load current through the stator windings increases significantly, and consequently, the power factor increases until reaching the maximum at the full-load point. Then, the power factor falls again as the motor approaches the full speed. In engineering practice, *PF* is determined at each load point using the following formula:

$$PF = \frac{P_{in}}{\sqrt{3}\,VI} \tag{1.25}$$

where
P_{in} is the motor input power
V and I are line-to-line voltage and current, respectively

The full-load power factor of an IM can vary from 0.5 for a small low-speed motor up to 0.9 for a large high-speed machine.

1.2.5 Torque–Speed Characteristics

In the power industry, a commonly used method of displaying motor performance characteristics graphically is to use motor torque–speed curves, as shown in Figure 1.13 for

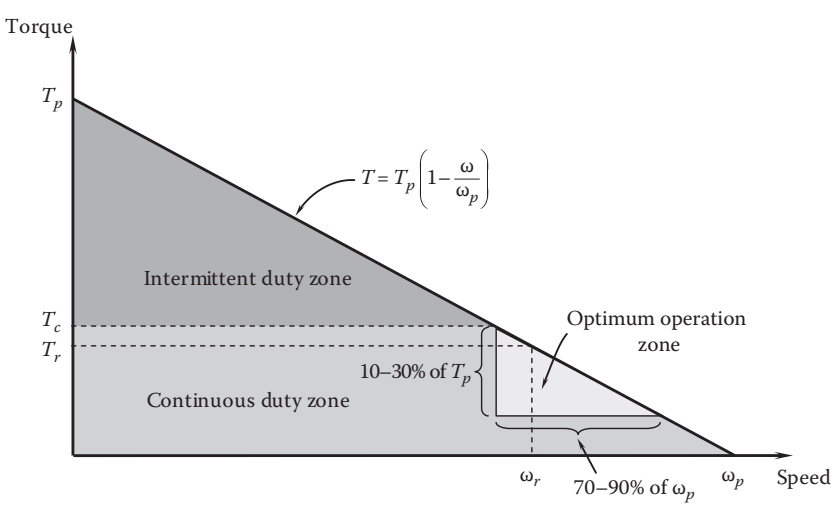

FIGURE 1.13
Torque–speed characteristics of a typical DC motor.

a typical DC motor. There are two pairs of parameters used to define the DC motor performance: one pair of torque, which includes peak torque T_p and rated torque T_r, and another pair of speed, which includes peak speed ω_p and rated speed ω_r. Since the peak torque occurs at $\omega = 0$, it also called the stall torque. The peak rotating speed is also called no load speed because the motor generates no torque at the point. As depicted in the figure, the linear relationship between the motor torque and the rotating speed can be expressed as

$$T = T_p\left(1 - \frac{\omega}{\omega_p}\right) \tag{1.26}$$

As shown in Equation 1.21, the motor output power is the product of torque and angular rotating speed. Thus, the power of a DC motor is given as

$$P_{out} = T_p\omega\left(1 - \frac{\omega}{\omega_p}\right) \tag{1.27}$$

This indicates that $P_{out} = 0$ at both $\omega = 0$ and $\omega = \omega_p$. Differentiating P_{out} with respect to ω and letting $dP_{out}/d\omega = 0$, the maximum power output is found to occur at $\omega = \omega_p/2$ where $T = T_p/2$. However, at this operating point, the motor efficiency is rather low, causing higher power losses and higher temperature rises. For optimal continuous performance, the operating speed may be set between 70% and 90% of the no load speed and the operating torque between 10% and 30% of the stalled torque [1.31]. The optimum operating zone is shown in Figure 1.13 as a small triangle.

With the two pairs of parameters (torque and speed), two motor operation zones can be identified: the intermittent duty zone and the continuous duty zone. In the intermittent duty zone, the motor operates intermittently with a higher torque. This is especially useful when a rotor requires frequent starts and frequent reversals in rotating direction. In such cases, extra torque is required to overcome the inertia of the load as well as the rotor itself. However, it is specially noted that in the intermittent duty zone, the motor can only produce torque and speed for a limited amount of time; otherwise, it will cause the motor overheating. As the combination of torque and speed produced by the motor falls in the continuous operation zone, the motor can be loaded until the rated torque remains constant for a speed range up to the rated speed. In this zone, the motor can run as long as needed without any chance of overheating. The slope of the torque–speed curve represents inherent motor damping. For DC motors, damping is a constant.

The torque–speed characteristics of a typical AC IM are displayed in Figure 1.14. When the motor is initially started from standstill at the starting current I_s, the starting torque (also called LRT) is produced by the motor to overcome the inertia of the motor drive system. The starting torque depends on the terminal voltage and the stator and rotor design. As the motor accelerates, the torque generated by the motor may drop slightly to the local minimum point known as the pull-up torque. In the case that the pull-up torque of the motor is less than that required by its application load, the motor will overheat and eventually stall. Then, a further increase in motor speed will lead to the increase in torque until it reaches the breakdown torque, which is the highest torque the motor can attain without stalling. Starting from this point, the continuous increase in speed causes the sharp

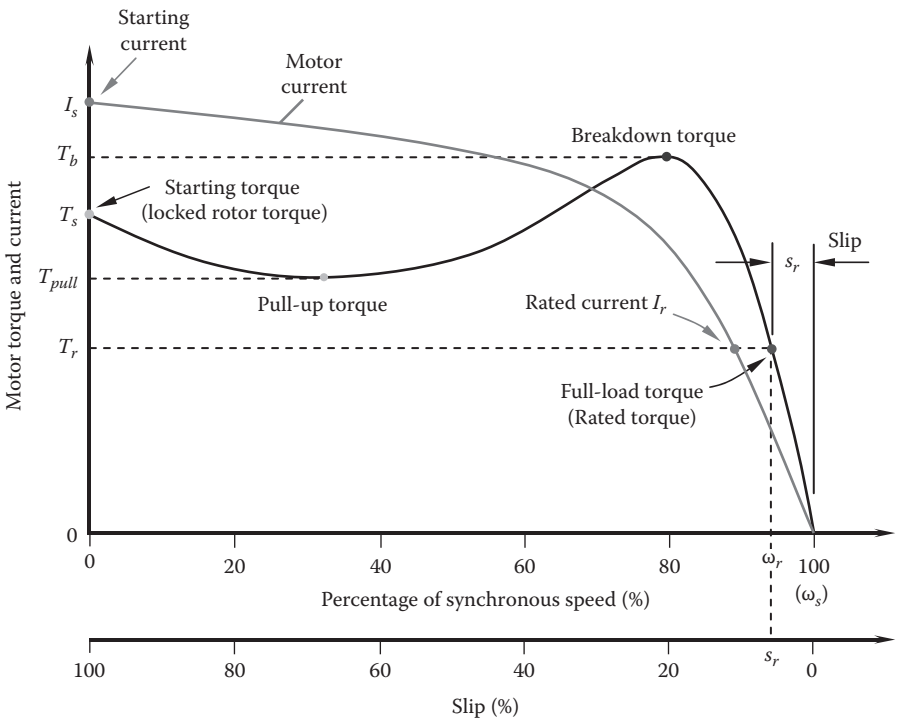

FIGURE 1.14
Torque–speed characteristics of a typical AC IM.

decrease in torque, as well as in motor current. When the motor reaches its full operation speed ω_r, it is loaded to its full-load torque T_r and the corresponding rated current I_r and slip s. At the synchronous speed, no torque can be developed as zero slip ($s=0$) implies no induced rotor current ($I=0$) and thus no torque ($T=0$). This situation only occurs for motors that run while not connected to a load. Therefore, in the strict sense, an IM can never reach the synchronous speed.

In order to clearly present the relationship between rotor torque and speed, an absolute value of torque (usually N-m) is used in Figure 1.14. More frequently, torque is expressed in terms of a percentage of full-load torque, together with speed in terms of a percentage of synchronous speed.

The torque–speed curve for a servomotor is given in Figure 1.15. The whole working zone is defined by the peak torque line $T=T_p$, the peak speed line $\omega=\omega_p$, and a diagonal line equation

$$T = T_p - \left(T_p - T_{mc}\right)\frac{\omega - \omega_k}{\omega_p - \omega_k} \tag{1.28}$$

where T_{ms} is the peak torque at the motor maximum speed ω_p and ω_k is the speed at the knee in the peak envelop.

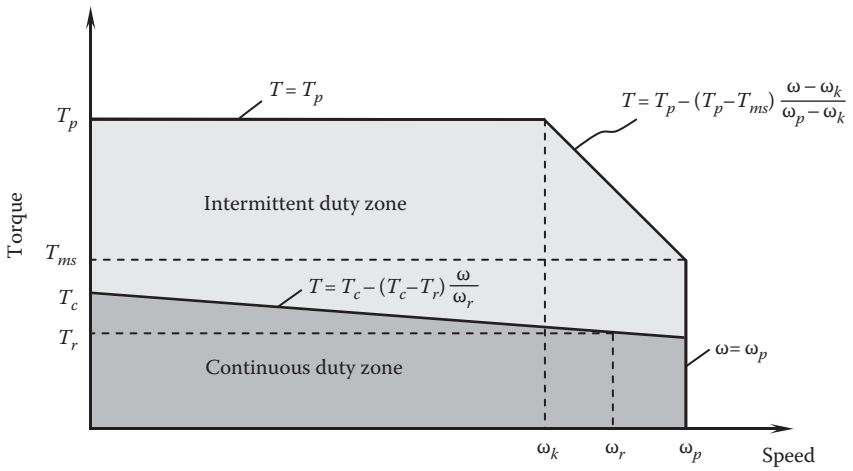

FIGURE 1.15
Torque–speed characteristics of a servomotor.

The two duty zones, that is, the intermittent duty zone and the continuous duty zone, are separated by the maximum continuous torque line, which is expressed as

$$T = T_c - (T_c - T_r)\frac{\omega}{\omega_r} \tag{1.29}$$

At normal operation, a motor runs at the continuous duty zone to provide a continuous torque to drive external loads.

Unlike DC motors, motor damping in AC motors always vary along with the motor speed.

1.2.6 Mechanical Resonance and Resonant Frequency

Mechanical resonance occurs when an external source amplifies the vibration level of a mass or structure at its natural frequency. For a rotating mass like a motor or a pump, this occurs at what is called the *critical speed*.

Every mechanical system can be resonated at a certain frequency, defined as resonant frequency. However, when two systems (e.g., a motor and a driven machine) are connected together by some power transmission components such as shaft coupling, gearboxes, and belts, it forms a new resonant frequency, based on all components in the system.

As illustrated in Figure 1.16, in a regular motor drive system, the total system inertia J_t is the sum of the motor inertia J_m and the reflected load inertia J_{rl}:

$$J_t = J_m + J_{rl} = J_m + J_c + J_{i,gb} + \frac{J_{o,gb} + J_l}{\gamma_g^2} \tag{1.30}$$

The unit of inertia is kg-m^2 in the SI system and lb$_m$-ft^2 in the English system. It is worth to note that 1 kg-m^2 = 1 N-m-s^2 and 1 lb$_m$-ft^2 = 1/32.185 lb$_f$-ft-s^2.

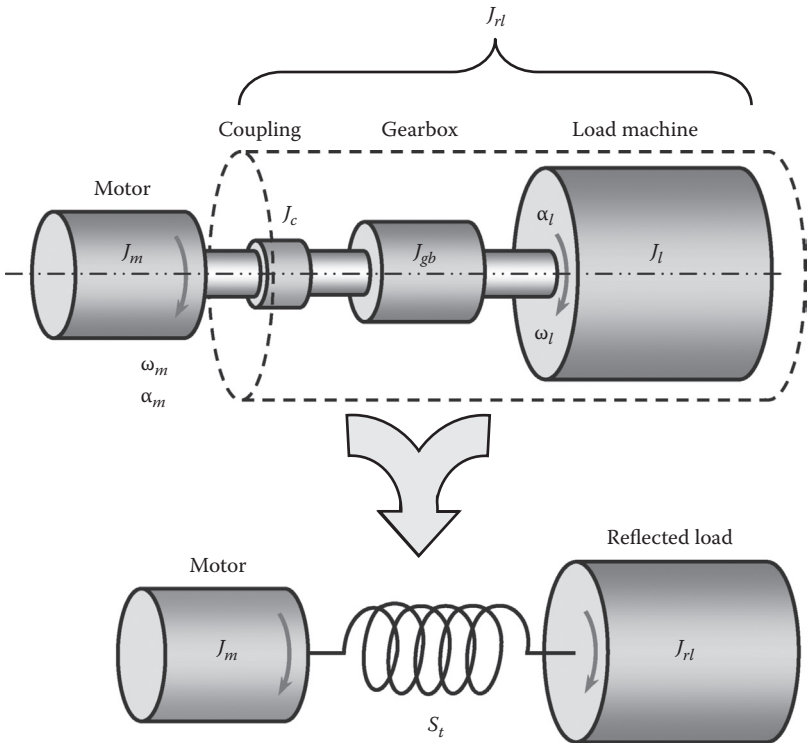

FIGURE 1.16
The equivalent motor-load model, consisting of two masses connected by a massless torsionally elastic spring.

Because the motor-load system is not rigid (i.e., the stiffness is not infinitely large), as the motor torque is applied on the system, each of these connecting components twists slightly like a torsional spring.

To calculate the resonant frequency, motor and load inertias must be distinguished from each other. As discussed previously, load inertia is the inertia of the load reflected to the motor shaft J_{rl}. It is the lumped inertia of the shaft coupling, gearbox, and driven load machine:

$$J_{rl} = J_c + J_{i,gb} + \frac{J_{o,gb} + J_l}{\gamma_g^2} \tag{1.31}$$

The total motor inertia J_m is the lumped inertia of the rotor (including the rotor core and shaft), bearing, and other rotating components:

$$J_m = J_{rotor} + J_{bearing} + \sum J_{other} \tag{1.32}$$

The effects of interference fit on the shaft stiffness can vary depending on the actual interference fit. For a very tightly fitted rotor, the rotor assembly can be viewed as one body with variable outer diameters (ODs) along its axis. Thus, the rotor core virtually increases

the shaft stiffness. On the contrary, if the rotor is loosely coupled with the driven machine, its compliance can contribute to resonance.

For a rotor with a hollow shaft, the torsional stiffness (or spring constant) at each segment is calculated as

$$S_{t,rotor,i} = \frac{\pi\left(d_{out,i}^4 - d_{in,i}^4\right)G}{32l_i} \tag{1.33}$$

where

$d_{out,i}$ and $d_{in,i}$ are the outer and inner diameter (ID) at ith segment, respectively
l_i is the length of the ith segment
G is the shear modulus of elasticity

It is noted that the stiffness of the motor shaft can be influenced by the various types of construction. In general, the machined or welded webs on the motor shaft can add significant stiffness (typically 10%–40% over the base shaft diameter stiffness), while keyed on laminations typically add minimal stiffness. A finite element analysis (FEA) has confirmed that with six welded spider arms on an IM shaft, the equivalent diameter is 7% larger than the base shaft diameter, which corresponded to a 33% increase in torsional stiffness [1.32].

Similarly, the torsional stiffness of the load system at each segment becomes

$$S_{t,oad,i} = \frac{\pi\left(d_{out,i}^4 - d_{in,i}^4\right)G}{32l_i} \tag{1.34}$$

For a solid shaft, $d_{in,i} = 0$.

Thus, the total torsional stiffness (spring constant) for the rotor and load machine are given as, respectively,

$$S_{t,rotor} = \frac{1}{\sum\left(1/S_{t,rotor,i}\right)} \tag{1.35a}$$

$$S_{t,load} = \frac{1}{\sum\left(1/S_{t,load,i}\right)} \tag{1.35b}$$

For two geared shafts with a gear ratio γ_g (where $\gamma_g = \omega_i/\omega_o$), the torsional stiffness is given as [1.33]

$$\frac{1}{S_{t,gb}} = \frac{1}{S_{t,i}} + \frac{1}{S_{t,o}/\gamma_g^2} \tag{1.36}$$

It follows that

$$S_{t,gb} = \frac{S_{t,i}S_{t,o}}{S_{t,i}\gamma_g^2 + S_{t,o}} \tag{1.37}$$

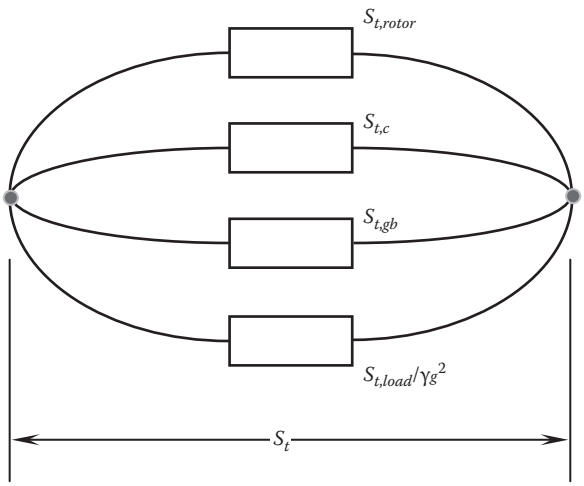

FIGURE 1.17
Taking advantage of the analogy between mechanical and electric systems to calculate the total torsional stiffness S_t.

Utilizing the analogy between the mechanical and electric systems, an electric circuit is developed for the total torsional stiffness S_t, as shown in Figure 1.17. Thus, S_t, which is measured in newton-meter per radians (N-m/rad), can be determined as

$$S_t = \frac{1}{\frac{1}{S_{t,rotor}} + \frac{1}{S_{t,c}} + \frac{1}{S_{t,gb}} + \frac{1}{S_{t,load}/\gamma_g^2}} \tag{1.38}$$

Resonant frequency (Hz) is thus calculated as

$$f_R = \frac{1}{2\pi}\sqrt{S_t\left(\frac{1}{J_m} + \frac{1}{J_{rl}}\right)} = \frac{1}{2\pi}\sqrt{\frac{S_t\left(J_m + J_{rl}\right)}{J_m J_{rl}}} \tag{1.39}$$

This shows that J_m and J_{rl} have the same effect on the resonant frequency. From this equation, it can be seen that there are four ways to increase the system resonant frequency:

- Make the motor shaft more rigid—this increases the stiffness and, in turn, increases the overall torsional stiffness S_t.
- Reduce motor inertia—this actually increases the ratio of load-to-motor inertia, but it also results in higher performance of servo system.
- Reduce reflected load inertia.
- Increase stiffness of components attached/mounted to shafts.

In a direct drive system, a direct drive rotary (DDR) motor is connected with a load without using a gearbox (Figure 1.18). The coupling inertia is considered as a part of the load

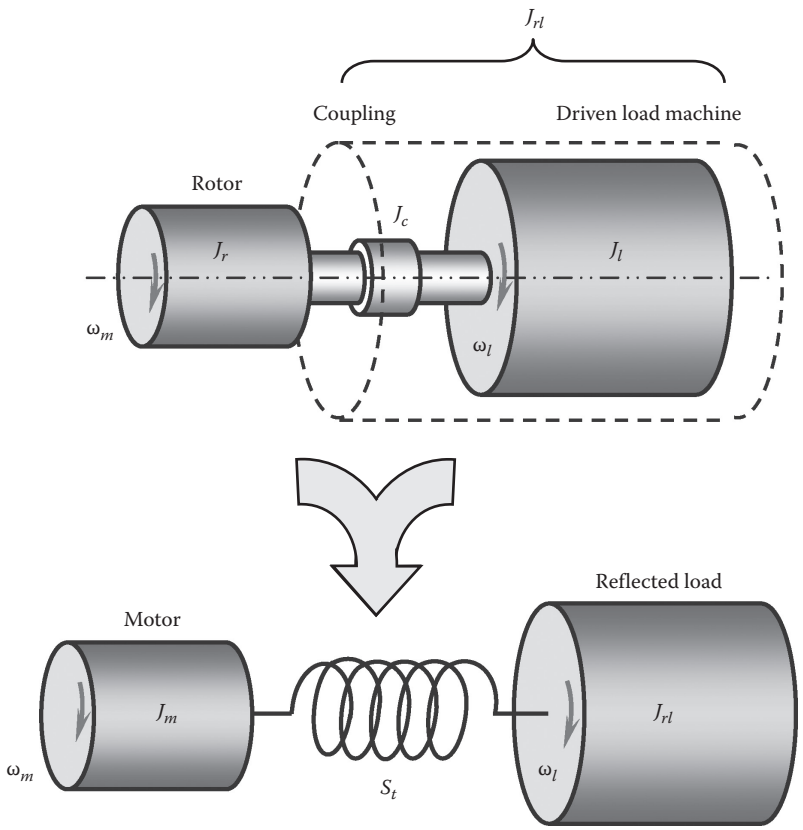

FIGURE 1.18
The equivalent motor-load model for direct drive system.

inertia. Therefore, the system model can be reduced to two lumped masses; the resonant frequency of the system is given by

$$f_R = \frac{1}{2\pi}\sqrt{\frac{S_t\left(J_m + J_{rl}\right)}{J_m J_{rl}}} = \frac{1}{2\pi}\sqrt{S_t\frac{J_m + \left(J_c + J_l\right)}{J_m\left(J_c + J_l\right)}} \tag{1.40}$$

The torsional stiffness is

$$S_t = \frac{1}{\dfrac{1}{S_{t,rotor}} + \dfrac{1}{S_{t,c}} + \dfrac{1}{S_{t,load}}} \tag{1.41}$$

For a three-mass system shown in Figure 1.19, the resonant frequencies are [1.33]

$$f_R = \frac{1}{2\pi}\sqrt{A \pm \left(A^2 - B\right)^{1/2}} \tag{1.42}$$

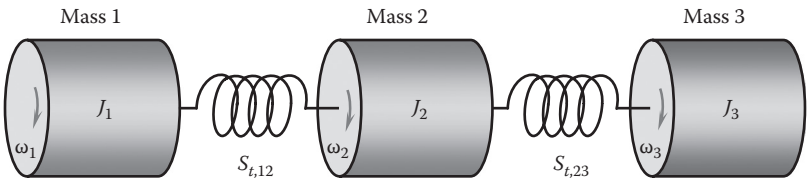

FIGURE 1.19
Three-mass system with massless torsionally elastic springs between them.

where

$$A = \frac{S_{t,12}(J_1 + J_2)}{2J_1J_2} + \frac{S_{t,23}(J_1 + J_2)}{2J_1J_2}$$

$$B = \frac{(J_1 + J_2 + J_3)S_{t,12}S_{t,23}}{J_1J_2J_3}$$

The notations $S_{t,12}$ and $S_{t,23}$ indicate that the torsional stiffness applies to the shaft between rotors 1 and 2 and rotors 2 and 3, respectively.

1.2.7 Load-to-Motor Inertia Ratio

Load-to-motor inertia ratio is defined as

$$\xi = \frac{J_l}{J_m} \tag{1.43}$$

The mismatch of the load-to-motor inertia is very important for the performance of electric motors. The importance of the inertia mismatch is relative to how responsive the system needs to be and how stiff the system is. In designing motion systems, the generally used rule of thumb is that the motor inertia should match the load inertia, that is, a ratio of 1:1 between load and motor inertia would be the ideal scenario. Regularly, the load-to-motor inertia ratio should stay within 10:1. Lower load-to-motor inertia ratios improve motor response, reduce mechanical resonance, and minimize power dissipation. An inertia mismatch of greater than 10:1 may cause motor speed oscillations (Figure 1.20), produce less than optimal response, waste power, and reduce system bandwidth.

In terms of efficiency, a 1:1 ratio between load and motor inertia provides the optimum power transfer. However, a 1:1 ratio is rarely useful in an actual application, because it requires an oversized and unnecessarily expensive motor. Furthermore, it wastes energy and may not perform to specifications [1.8]. In a typical servo system with a *stiff* coupling methodology, a load-to-motor inertial mismatch of 5:1 is generally accomplished.

However, in some cases, the inertia ratio for servomotors can be much higher than 5:1. As an example, direct drive elevator PM traction machines can have 40:1 inertia mismatches. More recently, Kollmorgen has developed a new generation of drive with digital biquadratic filters, enabling servomotors to be successfully applied to medical imaging gantry applications with high inertia mismatches up to 1000:1 [1.34]. To overcome the challenges of inertia mismatch, DDR motors, which directly couple to the load, have been developed in last two decades. DDR motors do not require a high degree of responsiveness and thus

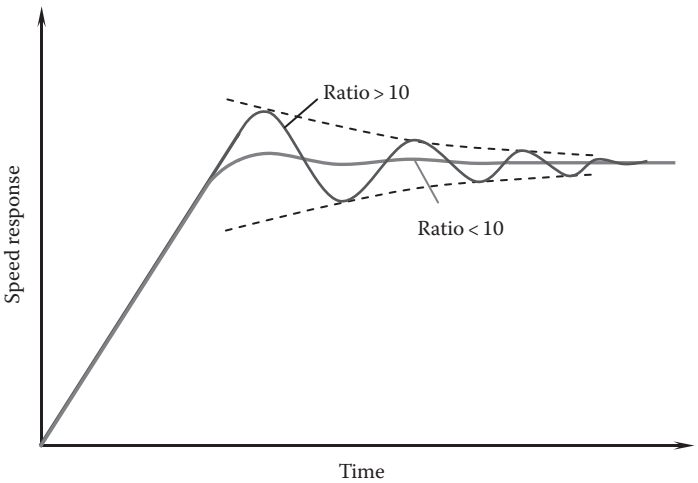

FIGURE 1.20
The effect of load-to-motor inertia ratio on motor speed response. For ratio >10, the speed response curve oscillates and asymptotically approaches to its final value in a long period of time.

significantly reduce inertia mismatch concerns. Directly coupled motors have been successfully tuned to ratios as high as 1600:1 [1.35].

Some servomotor applications require larger inertia rotors to achieve good system controllability. This is due to mass or inertia acting as mechanical filters to load disturbances. The easiest way is to attach an inertia disk or wheel to the shaft [1.36]. If possible, it is preferred to arrange the inertia disk inside the motor or have a larger diameter rotor in the same frame size. Otherwise, the inertia disk has to be arranged outside of the motor (Figure 1.21). As an example, by adding an inertia wheel or wheels to servomotors, Kollmorgen's engineers increase the motor inertia by a factor of 7. Thus, low-inertial motors that have a 14:1 inertia ratio can be changed to medium-inertia motors with a 2:1 inertia ratio. Correspondingly, the resonant frequency decreases from almost 4 times the antiresonant frequency to about 1.6 times the antiresonant frequency.

1.2.8 Duty Cycle

In the power industry, duty cycle is a measure of the fraction of time that a power device is in an active state, that is, $t_{on}/(t_{on}+t_{off})$. For electric motors, duty cycle is defined as the ratio the motor produces rated continuous power divided by the total elapsed time. In fact, duty cycle is a variation of load over a given period of time. The load variation may have a repetitive pattern or a fluctuating pattern.

Duty cycle is used to determine the acceptable level of running time so that the rated motor temperature is not exceeded. For a fixed repetitive load pattern, duty cycle is determined as the ratio of on-time to total cycle period. When operating cycle is such that electric motors operate at idle or a reduced load for more than 25% of the time, duty cycle becomes a factor in sizing electric motors. Also, energy required to start electric motors (i.e., accelerating the inertia of the electric motor as well as the driven load) is much higher than for steady-state operation, so frequent starting could overheat the electric motor.

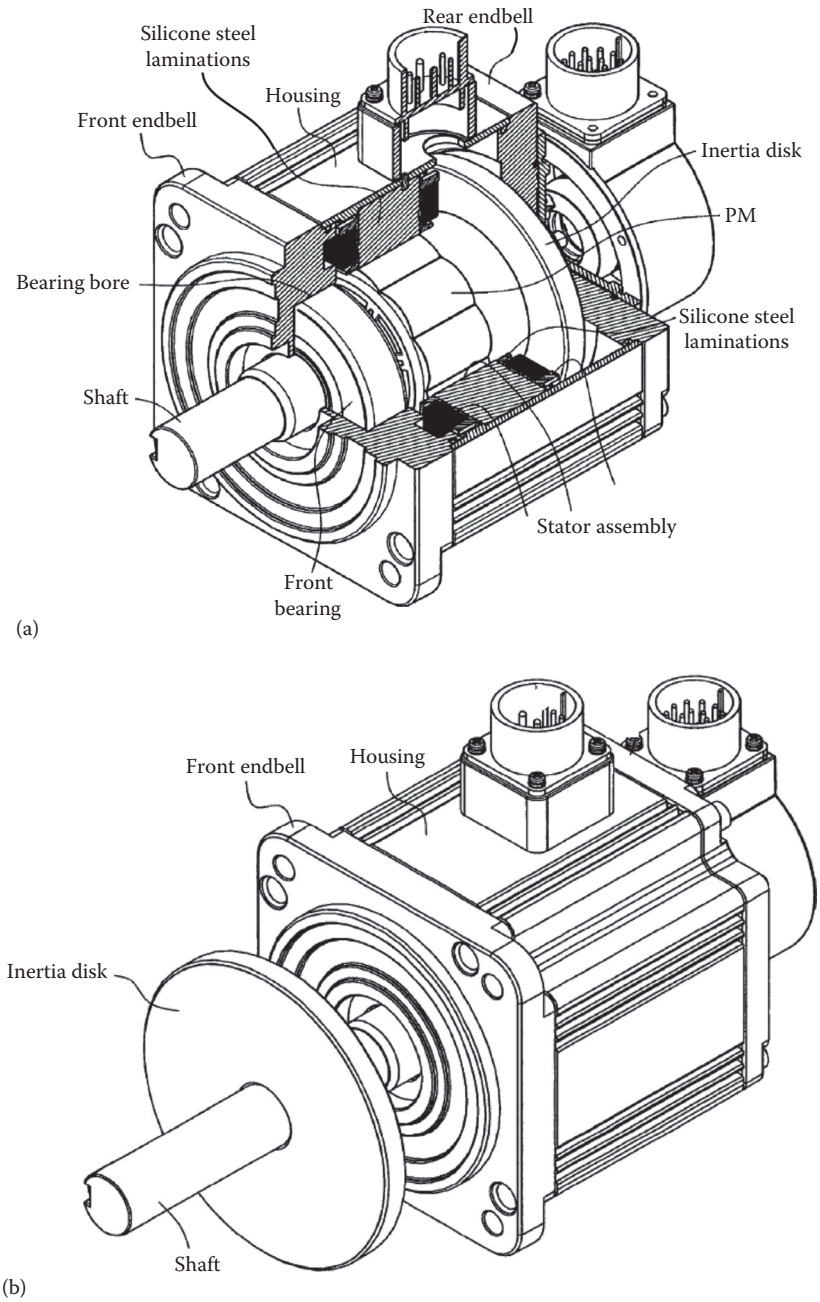

FIGURE 1.21
Addition of an inertia disk either inside (a) or outside (b) of a motor to increase the rotor inertia (U.S. Patent 7,911,095) [1.36]. (Courtesy of the U.S. Patent and Trademark Office, Alexandria, VA.)

According to the applications of electric motors, a running load on an electric motor can be either steady or variable (e.g., follows a repetitive cycle of load variation or has pulsating torque shocks). For instance, electric motors in ventilating fans or blowers run continuously over an extensive period of time with almost constant loads. By contrast, electric motors in electric vehicle systems (EVSs) have wide variations in running loads. Elevator machines have typical duties of 120, 180, and 240 starts per hour ratings but may only run at those rates for a few hours a day during heavy traffic time. The temperature variations of electric motors under different operation conditions are presented in Figure 1.22.

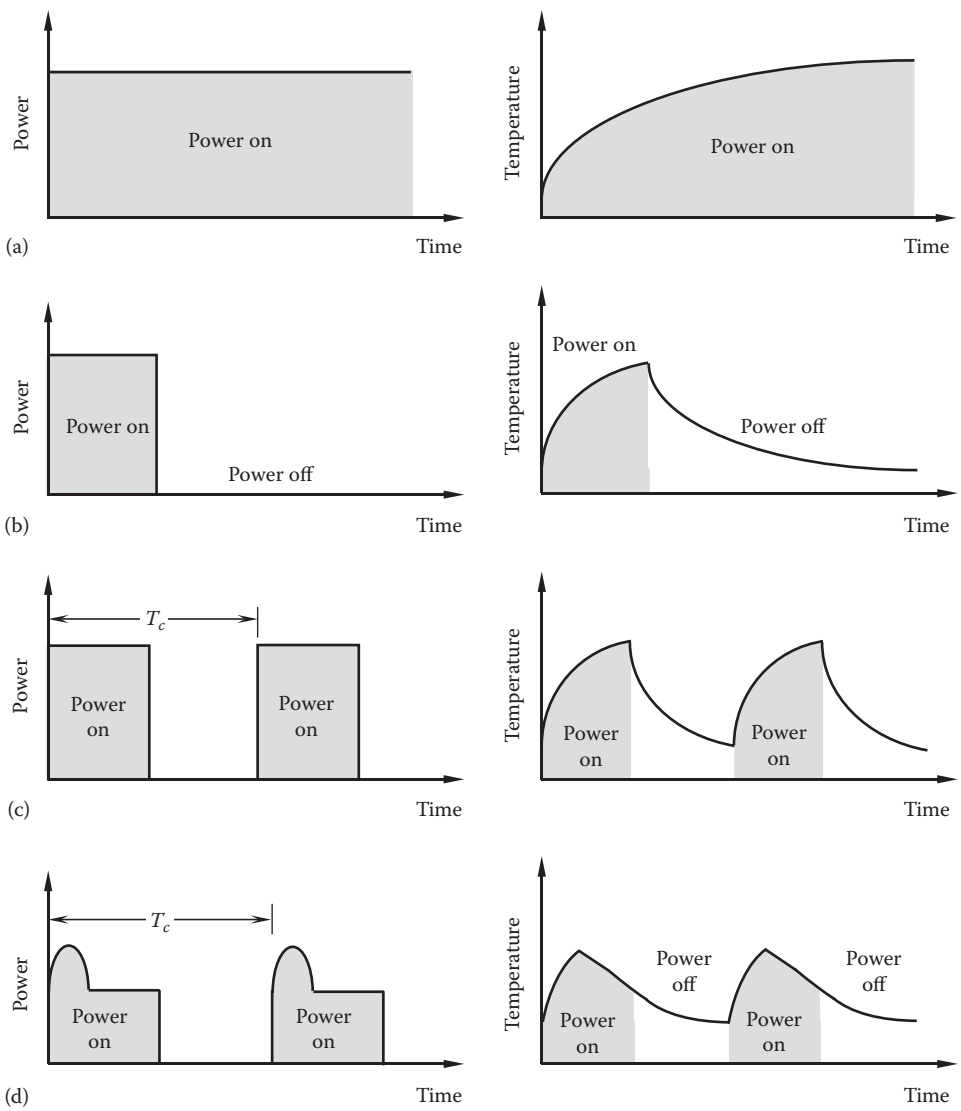

FIGURE 1.22
Temperature variations under different operation conditions: (a) S1—continuous operation; (b) S2—short time operation; (c) S3—intermittent periodic operation, where the start current has no impact on temperature rise; and (d) S4—intermittent periodic operation, where the start current has an impact on temperature rise.

TABLE 1.1

Operating Conditions of Electric Motors

Class	Motor Duty	Note
S1	Continuous duty	The motor operates at a constant load over an extensive period of time to reach temperature equilibrium.
S2	Short-time duty	The motor operates at a constant load over a period of time not sufficient to reach the thermal equilibrium. The rest periods are long enough for the motor to cool down.
S3	Intermittent periodic duty	The motor operates with repeated cycles consisting of a constant output power period followed by an off period. Temperature equilibrium is never reached. Starting current has little effect on temperature rise.
S4	Intermittent periodic duty with starting	Sequential, identical start, run, and rest cycles with constant load. Temperature equilibrium is not reached, but starting current affects temperature rise.
S5	Intermittent periodic duty with electric braking	Sequence of identical duty cycles—starting, operation, braking, and rest. Thermal equilibrium is not reached.
S6	Continuous operation with intermittent load	Sequential, identical cycles of running with constant load and running with no load. No rest periods.
S7	Continuous operation periodic duty with electric braking	Sequential identical cycles of starting, running at constant load, and electric braking. No rest periods.
S8	Continuous operation with periodic changes in load and speed	Series of identical repeating duty cycles, where within each cycle the motor operates at several different load levels and speed. There is no stopped time and thermal equilibrium is not reached.
S9	Duty with nonperiodic load and speed variations	Load and speed vary periodically within the permissible operating range. Frequent overloading may occur.
S10	Duty with discrete constant loads and speeds	Duty with discrete number of load/speed combinations, with these maintained long enough to reach thermal equilibrium.

The International Electrotechnical Commission (*IEC*) defines ten duty cycle designations to describe operation conditions of electric motors, denoted S1–S10, as shown in Table 1.1 [1.37].

1.2.9 Motor Efficiency

The fast rising energy demands all over the world and continuously increasing energy costs have created motivations for many developed and developing countries to focus on energy saving and consumption reduction. Improvements in energy efficiency are most often achieved by producing more efficient machines or adopting more advanced technologies. Because electric motors consume a significant amount of electric energy, motor manufacturers in recent years have committed to the development of more efficient electric motors to save energy.

1.2.9.1 Definition of Motor Efficiency

Motor efficiency is a measure of how effectively a motor converts electrical energy into mechanical energy. Given as a percentage, motor efficiency is defined as the ratio of the power output P_{out} to the power input P_{in}. Since the power output P_{out} represents the difference between the power input P_{in} and the variety of power losses $\sum P_{loss}$ and the

power input P_{in} represents the summation of the power output P_{out} and the variety of power losses $\sum P_{loss}$, motor efficiency can be expressed in several different forms:

$$\eta = \frac{P_{out}}{P_{in}} = \frac{P_{in} - \sum P_{loss}}{P_{in}} = \frac{P_{out}}{P_{out} + \sum P_{loss}} \tag{1.44}$$

This equation shows that in order to increase motor efficiency, it must minimize various power losses in motor, such as copper losses, iron losses, mechanical losses, and windage losses. Thus, the efficiency of electric motors can be boosted by the following [1.38]:

1. Reducing the copper losses in the motor windings. This can be done by increasing the cross-sectional area of the conductor or by improving the winding technique to reduce the winding length, especially at the end turns.
2. Using better materials for lowering eddy-current-related power losses.
3. Taking advantage of advanced nanotechnology to fabricate thinner laminations.
4. Improving the aerodynamics of motor ventilating system for reducing motor windage losses.
5. Applying more efficient cooling methods in motor cooling. (6) Improving manufacturing tolerances.

For electric motors, high efficiency and high torque density are two of the most desirable features. Today, motor efficiency is normally in the range of 80%–95%. Usually, larger motors with higher power output have higher efficiency than smaller motors. High-efficiency motors can provide significant benefits, including reductions in energy consumption and carbon emissions over their entire life cycles. Because operating costs comprise the majority of lifetime motor costs, even a 1% gain in efficiency can make a big difference to costs.

1.2.9.2 IEC Standards on Efficiency Classes of AC Electric Motors

In 2008, IEC published the standard IEC 60034-30: 2008 [1.39] on efficiency classes of AC electric motors. The scope of this standard covers almost all motors (e.g., standard, hazardous area, marine, and brake motors) but excluded motors made solely for converter operation and completely integrated into a machine:

- Single speed, three phase, and 50 and 60 Hz
- 2, 4, or 6 pole
- Rated output from 0.75 to 375 kW (1–500 hp)
- Duty type S1 (continuous duty) or S3 (intermittent periodic duty) with a rated cyclic duration factor of 80% or higher

This standard defines the requirements for the efficiency classes and aims to create a basis for international consistency. The international efficiency (IE) classes IE1, IE2, and IE3 defined in this standard are based on test methods specified in IEC 60034-2-1 [1.40]. It is noted that the methods with this standard determine efficiency values more accurately than the methods previously used.

TABLE 1.2

Electric Motor Efficiency Level, Class, Testing Standard, and Regulation over Time

Efficiency Level	Efficiency Class Standard	Test Standard	Regulation over Time
Standard efficiency	IE1 IEC 60034-30	IEC 60034-2-1 Medium uncertainty	China Taiwan 2003 Switzerland 2010
High efficiency	IE2 IEC 60034-30	IEC 60034-2-1	Australia 2006 Brazil 2009 Canada 1997 China 2009 Europe 2011 Korea 2008 Switzerland 2011
Premier efficiency	IE3 IEC 60034-30	IEC 60034-2-1 Low uncertainty	Europe 2015–2017 United States 2011
Super premier efficiency	IE4 IEC 60034-31		

In order to promote a competitive motor market transformation, a new international standard IEC 60034-31 [1.41] was released in 2010 for the addition of the IE4 motor efficiency level. Since no sufficient market and technological information is available to allow IE4 standardization, this efficiency class is intended to be informative. It is expected that advanced technologies will be developed in the near future that can enable manufacturers to design motors for the IE4 class efficiency levels, while maintaining motor dimensions compatible with the existing motors having lower efficiency classes. The four electric motor efficiency classes, testing standards, and regulation over time are listed in Table 1.2.

A rated efficiency of a motor is a function of its rated output. The comparisons of the efficiencies for all four efficiency classes (IE1, IE2, IE3, and IE4) are presented in Figures 1.23 and 1.24 for 50 Hz and 60 Hz electric motors, respectively.

Furthermore, the comparison of four efficiency classes for 50 Hz and 4-pole motors is given in Figure 1.25.

1.2.10 Motor Insulation

The maximum operating temperature of a motor depends on the selection of motor insulation. As the maximum temperature is determined, the maximum motor load, typically specified as the amount of power the motor can deliver on a continuous basis, can be also determined. Thus, motor insulation needs to be defined at the motor's conceptual design stage.

According to the maximum allowable operating temperature that insulation systems can withstand, electric insulation can be categorized into several classes, characterizing the capability of the insulator to resist aging and failures due to overheating. During motor operation, an insulation material may gradually lose its insulating ability to perform the task. The lifetime of insulation materials depends on thermal, chemical, electrical, and mechanical factors. Among them, thermal and electrical stresses are most important.

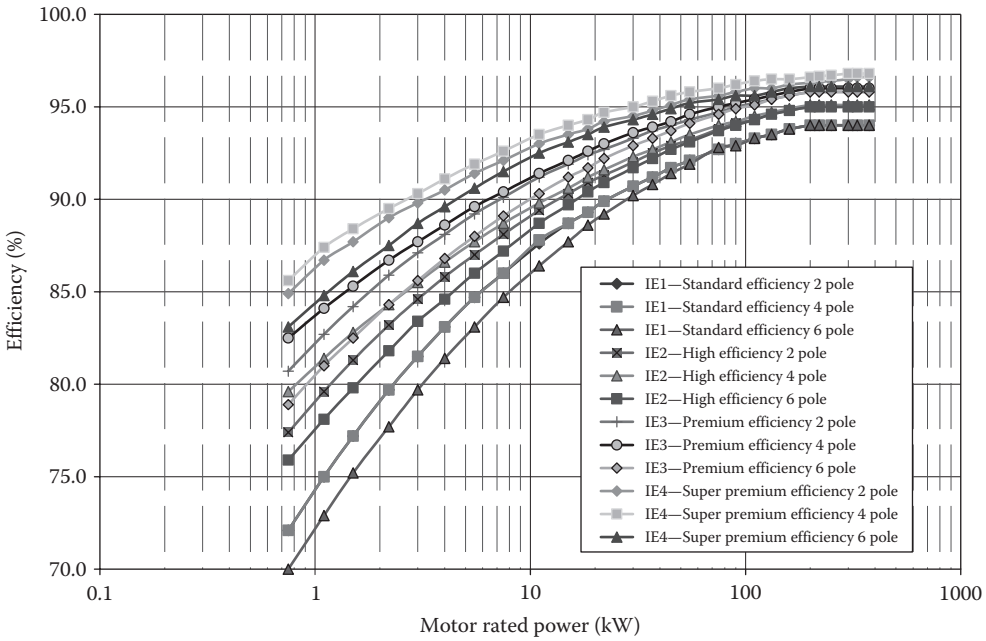

FIGURE 1.23
Comparison of four efficiency classes for electric AC motors with 50 Hz.

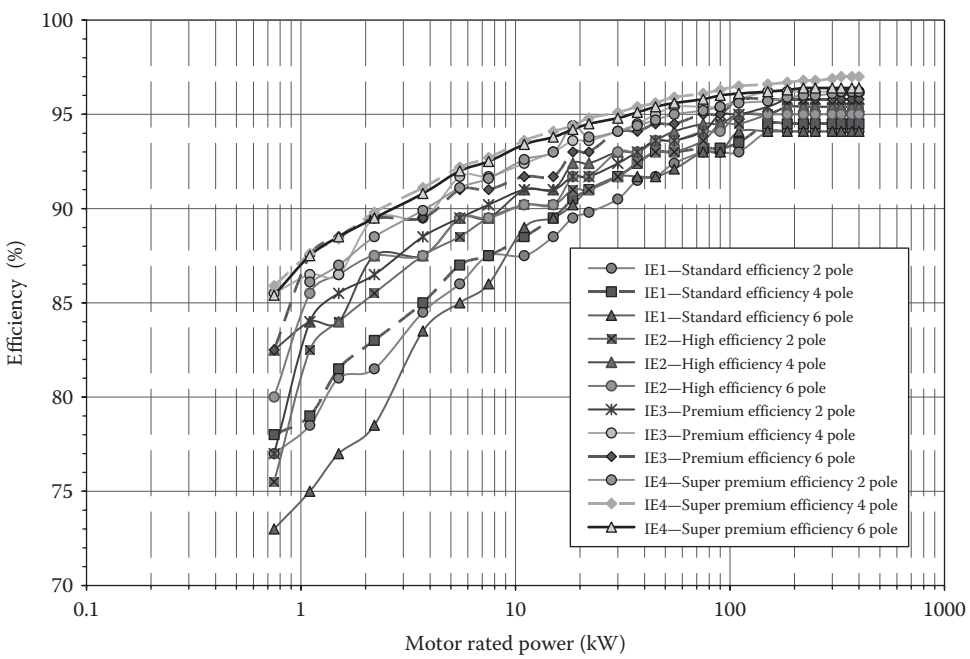

FIGURE 1.24
Comparison of four efficiency classes for electric AC motors with 60 Hz.

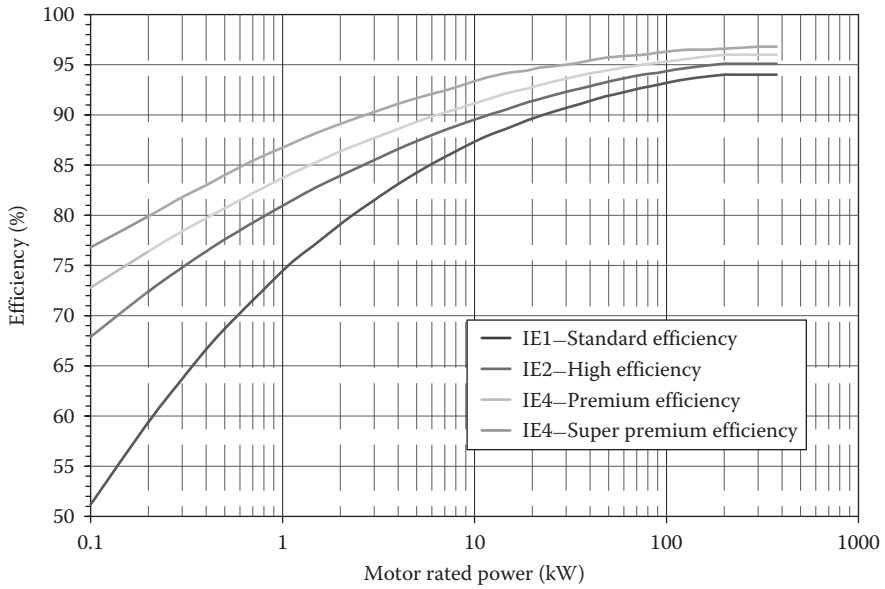

FIGURE 1.25
Comparison of four efficiency classes for 50 Hz, 4 pole electric motors.

In fact, dielectric strength of insulation is very sensitive to temperature aging. Average insulation lifetime decreases rapidly with the increase in motor internal temperatures. A generally accepted rule of thumb is that each 10°C rise above the rating temperature may reduce the motor lifetime by one-half.

There are generally five specialized insulation elements used in an electric motor, including turn-to-turn insulation between separate wires in each coil, phase-to-phase insulation between adjacent coils in different phase groups, phase-to-ground insulation between windings and the electrical ground, slot wedge to hold conductors firmly in the slot, and impregnation to bring all the other components together and fill in the air space.

Dielectric strength refers to the maximum electric field (in V/m in the SI system, and V/mil in English system, where 1 mil = 0.001 in.) that a material can withstand without breaking down and losing its insulating capabilities. The dielectric strength of a material depends on the specimen thickness, the electrode shape, the rate of the applied voltage increase, the shape of the voltage–time curve, and the medium surrounding the sample (e.g., air, gas, or liquid). It should be noted that in strong electric fields, Ohm's law does not hold for insulation materials that have extremely high electric resistance. The current density increases almost exponentially with the electric field, and at a certain value, the current jumps to very high magnitudes at which a specimen of the material is destroyed [1.42].

Dielectric strength values of some solid insulation materials at room temperature and normal atmospheric pressure are presented in Table 1.3.

Based on an average 20,000 h lifetime, the maximum allowable temperature and insulation materials for each insulation class are listed in Table 1.4. The motor classification is based on the temperature rating of the lowest-rated component in the motor.

Thermal aging is an irreversible, permanent reduction of material properties, defined as deterioration. Many of the insulation failures can be attributed to the fact that the

TABLE 1.3

Dielectric Strength of Some Solid Insulation Materials

Insulation Material	Dielectric Strength ($V/m \times 10^6$)	Reference
Ceramics		
• Porcelain	35–160	[1.43]
• Titanates of Mg, Ca, Sr, Ba, and Pb	20–120	[1.44]
Glasses		
• Fused silica, SiO_2	470–670	[1.43]
• Alkali–silicate glass	200	
Insulating films and tapes		
• Low-density polyethylene film	300	[1.45]
• Poly-*p*-xylylene film	410–590	[1.46]
• Aromatic polymer films		[1.47]
– Kapton H (DuPont)	389–430	
– Ultem	437–565	
– Hostaphan	338–447	
– Amorphous Stabar K2000 (ICI film)	404–422	
– Stabar S100 (ICI film)	353–452	
• Polyetherimide film (26 μm)	486	[1.48]
• Parylene N/D (25 μm) film	275	[1.49]
• Cellulose acetate film	157	[1.49]
• Cellulose triacetate film	157	[1.49]
• Polytetrafluoroethylene film	87–173	[1.49]
• Fluorinated ethylene-propylene copolymer film	157–197	[1.49]
• Ethylene-tetrafluoroethylene film	197	[1.49]
• Ethylene-chlorotrifluoroethylene copolymer film	197	[1.49]
• Polychlorotrifluoroethylene film	197	[1.49]
	118–153.5	[1.49]
Micas		
• Muscovite, ruby, natural	118	
• Phlogopite, amber, natural	118	[1.49]
• Fluorophlogopite, synthetic	118	
Potassium bromide, KBr, crystalline	80	[1.43]
Sodium chloride, NaCl, crystalline	150	[1.43]
Varnish		
• Vacuum-pressure-impregnated baking-type solventless varnish	79.9	
• Epoxy baking-type varnish	90.6	
– Solventless, rigid, low viscosity, one part	82.7	
– Solventless, semiflexible, one part	106.3	[1.49]
– Solventless, semirigid, chemical resistant	181.1	
– Solvable, for hermetic electric motors		
• Polyurethane coating—clear conformal, fast cre	78.7	
– Standard conditions	47.2	
– Immersion conditions		

TABLE 1.3 (continued)

Dielectric Strength of Some Solid Insulation Materials

Insulation Material	Dielectric Strength (V/m × 10^6)	Reference
Various insulations		
• Natural rubber	100–215	[1.43]
• Silicon rubber	26–36	[1.44]
• Aramid paper, calendered	28.7	[1.44]
• Aramid with mica	39.4	[1.44]

TABLE 1.4

Standard Insulation Classes

Insulation NEMA Class [1.50]	Maximum Temperature Rating (°C)	Insulation Materials
Class A	105	Cotton, silk, paper, synthetic fibers, vinyl acetate
Class E[a]	120	Polyurethane, epoxy resins, polyethylene terephthalate, phenolics, alkyds, leatheroid
Class B	130	Shellac, bitumen, silk, mica, polyesters
Class F	155	Epoxy, polyamides, silicone, mica, glass
Class H	180	Silicone elastomers, epoxy, polymides, silicone, mica, glass
Class N	200	Glass fibers, mica, asbestos, Teflon
Class R	220	Glass, silicone, mica, Nomex, Teflon

[a] IEC 60085 Thermal class [1.51].

operation temperature exceeds the temperature limits of insulation materials. In fact, temperature has a strong impact on the lifetime of insulations. As the temperature rises above the normal operating temperature, the lifetime of insulation can be quickly shortened (Figure 1.26). This phenomenon is called thermal aging. As discussed by Bonnett and Soukup [1.52], the increase in temperature may have resulted from various causes, including the following: (1) voltage variation or unbalance (per Bonnett and Soukup, 3.5% voltage unbalance per phase will lead to an increase of winding temperature of 25% in the phase with the highest current), (2) frequent motor starts and stops, (3) improper motor cooling, (4) severe environmental conditions such as high ambient temperature, and (5) motor operation under overloading conditions.

In many motor manufacturers, the reference ambient temperature T_a is assumed to be 40°C. The temperature rise of a motor is referred to as the difference between the measured temperature of the motor winding and the ambient temperature, that is, $\Delta T = T_w - T_a$. However, the standard method of measuring the winding temperature involves taking the ohmic resistance of the winding. This provides the average temperature of the whole winding, including the motor leads, end turns, and wires deep inside the stator slots. Therefore, to reflect the temperature difference within the winding, a so-called hot spot allowance must be added to adjust the allowable temperature rise. The hop spot allowance T_{hs} is usually assumed to be 5°C–15°C, depending on the insulation class. For a specific insulation class, the allowable temperature rise of a motor is determined for preventing motor overheating under all loading conditions (no load, full load, locked rotor, etc.):

$$\Delta T = T_{\max} - (T_a + T_{hs}) \tag{1.45}$$

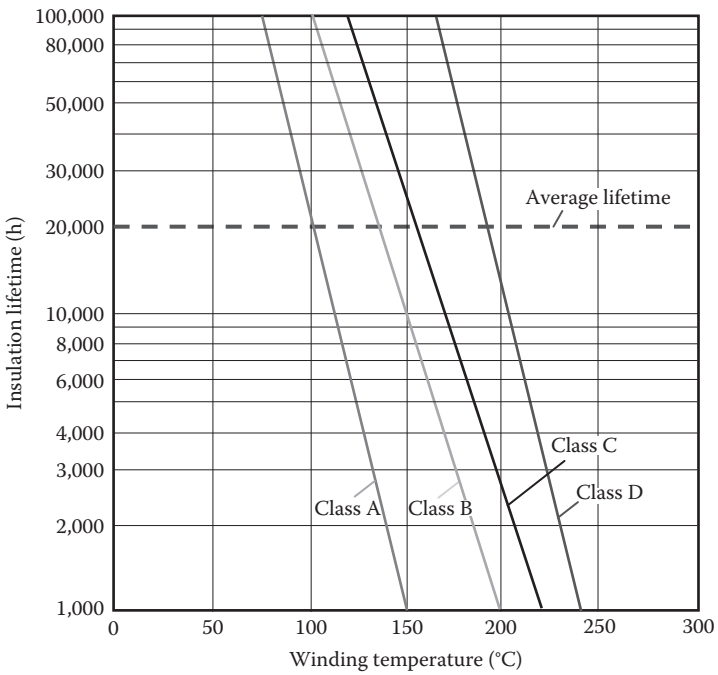

FIGURE 1.26
Thermal aging effect on lifetime of different insulation classes.

1.2.11 Motor Operation Reliability

Motor operation reliability and testing are two key components for design optimization and safe operation of motors. Motor reliability is the measure of the chance that the motor can operate normally over a period of time without failure. In the motor industry, one of the useful parameters is the mean time between failures, defined as the reciprocal of the failure rate (identified as $\ddot{e}$).

Two failure modes dominate the life of motors: bearing failures and winding failures. In all motor failures, bearing failures account the majority. Winding failures generally occur in the early stage of motor running and are attributed to shorts and grounds resulted from assembly quality rather than the long-term insulation degradation. By utilizing more than 2000 actual failure cases of fractional horsepower motors in the existed data failure bank, Wilson and Smith [1.53] developed a mathematical reliability model for each failure mode by means of Weibull cumulative distribution function and regression technique for use in predicting overall motor life and failure rates.

1.3 Classifications of Electric Motors

Electric motors can be classified in a variety of ways according to their operating characteristics, such as the source of electric power, type of rotor winding, type of motion, control pattern, the magnetic flux orientation, structure topology, power rating, and the cooling methods. A brief classification of rotary electric motors is given in Figure 1.27.

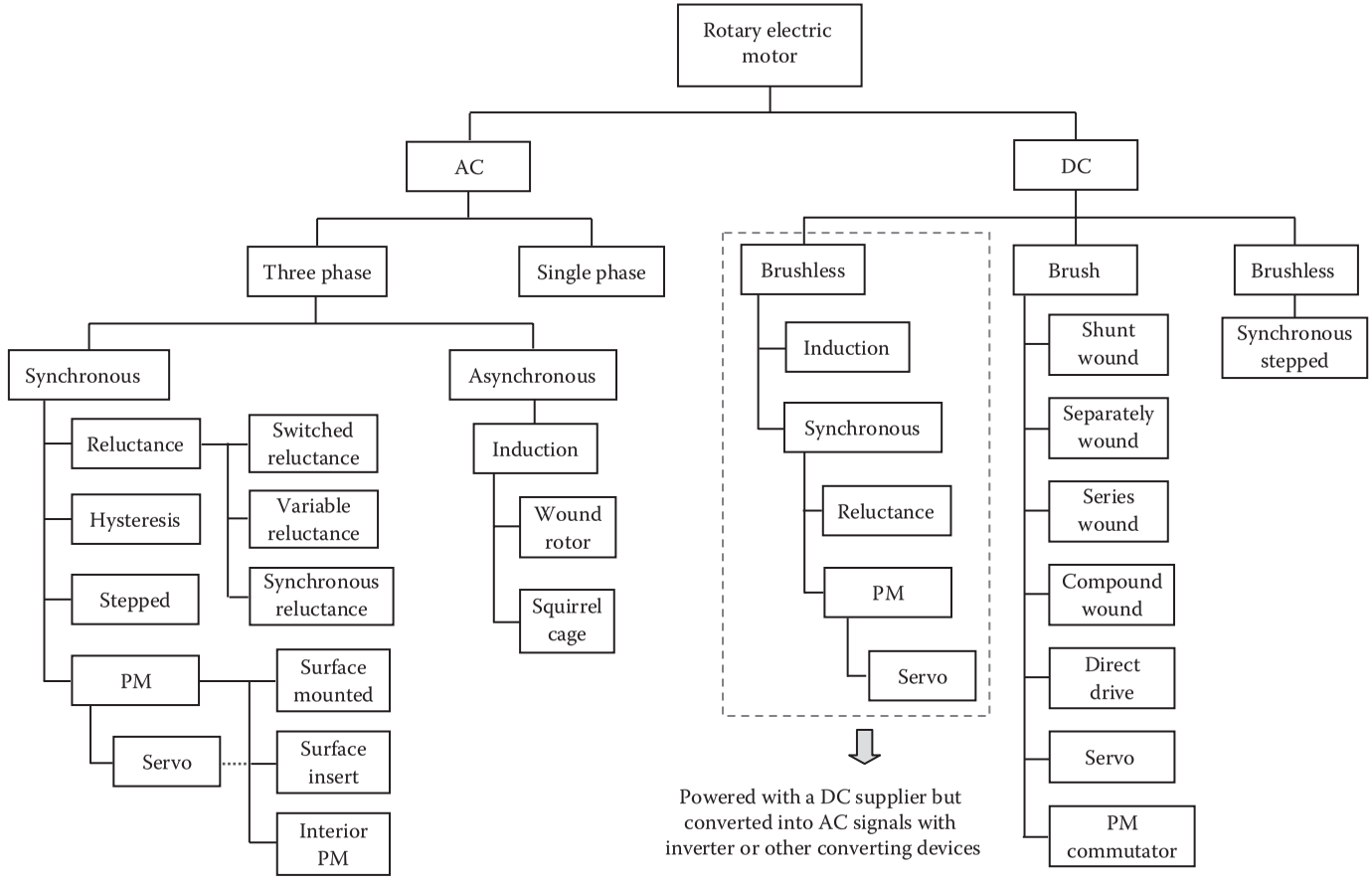

FIGURE 1.27
The classification of rotary electric motors.

1.3.1 DC and AC Motors

DC motors are designed to run on DC power. This type of motors was invented much earlier than the type of AC motors. They are often used when high torque at low speed is required. The speed adjustments of DC motors can be as much as 20:1, and they can operate at 5%–7% of the motor's base speed (some can even operate at 0 rpm) [1.54]. There are a number of different types of DC motors:

- Shunt wound motor—In this motor, the rotor and stator windings are connected in parallel. Hence, the current in the rotor and stator windings are independent of one another. The characteristics of a shunt motor provide it very good speed regulation.
- Separately excited motor—In this motor, the rotor and stator winding are connected with different power suppliers. For a long time, it has been the most common configuration used in industrial applications for DC motors with electronic speed control. Due to their excellent controllability and simple operational performance, separately excited motors are extensively used in speed or position control systems.
- Series motor—As its name indicates, the rotor and stator windings in a series motor are connected in series. The torque is proportional to I^2 so it gives the highest torque per current ratio over all other DC wound field motors at economical costs. It is therefore used in starter motors of cars and some old generation elevator motors [1.55].
- Compound motor—As the combination of the series motor and the shunt motor, the motor has the torque characteristics of the series motor and the regulated speed characteristics of the shunt motor. A compound motor comprises an armature winding on the rotor and two field windings on the stator. The stator is connected to the rotor through a compound of shunt and series windings. Compound motors are often adopted to drive loads such as shears, presses, and reciprocating machines.
- Brushed DC PM field motors—Field windings are now replaced by PM materials and the winding has a series of commutator bars with carbon brushes arranged to provide mechanical commutation of the motor. Commutation is the switching of the current direction in the winding at the right timing to produce continuous torque vectors in one direction for continuous rotating speeds of the shaft.
- Universal motors with brushes and commutators have been designed to operate on either AC or DC power. For this type of motor, the stator's windings are connected in series with the rotor windings through a commutator. The advantages of universal motors are high starting torque, compact size, and ability to run at high operating speed. The negative aspects include the short lifetime caused by the commutator and brushes and high noise and vibration. Therefore, this type of motor is often used in applications where the motor only operates intermittently. Universal motors generally run at high speeds, making them suitable in home appliances (e.g., vacuum cleaners and food mixers) and home power tools (e.g., electric drills) where single-phase wall plug in power is abundant.
- Brushless DC motor—This special type of motors has been developed to overcome the limitations and drawbacks of brushed DC motors. Practically, brushless motors are powered by a DC electric source via an integrated inverter/switching power supply, which produces an AC electric signal to drive/commutate the motor. It usually requires sensors and electronic control system for controlling the

inverter output amplitude, waveform, and frequency. Though a number of brushless motors are available (e.g., induction, switched reluctance), typical brushless motors are made with PMs. With built-in PM, the motor does not need a separate excitation winding, resulting in reduced power losses and increased efficiency. The size of the PMDC motor is the smallest (high power density) among all other DC motors. Often, PMDC motors are served as servomotors.

Advantages of brushed DC motors include low initial cost, high reliability, and simple speed and torque control characteristics. Brushless DC motors have evolved from brush DC motors as power electronic devices and became available to provide electronic commutation in place of the mechanical commutation provided by brushes. Brushless motors have increased reliability, longer lifetime, higher efficiency, less maintenance, reduced noise, elimination of ionizing sparks from commutator, and overall reduction of electromagnetic interference.

Today, DC motors are still used in a wide range of applications, especially for those applications requiring precise speed control over a large range around the rated speed, such as steel mills, mines, and electric trains. However, DC motors usually require additional operational elements such as brushes and commutators that transfer electric power to motor armatures. However, commutators usually can cause power ripples and limit the rotor speed and brushes increase the frictional power lower and radiofrequency interference. Furthermore, as brushes wear and tear, carbon dust spreads throughout the motor, causing some operation and performance problems. As a consequence, the maintenance of the interface between the brush and commutator becomes critical for motor operation reliability. In addition, the use of brushed can enhance the motor acoustic noise.

AC motors are driven by AC power sources. By eliminating commutators and brushes, AC motors offer several advantages over DC motors, including increased operation reliability, longer lifetime, higher efficiency, less maintenance, reduced cost, shorter frame size, and simpler motor structure. AC motors are dominant in industrial motion control for cost/performance reasons. As the most common type, single-phase AC motors are mainly used for residential and commercial applications. Three-phase AC motors are especially suitable for high-power applications. In general, single-phase motors operate less efficiently than three-phase motors.

Brushless DC motors are similar to AC synchronous motors. The major difference is that the waveform used to drive AC motors is typically sinusoidal and could come directly from an AC source or could be using the pulse-width modulation (PWM) technique. Therefore, AC synchronous motors develop a sinusoidal back EMF, as compared to a rectangular or trapezoidal back EMF for brushless DC motors.

Motors used in hospital equipment or other patient-care facilities are required to comply with low noise level standards to endorse patient comfort and reduce anxiety. Brushless DC motors are ideal for noise-sensitive environments due to the lack of brushes, which emit audible noise during rotation [1.56].

The disadvantages of AC motors include difficulty of speed control, high control complexity, less torque density, inability for operating at low speeds, induced eddy current and hysteresis power losses in the stator and rotor cores, high cost, and poor positioning control.

1.3.2 Single-Phase and Three-Phase Motors

In most countries, household power is usually single phase due to the low cost of single-phase power distribution. A single-phase motor is run from an AC single-phase power

system. The most standard frequencies of single-phase power systems are either 50 or 60 Hz, although other frequencies may be also available. However, unlike three-phase motors, a single-phase motor is unable to produce the start torque itself; it must be started by some external means such as an auxiliary start winding or a start capacitor. Single-phase motors need some other forcing functions to set direction of rotation (DIR). The auxiliary start winding or start capacitor creates a simulated phase to set the DIR.

Three-phase power is a common form of electric power due to its inherent benefits in high-powered transmission and electric equipment operation. In a three-phase power system, ACs are carried by three circuit conductors with the same frequency and amplitude but different phases. As sinusoidal functions of time, the current at each conductor has shifted 120° in phase from each other. Correspondingly, in a three-phase motor, there are also three windings (separated equally in space by 120°) per pole on stator to produce a rotating magnetic field.

Because of higher efficiencies and favorable torque–current characteristics versus single-phase motors, the three-phase AC motors dominate in almost all industries and consume more than half of all the electricity used in industry. In contrast, three-phase motors are more efficient and compact than single-phase motors of comparable power rating. Three-phase motors have generally lower vibrations and last longer than single-phase motors under the same conditions. As a matter of fact, the effectiveness and low cost of three-phase motors are major reasons for three-phase power to be extensively used in industry.

1.3.3 Induction and Permanent Magnet Motors

Depending upon the method of generation of the magnetic field in the rotor, an AC motor can be classified either a PM AC motor, where the magnetic field of the rotor is directly produced by PMs, or an IM, where the magnetic field of the rotor is produced though the induction effect onto the rotor bars/winding.

In an IM, the AC power supply is connected to the stator winding to generate a rotating magnetic field. Because of this rotating field, the rotor is powered by means of electromagnetic induction. The change in magnetic flux through the rotor induces AC in rotor windings and in turn creates its own magnetic field. The induced current in the rotor gives rise to magnetic forces, which cause the rotor to rotate in the direction defined by the stator rotating magnetic field. In actual operation, the rotor speed always lags the magnetic field speed, which is defined as the synchronous speed, allowing the rotor windings or conducting bars to cut magnetic lines of force and produce useful torque.

According to the rotor structure, IMs can be further divided into two subcategories: (1) squirrel cage motors in which the rotor is made of conductive aluminum/copper bars that are parallel (or have a small skew angle) to the rotor centerline and short-circuited by the end rings (Figure 1.28) and (2) wound rotor motors where windings are made on the rotors (Figure 1.29).

IMs are perhaps the simplest and most rugged motors, which have been extensively used in a variety of applications, from household appliances to heavy industrial equipment, due to their simple structures and low costs. In modern squirrel cage IMs, the conducting bars are formed in the skewed slots distributed axially along the rotor surface by casting. These conducting bars are connected at the ends of the rotor slots as the end rings to form the closed electric circuit.

For IMs, the stator operates with the power supply frequency f ($f=60$ Hz in North America and $f=50$ Hz in most countries of the world) and the rotor winding contains

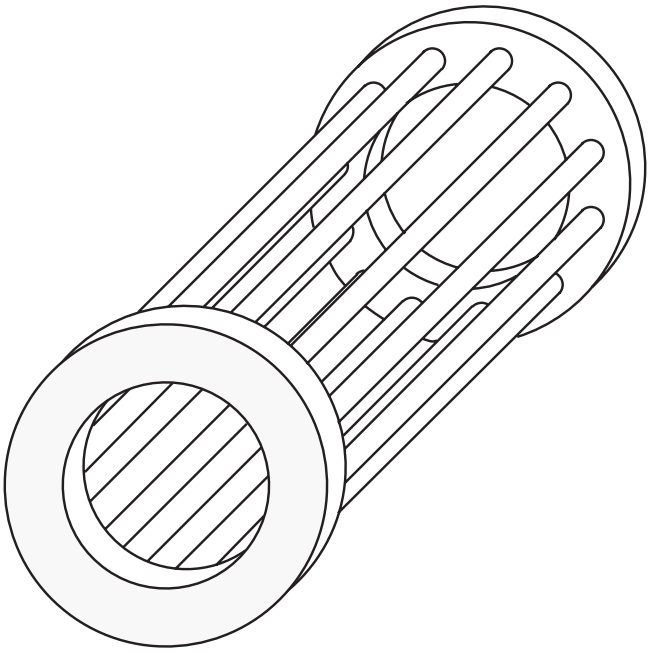

FIGURE 1.28
Conductive bars and end rings in a squirrel cage motor with closed slots.

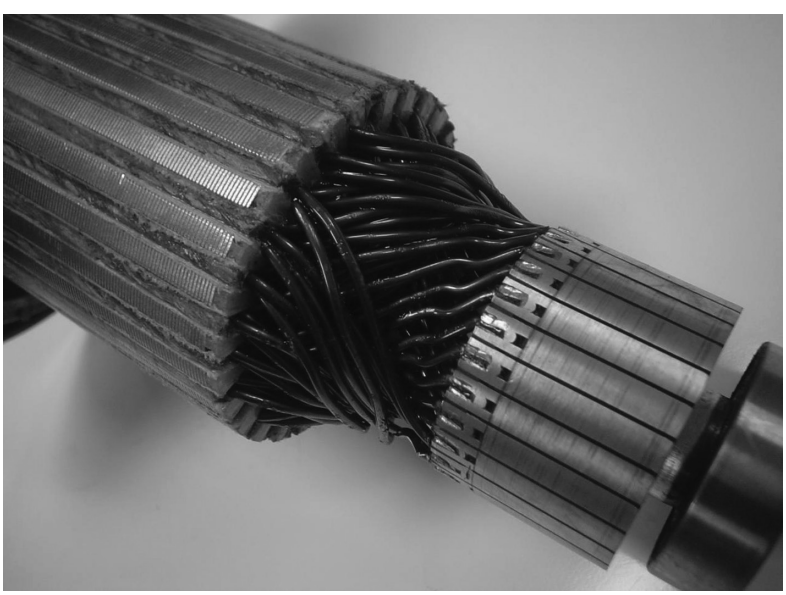

FIGURE 1.29
Rotor winding in a wound IM.

current and voltage with slip frequency f_{slip} or sf, where f_{slip} is defined as the frequency corresponding to the slip speed $n_{slip} = (n_s - n_r)$.

A low rotor resistance will result in the current being controlled by the inductive component of the circuit, yielding a high out-of-phase current and a low torque.

PMMs use permanent magnets to generate the required magnetic field and thus separated excitation windings are no longer required. A permanently excited synchronous motor has a sinusoidal back EMF and therefore operates with a sinusoidal voltage. PMMs are designed to provide a wide operation speed and load range with high motor efficiency, usually in excess of 90% from less than 50% speed driving a typical pump or compressor load to a peak range in excess of 97% for high-speed applications [1.57]. The structure of a PMM is shown in Figure 1.30.

PMMs have numerous advantages over IMs. First, the built-in PMs in a PMM eliminate rotor windings that are required in an IM. Hence, it greatly reduces the rotor inertia and power losses and, consequently, increases operational reliability and improves dynamic load response. Second, since the stator current in a PMM is only for torque production and thus magnetizing current through the stator is no longer necessary, a PMM operates at a higher power factor and thus a higher efficiency over an IM for the same power output. Third, the application of rare-earth PMs makes PMMs with high power density and high torque-to-inertia ratio, which lead to fast dynamic response capability. As a matter of fact, rare-earth PMMs have the highest power density of any motor type. This feature is especially desirable for applications in which the motor size is a main consideration. Today, PMMs have become increasingly popular in various industrial and commercial sectors. They are especially ideal in high-accuracy, high-performance motion control applications, for instance, computer numerical control (CNC) machine tools, robots, embedded motion, engraving machines, packaging and printing machines, semiconductor fabrication facilities, medical equipment, and satellite servo systems.

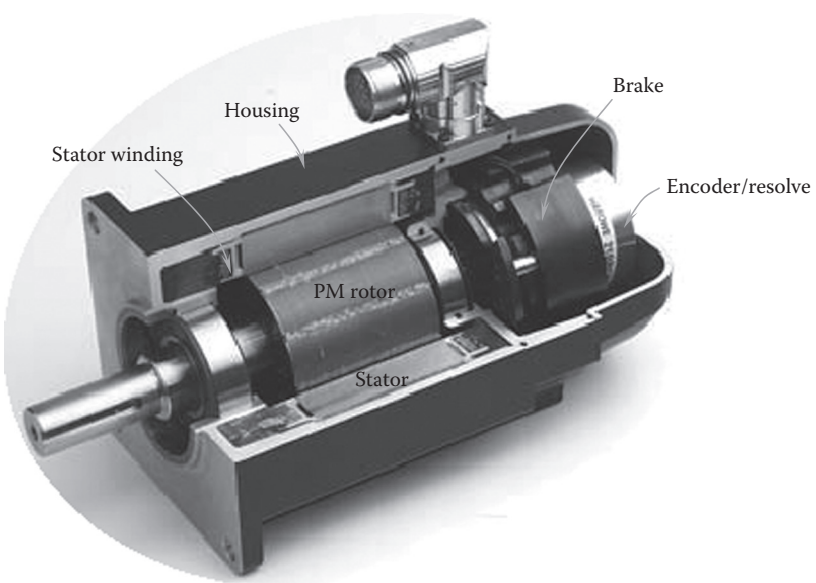

FIGURE 1.30
The typical structure of a PMM. (Courtesy of Kollmorgen Corporation, Radford, VA.)

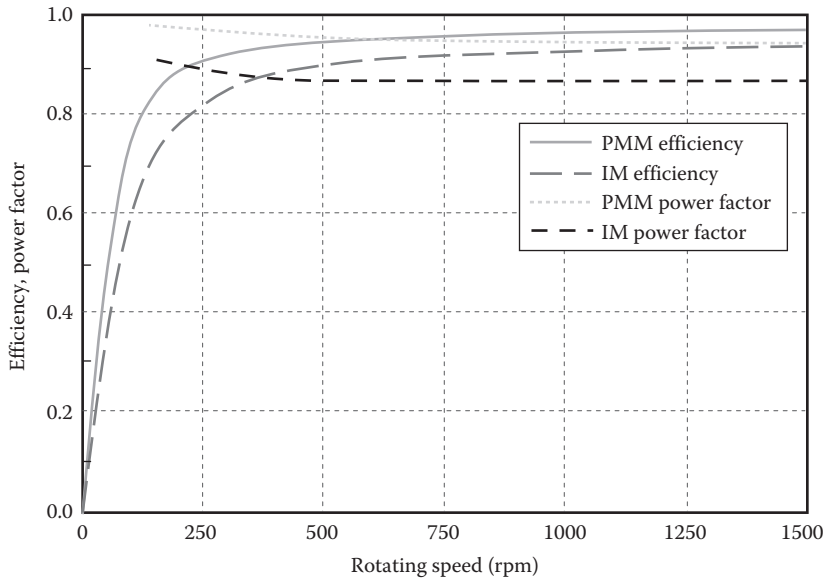

FIGURE 1.31
Comparison of calculated motor efficiency and power factor between a 55 kW, 1500 rpm IM and a PMM under an identical operation condition.

The comparison of motor efficiency and power factor between a 55 kW, 1500 rpm IM and a PMM under an identical operation condition and power rating is given in Figure 1.31 [1.58].

According to the mounting pattern of PMs, PMMs can be further divided as surface mounted, surface insert, core insert, and pole shoe. Surface-mounted PM (SPM) motors have dominated for decades. In recent years, some emerging markets and perhaps the sharp price rise of rare-earth magnets have boosted demand for IPM motors. With advantages such as high-speed performance, robust mechanical structure, low heat generation in rotor, and special designs that can support near-constant power over a broad range of speed, IPM motors provide an excellent solution for applications like traction motors, machine tools, or high-speed rotors.

In the surface-insert method, PMs are buried inside the rotor core. This method can offer some distinct advantages, for instance, the simple and robust rotor structure, high torque density, easy-to-achieve flux-weakening operation, and potentiality of fully sensorless operation [1.59].

Torque produced by an IPM motor is based on two different mechanisms [1.60]: one is the same as an SPM motor; PM torque is generated by the magnetic flux linkage between the PM rotor field and the electromagnetic field of the stator. Another is known as reluctance torque. PMs buried inside a rotor pole piece exhibit high reluctance directly along the magnetic axis due to the low permeability of the PMs and pole pieces between the magnetic poles or magnet barriers, creating inductance saliency and reluctance torque. Thus, IPM motor designs augment PM torque with reluctance torque. As a result, the magnets used in IPM motors can be thinner, achieving significant cost reductions.

1.3.4 Synchronous and Asynchronous Motors

A synchronous motor refers to a three-phase AC motor in which the rotor runs at the same speed of the rotating magnetic field of the stator. The synchronous speed n_s can be expressed in different ways, depending on the unit it adopted:

$$n_s = \frac{f}{p} \quad \text{in rps (Hz)} \tag{1.46a}$$

$$n_s = \frac{60f}{p} \quad \text{in rpm} \tag{1.46b}$$

where
f is the frequency of the AC supply current in Hz
p is the number of magnetic pole pairs per phase

The synchronous speeds of 50 and 60 Hz machines are presented in Figure 1.32 for various magnetic pole pairs.

If N denotes the number of magnetic poles per phase, then it gives that $N = 2p$ and yields

$$n_s = \frac{120f}{N} \quad \text{in rpm} \tag{1.47}$$

Therefore, synchronous speed can be altered by changing either the frequency applied to the motor or the number of magnetic poles. Some multispeed motors adopted external connections that enable to switch the stator poles, for example, from 4 to 6 poles. By using an adjustable frequency drive, motor speed can vary in a large speed range under a constant voltage.

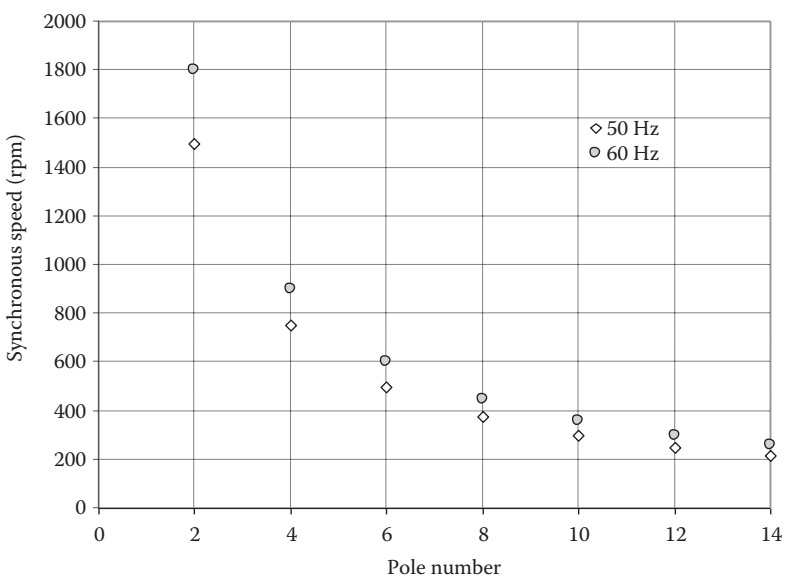

FIGURE 1.32
Synchronous speeds of 50 and 60 Hz machines under various pole numbers.

In the unit of radians per second (rad/s), the angular synchronous speed ω_s is given as

$$\omega_s = \frac{\pi n_s}{30} = \frac{2\pi f}{p} = \frac{4\pi f}{N} \tag{1.48}$$

In contrast, in an IM, the stator windings are wound around the rotor to produce a rotating magnetic field with a three-phase power supply. It is the varying magnetic field that induces currents in the rotor conductors/end rings (or rotor windings). Thus, the interaction between the magnetic fields of the stator and rotor causes a rotational motion of the rotor.

Because current in the rotor conductors/end rings is induced by the stator windings, the rotating speed of the rotor must lag the rotating speed of the stator's magnetic field (i.e., the synchronous speed). This speed difference is called slip, which is defined as

$$s = \frac{n_s - n_r}{n_s} = \frac{\omega_s - \omega_r}{\omega_s} \tag{1.49}$$

where

n_s and n_r are the synchronous speed and rotor speed in rpm

ω_s and ω_r are the angular synchronous speed and angular rotor speed in rad/s, respectively

Thus, the rotor rotating speed of an asynchronous motor becomes

$$n_r = n_s(1-s) \quad \text{in rpm} \tag{1.50a}$$

$$\omega_r = \omega_s(1-s) \quad \text{in rad/s} \tag{1.50b}$$

Slip increases with load. Usually, full-load slip ranges from less than 1%–3% for larger-power motors to 4%–6% for small-power motors.

Synchronous motors can be built with either salient pole rotor or nonsalient pole (cylindrical) rotors, depending on the customers' specifications and applications. Generally, salient pole motors are typically found in high-power, low-speed applications. Motors with cylindrical rotors are typically found in high-power, high-speed applications such as spindle motors in machine tools.

1.3.5 Servo and Stepper Motors

There are two main types of motion control systems: closed loop and open loop. A closed-loop system applies a feedback system to verify whether or not the desired output has been reached. For instance, an encoder is commonly attached with a servomotor to measure the velocity and position of the servomotor for providing the information to the motion controller. Obviously, servomotor systems require the use of the closed-loop system. As a contrast, an open-loop system does not need any feedback for verifying the output. In practice, most step motor systems use open-loop system. The difference between the two control schemes is whether or not the use of feedback system (Figure 1.33).

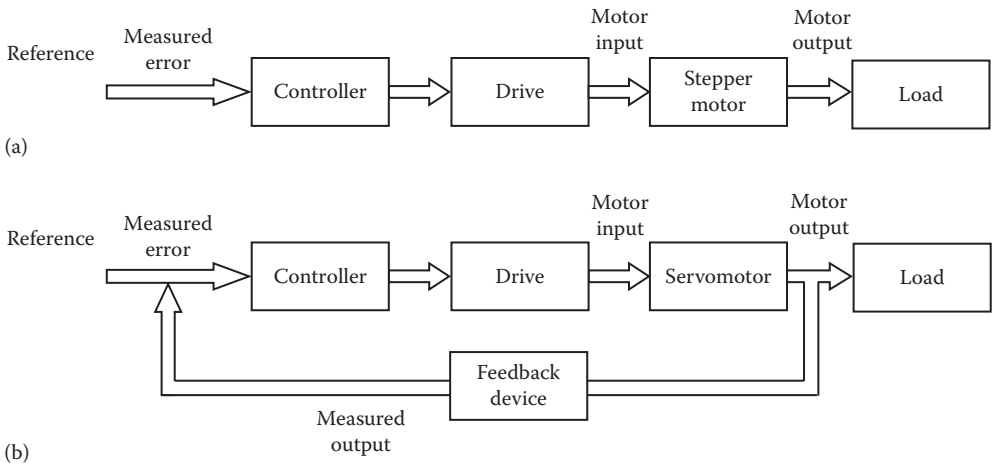

FIGURE 1.33
Comparison of two control schemes: (a) the open control loop and (b) the closed control loop.

An open motion control system usually consists of a motion controller, a feedback system, an electric motor, and a motor drive. The motion controller acts primarily as the brain of the motion control system. Its main function is to make sure the output of the system is as close as possible to the desired result. Based on the information from the feedback system (such as encoder, resolver, sensors), the motion controller sends the electronic signals to the motor drive to adjust motion path or trajectory. The feedback system is to obtain the motor motion information (e.g., displacement and speed), which are then converted into a set of digitized output signals and fed to the motion controller for making necessary adjustments. The motor drive takes the low-power electronic signal from the motion controller and converts it into high-power current/voltage to the motor, which executes the tasks from the drive as an actuator. All these components are integrated to form the complete motion control system to provide the desired movement for various applications.

The word *servo* originally comes from the Latin word *servus*, meaning slave or servant. NEMA [1.61] defined a servomotor as "an electric motor that employs feedback with the purpose of producing mechanical power to perform the desired motion of the servo mechanism." Simply speaking, any control element that employs feedback is a servo.

Today, servomotors are increasingly being used in a variety of applications due to their high power density, high efficiency, and excellent dynamic performance as compared with other motor drive technologies. Servomotors operate with closed-loop control systems. The ability of the servomotor to adjust to differences between the motion profile and feedback signals depends greatly upon the types of control systems and servomotors. There are two types of servomotors: one is classical DC servomotor and another is AC servomotor. Generally, AC servomotors can handle higher current surges compared to DC servomotors. It is to be noted that in some references, AC servomotors are referred to as brushless DC motors, causing confusion to some readers. An AC servomotor or the so-called brushless DC motor is essentially a three-phase AC synchronous motor. It has a position transducer inside the motor to transmit motor shaft position to the drive amplifier for the purpose of controlling current commutation in the three phases of the motor windings.

Stepper motors are special motors used in motion control systems. This type of motor has high torque at low speeds, high reliability, low cost, and simple rugged construction that operates in almost any environment. Typical applications include printers, image scanners, CNC machines, and volumetric pumps. Unlike common AC and DC motors rotating continuously, a stepper motor moves in fixed angular increments, called the step angles. In a stepper motor, a full revolution is divided into a large number of discrete steps. In fact, a stepper motor is an actuator that converts electrical pulse signals into angular displacements. Once the stepper motor receives an electrical pulse signal, it moves a fixed step angle in a predefined direction. Thus, by controlling the pulse number, the angular displacement (i.e., the motor positioning) can be controlled precisely. By altering the pulse frequency, the accurate control of the motor rotating speed and acceleration can be achieved. It is important to note that in this control mechanism, no feedback systems are required. This allows the stepper motor to operate in an open-loop system, making the motion control easier and less expensive. In addition, stepper motors can operate at a set speed regardless of load as long as the applied load is less than the limited torque rating.

As an open-loop control system, the stepper motor requires only the input of the current state. The number of steps per revolution varies by model and manufacturer. Stepper motors were introduced in the early of 1960s as an economical replacement to closed-loop DC servo systems. Unlike conventional motors that rotate continuously, stepper motors rotate in fixed angular increments. One revolution of a stepper motor involves taking a number of steps, depending on the number of rotor teeth, motor construction, and type of drive scheme used in the motor control.

Stepper motor technology does have some disadvantages. The most critical drawback is the loss of synchronization and torque if a large load exceeds the motor's capacity. A high-inertia load can cause the rotor to slip, or not advance when the step pulse is given. Consequently, the user typically selects a stepper motor's capability with 2:1 factors of safety (FS) to torque to minimize or eliminate loss of synchronization. Stepper motors also tend to run hot because phase current is independent of the load. In some applications, if the motor needs to be overdriven by the load, it may be undesirable to feel the poles of the stepper motor as the rotor is being pulled by the load [1.62].

Today, stepper motors are available in many topologies and step sizes for various industrial and commercial applications due to their advantages of low cost, high reliability, no cumulative error, high torque at low speeds, simple and rugged construction, and excellent response to start-up, stopping, and reverse operation.

There are basically three types of stepper motors: PM, variable reluctance, and hybrid [1.63]. The PMM has relative low torque and low speed with large step angles. Its simple construction and low cost make it an ideal choice for nonindustrial applications. The variable reluctance motor (VRM) usually has three-phase stator windings. It can achieve large torque outputs. However, due to their large vibrations and high noise emissions, VRMs are gradually out of the main industrial market. The hybrid stepper motor combines the best characteristics of the variable reluctance and PMMs by constructing multistator poles and PMs inside the rotor. Therefore, the hybrid stepper motor is the most widely used stepper motor today. The comparison of three types of stepper motors is listed in Table 1.5.

A cutaway diagram of hybrid stepper motors is demonstrated in Figure 1.34. The stator coils are wound on stator poles. The rotor is a cylindrical PM, magnetized along the axis with radial soft iron teeth. Thus, one pole of the rotor may align with the stator in distinct positions.

The polarity of rotor laminations is shown in Figure 1.35. Unlike conventional motors, the magnet in a stepper motor is magnetized axially rather than radially. As shown in

TABLE 1.5

Comparison of Three Types of Stepper Motors

Stepper Motor Type	Phase	Step Angle	Torque	Vibration and Noise	Note
Permanent magnet	2 or 4	7.5° or 15°	Low	Low vibration at low frequencies, low noise	High efficiency, low current, low heat generation
Variable reluctance	3	1.5°	High	Large	Out of main industrial market
Hybrid	2 5	1.8° 0.72°	High	Low	With the most wide applications

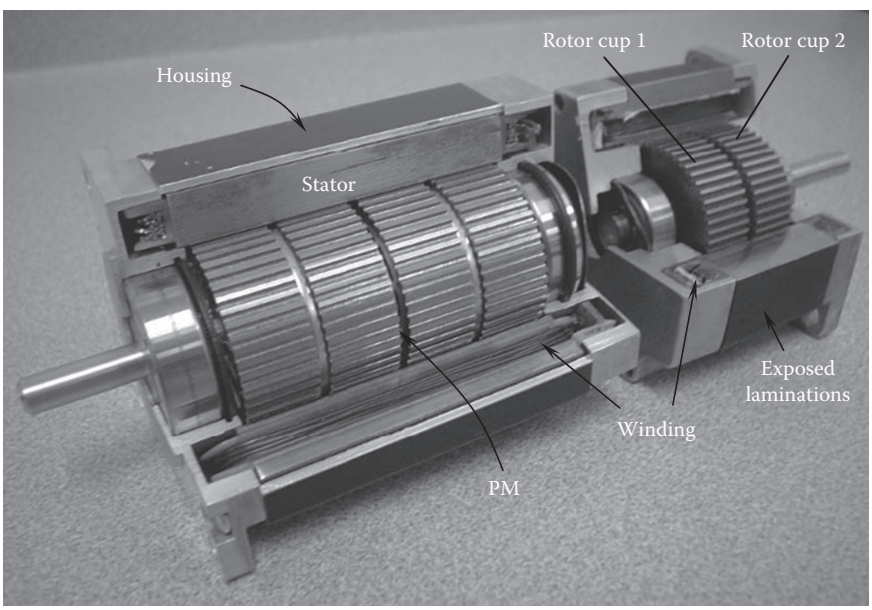

FIGURE 1.34
Structures of hybrid stepper motors, which combines features of the PM stepper and the variable reluctance stepper motors.

Figure 1.35, two axially spaced sections each formed with radially projecting and angularly spaced teeth. In addition, the teeth on the north end of the rotor are displaced by a half of a pole pitch from the teeth on the south end. Both of these two features make stepper motors unique from other motors.

For standard reluctance stepper motors (e.g., without PM), the rotors look similar to the aforementioned rotor except there is no PM and the magnetic field is not permanently present in the rotor lamination. The coils in the stator create a magnetic field in the stator that attracts or repels the soft iron rotor laminations into position. Then the coil current is reversed to reverse the coil magnetic field and keeps the rotation moving. A stepper motor drive is required to switch the currents.

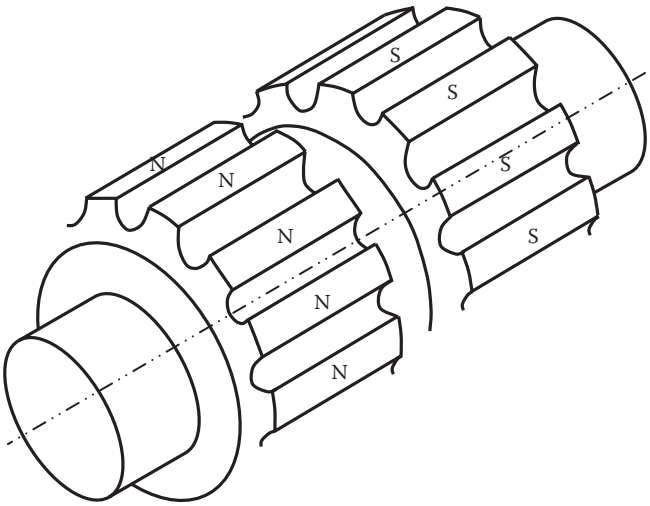

FIGURE 1.35
Magnetic polarity of rotor laminations in a hybrid step motor. The PMs are magnetized axially and placed in the center of lamination stacks. The rotor teeth on the north end of the magnet are magnetized north and the rotor teeth on the south end of the magnet are magnetized south. The north and south halves are displaced by a half of a pole pitch from the teeth on the south end.

1.3.6 Gear Drive and Direct Drive Motors

There are several motor driving patterns in motion control applications: (1) gear drive, (2) direct drive, (3) tangential drive (e.g., belt, chain), (4) ball/lead screw drive, and (5) worm drive.

Gear drive is a conventional mechanism in connecting electric motors to external mechanical loads. The shaft of a motor is attached to one end of the gearbox and, through the internal configuration of gears of the gearbox, provides a given output torque and speed determined by the gear ratio. In such a way, a motor is coupled with a transmission device (e.g., gearbox) to reduce the rotating speed and increase the output torque. The most important design parameter of gearboxes is the gear ratio γ_g, which is defined as the ratio of the input speed to the output speed. In a gear drive system, the ratio of the load torque T_l (the output torque) to the motor torque T_m (the input torque) is determined by the gear ratio γ_g and the gearbox efficiency η_{gb}:

$$\frac{T_l}{T_m} = \gamma_g \eta_{gb} \tag{1.51}$$

Gearboxes are available in many different types, sizes, gear ratios, efficiencies, and backlash characteristics. They can be generally categorized into several different types: parallel shaft gearbox (e.g., spur and helical gearbox), perpendicular shaft gearbox (e.g., bevel gearbox), planetary gearbox, and worm gearbox, just to name a few. For the type of parallel shaft gearbox, according to the number of shafts, gearboxes can be further classified as single-stage (two shafts), dual-stage (three shafts), and multistage (more than three shafts) gearboxes. Usually, this type of gearboxes takes more space than other gearbox types.

Planetary gearboxes are the most commonly used gearboxes in the motion control market due to their high torsional rigidity, high torque, high efficiency, low inertia, and low backlash.

However, there are some disadvantages in using gearboxes. The main problem is backlash introduced by gearboxes. Backlash is the gap between the teeth of two adjacent gears. Thus, the rotational backlash of a gearbox is the accumulated backlash from all paired gears. It can be measured as the free rotational angle at the gearbox output shaft when the input shaft is locked, or vice versa. In precise motion control applications involving frequent load reversals (e.g., CNC machines, elevators, wind pitch control systems), backlash plays a crucial role to determine the repetitive positioning accuracy. For this type of applications, gearboxes must be made with low, strictly controlled backlash and high stiffness. For demonstration purpose, the theoretical backlash of gearbox and torsional stiffness are shown in Figure 1.36.

The use of separated motor and gearbox may greatly increase the system volume and lower the torque density and system reliability. To solve these problems, some motor manufacturers have designed motors with built-in gearboxes for achieving the solution of high torque capacity, smooth operation, minimal maintenance, and high-efficiency motors in compact sizes, as shown in Figure 1.37.

DDR motors are designed to directly drive an external loaded machine. They can be housed or frameless component sets of a PM field assembly and wound stator. The frameless part set can be built into a machine as *embedded motion* onto the user's shaft, housing, and bearing assembly and offers the most compact form factors. By eliminating the need for additional mechanical transmission devices, it allows improved motor reliability, efficiency, dynamic performance, torque density, motion accuracy, and disturbance response. This also leads to large mass savings in the mechanical structure and enables further cost reductions. There are other advantages such as better load inertia matching, ease of control, low noise emission, and streamlined machine design.

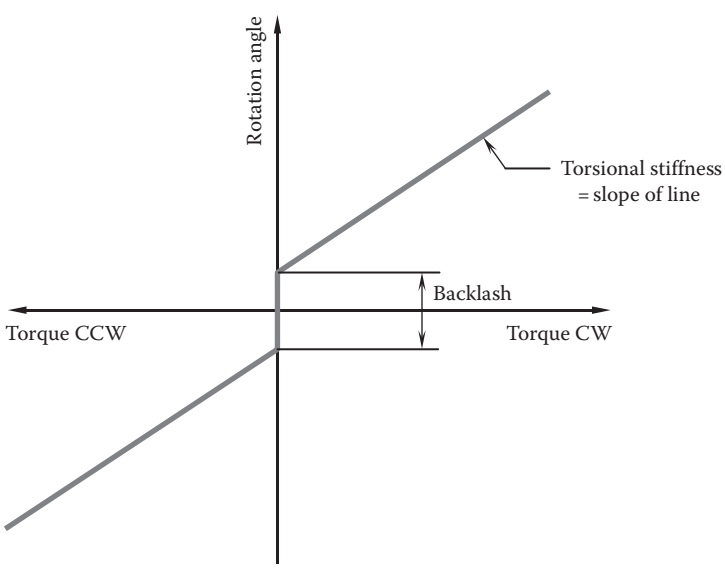

FIGURE 1.36
Theoretical backlash of a gearbox and stiffness curve.

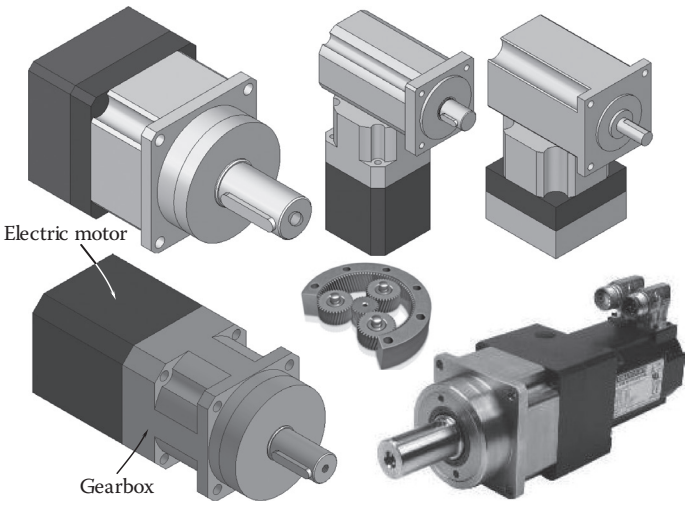

FIGURE 1.37
Integration of electric motor and gearbox as gearmotor.

Typical DDR motors are shown in Figure 1.38, which offer many high-performance features and zero maintenance in a precision servo solution. Among them, the cartridge DDR motor, developed by Kollmorgen in 2005, is the first in the motor industry to combine the space-saving and performance advantages of frameless DDR technology. The cartridge DDR motors are supported by customers' bearings, thus providing up to 50% more torque density than comparably sized conventional servomotors and the ability to remove the motor without dissembling the machine. By making direct drive benefits available to simple mechanisms, this type of motors has been successfully used in many applications such as packaging, printing, medical equipment, converting, and others.

For a DDR motor, torque is proportional to rotor diameter squared. Thus, in order to increase motor torque, DDR motors are typically designed with high diameter-to-length ratios, that is, large diameters and short axial lengths. In addition, a DDR motor can simultaneously have both a very large OD and ID. This implies that the DDR motor looks more like a thin ring. In fact, the large OD and ID help develop the large motor torque. This thin-ring shape may be particularly suitable for some applications requiring large diameters and short lengths such as computerized tomography (CT) scanners, magnetic resonance imaging (MRI) scanners, and wind turbines. As an example, a DDR motor for a telescope drive has a diameter of 2.5 m and a length of less than 50 mm. This motor can produce a continuous torque exceeding 10,000 N-m [1.64]. In large machine tool applications, DDR diameters of 1 m or so are commonly encountered.

Frameless DDR motors do not contain housings, bearings, or feedback devices, as shown in Figure 1.39. This implies that a frameless DDR motor must be integrated into the user's machine. To help integrate the motor, motor manufacturers often provide a reusable assembly tool called *bridge* to maintain the alignment of the rotor and stator during assembly.

The design of DDR motors is mainly influenced by its rotating speed, torque, and power. The achievable power of a motor is approximately proportional to the square of the air gap diameter and to the axial length of the motor at the air gap. This indicates that with a doubling of the air gap diameter, the motor power can increase four times. As a matter of fact, direct motors with low rotating speeds usually have a large diameter and a short length.

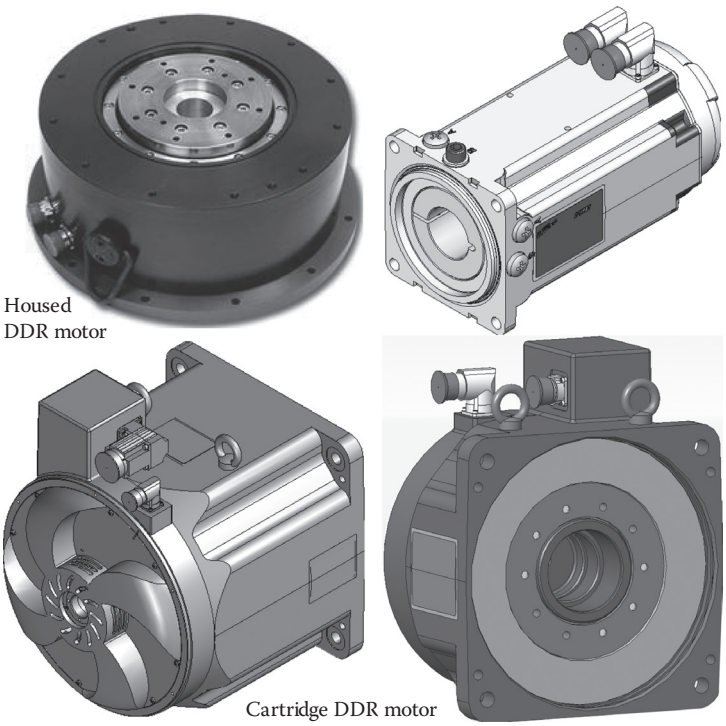

FIGURE 1.38
Various DDR motors. (Courtesy of Kollmorgen Corporation, Radford, VA.)

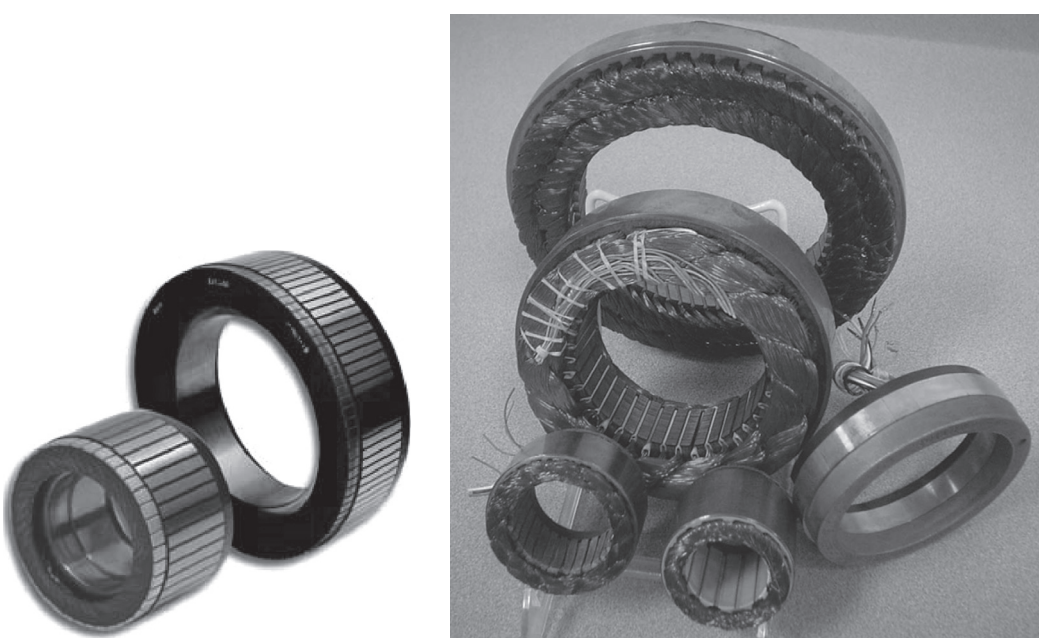

FIGURE 1.39
Frameless DDR motors. (Courtesy of Kollmorgen Corporation, Radford, VA.)

Comparing with conventional servo systems, the advantages of direct drive systems include the following:

- It significantly increases system efficiency by eliminating inefficient gearboxes.
- Because the gearbox in a motor system is a primary noise source, the elimination of the gearbox greatly reduces the noise emission from the motor.
- Motor reliability increases due to the reduction in the number of rotating parts.
- The positioning inaccuracy from transmission compliance no longer existed.
- Lower inertia enables fast and accurate positioning.
- A direct drive servomotor is capable of precise revolution control with high resolutions.
- Without speed reduction devices, mechanical backlash, hysteresis, and elasticity in gear transmission systems are eliminated.
- There is no need for gearbox lubrication and it simplifies maintenance.

However, direct drive motors require more precise control systems. Since the direct drive motors need special design, their individual costs are much higher than other servomotors, but system costs utilizing them can be lower than the total installed cost.

1.3.7 Brush and Brushless Motors

Brush motors have a long history of applications since the first electric motor was invented in the late nineteenth century. For a classical DC motor, an electrical power source is connected to the rotor winding through a commutator and brushes. A commutator usually consists of a set of contact bars attached to the rotating shaft of a motor. As the stator windings are sequentially energized to generate a rotating magnetic field, the rotor aligns itself with the magnetic field of the stator. A number of stationary brushes come into contact with corresponding the contact bars of the commutator for reversing the flow of current in the rotor winding. In order to reduce the contact electric resistance at the contacting surface, brushes are pressed against the commutator and thus result in some friction between the brushes and commutator. In addition, at high rotating speeds, brushes become increasingly difficult to maintain reliably in contact with the commutator. Brushes may bounce off from the commutator surface to produce sparks and consequently break the circuit in a very short period of time. Continuous sparking can cause overheat, erode, or even melt the commutator. For this reason, brush motors are restricted to relative low speeds to avoid brushes excessively bouncing and sparking.

To overcome these drawbacks, brushless motors have been developed to replace brushed motors in some motion control applications. Brushless DC motors typically operate with PM rotors, offering distinct mechanical and electrical advantages over conventional systems. Attachment of PMs on rotor and elimination of rotor coil windings allow significant reductions in rotor inertia and increase in motor acceleration and efficiency. Winding heat can be dissipated directly from the stator into the environment and rotor heating is much lower than that in a brush motor. Generally, comparing to brush motors, brushless motors offer higher operation reliability, higher dynamic accuracy, higher efficiency, less product variation, and smaller size but require complex and expensive electronic control systems.

With the widespread use of brushless AC motors in industrial, commercial, and military applications, brushes are gradually exiting the electrical machine market.

1.3.8 Reluctance Motors

Reluctance motors are special motors that use salient pole rotors but without windings and PM on the rotors. There are several types of reluctance motors, with different construction and slightly different functions [1.65]:

- Switched reluctance motor (SRM)—By eliminating windings and PMs from the rotor, this type of motor has inherent advantages over some DC and AC motors, such as simple structure, structure robustness, low cost, and operation in high temperatures. SRMs have been designed mainly for the applications in high-power, high-efficiency, variable speed drives, enabling to deliver a wide range of torque. This type of motor requires the closed-loop position control.
- VRM—This type of motor is an evolution of the stepper motor but with less salient poles. The motors are generally designed for use in low-power, open-loop position and speed control systems where efficiency is not of prime importance. In fact, there are similarities between switched and VRMs such as the operating principles, mechanical structures, performing characteristics, and power losses. Both of the types are similar to the brushless PMMs except that the rotors are made from laminated *soft* magnetic materials.
- Synchronous reluctance motor—This type of motor is similar to synchronous AC motors. The rotor has salient poles but the stator has smooth, distributed poles, whereas both the switched and variable motors have salient poles for both the rotor and stator.

SRMs can be traced back to the invention of Robert Davidson in 1938 [1.66]. However, this type of motors did not find widespread use until the late 1970s due to the difficulty in controlling the machine. For an SRM, there are no windings or PMs on the rotor. When the stator windings are powered, the rotor's magnetic reluctance produces a force that attempts to align the rotor with the exited stator poles. The coils in the adjacent slots are powered successively so that the rotor can rotate continuously. This operation principle is based on the difference in magnetic reluctance for magnetic field lines between aligned and unaligned rotor position when a stator coil is excited; the rotor experiences a force that will pull the rotor to the aligned position [1.67].

Due to the elimination of magnets and rotor windings, SRMs offer several performance, efficiency, and cost advantages. In an SRM, torque is produced by the tendency of its moveable part to move to a position of least reluctance. The SRM has salient poles on both the rotor and the stator, but only the stator poles carry windings. When the stator windings are energized, they create a magnetic field that pulls the nearest pole on the rotor toward it. Consequently, the performance of SRMs is largely a function of the power electronics that control the sequencing of pole energizations. Besides, the SRMs have characteristically high power-to-weight ratios and are well suited for vehicle applications [1.68].

SRMs have been found to offer important advantages over conventional motors in many industrial and commercial applications. In recent years, SRMs have been receiving increasing attention because they can provide similar performance to brushless DC motors without using expensive rare-earth magnets. In addition, their robust construction and efficiency over a wide speed range make them well suited to a variety of applications including hybrid and electric vehicles. However, the main drawbacks are its high-torque ripple and consequently high audible noise. As shown in Figure 1.40, the stator of an SRM is similar to a brushless DC motor but the rotor has no magnets or windings attached.

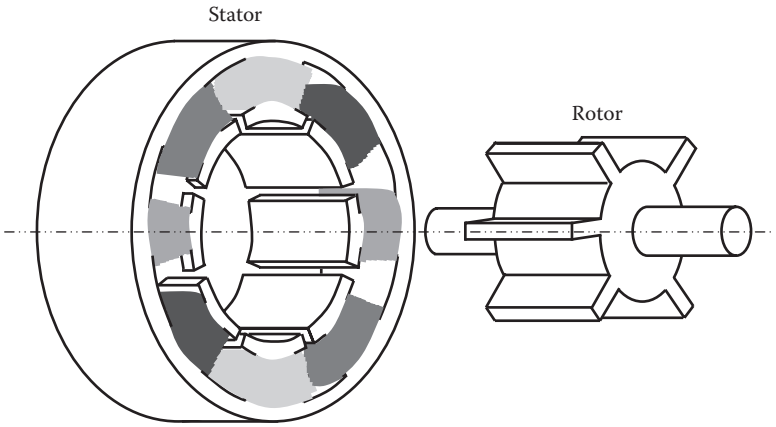

FIGURE 1.40
The salient rotor in an SRM.

1.3.9 Radial-Flux and Axial-Flux Motors

The configuration of the electromagnetic field in a motor determines the motor's geometry and structural topology. Electric motors in which the magnetic flux travels in the radial direction are classified as radial-flux (RF) motors. This type of motors is cylindrical in shape, and the rotor is typically located inside a stator but can also be placed outside the stator in some special applications, sometimes referred to as *inside out* motors or outer rotating rotor motors. As a contrast, motors in which the magnetic flux travels in the axial direction are classified as axial-flux (AF) motors. This type of motors usually has multiple disk- or pancake-shaped rotors and stators. A typical brushless AF motor is demonstrated in Figure 1.41, showing a stator–rotor–stator structural topology. AF motors offer low axial

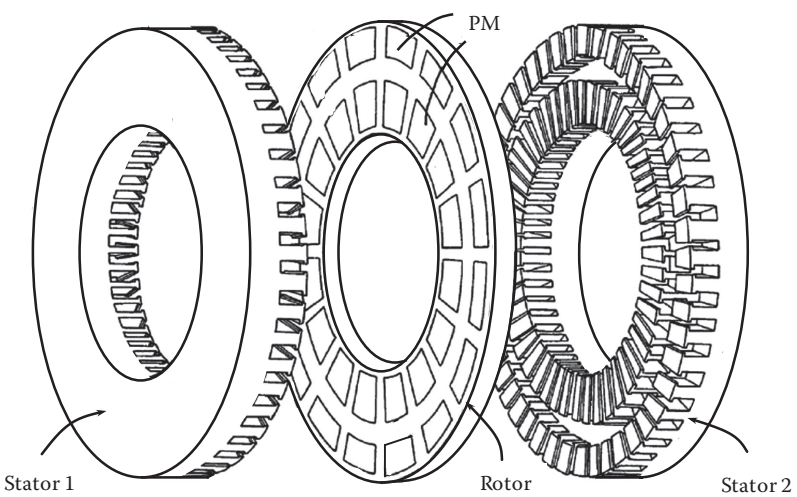

FIGURE 1.41
Brushless AF motor with the stator-rotor-stator structural topology, where PMs mounting on the rotor side surfaces and rotating with the rotor.

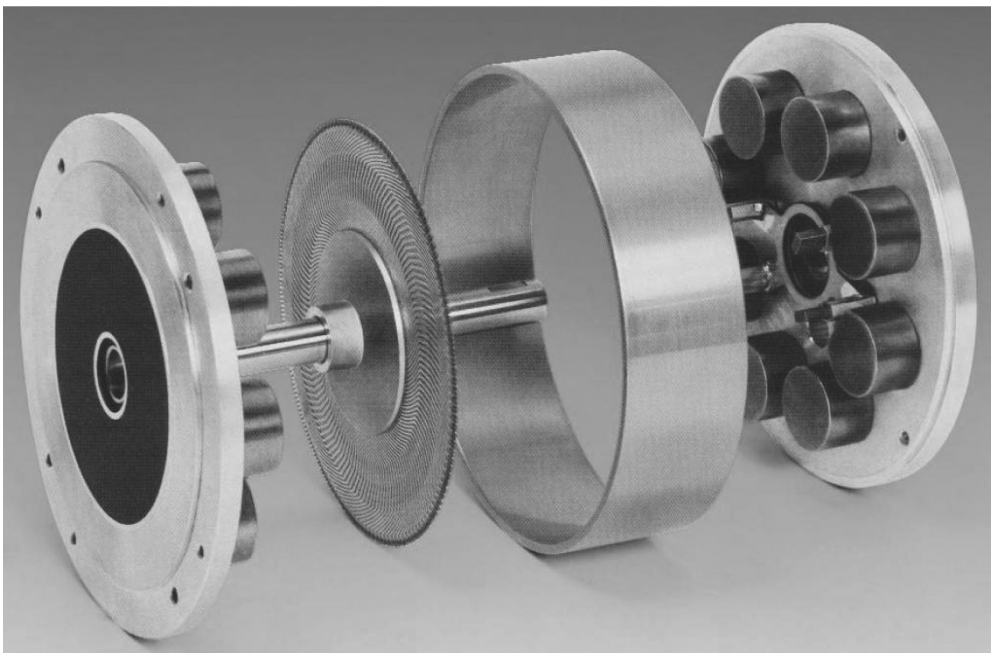

FIGURE 1.42
DC brush AF motor, where PMs are mounted on the stators to create an axial magnetic field. (Courtesy of Kollmorgen Corporation, Radford, VA.)

length and are common in automotive radiator cooling fan applications, table top medical or lab devices, and specialized elevator machines to name but a few. The structure of a DC brush AF motor is shown in Figure 1.42. As can be seen from the figure, the armature is constructed from several layers of copper conductors in a unique flat-disk configuration. Because it adopts ironless design, the thin, low-inertia armature design leads to exceptional torque-to-inertia ratios. The ironless armature enables the motors to deliver more torque over their entire speed range. In fact, the torque is almost constant from 0 to 3000 rpm, which is not attainable with conventional ironcore motor designs. In addition, this type of motors can accelerate from 0 to 3000 rpm in only 60° of rotation [1.69].

1.3.10 Rotary and Linear Motors

According to the motion pattern of motor, an electric motor can be classified as either rotary or linear motor. As indicated in their names, the rotor in a rotary motor always rotates with respect to its rotating axis and the rotor in a linear motor moves linearly along the flat stator. Actually, a linear motor has the motion of a rotary motor if it was laid out in a flat state.

Linear motors are typically used in the applications that require linear or reciprocating motions (Figure 1.43). A famous example is the high-speed maglev train that was built in 2004 at Shanghai, China, and has been in normal commercial operation thereafter. Similar to rotating motors, linear motors can be grouped as induction or PM linear motors. When very fast linear acceleration or high linear forces are required, linear motors are often employed. A disadvantage is the mechanical structure to support them is more expensive than rotary motor structures.

FIGURE 1.43
A linear motor. (Courtesy of Kollmorgen Corporation, Radford, VA.)

1.3.11 Open and Enclosed Motors

An open motor refers to the motor that has ventilating openings that permit passage of external cooling air to get in the motor for flowing over and around the windings. With the openings on the motor housing, it makes possible for the external objects such as dusts and moisture to enter into the motor, causing motor damage even failure. Therefore, this type of motors cannot work under harsh environments.

An enclosed motor refers to the motor that is completely enclosed to prevent the free exchange of air between inside and outside of the motor housing. In such a configuration, heat is usually dissipated relying on conduction from the heat source (i.e., stator windings) to the motor housing and then from the housing to the environment by convection. This cooling mode is applicable only to small motors with relative low heat loads. For high-powered motors, a build-in cooling system such as a liquid cooling system or using heat pipes is necessary. This type of motors usually has high International Protection Rating or Ingress Protection Rating (IP) values and thus can be used in harsh and dangerous environments.

1.3.12 Motor Classification according to Power Rating

According to the motor nominal power, electric motors can be briefly divided into five categories:

- Micromotors are electric motors with rated output poser of 0.05 hp (<37 W) or less. Micromotors have been used across a wide range of commercial and industrial applications for light duty, especially in microelectronics, computer, and precision instrument industries.

- Small motors are larger than 0.05 hp but less than 1 hp (37–746 W). Their applications focus primarily on power hand tools, appliances, medical devices, small fans, optical devices, electrical cars, precise motion control systems, and other small machinery.
- Medium motors are considered to be in the range of 1–100 hp (746 W–74.6 kW). The majority of medium motors are used in various industrial applications such as industrial fans, pumps, motion-control systems, machine tools, and vehicles.
- Large motors occupy the power range of 100–1000 hp (74.6 kW–746 kW). They are normally designed for use in medium-duty applications as in elevators, large vehicles, industrial blowers/fans, printing machines, package machines, air compressors, and other industrial large machines.
- Extra large motors range from 1000 to 10,000 hp (746 kM–7.46 MW), which are usually used in heavy-duty applications, such as large rolling mills, large machine tools, high-speed trains, skyway elevators, ship propulsion, and mining machinery.
- Ultra large motors are considered to be larger than 10,000 hp (>7.46 MW). NASA used a motor that is rated 135,000 hp for a wind tunnel. In addition, the industry's largest players such as GE, Siemens, TECO-Westinghouse, ABB, and Toshiba have developed their own ultra large motors.

It is worth to note that the range for each motor category shown earlier has not been clearly defined by international, national, or professional standards yet.

1.4 Motor Design and Operation Parameters

In designing, selecting, and repairing electric motors, it often involves a number of constants that reveal the relationships of torque, current, speed, voltage, power loss, and other operating characteristics. Among these constants, the back EMF constant and torque constant are the two most important constants for evaluating motor performance.

1.4.1 Back EMF Constant, K_e

The induced voltage in motor conductors under a rotating magnetic field is defined as the back EMF V_e and is directly proportional to the angular velocity of the motor. Thus, the proportionality constant, referred to back EMF constant, is defined as the ratio of back EMF to motor rotational speed, in the unit of V/(rad/s) or V/rpm (in some applications, V/krpm):

$$K_e = \frac{V_e}{\omega} \tag{1.52}$$

Thus, K_e is a measure of how many volts per rpm the motor would produce if driven as a generator. It can be also used to determine how fast a motor will run with a given voltage applied to it.

1.4.2 Torque Constant, K_t

K_t is called torque constant (N-m/A) or torque sensitivity, which is defined as the torque T (in N-m) generated by a motor to the motor input current I (in A), that is,

$$K_t = \frac{T}{I} \tag{1.53}$$

For a sinusoidal commutated motor, the root-mean-square (*rms*) current i_{rms} should be used to replace I in the aforementioned equation, where i_{rms} is related to the peak AC current i_p as

$$i_{rms} = \frac{i_p}{\sqrt{2}} \tag{1.54}$$

Figure 1.44 presents the block diagram of conventional circuit for estimating motor torque constant. This conventional engineering method assumes that when the motor is accelerated, the motor torque constant is proportional to a position change as the output of the motor, regardless of the input current of the motor. However, motor torque constant actually depends on the input current during acceleration of the motor. Hence, the conventional method cannot provide the accurate result for motor torque constant. Based on a new block diagram shown in Figure 1.45, a new method was proposed to calculate motor torque constant by a multiplicity of measured current and speed values [1.70]:

$$K_t = \frac{\sum_1^n i(k-1)\left[v(k)-v(k-1)\right]}{\sum_1^n i(k-1)^2} \tag{1.55}$$

where

$i(k)$ and $v(k)$, respectively, indicate the current and the speed of the motor at a sampling time k

n indicates a natural number greater than 1

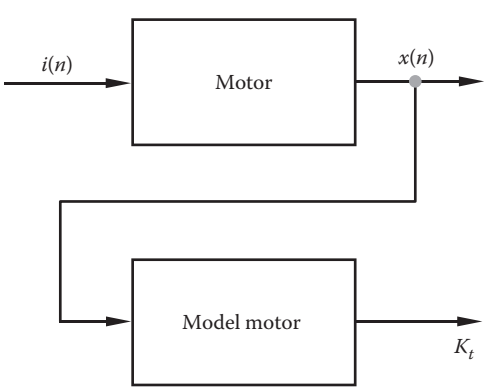

FIGURE 1.44
The block diagram of conventional circuit for estimating motor torque constant.

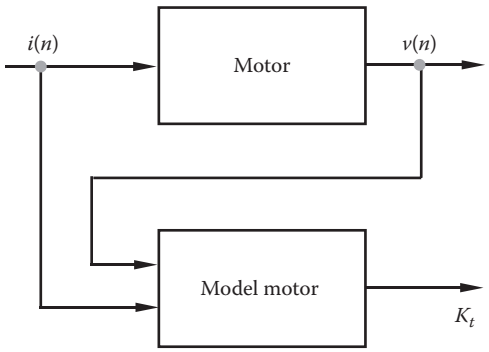

FIGURE 1.45
The block diagram of proposed new circuit for estimating motor torque constant.

1.4.3 Velocity Constant, K_v

K_v is the motor velocity constant, measured in rpm or rad/s per volt. In fact, K_v is the reciprocal of K_e. For brushless motors, K_v is the ratio of the motor's unloaded rpm or rad/s to the peak voltage. This parameter is used for selecting the winding in the motor.

It can be shown that if the torque constant K_t is in N-m/A and the back EMF constant K_e in V/(rad/s), then,

$$K_t = K_e = \frac{1}{K_v} \tag{1.56}$$

1.4.4 Motor Constant, K_m

K_m is the motor constant, defined as the torque constant K_t divided by the square root of the resistive power loss P_r:

$$K_m = \frac{K_t}{\sqrt{P_r}} \tag{1.57}$$

- For DC motors,

$$P_r = I^2 R_{DC} \tag{1.58a}$$

- For three-phase AC motors,

$$P_r = i_{rms}^2 R_{AC} = \frac{3 i_p^2 R_{AC}}{2} \tag{1.58b}$$

where R_{DC} and R_{AC} are the winding resistances for DC and AC motors, respectively.

Substituting (1.58a) into (1.57), it yields

$$K_m = \frac{K_t}{I\sqrt{R_{DC}}} = \frac{T}{I^2\sqrt{R_{DC}}} \tag{1.59}$$

Since $P_{in} - P_{out} = \sum P_{loss} > I^2 R_{DC}$, it follows that

$$\sqrt{P_{in} - P_{out}} > I\sqrt{R_{DC}} \tag{1.60}$$

Therefore, the minimum torque constant is obtained as

$$K_{m,\min} = \frac{T}{\sqrt{P_{in} - P_{out}}} \tag{1.61}$$

Similarly, substituting P_r for the corrected 3-phase AC motor and thus obtaining another K_m equation as

$$K_m = \frac{K_t}{1.225 i_p \sqrt{R_{AC}}} \tag{1.62}$$

In fact, K_m represents the ability of a motor to convert electrical power to mechanical power. A motor with a higher value of K_m can generate torque more efficiently. K_m is winding independent and is used as a rating comparison factor in selecting the motor size in various motor applications. In some references, K_m is also called motor size constant.

1.4.5 Mechanical Time Constant, τ_m

In design and analysis of servomotors, it often deals with two time constants: mechanical time constant τ_m and electrical time constant τ_e. A servomotor's dynamic motion response is controlled by these two time constants. Usually, τ_m and τ_e are listed in the servomotor specifications. However, it should be cautioned that these two time constants in the specifications are for the motor alone with no load inertia connected to the motor shaft. It is important to understand the impact of actual load conditions on the time constants [1.71].

The mechanical time constant τ_m (in unit of second s) is usually defined as the ratio of motor moment of inertia to the damping factor with a zero-impedance power source:

$$\tau_m = \frac{RJ_m}{K_t K_e} \tag{1.63}$$

where

R is the motor winding resistance
J_m is the motor moment of inertia

To take into account the impact of load on τ_m, the previously mentioned definition may be modified as

$$\tau_m = \frac{R_t J_t}{K_t K_e} \tag{1.64}$$

where

R_t is the total motor winding resistance of all phases plus the external circuit resistance and the total inertia
J_t is the sum of the motor inertia and the reflected inertia from the load to the motor shaft

According to NEMA [1.61], the mechanical time constant refers to the time taken by an unloaded motor to reach $(1 - 1/e)$ (where $1 - 1/e \approx 63.2\%$) of its maximum rated speed in a no-load condition. τ_m can be measured by applying a constant voltage to the motor, then measuring the velocity, and determining the time it takes to reach 63.2% of maximum rated speed.

One important factor to affect the mechanical time constant is temperature. During a normal operation process, the motor temperature rises from the ambient time (usually 40°C) to its normal operation temperature that is below the allowable maximum value. The electric resistance of the winding changes accordingly as

$$R(T) = R(T_o)[1 + \alpha(T - T_o)] \tag{1.65}$$

where α is temperature coefficient of resistance ($°C^{-1}$ or K^{-1}).

Similarly, for PMMs, the back EMF constant K_e and torque constant K_t are also affected by temperature. Both K_e and K_t have the same functional dependence on the motor's air gap magnetic flux density that is produced by the motor's magnets. All PMMs are subject to both reversible and irreversible demagnetization. It has been reported [1.72] that within the temperature range of −60°C to 200°C, all four types of PMs (aluminum–nickel–cobalt [alnico], SmCo, NdFeB, and ferrite/ceramic magnets) exhibit linear, reversible thermal reduction in field strength such that the amount of magnetic flux density produced by each magnet decreases linearly with increasing magnet temperature. Hence, the expression for the reversible decrease in both $K_e(T)$ and $K_t(T)$ with increasing magnet temperature is given as

$$K_e(T) = K_e(T_o)\left[1 - \alpha(T - T_o)\right] \tag{1.66a}$$

$$K_t(T) = K_t(T_o)\left[1 - \alpha(T - T_o)\right] \tag{1.66b}$$

where temperature coefficient of resistance α takes different values according to the different types of PM:

α (Alnico) = 0.0001/°C
α (SmCo) = 0.00035/°C
α (NdFeB) = 0.001/°C
α (Ferrite) = 0.002/°C

Thus, a 100°C rise in magnet temperature causes a reversible decrease in K_e and K_t as –1% for alnico, –3.5% for SmCo, –10% for NdFeB, and –20% for ferrite or ceramic magnets. This indicates that the motor operation temperature has the strongest impact on ferrite magnets.

By taking into account both load and temperature, the mechanical time constant becomes

$$\tau_m(T) = \frac{R_t(T)J_t}{K_t(T)K_e(T)} \tag{1.67}$$

Taking the ambient temperature of 40°C (104°F), the normalized mechanical time constant ratio, $\tau_m(T)/\tau_m(40°C)$, for each type of PMs is plotted in Figure 1.46 as a function of

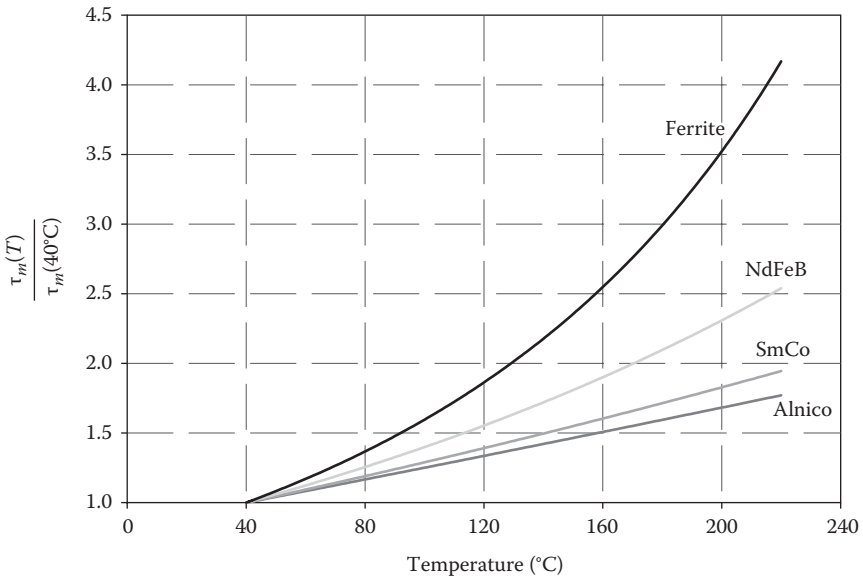

FIGURE 1.46
The temperature influence on mechanical time constant ratio for four types of PMs, with the ambient temperature of 40°C.

temperature. The increase in the mechanical time constant ratio is resulted from the combined effects of increasing electrical resistance and thermal demagnetization. It can be seen from the figure that the largest increase occurs in ferrite magnets with the mechanical time constant ratio increasing by a factor of 2.45 at 155°C. At the same temperature, it increases by a factor of 1.85, 1.57, and 1.49 for NdFeB, SmCo, and alnico magnets, respectively. These results have confirmed that the operation temperature has a strong impact on servomotor's dynamic motion response. Therefore, ignoring the temperature effect can lead to erroneous predictions of the servomotor's dynamic motion response to the applied voltage command. Rare-earth and ferrite/ceramic magnets have increased in magnetic flux at cold temperatures. Rare-earth magnets have improved resistance to demagnetization at cold temperatures, whereas ferrite/ceramic magnets have an increase in demagnetization risk at low temperatures.

1.4.6 Electrical Time Constant, τ_e

According to NEMA [1.61], the electrical time constant of a servomotor is the time required for the current to reach $(1 - 1/e)$ (i.e., 63.2%) of its final value after a zero source impedance, and the stepped input voltage is applied to the motor that maintained in the locked rotor or stalled condition (i.e., $\omega = 0$). A small electrical time constant indicates the high dynamic response of a servomotor.

Mathematically, the electrical time constant τ_e is defined as the ratio of armature inductance L to its winding electric resistance R:

$$\tau_e = \frac{L}{R} \tag{1.68}$$

Similarly, by taking into account the load and temperature effect, the equation becomes

$$\tau_e(T) = \frac{L}{R_t(T)} \tag{1.69}$$

where $R_t(T)$ is the total resistance, including the resistance of all phase windings and the external circuit resistance, at the temperature T. This equation indicates that with the increasing temperature, electrical time constant τ_e decreases due to the increase in $R_t(T)$.

1.4.7 Thermal Time Constant, τ_{th}

The thermal time constant τ_{th} is an indicator of the heat capacity of a motor, showing how fast or how slow the generated heat can be built up in the motor and can be effectively dissipated to the environment. In another words, it is a measure of how long it takes a motor to reach thermal equilibrium.

The thermal time constant τ_{th} can be expressed as

$$\tau_{th} = \frac{\rho c_p V_e}{h A_s} \tag{1.70}$$

where
- ρ is the density
- c_p is the specific heat
- V_e is the effective motor volume (this is because a motor is not a solid)
- h is the convective heat transfer coefficient
- A_s is the motor outer surface area

This equation indicates that larger mass m ($m = \rho V_e$) and specific heat c_p lead to larger τ_{th}, that is, larger heat storage capability and slower changes in temperature. Higher heat transfer coefficient h and larger motor outer surface area A_s help dissipate the generated heat quickly from the motor to the ambient, leading to smaller τ_{th}, that is, faster changes in temperature. Obviously, a lower value of thermal time constant is highly desired.

The motor thermal time constant may be used to estimate the temperature rise of a motor. The motor temperature rise ΔT can be predicted as [1.73]

$$\Delta T = T - T_a = P_{loss} R_{th} + \left(T_a + T_i - P_{loss} R_{th}\right) e^{-t/\tau_{th}} \tag{1.71}$$

where
- T_a is the ambient temperature
- T_i is the motor initial temperature at the start of operation
- P_{loss} is the motor total power losses that must be dissipated from the motor
- R_{th} is the overall motor-to-ambient thermal resistance
- t is the motor operation time

If ΔT is specified, the aforementioned equation can be used to determine how long of the motor could reach the specified value of temperature rise.

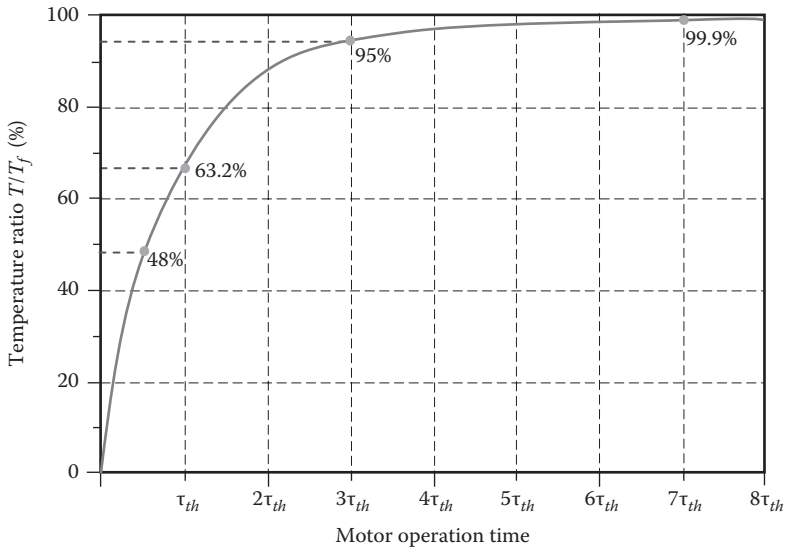

FIGURE 1.47
Variation of temperature ratio T/T_f as a function of motor operation time for a constant applied power.

Mathematically, as t approaches infinity (i.e., $e^{-t/\tau_{th}}$ approaches zero), the system attains thermal stability and the motor temperature reaches its final temperature T_f. Hence, the temperature rise ΔT becomes

$$\Delta T = T - T_a = P_{loss} R_{th} \tag{1.72}$$

The variation of the temperature ratio T/T_f with respect to motor operation time is plotted in Figure 1.47. At $t = 0$, the power is supplied to the motor and the motor temperature starts to rise exponentially until it reaches its final temperature at the thermal equilibrium. According to the engineering definition, thermal time constant is the time required to reach 63.2% of the final temperature.

It is worth to note that in practice, it is found that the thermal time constant of motor is not constant. It varies correspondingly to the change in heat load rates. For example, motors running in intermittent operation will have a shorter time constant than a motor running up to temperature in a continuous load operation. This is due to the definition of τ_{th} that assumes no internal heat generation and uniform heat distribution. Both are not purely true in motor operation.

1.4.8 Viscous Damping, K_{vd}

In general, damping can be divided into three types: viscous damping, coulomb or dry-friction damping, and hysteretic or structural damping. From the standpoint of physics, viscous damping is the dissipation of energy as occurred in liquid or air between moving parts. An example of viscous damping is ball bearing lubrication. It results in lower torque delivered at the output shaft to the torque developed at the rotor. Viscous damping in a single-degree-of-freedom torsional system is referred to as torsional viscous damping $K_{vd,t}$,

which is directly proportional to the damping torque T_d and inversely proportional to the angular velocity ω and is always opposite to the direction of motion, that is,

$$K_{vd,t} = \frac{T_d}{\omega} \tag{1.73}$$

The unit of viscous damping is N-m/rpm or N-m/(rad/s).

For reciprocating or linear motion systems, viscous damping $K_{vd,r}$ is defined as the ratio of the damping force F_d over the velocity $\dot{x}(t)$ with the unit of N-s/m:

$$K_{vd,r} = \frac{F_d}{\dot{x}(t)} \tag{1.74}$$

Another example of viscous damping is iron losses in a motor that are functions of frequency, circulating currents and iron mass.

1.5 Sizing Equations

The determination of appropriate motor size is an essential task in motor design. An oversized motor can provide itself a higher safety factor in stress and structural firmness but waste energy and can potentially create performance problems with the driven equipment, especially in turbomachinery such as fans or pumps. In some circumstances, an oversized motor may compromise the reliability of both the components and the entire system.

Empirical sizing equations are very useful for motor engineers to preliminarily determine the motor design at the early stage of motor design. Various sizing equations have been developed by different researchers and designers in the history of motor development. A set of sizing equations was proposed by Honsinger [1.74] for induction machines. This method focuses on the optimal electrical loading and the machine internal geometry for a given power level:

$$\frac{P}{n_s} = \xi_s D_{s,o}^3 L_e \tag{1.75}$$

$$\frac{P}{n_s} = \xi_r D_{r,o}^2 L_e \tag{1.76}$$

Based on these two sizing equations, the $D^{2.5}L_e$ sizing equations can be derived as

$$\frac{P_o}{n_s} = \xi_s' D_{s,o}^{2.5} L_e \tag{1.77}$$

$$\frac{P_o}{n_s} = \xi_r' D_{r,o}^{2.5} L_e \tag{1.78}$$

where

$D_{s,o}$ and $D_{r,o}$ are the OD of stator and rotor, respectively
P_o is the output power
n_s is the rotor rotating speed
L_e is the effective stack length and ξ_s, ξ_s' and ξ_r, ξ_r' are coefficients for stator and rotor, respectively

These coefficients contain the information regarding motor structure.

However, traditional sizing equations are based on the premise that the excitation of the electrical machine is provided by a sinusoidal voltage source to produce a sinusoidal EMF. In order to eliminate the deficiencies of traditional sizing equations, scientists at University of Wisconsin [1.75–1.77] have developed a general-purpose sizing equation that could take into account different waveforms of back EMF and machine characteristics. A particular effort has been made to express the sizing equation that characterizes the output power P_o as a function of overall volume of the machine. This sizing equation is easily adjustable for different motor topologies, such as RF, AF, and transverse-flux (TF) motors. The general-purpose sizing equation takes the form of

$$P_o = \frac{1}{1+K_\phi}\frac{m}{m_1}\frac{\pi}{2}K_e K_i K_p \eta B_g A \frac{f}{p}\lambda_o^2 d_{s,o}^2 L_e \tag{1.79}$$

where

$K_\phi = A_r/A_s$ is the ratio of electrical loading on rotor and stator
$A = A_r + A_s$ is the total electrical loading
m is the number of phases of the motor
m_1 is the number of phases of each stator (if there is more than one stator, each stator has the same m_1)
K_e is the EMF factor
K_i is the current waveform factor, defined as the peak phase current I_p to the *rms* value of the phase current I_{rms}
K_p is termed the electrical power waveform factor
η is the motor efficiency
f is the frequency
p is the motor pole pairs
λ is the ratio of the air gap surface diameter to the stator OD ($\lambda = d_g/d_{s,o}$)

The application of this general-purpose sizing equation can provide motor engineers with a useful tool in designing new high power density motors.

1.6 Motor Design Process and Considerations

The design of electric motor is a complex task, involving multidisciplines such as electromagnetics, mechanics, thermal science, material science, vibrations, acoustics,

rotordynamics, electronics, tribology, control theory, and mathematics. The design process of electric motors involves continuous iterations between electromagnetic, thermal, structural, rotordynamic, and systematic designs based on a variety of theoretical analyses, numerical simulations, and lab tests. To achieve an optimum design, all design parameters and criteria must be considered comprehensively.

There are two basic approaches in motor design: a subsystem/component approach and a system approach. Traditionally, a common engineering approach is to break down the system into subsystems or components (e.g., stator, rotor, feedback, cooling, coupling), design and optimize these subsystems, and then assemble them as a whole system. This is more likely the conventional bottom-up design strategy in engineering design. In the subsystem/component approach, the design of each subsystem/component is essentially independent of each other and all the work carry out in parallel. Thus, one of the benefits of this approach is its short design time with simplified problem. However, this approach ignores the interactions among different subsystems/components. This leads to a possible result that even if each subsystem/component performs well, the system as a whole may not perform well. This is because the sum of the functioning of the individual subsystem/component is quite often not equal to the functioning of the whole.

A system approach focuses on overall system performance and creates a technical solution that satisfies the functional requirements for the system. This is the result of the synthetic mode of thinking applied to physical problems. This approach takes account of the intrinsic connections and interactions among different subsystems/components. In this approach, the design engineers evaluate the entire system to determine how end-use requirements can be provided most effectively and efficiently. The system approach is actually based on a top-down design strategy, in which the requirements are always satisfied at every step of the design process.

In modern motor designs, engineers often involve some degree of compromise and trade-offs among various competing requirements and design features such as motor efficiency, operation reliability, torque density, IP rating, cooling, noise, and cost-effectiveness, to name a few. Decisions on trade-offs involve systematic comparisons of all benefits and costs for achieving a satisfactory overall design.

It is worth to note that the two design approaches are not always absolutely opposite. Under some circumstances, engineering designs may gainfully employ both methodologies [1.78].

1.6.1 Design Process

Good design of electric motor involves many engineering aspects upon which the success of the design work depends, including customer's specifications, motor operation condition, material selection, system integration, technical analysis, and manufacturing process, as demonstrated in Figure 1.48. In finding the best design solution, engineers must make trade-offs among many factors that determine the final design and cost of the motor. In addition, identifying and understanding the design constraints and limitations are critical to the success of the motor design.

The general design flow chart of electric motor is presented in Figure 1.49. The design process starts with the careful reviewing of customer's specifications and requirements, especially the requirements of motor operation and performance. Based on these information, the motor type and topology can be determined, such as PMM or IM, synchronous or asynchronous motor, and RF or AF motor. Then, the main motor design parameters are primarily set by using empirical equations. The overall sizing of the machine is of

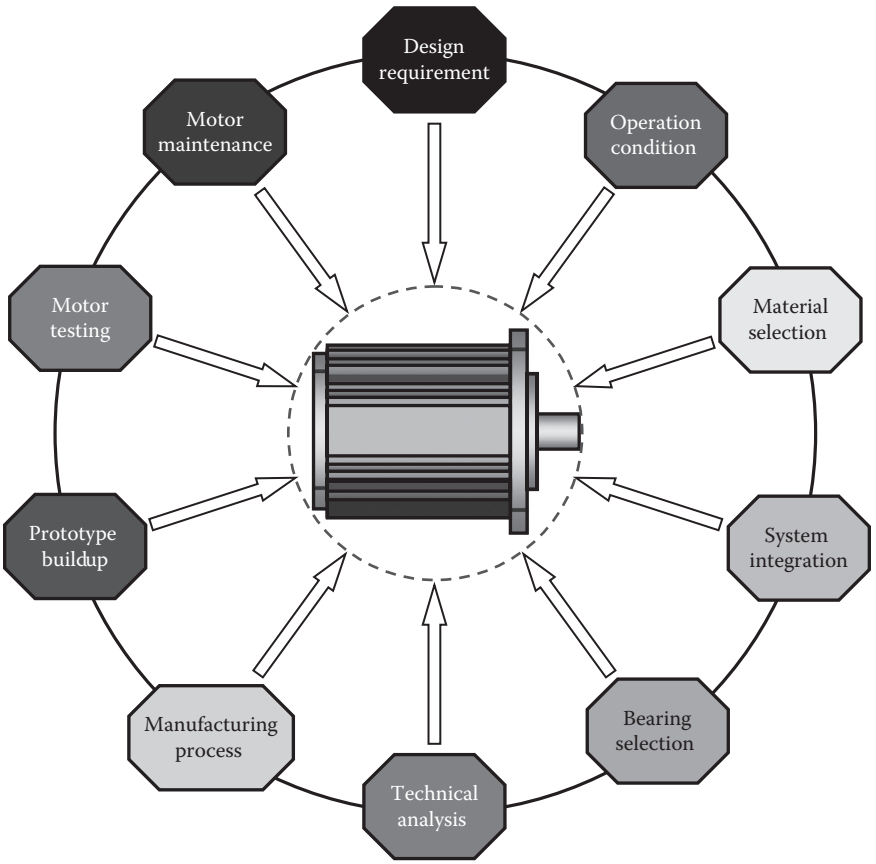

FIGURE 1.48
Motor design chart, indicating that in the motor design process many different design aspects must be taken into account.

great importance in terms of performance, structural integrity, cost, and weight. The major motor dimensions are determined via sizing equations available in the literature.

In the design of modern electric motors, none of technical design is isolated from the other designs. As a matter of fact, all designs in different fields have strongly influenced each other. Hence, these design processes are neither in series nor in parallel, rather, they form a crossover network. During this design stage, engineers/designers must communicate frequently to exchange their design concepts, innovative ideas, experience, and other useful information, especially the modifications that could impact on other designs. The design iterations between different design processes continue to carry out until the initial design is fully implemented.

Electromagnetic design is the core part of the motor design for determining motor key operating and performing characteristics. The electromagnetic design is highly dependent on the motor structure and rotordynamics analyses performed on the rotor. Recently, with the increasing demands for high-efficiency and high-reliability motors, one of the trends in novel motor development is to integrate the electromagnetic structure and mechanical transmission structure into a functional system for not only simplifying the motor structure but also increasing torque density, motor efficiency, and operation reliability.

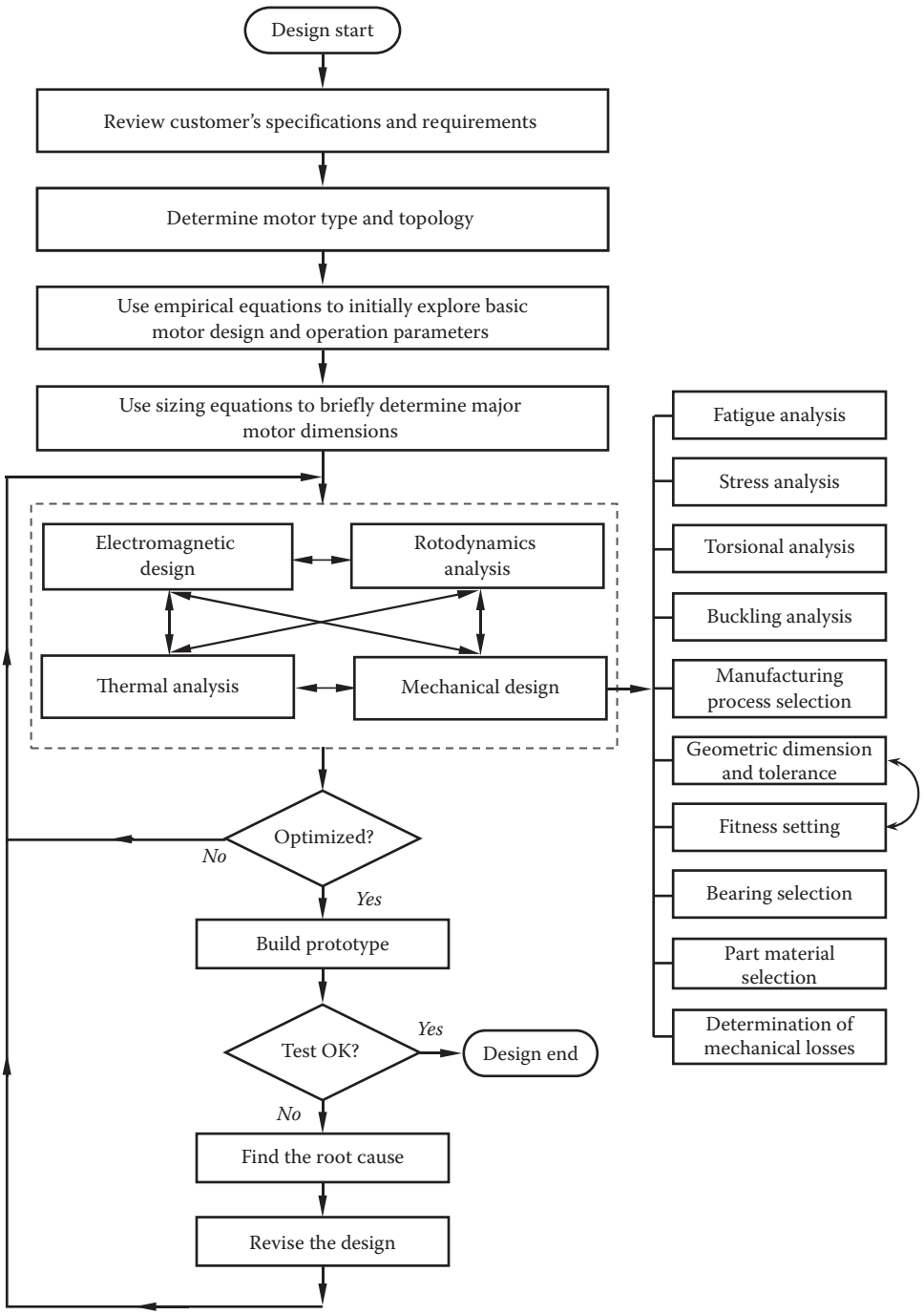

FIGURE 1.49
The flowchart of motor design.

The calculated power losses from electromagnetic design are passed into thermal analysis. With the fast development of computational technologies in last several decades, it becomes more popular today for thermal analysis to be executed by means of advanced computational fluid dynamics (CFD) software package. In the current CFD market, many powerful commercial software packages are available, either for general-purpose or specific applications, to solve heat transfer and fluid dynamics problems. CFD methods are used to provide detailed information of motor cooling such as temperature distribution, velocity field, pressure drop, and thermal interaction between solid surfaces and fluid flows in electric motors and to confirm and refine the preliminary designs. However, performing a CFD analysis still remains a challenging task and requires highly skilled engineers due to the complexities involved, such as the complexity of highly nonlinear partial differential equations, CFD model meshing, large amount demanding of computational resources, determination of models and parameter of turbulent flows, convergence of simulation, and complexity of inputs and related tasks. Extensive design iterations exist between the thermal, mechanical, and other design processes for achieving the optimized motor design.

Mechanical design consists of a number of design components:

- Fatigue analysis—As a material is subject to cyclic loads, a fatigue crack nucleus may be initiated on a microscopically small scale, and then the crack grows to a macroscopic size, finally causing material failure suddenly at a stress level below the material ultimate tensile strength or even yield tensile strength. During normal operation, some motor components are subject to alternative loads. One example is the motor shaft that is subject to gravitational force from the rotor core and drag force from a load machine (e.g., using belt or gear driving). When the rotor rotates, the shaft experiences cyclic loads creating a compression–expansion cycle for every revolution.
- Mechanical stress/strain analysis—The performance of mechanical stress/strain analysis is to determine whether the motor structure or components can withstand various loads without failure. The analysis allows for design optimization to achieve the best performance of electric motors. Due to the increasing complexity of modern motors, the stress/strain analysis today is mostly carried out using 3D finite element models. Recently, 3D finite element models have been used to perform thermomechanical analyses for providing more complete and accurate simulation results.
- Torsional analysis—When a motor is in normal operation, it may be subject to torsional vibration due to various causes. In analytically determining the torsional response, it requires to calculate the torsional resonance frequencies of the motor. To do this requires the torsional stiffness and mass inertia of both the motor and the load system, as addressed previously.
- Buckling analysis—Bucking is a phenomenon that a structural member subjected to compressive stress suddenly fails due to the loss of its stability. The actual compressive stress of the structural member at the point of failure is much lower than the ultimate strength that the material can withstand. For instance, some motors have a number of ventilation ducts within the lamination core (either stator or rotor or both). These ventilation ducts are constructed by I-beams or Π-beams that function like spacers. It is highly desired to perform bucking analysis to avoid the instability failure of beams.
- Determination of manufacturing process for motor components—Each motor part can be fabricated by many different manufacturing processes. The selection

of manufacturing process is based on many factors, including cost-effectiveness, productivity, process cycle time, availability, motor part geometry, requirements for part strengths, vibration and dampness, surface finishing, material properties, porosity/void, and environment friendliness. As an example, for a large volume of motor endbells, the most suitable manufacturing method is die casting.

- Determinations of geometric dimension and tolerance (GD&T)—The purpose of GD&T is defined as describing the geometric requirements for part and assembly geometry. Proper applications of GD&T can ensure allowable part and assembly geometry defined on the drawings leads to right size, shape, form, location, orientation, and location, define the proper assembly of mating parts, and enable assembled motors to function as intended. Mechanical engineers are responsible to provide the information for drafters and manufacturing engineers for the fabrication of motor components and the layout of motor assembly. Based on the information, 3D solid models can be generated to explicitly describe nominal geometries and their allowable variations at both the component level and system level.
- Setting up an appropriate fitness between mechanically mating components—Improper fitness between mating parts may greatly reduce the motor lifetime or lead to motor failure. For example, a loose fitting between a shaft and a bearing can cause the relative movement between the two components, resulting in a fast wear of the shaft and thus high heat generation due to the friction. In addition, an improper fitness may cause motor vibration.
- Selection of motor bearings—It has been reported that more than a half of motor failures can be attributed to the failure of bearings. Among them, improper selection of bearings is one of the major causes, usually dominated by wrong grease or lubrication selection.
- Selection of materials of motor components—Material selection in the motor industry is an artful balance between material performance, motor reliability, manufacturing process, and total cost. Apparently, material selection can heavily influence the motor performance and lifetime. None of the materials is perfect to satisfy all requirements. It is the responsibilities of engineers to make trade-offs between various design factors, for example, material performance and cost, and strength and durability.
- Determination of mechanical, electric, and electromagnetic power losses—The mechanical losses in a motor usually consist of friction losses and windage losses. The electric losses (also referred to as copper losses) represent all the resistive losses in motor windings and cables and are usually the main loss component in electric motors. The electromagnetic losses (i.e., iron losses), including eddy current and hysteresis losses in motor cores and other components, are often obtained through electromagnetic analysis conducted by electrical engineers. All the information is requested by thermal engineers for performing CFD or numerical heat transfer analysis.

Design optimization is the top goal of motor design. When the preliminary design is complete, the engineers need to examine whether the predetermined optimum objectives of the design have been reached. For different applications, these optimum objectives can be different, namely, the maximum peak torque, the highest torque density ratio, the most efficient cooling, and the total weight. If the design does not satisfy certain requirements,

the design engineers need to review their designs to identify the design gap and do the design iteration again until all optimum objectives are gained.

The next step is to build a prototype motor for validating the motor design as a whole unit. This is the critical step for the success of products. No matter how perfect the results achieved from engineering analyses are, prototype motor testing is an essential and necessary step to validate the conceptual design and ensure normal motor operation. Only after a series of successful tests, the motor can start mass production.

1.6.2 Design Integration

An electric motor usually consists of dozens to even thousands of components. In order to increase motor operation reliability, reduce the manufacturing cost, and simplify the assembly process, it is desired to integrate some of the components together in one self-contained package, including (1) motor-transmission device (e.g., gearbox, belt, chain) integration, (2) mechanical–electromagnetic system integration, and (3) motor control (e.g., feedback, drive).

As one of the most important constituents in an automated electric driving system, an electronic drive is used to deliver a useable form of power to control the performance of a servomotor for an end user. As presented in Figure 1.50, the integrated motor drive assembly system includes a motor, a fan, and a drive unit. One remarkable advantage of such integrated assembly systems is their compactness in size and ease of installation into a small industrial or other application. Generally, the drive is disposed on the motor or arranged in an integral housing with the motor. Both the motor and drive are shared with the same cooling fan [1.79].

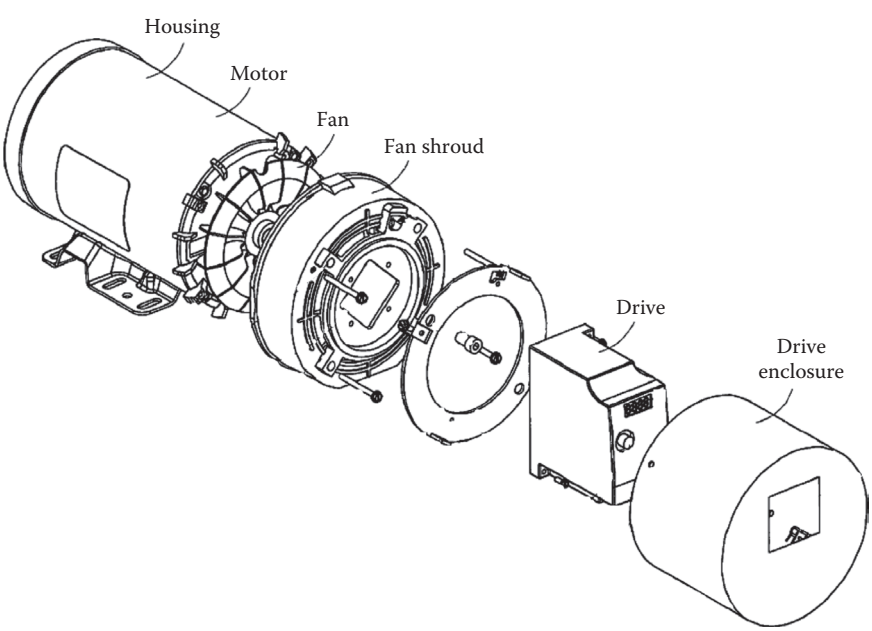

FIGURE 1.50
Integration of electric motor, drive, and fan as one unit (U.S. Patent 7,362,017) [1.79]. (Courtesy of the U.S. Patent and Trademark Office, Alexandria, VA.)

A growing trend in motor control is the integrated system that combines motor, feedbacks, and controller in one self-contained package. By integrating the controller with the motor, the possibility of mismatch is eliminated. Based on the integrated modular motor drive concept, an integrated traction drive has been developed recently. The integration of motor and drive offers a number of attractive features such as reduced drive volume and the elimination of power transmission cables. Correspondingly, it reduces radiated electromagnetic interference and voltage transient due to power transmission over long cable distances [1.80]. Furthermore, the integration of motor and drive can offer fault-tolerant features not possible with conventional drives [1.81,1.82]. On the caution side, significant thermal management and analysis are required to protect the electronic drive and motor combination.

1.6.3 Mechatronics

Mechatronics is the confluence of classical engineering disciplines with mechanical, electrical, and electromagnetic engineering, sensor technology, drive and actuator technology, control theory, and computer science. In recent years, one of the design trends in the electric machine industry is to design intelligent mechatronics products. Mechatronics is not just a new design strategy but also a new way of doing business to gain competitive advantage in the global market. As a result, it has been extensively used to design improved products and processes [1.83].

In fact, the mechatronic design approach that involved multidisciplinary is expected to become a key technology to gain a competitive advantage in the era of modern manufacturing. The development of mechatronics will therefore be crucial to the continued competitiveness of national economies.

The magnetic hard disk drive (HDD) is believed to be one of the most successful examples of modern mechatronics systems. In a state-of-the-art HDD servo system, a high-speed servomotor, a read/write head, a data storage disk, and other components are designed as one unit. The precision position control of HDD enables the tolerance to be less than one micrometer while operating at high speed [1.84]. As the mechatronics technology advances, new application areas of motor mechatronics can be developed in promising directions, such as mobile robots and medical devices.

1.7 Motor Failure Modes

There are a number of different approaches to assess motor failure modes. Generally, there are three primary failure modes identified from motor root cause analyses. The most important failure mode is electrical-related failure, caused by the breakdown of motor winding insulations, overloading condition, winding short circuit, and other issues. In a typical case, the breakdown of insulation material is attributed to exceeding of the temperature limit of windings. An overloading condition can cause the winding current exceeding its limit to damage coils. The second failure mode is magnetic failure, which usually resulted from the thermal demagnetization of PM (for PMMs). The thermal demagnetization of PM may be attributed to high motor operation temperature, shock, vibration, or strong magnetic field generated by a stator. The third failure mode is mechanical failure of motor structure and components. In this failure mode, bearing failures are encountered frequently. Another common failure mode is loose/broken rotor bars. Usually, most

mechanical failures result from slow processes such as mechanical wear and gradual degradation of material properties. During the process, the defective parts continue to display characteristic signs until they completely fail. This is different from most electronic component failures that happen suddenly and without warning.

Statistics have shown that despite the reliability and simplicity of construction of IMs, annual motor failure rate is conservatively estimated at 3%–5% per year, and in extreme cases, up to 12%, as in the pulp and paper industry [1.85]. The downtime in a factory due to motor failure may lead to a high cost, even exceeding the cost of motor replacement. In some instances, a motor failure may cause the entire production line to stop and thus interrupt the production process.

Based on the data collected from 1141 motors, those larger than 200 hp and less than 15 years in service, *IEEE* published a long report in three parts [1.86–1.88] to address motor failure modes according to the root causes of failure. In this report, Part I presented general results based on categories of motor types. Part 2 combined various categories and addressed some questions resulting from Part 1. Part 3 of the survey results was to address new questions and comments and to add more specific analyses of areas not yet explored previously.

A similar investigation of motor failure modes has been conducted by *Electric Power Research Institute* (*EPRI*) [1.89]. Though the approach of *EPRI* is different from *IEEE* (*EPRI* focused on failed motor components), their results are consistent. The integration of these two surveys was made by Venkataraman et al. [1.85], as presented in Table 1.6.

TABLE 1.6

Comparison of Failure Modes for Large-Size Motor

***IEEE* Survey**		***EPRI* Survey**		
Failure Contribution	**%**	**Failure Contribution**	**%**	**Average (%)**
Persistent overload	4.2	Stator ground insulation	23	Electrical-related failure
Normal deterioration	26.4	Turn insulation	4	
		Bracing	3	
		Core	1	
		Cage	5	
Electrical-related total	30.6	*Electrical-related total*	36	33.3
High vibration	15.5	Sleeve bearings	16	Mechanical-related failure
Poor lubrication	15.2	Antifriction bearings	8	
		Thrust bearings	5	
		Rotor shaft	2	
		Rotor core	1	
Mechanical-related total	30.7	*Mechanical-related total*	32	31.35
High ambient temperature	3.0	Bearing seals	6	Failures related to environmental maintenance and other reasons
Abnormal moisture	5.8	Oil leakage	3	
Abnormal voltage	1.5	Frame	1	
Abnormal frequency	0.6	Wedges	1	
Abrasive chemicals	4.2			
Poor ventilation cooling	3.9			
Other reasons	19.7	Other components	21	
Environmental reasons and other reasons total	38.7	*Maintenance-related and other parts total*	32	35.35

Data from *IEEE* and *EPRI* motor reliability surveys.

From the table, it can be seen that the most common reasons of the motor failures are bearing failures and failures related to the stator insulation. High vibration can lead to mechanical failures. Furthermore, many failures are related directly or indirectly to high operation temperature.

1.8 IP Code

Electric motors are designed to withstand various harsh environments such as flammable and explosive environments, high ambient pressure or vacuum, extreme temperatures, and high shock loads and vibrations. In some cases, they may operate in space or under deep water.

The IP code is an international standard for electric devices. It applies to the classification of degrees of protection provided by enclosures for electrical equipment against the insertion or intrusion of solid and liquid objects, external influences, or conditions such as dust, moisture, water, icing, corrosive solvents, and mechanical impacts. The IP code consists of two digits and optional letters. The indications of digits and optional letters are shown in Tables 1.7 and 1.8, respectively [1.90].

TABLE 1.7

Indications of IP Digits

First Digit: Protection against Ingress of Particles			Second Digit: Protection against Ingress of Water	
IP	**Protection of Person**	**Protection of Equipment**	**IP**	**Protection of Equipment**
0	No protection	No protection	0	No protection
1	Protected against contact with large areas of the human body (back of hand)	Protected against objects over 50 mm in diameter	1	Protected against vertically falling drops of water, e.g., condensation
2	Protected against contact with fingers	Protected against solid objects over 12 mm in diameter	2	Protected against direct sprays of water up to 15° from vertical direction
3	Protected against tools and wires over 2.5 mm in diameter	Protected against solid objects over 2.5 mm in diameter	3	Protected against sprays to 60° from vertical direction
4	Protected against tools and wires over 1 mm in diameter	Protected against solid objects over 1 mm in diameter	4	Protected against water sprayed from all directions (limited ingress permitted)
5	Protected against tools and wires over 2.5 mm in diameter	Protected against dust (limited ingress, no harmful deposit)	5	Protected against low-pressure jets of water from all directions (limited ingress permitted)
6	Protected against tools and wires over 2.5 mm in diameter	Totally protected against dust	6	Protected against strong jets of water
			7	Protected against the effects of immersion between 15 cm and 1 m
			8	Protected against long periods of immersion under pressure
			9K	Protected against ingress of high-temperature (steam) and/or high-pressure water

TABLE 1.8

Indications of Optional Letters in IP

First Letter (Optional)		Second Letter (Optional)	
Letter	**Protected against Access to Hazardous Parts with**	**Letter**	**Indication**
A	Back of hand	H	High-voltage device
B	Finger	M	Device moving during water test
C	Tool	S	Device standing still during water test
D	Wire	W	Weather condition

TABLE 1.9

Typical IP Codes Used for Different Motor Applications

IP Classification	Application
IP00	Open motor
IP12	Open drip-proof motor [1.91]
	Drip-proof motor [1.91]
IP13	Splash-proof motor [1.91]
IP21	Elevator motor
IP23, IP24	Weather protected motor [1.91]
IP42	Commercial refrigeration application
IP44	Totally enclosed fan-cooled motor [1.91]
	Totally enclosed pipe-ventilated motor [1.92]
IP54	Regular for commercial applications (fans, blowers)
	Totally enclosed force-ventilated motor [1.91]
	Totally enclosed air-to-air–cooled motor [1.92]
	Totally enclosed air-over motor [1.91]
	Totally enclosed air-to-water–cooled motor [1.91]
	Totally enclosed water-cooled motor [1.92]
IP55	Waterproof motor [1.92]
IP65	Motor used in hybrid vehicles
	Elevator motor
	High-speed spindle servomotor
	Some direct drive motor
IP67	Motor used under severe operation conditions (e.g., pitch and yaw control motors in wind turbines, driving motors in chemical reactors and in machine tools)
	Motor used outdoor under harsh environments
	Motor used in aerospace and defense applications (military vehicle, submarine, satellite, etc.)
	Motor used in food processing, beverage, and pharmaceutical applications
IP69K	Motor operating under ultra-harsh or aggressive environments (e.g., autoclaving, high-pressure spray, and frequent washdown with caustic chemicals)
	Motor used in deep water such as in propelling systems
	Liquid immersion pumps

The IP code has a strong impact on the motor design. With the IP defined, a number of design factors, such as motor construction, insulation, sealing method, coating, cooling technique, and component material, must be specifically determined to satisfy the requirements and regulations of the IP code.

As a reference, common IP codes used in electric motors in practice are summarized in Table 1.9.

References

[1.1] Waide, P. and Brunner, C. U. 2011. Energy-efficiency policy opportunities for electric motor-driven systems. International Energy Agency, Paris, France.

[1.2] Malcolm, D. R. 2006. Turn energy waste into profit. Plant services, http://www.plantservices.com/articles/2006/313/?show=all.

[1.3] Scheihing, P. E. 2007. A national strategy for energy efficient industrial motor-driven systems. In *Energy Efficiency Improvement in Electric Motors and Drives*. Part VIII, Springer, Berlin Heidelberg, pp. 377–389.

[1.4] Gee, W. 2004. Sturgeon, William (1783–1850). *Oxford Dictionary of National Biography*. Oxford University Press, Oxford, U.K.

[1.5] Davenport, T. 1837. Improvements in propelling machinery by magnetism and electromagnetism. U.S. Patent 132.

[1.6] Tesla, N. 1888. Electro magnetic motor. U.S. Patent 381,968.

[1.7] Hubbell, M. W. 2011. *The Fundamentals of Nuclear Power Generation: Questions and Answers*. AuthorHouse, Bloomington, IN.

[1.8] Armstrong, A. W. Jr. 1998. Load to motor inertia mismatch: Unveiling the truth. *Drive and Controls Conference*, Telford, U.K. http://www.diequa.com/download/articles/inertia.pdf.

[1.9] Voss, W. 2007. *A Comprehensible Guide to Servo Motor Sizing*. Copperhill Technologies Corporation, Greenfield, MA.

[1.10] IEEE Power Engineering Society. 2004. IEEE 112-2004 Standard test procedure for polyphase induction motors and generators. IEEE, New York.

[1.11] Hanselman, D. C. 1997. Effect of skew, pole count and slot count on brushless motor radial force, cogging torque and back EMF. *IEE Proceedings of Electric Power Applications* **144**(**5**): 325–330.

[1.12] Hanselman, D. C. 2006. *Brushless Permanent Magnet Motor Design*, 2nd edn. Magna Physics Publishing, Lebanon, OH.

[1.13] Lu, K. Y., Rasmussen, P. O., and Ewen Ritchie, E. 2006. An analytical equation for cogging torque calculation in permanent magnet motors. *17th International Conference on Electrical Machines*, Chania, Crete, Greece.

[1.14] Hitachi Metals, Ltd. 2013. Permanent magnets. http://www.hitachi-metals.co.jp/products/auto/el/pdf/hg-a27.pdf.

[1.15] Hsu, J. S., Scoggins, B. P., Scudiere, M. B., Marlino, L. D., Adams, D. J., and Pillay, P. 1995. Nature and assessments of torque ripple of permanent-magnet adjustable-speed motors. *IEEE Industry Application Conference*, vol. 3, pp. 2696–2702.

[1.16] Bianchi, N. and Bolognani, S. 2002. Design techniques for reducing the cogging torque in surface-mounted PM motors. *IEEE Transaction Industry Applications* **38**(**2**): 1259–1265.

[1.17] Zhu, Z. Q., Ruangsinchaiwanich, D., Ishak, D., and Howe, D. 2005. Analysis of cogging torque in brushless machines having non-uniformly distributed stator slots and stepped rotor magnets. *IEEE Transaction on Magnetics* **41**(**10**): 3910–3912.

[1.18] Aydin, M., Zhu, Z. Q., Lipo, T. A., and Howe, D. 2007. Minimization of cogging torque in axial flux permanent magnet machines—Design concepts. *IEEE Transaction on Magnetics* **43**(**9**): 3614–3622.

[1.19] Salminen, P. 2004. Fractional slot permanent magnet synchronous motor for low speed applications. PhD thesis, Lappeenranta University of Technology, Lappeenranta, Finland.
[1.20] Martin, J. P., Meibody-Tabar, F., and Davat, B. 2000. Multiple-phase permanent magnet synchronous machine supplied by VSIs working under fault condition. *IEEE Industry Application Conference*. *35th IAS Annual Meeting*, Rome, Italy.
[1.21] Li, T. and Slemon, G. 1988. Reduction of cogging torque in permanent magnet motors. *IEEE Transactions on Magnetics* **24**(**6**): 2901–2903.
[1.22] Dosiek, L. and Pillay, P. 2007. Cogging torque reduction in permanent magnet machines. *IEEE Transactions on Industry Applications* **43**(**6**): 1565–1571.
[1.23] Ishikawa, T. and Slemon, G. R. 1993. A method of reducing ripple torque in permanent magnet motors without skewing. *IEEE Transaction on Magnetics* **29**(**2**): 2028–2031.
[1.24] Lateb, R., Takorabet, N., Meibody-Tabar, F., Enon, J., and Sarribouette, A. 2006. Design technique for reducing the cogging torque in large surface-mounted magnet motors. In *Recent Developments of Electrical Drives* (Eds.: S. Wiak, M. Dems, and K. Komeza). Springer, Dordrecht, the Netherlands, pp. 59–72.
[1.25] Muljadi, E. and Green, J. 2002. Cogging torque reduction in a permanent magnet wind turbine generator. *ASME 2002 Wind Energy Symposium*. Paper no. WIND2002-56, Reno, NV, pp. 340–342.
[1.26] Lao, Y. D., Huang, D. R., Wang, J. C., Liou, S. H., Wang, S. J., Ying, T. F., and Chiang, D. Y. 1997. Simulation study of the reduction of cogging torque in permanent magnet motors. *IEEE Transactions on Magnetics* **33**(**5**): 4095–4097.
[1.27] Soleimani, J., Vahedi, A., and Mirimani, S. M. 2011. Inner permanent magnet synchronous machine optimization for HEV traction drive application in order to achieve maximum torque per ampere. *Iranian Journal of Electrical & Electronic Engineering* **7**(**4**): 241–248.
[1.28] Hsu, J. S., Scoggins, B. P., Scudiere, M. B., Marlino, L. D., Adams, D. J., and Pillay, P. 1995. Nature and assessments of torque ripples of permanent-magnet adjustable-speed motors. *Proceedings of IEEE Industry Application Conference* **3**: 2696–2702.
[1.29] Holtz, J. and Springob, L. 1996. Identification and compensation of torque ripple in high-precision permanent magnet motor drives. *IEEE Transactions on Industrial Electronics* **43**(**2**): 309–320.
[1.30] Parker Hannifin Electromechanical Division. 2011. Factors affecting velocity and current ripple. http://www.parkermotion.com/dmxreadyv2/blogmanager/blogmanager.asp?category=drives.
[1.31] Hunt, G. How to select a DC motor: The different characteristics of each group of DC motors. http://insidepenton.com/machinedesign/nl/MicroMO-DCmotor-select.PDF.
[1.32] Feese, T. and Hill, C. 2009. Prevention of torsional vibration problems in reciprocating machinery. In *Proceedings of the Thirty-Eight Turbomachinery Symposium*, Houston, TX, pp. 213–238.
[1.33] Eshleman, R. L. 2009. Torsional vibration in reciprocating and rotating machines. In *Harris' Shock and Vibration Handbook* (Eds.: A. G. Piersol and T. L. Paez), 6th edn. McGraw-Hill, New York, Chapter 37.
[1.34] Stephens, L. 2011. Servo controls deliver performance benefits for medical imaging systems. Kollmorgen Paper 2-09-11.
[1.35] Stephens, L. 2010. The significance of load to motor inertia mismatch. Kollmorgen Paper 08-12-10.
[1.36] Shu, H.-C. and Chen, C. H. 2011. Servo motor with large rotor inertia. U.S. Patent 7,911,095.
[1.37] IEC. 2004. *International Standard IEC 60034-1. Rotating Electrical Machines—Part 1: Rating and Performance*, 11th edn. IEC, Geneva, Switzerland.
[1.38] Mirchevski, S. 2012. Energy efficiency in electric drives. *Electronics* **16**(**1**): 46–49.
[1.39] IEC. 2008. IEC 60034-30. Rotating electrical machines—Part 30: Efficiency classes of single-speed, three-phase, cage-induction motors. IEC, Geneva, Switzerland.
[1.40] IEC. 2007. IEC 60034-2-1. Rotating electrical machines—Part 2-1: Standard methods for determining losses and efficiency from tests. IEC, Geneva, Switzerland.

[1.41] IEC. 2010. IEC 60034-31. Rotating electrical machines—Part 31: Guide for the selection and application of energy-efficient motors including variable-speed applications. IEC, Geneva, Switzerland.
[1.42] Berger, L. I. 2006. Dielectric strength of insulating materials. In *CRC Handbook of Chemistry and Physics* (internet version 2006) (Eds.: D. R. Lide), Chapter 15. Taylor & Francis, Boca Raton, FL, pp. 42–46.
[1.43] Skanavi, G. I. 1958. Fizika dielektrikov: Oblast' sil'nykh poleĭ (Physics of dielectrics: Strong fields domain). Moscow: *Fizmatgiz* **26**: 609–612.
[1.44] Vedensky, B. A. and Vul, B. M. 1965. *Encyclopedic Dictionary in Physics*, Vol. 4. Soviet Encyclopedia Publishing House, Moscow, Russia.
[1.45] Suzuki, H., Mukai, S., Ohki, Y., Nakamichi, Y., and Ajiki, K. 1997. Dielectric breakdown of low-density polyethylene under simulated inverter voltages. *IEEE Transactions on Dielectrics and Electrical Insulation* **4**(**2**): 238–240.
[1.46] Mori, T., Matsuoka, T., and Muzitani, T. 1994. The breakdown mechanism of poly-p-xylylene film. Prestress effects on the breakdown strength. *IEEE Transactions on Dielectrics and Electrical Insulation* **1**(**1**): 71–76.
[1.47] Bjellheim, P. and Helgee, B. 1994. AC breakdown strength of aromatic polymers under partial discharge reducing conditions. *IEEE Transactions on Dielectrics and Electrical Insulation* **1**(**1**): 89–96.
[1.48] Zheng, J. P. Cygan, P. J., and Jow, T. R. 1996. Investigation of dielectric properties of polymer laminates with polyvinylidene fluoride. *IEEE Transactions on Dielectrics and Electrical Insulation* **3**(**1**): 144–147.
[1.49] Shugg, W. T. 1995. *Handbook of Electrical and Electronic Insulating Materials*, 2nd edn. IEEE Press, New York.
[1.50] National Electric Manufacturers Association (NEMA). 2011. NEMA MG 1-2011 motors and generators. NEMA, Rosslyn, VA.
[1.51] International Electrotechnical Commission (IEC). 2004. IEC 60085 Electrical insulation—Thermal evaluation and designation. 4th edition.
[1.52] Bonnett, A. H. and Soukup, G. C. 1992. Cause and analysis of stator and rotor failures in three-phase squirrel-cage induction motors. *IEEE Transactions on Industry Applications* **28**(**4**): 921–937.
[1.53] Wilson, D. S. and Smith, R. 1977. Electric motor reliability model. Report number RADC-TR-77-408. Rome Air Development Center, Griffiss Air Force Base, New York.
[1.54] U.S. Department of Energy. 2008. *Improving Motor and Drive System Performance: A Sourcebook for Industry*. National Renewable Energy Laboratory. https://www1.eere.energy.gov/manufacturing/tech_assistance/pdfs/motor.pdf.
[1.55] Chapman, S. J. 2005. *Electric Machinery Fundamentals*, 4th edn. McGraw-Hill, New York.
[1.56] NMB Technologies Corporation. The emergence of brushless DC motors within medical applications. http://www.nmbtc.com/pdf/engineering/motors_emergence_of_brushless_dc.pdf.
[1.57] Smith, J. S. and Watson, A. P. 2005. Design, manufacturing, and testing of a high speed 10 MW permanent magnet motor and discussion of potential application. *Proceedings of 35th Turbomachinery Symposium*, Houston, TX, pp. 19–24.
[1.58] Parviainen, A. 2005. Design of axial-flux permanent-magnet low-speed machines and performance comparison between radial-flux and axial-flux machines. PhD thesis, Lappeenranta University of Technology, Lappeenranta, Finland.
[1.59] Jian, L. N., Chau, K. T., Yu Gong, Y., Yu, C., and Li, W. L. 2009. Analytical calculation of magnetic field in surface-inset permanent magnet motors. *IEEE Transactions on Magnetics* **45**(**10**): 4688–4691.
[1.60] Lewotsky, K. 2012. Interior permanent magnet motors power traction motor applications. Motion Control Association. http://www.motioncontrolonline.org/i4a/pages/index.cfm?pageID=4379.

[1.61] National Electric Manufacturers Association (NEMA). 2004. Industrial control and systems: Motion/position control motor, controls and feedback devices. ICS 16-2001. Section I.
[1.62] Schneider Electric Motion. 2012. Electric motors: General information for all motors. http://motion.schneider-electric.com/downloads/whitepapers/Electric_Motors_whitepaper.pdf.
[1.63] Condit, R. and Jones, D. W. 2004. Stepping motors fundamentals. Microchip Technology Inc. Publication no. AN907. http://www.bristolwatch.com/pdf/stepper.pdf.
[1.64] Wavre, N., Vaucher, J.-M., and Piaget, D. 1998. *Drive Systems for Demanding Applications—Linear and Torque Motors in the Industrial Environment*. Carl Hanser Verlag, Munich, Germany.
[1.65] Electropaedia. 2005. Electric drives—Brushless DC/AC and reluctance motors (description and applications). http://www.mpoweruk.com/motorsbrushless.htm.
[1.66] Ahn, J.-W. 2011. Switched reluctance motor. In *Torque Control* (Eds.: M. T. Lamchich). InTech, pp. 201–252.
[1.67] Vaithilingam, C. A., Misron, N., Aris, I., Marhaban, M. H., and Nirei, M. 2013. Electromagnetic design and FEM analysis of a novel dual-air-gap reluctance machine. *Progress in Electromagnetics Research* **140**: 523-544.
[1.68] McMahon, J. 2010. Piezo motors and actuators: Streamlining medical device performance. *European Medical Device Technology*. http://www.emdt.co.uk/article/piezo-motors-and-actuators.
[1.69] Kollmorgen. 2011. Servodisc catalog. http://www.electromate.com/db_support/downloads/KollmorgenGearmotorSeries.pdf.
[1.70] Kang, C.-i. 2001. Method of estimating motor torque constant. U.S. Patent 6,320,338.
[1.71] Younkin, G. W. Electric servo motor equations and time constants. http://www.ctc-control.com/customer/elearning/younkin/driveMotorEquations.pdf.
[1.72] Welch, R. H. Jr. and Younkin, G. W. 2002. How temperature affects a servomotor's electrical and mechanical time constants. *IEEE Industry Applications Conference. 37th IAS Annual Meeting*, Pittsburgh, PA, Vol. 2, pp. 1041–1046.
[1.73] Mazurkiewicz, J. Check temperature when specifying motors. http://www.motioncontrolonline.org/files/public/Check_Temperature_when_Specifying_Motors.pdf.
[1.74] Honsinger, V. B. 1987. Sizing equations for electrical machinery. *IEEE Transaction on Energy Conversion* **EC-2**(**1**): 116–121.
[1.75] Huang, S., Luo, J., Leonardi, F., and Lipo, T. A. 1998. A general approach to sizing and power density equations for comparison of electrical machines. *IEEE Transactions on Industry Applications* **34**(**1**): 92–97.
[1.76] Huang, S., Aydin, M., and Lipo, T. A. 2001. Torque quality assessment and sizing optimization for surface mounted permanent magnet machines. *IEEE Industry Applications Conference*, Chicago, IL, Vol. 3, pp. 1603–1610.
[1.77] Huang, S., Aydin, M., Lipo, and T. A. 2002. A direct approach to electrical machine performance evaluation: Torque density assessment and sizing optimization. *Proceedings of International Conference on Electrical Machines, ICEM'02*, Brugge, Belgium.
[1.78] Misra, K. B. 2008. Engineering design: A system approach. In *Handbook of Performability Engineering* (Eds.: K. B. Misra). Springer, London, U.K., pp. 13–24.
[1.79] Piper, J. A., Dudas, M. J., and Sudhoff, D. H. 2008. Motor with integrated drive unit and shared cooling fan. U.S. Patent 7,362,017.
[1.80] Choi, G., Xu, Z., Li, M., Gupta, S., Jahns, T. M., Wang, F., Duffie, N. A., and Marlino, L. 2011. Development of integrated modular motor drive for traction applications. *SAE International Journal of Engines* **4**(**1**): 286–300.
[1.81] Brown, N. R., Jahns, T. M., and Lorenz, R. D. 2007. Power converter design for an integrated modular drive. *IEEE Industrial Applications Society Annual Meeting*, New Orleans, FL, pp. 1322–1328.
[1.82] Sylora, B. J., Jahns, T. M., and Lorenz, R. D. 2008. Development of a demonstrator model of an integrated modular motor drive. *2008 NSF-CPES Annual Conference*, Blacksburg, VA.

[1.83] Ashley, S. 1997. Getting a hold on mechatronics. *ASME Mechanical Engineering Magazine*, May issue: 60–63.

[1.84] Oonsivilai, A. and Meeboon, N. 2008. Verification skip writes head-positioning error mechanism using skip writes problem detection. *Eighth World Scientific and Engineering Academy and Society (WSEAS) International Conference on Robotics, Control and Manufacturing Technology*, Hangzhou, China.

[1.85] Venkataraman, B., Godsey, B., Premerlani, W., Shulman, E., Thakur, M., and Midence, R. 2005. Fundamentals of a motor thermal model and its applications in motor protection. *Proceeding of 58th Annual Conference for Protective Relay Engineers*, College Station, TX, pp. 127–144.

[1.86] Motor Reliability Working Group. 1985. Report of large motor reliability survey of industrial and commercial installations, Part I. *IEEE Transactions of Industry Applications* **IA-21**(**4**): 853–864.

[1.87] Motor Reliability Working Group. 1985. Report of large motor reliability survey of industrial and commercial installations, Part II. *IEEE Transactions of Industry Applications* **IA-21**(**4**): 865–872.

[1.88] Motor Reliability Working Group. 1987. Report of large motor reliability survey of industrial and commercial installations, Part III. *IEEE Transactions of Industry Applications* **IA-23**(**1**): 153–158.

[1.89] Cornell, E. P., Owen, E. L., Appiarius, J. C., McCoy, R. M., Albrecht, P. F., and Houghtaling, D. W. 1982. Improved motors for utility applications: Final report. The Institute, Palo Alto, CA.

[1.90] IEC. 2001. International Standard IEC 60529. Degree of protection provided by enclosures (IP Code), 2.1 edn. IEC, Geneva, Switzerland.

[1.91] Teco-Westinghouse. Wound rotor motor technology. http://www.tecowestinghouse.com/PDF/woundrotor.pdf.

[1.92] NEMA. 2002. NEMA standards publication MG 1-1998 (revision 3, 2002) interfiled: Motors and Generators. http://www.homewoodsales.com/PDFs/tech-library/Motors/NEMA/CompleteMG1-1998Rev3.pdf.

2

Rotor Design

An electric motor primarily consists of a rotor and a stator, which are separated by an air gap and integrated together via bearings and a motor frame. The rotor is the rotating component to drive an external loading machine, and the stator is the stationary component to produce a rotating magnetic field.

Rotor design involves a wide range of knowledge, skills, and experience across various disciplines including material science, rotor dynamics, electromagnetics, structural mechanics, aerodynamics, manufacturing technology, tribology, thermal engineering, and fluid dynamics. Furthermore, during the rotor design, a large number of design parameters must be carefully considered and determined.

As discussed previously, an AC motor can be primarily classified as either an induction motor (IM) or a permanent magnet motor (PMM), depending on how the rotor is constructed. Because the structure and the working principle of these two types of motors are fundamentally different, IM and PMM are addressed separately in the following sections.

2.1 Rotor in Induction Motor

A typical rotor in an IM comprises a cylindrical core that is made up of silicon steel laminates and pressed onto the cylindrical motor shaft. There are two types of IMs: wound rotor IMs and squirrel cage rotor IMs. The primary difference between these two types of IM motor is the design of the motor rotor. While the design of stators for all IMs is almost the same, the rotor construction is quite different for different types of IMs.

2.1.1 Wound Rotor

In a wound rotor, a set of insulated rotor windings, which are similar to the stator windings, are utilized to accept external impedances. A set of rotor windings are correspondingly connected to a set of insulated slip rings mounted on the rotor shaft. The carbon-composite brushes riding on the slip rings connect to a set of external rheostats (Figure 2.1). This rotor construction design allows the external rheostats to be placed in series with the rotor windings. These rheostats, varying from almost short-circuit condition to an open-circuit condition with infinite external resistance, can remarkably improve motor starting characteristics, of which low inrush current is being the most significant.

Wound rotor IMs have some distinct advantages over other types of IMs. A special feature of the wound rotor motor is its capability to control the motor velocity at different load levels by controlling the rotor currents. By varying the rheostat resistance, it is possible to change the slip and thus to change the rotor rotating velocity. This feature has been used to improve the motor performance. For instance, a wound rotor has ability to gradually bring up to speed for high-inertia and large load equipment.

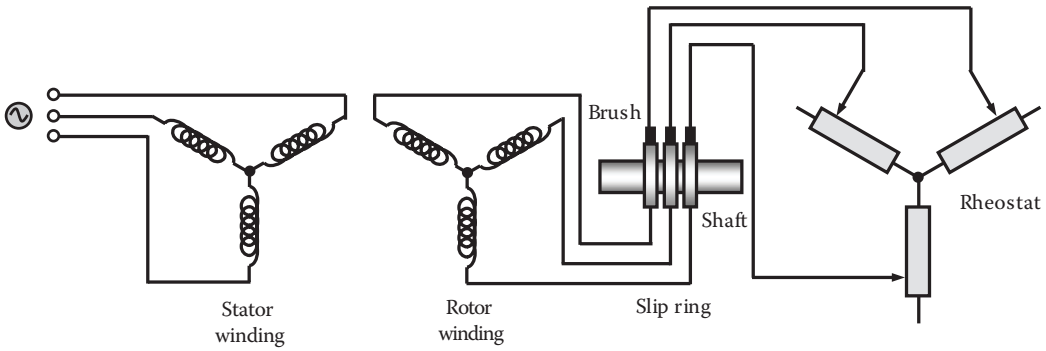

FIGURE 2.1
Wound rotor IM using slip rings and brushes to contact rotor winding and external resistances for improving motor start characteristics

Long motor life is ensured with the use of external resistor banks during motor start-up. For these reasons, the wound rotor IMs are conventionally used for high-power industrial applications.

Using this feature can optimize the torque–speed characteristics for different applications [2.1]. The impact of the rotor resistance on the torque–speed characteristics is shown in Figure 2.2. It can be seen that increasing rotor resistance can result in the shift of the breakdown torque toward zero speed. This can eventually alter motor performance characteristics: (1) The increase in the rotor resistance causes the significant

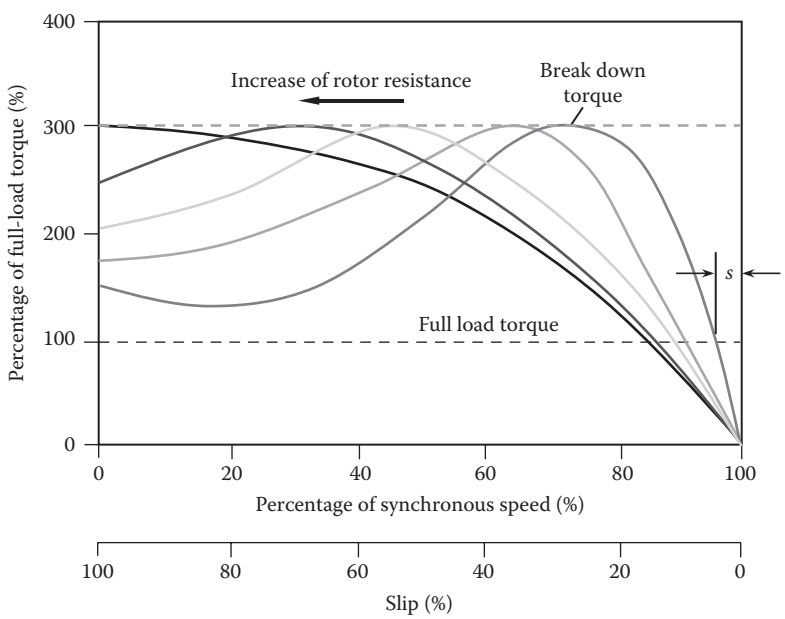

FIGURE 2.2
Variations of torque–speed characteristics of wound IMs as a function of rotor resistance. Increasing rotor resistance results in the shift of the breakdown torque toward zero speed, causing the increase of slip and starting torque and the decrease of full-load speed.

increase in the starting torque and the decrease in the corresponding starting current. (2) A higher rotor resistance leads to the reduction of the rotating speed of the rotor, that is, the increase of slip. (3) For a given full-load torque, the motor full-load speed decreases as the motor rotor resistance increases. However, the reduction of the full-load speed in such a way is highly undesirable since it lowers the motor efficiency and power output as the increase in the resistive losses (i.e., I^2R losses). (4) Under high rotor resistance conditions, the pull-up torque may be eliminated from the torque–speed curves. In fact, a high rotor resistance causes the motor torque to decrease more rapidly than those with lower rotor resistances. (5) The higher rotor resistance is always related to the larger variation in the rotation speed as the torque varies. This indicates that wound rotor IMs having high rotor resistances are more susceptible to speed variations as the load torque changes [2.2].

The rotor windings are made up of copper coils inserted into rotor slots. Essentially, the rotor windings exhibit inductance and resistance, and these characteristics can effectively depend on the frequency of current flowing in the rotor. Today, the wound rotor IMs are less used in industrial applications due to frequent maintenances for slip rings and brushes, high rotor inertia, and requirement of bulky resistor banks.

2.1.2 Squirrel Cage Rotor

Most IMs used today are of squirrel cage type. A squirrel cage rotor consists of a rotor core made by stacked laminations and a shaft fitted in the rotor core. A number of equally spaced open or closed slots are punched at the outer circumference of the laminations (Figure 2.3). In fact, the selection of open or closed rotor slot design involves the trade-off because each design has its own advantages and disadvantages, depending on different applications. Open rotor slots allow a substantial reduction of the rotor leakage inductance with the possibility to increase the constant power range speed regulation. As contrast, closed slots tend to produce lower surface loss and have higher rotor leakage inductance for a better filtering in presence of inverter supply [2.3,2.4].

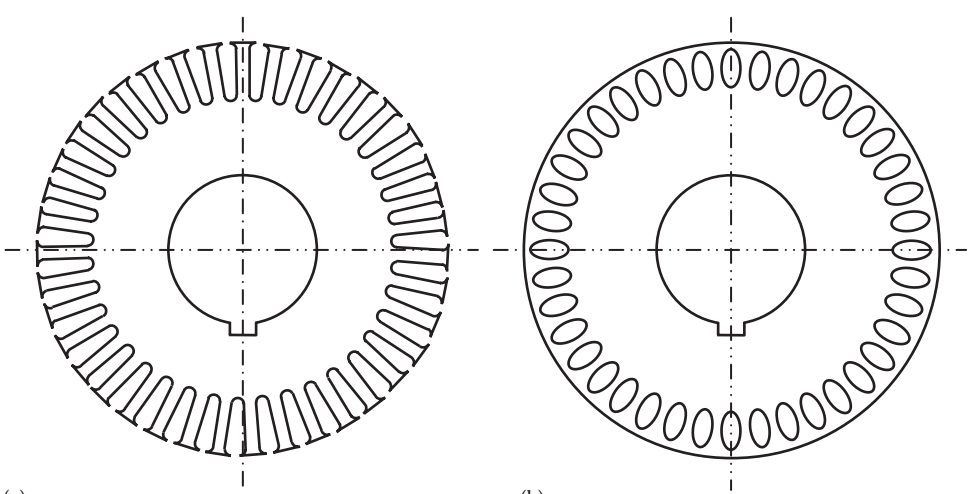

FIGURE 2.3
Rotor slots of a squirrel cage motor: (a) open slots and (b) closed slots.

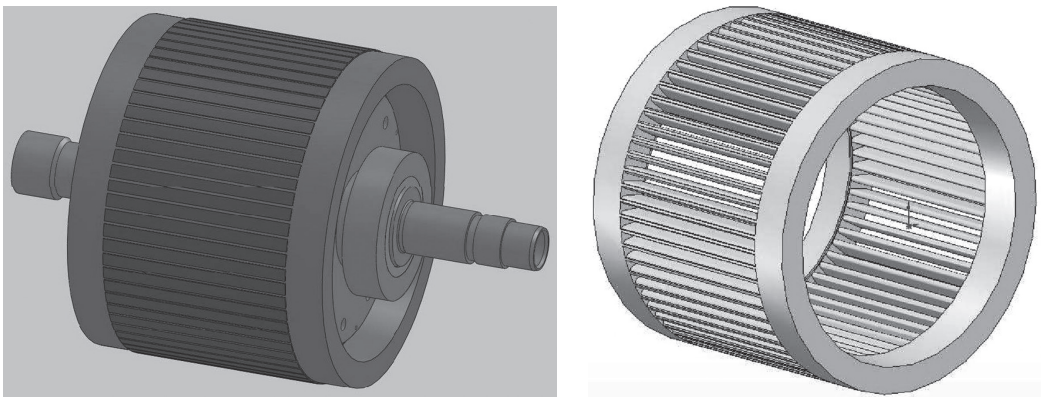

(a) (b)

FIGURE 2.4
Casted copper rotor assemble: (a) the rotor is assembled by integrating two hollow shafts with the casted copper rotor core. (b) Conducting bars and end rings form a closed loop for inducted current as the steel rotor laminations are removed from the rotor core.

A transient 2D FEA has shown that the closed slot rotor geometry gives less spatial rotor harmonics and less stator current harmonics, leading to a significantly lower level of stator vibrations for frequencies above 1 kHz of induction machines [2.5]. In addition, closed slot rotor helps improve the die-casting process.

Rotor conducting bars are made by casting a conducting material (usually aluminum or copper) directly into rotor slots. These casted conducting bars are usually slightly skewed to the axis of the rotor for reducing cogging torque and connected together with an end ring at each of the rotor end to form a closed electric circuit. Thus, the stator windings set up a rotating magnetic field around the rotor to induce electric current in the conductive bars and end rings. In turn, the induced currents in the conducting bars/end rings react with the magnetic field of the stator to produce forces acting at a tangent orthogonal to the rotor, resulting in continuous torque on the motor shaft to drive external loads. As shown in Figure 2.4, by removing the steel laminations, the conducting bars and end rings form a squirrel cage. Thicker end rings can not only reduce current densities but also increase the heat dissipation capability of the rotor.

2.1.2.1 Factors Impacting Resistance of Squirrel Cage Rotor

There are a variety of factors impacting characteristics and performance of squirrel cage rotors, including the conducting bar material, number of conducting bars, cross-sectional area, bar configuration and shape, skew angle, and bar position relative to the rotor surface.

A conducting bar with a large cross-sectional area exhibits a low resistance. Moreover, the electric conductivity of copper is nearly 60% higher than that of aluminum. Thus, it is commonly accepted that copper rotor bars are superior over aluminum bars because of lower power losses, better performance, and higher motor efficiency. It has been reported that the incorporation of casting copper for conducting bars and end rings in place of aluminum would result in attractive improvements in motor energy efficiency through reductions in motor losses ranging from 15% to 20% [2.6]. With an FEA software, Daut et al. [2.7] have analyzed and investigated the performance of the

three-phase 0.5 hp IM using either copper or aluminum rotor bars. The FEA results fall into four groups: torque versus speed, torque versus slip, power loss versus speed, and power loss versus slip. Comparisons between copper and aluminum rotor bars have been performed in these four groups and shown that the copper rotor bars excel in all investigated performance issues.

The position of conducting bars in a squirrel cage IM is an important design parameter to affect the motor performance. The impedance of a conducting bar is comprised of both the resistance and inductance. According to the position of the conducting bar relative to the rotor surface, the conducting bar exhibits different magnetic leakage flux and inductance. Positioning the conducting bars near the rotor surface (i.e., near the stator) will produce a relatively small leakage flux and a small inductance. In contrast, positioning the conducting bar deeper radially into the rotor slots (i.e., away from the stator) will result in more leakage and a higher inductance and consequently a higher impedance. Due to the skin effect, at high frequencies, the AC impedance of the outer portion of the conducting bar is lower than that of the inner portion.

2.1.2.2 Double-Cage Rotor

The invention of double-cage rotor was motivated to develop a type of motor that is characterized by a variable rotor resistance during motor operation. This type of motor offers preferably high rotor resistance at the motor start-up, high locked torque, low starting current, and high pull-up torque, while maintaining higher efficiencies when compared to the same power ratings with single-cage designs. For the specific rotor designs and operating conditions, the comparison of torque–speed curves of double-cage and single-cage rotors is presented in Figure 2.5.

As presented in Figure 2.6, a double-cage consists of a large cage buried deeply in the rotor and a small cage located near the rotor surface. The conducting bars in the large cage are loosely linked with the stator and have low resistance and high leakage inductance. In contrary, the conductors in the small cage are closely linked with the stator and have high resistance and low leakage inductance. At the motor start-up stage, only the conductor

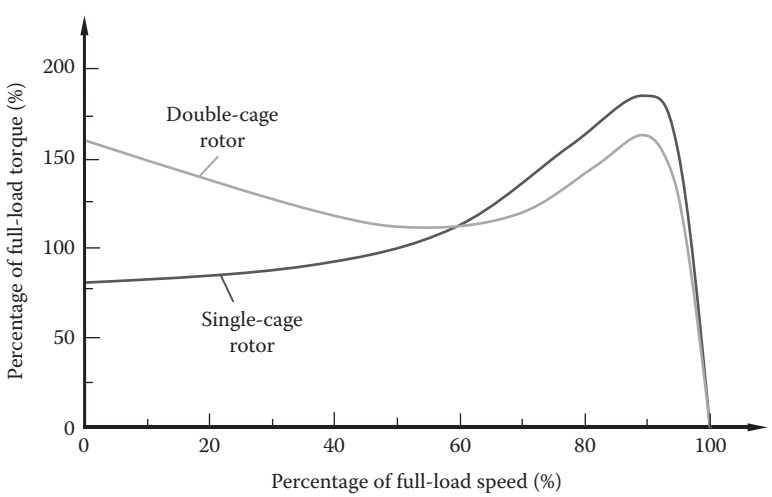

FIGURE 2.5
Comparison of torque–speed curves between double-cage and single-cage rotors.

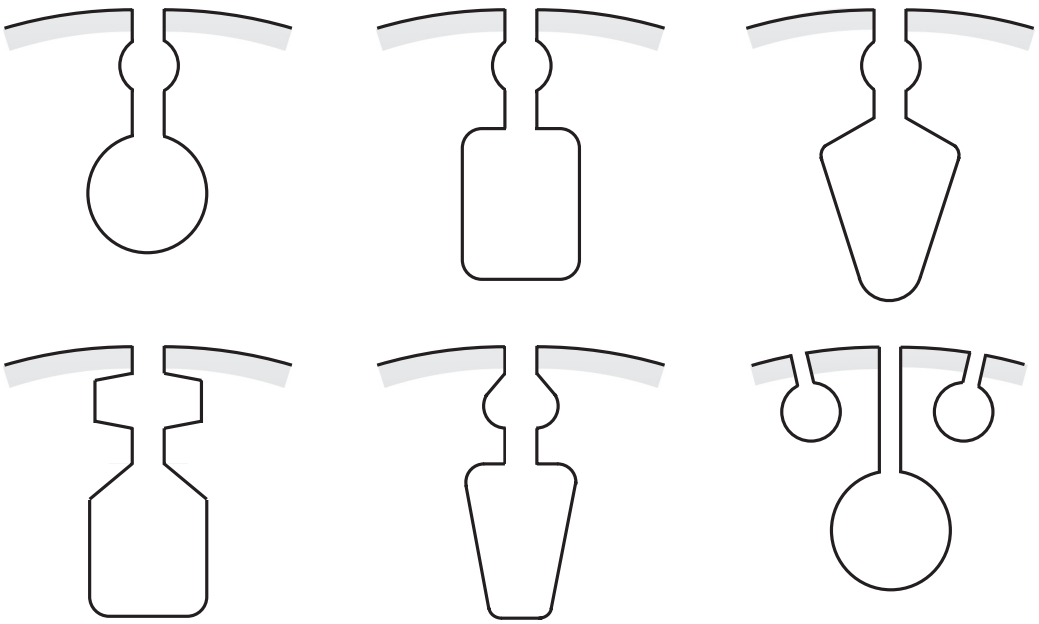

FIGURE 2.6
Various double-cage rotor designs for improving motor start-up and normal operation.

bars in the small cages that have high resistance are effective, providing high starting torque. In the motor normal operation stage, the conducting bars in both large and small cages become effective. Because the two resistances are connected in parallel, the rotor resistance is

$$R_r = \frac{R_i R_o}{R_i + R_o} \tag{2.1}$$

where R_i and R_o are the resistances of the conductors in the inner and outer cages, respectively. In a case that $R_o \gg R_i$, $R_r \approx R_i$. Therefore, under normal operation conditions with low rotor frequencies, the rotor current mainly goes through the conducting bars in the inner cage with lower I^2R losses. For this reason, some motor manufacturers use a high-resistance material such as brass for the outer cage and a low-resistance material such as copper for the inner cage.

Some large-size motors with double-cage rotors may employ separated end rings to connect the inner and outer cage, respectively. One of the reasons for this is to reduce thermal stresses induced in the end rings due to the different coefficients of thermal expansion of the inner and outer cages.

2.1.2.3 Casting Squirrel Cage Rotor

Several casting processes can be used for making squirrel cage rotors, including centrifugal casting and high- and low-pressure die casting. Low-pressure die casting is usually used for large rotors. In a casting process, the stack of laminations is placed in a die-casting

TABLE 2.1

Comparison of Properties of Copper and Aluminum

Property	Copper UNS C10100[a] [2.8]	Aluminum 383 [2.9]
Density (kg/m^3)	8890–8940	2700
Hardness, Vickers	75–90	85
Yield tensile strength (MPa)	69–365	152
Ultimate tensile strength (MPa)	221–455	310
Elongation at break (%)	55	3
Modulus of elasticity (GPa)	115	71
Poisson ratio	0.31	0.33
Shear modulus (GPa)	44	27
Machinability (%)	20	70
Melting temperature (°C)	1083	660
Thermal conductivity (W/m·K)	391	96.2
CTE (μm/μm/K)	1.692×10^{-5} (20°C–100°C)	2.11×10^{-5} at 20°C
	1.728×10^{-5} (20°C–200°C)	2.25×10^{-5} at 250°C
	1.692×10^{-5} (20°C–300°C)	

[a] Due to casting, C10100 is assumed the annealed properties.

die or a permanent mold containing a space at the top and bottom for the simultaneous casting of end rings. The molten material is poured or forced into the mold.

Two conducting materials are commonly used in casting squirrel cage rotors: (1) aluminum, which is the popular casting material of choice by most motor manufacturers due to its low melting temperature (660°C), low cost, and low density, which means that an aluminum rotor is subject to less starting inertia, less stress from centrifugal forces, and less vibration, and (2) copper, which is the promising material to significantly reduce rotor power losses as the result of high electric conductivity. The melting temperature of copper is 1083°C. The comparison of properties of copper and aluminum is presented in Table 2.1.

It is well known that incorporation of copper for the rotor bars and end rings in place of aluminum would result in attractive improvements in motor energy efficiency. Manoharan et al. [2.10] have reported that for the same output power, by merely replacing an aluminum rotor with a copper rotor and keeping all other parameters unchanged, the motor efficiency is increased by nearly 2.6%. It is observed that this increment in efficiency in the copper rotor is attributed to the higher electrical conductivity of the copper rotor. For instance, under a temperature of 20°C, the electric resistance of copper is 44% lower than that of aluminum. Hence, for the same current, the substitution of aluminum by copper can result in 44% reduction in the electric resistance loss.

Figure 2.7 presents an example of applying copper rotor in vehicles. It is benefited with low resistance losses and low starting torque and increased torque density. This leads to small motor size with the same power output or more power output for the same motor size. Furthermore, the much simpler design of a copper rotor compared to an aluminum rotor can significantly lower the manufacturing costs [2.11].

It was reported [2.12] that the advantage of using die-casting copper motors is not only the reduction in power losses but also the increase in power density. The die-cast copper rotor motors would be 18%–20% lighter and 14%–18% less expensive than the aluminum rotor motor at the same efficiency when a frame size reduction is possible.

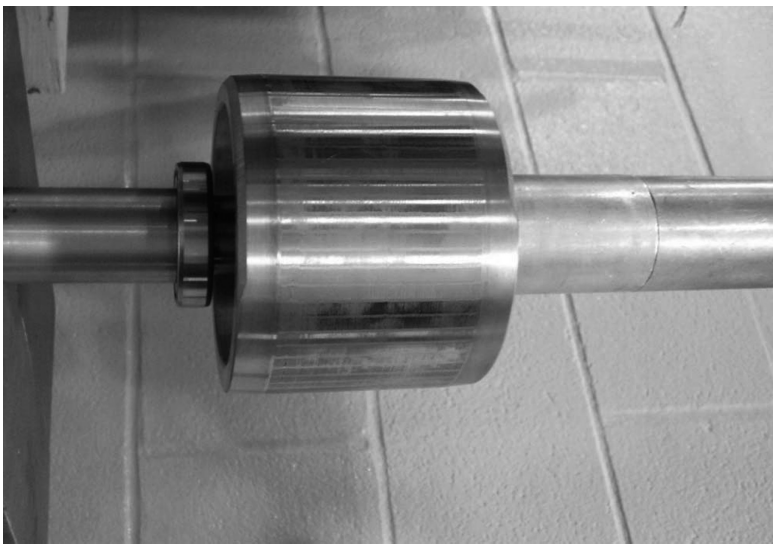

FIGURE 2.7
Rotor with casted copper conducting bars and end rings.

However, two difficulties must be addressed before cast copper rotors are fully commercialized: (1) Casting copper into a rotor is still a challenge today due to high casting temperatures (>1000°C) that are detrimental to the rotor laminations. (2) Copper has a higher coefficient of thermal expansion (CTE) than aluminum. As a motor passes through temperature cycles during its lifetime, the difference in CTE between copper conductors and steel laminations may develop fatigue stresses at the interfaces between the rotor conducting bars and stator core slots. The fatigue stresses may initiate cracks on the conducting bars and eventually lead to fatigue failure of the conductor bars. In some cases, it may result in the separation of the conducting bars/end rings from the rotor core. For the same reason, sometimes breaks may occur at the joints of the conducting bars to the end rings.

The advantages of squirrel cage IMs include their low cost, ruggedness, and maintenance free operation. However, since the rotor conducting bars and end rings are permanently short-circuited, it is unable to add any external resistance in series with the rotor circuit for starting purpose, leading to high starting current and low starting torque. In fact, this is the major disadvantage of the squirrel cage motors. Because squirrel cage IMs have good constant speed characteristics, they are preferred for driving machinery with constant operating speeds such as fans, blowers, water pumps, grinders, lathes, and printing and drilling machines.

As a rotor is subjected to a very high rotating speed, a retention mechanism may be required to keep the end rings connected to the rotor against high centrifugal forces. A number of solutions are effective in reducing the stress concentration at certain areas and are also effective in keeping the rotor together at the high speed. These include the following: (1) Each end ring can be secured using a band of a high-strength material. (2) Rivets can be cast into the rotor to secure the end rings to the body. (3) Specially designed laminations can be used for securing the end rings in rotors used today with the rotor body. (4) By breaking the end ring into sections, limiting the thermal growth of each section, thus reducing the thermal growth of the entire the ring. The specially designed geometry of the end ring in rotor used today helps contain the end ring at high speed by acting like a band as used in rotors today [2.13].

2.1.2.4 Skin Effect

In power systems, skin effect refers to the tendency of AC current to concentrate near the outer surface of a conductor and to decay exponentially toward the center. This indicates that the induced current in conducting bars is unevenly distributed over the cross-sectional area of the conducting bars. The current density increases from the center to the outer surface of the bar. Because of the skin effect, as well as the proximity effect between the conductor bars, the nonuniform current distribution causes more resistive loss. As a result, the AC resistance of a conducting bar is much higher than its DC resistance. Generally, the AC resistance increases with the increase of the frequency of rotor currents. The distribution of current density in a round conducting wire is given as

$$J = J_o e^{-d/\delta} \tag{2.2}$$

where

J_o is the current density at the conductor surface
e is the base of the natural logarithm ($e = 2.718$)
d is the distance measured from the surface toward the center of the conductor
δ is the skin depth, which is defined as the distance at which the current decreases to e^{-1} ($e^{-1} = 0.3679$) of its original value

The skin depth δ is inversely proportional to the square root of the frequency (in Hz).

2.1.3 Induction Motor Design Types and Their Performing Characteristics

The National Electrical Manufacturers Association (NEMA) standard has specified four major design classifications of AC IMs: designs *A*, *B*, *C*, and *D*. These design classifications apply particularly to the rotor design and hence affect the performance characteristics of the motors. Figure 2.8 displays a series of torque–speed curves for these design classifications with identical power rating and rotating speed [2.14]. It illustrates that the design characteristics such as starting torque, speed, and breakdown torque can be combined in different ways:

- Design *A* motors are used for applications that may undergo frequent but short-time overloading and thus require high breakdown torque, such as injection molding machines. This type of motor has normal starting torque (typically 150%–170% of the rated torque) and relatively high starting current.
- Design *B* motors are general-purpose motors, designed for applications that require normal starting and running torques, such as machine tools, fans, and centrifugal pumps. This type of motor usually has a comparable starting torque with Design *A* but offers low starting current. The locked rotor torque is good enough to start many loads encountered in the industrial applications. The slip is about 5%.
- Design *C* motors are selected for applications that require high starting torque, such as inclined conveyors and gyratory crushers.
- Design *D* motors, called *high slip* motors, are sometimes used to power hoists and cycling loads, such as oil well pump jacks and low-speed punch presses.

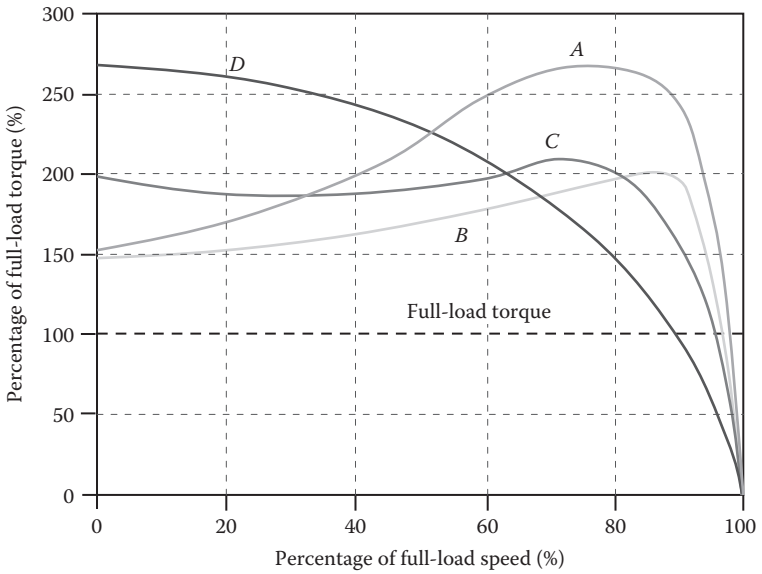

FIGURE 2.8
Torque–speed characteristics for design *A*, *B*, *C*, and *D* motors defined by NEMA.

Note that the starting torque ranges broadly among the design classifications, from about 150% of full-load torque for Design *A* motors to about 260% of rated torque for Design *D* motors. In addition, the speed at full-load for Design *A* motor is several percent less than the Design *D* motor.

2.2 Permanent Magnet Rotor

A PMM adopts PMs attached to the rotor in place of rotor windings or conductors/end rings to generate magnetic fields. The first motor invented by Faraday in 1821 was practically a primitive PM DC machine [2.15]. The first attempt to introduce rare-earth PM motors into the market of electric machines was in the 1980s using samarium–cobalt (Sm–Co) magnets that were invented in 1960s. Since then, more manufacturers have successfully launched rare-earth PM motors into the market. Neodymium–iron–boron (Nd–Fe–B) magnets were added into the rare-earth PM family in the mid-1980s. Like Sm–Co, Nd–Fe–B has demonstrated many design advantages and superior performance over common PMs. Because Nd–Fe–B is more abundant than Sm–Co, it is extensively used in energy-conversion devices today. In the recent years, modern PM motors have presented a momentum of rapid development. However, PM motor applications have been generally limited to relatively low-power motors, usually less than 500 kW, in most cases, less than 100 kW.

2.2.1 Discovery of Phenomenon of Magnetism

Ancient Chinese discovered the phenomenon of magnetism. Utilizing the magnetism of natural lodestone, the first compass was invented around the fourth century BC and was

(a)

(b)

FIGURE 2.9
Invented compass in ancient China: (a) Appeared on a Chinese stamp of 1953. (b) A replica.

called *south pointer* or *Si Nan* (司南). In the book of *Guiguzi* (鬼谷子), which was written in the early third century BC, it stated that "the lodestone makes iron come or it attracts it." The author Wang Yu (a thinker and strategist at approximately 300 BC) noted that in addition to its main purpose of serving as designators of direction, the Chinese primarily used it to order and harmonize their environments and lives (it refers to as *Feng Sui*—风水). The compass could be carried with jade hunters to prevent them from getting lost during their journeys.

The earliest Chinese records show the spoon-shaped compass *south pointer* could be dated back to sometime during the Han Dynasty (from the second century BC to the second century AD). As shown in Figure 2.9, a spoon-shaped lodestone is placed on a cast bronze plate that had the 8 trigrams (i.e., *Ba Gua*—八卦), as well as the 24 directions (based on the constellations) and the 28 lunar mansions (based on the constellations dividing the equator). Because the shape of the spoon bottom is spherical, the spoon can rotate freely on the bronze plate. Toggling the spoon to rotate, when it stops, its handle will point to the south.

2.2.2 Permanent Magnet Characteristics

The use of PMs in electric motors is highly desirable since they have great potential for reducing motor weight and increasing efficiency. In a PMM, the magnetic field of rotor

is produced by PMs. Because there is no need of rotor windings or conducting bars, the motor structure is greatly simplified. However, due to the limited magnetic strength of PMs, IMs are still dominant in large-size electric motors.

PMs are key parts in PM motors to generate magnetic fields along with stator windings. The advantages of PM motors include the following:

- Having higher efficiency than IMs
- Simplifying the rotor structure
- Requiring less maintenance
- Lowering the rotor inertia under the same power rating
- Eliminating the need for field exciter and slip rings
- Reducing cooling requirements due to less rotor losses
- Offering more precise speed control
- Lowering bearing currents
- Achieving higher power/torque density

With the fast developments of advanced magnetic materials and continuous improvements in operation performance, PM motors have been extensively used in various military and industrial applications. However, in comparison with conventional IMs, PM motors are generally more expensive due to high costs of magnets, especially for the rare-earth magnets.

The most important relationship of a magnetic material is the nonlinear behavior between the magnetic flux density **B** and the magnetic field strength **H**, where **B** and **H** are measured in gauss and oersteds and are analogous to current and voltage in an electric circuit, respectively. A typical **B**–**H** hysteresis loop of a magnetic material is shown in Figure 2.10. This hysteresis loop is useful for evaluating the response of a magnetic material to the applied magnetic field. It is readily noted the **B**–**H** hysteresis loop is skew-symmetric with respect to the *H*-axis. An unmagnetized PM is composed of a large number of small magnetic domains that randomly oriented and cancel one another, resulting in a net magnetic moment of zero on a large scale. This indicates that for the material in the unmagnetized state, both **B** and **H** are at the origin in Figure 2.10. During a magnetizing process, these randomly oriented domains are forced to be aligned with respect to the applied external magnetic field, and the magnet is thus magnetized following the initial magnetization curve (as market as curve #1). As it reaches the point of magnetic saturation, an additional increase in **H** will produce little increase in **B**. When driving magnetic field strength **H** to zero (curve #2), the magnet still retains a considerable degree of magnetization because of hysteresis of the magnet. This phenomenon is referred to as residual magnetism and the corresponding magnetic flux density is denoted as $\mathbf{B}_r$. To move the magnetic flux density **B** to zero, **H** must be reversed. This is referred to as coercivity (curve #3—also refers to demagnetization curve). The force required to remove the residual magnetism from the magnet is called the coercivity force, expressed as $-\mathbf{H}_c$ in Figure 2.10.

As the magnetic field strength continues to decrease in the negative direction, the magnet is magnetized again but in the opposite direction (curve #4). Similarly, as it reaches the point of magnetic saturation (but in opposite direction), any changes of $-\mathbf{H}$ in the negative direction will result in little variation of $-\mathbf{B}$. From this point, increasing **H** back in the positive direction will lead the increase of **B** (curve #5). As **H** becomes zero again, the material

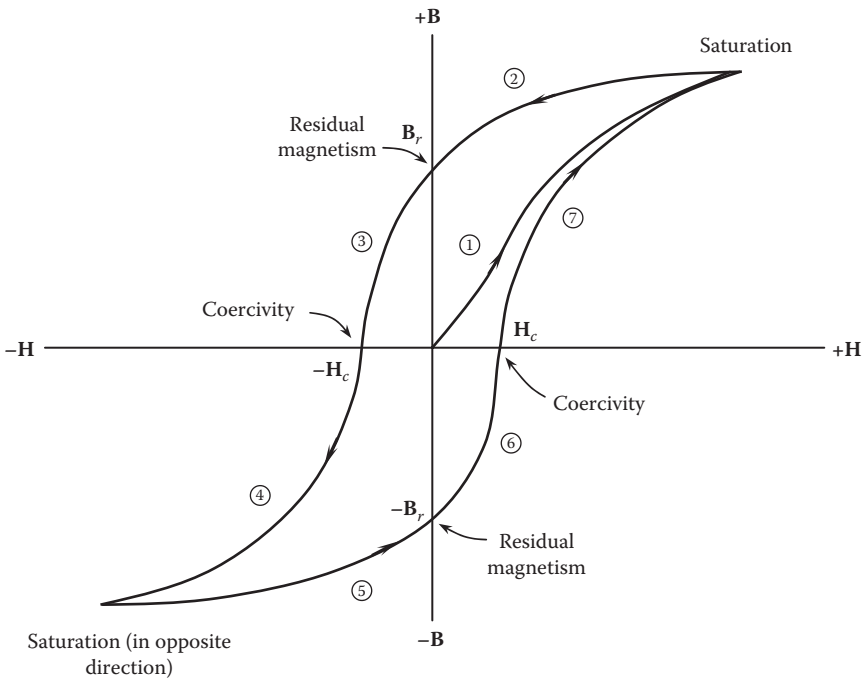

FIGURE 2.10
The magnetization hysteresis loop of a PM.

still remains negative flux density $-\mathbf{B}_r$. Further increasing **H** will bring **B** to zero (curve #6) and reach the point of magnetic saturation (curve #7). It is noted that this curve did not pass through the origin because the positive magnetic field strength is required to remove the residual magnetism.

A magnetized PM may lose partly or completely its magnetism under certain circumstances. The demagnetization of the PMs in a motor can cause performance degradation or complete failure of the motor.

The electromagnetic properties of PMs are strongly influenced by temperature [2.16]. An increase in temperature can increase kinetic energy of the molecules in a magnetic material, causing them to wiggle and jiggle around and the domains to lose alignment. Studies have shown that temperature variations normally produce changes in the hysteresis loop width, induction amplitude, maximum differential permeability, and other magnet properties [2.17], impacting the performance of PM motors. An FEA was conducted to investigate the influence of PM materials and temperature on the performance of interior PM motors [2.18]. The results show that along with the increase in temperature, remanent flux density $\mathbf{B}_r$ decreases, resulting in the decrease of the average torque and cogging torque but the increase in torque ripple.

2.2.3 Permanent Magnet Materials

PMs have been used in electric machines for more than a century. However, the modern history of PMs started in the 1930s with the introduction of alnico. As the strongest type of magnets at that time, alnico alloys dominated the market of electric machines due to their

TABLE 2.2

Magnetic Characteristics for Various Magnetic Materials

Magnetic Material	Grade	B_r (Gauss)	H_c (Oe)	H_{ci} (Oe)	BH_{max}[a] (MGOe)	T_{max} (°C)	T_c (°C)	Reference
Ferrite magnet	8	3,900	3,200	3,250	3.5	300	450	[2.19]
Nd–Fe–B	39H	12,800	12,300	21,000	40	150	310	[2.19]
Sm–Co	26	10,500	9,200	10,000	26	300	750	[2.19]
Alnico	5	12,500	640	640	5.5	540	860	[2.19]
Ceramic	8	3,900	3,200	3,250	3.5	300	460	[2.19]

[a] BH_{max} represents energy product, given in MGOe. Nd–Fe–B magnets have the highest energy product of any magnetic materials available below 200°C.

excellent remanence, high thermal stability, and high chemical stability until the development of rare-earth magnets in the 1970s.

In the last several decades, dramatic improvements have been made in magnetic properties and availability of PMs. Applications of PMs in electric machines are increasingly growing. There are several main types of PM materials used in motor manufacturing, including ferrite PMs, alnico PMs, and rare-earth PMs. The comparison of magnetic characteristics for various magnetic materials is presented in Table 2.2.

2.2.3.1 Ferrite Permanent Magnets

Ferrite PMs are made from some oxides (SrO, BaO, or Fe_2O_3). Due to low costs of raw materials and simple manufacturing technique, the magnets are considerably cheap. The corrosion resistance of the oxides is considered excellent, and no surface treatments are required. Ferrite PMs can work under severe environmental conditions such as high temperature, dust, salt fog, and moisture. Therefore, they are extensively used in automobile motors and power tools.

Alnico magnets are alloys made of aluminum, nickel, cobalt, copper, iron, and other materials by either sintering or casting. The remarkable advantage of alnico magnets is that they have the widest range of temperature stability and the lowest temperature coefficient of any commercial magnet materials (0.02% per degree centigrade). Their maximum working temperatures can be up to 450°C–550°C. Due to good corrosion resistance, there are no surface treatments required. This type of magnet is usually used in temperature-sensitive devices such as instruments and sensors.

2.2.3.2 Rare-Earth Permanent Magnets

Rare-earth PMs are made from alloys of rare-earth elements such as neodymium (Nd) and samarium (Sm). In comparing with regular ferromagnets, rare-earth magnets have higher residual magnetic flux density and much higher coercivity but lower Curie temperature. Today, rare-earth magnets are widely used in various PM motors for producing high-efficiency, high-torque-density, and high-performance motors and reducing motor vibration and noise. Because Sm–Co magnets can work at higher temperatures (up to 250°C–350°C) than Nd–Fe–B magnets (usually 80°C–220°C), they are more suitable for manufacturing various high-performance PM motors. In addition, due to the strong anti-corrosion ability, electroplating of Sm–Co magnets is generally unnecessary. However, because of the low reserve of samarium on the earth, Sm–Co magnets are very expensive.

Among rare-earth magnets, Nd–Fe–B magnets offer the largest energy product of any magnetic materials available below 200°C (392°F). Compared to Sm–Co and alnico magnets, Nd–Fe–B magnets are capable of picking up more than 600 times its own weight. Nd–Fe–B magnets have not only the excellent qualities of high remanent magnetization, high coercive force, and high magnetic energy product but also the better mechanical properties for processing of complex shapes. According to the current trend, the Nd–Fe–B magnetic material may become the dominant magnetic material in the future in electric machines, energy, transportation, medical devices, computers, home appliances, and other fields. However, because the material contains large amounts of neodymium and iron, the Nd–Fe–B magnets are easily corroded and thus must be coated with nickel (Ni), zinc (Zn), gold (Au), chromium (Cr) epoxy resin, etc. One of the disadvantages of Nd–Fe–B magnets is its low performance temperature. The magnetic loss at high temperature is relative large.

2.2.3.3 New Developments of Permanent Magnets

In the last two decades, new materials have played a major role in the technological innovations needed to propel the rapid development of high-performance, high-powered electric machines that are ever lighter and smaller.

The rapid developments of nanotechnology in recent years shed a new light on research and development of nanoalloy magnets. Nanoalloy magnets are especially interesting to the motor industry because it can further reduce the power density of electric motors. Previous studies showed that arrays of nanomagnets displayed various magnetization patterns that are closely related to the nature of the magnetic interactions between neighboring nanomagnets [2.20,2.21].

It is known that the strength of a magnet is measured in terms of coercivity and saturation magnetization values. These values increase with a decrease in the grain size and an increase in the surface to volume ratio. Therefore, the magnets made of nanocrystalline yttrium–samarium–cobalt grains may possess very unusual magnetic properties due to their extremely large surface area [2.22].

Japanese engineers and scientists have committed to developing new types of magnets for replacing rare-earth magnets. The government-affiliated New Energy and Industrial Technology Development Organization and Hokkaido University announced in 2010 that it had developed motors for hybrid vehicles that used cheap and readily available ferrite magnets [2.23].

More recently, a team of researchers mainly from Tohoku University and Toda Kogyo Corporation has succeeded in generating $Fe_{16}N_2$ powder with a purity of 91% and a reproducibility for the first time in the world. Thus, a new powerful magnet can be made from the material using the synthesizing technology developed by Toda Kogyo without any rare-earth element. The new magnet is aimed to be commercialized in 2023 [2.24]. Toshiba recently announced that the company has developed a high-iron-concentration samarium–cobalt (Sm–Co) magnet that is free of dysprosium, a rare-earth mineral. The magnet exceeds the heat-resistant neodymium magnet in magnetic force by 1% at an operating temperature of 100°C and by 5% at 150°C [2.25].

At the end of 2012, a company based in the United States [2.26] announced that it has made a breakthrough in the development of non-rare-earth magnet electric motor. The key design is the patent-pending motor geometry, which in part defines the shape and magnetization direction of the PMs. This new technique provides an alternative way in PM motor designs. According to this company, the electromagnetic design and analysis task was completed. The next phase is the mechanical design and the concept unit will be built in 2013.

Scientists at University of Minnesota have developed a new type of magnets using the iron nitride ($Fe_{16}N_2$) magnet and achieved 130 megagauss–oersteds (MGOe), which is more than twice the maximum reported magnet energy product for a rare-earth neodymium magnet [2.27].

2.2.4 Magnetization

The full performance of PMs can only be guaranteed if it is magnetized properly to saturation. The magnetization of PMs can be implemented either prior to or posterior to rotor assembly. Premagnetized magnets can easily achieve 100% of saturation. This approach may be especially suitable for some cases. For example, since a large PM motor is hard to place in a magnetizer, the premagnetization of magnets is the only solution. However, there are some apparent disadvantages for premagnetized magnets. First, the magnetized magnets are difficult to handle during rotor assemblies because of its attraction to steel parts or attraction/repulsion with other magnets. Second, premagnetized magnets may pick up magnetically permeable dirt in their assembly and transportation processes. Third, magnets are usually brittle and easily damaged in shipment if they are not packaged properly. Therefore, it is preferred to magnetize assembled systems at the assembly locations. However, in such a way, the magnetized saturation level may be slightly lower (about 99%) due to the fact that the magnets are too close to one another [2.28].

Usually, postmagnetization works efficiently for surface-mounted PM and interior PM that are located near the rotor surface. In the motor industry, because of the high production efficiency and ease of assembly, a majority of small PM motors are postmagnetized by means of magnetizers, as depicted in Figure 2.11.

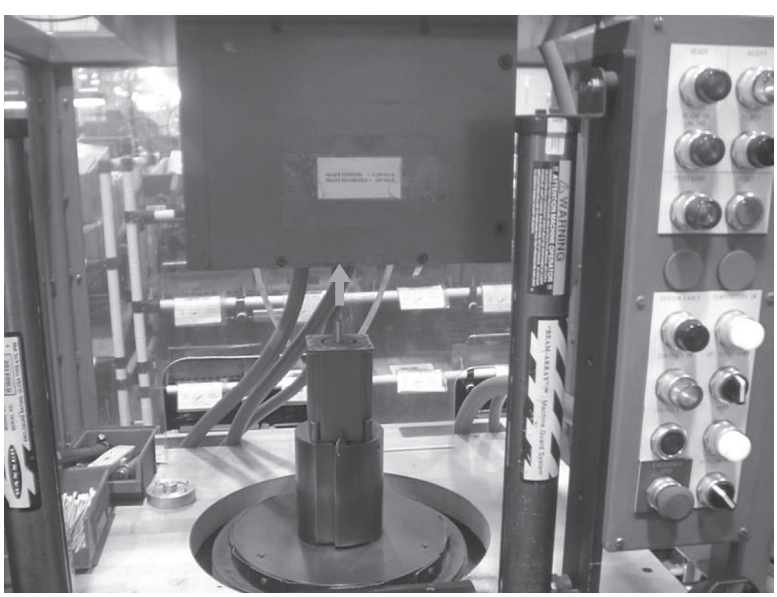

FIGURE 2.11
Postmagnetizing of a PM motor by means of a magnetizer.

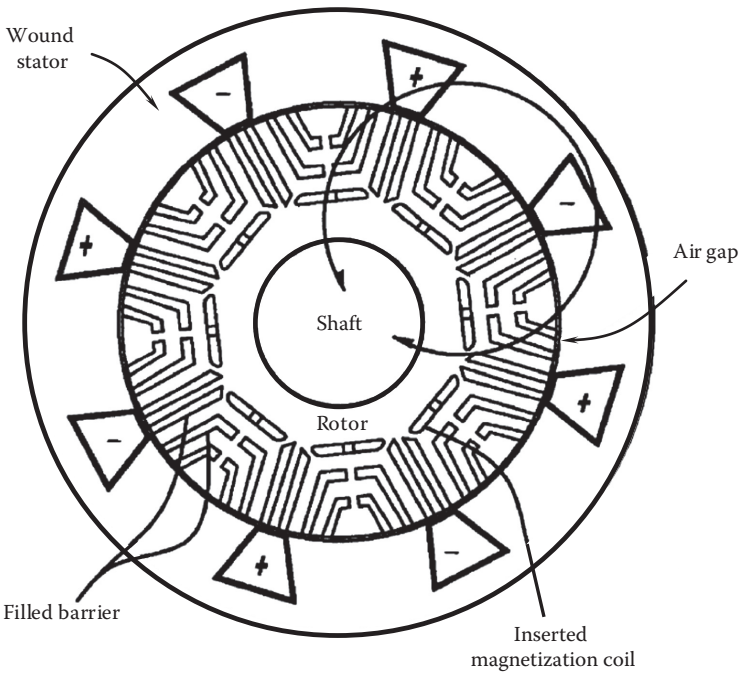

FIGURE 2.12
Cross-section of a multilayer interior magnet motor with a magnetizing auxiliary winding for magnetizing interior magnets (U.S. Patent 6,674,205) [2.29]. (Courtesy of the U.S. Patent and Trademark Office, Alexandria, VA.)

For multilayer buried magnet rotors, postmagnetization would result in a large amount of magnetic material buried deep within the rotor to be only partially magnetized or even not magnetized at all. To solve this problem, an innovative method is presented in Figure 2.12. It removes magnetic material from the regions of the rotor that cannot be effectively or strongly magnetized during the postmagnetization process and inserts magnetizing coils. Thus, the inserted magnetizing coils enhance the magnetizing field produced by the stator or other magnetizing fixture for improving the rotor magnetization. Then, the magnetizing coils are removed from the rotor [2.29].

2.2.5 Factors Causing Demagnetization

During assembly process, magnetic properties of PMs may change due to the improper installation processes and changes in environmental conditions. As a result, the variation in magnetic properties can directly affect the reliability and performance of electric motors. A primary cause of demagnetization of PMs is high temperature. When a PM is heated, the internal energy increases to make the atoms in the PM vibrate actively. The vibration of the atoms may shift the alignments of some atoms from an ordered pattern to a nonaligned disordered pattern. As a result, the PMs may be partially demagnetized. In a worse case, excessive temperatures may lead the PMs to completely lose their magnetic properties, causing electromechanical failure, power loss, or erratic power fluctuation. This is especially true for rare-earth PMs.

The temperature effect on magnet demagnetization usually falls into three categories:

1. Reversible losses: At the early stage, the rise in temperature will gradually decrease the magnetism of a magnetic material. For example, the reduction in magnetism of Nd–Fe–B magnets is 0.13% per degree Celsius. At this stage, the losses in magnetism can be recovered automatically as the magnetic material returns to its original temperature.
2. Irreversible but recoverable losses: Continuously increasing the temperature will result in the irreversible drop in the magnetism due to the reduction in the coercive force. The losses in magnetism can be only recovered by remagnetizing. This is also applicable for the partial demagnetization due to the interference of external magnetic fields.
3. Irreversible and unrecoverable losses: Each magnetic material has a specific temperature, the Curie temperature T_c, at which all magnetic properties are completely lost. Because the crystal microstructure of magnetic materials changes at the Curie temperatures, remagnetization cannot bring its magnetism back again. When the temperature is much higher than the Curie temperature, the lattice of the magnetic material will be melted and recrystallized, resulting in the permanent loss of the characteristics as the permanent magnetic material.

The impact of temperature on the demagnetization characteristics of PMs has been extensively investigated by many researchers and engineers. This is normally studied by looking at the **B**–**H** hysteresis loop at the second quadrant. A demagnetization curve represents the relationship of the magnetic flux density generated by a magnet and the demagnetization force imposed on the magnet. As examples, the demagnetization curves for a typical ferrite PM under various temperatures are shown in Figure 2.13 [2.30]. It can

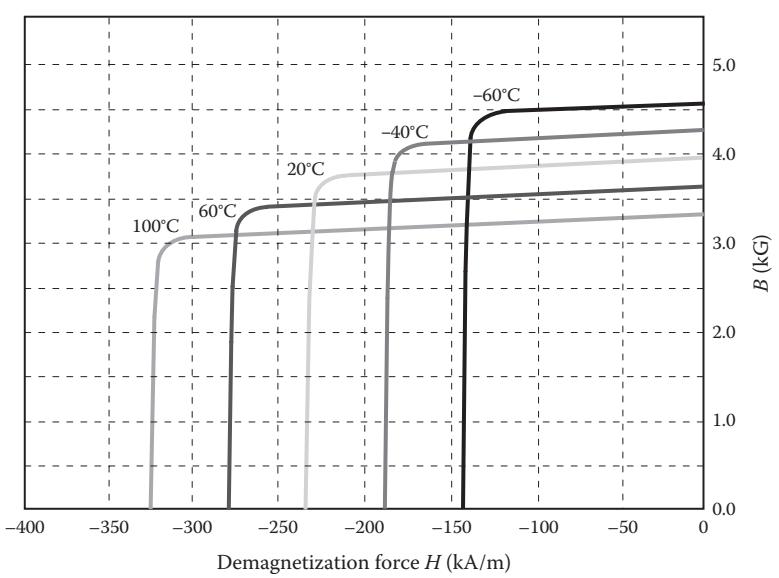

FIGURE 2.13
Impact of temperature on demagnetization characteristics of a typical ferrite magnet.

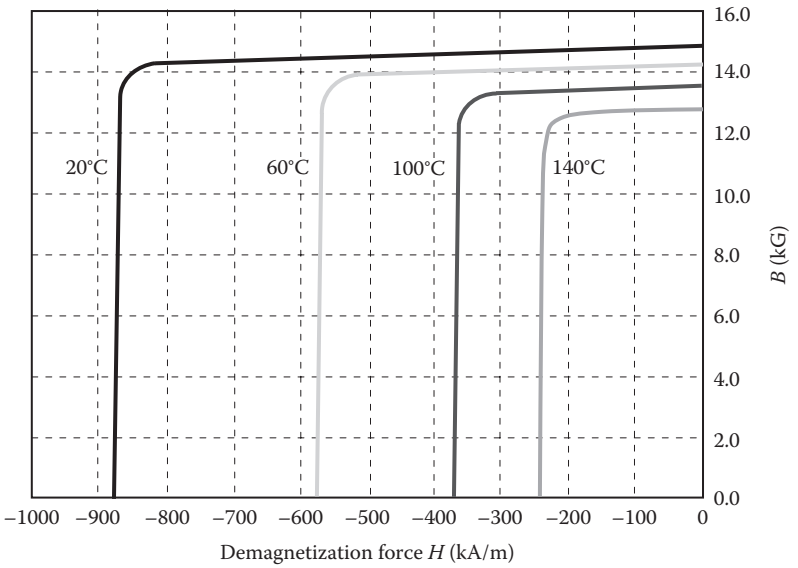

FIGURE 2.14
Impact of temperature on demagnetization characteristics of a typical Nd–Fe–B magnet.

be seen from this figure that the shapes of all demagnetization curves are similar. These curves decrease slowly initially with the increase in **−H** and then drop off abruptly when the *knees* are passed. At the knee points, the irreversible demagnetization starts to take place. The knee occurs at approximately −130 kA/m at the temperature of −60°C but occurs −320 kA/m as the temperature is raised to 100°C. Increasing operation temperature from −60°C to +100°C, the demagnetization curves in sequence reduce in both their magnetic field strength **H** (i.e., move toward **−H**) and magnetic flux density **B** (i.e., move toward **−B**).

For a typical Nd–Fe–B PM, the demagnetization curves are shown in Figure 2.14 [2.31]. Unlike in ferrite magnets, the temperature impact on the magnetic characteristics of Nd–Fe–B magnets is somewhat different. When the operation temperature increases from 20°C to 140°C, the demagnetization curves increase in their magnetic field strength **H** (i.e., move toward **+H**), while they decrease in their magnetic flux density **B** (i.e., move toward **−B**). This indicates that for a PM motor subject to a large range of operating temperature, its maximum torque capacity and efficiency of the motor can vary over a wide range.

Furthermore, it has been observed that the magnetic properties change with temperature due to the change in the magnetic domain structure. The effect of the operational temperature on Nd–Fe–B magnets has been investigated on a 2.5 kW, 24-pole surface PM prototype motor by Beniakar et al. [2.32]. Their results show that the rise of the operational temperature from 20°C to 140°C causes a significant decrease of the air gap flux density, thus deteriorating the machine's overall performance.

In addition to temperature, other factors can also cause demagnetization of magnetic materials. A strong external magnetic field can distort the magnetic field of a PM, causing some atoms to orient their electron spins to conform to the external magnetic field. This will turn some magnetic domains in the PM from an aligned orientation to a random orientation. In fact, it is possible to demagnetize a PM by applying an external magnetic field in a direction opposite to the direction of magnetization of the PM.

Mechanical disturbances also tend to randomize the magnetic domains and thus to demagnetize PMs. Thus, it is important to avoid strong mechanical shocks such as hammering or jarring on PMs. It is usually preferable to ship PMs in an unmagnetized state to prevent damages to themselves and things close to them. In order to safely and reliably ship magnetized PMs, special care must be taken to ensure that the PMs are packaged well with damping materials.

Radiation-induced demagnetization of PMs has been studied for various insertion devices [2.33,2.34]. It has been reported that Sm–Co magnets exhibit significant demagnetization when irradiated with a proton beam of 10^9–10^{10} rad. Nd–Fe–B test samples were shown to lose all of their magnetization at a dose of 7×10^7 rad and 50% at a dose of 4×10^6 rad [2.35]. When a PM motor is subjected to electron beam or γ-ray irradiation, this type of losses must be carefully considered.

Studies have demonstrated that PMs are affected by time, known as magnetic creep. PMs undergo changes immediately after magnetization. At this stage, the PMs are less stable, showing significant variations in magnetic properties by fluctuations in thermal and magnetic energy. After a period of time, the PMs become more stable as unstable magnetic domains decrease.

The time effect on modern PMs is minimal. It has been reported that over 100,000 h, the losses are in the range of essentially zero for samarium–cobalt materials to less than 3% for alnico five materials at low permeance coefficients [2.36]. Due to the extremely high coercivities, rare-earth magnets experience a much less time effect than other types of magnets. Furthermore, most losses of rare-earth magnets are reversible or recoverable.

2.2.6 Maximum Operation Temperature

Maximum operation temperature is defined as the temperature below which magnets can operate normally with a small demagnetization. For PM motors, the maximum operation temperature provides an important reference temperature for the design of motor cooling. It is important to maintain the maximum operating $T_{\max}$ well below the Curie temperature T_c for preventing losses in magnetism, as well as the structural or mechanical damage of magnets. In fact, for a particular magnetic material, $T_{\max}$ is determined by not only the magnetic material but also the material processing process.

2.2.7 Permanent Magnet Mounting and Retention Methods

In practice, PMs may be either mounted on the rotor outer surface or inserted into retention slots passing axially through the rotor core. A motor with surface-mounted PM is simple in construction and easy to manufacture. However, the magnets in this design are exposed to all the time and space harmonics of the stator winding magnetomotive force (MMF).

For surface-mounted PM motors, one of the most important issues is to hold the magnets in place firmly to prevent them from flying off during motor operation [2.37]. Some surface mounting methods are presented in Figure 2.15, where PMs are positioned either directly on the rotor surface or on the sunken portions made on the rotor surface.

A retention device must be capable of withstanding both high centrifugal forces due to high rotating speed of the rotor and the axial forces that may arise during manufacturing, assembly, or installation. In addition, the retention device must have low permeability to avoid short-circuiting the magnetic flux, low electric conductivity to minimize space and time harmonic losses, and sufficient strength to provide for magnet retention and must be thin enough to not increase the air gap.

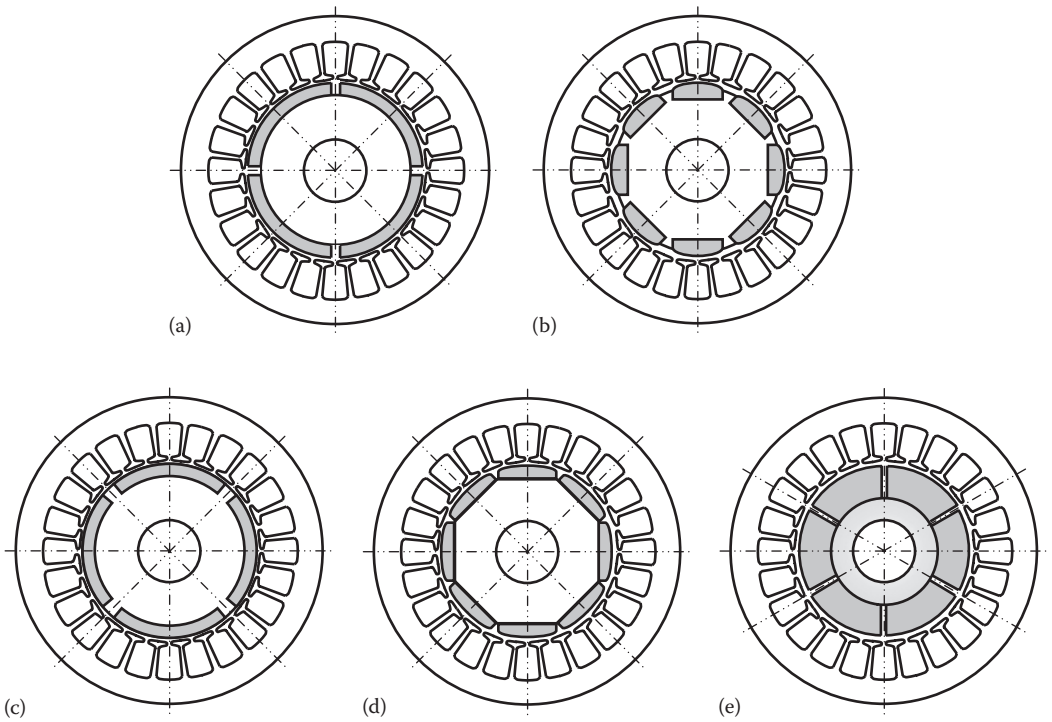

FIGURE 2.15
Various mounting methods on rotor surface: (a) tile-shaped magnets mounted on the rotor surface, (b) bread loaf magnets partially positioned in the sunken portions of the rotor, (c) tile-shaped magnets fully positioned in the sunken portions of the rotor, (d) bread loaf magnets mounted on the surface of an octagon rotor, and (e) thick magnets mounted on the thin rotor core, generating strong magnetic field.

PMs can be mounted on rotor surfaces by either mechanical retaining methods (e.g., using clamps, wedges, and wrapped fibers), chemical retaining methods (e.g., using adhesives), physical retaining methods (e.g., using soldering), or combinations of these methods. A common method is to glue arc magnets on the rotor core surface with adhesives and secure the magnets with reinforcing fine fiber (e.g., Kevlar™ aromatic polyamide fiber) or fiberglass bands/strings wrapped around the magnets (Figures 2.16 and 2.17). This technique offers a simple and effective solution for the magnet assembly but decreases the effective air gap and consequently increases the magnetic leakage flux. In order to minimize eddy-current losses in the magnets, it is desirable to use multiple small magnets. However, the installation of small magnets increases the working load, leading to low efficiency.

Adhesives provide strong bonds between magnets and the rotor core. Thus, the magnets become load-bearing members, thus subject to centrifugal load that may potentially exceed their strength limitations. Additionally, the bonded magnets become permanently attached to the rotor, making it difficult or otherwise infeasible to replace them, wholly or individually. Adhesive is also susceptible to failure due to extreme temperatures, aging, and chemical exposure [2.38].

An innovative retention method [2.39] combines the two magnet mounting methods, that is, surface-mounted and slot insertion methods, as shown in Figure 2.18. This method utilizes a number of dovetail slots that are made circumferentially on the rotor core surface

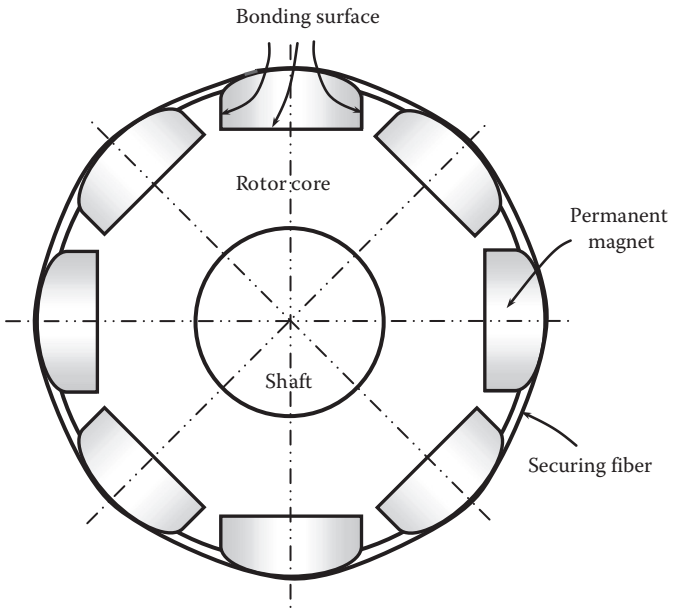

FIGURE 2.16
Gluing PMs on rotor surface and securing with wound special fiber string outside the magnets.

to hold wedge-shaped magnets robustly. Correspondingly, the magnet shape must match with that of the dovetail slots. Because magnets are usually fragile and unable to withstand large forces, the interference fit is inapplicable in assembling the magnets into the dovetail slots. Instead, the magnets are fixed in the dovetail slots by an adhesive.

Compared to mechanical retention methods, soldering takes less space that can be critical for high-power-density motors. It has a lesser outgassing rate than gluing. However, the primary disadvantage of soldering in comparison to mechanical attachment and gluing is the necessity to raise the temperature of the PM to above the solder melting point during the soldering process, which can easily demagnetize the magnets. Therefore, special measures in magnet cooling must be carefully considered and taken.

Another alternative method for the magnet retention is to use high-strength metallic sleeves over the magnets [2.40], as shown in Figure 2.19. The metallic sleeve is advantageously resistant to high temperature and easy to process with a high productivity. The thin-wall metallic sleeve has a capability of restraining the magnets against centrifugal forces. By extending the sleeve beyond the ends of the rotor core and bending the sleeve toward the magnets, the metallic sleeve thus prevents the magnets from shifting in the axial direction (Figure 2.20). However, because of electrically conductive properties of the material, the metallic sleeve produces an eddy-current loss, which in turn reduces the efficiency of the motor. To minimize the influence of the metallic sleeve on motor performance, the sleeve is preferably made of the materials with low conductivity such as titanium or chromium alloys. However, these materials are expensive and hence impractical. In practice, stainless steel and corrosion-resistant Inconel™ alloys that contain primarily nickel, chromium, and iron are commonly used for metallic sleeves. For small motors, the thickness of the sleeve preferably ranges from about 0.1 mm (0.004 in.) to about 0.6 mm (0.024 in.). For large motors, the thickness can go up to 3 mm (0.12 in.). With such a thin wall, the sleeve can be mounted over magnets by various operations such as heat shrinking or pressing

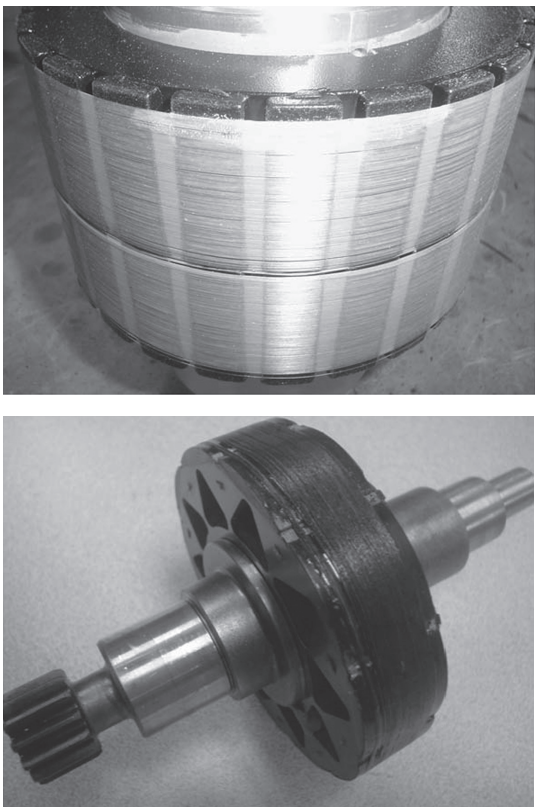

FIGURE 2.17
PM rotors are commonly wound with reinforcing fine fibers to provide large mechanical strength for retaining PMs on rotors.

fitting [2.41]. However, the use of metallic sleeves increases the thermal resistance and thus lowers the rotor cooling efficiency.

Magnets can be also retained by a molded plastic cylindrical sleeve. As illustrated in Figure 2.21, the magnets are encapsulated entirely by the plastic sleeve. This method provides a perfect solution for the magnet corrosion problem and increases the magnet retention strength against the centrifugal forces [2.42].

The schematic diagram for PMs embedded in the interior of a lamination rotor core is shown in Figure 2.22. There are a number of advantages with this technique over the surface-mounted technique: (1) Inserted PM can generate higher torque because it utilizes both the PM and reluctance torques (e.g., the design *f* in Figure 2.22) generated by the magnetic saliency. (2) Because magnets are placed inside slots that pass axially through the rotor core, magnet retention is thus enhanced and yields to simplification in the manufacturing process. This is especially true for high-speed motors. (3) With this technique, rectangular magnets, which are less expensive than arc magnets, can be used. (4) The centrifugal forces acting on the magnets will be transferred to the rotor core. (5) When a magnet is broken due to corrosion, heating, or shock load, its fragments will not directly fly off into the air gap to damage the motor. However, for the same power and same machine size, the surface-mounted magnet machine requires less magnet material than the corresponding embedded magnet machine.

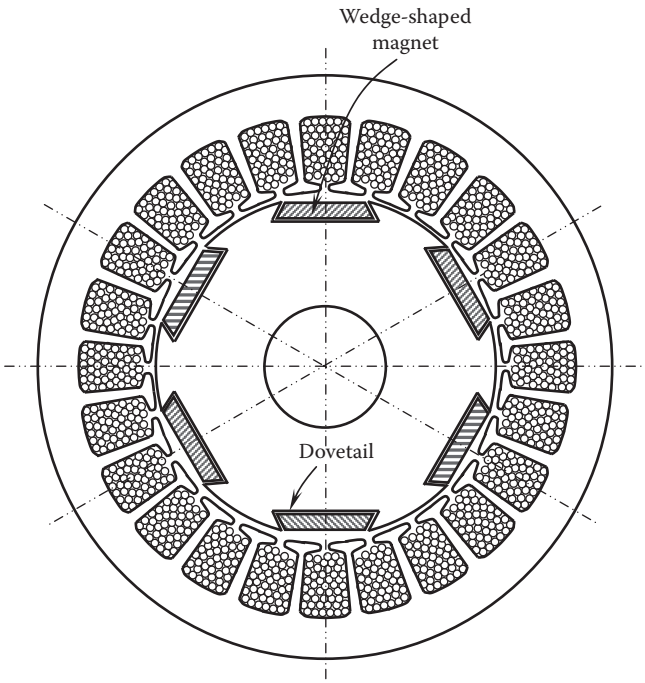

FIGURE 2.18
An innovative method for magnet retention by inserting wedge-shaped magnets into the dovetails on the rotor surface.

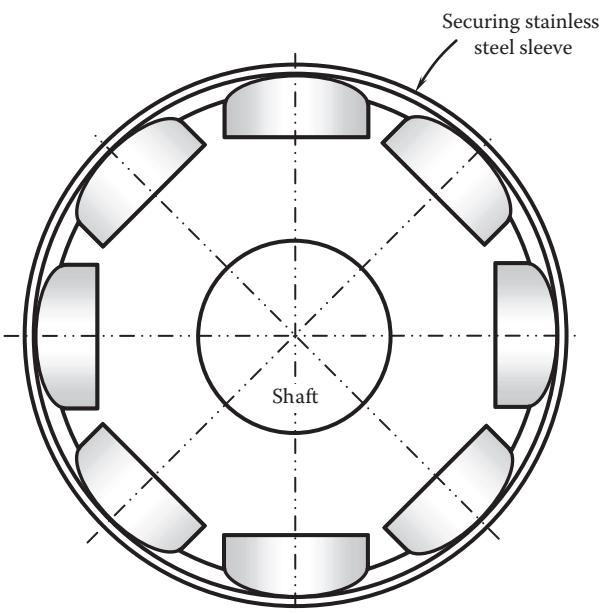

FIGURE 2.19
Using securing stainless steel sleeve for holding magnets on the rotor core.

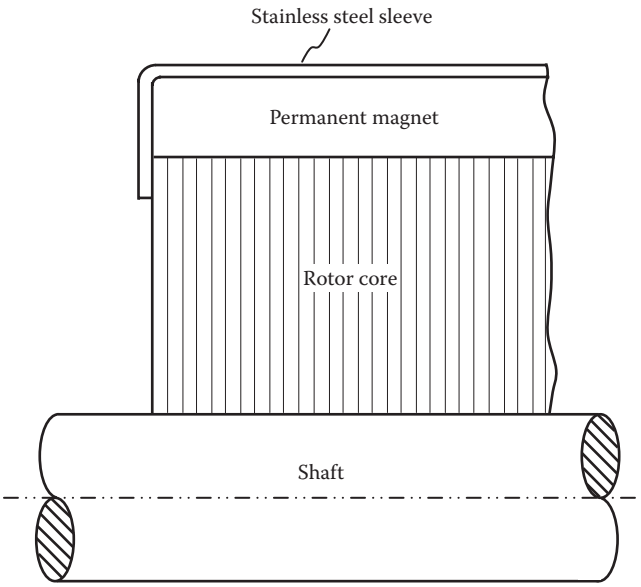

FIGURE 2.20
Bending of stainless steel sleeve at the end of rotor core for preventing magnets from shifting in the axial direction.

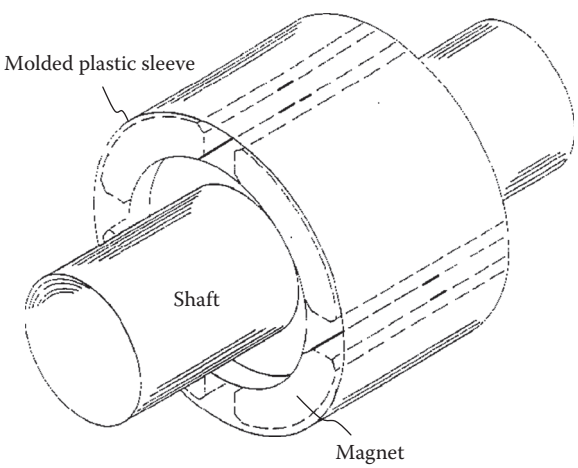

FIGURE 2.21
Retention of magnets with a molded plastic sleeve (U.S. Patent 4,973,872) [2.42]. (Courtesy of the U.S. Patent and Trademark Office, Alexandria, VA.)

For a motor with embedded magnets, the stator synchronous inductance in the *d*-axis is lower than the synchronous inductance in the *q*-axis.

2.2.8 Corrosion Protection of Permanent Magnets

Electric motors may work under severe environmental conditions. Therefore, the protection of PMs from corrosion could be critical for motor normal operation and lifetime in

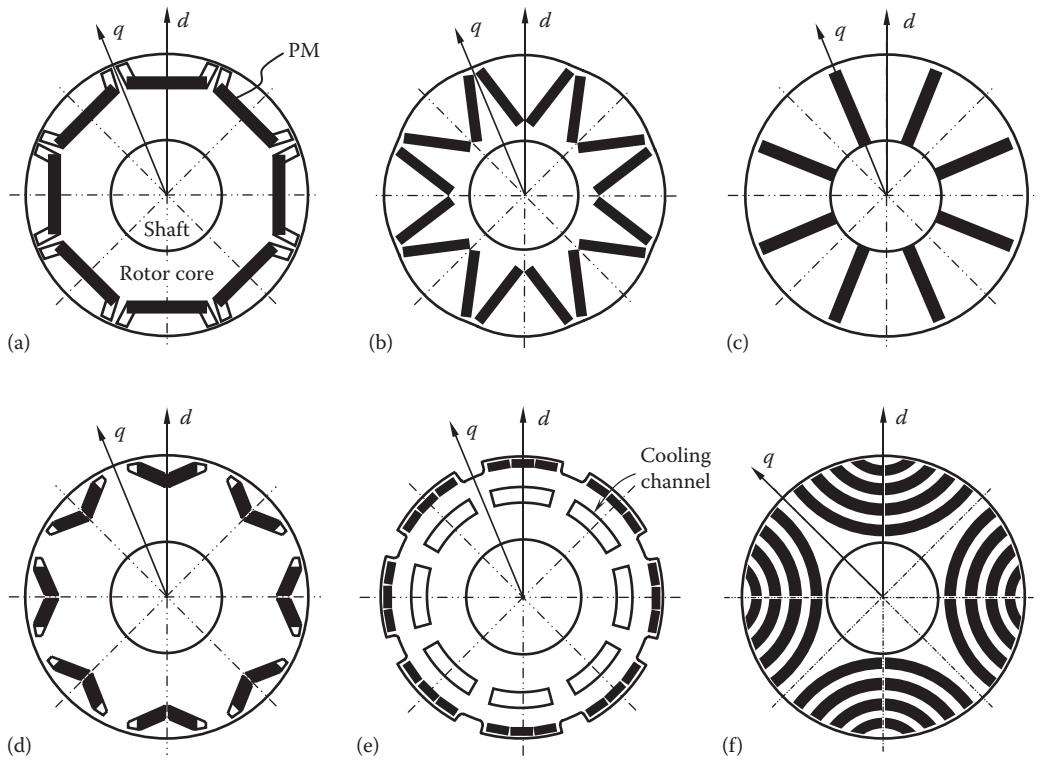

FIGURE 2.22
PMs placed in the interior of the rotor core, allowing for high-speed operation than surface-mounted magnet design: (a) buried tangential magnets near the rotor surface; (b) buried splitted V-magnets with 1/cosine-shaped air gap outline; (c) buried radial magnets so that their magnetization is azimuthal; (d) embedded splitted magnets in *V*-shaped slots near the rotor surface; (e) embedded splitted magnets in slots near the rotor outer surface (EP 1420501), similar to surface mount method but more secure magnet retention; (f) buried multilayer splitted arc magnets in saliency slots, exhibiting excellent performing characteristics of a motor.

some applications. For instance, rare-earth magnets exposed to acid/alkaline solution, salt, deleterious gas, or some chemical substances can result in corrosion of them. Even under a high-humidity condition, some magnets are easy to be eroded. It is noted that though the corrosion itself does not actually cause the part failure, the corrosion is the catalyst that starts a long chain of events over a long time of motor operation that eventually leads to the motor failure.

The detrimental effects of magnet corrosion include the following: (1) Excessive corrosion on magnet surfaces can cause premature wear of magnets. This in turn will cause magnet degradation and even failure of motor. (2) Debris and powders detached from corrosive magnets may block the air gap between the stator and rotor. (3) Microscale cracks may develop on magnet surfaces as a result of corrosion. This will eventually lower the strength of magnets.

The corrosion process of a magnet begins with the diffusion of oxygen, water vapor, or hydrogen along grain boundaries inside the magnet. The most common method to protect magnets against corrosion is to use coatings on magnet surfaces. Coatings can isolate magnets from all harmful chemical substances and thus enhance the corrosion resistance. A number of materials can be used for coating, such as polyurethane, phtal-uretane and

epoxy lacquer, polymer epoxide, polyester, polyester–epoxy, zinc, nickel, copper, and chromium. Experimental results [2.43] show that polymer coatings demonstrate the best resistance. The lacquer coatings are resistant in the water environment. Metal coatings have a lower corrosion resistance compared to the polymer and lacquer in corrosive environments.

Another method is to improve the intrinsic properties of the magnetic material by controlling the chemistry of the grain boundary in the magnet. For example, the addition of certain transition elements (e.g., Co, Ga, Nb, Mo, and V) can reduce the corrosion rate of rare-earth magnets [2.44].

2.3 Rotor Manufacturing Process

The manufacturing process for both induction and PM rotors starts from the material section. This is a critical step because it determines rotor core losses, rotor operating performance, and motor efficiency. Usually, motor manufacturers directly purchase thin lamination sheets from steel suppliers. The lamination sheets are punched by stamping machines or cut by laser devices to make desired lamination patterns. The stamped laminations are usually required to pass a heat treatment process to stabilize their electromagnetic, thermal, and mechanical properties and to release the internal stresses for dimension stabilization. Finally, these laminations are stacked together to form rotor cores.

The rotor assembly is achieved when a shaft is interference fitted into a rotor core. The design of the fitting method is very important for reliable motor operation and securely transmitting its torque to an external loaded machine. An improper fitting may lead to the separation of the shaft and the rotor core during motor operation. The final step in the rotor manufacturing is to carefully perform the rotor balance under a dynamic condition.

2.3.1 Lamination Materials

It has been commonly accepted that high motor torque can be achieved with the magnetic core material having high saturation magnetic flux density, low coercivity, and low-core-loss characteristics. The selection of rotor core material is based on the electromagnetic, thermal, and mechanical properties of materials, as well as the material cost. It has long been recognized that no material is perfect in all aspects and optimum for all applications. During design processes, trade-offs are often made between material properties (e.g., permeability, saturation flux density, density, and tensile strength), core losses, cost, fabrication processes, formation of lamination insulations, and other factors.

Of all the soft magnetic core materials, the most widely used materials are known as electrical steels, which are divided into several general classes. Among them, a major class is silicon steel, in which silicon is the principal alloying element. Alloying the steel with silicon can considerably increase the volume resistivity of the steel and thereby reduce the eddy-current loss. In addition, silicon can affect the grain structure of the steel and thus gives somewhat improved core loss by the reduction of the hysteresis loss in nonoriented electrical steels [2.45]. Hence, the electric and magnetic characteristics of silicon steel make it well suited for making rotor and stator lamination cores.

Silicon steel consists of body-centered cubic crystals. During a rolling process, these crystals are stretched and flattened. If they are left in that state, the magnetic properties

are maximized in the rolling direction (i.e., along the length of the strip). Hence, this type of steel is defined as oriented steel. Taking advantage of this characteristic, the maximum performance can be achieved by applying the material in the same direction that magnetic flux is expected. When an annealing heat treat (usually 850°C–1100°C) is performed, it may eliminate the grain structure in the material needed for achieving approximately isotropic properties within the material. This material is defined as nonoriented steel.

Silicon content in electrical steels is usually between 1.5% and 3.5%. Oriented silicon steel contains more silicon than nonoriented steel, approximately 3.0%–3.5%. However, it must be noted that very high silicon content (e.g., >4.0%) may result in lowering of induction permeability saturation density. To minimize hysteresis losses, the impurities such as oxides, nitrides, and sulfides in silicon steel must be tightly controlled.

Carbon content in all silicon steels is usually considerably low, approximately 0.003%. This helps minimize the hysteresis loss in the silicon steels, make them easier in rolling and other fabrication processes, and increase the lifetime of tooling.

Silicon steel is available in an array of grades and thicknesses, suited for applications in different types of electric motors. According to American Iron and Steel Institute (AISI), the silicon steel is graded by core loss, represented by a series of M numbers. The lower the M number, the lower the core loss and thus the higher the cost.

As a reference, some silicon steels are listed in Table 2.3. Among all grades, M19 is probably the most common grade for motion control products, as it offers nearly the lowest core loss in this class of material.

An alternative material commonly used for rotating electric equipment is the nickel alloy due to its high permeability and low core losses. These characteristics make it ideal for motors. However, its cost is significantly higher than silicon steel. Nickel alloys require a very careful annealing cycle. During the annealing process, surface insulation films are formed on the surfaces of the nickel alloy laminations.

In some applications that require high flux density without saturation, cobalt alloys may be used to make motor laminations. This type of alloys is also used in weight-sensitive applications such as space shuttles and satellites. The commonly used cobalt alloys contain 48%–50% cobalt and 2% vanadium, making them high tensile strengths. Hence, for some high-speed, large-power motors, silicon steel is no longer applicable due to its low mechanical strengths, and cobalt alloys become an excellent choice for the lamination material. Like nickel alloys, cobalt alloys require careful annealing after stamping and making oxide coatings on lamination surfaces is a separate process.

Other elements such as manganese and aluminum can also help reduce core losses due to the different mechanisms from silicon. The addition of these elements into steel will alter the metallurgical grain structure to contribute to lowering of the core loss.

Cold rolled lamination steel is the most cost-effective and most common material for core laminations of low-cost motors. Similar to carbon steel, this material has relative high core losses. It usually requires annealing after stamping to develop optimum properties and to add oxide coatings on the lamination surfaces.

The rotor core is assembled onto the rotor shaft with an interference fit. The radial interference value is optimized to provide adequate radial contact pressure to transmit torque under full-load and full-rotating speed.

One of the most critical issues for a high-speed motor is the extreme high centrifugal force acting on the rotor core, resulting in a high level of spin stress. In addition, interference fit preload stress also contributes to the loading of the rotor core. Thus, it becomes critical to carefully select lamination materials based on not only their magnetic properties but also mechanical properties, especially for high-speed motors.

TABLE 2.3

Silicon Steel Grades

Silicon Steel	AISI Grade	Thickness, mm (in.)	Note
Nonoriented silicon steel	M15	0.36 (0.014) 0.47 (0.0185)	The magnetic properties are practically the same in any direction of magnetization in the plane of the material.
	M19	0.36 (0.014) 0.47 (0.0185) 0.64 (0.025)	
	M22	0.36 (0.014) 0.47 (0.0185) 0.64 (0.025)	
	M27	0.36 (0.014) 0.47 (0.0185) 0.64 (0.025)	
	M36	0.36 (0.014) 0.47 (0.0185) 0.64 (0.025)	
	M43	0.36 (0.014) 0.47 (0.0185) 0.64 (0.025)	
	M45	0.47 (0.0185) 0.64 (0.025)	
	M47	0.47 (0.0185) 0.64 (0.025)	
Orientated silicon steel	M2	0.18 (0.007)	The magnetic properties are strongly oriented with respect to the direction of rolling.
	M3	0.23 (0.009)	
	M4	0.27 (0.011)	
	M6	0.36 (0.014)	
High permeability orientated	—	0.23 (0.009) 0.27 (0.011)	Low core losses with very thin laminations.

Source: Data from AK Steel, Selection of electrical steel for magnetic cores, http://www.aksteel.com/pdf/markets_products/electrical/Mag_Cores_Data_Bulletin.pdf.

2.3.2 Lamination Cutting

There are primarily two ways used by lamination manufacturers in lamination cutting: laser beam cutting and stamping machine cutting, depending on applications. For large-volume production manufacturing, stamping machine cutting is more appropriate for its high efficiency and low cost. For achieving high productivity, most lamination manufacturers adopted high-speed stamping machines in production lines. By supplying silicon steel sheets automatically, stamping machines operate continuously with press capabilities of over 250 strokes per minute and up to 1250 tons of force. To fully utilize the material, some motor manufacturers stamp slotted laminations of the stator and rotor from the same sheet of core steel simultaneously, with the outer doughnut-shaped punching as the stator lamination and the inner as the rotor lamination.

One problem often encountered in stamping cutting is that burrs are left at the lamination edges after a stamping process. Without passing through special treatments, these burrs may form electric paths for interlaminar eddy current under assembly pressures. Consequently, control of stamping operation must be carefully designed to keep the stamping burrs as small as possible. If necessary, all stamped edges are debarred when effective control is difficult or impossible.

Laser cutting is typically applied to large-size motor laminations in which stamping machines may not be suitable. This technique is also suitable for fast fabrication of motor prototypes for its flexibility, dimensional accuracy, and short lead time. By concentrating a very high temperature into a tiny spot during a short time, laser cutting provides superior cutting quality with small burrs, low deformation, low residual stress, and tight control of dimensions. During the cutting process, an oxide film is naturally generated on the burrs, thereby reducing the conductivity of burr contact and reducing interlaminar losses. The drawbacks of laser cutting are its low productivity and high cost.

2.3.3 Lamination Surface Insulation

When a laminated core is subjected to an alternating electric field, eddy current is induced in each lamination and between the laminations (Figure 2.23). The resistance to the eddy current within a lamination depends on the lamination dimensions (thickness, length, and width) and material properties. In most circumstances, the eddy-current losses vary approximately as the square of the thickness of flat-rolled magnetic materials, that is, $P_e \propto t^2$, where t is the lamination thickness. This indicates that reducing the lamination thickness by half will lead to the reduction in the eddy-current losses by one-fourth. With today's advanced nanotechnology, magnetic core laminations may be possibly made extremely thin so that eddy-current losses within the laminations become negligibly.

Referring to Figure 2.23, in addition to the eddy current within each lamination, eddy current may occur between laminations, called interlaminar eddy current. In order to minimize eddy-current losses between laminations, silicon steel laminations must be insulated from one another to maximize the lamination surface resistance by coating a thin layer on two sides of each lamination with either an organic, inorganic, or magnetite material.

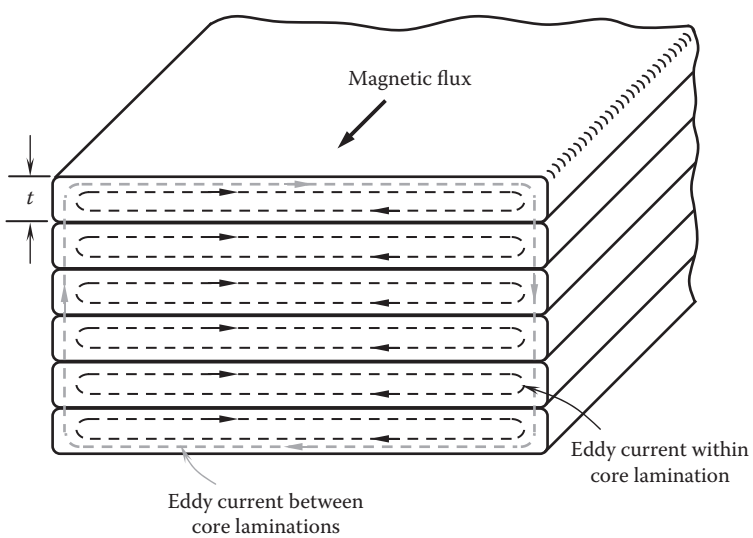

FIGURE 2.23
Eddy current within each core lamination and between core laminations.

The simplest way for making lamination insulation is to oxide laminations through annealing. This will create an oxide film on all lamination surfaces, as well as burrs. Thus, it greatly reduces the conductivity of laminations and minimizes eddy-current losses.

Lamination recoating restores interlaminate resistance to bring magnet core laminations back to optimal operating specifications. Recoating on stamped or laser cut laminations eliminates the possibility of interlaminate shorts.

2.3.4 Lamination Annealing

Lamination annealing is used to restore the electromagnetic, thermal, and mechanical properties of newly stamped or laser cut laminations. During a stamping process, plastic deformation, stress, and strain are produced at the cut zone, causing nonfavorable effects on magnetic properties of laminations. Though laser cutting produces little plastic deformation at cut edges, it induces a thermal shock wave and high temperatures to the cut laminations, resulting in thermal stresses and/or permanent damage to magnetic properties, such as reduced remanence and permeability. It has been reported that annealing processes can increase permeabilities and reduce power losses for both stamping and laser cutting [2.46]. Usually, the annealing temperature for the recrystallization ranges at 830°C–890°C. A higher annealing temperature up to 1100°C is also applicable for some lamination materials.

2.3.5 Lamination Stacking

A stack of laminations is assembled for a rotor core. Laminations are often stacked on a mandrel and then compressed under high pressure for obtaining the rigidity of the rotor core in the axial direction. Traditionally, laminations have been bonded using either adhesives or pins. Obviously, these stacking methods require additional operations and thus increase manufacturing costs and production lead time. In last several decades, a number of manufacturing processes have been developed to simplify the lamination stacking operation without using adhesives or pins. A simple method is to weld the rotor core when it is compressed. Another process involves interlocking the laminations at their outer tips with a die-punching machine so that corresponding laminations can interlock one another during assembly. Interlocking dimples on internal regions is another method. For large motors, the finished rotor cores are kept tightly in the axial direction by through bolts with a plate at each end of the stacked rotor core. A coated thin layer of insulation on each surface of each lamination reduces eddy current to minimize energy loss and boost performance.

An alternative method for fabricating rotor core is referred to as the slinky method. As demonstrated in Figure 2.24 [2.47], a rotor core is made by coiling up a straight continuous strip of sheet metal with respect to its centerline. To help bend the strip into a generally spiral and arcuate configuration, a V-shaped notch is formed between adjacent teeth at the ID of the core. The predetermined holes are used to receive suitable fastening means such as rivets to hold the rotor core firmly. All the slots, notches, and holes are punched together into a continuous longitudinally extending metal band of relative ductile material such as silicon steel.

2.3.6 Rotor Casting for Squirrel Cage Motor

A squirrel cage rotor has conducting bars and end rings made by casting either aluminum or copper into the rotor core slots and at the end surfaces of the rotor. The conducting bars

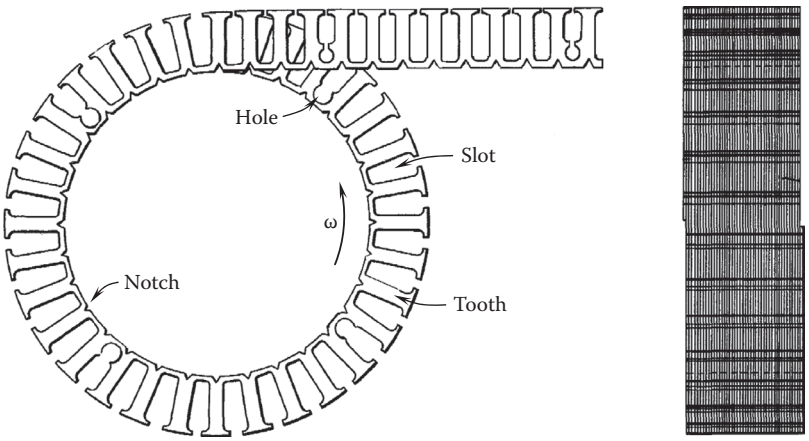

FIGURE 2.24
Applying slinky method for fabricating motor core for using as either rotor or stator (U.S. Patent 3,188,505) [2.47]. (Courtesy of the U.S. Patent and Trademark Office, Alexandria, VA.)

are parallel to the rotor axis with a small skew angle, and the end rings serve to connect electrically all of the rotor bars, forming closed loop paths for electric current.

Cast rotors can be made by either permanent casting or die-casting process. In a permanent casting process, a rotor core is placed in a permanent mold with a desired space at the core top and bottom for the casting of end rings. Then, the mold is clamped together and a molten aluminum alloy is poured or forced into the mold. In a die-casting process, a rotor core can be cast either vertically or horizontally. One of the advantages using a die-casting process is its high pressure acting on the molten aluminum to force it to fill the rotor slots in a very short period of time for minimizing porosities in cast rotors. To achieve high casting quality, the key casting parameters including the aluminum temperature, injection speed, casting pressure, and casting time must be controlled strictly. In addition, to achieve high casting efficiency and rotor strength, all conducting bars, end rings, and fans are cast as one integral unit, resulting in a robust and rigid assembly to withstand high loads.

In a rotor casting process, a shaft may or may not be inserted into a rotor core, depending on the succeeding finishing steps required and the particular manufacturing process being used. With the shaft insertion, high casting temperatures may result in the deformation of the shaft and the reduction of the hardness on the shaft surface.

2.3.7 Heat Treatment of Casted Rotor

Heat treatment of casted rotors is important for optimizing the motor performance. By heating casted rotors at 300°C–450°C (570°F–840°F) for about 1–2 h, it helps break metallurgical bonds between steel laminations and the conductor bars, as the result of a large differential in thermal expansion of the two metallic materials. This greatly increases the electric resistance between the conducting bars and laminations. A theoretical analysis has shown that even a partial improvement in the insulation between the conducting bars and laminations can immediately result in noticeably reduced eddy-current losses. In addition, heating of casted rotor creates a thin protective insulation of naturally formed oxide film at the cutting edges of the laminations to further reduce interlaminar eddy-current losses.

2.3.8 Rotor Assembly

The most economic and reliable rotor assembly method is to use interference fits to firmly integrate shafts and rotor cores together, such as press fit and shrink fit. Generally, press fit is used for relative small rotors without exceeding the capacity of axial hydraulic pressing forces. However, the axial force required to assemble large rotors is considerably high in some instances and thus may bend or damage shafts or cause overstressed rotor cores. As a result, heat shrink processes are often used for larger rotors. The rotor assembling process is shown in Figure 2.25. In this case, shrink fit is made by heating rotor cores with induction heating (Figure 2.25a) while maintaining shafts at room temperature. When a rotor core reaches a preset temperature, its ID expands to become a little larger than the OD of the shaft, allowing the shaft to be easily inserted into the bore of the rotor core with little or no axial force (Figure 2.25b). The preset heating temperature is determined based on the rotor-shaft interference and ID of the rotor core. The rotor core is then shrunk as cold compressed air is applied on the rotor assembly. Once the shaft seizes to the core, shrinkage causes the core to pull away from the shaft shoulder. The end of the rotor core is hit with a rubber hammer to ensure the shaft shoulder is banked on the core face (Figure 2.25c). Finally, the rotor assembly is covered with a cooling hood for complete cooling of the rotor assembly.

2.3.9 Rotor Machining and Runout Measurement

A rotor assembly process involving heat shrinking or high mechanical pressuring may cause a change in shaft runout. Therefore, after rotor assembly is complete, it is preferred to check the runout of shafts to ensure the changes of runout are in the range of acceptance (Figure 2.26).

Kollmorgen engineers have investigated the effect of heat shrinking on shaft runout [2.48]. Thirty shafts were measured before and after the heat-shrinking assembly process. The runout of the shafts was inspected in seven locations with a 0.00254 mm (0.0001 in.) dial indicator using the bearing journals as the datum. The mean change in runout for shafts was 0.00414 mm (0.000163 in.) with a standard deviation of 0.00676 mm (0.000266 in.). The average runout from the rotor OD (measured at two locations) to the bearing journals was 0.01707 mm (0.000672 in.) with a standard deviation of 0.01034 mm (0.000407 in.). Data collected from the runout testing have shown that the heat shrink process for rotor assembly has minimal to no effect on shaft runout.

Then, the rotor is placed on a lathe, where the rotor outer surface is machined to a smooth finish for ensuring a uniform air gap between the rotor and stator and for minimizing the runout of the rotor outer surface to the axis of rotation (Figure 2.27). However, machining the rotor outer surface may smear the casted conducting bars and steel laminations, resulting in the increase in the core losses, creating some hot spots and the decrease in motor efficiency. To reduce the smearing effect on motor performance, some motor manufacturers grind the rotor outside surfaces.

After the rotor is machined, it requires inspecting the runout on both the rotor and shaft for ensuring the centricity of the rotor to the rotating axis and uniform air gap, as demonstrated in Figure 2.28. The measured shaft runout data should be compared with those measured prior to the rotor assembly.

2.3.10 Rotor Balancing

Motor manufacturing involves a variety of mechanical processing techniques, such as machining, milling, forging, stamping, welding, grinding, drilling, and casting. When

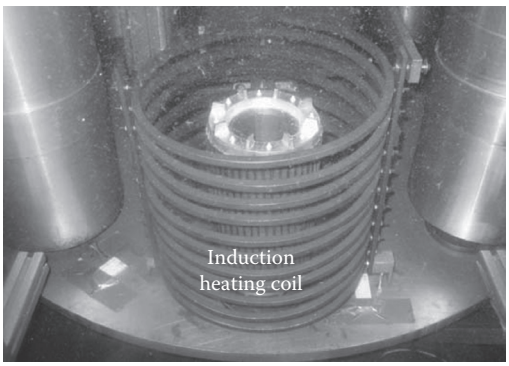

(a)

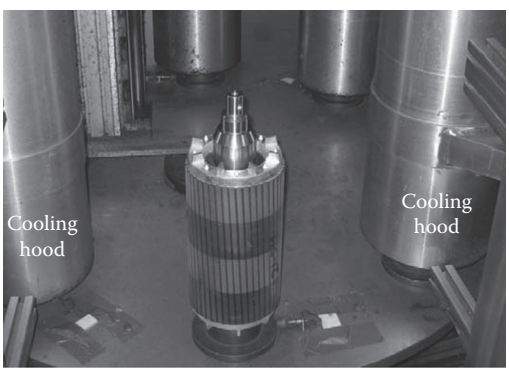

(b)

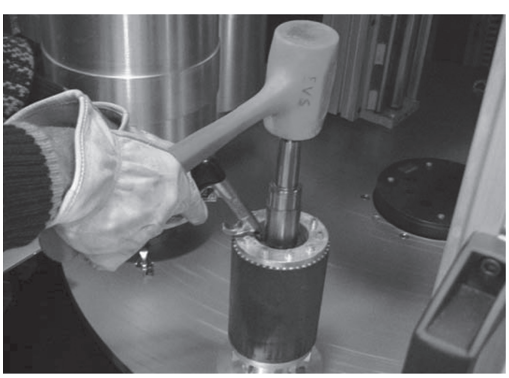

(c)

FIGURE 2.25
Rotor assembly process with the shrink fit technique: (a) heating the rotor core, (b) inserting the shaft, and (c) quenching the assembly and hammering the shaft to reaching its desired position.

a rotor has been fabricated and assembled, unbalance of the rotor is likely experienced due to a number of factors, including improper manufacturing tolerances, material defects (e.g., porosity, voids, and blowholes), unsymmetrical structures (e.g., keys and key ways), poor assembly, and improper fabrications (e.g., misshapen casting and eccentric machining). Rotor unbalance can result in vibration and variable stress in rotors and their related

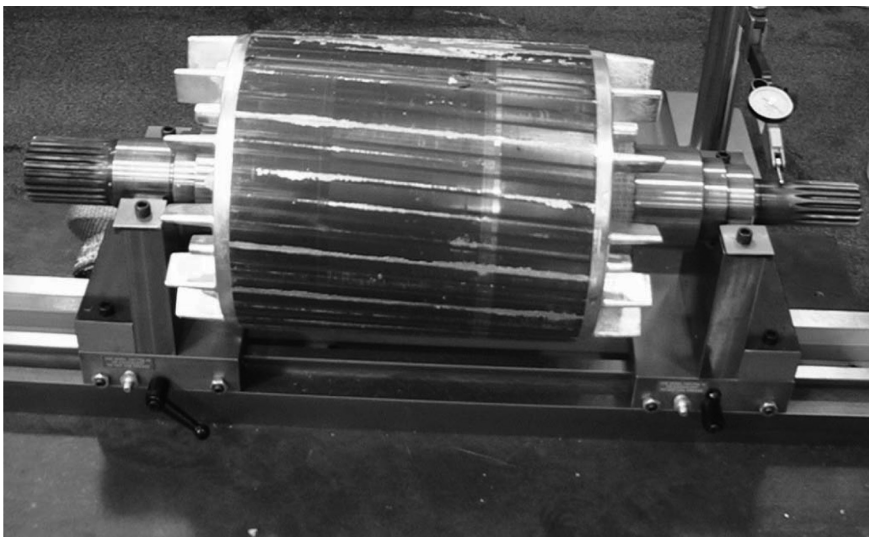

FIGURE 2.26
Measurement of shaft runout after rotor assembly but before rotor machining.

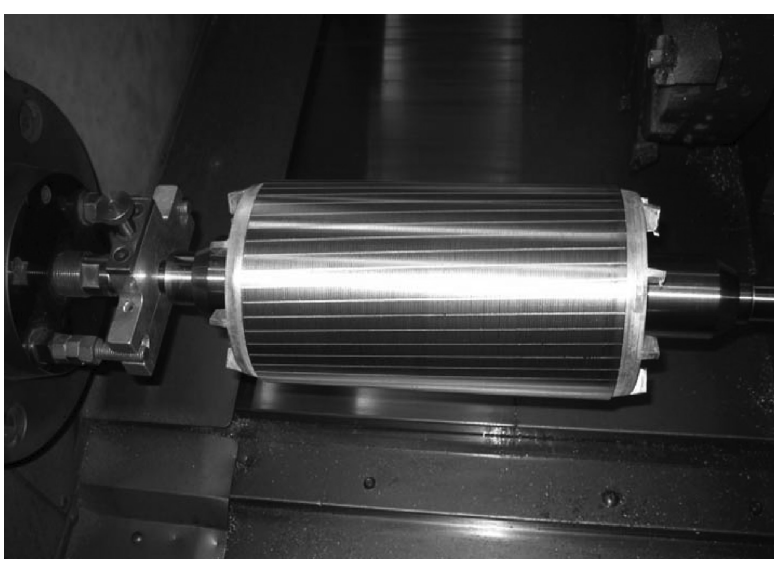

FIGURE 2.27
Machining the outer surface of a casted rotor with a CNC.

supporting structures. Rotor balancing is extremely important to motors that have very high rotating speeds for ensuring safe and normal operation.

Rotor balancing involves the entire rotor structure, including a shaft, a rotor core, rotor conducting bars/end rings, fans, and other auxiliary components.

There are a number of international standards available for rotor balance. One commonly used standard in motor industry is ISO Standard 1940/1 [2.49], which provides a method for applying unbalance tolerances based upon the static and coupled

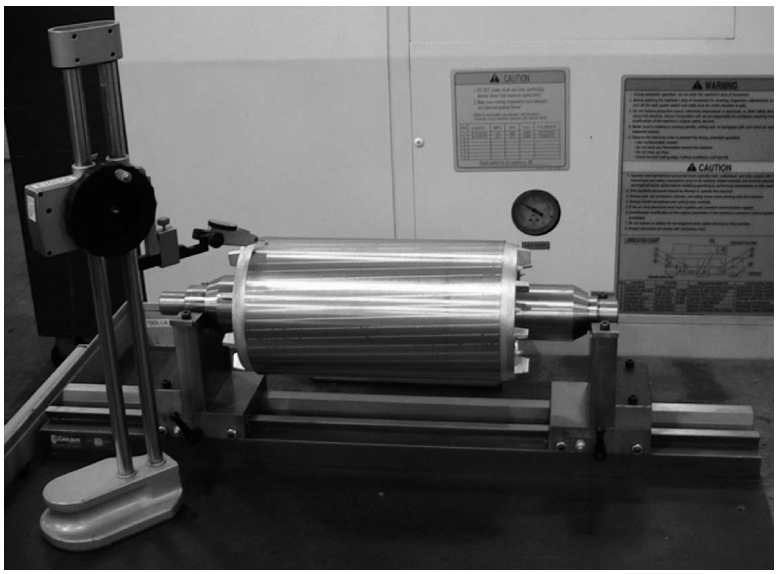

FIGURE 2.28
Runout measurement made on the outer surface of a cast rotor after it was machined.

components. This standard defines common levels of acceptable unbalance for various types of machines and applications.

2.3.10.1 Types of Unbalance

There are three types of unbalance: (1) static unbalance is when the principal inertia axis of a rotor is offset from and parallel to the axis of rotation and is corrected only in one axial plane (Figure 2.29a); (2) coupled unbalance is when the principal inertia axis intersects the axis of rotation at the center of gravity (Figure 2.29b); and (3) dynamic unbalance is the vectorial summation of static unbalance and coupled unbalance (Figure 2.29c). Thus, it is equivalent to two unbalance vectors in two specified planes that completely represent the total unbalance of the rotor. Because dynamic unbalance is a multiplane unbalance, the correction of dynamic unbalancing requires at least two correction masses. In all cases, the center of gravity C_g is located on the principal inertia axis, rather than on the axis of rotation.

It has been widely accepted that dynamic unbalance is one of the most common sources of motor vibration and noise. As reported previously, dynamic unbalance is the main source in about 40% of the excessive vibration situations [2.50]. In severe situations, this type of unbalance can cause failures of rotor and bearings.

As the simplest form of unbalance, static rotor unbalance U_s can be determined as

$$U_s = M_r e = m_u r_u \tag{2.3}$$

where

M_r and m_u are the rotor and unbalance masses, respectively
e is the mass eccentricity measured as the distance between the principal inertia axis and the axis of rotation
r_u is the distance between the center of the unbalance mass and the axis of rotation

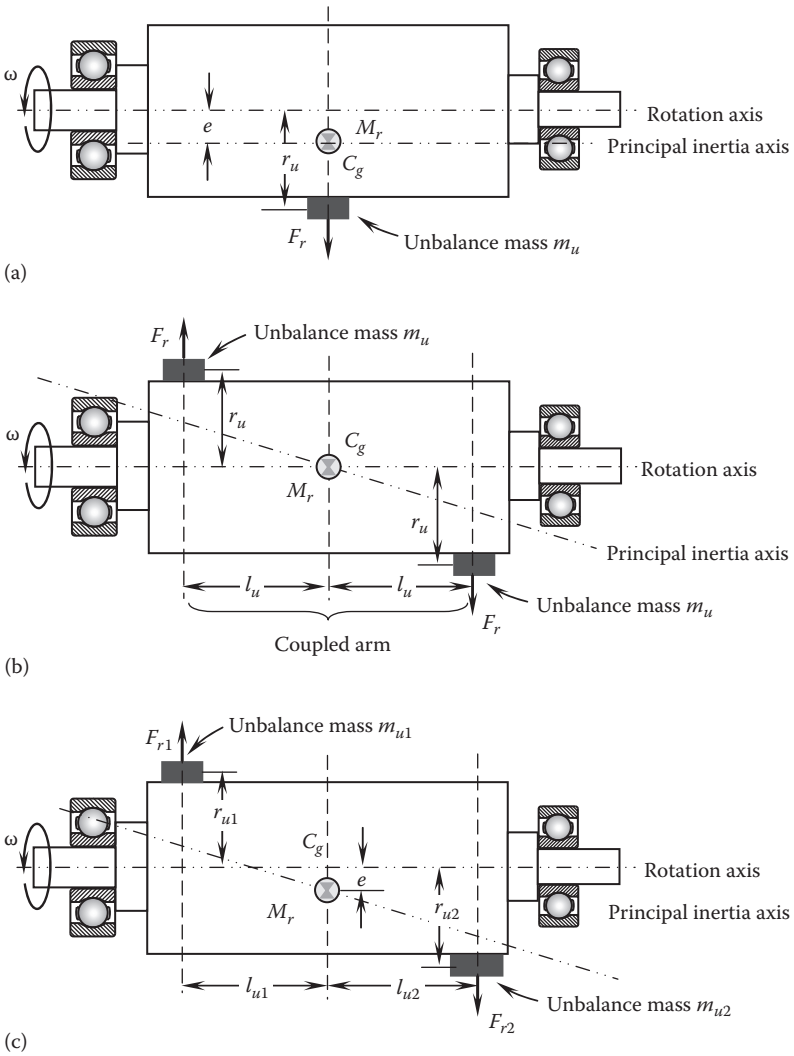

FIGURE 2.29
Three types of unbalance: (a) static unbalance, (b) coupled unbalance, and (c) dynamic unbalance. In all cases, the center of gravity is located on the principal inertial axis.

Thus, the mass eccentricity e can be obtained:

$$e = \frac{m_u r_u}{M_r} \tag{2.4}$$

Referring to Figure 2.29a, the magnitude of unbalance force or centrifugal force is expressed as

$$F = (m_u r_u + M_r e)\omega^2 \tag{2.5}$$

This indicates that centrifugal force is exponentially sensitive to the rotor rotating speed.

Coupled unbalance is expressed as

$$U_c = m_u r_u (2l_u) \tag{2.6}$$

where $(2l_u)$ is defined as the coupled arm, which is the distance between the two unbalance masses. Thus, coupled unbalance is described as a mass times a length squared.

2.3.10.2 Rotor Balancing Machine

To prevent possible damages to motor due to vibration caused by rotor unbalance, balancing operation is a necessary corrective action before assembling rotors to motors. Many motor manufacturers use balancing machines to detect the amount and location of unbalanced masses on rotors. Some precise balancing machines can sensitively and accurately identify any mass axis 0.001 mm off the axis of rotation.

A simplest type of balancing machine is used for static balancing only. This type of machine is suitable for balancing disk-shaped rotors. For a majority of rotors, the type of balancing machine required must be capable of identifying dynamic unbalance in two axial planes. This type of machine is suitable for balancing rotors with long span length and small shaft diameter (i.e., $L/D \gg 1$).

The principle of rotor balancing is very similar to that of car wheel balancing. With an advanced balancing machine, masses have to be either removed from or added to a rotor to minimize the uneven mass distribution so that rotor vibration can be minimized. It must be noted that the added mass must be firmly installed to the rotor and thus will not fall off when the rotor rotates at a high speed. For this reason, the material removal method is ideal.

An advanced balancing machine is shown in Figure 2.30. This machine can implement the whole balancing process with full automation, from measuring the location and

FIGURE 2.30
Rotor balancing machine.

amount of unbalance, displaying unbalancing results in polar graphs, drilling on the testing rotor, and repeating the process until unbalance is lower than an allowable level.

2.3.10.3 Balancing Operation

Not all unbalanced rotors need to be corrected. In common practices, a permissible unbalance is set by motor manufacturers as the balancing acceptance limit. The permissible unbalance can be determined based on experiments from similar machines, permissible bearing forces, or standards. Balancing corrections would be taken only when the existing balance is larger than the permissible unbalance.

The principle of rotor balancing is that all forces and moments acting on the rotor must be balanced under both static and dynamic conditions, so that the resultant force and moment on the rotor must be zero, that is,

$$\sum_{i=1}^{n} F_i = 0 \tag{2.7a}$$

and

$$\sum_{i=1}^{n} M_i = 0 \tag{2.7b}$$

Static unbalance can be detected without spinning the rotor and can be most easily corrected. As shown in Figure 2.31, a static unbalance can be corrected in two ways. One method is to add directly a correct mass m_c at the opposite location of the unbalance mass m_u in the plane that contains the center of gravity (Figure 2.31a). As long as the product of the correct mass m_c and the radius from the center of the correct mass to the axis of rotation r_c is equal to the product of the unbalance mass m_u and the radius from the center of the unbalance mass to the axis of rotation r_u ($m_c r_c = m_u r_u$), the static balance is achieved. In a case that $r_c = r_u$, it leads to $m_c = m_u$.

An alternative method is to use two pieces of correct mass on the rotor in planes equidistant from the plane that contains the center of gravity at the radius r_c (Figure 2.31b). The static balance is achieved when $2m_c r_r = m_u r_u$. If $r_c = r_u$, then $m_c = m_u/2$.

An advantage of using these methods for correcting static unbalance is their simplicity and flexibility. Rotor balancing can be done without using a complex balance machine. However, these methods are only suitable for the disk-shaped rotors that are dominated by static unbalance.

Unlike static unbalance that is measured under a nonrotating condition, coupled unbalance can only be measured by spinning the motor rotor. There are two methods to correct coupled unbalance. The first method is to use two equal masses, in which each is to be added on the rotor at an angle of 180° apart from the unbalance mass, as shown in Figure 2.32a. In the second method, coupled unbalance is corrected in any two planes. However, each correcting mass and the distance to the plane that contains the center of gravity must be carefully determined, as shown in Figure 2.32b.

Because dynamic unbalance is the vectorial summation of static unbalance and coupled unbalance, the correction of dynamic unbalance is thus the combination of the corrections of static unbalance and coupled unbalance.

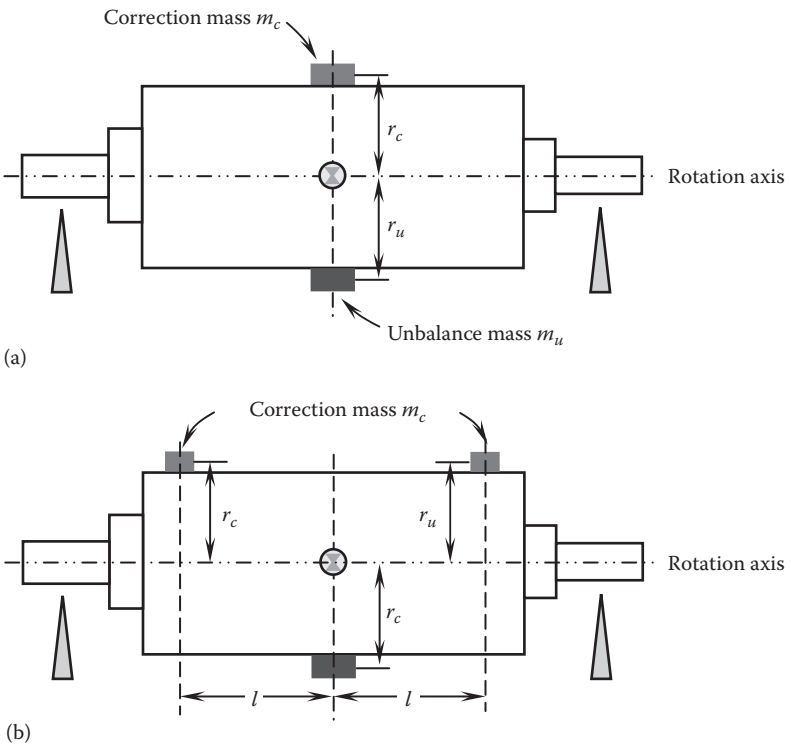

FIGURE 2.31
Two alterative balancing operations for static unbalance: (a) adding one piece of correction mass in the plane containing the center of gravity and (b) adding two pieces of correction mass in two planes with equal distance from the plane containing the center of gravity and equal radius from the rotation axis.

A real balancing operation is shown in Figure 2.33. An assembled rotor is placed in a rotor balancing machine. The bearing journal at each end of shaft is put on a pair of bearing rollers. The rotor is driven by a driving belt that is placed over the rotor surface near the rotor center.

2.4 Interference Fit

A rotor primarily consists of a rotor core and a shaft. In order to integrate these two parts together as the rotor to transmit the motor torque, the fit between the rotor core and shaft must be carefully designed. For example, too loose a fit could result in a corroded or scored rotor core and shaft, while too tight a fit could result in unnecessarily large mounting and dismounting forces, even damages of the mating surfaces or deformation/cracks of the fitting parts.

The term *interference* refers to the fact that one part slightly interferes with the space that the other is taking up. Interference fit is often used to joint two mating parts together either semipermanently or permanently. Interference fit can be generally achieved by shaping

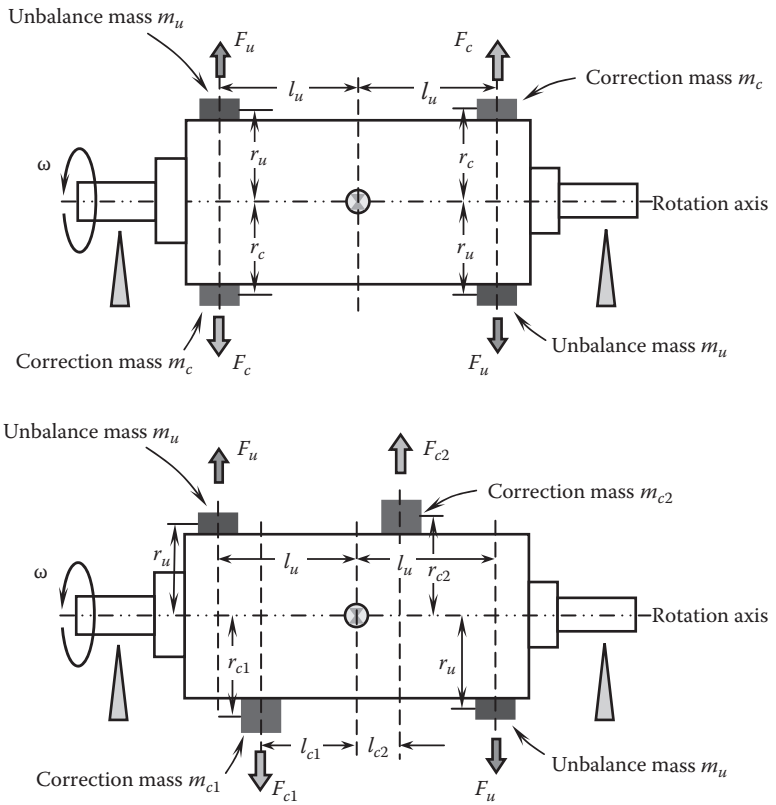

FIGURE 2.32
Balancing operation for coupled unbalance.

the two mating parts so that one or the other (or both) slightly deviates in size from the nominal dimension. In the motor industry, interference fit is extensively used to join rotor cores and shafts, as well as stator cores and housings, for its high joining strength and concentricity between the mating parts. Interference fit can be divided into several types as discussed in the following.

CTE is the material property of primary influence on dimensional stability as it represents the material response to changes in temperature. This material property can be exploited in an interference fit such as shrink fit. It is to be noted that in the interference fit design, it is critical to carefully consider the temperature effect on the fitting strength and component stresses in the whole temperature range including both motor operation and storage. In some improper designs, interference fits work fine near room temperature. However, as the temperature becomes extremely high or extremely low, due to the large differential in thermal expansion between the assembly parts, the two assembled parts may separate from each other or pressed against each other, causing one of them to be broken.

Consequently, to avoid failure of the interference-fitted assembly and minimize thermal stresses arising from the difference in CTE during temperature variations, it is highly desired to select materials of the mating parts that have close CTE values.

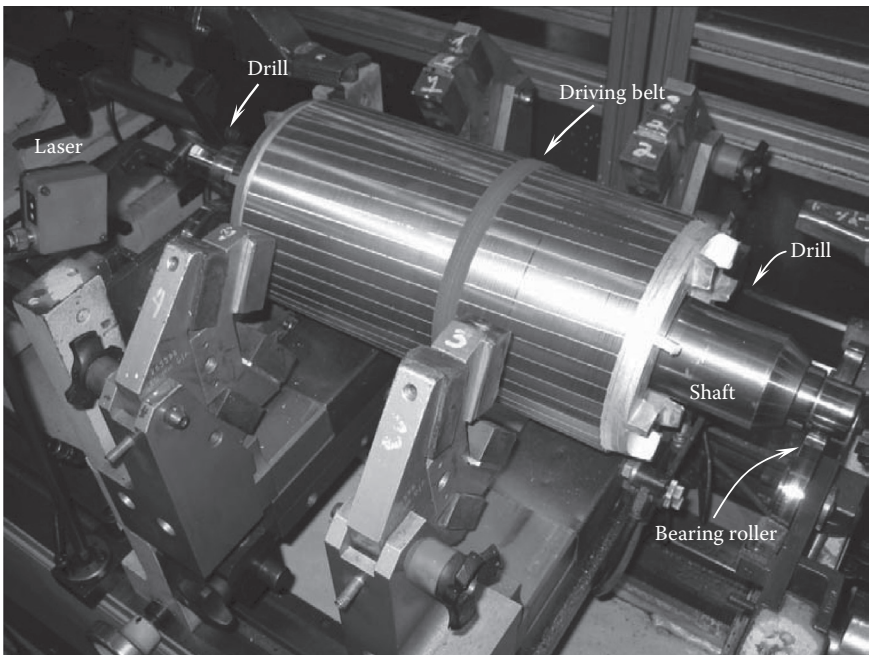

FIGURE 2.33
Automatically controlled rotor balancing process.

2.4.1 Press Fit

Press fit is generally chosen for its high operation reliability in rotor assemblies. Press fit can be obtained by selecting the proper interference between a shaft and a rotor core, that is, the OD of the shaft is slightly larger than the ID of the rotor core. Thus, at room temperature, the shaft must be pressed into the rotor core under an axial pressing force. During this insertion process, the shaft reduces its original OD due to the compressive force, and the rotor core increases its original ID due to the expansion force, producing a radial contact stress at the interface. This radial stress is referred to in the literature as contact pressure or interference pressure. In general, the contact pressure changes in response to the interference, ambient temperature, shaft dimensions, and material properties of both the shaft and rotor core.

As shown in Figure 2.34, the original inner and outer radii of a hollow shaft and the rotor core are a and b and c and d, respectively. For the case that $b > c$, the interference between the shaft and the rotor core is defined as

$$\delta = b - c \tag{2.8}$$

when the shaft is pressed into the rotor core, the shaft radius becomes b' and

$$b' = b - \delta_s \tag{2.9}$$

where δ_s is the decrease of the shaft radius. As the same matter, the internal radius of the rotor core becomes c'

$$c' = c + \delta_{rc} \tag{2.10}$$

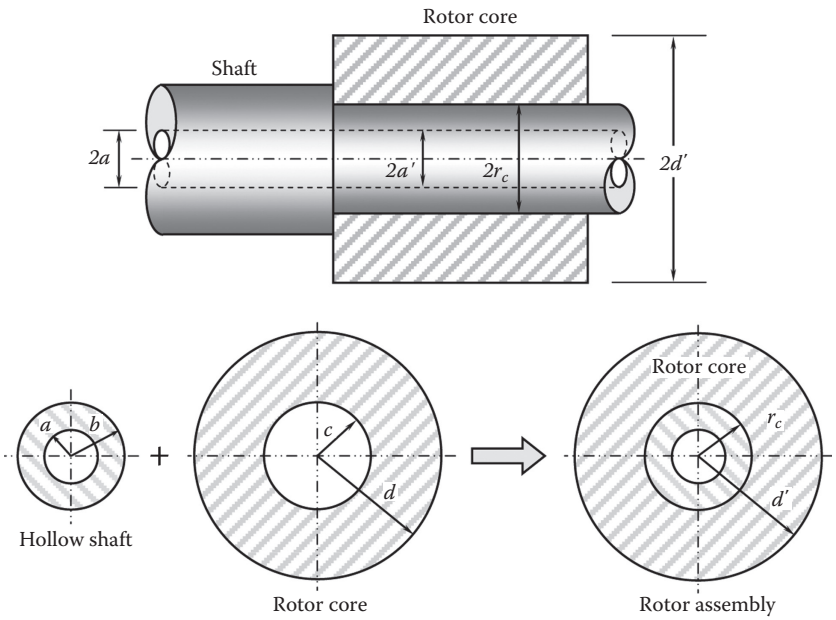

FIGURE 2.34
Dimensions of the hollow shaft and rotor core before and after assembly.

where δ_{rc} is the increase in the internal radius of the rotor core. Because that $b' = c' = r_c$, it follows that

$$\delta = b - c = \delta_s + \delta_{rc} \tag{2.11}$$

A contact pressure p is thus created at the contacting surface at $r = r_c$ (Figure 2.35). It can be derived that the radial stresses $\sigma_r = -p$ in each member at the contacting surfaces. The tangential stresses of the rotor core bore and the shaft surface are [2.51]

$$\sigma_{t,rc} = p\frac{d^2 + r_c^2}{d^2 - r_c^2} \tag{2.12}$$

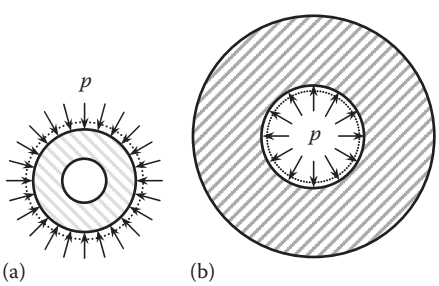

FIGURE 2.35
Contact pressure acting on (a) the hollow shaft and (b) the rotor core.

$$\sigma_{t,s} = -p\frac{r_c^2 + a^2}{r_c^2 - a^2} \tag{2.13}$$

respectively.

The tangential strain of the rotor core is determined as the ratio of the change in circumference to the original circumference, that is,

$$\varepsilon_{rc} = \frac{2\pi(r_c - c)}{2\pi c} = \frac{\delta_{rc}}{c} \tag{2.14}$$

This gives that

$$\delta_{rc} = c\varepsilon_{rc} \tag{2.15}$$

Since

$$\varepsilon_{rc} = \frac{\sigma_{t,rc}}{E_{rc}} - \nu_{rc}\frac{\sigma_r}{E_{rc}} \tag{2.16}$$

where

ν is Poisson's ratio

E is Young's modulus (modulus of elasticity)

Combining Equations 2.14 and 2.16, it yields

$$\delta_{rc} = \frac{c}{E_{rc}}(\sigma_{t,rc} - \nu_{rc}\sigma_r) \tag{2.17}$$

Noting that $\sigma_r = -p$ and substituting Equation 2.12 into 2.17 yields

$$\delta_{rc} = \frac{cp}{E_{rc}}\left(\frac{d^2 + r_c^2}{d^2 - r_c^2} + \nu_{rc}\right) \tag{2.18}$$

Similarly to Equations 2.14 and 2.16 for the tangential strain of the rotor core, the governing equations for the tangential strain of the shaft are as follows:

$$\varepsilon_s = \frac{2\pi(r_c - b)}{2\pi b} = -\frac{\delta_s}{b} \tag{2.19}$$

$$\varepsilon_s = \frac{\sigma_{t,s}}{E_s} - \nu_s\frac{\sigma_r}{E_s} \tag{2.20}$$

Therefore, from the previous two equations, the reduction in the shaft radius δ_s can be expressed as

$$\delta_s = \frac{bp}{E_s}\left(\frac{r_c^2 + a^2}{r_c^2 - a^2} - \nu_s\right) \tag{2.21}$$

Thus, Equation 2.11 can be rewritten as

$$\delta = \delta_s + \delta_{rc} = \frac{cp}{E_{rc}}\left(\frac{d^2 + r_c^2}{d^2 - r_c^2} + \nu_{rc}\right) + \frac{bp}{E_s}\left(\frac{r_c^2 + a^2}{r_c^2 - a^2} - \nu_s\right) \tag{2.22}$$

It must note that the interference δ is associated with radius, rather than diameter. This equation can be solved for the contact pressure p when the interference δ is known:

$$p = \frac{\delta}{\frac{c}{E_{rc}}\left(\frac{d^2 + r_c^2}{d^2 - r_c^2} + \nu_{rc}\right) + \frac{b}{E_s}\left(\frac{r_c^2 + a^2}{r_c^2 - a^2} - \nu_s\right)} \tag{2.23}$$

For a solid shaft (i.e., $a = 0$), the previous equation is simplified as

$$p = \frac{\delta}{\frac{c}{E_{rc}}\left(\frac{d^2 + r_c^2}{d^2 - r_c^2} + \nu_{rc}\right) + \frac{b}{E_s}(1 - \nu_s)} \tag{2.24}$$

The contact area between the shaft and the rotor core is

$$A_c = 2\pi r_c L \tag{2.25}$$

where L is the contact length between the rotor core and the shaft. Thus, for a given interference δ, the maximum torque that can be carried by the shaft is

$$T_{\max} = \mu_s F_c r_c = \mu_s p A_c r_c = 2\pi r_c^2 \mu_s p L \tag{2.26}$$

where μ_s is the static coefficient of friction between the shaft and the rotor core.

The axial force required for the press in assembly is (see Figure 2.36)

$$F_a = \mu_k p A_c = 2\pi r_c \mu_k p L \tag{2.27}$$

where μ_k is the kinetic coefficient of friction between the shaft and the rotor core.

It is noted that $b = r_c + \delta_s$ and $c = r_c - \delta_{rc}$. Because $(b + c) \gg (\delta_{rc} - \delta_s)$, r_c can be expressed as

$$r_c = \frac{b + c}{2} + \frac{\delta_{rc} - \delta_s}{2} \approx \frac{b + c}{2} \tag{2.28}$$

When a shaft is pressed into a rotor core, the force driving the shaft should be applied uniformly to the end of the shaft to avoid galling, peening, or damaging the rotor core. The mating surfaces of both the shaft and rotor core should be thoroughly cleaned and free of imperfections.

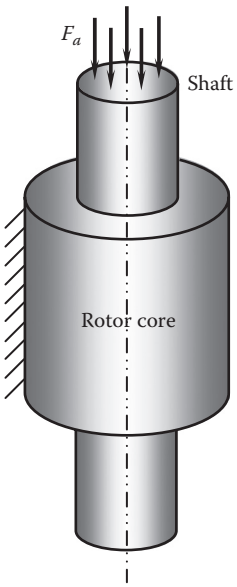

FIGURE 2.36
Axial pressing force applied in press fit rotor assembly.

2.4.2 Shrink Fit

Shrink fit is a semipermanent assembly system that can transmit large torques through the creation of high contact pressure at the interface of its mating components. Being a tight joining method, shrink fit has been extensively used in various industries due to its high joining strength and reliability. There are a number of benefits to using shrink fit over press fit: (1) shrink fit can minimize mechanical stresses associated with the pressing operation and thus reduce the deformation of the rotor core; (2) it allows a rotor core to shrink onto a shaft symmetrically; (3) the requirement of surface finishing for shrink fit is relatively lower than that for press fit; and (4) the process of shrink fit is completely controllable.

Most materials are subjected to thermal expansion as the temperature goes up and thermal contraction as the temperature goes down. Shrink fit techniques utilize such the material properties in machine assembly processes.

For a solid material, the coefficient of linear thermal expansion is typically a function of temperature, for measuring how much the material expands for a change in temperature. It is defined as the linear dimension change with respect to the change in temperature per unit linear dimension (i.e., length) under a constant pressure p_o:

$$\alpha_L = \frac{1}{L}\left(\frac{\partial L}{\partial T}\right)_{p_o} \tag{2.29}$$

If the desired expansion in length ΔL is provided, the temperature rise ΔT can be determined as

$$\Delta T = \frac{1}{\alpha_L}\frac{\Delta L}{L} \tag{2.30}$$

TABLE 2.4

Coefficient of Linear Thermal Expansion of Some Common Materials

Material	Coefficient of Linear Thermal Expansion × 10^{-6} (at 20°C) (mm/mm-°C)
Aluminum	23
Aluminum nitride	5.3
Brass	19
Carbon steel	10.8
Copper	17
Gold	14
Iron	11.8
Nickel	13
Stainless steel	17.3
Steel	11–13

The coefficients of linear thermal expansion for some common materials are listed in Table 2.4.

Similarly, the area and volume thermal expansion coefficients are defined as follows:

$$\alpha_A = \frac{1}{A}\left(\frac{\partial A}{\partial T}\right)_{p_o} \tag{2.31}$$

$$\alpha_V = \frac{1}{V}\left(\frac{\partial V}{\partial T}\right)_{p_o} \tag{2.32}$$

In shrink fit applications, the ID of a rotor core is slightly smaller than the OD of a shaft. In an assemble process, to achieve a shrink fit joint between the two components, either the rotor core or the shaft (or both) must be treated. This can be done by either heating the core to increase the internal diameter or cooling the shaft to reduce the external diameter. Thus, according to the fitting conditions, shrink fit techniques can be categorized into three groups: (1) heating technique, (2) cooling technique, and (3) mixing technique, which is the combination of (1) and (2).

Most motor manufacturers utilize heating techniques in rotor shrink fits, that is, heating rotor cores to a certain temperature and maintaining shafts at room temperature. With the desired expansion and shrinkage, the rise in temperature can be determined. For example, if the shaft OD is 31.75 mm and the rotor core ID is 31.70 mm. This gives the diametrical interference fit of 0.05 mm. Thus, by adding the minimum desired slip fit clearance of 0.07 mm (≈ 0.003 in.), the total differential expansion is 0.12 mm. The temperature rise ΔT required on the rotor core to give 0.12 mm expansion in the diameter is calculated as

$$\Delta T = \frac{0.12/31.70}{10.8\times10^{-6}} = 350.5°\text{C}$$

Therefore, the total temperature would be 350.5°C plus the ambient temperature.

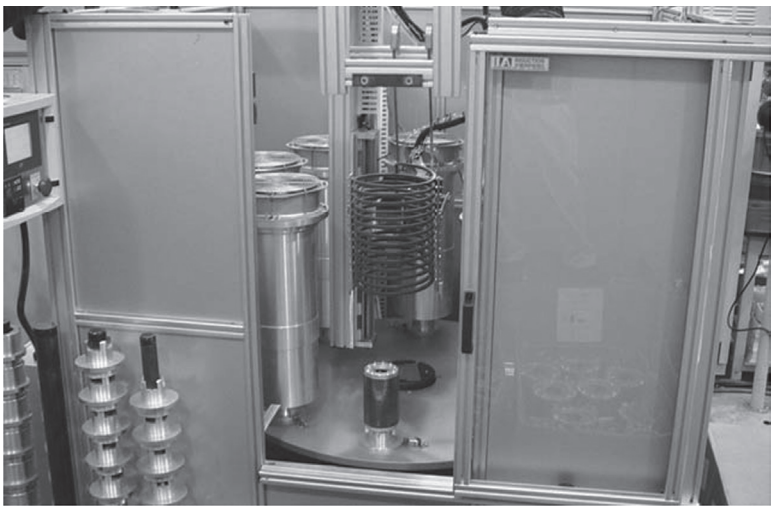

(a)

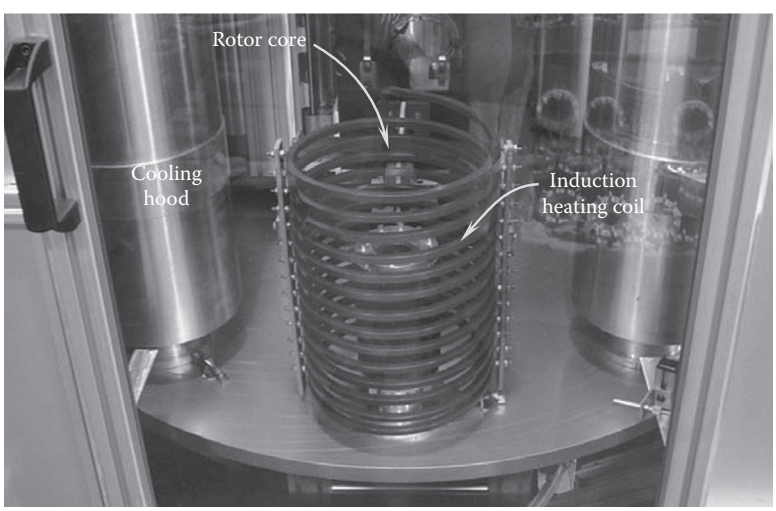

(b)

FIGURE 2.37
Inducting heating process for rotor core prior to shaft insertion: (a) loading and inducting heating coil on the rotor core and (b) heating the rotor core.

Induction heating is a noncontact process of providing fast, consistent, and controllable heating for bonding, hardening, or softening metals or other electrically conductive materials. The process relies on induced electric currents within metallic components for heating themselves. By using this technique, shrink fit can be achieved by heating rotor cores to preset temperatures while maintaining shafts at room temperature. As demonstrated in Figure 2.37, a rotor core is placed in an induction heating equipment. As the induction heating coil is placed around the rotor core, it requires only a few seconds to achieve the desired temperature of the rotor core. The power supply to the heating coil is controlled and monitored with the front panel LCD and sealed touchpad.

As a rotor core is heated up, its internal diameter increases, allowing a shaft to insert into position. Then, as the rotor core is cool down, it shrinks back to its original size and holds the shaft tightly. By contrast, in a cooling technique, shrink fit is achieved by chilling shafts with a suitable median, such as liquid nitrogen or dry ice. An alternative way is to place shafts into a freezer. During the time, the rotor core remains at the room temperature. In such a way, the shaft shrinks to allow it to pass through the rotor core bore. When the shaft restores to the room temperature, it expands to its original size to gain a tight fit with the rotor core. One of the advantages of the cooling technique is that it causes little distortions on effected parts.

In some applications, it is preferred to cool down shafts rather than to heat up rotor cores. This is because high temperature may cause the damage of the rotor winding insulation (as in IMs) or irreversible demagnetization of magnets (as in PMMs). In addition, since a shaft has a relatively low weight compared with that of a rotor core, it is easier to deal with the shaft than the rotor core. During the cooling shrink fit process, the shaft is usually cooled via exposure to a cryogen, typically solid carbon dioxide (–78.5°C at normal atmospheric pressure), liquid carbon dioxide (–56.6°C at 518 kPa), or liquid nitrogen (–195.8°C at normal atmospheric pressure) in order to reduce its size through the contraction.

In comparison with heating, the cooling process cannot achieve as much change in diameter. Thus, for some special fitting applications, both the heating and cooling technique are used to provide the desired fitting strength.

The mechanical design of shrink fit set is based on either the classical Lamé elastic solution of a thick-walled cylinder or the elastoplastic solution that is based on the yield criterion of von Mises. Various analytical, experimental, and numerical studies have been performed by many investigators. Horger and Nelson [2.52,2.53] discussed the detail design of shrink fit assemblies based on linear elasticity solutions. An analysis of the shrink fit in the context of nonlinear elasticity was presented by Antman and Shvartsman [2.54]. Using the von Mises yield criterion and the Hencky deformation theory, Lundberg [2.55] presented the first elastoplastic solution for the shrink fit problem. Late, based on the work of Lundberg, Gao and Atluri [2.56] proposed an analytical solution for the axisymmetric shrink fit problem with a thin strain-hardening hub and an elastic solid shaft.

The difference between shrink fit and press fit is in method of assembly: press fit applies an axial force during the assembling process at room temperature, and shrink fit takes advantage of thermal expansion or shrinkage of the materials. In some cases, shrink fit is the only way to join parts that have low mechanical strengths.

2.4.3 Serration Fit

Serration fit is referred to a special press fit technique under partial interference conditions. In serration fit, a number of serrations are made symmetrically on the outer circumference of a shaft at the room temperature to form local deformations on the shaft (Figure 2.38). Due to the hardening effect of cold forging, the local strength near the serrations can increase 15%–30% of the material strength. When the shaft is pressed into a rotor core, the interference occurs at the vicinity of each serrated groove on the shaft. During the fitting process, the serrations are deformed to generate a contact pressure at the small areas near deformed serrated grooves. Unlike in press fit and shrink fit, the requirements for surface finish and dimension tolerance of mating components can be significantly reduced because of the limited contact area in serration fit.

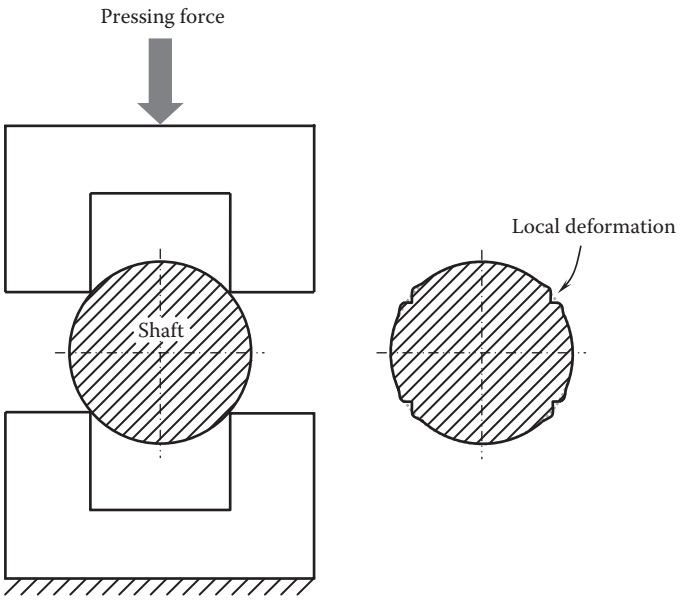

FIGURE 2.38
Fabrication of serrations on a shaft.

In the motor industry, the serration fit technique is adopted in rotor assemblies for relative low torque applications. Figure 2.39 demonstrates the V-shaped serrated grooves disposed in the axial direction on the outer surfaces of the shafts.

2.4.4 Fitting with Adjustable Ringfeder® Locking Devices

Ringfeder locking devices generate easily adjustable and releasable mechanical fits. As shown in Figure 2.40, these locking devices feature either a single- or double-tapped thrust rings with self-releasing tapers. Thus, they can bridge relatively large fit clearances between shafts and rotor cores. Because of their advantages over other interference fitting methods, they have been successfully used in various industries for more than a half century.

2.4.5 Fitting with Tolerance Rings

Tolerance ring is a precision-engineered device usually made from a thin strip of spring steel or stainless steel. The application of tolerance rings can provide robust fitting joints in rotor assemblies. Wave pitches pressed on tolerance rings are used to provide the radial contact pressure between mating components. When the tolerance ring is assembled between mating parts, the wave pitches are compressed and elastically deflected, resulting a large contact pressure between the mating parts for tightly holding them together. In motor manufacturing, a tolerance ring presented in Figure 2.41 can be used for assemblies of shafts and rotor cores and bearings. The wave pitch of the tolerance ring is carefully designed so that the desired spring rate can be achieved.

Tolerance rings work on the two physics principles of spring and friction. The corrugations on a tolerance ring act like stiff radial spring. Like regular springs, the

FIGURE 2.39
Serrations on motor shafts.

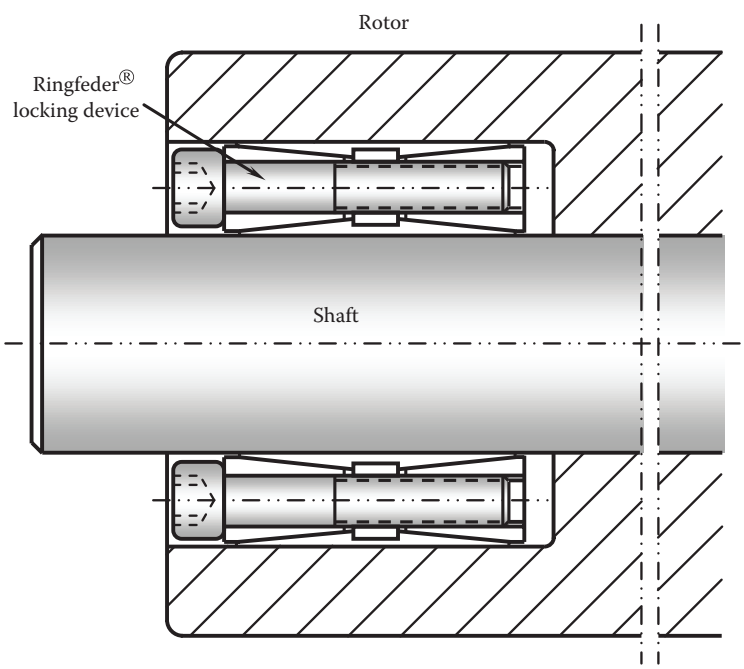

FIGURE 2.40
Keyless connection between shaft and rotor/hub using Ringfeder® locking device.

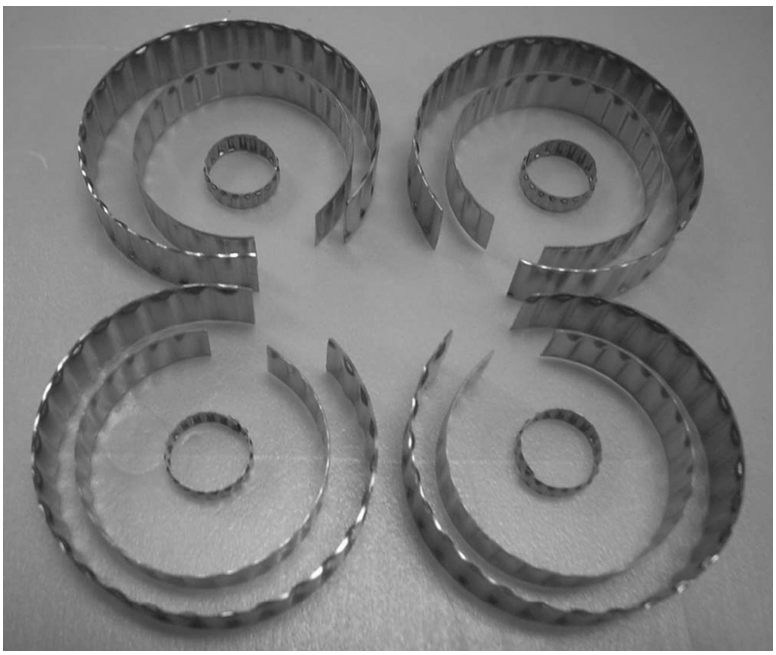

FIGURE 2.41
Using tolerance rings between mating parts such as shaft and rotor core.

relationship between the spring force F_s applied on the tolerance ring and the deflection of the ring is given as

$$F_s = -kx \tag{2.33}$$

This minus sign means that the spring force F_s is always in the opposite direction of the displacement x. In fact, the compressive force acting on the tolerance ring always flattens the corrugations.

The friction force of tolerance springs is determined as

$$F_f = \mu N \tag{2.34}$$

where

μ is the coefficient of static friction
N is the normal force on the contacting surfaces

This force is important for holding the mating parts together firmly without sliding on each other. While motor torque capacities are related to the amount of interference and coefficient of static friction, motor radial load capacities relay on yield limit of the material, the preload, and the cumulative compression of the corrugations caused by interference fit.

Tolerance rings provide many design advantages over other conventional fitting methods. They are used with great success in compensating for different thermal expansion of mating parts. As shown in Figure 2.42, without using tolerance rings, the pressing force between mating parts reduces sharply as the temperature goes higher due to the

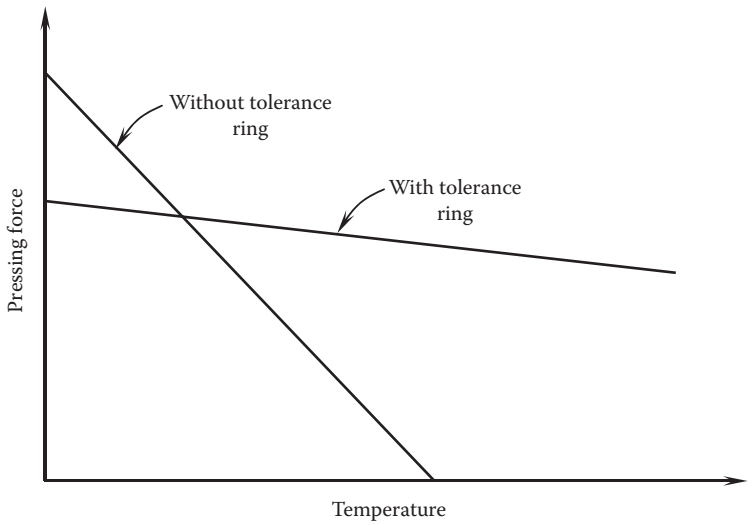

FIGURE 2.42
Comparison pressing forces at different temperatures with and without tolerance rings.

thermal expansion of the mating parts. In contrast, with the tolerance rings, the pressing force only reduces slightly with the temperature increase. For instance, for a 50.8 mm (2 in.) diameter ball bearing on an aluminum housing, the installation pressing force is 2224 N (500 lb_f) at room temperature. The bearing becomes loose at a temperature of 77°C (170°F) as the result of the higher thermal expansion of the aluminum housing than that of the steel bearing. With the tolerance ring, an initial installation pressing force is only (320 lb_f), and retention still remains high at 1023 N (230 lb_f) even at the temperature of 132°C (270°F).

Because tolerance rings allow for a broad range of tolerance, this permits the use of loosen tolerances for the mating parts (e.g., shaft and rotor core). As a result, the requirements for the surface finish on the mating parts are obviously reduced. Another advantage is that the use of tolerance rings can reduce the vibration of the system and lower the noise emission from the system. Finally, the use of tolerance ring can significantly simplify the assembly and disassembly processes.

However, the transmitted torque through the tolerance ring fitting is not as high as those through press fitting and shrink fitting, indicating that the application of tolerance rings is limited to small-rating motors.

2.5 Stress Analysis of Rotor

One of the most important parameters in the rotor design is the length-to-diameter aspect ratio (i.e., *L/D* ratio). A rotor with a low aspect ratio has high rotor stiffness and thus has a high critical speed. The determination of *L/D* ratio is based on factors such as motor torque, spin stresses, rotor dynamic characteristics, and heat loads. Small *L/D* ratios mean high tangential speed and high centrifugal forces at the rotor surface. However, a rotor with a large diameter and a small *L/D* ratio may have large windage losses, especially for

high-speed motors. Normal *L/D* ratio ranges 0.5–1.0 for wound rotor motors and 1–3 for PM motors [2.57]. The tangential speed on the rotor surface u_t is calculated as

$$u_t = r\omega = \frac{d\omega}{2} \tag{2.35}$$

To restrict the centrifugal force of a rotor, the upper limit of the rotor tangential speed is set in the range of 100–250 m/s, depending on motor applications.

During rotor rotation, centrifugal forces are produced in the rotor and in turn generate stresses in the circumferential and radial directions. In general, hoop tensile stresses are dominant and play a decisive role in the selection of rotor material. The stress resulted from centrifugal loading is governed by the radial equilibrium equation in the cylindrical coordination system [2.58]:

$$\frac{d\sigma_r}{dr} + \frac{1}{r}(\sigma_r - \sigma_\theta) + \rho\omega^2 r = 0 \tag{2.36}$$

where

σ_r and σ_θ are the radial and circumferential stresses, respectively
ρ is the density
ω is the rotational angular speed

Thus, a linear relationship between stress vector $\boldsymbol{\sigma}$ and strain vector $\boldsymbol{\varepsilon}$ can be written as

$$\boldsymbol{\sigma} = \mathbf{k}(\boldsymbol{\varepsilon} - \boldsymbol{\alpha}\Delta T) \tag{2.37}$$

where

$\mathbf{k}$ is the stiffness matrix
$\boldsymbol{\alpha}$ is the vector of thermal expansion coefficient
ΔT is the temperature difference

The previous equation can be expressed in the matrix form as

$$\begin{Bmatrix} \sigma_\theta \\ \sigma_z \\ \sigma_r \end{Bmatrix} = \begin{bmatrix} k_{11} & k_{12} & k_{13} \\ k_{21} & k_{22} & k_{23} \\ k_{31} & k_{32} & k_{33} \end{bmatrix} \begin{Bmatrix} \varepsilon_\theta \\ \varepsilon_z \\ \varepsilon_r \end{Bmatrix} - \begin{bmatrix} \alpha_\theta \\ \alpha_z \\ \alpha_r \end{bmatrix} \Delta T \tag{2.38}$$

By ignoring the quadratic terms of the deformation, the strains in circumferential and radial directions can be lineally related to the radial displacement u_r; the strain in the axial direction (z) is assumed to linearly vary along the radial direction:

$$\begin{cases} \varepsilon_\theta = \dfrac{u_r}{r} \\ \varepsilon_r = \dfrac{\partial u_r}{\partial r} \\ \varepsilon_z = \varepsilon_o + \varepsilon_1 r \end{cases} \tag{2.39}$$

Substituting Equations 2.38 and 2.39 into 2.36, the governing equation for radial displacement u_r is obtained. A closed-form solution is derived in detail by Ha et al. [2.59].

2.6 Rotordynamic Analysis

Rotordynamics is a specialized branch of applied mechanics concerned with the behavior and stability of rotating machinery. It plays an important role in improving the safety and reliability of electric motors. To design a robust motor, it is necessary to perform both steady-state and transient lateral and torsional calculations.

With the fast development of advanced computing techniques in recent decades, there are many software packages that are capable of solving the rotordynamic system of equations. Each software package has its specific capabilities and applications. Today, because of the complexity of the modern rotating machinery, rotordynamic software packages have been extensively used to analyze the behavior of structures ranging from gas and steam turbines to auto engines.

Rotordynamic results strongly rely on many factors such as motor structure, bearing type, rotor inertia, rotating speed, mass distribution in rotating system, motor component materials, and motor mounting pattern. As illustrated in Figure 2.43, a motor is fixed on the frame of a machine via the drive-side endbell of the motor. In order to perform rotordynamic analysis of the rotor, the stiffness and damping of the bearings, endbells, and the motor housing must be determined prior to the analysis. The rotordynamic model is shown in Figure 2.44, where S_{br1} and S_{br2} and c_{br1} and c_{br2} are the stiffness and damping of the bearings 1 and 2; S_{ed1} and S_{ed2} are the stiffness of the endbells 1 and 2, respectively; and S_h is the housing stiffness. The bearing stiffness and damping are functions of the rotor rotating speed ω. The support properties of the endbells and housing may be also speed dependent.

2.6.1 Rotor Inertia

In high-speed or large-scale motors, the rotor inertias can be considerably large. The total inertia of the motor rotating system can be obtained by summing the component

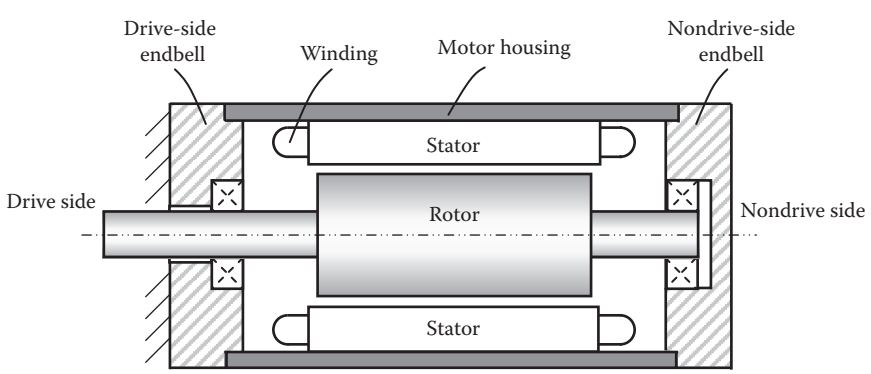

FIGURE 2.43
A motor is mounted to the driven machine via drive-side endbell.

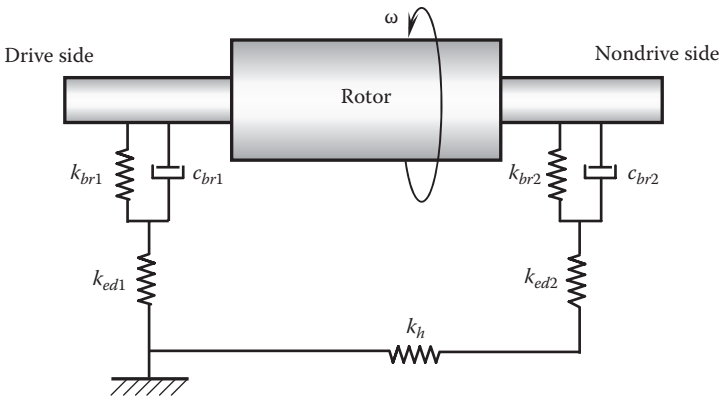

FIGURE 2.44
Rotordynamics model for a motor mounted at one end.

inertias together, such as the rotor core inertia, shaft inertia, and bearing rotating component inertia:

$$J_r = J_{core} + J_{shaft} + J_{bearing} \tag{2.40}$$

The formulas for determining the inertia and spring constant of rotating bodies with various shapes are given in Figure 2.5. The bearing inertia consists of two components: the inertias of the inner raceway and rolling elements

$$J_{bearing} = J_{ir} + NJ_{rolling} \tag{2.41}$$

where N is the number of rolling elements. The inertia of the inner ring is

$$J_{ir} = \frac{\pi l \rho (d_{ir,o}^4 - d_{ir,i}^4)}{32} \tag{2.42}$$

where $d_{ir,o}$ and $d_{ir,i}$ are the outer and inner diameters of the bearing inner ring, respectively (Figure 2.45). For a rolling bearing, the inertia of each rolling element with respect to the bearing centerline is

$$J_{roll} = m\left[K\left(\frac{d_{roll}}{2}\right)^2 + l^2\right] \tag{2.43}$$

where

m and d_{roll} are the mass and diameter of the rolling element, respectively
l is the distance from the center of the rolling element to the bearing centerline
K is the geometric constant of the rolling element, where $K = 2/5$ for sphere bolls and $K = 1/2$ for rollers

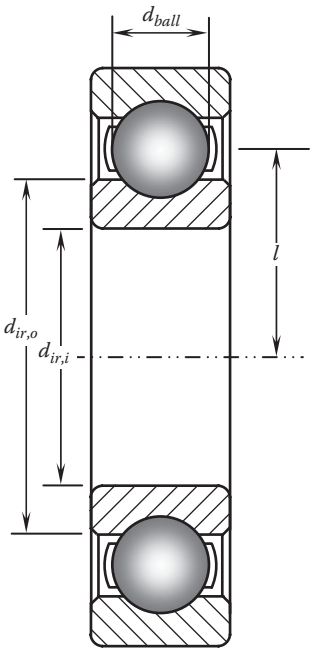

FIGURE 2.45
Calculation of inertia of rolling bearing with respect to the bearing centerline.

2.6.2 Motor Critical Speed and Resonance

A rotor assembly consists of a rotor core and a shaft, fitted together tightly. The rotor critical speed refers to the speed at which a system resonance is excited. In such a case, the centrifugal force associated with even a small mass unbalance can cause a vibration of high amplitude. In worse cases, it may lead to a disintegration of a motor within a few seconds.

For some small lightweight motors with low rotating speeds, the operation speed is far below the critical speed. Therefore, the verification of critical speed for this type of motor may be unnecessary. Some motors are designed to operate at a rotational speed above the critical speed. It can work well if the motors accelerate quickly through the critical speed before the vibration buildup to an excessive amplitude.

Every rotating machine has its own natural frequency at which all attached components and the machine structure self-vibrate, known as resonance. Theoretically, natural frequency is directly proportional to the stiffness and inversely proportional to the mass of the machine. The accurate calculation of critical speed and natural vibration frequency is quite complex if all factors are taken into account. In practice, there are two methods used to predict critical speed and natural frequency: Rayleigh-Ritz and Dunkerley methods. Both Rayleigh-Ritz and Dunkerley methods are an approximation to the first natural frequency of vibration. Generally, the Rayleigh-Ritz equation overestimates and the Dunkerley equation underestimates the natural frequency. Good practice suggests that the maximum operation speed should not exceed 75% of the critical speed [2.60].

Both resonance and critical speeds are frequencies that are governed by natural frequencies, damping, and vibration forces. A resonance is a condition in a structure in which the

frequency of the vibrating force is equal to the natural frequency of the system. For the rotation-excited vibration, the resonance is defined as the critical speed.

During operation, a motor is subject to a variety of forces, including mechanical and electromagnetic forces. Though the calculation of all motor forces is considerably complex, some factors can be identified as follows:

- When a rotor is spinning, any unbalance on the rotor causes a large centrifugal force deflection.
- Because of finite number of stator and rotor slots (or magnets in a PM motor), it generates the unbalanced magnetic force.
- Force due to the torque is transmitted to the load.

Regularly, torsional critical speed is less of a problem in motors but can be significant for large *L/D* ratio motors.

Considering a rotor assembly in a motor as presented in Figure 2.46a, the rotor is positioned at the center of the system, supported by two roller bearings at the each end of the rotor shaft. This physical model can be converted into a rotordynamic model, as shown in Figure 2.46b.

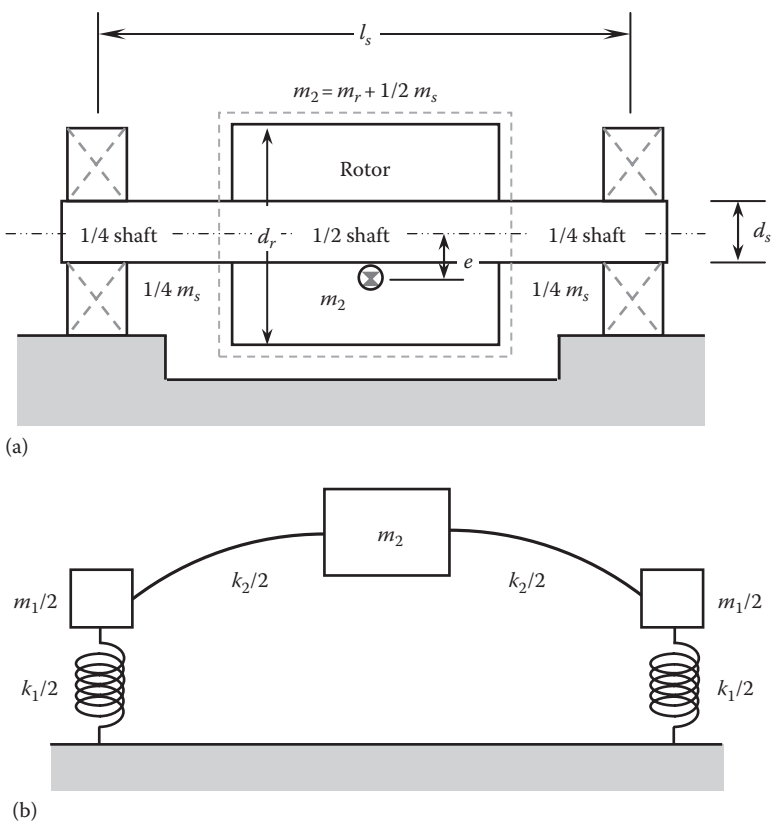

FIGURE 2.46
Rotor models: (a) physical model and (b) rotordynamic analytical model.

The system can be divided into three sections: the middle section, which contains the rotor core and one-half of the shaft, and two end sections, each containing one-quarter of the shaft. In order to perform the rotordynamic analysis, this system can be further simplified to a two-degree-of-freedom model with two masses, m_1 and m_2 [2.61]:

$$m_1 = \frac{1}{2} m_s \tag{2.44}$$

$$m_2 = m_r + \frac{1}{2} m_s \tag{2.45}$$

where m_s and m_r are the shaft and rotor mass, respectively. The exciting force F_u is resulted from the eccentric mass m_2 in the rotor system and is given by

$$F_u = m_2 e\omega^2 \sin(\omega t - \varphi) \tag{2.46}$$

The above system can be simplified as a two-degree-of-freedom rotordynamic model, as shown in Figure 2.47. There are two equations of motion for this system, one for each degree of freedom. These two equations are generally in the form of coupled differential equations:

$$m_1 \frac{d^2 x_1(t)}{dt^2} + (k_1 + k_2)x_1 - k_2 x_2 = 0 \tag{2.47}$$

$$m_2 \frac{d^2 x_2(t)}{dt^2} + k_2 x_2 - k_2 x_1 = (m_2 e\omega^2)\sin(\omega t - \varphi) \tag{2.48}$$

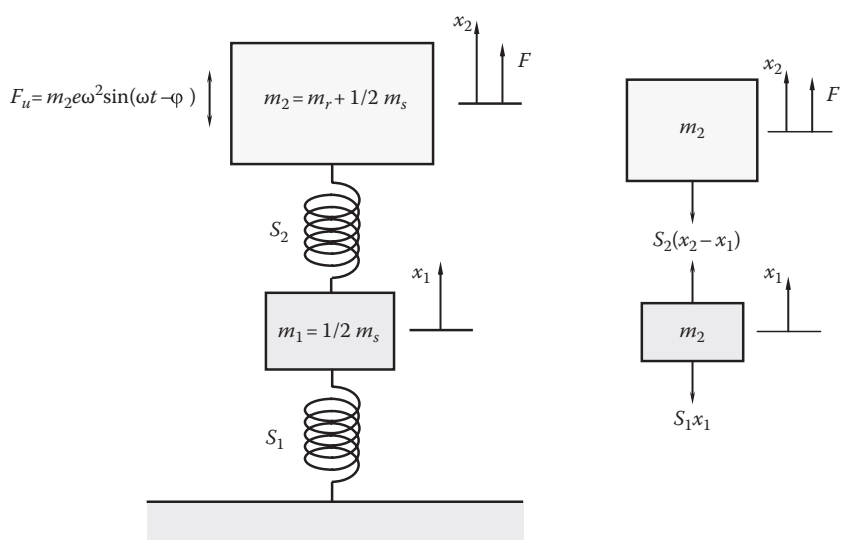

FIGURE 2.47
Reduced two-degree-of-freedom rotordynamic model for rotor assembly, where the exciting force is produced due to the rotor unbalance.

The solutions of the motion equations may take the form

$$x_1(t) = X_1 \sin(\omega t - \varphi) \tag{2.49}$$

$$x_2(t) = X_2 \sin(\omega t - \varphi) \tag{2.50}$$

where
X_1 and X_2 are constants denoting the maximum amplitudes of $x_1(t)$ and $x_2(t)$
φ is the phase angle

Thus, the motion equations become

$$[-m_1\omega^2 + (k_1 + k_2)]X_1 - k_2X_2 = 0 \tag{2.51}$$

$$-k_2X_1 + (-m_2\omega^2 + k_2)X_2 = m_2e\omega^2 \tag{2.52}$$

These two equations can be expressed in a matrix form

$$\begin{bmatrix} (k_1 + k_2) - m_1\omega^2 & -k_2 \\ -k_2 & k_2 - m_2\omega^2 \end{bmatrix} \begin{Bmatrix} X_1 \\ X_2 \end{Bmatrix} = \begin{bmatrix} 0 \\ m_2e\omega^2 \end{bmatrix} \tag{2.53}$$

This can be solved to obtain X_1 and X_2:

$$X_1 = \frac{k_2m_2e\omega^2}{AB - k_2^2} \tag{2.54}$$

$$X_2 = \frac{m_2e\omega^2}{B - \dfrac{k_2^2}{A}} \tag{2.55}$$

where
$A = (k_1 + k_2) - m_1\omega^2$
$B = k_2 - m_2\omega^2$

By setting the determinant of the dynamic stiffness matrix in Equation 2.53 to be equal to zero, the fourth-order frequency equation can be obtained as

$$\omega^4 + \left(-\frac{k_1 + k_2}{m_1} + \frac{k_2}{m_2}\right)\omega^2 + \frac{k_2(k_1 + k_2)}{m_1m_2} = 0 \tag{2.56}$$

This equation can be solved using the quadratic formula,

$$\omega^2 = \frac{-B \pm \sqrt{B^2 - 4C}}{2} \tag{2.57}$$

where

$$B = -\frac{k_1 + k_2}{m_1} + \frac{k_2}{m_2}$$

$$C = \frac{k_2\left(k_1 + k_2\right)}{m_1 m_2}$$

This leads to the two natural frequencies

$$\omega_1 = \left[\frac{-B + \sqrt{B^2 - 4C}}{2}\right]^{1/2} \tag{2.58a}$$

$$\omega_2 = \left[\frac{-B - \sqrt{B^2 - 4C}}{2}\right]^{1/2} \tag{2.58b}$$

2.7 Rotor Burst Containment Analysis

For high-speed motors, a key technical issue is the operation safety of electric motor. This is especially true for some applications such as elevators, roller coasters, and cableways. According to rotordynamics, rotor burst refers to the phenomena that a rotor breaks suddenly at high rotating speeds. When this failure occurs, the motor stator and housing must function as a containment to retain all debris to avoid severe personal injuries or disasters. For this reason, rotor burst containment is a critical design requirement regarding motor safety.

2.7.1 Rotor Burst Speed

The rotor burst speed can be predicted using different approaches. A logical approach is that rotor burst occurs when the hoop stress of a rotor is equal to the ultimate tensile strength of the rotor material. Consider a rotor core assembled with a shaft to form a rotor, with an inner and outer radii r_i and r_o, respectively, and a length l. The rotor is contained inside a stator and a housing (Figure 2.48). A differential element in the rotor has the radial thickness dr and the circumferential length $rd\theta$. The centrifugal force acting on the rotor element due to the rotor rotating is given as

$$dF = (r\omega^2)dm \tag{2.59}$$

where the mass of the element dm is found as the product of the material density ρ and the element volume dV:

$$dm = \rho dV = \rho l(rd\theta)dr \tag{2.60}$$

At an equilibrium condition, all forces acting on the element must be balanced, that is,

$$\sum_i F_i = 0 \tag{2.61}$$

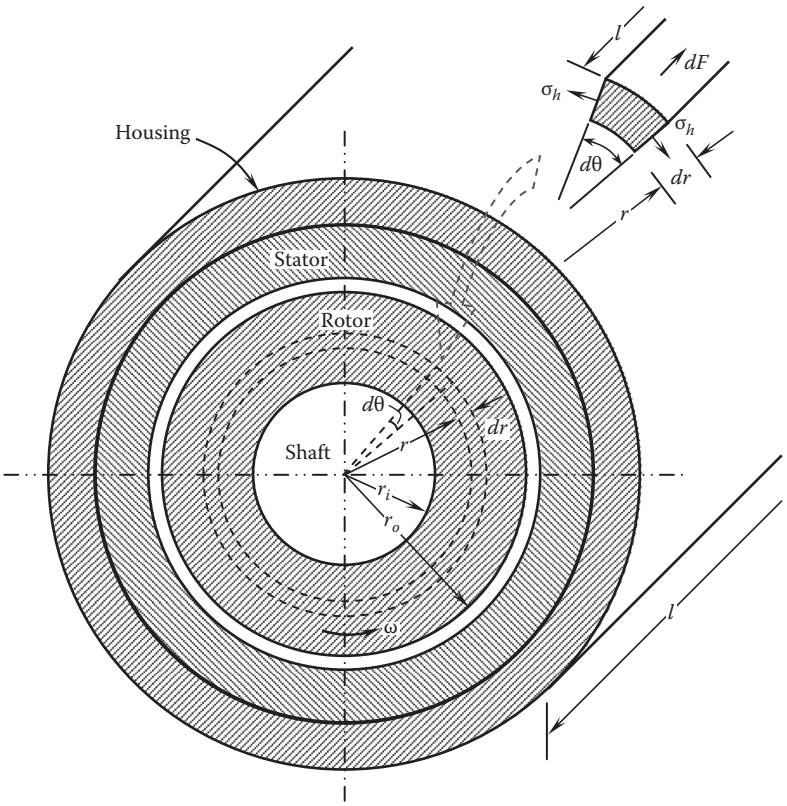

FIGURE 2.48
Rotor is contained inside a stator and a housing that functions as the containment of the rotor.

It follows that

$$dF = 2l(dr)\sigma_h \sin\left(\frac{d\theta}{2}\right) \cong l(dr)\sigma_h\theta \tag{2.62}$$

where σ_h is the hoop stress on the element and $\sin(d\theta/2) \cong d\theta/2$ for small angle of $d\theta$. Thus, the hoop stress σ_h at any radius r becomes

$$\sigma_h = \rho(r\omega)^2 \tag{2.63}$$

This equation indicates that the hoop stress of the rotor is independent of the rotor length l. The maximum hoop stress occurs at the rotor outer surface where $r = r_o$:

$$\sigma_{h,\max} = \rho(r_o\omega)^2 \tag{2.64}$$

The rotor burst speed ω_b is thus determined as $\sigma_{h,\max}$ is equal to or larger than the ultimate tensional strength of the rotor material S_{ut}:

$$\omega_b = \frac{1}{r_o}\sqrt{\frac{S_{ut}}{\rho}} \tag{2.65}$$

This indicates that the rotor burst speed ω_b is both design-dependent (the rotor OD r_o) and material-dependent (square root of the material's ultimate strength-to-density ratio).

2.7.2 Energy in Rotating Rotor

For a rotating rotor, the dominate energy stored in the rotor is the kinetic energy about the center of the rotor mass. In addition, the elastic potential energy is also stored in the rotating rotor because of circumferential tensile stress and elongation during operation.

2.7.2.1 Kinetic Energy in Rotor

The kinetic energy of a rotating rotor is proportional to the product of the polar moment of inertia of the rotor J_p and the square of rotor rotating speed ω, that is,

$$KE = \frac{1}{2} J_p \omega^2 = \frac{1}{2} J_p \left(\frac{\sigma_h}{\rho r^2} \right) \tag{2.66}$$

From this equation, it can be deduced that the kinetic energy of the rotor increases quadratically with the angular velocity ω. Furthermore, Equation 2.66 indicates that the rotor diameter also has a greater influence on kinetic energy. In the previous equation, J_p can be expressed as

$$J_p = \int r^2 dm = \int r^2 \rho dV \tag{2.67}$$

Referring to Table 2.5, the differential volume of the rotor dV is

$$dV = 2\pi r l dr \tag{2.68}$$

Hence, for a hollow cylinder, the polar moment of inertia becomes

$$J_p = 2\pi l \rho \int_{r_i}^{r_o} r^3 dr = \frac{\pi l \rho}{2} \left(r_o^4 - r_i^4 \right) \tag{2.69}$$

The kinetic energy of a rotor at any rotating speed of ω is given as

$$KE = \frac{1}{2} J_p \omega^2 = \frac{\pi l \sigma_h}{4 r_o^2} \left(r_o^4 - r_i^4 \right) \tag{2.70}$$

At the burst rotating speed $\omega = \omega_b$, the hoop stress is equal to the ultimate tensile strength of the rotor material. The kinetic energy of the rotor is

$$KE_b = \frac{1}{2} J_p \omega_b^2 = \frac{\pi l S_{ut}}{4 r_o^2} \left(r_o^4 - r_i^4 \right) \tag{2.71}$$

TABLE 2.5

Polar Moment of Inertia J_p and Torsional Stiffness S_t for Various Types of Shafts

Shaft Type	Shaft Shape	Polar Moment of Inertia J_p (kg-m²)	Torsional Stiffness S_t (Nm/rad)
Solid circular shaft	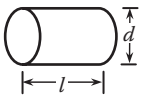	$J_p = \frac{\pi l \rho d^4}{32}$	$S_t = \frac{\pi G d^4}{32l}$
Hollow circular shaft	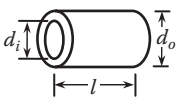	$J_p = \frac{\pi l \rho \left(d_o^4 - d_i^4\right)}{32}$	$S_t = \frac{\pi G \left(d_o^4 - d_i^4\right)}{32l}$
Tapped circular shaft	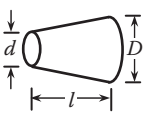	$J_p = \frac{3\pi}{32} \frac{l \rho d^4}{(n + n^2 + n^3)}$ $n = \frac{d}{D}$	$S_t = \frac{3\pi}{32l} \frac{G d^4}{(n + n^2 + n^3)}$ $n = \frac{d}{D}$
Stepped shaft	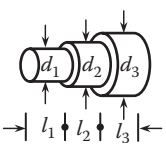	$J_p = \sum_i J_{p,i} = \sum_i \frac{\pi l_i \rho d_i^4}{32}$	$S_t = \frac{1}{\sum_i \frac{1}{S_i}}$

2.7.2.2 Elastic Potential Energy in Rotor

The elastic potential energy in a rotating rotor is given as [2.62]

$$PE = \frac{1}{2} \int_V \sigma_h \varepsilon_h dV \tag{2.72}$$

where ε_h is the hoop strain (circumferential strain) in the rotor and

$$\varepsilon_h = \frac{\sigma_h}{E} = \frac{\rho r^2 \omega^2}{E} \tag{2.73}$$

where E is the Young's modulus. Thus, the elastic potential energy is expressed as

$$PE = \frac{\pi l \rho^2 \omega^4}{6E} \left(r_o^6 - r_i^6\right) \tag{2.74}$$

At the rotor burst speed, the elastic potential energy reaches its maximum value

$$PE_b = \frac{\pi l \rho^2 \omega_b^4}{6E} \left(r_o^6 - r_i^6\right) = \frac{\pi l S_{ut}^2}{6E r_o^4} \left(r_o^6 - r_i^6\right) \tag{2.75}$$

This indicates that the elastic potential energy at the burst speed is dependent on the rotor geometry and material properties but independent of the rotor mass.

2.7.2.3 Ratio of Potential Energy to Kinetic Energy of Rotor

The ratio of the potential energy to the kinetic energy becomes

$$\frac{PE}{KE} = \frac{2}{3}\frac{\rho r_o^2 \omega^2}{E}\left[\frac{1-(r_i/r_o)^6}{1-(r_i/r_o)^4}\right] \tag{2.76}$$

When the rotor fails at the rotor burst speed, this ratio becomes

$$\frac{PE_b}{KE_b} = \frac{2}{3}\frac{S_{ut}}{E}\left[\frac{1-(r_i/r_o)^6}{1-(r_i/r_o)^4}\right] \tag{2.77}$$

As pointed out by Genta [2.63], the kinetic energy is at least one or two orders of magnitude greater that the energy needed to deform the rotor until failure occurs.

2.7.3 Rotor Burst Containment Design

At the rotor burst speed, a rotor splits into fragments that attempt to follow tangential trajectories to strike the internal wall of the stator. When the fragments impact with the stator, it is the kinetic energy of the fragments that get converted into kinetic and strain energy of the stator. Also, part of the energy gets dissipated in the form of heat energy due to the fragments rubbed with the stator inner surface. The released fragments can be contained within the stator if the kinetic energy of the fragments is less than the sum of the shear and strain energy of the stator material. In any cases, stators have to withstand very high-energy impact resulting from broken rotors.

However, the accurate prediction of the containment response is considerably complex due to the following factors: (1) the prediction of the shape and size of rotor debris would be very difficult, if not impossible; (2) there are uncertainties associated with the kinetics of the rotor debris; and (3) the determination of the impact parameters such as the impact area, points, and angle of each fragment relative to the containment wall is extremely difficult. Therefore, in practical containment design, rotor burst tests and FEMs are often used to determine the key design parameters of the containment structure.

Pichot et al. [2.64] have developed the loading models to analyze the containment response following rotor burst. With these models, the radial, axial, and torsional loadings on the containment wall are determined using fundamental energy and momentum principles. In order to overcome the difficulties due to the uncertainties associated with the kinetic energy of the debris, two separate models were developed. The first model is called the debris deflection model, in which the debris is assumed to impact the inside wall of the containment and to be immediately deflected axially without any accumulation on the wall. The second model is called the debris accumulation model, which assumes that all of the fragments pack into a debris bed against the wall without any axial deflection. In fact, these two models represent two extreme cases and thus provide the bounds for the real case. In analyzing the containment response, the debris deflection model tends to produce an impulsive loading that maximizes the magnitude of the axial loading. On the other hand, the debris accumulation model tends to produce longer duration loading and maximizes the torque on the containment.

Hagg and Sankey [2.65] have derived an analytical solution to predict the thickness of the containment shell in the event of turbine disk burst by comparing strain and shear energy with the total energy of disk fragmented missile before impact. Their solution is based on the assumption that the kinetic energy lost by the disk fragments during impact is converted into kinetic energy in the containment shell and energy loss to plastic strain and shear failure in the shell. The minimum perforation energy occurs with the normal force imposed by the translational motion of an impacting fragment.

In the studies of Hagg and Sankey [2.65], the containment process consists of two stage events. The first stage accounts for localized perforation failure where the fragments perforate the containment shell upon initial impact. The equations assume that perforation failure occurs when the energy transfer during impact as measured by the energy loss of the burst fragment exceeds the maximum compression and shear strain energy that the contact zone of the containment shell is capable of absorbing. The maximum compression and shear strain energies in the shell are based on the compressive flow stress, the failure strain, and the shear strengths of the shell material. Assuming that the impact is entirely inelastic and there are no losses to friction or heat, the energy lost during the impact process E_{loss} equals the kinematic energy of the fragment before the impact KE_f minus the residual energy E_{res} [2.66]:

$$E_{loss} = KE_f - E_{res} = \frac{1}{2} m_f v_f^2 \left(1 - \frac{m_f}{m_f + m_c} \right) \tag{2.78}$$

where the kinematic energy of the fragment KE_f is based on the normal velocity of the fragment to the wall of the containment shell v_f and m_f and m_c are the mass of the fragment and the effective mass of the containment shell that responds to the initial contact and momentum transfer, respectively.

The energy required for straining the fragments E_{strain} consists of compressive strain energy in compression E_{comp} and shear strain energy in shearing E_{shear} [2.67]:

$$E_{strain} = E_{comp} + E_{shear} = At\varepsilon\sigma_d + C\tau_d pt^2 \tag{2.79}$$

where

A is the striking area
t is the thickness of the containment shell
ε is the per unit plastic strain
σ_d is the dynamic stress of the containment shell in compression
τ_d is the dynamic shear stress of the containment shell in shearing
p is the perimeter of the sheared area
C is the experimental constant with a value in the range of 0.3–0.5

Hence, the necessary and sufficient condition for straining released fragments is

$$E_{loss} < E_{strain} \tag{2.80}$$

That is,

$$\frac{1}{2} m_f v_f^2 \left(1 - \frac{m_f}{m_f + m_c} \right) < At\varepsilon\sigma_d + C\tau_d pt^2 \tag{2.81}$$

Therefore, the minimum thickness of the containment shell is determined as

$$t_{\min} = \frac{1}{2C}\left(\frac{A}{p}\right)\left(\frac{\varepsilon\sigma_d}{\tau_d}\right)\left[-1+\sqrt{1+\frac{2C\tau_d p}{\left(A\varepsilon\sigma_d\right)^2}\left(m_f v_f^2\right)\left(1-\frac{m_f}{m_f+m_c}\right)}\right] \tag{2.82}$$

This calculated value of $t_{\min}$ is to be compared to the total thickness of the stator and housing. In a case that $t_{\min}$ is larger than the total thickness, either the stator or housing must be redesigned.

If localized perforation failure does not occur, the process moves to the second stage. In this stage, the residual energy is dissipated in the form of tensile strain throughout an extended volume of the shell material. As discussed previously, the residual energy is

$$E_{res} = \frac{1}{2}m_f v_f^2\left(\frac{m_f}{m_f+m_c}\right) \tag{2.83}$$

Failure occurs when the remaining energy exceeds the allowable strain energy in this extended volume.

Alternatively, several turbine manufacturers have presented their models to estimate the minimum thickness of the containment shell. Each of the models may involve different operation conditions and applications. These empirical formulas are listed here for the purpose of reference:

General Electric [2.68]

$$t_{\min} = C_1\sqrt{KE_f} \tag{2.84}$$

Pratt and Whitney [2.69]

$$t_{\min} = C_2\sqrt{\frac{B(KE_f)}{\tau_d p}} \tag{2.85}$$

Snecma [2.70]

$$t_{\min} = \sin(\alpha)\sqrt{\frac{KE_f}{\tau_d p}} \tag{2.86}$$

where

C_1 and C_2 are the empirical constants
KE_f is the translational kinetic energy of the fragment
B is the blade buckling factor
α is the fragment impact angle

It is worth to note that no matter how advanced computational techniques have been developed for predicting the rotor burst, development of a reliable and effective containment system for electric motor eventually requires extensive experimental testing to verify the analytical predictions. This usually requires a large amount of investment to build up a specific testing lab.

References

[2.1] TECO-Westinghouse. 2009. Wound rotor motor technology. http://www.tecowestinghouse.com/PDF/woundrotor.pdf.

[2.2] Lab-Volt Ltd. 2011. Three-phase wound-rotor induction machines: courseware sample. http://www.labvolt.com/downloads/86367_F0.pdf.

[2.3] Boglietti, A., Ferraris, P., Lazzari, M., and Profumo, F. 1997. About the design of very high frequency induction motors for spindle applications. *Electric Machines & Power Systems* **25**(**4**): 387–409.

[2.4] Boglietti, A., Bojoi, R., Cavagnino, A., and Guglielmi, P. 2011. Analysis and modeling of rotor slot enclosure effects in high speed induction motors. *Proceeding of IEEE Energy Conversion Congress and Exposition*, Phoenix, AZ, pp. 154–161.

[2.5] Delaere, K., Belmans, R., and Hameyer, K. 2003. Influence of rotor slot wedges on stator currents and stator vibration spectrum of induction machines: A transient finite-element analysis. *IEEE Transactions on Magnetics* **39**(**3**): 1492–1494.

[2.6] Peters, D. T., Cowie, J. G., and Brush, E. F., Jr. 1999. Die casting copper motor rotors: Mold materials and processing for cost-effective manufacturing. *Proceedings of EEMODS Second International Conference*, London, U.K. http://www.copper.org/applications/electrical/motor-rotor/pdf/eemods_paper.pdf.

[2.7] Daut, I., Gomesh, N., Ezanni, M., Yanawati, Y., Nor Shafiqin, S., Irwan, Y. M., and Irwanto, M. 2011. Modeling of 0.5 HP induction motor using AC analysis solver for rotor copper bar material. *Proceeding of the International Conference on Advanced Science, Engineering and Information Technology 2011*, Bangi, Malaysia, pp. 456–459.

[2.8] Azom.com. 2012. Oxygen free copper—UNS C10100. http://www.azom.com/article.aspx?ArticleID=6314.

[2.9] MatWeb. Aluminum 383.0-F die casting alloy. http://www.matweb.com/search/DataSheet.aspx?MatGUID=2d5590682b514946b8f77c47f2908356&ckck=1.

[2.10] Manoharan, S., Devarajan, N., Deivasahayam, M., and Ranganathan, G. 2010. A comparative analysis of performance characteristics of 2.2 kW 3 phase induction motor using DAR and DCR technology. *International Journal of Computer and Electrical Engineering* **2**(**3**): 1793–8163.

[2.11] Kimmich, R., Doppelbauer, M., Kirtley, J. L., Peters, D. T., Cowie, J. G., and Brush, E. F., Jr. 2005. Performance characteristics of drive motors optimized for die-cast copper cages. *Conference Proceedings of the 4th International Conference on Energy Efficiency in Motor Driven Systems*, Heidelberg, Germany, Vol. I, pp. 110–117.

[2.12] Fassbinder, S. 2007. Saving energy with high-efficiency motors. Briefing paper. http://www.leonardo-energy.org/sites/leonardo-energy/files/root/pdf/2007/HEM.pdf.

[2.13] Czebiniak, D. J. 2013. Die cast rotor with steel end rings to contain aluminum. U.S. Patent 8,368,277.

[2.14] NEMA Standards Publication MG 1-2011. Motors and generators.

[2.15] Atherton, W. A. 1984. *From Compass to Computer: A History of Electrical and Electronics Engineering*. Palgrave Macmillan, London, U.K.

[2.16] Robert, W. H. 1958. Performance of permanent magnets at elevated temperatures. *Journal of Applied Physics* **29**(**3**): 405–407.
[2.17] Kadochnikov, A. I., Ivanov, V. P., and Malyuk, V. P. 1979. Effect of temperature on the characteristics of reference materials for magnetic properties of iron-nickel alloys. *Measurement Techniques* **22**(**5**): 584–586.
[2.18] Wang, A.-M. and Li, H.-M. 2008. Influence of permanent magnet material and temperature on interior permanent magnet machine performance and torque ripple (in Chinese). *Journal of North China Electric Power University* **35**(**3**): 24–32.
[2.19] Magnet Sales & Manufacturing Inc. 1995. High performance permanent magnets. Catalog 7. http://www.magnetsales.com/Info_R2.htm.
[2.20] Gatteschi, D., Sessoli, R., and Villain, J. 2006. *Molecular Nanomagnets*. Oxford University Press, Oxford, U.K.
[2.21] García, S. M. 2008. The nanofabrication and magnetic properties of nanomagnets patterned with thin films. PhD thesis, University of the Basque Country, Basque Country, Spain.
[2.22] Azom.com. 2001. Nanomaterials and their applications. http://www.azom.com/article.aspx?ArticleID=1066.
[2.23] Tabuchi, H. 2010. Japan recycles minerals from used electronics. *New York Times*, October 4, 2010. http://www.nytimes.com/2010/10/05/business/global/05recycle.html?pagewanted=all&_r=0.
[2.24] Tomioka, T. and Monozukuri, N. 2011. Iron nitride powder produced as substitute for rare metal. http://techon.nikkeibp.co.jp/english/NEWS_EN/20110307/190128/.
[2.25] Green Car Congress. 2012. Toshiba develops dysprosium-free samarium-cobalt magnet to replace heat-resistant neodymium magnet in motors. http://www.greencarcongress.com/2012/08/toshiba-20120816.html#more.
[2.26] UQM Technologies. 2012. UQM Technologies makes breakthrough in non-rare-earth electric motor design under DOE development program. http://www.uqm.com/.
[2.27] Ji, N., Liu, X. Q., and Wang, J. P. 2010. Theory of giant saturation magnetization in α″-Fe16N2: Role of partial localization in ferromagnetism of 3d transition metals. *New Journal of Physics* **12**(**2010**): 063032.
[2.28] Brown, R. D. and Cost, J. R. 1989. Radiation-induced changes in magnetic properties of Nd-Fe-B permanent magnets. *IEEE Transaction on Magnetics* **25**(**4**): 3117–3120.
[2.29] Biais, F. J. and Rahman, K. M. 2004. Auxiliary magnetizing winding for interior permanent magnet rotor magnetization. U.S. Patent 6,674,205.
[2.30] Hitachi Metals Corporation. High energy ferrite magnets NMF series—Demagnetization curve (NMF-3C). http://www.hitachi-metals.co.jp/e/products/auto/el/pdf/nmf_a.pdf.
[2.31] Hitachi Metals Corporation. Nd-Fe-B magnet—NEOMAX: demagnetization curve (S54). http://www.hitachi-metals.co.jp/e/products/auto/el/pdf/nmx_a.pdf.
[2.32] Beniakar, M., Kefalas T., and Kadas, A. 2011. Investigation of the impact of the operational temperature on the performance of a surface permanent magnet motor. *Materials Science Forum* **670**: 259–264.
[2.33] Simos, N. and Mokhov, N. 2008. An experimental study of radiation-induced demagnetization of insertion device permanent magnets. *Proceedings of 11th European Particle Accelerator Conference*, Genoa, Italy, pp. 2112–2114.
[2.34] Alderman, J., Job, P. K., Martin, R. C., Simmons, C. M., Owen, G. D., and Puhl, J. 2000. Radiation-induced demagnetization of Nd-Fe-B permanent magnets. U.S. Department of Energy Report LS-290, Washington, DC.
[2.35] Magma Magnetic Technologies. 2010. Permanent magnet stability. http://www.magmamagnets.com/permanent-magnet-stability.
[2.36] Integrated Magnetics. 2013. Magnetics 101. http://www.intemag.com/magnetics_101.html.
[2.37] Degner, M. W., Van Maaren, R., Fahim, A., Novotny, D. W., Lorenz, R. D., and Syverson, C. D. 1996. A rotor lamination design for surface permanent magnet retention at high speeds. *IEEE Transactions on Industry Applications* **32**(**2**): 380–385.

[2.38] UPM Raflatac. 2012. *The Adhesive Book*. UPM Raflatac, Tampere, Finland. http://www.upmraflatac.com/europe/eng/images/51_783.pdf.
[2.39] Gan, J., Chau, K. T., Chan, C. C., and Jiang, J. Z. 2000. A new surface-inset permanent brushless DC motor drive for electric vehicles. *IEEE Transactions on Magnetics* **36**(**5**): 3810–3818.
[2.40] Johnson, R. N., Kliman, G. B., Liao, Y. F., and Soong, W. L. 1998. Rotors with retaining cylinders and reduced harmonic field effect losses. U.S. Patent 5,801,470.
[2.41] Schaefer, E. J. and Antrim, T. K. 1988. Permanent magnet rotor for electric motor. U.S. Patent 4,742,259.
[2.42] Dohogne, L. R. 1990. Dynamoelectric machine rotor assembly with improved magnet retention structure. U.S. Patent 4,973,872.
[2.43] Dobrzanski, L. A., Drak, M., and Trzaska, J. 2005. Corrosion resistance of the polymer matrix hard magnetic composite materials Nd-Fe-B. *Proceedings of 13th International Scientific Conference on Achievements in Mechanical and Materials Engineering*, Gliwice-Wista, Poland.
[2.44] Trout, S. 2004. Optimum corrosion protection of Nd-Fe-B magnets. *Proceedings of Advanced in Magnetic Application, Technology and Materials*, Dayton, OH.
[2.45] AK Steel Corporation. 2007. Selection of electrical steel for magnetic cores. Product data bulletin 7180-0139. http://www.aksteel.com/pdf/markets_products/electrical/Mag_Cores_Data_Bulletin.pdf.
[2.46] Emura, M., Landgraf, F. J. G., Ross, W., and Barreta, J. R. 2003. The influence of cutting technique on the magnetic properties of electrical steels. *Journal of Magnetism and Magnetic Materials*, **254–255(2003)**: 385–360.
[2.47] Wiley, J. B. 1965. Dynamoelectric machine means. U.S. Patent 3,188,505.
[2.48] Rosenquist, S. 2005. Test of the effects of the heat shrink process on shaft run-out and torsional strength of EVS rotor assemblies. Kollmorgen report.
[2.49] International Organization for Standardization. 2003. ISO 1940-1:2003 Mechanical vibration. Balance quality requirements for rotors in a constant (rigid) state.
[2.50] Mobley, R. K. 2004. *Maintenance Fundamentals*, 2nd edn. Elsevier Butterworth-Heinemann, Amsterdam, the Netherlands.
[2.51] Budynas, R. G. and Nisbett, K. J. 2010. *Shigley's Mechanical Engineering Design*, 9th edn. McGraw-Hill, New York.
[2.52] Horger, O. J. and Nelson, C. W. 1937. Design of press- and shrink-fitted assemblies: Part I. *Journal of Applied Mechanics* **4**: A183–A187.
[2.53] Horger, O. J. and Nelson, C. W. 1938. Design of press- and shrink-fitted assemblies: Part II. *Journal of Applied Mechanics* **5**: A32–A32.
[2.54] Antman, S. S. and Shvartsman, M. M. 1995. The shrink-fit problem for aeolotropic nonlinear elastic bodies. *Journal of Elasticity* **37**: 157–166.
[2.55] Lundberg, G. 1944. Die festigkeit von pressitzen. *Das Kugellager* **19**: 1–11.
[2.56] Gao, X.-L. and Atluri, S. N. 1995. An elasto-plastic analytical solution for the shrink-fit problem with a thin strain-hardening hub and an elastic solid shaft. *Mathematics and Mechanics of Solids* **2**: 335–349.
[2.57] Bianchi, N. and Lorenzoni, A. 1996. Permanent magnet generators for wind power industry: An overall comparison with traditional generators. *International Conference on Opportunities and Advances in International Power Generation*, Durham, United Kingdom, Conference Publication No. 419.
[2.58] Lekhniskii, S. G. 1968. *Anisotropic Plates*. Gordon and Breach Science Publishers, New York.
[2.59] Ha, S., Kim, D., and Sung, T. 2001. Optimum design of multi-ring composite flywheel rotor using a modified generalized plane strain assumption. *International Journal of Mechanical Sciences* **43**(**4**): 993–1007.
[2.60] Ameridrives Power Transmission. 2009. Americardan universal joints: 5000 series high torque density. P-1751-APT. http://www.gmbassociates.co.uk/downloads/AmericardanUniversalJoints5000SeriesCatalogue.pdf.

[2.61] Kirk, R. G. and Keesee, J. 1989. Influence of active magnetic bearing sensor location on the calculated critical speeds of turbomachinery. *Proceeding of ASME Design Technical Conferences*, Montreal, Quebec, Canada, DE-Vol. 18-1, pp. 309–316.
[2.62] Kass, M. D., McKeever, J. W., Akeman, M. A., Goranson, P. L., Litherland, P. S., and O'Kain, D. U. 1996. Evaluation of demo of 1C component flywheel rotor burst test and containment design. ORNL/TM-13159. Oak Ridge National Laboratory, Oak Ridge, TN.
[2.63] Genta, G. 2005. *Dynamics of Rotating Systems*. Springer, New York.
[2.64] Pichot, M. A., Kramer, J. M., Thompson, R. C., Hayes, R. J., and Beno, J. H. 1997. *The Flywheel Battery containment Problem*. SAE Technical Paper Series, Warrendale, PA, Book Number: SP-1243, Document Number: 970242.
[2.65] Hagg, A. C. and Sankey, G. O. 1974. The containment of disk burst fragments by cylindrical shells. *ASME Journal for Engineering for Power* **96(2)**: 114–123.
[2.66] Stamper, E. and Hale, S. 2008. The use of LS-DYNA® models to predict containment disk burst fragments. *10th International LS-DYNA®* Users Conference, Dearborn, MI.
[2.67] Jain, R. 2010. Prediction of transient loads and perforation of energy casing during blade-off event of fan rotor assembly. *Proceedings of the IMPLAST 2010 Conference*, Providence, RI.
[2.68] Stotler, C. L. 1981. Development of advanced lightweight systems containment: final report. NASA report no. CR-165212. http://www.dtic.mil/cgi-bin/GetTRDoc?AD=ADA305415.
[2.69] Gunderson, C. O. 1977. Study to improve airframe turbine engine rotor blade containment. U.S. Department of Transportation, Federal Aviation Administration. Report No. FAA-RD-77-44. http://www.tc.faa.gov/its/worldpac/techrpt/rd77-44.pdf.
[2.70] Payen, J. M. 1983. Containment of turbine engine fan blades. *6th International Symposium on Air Breathing Engines*. Symposium papers A83-35801 16-07, Paris, France, pp. 611–616.

3

Shaft Design

A shaft in an electric motor is used to transmit torque and power from the motor to an external loading machine. Because motor shafts are subjected to various combined effects of tension, compression, bending, and torsion during operation, they are typically designed for maximum stiffness and rigidity and minimum deflection to maintain shaft stress/strain below allowable limits under various loading and operating conditions. The achievement of such design objectives relies on the selection of shaft material, determination of suitable shaft dimensions (especially shaft diameter and span between the bearings) and structures, mitigation/elimination of stress concentrations, and other design activities. Obviously, each of these can affect the long-term reliability of motor.

As a rotating component, the motor shaft is subject to a completely reversed bending load that results in an alternating bending stress in the shaft. Furthermore, some motors require to frequently change the direction of rotation or experience frequent starts and stops during operation, causing cyclic torsional stress in motor shafts. Therefore, the prevention of fatigue failure is an important consideration in the shaft design.

A typical shaft of an electric motor is illustrated in Figure 3.1. Typically, the motor shaft is supported by two bearings at its ends and a rotor core mounted on the shaft between the two bearings. Motor shafts usually carry keyed or splined power-transmitting components (e.g., sheaves, pulleys, couplers, and sprockets) on the overhanging end to transmit torque to an externally driven machine. The shaft span is generally designed as short as possible to increase the shaft stiffness and reduce the shaft stress and lateral deflection. In addition, minimizing the shaft overhang is highly desired for lowering shaft bending stress.

The importance of engineering analysis and design of shafts has been widely recognized by engineers and designers. However, most machine design textbooks have mainly focused on shafts with uniform diameters. Such shafts are easy to produce but rare in practice. To help design motor shafts, this chapter emphasizes on the design for stepped motor shafts.

3.1 Shaft Materials

The selection of proper shaft material is critical for ensuring motor normal and safe operation. Depending on different applications, motor shafts can be made of low- to medium-carbon steel, cast iron, stainless steel, aluminum alloys, brass, and bronze. The criteria of the shaft material selection include material mechanical and thermal properties, rigidity, hardness, wear resistance, machinability, noise absorption, manufacturing process, and cost.

By far the most widely used shaft material is carbon steel. The mechanical and thermal properties of carbon steel primarily depend on the amount of carbon it contains. Increasing

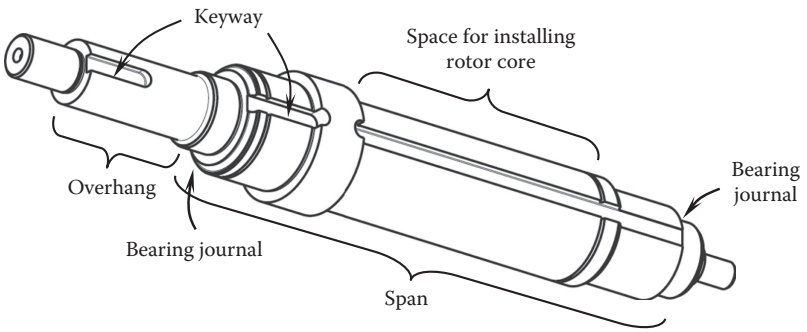

FIGURE 3.1
Structure of a motor shaft.

carbon contents can result in the increase of hardness, yield tensile strength, and ultimate tensile strength. However, higher carbon contents also increased material brittleness and reduced weldability, machinability, and elongation.

According to the content of carbon in steel, carbon steel can be categorized into approximately three types: low-carbon, medium-carbon, and high-carbon steel. Low-carbon steel contains carbon up to 0.25%. Medium-carbon steel has carbon content ranging from 0.25% to 0.70%. High-carbon steel contains carbon in the range of 0.70%–1.50%. Most motor shafts are made of steel containing 0.2%–0.5% carbon. With a single-digit elongation, high-carbon steel is too brittle to be used as shaft material.

To improve the mechanical properties of shafts, such as hardness, yield and ultimate tensile strength, fatigue strength, and other material properties, motor shafts are often heat-treated. Heat treatment processes include spheroidizing, annealing, normalizing, carburizing, quenching, martempering, and austempering. Each process has its own purpose and is applied to certain types of materials.

A spheroidizing process is especially used for high-carbon steel with carbon content more than 0.6%. Spheroidite forms when carbon steel is heated to approximately 700°C for more than 30 h. The purpose of this process is to soften high-carbon steels and allow more formability. An annealing process is often used to relieve residual stresses in the cold-worked steel with the carbon content of 0.3% or above. Fully annealed steel has no residual stresses and becomes ductile. Normalizing helps steel with a fine and more uniform pearlitic structure. Normalized steel still maintains high strength and durability. For low-carbon steel, carburizing can increase the hardness and improve other mechanical properties. During the process, carbon molecules penetrate into the material surface. The affected area and depth of carbon content are dependent on the heating time and temperature. Generally, higher temperatures and longer heating time lead to greater carbon diffusion into steel. The carbon content of quenchable steel must be 0.3% or above. A quenching process can increase yield and ultimate tensile strength, fatigue strength, and hardness but decrease material elongation. Usually, quenched steel is about three or four times harder than normalized steel. However, residual stresses can be introduced during the quenching process in the bulk of the shaft that may cause cracks on the shaft surface. In all heat treatment processes, the heating and cooling rate and temperature holding time are critical parameters to impact the metallographic microstructure of steel.

Either cold-rolled or hot-rolled carbon steel can be used for making motor shafts. Hot-rolled steel is produced at temperatures above the recrystallization temperature of steel.

As a contrast, cold-rolled steel is produced under the recrystallization temperature of steel (more regularly, at the room temperature). The benefits of cold-rolled steel over hot-rolled steel are as follows: (1) The strength of cold-rolled steel can increase by 15%–30% due to the strain-hardening mechanism. (2) Cold-rolled steel has smooth surface finish compared to hot-rolled steel. (3) Cold-rolled steel products have tight dimensional tolerances. However, the cold rolling process can generate residual stresses remaining in the rolled steel. Furthermore, the cost of cold rolling process is usually higher than that of hot rolling.

For some applications that require high material strengths or operate under severe environmental conditions (e.g., low or high temperatures, high humidity, acid and alkali corrosion), motor shafts may be also made of special steel alloys.

Stainless steel can be used as a shaft material when motors work under corrosive environments or for some special applications such as food industry and medical equipment. With a minimum chromium (Cr) content of 10.5%, stainless steel is continuously protected by a passive layer of chromium oxide that forms naturally on the surface through the combination of chromium and moisture in the air. This enhances corrosion resistance of stainless steel. The addition of nickel (Ni) can also raise the corrosion resistance of stainless steel. However, machining stainless steel is more difficult than carbon steel because of heat buildup during the machining process and difficulties in chip breaking. Stainless steel alloy 304 is one of the most widely used stainless steel that contains 18% of chromium, 8% of nickel, and lower carbon (0.08%) to minimize carbide precipitation. This type of stainless steel possesses an excellent combination of strength, corrosion resistance, and fabricability [3.1]. However, because the coefficient of thermal expansion (CTE) of stainless steel is approximately 25%–50% higher than that of carbon steel, high thermal stresses on stainless steel shafts may be developed as the result of temperature rise in motors.

Cast iron is a large family of ferrous alloys in which four types can be categorized: gray cast iron, ductile iron, white iron, and metallurgic iron. Cast iron has been widely used to make crankshafts in internal combustion engines (ICEs). Crankshafts convert the reciprocating motion into rotation by crankpins. One of the main reasons to use cast iron is that it has excellent vibration damping properties to reduce the pulsation influence of the four-stroke cycle. In addition, cast iron exhibits low notch sensitivity, low modulus of elasticity, high thermal conductivity, moderate resistance of thermal shock, and outstanding castability. It is interesting to note that unlike most ferrous materials, shear strength of gray cast iron is much higher than ultimate tensile strength, indicating that gray cast iron can withstand higher shear forces than tensile forces. However, until now, it is still rare to use cast iron as the shaft material in electric motors.

Aluminum is a versatile and corrosion-resistant material. Advanced high-tensile aluminum alloys such as scandium- and titanium-enhanced aluminum alloys have been used to replace steel today in making shafts, vehicle body, and other important components in the automotive industry. Their advantages are ease of fabrication, high strength-to-density ratio, and resistance to the corrosive atmospheres. High-performance race cars utilize extensively lightweight aluminum parts as engineers strive to improve speeds and reduce corrosion under high-temperature and high-stress conditions. For example, high-grade 7075-T6 aluminum alloy may be acceptable as a shaft material in some applications due to its high strength, low weight, and good fatigue strength properties [3.2]. In the motor industry, the use of aluminum shafts is limited to small-size and low-torque motors.

The properties of some typical shaft materials are listed in Table 3.1. The machinability rating is an indicator of how easy or how difficult a material can be mechanically processed based on the reference material AISI 1212 steel as 100% machinability.

TABLE 3.1

Properties of Some Shaft Materials

Material	Yield Tensional Strength (MPa)	Ultimate Tensional Strength (MPa)	Shear Strength (MPa)	Fatigue Strength (MPa)	Elongation (%)	Hardness Brinell (HB)	Machinability Rating (%)	Vibration Damping
AISI 1008 cold rolled	285	340	196	170	20	95	55	OK
AISI 1020 cold rolled	350	420	242	193[a]	15	121	65	OK
AISI 1045 cold rolled, annealed	505	585	338	268[a]	12	170	65	OK
304 SS	241	586	334	241[b]	55	149	45	A little better than steel
Ductile iron 65-45-12	310	448	336	179	12	131–220	160	Good
Gray cast iron 40	—	293	393	128[b]	<1	235	70	Best
A7075-T6	503	572	331	159[c]	11	150	120	Poor

[a] Based on 10^7 cycles.
[b] Based on 10^8 cycles.
[c] Based on 5×10^8 cycles.

3.2 Shaft Loads

Motor shafts are generally subject to combined, variable loads during operation. The motor loads can be categorized into various types:

a. Because a shaft transmits torque from a motor to an externally driven machine, the shaft is subject to the torsional load. Hence, the shaft must have adequate torsional strength to withstand the load.
b. Transverse loads are most significant in various motor applications. As a shaft is subject to transverse loads, it undergoes bending or flexural deformations and possibly shearing at the joints of the shaft and the rotor core. There are several types of transverse forces acting on the shaft: (1) The gravitational force acting on the mass of the rotor assembly (the rotor core, shaft, and other components) is perpendicular to the shaft axis for a horizontally installed motor and (2) the shaft usually carries power-transmitting components such as sheaves, gears, pulleys, and chain sprockets, exerting forces at the end of the shaft in the transverse direction. (3) For a nonuniform air gap between a stator and a rotor, the unbalanced magnetic pull may develop and act on the rotor and shaft. As the shaft rotates, all these transverse forces cause reverse bending moments on the shaft. Thus, it is required to perform fatigue analysis to avoid fatigue failures.
c. A motor shaft is usually subject to low axial loading compared to its transverse loads. However, for some applications such as high-speed PCB drilling machines that experience high acceleration and deceleration in a very short time period in the motor axial direction, the axial load on the shaft can become considerably high. Furthermore, buckling analysis may be required for assessing rotor stability.
d. The coupling between a motor and a driven machine can be achieved by using flanges, splines, belts, chains, and other flexible or rigid coupling devices. For using belts or chairs, a bending moment is applied on the overhanging portion of the shaft.
e. One of the major concerns during motor design is the motor's resonant behavior. As a motor starts up, the motor shaft is subject to a shearing force. Mechanical resonance occurs as an external source amplifies the vibration level of a motor at its natural frequency. The increase in amplitude of vibration level leads to high shear stress on motor shaft and other components.
f. The preload acts on a shaft due to interference fitting of rotor core, bearing, and other mechanical components.
g. A motor may encounter shock loads at normal operation. Shock loads can be created when motors experience interrupted motions in rapid sequence, such as repeated sudden start and stop, high acceleration and deceleration, forward–reverse, and indexing motions. In addition, with high rotating speeds, electric motors act like flywheels. Typically, they represent approximately 80%–90% of the total kinetic energy in the drive systems. This flywheel effect can produce inertia shock loads far above the rated torque when the driven equipment is abruptly stopped [3.3].

If shock loads cannot be completely avoided, the motor components must be designed by taking into account an additional factor of safety (shock factors).

Earthquakes can always cause shock loads on motors. For the safe operation of the motor, this scenario must be carefully considered at the motor design stage. This is extremely important for some types of motors, such as elevator motors.

3.3 Shaft Design Methods

There are several methods available in design of motor shafts; each of them has its specific scope of application and advantages/disadvantages when compared with others.

3.3.1 Macaulay's Method

This method is relatively simple to deal with the stiffness, radius of curvature, deflection, and bending moments in a beam. The method enables discontinuous bending moment functions to be represented by a continuous function. It allows the contributions, from individual loads to the bending moment at any cross section to be expressed as a single function, which takes zero value at those sections where particular loads don't contribute to the bending moment [3.4].

As shown in Figure 3.2, when a beam is subject to a uniform load along its length, the bending moment M (in unit of N-m) is given by

$$M = \frac{EI_a}{R} \tag{3.1}$$

where

E is Young's modulus of elasticity (in unit of Pa)
I_a is the second moment of area (in unit of m^4)
R is the radius of curvature (in unit of m)

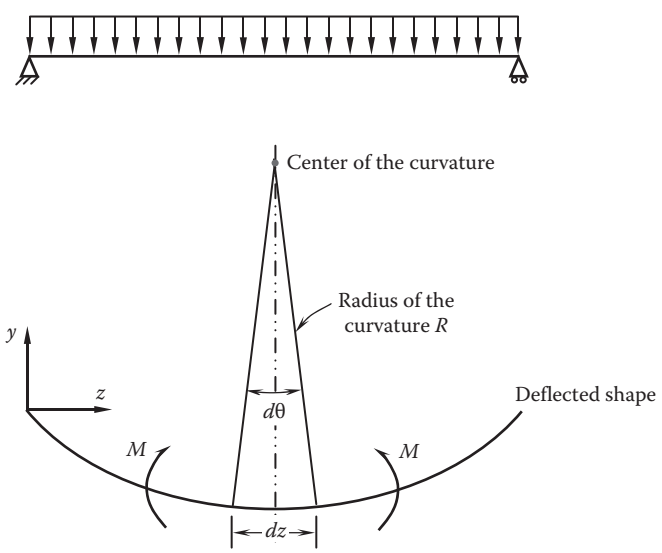

FIGURE 3.2
Beam deflection under uniformly distributed load.

In some textbooks, EI_a is defined as the beam flexural rigidity.

The curvature $1/R$ equals the reciprocal of the radius and is expressed as the second derivative with respect to the beam deflection y, that is,

$$\frac{1}{R} = \frac{d^2y}{dz^2} \tag{3.2}$$

It gives that

$$EI_a \frac{d^2y}{dz^2} = M \tag{3.3}$$

Hence, the differential equation of an elastic curve may be given as

$$\frac{d^2y}{dz^2} = \frac{M}{EI_a} \tag{3.4}$$

Macaulay's method enables discontinuous bending moment functions to be represented by a continuous function, thus avoiding the need to deal with the beam section by section between discontinuities in the bending moment function. This is very desirable since it avoids the need to evaluate, and therefore eliminate, a large number of constants of integration.

3.3.2 Area–Moment Method

The area–moment method is commonly used to determine the deflection and slope of a shaft based on two theorems: the first is used to find rotations and the second is used to find displacements. It is effective for calculating the deflections of shafts with various cross sections.

In Figure 3.3, consider a section of an elastic curve between points A and B. Both the slope and M/EI_a change along the elastic curve from A to B. Thus, integrating both sides of Macaulay's equation with respect to dz yields

$$\int_A^B \frac{M}{EI_a} dz = \int_A^B \frac{d^2y}{dz^2} dz = \left[\frac{dy}{dz}\right]_A^B = \theta_B - \theta_A \tag{3.5}$$

This indicates that the difference in slope between the points A and B on a beam is equal to the area of the M/EI_a diagram between these two points.

Multiplying both sides of Macaulay's equation by zdz and integrating from A to B, it gives that

$$\begin{aligned}\int_A^B \frac{M}{EI_a} z dz &= \int_A^B \frac{d^2y}{dz^2} z dz = \int_A^B \left[\frac{d}{dz}\left(z\frac{dy}{dz}\right) - \frac{dy}{dz}\right] dz = \left[z\frac{dy}{dz}\right]_A^B - \left[y\right]_A^B \\ &= z_B\left(\frac{dy}{dz}\right)_B - z_A\left(\frac{dy}{dz}\right)_A - y_B + y_A\end{aligned} \tag{3.6}$$

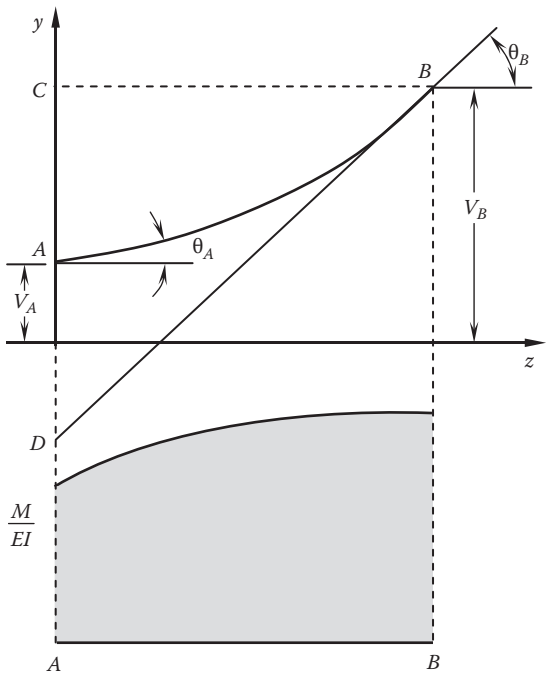

FIGURE 3.3
The changes in the slope and M/EI along the elastic curve between points A and B.

If the origin is shifted below the point A (i.e., $z_A = 0$), the second term in the previous equation vanishes, giving that

$$\int_A^B \frac{M}{EI_a} z dz = z_B \theta_B - y_B + y_A \tag{3.7}$$

where $z_B\theta_B$ is represented by the distance CD in Figure 3.3. This indicates that the moment about a point A of the M/EI_a diagram between points A and B provides the deflection of point A relative to the tangent at point B.

3.3.3 Castigliano's Method

Castigliano's method is widely used to determine displacements of linear-elastic systems based on strain energy of the systems. When such a system is subject to external loads, the deflection δ_i at any loading point in a direction of any external load Q_i can be determined by taking the partial derivative of the total strain energy U stored in the system with respect to the applied load Q_i in that direction, that is,

$$\delta_i = \frac{\partial U}{\partial Q_i} \tag{3.8}$$

If the displacement is in the same direction of the force, the displacement is positive.

The general energy and deflection equations corresponding to different load types are listed in Table 3.2, where F, M, and T are the force, bending moment, and torque acting on

TABLE 3.2

General Deflection Equations Using Castigliano's Method

Load Type	General Energy Equation	General Deflection Equation
Axial force	$U = \int_0^l \frac{F^2}{2EA}\,dx$	$\delta = \int_0^l \frac{F}{EA}\left(\frac{\partial F}{\partial Q}\right)dx$
Bending moment	$U = \int_0^l \frac{M^2}{2EI_a}\,dx$	$\delta = \int_0^l \frac{M}{EI_a}\left(\frac{\partial M}{\partial Q}\right)dx$
Torsional moment	$U = \int_0^l \frac{T^2}{2GJ}\,dx$	$\delta = \int_0^l \frac{T}{GJ}\left(\frac{\partial T}{\partial Q}\right)dx$
Transverse shear	$U = \int_0^l \frac{f_s V^2}{2GA}\,dx$	$\delta = \int_0^l \frac{f_s V}{GA}\left(\frac{\partial V}{\partial Q}\right)dx$

the shaft, respectively, E is the modulus of elasticity of the shaft material, A is the cross-sectional area of the shaft, I_a is the second moment of area, G is the shear modulus of elasticity, J is the second polar moment of area (sometimes improperly referred to as the *polar moment of inertia*), and f_s is the form factor for shear:

$$f_s(x) = \frac{A(x)}{I_a^2(x)} \int_A \frac{Q^2(x,y)}{t^2(y)}\,dA \tag{3.9}$$

The form factor is a dimensionless quantity that depends only on the shape of the cross section of shaft. In most cases, f_s is constant. For a circular shaft, $f_s = 10/9$.

3.3.4 Graphical Method

The graphical method has been primarily used in earlier time when computational techniques have not been fully developed [3.5]. With this method, design engineers graphically analyze shaft stresses and deflections. Today, with the fast development of sophisticated computational techniques, design engineers more and more concentrate on the analytical approach. However, the graphical approach to the shaft design and analysis has not lost its utility, especially in some applications where the graphical technique can provide the most efficient and quickest solution and physical insight to visualize the response of a shaft to applied loads.

3.4 Engineering Calculations

Engineering calculation is a key part in motor shaft design, which is conducted to ensure proper operation of shafts, including stress and strain, shaft deflection, critical speed, and stiffness.

For most loading types (forces, bending moments, etc.), the stress developed in a shaft is linearly related to the loading. As long as the stress in the material remains within the linear-elastic region, the stress is also linearly related to the deflection.

3.4.1 Normal Stress for Shaft Subjected to Axial Force

When a shaft of uniform diameter is subjected to an axial force F (Figure 3.4), the normal stress σ of the shaft is obtained as

$$\sigma = \frac{F}{A} = \frac{4F}{\pi d^2} \tag{3.10}$$

where A is the cross-sectional area of the shaft.

More general, when the cross-sectional area of a shaft varies along the z direction, that is, $A = A(z)$, the normal stress becomes a function of z:

$$\sigma(z) = \frac{F}{A(z)} = \frac{4F}{\pi\left[d(z)\right]^2} \tag{3.11}$$

A common example is a tapered shaft that can be characterized by a small (or large) diameter d_1 (or d_2) and a cone angle α, as shown in Figure 3.5. Thus,

$$d(z) = d_1 + 2z\tan\alpha \tag{3.12}$$

Substituting Equation 3.12 into 3.11, it yields

$$\sigma(z) = \frac{4F}{\pi[d_1 + 2z\tan\alpha]^2} \tag{3.13}$$

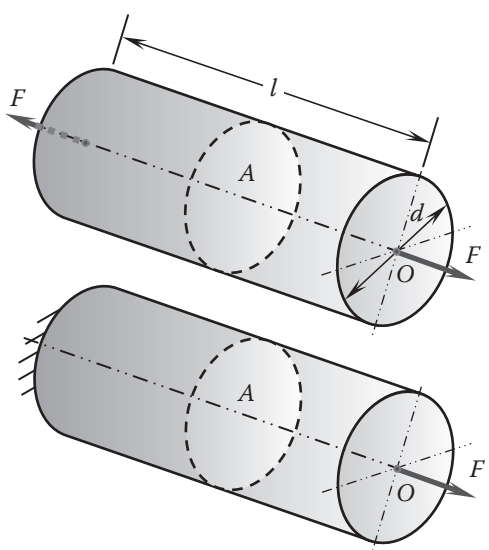

FIGURE 3.4
A single-section shaft subjected to axial force.

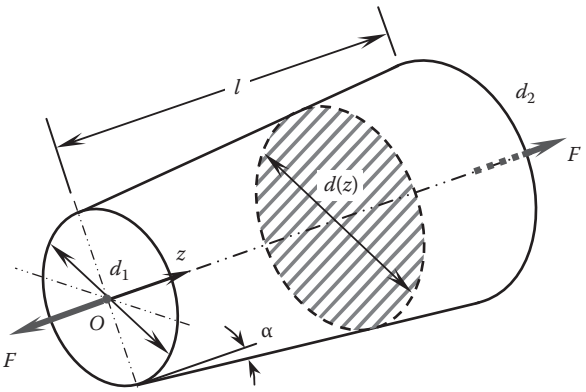

FIGURE 3.5
A tapered shaft with a cone angle α is subject to an axial force *F*.

For a stepped shaft that has an individual diameter at each segment, the normal stress at each segment *i* is given as (see Figure 3.6)

$$\sigma_i = \frac{F}{A_i} = \frac{4F}{\pi d_i^2} \tag{3.14}$$

This indicates that the maximum normal stress occurs at the segment having the smallest diameter.

3.4.2 Bending Stress for Shaft Subjected to Bending Moment

When a shaft is subjected to pure bending moment, there is bending stress generated in the shaft. As shown in Figure 3.7, compressive stresses are developed for $y > 0$ and tensional stresses for $y < 0$. At $y = 0$, there is neither compressive nor tensile stress. Thus, $y = 0$ is defined as the neutral axis. The classic formula for determining the bending stress is

$$\sigma(y) = \frac{My}{I_a} \tag{3.15}$$

- For a solid circular shaft,

$$I_a = \frac{\pi d^4}{64} \tag{3.16a}$$

- For a hollow circular shaft,

$$I_a = \frac{\pi\left(d_o^4 - d_i^4\right)}{64} \tag{3.16b}$$

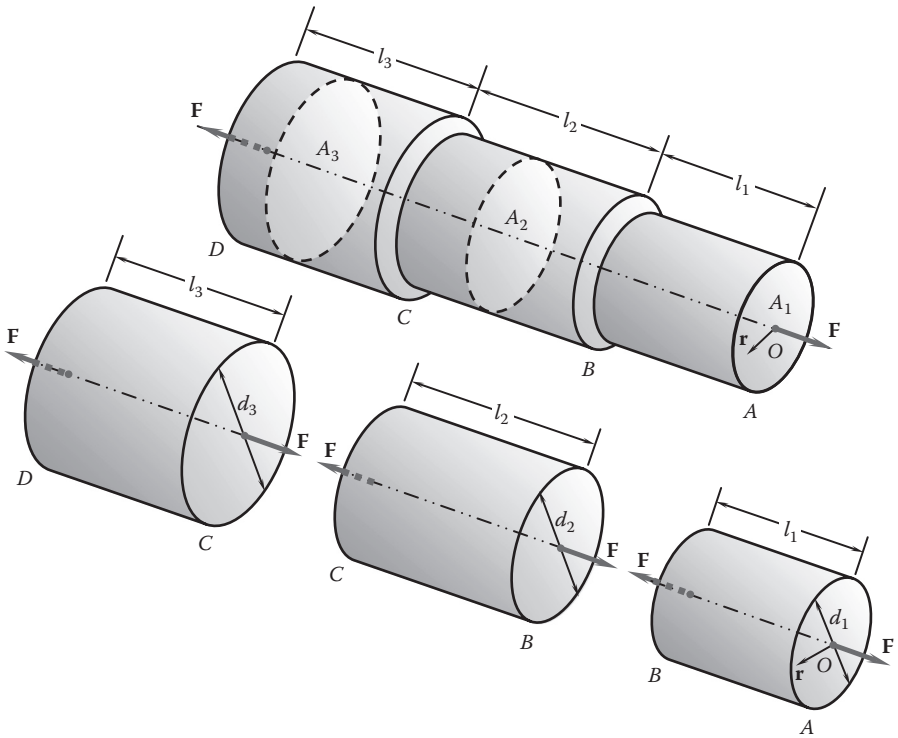

FIGURE 3.6
A stepped shaft subjected to an axial force.

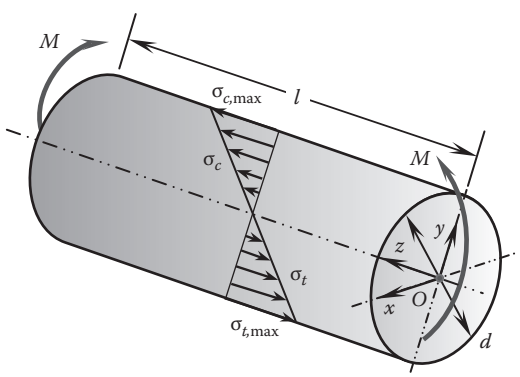

FIGURE 3.7
A single-section shaft subjected to pure bending moment.

The maximum compressive and tensional stresses occur at $y = d/2$ and $-y = d/2$, respectively:

- For a solid circular shaft,

$$\sigma_{c,\max} = \sigma_{t,\max} = \frac{32M}{\pi d^3} \tag{3.17a}$$

- For a hollow circular shaft,

$$\sigma_{c,\max} = \sigma_{t,\max} = \frac{32Md_o}{\pi\left(d_o^4 - d_i^4\right)} \tag{3.17b}$$

For a stepped shaft subjected to multiple bending moments (Figure 3.8), the bending stress at each segment is given as

$$\sigma_i(y) = \frac{My}{I_{a,i}} \tag{3.18}$$

- For a solid circular shaft,

$$I_{a,i} = \frac{\pi d_i^4}{64} \tag{3.19a}$$

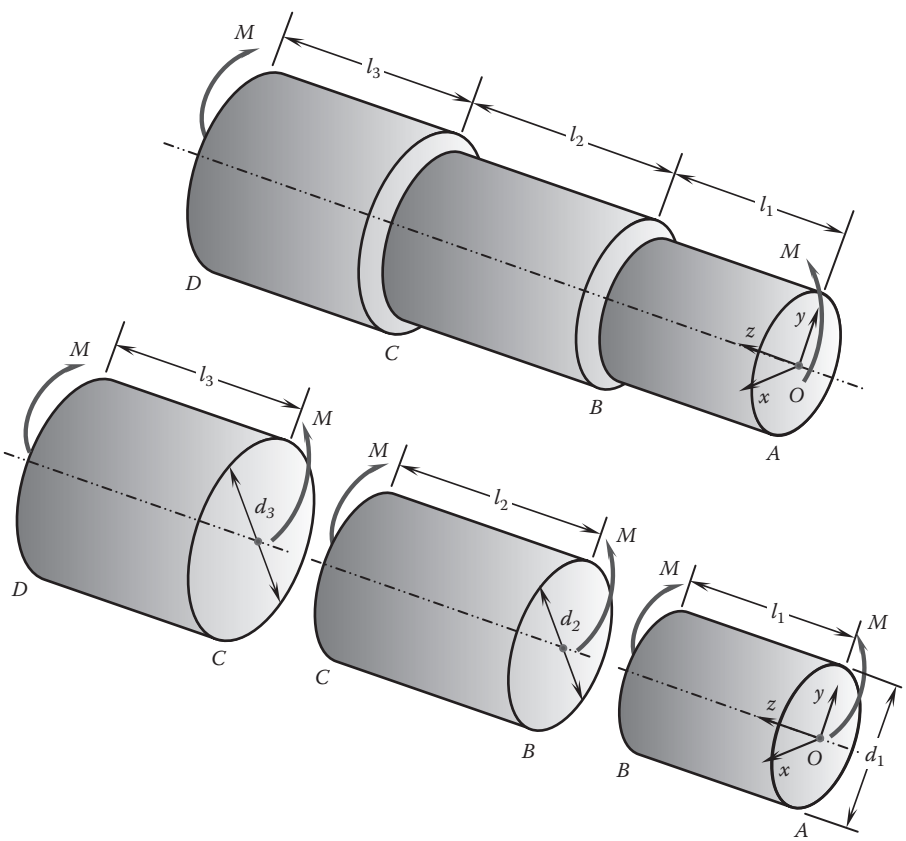

FIGURE 3.8
A stepped shaft subjected to pure bending moment.

- For a hollow circular shaft,

$$I_{a,i} = \frac{\pi\left(d_{o,i}^4 - d_{i,i}^4\right)}{64} \tag{3.19b}$$

3.4.3 Torsional Shear Stress and Torsional Deflection

Figure 3.9 shows that a pair of twist forces F is applied on a single-section shaft with a uniform diameter. This is equivalent to the case that the shaft is fixed at one end and a torque T is applied at the other end. In such a case, the radial line at the shaft end surface is rotated through an angle ϕ, defined as the shaft torsional deflection (or angular deflection in some textbooks). The length of the arc produced in the case is $R\phi$. Correspondingly, the straight line parallel to the shaft axis is rotated through an angle γ, defined as the shaft shear strain.

The rate of twist $d\phi/dz$ can be derived as

$$\frac{d\phi}{dz} = \frac{T}{GJ} \tag{3.20}$$

where

G is the shear modulus of elasticity (in unit of Pa)

J is the second polar moment of area (in unit of m^4)

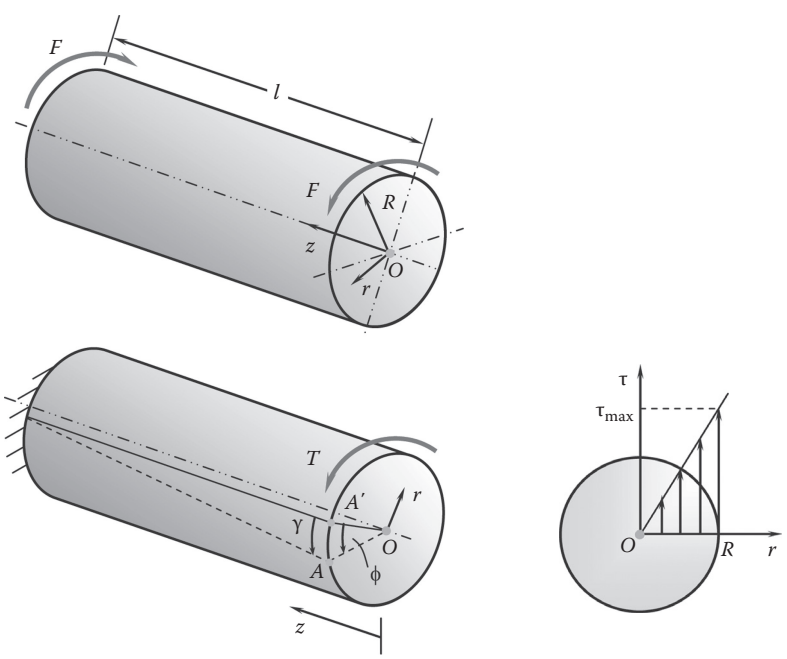

FIGURE 3.9
Torsional shear stress and torsional deflection of a single-section shaft subjected to torsional bending moment $M = F \times R$ or torque T.

It can be seen from this equation that the higher the value of GJ, the lower the rate of twist $d\phi/dz$ for a given torque T. This means that the rigidity of the shaft increases with the increase of GJ. The quantity GJ is thus defined as torsional rigidity.

For a solid circular shaft,

$$J = \frac{\pi d^4}{32} \tag{3.21}$$

For a hollow shaft with an OD and ID, d_o and d_i, respectively, the second polar moment of area J is

$$J = \frac{\pi\left(d_o^4 - d_i^4\right)}{32} \tag{3.22}$$

Integrating Equation 3.20 for obtaining torsional deflection of the shaft ϕ (in radians) yields

$$\phi = \frac{Tl}{GJ} \tag{3.23}$$

This equation shows that torsional deflection in a shaft is inversely proportional to the diameter of the fourth power. Taking a solid shaft as an example, a 10% increase in shaft diameter can result in a 31.7% reduction in torsional deflection ($1/1.1^4 - 1 = -31.7\%$). However, for practical and economical reasons, shaft size is often minimized to just satisfy the basic requirements.

Torsional stiffness of a shaft is a measure of the resistance offered by the elastic shaft to torsional deformation. This design parameter is very important in positional systems. In practice, shaft torsional stiffness is specified as a torque per unit torsional deflection, that is,

$$S_t = \frac{T}{\phi} = \frac{GJ}{l} \tag{3.24}$$

Torsional stiffness may be expressed in several different units, but the most common and easiest to work with is N-m/rad.

Another design parameter closely related to torsional stiffness is torsional flexibility, which is defined as the reciprocal of the torsional stiffness.

The torsional shear stress τ at a certain radius r of shaft is expressed as

$$\tau = \frac{Tr}{J} \tag{3.25}$$

This reveals that the torsional shear stress is independent of the choice of shaft material.

It can be seen from Figure 3.9 that the torsional shear stress is a linear function of shaft radius r; it vanishes at the shaft center (where $r = 0$) and reaches the maximum at the outer surface of the shaft (where $r = R = d/2$):

$$\tau_{\max} = \frac{TR}{J} = \frac{Td}{2J} \tag{3.26}$$

- For solid shaft,

$$\tau_{\max} = \frac{16T}{\pi d^3} \tag{3.27a}$$

- For hollow shaft,

$$\tau_{\max} = \frac{16Td_o}{\pi\left(d_o^4 - d_i^4\right)} \tag{3.27b}$$

This indicates that the shaft core has little contribution to the shaft torsional strength, and thus, the shaft can be designed as a hollow shaft minimal influence on its strength while significantly reducing weight.

Comparing Equations 3.25 and 3.26 gives

$$\tau = \frac{r}{R}\tau_{\max} \tag{3.28}$$

The shaft shear strain γ, measured as the twist angle, can be expressed as the product of the radial coordinate r and the rate of twist $d\phi/dz$:

$$\gamma = r\frac{d\phi}{dz} \tag{3.29}$$

Since $d\phi/dz$ is a constant, the shaft shear strain γ is a linear function of the shaft radius r and reaches its maximum value $\gamma_{\max}$ at the outer surface (where $r = R$):

$$\gamma = \frac{r}{R}\gamma_{\max} \tag{3.30}$$

From Hook's law, the shear stress τ can be expressed as

$$\tau = G\gamma = Gr\frac{d\phi}{dz} \tag{3.31}$$

Substituting Equation 3.20 into 3.31, it becomes

$$\tau = \frac{Tr}{J} \tag{3.32}$$

This is identical to Equation 3.25.

For a stepped shaft having a different diameter and length in each segment, when the shaft is subjected to a single torque (Figure 3.10), the torsional deflection at each shaft segment becomes

$$\phi_i = \frac{Tl_i}{GJ_i} \tag{3.33}$$

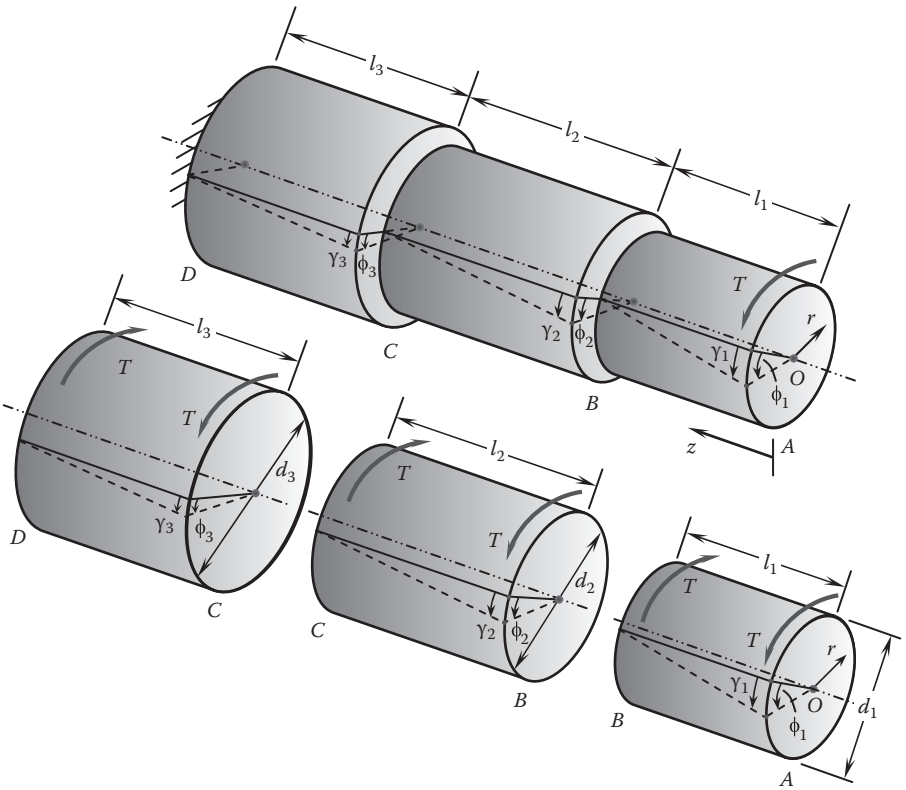

FIGURE 3.10
Torsional deflection of a stepped shaft subjected to a single torque and made from of single material.

It is noted that all torsional deflections ϕ_i have the same sign. The total torsional deflection is

$$\phi = \sum_i \phi_i = \frac{T}{G} \sum_i \frac{l_i}{J_i} \tag{3.34}$$

Similarly, the torsional shear stress on each shaft segment is

$$\tau_i = \frac{T r_i}{J_i} \tag{3.35}$$

For a stepped shaft with individual diameter d_i, length l_i, torque T_i, and material shear modulus G_i at each segment (Figure 3.11), the total torsional deflection becomes [3.6]

$$\phi = \sum_i \phi_i = \sum_i \frac{T_i l_i}{G_i J_i} \tag{3.36}$$

For this case, the sign of each torsional deflection ϕ_i depends on the torque applied on the segment.

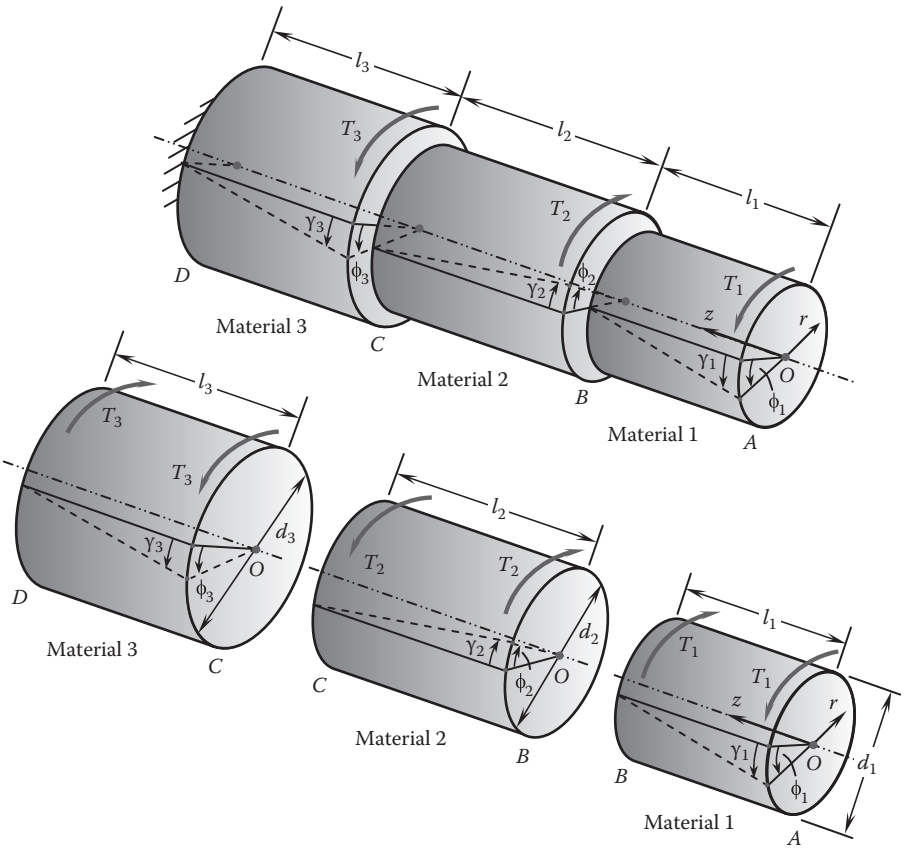

FIGURE 3.11
Torsional deflection of a stepped shaft having an individual diameter, length, torque, and material at each segment.

Correspondingly, shaft torsional stiffness at each segment is expressed as

$$S_{t,i} = \frac{T_i}{\phi_i} = \frac{G_i J_i}{l_i} \tag{3.37}$$

The total shaft torsional stiffness is given as

$$S_t = \left(\sum_i \frac{1}{S_{t,i}} \right)^{-1} \tag{3.38}$$

3.4.4 Lateral Deflection of Shaft

One of the critical design parameters of motor shaft is the maximum allowable deflection. If a motor shaft experiences a large lateral deflection, the rotating rotor may possibly contact the stator bore, causing a severe damage of the motor. Thus, the shafts must be rigid enough to avoid excessive deflection.

3.4.4.1 Lateral Deflection due to Bending Moment

When a shaft is subjected to a bending moment, the longitudinal centroidal axis of the shaft becomes a curve defined as elastic curve, as shown in Figure 3.12 with an exaggerated shape. When the bending moment is a function of the position along the shaft, that is, $M = M(z)$, the lateral deflection y of the shaft that has a uniform diameter can be derived from the following equation [3.7]:

$$\frac{d^2y}{dz^2} = \frac{M(z)}{EI_a} \tag{3.39}$$

Integrating the previous equation with respect to z, the slope of the shaft (in radians) is obtained as

$$\theta = \frac{dy}{dz} = \frac{1}{EI_a}\int M(z)\,dz \tag{3.40}$$

Continuously integrating the previous equation with respect to z, the lateral deflection of the shaft is found as

$$y = \int \theta\,dz = \frac{1}{EI_a}\iint M(z)\,dz\,dz \tag{3.41}$$

In an electric motor, the shaft diameter is often nonuniform. For a stepped shaft having an individual diameter at each segment, $I_{a,i} = I_{a,i}(z)$, the lateral deflection y and the slope of the shaft θ can be determined, respectively:

$$y_t = \sum_i y_i = \sum_i \int \frac{d\theta}{dz} = \sum_i \frac{1}{E}\iint \frac{M_i(z)}{I_{a,i}(z)}\,dz\,dz \tag{3.42}$$

$$\theta_t = \sum_i \theta_i = \sum_i \frac{dy_i}{dz} = \sum_i \frac{1}{E}\int \frac{M_i(z)}{I_{a,i}(z)}\,dz \tag{3.43}$$

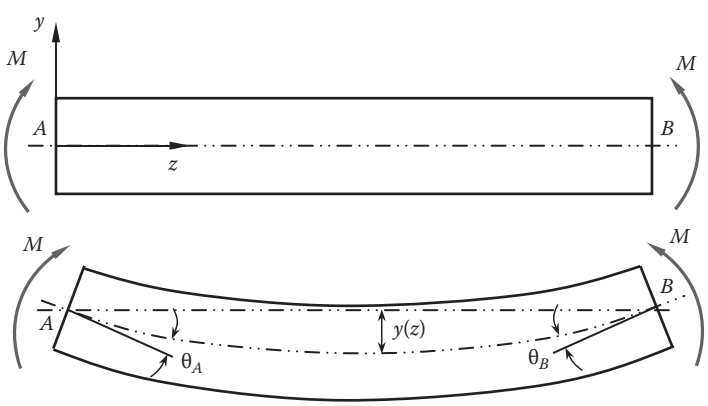

FIGURE 3.12
Deflection of a single-section shaft subjected to bending moment.

The previous equations can be used in a stepwise fashion to solve the deflection problem for stepped shafts.

For the simple case as shown in Figure 3.12, the deflection is given as

$$y(z) = \frac{Mz}{6EI_a l}\left(z^2 + 3a^2 - 6al + 2l^2\right) \tag{3.44}$$

$$\theta_A = \frac{M}{6EI_a l}(3a^2 - 6al + 2l^2) \tag{3.45}$$

3.4.4.2 Lateral Deflection due to Transverse Force

As shown in Figure 3.13, a shaft is simply supported at the two ends and loaded by a transverse force *F*. At the equilibrium condition, all forces and bending moments acting on the shaft must be balanced:

$$\sum F = 0 \Rightarrow R_A + R_B - F = 0 \tag{3.46}$$

$$\sum M = 0 \Rightarrow R_B l - Fa = 0 \tag{3.47}$$

This gives

$$\begin{cases} R_A = \dfrac{F}{l}(l-a) \\ R_B = \dfrac{Fa}{l} \end{cases} \tag{3.48}$$

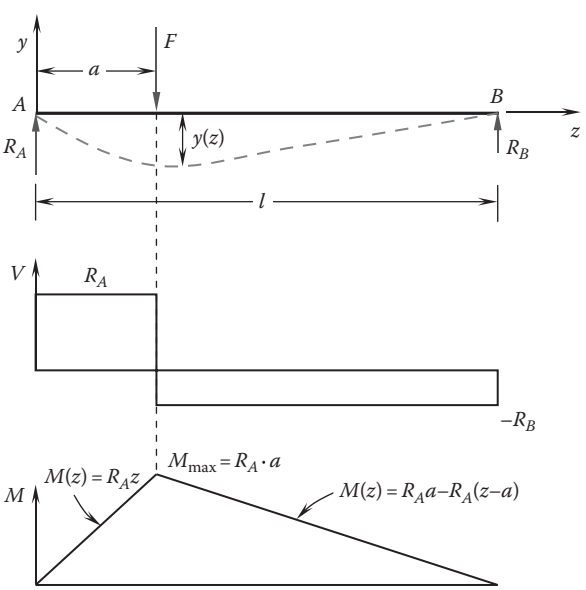

FIGURE 3.13
Deflection of a shaft subjected to a transverse force.

and

$$\begin{cases} M(z) = R_A z = \dfrac{Fz}{l}(l-a) & 0 \le z \le a \\ M(z) = R_A a - R_B(z-a) = \dfrac{Fa}{l}(l-z) & a \le z \le l \end{cases} \tag{3.49}$$

The deflection of the shaft is

$$\begin{cases} y(z) = \dfrac{F(l-a)z}{6EI_a l}\left[z^2 + (l-a)^2 - l^2\right] & 0 \le z \le a \\ y(z) = \dfrac{Fa(l-z)}{6EI_a l}\left(z^2 + a^2 - 2lz\right) & a \le z \le l \end{cases} \tag{3.50}$$

$$\begin{cases} \theta_A = \left(\dfrac{dy}{dz}\right)_A = -\dfrac{Fa}{6EI_a l}\left(2l^2 - 3al + a^2\right) \\ \theta_B = \left(\dfrac{dy}{dz}\right)_B = -\dfrac{Fa}{6EI_a l}(l^2 - a^2) \end{cases} \tag{3.51}$$

For this case, the maximum deflection occurs at $z = a$:

$$y_{\max} = -\frac{Fa^2(l-a)^2}{3EI_a l} \tag{3.52}$$

In Figure 3.14, a shaft with uniform diameter is subjected to multitransverse forces. In such a case, each deflection $y_i(z)$, which resulted from each of the transverse force F_i, is obtained as

$$\begin{cases} y_i(z) = \dfrac{F_i(l-a_i)z}{6EI_a l}\left[z^2 + (l-a_i)^2 - l^2\right] & 0 \le z \le a_i \\ y_i(z) = \dfrac{Fa_i(l-z)}{6EI_a l}\left(z^2 + a_i^2 - 2lz\right) & a_i \le z \le l \end{cases} \tag{3.53}$$

$$y_t(z) = \sum y_i(z) \tag{3.54}$$

Therefore, the total deflection is obtained by superimposing each of the deflection $y_i(z)$:

$$\begin{cases} \theta_A = -\sum \dfrac{F_i a_i}{6EI_a l}\left[2l^2 - 3a_i l + a_i^2\right] \\ \theta_B = -\sum \dfrac{F_i a_i}{6EI_a l}\left(l^2 - a_i^2\right) \end{cases} \tag{3.55}$$

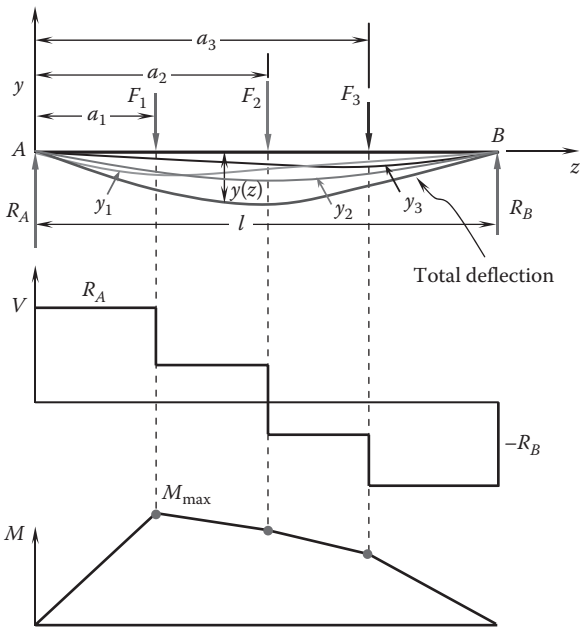

FIGURE 3.14
Deflection of a shaft subjected to multitransverse forces. The total deflection $y(z)$ is the superposition of each deflection $y_i(z)$, corresponding to each transverse force.

3.4.4.3 Lateral Deflection due to Shear Force

A shear condition is considered when a shaft is subject to a pair of equal, opposite, and parallel forces that are so close so that the bending moment is negligible. Typically, deflections due to direct shear is very small (<5%) compared to deflections due to bending moments. However, for short and heavily loaded shafts, this deflection may become significant.

As shown in Figure 3.15, two equal and opposite forces act on a shaft apart by Δz. Because Δz is small enough, the bending effect on the shaft can be ignored. The deflection due to each force is easily obtained. Thus, the total shaft deflection $y(F_1+F_2)$ can be determined using the superposition method.

3.5 Shaft Design Issues

3.5.1 Shaft Design Considerations

The design of highly reliable shafts involves many aspects of mechanical design; some of them are listed in the following:

- The determination of shaft diameter is greatly affected by many design factors such as shaft loads, transmitted torque, support span, bearings, mating methods, stress concentrations, and motor cooling. Many of these factors have been discussed previously and integrated into the derivation of the equations for calculating the shaft diameter.

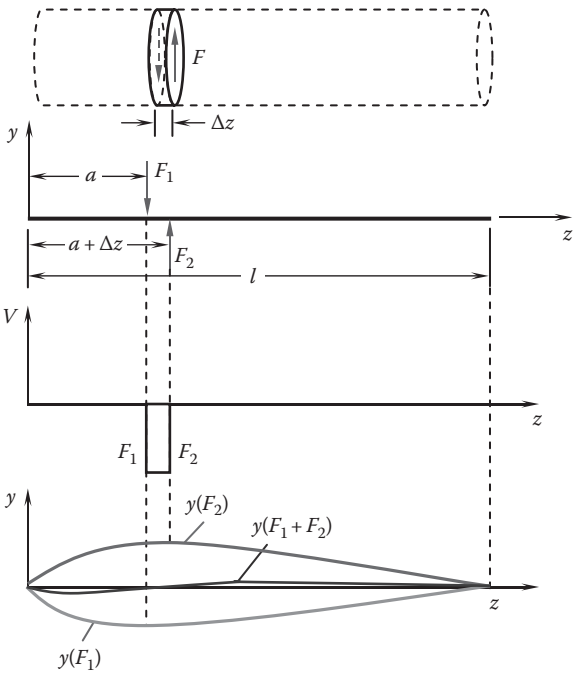

FIGURE 3.15
Deflection of a shaft subjected to shear load.

- In order to reduce stress concentration, the radius of the fillet between two adjacent steps must be larger than 0.2*d*. Sharp corners are absolutely not allowed.
- To lower bending stress and shaft deflection, the shaft length must be kept as short as possible. So does the shaft overhang length.
- Factor of safety (FS) in shaft design can vary in a large range, mostly depending on applications. For some specific applications such as elevate motors, FSs are often mandated by applicable international, national, or industrial standards, policies, or law.
- The shaft shoulder in contact with the face of a bearing must keep perpendicular to the shaft centerline. To avoid interference, the shaft fillet radius must be smaller than the bearing radius. The shoulder height is an important parameter to provide enough support to bearing loads. This is especially true for tapered roller bearings subject to high axial loads. Sometimes the shoulder height is roughly assumed to be 50%–80% of the thickness of the inner race of the bearing that directly contacts with the shaft. For more accurate design, shaft shoulders are determined using bearing catalogs for the specific bearing type and different load conditions. When the shoulder at a bearing becomes critical, it is necessary to check the stress and stress concentration on the shaft shoulder.
- Although there are many methods of fixing bearings in position on shafts, the most common way is to use retaining (snap) rings, which fit into grooves of shafts and take axial loads. However, the grooves can cause stress concentrations in the shafts.

3.5.2 Shaft Rigidity

Shaft design involves two types of shaft rigidity:

- Torsional rigidity: Torsional rigidity is a measure of a shaft's ability to resist twisting loads. It is expressed as the product of the shear modulus of elasticity G (in unit of Pa) and the second polar moment of area J (in unit of m^4). Thus, the torsion angle (in rad) of the shaft that is subject to a torque T is determined:

$$\theta = \frac{Tl}{GJ} \tag{3.56}$$

  where
  T is the torque or torsional moment
  l is the shaft length subjected to twist moment

  This equation indicates that the torsion angle θ decreases with the increased shaft torsional rigidity GJ. In the unit of degree, the torsion angle can be expressed as

$$\theta = \frac{180}{\pi}\frac{Tl}{GJ} \tag{3.57}$$

  The permissible angle of twist changes case to case. For instance, for machine tool applications, it is 0.25° per meter length of shaft.
- Lateral rigidity: Lateral rigidity is a measure of a shaft's ability to resist forces or bending moments, defined as the product of modulus of elasticity E and second moment of area I. Generally, the higher the lateral rigidity EI, the lower the shaft lateral deflection y. In certain applications, the shaft is designed on the basis of the lateral rigidity rather than on strength. Usually, the maximum permissible deflection for the transmission shaft is taken as $0.001l$–$0.003l$, where l is the span between two bearings. For electric motors, the gap depth must be taken into account in the determination of the maximum shaft deflection. Generally, the shaft lateral deflection depends on shaft dimensions, load condition, material properties, bearing span, and supporting patterns.

3.5.3 Critical Shaft Speed

A rotating shaft deflects during rotation due to its own weight, external loads, imperfect geometry, and uneven mass distribution. This deflection can significantly impact the motor performance. It has been found that there are a number of specific rotational speeds, at which the vibration amplitude increases dramatically. As the rotational speed passes beyond these speeds, the vibration amplitude decreases significantly. These speeds are defined as *critical speeds*.

The critical speed of a shaft generally depends on the magnitudes and locations of mass/load carried by the shaft, shaft support span, stiffness of the shaft, moment of inertia of the shaft, properties of shaft material (e.g., density, modulus of elasticity), shaft varying diameter, type of end supports, bearing type, and system configuration. Typical shaft design requires the critical speeds to be much higher than the anticipated operating speeds of motors, usually 20%–25% of the operating speed.

As discussed in Chapter 2, two methods are commonly used to calculate shaft critical speed. Rayleigh–Ritz method is an approximate method of finding displacements that is based on the theorem of minimum potential energy. However, the Rayleigh–Ritz method overestimates the critical speed by a few percent [3.8]. Another method is called the Dunkerley method, which underestimates the critical speed.

3.5.3.1 Shaft with Uniform Diameter

For a shaft of uniform diameter, the calculation of critical speed is relatively straightforward.

- For a shaft itself, the critical speed is

$$n_c = \left(\frac{\pi}{l}\right)^2 \sqrt{\frac{gEI_a}{A\gamma}} \tag{3.58}$$

- For the shaft with one element (e.g., rotor core) attached to it, the critical speed is

$$n_c = \frac{30}{\pi}\sqrt{\frac{g}{\delta_{st}}} \tag{3.59}$$

where
n_c is the critical speed in rpm
g is the acceleration of gravity
δ_{st} is the static deflection

3.5.3.2 Stepped Shaft

For a stepped shaft that has multiple elements, the critical speed can be calculated by the Rayleigh method after calculating the static deflection at each and every change of cross section [3.9]:

$$n_c = \sqrt{\frac{g\sum_i^m F_i y_i}{\sum_i^m F_i y_i^2}} \tag{3.60}$$

3.5.4 Dimensional Tolerance

The key tolerances of a shaft can strongly influence motor normal operation and reliability. Motor design engineers should pay special attention to the shaft dimensional tolerances at these locations:

- Bearing journals. It usually requires the press fits for assembling shafts with bearings.
- Rotor core. To ensure a rotor to withstand various loads, the interference fit (e.g., press or shrink fit) adopted in the rotor–shaft assembly.
- Coupling attached to the shaft. Improperly installed couplings may initiate additional forces acting on shafts.

- Shaft seal. Because a seal may contact with the shaft, it generates a frictional force on the shaft. To help prevent scratches and nicks, the shaft must maintain certain levels of hardness (usually HRc > 45, more desirable hardness is at the range of 60–65 HRc), smoothness, and roundness.
- Keyseats, retaining ring grooves. These may also use the press fit method.

3.5.5 Dynamic Shaft Runout

Dynamic shaft runout refers to the phenomenon that during operation, a shaft does not rotate around the true center. A number of factors may cause shaft runoff such as shaft deflection, vibration, bearing misalignment, shaft imbalance, machining tolerance, and other inaccuracies. Shaft runouts can deteriorate motor operation, produce additional stresses inside the shaft, and enlarge sealing gap, which leads to a certain level of leakage.

Dynamic shaft runout data can be captured using a dial indicator when a shaft rotates slowly. Runout measurements are usually taken at a number of positions along the shaft. Alternatively, measurements can be performed more efficiently by using a coordinate measuring machine (CMM).

3.5.6 Shaft Eccentricity

Shaft eccentricity can be resulted from the shaft deformation due to unbalance forces on the shaft, the shaft-to-bore misalignment due to machining and assembly inaccuracies, as well as the bearing radial clearance, and dynamic runout from the shaft itself. Among them, the shaft-to-bore misalignment is involved by both the shaft and the bore and almost always exists to a certain extent in practice. Apparently, shaft eccentricity must be minimized to prevent vibration, noise, leakage, and possible motor failure, especially for high-speed motors.

Eccentricity is a measure of shaft bow that is caused by any or a combination of mechanical, thermal, and gravity bow. This bow is measured while a motor runs at slow speed for detecting the peak-to-peak motion of the shaft. The measured data are critical for identifying the primary root cause of shaft eccentricity. There are a number of ways to reduce shaft eccentricity, including the following: (1) Both the shaft and its mating bore must be machined within the tolerance. (2) The shaft runout is controlled within the tolerance. (3) To reduce the gravity-induced shaft deformation, shafts that have been completely machined should be placed vertically. (4) All fits need to be carefully inspected, including bearing to bearing bore, shaft to bearing, and shaft to rotor core. (5) Rotor unbalance must be minimized. In addition, unbalance inspection includes all mechanical components mounted on the shaft, such as couplings and pulleys. (6) Bearings need to be inspected to ensure their performance. (7) Since one of the root causes of shaft eccentricity is overloading, sometimes reducing load can mitigate the extent of shaft eccentricity. (8) The selection of appropriate couplings is an important part impacting motor's overall performance. The adoption of flexible couplings helps reduce shaft misalignment and eccentricity.

Because shaft eccentricity is so critical for motor performance, it is highly desired to proactively solve it in the early stage of design process.

3.5.7 Heat Treatment and Shaft Hardness

The purpose of heat treatment on motor shafts is to improve shaft mechanical properties as a result of the change in material microstructures. Medium- and high-carbon steel

is heat-treated to increase strengths, hardness, wear resistance, and fatigue life. For low-carbon steel, the improvement of material properties can be achieved by means of carburization technology.

Hardness is a measure of a material's ability to resist mechanical abrasion and indentation. In fact, there is a positive correlation between the material hardness and the yield tensile and ultimate tensile strengths. Shaft surface hardness has a direct influence on its load capacity, performance, lifetime, and sealing.

It has been reported that a shaft of 40 HRc hardness has only 20% of the rated life of a system with a shaft at 60 HRc. To get the most rated life, heat treating shafts to a surface hardness of 60–65 HRc is essential [3.10]. For instance, by changing a shaft hardness of 50–55 HRc to 60–65 HRc, the shaft life can increase eight times.

The ability of the material to absorb a significant deformation before fracture is referred as ductility. An indicator of the material ductility is its elongation under a tensile load. Toughness is the material's ability to sustain impact and shock loading. For a motor shaft, it is desired to maintain high hardness at the shaft surface and good ductility and toughness at its core.

There are many types of heat treatment processes available to motor shafts. The combination of inductive heating and water quenching is the most effective heat treatment process of carbon steel shafts. As illustrated in Figure 3.16, during an inducting heating process while a single inductive coil moves along the shaft axis to heat a certain length of the shaft, the motor shaft rotates slowly around its axis to ensure uniform heating all over the shaft surface and through the shaft cross sections. The surface temperature of the shaft during induction heating changes sharply from room temperature to above 1000°C. The optimal heating time for required shaft properties is found out to be a few seconds, followed by a quenching period with oil–water emulsion.

The thickness of the surface hardened layer of steel parts through the induction hardening process is determined by many factors such as frequency of the AC field, heating and quenching time, current, moving speed of the heating coil, shaft material, and shaft shape, to name a few. Microscopic photos are commonly used to demonstrate the variation of the microstructure underneath the shaft surface. It has shown that at the shaft surface is completely martensitic. At a certain depth, the microstructure is composed of martensite

FIGURE 3.16
Inductive heating and water quenching of a motor shaft.

and ferrite. The ferrite in the microstructure indicates that the transformation to austenite was not completed during induction heating period because the time for transformation was not long enough. Beneath the hardening depth, the microstructure is composed of pearlite and ferrite [3.11].

One of the most important factors in a shaft heat treatment is to minimize the distortions in shaft shape and size. The larger the mass of the metal heated, the greater the metal's thermal expansion and, thus, distortion.

3.5.8 Shaft Surface Finishing

Shaft surface finishing is important on the shaft fatigue life and seal performance, as well as the reduction of windage losses. Shaft surface finishing contains two features: surface texture and shaft lead. Surface texture is characterized by three parameters: average roughness R_a, average peak-to-valley height R_z, and average peak-to-mean height R_{pm}, as shown in Figure 3.17.

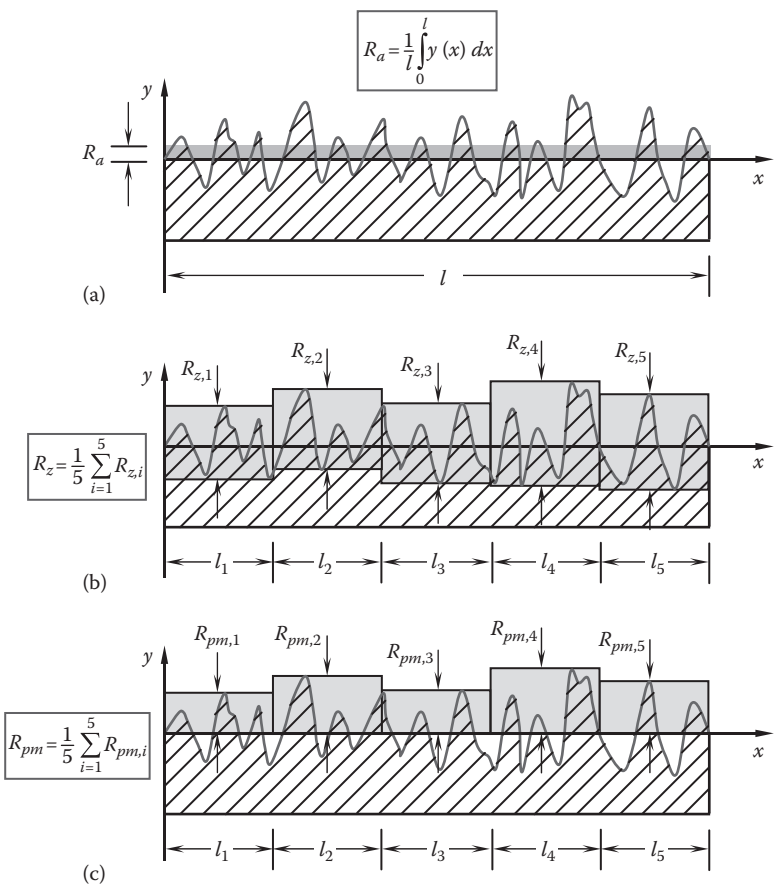

FIGURE 3.17
Three surface texture characteristic parameters: (a) average roughness R_a, (b) average peak-to-valley height R_z, and (c) average peak-to-mean R_{pm}.

R_a is the average value of the deviations from the mean line over the evaluation length l and can be determined as

$$R_a = \frac{1}{l}\int_0^l |y(x)|\,dx \tag{3.61}$$

In general, R_a less than 0.5 μm and a shaft lead angle less than 0.05° can achieve the optimum seal performance.

Steel manufacturing process has a strong impact on surface finish. For example, cold-rolled stainless steel has a roughness of $R_a = 0.2–0.5$ μm and therefore usually does not need to be polished to meet surface roughness requirements. The surface treatment of stainless steel and the resultant surface topography are listed in Table 3.3 [3.12].

Similarly, the rms roughness R_q is defined as follows:

$$R_q = \sqrt{\frac{1}{l}\int_0^l y^2(x)\,dx} \tag{3.62}$$

TABLE 3.3

Surface Treatments of Stainless Steel and Resultant Surface Topography

Surface Treatment	Approximate R_a Values (μm)	Typical Features of the Technique
Hot rolling	>4	Unbroken surface
Cold rolling	0.2–0.5	Smooth unbroken surface
Glass bead blasting	<1.2	Surface rupturing
Ceramic blasting	<1.2	Surface rupturing
Micropeening	<1	Deformed (peened) surface irregularities
Descaling	0.6–1.3	Crevices depending on initial surface
Pickling	0.5–1.0	High peaks, deep valleys
Electropolishing		Roundoff peaks without necessarily improving R_a
Mechanical polishing with aluminum oxide or silicon carbide		
Abrasive grit number		Surface topography highly dependent on process parameters, such as belt speed and pressure
500	0.1–0.25	
320	0.15–0.4	
240	0.2–0.5	
180	0.6	
120	1.1	
60	3.5	

R_z is the average peak-to-valley height and can be obtained by averaging $R_{z,i}$ values from a number of consecutive lengths along the contact surface, where

$$R_z = \frac{1}{N}\sum_{i=1}^{N} R_{z,i} \tag{3.63}$$

where N is the number of sections.

Besides R_a and R_z, another important parameter is the average peak to mean, defined as R_{pm}:

$$R_{pm} = \frac{1}{N}\sum_{i=1}^{N} R_{pm,i} \tag{3.64}$$

By cutting surface roughness with the depth of C ($C = R_z/2$), the area can be distinguished as the contact areas and noncontact areas. The surface contact area ratio R_c is defined as the summation of all surface contact areas to the total surface area (Figure 3.18), that is,

$$R_c = \frac{1}{l}\sum_{i=1}^{N} x_i \tag{3.65}$$

3.5.9 Shaft Lead

Fluid leakage in electric motors may be encountered when defective shafts that were not properly manufactured are used. A number of factors can affect the shaft sealing performance such as shaft surface finish, dimensional accuracy, and operating conditions. During a shaft finishing process, spiral grooves may be generated on the shaft surface. As shown in Figure 3.19, while the shaft rotates counterclockwise at an angular velocity $\boldsymbol{\omega}$, a finishing tool (a lathe cutter or a grinding wheel) moves axially along the shaft toward the lathe chuck at a feeding speed $\mathbf{u}$, forming the shaft lead angle α

$$\alpha = \tan^{-1}\left(\frac{u}{r\omega}\right) \tag{3.66}$$

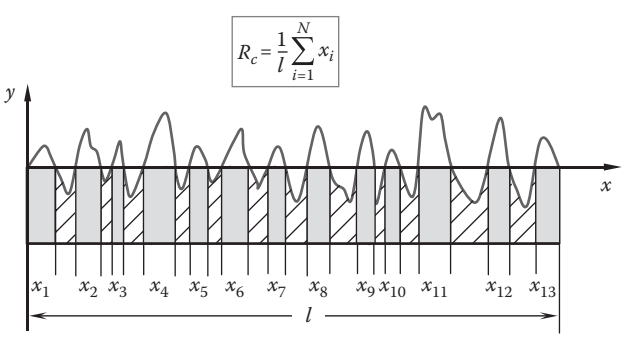

FIGURE 3.18
Surface contact area A_c, which is defined as the ratio of the summation of each contact area to the total area.

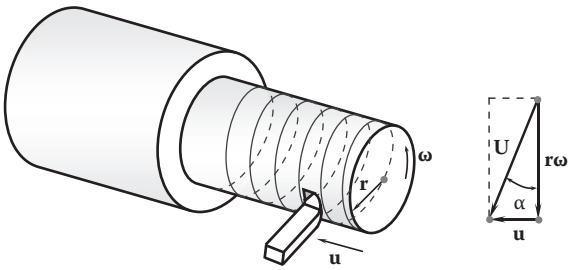

FIGURE 3.19
Formation of spiral grooves on shaft surface during shaft finishing machining.

and the magnitude of the resultant speed vector **U** is

$$U = \sqrt{u^2 + (r\omega)^2} \tag{3.67}$$

Figure 3.19 indicates that the lead angle α is proportional to the feeding speed u but inversely proportional to the angular velocity ω and the shaft radius r. Regardless of shaft finishing conditions, the shaft lead angle α is generally recommended to be controlled less than 0.05°. With a large feed speed or a slow shaft rotating speed, or both, spiral grooves are formed on the shaft surface. This phenomenon, known as shaft lead, can result in shaft seal failure during motor normal operation.

A quick and simple test can be adopted by using the suspended weight method for establishing the presence of shaft lead. As illustrated in Figure 3.20, a shaft is mounted on a lathe chuck and a small weight (e.g., 1 oz) is suspended on a testing shaft. As the lathe rotates slowly either counterclockwise or clockwise, observe whether the weight moves along the shaft and which direction it goes. The ideal case is that the weight remains in the same location with the rotating shaft, indicating there is no leakage problem.

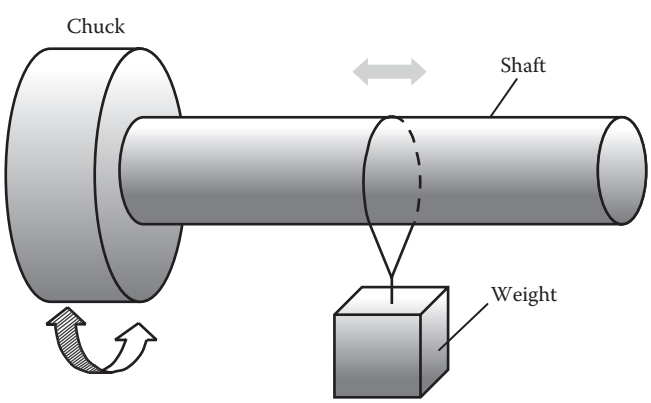

FIGURE 3.20
Motor shaft string testing.

3.5.10 Shaft Seal

Sealing is one of the main concerns in the design of rotating machinery such as motors, engines, gas turbines, generators, pumps, compressors, and other variety of rotational machines. A sealing system in a rotating machine is used to control (1) fluid (liquid or gas) leakage, (2) dynamic performance, (3) tolerance to boundaries, (4) coolant or lubricant flow, and (5) windage losses. All these functions can directly affect the performance of rotating machines through parasitic losses, life, or limit cycles [3.13]. In a worse case, a failure of the sealing system may lead to the whole system failure or disaster (e.g., exploration in a hydrogen-cooled machine).

In some motor applications, shaft seals can be critical for motor performance. For instance, in the food, pharmaceutical, and semiconductor industries, any leakages from motors that are associated with the production processes are not allowed. If using individual sealing elements, shaft seals may involve both static seals, where both the mating surfaces are stationary, and dynamic seals, where there is relative motion between the mating surfaces. For a motor using an individual sealing element, the static seal occurs between the stationary sealing element and the motor endbell and the dynamic seal occurs between the shaft and the sealing element. In most applications, seal elements are directly integrated into the motor components (e.g., motor endbell). For such a circumstance, there exists only dynamic seal between the seal element and rotating shaft. Because of the dimensional variations in dynamic seal surfaces, the design of a dynamic seal system is much more difficult than a static seal system.

Seal performance and lifetime depend upon many parameters, including shaft hardness and surface finish, shaft spiral lead, runout, rotating speed, operation temperature, pressure, seal material, and lubrication conditions. To achieve longer seal life, shaft hardness is expected to be higher than HRc 45. Most effective sealing is obtained with optimum shaft surface finishes. However, highly polished shafts may lead to high seal temperatures.

Many contacting and noncontacting shaft seals have been developed and used to rotating machinery, reflecting the need for specific solutions for individual applications. As always, each type of seal has its pros and cons. Some common seal types will be addressed in the following sections.

3.5.10.1 O-Ring Seal

O-ring seals are indispensable to a wide variety of applications, from vehicles, machine tools, pumps, and air conditioners to washing machines and vacuum cleaners. Advantages of O-rings include the following [3.14]:

- Having sealing ability over a wide range of pressure, temperature, and tolerance
- Normally requiring very little room and are light in weight
- Reusable in many cases
- Ease of service and installation
- Duration of life depending upon the normal aging period of its material
- Providing cost-effective sealing solution

The dimensions of O-ring are defined by the OD (or ID) and its cross section diameter d. O-rings are typically made of elastomers, including acrylonitrile–butadiene, carboxylated

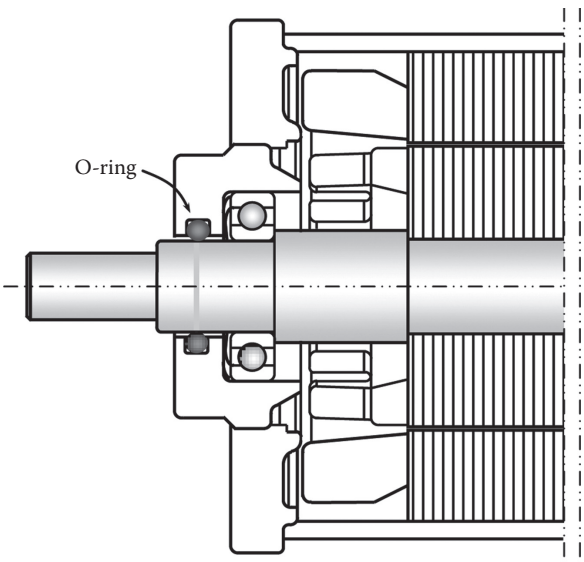

FIGURE 3.21
O-ring seal between a shaft and a motor endbell. Note that groove size prevents rotation of O-ring.

nitrile, ethylene–propylene rubber, fluorocarbon, and silicone rubber (high-temperature applications up to and above 300°C), to name a few.

As demonstrated in Figure 3.21, an O-ring is radially squeezed in an O-ring cavity groove that is machined on the endbell, providing dynamic sealing ability for the bearing. To ensure effective sealing and prevent O-ring rotation, the O-ring's OD must be slightly larger than the groove's diameter. Thus, the O-ring is slightly squeezed in the groove. Furthermore, it is important to keep the shaft diameter no greater than the O-ring's ID. When the O-ring operating temperature increases, it tends to contract. This contraction can result in a tendency for the O-ring to seize the rotating shaft and cause more friction.

There are several parameters for quantitatively describing the squeezing degree of O-ring in rotary O-ring sealing applications:

1. Relative interference, which is defined as the ratio between the differential diameter of the O-ring OD and the groove diameter, and the O-ring OD, that is, $(OD_{O\text{-ring}} - d_{groove})/OD_{O\text{-ring}}$. The maximum relative interference is usually 2%–5%, depending on different applications.
2. Compression squeeze, which is defined as the difference between the uncompressed O-ring cross-section diameter and its radial height after it compressed. Although the recommended minimum value of compression squeeze by many O-ring manufacturers is about 0.005 in. (0.127 mm), reduced compression squeeze, as small as 0.002 in. (0.051 mm), may be used in some rotary sealing systems to minimize friction.
3. Compression ratio, which is defined as the ratio between the compression squeeze and the uncompressed O-ring cross-section diameter. For rod- or piston-type seal, the recommended compression ratio ranges between 5% and 30%, with the target value of 20%.

In a continuously rotary application such as an electric motor, the shaft continuously rotates in the ID of the O-ring. Heat due to friction is generated at the same location of the contact and builds up inside the O-ring. Because elastomers are poor thermal conductors, high temperatures can cause O-ring swelling and finally lead to seal failure. This is especially true as the shaft surface speed exceeds 180 ft/min (0.91 m/s) or an O-ring is excessively squeezed.

However, O-ring seals are not recommended for rotary applications under the following conditions [3.15]:

- Pressure exceeding 5.52 MPa (800 psi)
- Temperature lower than −40°C (−40°F) or higher than 107°C (225°F)
- Surface speeds exceeding 3 m/s (9.8 ft/s)

Because O-ring seals are directly in contact with rotating shafts, O-ring wear and sealing life are some of the main concerns in O-ring seal design. Furthermore, rotary seals do not efficiently dissipate heat themselves compared to reciprocating seals. Thus, special care must be taken on the seal operating temperature to avoid seal failures during the service life.

3.5.10.2 Universal Lip Seal

A universal lip seal is used to seal a rotating shaft against the stationary motor housing. As an example presented in Figure 3.22, the seal system has a dual-lip structure: an auxiliary lip seal rides in the face of the motor endbell to establish the first barrier for solid particles such as dusts, and a primary lip seal is closer to the bearing to set the second barrier for fluid leakage. The dimensions of the dual lip are set based on material properties, sealing size, rotating speed, and lip geometry. Optimization of these ensures larger sealing capability, more reliable operation, and longer seal life. The use of a lubricant at the seal tip can promote seal durability and increase the seal life. Contaminations are always harmful for seal performance and should be avoided. With the well-designed seal and proper selections of seal material and lubricant, seals can often last over 10,000 h under clean environmental conditions [3.16]. This type of seal is primarily designed for low-pressure and low-speed applications.

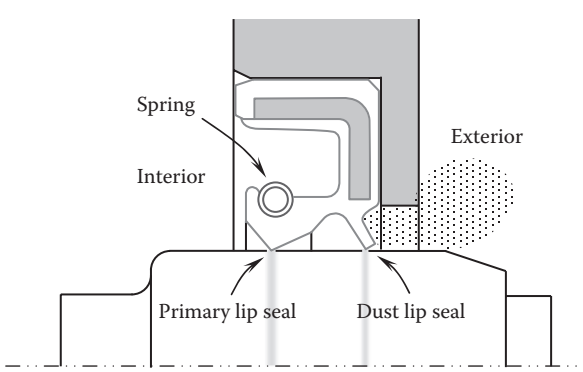

FIGURE 3.22
Universal lip seal with dual lip: a primary lip for sealing fluid and an auxiliary lip for sealing dusts.

3.5.10.3 V-Shaped Spring Seal

This type of seal differs from the previous one in some respects. First, the seal is stretched and mounted onto a rotating shaft rather than on a stationary motor endbell. Typically, the main function of the seal is to act as a face seal to prevent the ingress of dirt, dust, oil, and water. Secondly, the sealing face is the flat end surface of an endbell rather than the cylindrical shaft surface (Figure 3.23). Because the shaft radial runout is generally larger than its axial displacement, this sealing configuration can help improve the sealing performance. In fact, sealing on a flat face is easier than on a curved face. Third, the sealing pressure can be changed by adjusting the relative position of the seal to the sealing face. Finally, a high external pressure always pushes the seal lip closer to the sealing face, leading to the enhanced sealing performance but increased friction on the sealing face.

3.5.10.4 Brush Seal

The initial concept of brush seal was proposed by General Electric in 1955. Since then, the brush seal technique has been greatly developed and found more applications in a variety of industries. In the last three decades, brush seals have attracted more industrial attention in replacing conventional labyrinth seals for their improved resistance to leakage. Today, the brush seal technology represents a promising advance in constructing seal systems with high sealing effectiveness and possible small size. The brush seal uses a biased pattern of wire Kevlar® fibers in contact with the surface of a shaft. This type of seal is remarkably effective in reducing leakage.

Brush seals typically comprise a plurality of elongated Kevlar fibers or wire bristles in contact with a rotating surface. The Kevlar fibers provide a tight rub-tolerant seal that experiences only slight degradation over time. The Kevlar fibers of the seal are compliant in use, and this minimizes damage due to transient impact between the sealing components. A typical brush seal is formed by sandwiching Kevlar fibers between a pair of supporting metal plates that are welded together on their top surfaces (Figure 3.24).

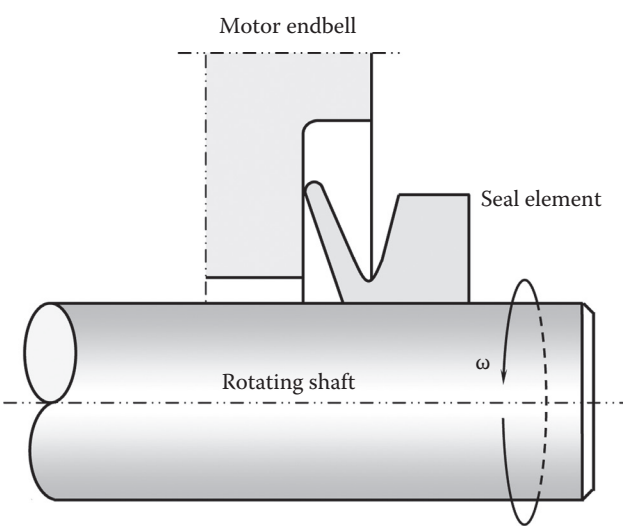

FIGURE 3.23
A V-shaped seal attached to rotating shaft for sealing the shaft at the end surface of motor endbell.

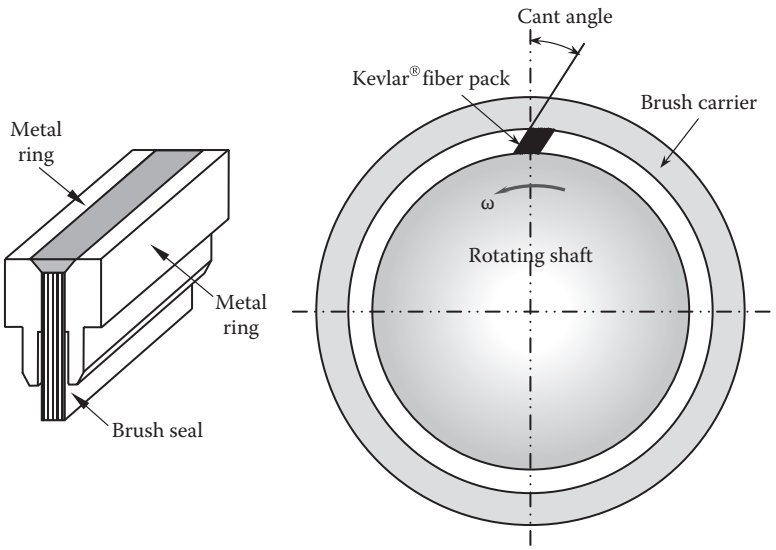

FIGURE 3.24
Brush seal employed Kevlar® fiber pack for sealing rotating shaft.

The Kevlar fibers or bristles of the seal are compliant in use, and this minimizes damage due to transient impact between the sealing components. Brush seal construction consists of three main components: Kevlar pack and back and front steel rings. The brush fibers lie at a cant angle affording the capability of accommodating radial excursions of the rotating shaft. For bidirectional rotating motors, the cant angle is set at zero.

Figure 3.25 presents an example that uses the combination of a flexible silicone rubber brush seal and a labyrinth seal to seal the shaft of rotating machinery for minimizing leakage flows. The brush seal comprises a plurality of elongated wire bristles in contact

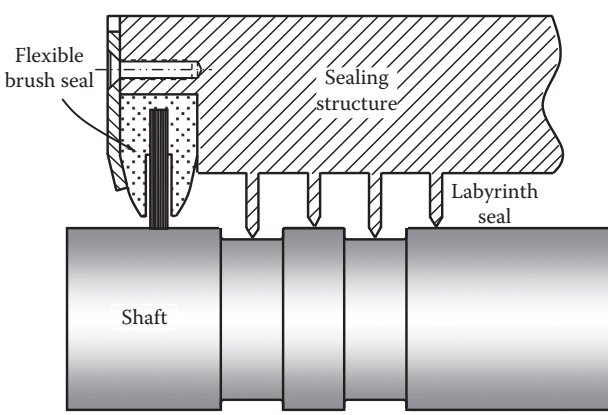

FIGURE 3.25
A flexible silicone rubber brush seal combined with a labyrinth seal to seal the shaft of rotating machinery. The brush seal body is made of heat-resistant magnetic silicone rubber material for high temperature applications (U.S. Patent 6,390,476) [3.17]. (Courtesy of the U.S. Patent and Trademark Office, Alexandria, VA.)

with the rotating shaft. The bristles provide a rub-tolerant seal that experiences only slight degradation over time. In order to use the brush seals under high-temperature conditions, they are fabricated with the flexible heat-resistant magnetic silicone rubber material. Therefore, this type of brush seal can fit a wide range of sealing dimensions and complex sealing geometry. By changing the brush bending pattern, the brush seal can be used for either inner sealing where the bristles point radially inward, outer sealing where the bristles point radially outward, or axial sealing where the bristles point parallel to the rotor–shaft axis. Additionally, by forming the brush seal body from the magnetic silicone rubber, the seal may be readily adhered to the metallic sealing components. In fact, this type of brush seal is particularly suitable for applications with large sealing dimensions [3.17].

3.5.10.5 PTFE Seal

PTFE, or more formally polytetrafluoroethylene, was discovered by accident in 1938 by a DuPont scientist. This material has some unique and remarkable properties, including the following [3.18]:

- PTFE has thermal stability across a wide temperature range. It can be used in cryogenic temperatures to seal liquid nitrogen (–196°C), liquid hydrogen (–253°C), and liquid helium (–269°C). It also can keep normal service at temperature up to 260°C for virgin PTFE.
- PTFE has the lowest friction coefficient of any known solid. The material has self-lubricating capability, making it as the excellent seal material in dynamic seal applications.
- Comparing with other main polymeric materials (e.g., UHMW-PE, PEEK, PCTFE, and PI), PTFE has the highest elongation, up to 300%.
- PTFE has very strong chemical resistance and chemical stability. It is inert to virtually all industrial chemicals and solvents even at elevated temperatures and pressures.
- The exceptional insulating properties of PTFE make the material ideally suited for using in electric machines.

High-pressure, high-speed shaft seals are often encountered in equipment or rotating machinery relevant with chemical processing under severe operating conditions. PTFE seals are especially suitable for these applications due to their superior material properties. Some specially designed PTFE seals can withstand pressures up to 55 MPa (7252 psi) and surface speeds up to 15 m/s (49.2 ft/s) [3.18]. A high-pressure, high-speed PTFE shaft seal is presented in Figure 3.26.

3.5.10.6 Noncontact Seal

As one of noncontact seal types, labyrinth seals are the most commonly used sealing configuration in rotating machinery to control the internal leakage of fluid. A typical labyrinth seal is generally characterized by a series of grooves formed along the adjacent surfaces of a rotating shaft. The circumferential grooves make a tortuous axial path that restricts fluid flow across it, as shown in Figure 3.27a [3.19].

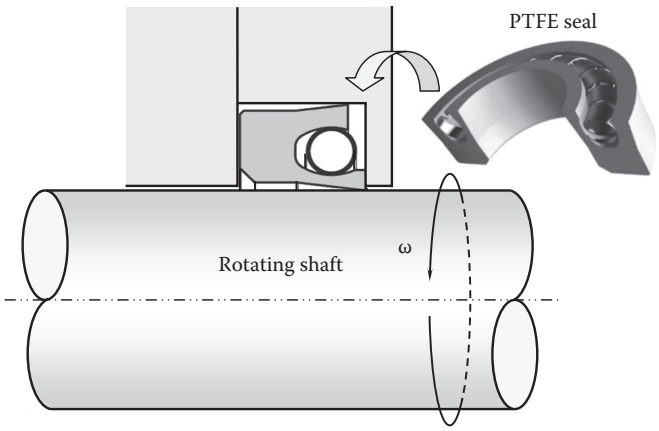

FIGURE 3.26
High-pressure, high-speed dynamic PTFE seal.

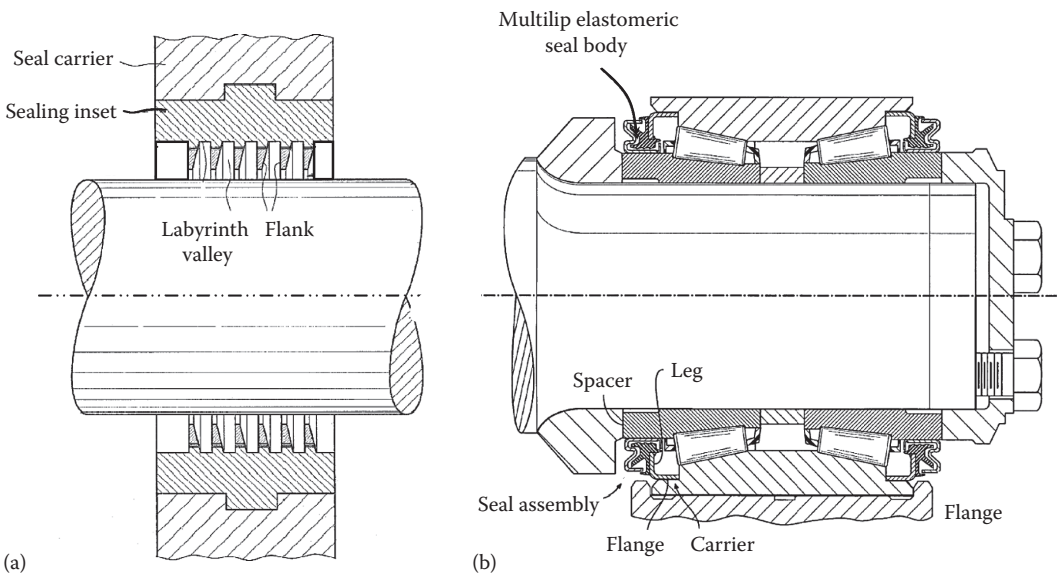

FIGURE 3.27
Noncontact labyrinth seals used in rotating machinery: (a) tooth-groove labyrinth seal (U.S. Patent Application 2012/0228830) [3.19] and (b) multilip labyrinth seal (U.S. Patent 8,342,535) [3.20]. (Courtesy of the U.S. Patent and Trademark Office, Alexandria, VA.)

In motor operation, the labyrinth seal on a rotating shaft provides noncontact sealing action by controlling the passage of fluid. With the labyrinth design, the leakage fluid has to pass through a long and tortuous path, producing high friction forces against the movement of the fluid. In addition, at high rotating speeds, the leakage fluid is subjected to a high angular momentum and hence is flung radially outward. In such a way, the leakage fluid along the tortuous path is disturbed and pushed away from the passage. Consequently, the combination of these two effects makes this type of seal have good sealing capability.

Another type of labyrinth seal is presented in Figure 3.27b, where an elastomeric seal body has multiple radially outward lips in different directions, creating even more complicated flow path for improving sealing performance [3.20].

This type of labyrinth seals is known for its low manufacturing cost, small fiction (only fluid friction involved), no wear, tight radial clearance between the seal and shaft, and acceptable leakage control effectiveness. One important issue in using labyrinth seals is that they are prone to developing cross-coupled forces, which can induce rotor dynamic instability. The effects of pressure differential, rotor speed, entry flow conditions, and seal geometry on the rotordynamic stability were addressed by Benckert and Wachter [3.21] in detail.

3.5.11 Diametrical Fit Types

There are two diametrical fit types: hole-based fitting and shaft-based fitting. In the hole-based fitting, the dimension of the hole is taken as the basis and the clearance or interference is applied to the shaft dimension. In contrast, in the shaft-based fitting, the dimension of the shaft is taken as the basis. Generally, the hole-based fitting is considered better than the shaft-based fitting. This is because holes are often machined by standard tools (drills or reamers) with fixed dimensions and shafts are machined by CNC lathes to any given dimensions. In addition, some standard mechanical parts such as bearings, pulleys, and gears often have standard internal diameters with tight tolerances. However, the shaft-based fitting may be also used in some special applications.

3.6 Stress Concentration

It has long been recognized that any structural and discontinuity in machinery components can alter the stress or strain distributions in the vicinity of the discontinuity and significantly raise the local stress or stain levels. The structural discontinuities can be geometric discontinuity such as grooves, holes, notches, shoulders, keyseats, threads, splines, and sudden changes in geometry and material discontinuities such as voids, cracks, and porosities. As the sources of stress/strain intensification, these discontinuities affect only small regions of actual machinery components or structural members but have little impact on the overall stress/strain pattern. This is extremely dangerous because without any apparent signs, the machinery components or structural members may suddenly fail due to the cracks developed at the stress concentration locations.

In order to quantitatively describe the phenomenon of stress concentration, a dimensionless factor, known as stress concentration factor K, is introduced as the ratio of the actual maximum stress with the stress riser to the nominal stress without the stress riser, that is,

$$K = \frac{\text{Actual maximum stress}}{\text{Nominal stress}} \tag{3.68}$$

More specifically, the normal and shear stress concentration factors, K_t and K_{ts}, are defined respectively as

$$K_t = \frac{\sigma_{\max}}{\sigma_o} \quad \text{for normal stress (underbending, tension, or compression)} \tag{3.69a}$$

$$K_{ts} = \frac{\tau_{max}}{\tau_o} \quad \text{for shear stress (undertorsion)} \tag{3.69b}$$

where the stresses σ_{max} and τ_{max} are the real maximum normal and shear stresses and the nominal stresses σ_o and τ_o are the normal and shear stresses without stress raisers, respectively.

Stress concentration factors for different discontinuity types, loadings, and geometries can be found from some typical mechanical engineering design textbooks [3.6,3.22,3.23].

3.7 Torque Transmission through Mechanical Joints

For a shaft to transmit torque or power to a driven machine, some mechanical components are needed to be mounted on the shaft, such as coupling, pulley, gear, hub, sheaves, sprocket, and/or cam, to name a few. To ensure that these mechanical components are firmly connected with the shaft, it must satisfy the following design requirements: (1) no relative motion between the shaft and the attached components, (2) easy and rapid assembly/disassembly, (3) easy to manufacture, (4) minimized stress concentration, and (5) induced less vibration and acoustic noise.

Motor torque is normally transmitted from the motor shaft to the mounted components using keys, splines, pins, or other torque-transmitting elements.

3.7.1 Keyed Shafts

Most motor shafts use keys for securing mating elements rotating together to transmit motor torque to external equipment. The advantages of using keys include cost-effectiveness, ease of installation, and high reliability. In addition, keys used in the joint systems may function as mechanical *fuses* to prevent further damage to joints or other parts of the machine.

3.7.1.1 Selection of Key Material

In the design of keyed connections, it is important to select proper key material. An improper key material may cause damage to the key itself, shaft, hub, or even motor failures in severe cases. In transmitting power/torque, there are two basic failure modes: shear across the shaft–hub interface and compression due to the bearing forces between the key (lower portion) and shaft and key (upper portion) and hub. Since shafts are subjected to combined loads, the key material must have high strengths, high hardness, proper elongation, and tolerance to shock loads.

The required key strengths are closely associated with the key length. As the key length is 1.6 times the shaft diameter, the key stress is equal to the shaft stress. As the key length is comparable to the shaft diameter, the key stress becomes much higher than the shaft stress. However, because there is a high contact pressure between the shaft and the hub bore due to the interference fit to transmit a considerably large portion of power/torque, it is generally accepted that the key material can be chosen with the same strengths and hardness as the shaft. In practice, carbon steel is the most common material for keys.

3.7.1.2 Stress Analysis of Key and Keyseat

Numerous types of keys are available, including flat keys, square keys, round keys, gib-head keys, feather keys, and Woodruff keys. Among these, flat keys are widely used in the motor industry. To accept a key, longitudinal grooves are made into a shaft and its mating element (e.g., sheave, hub), known as keyways or keyseats. According to the milling pattern, a shaft keyseat can be classified as either sled runner keyseat or profile keyseat. The sled runner keyseats are milled with a disk milling cutter that has the same width of the keyseat. The profile keyseat is produced by a circular endmill that has a diameter equal to the keyseat width (Figure 3.28). Though the type of profile keyseat is widely used in industries, the type of sled runner keyseat is desirable for its lower stress concentration factor. Figure 3.29 presents a PM rotor with a profile keyseat.

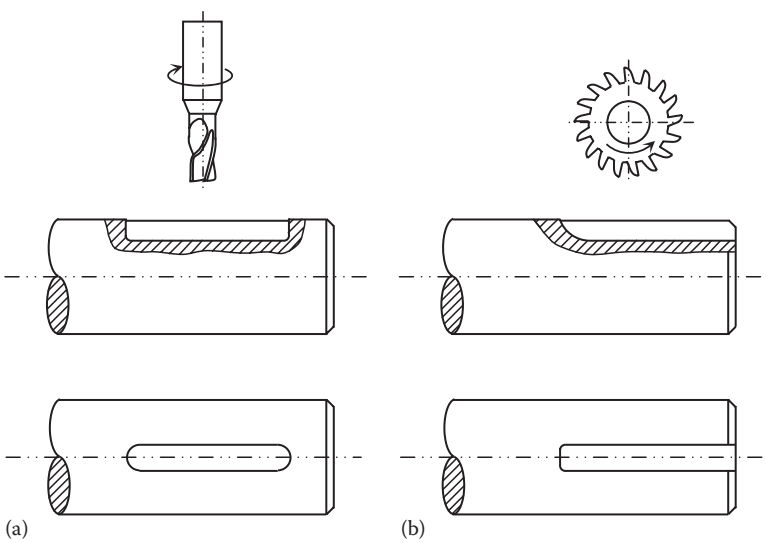

FIGURE 3.28
Keyseat types: (a) profile keyseat and (b) sled runner keyseat.

FIGURE 3.29
A keyseat is machined at the drive side of a PM rotor.

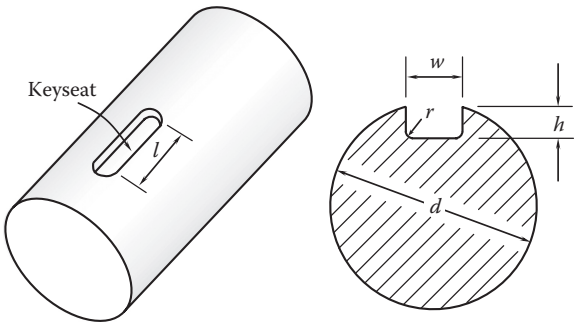

FIGURE 3.30
Dimensions of the profile keyseat made on the motor shaft. Small fillets are made at the keyseat corners to decrease stress concentration.

A keyed shaft is primarily characterized by five variables: shaft diameter d, keyseat width w, keyseat depth h, effective keyseat length l, and the fillet radius at the keyseat bottom edge r (Figure 3.30). Usually, the fillet radius is about 2% of the shaft diameter. This gives the stress concentration factor of the keyseat approximately 3. If a keyseat has sharp corners at the bottom, the stress concentration factor can be significantly high. As reported by Peterson, typical stress concentration factors are approximately 1.1–2.0 for stepped shafts and 2.5–4.0 for keyseats [3.24]. It is noted that the rounded key ends avoid high local stresses.

As illustrated in Figure 3.31, a key is inserted in the keyseats of the shaft and sheave/hub. To avoid interference with the keyseats at the key edges, the radii of the key must be larger than those of the keyseats. The key must be precisely fitted to the keyseat in the shaft and sheave/hub with a small radial clearance on the top. Thus, motor torque is transferred from the shaft to the sheave/hub through two contact surfaces at the sides of the key. While the contact force of the shaft F exerts on the lower section of the key, the opposite reaction force F' from the sheave/hub exerts on the upper section of the key (where F is slightly larger than F'). These resulting forces cause shear and compressive stresses. Thus, for this locking system, there are two major failure mechanisms: shear failure and crushing failure, which are applicable to all components (shaft, key, and sheave/hub).

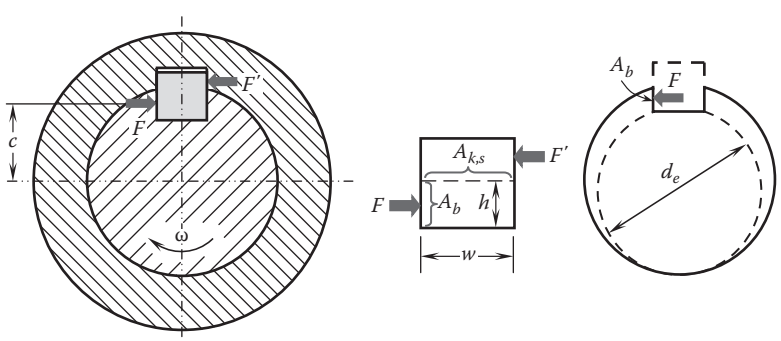

FIGURE 3.31
Shear failure and crushing failure applied on a flat key and a keyed shaft.

In the shear failure mechanism, a key withstands opposite forces on its upper and lower sections, causing a shear stress on the key shear plane $A_{k,s}$,

$$A_{k,s} = lw \tag{3.70}$$

The maximum shear stress $\tau_{\max}$ is reached when the force F approaches its maximum value $F_{\max}$:

$$\tau_{\max} = \frac{F_{\max}}{A_{k,s}} \tag{3.71}$$

The factor of safety for the shear failure is defined as

$$n_s = \frac{S_{sy}}{\tau_{\max}} = \frac{0.577\, S_y}{\tau_{\max}} \tag{3.72}$$

where S_{sy} and S_y are shear yield strength and tensile yield strength (according to the distortion-energy theory, $S_{sy} = 0.577 S_y$), respectively. Thus, the maximum torque that can be transmitted by the key is

$$T_{k,\max} = F_{\max} c \approx F_{\max}\left[\frac{1}{2}(d-h)\right] = \frac{0.289\, lw(d-h) S_y}{n_s} \tag{3.73}$$

The stress analysis of a keyed shaft is different from the analysis of the key. As a good practice to estimate the torque that can be transmitted by the keyed shaft with a reduced shaft diameter, the concept of an effective diameter d_e is introduced into the analysis:

$$d_e \cong \sqrt{(d-h)^2 + w^2} \tag{3.74}$$

Correspondingly, shear stress resulting from the applied torque T is

$$\tau = \frac{Tr}{J} \tag{3.75}$$

where r is the shaft radius and

$$J = \frac{\pi d_e^4}{32} \tag{3.76}$$

The maximum shear stress is reached at $r = d_e/2$:

$$\tau_{\max} = \frac{T_{\max}(d_e/2)}{\pi d_e^4/32} = \frac{16 T_{\max}}{\pi d_e^3} \tag{3.77}$$

Combining the previous equation, it follows that

$$T_{\max} = \frac{0.1133 d_e^3 S_y}{n_s} \tag{3.78}$$

In the crushing failure mechanism, the compressive force F acts on the bearing area A_b of the shaft and the key, respectively. The maximum bearing stress is given as

$$\sigma_{\max} = \frac{F_{\max}}{A_b} = \frac{F_{\max}}{hl} \tag{3.79}$$

The factor of safety for the crushing failure is defined as

$$n_c = \frac{S_{cy}}{\sigma_{\max}} \tag{3.80}$$

where S_{cy} is the compressive yield strength. Hence, the corresponding maximum torque becomes

$$T_{\max} = F_{\max} c \approx F_{\max}\left[\frac{1}{2}(d-h)\right] = \frac{hl(d-h)S_{cy}}{2n_c} \tag{3.81}$$

For steady loads, $n_s = n_c = 2$ is frequently adopted. As for shock loads, the factor of safety can be chosen between 2.5 and 4.5 [3.25].

3.7.1.3 Key Fitting

Usually, higher motor torques require tight fits (e.g., interference fits) between keys and keyseats. When a key is loosely fitted into the mating keyseat as a clearance fit. Thus, as the key is subject to the transverse forces from both the shaft and hub. Thus, the key rolls in the keyseat to pit the edges and surfaces of the keyseat (Figure 3.32). This condition can cause high loadings between the key and keyseats, leading to the failure of either the key or shaft, or both. It becomes even worse if the motor frequently changes its rotating direction. On the other hand, too tight fitted keys and keyways may also result in mechanical failures. To ensure appropriate fit, the width and height dimensions of

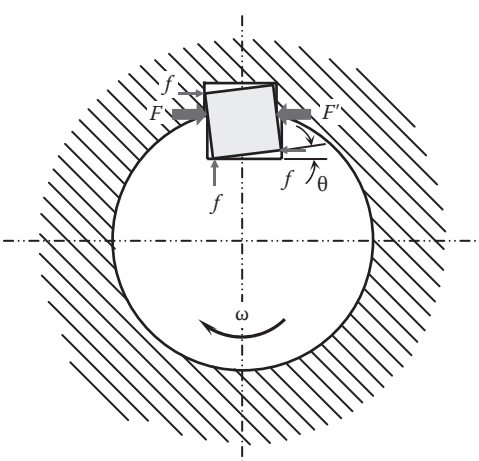

FIGURE 3.32
A key inserted loosely in a keyseat, causing high edge loadings between the key and keyseat.

keys and keyways must be held to recommended tolerances, as defined in industrial or national standards.

Because the stress analysis of key fitting is very complicated, it is usually performed using FEM tools.

3.7.1.4 Stress Concentration Factors of Keyed Shafts

A machined keyseat in a shaft does not only reduce the shaft strength and stiffness but also cause stress concentration in the shaft. The impacts of keyseats on the torsional stiffness of shafts were addressed first by Filon in 1900 [3.26]. Subsequent to that, a large number of theoretical, experimental, and numerical investigations have been conducted for determining stress concentration factors in keyed shafts [3.7,3.27–3.35, as some examples]. Pilkey [3.22] proposed a correlation of stress concentration factor for a specific case of $w/d = 1/4$ and $h/d = 1/8$:

$$K_t = 1.9753 + 0.1434\left(\frac{0.1}{r/d}\right) - 0.0021\left(\frac{0.1}{r/d}\right)^2 \quad r/d \in [0.005 : 0.07] \tag{3.82}$$

This correlation is found overestimating the K_t values. More recently, Pedersen [3.35] reported a better correlation for the same case:

$$K_t = 1.8755 + 0.1397\left(\frac{0.1}{r/d}\right) - 0.0018\left(\frac{0.1}{r/d}\right)^2 \quad r/d \in [0.003 : 0.07] \tag{3.83}$$

The comparison of the two previous correlations is given in Figure 3.33. It can be seen for $r/d < 0.005$, the predicted K_t values from two correlations are almost identical. For large r/d ratios, the correlation of Pilkey is about 4%–5% higher than that of Pedersen.

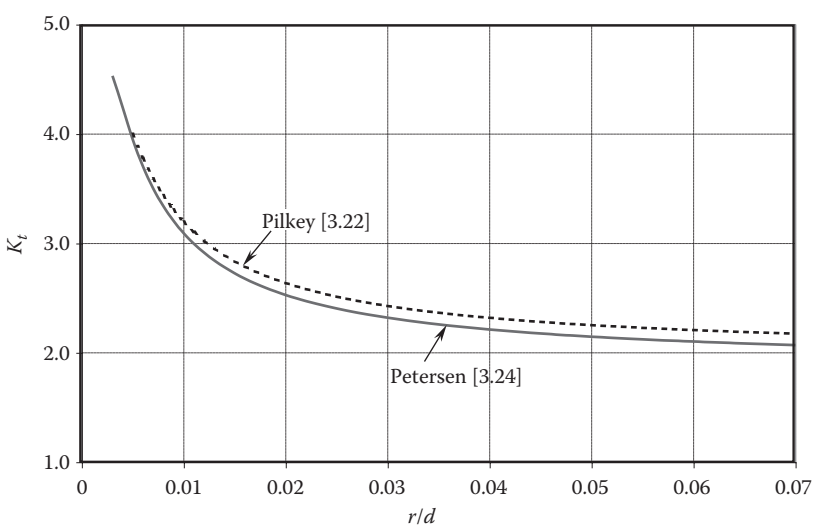

FIGURE 3.33
Comparison between two correlations of stress correlation of keyed shaft for the case of $w/d = 1/4$ and $h/d = 1/8$.

More general, stress concentration factors of keyed shaft depend on three ratios: fillet radius to shaft diameter ratio r/d, keyseat width to shaft diameter ratio w/d, and keyseat height to shaft diameter ratio h/d. As discussed by Pedersen [3.35], the width ratio and height ratio can be linked together and fall naturally into two groups depending on the shaft diameter:

$$\frac{w}{d} = 1.2662\frac{h}{d} + 0.0866 \quad d \in [6:38]\,\text{mm} \tag{3.84a}$$

$$\frac{w}{d} = 1.6683\frac{h}{d} + 0.1055 \quad d \in [38:500]\,\text{mm} \tag{3.84b}$$

Corresponding to these two diameter ranges, stress concentration factors can be correlated as

$$K_t = \left(1.4786\frac{h}{d} + 0.6326\right)\left(\frac{r}{d}\right)^{\left[0.868(h/d)^2 - 0.4392(h/d) - 0.2369\right]} \quad d \in [6:38]\,\text{mm} \tag{3.85a}$$

$$K_t = \left(1.0428\frac{h}{d} + 0.5355\right)\left(\frac{r}{d}\right)^{\left[2.8074(h/d)^2 - 0.8091(h/d) - 0.2476\right]} \quad d \in [38:500]\,\text{mm} \tag{3.85b}$$

respectively.

Many researchers and investigators have contributed to determine shear stress concentration factor K_{ts} for keyed shaft. Leven [3.28] did the early work for the stress concentration arising from torsion in a shaft containing a keyseat and obtained K_{ts} values at the straight part of a keyseat as a function of r/d. Using the electroplating method, Okudo et al. [3.32] experimentally examined stresses in keyseats under the most practical conditions. To obtain the limit value for a shaft twisted only through a key, the fitting is devised so as to minimize the surface friction at the fitted portion. From the Peterson's charts [3.22], for a ratio of $r/d = 0.02$, $K_{ts} = 2.60$ without the key in place, and $K_{ts} = 3.0$ with the key in place.

Thus, the allowable maximum torques transmitted by a keyed shaft in the shear failure and crushing failure become

$$T_{sh,\max} = \frac{0.289 d S_y}{n_s K_{ts}} A_{sh,s} \tag{3.86}$$

$$T_{\max} = \frac{hl(d-h)S_{cy}}{2n_c K_t} \tag{3.87}$$

3.7.2 Spline Shafts

Spline shafts are widely used in various industries such as automotive, aerospace, heavy machinery, machine tool, textile machinery, and mining. Splines perform the same function as keys in transmitting torque from a motor to a driven machine. In fact, a spline can be viewed as a series of axial keys machined into the shaft (Figure 3.34), with corresponding

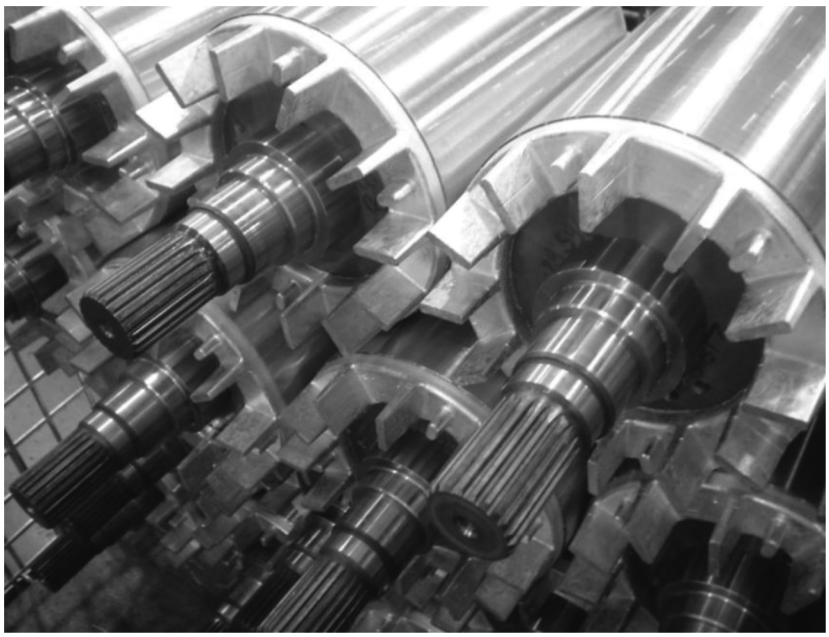

FIGURE 3.34
Spline shafts used in induction motors.

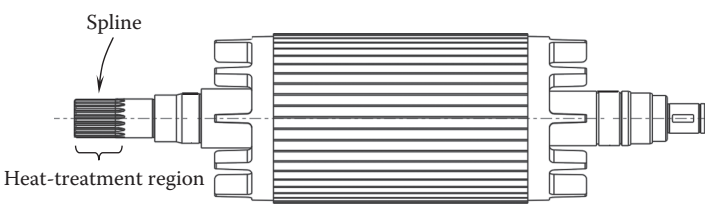

FIGURE 3.35
The spline is heat treated for increasing surface hardness, wear resistance and fatigue life.

grooves machined into the bore of the mating element. As demonstrated in Figure 3.35, the spline is machined at the drive side of the shaft. To increase the surface hardness, wear resistance, and fatigue life, shaft splines must go through heat treatment processes. It should be noted that to prevent shaft deformation, heat treatment is applied to the limited region that contains only spline. However, improper heat treatment of steel and alloys may lead to temper embrittlement, tempered martensite embrittlement, or hydrogen embrittlement, depending on different heat treatment processes [3.36]. Consequently, all of these embrittlement types could cause spline shaft failure, as shown in Figure 3.36.

3.7.2.1 Advantages of Spline Shafts

There are a number of advantages of spline connections over key connections: (1) Because the spline is machined directly on the shaft, no relative motion can occur between the spline teeth and the shaft. (2) With multiple spline teeth, the torsion and bending loads are uniformly distributed to the teeth. (3) Each spline tooth transfers a much lower torsion

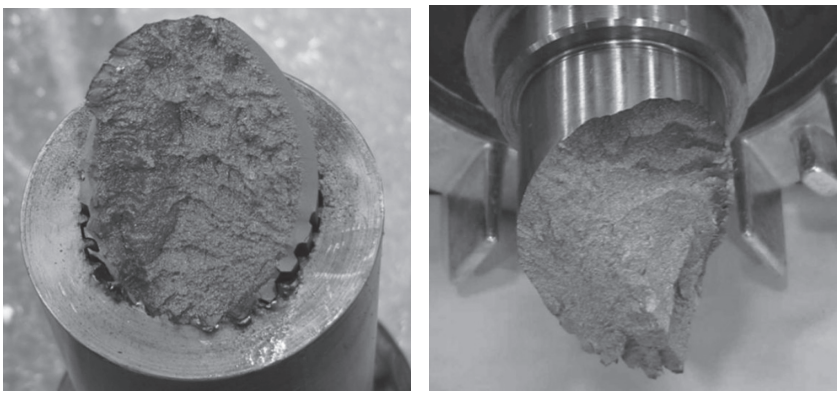

FIGURE 3.36
Failure of spline shafts due to improper heat treatment.

load compared with a keyed shaft. Thus, spline shafts can transmit large torque or power. (4) A spline shaft has an ability to accommodate large axial movements between the shaft and the mating part while simultaneously transmitting torque. (5) An involute spline shaft has an autocentering dynamics that allows a semi- or full-floating coupling. (6) The mating part can be indexed to various positions with respect to the shaft spline. (7) A helical spline shaft can drive the axial and rotary motion at the same time. (8) Using the hob to cut spline shafts can offer notable advantages both in terms of manufacturing efficiency and spline profile accuracy over the manufacturing method for keyed shafts. (9) Splines are usually heat-treated to increase the surface hardness and wear resistance. By contrast, it is very rare to do heat treatment to shaft keyseats. (10) Uniformly distributed spline teeth have little impact on shaft unbalance. For a keyed shaft, the keyseat can bring an unbalance problem. (11) While a shaft with an external key is subject to a high stress concentration at the mouth of keyseat, a spline shaft has much lower stress concentration due to the distribution of loads to all teeth.

3.7.2.2 Spline Types

Although a number of spline types exist, the most commonly used splines across a wide variety of industries are involute splines and straight-sided splines (sometimes also referred to as parallel key splines), as shown in Figure 3.37. Involute splines typically have pressure angles of 30, 37.5, or 45. This type of splines tends to be self-centering that equalizes bearing and stresses among all teeth. This characteristic feature also helps achieve better concentricity between the shafts of the motor and its mating machine. In contrast with involute splines, straight-sided splines have ridges with a rectangular profile. This type of splines has been standardized by SAE to have 4, 6, 10, or 16 splines, which is equally distributed around the circumference of a shaft. Today, straight-sided splines still remain popular in many applications, especially in the machine tool and automotive industries.

Involute splines are favored over straight-sided splines because of their self-centering capability, higher torque-transmitting capacity, and greater strength, as well as some manufacturing advantages (e.g., for any given pitch, the spline cutting tools can cut any number of teeth).

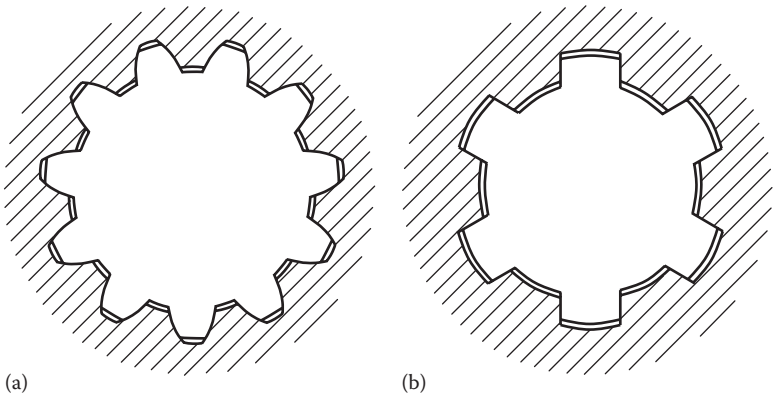

FIGURE 3.37
Spline types: (a) involute spline and (b) straight-sided spline.

3.7.2.3 Stress Concentration Factors of Spline Shafts

When spline motor shafts transmit torque or power to a driven machine, they are subject to torsion loads. A mathematical analysis was conducted by Okubo [3.37] for a shaft with a number of longitudinal semicircular grooves. It was found that as r/d approaches zero (where r is the fillet radius at the tooth root and d is the shaft diameter), the stress concentration factor $K_{ts}=2$. By using the 3D photoelastic technique, Yoshitake [3.38] performed an experimental investigation on eight-tooth splines. In his work, the torsion stress concentration factors were measured by the wedge method with varied tooth fillet radius. The test results indicate that the involute splines are more advantageous than parallel side splines from the standpoint of torsion stress concentration factor. It was reported that the torsion stress concentration factor is 2.8 for an involute spline and is 3.1 ($r=1.5$ mm), 3.4 ($r=1.0$ mm), and 4.4 ($r=0.5$ mm) for parallel splines.

3.7.3 Tapered Shafts

Since keys and splines usually produce stress concentrations on motor shafts, tapered shafts may provide a promising solution with keyless designs. As shown in Figure 3.38, a taper is made at the drive end of a motor shaft with a small cone angle α and inserted in the bore of the traction sheave/hub. A number of fasteners (screws or bolts) are engaged with the shaft to ensure the close contact of the tapered shaft with the sheave/hub. As the fasteners are tightened, the tapered shaft is further pushed into the bore of the sheave/hub, creating a contact pressure at the contact surface.

By comparing with conventional shafts, tapered shafts are more expensive and may require special tooling. In addition, this method may not be suitable for very high torque conditions.

Assume the tapered shaft is perfectly contacted with the sheave/hub, the contact diameter d is a function of the contact distance x, as

$$d(x)=d_1+\frac{d_2-d_1}{L}x \tag{3.88}$$

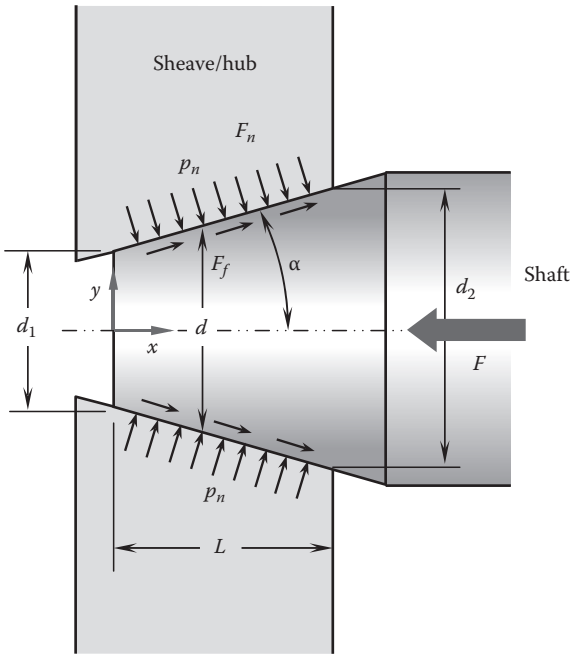

FIGURE 3.38
A tapered motor shaft against a sheave/hub.

The area of the contact surface between two components is thus

$$A = \pi \int_0^L d(x)\,dx = \pi \int_0^L \left(d_1 + \frac{d_2 - d_1}{L} \right) x dx = \frac{\pi L}{2}(d_1 + d_2) \tag{3.89}$$

With the normal contact pressure p_n applying on the interface of the tapered shaft and the sheave/hub, the force acting on the contact surface can be decomposed as the normal contact force F_n, which is perpendicular to the contact surface, and the friction force F_f, which is parallel to the contact surface. Since the two components are perfectly contacted each other, the contact pressure p_n is uniform on the interface, following that

$$F_n = \pi p_n \int_0^L d(x)\,dx = \pi p_n \int_0^L \left(d_1 + \frac{d_2 - d_1}{L} x \right) dx = \frac{\pi L p_n}{2}(d_1 + d_2) \tag{3.90a}$$

$$F_f = \mu F_n = \frac{\pi \mu L p_n}{2}(d_1 + d_2) \tag{3.90b}$$

where μ is the friction coefficient between two contact components.

At the equilibrium condition, all forces are balanced with each other, $\sum F = 0$. The axial pressing force F can be expressed as

$$F = p_n A(\sin\alpha + \mu \cos\alpha) \tag{3.91}$$

The torque transmitted by the shaft can be determined as

$$T = \int \frac{d}{2} \mu p_n \, dA = \frac{\mu}{2} \int_0^L \frac{\pi d^2 p_n}{\cos\alpha} dx = \frac{\pi \mu p_n L}{6 \cos\alpha} \left(d_1^2 + d_1 d_2 + d_2^2 \right) \tag{3.92}$$

In a similar manner, a governing equation for calculating the brake torque of a cone clutch was derived in Shigley's textbook [3.39]. By assuming uniform contact pressure, the brake torque can be expressed as

$$T = \frac{F_n \mu}{3 \sin\alpha} \frac{d_2^3 - d_1^3}{d_2^2 - d_1^2} \tag{3.93}$$

where

$$F_n = \frac{\pi p_n}{4} \left(d_2^2 - d_1^2 \right) \tag{3.94}$$

Combining Equations 3.93 and 3.94 yields

$$T = \frac{\pi \mu p_n}{12 \sin\alpha} \left(d_2^3 - d_1^3 \right) \tag{3.95}$$

Note that in Equation 3.92, the length of the tapered shaft L can be expressed as

$$L = \frac{d_2 - d_1}{2 \tan\alpha} \tag{3.96}$$

Substituting Equation 3.96 into 3.92, Equation 3.92 is identical to Equation 3.95.

However, there is a difference in force (or pressure) equation between two systems. By replacing L in Equation 3.90a with 3.96, it gives

$$F_n = \frac{\pi p_n}{4 \tan\alpha} \left(d_2^2 - d_1^2 \right) \tag{3.97}$$

Comparing Equations 3.97 and 3.94, it can be clearly seen that a factor of $1/\tan\alpha$ is missing in Equation 3.94 (Shirgley's equation). This indicates that Equation 3.94 is a special case of Equation 3.97 with $\tan\alpha = 1$ (i.e., $\alpha = 45°$). This has been confirmed by Keesee [3.40] by using an FEA analysis to calculate the contact pressure and contact force on the interface. The numerical results have shown good agreement with the data obtained from Equation 3.97.

3.8 Fatigue Failure under Alternative Loading

Rotating shafts are frequently subject to partial or complete reversing loads, resulting fatigue failure.

The fatigue stress concentration factor is defined as

$$K_f = \frac{\text{Maximum stress with discontinuity}}{\text{Nominal stress without discontinuity}} \tag{3.98}$$

The relationship between K_f and K_t is found as

$$K_f = 1 + q(K_t - 1) \tag{3.99}$$

where q is the notch sensitivity of a material and $0 \le q \le 1$. Thus, it gives that $1 \le K_f \le K_t$. If notch sensitivity data are not available, it is conservative to use K_t in fatigue calculations.

3.9 Shaft Manufacturing Methods

There are a variety of shaft manufacturing methods in manufacturing industries. None of the manufacturing methods is perfect. Each has its own set of advantages and disadvantages. The determination of the optimal manufacturing process depends on many factors, such as production efficiency, dimension accuracy, surface finishing, influence on part's strength, processing cycle, shaft material, shaft size, equipment availability, and cost.

3.9.1 Machined Shaft

A majority of motor shafts are manufactured by machining for high productivity, low cost, and easy tolerance control.

A machined shaft usually passes through a series of machining processes. As the shaft is machined from a raw material, in order to increase the productivity, it is typical to use a common lath first to quickly machine it to the dimensions that are close to its final dimensions. Then, use a precise machine such as a CNC to machine the shaft to the final dimensions. For some important sections, such as bearing journals, the shaft may go through a heat treatment and finally grinding it to the final dimensions.

During these processes, the shaft has to be machined on different machines. Therefore, holding the shaft's geometric tolerances such as roundness, cylindricity, runout, concentricity, and straightness is critical in obtaining satisfactory shaft balance and lowing motor vibration. As a matter of fact, this depends entirely on the success of the initial centering phase of the machining operation. The key is providing a good reference point for machining between centers.

In motor shaft manufacturing, endworking of shafts is often incorporated as a primary operation of a series of machining processes. Endworking can eliminate some secondary machining operations by combining them with initial end finishing, thereby increasing productivity and helping to decrease the part process scrap rate for subsequent operations [3.41].

Major benefits of the endworking process include the improved concentricity, roundness, and squareness of the machined surfaces. This greatly reduces the shaft runout. Practically, the more accurate shaft centers allow for more accurate dimension and position controlling, in favor of shortening the production cycle time and costs.

Endworking is conventionally used for centering and facing a shaft that is loaded on a lathe between centers in high-volume production of shafts. Presently, the endworking process is often performed by a CNC double-end machine to work on both shaft ends at the same time for achieving cost savings and high productivity.

3.9.2 Forged Shaft

Forging is a manufacturing process that has been extensively used in industries for producing high-strength and high-quality machine parts. In a forging process, under high pressure, a metal workpiece undergoes large plastic deformation, resulting in an appreciable change in shape or cross section. Unlike in a conventional machining process that the material grain is cut off, forging increases the strengths and toughness of metal by aligning the grain along the line of potential stress. Moreover, because of the enormous pressure involved during forging process, a forged part is denser in the bulk due to the reduction or elimination of porosities and voids. Thus, the forged shafts have higher strength-to-weight ratio and higher corrosion resistance. However, because of the high cost of forging tooling and required multiple steps, forging is generally more expensive than most manufacturing processes. Motor manufacturers often use medium-carbon steel to make forged motor shafts.

Several forging processes are available, including cold forging and hot forging. Cold forging is performed at room temperature and requires a very high forging pressure to overcome the deformation resistance of the material. This indicates that cold forging is limited to relative small shafts with simple geometries. Cold forging can achieve product features such as smooth surfaces, tight tolerances, concentric diameters, and beneficial grain flow. It offers significant cost-saving advantages as the result of the material saving. In contrast, hot forging is performed above the material recrystallization temperature and thus generates oxide scales on the forged shaft surface.

A method for forging a stepped shaft through a combination of forging operations has been reported recently [3.42]. The method includes providing a billet of a predetermined mass; heating the billet; cross-wedge rolling the billet to form an intermediate workpiece having a first cylindrical portion and a second cylindrical portion that are axially spaced apart by a neck that has a smaller diameter than the two portions; and performing at least one upset forging operation on the end of the intermediate workpiece to enlarge the first cylindrical portion such that in at least one location, its diameter is larger than a diameter of the billet and a diameter of any other shaft portion (Figure 3.39).

3.9.3 Welded Hollow Shaft

Motor weight can be very sensitive in some applications such as satellites and aircrafts. Motor designers always take tremendous efforts to reduce the machine weight and increase its torque density. One of the effective methods is to use hollow shafts to lower the shaft weights without affecting their functions and performances. In fact, a hollow motor shaft can not only reduce its weight and inertia but also provide a passage for a cooling fluid (air or liquid) passing through the shaft interior to cool the rotor.

Hollow shafts are often used in direct drive motors and vehicle motors that have large shaft diameters. Because of the larger diameter, a hollow shaft has a higher stiffness/mass ratio, a higher natural frequency, and lower deflection, compared with a solid shaft having the same mass.

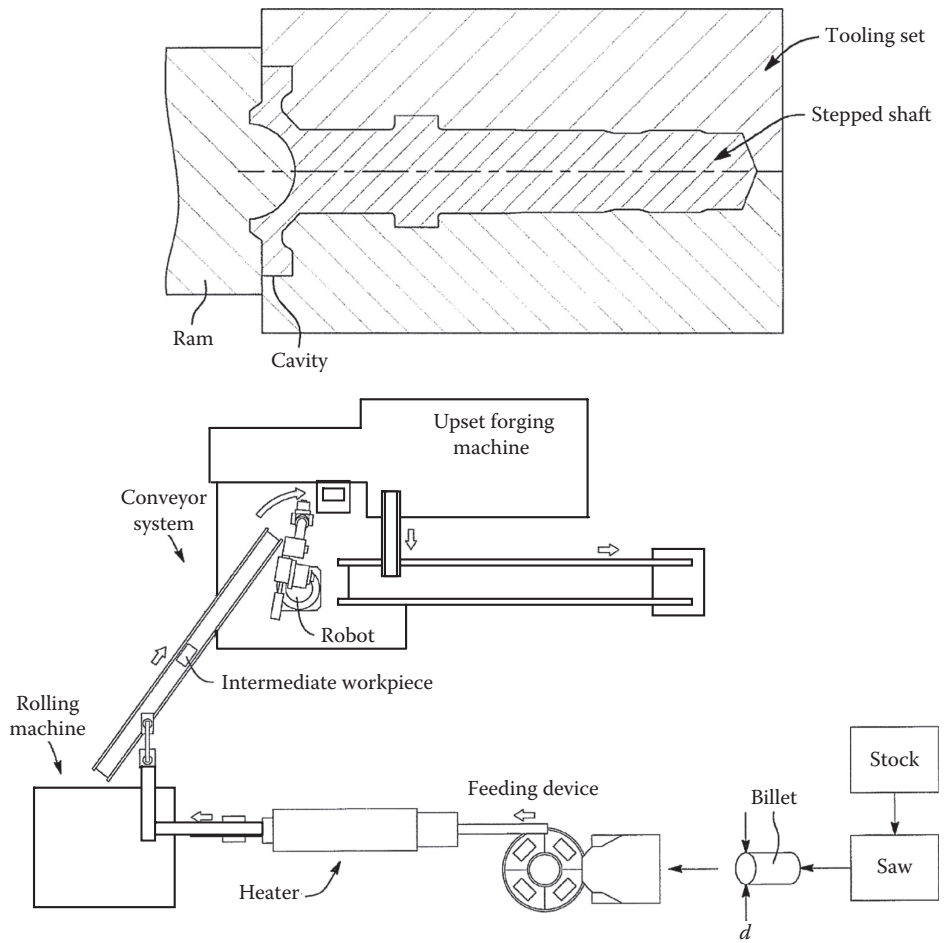

FIGURE 3.39
Fabrication system for producing forged stepped shafts (U.S. Patent 7,866,198) [3.42]. (Courtesy of the U.S. Patent and Trademark Office, Alexandria, VA.)

The fabrication of hollow shafts may involve several different manufacturing processes such as welding, machining, and casting. Among them, welding is the most cost-efficient way for making hollow shafts. Therefore, it requires that the shaft material has a good weldability.

The weldability of steel strongly depends on the chemical composition of steel, especially carbon. Higher quantities of carbon and other alloying elements result in a lower weldability. To quantitatively evaluate the influence of the contributions of the various alloying elements on the difficulties encountered in alloy welding, a concept of carbon equivalent (CE) is introduced in an effort to measure weldability with a single number. CE is an empirical value expressed in weight percent. Several empirical formulas are available in literature. One popular expression, which is recommended by the International Institute for Welding and most often used in ASME applications [3.43,3.44], is given in the following (all elements in mass percentage):

$$CE = C + \frac{Cr + Mo + V}{5} + \frac{Mn + Si}{6} + \frac{Ni + Cu}{15} \tag{3.100}$$

Another popular formula for predicting CE is known as Dearden and O'Neill formula, which is similar to (3.100) but without the Si term. Dearden and O'Neill [3.45] first proposed the CE to assess the weldability of alloy steels. Later, their formula was revised slightly by the International Institute of Welding (IIW).

A CE value of 0.30 or less is considered to be good for welding and no special precautions are required. For $0.30 < CE < 0.4$, modest preheat is necessary. Steel with a CE value in excess of about 0.5 cannot be easily welded because of their increased tendency to develop hydrogen-induced cracking in the heat-affected zone. Hence, welding of steel with a high CE value requires a special care for the preheat process. Figure 3.40 is an example of hollow shaft used in hybrid vehicles.

An alternative design of hollow shaft is presented in Figure 3.41. It can be seen that the hollow shaft is formed by integrating two shafts together with the rotor laminated core through the interference fitting. In order to ensure the firmness of the rotor assembly, welding is used between shaft 1 and the rotor core.

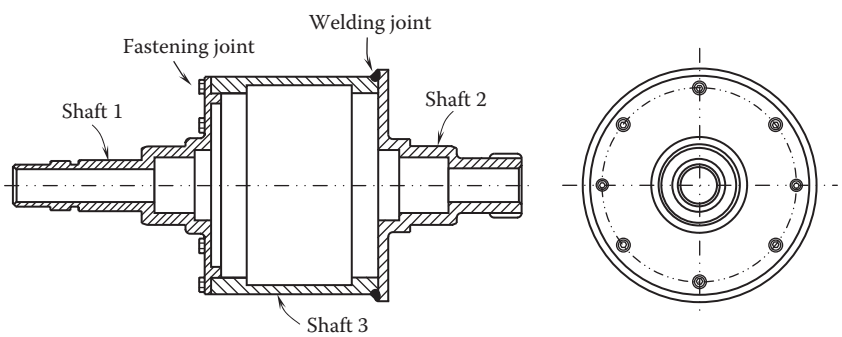

FIGURE 3.40
Three-piece hollow shaft design using fastening and welding joint methods.

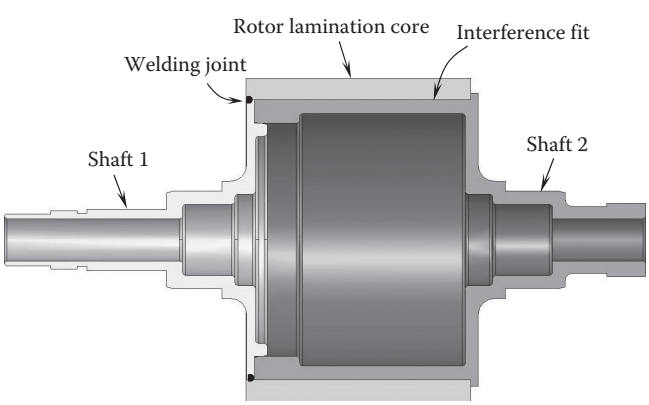

FIGURE 3.41
Alternative hollow shaft design: two shafts are integrated together with the rotor lamination core.

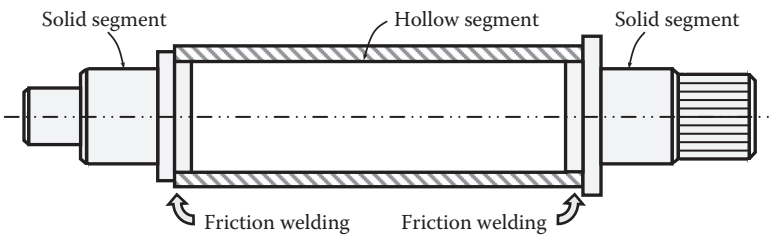

FIGURE 3.42
Hollow shaft fabricated by friction welding technology.

A hollow shaft can be also fabricated by utilizing the friction welding technology. Friction welding is a melt-free process that generates heat through mechanical friction between a rotating and a stationary component. Because there is no melt involved, this processing method is not a truly welding process in the traditional sense but more like a forging process. One of the advantages of this technology is to allow different materials to be joined together, such as aluminum and steel and stainless steel and carbon steel. A hollow shaft generally consists of three segments: two solid segments and one pipe segment. Two solid segments are friction welded to both ends of the center pipe segment (Figure 3.42). The formed shaft is then machined to its final dimensions. With this manufacturing technique, the hollow shafts can achieve up to 50% or more weight reduction compared to the similar solid shafts.

3.9.4 Shaft Measurement

Confirming that manufactured shafts meet all requirements requires validating shaft hardness, geometric dimensions and tolerances, and other items. Figure 3.43 shows a coordinate measurement machine (CMM) that is used to measure the geometric dimensions and other characteristics of shafts. The CMM is composed of three axes, that is, *X*, *Y*, and *Z*, forming a regular 3D coordinate system. In a measurement, the shaft is put on a pair of *V*-shaped stands on the table, which is defined as the *X*–*Y* plane. Measurements are executed using a probe attached to the movable third axis, that is, *Z*-axis. As the probe touches the shaft surface, the CMM takes readings in six degrees of freedom. In such a way, a measuring point is generated with its three coordinates (*X*, *Y*, and *Z*). All collected points are analyzed via regression algorithms for the shaft constructive features. Usually, dimensional measurement capabilities of a CMM include position, perpendicularity, parallelism, angularity, profile of a surface, profile of a line, straightness, flatness, circularity, cylindricity, symmetry, concentricity, and total/circular runout.

3.10 Shaft Misalignment between Motor and Driven Machine

Shaft alignment has a strong impact on motor and driven machine operation and performance. Shaft misalignment, occurring as the centerlines of the motor and the driven machine shafts are not in line with each other, can result in excessive vibration, noise, and

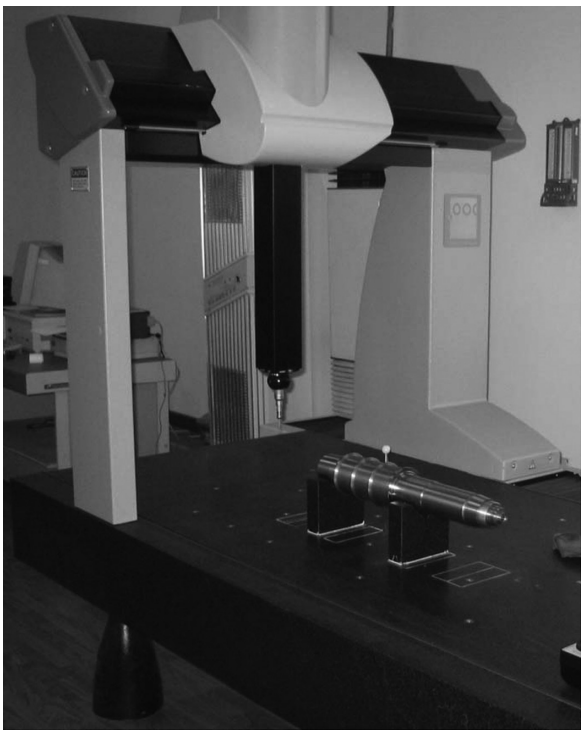

FIGURE 3.43
A coordinate measurement machine for measuring shaft geometric dimensions.

additional loads in motor and driven machine components, such as coupling, bearings, seals, shafts, and other machine components. It can lead to premature wear or even catastrophic failure of these components.

3.10.1 Types of Misalignment

Because the motor and driven machine are in 3D space, the misalignments between their shafts can exist in any direction. In actual applications, it is most convenient to break up this 3D space into the horizontal and vertical planes. As demonstrated in Figure 3.44, there are basically two types of motor misalignment:

- Angular misalignment can be further divided into the horizontal and vertical angular misalignments. Both of the misalignments occur when a motor is set at an angle to the driven machine in the horizontal or vertical direction, or both. It can be seen that from Figure 3.44a, as the centerlines of the shafts of the motor and driven machine are extended, the two centerlines cross each other with an angle. Angular misalignment can cause severe damage to motors and driven machines.
- Axial misalignment occurs when a motor has an axial distance with its mating machine (Figure 3.44b). This type of misalignment, sometimes referred to as *shaft end float*, often results from the dimensional variations due to the thermal expansion/contraction of the shafts. In practice, axial misalignment is easily measured and corrected compared to angular misalignment.

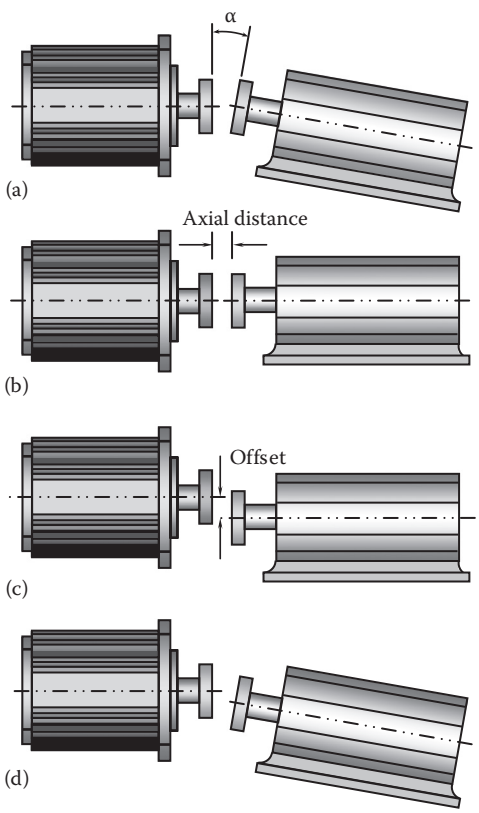

FIGURE 3.44
Misalignment of the motor shaft with the shaft of driven machine: (a) angular misalignment, (b) axial misalignment, (c) parallel misalignment, and (d) combination of angular, axial, and parallel misalignments. Only vertical misalignments are presented in this figure. Horizontal misalignments are in the similar manner.

- Similar to angular misalignment, parallel misalignment can be further divided into horizontal and vertical parallel misalignments. These two misalignments occur when the two shaft centerlines are parallel do not line up either horizontally or vertically or both (Figure 3.44c). Parallel misalignment may be resulted from manufacturing processes such as improper tolerances and shaft runouts, as well as poor installation practices.
- In practice, angular, axial, and parallel misalignments may occur simultaneously, as shown in Figure 3.44d.

3.10.2 Correction of Shaft Misalignment

Misalignments have long been recognized as one of the leading causes of electric machine damage and have been responsible for huge economic losses. In order to achieve best results in correcting shaft misalignment, it must take into account the machine sizes, shaft geometries, coupling type and condition, rotating speed, and operating temperature of both the motor and driven machine.

During motor normal operation, the alignment condition may change as the results of variations in a number of operating characteristics, such as operating temperature, transmitted torque, load, coupling, bearing play, and mounting conditions of both the motor and driven machine. Therefore, it is highly desired to measure motor-driving machine alignments under actual operating conditions (sometimes referred to as dynamic alignments).

There are good practices for measuring and correcting shaft misalignments [3.46]. The first step is to check alignments using appropriate tools. Modern laser alignment systems have been developed since the 1980s. Today, laser alignment becomes an essential component of a viable maintenance strategy for rotating machines. One of the notable features of laser alignment systems is their capability of performing real-time measurements to monitor the changes in machine's alignments.

As the misalignments have been detected, the next step is to follow suitable procedures to correct them. Soft foot is one of the most prevalent conditions found in shaft misalignments. Some laser alignment tools have a soft foot operation capability that guides engineers through the correction procedure. In practice, a set of precision shims is often used to bring the machines back into both vertical and horizontal alignment [3.47].

3.11 Shaft Coupling

The term coupling refers to a device that is used to connect two shafts together at their ends. The primary function of a motor coupling is to transmit torque or power from a motor shaft to the shaft of the driven machine. According to the connection pattern and relative motion, motor couplings can be briefly classified as rigid and flexible couplings.

3.11.1 Rigid and Semirigid Couplings

Rigid couplings are designed to draw two shafts together tightly so that no relative motion can occur between them. Rigid couplings are only applicable when the alignment of the two shafts can be maintained very accurately during motor operation lifetime. This type of coupling does not compensate for any misalignment between a motor and a driven equipment. If there is any significant angular, radial, or axial misalignment between them, additional loads (either bending moment, or tensional or axial stress) will be applied on the shafts of the motor and the driven equipment, as well as the coupling itself. The effects of these loads include premature bearing, seal or coupling failures, shaft cracking and breaking, and excessive radial and axial vibrations.

One of the most commonly used rigid couplings is a flange coupling, as shown in Figure 3.45. The motor shaft and the driven machine shaft are connected tightly through two flanges using bolt fasteners. Thus, in addition to tensile forces, the bolts are also subject to shear forces. This type of coupling uses a sleeve to align the two shafts.

A semirigid coupling is shown in Figure 3.46. This coupling is similar to the previous one, but there is no common sleeve shared between two shafts. As shown in the figure, the motor shaft and driven machine shaft are firmly assembled together with their hubs/flanges respectively. Each flange is bolted with a ring-shaped annular element which is securely fixed on the outer surface of the split tube. To avoid distortions of the split tubes under loads, the split tubes are supported internally with two reinforcing half-rings.

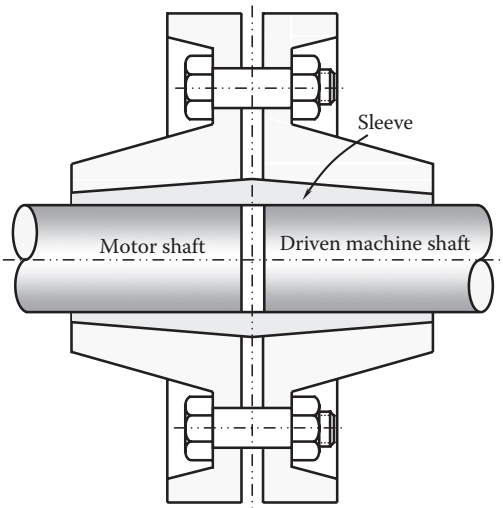

FIGURE 3.45
Flange rigid coupling. The sleeve is for aligning two shafts.

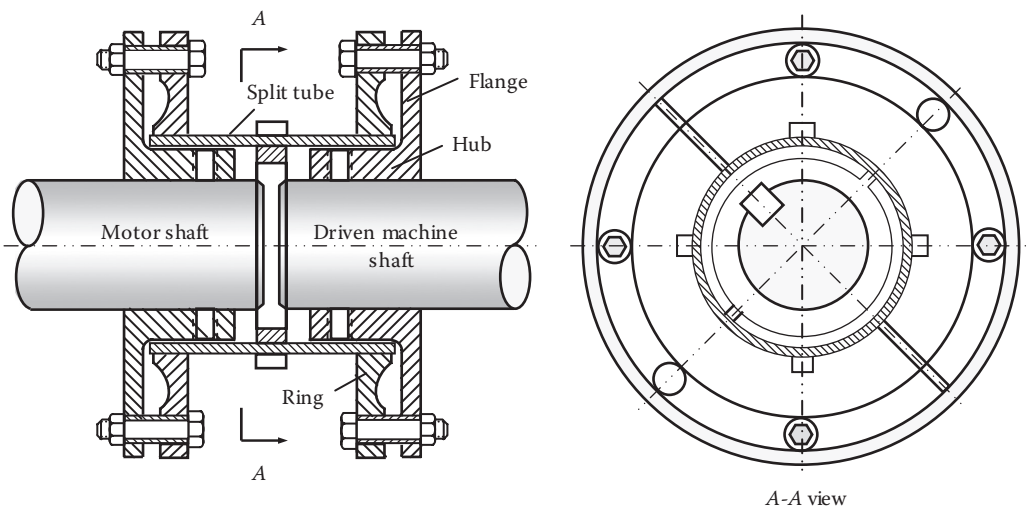

FIGURE 3.46
Semirigid coupling used in torque/power transmission. The motor shaft and driven machine shaft are indirectly connected together through two ring-shaped annular elements and split tubes for gaining a certain degree of flexibility.

This type of coupling can provide a certain degree of freedom to accommodate a small misalignment between two shafts.

In order to further increase the coupling flexibility, the two ring-shaped annular elements may be made of flexible elastomeric materials such as polyurethane elastomer, as suggested by Zilberman et al. [3.48]. However, one of the unfortunate consequences of increasing the coupling flexibility is a corresponding reduction in torque transmission

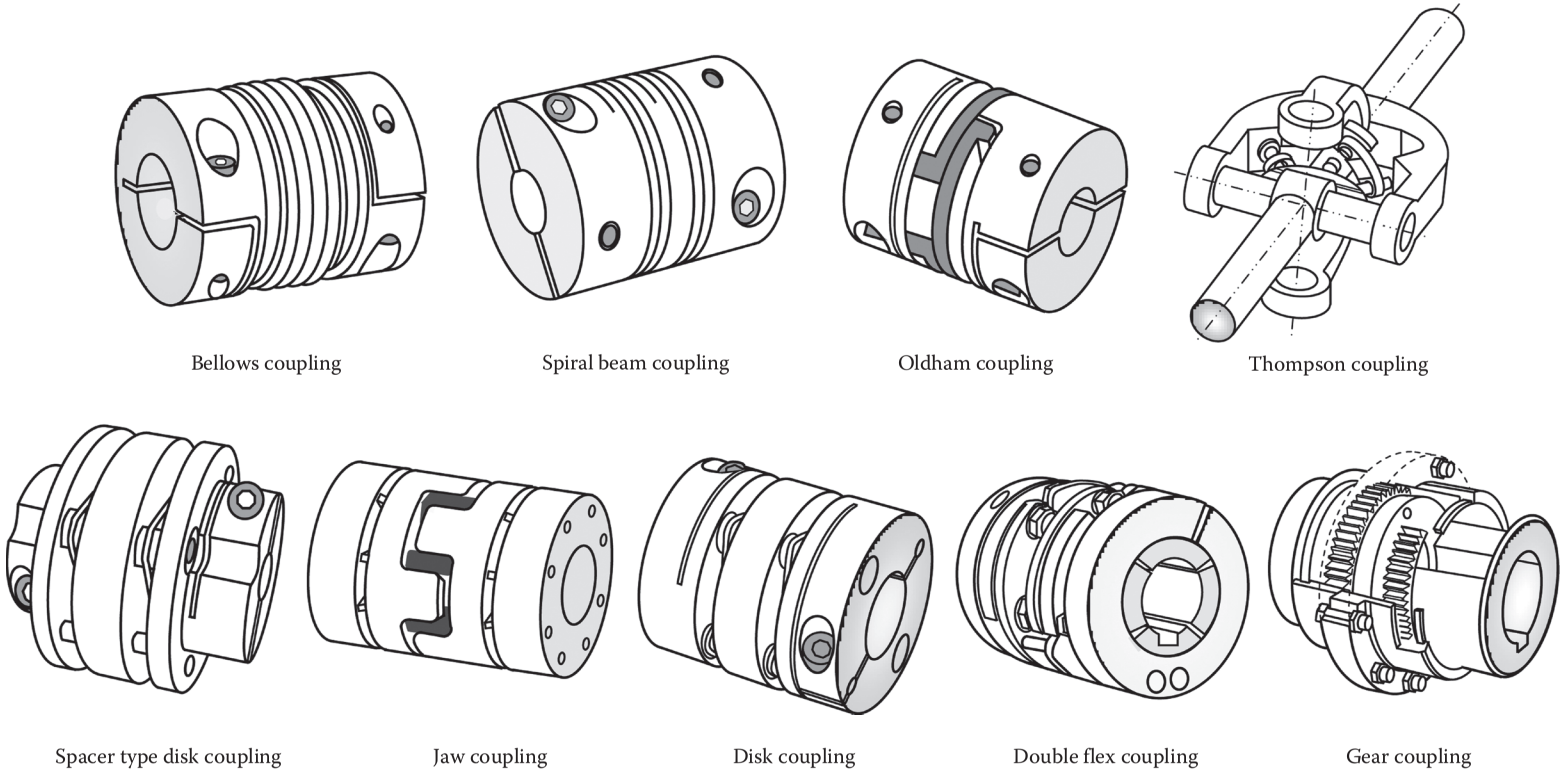

FIGURE 3.47
A variety of flexible couplings used in motor applications.

reliability. This indicates that such couplings may be restricted to use in relatively low-torque transmission applications.

3.11.2 Flexible Couplings

Flexible couplings are designed to transmit motor torque smoothly while accommodating minor misalignment in the axial, radial, or angular directions. The flexibility is such that when misalignments do occur, the coupling components move with little resistance. It is noted that with today's technology, flexible couplings are designed to tolerate more misalignments.

A large variety of flexible coupling types are available, as displayed in Figure 3.47. Each of them has its special features and is suitable for particular applications. Motor engineers need to trade-off their strengths and limitations to correctly select the coupling for the particular application.

References

[3.1] AK Steel Corporation. 2013. 304/304L stainless steel. Product data bulletin. http://www.aksteel.com/pdf/markets_products/stainless/austenitic/304_304L_Data_Bulletin.pdf.

[3.2] CRP Technology. Aluminum 7075-T6; 7075-T651. http://www.crptechnology.com/sito/images/PDF/Aluminum7075-T6-7075-T651.pdf.

[3.3] PT Tech. Specialized clutches and brakes for heavy industry. http://www.pttech.com/images/company_assets/AA63FEEA-0BF3-4414-88E1-FD86F132AE9C/PTTechSpecializedClutchesBrakesb320_4a3a.PDF.

[3.4] Rostom, F. R. S. 2008. *Computer Analysis and Reinforced Concrete Design of Beams*. Fadzter Media. http://www.fadzter.com/engineering/downloads/Fadz_BeamDoc.pdf.

[3.5] Richmond, E. L. and Feng, R. H. 1953. Graphical methods for determining beam deflections. *Machine Design*, September Issue, pp. 177–183.

[3.6] Budynas, R. G. and Nisbett, J. K. 2008. *Shigley's Mechanical Engineering Design*, 8th edn. McGraw-Hill, Boston, MA.

[3.7] Ugural, A. C. 1991. *Mechanics of Materials*. McGraw-Hill, New York.

[3.8] Norton, R. L. 2000. *Machine Design: An Integrated Approach*, 4th edn. Prentice-Hall, Boston, MA.

[3.9] Central Machine Tool Institute. 1985. *Machine Tool Design Handbook*. Tata McGraw-Hill, New Delhi, India.

[3.10] Ng, A. 2000. Better shafts for better linear motion performance. *Motion System Design*. http://machinedesign.com/linear-motion/better-shafts-better-linear-motion-performance.

[3.11] Kosec, B., Karpe, B., Budak, I., Ličen, M., Đorđević, M., Nagode, A., and Kosec, G. 2012. Efficiency and quality of inductive heating and quenching planetary shafts. *Metalurgija* **51(2012)**: 71–74.

[3.12] Hauser, G., Curiel, G. J., Bellin, H.-W., Cnossen, H. J., Hofmann, J., Kastelein, J., Partington, E., Peltier, Y., and Timperley, A. W. 2004. Hygienic equipment design criteria. Doc 8, 2nd edn. European Hygienic Engineering and Design Group (EHEDG), Frankfurt, Germany. http://www.ehedg.org/uploads/DOC_08_E_2004.pdf.

[3.13] Hendricks, R. C., Braun, M. J., Canacci, V., and Mullen, R. L. 1991. Brush seals in vehicle tribology (Section IX). In *Vehicle Tribology* (Eds.: D. Dowson, C. M. Taylor, and M. Godet). Elsevier Science Publishers, pp. 231–242.

[3.14] Parker Hannifin Corporation. 2007. *Parker O-ring Handbook*. ORD 5700. http://www.parker.com/literature/ORD 5700Parker_O-Ring_Handbook.pdf.
[3.15] R. L. Hudson & Company. 2008. *O-Ring Design & Material Guide*. http://www.rlhudson.com/O-RingBook/opening.html.
[3.16] Simrit. 2011. *Radial Shaft Seal Technical Manual*. Publication no. 4100. http://www.simritna.com/news/brochures/RSSTechManual.pdf.
[3.17] Tong, W. and Zhuo, Z. Q. 2002. Heat-resistant magnetic silicone rubber brush seal in turbomachinery and methods of application. U.S. Patent 6,390,476.
[3.18] Parker Hannifin Corporation. 2011. *PTFE Seal Design Guide*. http://www.parker.com/literature/Packing/Packing-Literature/Catalog_PTFE-Seals_PDE3354-GB_1103.pdf.
[3.19] Bode, R. 2012. Labyrinth seal and method for producing a labyrinth seal. U.S. Patent Application 2012/0228830.
[3.20] Lattime, S. B., Dillon, K. M., Borowski, R., Trntman, R., Brister, S. E., Meadows, C. F., Hupp, B. M., and Toth, D. G. 2013. Non-contact labyrinth seal assembly and method of construction thereof. U.S. Patent 8,342,535.
[3.21] Benckert, H. and Wachter, J. 1980. Flow induced spring coefficient of labyrinth seals for applications in turbomachinery. NASA CP2133. Texas A&M University, College Station, TX, pp. 189–212.
[3.22] Pilkey, W. D. and Pilkey, D. F. 2008. *Peterson's Stress Concentration Factors*, 3rd edn. John Wiley & Sons, Hoboken, NJ.
[3.23] Ugural, A. C. 2004. *Mechanical Design: An Integrated Approach*. McGraw-Hill, Boston, MA.
[3.24] Peterson, R. E. 1974. *Stress Concentration Factors*. John Wiley & Sons, New York.
[3.25] Calistrat, M. M. and Calistrat, A. B. 1994. *Flexible Couplings: Their Design, Selection and Use*. Caroline Publishing, Houston, TX.
[3.26] Filon, L. N. G. 1900. On the resistance to torsion of certain forms of shafting, with special reference to the effect of keyways. *Philosophical Transactions of the Royal Society of London, Series A* **193**: 309–352.
[3.27] Peterson, R. E. 1933. Stress concentration phenomena in fatigue of metals. *Journal of Applied Mechanics* **1**(**4**): 157–171.
[3.28] Hetényi, M. 1939. The application of hardening resins in three-dimensional photoelastic studies. *Journal of Applied Physics* **10**(**5**): 295–300.
[3.29] Leven, M. M. 1949. Stresses in keyways by photoelastic methods and comparison with numerical solution. *Proceedings of the Society for Experimental Stress Analysis* **7**(**2**): 141–154.
[3.30] Peterson, R. E. 1953. *Stress Concentration Design Factors*. John Wiley & Sons, New York.
[3.31] Nisida, M. 1963. New photoelastic methods for torsion problems. *Proceedings of International Symposium on Photoelasticity* (Ed.: M. M. Frocht). Pergamon, New York, pp. 109–121.
[3.32] Okubo, H., Hosono, K., and Sakaki, K. 1968. The stress concentration in keyways when torque is transmitted through keys. *Experimental Mechanics* **8**(**8**): 375–380.
[3.33] Fessler, H., Rogers, C. C., and Staley, P. 1969. Stresses at end-milled keyways in plain shafts subjected to tension, bending and torsion. *The Journal of Strain Analysis for Engineering Design* **4**(**3**): 180–189.
[3.34] Orthwein, W. C. 1975. Keyway stress when torsional loading is applied by the keys. *Experimental Mechanics* **15**(**6**): 245–248.
[3.35] Pedersen, N. L. 2010. Stress concentration in keyways and optimization of keyway design. *The Journal of Strain Analysis for Engineering Design* **45**(**8**): 593–604.
[3.36] Eliaz, N., Shachar, A., Tal, B., and Eliezer, D. 2002. Characteristics of hydrogen embrittlement, stress corrosion cracking and tempered martensite embrittlement in high-strength steels. *Engineering Failure Analysis* **9(2002)**: 167-184.
[3.37] Okubo, H. 1950. Torsion on a circular shaft with a number of longitudinal notches. *Transactions of ASME, Applied Mechanics Section* **72**: 359.
[3.38] Yoshitake, H. 1962. Photoelastic stress analysis of the spline shaft. *Bulletin of Japanese Society of Mechanical Engineering* **5**(**17**): 195–201.

[3.39] Budynas, R. G. and Nisbett, J. K. 2008. *Shigley's Mechanical Engineering Design*, 8th edn. McGraw-Hill, Boston, MA, pp. 834–835.
[3.40] Keesee, J. 2010. Shaft taper analysis—Peer review. Kollmorgen Corporation.
[3.41] Felix, C. 2008. Endworking enhances shaft manufacturing process. *Production Machining Magazine*. September Issue. http://www.productionmachining.com/articles/endworking-enhances-shaft-manufacturing-process.
[3.42] Chilson, T. R., Khetawat, M. P., and Pale, J. A. 2011. Method of producing a stepped shaft. U.S. Patent 7,866,198.
[3.43] ISO/TR 17671-2:2002 (EN 1011-2). 2002. Welding—Recommendations for welding of metallic materials—Part 2: Welding of ferritic steels.
[3.44] Yurioka, N. 2004. Comparison of preheat predictive methods (Report III). IIW Doc. IX-2135-04.
[3.45] Dearden, J. and O'Neill, H. 1940. A guide to the selection and welding of low-alloy structural steels. *Transactions of the Institute of Welding* (UK) **3**: 203–214.
[3.46] Piotrowski, J. 1995. *Shaft Alignment Handbook*, 2nd edn. CRC Press, Boca Raton, FL.
[3.47] Michalicka, P. 2010. Correcting shaft misalignment: three steps to smooth production. *Engineering and Mining Journal* **211(7)**: 82–84.
[3.48] Zilberman, J., Munyon, R. E. and Meier, W. R. 2003. Split spool type flexible coupling. U.S. Patent 6,508,714.

4

Stator Design

The stator is usually the outer body (or the inner body in some special cases) of an electric motor to house the driven windings on a laminated steel core for creating a rotating magnetic field. The stator core is made up of a stack of prepunched laminations assembled into a motor housing that is made of aluminum or cast iron or no separate housing designs. The inner surface of the stator is made up of a number of deep slots or grooves, distributed either uniformly or nonuniformly in the circumferential direction. It is into these slots that the stator windings are positioned. The arrangement of the windings within the stator determines the number of poles that the motor has.

4.1 Stator Lamination

The considerations in lamination design include the selection of the lamination material, optimization of the lamination stamping/cutting process, and determination of the lamination profile and pattern, dimension tolerances, core losses, grain orientation, unique shape requirements, and, of course, lamination manufacturing costs.

4.1.1 State Lamination Material

In practice, the base lamination material used for stators is fundamentally the same for rotors when it is desirable to punch the stator and rotor laminations simultaneously with the same die. However, some differences may exist between these two applications: (1) Because the main function of a stator is to generate a rotating magnetic field, the lamination material of the stator has higher requirements for electromagnetic properties. (2) Unlike a rotor that is subject to large centrifugal forces as it rotates, the forces acting on the stator are much lower, leading to lower requirements for mechanical strength properties. Based on these reasons, segmented cores are extensively used in stators for all types of motors but are restricted from use in high-speed rotors due to high centrifugal forces.

4.1.2 Stator Lamination Patterns

One of the factors that affect the efficiency of electric motors is the ability of steel laminations used in the stator to carry magnetic flux. There are several lamination patterns available for either enhancing the magnetic flux or simplifying the manufacturing processes, or both, depending on different applications.

4.1.2.1 One-Piece Lamination

Stators and rotors of electric machines are usually manufactured using a stack of one-piece laminations, made by punching the desired pattern from large insulated sheets of steel.

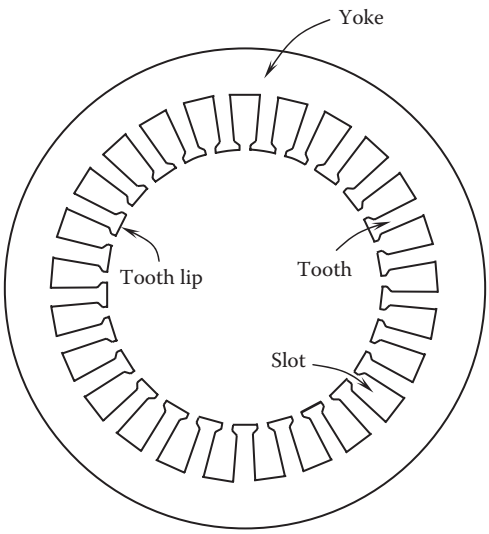

FIGURE 4.1
One-piece lamination is made by an undivided piece of steel sheet in full revolution. Stator slots are for receiving stator windings.

One-piece lamination is fabricated from an undivided piece of steel sheet and continuous in the 360° circumference, as shown in Figure 4.1. Obviously, the one-piece lamination method offers the advantage of fabrication and assembly simplicity. Multiple pieces are always used over the stator circumference and will be discussed in the following sections.

As illustrated in the figure, a one-piece lamination contains a number of teeth facing inward and connecting with the yoke. Slots are formed between adjacent teeth for receiving stator windings. The tooth tips, as well as the insulation sleeves or wedges, help keep the stator windings inside the slots. Tooth tips also have many electromagnetic functions.

4.1.2.2 T-Shaped Segmented Lamination

Segmented stator laminations are frequently encountered in large-size motors (Figure 4.2) wherein stamping one-piece laminations is no longer practical, either due to the limitation of the capability of stamping machines or due to the incredible high costs. For such cases, segmented laminations are the best choice for the stator core fabrication.

The recent trend toward using segmented laminations in small motors is a means to not only increase the slot-filling rate and facilitate automated fabrication of electric motors

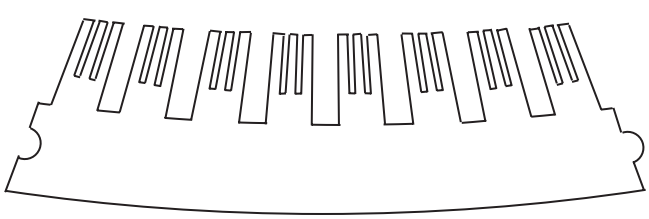

FIGURE 4.2
A segmented stator lamination containing a number of teeth for a large-size motor. The wide radial slots are used for receiving stator windings and the narrow radial slots for reducing eddy-current losses.

but also increase the continuous torque (well designed segmented lamination stators may increase motor torque by up to 50% over conventional motors). The segmented lamination technology is probably best suited to electric machines where the size of the effective air gap is insensitive to small variations, as in PM machines. It has been developed for high power density, cost-effective modern motors with better heat transfer within small overall packages, offering some benefits over traditional one-piece lamination stator cores [4.1,4.2]:

- The segmented design lowers the requirements for stamping machines and thus reduces both the machine and tooling costs. However, handling and assembly costs of the larger number of pieces to assemble increase or require automation tooling.
- The adoption of the segmented lamination technology can make a full use of the lamination material for significantly reducing the material consumption and material cost.
- Because each lamination section can be machine wound it allows placing more copper wires in stator slots. Generally, segmented lamination stators allow for 20%–30% higher slot-filling rate. This makes it able to use a larger diameter copper wire to fabricate the stator windings, thereby reducing the I^2R power loss.
- The segmented type stator may significantly increase in continuous motor torque over conventional integral type stator.
- The segmented lamination technology and single-tooth windings enable a motor to have significantly shortened end turns. This feature allows the motor to be much shorter, comparing with the long end turns found in conventionally random-wound servomotors.
- In manufacturing segmented stator coils, there are more choices in coil insertion methods. Many innovative ideas have been awarded patents over the past decade.
- Eddy-current loss is lowered due to the restriction of eddy-current paths. Thus, it could increase the motor efficiency. However, there are increases in electromagnetic ampere-turn drops due to the increase in mechanical gaps that can also reduce the total performance gain.
- T-shaped or I-shaped segmented laminations allow forming stator cores with different diameters to greatly save the tooling costs on very large motors. Again, one has to factor in the increase part handling and possible automation costs if employed on small motors.
- By taking advantages of the permeability of a grain-oriented material, the motor performance is correspondingly enhanced.

However, the adoption of the segmented core structure in electric machines comes with a penalty of increased core losses at the segment joints due to several factors, such as the degraded material conditions, the increased amount of punched edges with induced residual stress, and the effect of compressive stress applied on segmented stator cores. Furthermore, a potential cause of increased core losses may result from the increase in eddy current losses at the edge-to-edge butt joints [4.1]. Punching electrical steel drastically alters its magnetic properties near the cutting edges, resulting in the increase in core losses in two different ways [4.3]:

1. In a direct way, the cutting process creates residual stresses in the laminations at the vicinities of the cut edges, which can significantly increase the hysteresis losses and hence the total core losses at these locations.

2. In an indirect way, cutting can alter the magnetization profile inside the lamination. Due to the permeability drop, the polarization obtained with a given excitation is significantly reduced at the cut edge. Hence, in order to have the same flux across the sample (i.e., the same average polarization), a higher polarization in the bulk of the lamination is required. This higher polarization induces higher total losses.

Moses et al. [4.4] found that for a T-joint transformer core, the inner edges of the yoke and limb laminations are the highest power loss areas, up to 30% higher than the mean core loss. The third circulating harmonics causes additional losses calculated to be 20% of the nominal core loss [4.5].

Segmented laminations are made by punching one or several lamination teeth as an individually segmented piece. To save the tooling cost, all segmented laminations are usually designed to have an identical shape. As illustrated in Figure 4.3, T-shaped segmented laminations are jointed together by interlocking convex and concave portions to form a complete piece of a lamination. As all segmented lamination pieces are put into positions, the geometric pattern and magnetic circuit are approximately the same as for one-piece laminations. To enhance the motor performance, the grain orientation is arranged in the radial direction on all T-shaped segmented laminations.

A grain-oriented material has a superior performance in respect of less saturation and lower losses in the direction of the grain orientation. For this material, both core loss and permeability vary markedly, depending on the direction of the magnetic flux relative to the material rolling direction. To further take the advantage of the permeability and core loss of the grain-oriented material, it is to split the T-shaped segmented lamination into two pieces, as shown in Figure 4.4. Thus, by arranging the grain orientation in the radial direction on the tooth piece and in the circumstantial direction on the yoke piece, the stator performance is maximized.

A large number of patents are available on the segmented lamination design. Similar to the design in Figure 4.3, an innovative design that was awarded as a US patent [4.6] is presented in Figure 4.5. The lamination pieces are secured by means of the curved arc mating surfaces. A patented design is illustrated in Figure 4.6 [4.7], where both the teeth and yoke are made by segmented pieces. In Figure 4.7, the stator core consists of segmented large and small components, arranged alternately. Each stator slot is formed between a large and a small component, forming nonuniform slots in the circumference of the stator. It has been reported [4.8] that the periodicity of the cogging torque waveform for the motor with nonuniformly distributed slots is half that for the motor with uniformly distributed slots. However, the amplitude of the cogging torque is increased significantly due to the fact

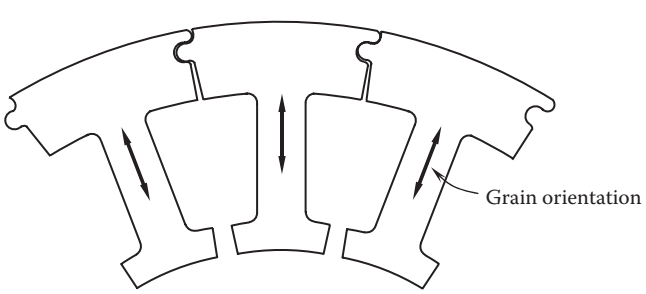

FIGURE 4.3
Segmented stator laminations, jointed with interlocking convex and concave portions.

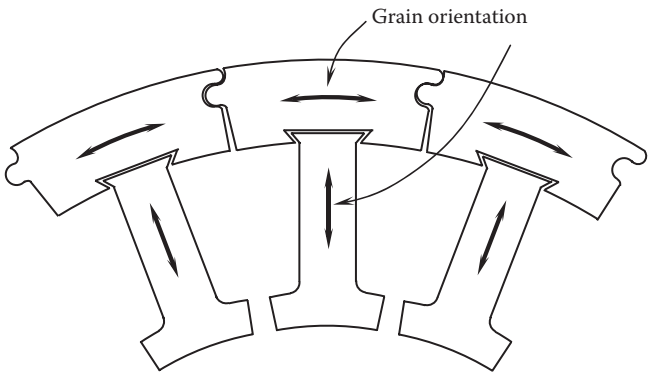

FIGURE 4.4
Grain-oriented segmented laminations.

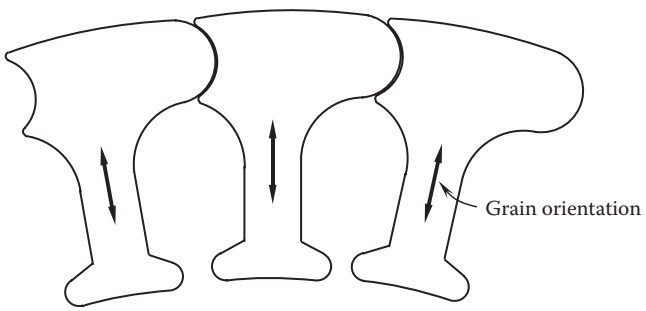

FIGURE 4.5
Patented segmented stator laminations with curved arc mating surfaces (U.S. Patent 5,212,419) [4.6]. (Courtesy of the U.S. Patent and Trademark Office, Alexandria, VA.)

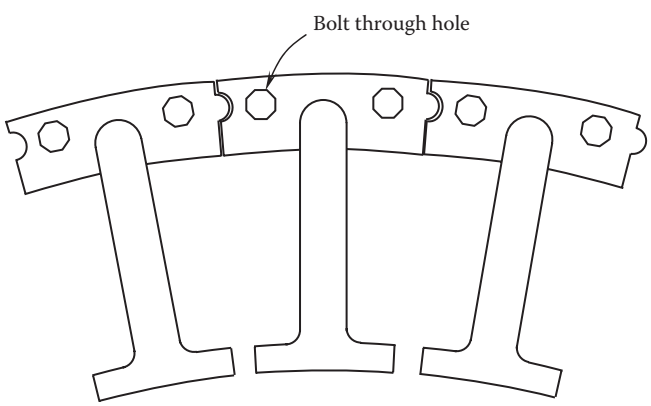

FIGURE 4.6
Patented segmented stator laminations in which both the tooth and yoke are segmented (U.S. Patent 7,816,830) [4.7]. (Courtesy of the U.S. Patent and Trademark Office, Alexandria, VA.)

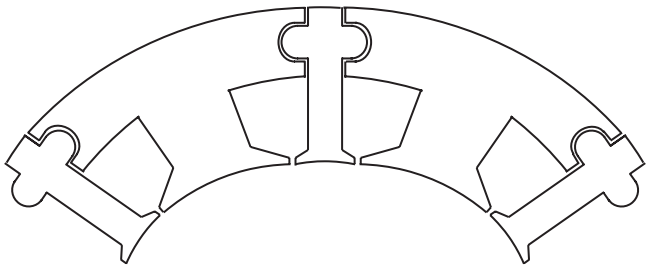

FIGURE 4.7
Alternative segmented stator laminations, showing each stator slot is formed between a large and a small segmented piece.

that the tooth tips of the wider teeth are approximately equal to the pole pitch in order to maximize the flux linkage per coil.

4.1.2.3 Connected Segmented Lamination

In order to increase the productivity of segmented laminations, the manufacturing process shown in Figure 4.3 can be improved. In this new process, instead of stamping individual segmented laminations, a long string of lamination pieces may be continuously stamped. These lamination pieces are connected together at the lamination outer tips (Figure 4.8). Then, these pieces are easy to roll together to form a complete lamination.

An alternative design of punched segmented laminations that connected together at the outer tips of the laminations is shown in Figure 4.9. The laminations are fabricated by stamping steel sheets in a progressive die. To reduce the bending force, circular edges and large semicircles are arranged at the tips of each lamination [4.9].

4.1.2.4 Two-Section Stator Lamination

In this design, a stator lamination is integrated by two lamination pieces: a section of teeth and a section of yoke (Figure 4.10). The stator windings are wound on the section of teeth. When all windings get in their positions, the section of yoke covers at the outer surface of the section of teeth, for housing the stator windings [4.10]. The section of teeth is positioned in the concave slots that are made at the yoke inner surface.

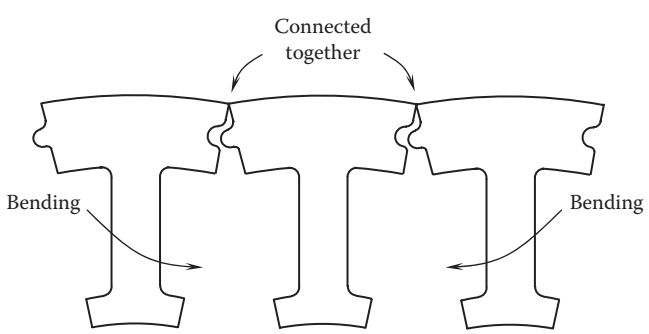

FIGURE 4.8
Punched segmented laminations are connected together at the outer tips of the laminations.

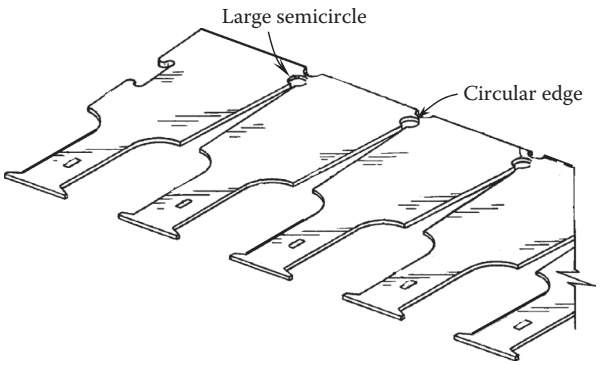

FIGURE 4.9
An alternative design of punched segmented laminations that connected together at the outer tips of the laminations (U.S. Patent 7,062,841) [4.9]. (Courtesy of the U.S. Patent and Trademark Office, Alexandria, VA.)

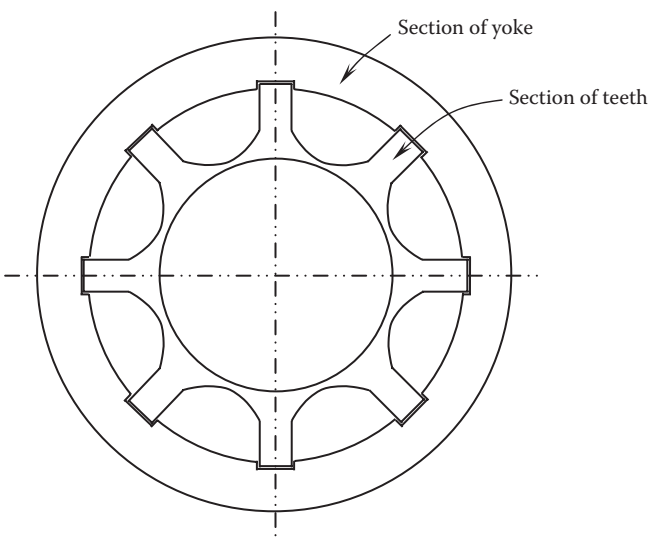

FIGURE 4.10
Integrated stator core with a section of teeth and a section of yoke; the section of teeth is positioned in the concave slots at the yoke inner surface.

For this design, the use of nonoriented materials, in which the magnetic properties are primarily the same in all directions, is more appropriate.

4.1.2.5 Stator Lamination Integrated by Individual Teeth and a Yoke Section

An alternative design of segmented laminated core is presented in Figure 4.11. It can be seen that all teeth are no longer connected together. Each tooth is individually positioned in the concave slot made at the inner surface of the yoke. Thus, this design can use the grain-oriented material to make the teeth, arranging the grain orientation in the radial direction.

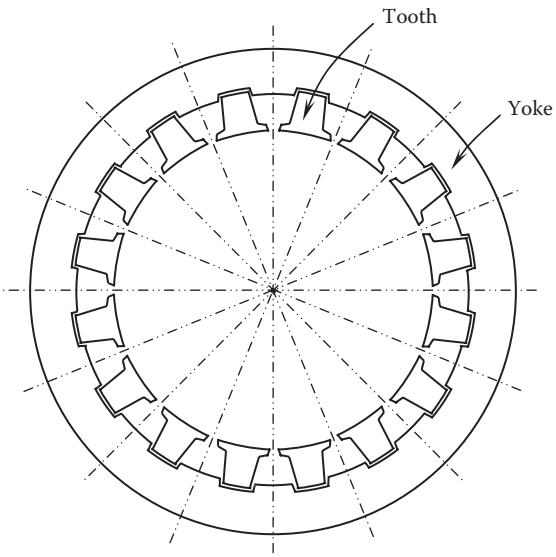

FIGURE 4.11
Integrated stator core with individual teeth and yoke; the teeth are positioned in the concave slots on the inner surface of the yoke.

The segmented lamination design in Figure 4.12 is similar to that in Figure 4.11 but with the opposite orientation of the yoke and the teeth. As a novel PM motor, the teeth are put outer forward and the yoke is located in the inner of the stator core [4.11]. In the assembly process, the sheets for a tooth are glued together to form a component, which are then glued onto the stator yoke (Figure 4.13). Rectangular-shaped concentrated fractional-pitch windings are inserted in the stator slots.

4.1.2.6 Slotless Stator Core

In brushless PM machines, cogging torque is generated from the interaction between the PMs on the rotor and the stator slots. Cogging torque can result in torque/speed ripples, rough running, vibration, and acoustic noise. Motor engineers always struggle with reducing cogging torque. As a result, slotless stator designs have emerged as a solution to zero cogging in conventional PM motors. The slotless stators totally eliminate the cogging torque, simplify the lamination process, and smooth the motor performance. In this type of motor, stator wires are wound into a cylindrical shape and assembled inside the stator core in a radial inward compressed condition [4.12]. Since the stator winding effectively functions as a spring pressure at the internal wall of the stator core, it is mechanically secured to the inner periphery of the stator core and a special fixation mechanism is not required. Then, the stator assembly is immersed in high-temperature epoxy resins and finally cured in an oven. Thus, the stator winding maintains its orientation with respect to the stator laminations and housing assembly (Figure 4.14).

However, the slotless winding requires increasing the air gap and in turn reduces PM excitation field. To maintain the same air gap flux density, the height of the PM must be increased. Therefore, slotless PM motors use more PM materials than slotted motors [4.13]. The cross-sectional view of the slotless stator is shown in Figure 4.15. Like all technologies, there are pros and cons to the differences.

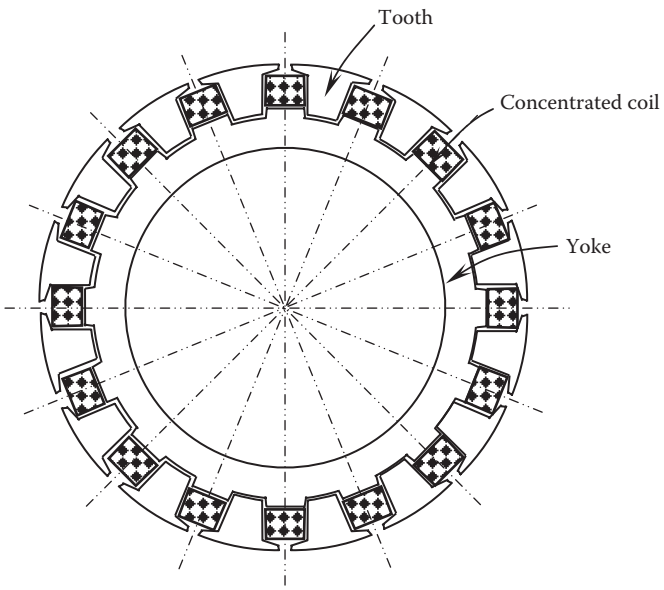

FIGURE 4.12
Integrated stator core with teeth and an internal yoke section; the teeth are positioned in the concave slots on the outer surface of the yoke, and the concentrated coils are inserted into the stator slots.

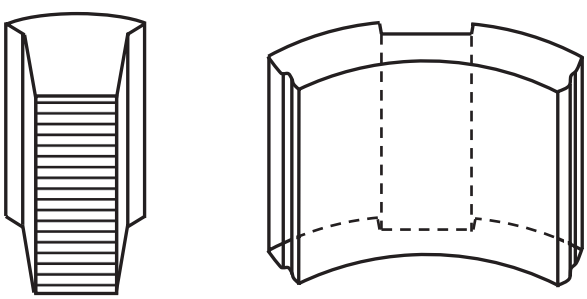

FIGURE 4.13
The sheets of teeth are held together as a subsection and then integrated with the yoke laminations.

4.1.2.7 Slinky Lamination Stator Core

Using new methods for fabricating stator cores is highly desired for both the cost reduction and manufacturing efficiency. One such design is known as the slinky method [4.14,4.15]. With this method, a stator core is built up from a continuous slotted strip of silicon steel rather than cross-sectional laminations in a conventional manufacturing process (Figure 4.16). The strip is wound edgewise in a helical configuration by a coiling machine that consists of three flanged rolls. By making the stacked strip to the desired thickness, the rolled core is compressed longitudinally and welded at the outer circumferential surface of the core, avoiding noise caused by vibration. The advantages of this manufacturing method include the following: (1) Using the slinky design provides the induced magnetic field with a preferable grain orientation in the rotor rotation, which would subsequently boost the overall efficiency of the motor. (2) It reduces the iron losses, noise generation, and

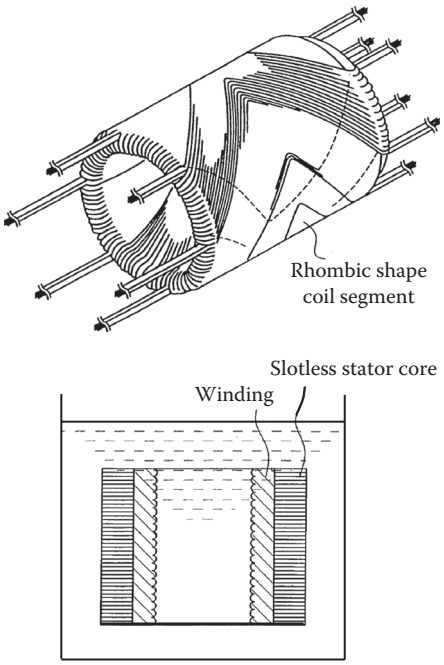

FIGURE 4.14
Fabrication of slotless stator (U.S. Patent 6,525,437) [4.12]. (Courtesy of the U.S. Patent and Trademark Office, Alexandria, VA.)

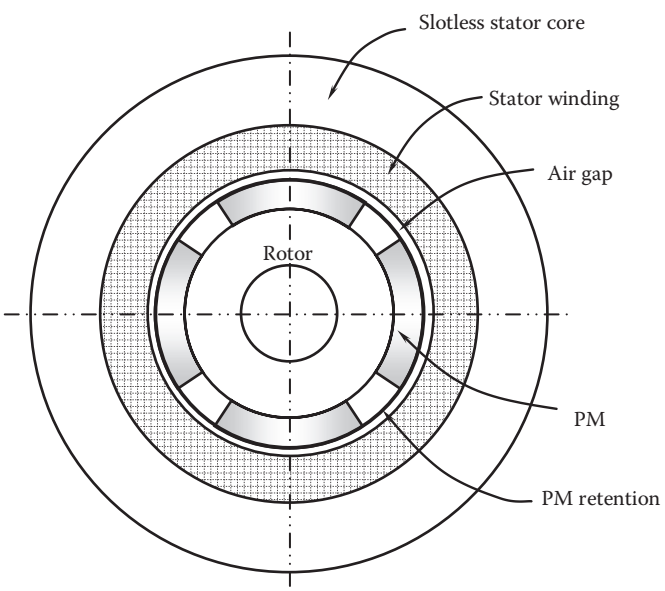

FIGURE 4.15
Structure of a four-pole slotless PM motor.

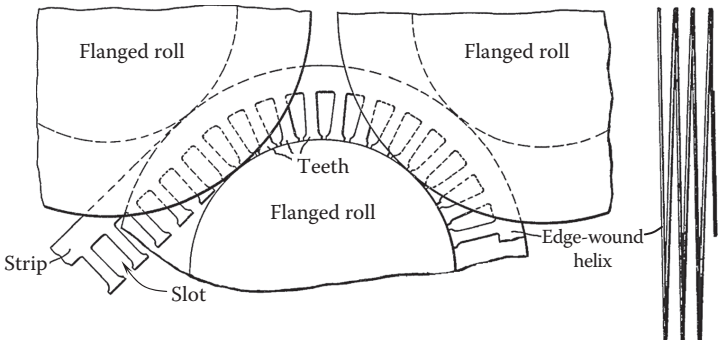

FIGURE 4.16
Fabrication of helical stator core with three flanged rolls (U.S. Patent 1,920,354) [4.11]. (Courtesy of the U.S. Patent and Trademark Office, Alexandria, VA.)

power draw as compared to the conventional process. (3) This method can lead to great savings in material and winding labor.

This technique can be used in a slotless stator design. With the additional elimination of the teeth on the steel back iron, cogging of the motor is eliminated. It also simplifies the manufacturing process, as shown in Figure 4.17 [4.16].

In order to gain full advantages of core loss reductions from a laminated core, an adequate surface insulation must be maintained between the laminations. Stator laminations

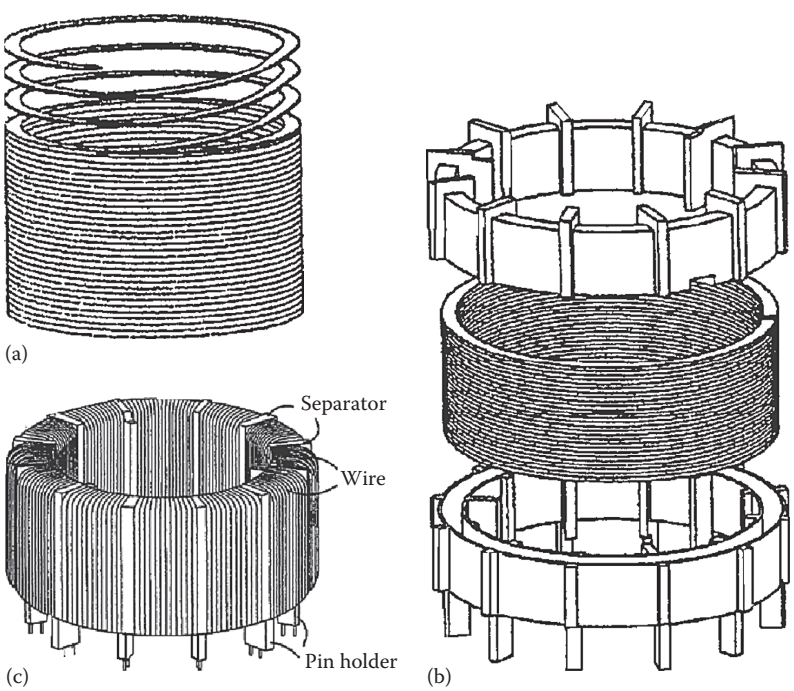

FIGURE 4.17
Using slinky method in designing slotless stator: (a) fabricating a helical stator core, (b) adding a molded plastic annular insulator at each end of the stator core, and (c) making the stator winding over the insulators (U.S. Patent Application 2005/0073210) [4.15]. (Courtesy of the U.S. Patent and Trademark Office, Alexandria, VA.)

are usually coated with inorganic nonconductive materials as the insulation. The selection of coating materials is based on material properties especially electrical resistance, operation temperature, cost, and processing time. Furthermore, the application of a suitable coating can promote a better stamping performance such as low burr and long tool life.

4.2 Magnet Wire

The most common materials used for stator windings are copper and aluminum for their excellent electrical properties especially high electrical conductivity. By comparing with aluminum, copper has better electrical properties but higher melting temperature. At the temperature of 20°C, the conductivity of copper is 70% higher than that of aluminum. Though silver has the highest electrical conductivity (its conductivity is 5.7% higher than that of copper at 20°C) and highest thermal conductivity of any metal, its high cost and tarnishability have prevented it from being used for motor windings. Magnet wires are widely used in small and medium electric motors for fabricating stator windings. For heavy-duty large-size electric motors, electric conducting cables are more commonly used to make stator windings.

Magnet wire is coated with insulation materials (such as enamels) to allow winding wires to contact each other without forming electricity short circuits between them. The selection of the magnet wire is based on the motor operation conditions (working frequency, current, voltage, temperature, etc.), wire material properties, wire diameter for allowing maximum current density, thermal class, coating material, thickness of coating layer, and others. Magnet wire received its name undoubtedly from its use to make electromagnets.

4.2.1 Regular Magnet Wire

Regular magnet wire consists of a base metal, commonly copper or aluminum, and coated one- or multilayer of insulation materials, such as enamel, fibrous polyester, fiberglass yarn, and polyamide. For multilayer coatings, it is often necessary to use different compositions to achieve the most optimal insulation result. Several cross-sectional shapes of magnetic wires are available in stator windings, including round, square, and rectangular (Figure 4.18). The use of square wires can significantly increase the slot-filling rate. This is especially useful where space constraints are concerned.

4.2.2 Self-Adhesive Magnet Wire

As shown in Figure 4.19, a self-adhesive magnet wire has a thermoplastic adhesive film superimposed over standard film insulation. When activated by heat or solvent, the bond coating cements the winding turn-to-turn to create a self-supporting coil. This type of wires opens up new avenues for some special applications, especially where regular magnetic wires are not suitable. For instance, bobbin-free deflection yoke coils in television sets can be conveniently made by self-adhesive wires. With a coated thermoplastic cement on the outer surface of the wire, a strong turn-to-turn bond throughout a winding can be achieved, and thus the need for varnish impregnation can be eliminated.

The adhesive can be activated by different ways. An easy way is to allow the wire passing through a solvent while winding. As the solvent is evaporated, all turns are bonded

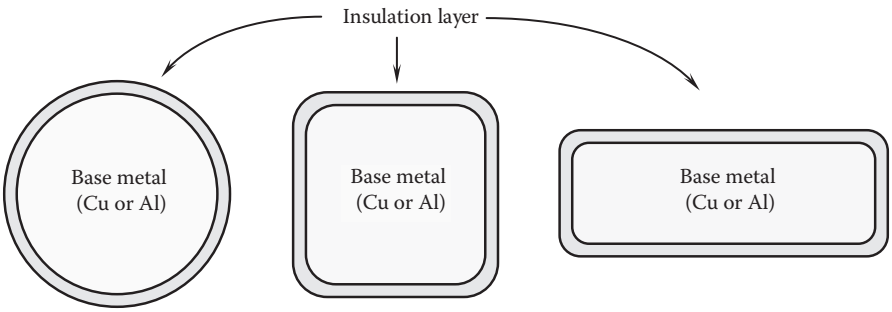

FIGURE 4.18
Modern magnet wires with different shapes.

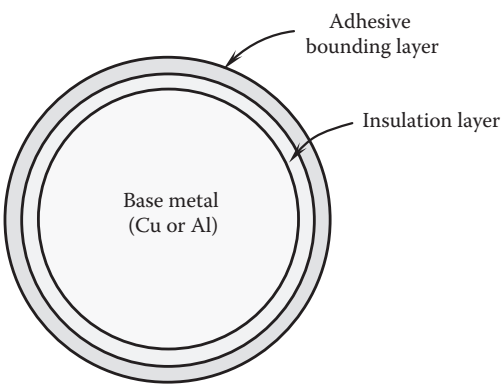

FIGURE 4.19
Self-adhesive magnet wire; an adhesive bounding layer is added on magnet wire.

together as the whole coil. Another effective way is called resistance heating, which is accomplished by passing electric current through the coil. Due to the resistance of the coil itself, heat is generated in the coil, and a desired temperature can be reached by controlling the heating time. When the desired temperature of the coil is reached, the coil is compressed so that the wires contact closely and thus bounded together. In fact, high resoftening temperature of cement allows the self-adhesive wires to compare with varnish-impregnated heavy-grade magnet wires.

As an example, the dimensions of a self-adhesive wire are presented in Table 4.1. It can be seen from the table that the thickness of both the insulation layer and the cement layer is proportional to the bare wire diameter. The thickness of the cement layer is about half of that of the insulation layer. This type of wires can withstand 180°C, which is well suited for electric motors.

The optimum bonding of the wires is reached when the coil temperature is raised to the range of 220°C–240°C, measured by the change in the coil electrical resistance.

4.2.3 Litz Wire

Litz wire is basically used for high-frequency applications. It contains many thin wire strands that are individually insulated and twisted together. Litz wire utilizes the full

TABLE 4.1

Dimensions of Self-Adhesive Magnet Wires (Bondeze®M)

AWG Size	Nominal Bare Wire Diameter, mm (in.)	Minimum Insulation, mm (in.)	Minimum Cement, mm (in.)	Maximum OD, mm (in.)
15	1.4503 (0.0571)	0.0406 (0.0016)	0.0203 (0.0008)	1.5392 (0.0606)
16	1.2903 (0.0508)	0.0381 (0.0015)	0.0203 (0.0008)	1.3741 (0.0541)
17	1.1506 (0.0453)	0.0381 (0.0015)	0.0203 (0.0008)	1.2344 (0.0486)
18	1.0236 (0.0403)	0.0356 (0.0014)	0.0203 (0.0008)	1.1506 (0.0453)
19	0.9119 (0.0359)	0.0356 (0.0014)	0.0203 (0.0008)	0.9931 (0.0391)
20	0.8128 (0.0320)	0.0330 (0.0013)	0.0178 (0.0007)	0.8865 (0.0349)
21	0.7239 (0.0285)	0.0330 (0.0013)	0.0178 (0.0007)	0.7976 (0.0314)
22	0.6426 (0.0253)	0.0305 (0.0012)	0.0178 (0.0007)	0.7137 (0.0281)
23	0.5740 (0.0226)	0.0279 (0.0011)	0.0152 (0.0006)	0.6401 (0.0252)
24	0.5105 (0.0201)	0.0279 (0.0011)	0.0152 (0.0006)	0.5740 (0.0226)
25	0.4547 (0.0179)	0.0254 (0.0010)	0.0152 (0.0006)	0.5156 (0.0203)
26	0.4039 (0.0159)	0.0254 (0.0010)	0.0127 (0.0005)	0.4623 (0.0182)
27	0.3607 (0.0142)	0.0229 (0.0009)	0.0127 (0.0005)	0.4140 (0.0163)
28	0.3200 (0.0126)	0.0203 (0.0008)	0.0127 (0.0005)	0.3708 (0.0146)
29	0.2870 (0.0113)	0.0203 (0.0008)	0.0102 (0.0004)	0.3353 (0.0132)
30	0.2540 (0.0100)	0.0178 (0.0007)	0.0102 (0.0004)	0.2997 (0.0118)

cross-sectional area of the wire to carry current. Because each individual strand is thinner than the skin depth, the use of Litz wire can greatly minimize the skin effect and proximity effect losses in high-frequency windings.

A size of a Litz wire is often expressed in abbreviated format of *N*/*XX*, where *N* is the number of strands and *XX* is the AWG size of each strand. The twist per inch or meter is also an option to specify.

4.3 Stator Insulation

As magnet wires are wound into stator slots to form stator windings, electrical insulation is required wherever there is a difference of electric potential between two electric conductors to prevent the conductors from short circuiting to one another, including (1) one turn of a coil to adjacent turns, (2) coils to adjacent coils, (3) stator windings to the ground (i.e., the stator core), and (d) one phase winding to adjacent phase windings.

The insulation of stators can be done by various methods, for example, using aramid or mylar layered paper, fluidized-bed powder coating, or overmolding with thermoplastic materials. For low- or moderate-voltage stators, the magnet wire insulating varnish can usually satisfy the requirements of turn-to-turn insulation. However, as the stator voltage increases, an additional insulation becomes necessary. For instance, wrapping an insulating tape around the conducting wire can effectively enhance the dielectric strength. Similarly, for low-voltage stators, coil-to-coil insulation is provided by the wire insulation to avoid the risk of short circuiting in various series or parallel connected coils. The practical method for winding-to-ground insulation is usually to employ slot liners and slot wedges at the bottom and at the top of stator slots,

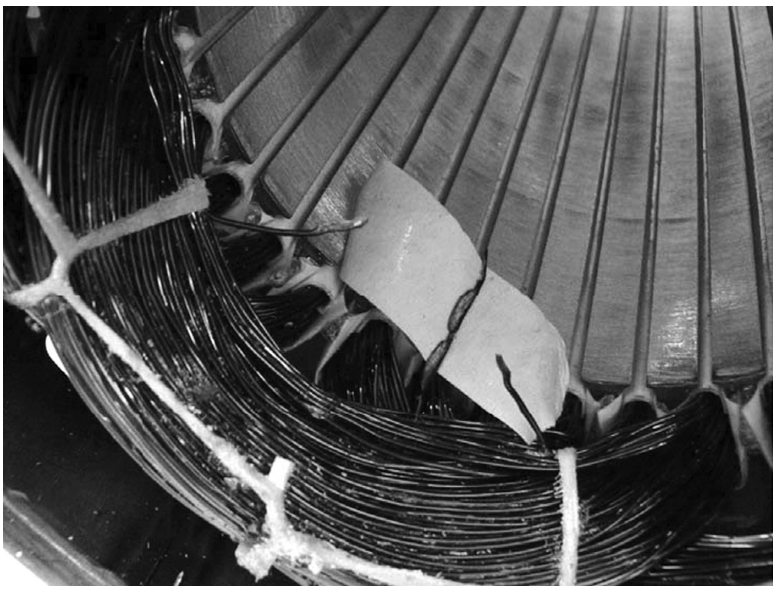

FIGURE 4.20
The damage of stator winding due to the failure of electric insulation.

respectively, to separate the stator windings to the adjacent lamination surfaces for preventing any part of the stator windings from shorting to the stator core. These are available in many shapes, sizes, and materials. Phase-to-phase insulation can be achieved by completely insulating the winding of one phase from those of adjacent phases. Failure of electric insulation can lead to the damage of the stator winding (Figure 4.20), causing permanent failure of the electric motor.

4.3.1 Injection Molded Plastic Insulation

Injection molded plastic insulation provides highly reliable insulating properties to laminated stator stacks. The use of molded plastic insulation prior to winding assures consistent and durable insulation of wound winding to the stator cores. Figure 4.21 is an example of the molded plastic insulation, which consists of a main body and an end cap. Using the molded plastic insulation can offer proven engineering advantages in the stator assembly, including consistent insulation thickness, reliable and long lasting insulation, and reduced labor time. The use of such insulation in small motors is presented in Figure 4.22.

A specially designed molded plastic insulator is applied at the motor end, providing the insulation for lead wires, as shown in Figure 4.23.

4.3.2 Slot Liner

As shown in Figure 4.24, heat-resistant and mechanically stable insulation papers or thermoplastic materials are inserted in stator slots for preventing coils from shorting to the stator core. The typical thickness of an insulation material may have a range of 0.1–0.65 mm, depending on liner materials and stator operation conditions. Although the material is inexpensive, it takes a longer labor time for fabricating stator windings.

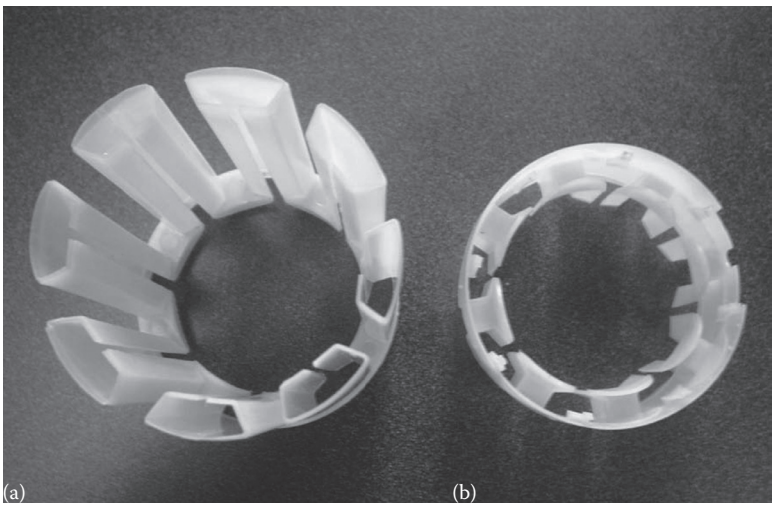

FIGURE 4.21
Molded plastic insulator: (a) main body; (b) end cap.

FIGURE 4.22
A variety of molded plastic insulators applied to stator windings.

4.3.3 Glass Fiber–Reinforced Mica Tape

For large-size *KV* motors, stator windings are often made of conducting bars that are continuously wrapped with mica tape. The taped winding bars are placed in a vacuum impregnation tank and flooded with a low-viscosity epoxy resin. After being completely impregnated, the insulation is cured at high temperatures in large chamber ovens.

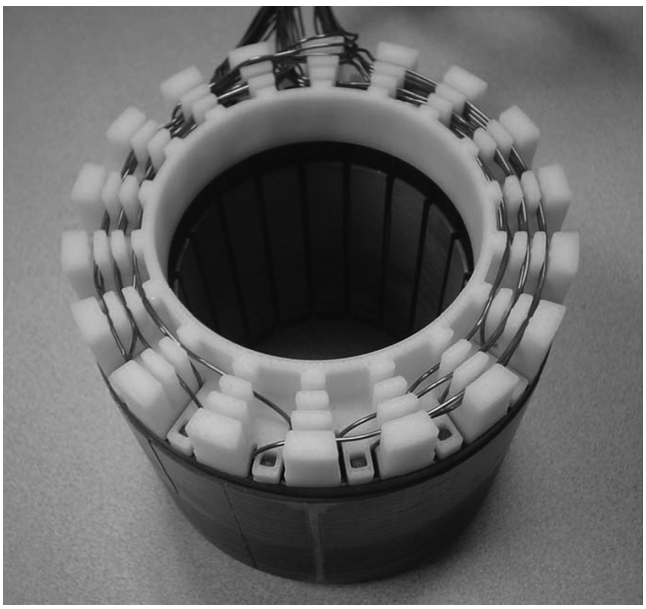

FIGURE 4.23
Specially designed molded plastic insulation part used at the motor ends for insulating the lead wires.

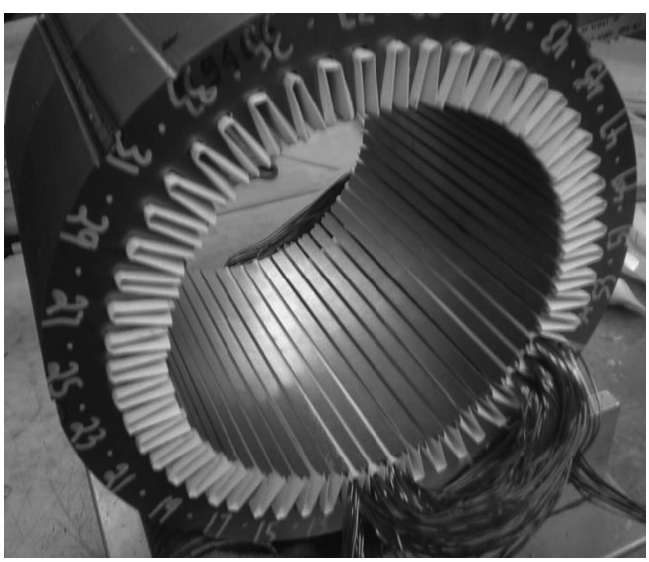

FIGURE 4.24
Insulation papers inserting in the stator slots for receiving winding coils.

4.3.4 Powder Coating on Stator Core

Powder coating technology (fluidized-bed coating) has been successfully applied in motor manufacturing since the early 1950s and is recognized as a superior and powerful method of applying a protective finish on electrical components. As an example, motor stators

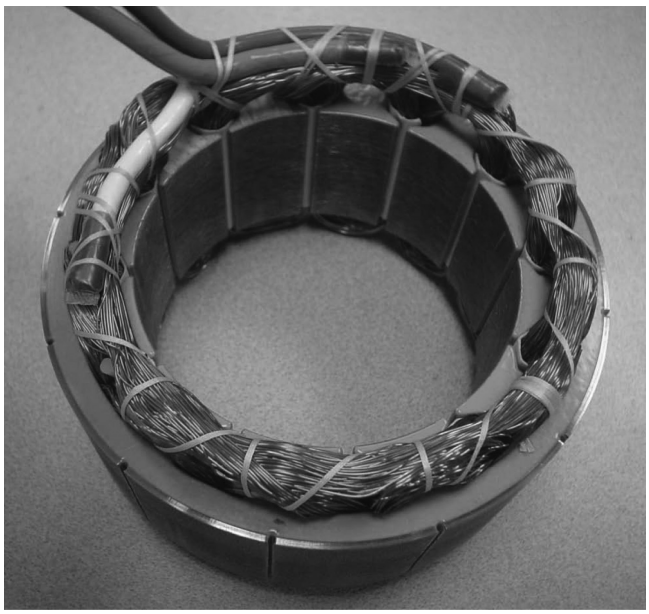

FIGURE 4.25
A stator core having a coated insulation layer on the slot surfaces and partially end surfaces with powder coating technique.

are often shaped cylindrically with inwardly facing slots configured to receive stator windings. It is required to insulate the copper windings from the stator metal surfaces. This can be achieved by applying power coating techniques to provide uniform insulating coating layers on the stator slot surfaces, as well as partially on the stator end surfaces (Figure 4.25). There are a number of insulation materials suitable for powder coating such as epoxy, Glyptal®, and Loctite®. Epoxy powder coating has been effectively used as a high dielectric insulator on copper/aluminum conductors by many motor manufacturers for its high durability and superior dielectric strength. Numerous ways of distributing powder throughout motor parts are available. One approach that offers significant advantages over a wide range of other approaches is to use a specially designed apparatus that is equipped with a power fluidized bed to get uniform coating layers [4.17]. The thickness of the coating layer typically has a range of 0.1–0.5 mm.

4.4 Manufacturing Process of a Stator Core

The manufacturing process of a stator core includes lamination stamping, annealing, stacking, winding, and impregnating/encapsulating. The selection of stator core materials is similar to that of rotor cores. Since there are no centrifugal forces acting on stator cores, the requirement for material strengths can be lower than that of rotor cores.

In order to reduce eddy current and hysteresis losses, a stator core is manufactured by stacking a large number of thin laminations made of silicon steel. Without the lamination process, a solid steel core would become an electrical heater. The addition of silicon

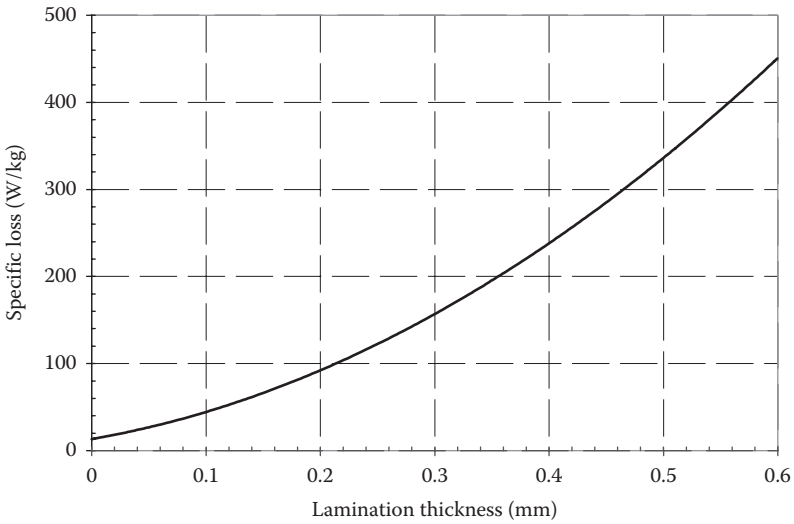

FIGURE 4.26
Specific iron loss in a PM motor versus lamination thickness at $B = 2T$ and $f = 1200$ Hz, showing that the reduction in lamination thickness can significantly reduce stator power loss.

to steel can significantly increase the permeability and volume resistivity to eddy current and thus enhance motor efficiency. It was shown that the iron loss of stator core can be reduced considerably by employing 6.5% silicon steel laminations rather than 3% silicon steel [4.18].

Silicon steel is available in an array of grades and thicknesses so that the material can be tailored for various applications. Generally, the thickness of motor laminations is in the range of 0.36 mm (0.014 in. for 29 gage) to 0.64 mm (0.025 in. for 24 gage). Thinner laminations are also available at 0.051 mm (0.002 in.), 0.102 mm (0.004 in.), and 0.178 mm (0.007 in.), considered for use in high-performance and high-frequency applications. It has been reported that at high flux densities and high frequencies, the specific iron loss is proportional to the square of the lamination thickness [4.19]. For the purpose of demonstration, the specific iron loss in a PM motor versus the lamination thickness for high saturated cobalt iron alloy at $B = 2T$ and $f = 1200$ Hz is presented in Figure 4.26. This indicates for a lower iron loss; the lamination thickness should be less than 0.1 mm. However, the determination of the lamination thickness is a trade-off between core loss and fabrication cost. Thinner laminations are always more expensive and have lower stacking efficiency.

Two major distinctions of laminated materials are the fully processed electrical steel and annealed electrical steel. The annealed electrical steels are most common in North America and have higher-performing electrical properties than the fully processed steels. A fully processed steel is usually a silicon electrical steel with an insulator coating and is not annealed after punching to save time and cost of the anneal process. When a lamination supplier is set up with high output flow through ovens, the anneal process can be down very economically.

4.4.1 Stator Lamination Cutting

Stamping is the most popular method used for lamination fabrication by most lamination manufacturers. The advantages of stamping include high productivity, low cost, and

simplicity of stamping process. The accuracy of the lamination cutting is typically controlled within ±0.0254 mm (±0.001 in.). However, burrs and warps near the lamination edges due to stamping can lead to difficulties in stacking and tolerance control. As discussed by Brown [4.20] for a high-speed stamping machine, these inaccuracies sometimes can be 50% or more of the design gap between laminations. In addition, burrs provide current paths between laminations and thus increase eddy-current losses.

Laser cutting is often used in special cases, such as prototype buildup, stators with extra large dimensions, or very complex geometries and shapes. Since the design information of lamination is computerized and loaded in a laser cutting machine, there is no need for tooling as in the stamping process.

In laser cutting, a high-energized laser beam is focused in a very tiny spot so that the local temperature rises extremely high to melt lamination sheets. Hence, this process generates much smaller residual stresses, lower distortion, better surface finishing, and high precise dimension control than the stamping process. However, laser cutting has lower productivity, higher power consumption, and higher costs. During a cutting process, some deterioration to the magnetic characteristics may occur, but it is too small to require annealing. This fabrication process is suitable for small quantities of laminations. The required tolerances for laser cutting are typically set at ±0.0254 mm (±0.001 in.).

Electrical discharge machining (EDM) is a manufacturing cutting process. An unwanted material is removed from the workpiece by a series of rapidly recurring current discharges between two electrodes—one is called the tool electrode and another is called the workpiece electrode. In a normal operation, the two electrodes are separated by a dielectric liquid. Similar to laser cutting, EDM can do a good job in cutting laminations but suffers its low productivity, excessive tool wear, and high power consumption.

Chemical etching is a very low-cost procedure that requires only a few chemicals (such as sodium persulfate and hydrochloric acid) and very little equipment. In practice, this method has been extensively used in manufacturing printed circuit boards (PCBs). The chemical etching process can generate burr-free and stress-free laminations that do not require annealing. The process starts to create a photographic image (*mask*) with the desired stator pattern. The mask is then illuminated with UV light onto lamination sheets. The lamination sheets need to be immediately placed into a developer solution such that the desired stator design is chemically etched onto the laminations.

4.4.2 Lamination Fabrication Process

An effective way to produce stator and rotor laminations together was presented by Isayama [4.21]. This method uses a sequence of stamping operation on strip materials to generate first the rotor sheet piece and then the stator sheet piece. As demonstrated in Figure 4.27, the stamping operation starts to punch pilot holes (Stage A) and then a shaft hole (Stage B), rotor ventilating holes (Stage C), and rotor teeth to complete the rotor lamination fabrication (Stage D). The following operation is for the stator lamination. The slots are made in Stage E. At Stage F, an annular punch is used to generate a concentric thin portion, located inside the ID end. In Stage G, round calking portions are formed. Following, stator teeth are punched (Stage H). In the last stage (Stage I), the stator lamination is blanked away from the metal sheet.

This method has numerous advantages over conventional methods, including (1) reducing the residual stress in stator and rotor laminations, (2) reducing the lamination deformation, (3) lowering production cost because all operations complete on a single strip material with the use of a single press machine and a single die machine, (4) enabling

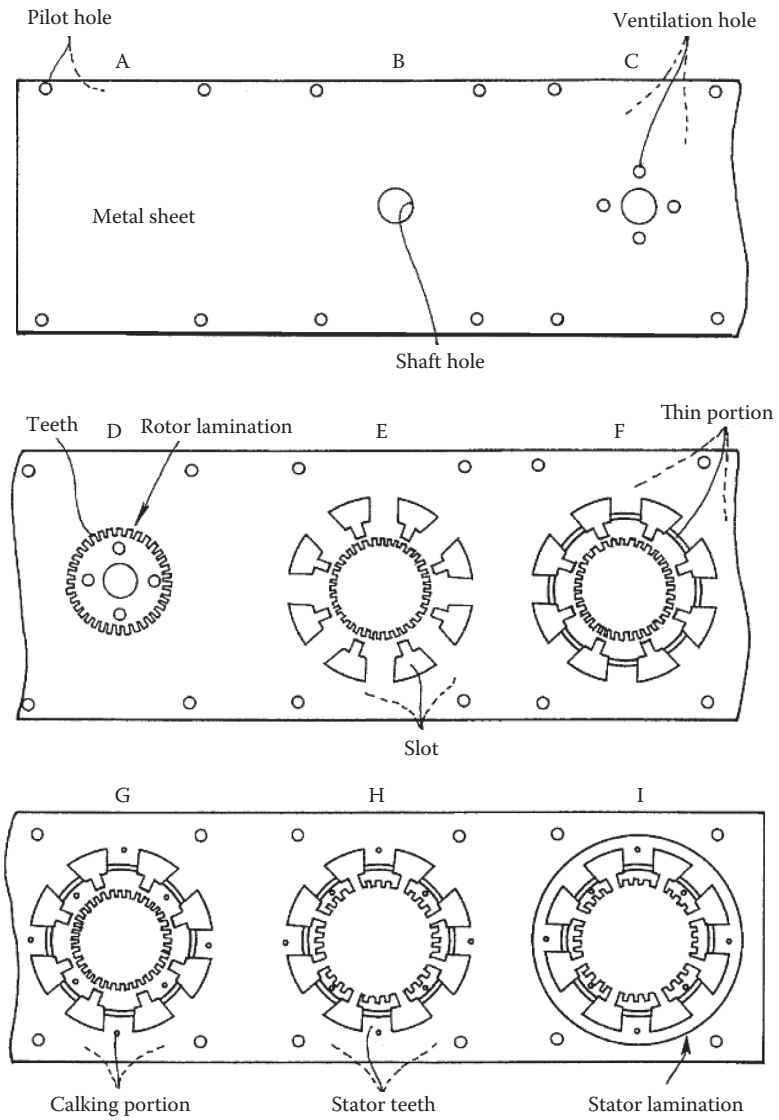

FIGURE 4.27
Rotor and stator laminations are made by a sequence of stamping operations (U.S. Patent 5,539,974) [4.21]. (Courtesy of the U.S. Patent and Trademark Office, Alexandria, VA.)

to deal with complex shapes of stator and rotor, and (5) obtaining laminations that are excellent in such high shape precision as squareness and parallelism and highly suitable for use in accurate electric motors.

4.4.3 Lamination Annealing

During a lamination cutting process, residual stresses are introduced in processed laminations, leading to the degradation of material magnetic properties near the edges of the laminations and possible large cogging torque in motor operation. The smaller the stator

size, the larger the cut-affected zone relative to the whole lamination area. Therefore, annealing is a necessary step for stress relief and for optimum properties of laminations, especially for stamped small laminations. The annealing cycle requires to maintain processed laminations for several hours at the temperature range of 730°C–790°C under nonoxidizing and noncarburizing conditions (such as a vacuum or nitrogen-filled chamber) and then to naturally cool them to room temperature. Fully processed steels skip this step and perform very satisfactorily, but the highest performance is achieved with the anneal cycle.

4.4.4 Lamination Stacking

With the development of industrial automation, automatic lamination stacking becomes more popular today for modern motor manufacturers. This increases production efficiency and reduces the requirement for the storage capacity, especially for a rotary stacking.

A stator stack is formed by stacking laminations into a pack. There are several methods to assemble stack laminations into stator cores [4.22]:

- Welding—This method can robustly join laminations together to withstand large forces without lamination separation (Figure 4.28). However, welding across laminations may increase local stator core losses to impact motor performance, particularly for small motors. Designing geometry for welding can eliminate or minimize the shorting concerns. If improperly designed or welded, an increase in cogging torque can occur. Therefore, in order to avoid this undesired result, it must keep welds out of critical flux return path locations.
- Bonding with adhesive materials—This method is to deposit a thin film of adhesive on lamination surfaces to be bonded and assemble the laminations into the stator core. The core and winding are reheated to cure the adhesive material. Thus, it has bounded together the laminations of the core to provide adequate

FIGURE 4.28
Stator laminations are integrated by welding.

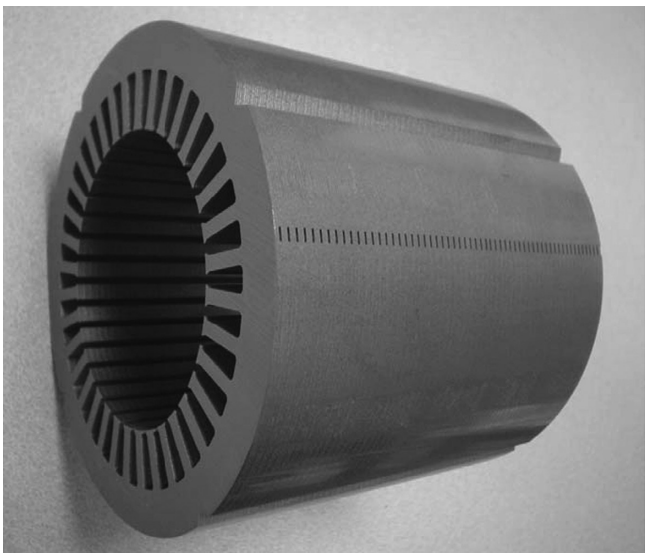

FIGURE 4.29
Stator core is fabricated using spot bonding technique with epoxy adhesive.

core strength (Figure 4.29). By comparing with other methods such as welding and riveting, this method provides the relatively low mechanical strength of the stack.

- Riveting—This is an economical and reliable method for securing stator cores. It requires punching small holes or slots on laminations. However, the heads of the rivets may obstruct the stator end windings.
- Fastened by pins—This method is similar to riveting but without the problem of the obstruction of the rivet heads to the stator end windings.
- Lamination interlocking—This is a convenient way of assembling a stack. As can be seen in Figure 4.30, 10 dimples are placed at the back iron on each stator lamination. When the laminations are stacked together, they nest inside each other. The main disadvantage of this process is that it requires a complex die that is very expensive.
- Self-cleating—This method rolls V-shaped strips and then flattens them down into dovetail slots at the OD of the stator laminations.
- Using slot liners—This method is commonly used for stator cores less than 150 mm. Cuffed slot liners hold the stator core together, as described in [4.23].
- Using thin sleeves—As demonstrated in Figure 4.31, this method for the stator core retention is to use thin metallic sleeves outside of the core. Due to high strength of the sleeve, the stator core can withstand large forces with only tiny deformation. The installation of the sleeve usually relies on the shrink fit technique.
- Bolting—This method is similar to riveting for providing reliable lamination integration. A plurality of bolts is extended through boltholes in the lamination stack and engaged with nuts. Upon tightening of the bolds, the laminations are forced together to establish a generally axial compression on the lamination stack. However, bold heads have even larger heads than rivets to obstruct the stator end windings.

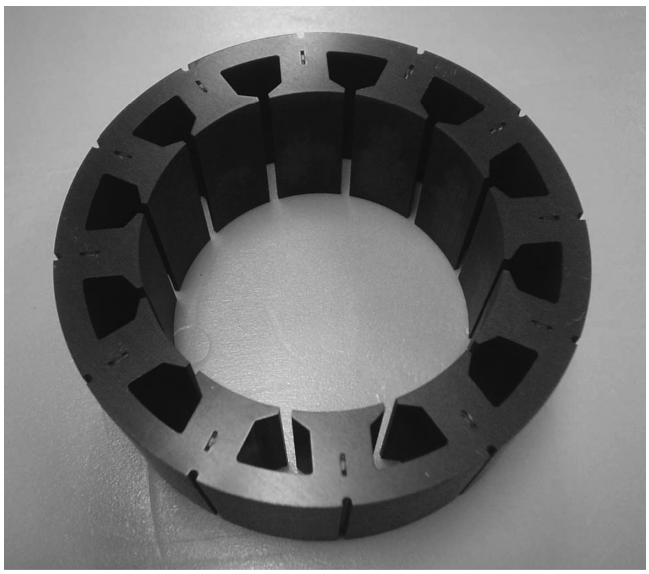

FIGURE 4.30
Stator core is made from dimpled laminations.

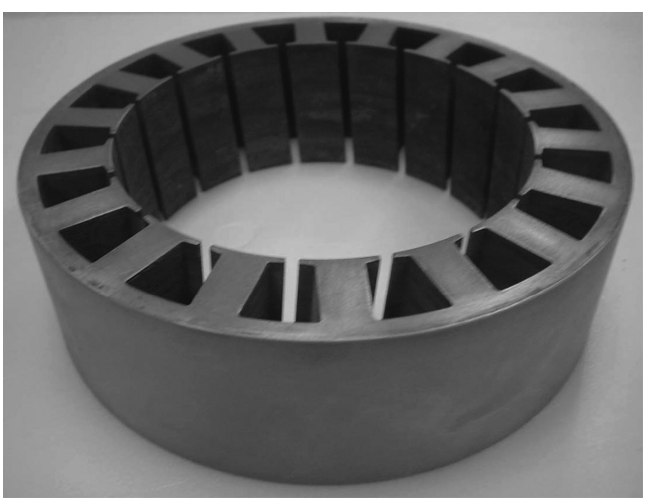

FIGURE 4.31
Stator core is secured with a thin sleeve at the outside of the core.

4.4.5 Stator Winding

One of the important parameters in stator winding is the slot fill ratio, which is defined as the percentage of the space occupied by magnet wires to the total available space of the slot. In order to lower the wire resistive loss and increase the power density, it is highly preferable to have the maximum copper fill, that is, maximum slot fill ratio.

A winding end turn refers to the amount of the winding extending beyond each end of the stator's magnetic core structure. Though the end turns are necessary to complete the

electrical path within the winding, they contribute little to the motor torque output. Motor torque is only generated by the winding that lies within the stator's magnetic core structure. Consequently, it is highly desired to minimize the length of the winding end turns. This can not only save the wiring material and lower the material cost but also reduce the copper loss and increase the motor efficiency. The shorter the winding stack length, the greater the impact of the end turn length on motor efficiency.

4.4.5.1 Random Winding by Hand

The advantages of random winding by hand include the flexibility and suitability to some manufacturing processes, such as prototypes, low-volume production, and/or motor rewinding. Slot fill can also be higher than single slot designs wound with typical needle winding machines. However, this winding method may have more winding variabilities and require highly skilled operators. Hand wiring can have different configurations and is best to clarify if (1) coils are hand wound and hand inserted, (2) coils are wound around stator teeth by hand, and (3) coils are machine wound and hand inserted.

4.4.5.2 Coil Formation: Distributed Winding

This type of winding is made by arranging winding turns in several full-pitch or fractional-pitch coil. Then, this coil is housed in the slots spread around the air gap periphery. Because a distributed overlapping winding generally results in a more sinusoidal MMF distribution and EMF waveform, it is used extensively in PM brushless AC machines [4.24]. High slot fills can be achieved depending upon the motor size. Generally, the larger the motor, the higher the slot fill.

4.4.5.3 Coil Formation: Concentrated Winding

The interest in motors with concentrated windings is growing due to their short end windings and simple winding structures that are highly desired for high-volume automated manufacturing. For this type of windings, all the winding turns are wound together in series to form one multiturn coil. The concentrated winding motors have potentially more compact designs compared to conventional motors with distributed windings.

It has been reported that based on FEM calculations, the performance of an electric machine with concentrated winding is superior, because the minimization of the copper volume greatly reduces power losses and manufacturing costs. Induced EMF in concentrated windings is greater than distributed windings. In addition, harmonic or noise in distributed windings is lesser than concentrated windings. Furthermore, distributed windings have less armature reaction. The distributed and concentrated windings are given in Figure 4.32.

4.4.5.4 Coil Formation: Conductor Bar

In building large-size motors and generators, it is often necessary to bundle several individual conductors that are insulated against one another to form a so-called conductor bar (Figure 4.33). The insulation between the conductor bar and stator core is defined as the main insulation. To fabricate stator windings, several conductor bars are connected to each other at the machine ends, as shown in Figure 4.34.

Conductor bars are prefabricated with either round or rectangular shape copper wires, coated with mica tape and impregnated with epoxy resin. They are then heated up and

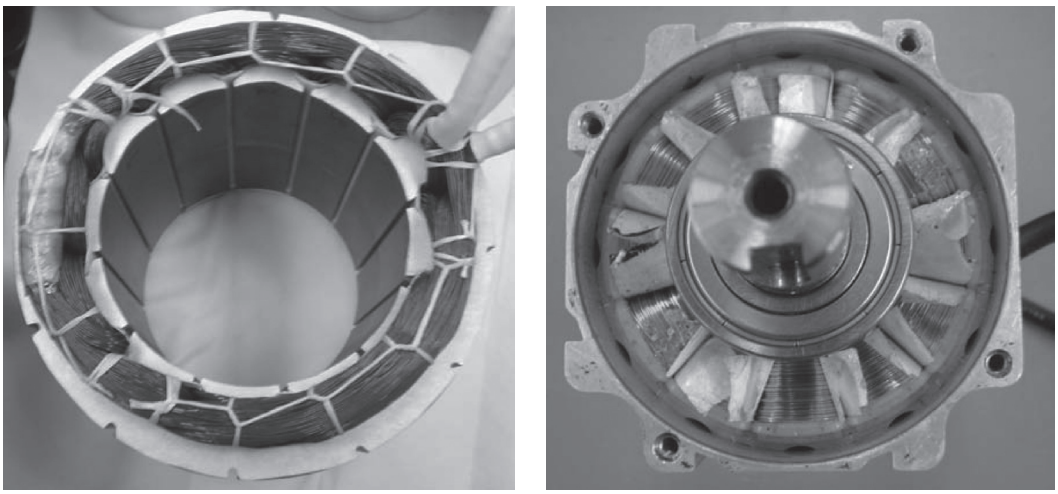

(a) (b)

FIGURE 4.32
Coil formation: (a) distributed winding; (b) concentrated winding.

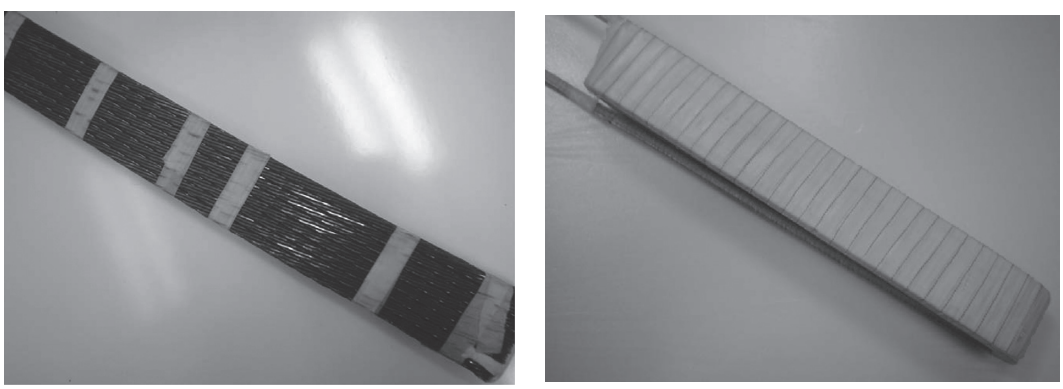

(a) (b)

FIGURE 4.33
Bundled conducting bars used in electric motors: (a) rectangular magnetic wires are twisted to reduce eddy-current loss and (b) stator winding is wrapped by an insulating strip.

cured resulting in high winding mechanical strength. Generally, a conductor bar with a rectangular cross section is preferred for its high filling rate in stator slots. In producing conductor bars, the individual conductor can be either twisted around each other or maintained parallel each other. During a manufacturing process, sometimes, conductor bars are required to be compressed to make them into a desired shape and compact size. It has been found that an improper compressing method may potentially damage the conductor's insulation, causing stator winding failure. The connection efforts are more labor intensive with individual coils.

Before and after the winding impregnation, stators must undergo a series of tests such as hipot (dielectric voltage withstand test), surge (impulse test), resistance, and contact resistance to verify the stator condition.

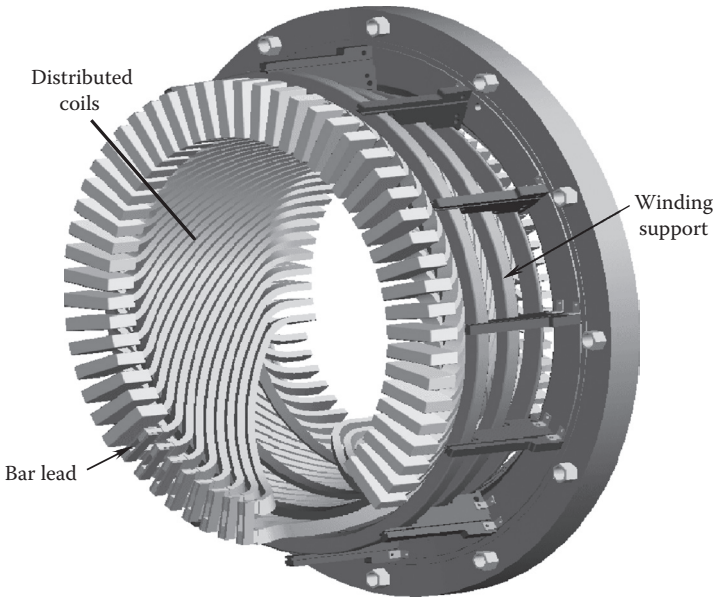

FIGURE 4.34
Conducting bars are commonly used in large electric machines. It shows the joints of conducting bars at the end turn region.

4.5 Stator Encapsulation and Impregnation

Encapsulating and impregnating stators can strengthen stator winding electrical insulation, provide reliable protection to chemicals and harsh environments, enhance thermal dissipation, promote stator structure integrity, and stabilize motor operation.

4.5.1 Encapsulation

Encapsulation has been widely used in electric machines. According to different applications, electric motors can be either partially or entirely encapsulated. Partial encapsulation is basically applied to the stator end windings for integrating them with other stator components against vibration and for enhancing heat transfer. Entire encapsulation is applied to the whole stator assembly for achieving better protection of the stator from moisture, dirt, debris, and erosions caused by chemicals such as acids. This treatment can provide very robust, durable, and long-life stators.

4.5.1.1 Encapsulation Materials

A wide variety of encapsulation materials are available for electric machines, as given in Table 4.2. These materials usually exhibit high dielectric strengths and relatively high thermal conductivity and are developed for different applications.

Thermoset plastics (also known as thermosets), such as epoxies, phenolics, and thermoset polyesters, have long been applied to electric machines as encapsulation materials. They can form irreversible chemical bonds during the curing process and have good

TABLE 4.2

Encapsulation Materials

Encapsulation Material	Thermal Conductivity (W/m-K)	Dielectric Strength (V/mil)	CTE (10^{-6}/K) (%)	Note	Reference
E88 epoxy	1.049 (at 23°C)	780	3.49	A two-component flame retardant resin system used for the impregnation and encapsulation of high-voltage electrical components.	[4.25]
C89 hardener	1.069 (at 50°C) 1.083 (at 75°C) 1.074 (at 100°C) 1.043 (at 125°C) 1.004 (at 140°C)				
Araldite CW 229-3 Aradur HW 229-1	0.75	508	27	It is a prefilled resin system that provides high crack and thermal shock resistance.	[4.26]
Altherm XB 2710 Aradur XB 2711	1.5	508	24	It is a good choice for stator encapsulation for its high thermal conductivity.	
Araldite XB 2252 Aradur XB 2253	0.7	508	60	The system is mineral filled with excellent flowability and impregnation capability.	
Araldite CW 1312 Aradur HY 1300	1.1	381	100	It has higher thermal conductivity and adequate impregnation capability. High filler loading results in higher viscosity.	
Arathane CW 5631 Arathane HY 5610	0.6	508	70	The curing reaction is fast and exothermal at room temperature. It is easy to process and has good impregnation capability.	
Aratherm CW 2731	3.0		20	One-component product. Developed for end turn encapsulation of motors and generators.	

Catalyst 11	1.28	380	97.9[a]	It is a two-component, thermally conductive epoxy encapsulant. It features a low CTE and excellent electrical insulative properties.	[4.27]
EP 234	3.77	415		It is room temperature cured and designed for medium-voltage devices.	
EP 1121	0.14	440		Its low viscosity allows for good wicking and penetration into components and circuitry and also gives good air release.	[4.28]
EP 1282	0.14	440		EP 1282 is a two-part unfilled electronic grade epoxy encapsulant. It cures at room temperature to a tough, semirigid polymer.	
EP 1285	1–1.27	365–400		Designed for applications requiring a high degree of thermal conductivity and a low CTE combined with a moderate free-flowing viscosity.	
Thermoset® SC-320 silicone	3.2			A two-component silicone elastomer that provides excellent thermal conductivity, high thermal shock resistance, and improved coefficient of expansion.	[4.29]

[a] Samples tested were cured for 24 h at 25°C.

mechanical and thermal properties. In recent years, with the recognitions by IEC-85 and UL-1446, thermoplastics as encapsulation materials are used for some encapsulated motors, solenoids, and transformers. Thermoplastics offer some performance benefits such as high strength and shrink resistance.

Though these two types of encapsulation materials sound similar, they have very different properties and applications. One of the remarkable differences is that the volatile organic solvents used in thermoset plastic encapsulation processes are eliminated in thermoplastic processes. As a result, the harmful solvent emissions to the environment are eliminated. Another important characteristic feature is that the curing process of thermoplastics is completely reversible as no chemical bonding takes place. This indicates that thermoplastics can be remelted at high temperatures. This special characteristic feature allows thermoplastics to be remolded and recycled but restricts their use for relatively low-temperature applications.

4.5.1.2 Encapsulation Process

In practical operation, prior to the encapsulation process, the stator is preheated in an oven to drive off any moisture or volatile components.

Thermally conductive thermosets are ideally suited for the full stator encapsulation due to their outstanding electrical and thermal properties and mold flow characteristics [4.30]. Among them, epoxy resins are most popular in the motor industry. They are generally hard and tough, exhibit low shrinkage on cure, and offer superior chemical and environmental resistance. The key features of encapsulating materials include high heat conductivity, high dielectric strength, and low shrinkage, thermal endurance, and chemical resistance. It is worth to note that thermal conductivity in an encapsulation system is determined by all its components, such as epoxy resin, hardener, and filler. Generally, thermal conductivity increases as more fillers are added. However, a high filler volume may significantly increase the viscosity of the mix, making it much more difficult to fill tight spaces. One way to get high filler volume in an encapsulation system is to use fillers with a spherical shape; angular fillers require much resin between them to maintain the necessary liquidity of the encapsulating materials.

Epoxy resins usually contain diluents or reducers to help their fluidity during the process. The hardener used with the epoxy resin plays a very important role for the final properties and has an impact on the speed of cure. Many epoxy resin systems use solid fillers as the constituent for cost reduction and increased hardness and stiffness of the cured product. Moreover, by carefully choosing the solid filler materials, it may lead to the increase in thermal conductivity in the cured encapsulation. It was reported that the types of filler that can help increase thermal conductivity include ceramic material, glass fiber, Kevlar® fiber, carbon fiber, silicon nitride fiber, and other materials [4.31]. The filler materials can be in the form of particles, granular powder, whiskers, fibers, or any other suitable forms. The thermally conductive polymer composition used to form the encapsulating polymer layer for the stator assembly comprises a base polymer and a thermally conductive filler material and has a thermal conductivity of at least 0.6 W/(m-K) and up to 5 W/(m-K) or higher.

Different encapsulation processes are available such as vacuum casting, gravity casting, and pressure gelation to allow highly automated production lines with short cycle time. Prior to casting, a sealing core is placed in the middle of the stator for preventing an encapsulant contamination of stator laminations.

A stator encapsulation process starts with the heating of an encapsulant to a certain temperature for the purposes of degassing and increasing the fluidity of the encapsulant. The higher the fluidity of the encapsulant, the shorter the filling time. With a gravity casting technique, liquid encapsulant is induced at the bottom of the stator to avoid air bubbles trapped in the encapsulation. Then, the stator is put in the oven for curing. The curing temperature and time can be optimized to minimize volume shrinkage and maximize mechanical strengths.

A standard casting process is typically controlled and executed by an encapsulating equipment, which consists of two independent systems for dealing with the encapsulant (e.g., epoxy resin) and the hardener individually before they are mixed. The epoxy resin is stored separately with the hardener in its packaging drum and goes to the vacuum premixers for degassing and the metering mixer for further mixing. This is the same process for the hardener. After this step, both materials get in the static mixer to get them to be mixed together. The well-mixed epoxy resin is pumped to fill the mold.

The cutaway view of an encapsulated stator shows that the epoxy completely penetrated into the stator coils (Figure 4.35).

The entire stator assemblies are immersed into a liquid epoxy resin in a vacuum tank. The vacuum helps to not only completely fill voids in the windings but also exhaust moisture and other vapors from the windings.

4.5.2 Varnish Dipping

Varnishing dipping is an effective way of securing stator windings. In this method, a stator is immersed into an open varnish tank. After a certain time, the stator is removed from

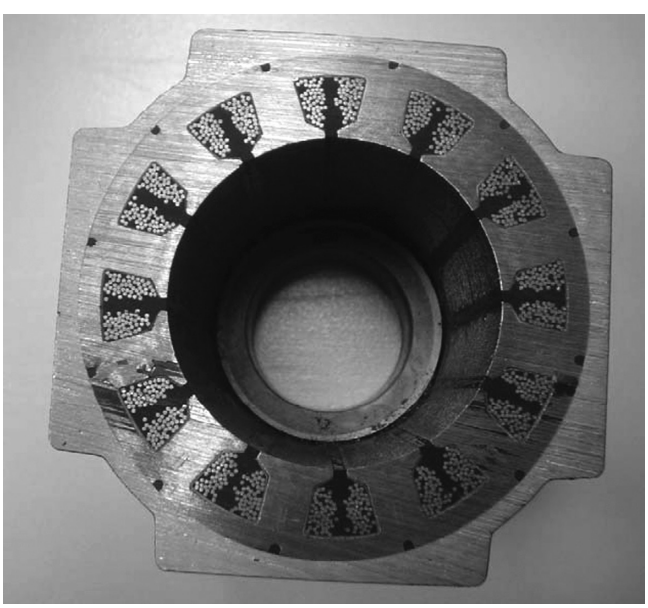

FIGURE 4.35
A cutaway view of an encapsulated stator shows that epoxy penetrates into stator coils and forms void-free encapsulation.

the varnish tank to allow excess varnish dipping. Then, place the stator in an oven to dry off solvent.

However, during varnish dipping and baking processes, solvent is continuously evaporated and released into the environment air, causing air pollution problems.

4.5.3 Trickle Impregnation

Trickle impregnation is extensively used in many motor manufacturers. In practice, a trickle varnish machine is usually used to impregnate the stator winding with a varnish that rigidly secures the wires. Prior to the impregnation process, stators need to be preheated to the desired temperature. A thin stream of impregnating resin is poured/dripped onto the winding. In such a way, the impregnating resin fills the voids of the winding and gets polymerized in a short time. This method offers several advantages, including short processing time, high retention, no need of postoven curing, and consistent quality of impregnation.

The varnish improves heat transfer within the winding and between its surrounding magnetic core structure. This improves motor cooling and in turn increases the motor's continuous torque and power density. In addition, trickle impregnation helps the stator winding to withstand vibrations, avoiding motor failure due to the damage of wire insulation.

The utilization of a thermally conductive epoxy instead of a regular varnish to impregnate the stator winding can enhance motor cooling remarkably, for example, using a potting epoxy that is a recognized component in a UL-1446 insulation system that has a Class H (180°C) temperature rating. Actual measurement shows that potting the stator winding using this thermally conductive epoxy lowers its winding-to-ambient thermal resistance, R_{th} (in °C/W), by 50% compared to impregnating the winding with a typical varnish [4.32].

4.5.4 Vacuum Pressure Impregnation

The vacuum pressure impregnation (VPI) technology has been extensively used in a wide range of applications in the electric machine manufacturing industry from insulating coil windings to sealing porous metal castings. The characteristic of this technology is to use a VPI tank (Figure 4.36) that is vacuumed first and then pressurized to achieve the best insulation effect on stators. This method can provide the highest industrial standards for electric machines. By driving out voids from the electric winding through the VPI process, the thermal conductivity of the winding is remarkably enhanced so that the hot spots are eventually eliminated. This also reduces the risk of partial discharge in the winding. In fact, the VPI can make the high stator mechanical integration to reduce vibration of the motor. Since the resins contain no solvents and only a small amount of resin vaporizes during curing, the VPI process has a negligible environmental impact. Presently, this state-of-the-art method is primarily applied on heavy-duty motors.

The primary VPI process involves (Figure 4.37) the following:

- Place a stator in a VPI tank.
- Pull the vacuum of the container for a period of time to remove air and moisture from the stator winding.

FIGURE 4.36
VPI tank used for large electric motors.

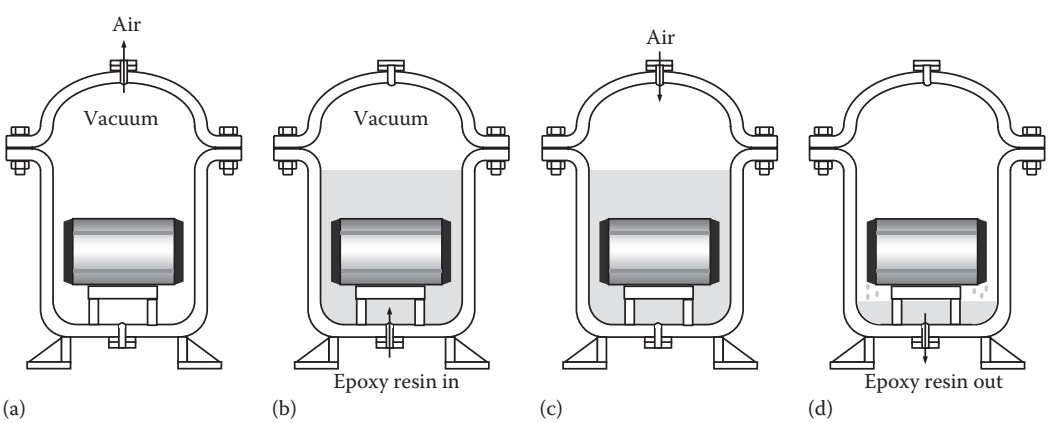

FIGURE 4.37
VPI process: (a) evacuating the container into deep vacuum, (b) introducing epoxy resin into the container until the stator is completely submerged, (c) releasing the vacuum of the container and applying pressure over the resin-covered stator to force resin completely into the stator, (d) draining epoxy resin out of the container, and (e) placing the stator into an oven and baking it for curing the epoxy resin (not shown).

FIGURE 4.38
The temperature controlled oven for curing and baking epoxy resins of impregnated motors.

- Introduce a preheated solventless epoxy resin into the vacuum container until it fully covers the stator and hold the vacuum of the container for a period of time.
- Release the vacuum of the container and pressurize the container to a desired level to achieve maximum impregnation for deep penetration of epoxy resin into voids.
- Draw the epoxy resin from the container.
- Place the impregnated stator into a temperature controlled oven (Figure 4.38) and bake it to cure the epoxy resin and fully develop the properties of the insulation system for a period of time at a desired temperature. In today's motor workshops, the baking process is fully controlled by a built-in computer in the oven to followup the preset temperature chart. To prevent *thermal shock* to motor insulation systems, the oven temperature is brought up and down slowly. Ovens are typically equipped with digital panel meters to monitor baking temperatures.

This VPI process can achieve complete penetration of resin throughout turns, coils, slots, and insulation and thus is primarily applied on heavy-duty applications. The VPI technology is superior to solvent varnishes in many aspects. As discussed previously, solvent varnishes lose 50%–70% of volume during baking, leaving voids and air pockets in

the windings. In contrast, VPI provides a 100% solid mass structure that increases the mechanical strength, minimizes the hot spots, and reaches the highest level of environmental protection. A motor winding that undergoes a VPI process is virtually impervious to oil, moisture, and chemical contaminants [4.33].

4.6 Stator Design Considerations

4.6.1 Cogging Torque

Cogging torque is one of inherent characteristics of PM motors, resulted from the interaction of the PM MMF harmonics and the air gap permeance harmonics due to slotting. Since cogging torque can cause speed ripples, induce motor vibration, and deteriorate motor performance, it is one of the major design goals for motor engineers to reduce cogging torque.

Electromagnetic design primarily determines the level of cogging torque. As addressed in Chapter 1, there are many methods for reducing the amount of cogging torque, for instance, skewed stator stack, optimized slot and pole combination [4.34], uneven distribution of stator slots, stator tooth notching, and pole shifting.

In addition to EM design, a cogging condition may be inadvertently set up from improper stator fabrication processes, including the following: (1) The lack of a proper annealing after lamination stamping will directly lead to high residual stresses in the stamped laminations, as well as the degradation of magnetic properties, and thus results in cogging torque. (2) The lack of deburring will increase eddy-current losses. (3) Machining defects (e.g., concentricity and roundness) on the stator ID may result in unequal air gap and thus greatly induce a large amount of cogging torque. (4) Exceeding roundness or concentricity tolerance of the stator ID can significantly change cogging torque. A decrease in the air gap or air gap variations can considerably increase cogging torque. (5) Exceeding tolerance of slot opening is very sensitive to change cogging torque. (6) Welding a stack of stator laminations may increase the core loss at the welded area, cause the deformation of the stator core, and alter magnetic flux distribution. All these factors could change cogging torque. A more important issue is the welding location. Welding in the back iron between the teeth could increase cogging torque.

4.6.2 Air Gap

The radial distance between the rotor and stator in a motor is defined as the air gap. Normally, a smaller air gap provides a more efficient and powerful motor. Hence, it is highly desired to maintain the air gap dimension as small as possible and within a small variation in operation. The control of the air gap dimension involves the design of several components such as the stator, rotor, motor housing, and endbells. An important factor that affects the air gap dimension is the accuracy of the coincidence of the stator and rotor axes. Thus, to provide a motor with a small air gap dimension within only a small tolerance, preciseness in manufacturing of these parts is required.

In attempting to obtain concentricity, it has been proposed [4.35] to mechanically fit the metal rotor bearing support members to the stator stack in a matter that form a cavity. A hardenable plastic material is ejected to fill the cavity and bond the parts together. The assembly is then machined to the desired dimensions.

4.6.3 Stator Cooling

An important objective in motor design is to control the motor temperature below its allowable value. Increased motor temperature often reduces motor efficiency and affects bearing life. The Arrhenius equation predicts that the failure rate of an electric device is exponentially related to its operation temperature.

In designing a motor cooling system, thermal engineers always focus on stator cooling for several reasons: (1) The stator winding is usually the main heat source in a motor. Test data show that in most applications heat generated in a motor is primarily attributed to the stator. (2) Cooling in the stator end-winding region is particularly difficult and still remains a challenge due to various factors [4.36]. (3) As a stationary component, the stator is much easier to be cooled compared with the rotor. In fact, the stator often serves as a heat sink for the motor. (4) For some electric motors, the pumping effect, which is resulted from the rotor rotation, is strong enough to generate turbulent circulating flows for making the motor self-cooling [4.37].

4.6.4 Robust Design of Stator

The root causes of motor failure are often related to mechanical deterioration such as vibration, static and cyclic loads (e.g., centrifugal and differential expansion forces), insulation fracture, and bearing lubricant contamination and leakage, to name a few. Robust design techniques can optimize the stator design and ensure adequate motor performance over a wide range of operating conditions.

Because the rotor is supported on bearings located at the endbells of the machine, the stator design is significantly impacted by the dynamic behavior of the rotor. As a matter of fact, the loads carried by the rotor are essentially transmitted to the stator and finally to the motor base. In this load configuration, the structural vibratory loads caused by the rotor, and loading caused by stator vibration that drives rotor behavior, are intertwined. This requires a full understanding of the structural interactions for all motor components, as well as the interaction between the motor and its base.

Motor vibration is greatly influenced by its base. A weak motor base usually results in high vibration. Thus, it is essential to design a motor base strong enough to withstand all motor loads for preventing resonance and vibration.

4.7 Mechanical Stress of Stator

Electric motors are exposed to many kinds of disturbances and stress. Some disturbances are due to imposed external conditions such as mechanical or electric unbalanced system; harmonics; supply interruptions; variations in voltage, current, and frequency; unstable cooling system; and large variations in ambient temperature and humidity. Stress factors include frequent successive start-ups, abnormal use of the motor, stall, and overload situations. These stress and disturbances deteriorate the winding insulation mechanically and increase thermal aging rate and thus may eventually lead to an insulation failure [4.38].

Stresses and strains in stator cores can not only cause mechanical problems but also change the magnetic properties of electrical steels (e.g., silicon steel). A stator is subjected

to a variety of forces during operation. When the forces are relatively small, only elastic deformations are generated on the stator core. Removal of the forces will permit the stator core to return to essentially a stress-free condition. However, under large load conditions, the stator core has to withstand high stresses that produce plastic deformations of the stator core. These plastic deformations can distort the metal crystals or atomic structure and, in turn, affect the magnetization characteristics of the material. As a result, a set of the maximum stress on magnetic core materials must consider both the mechanical and electromagnetic requirements.

There are three main sources of mechanical stress for stators. The first common mechanical stress is caused by power frequency current. When a motor starts, the current through the stator winding reaches its maximum value that gives rise to a magnetic force oscillating at twice the power frequency [4.39]:

$$F = \frac{k i_{rms}^2}{w} \tag{4.1}$$

where
i_{rms} is the rms current
w is the stator slot width
$k = 0.96$

If the current in a stator winding is

$$i_{rms} = A \sin \omega t \tag{4.2}$$

Equation 4.1 can be rewritten as

$$F = \frac{kA^2 (1 - \cos 2\omega t)}{2w} \tag{4.3}$$

Noting that $\omega = 2\pi f$, this equation describes the oscillation force in the radial direction at twice the power frequency. If the stator winding resonates at this frequency, the insulation of the winding will be damaged. More likely, the damage occurs at the stator end-winding regions. In fact, resonances cause serious vibration levels of end windings and develop high stress in these windings. As discussed previously, stator encapsulation can provide a good solution to avoid it.

In addition, there is also a force at twice the power frequency in the circumferential direction caused by the rotor's magnetic field interacting with the current in the stator winding. However, this circumferential force is only about 10% of the radial force.

The second mechanical stress is caused from the transient effect. For synchronous machines, switching on of motors or out-of-phase synchronization can give rise to a large transient power frequency current that may be five times (or even more) greater than the normal operating current in the stator. This results in that the magnetically induced mechanical force is 25 or more times stronger than the normal service. This alternative force tends to bend the stator winding, especially in the end-winding regions. If the force is too large, the stator winding may crack.

The third source of mechanical stress resulted from rotors. In a motor, the rotor rotates at a high speed with a coupled externally driven machine. While the rotor is subject to a larger centrifugal force, it transmits its radial and axial loads to the stator via bearings.

References

[4.1] Klontz, K. W. and Li, H. D. 2008. Reducing core loss of segmented laminations. *Power Transmission Engineering*, June Issue: 26–32.

[4.2] Welch, R. 2009. Think thermal to increase motor efficiency. *Motion System Design—Motors & Drives* **51(8)**: 32. http://motionsystemdesign.com/motors-drives/think_thermal_increase_0809/.

[4.3] Vandenbosschel, L., Jacobs, S., Henrotte, F., and Hameyer, K. 2010. Impact of cut edges on magnetization curves and iron losses in e-machines for automotive traction. *The 25th World Battery, Hybrid and Fuel Cell Electric Vehicle Symposium & Exhibition*, Beijing, China.

[4.4] Moses, A. J., Thomas, B., and Thompson, J. E. 1972. Power loss and flux density distributions in the T-joint of a three-phase transformer core. *IEEE Transactions on Magnetics* **8(4)**: 785–790.

[4.5] Jones, M. A. and Moses, A. J. 1974. Problems in the design of power transformers. *IEEE Transactions on Magnetics* **10(2)**: 148–150.

[4.6] Fisher, G. A. and Jacobs, J. T. 1993. Lightweight high power electromotive device. U.S. Patent 5,212,419.

[4.7] Dicks, G. 2010. Permanent magnet alternator with segmented construction. U.S. Patent 7,816,830.

[4.8] Zhu, Z. Q., Ruangsinchaiwanich, S., Ishak, D., and Howe, D. 2005. Analysis of cogging torque in brushless machines having nonuniformly distributed stator slots and stepped rotor magnets. *IEEE Transactions of Magnetics* **41(10)**: 3910–3912.

[4.9] Neuenschwander, T. R. 2006. Method of manufacturing a formable laminated stack in a progressive die assembly having a choke. U.S. Patent 7,062,841.

[4.10] Magnussen, F., Svechkarenko, D., Thelin, P., and Sadarangani, C. 2004. Analysis of a PM machine with concentrated fractional pitch windings. *Proceedings of Nordic Workshop on Power and Industrial Electronics* (NORPIE). Trondheim, Norway.

[4.11] Carpenter, D. E. 1933. Edge-wound core. U.S. Patent 1,920,354.

[4.12] Ozawa, M. and Fukuda, T. 2003. Rotating electrical machine stator. U.S. Patent 6,525,437.

[4.13] Gieras, J. F. 2002. *Permanent Magnet Motor Technology: Design and Applications*, 2nd edn. Marcel Dekker: New York.

[4.14] Aoki, K. and Yamaguchi, T. 1969. Method of making the stator core for rotary electric machinery. U.S. Patent 3,436,812.

[4.15] Rocky, D. M., O'Connor, Jr., J. F., Marvin, R. H., Charwick, E. R., Tribodeau, P., and Won, B. 2005. Permanent magnet motor. U.S. Patent Application 2005/0073210.

[4.16] Knapp, J. M., Cain, S. A., Pesek, S. A., Tran, T. Q., and Parmeter, L. J. 2012. Systems and methods for electric motor construction. U.S. Patent Application 2012/0275942.

[4.17] Bellemare, D. J., Donahue, J., Fagan, M., and Vollono, R. 2002. Electrostatic fluidized bed coating method and apparatus. U.S. Patent 6,458,210.

[4.18] Paulides, J. J. H., Jewell, G. W., and Howe, D. 2004. An evaluation of alternative stator lamination materials for a high-speed, 1.5 MW, permanent magnet generator. *IEEE Transactions of Magnetics* **40(4)**: 2041–2043.

[4.19] Nagomy, A. S., Dravid, N. V., Jansen, R. H., and Kenny, B. H. 2005. Design aspects of a high speed permanent magnet synchronous motor/generator design for flywheel applications. *IEEE International Electric Machines and Drives Conference*, pp. 635–641, San Antonio, TX.

[4.20] Brown, C. P. 1996. Design for manufacturability of a high-performance induction motor rotor. MS thesis, Massachusetts Institute of Technology, Cambridge, MA.

[4.21] Isayama, M. 1996. Method for producing laminated iron cores. U.S. Patent 5,539,974.

[4.22] Hendershot, Jr. J. R. and Miller, T. J. E. 1994. *Design of Brushless Permanent-Magnet Motors*. Magna Physics Publishing, Hillsboro, OH.

[4.23] Crawford, D. E. and Fields, H. T. 1990. Core and slot liner. U.S. Patent 4,922,165.

[4.24] EL-Refaie, A. M. 2010. Fractional-slot concentrated-windings synchronous permanent magnet machines: Opportunity and challenges. *IEEE Transactions on Industrial Electronics* **57(1)**: 107–120.
[4.25] The P.D. George Company. 2001. Technical data sheet: Pedigree No. E-88 epoxy and No. C-89 hardener. http://www.elantas.com/.
[4.26] Hollstein, W. 2012. Thermosetting resin systems for stator encapsulation in electro-mobility and industrial motors. http://www.lindberg-lund.fi/files/PDFkataloger_FI/WHollstein_Inductica_EncapsulationofStatorsforemobility_2012.pdf.
[4.27] Emerson & Cuming. 2001. Technical data sheet—STYCAST® 2850 FT-thermally conductive epoxy encapsulant. http://lartpc-docdb.fnal.gov/0000/000059/001/stycas2850.pdf.
[4.28] Resinlab. Thermally conductive encapsulants. http://www.resinlab.com/encapsulant/thermal.html.
[4.29] Lord Corporation. 2005. SC-320—Highly thermally conductive encapsulating system. http://www.lord.com/Products-and-Solutions/Electronic-Materials/Product.xml/561.
[4.30] Du Pont. 1997. Electrical/electronic thermoplastic encapsulation. H-58633. http://plastics.dupont.com/plastics/pdflit/europe/markets/TEncap_e.pdf.
[4.31] Neal, G. D. 2002. Stator assembly. U.S. Patent 6,362,554.
[4.32] Welch, R. Jr. 2012. A more efficient servomotor. http://www.exlar.com/pages/380-A-More-Efficient-Servomotor.
[4.33] Inman Electric, Inc., 2012. Vacuum pressure impregnation (VPI). http://www.inmanelectric.com/vacuum.html
[4.34] Zhu, Z. Q. 2000. Influence of design parameters on cogging torque in permanent magnet machines. *IEEE Transactions on Energy Conversion* **15(4)**: 407–412.
[4.35] Kaufman, Jr., G. A. 1977. Electric motor with plastic encapsulated stator. U.S. Patent 4,048,530.
[4.36] Tong, W. 2008. Numerical analysis of flow field in generator end-winding region. *International Journal of Rotating Machinery* **2008**: Article ID 692748.
[4.37] Tong, W. 2001. Numerical analysis of rotating pumping flows in inter-coil rotor cavities and short cooling grooves of a generator. *International Journal of Rotating Machinery* **7(2)**: 131–141.
[4.38] ABB. 2010. Power system protection: Motor protection (Section 8.11). *In Distribution Automation Handbook*. ABB Oy: Vaasa, Finland. http://www.abb.com/product/ap/db0003db004281/a40c9d1981558a3cc1257a060018bfb1.aspx.
[4.39] Stone, G. C., Boulter, E. A., Culbert, I., and Dhirani, H. 2004. *Electrical Insulation for Rotating Machines*. Wiley-Interscience, Hoboken, NJ.

5

Motor Frame Design

Electric motors are manufactured in a variety of types and configurations. Typically, an electric motor assembly includes a hollow, substantially cylindrical-shaped housing with a stator and a rotor disposed within the housing interior and an endbell at each end of the housing for providing protections to the motor components against the insertion or intrusion of solid/liquid objects under various environmental conditions. In addition to rotors and stators, some motors may have electronic components that are used to improve operating characteristics for particular applications. These electronic components also need to be well protected.

For radial air gap motors, the stator coils are wound axially through the stator slots, and the end turns of the stator winding are positioned adjacent to the stator end surfaces. The endbells and the motor housing form an enclosure to protect the stator windings and end turns from inadvertent contact and grounding while providing a mounting surface for rotor bearings and shaft bushings. The endbells also prevent debris from entering the hollow interior of the stator and interfering with operation of the motor.

5.1 Types of Motor Housing

Motor housings are designed to provide the support for the stator core and protect motor components from foreign objects such as water, dust, sand, and moisture (see Figure 5.1). Motor housing can be made by a variety of manufacturing processes such as wrapping, casting, extruding, machining, and stamping. For rare-earth magnet motors, either magnetic or nonmagnetic materials can be used to fabricate motor housings. However, for Alnico magnet motors, the housings must be made from only nonmagnetic materials such as aluminum, brass, and stainless steel to preserve specified performance characteristics of the motors. The requirements for the motor housing design include high structural strength for supporting the stator, low vibration transmission, light weight, corrosion resistance, and low cost.

5.1.1 Wrapped Housing

A wrapped motor housing is made from a flat sheet metal that passes through a 3-roll bending machine to form a cylindrical-shaped form. Figure 5.2 illustrates the manufacturing process of wrapped housing. The first step is to prepare a metal sheet with prepunched apertures for installing motor fasteners and notches for receiving electric connection cables (Figure 5.2a). At each edge of the sheet metal, a small notch is left. When the two edges come together nicely, these notches form a narrow clearance for receiving welding operation. Subsequently, the sheet metal is rolled by a bending machine with three adjustable rolls to control the radius of the rolled sheet metal (Figure 5.2b). When the stator core is

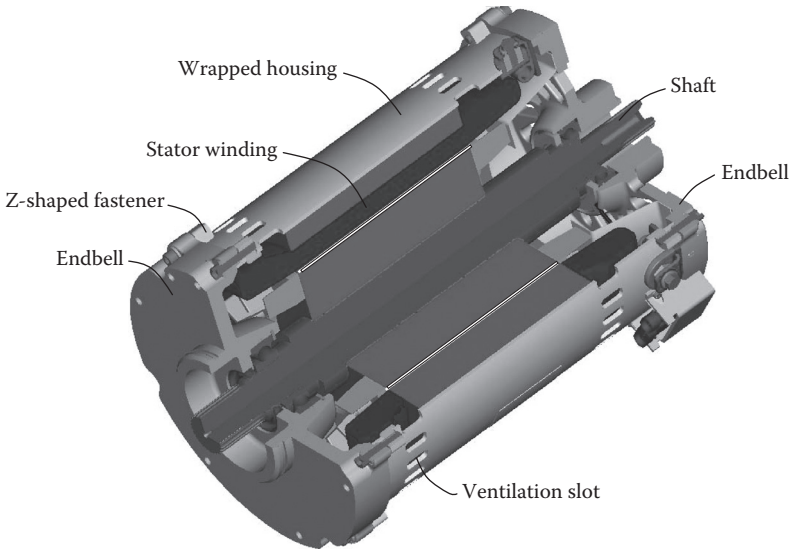

FIGURE 5.1
Cutaway view of electric motor with wrapped housing.

inserted, the wrapped housing is pressed tightly with a special tool for welding along the welding seam (Figure 5.2c). Lastly, the two ends of the housing are machined for receiving the endbells that block off the axial ends.

During the welding process of the wrapped housing, a large amount of heat is produced and conducted into the motor housing and stator core. Excessive heating can cause the deformation and distortion of the housing and stator core, resulting in permanent damage to these parts. High heat input can also adversely affect the mechanical properties of the welded parts. Therefore, it is critical to control the temperature on the welded parts and enable efficient heat dissipation from them to the environment. For example, using a higher welding speed, a lower welding current, and/or an active/passive cooling technique (e.g., cooling via cold plate) can essentially solve most welding overheating problems. While the control of heat input is highly desired in the welding process, it must be noted that the rapid cooling, on the other hand, may lead to the change of metallographic microstructure in welded materials, resulting in the formation of large grains and the reduction in resistance to cracking.

5.1.2 Casted Housing

Casting refers to a manufacturing process that involves a phase change of casting materials between liquid and solid. Metal casting processes can be traced back to approximately 3600 BC as ancient Egyptians utilized casting to make bronzes. In China, the discovery of "Three-Star Piles" civilization in the last century has revealed that about 4000 years ago, ancient Chinese casted out exquisite bronzes. The cast iron technique was invented in China in the seventh century BC. The earliest cast iron pieces in the world were discovered in Shanxi, China, by archaeologists in the 1980s.

A casting process begins by heating up of casting material to reach the material melting temperature or above, at which the casting material is in the liquid state. The molten casting material is maintained at the temperature for a period of time for degassing, then poured

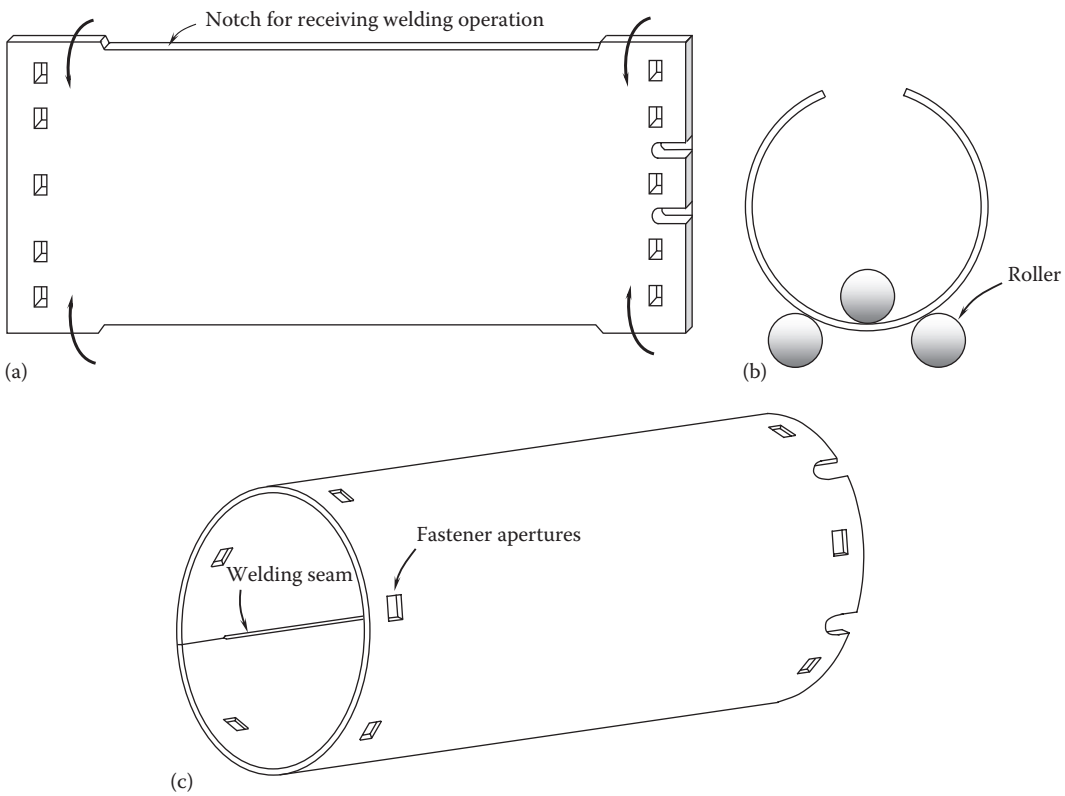

FIGURE 5.2
Manufacturing procedure of wrapped motor housing: (a) punching apertures for installing fasteners and notches for receiving motor cables on a sheet metal using a high-speed punching machine and cutting the sheet metal, (b) rolling the sheet metal to form an open hollow tube with a 3-roll bending machine, and (c) welding at the notched edges to form the motor housing.

into a mold with a desired shape, and allowed to solidify. Therefore, casting technologies are especially suitable for producing motor housings, endbells, and other components with a wide variety of shapes and geometries. In fact, with the ability to effectively produce high-quality and low-cost mechanical components with a wide range of sizes and materials, various casting processes are extensively used in almost all industries, especially in automobile, aerospace, and power industries. Figure 5.3 is a typical servomotor with a casted housing. In this design, the housing is integrated with the front endbell as a single-casted part.

5.1.2.1 Casting Materials

Common casting materials include aluminum, iron, copper, magnesium, zinc, and steel alloys. Among them, aluminum is the most popular material extensively used by motor manufacturers. Benefited with a low melting temperature, high liquidity, light weight, high thermal conductivity, and other good casting characteristics, aluminum alloys have been commonly used for manufacturing motor housings, endbells, and other components. Furthermore, reusability is one of the principal advantages for aluminum. With the improvement of aluminum alloys and casting processes and good balance between

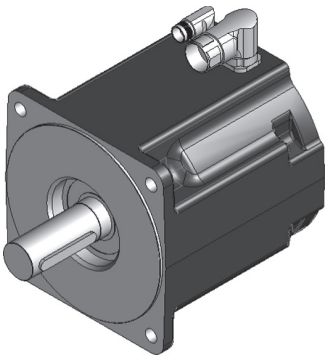

FIGURE 5.3
Casted servomotor housing, showing that the front endbell is integrated with the motor housing.

mechanical properties and lightness, it is expected that more and more aluminum-casting parts will be demanded by the motor industry.

Today, cast iron housings are commonly used in heavy-duty and large-size electric motors, as cast aluminum is unable to offer the required strength and hardness. Cast irons are ternary alloys of Fe–C–Si. The microstructure and mechanical properties of cast irons vary considerably depending on the form of the carbon element presented in the irons. There are four main types of cast irons with different carbon forms: gray, malleable, ductile, and white cast iron. Carbon is mainly present as graphite in gray, malleable, and ductile cast iron, while exists as cementite (Fe_3C) in white cast iron. Gray cast iron contains 2.5%–4% carbon and 1%–3% silicon [5.1]. Silicon is essentially needed as a graphite stabilizing agent that makes cementite (Fe_3C) more difficult to form in the cast irons. Graphite is a relatively soft material, and its presence in gray iron gives it some unique and useful properties:

- Excellent vibration damping capacity, being 25–100 times better than that of a 1080 steel [5.2]. Damping is the ability of a material to absorb vibration energy by converting it into other forms of energy such as heat. The quelling of vibration is very important for structures and devices with moving parts. Damping capacity of gray iron strongly depends on its graphite structure and size. For instance, the damping capacity for a gray iron with course flake graphite can be 5–10 times higher than that for a gray iron with fine flake graphite. The strength and hardness of the gray iron is provided by the metallic matrix in which the graphite occurs. Generally, damping capacity decreases with increasing strength since a smaller amount of graphite present in the higher strength irons decreases the energy absorbed. The primary damping mechanism is localized microplastic behavior. Under cyclic loading conditions, this microplastic behavior produces a hysteresis loop whose area is proportional to the energy absorbed during each cycle [5.3]. This property is especially desirable as it reduces the acoustic noise and vibration emitted by motors.
- Superior wear resistance as the metallic matrix microstructure being primarily pearlite. Among the casting materials in Table 5.1, gray cast iron has the highest hardness.
- High compressive strength. Gray iron's compressive strength is typically three to four times higher than its tensile strength [5.4]. Thus, the parts made by gray cast iron are mainly designed to withstand compressive forces rather than tensile forces.

TABLE 5.1

Properties of Some Common Casting Materials for Electric Motors

Material Property	Aluminum 383	Aluminum 356-T6	Aluminum 6061-T6	Ductile Iron 65-45-12	Gray Cast Iron
Melting point (°C)	516–543	557–613	582–652	1148	1180
Density (kg/m^3)	2700	2670	2700	7096	7150
Yield tensile strength (MPa)	152	>165	276	310	—
Ultimate tensile strength (MPa)	310	>234	310	448	276
Elongation (%)	3.5	3.5	17	12	1
Poisson ratio	0.33	0.33	0.33	0.29	0.29
Hardness (Brinell)	75	70–105	95	170–207	183–234
Modulus of elasticity (GPa)	71.0	72.4	68.9	163	90–113
Shear modulus (GPa)	27	27.2	26.0	65	36–45
Fatigue strength (MPa)	145	90	96.5	210	110
Shear strength (MPa)	187	143	207	400	334
Machinability (%)	70	50	50	0	0
Thermal conductivity (W/m-K)	96.2	151	167	32.3	47
Coefficient of thermal expansion @ 20°C (mm/m-K)	21.1	21.4	23.6	14.6	10.8

- Internal lubricating qualities and machinability. Graphite has little strength or hardness. The presence of the graphite provides several valuable characteristics to gray iron, including the ability to produce sound castings, dimensional stability, borderline lubrication, and excellent machinability. In fact, cast iron is the easiest ferrous material for dry machining.
- Improved thermal properties. Gray iron has a better thermal conductivity and a lower coefficient of thermal expansion compared with ductile iron.

Due to these superior properties, gray cast iron has been a staple in automotive manufacturing for many years. As a desired material in vibration damping for achieving low-noise performance, there is a steady increase in the use of cast iron in certain types of motors, such as those in medical equipment.

As a member of the cast iron family, ductile iron contains 3%–4% carbon and 1.8%–2.8% silicon. This type of cast iron has a high strength. Unlike gray cast iron in which graphite is presented as flakes, ductile iron contains tiny graphite nodules, which make cracking more difficult. Therefore, ductile cast iron is much stronger and has much higher ductility than gray cast iron. In addition to high strength, the toughness and shock resistance also increase for ductile cast iron [5.5]. Furthermore, the damping capacity of ductile iron is considerably greater than most other ferrite materials (except for gray iron). These superior properties of ductile iron make it ideally suited for various industrial applications. In the motor industry, ductile iron is often used to make motor housings and endbells.

For ductile iron with high silicon contents, a silicon-rich surface layer is formed to resist oxidation, corrosion, and heat. Stabilization of the ferrite phase reduces the influence of high temperature in two ways: (1) silicon raises the critical temperature at which ferrite transforms to austenite; (2) the strong ferritizing tendency of silicon stabilizes the matrix against the formation of carbides and pearlite, thus reducing the growth associated with the decomposition of these phases at high temperature [5.6].

Steel casting is a specialized form of casting, adapted for parts that must withstand heavy loads and shocks. There are generally two types of steel castings to meet different needs of various applications: carbon steel casting and alloy steel casting. Carbon steel casting is the most popular type, which uses low-, medium-, and high-carbon steel in casting to obtain different ranges of strength. For alloy steel castings, special alloy elements (e.g., manganese and chromium) are added to casting steels to enhance the desirable material properties. Among alloy steel castings, stainless steel casting is designed to resist corrosion and thus widely used in the chemical, shipbuilding, and renewable energy industries. However, steel casting is seldom used for making motor components unless casting iron cannot deliver enough strength or motors have strict anticorrosion requirements.

Compacted graphite iron has been developed since the mid-1970s. Because the graphite in this type of iron takes a form between that in gray iron and ductile iron, it has the benefit of combining the high thermal conductivity of gray iron with the high strength and high modulus of elasticity of ductile iron [5.7]. Since it has high thermal-shock resistance, this type of iron is especially suitable in applications involving thermal shocks.

In the selection of materials for casting housings, a number of mechanical and thermal properties must be taken into account, including mechanical strength, elongation, hardness, modulus of elasticity, dimensional stability, shrinkage, machinability, thermal conductivity, among other indices. The properties of the most common casting materials are given in Table 5.1.

5.1.2.2 Casting Process

Casting processes can be divided into two broad groups, gravity-fed and pressure-fed processes, where the gravity fed involves pouring molten metal into mold cavities under gravity and the pressure fed involves injecting molten metal under pressure. The choice of casting process is greatly influenced by product geometric complexity, size, material, dimensional accuracy, surface finish, tooling and other costs, and production volume.

As one of the oldest known manufacturing techniques, casting still remains a highly efficient and cost-effective manufacturing process today. Modern advances in casting technology have led to a wide array of specialized casting methods. In manufacturing industries, four main casting methods are commonly used to make a variety of cast products—die casting, sand casting, permanent-mold casting, and evaporative pattern casting (EPC)—each having its own unique fabrication advantages and limitations.

Die casting is a manufacturing casting process that can produce geometrically complex metal parts through the use of reusable molds (i.e., dies). There are traditional high pressure and also low pressure die casting processes. The casting materials typically are nonferrous alloys such as aluminum, zinc, magnesium, and copper. In a die-casting process, molten metal is injected under high pressure over a very short period of time into a hardened steel or cast iron die (Figure 5.4). Then, the ejection die is removed, and the die-casting part is ejected by means of ejection pins. The total cycle time is very short, typically between a few seconds to less than a minute. High casting pressures help reduce porosities in casting parts, increase casting uniformity, and improve the surface finish and dimensional accuracy. Because die casting can provide good surface finishing and dimensional accuracy, only light machining is required to enforce the accuracy of a few critical dimensions. In some cases, post machining can be completely eliminated. A key feature in die design is the positioning of the runners and gates. Well-designed gates permit rapid flow into the die cavity, minimizing turbulence and long flow paths for the molten metal.

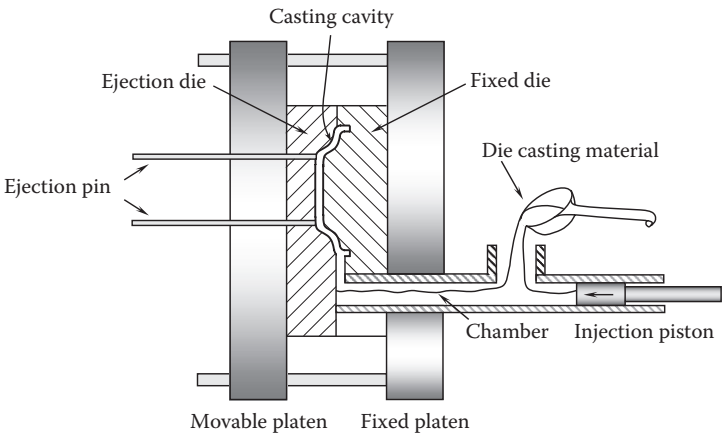

FIGURE 5.4
Illustration of die-casting process.

Die-casted housing is most popular in the motor industry due to its inherent advantages of light weight, low cost, high thermal conductivity, and high productivity. In the design of die-casting housing, the most important thing is to determine the departing line as it has a direct impact on the success of the casting process. Secondly, it is better to make the wall thickness as uniform as possible to reduce casting deflects caused by nonuniform cooling rates and residual stresses in casting housings. Reinforced ribs are often employed in motor housings to reduce the housing weight and casting material. All corners of casting parts should be radiused generously to avoid stress concentrations and cracks. The set of the draft angle allows casting parts to be easily removed from dies. The minimum draft angle per side in the parting direction depends on the casting materials: usually 0.25° for zinc alloys, 0.5° for aluminum alloys, and 0.75° for brass. In practice, a draft angle of 1°–2° on all walls in the parting direction is suitable for most applications. The arrangement of ejection pins is critical for allowing casting parts to be effectively ejected from dies.

Sand casting applies reusable sand to make sand molds. The advantages of sand casting include low cost of mold, large-size casting part, and wide variety of metals and alloys. However, sand-casted parts also suffer rough surface and poor dimensional accuracy. In this technique, the preparation and bonding of the sand mold are the critical steps. A typical structure of a sand-casting mold is shown in Figure 5.5. For casting parts with a simple geometry, the mold may be consisted of two components, that is, the upper mold and the lower mold. Depending on the geometry requirement, cores may be placed in the mold. The paths of molten metal are usually arranged on the department surface. Gas vents are left on the upper mold to allow air to escape from the mold during the casting process. In sand casting, molten metal is poured into the sand mold with the aid of the gravitational force.

Permanent-mold casting refers to the casting process that employs reusable metal molds to produce casting products repeatedly. This casting process usually requires the preheat of mold. Therefore, when the molten metal is poured into the mold under the gravitational force, the expansion of the mold is smaller than that in sand casting without preheating. The molds are usually made of high-strength steel or iron alloys. To achieve the desired lifetime of the mold, this casting process is mainly used for lower-melting-temperature

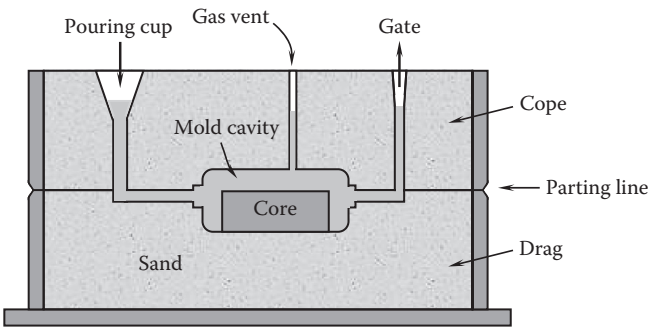

FIGURE 5.5
Typical sand-casting mold and casting process.

materials such as aluminum alloys. When the process is used to cast steel or iron alloys that have much higher melting temperatures, the mold life is extremely short [5.8].

For the ease of manufacturing and casting, the mold usually consists of two or more components. To reduce the temperature effect on the mold dimensions, a thin layer of heat-resistant material (such as clay or sodium sulfate) is coated on the inner surfaces of the mold.

Permanent-mold casting produces castings with excellent structural characteristics. There are some inherent advantages that the permanent-mold-casting process has over other casting processes: (1) because of the reusable molds, the unit tooling cost is lower than other casting processes under high-volume production conditions; (2) some mechanical properties of casted parts via permanent-mold casting are more favorable; (3) the dimensional accuracy is increased; (4) the surface finish is improved; and (5) the directional solidification rate can be controlled by varying the mold wall thickness or selectively heating or cooling certain positions of the mold. The fast cooling rates created by using a metal mold result in a finer grain structure than sand casting [5.8]. However, because of the high tooling cost, this casting process is obviously uneconomical for low-volume productions. The permanent-mold-casting process is especially suitable for making motor housings with thick walls. Figure 5.6 illustrates the permanent mold for elevator motor housings.

The EPC technique has been developed for providing a cost-effective and low-pollution solution in the foundry industry. EPC takes advantage of certain materials that are easy to evaporate under high temperatures (e.g., foam plastic) to fabricate casting patterns. The pattern is coated with refractory materials and buried into dry sand.

There are two main cast processes in EPC. The lost-foam-casting process is demonstrated in Figure 5.7 [5.9]. In this casting process, a pattern is positioned in a suitable container. Dry sand is placed in a container to surround and cover the pattern. Sand is vibrated to ensure that the pattern is completely surrounded without leaving undesirable voids. As the molten alloy is introduced into the mold through a sprue, the pattern material evaporates immediately upon contacting the molten alloy. As a consequence, the molten alloy replaces the space of the pattern and forms a seamless casting piece, which has exactly the same shape as the pattern. Therefore, there is no need for removing the pattern from the mold during the whole casting process.

Full-mold casting combines sand casting and lost-foam casting. It employs an expandable polystyrene (or foamed polystyrene) pattern, which is supported by sand in a single-piece sand mold. The molten metal is then poured through the sprue into the mold. With the

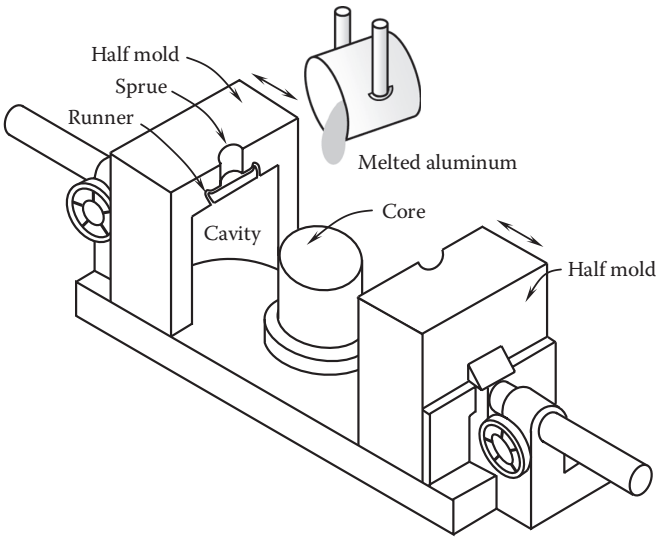

FIGURE 5.6
Permanent-mold casting for motor housing.

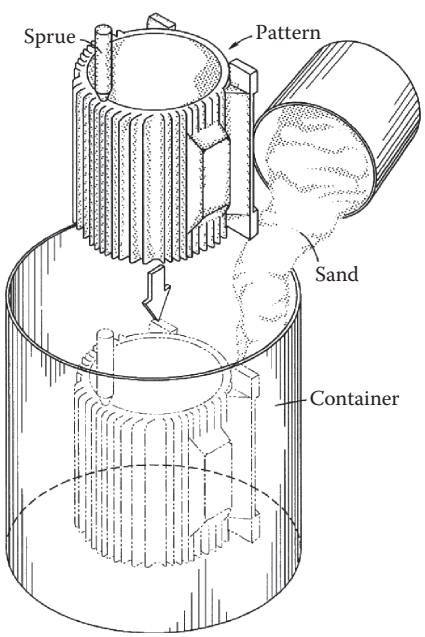

FIGURE 5.7
Making motor housing with lost-foam-casting process (U.S. Patent 6,109,333) [5.9]. (Courtesy of the U.S. Patent and Trademark Office, Alexandria, VA.)

progressive evaporation of the pattern material, the molten metal fills the available space. This casting process can make complex-shaped parts (e.g., automobile engines) without using cores and drafts.

5.1.2.3 Pressure Casting

In order to reduce porosities in casting parts, pressure casting is widely adopted by many motor manufacturers, especially for large-size, high-power-density motors. In this casting technique, the molten metal is forced into a metal mold under pressure. The higher the applied casting pressure, the shorter the casting time and the less the porosities in casting parts.

Figure 5.8 presents a low-pressure-casting process. While the molten metal is poured into the crucible, a pressurized gap forms. The pressure acts on the surface of the molten metal to force the molten metal into the mold through the refractory tube. The air pressure is maintained until the casting part has hardened within the mold. Once the casting part has solidified, the mold is opened and the casting part is removed. In this casting process, since the molten metal is drawn from the lower part of the crucible, it has less exposure to the environment and thus contains less trapped gas and other undesired contaminants, compared with the molten metal at the upper part of the crucible. Therefore, casting quality is remarkably improved.

5.1.2.4 Heat Treatment

During a casting process, the solidification rate of the casting part is far from uniform. This is especially true for permanent-mold casting in which the liquid aluminum contacted with the metal mold surfaces solidifies much faster than that in the bulk of the part. Consequently, large residual stresses are created inside the casted part with nonuniform mechanical properties.

There are several heat treatment methods, each having a unique combination of temperature and time depending on the casting process, casting material, and cast requirements. Standard T6 heat treatment can enhance material properties such as improved ductility and fracture toughness through spheroidization of the eutectic silicon particles

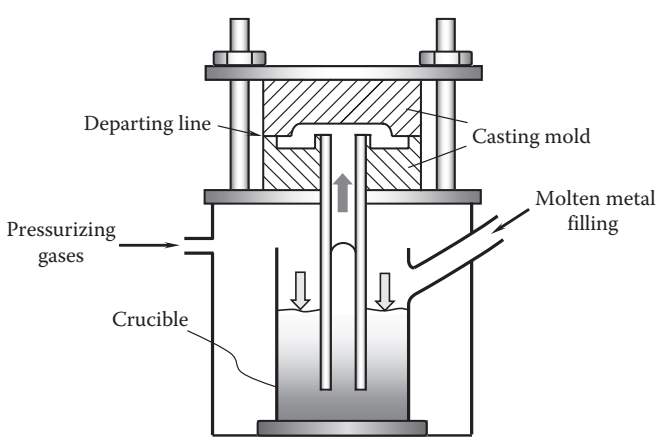

FIGURE 5.8
Pressure-casting process.

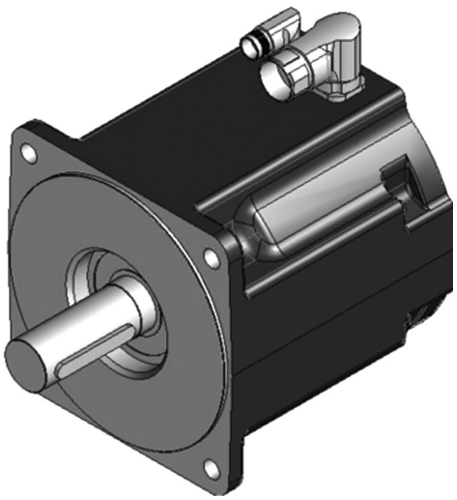

FIGURE 5.9
Furnace for casted housing heat treatment.

in the microstructure and increase yield strength through the formation of a large number of fine precipitates [5.10].

As part of T6 heat treatment, artificial aging at a relatively low-temperature range of 120°C–210°C can effectively reduce residual stresses. During this stage, the precipitation of dissolved elements occurs. These precipitates are responsible for the strengthening of the material [5.11]. It is interesting to note that a casting process normally takes less than 10 min, while a typical T6 heat treatment cycle may take more than 10 h. Figure 5.9 shows a casted aluminum housing of an elevator motor placed in the furnace, waiting for the heat treatment.

5.1.3 Machined Housing

For fast fabrication of motor prototypes, motor housings are often machined to reduce the lead time and avoid high tooling costs in casting processes. In such a way, motor housings can be machined to exact dimensions from raw materials by means of CNC machining centers. However, this method is not suitable for housings with very large sizes and/or complicated structures.

5.1.4 Stamped Housing

In stamping processes, metal sheets are deformed to desired shapes and dimensions under high stamping forces at room temperature. Because of its high productivity and acceptable accuracy of shape and size, stamping process is extensively used in various industries. In motor manufacturing, stamped housings and endbells are typically used for small-size, large-volume, and ordinary motors such as vacuum cleaner motors (Figure 5.10).

5.1.5 Extruded Aluminum Motor Housing

In various industries, aluminum extrusions provide engineering solutions for a diverse range of machinery and equipment needs due to their complex shapes, light weight,

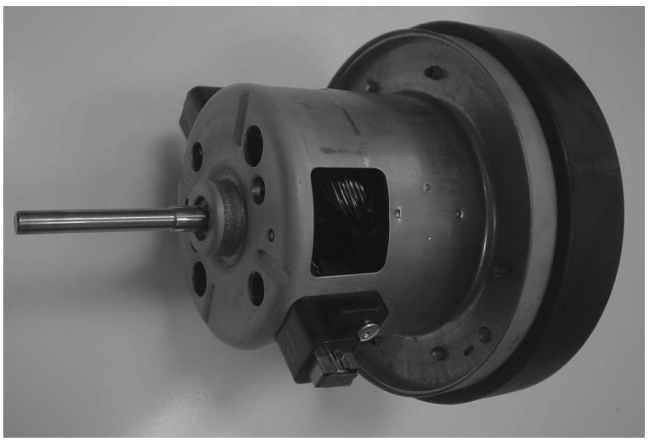

FIGURE 5.10
Stamped motor housing of a vacuum cleaner DC brush motor, showing that the drive-side endbell has been integrated with the housing.

high thermal conductivity, dimension precision, high strength, and minimal maintenance. For instance, properly designed and fabricated aluminum extrusions are an excellent choice for electric motor housings. An extruded motor housing with extruded fins and cooling channels on the housing wall can literally be obtained as a finished component by cross-cutting from extruded materials. Even with small or moderate production runs, the manufacturing costs of extruded motor housings are well below those of cast aluminum housings [5.12]. In addition, since cooling fins are designed on the extruded materials in all sides, as shown in Figure 5.11, the extruded housing design can give electric motor an outstanding cooling.

5.1.6 Motor Housing with Composite Materials

The use of composite materials in motor housing facilitates the fabrication of motors with reduced weight, lowered vibration transmission, improved mechanical damping, increased corrosion resistance, enhanced cooling, and improved motor performance. Variation of the thickness and fiber laying geometry in the composite housing may be used to control motor housing strength, stiffness, and damping characteristics. The motor housing contains both metal and composite resin material that may take more than 50%, making it lighter and easier to fabricate [5.13].

5.1.7 Motor Housing Fabricated by 3D Printing Technology

The 3D printing technique was originally proposed by researchers in MIT in the early 1990s [5.14,5.15] as a means to produce relatively inexpensive prototype parts for industrial and automotive design work. Unlike traditional manufacturing processes, this new manufacturing process allows computer-generated 3D models to be directly transformed into physical objects through a layered printing process. Because of its cost-effectiveness and versatility, the advent of this new manufacturing process ultimately has the potential to become as important and game changing as the introduction of the assembly line a hundred years ago [5.16].

FIGURE 5.11
Motor housings are made by cutting from extruded aluminum. The fins are extruded in the axial direction on all sides of the extruded aluminum for enhancing heat dissipation.

In recent years, this technique has been developed to become a manufacturing process for producing solid parts. This technique is an extremely versatile and rapid process accommodating geometry of varying complexity in a wide range of industrial applications. Because this technique can support many types of materials, it is especially suitable for the fabrication of prototypes.

With newly developed 3D printing techniques such as laser sintering and electron beam melting, this manufacturing process has been extended to produce metal parts. Although it has not been used for fabricating motor parts today, the 3D printing techniques, with the continuous improvement and cost reduction, may be applied to the fabrication of motor parts and casting toolings in the near future.

5.1.8 Frameless Motor

Frameless motors (see Figure 5.12) are especially suitable for certain applications such as airplanes and satellites for its reduced volumes and weights. The advantage of frameless motors, as compared with conventional housed motors, resides in its high reliability and efficiency, as well as its capability to form a compact mechatronic system without using redundant parts or components.

A typical type of frameless motors is the frameless DDR motor (Figure 5.13). A DDR motor generally consists of two separate components, that is, rotor (field) and stator (armature). Frameless motors are integrated directly with the load where the same bearings that support the load also support the motor. This configuration eliminates shaft, bearings, endbells, and couplings, which offer reduced volume, weight, and complexity, and also results in improved servo stiffness and quicker response [5.17]. In addition, the frameless DDR motor eliminates mechanical transmissions, such as

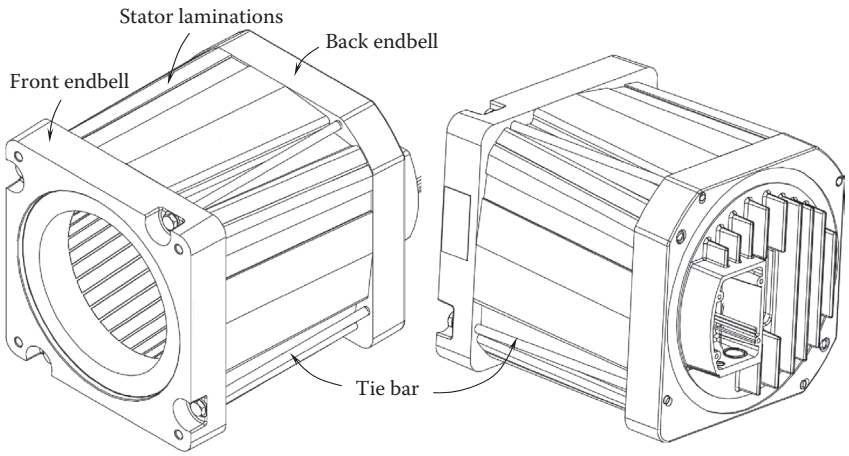

FIGURE 5.12
Frameless motor, assembled with tie bars on endbells.

FIGURE 5.13
Stators of frameless DDR motor.

gearboxes, belts, and pulleys, resulting in zero backlash, quiet operation, and zero-maintenance servo solution.

Frameless motors are attractive to those customers whose applications demand a minimized motor size and weight along with a maximized dynamic performance. Since the load is often supported on its own bearing structure, the frameless motor can be integrated directly into the system/load shaft and be suspended on the same bearings with the load.

The advantages of the frameless motor include the following:

- By eliminating the motor housing, the thermal resistance between the heat sources (e.g., stator and rotor windings) and the environment is greatly reduced.
- Compared with the conventional framed motor, a frameless motor has a smaller volume for a given power rating. Thus, frameless motors offer the most compact and lightweight solution for the motion control industry.

- Frameless motor has a high overall stiffness. Shaft stiffness is a function of the cube of the shaft diameter. For a frameless DDR motor, the shaft diameter can be approximately three times larger than that of a conventional motor.
- Hollow shafts with large diameters can be used in frameless motors for not only reducing rotor inertia but also improving motor cooling.
- Frameless motors can reduce not only the part cost but also assembly time. Therefore, the total motor cost is reduced.

For frameless motors, the motor sealing system must be carefully designed to prevent any potential damages to the motor parts.

5.2 Testing Methods of Casted Motor Housing

Testing machines are commonly used by motor manufacturers to determine mechanical properties of materials, such as yield strength, ultimate strength, strain, and elongation. As shown in Figure 5.14, a typical tension testing machine possesses a movable upper head and a stationary lower head. The grips, which are attached to the heads of the testing machine, hold the specimen firmly at each end. A tensile load is then applied to the test specimen by controlling the separating rate of the two heads until the specimen fractures. This process produces a stress–strain curve showing how the testing specimen behaves throughout the testing process. The test data are recorded by a monitoring/measuring system during the test and are used to determine the mechanical properties of the material.

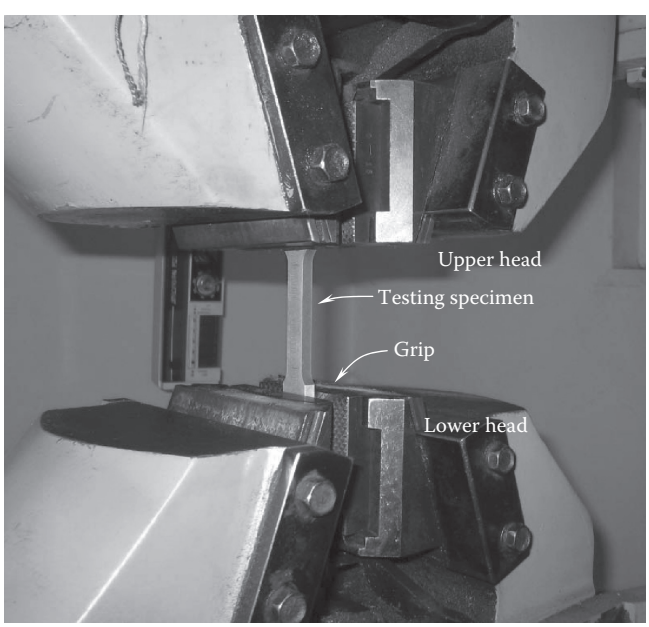

FIGURE 5.14
Standard configuration for tensile testing strip material cutting from casting housing and endbell.

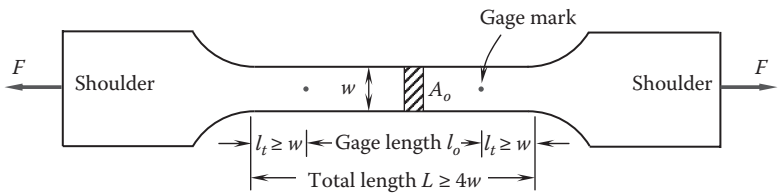

FIGURE 5.15
Typical tensile specimen, showing a reduced gage section at the middle and enlarged shoulders at the ends of the specimen.

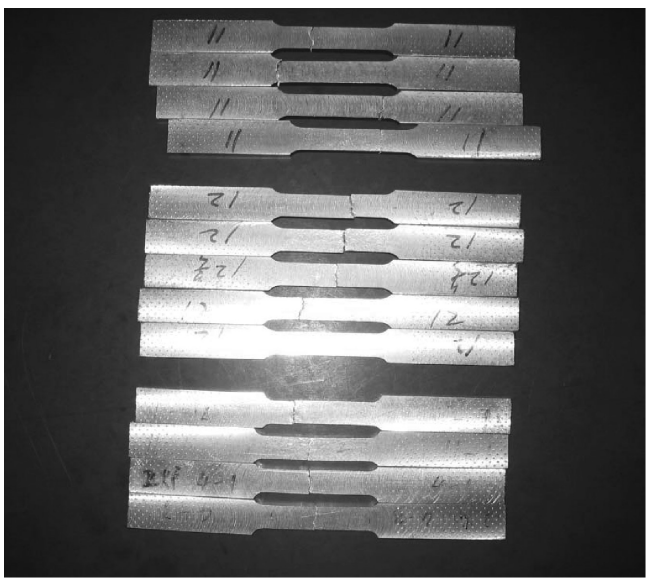

FIGURE 5.16
Testing specimens cutting from different locations of a casting housing.

In order to understand the strength distribution over the whole motor housing, the test specimens are specifically sampled at different locations of the housing. The dimension and size of testing specimen are described in the standard [5.18] and are shown in Figure 5.15. The specimen has a reduced gage section in the middle and enlarged shoulders at the ends for being held by serrated grips. To avoid the effect from the shoulders, the length of the transition region x should be at least as big as the specimen width w, and the total length of the reduced section L should be at least four times the width w.

Figure 5.16 illustrates the tested specimens that were cut from the different locations of the same casted aluminum housing. It shows clearly that all fractures occurred in the test area between the gage marks.

The stress σ is determined from the measured load F and the original specimen cross-sectional area A_o:

$$\sigma = \frac{F}{A_o} \tag{5.1}$$

The strain ε is calculated as the ratio of the length change Δl during the test to the original specimen length l_o, which is measured between the gage marks before the test:

$$\varepsilon = \frac{l - l_o}{l_o} = \frac{\Delta l}{l_o} \tag{5.2}$$

After fracture, the fractured specimen needs to be put together to measure its gage length l_1. Thus, the elongation of the material is calculated as

$$\varepsilon_e = \frac{l_1 - l_o}{l_o} = \frac{\Delta l_e}{l_o} \tag{5.3}$$

Stress–strain curves are an extremely important graphical measure of a material's mechanical properties. As an example shown in Figure 5.17, for low strains, the material obeys Hooke's law to a reasonable approximation so that stress is proportional to strain with a constant of proportionality (the line *AB*). The Young's modulus *E* is computed as

$$E = \frac{\sigma}{\varepsilon} \tag{5.4}$$

As strain is increased, the material eventually deviates from this linear proportionality and exhibits nonlinear behavior between stress and strain. The highest point attained before the stress–strain line begins to bend is defined as the proportional limit, which is the maximum point at which the material obeys Hooke's law.

Material yield strength refers to the point on the stress–strain curve beyond which the material experiences deformations plastically, as the molecular or microscopic structure undergoes a rearrangement and atom lattice planes slide over each other. This indicates that the yield point and the proportional limit refer to the same point. The only difference is that one is defined from the microscopic perspective and another from the macro perspective.

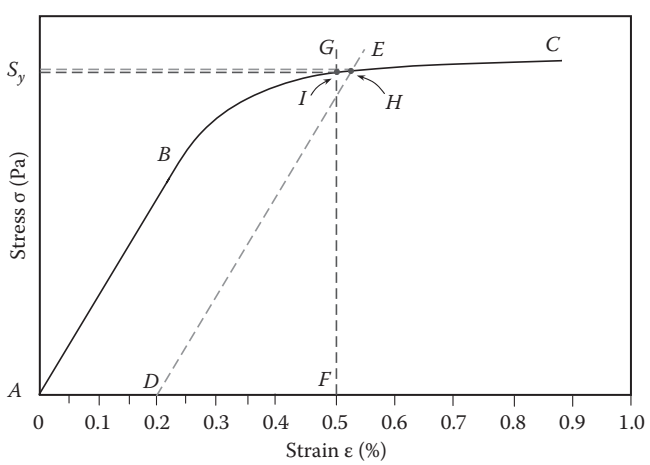

FIGURE 5.17
Determination of yield strength from the offset method and the extension under load method.

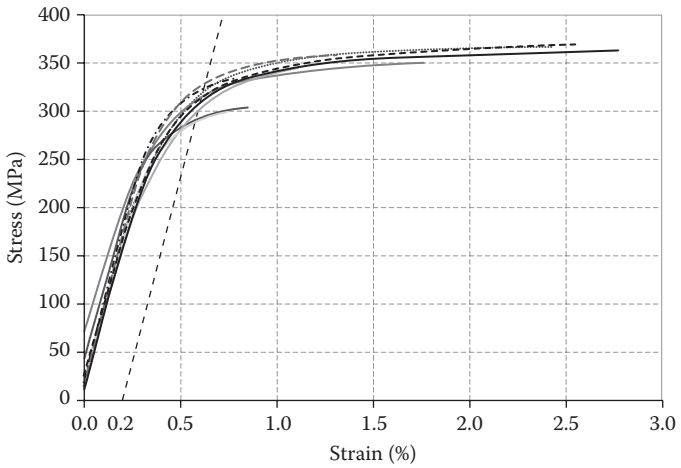

FIGURE 5.18
Stress–strain curves obtained from tested specimens cutting from different locations of the casted aluminum housing. Each curve represents the stress level at that location.

In practice, it is often difficult to pinpoint the exact yield strength at which plastic deformation begins curve. There are primarily two common methods to determine yield strength from the stress–strain curve: the offset method and the extension under load method. The offset is the horizontal distance between the modulus line (the line *AB*) and any line running parallel to it. In industries, tensile yield strengths are often determined by this method at an offset of 0.2% of strain. The intersection of the offset line and the stress–strain curve (the point *H*) thus gives the yield strength.

The extension under load method involves drawing an ordinate line *FG* from the point on the *x*-axis where the strain equals the specified extension, typically 0.5%. The intersection of the line FG and the stress–strain curve (the point *I*) defines the yield strength. From Figure 5.17, it can be seen that the values determined by two methods are very close.

The measured stress–strain curves from the samples being cut from different locations of the housing are displayed in Figure 5.18. It can be seen that the ultimate tensile strength and strain data distribute in the range of 300–370 MPa and 0.7%–2.7%, respectively. These results are very important for optimizing the motor housing design and improving casting processes.

5.3 Endbell Manufacturing

As an integral part of the motor structure, motor endbells are used to cover the ends of motor housing, to house bearings at the ends of a motor for supporting the rotor, to provide paths for cooling air flows, and to protect internal electrical and mechanical parts from moisture and dirt. Motor endbells can be made by many manufacturing processes, such as casting, machining, stamping, forging, extruding, and powder metallurgy sintering. In considering the production efficiency, cost, appearance, and other factors, casting processes have been widely adapted to produce motor endbells.

5.3.1 Casted Endbell

Similar to casting motor housings, motor endbells are often produced through a casting process. As shown in Figure 5.19, an endbell is made of die casting with an aluminum alloy. In any cases, endbells must be designed to provide a rigid and stable support for the stator and rotor assembly. For the consideration of safety, a minimum clearance gap of 1.5 mm must be provided between the coil end turns and the endbell wall.

Motor endbells can be made by either die casting or sand casting. Compared with sand casting, die casting produces parts with thinner walls, higher-dimensional accuracy, and smoother surfaces. Production is faster and labor cost per casting is lower.

For some motors with low IP requirements, endbells may be designed to have cooling openings serving as the passage of air over and around the windings. For totally enclosed motors, the endbells must have reliable and tight sealing capabilities. Therefore, no openings are allowed on the endbells.

In the design of casting endbells, it is important to consider the effect of material impurity and porosity on the strength of casting parts. In order to ensure good quality of casting, it is common to cut the casted parts to inspect casting defects, especially porosities and voids, as demonstrated in Figure 5.20. However, due to the multiparameter control in casting processes and the complex geometry of motor components, it is difficult to completely avoid casting defects. As an example, a broken endbell is presented in Figure 5.21.

5.3.2 Stamped Endbell

To provide an economic solution for endbell production, stamped endbells are often used in low- or mid-end motors. As a matter of fact, stamped parts are widely used in many advanced industries such as automotive, aerospace, and energy due to their good mechanical properties (e.g., light weight), low cost, and quick production. In practice, stamped parts have replaced many expensive casted, forged, and machined products in small motors.

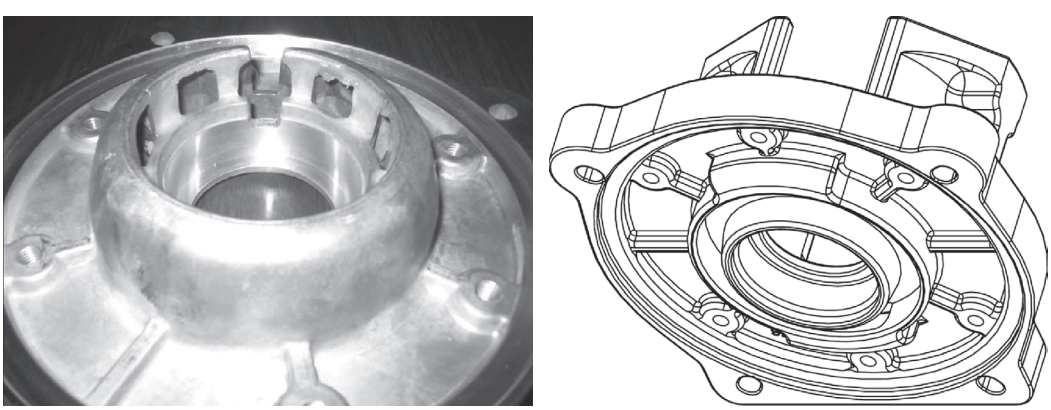

(a) (b)

FIGURE 5.19
Aluminum endbells made by die-casting process: (a) with ventilation passages and (b) without ventilation passages.

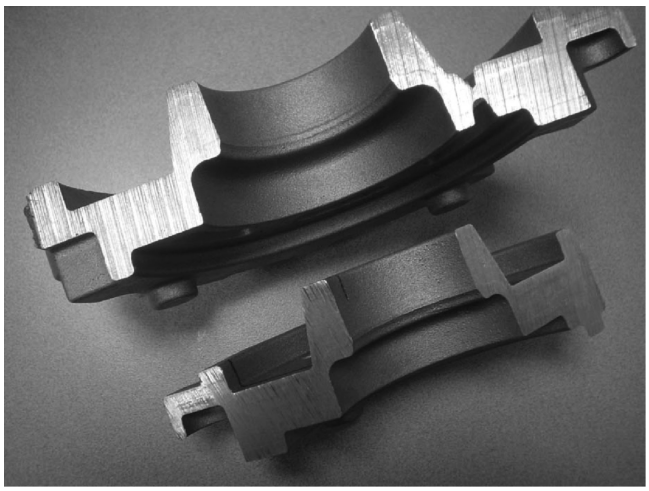

FIGURE 5.20
A casted endbell is cut to inspect the casting defects, particularly for porosities and voids.

FIGURE 5.21
Broken aluminum die-casting endbell due to the porosity and impurities in the part.

5.3.3 Iron Casting versus Aluminum Casting

A number of metal alloys are available for die casting such as aluminum, zinc, magnesium, iron, and copper. In most modern small motors, the endbells are made from aluminum alloys for their good corrosion resistance, light weight, high-dimensional accuracy, stability, and high thermal conductivity. Endbells made from high-grade cast iron are often used for large motors due to its strength, rigidity, and the ability to attenuate motor vibration and noise.

5.3.4 Machined Endbell

Similar to machined housings, machined endbells are often used for motor prototypes or small quantities of products for a short lead time and no need of tooling. It is apparent that machined endbells are more expensive than those made by other manufacturing processes such as die casting for a mass production. With the rapid development of 3D printing technology, it is possible to use the 3D printing technology to replace the machining technology for making motor endbell prototypes in the future.

5.3.5 Forged Endbell

Forging is a manufacturing process involving the shaping of metal by pressing or hammering. Metals can be either cold-forged or hot-forged depending on applications. Forging refines the grain structure in the direction of the deformation and develops the optimum grain flow. The modified structure gives forged parts better mechanical properties than machined parts in which the grain flow is broken by machining. Generally, forging technology is suitable for making parts that have simple geometries. For endbells with complicated structures, casting is more convenient than forging as the manufacturing process.

5.4 Motor Assembly Methods

There are a number of different ways to secure motor assembly, each of which is applicable to certain applications depending on the motor size, motor type, IP, and mounting requirements.

5.4.1 Tie Bar

This method is to use nuts, in coordination with long bolts (or in the alternative key bars), which extend through a distal side of one endbell, the housing and the opposite endbell, to secure the assembly together, as shown in Figure 5.22 [5.13]. The high compressive forces produced by bolts act to maintain the end shields in a static position with respect to the housing. This assembly method is especially suitable for a motor with a low length-to-diameter ratio. For motors with large length-to-diameter ratios, however, this assembly method is prohibitive due to the inherent structural instability caused by the increased bolt length to match the long motor body.

5.4.2 Tapping at Housing End Surface

A frame assembly method incorporates tapping directly at the housing end surfaces, creating attachment sites (i.e., threaded spaces) integrally as part of the housing itself (Figure 5.23). Specifically, short screws are threaded into the tapped housing through the endbells. However, this necessitates either a significant increase in the housing wall thickness or a housing design with complex structures formed with additional material that integrally provide a portion of the housing configured to receive the screws.

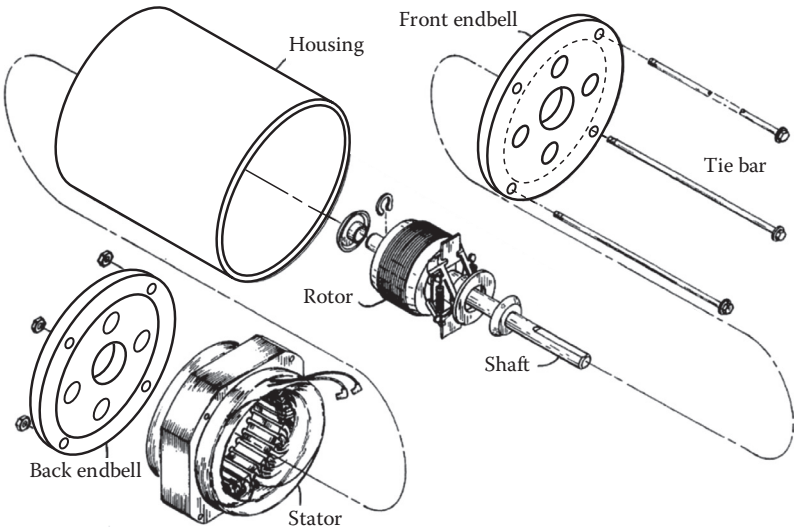

FIGURE 5.22
Motor assembly is secured by tie bars (U.S. Patent 5,412,270) [5.13]. (Courtesy of the U.S. Patent and Trademark Office, Alexandria, VA.)

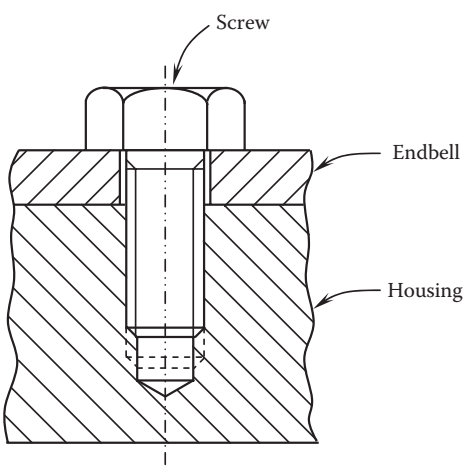

FIGURE 5.23
The motor housing is tapped for receiving short screws, which go through the endbell to complete the construct of the motor frame.

5.4.3 Forged Z-Shaped Fastener

Forging refers to the shaping of metal by plastic deformation. Forging is one of the most economical metal-forming methods for its advantages of significant material saving, simplified production process, high production rate, superior surface quality (especially for cold forging), high shear strength, and high fatigue resistance. During a forging process, internal grain deforms to follow the general shape of the part. As a

result, the grain is continuous throughout the part, giving rise to a piece with improved strength characteristics [5.19].

Cold forging is done at room temperature while conventional hot forging is done at temperatures higher than material recrystallization temperature (for instance, up to 1150°C for steel, 360°C–520°C for aluminum alloys, and 700°C–800°C for copper alloys). Motor manufacturers may choose cold forging over hot forging for a number of reasons, including little or no finishing work, higher-dimensional accuracy, better surface finishing, and improved reproducibility and interchangeability.

One of the most common types of cold forging is a process called impression-die forging, where the metal is placed into a die. Then, the metal is forced into the die by a pressing machine or a descending hammer. In cold-forging operations, pressures as high as 2500 MPa are developed at the forming tool–workpiece interface [5.20]. In order to minimize the friction between the tool and the processed workpieces, phosphate coatings together with lubricants are applied prior to cold forging.

It is widely recognized that surface finish has a significant effect on fatigue behavior. During a forging process, oxide and scaling layers are formed on the surfaces of the forged workpieces. Thus, it requires using either chemical methods such as acid pickling or mechanical methods such as sand blasting and shot peening to remove such oxide and scaling layers. In addition, the residual stress, produced in forgings as a result of inhomogeneous deformation in the forged workpieces, must be relieved through the annealing process following the forging process.

To provide robust motor frame assemblies, Boyland et al. [5.21] invented Z-shaped fasteners for reinforcing the joints between endbells and motor housings (Figure 5.24). Fastening apertures are formed in the lateral ends of the housing. The fastener includes elements that engage the housing through a plurality of contact areas. Specifically, the fastener includes a central portion that establishes a contact area in the plane of the aperture, as well as a

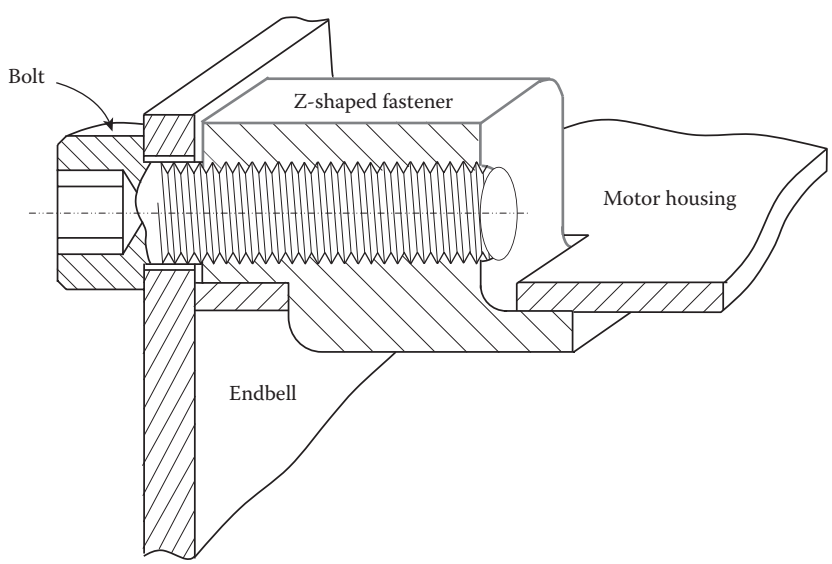

FIGURE 5.24
Jointing motor housing and endbell with Z-shaped fastener.

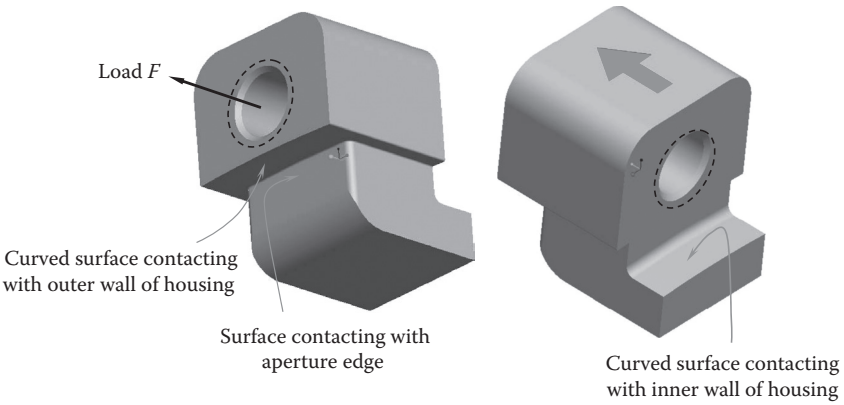

FIGURE 5.25
Contacting surfaces of Z-shaped fastener to housing.

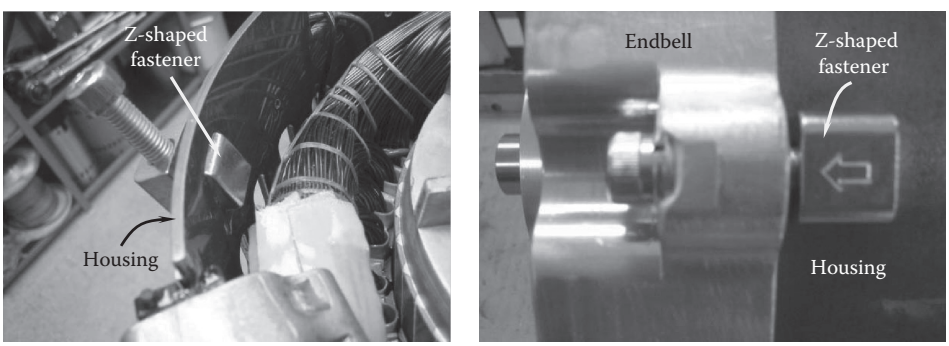

(a) (b)

FIGURE 5.26
Configuration of Z-shaped fastener to housing (a) and housing endbell (b).

base extension tab that establishes at least one contact area with the interior wall of the housing (Figure 5.25). The fastener also includes an extension block that establishes a contact area with the exterior of the housing and engages a securing bolt. The securing bolt threads through an aperture in the endbell and engages the fastener, thereby securing the endbell to the housing. The configuration of Z-shaped fastener to a housing and housing endbell is given in Figure 5.26.

Advantageously, this type of fastener reinforces the motor housing so as to provide additional support to the assembly by reinforcing the joints between the endbell and the motor assembly main body. Furthermore, the invention secures the endbell to the housing by simply engaging the housing and the securing bolt. Accordingly, the fastener acts to simplify housing/endbell manufacturing and the assembly process.

5.4.4 Rotary Fasteners

Rotary fasteners refer to the fasteners that insert through the apertures of joint members and rotate certain angles to secure the joint members together. This type of fasteners is capable of quickly and easily securing and releasing joint members.

5.4.4.1 Triangle-Base Rotating Fastener

Figure 5.27 illustrates a triangle-base rotating fastener with a triangle-shaped base extension tab. The fastener utilizes both horizontal and vertical forces in relation to the housing while engaging the housing's fastening aperture. The extension block and base extension tab may exert forces on the exterior and interior housing walls in a vertical direction. These vertical forces work in coordination with horizontal forces exerted by the central portion of the fastener and the force created by engaging a securing bolt with the extension block.

With regard to engaging the securing bolt with the extension block, the securing bolt used during the fastening process applies a load to the fastener. The load works, in coordination with the fastener contact areas, to maintain the vertical and horizontal fastener position with respect to the housing, the endbell, and the securing bolt. The contact areas apply a retaining force or pressure to the interior and exterior walls of the housing as well as apply a force in the plane of the fastening aperture portion of the housing.

The underside of the extension block joins the central portion to create a second section of the fastener. The central portion lies in the plane of the fastening aperture as the fastener engages the housing. The central portion also separates the base extension tab and the extension block in the fastener. The central portion is formed such that after the fastener is rotated, the central portion provides additional structural support along with an additional contact area between the fastener and the housing. Generally, both the extension block and the base extension tab extend beyond the central portion to engage the surface of the housing. This advantageously allows for the fastener to firmly engage both the interior and exterior sides of the housing wall, as well as a securing bolt.

The cross-sectional view of triangular base extension tab is shown at the right-hand side in Figure 5.27, taken along lines *A–A*. It is to be understood that for a given embodiment, both fastening aperture and the base extension tab are designed to match and work together. Generally, the base extension tab is formed with a similar contour as the fastening aperture. The shape of the fastening aperture on the housing also contributes to determining the shape of the central portion (shown shaded). The wedge shape of the central portion allows it to engage the triangular fastening aperture. It can be seen from the figure that making the fastening aperture a triangular shape leads to a complementary contoured triangular base extension tab. Varying the shape of the fastening

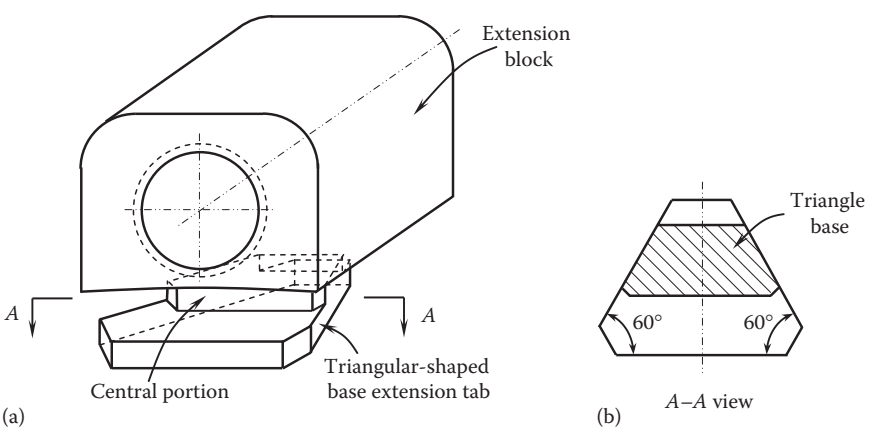

FIGURE 5.27
Triangle-base rotating fastener.

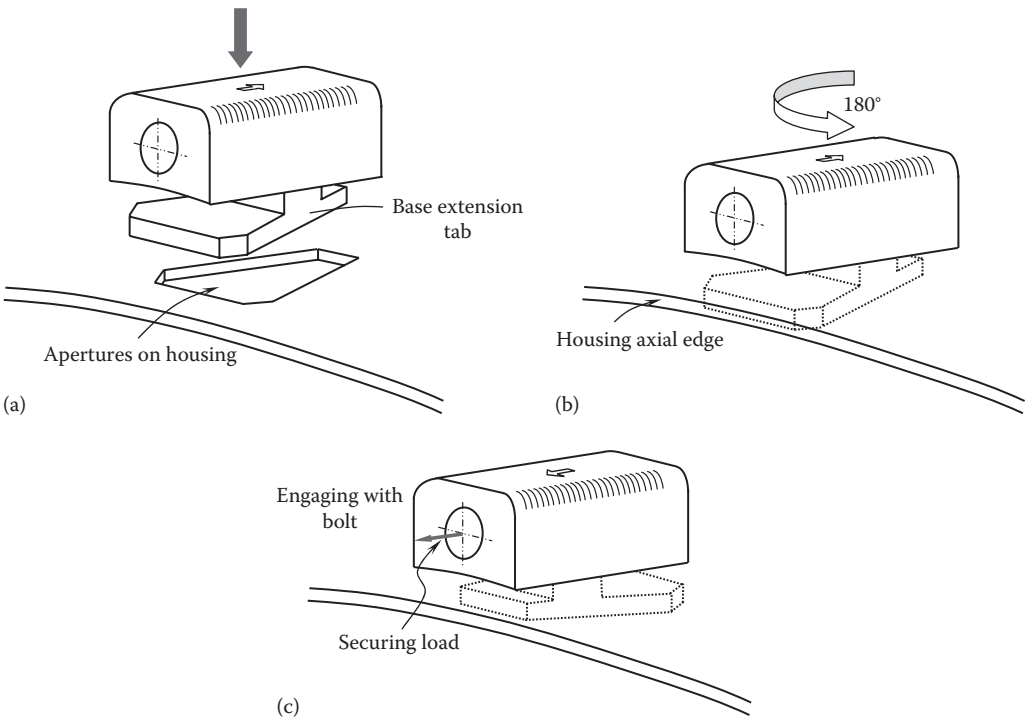

FIGURE 5.28
Fastening mechanism of triangle-base rotating fastener: (a) inserting a fastener into an aperture on the housing, (b) rotating 180° of the fastener, and (c) applying the securing load to the fastener.

aperture leads to subtle implementation variances in the placement of the retention forces securing the elements.

Figure 5.28 illustrates the steps of engaging the fastener having a triangular base extension tab with a motor housing. Initially, as shown in Figure 5.28a, the fastener is positioned above a fastening aperture, thereby aligning the complementary contours of the triangular base extension tab with the fastening aperture. After the elements are aligned, the fastener is inserted into the fastening aperture. In Figure 5.28b through d, the central portion and the triangular base extension tab are represented with dashed lines as they are hidden beneath the fastening aperture and in the interior side of the housing. To ensure a secure connection between the fastener and the housing, the thickness of the central portion is equal to the housing thickness. Figure 5.28b shows the fastener with the central portion, and the base extension tab is inserted into fastening aperture. The extension block prevents the fastener from fully passing through the aperture and advantageously provides additional contact area between the fastener and the housing. As shown in Figure 5.28c, upon insertion, the fastener is rotated by 180° with respect to the axial edge of the housing. The degree of rotation is one of the subtle implementation-specific aspects of the fastening processes referenced earlier.

Figure 5.29 illustrates a fastener viewed from top before and after its rotation. The 180° rotation illustrated creates staggered contact areas for the apex and the base corners of the base extension tab and the triangular aperture. In Figure 5.29, the base extension tab and the complementary aperture are aligned to facilitate insertion of the fastener into the aperture. As shown, the central portion is set back from the leading edge of the base extension tab.

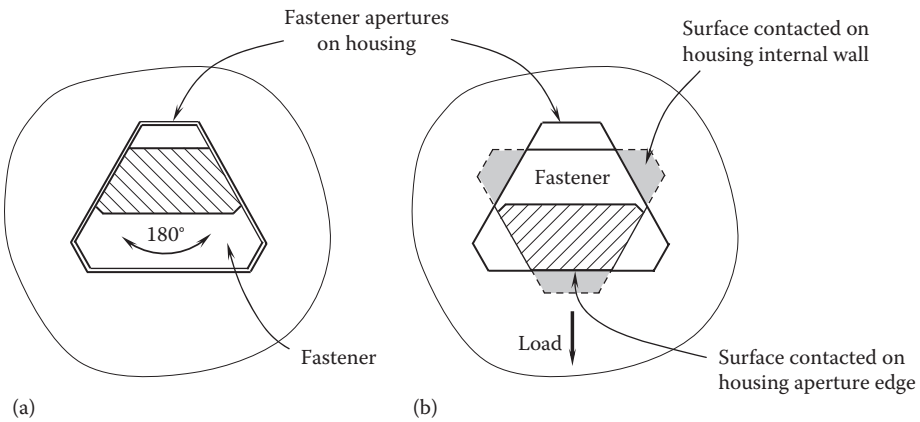

FIGURE 5.29
Installation of triangle-base rotating fastener: (a) inserting the triangle-base fastener and (b) rotating the fastener by 180° so that the three corners of the fastener base come in contact with the interior of the housing (the dark areas).

Rotating the fastener provides three contact areas on the interior surface of the assembly housing, which, in turn, provide additional structural support for the fastening assembly. Specifically, as the hook nut is inserted into the slot and turned by 180°, the three corners of the base extension tab engage the housing's internal wall, thereby providing radial support for balancing the bending moment acting on the fastener as the securing bolt is engaged.

Once the fastener is engaged with the housing, the other elements of the assembly may be secured to the housing. The fastener also includes an extension block that establishes a contact area with the exterior of the housing and engages a securing bolt (not shown). The securing bolt threads through an aperture in the endbell and engages the hollow portion of the extension block. The engaged securing bolt and fastener rigidly secure the endbell between the securing bolt head and the fastener's extension block. It is to be understood that the fastener may work alone or in coordination with other fasteners located at areas along the circumference of the axial end to secure the endbell to the housing.

5.4.4.2 Square-Base Rotating Fastener

A square-base rotating fastener is presented in Figure 5.30. This type of fastener is similar to the triangle-base rotating fastener, except that the central portion and the base extension tab of the fastener are substantially square shaped. As can be seen in Figure 5.30a and b, the central portion of the fastener is set back from the edge of the base extension tab, allowing for an additional contact area when the fastener engages the housing. Figure 5.30c and d illustrates the process of applying the square-base rotating fastener. As discussed previously, varying the geometry of the fastening aperture, the base extension tab, and the central portion leads to subtly different placement of the retention forces. Specifically, as the fastener engages the securing bolt (not shown) and the housing, there are different retaining forces exerted on the interior wall of housing by the square-base extension tab. The square-shaped base extension tab has four independent areas of contact with the interior wall of the housing. Further, due to the geometry associated with this embodiment, the fastener is rotated 45° to engage the housing. The other aspects of engaging the fastener, the housing, the endbell, and the securing bolt are similar to those discussed previously with regard to triangle-base fastener.

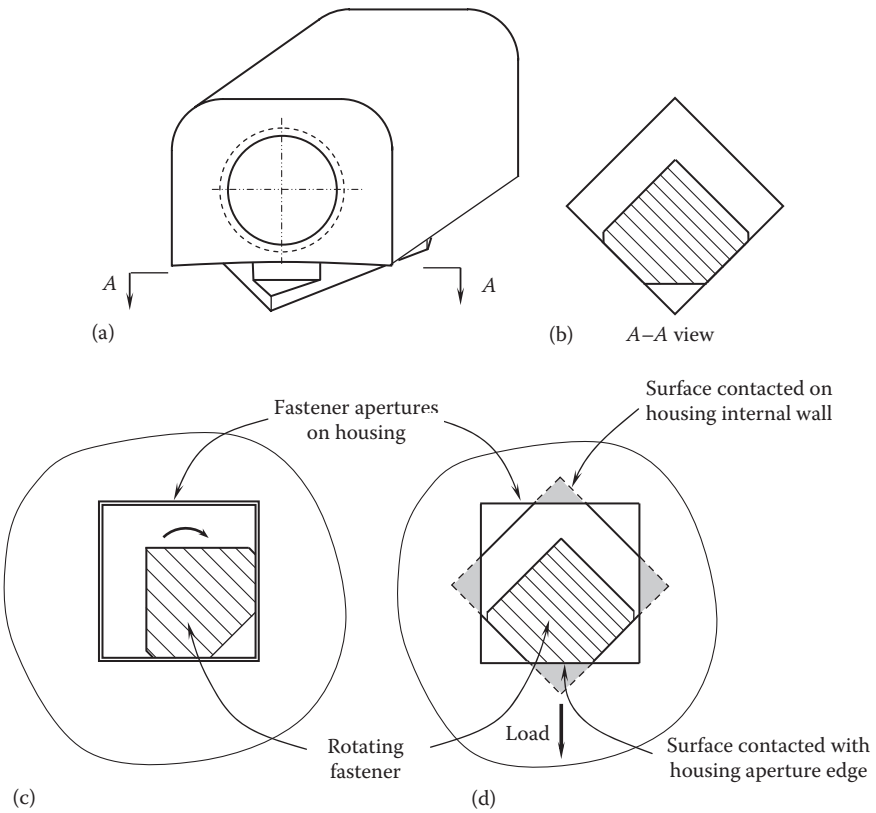

FIGURE 5.30
Installation of square-base rotating fastener: (a) a perspective view of square-base rotating fastener, (b) a cross-sectional view of the square-base extension tab, (c) inserting a fastener into an aperture on the housing, and (d) rotating 45° of the fastener and applying the load on the fastener.

5.4.4.3 Butterfly-Base Rotating Fastener

A butterfly-base rotating fastener is demonstrated in Figure 5.31. It is similar to the triangle-base and square-base fasteners, except the base extension tab is substantially butterfly shaped. The contact surface to the housing is shown at the bottom horizontal wedge of the central portion.

Figure 5.31a illustrated a perspective view of the butterfly-base rotating fastener, and Figure 5.31b presents the cross-sectional view of butterfly-base extension tab taken along lines *A–A* in Figure 5.31a. Figure 5.31c and d presents the top views before and after the rotation of the fastener, respectively. The base extension tab and the complementary aperture are aligned to facilitate insertion of the fastener into the aperture. The final orientation of the fastener after its 90° clockwise rotation is shown in Figure 5.31d. It shows the interior contact areas at the front and the back of the fastener aperture.

5.4.5 Other Types of Fasteners

There are other types of fasteners that may be applied in motor assemblies, each type being appropriate for certain types of motors.

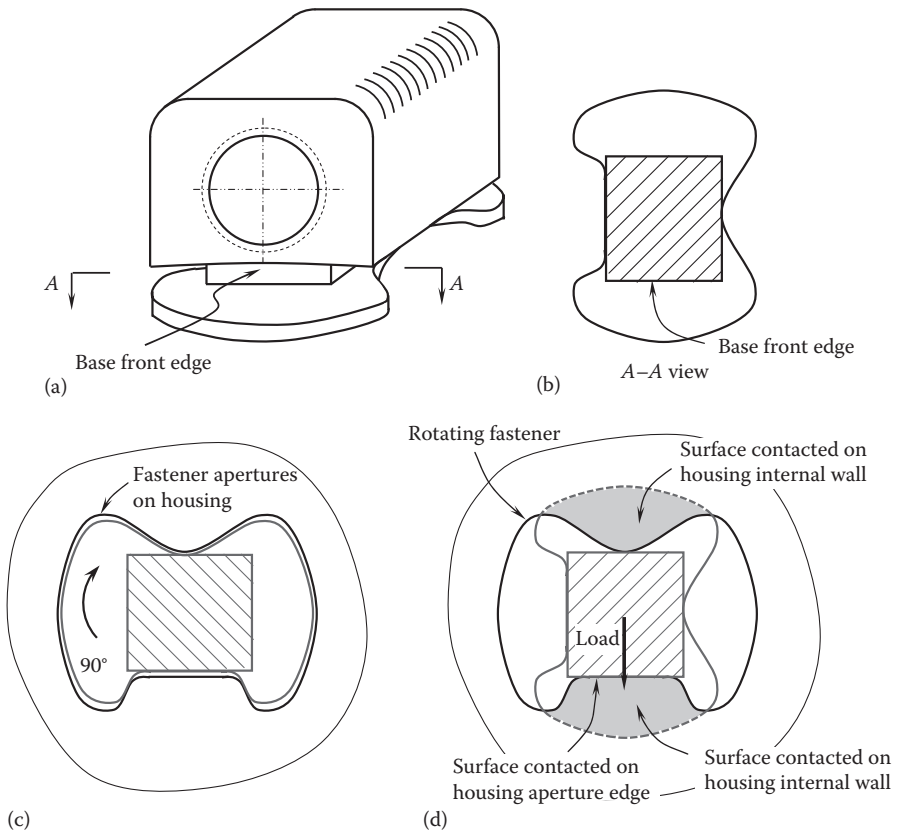

FIGURE 5.31
Installation of butterfly-base rotating fastener: (a) a perspective view of butterfly-base fastener, (b) a cross-sectional view of the butterfly-base extension tab, (c) inserting the fastener into an aperture on the housing, and (d) rotating 90° of the fastener and applying the load on the fastener.

5.4.5.1 Cylinder-Base Fastener Locked with Retaining Ring

Figure 5.32 demonstrates a cylinder-base fastener that is locked with a retaining ring. The fastener has two grooves at the cylindrical base to receive the retaining ring. To ensure normal performance of the fastener, the fastener base is designed to have a sliding fit with the hole on the motor housing, and the surface of the retaining ring must be in contact with the inner wall of the housing. This type of fastener may lead to less production costs associated with the simple elements, as well as a less complex manufacturing and assembly process.

An alternative locking mechanism may also be implemented as a securing pin engaged with a hole through the cylindrical base.

5.4.5.2 Cylinder-Base Fastener with Self-Locking Aperture

This design is essentially similar to the fastener design addressed previously. As shown in Figure 5.33, instead of using a retaining ring to lock the fastener, this type of fastener can be self-locked by engaging an aperture on the motor housing. For this purpose, the

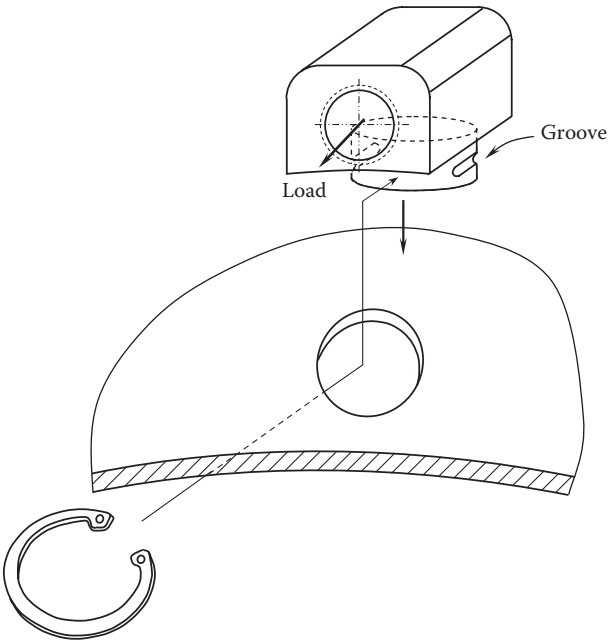

FIGURE 5.32
Cylinder-base faster, locked with a retaining ring at the grooves of the cylindrical base.

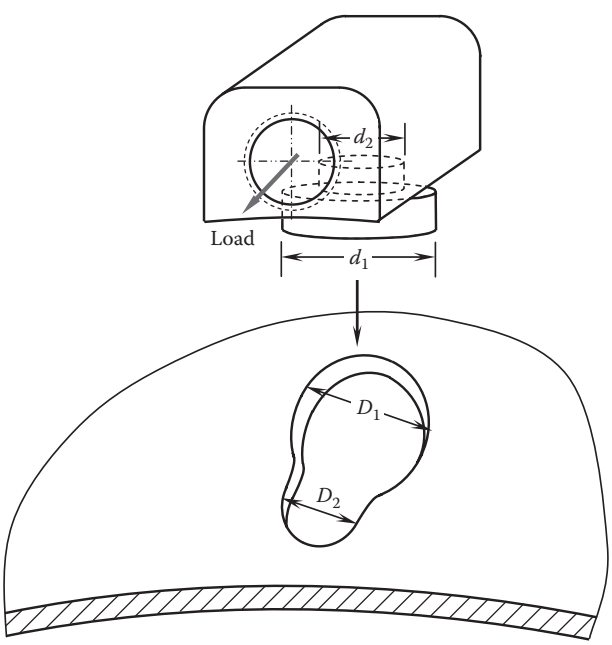

FIGURE 5.33
Cylinder-base fastener with a self-locking aperture on the motor housing.

fastener consists of two cylinders having the diameter d_1 and d_2, respectively. The self-locking aperture consists of two circles that have the diameter D_1 and D_2, respectively. The two circles are connected smoothly by two arcs to form a pear-shaped aperture, with the smaller end disposed toward the axial end of the housing. The diameter d_1 is designed to be a little smaller than D_1, and d_2 is a little larger than D_2. This geometry facilitates the fastener's insertion through the larger circle of the aperture and the engagement to a securing bolt (not shown). With the tightening load applied on the fastener, the small cylinder achieves an effective interference fit with the small circle of the aperture.

5.4.5.3 Fastener Engaged with Housing from Housing Interior

Figure 5.34 illustrates a rectangular base fastener inserted into the fastening aperture from the interior side of the housing. As shown in the figure, the extension block of the fastener is inserted along the arrow into the fastening aperture. The continuous base contacts the entire circumference of the interior wall of housing along the fastening aperture. Once the fastener is inserted into the fastening aperture, a securing bolt (not shown) acts to apply a load along the arrow. The securing bolt acts in coordination with the continuous base extension tab to secure both the fastener and the endbell (not shown) to the housing.

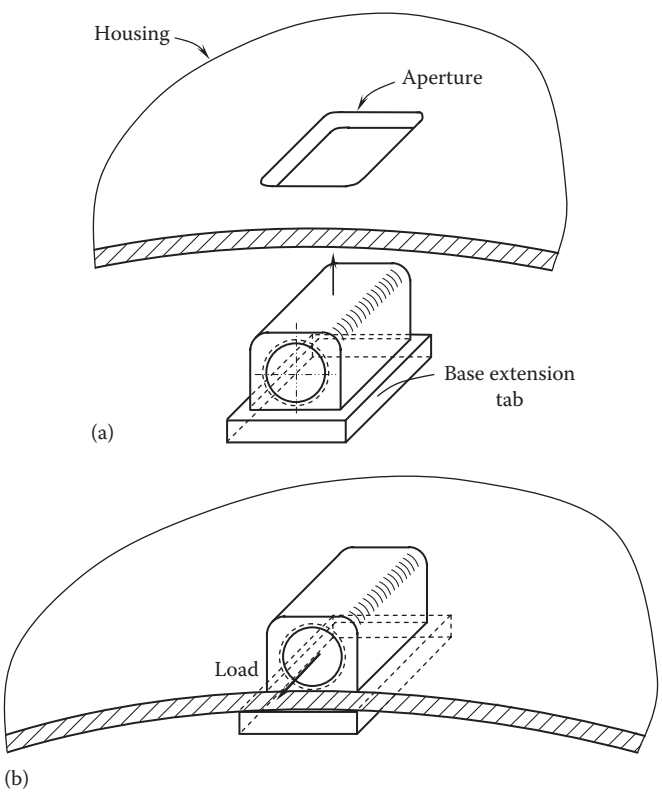

FIGURE 5.34
Installing process of the nut: (a) inserting the nut from the interior of the housing and (b) engaging the nut with the endbell using a bolt.

5.5 Fastening System Design

In the motor industry, it is very common to use fasteners (bolts, nuts, screws, etc.) for joining motor components together and for installing motors into places.

5.5.1 Types of Thread Fasteners

Though a wide variety of threaded fasteners are used in engineering practice, two types of thread fasteners primarily used in motor assemblies and installations are as follows:

- Bolt–nut fasteners, in which a bolt passes through slightly larger holes in two joint members and is engaged with a hexagonal nut. The desired tightness of fastener can be achieved by applying a wrench to either the bolt head or nut. In this way, the two joint members are clamped between bolt head and nut, as shown in Figure 5.35. The grip length l_g is the sum of the thicknesses of both joint members:

$$l_g = l_1 + l_2 \tag{5.5}$$

- Screw-threaded member fasteners, in which the threads of the screw are threaded into an internally threaded hole of the lower joint member, as shown in Figure 5.36. The effective grip length is determined according to the bolt diameter relative to the thickness of the first joint member:

$$l_g = \begin{cases} l_1 + l_2/2 & \text{for } l_2 < d \\ l_1 + d/2 & \text{for } l_2 \geq d \end{cases} \tag{5.6}$$

In both cases, while bolts are subjected to tensile forces, joint members withstand compressive (clamping) forces.

5.5.2 Thread Formation

Fastener threads can be produced by either rolling or cutting operations. Rolled threads are formed by rolling the reduced diameter portion of a shank between two reciprocating serrated dies. The advantages of rolled threads include more accurate and uniform thread dimensions, smoother thread surfaces, higher thread strength (usually 10%–20% in tensile strength), improved fatigue and wear resistance, and material savings. In addition, the grain structure in rolled threads maintains continuous unbroken lines, as opposed to the broken grains in cut threads. Usually, cut threads are used for large diameter or nonstandard fasteners.

5.5.3 Fastener Preload

The preload P_p, or the clamp load, of a fastener is created as a tightening torque is applied on the fastener before receiving any external loads. The tightening process exerts an axial preload tension on the bolt and an axial compression on the joint members, where the generated bolt tension load exactly counterbalances the compression load applied on the assembled

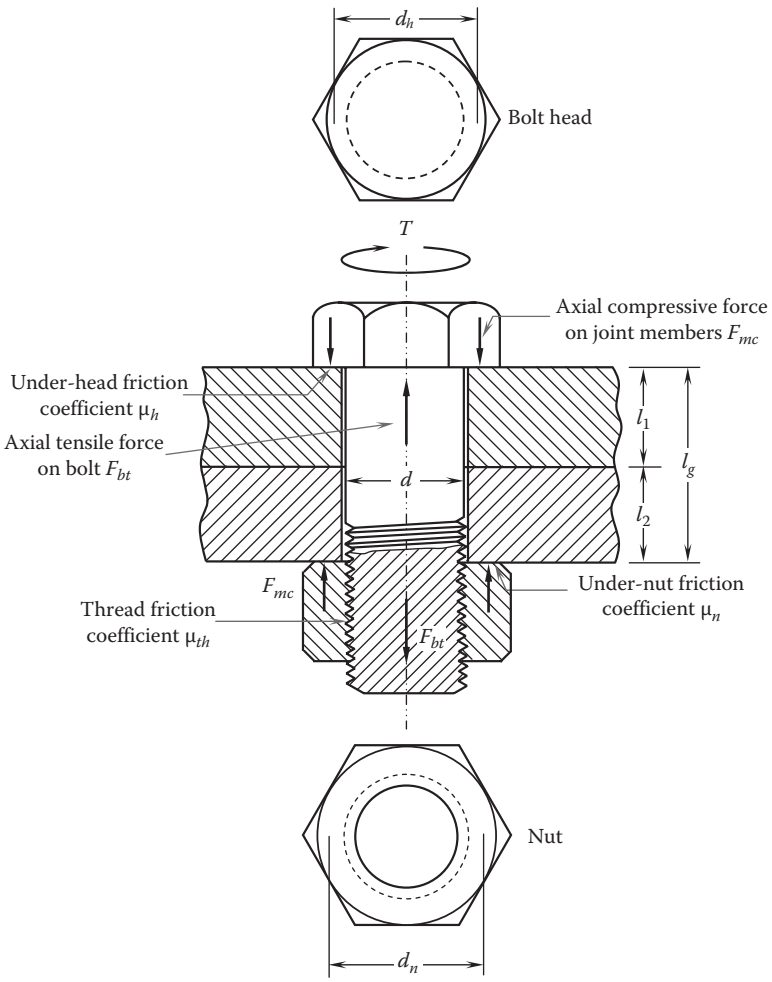

FIGURE 5.35
Bolt–nut fasteners with drilled holes through joint members.

components. It has been reported that when an external load is applied on a preloaded joint, only a portion (usually 80%) of the external load acts on the jointed members [5.22].

In order to achieve high strength and long lifetime of a bolted joint, it is critical to set appropriate bolt tightening torque. Excessive tightening of bolts can cause thread damage or bolted joint failure, and insufficient tightening may lead to separation of jointed members or poor motor performance (such as large vibration). Many surveys have shown that among the possible causes of bolted assembly failure, the most frequent cause is poor assembly. Improper and irregular bolt tightening alone accounts for over 30% of all assembly failures and 45% of all fatigue incidents [5.23].

5.5.4 Fastener-Tightening Process

During a fastener-tightening process, a desired tightening torque is applied to a threaded fastener to stretch the bolt while compressing the clamped joint members elastically according

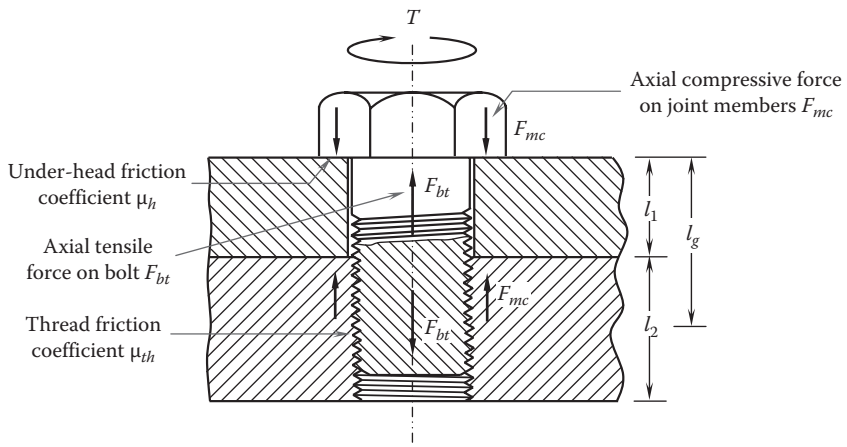

FIGURE 5.36
Screw-threaded member joint. Due to the elimination of a nut, the friction under nut-bearing surface no longer exists.

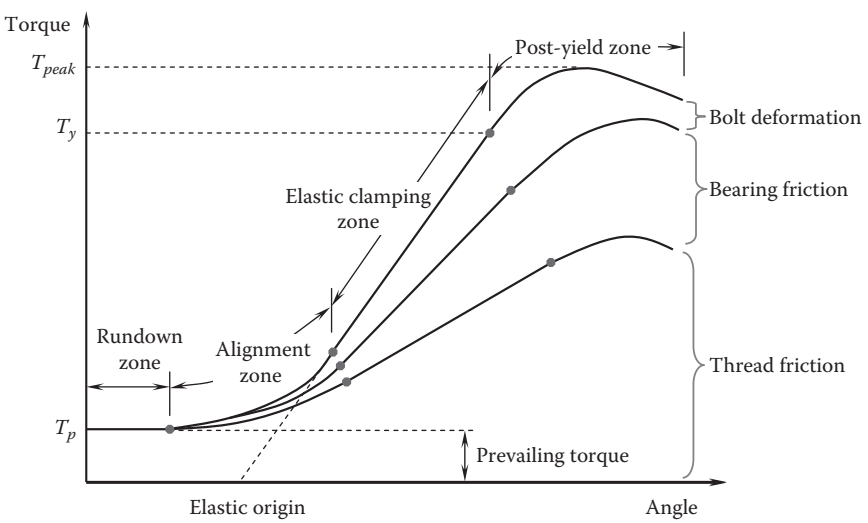

FIGURE 5.37
Four distinct zones in fastener-tightening process.

to the effective spring rates of the bolt and the joint members. This process can be characterized by plotting the input torque against the angular displacement of the bolt. As illustrated in Figure 5.37, four distinct zones can be identified in a fastener-tightening process:

1. Rundown or prevailing torque zone. In this zone, the fastener has not yet touched the bearing surfaces. There is no axial load acting on both the fastener and joint members. The torque needs only to overcome the friction between the fastener threads.
2. Alignment zone. In this zone, the fastener and bearing surfaces are drawn into alignment, and the torque–angle curves is nonlinear. The compressive force

acting on the joint members begins to increase but not at the same rate as the bolt tensile force.

3. Elastic clamping zone. This is the working zone of the fastener. In this zone, the angular displacement of the fastener is proportional linearly to the applied torque on it. The slope of the torque–angle curve at this zone is a function of the stiffness of the assembly and the friction between the threads and on the bearing areas.
4. Post-yield zone. This zone begins with the yield point. Yielding may occur in the bolt or in the joint members or both. Correspondingly, the slope of the torque–angle curve decreases. Continuous increase in the angular displacement will cause the failure of the joint.

The fastener yield torque improvement due to cold working is demonstrated in Figure 5.38. During a tightening process, both the torque applied to the fastener and the angular displacement of the fastener increase simultaneously along the torque–angle curve. Tightening the fastener beyond the yield point but below the ultimate tensile strength can achieve the maximum preload for a given fastener size [5.24]. Due to the plastic deformation of the fastener, releasing the load will not return the fastener to its original state. Then, retightening the fastener again, it is found that the torque and angular displacement increase along the offset curve that is approximately parallel to the first torque–angle curve and the yield torque appearing at a higher level ($T_{y2} > T_{y1}$).

It should be noted that while the yield strength, tensile strength, and hardness of the fastener increase as the consequence of cold working, the ductility decreases along a path opposite to that of hardness. Since the yield strength increases faster than ultimate tensile strength, the yield strength comes closer to the ultimate strength after each cold working cycle. After several repeated load/unload cycles, the fastener exhibits brittle behavior

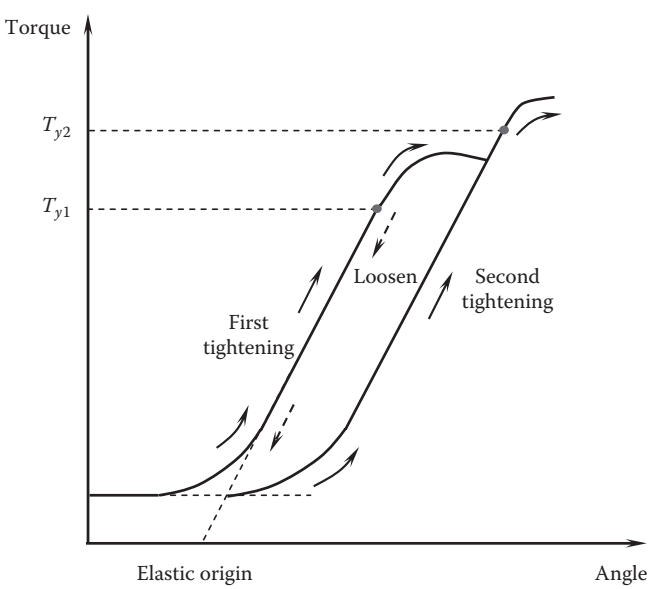

FIGURE 5.38
By loading fastener beyond the yield point, then unloading and reloading again, yield strength, tensile strength, and hardness of the fastener increase, but its ductility decreases.

and may suddenly fail without warning signs. Therefore, for critical joints or applications, the reuse of fasteners (bolts, nuts, washers, and other mechanical fasteners) is not recommended.

5.5.5 Tightening Torque

In the elastic clamping zone, when a bolt fastener turns an angle of $\Delta\varphi$ under a tightening torque T, the work done by the tightening torque is (Figure 5.39),

$$W_t = T\Delta\varphi = F_t l\Delta\varphi \tag{5.7}$$

In practice, the work W_t is balanced with three components: the work done by the axial tensile force F_{bt} toward the elastic elongation of the bolt and the clamping force F_{mc} ($F_{bt} = -F_{mc}$) toward the compression of the joint members, W_{def}; the work done by the thread friction between the threads of the fastener system (e.g., bolt and nut), W_{th}; and the work done by the friction on the bearing surfaces under the bolt head and the nut, W_f, as referred to in Figure 5.35.

As shown in Figure 5.40, when a wrench tightens a fastener in a full circle (i.e., 2π in radians) in the elastic clamping range, the corresponding change in the bolt length is the thread pitch p. Thus, as the wrench turns a small angle of $\Delta\varphi$, the change in the bolt length is δ:

$$\frac{\delta}{p} = \frac{\Delta\varphi}{2\pi} \tag{5.8}$$

As a result, the work done due to the bolt deformation becomes

$$W_{def} = F_{bt}\delta = F_{bt}p\frac{\Delta\varphi}{2\pi} \tag{5.9}$$

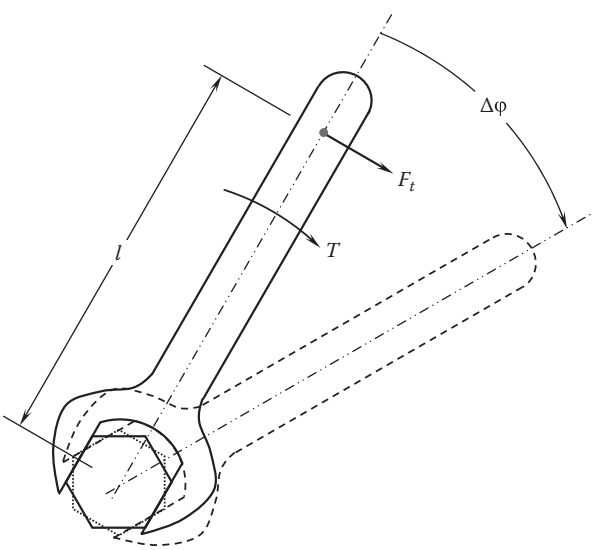

FIGURE 5.39
Work is done by tightening torque over a small angle of $\Delta\varphi$.

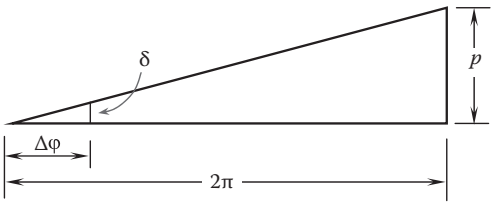

FIGURE 5.40
When a tightening wrench rotates a full circle in the elastic clamping zone, the change in the axial length of bolt is p (thread pitch). As it turns a small angle of Δφ, the change in length is δ.

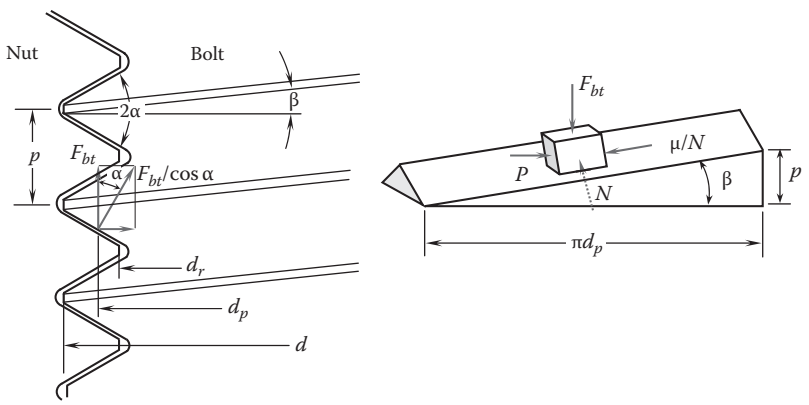

FIGURE 5.41
Work is done by thread friction. Noting that 2α is the thread angle, β is the thread lead angle, d, d_r, and d_p are the major diameter, minor (root) diameter, and pitch diameter, respectively.

During a fastener-tightening process, the thread surfaces of the bolt and nut remain in contact with each other where a relative movement exists. As demonstrated in Figure 5.41, the forces acting on the entire thread surface are the bolt axial compressive force F_{bt}, the tangential force P, the normal force N, and the thread friction force $\mu_{th}N$, where μ_{th} is the coefficient of sliding friction between the bolt and nut threads. It is to be noted that the friction force $\mu_{th}N$ acts on the inclined plane opposite to the direction of motion. In this figure, the inclined angle β denotes the lead angle of the thread, and the angle α is the half of the thread angle. As a function of angle α, the normal contact force N is expressed as $F_{bt}/\cos\alpha$, and hence, the friction force acting on the threads becomes $\mu_{th}F_{bt}/\cos\alpha$. This indicates that an increase in α results in an increase in the friction force.

When the system is in equilibrium, the sum of all forces acting on the system is equal to zero. Therefore, two force–balance equations can be derived as

$$\sum F_h = 0 \quad P - N(\mu_{th}\cos\beta + \cos\alpha\sin\beta) = 0 \tag{5.10a}$$

$$\sum F_v = 0 \quad F_{bt} + N(\mu_{th}\sin\beta - \cos\alpha\cos\beta) = 0 \tag{5.10b}$$

Combining these two equations yields

$$P = F_{bt}\frac{\tan\beta\cos\alpha + \mu_{th}}{\cos\alpha - \mu_{th}\tan\beta} \tag{5.11}$$

Thus, the torque required to overcome thread friction is

$$T_{th} = P\left(\frac{d_p}{2}\right) = \frac{F_{bt}d_p}{2}\frac{\tan\beta\cos\alpha + \mu_{th}}{\cos\alpha - \mu_{th}\tan\beta} \tag{5.12}$$

where d_p is the pitch diameter. Thus, the work done by the thread friction can be expressed as

$$W_{th} = T_{th}\Delta\varphi = \frac{F_{bt}d_p}{2}\left(\frac{\tan\beta\cos\alpha + \mu_{th}}{\cos\alpha - \mu_{th}\tan\beta}\right)\Delta\varphi \tag{5.13}$$

For a very small angle β, tanβ approaches zero; thus,

$$W_{th} = \frac{F_{bt}d_p}{2}\frac{\mu_{th}}{\cos\alpha}\Delta\varphi \tag{5.14}$$

The necessary and sufficient condition for thread self-locking is that the coefficient of thread friction μ_{th} is greater than or equal to the product of the tangent of the thread lead angle β and cosine of the half thread angle α [5.25]:

$$\mu_{th} \geq \tan\beta\cos\alpha \tag{5.15}$$

This indicates that fine-thread fasteners are easier to reach self-locking than coarse-thread fasteners because of their smaller thread lead angles.

Other methods to prevent fastener slackening include using fastener retainers, bolts, nuts, and washers with serrated locking ribs, locked inserts, and adhesive retention materials (such as Loctite).

The work done due to the friction on the bearing surfaces under bolt head and nut becomes

$$W_h = \frac{F_{bt}}{2}(\mu_h d_h)\Delta\varphi \tag{5.16a}$$

$$W_n = \frac{F_{bt}}{2}(\mu_n d_n)\Delta\varphi \tag{5.16b}$$

respectively. In the above equations, μ_h and μ_n are friction coefficients on the bearing surface under the bolt head and nut; d_h and d_n are the effective diameters of the bolt head and nut, respectively:

$$d_h = d_n = \frac{d + 1.5d}{2} = 1.25\ d \tag{5.17}$$

Based on the preceding analysis, it gives that

$$W_t = W_{def} + W_{th} + W_h + W_n \tag{5.18}$$

That is,

$$\begin{aligned} T &= \frac{F_{bt}p}{2\pi} + F_{bt}\frac{d_p}{2}\left(\frac{\tan\beta\cos\alpha + \mu_{th}}{\cos\alpha - \mu_{th}\tan\beta}\right) + 0.625F_{bt}d(\mu_h + \mu_n) \\ &= \left[\frac{p}{2\pi d} + \frac{d_p}{2d}\left(\frac{\tan\beta\cos\alpha + \mu_{th}}{\cos\alpha - \mu_{th}\tan\beta}\right) + 0.625(\mu_h + \mu_n)\right]F_{bt}d \\ &= KF_{bt}d \end{aligned} \tag{5.19}$$

and

$$K = \sum_{i=1}^{3} K_i \tag{5.20}$$

where K_1, K_2, and K_3 are tightening factors due to the bolt tension, thread friction, and friction on bearing surfaces under the bolt head and nut:

$$K_1 = \frac{p}{2\pi d} \tag{5.21a}$$

$$K_2 = \frac{d_p}{2d}\left(\frac{\tan\beta\cos\alpha + \mu_{th}}{\cos\alpha - \mu_{th}\tan\beta}\right) \tag{5.21b}$$

$$K_3 = 0.625(\mu_h + \mu_n) \tag{5.21c}$$

For metric threads,

$$d_p = d - 0.649519p \tag{5.22}$$

It has been estimated that around 10% of the torque applied to the fastener is to produce the stretch of the bolt and compression of the joint, 40% of the torque is to overcome thread friction, and the remaining 50% is to overcome head- and nut-bearing friction (see Figure 5.37). This implies that approximately 90% of the total torque is to overcome friction, while only 10% does useful work [5.26].

5.5.6 Thread Engagement and Load Distribution

In bolted joints, thread engagement refers to the number or length of threads that are engaged between the bolt and nut threads. It has long been recognized that when a bolt is engaged with a nut, the axial load acting on the bolt and nut is distributed extremely

TABLE 5.2

Loading Distribution of Bolt Threads

Thread Number	Loading Distribution (%)		
	Tseng [5.27]	Timoshenko [5.28]	Young [5.29]
1	58.9	54.5	55.0
2	24.2	24.6	24.8
3	10.0	10.7	11.2
4	4.1	4.7	5.1
5	1.8	2.2	2.5
6	1.0	1.3	1.5

nonuniformly between the threads of threaded joints. During a tightening process, the first engaged thread takes the majority of the applied load. This suggests that the first thread and subsequently some of other threads may yield and proceed to plastic deformation. This plastic softness will redistribute the load over other engaged threads and, as a result, make the loading distribution more uniform.

A simple model has been proposed by Tseng [5.27] for determining the loading distribution on bolt threads. The results of his model are in good agreement with those of Timoshenko and Goodier [5.28] and Young et al. [5.29]. The data in Table 5.2 indicate that extra threads engaged do not increase joint strength.

Assuming both the bolt and nut are made with the same material, the minimum thread engagement length required is approximately 65% of the nominal diameter [5.30]. For instance, a M8 × 1.25 bolt needs a minimum of 5.2 mm of thread engagement, that is, 4.16 threads. In addition, it is appropriate to apply a safety margin of approximately 30% to the calculated minimum length to account for high-order effects.

5.6 Anticorrosion of Electric Motor and Components

Many metallic products produced by manufacturing industries may have bare metal surfaces, which require receiving some forms of protection from corrosion. The classification of corrosion protection methods includes active, passive, permanent, and temporary protection. Active anticorrosion methods can alter or control the proceeding reaction during a corrosion process so that corrosion is avoided. Examples of such an approach are the development of corrosion-resistant alloys and the formation of effective passivation layer on metal surfaces for impeding corrosion half-reactions. In passive protection, corrosion is prevented by mechanically isolating metal surfaces from aggressive, corrosive agents. A coating of this type of protection serves as a barrier layer precluding permeation of corrodent to the metal surface. Among various methods, protective layers, films, or other coatings have been usually chosen by motor manufacturers to provide overall protection against corrosion.

5.6.1 Surface Treatment Methods

By coating a thin layer of a certain metal on a motor component (e.g., a fastener) surface, the surface properties of the component can be changed to that of the metal applied. Thus, the

coated component becomes a composite material, consisting of a durable and corrosion-resistant layer and a core having the load-bearing capability. A number of metals are suitable for protective coating, such as chromium, nickel, copper, zinc, and cadmium. However, coating processes may cause inherent pollution problems.

There are many different methods of metal surface treatment for preventing corrosion on motor components. Metal surfaces can be treated chemically, mechanically, or physically. Some of these methods are addressed in the following sections.

5.6.1.1 Electroplating

Electroplating is achieved by passing an electrical current through a solution containing dissolved metal ions and the metal object to be plated. The most widely used metallic coating method for corrosion protection is galvanizing, which involves the application of metallic zinc to iron and steel products requiring protection from corrosion. Its excellent corrosion resistance in most environments leads to its successful use as a protective coating on a variety of products and in many exposure conditions.

5.6.1.2 Electroless Plating

The electroless plating technology has been developed for many decades. Electroless plating is the process of plating a coating with the aid of a chemical reducing agent (e.g., formaldehyde) in solution without the passage of external power. Compared with electroplating, electroless plating has some superior characteristics: (a) Without using electric current in the plating process, it is easier to obtain uniform coatings on parts. This feature is especially suitable for parts with irregular, complex-shaped geometries. (b) It is applicable to non-conductive substrates such as glass and plastic. (c) Electroless plating can deposit particles from different materials to obtain composite coatings readily for adapting to different application requirements. For instance, nickel–phosphorus coatings are used to enhance corrosion resistance. Alternatively, thin cobalt–phosphorus coatings offer superior sliding wear, enhanced lubricity and corrosion resistance, and improved fatigue properties. Because they exhibit some magnetic properties, they are also of interest to the magnetic recording community.

5.6.1.3 Physical Vapor Deposition

Physical vapor deposition (PVD) refers to the techniques used to deposit molecular thin films on solid surfaces in a vacuum environment. As its name implies, the PVD process is a physical process, without involving chemical reactions as in chemical vapor deposition (CVD). There are two common types of PVD processes: electron beam evaporation process and sputtering deposition process. During the electron beam evaporation process, a solid or liquid coating material evaporates into the vapor phase to travel in the vacuum space and then condensates on the solid surfaces, with the transition of its physical morphology to the solid phase. The sputtering deposition process, which is extensively used in the semiconductor industry, involves ejecting coating materials from the sputtering target to the substrates such as silicon wafers. One of its important characteristics is that it can deposit the materials with high melting points. The most outstanding feature of PVD is that the properties of one material can be imparted to the surface of the workpiece which is made from another material, thus creating a wholly different product. However, the PVD techniques require expensive equipment and instruments.

Furthermore, because the PVD process is usually carried out in a vacuum chamber, the size of the coated members is subject to certain restrictions.

5.6.1.4 Inorganic Coating

Inorganic coating can be produced by chemical reaction, with or without electrical assistance. The treatments change the immediate surface layer of metal into a film of metallic oxide or compound that has better corrosion resistance than the natural oxide film and provides an effective base or key for supplementary protection such as paint.

Black oxide is a process that provides a conversion coating on surfaces of ferrous alloys. The coating is formed from chemical reactions between the iron of ferrous alloys and black oxide solutions such as the alkaline aqueous salt solution. When workpieces are immersed in a hot black oxide solution at the operation temperature of 132°C–143°C (270°F–290°F), a layer of magnetite (Fe_3O_4) is produced on the workpiece surfaces about 30 min.

Unlike other coating processes, black oxide has some specific properties and characteristics that make it ideal for certain applications. One of the remarkable characteristics is that for a properly controlled coating process, black oxide has little contribution to hydrogen embrittlement. This is because that the black oxide process does not require an acid activation nor is it an electro process. However, if the workpieces are scaled or rusty such that an acid pickle is required, it may lead to hydrogen embrittlement problems.

5.6.1.5 Phosphate Coating

Phosphate coating is a crystalline conversion coating consisting of an insoluble crystalline metal-phosphate salt formed in a chemical reaction between ferrous metals and a phosphoric acid (H_3PO_4) solution containing metallic ions (e.g., zinc, iron, or magnesium). Phosphate coating can serve either as the foundation for subsequent coatings or the protective coating on ferrous parts for corrosion resistance. In addition, phosphate coating is often employed in cold-forging process for lubricity.

The primary types of phosphate coatings include manganese, iron, and zinc coating. Among them, manganese phosphate coating has the highest hardness and superior corrosion and wear resistance. Therefore, manganese phosphate coating is extensively used to improve friction properties of sliding components such as engine pistons, gears, camshafts, and power transmission systems. Iron phosphate coating inhibits corrosion and improves the adhesion and durability of paint finishes. Due to the low cost and moderate corrosion resistance, this type of phosphate coating is basically suitable for indoor equipment. Zinc phosphate coating can provide the highest corrosion resistance. Hence, it is widely used in the automotive industry and in certain sectors of the appliance and electronics industries.

5.6.1.6 Electropolishing

As a reverse plating technique, electropolishing is an electrochemical process that is typically used for surface polishing and corrosion resistance enhancing. While electroplating deposits a thin metal layer on surfaces on either metallic or nonmetallic parts, electropolishing removes surface metal, beginning with the high points within the microscopic surface texture, by using a combination of chemicals rectified electrical current. As a result, surface imperfections (e.g., surface crack, burr) and embedded contaminants (e.g., rust, oxide scale) of the parts are eliminated. Electropolished parts are left in a homogenous and passive condition which enhances surface resistance to corrosion tarnish or oxidation.

These properties are especially evident on stainless steel but also found on carbon steel, brass, aluminum, copper, and inconel. Even though all these materials are more corrosion resistant, electropolishing is generally applied to stainless steel today.

As a nondistorting process, electropolishing is especially suitable for applications in which mechanical deformation is not allowed. Other benefits of electropolishing include deburring, precise dimension control, ultra cleaning, stress sensitivity reduction, and weldability improvement.

5.6.2 Anticorrosion Treatment of Electric Motor

Almost all metals, with the exception of the common precious metals such as gold, silver, and platinum group metals (iridium, osmium, palladium, platinum, rhodium, and ruthenium), oxidize and corrode in corrosive environments, forming compounds such as oxides, hydroxides, and sulphides. In fact, corrosion has a great effect on motor performance and lifetime and may cause serious damage to motors or components in some severe cases. Therefore, corrosion control and treatment are of vital concern in motor design.

There are many anticorrosion methods in industrial technologies such as cathodic protection, chemical conversion, inhibition of surface reaction, rust preventive treatment, thermal spray, paint, electroplate, and anodic protection. Each of these methods can, in a certain extent, extend the life of electric motors. Among all the anticorrosion methods, the surface protective coatings are often adopted by motor manufacturers for their good rust inhibitive properties, durability, easy operation, and no requirement for special equipment.

The materials of the protective coatings can be generally categorized into two types: inorganic and organic materials. The inorganic materials include metal, glass, ceramics, and plastic. The organic materials include paint, resin, paraffin, ointment, rubber, and asphalt. Each of the protective coatings has its own properties and usage scopes. In selecting protective materials, the pros and cons of the material must be completely taken into account.

In practice, motor manufacturers commonly use thermally conductive paints on the external surfaces of motor frames at room temperature. The painting materials include plastic ferrite polyurethane, polyurethane acrylic varnish, expanded graphite, enamel, alkyd and epoxy-based paints. The paint thickness is typically less than 0.5 mm. If a motor has been over painted, the paint thickness may be greater than 1 mm. In such a case, low thermal conductivity paints could weaken the heat dissipation from the motor to the ambient. Black paint is commonly utilized on motor surfaces to achieve higher thermal emissivity (about 0.96) and thus higher thermal radiation from the motor. It should be noted that the primary thermal energy emitted by the motor is in the invisible infrared portion of the spectrum. All paint colors in the visible spectrum have small differences in thermal emissivity. All paint colors in the visible spectrum have small differences in thermal emissivity. For instance, white paint has an emissivity of 0.90–0.95, blue 0.94, green 0.92 and red 0.91.

The thermal spraying process involves the projection of small molten metal particles onto prepared motor surfaces to form a continuous coating. During the process, a certain amount of heat is transferred to the motor housing. It is thus important to access the distortion of the housing as a result of the heat transfer. This technique has been widely used in constructions, oil and gas plants, petrochemical equipment, and off shore wind turbines.

When a motor operates under harsh environmental conditions such as high temperature, high humidity, corrosive media, high G-shock, high contamination and/or high pressure, adequate precautions shall be taken to prevent the motor from corrosion. Conventionally, the motor is well sealed with sealing devices on the shaft, housing, and endbells to avoid moisture, corrosive media, and other contamination particles to enter the motor.

In fact, the use of seals can reduce but not completely eliminate moisture to penetrate into the motor. Usually, thermal cycling can develop tiny gaps in a motor. Thus, as the air inside the motor periodically experiences expansion and contraction, a small amount of moisture may be sucked inside the motor. Under this circumstance, the seals act as a barrier to the moisture removal, causing interior corrosion of the rotor, stator, PM, and other components. According to Lenzing and Chen [5.31], shaft seals typically cause a loss of 3%–15% of shaft torque due to friction.

A new technique for providing corrosion protection is to apply a protective coating to all the motor parts, including rotor and stator cores, PMs, windings, housing, and endbells, both internally and externally [5.31]. Using the standard salt-spray test as defined in MIL-STD-202G [5.32], in which testing machines are subjected to a fine mist of salt solution, a conventional motor develops a locked rotor and is unable to operate after 48 h of the salt-spray test. By contrast, the motor treated with this new technique still runs normally after 140 h of the test.

Alternatively, motor manufacturers often use stainless steel to make motor housing and endbells for some special applications, such as food processing–related applications. Stainless steel has long been thought of as the best material for withstanding caustic chemicals and high pressure. It is thus ideal for applications requiring high corrosion and heat resistance, frequent washdown, and long life. The drawback of stainless steel is its high price.

Kollmorgen has recently launched its AKMH stainless steel servomotors (Figure 5.42) that fulfill the European Hygienic Engineering & Design Group (EHEDG), National Sanitation Foundation (NSF), and 3A standards [5.33]. This type of motor is specially designed for food processing manufacturers with superior performance, long-life operation, low maintenance, and great corrosion protection. These IP69K rated hygienic servomotors feature stainless steel housings and can withstand water pressure up to 100 bars.

5.6.3 Hydrogen Embrittlement Issues

During some surface treatment processes, such as electroplating, acid pickling, phosphating, electrocleaning, and heat treatment, atomic hydrogen can enter into metallic materials

FIGURE 5.42
Stainless steel servomotor for food processing applications. (Courtesy of Kollmorgen Corporation, Radford, VA.)

(mainly steel) to degrade the fracture behavior or load-carrying ability of these materials. This phenomenon is often referred to as hydrogen embrittlement or hydrogen-induced brittle failure.

For instance, hydrogen can be produced from the reaction of the cathode with metal deposition in a zinc electroplating process [5.34],

$$Zn^{2+} + 2e^- \rightarrow Zn^0 \tag{5.23}$$

$$2H^+ + 2e^- \rightarrow H_2 \tag{5.24}$$

An acid pickling operation prepares the surfaces of workpieces prior to some processes such as electroplating, black oxide, and phosphate coating. The acid pickling operation is usually completed with sulfuric acid, but hydrochloric acid is also used.

In the acid pickling process, oxide and scaling layers are dissolved in acid pickling solutions without generating hydrogen. Hydrogen is formed as acid attacking the base material [5.35]:

$$Fe + 2H_3PO_4 \rightarrow Fe^{3+} + 2H_2PO_4^- + H_2 \tag{5.25}$$

The absorption and diffusion of hydrogen in steel are quite complicated [5.36]. When hydrogen atoms enter and diffuse through steel surfaces, they may present either as atomic or molecular hydrogen or in combined molecular form. Because these molecules are too large to diffuse through steel, pressure builds at crystallographic detects (dislocations and vacancies) or discontinuities (voids, inclusion/matrix interfaces) causing minute cracks to form [5.37]. The relief of hydrogen embrittlement is partially related to the nature of the coating applied. Simply speaking, if the coating is dense and nonporous, the escape of hydrogen may be difficult; if the coating is open and porous, the release of hydrogen is a matter of time and temperature [5.38].

Even today, hydrogen embrittlement still remains a major cause of fastener failure. In a root cause failure analysis, an essential step is to determine the failure mechanism. More specifically, it is important to distinguish hydrogen embrittlement and stress corrosion cracking from each other because both failures are associated with the interaction between hydrogen and metal workpieces (e.g., fasteners) and occur under tensile stresses well below the yield strength of the material. The major differences include [5.39–5.41] the following:

- While hydrogen responsible for embrittlement comes from manufacturing processes such as plating and cleaning, hydrogen in stress corrosion cracking is supplied from the environment.
- Stress corrosion cracking is associated with high-stress workpieces where the core hardness is larger than 32 HRC, more likely >36 HRC.
- Stress corrosion cracking is not only induced by hydrogen; it could be also resulted from various corrosive substances that attack small cracks, leading to the final brittle fracture.
- Though both hydrogen embrittlement and stress corrosion cracking are delayed failures, the delay time for hydrogen embrittlement is likely from a few minutes to 24 h after installation, whereas the delay time for stress corrosion, as the primary indication of this type of failure, is typically longer than 24–48 h after installation.
- Stress corrosion cracking often exhibits more crack branching and less pronounced dimples than cracking produced by hydrogen embrittlement.

TABLE 5.3

Recommended Baking Process by ASTM B850-98

Tensile Strength				
MPa	**ksi**	**Hardness (HRC)**	**Temperature (°C)**	**Baking Time (h)**
1000–1100	145–160	31–33	190–220	>8
1101–1200	160–174	33–36	190–220	>10
1201–1300	174–189	36–39	190–220	>12
1301–1400	189–203	39–43	190–220	>14
1401–1500	203–218	43–45	190–220	>16
1501–1600	218–232	45–47	190–220	>18
1601–1700	232–247	47–49	190–220	>20
1701–1800	247–261	49–51	190–220	>22

A number of methods can be taken to avoid hydrogen embrittlement failure, including the following:

a. The hydrogen removal process must be carried out following the electroplating process immediately. According to the ASTM standard [5.42], the hydrogen removal requires that the electroplated parts must be baked at 204°C–218°C (400°F–425°F) within 1 h after the plating process for at least 4 h. In ASTM B850-98 [5.43], the baking time varies from >8 to >22 h at 190°C–220°C (374°F–428°F), depending on the tensile strength and hardness of plated parts (see Table 5.3).

   It is worth to note that the baking temperature is limited for some metal coatings. For example, at 225°C, the zinc starts to oxidize in air.

b. A stress relief process is necessary to reduce the residual stress in the parts. For low-carbon steels, it requires to anneal 3–4 h at about 400°C.

c. A more direct and effective way for reducing the hydrogen embrittlement risk is to use low embrittling electroplating processes such as special solution compositions and operating conditions, which result in either a lower pickup of hydrogen or a deposit that allows easier removal of the absorbed hydrogen during the baking treatment.

d. For high-stressed parts, it is recommended to use a pickling-free process such as dry sand blasting or other mechanical means.

e. Some coating techniques can eliminate hydrogen embrittlement. One example is called PVD. This is because PVD processes are done in vacuum, and thus, the chance of embrittlement by hydrogen is precluded. Another example is the mechanical galvanizing process. In this process, zinc coatings are applied to workpieces at room temperature without hydrogen embrittlement, as described in ASTM B695-2000 [5.44]. The coating thickness can be controlled between 5 and 100 μm.

f. It is generally agreed that in plating of Cr, Zn, Cd, Ni, Sn, and Pb, hydrogen tends to remain in steel. By contrast, some elements such as Cu, Mo, Al, Ag, Au, and others lead to lower hydrogen diffusion and solubility and, consequently, lower hydrogen permeation through steel surfaces. Under the condition of honoring the technical requirements, it is preferred to use the coating materials that have low hydrogen permeation.

g. Use low-strength steel to replace high-strength steel. This can effectively reduce the risk of hydrogen embrittlement.
h. Because coating layers cover the surfaces of plated fasteners, they play the role as a hydrogen diffusion barrier. In fact, the coating thickness affects significantly the rate of hydrogen diffusion. Usually, the maximum coating thickness for fasteners with the hardness <32 HRC is 12 μm and 8 μm with the hardness ≥32 HRC.

While avoiding hydrogen embrittlement in some manufacturing processes, scientists and engineers have also taken full advantage of hydrogen embrittlement in other manufacturing processes. A typical example is the production of micro- and nanoparticles. This technique has been successfully adopted for making rare-earth PMs.

References

[5.1] Groover, M. P. 2010. *Fundamentals of Modern Manufacturing: Materials, Processes, and Systems*, 4th edn. John Wiley & Sons, Hoboken, NJ.
[5.2] Verhoeven, J. D. 2005. Metallurgy of steel for bladesmiths and others who heat treat and forge steel. Online eBook at http://www.feine-klingen.de/PDFs/verhoeven.pdf.
[5.3] Rio Tinto Iron and Titanium, Inc. 2013. *Ductile Iron Data for Design Engineers*. http://www.ductile.org/ductile-iron-data/.
[5.4] Davis, J. R. 1999. *Cast Irons*, 2nd edn., ASM International: Materials Park, OH.
[5.5] Karwa, R. 2006. *A Textbook of Machine Design*, 2nd edn. Laxmi Publications Ltd., New Delhi, India.
[5.6] ASM. 1990. ASM Handbook (vol. 1): *Properties and Selection: Irons, Steels, and High-Performance Alloy*. ASM International.
[5.7] Graham, D. 2006. Machining cast iron. *Manufacturing Engineering* **136**(**2**): 77–83.
[5.8] DeGarmo, E. P., Black, J. T., and Kohser, R. A. 2002. *Materials and Processes in Manufacturing*, 9th edn. John Wiley & Sons, New York.
[5.9] Pontzer, J. H. 2000. Method of manufacturing electric motor housing frame and foam pattern therefore. U.S. Patent 6,109,333.
[5.10] Zhang, D. L., Zheng, L. H., and St. John, D. H. 2002. Effect of a short solution treatment time on microstructure and mechanical properties of modified Al-7wt. %Si-0.3wt. %Mg alloy. *Journal of Light Metals* **2**(**1**): 27–36.
[5.11] Manente, A. and Timelli, G. 2011. Chapter 9: Optimizing the heat treatment process of cast aluminum alloys. In *Recent Trends in Processing and Degradation of Aluminum Alloys* (Ed.: Z. Ahmad). InTech, Rijeka, Croatia.
[5.12] Bauser, M., Sauer, G., and Siegert, K. 2006. *Extrusion*, 2nd edn. ASM International, Materials Park, OH.
[5.13] Van Dine, P., Odessky, V., Spencer, B. E., Smith, J. S., and Harring, W. R. 2000. Method for making a composite electric motor housing. U.S. Patent 6,125,528.
[5.14] Sachs, E. M., Haggerty, J. S., Cima, M. J., and Williams, P. A. 1993. Three-dimensional printing techniques. U.S. Patent 5,204,055.
[5.15] Sachs, E. M., Haggerty, J. S., Cima, M. J., and Williams, P. A. 1994. Three-dimensional printing techniques. U.S. Patent 5,340,656.
[5.16] Cima, M., Sachs, E., Fan, T. L., Bredt, J. F., Michaels, S. P., Khanuja, S., Lauder, A., Lee, S.-J. J., Brancazio, D., Curodeau, A., and Tuerck, H. 1995. Three-dimensional printing techniques. U.S. Patent 5,387,380.

[5.17] Kollmorgen Corporation. RBE(H) motor series. http://www.clemson.edu/ces/crb/procedures/WAM_Data_Files/WAM_motors_datasheet_rbe_series.pdf.
[5.18] ASTM Standard B557-06. Standard test methods for tension testing wrought and cast aluminum- and magnesium-alloy products.
[5.19] Black, J. T. and Kohser, R. A. 2007. *DeGarmo's Materials and Processes in Manufacturing*, 10th edn. John Wiley & Sons, Hoboken, NJ.
[5.20] Garietya, M., Ngaileb, G., and Altan, T. 2007. Evaluation of new cold forging lubricants without zinc phosphate precoat. *International Journal of Machine Tools and Manufacture* **47**(**2007**): 673–681.
[5.21] Boyland, J., Tong, W., Bartha, L., and Krogen, O. 2005. Hook nut connector assembly. U.S. Patent Application 2005/0123377.
[5.22] Budynas, R. G. and Nisbett, J. K. 2008. *Shigley's Mechanical Engineering Design*, Chapter 8. McGraw-Hill, New York, p. 422.
[5.23] SKF. 2001. *Bolt-Tightening Handbook*. SKF Group.
[5.24] Shoberg, R. S. 1999. Tightening strategies for bolted joints: Methods for controlling and analyzing tightening. *11th Annual Technical Conference on Fastening Technology*, Cleveland, OH. www.pcbloadtorque.com/pdfs/Tightening%20Strategies.pdf.
[5.25] Ugural, A. C. 2004. *Mechanical Design: An Integrated Approach*, Chapter 15. McGraw-Hill, Boston, MA, p. 608.
[5.26] Fernando, S. 2001. An engineering insight to the fundamental behavior of tensile bolted joints. *Steel Construction* **35**(**1**): 2–13.
[5.27] Tseng, S.-W. 2010. A simplified simulation on loading distribution at bolt threads. Bastion Technologies. http://www.bastiontechnologies.com/ogp/TechnicalPapers.html.
[5.28] Timoshenko, S. P. and Goodier, J. N. 1970. *Theory of Elasticity*, 3rd edn. McGraw-Hill, New York.
[5.29] Young, W. C., Budynas, R. G., and Sadegh, A. M. 2011. *Roark's Formulas for Stress and Strain*, 8th edn. McGraw-Hill, New York.
[5.30] Fernando, S. 2001. Minimum thread engagement—what is the optimum engagement length? Ajax Fasteners Innovations. Technical note: AFI/01/002. http://www.ajaxfast.com.au/downloads/Technical%20notehowmanythreads.pdf.
[5.31] Lenzing, R. and Chen, W. 2010. New stepper motors. *Design World*, February issue, pp. 62–64.
[5.32] Department of Defense, USA. 1980. Test method standard: Electronic and electrical component parts. MIL-STD-202G.
[5.33] Kollmorgen Corporation. 2013. HKM: New dimension stainless steel motors. http://www.heason.com/wp-content/uploads/2013/06/HKM-Servo-Motor-Flyer1.pdf.
[5.34] Ferraz, M. T. and Oliveira, M. 2010. Steel fasteners failure by hydrogen embrittlement. *Ciência & Tecnologia dos Materiais* **20**(**1**/**2**): 128–133.
[5.35] Bay, N. 1994. The state of the art in cold forging lubrication. *Journal of Materials Processing Technology* **46**(**1994**): 19–40.
[5.36] Grabke, H. J. and Riecke, E. 2000. Absorption and diffusion of hydrogen in steels. *Materiali in Technologije* **34**(**6**): 331–342.
[5.37] Herring, D. H. 2010. Hydrogen embrittlement. *Wire Forming Technology International* **13**(**4**): 24–17.
[5.38] Wolff, R. H. 1966. Hydrogen embrittlement of steel in metal finishing processes of black oxide and zinc phosphatize. U.S. Army Weapons Command. Rock Island Arsenal Research and Engineering Division. Technical Report 66-2008.
[5.39] Eliaz, N., Shachar, A., Tal, B., and Eliezer, D. 2002. Characteristics of hydrogen embrittlement, stress corrosion cracking and tempered martensite embrittlement in high-strength steels. *Engineering Failure Analysis* **9**(**2002**): 167–184.
[5.40] Woodtli, J. and Kieselbach, R. 2000. Damage due to hydrogen embrittlement and stress corrosion cracking. *Engineering Failure Analysis* **7(6)**: 427–450.
[5.41] Bickford, J. H. 2008. *Introduction to the Design and Behavior of Bolted Joints*, 4th edn., CRC Press, Boca Raton, FL.

[5.42] American Society for Testing and Materials. 1999. ASTM F1940-99 Standard test method for process control verification to prevent hydrogen embrittlement in plated or coated fasteners.
[5.43] American Society for Testing and Materials. 2009. ASTM B850-98 Standard guide for post-coating treatments of steel for reducing the risk of hydrogen embrittlement.
[5.44] American Society for Testing and Materials. 2000. ASTM B695-00 Standard specification for coatings of zinc mechanically deposited on iron and steel.

6

Motor Bearing

The purpose of using bearings in electric motors is to support and locate the rotating rotor in both radial and axial directions, maintain a uniform air gap between the rotor and stator over a wide range of operating speeds, reduce friction and wear between the rotating and stationary components, and transfer loads from the shaft to the motor frame and base. It has been reported that two major root causes of motor failure are bearing and insulation failure. Statistical data have further indicated that more than half of all motor failures can be attributed to the bearing failures [6.1]. Therefore, it is important to understand bearing performance characteristics and bearing failure mechanisms.

The most important bearing rating factors are speed and load because they have a great impact on bearing life, especially load. Bearings should have good dynamic operating characteristics over a wide range of speeds, low noise and vibration levels, minimized friction, high fatigue strength, less maintenance, long service lifetime, and low cost. To ensure motor operation, it is critical to select the appropriate bearing type, lubricant, lubrication method, and suitable bearing arrangement, according to different operational conditions and motor applications.

6.1 Bearing Classification

There are basically three types of bearings used in industrial, military, and commercial applications: journal (sliding) bearings, rolling bearings, and noncontact bearings. Each type has different performing characteristics and is intended for different applications. Besides these, there are also some special bearings, such as air bearings, maglev bearings, and superconducting bearings.

6.1.1 Journal Bearing

A journal bearing commonly uses a grease or mineral oil to form a thin layer on the bearing surface, withstanding the bearing load and separating the rotating shaft from the stationary bearing surface (Figure 6.1). The lubricant film thickness t_f is very small in comparison to the shaft radius R. In most lubricated journal bearings with incompressible lubricants, the ratio (t_f/R) is typically on the order of 10^{-3}. Due to the eccentricity and the difference in radius between the shaft and bearing, a convergent clearance is formed between the two components. Hydrodynamic pressure is thus developed in this film. It is the hydrodynamic pressure that allows journal bearings to tolerate dynamic loads or even momentary shock loads reasonably.

This type of bearing is often used for high-power and high-load industrial machinery such as engines, centrifugal compressors, pumps, and motors. A journal bearing consists of a shaft that rotates freely in a supporting metal sleeve. There are no rolling elements in

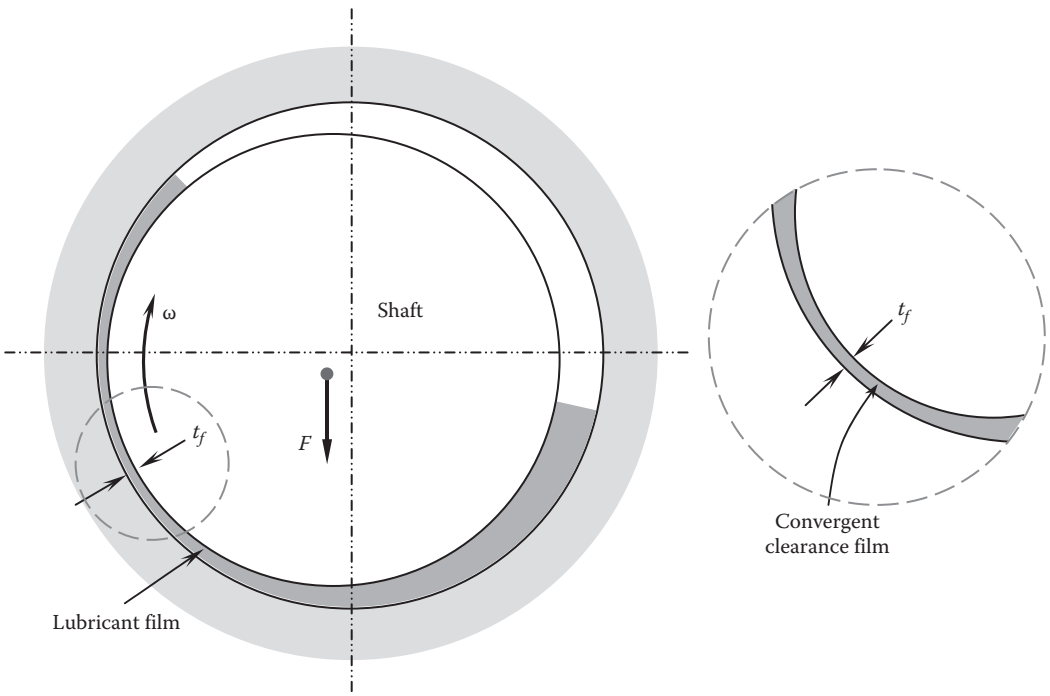

FIGURE 6.1
Lubricant film for supporting motor loads and separating the shaft and stationary bearing surface. Hydrodynamic pressure is developed in the convergent clearance film to lift the shaft.

this type of bearing. Journal bearings have various designs: (1) the self-lubricating bearings, which are made of porous materials and soaked with lubricants. When the temperature rises up due to bearing operation, the lubricant gets out of the pores for playing a role of lubrication. As the temperature decreases, the lubricant is sucked back into the pores due to the capillary effect. The most significant advantage of self-lubricating bearings is lubrication and maintenance-free. (2) The regular lubrication bearings, which require lubricants to form an oil film between the shaft and bearing to support the rotating shaft. (3) The hydrodynamic lubrication bearings, which require lubricants that elevates the rotating shaft by providing the pressurized lubricant from outside. Journal bearings are usually made from cast iron or Babbitt alloys and widely used for engines and large-size, heavy-duty motors.

Journal bearings have some advantages over other types of bearings, including the following:

- Low cost for manufacturing
- Less sensitive to contamination
- Enabling operation under severe conditions
- Requiring small radial space
- Available to work in split halves
- Better shock load–sustaining capacity
- Low operation noise

- Less-precise mounting
- Easy for maintenance

Tribology is a multidisciplinary science to study friction, lubrication, and wear in sliding lubrication systems. In fact, tribological behavior is a complex phenomenon in metallic materials. Many factors, such as loading, lubrication, surface roughness, and relative speed, can significantly affect the interaction between two sliding materials. Stribeck [6.2] had systematically studied the variation of friction between two liquid-lubricated surfaces. Based on the investigations, Stribeck claimed that the journal bearing friction is a function of load, lubricant viscosity, and shaft rotating speed. He showed that the friction in journal-type bearings started with high friction at very low speeds, decreased to a minimum friction when metal-to-metal contact was eliminated, and then increased again at higher speeds, which is well known as *Stribeck curve* today. As depicted in Figure 6.2, there are three friction regions: boundary friction, mixed friction, and fluid friction. In the boundary region, the hydrodynamic pressure between the mating surfaces (i.e., the surfaces of the shaft and journal bearing) has not been developed adequately to support the load. In this region, the lubricant boundary film is partly discontinuous, and the thickness of the film is very thin, approximately 200 Å [6.3]. There are solid contacts in some areas, causing high friction of the sliding system. With the increase in the speed, the film thickness of the lubricant increases rapidly to reduce the direct contact of the shaft and the bearing and consequently reduce the friction until it reaches the minimum value. In the fluid friction region, the film thickness of the lubricant becomes much larger (at least four times) than the surface roughness so that the shaft is completely isolated from the bearing. As a result, the friction between the shaft and the bearing is determined by the dynamic viscosity of the lubricant alone, which increases with the increased speed. The friction factors of different regions are presented in Table 6.1 [6.4] to compare with the dry friction.

The data in Table 6.1 indicate that in any cases, dry friction should be avoided.

Figure 6.2 also provides the comparison of friction between different types of bearings. It exhibits that ball bearings have the lowest friction over a wide range of rotating speeds,

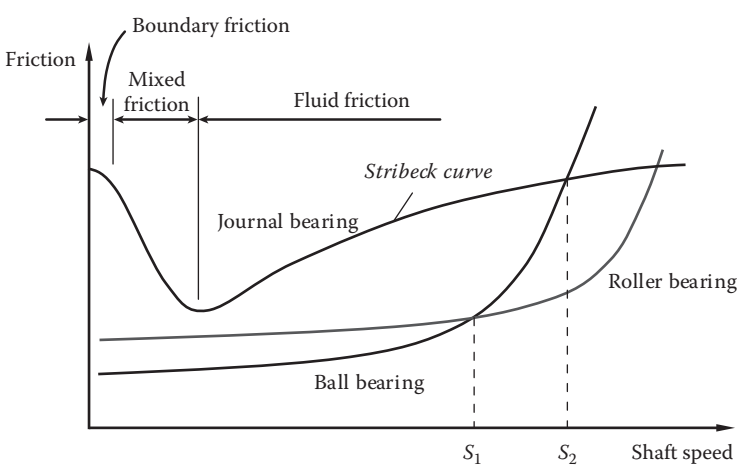

FIGURE 6.2
Comparison of friction between different types of bearings.

TABLE 6.1

Comparison of Friction Factors between Different Friction Regions

Friction Region	Friction Factor, f
Dry friction	0.15–0.8
Boundary friction	0.03–0.15
Mixed friction	0.005–0.03
Fluid friction	<0.005

Source: Mayer, E., *Mechanical Seals*, 3rd edn., Newnes-Butterworth, London, U.K., 1977.

where the rotating speed is lower than a certain value of S_1. Increasing the speed to S_1, the friction of ball bearings increases steeply and thus becomes larger than that of roller bearings. At very high rotating speeds ($>S_2$), the friction of journal bearings becomes lower than that of rolling bearings.

It should be noted that rotating machinery supported by journal bearings presents two kinds of self-excited vibrations, that is, oil whirl and oil whip; both can drive the rotating system to an unstable condition. Oil whirl is commonly masked by the rotor unbalance and occurs near half of the rotating speed, hence being rarely associated with instability problems. Oil whip is a severe vibration that occurs when the oil-whirl frequency coincides with the first flexural natural frequency of the shaft, hence near twice this natural frequency. When operating under this condition, the vibration amplitudes in the bearings are limited by the bearing's clearance. Based on the rotordynamic analysis, two different thresholds of fluid-induced instabilities have been reported by Mendes and Cavalca [6.5].

In designing journal bearings, the bearing static performance characteristics are related to a dimensionless parameter as Sommerfeld number S, which is defined as

$$S = \frac{\mu\omega}{P}\left(\frac{R}{\delta}\right)^2 \tag{6.1}$$

where

μ is the viscosity of the lubricant in Pa-s
ω is the shaft rotating speed in rad/s
R is the shaft radius
δ is the clearance between the shaft and bearing
P is the specific load in Pa

$$P = \frac{F}{ld} \tag{6.2}$$

where

F is the external force acting on the shaft
l and d are the length and diameter of the bearing, indicating the ratio of applied load to bearing projected area

For an unloaded bearing condition, $F=0$ and $P=0$, so that Sommerfeld number S approaches infinity. Thus, a weightless shaft will run concentrically with the bearing.

Either increasing the external load or decreasing the rotating speed will reduce *S*. Under such circumstances, the journal moves away from its concentric position to eccentric positions. As specific load becomes huge or speed approaches zero, *S* approaches zero. Under this condition, metal-to-metal contact occurs between the shaft and bearing.

6.1.2 Rolling Bearing

Rolling bearings have high loading capacity and exhibit very low rolling friction torques. A rolling bearing usually consists of an inner and outer ring, a number of rolling elements, and a cage to hold the rolling elements. Raceways are made on the inner and outer rings, on which the rolling elements rotate freely. The performance of bearing strongly depends on the hardness, surface finish, and accuracy of raceways and other parameters such as internal radial and axial clearance. The ring surfaces must go through grinding without producing waviness. Typically, when the surface roughness is larger than 0.2 μm, the bearing cannot fully play to its carrying capacity. In today's motor industry, the great majority of bearings are rolling bearings.

There are two major types of rolling bearings, distinguished mainly by the rolling element shape: ball bearings and roller bearings. According to the configuration of the bearing rings, ball bearings are further classified as deep-groove ball bearings and angular contact ball bearings. On the other hand, according to the shape of the rollers, roller bearings are classified as cylindrical, spherical, tapered, and needle roller bearings. To distinguish bearings from their functions, the bearing can be divided into radial bearings, which withstand primarily radial loads and axial loads to a certain extent, and thrust bearings, which withstand only axial loads.

6.1.2.1 Ball Bearing

As the most common type of bearing, deep-groove ball bearings are extensively used in electric motors. This type of bearing is not only capable of taking radial loads but also axial loads to some extent. As shown in Figure 6.3, a standard deep-groove ball bearing consists of a number of rolling balls and two concentric steel rings. Each of the concentric steel ring has a hardened ring on which the balls roll. The balls are separated from each other by a cage between the inner and outer rings. The cage is traditionally made of thin steel, but some bearing manufacturers now use plastic materials. To protect against contaminants, the bearing is sealed with plastic covers at the bearing-side surfaces between the inner and outer rings. To reduce the friction and wear in the rolling contacts, bearings are lubricated with greases or mineral oils. From Figure 6.3, it can be seen that a deep-groove ball bearing is symmetric with respect to its center line of cross section and is characterized by a number of primary dimensions, including the following:

- The bearing OD d_o is the fitting dimension with the bearing bore on the motor end-bell or housing, and the bearing ID d_i is the fitting dimension with the rotor shaft.
- d_{ir} is the inner ring diameter at the lowest point of the raceway.
- d_{or} is the outer ring diameter at the highest point of the raceway.
- d_p is the bearing pitch diameter.
- d_b is the ball diameter.
- δ_r is the radial clearance of the bearing.
- w is the bearing width.

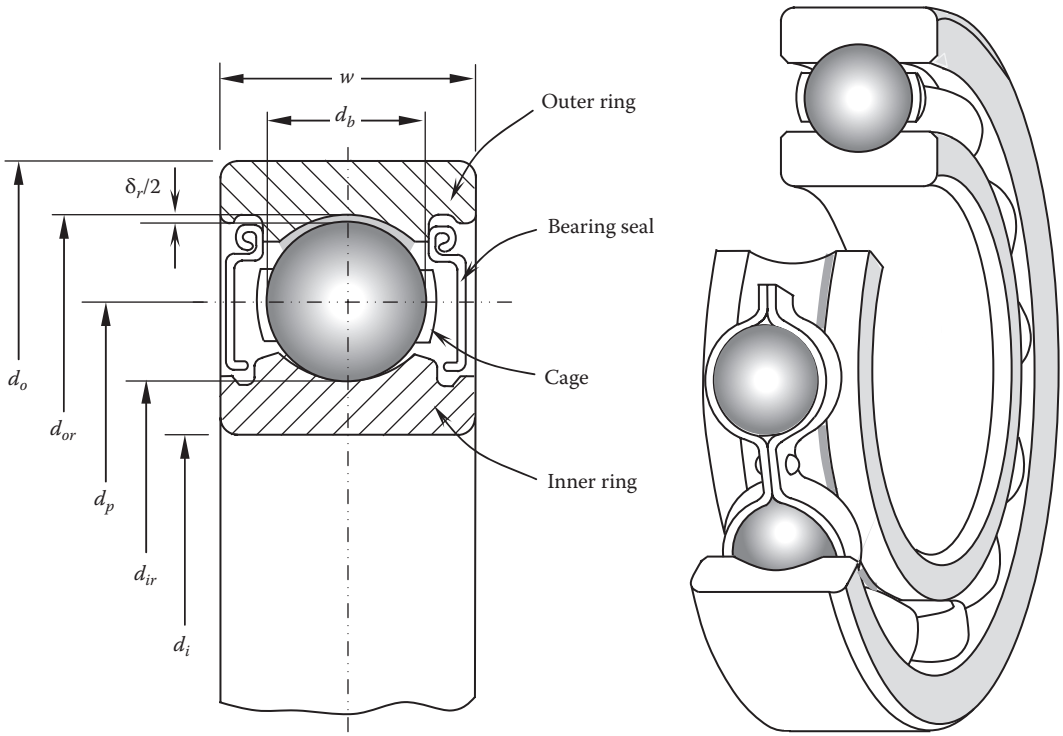

FIGURE 6.3
Deep-groove ball bearings (seals are removed from the right figure).

The bearing pitch diameter d_p is defined as the diameter going through the ball centers. From Figure 6.3, it can be easily derived that

$$d_p = d_{ir} + d_b \tag{6.3}$$

An alternative expression of the bearing pitch diameter d_p can be related to the bearing internal radial clearance δ_r as

$$d_p = \frac{d_{ir} + d_{or}}{2} - \frac{\delta_r}{2} \tag{6.4}$$

One of the key design features of the deep-groove ball bearing is the curvature of the outer and inner rings because they have a strong impact on the bearing stress, friction, and fatigue life. The curvatures of the outer and inner rings are r_o and r_i, as depicted in Figure 6.4. The ratio of the ring radius to the ball diameter is defined as race conformity, which is a measure of the geometrical conformity of the race to the ball in a plane passing through the bearing axis. Therefore, the outer and inner race conformities are expressed as

$$f_o = \frac{r_o}{d_b} \tag{6.5a}$$

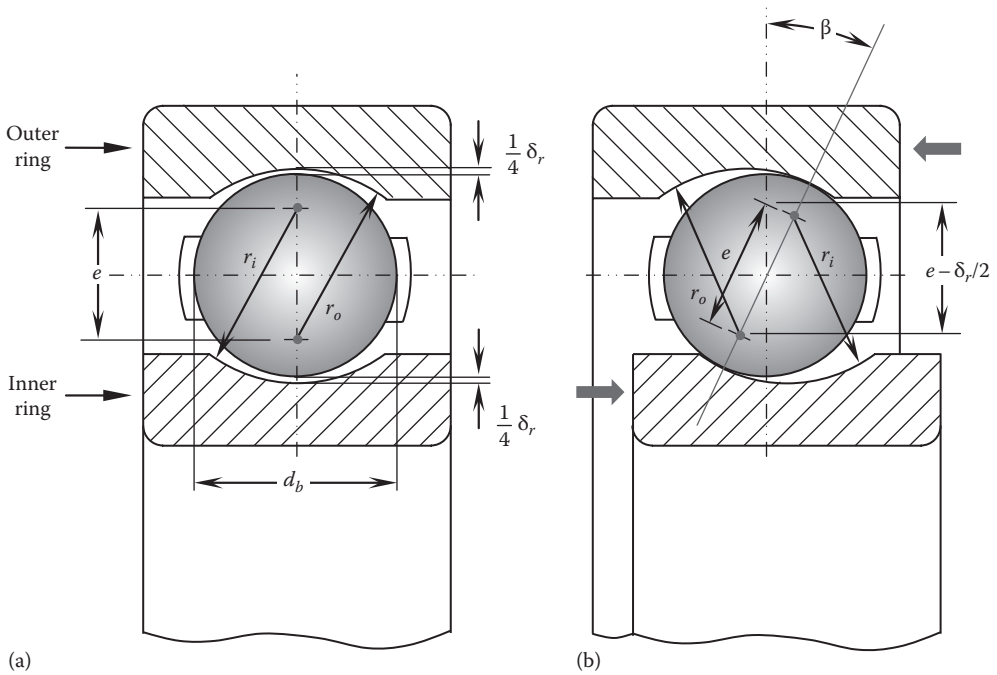

FIGURE 6.4
Cross section of a radial ball bearing, showing inner and outer ring radius (r_o and r_i) and the distance e between the centers of the radii r_i and r_o: (a) initial position and (b) shifted position under axial load.

$$f_i = \frac{r_i}{d_b} \tag{6.5b}$$

respectively. Usually, the outer and inner race conformities are around 52%.

Ball bearings are designed with a specific internal radial clearance because it provides free rotation of balls, compensation for thermal expansion, and optimum load distribution (Figure 6.4a). This parameter can significantly influence bearing operating characteristics. When the bearing is subject to axial load, the inner and outer rings shift relatively in the axial direction. As a result, the internal radial clearance no longer exists (Figure 6.4b).

The bearing contact angle β is defined as the angle between the bearing radial line and the contact line, which passes through the contact points between the rolling balls and the inner and outer raceways. From Figure 6.4b, the contact angle β can be expressed as

$$\cos\beta = \frac{e - \delta_r/2}{e} \tag{6.6}$$

where e is the distance between the radius centers of r_i and r_o and can be determined as

$$e = (r_o + r_i) - d_b \tag{6.7}$$

Combining Equations 6.5a and 6.5b with Equation 6.7, it follows that

$$e = (f_o + f_i - 1)\, d_b \tag{6.8}$$

where (f_o+f_i − 1) is known as the total conformity ratio, which is the measure of the combined conformity of both the outer and inner rings to the balls [6.6].

By optimizing the contact geometry between the balls and rings, the misalignment between the outer and inner rings can be minimized, providing 35% less friction and 50% less noise [6.7]. These optimized bearings are ideal for applications that require precise rotation with large range of torques, such as motors and machine tools. Other design features impacting bearing loss include the ring finish, cage material, and bearing lubrication.

Angular contact ball bearings are specially designed to accommodate combined radial and axial loads. Since this type of bearing uses axially asymmetric rings, the contact line that connects the contact points of the ball and the rings is no longer perpendicular to the axis of the bearing rotation. Rather, it forms an angle with the bearing radial line, called contact angle (Figure 6.5). The standard contact angles are 15°, 20°, and 25°, but the contact angles of 30° and 40° are also available for using in different loading conditions. Generally, the larger the contact angle, the higher the axial load that bearing can handle. It is very important to note that single-row angular contact ball bearings can take axial loads only in one direction. Under reverse loading conditions, the elliptical contact area on the outer ring is truncated by the low shoulder on that side of the outer ring, causing excessive stress and temperature rise at the contact area, and thus leading to high

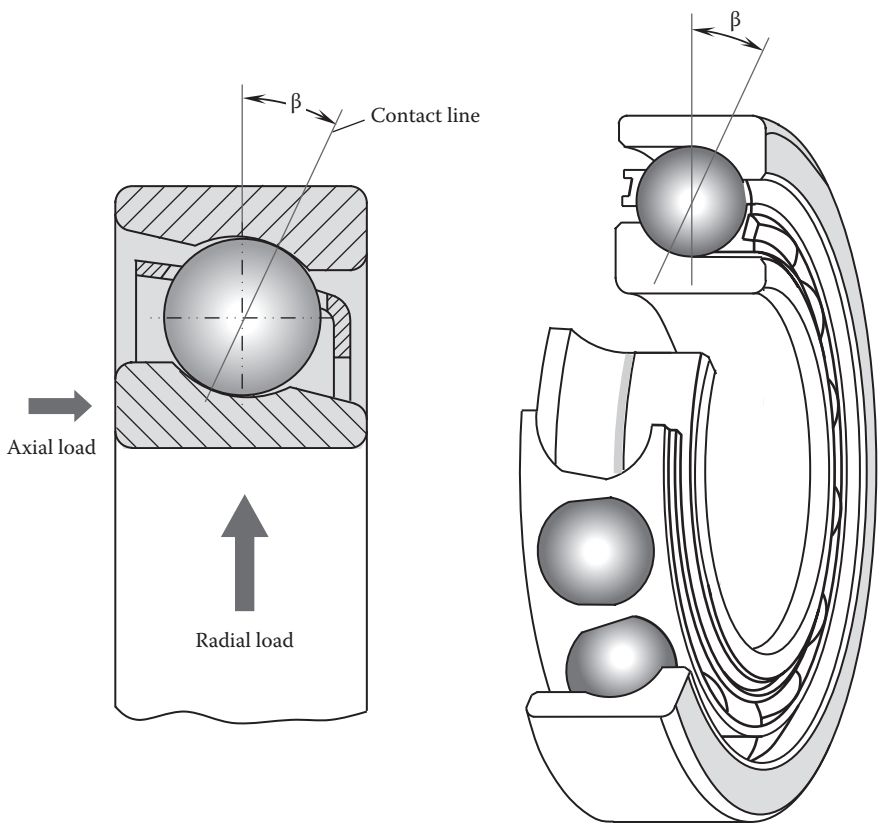

FIGURE 6.5
Angular contact ball bearing with the contact angle β. The bearing shown here has the outer ring cut away reveling the balls and ball cage.

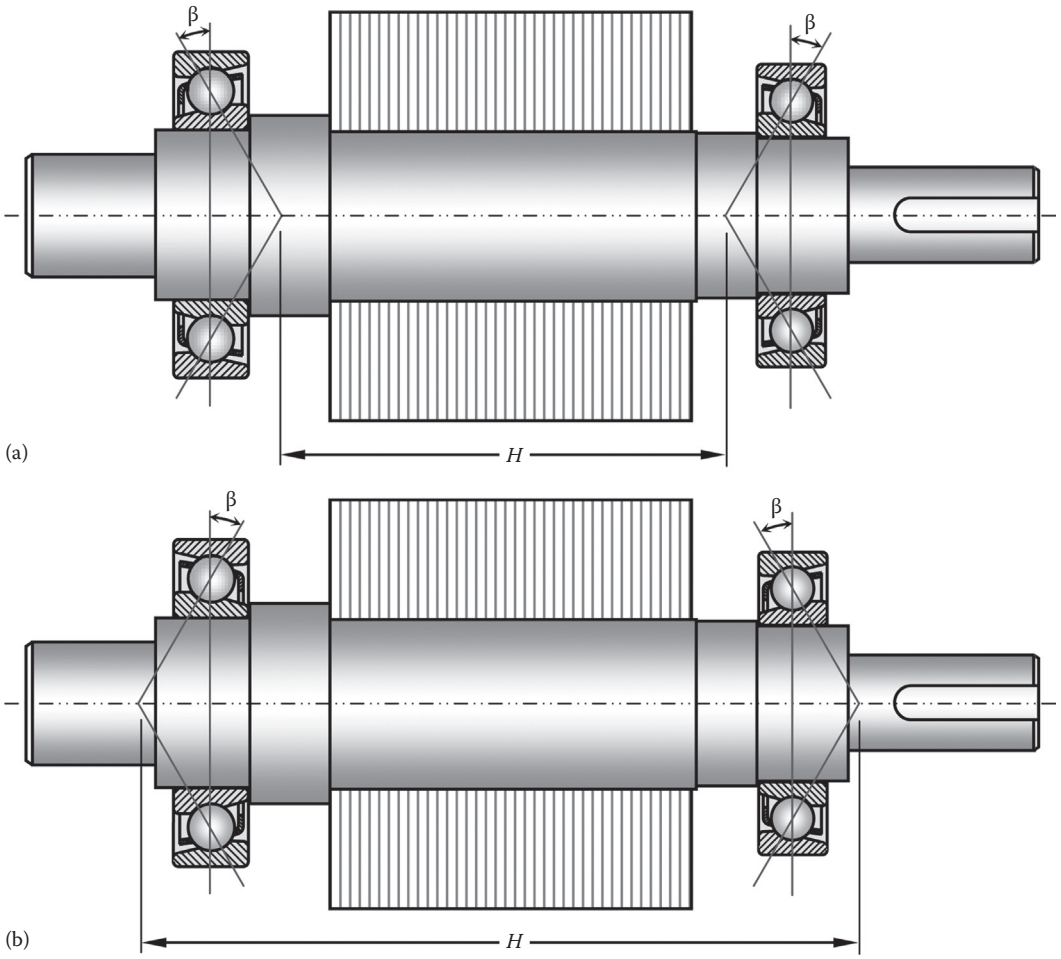

FIGURE 6.6
A pair of angular contact ball bearings used together to support rotor in a motor with two bearing arrangements: (a) contact line inwards (face-to-face); (b) contact line outwards (back-to-back).

vibration and bearing failure. Therefore, at least a pair of bearings must be used together, as shown in Figure 6.6. As can be observed, there are two bearing arrangements: face-to-face (contact line inwards) and back-to-back (contact line outwards). In the face-to-face arrangement (Figure 6.6a), the cones formed by the contact lines point inwards. The axial loads converge toward the bearing axis and may cancel each other out. However, because the support base length H is shorter than the back-to-back arrangement (Figure 6.6b), this arrangement provides a higher tilting clearance (which is defined as the differential mutual ring displacement in the axial direction). As a result, the face-to-face arrangement is not as stiff as the back-to-back arrangement and is not appropriate for the tilting moment loading.

The performance of the angular contact ball bearings is similar to that of the deep-groove ball bearings. However, this type of bearing is limited to lower rotating speeds and has slightly higher noise. For some applications, matched bearing sets that combine two,

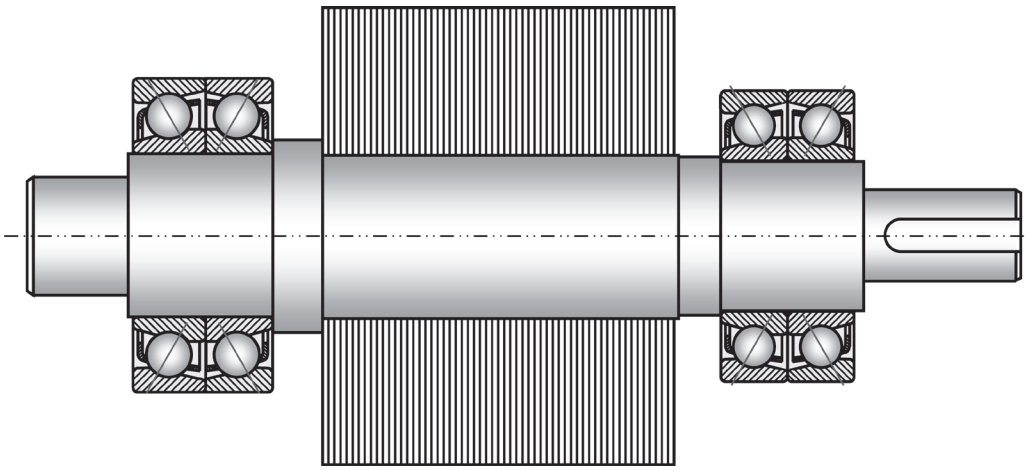

FIGURE 6.7
Matched angular contact ball bearings in a specific bearing arrangement for supporting heavy rotor.

three, or four angular contact ball bearings together may be used to meet special requirements for load capacity and rigidity (Figure 6.7).

The load analysis of an angular contact ball bearing is shown in Figure 6.8. The radial load F_r acting on the bearing is perpendicular to the bearing axis of rotation, while the thrust load F_a is parallel to the axis of rotation. Thus, the resultant force is formed from these two bearing loads. The load angle α is defined as the angle between the resultant load and the radial load, determined as

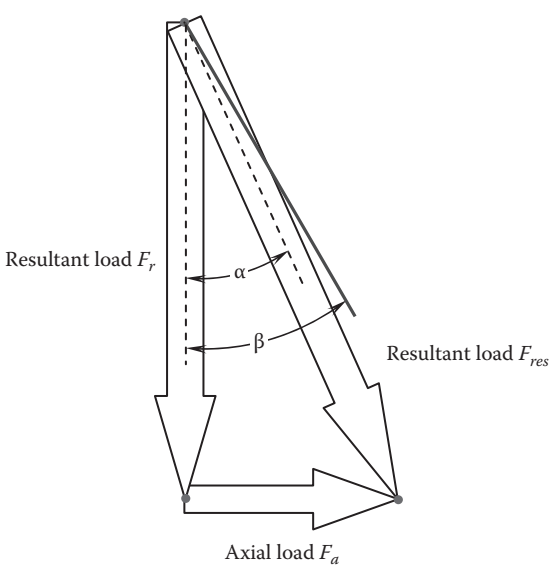

FIGURE 6.8
Loads acting on angular contact ball bearing. The load angle α is determined from the radial and axial load.

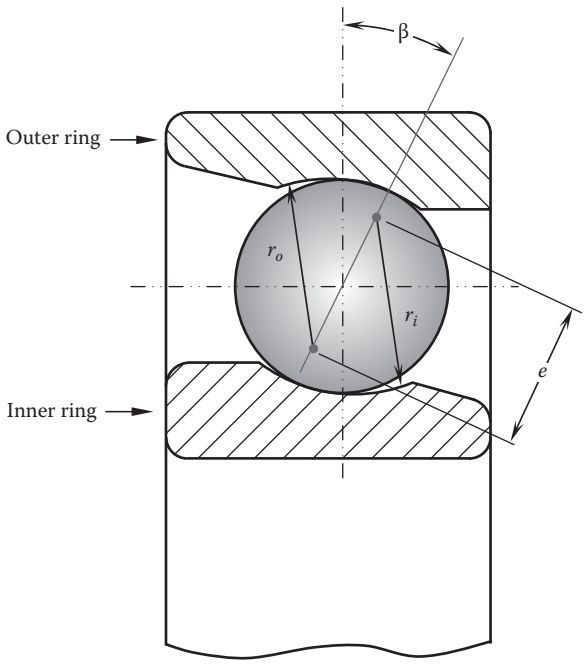

FIGURE 6.9
Cross section of an angular contact ball bearing, showing the outer and inner ring radius (r_o and r_i) and the distance e between the centers of the radii r_r and r_o.

$$\alpha = \arctan\left(\frac{F_a}{F_r}\right) \tag{6.9}$$

The radii of the outer and inner rings in an angular contact ball bearing are shown in Figure 6.9. It is noted that the centers of the radii are located at the bearing contact line.

6.1.2.2 Roller Bearing

In roller bearings, contact rollers may come in a variety of different shapes, including cylindrical, spherical, and conical (tapered roller). In general, the bearing running performance and noise generation depend to a large extent on the dimension precision and surface finish of rollers. Compared with ball bearings, roller bearings have much greater load-carrying capacity but also higher rolling resistance (typically 0.0015 for roller bearings and 0.0008 for ball bearings).

Cylindrical roller bearings improve load-carrying capacity and have been designed to support primarily high radial loads and, to a lesser extent, thrust loads. They have exceptionally low-friction torque characteristics that make them suitable for high-speed applications. The critical design features of this type of bearing include the surface finish, roundness, and waviness of the tracks and cylindrical rollers. As depicted in Figure 6.10, a single-row cylindrical roller bearing consists of an outer and an inner ring and a number of cylindrical rollers for enhancing the load-carrying capacity. The cylindrical rollers are parallel to the bearing axis of rotation and held in position by a bearing cage.

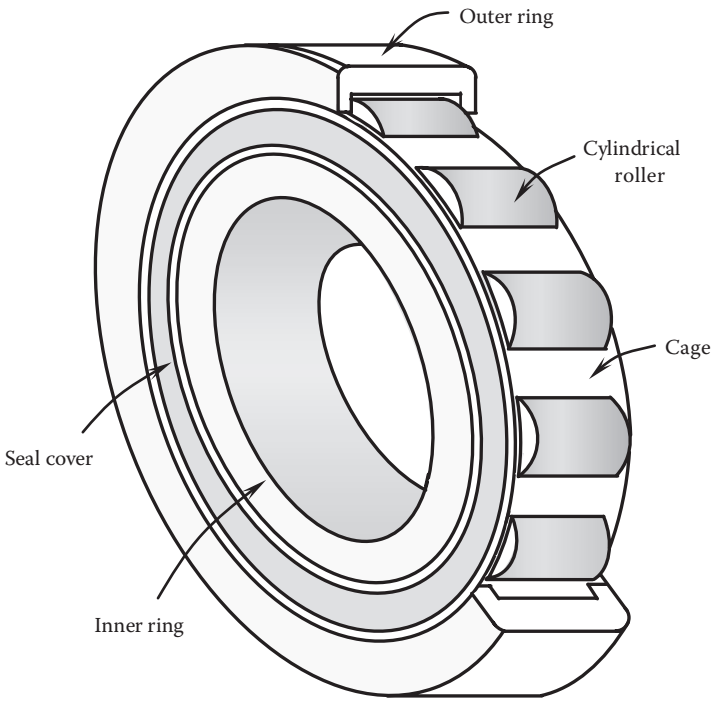

FIGURE 6.10
A single-row cylindrical roller bearing.

Tapered roller bearings have the ability to carry combinations of large thrust and radial loads. As shown in Figure 6.11, a taper angle is formed between the inner and outer ring. Nominal taper angles of 10° and 17° are commonly used in tapered roller bearings.

Thrust bearings are a particular type of rotary bearing, designed to support primarily thrust (axial) loads in a variety of applications (Figure 6.12). There are several thrust bearing types such as ball, crossed roller, cylindrical roller, tapered roller, needle, and spherical roller. Thrust bearings are often used in vertical motors. However, they are typically noisier than ball bearings.

6.1.3 Noncontact Bearing

Noncontact bearings, including air and magnetic bearings, are referred to as floating bearings that maintain a small gap with moving surfaces to completely avoid any kind of solid-to-solid contact under typical operating conditions. Unlike conventional bearings, noncontact bearings prevent problems of friction. Air bearings use a thin film of pressurized air to support a load (Figure 6.13) and offer much higher stiffness than rolling bearings because the air film fully supports the rotating rotor load, as opposed to rolling elements (i.e., balls or rollers) that have point or line contact. As air has a much lower viscosity than liquid, pressurized air bearings have lower load capacity and operate with essentially zero static and dynamic frictions as opposed to the liquid film bearings, which have much higher frictions and pumping losses within the bearings. These features, as well as their high precision capabilities, high damping, and silent operation, make air bearings excellently suitable for high-speed, low-load, and low-noise applications such as

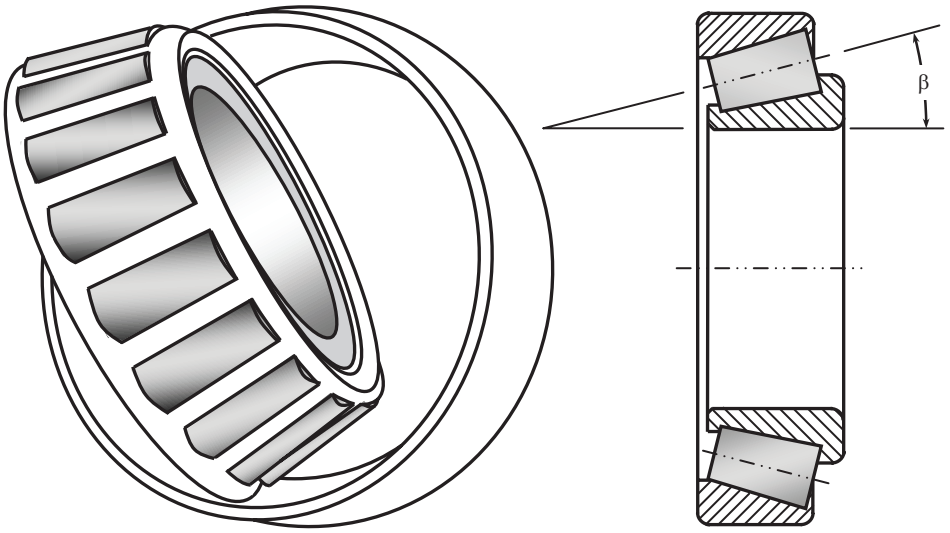

FIGURE 6.11
Tapered roller bearing, which can withstand both radial and axial loads. The cross-sectional view shows the specially designed tapered rollers and demonstrates their angular mounting, which gives their dual load ability.

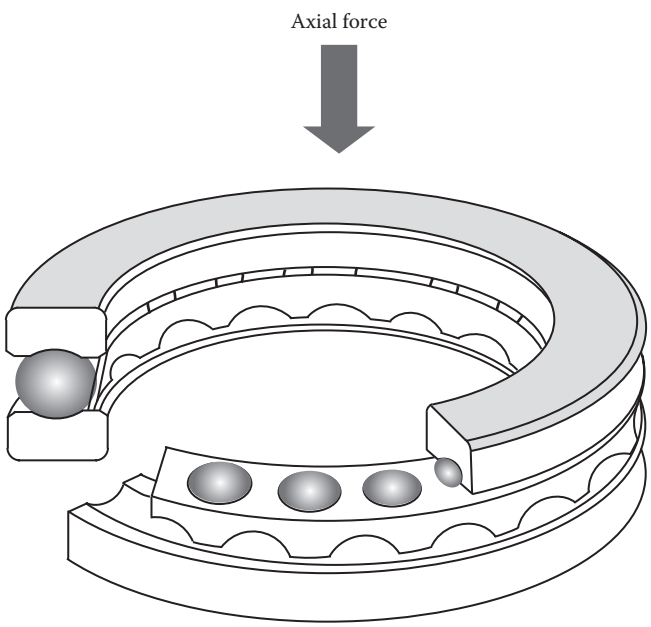

FIGURE 6.12
Thrust ball bearing designed for receiving thrust (axial) loads.

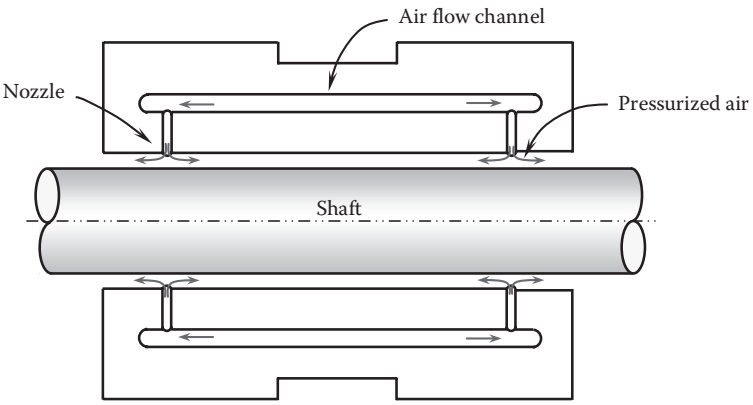

FIGURE 6.13
In air film bearing, load is supported by pressurized air.

dental drills and CMMs [6.8]. However, air bearings require very tight bearing gaps (about 10 μm compared 100 μm for liquid film bearings) and very high manufacturing accuracy. This directly leads to extremely tight tolerances, typically less than ±2.54 μm (±0.0001 in.) for the bearings with air gaps of 12.7 μm (0.0005 in.).

Magnetic bearings can provide superior performance over fluid film bearings and roller-element bearings. They generally have lower drag losses, higher damping properties, and moderate load capacity. The steady-state stiffness of magnetic bearings can be essentially infinite, depending on how the close-loop control system is designed. The dynamic stiffness depends on the frequency of applied load and the bandwidth of the control system [6.9]. Unlike other types of bearings, magnetic bearings do not require lubrication, thus eliminating lubricant, valves, pumps, filters, coolers, and other related components, which are typically responsible for adding system complexity and reducing machine's operating reliability.

Although magnetic bearings can use either attractive or repulsive magnetic forces to elevate the rotating shaft, magnetic bearings are efficient only in the attraction mode. In order to obtain high performance in systems with randomly oriented force components, magnetic bearings should be used in an opposed mode design. Air bearings use air pressure to support the rotating shaft. For this type of bearings, the ratio of δ_r/R is typically 0.0001. Noncontact bearings are often used for extremely high-speed applications such as gyroscopes and dental drills and for precision machinery such as CMM.

6.1.4 Sensor Bearing

In some motor applications, it is required to monitor the operational status of rotor, including rotor position (number of revolutions), rotating speed and direction, as well as acceleration and deceleration. A sensor bearing is made by integrating shielded Hall effect sensors, a magnetic impulse ring, and a versatile ball bearing to form a sensor-bearing unit to detect the required motor operation information and convert it into electrical signals.

As shown in Figure 6.14, while a magnetic impulse ring divided into a sequence of north and south poles is attached to the inner ring of the bearing, small sensors are attached to the outer ring of the bearing. When the bearing inner ring rotates, the impulse ring moves

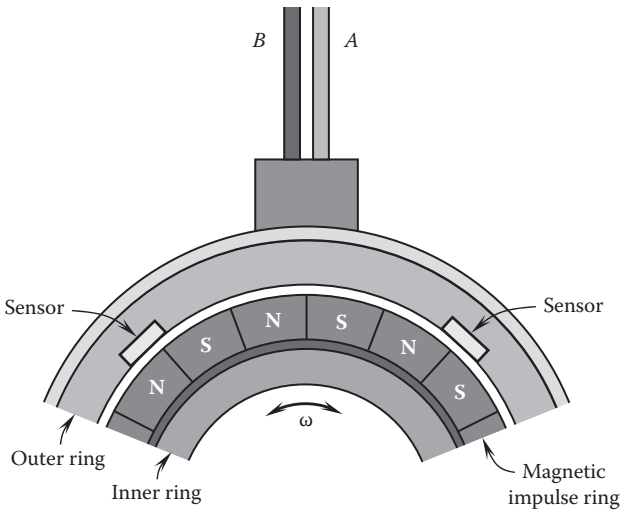

FIGURE 6.14
Operating principle of sensor bearing.

past the stationary sensor ring, generating a magnetic field of alternating polarity. The sensor outputs a pulse whose frequency depends on the number of polarity changes per second. Via the sensor-bearing connection cable, the sensor output signal is transmitted to an electronic unit normally developed by the user. This unit analyzes the signal and provides application-specific information [6.10].

6.2 Bearing Design

Bearing design involves several fundamental elements: selecting correct bearing materials, designing proper bearing lubrication and cooling approach, understanding bearing service environment and operating conditions, and choosing suitable values of bearing design parameter.

6.2.1 Bearing Materials

Bearings materials are classified as through-hardened materials used largely for ball bearings and case-hardened materials used largely for roller bearings. The commonly accepted minimum hardness for steel bearing components is 58 Rockwell, and the hardness for ceramic bearings ranges from 78 to 81 Rockwell [6.11]. For normal applications, Society of Automobile Engineers (SAE) 52100 (100Cr6 in Germany and GCR15 in China) is an excellent general purpose bearing steel, which has a carbon content of 0.95%–1.1% and a chromium content of 1.3%–1.6% [6.12]. This steel grade is generally suitable for applications in which high-strain strength and high resistance to wear under high alternate loads are required. Therefore, the steel is manufactured by induction vacuum melting process for minimizing porosity that might be caused by gas released from smelting process.

High-temperature and high-load applications often use hybrid bearings with rings made of SAE 52100 and balls made of ceramic (e.g., silicon nitride Si_3N_4). Under corrosive environment conditions, stainless steel AISI 440C (SUS440C in Japan and 9Cr18 in China) hardened to 58 Rockwell and above is used as the standard rolling bearing material. Due to the lower hardness, the bearings made from this material have a load-carrying capacity 20% lower than those made from SAE 52100.

Nickel–chrome alloys are often used for making bearings. The addition of elements nickel and chrome can increase the hardenability of steel. In addition, chromium brings high temperature strength and resistance to corrosion, oxidation, and abrasion. As a nickel–chrome alloy, SAE 8620 contains about 0.2% of carbon, 0.5% of chrome, and 0.55% of nickel.

Another alternative material is high-nitrogen steel (HNS), which is a new type of alloy with up to 0.9% nitrogen. This material has a good size stability, high strength, and enhanced resistance to pitting corrosion.

Because cylindrical roller bearings can take much higher loads than ball bearings, these bearings are widely used in large motors with heavy loads. In addition, the cylindrical roller bearing allows for floating of the inner race relative to the outer race. In some motor applications, the external load acting on a motor is far from uniform, that is, the motor drive end takes much higher load than the nondrive end. Thus, for such an application, it is common to use a cylindrical roller bearing on the drive end and a deep-groove ball bearing on the nondrive end.

For some special applications, spherical roller bearings may also be used for heavy radial load application. This type of bearing has a good bearing misalignment capability and can carry even more radial loads. However, the performance of sphere bearings is very sensitive to their lubrication conditions, requiring three to five times relubrication than similarly sized cylindrical roller bearings. Statistic results have shown that lubrication failures with these types of bearings are common. Consequently, these bearings are rarely found in motors today [6.13].

6.2.2 Bearing Internal Clearances

Bearing clearance is defined as the total free distance that one bearing ring can be shifted relative to the other either in the radial direction, which is defined as the internal radial clearance δ_r, or in the axial direction, which is defined as the internal axial clearance δ_a, as demonstrated in Figure 6.15. Both internal radial and axial clearances are important parameters that significantly affect bearing operating characteristics such as vibration, noise, lubrication, heat generation, friction, wear, and bearing fatigue life. If the radial clearance of a bearing is too large, it may lead to bearing vibration and inaccurate motion. If the radial clearance is too small, the lubrication film may break down, leading to metal-to-metal contact between rolling balls and raceways.

The axial internal clearance is established by ball diameter, inner and outer raceway radius, and the radial internal clearance. Depending on the bearing geometry, the axial clearance is 8.5–10 times larger than the radial clearance [6.14].

Bearing clearance is categorized as unmounted and mounted (effective) clearance. Unmounted clearance is referred to as the initial bearing clearance, which is provided by bearing manufacturers. As a reference value, the initial bearing clearance is chosen during the motor design and bearing selection process. Mounted clearance is referred to as the operational clearance as the bearing is fitted onto the shaft and into the housing bore and

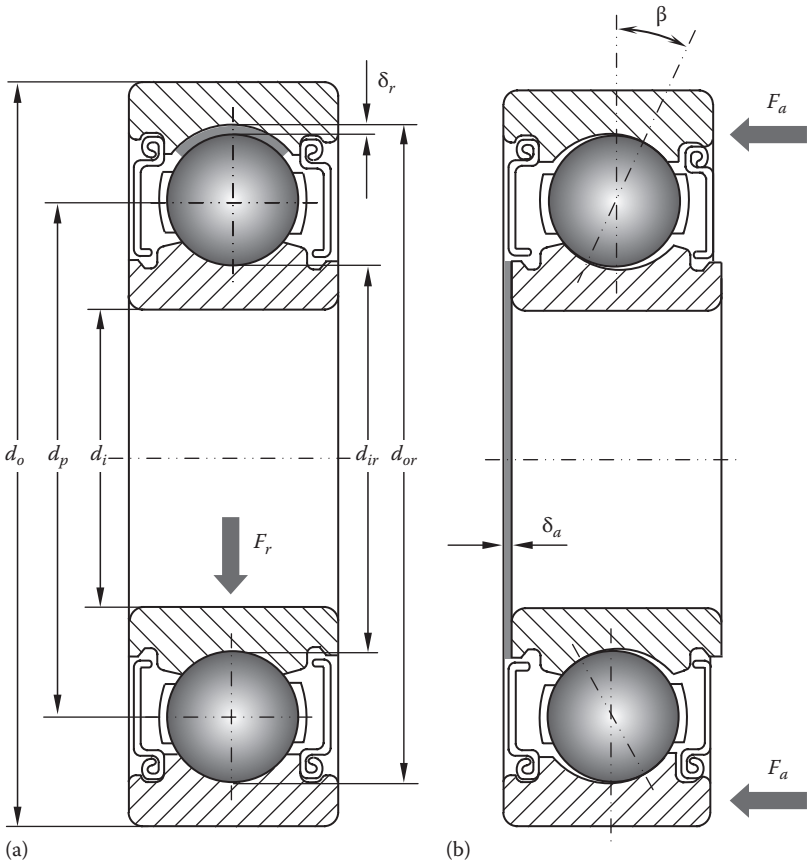

FIGURE 6.15
Bearing clearance: (a) when a bearing is subject to a radial load F_r, a radial clearance δ_r is formed between the inner and outer ring; (b) when a bearing is subject to axial load F_a, the axial clearance δ_a and contact angle β are formed, but the radial clearance disappears.

when the bearing reaches steady-state operating temperature. In practical applications, mounted clearance is difficult to measure in real time. Usually, the operational clearance is smaller than the bearing initial clearance due to several factors including bearing fit and the temperature difference between the inner and outer rings.

Because cooling the stator in a motor is typically easier than the rotor, the outer ring is often cooler than the inner ring by about 5°C–10°C. For water-cooled stator cases, the temperature difference between the two rings can even be greater to significantly reduce the bearing radial clearance. In some cases, the radial clearance can reach zero or even negative values. When the interference between the rolling elements and rings become quite large, it may damage bearing elements, accelerate bearing wear, or even lead to bearing failure. For each size of bearing, there is an optimum range of radial clearance depending on bearing applications.

The internal radial clearance δ_r is determined by the outer and inner ring diameters and ball diameter:

$$\delta_r = d_{or} - d_{ir} - 2d_b \tag{6.10}$$

where d_{or} and d_{ir} are the outer and inner ring diameter, respectively. From Equation 6.6, the internal radial clearance δ_r can be also expressed as

$$\delta_r = 2e(1-\cos\beta) \tag{6.11}$$

The interference fits of an inner ring to a shaft and an outer ring to a bearing bore can reduce the bearing radial clearance. As described by Harris [6.15], the increase in the inner ring diameter Δd_{ir} due to the interference fit between a bearing inner ring and a hollow shaft (with the ID of d_2) is given as

$$\Delta d_{ir} = \frac{2\delta d_{ir}/d_i}{[(d_{ir}/d_i)^2-1]\left\{\frac{(d_{ir}/d_i)^2+1}{(d_{ir}/d_i)^2-1}+\nu_b+\frac{E_b}{E_s}\left[\frac{(d_i/d_2)^2+1}{(d_i/d_2)^2-1}\right]-\nu_s\right\}} \tag{6.12}$$

where
- δ is the interference between the inner ring and the hollow shaft
- v_b and v_s are Poisson's ratio
- E_b and E_s are modulus of elasticity of the bearing and shaft, respectively

If both the bearing and shaft are made of the same material, v_b and E_b should be equal to v_s and E_s, respectively. The above equation can be simplified as

$$\Delta d_{ir} = \delta\frac{d_{ir}}{d_i}\left[\frac{(d_i/d_2)^2-1}{(d_{ir}/d_2)^2-1}\right] \tag{6.13}$$

Furthermore, for a solid shaft, $d_2=0$. By means of L'Hôpital's rule, it can be derived that

$$\lim_{d_2\to 0}\left[\frac{(d_i/d_2)^2-1}{(d_{ir}/d_2)^2-1}\right]=1 \tag{6.14}$$

Thus,

$$\Delta d_{ir} = \delta\frac{d_{ir}}{d_i} \tag{6.15}$$

Similarly, the decrease in the outer ring diameter $-\Delta d_{or}$ due to the interference fit between a bearing outer ring and a bearing bore (with the diameter of d_1) on the endbell or housing is given as

$$\Delta d_{or} = \frac{2\delta d_o/d_{or}}{\left[(d_o/d_{or})^2-1\right]\left\{\frac{(d_o/d_{or})^2+1}{(d_o/d_{or})^2-1}-\nu_b+\frac{E_b}{E_h}\left[\frac{(d_1/d_o)^2+1}{(d_1/d_o)^2-1}\right]+\nu_h\right\}} \tag{6.16}$$

where v_h and E_h are Poisson's ratio and modulus of elasticity of the bearing bore, respectively.

If both the bearing outer ring and the bearing bore are made of the same material, $v_b=v_h$ and $E_b=E_h$. The above equation can be simplified as

$$\Delta d_{or} = \delta \frac{d_o}{d_{or}} \left[\frac{(d_1/d_o)^2 - 1}{(d_1/d_{or})^2 - 1} \right] \tag{6.17}$$

Taking into account the influence of interference fits, the bearing internal radial clearance becomes

$$\delta_r = (d_{or} - \Delta d_{or}) - (d_{ir} + \Delta d_{ir}) - 2d_b \tag{6.18}$$

When selecting motor bearings, thermal expansion must be taken into consideration because it can significantly change the internal clearances. A temperature differential between the shaft and the motor endbell/housing always leads to a change in the internal clearances. Ricci [6.6] has investigated the influence of the radial temperature gradient between the inner and outer rings on the internal radial clearance. Assuming the temperature rises in the outer and inner rings over the ambient temperature are $(T_o - T_a)$ and $(T_i - T_a)$, respectively, the increases in d_{or} and d_{ir} are Δd_{or} and Δd_{ir}, respectively

$$\Delta d_{or} = \beta_{or} d_{or} (T_o - T_a) \tag{6.19a}$$

$$\Delta d_{ir} = \beta_{ir} d_{ir} (T_i - T_a) \tag{6.19b}$$

where β_{or} and β_{ir} are the coefficient of thermal expansion of outer and inner rings, respectively. Generally, $\beta_{or} = \beta_{ir} = \beta$.

Assuming the ball temperature takes the mean value of the outer and inner rings, the increase in the ball dimension is

$$\Delta d_b = \beta_b d_b \left(\frac{T_o + T_i}{2} - T_a \right) \tag{6.20}$$

Thus, the change in the bearing internal radial clearance due to the thermal expansion is

$$\Delta d_r = \beta d_{or} (T_o - T_a) - \beta d_{ir} (T_i - T_a) - \beta_b d_b \left(\frac{T_o + T_i}{2} - T_a \right) \tag{6.21}$$

The internal clearance is grouped into different classes, that is, *C*2, *C*3, *C*4, and *C*5, for which the lower number indicates the lower clearance. Some bearing manufacturers designate *CN* as the normal clearance which is between *C*2 and *C*3.

The clearance *C*3 is the most popular clearance used in most motor applications because it permits a sufficiently large tilting clearance even at high speeds. A bearing with a risk of increased thermal stressing for any reasons needs to select the clearance of *C*4.

It is noted from Figure 6.15 that when a ball bearing is subject to an axial load, the inner and outer rings are dislocated axially, resulting in an axial clearance δ_a. Correspondingly, the contact line is no longer perpendicular to the axis of bearing rotation; instead, the contact angle β is formed between the bearing contact line and the bearing normal line. Under this circumstance, the radial clearance δ_r no longer exists. Generally, internal axial clearance δ_a can be established by internal radial diameter δ_r, ball diameter d_b, and outer and inner ring radius r_o and r_i, respectively

$$\delta_a = 2\sqrt{\delta_r (r_o + r_i - d_b)} \tag{6.22}$$

6.2.3 Allowable Bearing Speed

High bearing speed often leads to temperature rise in the bearing due to the friction heating effect. When the temperature becomes high enough, it may cause the decomposition and degradation of the lubricant, thereby deteriorating bearing performance. Therefore, it is a common practice for most bearing manufacturers to set a maximum bearing rotating speed to avoid such detrimental situations. The allowable speed of a bearing varies with the bearing type, size, material, lubrication method, manufacturing precision, sealing type, loading condition, noise level, operation configuration, both bearing and cage structures, cooling condition around the bearing, etc. As the bearing speed exceeds 70% of its allowable speed, high-speed lubricants (grease or oil) of high quality must be applied to the bearing. Generally, ball bearings have higher allowable speed than roller bearings due to their lower friction.

As radial bearings are used in a vertically mounted motor, lubricant retention and cage guidance are not favorable compared to horizontal motor mounting. Thus, the allowable speed should be reduced to approximately 80% of the listed speed [6.16].

6.2.4 Bearing Fitness

For the majority of bearings used in electric motors, the rotating inner rings of bearings are fitted tightly with the rotor shafts via the interference fitting method for ensuring reliable torque transmissions. Meanwhile, the stationary outer rings are fitted less tightly (usually slip fitting) with the stationary bearing bores at the motor frame. This ensures that at least one bearing in the motor is able to slide when the shaft expands or shrinks due to the change in operation temperature. Also, it facilitates the motor assembling and disassembling processes.

It is recommended by bearing manufacturers [6.17] that tight interference fits be used when (1) the operating conditions involve large vibration or shock loads, (2) hollow shafts or housings with thin walls are used, and (3) housings made of light alloys or plastic are used. Similarly, loose interference fits are preferable for (1) requiring high running accuracy and (2) using small-sized bearings or thin-walled bearings.

The fit selection for bearings with shafts and housings is graphically presented in Figure 6.16. The bars designated by lower case letters and numbers (e.g., g6, h6) represent shaft diameter and tolerance ranges to achieve various fitness conditions (i.e., loosen and interference fits) required for various load and bearing rotation conditions. Similarly, the bars designated by upper case letters and numbers (e.g., F7, G7) represent housing bore diameter and tolerance ranges. The recommendations for bearing fits are usually provided by bearing manufacturers in their catalogs for different operating conditions and a variety of bearing types and sizes.

The selection of proper bearing fits is crucial for some motor applications. The selection depends on both bearing and motor operating conditions (such as rotating speed, operation temperatures, load conditions), shaft and housing materials, manufacturing accuracy of mating surfaces, among other factors. Too tight bearing fits can cause excessive stress, reduced radial clearance, and elastic deformation of rolling elements and raceways that may adversely influence the bearing performance. In a worse case, the bearing radial clearance may vanish, turning a loose interference into a tight interference. For such circumstances, the rolling elements may be excessively loaded, leading to rapid wear and temperature rise. On the other hand, too loose bearing fits can cause relative motion between mating parts, resulting in fretting corrosion on the matting surfaces.

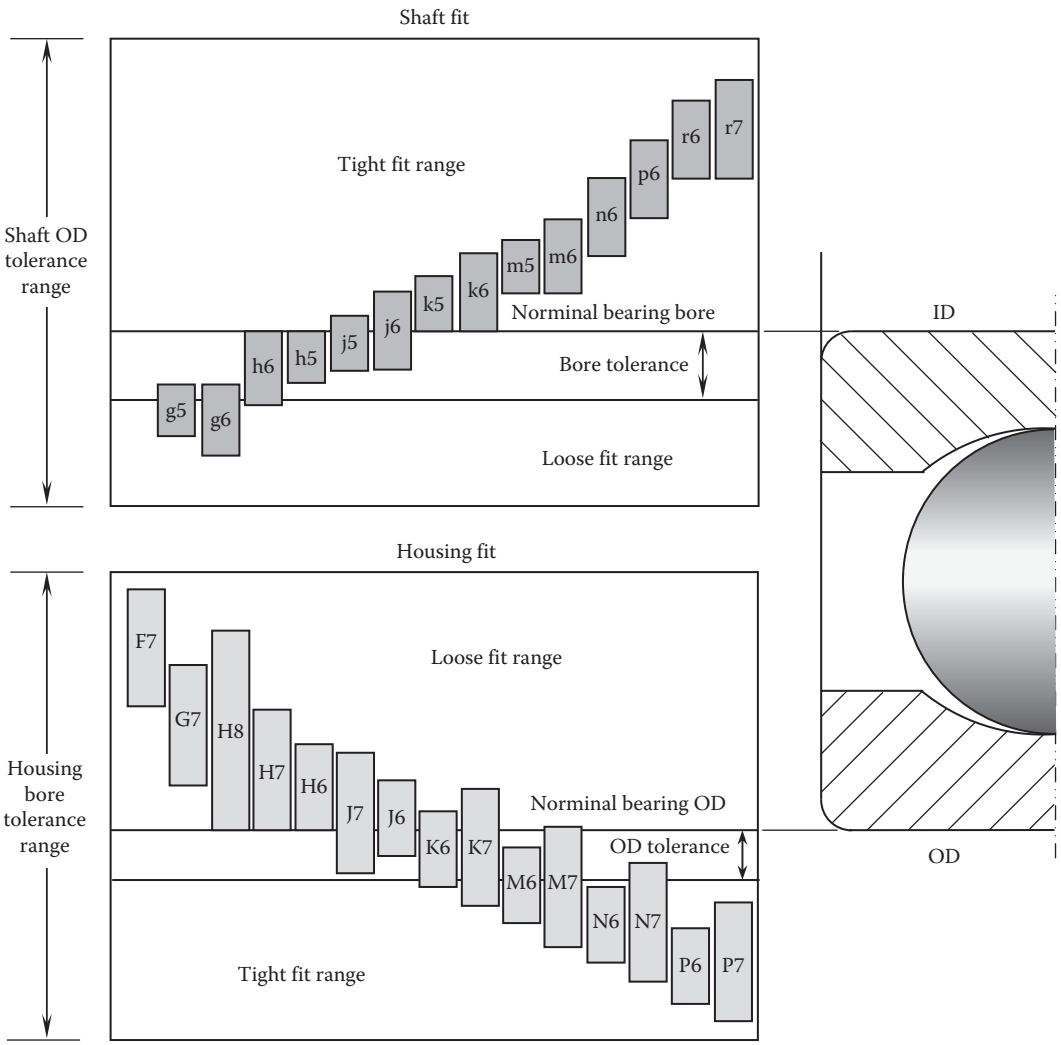

FIGURE 6.16
Fit section for bearings with shafts (top) and housings (bottom).

6.2.5 Prevention of Bearing Axial Movement

In normal motor operation, bearings must be held in their positions firmly. The axial movement of bearing may alter the load distribution on the bearings and thus possibly overload one of them, leading to the damage of the bearing, wave spring washer, endbells, or windings.

A motor shaft is generally supported at its ends by suitable bearings contained in motor endbells or motor frame. Typically, the inner ring of the bearing is pressed onto the shaft, and the outer ring is pressured into a bearing seat defined within an endbell/housing. A number of mechanical methods have been employed to prevent bearing axial movement. The most common way is to use shaft shoulders and retaining rings, which are inserted in machined grooves on the motor shaft to position the bearings precisely.

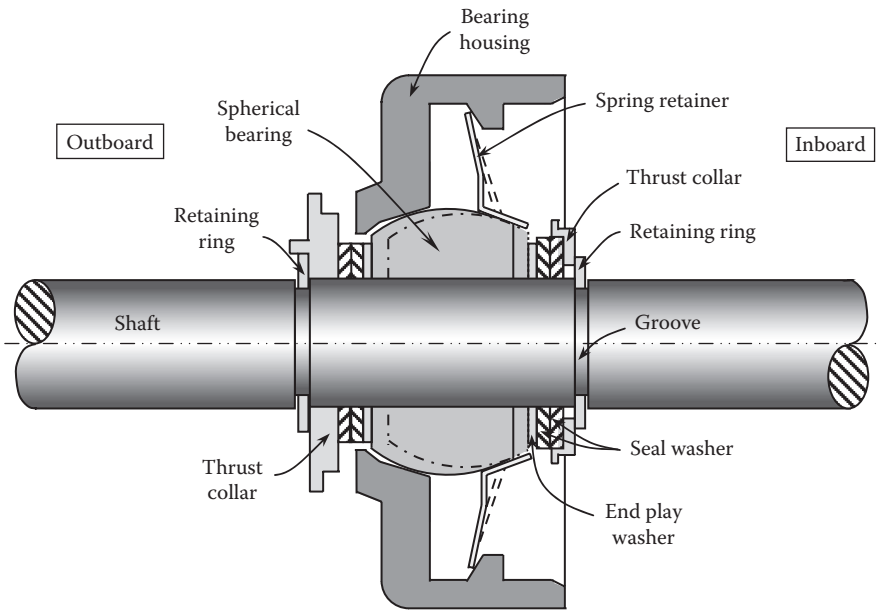

FIGURE 6.17
Using a simplified end play control system for preventing excessive axial movement of shaft and bearing.

In addition, proper fits of the bearing inner ring on the shaft and the outer ring in the bearing bore of the endbell/housing also help hold the bearings in their positions against axial movement.

Bischoff [6.18] proposed a method that uses a simplified end play control system to prevent excessive axial movement of the motor shaft in response to forces applied to the shaft. Figure 6.17 shows an endbell hub assembly, which consists of a rotor shaft, a self-aligning bearing carried on the shaft, and a bearing support structure surrounding the shaft and journaling the self-aligning bearing member. A resilient retainer biases the self-aligning bearing into engagement with its journal. The end play control system includes a thrust collar, a retaining ring, and washers at the outboard (left) and inboard (right) side, respectively. While the thrust collar and retaining ring at the outboard side are for preventing inward movement (i.e., movement to the right), the thrust collar and retaining ring at the inboard side are for preventing outward movement (i.e., movement to the left) of the shaft. It is desirable to insert a seal washer and a pair of washers between the thrust collar and the bearing to position the bearing properly. The seal washer also serves to dampen axial vibration that may occur during motor operation.

An alternative approach was proposed by Grund [6.19], as presented in Figure 6.18. This method uses a bearing holder to fix a bearing to a support structure such as a motor endbell or housing. As can be seen in the figure, the single platelike bearing holder is made from a single metal plate. A plurality of butt straps as a holding structure is formed on the side of the panel opposite to the bottom hooks. The butt straps are arranged to retain the bearing within the bearing holder and ideally to press the bearing axially against the bottom hooks.

Once the bearing has been inserted into the bearing holder with the bearing seated in contact with the bottom hooks, the butt straps are radially deformed to move the fingers radially inwardly so as to axially cover the bearing preventing its removal from the

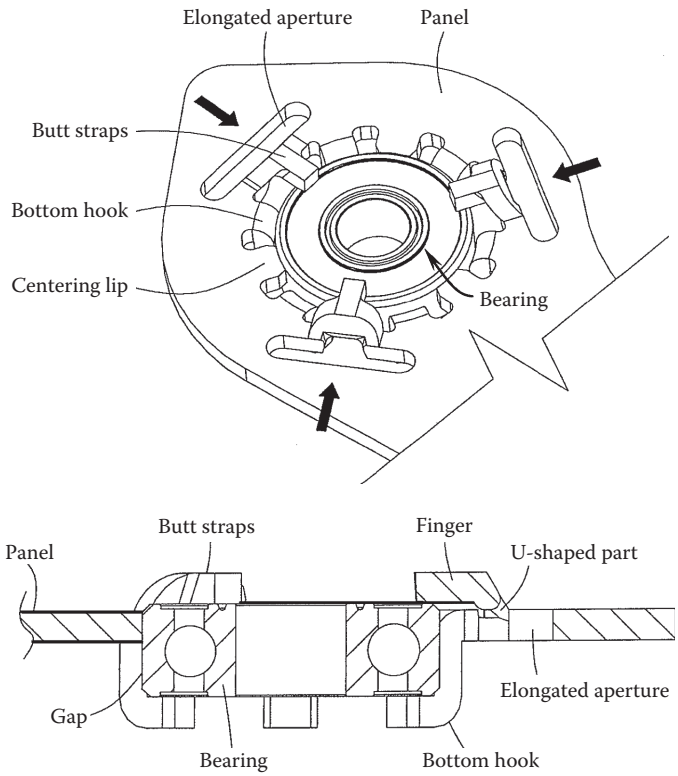

FIGURE 6.18
Bearing holder for fixing a bearing to a support structure using a single platelike body (U.S. Patent Application 2013/0169092) [6.19]. (Courtesy of the U.S. Patent and Trademark Office, Alexandria, VA.)

bearing holder. Centering lips extending inwardly from the hole edge may be provided to fix the lateral position of the bearing.

6.2.6 Bearing Load

Bearing load and speed are the most critical factors in bearing selection and bearing design. To ensure normal operation, both bearing loads and speeds must be within their limits.

6.2.6.1 Bearing Preload Arrangement

Wave spring washers are normally used to provide a preload on the outer ring of one of the bearings for compensating dimensional variations, absorbing impulse forces, and lowing motor operating vibration and noise (Figure 6.19). Many design variations have evolved to best serve these basic functions. The deflection rate for wave spring washers usually range from 20% to 80%, depending on the spring type, structure, material, and number of spring waves and turns (Figure 6.20).

The radial preload is often from an interference fit, usually between the motor shaft and the bearing inner ring and between the bearing bore and the outer ring. In some cases, improper fit can cause relative movements between the mating parts, leading to severe wear on either shaft or bearing born and reduced bearing life.

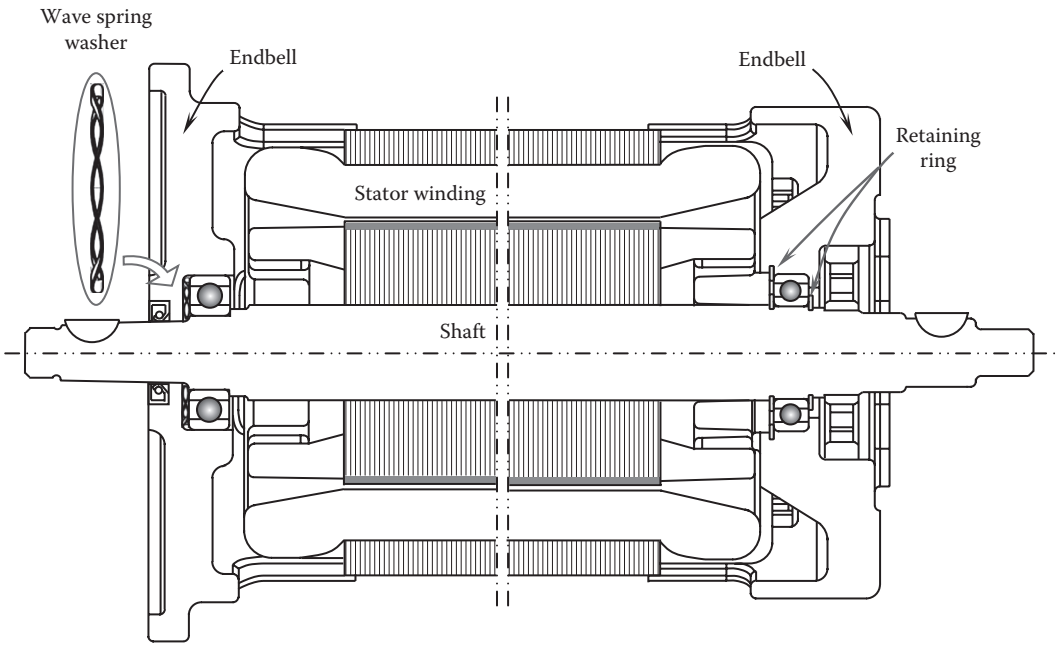

FIGURE 6.19
Using wave spring washer and retaining rings for providing preload to the shaft and positioning bearings axially.

6.2.6.2 Radial and Axial Bearing Load

Even though most radial rolling bearings used in electric motors are designed to take primarily radial load, they can also withstand smaller axial load, as a certain portion of their rated radial load.

The most important parameters of bearing loads are the load magnitudes and their directions. The external load, which comes from the interaction of the rotor and stator, acts firstly on the inner ring and is subsequently transferred to the outer ring through the rolling elements and finally to the bearing bore on the motor endbell or housing.

6.2.6.3 Load Distribution

When a rolling bearing is subject to radial load, the rolling elements are not equally loaded. Usually, at any given time, only less than half of the rolling elements are loaded. The actual load on each rolling element depends on its position in the bearing and other bearing characteristics such as motor internal clearance. Stribeck [6.20] conducted pioneering work on investigating the variation of loads on rolling elements of a radially loaded ball bearing. He found that the load zone for a radially loaded bearing with an internal clearance is less than $\pi/2$, and the load on the most heavily loaded ball is 4.37 times the average ball load for zero internal clearance. Later, Palmgren [6.21] determined that the theoretical value of Stribeck's constant for roller bearings at zero internal clearance is 4.08.

Oswald et al. [6.22] investigated the effect of motor internal clearance on the load distribution and the life of radially loaded ball and roller bearings. Their analysis was extended

FIGURE 6.20
Various types of wave spring washers.

to negative clearance (interference) conditions for producing a curve of life factor versus internal clearance. It was found that for a small negative clearance, rolling-element loads can be optimized and bearing life maximized. To compare with the results from previous investigators, the concept of Stribeck number is introduced as

$$St = \frac{P_{\max}}{P_r / z} \tag{6.23}$$

where
$P_{\max}$ is the maximum element load
P_r is the applied radial load
z is the number of rolling elements

Their analysis confirmed that $St = 4.37$ for ball bearings at zero internal clearance and $St = 4.08$ for roller bearings at zero clearance.

The load distribution of a rolling bearing is primarily determined by the load factor ε, the load angle, and the bearing internal clearance.

$$F(\phi) = F_{\max}\left[1 - \frac{1}{2\varepsilon}(1 - \cos\phi)\right]^n \tag{6.24}$$

where
$F_{\max}$ is the maximum load
ε is the load distribution factor
ϕ is the angle from the bearing lower center line (as shown in Figure 6.21)
$n = 10/9$ for ball bearings and $n = 3/2$ for roller bearings

For a bearing with a normal radial clearance, the maximum load $F_{\max}$ can be determined approximately as

$$F_{\max} = \frac{5F_r}{Z\cos\alpha} \tag{6.25}$$

where
F_r is the applied radial load
Z is the number of rolling element
α is the mounted contact angle

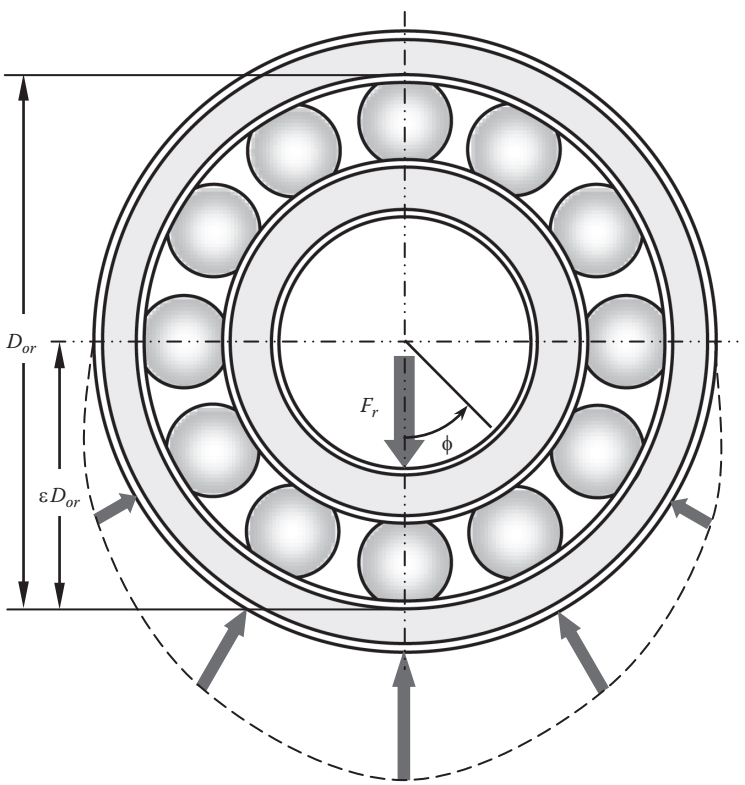

FIGURE 6.21
Load distribution of rolling bearing, $\varepsilon = 0.5$ in this case.

6.3 Bearing Fatigue Life

Each bearing has a limited life of service. The factors that determine bearing fatigue life include (1) bearing rotating speed, (2) external radial and axial loads, (3) bearing radial and axial clearances, (4) lubrication condition (e.g., formation of lubricant film, contamination), (5) lubricant type, (6) operation condition (e.g., temperature, corrosive environment, machine vibration), (7) bearing type and size, (8) bearing material, (9) fitting condition, (10) manufacturing process, (11) bearing installation condition, and (12) motor shaft misalignment. All of these factors must be taken into account in the bearing section and application.

Bearing operating temperature has a strong impact on bearing life by affecting bearing radial and axial clearances, viscosity of lubricant, rate of lubricant volatilization, and bearing sealing performance. Motor vibration and shock loading can not only bring additional loading to motor bearings to deteriorate bearing operation but also alter bearing lubrication condition and thus are detrimental to bearing life.

6.3.1 Calculation of Bearing Fatigue Life

Bearing life is defined as the length of time, or the number of revolutions, until a fatigue spall of a specific size develops. This spall size is usually defined as an area of 0.01 in^2 (6.5 mm^2). This life depends on many factors as mentioned above. Due to all these factors, the life of an individual bearing is impossible to predict precisely. Also, bearings that may appear to be identical can exhibit considerable life scatter when tested under the same conditions.

Basic bearing rating fatigue life or L_{10} is defined as the life that 90% of a sufficiently large group of apparently identical bearings is expected to reach or exceed. By contrast, bearing average life is the life that 50% of the bearings exceed.

Either in theory or in fact, with sound and robust design, correct bearing material selection, accurate manufacture, proper lubrication, and diligent maintenance, bearing life can be extremely long. A calculation was made by Orlowski [6.23] for a medium-duty ball bearing with a dynamic load ration of 7000 lb at an operating speed of 1800 rpm; the bearing life can be as high as 362 years!

Though there are several bearing fatigue life calculation methods available, the formula that is widely used by bearing manufacturers is given as

$$L_{10} = a\left(\frac{C}{P}\right)^b \frac{B}{N} \tag{6.26}$$

where

C is the radial-rated bearing load rating
P is the dynamic equivalent radial load applied on the bearing
B is the factor that depends on the method and units used in the equation
N is the bearing rotating speed
a is the life adjustment factor
$b = 3$ for ball bearings and $b = 10/3$ for roller bearings

In 2007, ISO [6.24] specifies methods of calculating the basic bearing rating life L_{10} of rolling bearings in its standard ISO 281: 2007, with commonly used high-quality material, good

manufacturing quality, and conventional operating conditions. By introducing a correction factor a_{ISO}, which provides an estimation of the influence of lubrication and contamination on the bearing life, the adjusted rating life (in one million revolutions) for a different level of reliability is given as

$$L_{n,a} = a_1 a_{ISO} L_{10} \tag{6.27}$$

where a_1 is the life adjustment factor for reliability. The value of a_1 is entirely determined by L_n, where the subscript n represents the failure probability, that is, the difference between 100% and the requisite reliability. For instance, $a_1 = 1$ for L_{10} (i.e., 90% reliability) and $a_1 = 0.21$ for L_1 (i.e., 99% reliability). The introduction of a_{ISO} is based on the assumption that the fatigue load is directly linked with the bearing's static capacity and the contamination factor is constant whatever the lubrication conditions.

Another popular bearing life formula was also released by ISO in 1978, which is still used today in industrial applications. This model uses three adjustment factors for taking into account reliability, bearing properties, and operating conditions, respectively [6.25]:

$$L_{n,a} = a_1 a_2 a_3 L_{10} \tag{6.28}$$

where a_1 is the adjustment factor for reliability as in Equation 6.27. a_2 is the adjustment factor for bearing special properties such as material processing, forming method, heat treatment, and other manufacturing methods. For standard bearing material and manufacturing method, $a_2 = 1$. As special steel or advanced manufacturing method (e.g., vacuum degassed or vacuum melt) is adopted for improving bearing quality, $a_2 > 1$. a_3 is the adjustment factor for operating condition, which takes into account a wide range of operating, mounting, and application conditions, as well as bearing features and design. For instance, it adjusts the impact of lubrication, contamination, mounting conditions, misalignment, etc., on fatigue life. Under ideal lubrication where the rolling elements and raceways are completely isolated by lubricant films and normal operation conditions, $a_3 = 1$. For poor lubrication cases, such as incomplete lubrication or low lubricant viscosity, and unusual loading or mounting conditions, $a_3 < 1$. Under especially excellent lubrication condition with very smooth operation, a_3 becomes larger than 1. Logically, for a poor operating case where $a_3 < 1$, the life adjustment factor for bearing special properties a_2 cannot exceed unity.

In addition to these standards, some major bearing manufacturers such as Timken and SKF have developed their own bearing life models to best predict bearing life of their products. For example, SKF has introduced the SKF life modification factor a_{SKF} to adjust the bearing rated life for each type of bearings (e.g., ball bearings, roller bearings, thrust ball bearings, and thrust roller bearings).

In recent years, with the advances in manufacturing, tribology, materials, bearing operation monitoring, and computational technology, the bearing life calculations continue to evolve and become increasingly accurate over time, reflecting the collective experience of the bearing industry.

6.3.2 Bearing Failure Probability Distribution

Bearing reliability is the probability of bearing performing without failure over a certain period of time under the operation conditions encountered. Reliability is intimately linked

with failure, failure rates, and component and system mortality. Depending on the type of application machines, there are various models available for dealing with bearing failure probability distributions. These models can be briefly categorized as age-related failure models (e.g., bathtub-shaped distribution, normal distribution, monotone distribution) and random failure models (e.g., exponential distribution).

The Weibull probability distribution is one of the most widely used lifetime distributions in industries for modeling failure data. The main advantages of the Weibull distribution include the following: (1) it is used extensively in many different disciplines due to its ability to fit a variety of data and to represent a variety of distributions; (2) it can easily handle suspensions (nonfailure points); and (3) it can provide simple graphical solutions. The cumulative distribution function (CDF) of the Weibull distribution $F(t, k, \lambda)$ is

$$F(t,k,\lambda)=\begin{cases}1-e^{-(t/\lambda)^k} & t\geq 0\\ 0 & t<0\end{cases} \tag{6.29}$$

where
- t is the bearing service time
- λ ($\lambda>0$) is the scale parameter
- k ($k>0$) is the shape parameter

By differentiating $F(t, k, \lambda)$ with respect to t, the probability density function (PDF) $f(t, k, \lambda)$ is obtained as

$$f(t,k,\lambda)=\begin{cases}k\left(\dfrac{t^{k-1}}{\lambda^k}\right)e^{-(t/\lambda)^k} & t\geq 0\\ 0 & t<0\end{cases} \tag{6.30}$$

The Weibull probability distribution is a versatile distribution that becomes either the normal or exponential probability distribution, based on the value of the shape parameter k. Figure 6.22 illustrates the variations of the PDF versus time t. When $k=2$ and 3.5, the PDF $f(t, k, \lambda)$ becomes the log-normal and normal distributions, respectively. By setting the shape parameter k to 1, Equation 6.29 becomes the exponential probability distribution, which has a constant failure rate

$$F(t,\lambda)=\begin{cases}1-e^{-(t/\lambda)} & t\geq 0\\ 0 & t<0\end{cases} \tag{6.31}$$

It can be observed in Figure 6.22 that the PDF curves exhibit obviously different behaviors for the $0<k\leq 1$ and $k>1$ cases. At $t=0$, $f(t, 0<k\leq 1, \lambda)$ approaches infinity and $f(t, k>1, \lambda)=0$. The increase in t results in the decrease of $f(t, 0<k\leq 1, \lambda)$ but the increase of $f(t, k>1, \lambda)$ until it reaches the peak value. At the peak point, any increase of t causes a

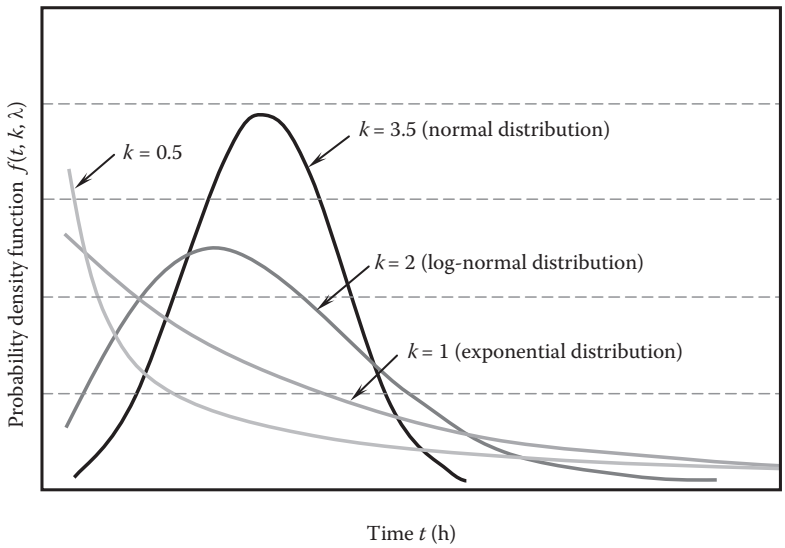

FIGURE 6.22
Weibull probability distributions with different values of the shape parameter k.

sharp decrease of $f(t, k>1, \lambda)$. As the time t becomes very large, both $f(t, 0<k\leq 1, \lambda)$ and $f(t, k>1, \lambda)$ approach zero.

Many studies suggested that bearing failures due to absent lubrication or other negligence generally conform to a Weibull exponential distribution. As an extension of Weibull distribution, this model has wide applications in many disciplines, such as bearing fatigue and windshield break. As addressed by Brake [6.26], the exponential distribution is an excellent model for describing bearing fatigue failures. Based on this model, the bearing failure rate is constant. It indicates that the bearing failure occurs randomly, regardless of the age of bearings. According to Nowlan and Heap [6.27] and Moubray [6.28], among all failure patterns, random failure patterns account for 89%. The detailed information can be found in Table 6.2.

As a real example, the bearing failure probability distribution versus the bearing operating time is presented in Figure 6.23, based on the real statistical data from a bearing manufacturer [6.29]. At the beginning of the bearing service, the bearing failure probability is rather low. Continuous bearing service results in the increase of bearing failure probability until it reaches the peak. Then, the failure probability decreases exponentially and asymptotically approaches a constant over a long time.

6.3.3 Influence of Unbalance on Bearing Fatigue Life

Excessive vibration in rotating machinery such as motors can cause unacceptable levels of noise and, more importantly, substantially reduce the life of shaft bearings. Vibration essentially results from residual imbalance, which is caused by an effective displacement of the mass center line from the true axis in a unit. Hence, it is desired to remove all inherent causes of vibration. Where vibrations are reduced, the size, mass, and/or complexity of the mounting structures can often be reliably reduced.

TABLE 6.2

Failure Patterns of the Conditional Probability

Type	Failure Patterns	Share (%)	Note
Age-related failure (11%)	A	4	The bathtub curve consists of an infant mortality region, a constant or gradually increasing failure probability region, and a pronounced wear-out region. An age limit may be desirable.
	B	2	Constant or gradually increasing probability, followed by a pronounced wear-out region. An age limit may be desirable.
	C	5	Gradually increasing failure probability, but with no identifiable wear-out age. It is usually not desirable to impose an age limit in such cases.
Random failure (89%)	D	7	Low failure probability when the item is new or just out of the shop, followed by a quick increase to a constant level.
	E	14	Constant probability of failure at all ages (exponential distribution).
	F	68	Infant mortality, followed by a constant or very slowly increasing failure probability (particularly applicable to electronic equipment).

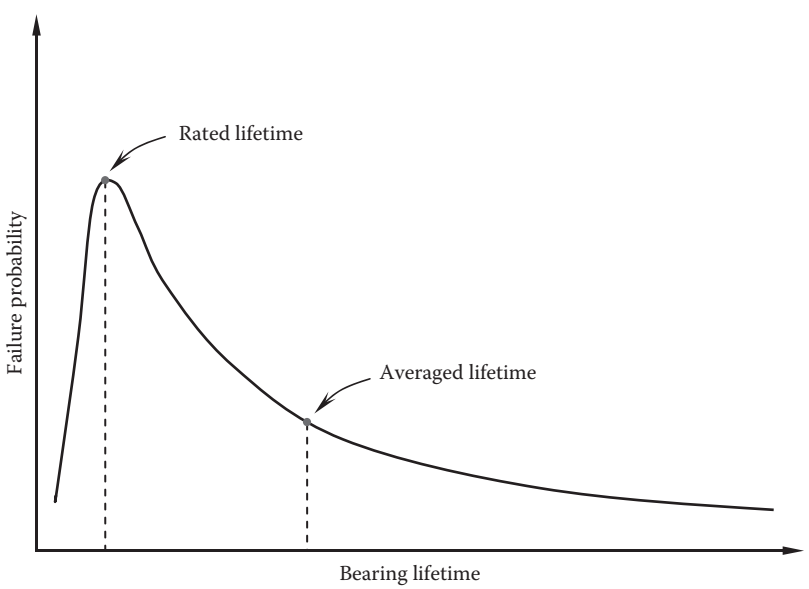

FIGURE 6.23
The bearing lifetime of motor as a function of bearing failure probability, suggested by NSK [6.29].

Mass unbalance in a motor commonly causes vibration of rotor-bearing systems. Usually, unbalance is caused by an asymmetry in the rotor that results in an offset between the shaft center line and the center of mass. Asymmetry can be attributed to an off-center weight distribution, or a thermal mechanism that produces uneven heating and bowing of the rotor, or an electrical effect that produces uneven magnetic field.

One purpose for a rotor to be balanced is to reduce the force at the bearings. This is because that under an unbalanced condition, an additional centrifugal force will be added to the bearing load. The centrifugal force can be calculated as

$$F_c = 1.77\left(\frac{n}{1000}\right)^2 WR \tag{6.32}$$

where

n is the rotational speed in rpm
W is the unbalance weight in ounce (oz)
R is the radius of unbalance weight in inch

For example, for $N = 600$ rpm, $W = 0.42$ oz (11.9 g), and $R = 1.26$ in. (32.0 mm), the calculated centrifugal force at 1g is 0.58 lb_f (2.58 N). With the increase of the centrifugal force to the radial load applied on the bearing (i.e., P) in Equation 6.32, the bearing fatigue life will be reduced for both 1g and high-g environments. The calculated results are given in Table 6.3.

For the present example, the reduction of the bearing life is less than 5% because of the small magnitude and radius of the unbalance weight. Increasing either the magnitude or radius of the unbalance weight results in a more decrease in the bearing fatigue life. It shows that bearing fatigue life is very sensitive to the radial load acting on the bearing. For instance, for the sensor bearing, as the radial load increases from 46 lb_f (205 N) to 460 lb_f (2050 N), the bearing life reduces from 33,847 to 15.7 years. The calculated results show that the reductions in bearing fatigue life make a little difference between 1g and high-g environments.

TABLE 6.3

The Impact of Rotor Unbalance on the Bearing Life

	Sensor Bearing at Rear Motor	Torque Bearing at Fount Motor	Sensor Bearing at Rear Motor	Torque Bearing at Fount Motor
Bearing Condition	**Hours**		**Year**	
Bearing life at balance condition at 1g	296,500,581	109,264,650	33,847.1	12,473.1
Bearing life at unbalance condition 1g	284,411,241 (−4.08%)	107,185,338 (−1.94%)	32,467.0 (−4.08%)	12,235.8 (−1.94%)
Bearing life at balance condition at 10g	137,623	50,716	15.71	5.79
Bearing life at unbalance condition 10g	132,012 (−4.08%)	49,751 (−1.90%)	15.07 (−4.08%)	5.68 (−1.90%)

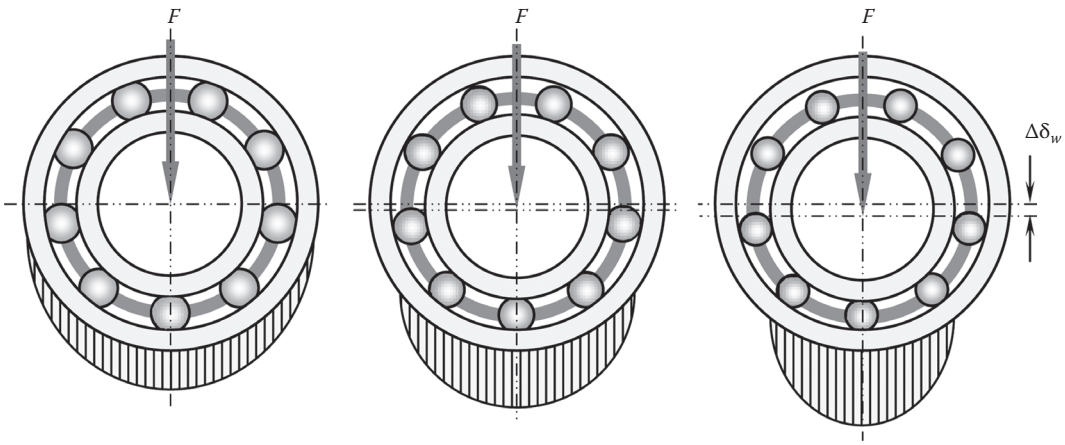

FIGURE 6.24
Influence of bearing wear on load distribution between rolling elements, where $\Delta\delta_w$ is the increased radial clearance due to bearing wear.

6.3.4 Influence of Wear on Bearing Fatigue Life

During bearing operation, the frictional sliding and rolling motion of rolling elements along raceways usually cause rolling bearing to wear. The wear allows the rolling elements to move out of position, increases the internal radial clearance, and makes the load distribution on both the rolling elements and rings even more uneven. As a result, it significantly reduces the life of rolling bearings.

Mitrović and Lazović [6.30] investigated the influence of wear on bearing life for rolling bearings. Their results indicate that the bearing internal geometries are changed due to wear, that is, the diameters of the balls and inner raceway decrease while the diameter of the outer raceway increases. The change of these dimensions leads to the increase in the internal radial clearances of the bearing and the changes in bearing operational characteristics (friction torque, vibration, noise, static and dynamic load rating, etc.). With increasing internal radial clearance, load distribution between rolling elements becomes more unequal (Figure 6.24), causing the reduction of the bearing life. Base on the bearing life theories, a mathematical model was proposed to analyze the wear influence on bearing service time using a newly developed load distribution factor.

6.3.5 Influence of Internal Radial Clearance on Bearing Fatigue Life

The internal radial clearance of radial loaded bearings can significantly alter the load distribution on rolling elements and thus impact the bearing operation reliability and fatigue life. The calculation of the bearing fatigue life is usually based on the assumption that the bearing internal clearance is zero. With a nonzero radial clearance δ_r, the function of load factor $f(\varepsilon)$ can be related to the bearing fatigue life with clearance L_ε [6.22]

- For deep-groove ball bearing

$$f(\varepsilon) = \frac{\delta_r d_b^{1/3}}{0.00044(F_r / Z)^{2/3}} \quad \text{in unit of Newton (N)} \tag{6.33}$$

- For cylindrical roller bearing

$$f(\varepsilon) = \frac{\delta_r l_{er}^{0.8}}{0.000077(F_r / Zi)^{0.9}} \quad \text{in unit of Newton (N)} \tag{6.34}$$

where
δ_r is the radial clearance (mm)
F_r is the radial load (N)
Z is the number of rolling elements
i is the number of rows of rolling elements
d_b is the ball diameter (mm)
l_{er} is the effective roller length (mm)

Under some circumstances, bearing radial internal clearance becomes zero or even negative (interference) at operating conditions. In fact, a slight interference helps reduce bearing vibration and noise, improve the load distribution on rolling elements, and achieve optimum bearing life and motor reliability. However, when the bearing radial interference becomes considerably large, high radial loads can act on rolling elements, causing damages to both rolling elements and raceways.

The bearing life factor is defined as the ratio of the bearing life L at any clearance condition to the life at zero clearance L_o

$$LF = \frac{L(\delta_r)}{L_o(\delta_r = 0)} \tag{6.35}$$

Hence, $LF = 1$ indicates zero clearance on any bearing.

ANSI/ABMA Standard 20-1996 [6.31] defines five ranges of radial clearance for various radial loaded bearings. Based on the investigation of 210-size, deep-groove ball bearings radially loaded to produce 1720 MPa inner race maximum Hertz stress under the zero clearance condition, Oswald et al. [6.22] provided radial clearance and corresponding *LF* values for four ANSI/ABMA clearance groups, as shown in Table 6.4.

The influence of internal radial clearance and interference on bearing life is presented in Figure 6.25 (using the data from [6.22]) under the same loading condition mentioned earlier. It can be seen that bearing life increases with the decrease in radial clearance. At zero clearance, $LF = 1$. With a continuously increasing radial interference (i.e., negative clearance), the bearing life increases accordingly until reaching its maximum at interference of about 0.009. Beyond this point, any increase in interference will cause a sharp decrease in bearing life.

TABLE 6.4

Life Factors and Internal Clearances in Different ANSI/ABMA Clearance Group

Group	Clearance Range (mm)	Corresponding *LF* Range
2	0.001–0.011	0.99–0.85
N	0.006–0.023	0.91–0.77
3	0.018–0.036	0.80–0.69
4	0.03–0.051	0.74–0.63

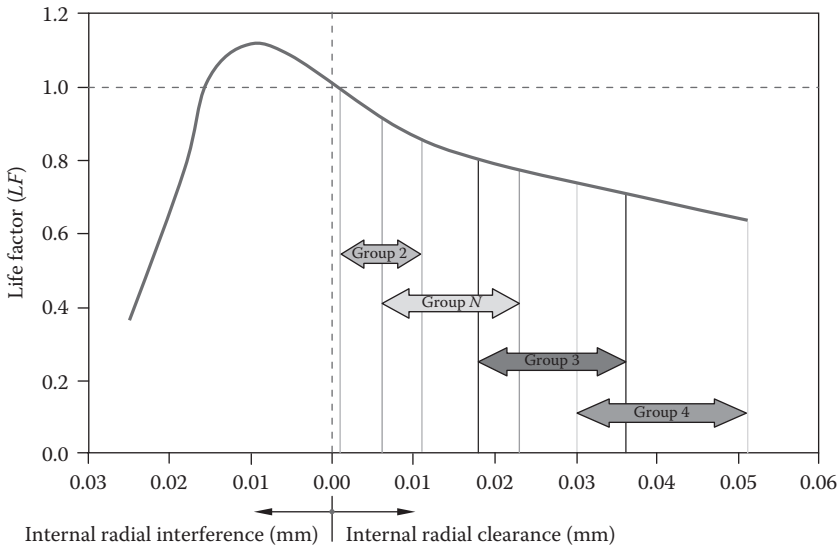

FIGURE 6.25
Effect of internal radical clearance on life factor for deep-groove bearings.

6.4 Bearing Failure Mode

Bearings are considered to be the most critical components of electric motors for maintaining motor normal operation and ultimately reducing unnecessary motor downtime. Many factors can impact bearing life, including operating condition, loads, environment condition, bearing type, bearing structure and quality (seal, surface finishing, dimension accuracy, etc.), bearing materials, heat treatment, lubrication condition, installation, and maintenance. It is commonly accepted that bearing failures that resulted from normal rolling fatigue are less than five percent [6.32].

The failure of a bearing may result in a considerable amount of consequential damage to other motor components. There are tremendous expenses associated with bearing failure in industrial and military motor applications each year. Because the rotor is fully supported by the motor bearings, any bearing defect may directly lead to the variation of the rotor position in the radial direction. This mechanical movement causes the motor air gap to vary in a manner that can be described by a combination of rotating eccentricities moving in both directions [6.33].

Bearing failure can be caused by a variety of factors, including manufacturing defects, unsuitable lubrication, improper bearing selection, inefficient sealing, incorrect fits, defective installation, system misalignment, and careless shipment. Statistical data show that bearing failure due to material fatigue accounts for only a small portion among all bearing failures. In fact, the prediction of theoretical bearing life is based on material fatigue. Most bearing failures are caused by some avoidable factors.

In diagnosing root causes of bearing failure, a fishbone diagram is a useful tool for identifying the potential suspects. It can help understand systematically how system components/factors interact and how they lead to undesirable results such as bearing failure. A fishbone diagram allows engineers to identify, explore, and graphically display all

of the possible causes related to a problem to reveal its real root causes. In fact, the fishbone diagrams work very well in many different areas.

As an example presented in Figure 6.26, the fishbone diagram has been successfully used in the root cause analysis for customers' bearing failure.

6.4.1 Major Causes of Premature Bearing Failure

Fatigue of rolling elements and raceways is an extremely complex and unpredictable process. Therefore, the analysis of bearing fatigue is based on statistical prediction depending on many different parameters, including steel type, steel processing, heat treatment, bearing precision, bearing type, lubricant, and operating conditions.

Bearing root cause analysis involves a structured investigative process that aims to identify the true cause of bearing failure and the actions necessary to mitigate and eliminate the failure. Among the factors that may lead to bearing failure are inadequate lubrication, improper bearing selection, excessive loading, overheating, contamination, high vibration, corrosion, misalignment, and loose or tight bearing fits. Among all failure modes for electric motor bearings, the lubrication-related bearing failure is the primary mode, as summarized in Table 6.5.

This table shows that the lubrication-related failure modes are the top three and account for 55% of all motor failures. The issues related to motor manufacturing and mechanical engineering account for about one-third.

Some more recent results of bearing failure modes have also been released, as shown in Table 6.6 [6.34]. Unlike the results in Table 6.5, the main bearing failure modes are corrosion, manufacturing defects, and bearing precision. The failure mode categorized under *other* includes bearing misalignment, true and false brinelling, excessive thrust/bearing overload, lubrication, heat and thermal preload, roller edge stress, cage fracture, element or ring fracture, skidding damage, and electric arc discharge. Some of these major causes will be addressed in the following sections.

For journal engine bearings, eight major causes of premature bearing failure are listed in Table 6.7 [6.35]. It is important to note that in many cases, a premature bearing failure is collectively caused by a combination of several of these causes.

6.4.2 Lubricant Selection

From the reference [6.1], it is clearly shown that the vast majority of bearing failures in electric motors are associated with lubrication-related problems. All of the rolling bearing systems require appropriate lubrication to ensure normal operation. The metal-to-metal contact of the rolling elements against the raceways necessitates the presence of grease or oil at all times. If the external lubricant is not present, the balls or rollers will begin to make direct contact with the rail material, resulting in galling and brinelling damage. Many manufacturers attempt to overcome this weakness in the design by adding oil-impregnated seals to the ends of the bearing for extending the bearing life [6.36].

In the vast majority of cases, correct lubrication is the most important factor in obtaining good performance of bearings. As a matter of fact, the selection of lubricant and lubrication method is as important as the selection of the bearing itself.

In most cases, greases are considered as the best lubricant for motor bearings. Today, grease manufacturers offer multitudes of greases suitable for a wide variety of bearing

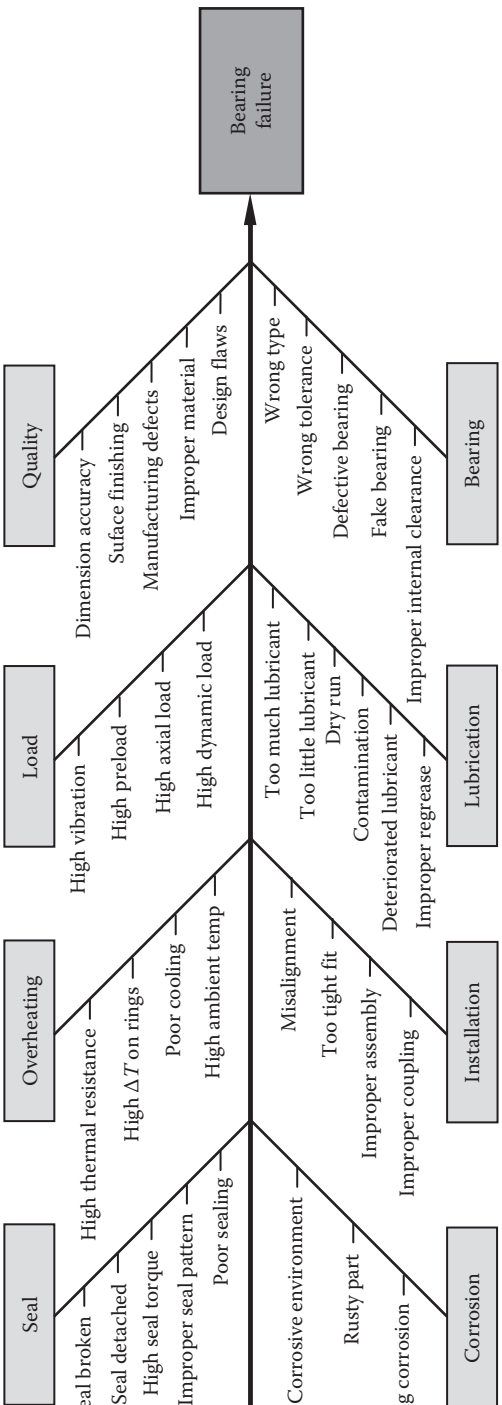

FIGURE 6.26
Fishbone diagram for root cause analysis of bearing failure.

TABLE 6.5

Common Reasons for Bearing Failures

Ranking	Reason of Bearing Failure	Weight (%)
1	Incorrect or aged lubricant	22
2	Dirty bearing, coarse particles, or liquid	19
3	Too much or too little grease	14
4	Incorrect alignment	11
5	Bearing currents/bearing insulation	9
6	Vibration from motor or load machine	8
7	Installation/maintenance failure	7
8	Manufacturing/dimensioning	6
9	Consequential damages/others	4

Source: Data from Lawrie, R., *Electrical Construction & Maintenance (EC&M) Magazine*, February Issue, 2001.

TABLE 6.6

Bearing Failure Mode

Probable Cause for Bearing Failure	Weight (%)
Fatigue (surface and subsurface origin)	3
Cage	3
Bearing wear	6
Handling damage	7
Dimensional discrepancies	17
Debris denting/contamination	20
Corrosion pitting	27
Other	17

TABLE 6.7

Major Causes of Premature Bearing Failure

Cause of Premature Bearing Failure	Weight (%)
Dirt	45.4
Misassembly	12.8
Misalignment	12.6
Insufficient lubrication	11.4
Overloading	8.1
Corrosion	3.7
Improper journal finish	3.2
Other	2.8

applications and operation conditions. The characteristic feature of greases is that they possess a high initial viscosity. The correct choice of grease depends on many factors, including grease viscosity, base oil type, additive requirements, thickener, and some other factors such as dropping point and operating temperature range.

For very high-speed applications such as spindle motors, the bearing temperature can be considerably higher due to friction between deformed rolling elements, raceways,

and cage. For these circumstances, bearing cooling becomes more important than bearing lubrication. Obviously, the use of greases is no longer appropriate and oil lubrication should be provided. Oil, as an efficient coolant, can provide good solutions not only for bearing lubrication but also for bearing cooling. There are three types of oil lubrications:

1. Oil mist lubrication. Oil mist is produced in an atomizer and conveyed to the bearings by an air current.
2. Oil–air lubrication. Oil droplets are carried by compressed air to lubricate/cool bearings.
3. Oil jet lubrication. Injection technique is often used in cooling of high heat flux devices. Oil jet can carry away a large amount of heat from the bearings and is cooled by an oil-to-water or oil-to-air heat exchanger. This lubrication method is especially suitable for high-load, high-speed bearings.

6.4.3 Improper Bearing Lubrication

Among all causes of bearing failure, a primary cause is over or under bearing lubrication. Improper lubrication may result in high temperature buildup in bearings, causing the grease to break down prematurely and thus, leading to the excessive wear of the bearing until its being completely scrapped.

Lubricants are usually made from various oils and additives. There are many different types of motor lubricants, including mineral oils (pure and refined) and synthetic oils for higher temperatures. Animal and vegetable oils are not normally used for bearing lubrication due to the risk of acid formation after a short operating period.

With too much added lubricant such as grease, bearings consume energy as the rolling elements begin churning the lubricant. The energy is then converted into heat that raises the temperature of the lubricant. As a result, the viscosity of the lubricant is reduced and, at elevated temperatures, varnish or coke may form. Furthermore, too much lubricant can effectively reduce the bearing internal clearance. On the other hand, too little lubricant cannot guarantee a sufficient lubrication of the bearing. With insufficient lubricant, an oil film with needed load-carrying capacity cannot fully form. This may result in metal-to-metal contact between rolling elements and raceways, leading to adhesive wear and bearing failure. As a matter of fact, more motor bearing failures are due to overgreasing rather than undergreasing [6.37].

6.4.4 Lubricant Contamination

One of the leading causes of premature bearing failure can be attributed to lubricant contamination, which increases energy consumption by causing abrasive friction at bearing surfaces, raising lubricant viscosity, generating dents on the raceway and rolling element surfaces, and consequently reducing the bearing operation life. Water from condensation of moisture-contained air can enter the lubricant via penetration through the bearing seal or some other ways. It has been reported [6.38] that as little as 0.002% water in the bearing lubricant will reduce bearing life by 48%, while 6% water content in the lubricant will reduce bearing life by as much as 83%.

Microscopic particles are the most harmful form of lubricant contamination as they initiate irreversible microscopic damages on the bearing contact surfaces. Over time, these

FIGURE 6.27
A rusty bearing with 2-year service in an electric mold nonsinusoidal oscillation system for slab caster in a steel plant.

microscopic damages may accumulate and progress into macroscopic damages and finally lead to premature bearing failure and breakdown of motors.

When bearings work under certain hazard conditions such as high temperature, high moisture, and other corrosive environments (e.g., steel or glass plants), corrosion on some bearing materials would be hardly avoidable. Figure 6.27 shows a rusty bearing after a 2-year service in an electric mold nonsinusoidal oscillation system for slab caster in a steel plant. Ferric oxide is an inorganic compound with the formula Fe_2O_3. During motor operation, Fe_2O_3 powder may enter critical areas of the bearing where sliding or rolling contact takes place, causing fretting damage on the bearing.

6.4.5 Grease Leakage

In a field motor inspection, it is common to encounter grease leakage problems. Grease may leak from a sealed bearing between the inner seal groove and the seal, especially for vertically installed motors. While a small amount of grease leakage may exert little impact on motor performance, an aggravated level of grease leakage can significantly shorten bearing life, degrade bearing performance, or even cause bearing failure.

When grease leakage occurs, it is important to check the questions listed in the following:

- Is the selected grease appropriate? The properties of the grease (e.g., viscosity, the allowable operation temperature) must be checked carefully.
- What is the operation temperature when the leakage occurs? As the operation temperature goes higher, the grease viscosity becomes significantly lower.
- What is the condition of the bearing seal? An improper or damaged bearing seal always results in grease leakage.
- What is the bearing load condition? An overloaded bearing tends to cause grease leakage.

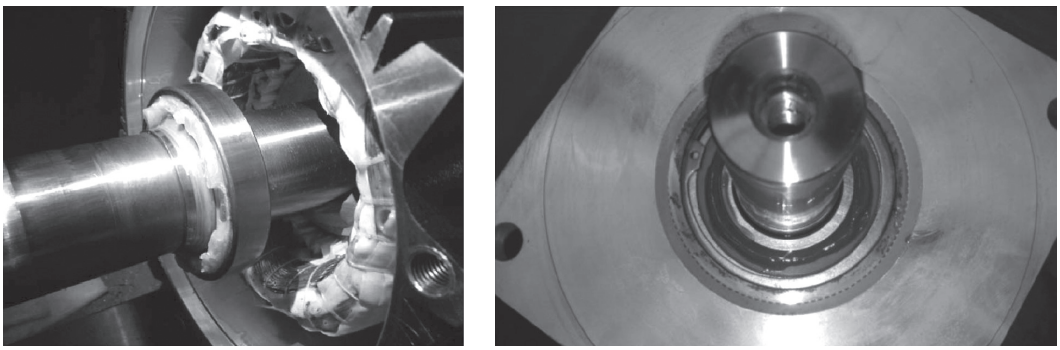

(a) (b)

FIGURE 6.28
Grease leakage from the bearings in the vertically mounted motors: (a) with a 2-year service in an electric mold nonsinusoidal oscillation system for slab caster and (b) with a 3600 h service in a CNC laser cutting machine.

- Is the bearing overfilled with grease? Grease overfilling can cause excess churning of the grease during operation and generate extra resistance in the bearing.
- What is the level of motor vibration? A high motor vibration can accelerate grease leakage from the motor bearings.

As demonstrated in Figure 6.28, lubricating grease leaks out of the bearings and accumulates on the bearing seals. It is noted that in both cases, the grease purge occurs from the vertically mounted motors with low-frequency vibration.

In order to improve the sealing capability and avoid grease purge from sealed deep-groove ball bearings, NTN engineers have designed new geometrical cages that differ in shape from that of the standard case [6.39]. The new type of cages has been confirmed experimentally to suppress the adherence of grease to the inner ring seal groove, improving the resistance to grease purge substantially.

6.4.6 Bearing Sealing

Bearing seals and shields are commonly used to retain the bearing lubricant and prevent ingress of external contaminations. Both seals and shields are available in a variety of materials and configurations. Briefly, a seal is retained to the bearing outer ring, but also makes light contact with the rotating inner ring. This provides a high degree of bearing sealing capability with a modest increase in friction and torque. Generally, when the sealing performance is enhanced, the torque required to turn the bearing increases with the friction caused by the seal. It is noted that some types of seals (e.g., lip seals) may generate a high pressure at the lip, resulting in greatly increased torque and friction losses, especially in high-speed applications.

In contrast, a shield is a noncontact closure piece, being staked to the bearing outer ring with a small gap between the shield ID and the bearing inner ring. Thus, bearing shields have virtually little compact on bearing performance. As a result, in torque-sensitive applications, it is advantageous to use shields rather than seals.

Retention of bearing seals/shields has a critical impact on achieving the best bearing sealing performance. This is especially true for vertically installed motors subject to high levels of vibration. It is interesting to note that even for the same model and bearing

(a) (b)

FIGURE 6.29
Different retention methods used for securing bearing seals for the same model and same brand bearings: (a) with a number of knocks equally distributed along the circumference of the outer ring ID and (b) a simple retention method without using knocks. It is obvious that the retention method used in (a) can provide better retaining capability than that in (b).

brand, the retention methods could vary depending on in which countries they are manufactured. As shown in Figure 6.29, one bearing uses 19 knocks that are equally distributed along the circumference of the outer ring ID to retain the seal firmly. However, the other bearing has no such feature. Obviously, the former has a much better seal retaining capability.

Figure 6.30 shows an example of a bearing failure due to the bearing seal being pushed down in a vertically mounted motor as a consequence of improper sealing. The field inspection has revealed that as the seal was dropped off, the grease was completely lost from the bearing. Under a dry run condition, the bearing temperature was raised dramatically, leading to the disintegration of bearing cage into pieces.

6.4.7 Excessive Load

Bearing load and speed are the most common rating factors impacting bearing service life. Of the two, bearing load has a greater influence on its lifetime. Generally, by doubling the load of a bearing, the bearing life can be reduced by a factor of ten for the ball bearing and eight for the roller bearing. As a contrast, doubling the speed reduces the bearing life by half.

Excessive loads usually lead to premature fatigue failure of the contact surfaces of the rolling elements. As excessively heavy loads repeatedly act on the contact rolling elements, microcracks start to develop on the surfaces of raceways or rolling elements (balls or rollers). After a period of time, these cracks grow and propagate on the fracture surfaces and finally cause flaking on the raceway or rolling element surfaces. When bearings are subject to very high loads or shock loads, it may lead to large cracks or fractures of bearing components.

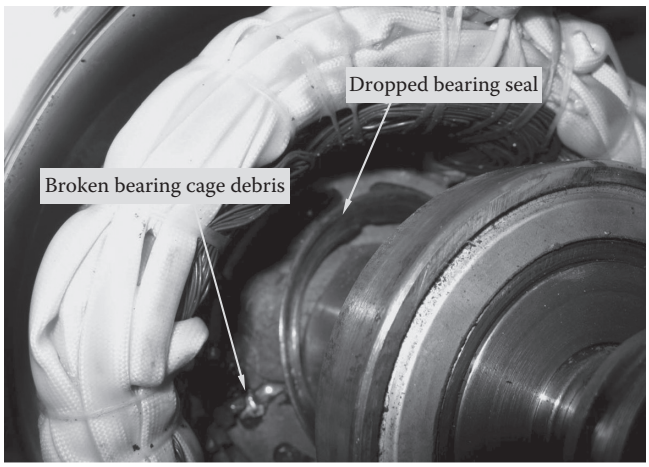

FIGURE 6.30
The bearing seal is dropped off from the bearing. The cage is severely destroyed, broken into pieces to scatter inside the motor.

6.4.8 Internal Radial Interference Condition

Regularly, bearing manufacturers always design bearings with certain internal radial clearances. However, under some operating conditions, the internal radial clearance in a bearing may be reduced or even completely eliminated. In some cases, the radial clearance may be further turned into the interference. With the bearing internal radial interference, the rolling elements and raceways are tightly fitted together, applying large frictions and loads to the bearing components.

The bearing effective radial operating clearance δ_{eff} is defined as the amount of radial internal free movement during bearing normal operation. It can be determined by three clearance components: (1) the initial bearing radial internal clearance before mounting, δ_o; (2) the reduced amount of radial clearance due to interference fit, δ_f; and (3) the reduced amount of radial clearance due to temperature difference between the outer and inner rings, δ_t [6.16], that is,

$$\delta_{eff} = \delta_o - (\delta_f + \delta_t) \tag{6.36}$$

When bearings are mounted on shafts and in bearing bores with interference fits, the inner ring will expand and the outer ring will contract, thus reducing the bearings' radial internal clearance to approximately 70%–90% of the effective interference.

$$\delta_f = (0.7 \sim 0.9)\Delta\varepsilon_{eff} \tag{6.37}$$

where $\Delta\varepsilon_{eff}$ is the effective interference

During motor normal operation, the bearing outer ring is typically about 5°C–10°C cooler than the inner ring due to the smaller thermal resistance from the stator to the surrounding environment. However, as the motor housing is subjected to forced convective cooling, the temperature difference between the outer and inner bearing rings

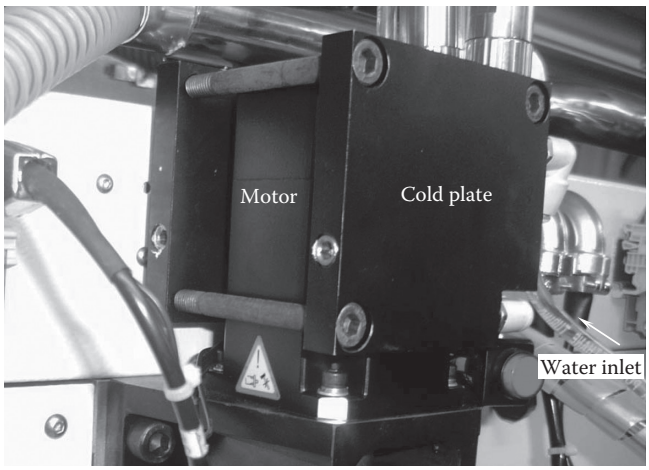

FIGURE 6.31
A motor is sandwiched by two water cold plates, causing a large temperature difference between the bearing outer ring and inner ring.

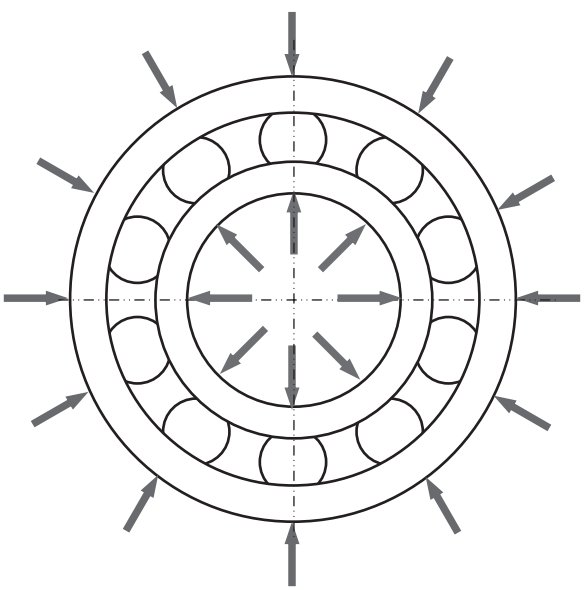

FIGURE 6.32
Due to the temperature difference on the bearing's outer and inner rings as a result of motor cooling, shrinkage occurs on the outer ring and expansion on the inner ring.

can be considerably larger. As shown in Figure 6.31, a motor is sandwiched by two water cold plates. A much lower temperature is measured at the bearing outer ring when the cooling systems start operating. Thus, the amount of radial internal clearance is further reduced due to the shrinkage of the outer ring and the expansion of the inner ring (Figure 6.32).

The decrease in radial internal clearance due to the temperature difference ΔT of the outer and inner rings δ_t can be calculated as

$$\delta_t = \alpha(\Delta T)d_{or} \tag{6.38}$$

where

α is the bearing material expansion coefficient, which, for stainless still, $\alpha = 12.5 \times 10^{-6}$
ΔT is the temperature differential between the inner and outer rings
d_{or} is the outer ring raceway diameter. For ball bearings, $d_{or} = 0.2\ (d_i + 4d_o)$

Using the above equations, the bearing effective radial operating clearance δ_{eff} can be displayed as a function of the temperature difference between the inner and outer rings. As an example, the results for a 6802 bearing with a normal clearance class CN (its radial clearance ranges of 3–18 μm) are shown in Figure 6.33.

It can be seen that for $\Delta T < 7.2$°C, the bearing has a positive radial clearance. At the point of $\Delta T = 7.2$°C, the radial clearance vanishes. As ΔT becomes larger than 7.2°C, it turns to the radial interference. Note that small interference is allowed and desirable for some applications for increasing bearing stiffness and reducing vibration and noise. However, excessive interferences result in extra rolling contact pressure, which can greatly reduce the fatigue life of the bearing. When the interference becomes high enough, the bearing balls may be completely held by the inner and outer raceways. As a result, these balls are unable to rotate freely but forcibly slide between the raceways, causing overheating, overwearing, and eventually the failure of bearing. It is to be noted that since large bearings usually have large radial clearances, they are unlikely experiencing overheating and overwearing situations. Even for the same bearing size, if the bearing has a higher radial clearance class,

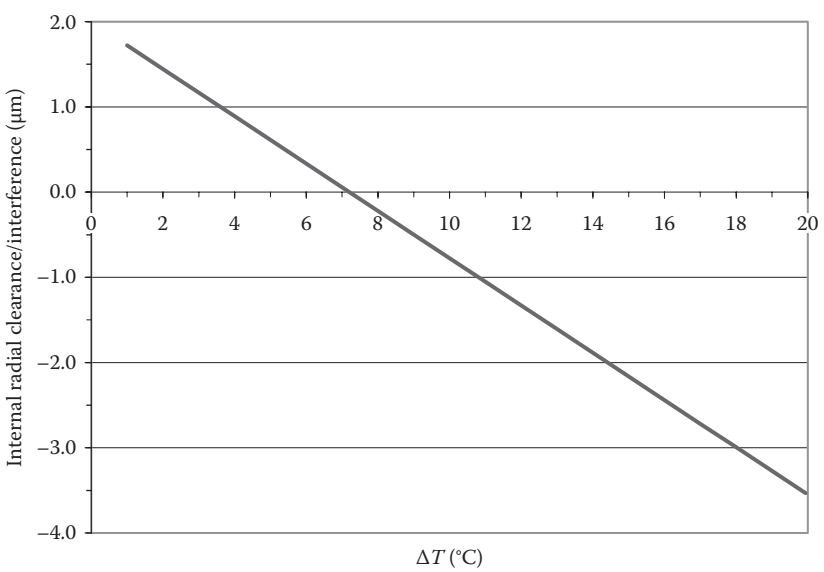

FIGURE 6.33
Effect of the temperature difference of the bearing inner and outer rings on the bearing radial clearance/interference for a specific bearing with the clearance class of *CN*.

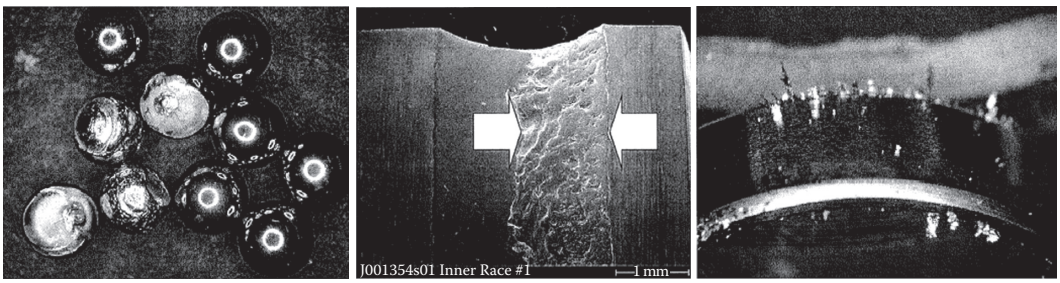

FIGURE 6.34
Damaged bearing balls, inner and outer raceways due to large axial load. It can be clearly seen that spalling occurs at one side of the inner raceway.

for instance, *C*3 or *C*4, it will significantly improve bearing operation condition under such circumstances.

Most bearings are designed to withstand primarily radial loads, and only certain extent of axial loads. As an example, for deep-groove ball bearings, the maximum axial load is typically about 50% of the maximum radial road. However, for small bearings, this value can be lowered to 25%. When a ball bearing is subjected to a large axial load, the internal radial clearance vanishes as the result of the shift of the inner ring axially relatively to the outer ring (see Figure 6.15). Correspondingly, the balls and raceways develop elastic deformation, resulting in an increase in the contact angle β (defined as the angle between the bearing contact line and bearing normal line) and contact width. This changes the bearing from the point contact to ellipse contact, which in turn causes asymmetric wear of the ring at their sides of the raceways, as demonstrated in Figure 6.34.

6.4.9 Bearing Current

The problem of bearing currents and shaft voltages has been recognized for almost a century [6.40]. A shaft voltage can cause the bearing current that flows through the bearings. A number of surveys have indicated that 30% of all motor failures operated with 60 Hz sine wave voltage are due to bearing current damage [6.41]. In recent years, there is an increase in motor failures due to bearing current.

The most common underlying cause of bearing currents in three-phase IMs is alternating magnetic flux, which is a result of asymmetric magnetic properties of the stator or rotor core. The asymmetrical flux through the steel results in time-varying flux lines that enclose the shaft. This can drive a current down to the bearings, endbell, housing, and back again to the bearings [6.42]. In addition, the use of variable frequency drives can induce the shaft voltage because of the extremely high-speed switching of the insulated gate bipolar transistors, which produce the pulse width modulation used to control AC motors. This shaft voltage can exceed the dielectric strength of the lubricant film in bearings, causing the bearings to discharge [6.43].

When electric current flows through IM bearings along internal closed-loop paths (Figure 6.35), it may generate electric arc, which tends to melt and damage internal bearing surfaces, just like a series of small lightning strikes. This can cause bearing surfaces to flake away and spall out, leaving behind microcraters on the bearing surfaces. As rolling elements roll on these damaged surfaces with contact pressures, the microcraters will

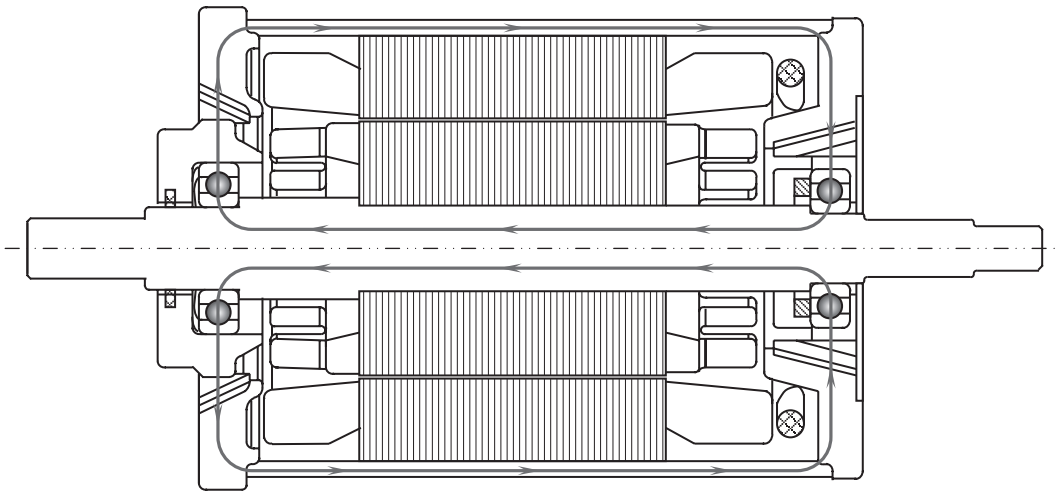

FIGURE 6.35
Bearing current resulted from time-varying magnetic flux in a motor.

be increasingly enlarged, further leading to the deterioration of bearing contact surface, acceleration of wear, elevation of noise and vibration levels, and eventually bearing failure. In addition, wear debris may be introduced into the lubricant, causing lubricant contamination problems.

There are a number of strategies and methods available for reducing/eliminating bearing currents:

- An effective way to eliminate bearing currents is to break the current path by insulating either bearings or endbells from the motor frame. Insulating bearings may be accomplished by the following [6.44]: (1) adding an insulation material to the bearing ring or bearing journal; (2) coating a ceramic material on bearing components; or (3) adopting ceramic bearing, which has been experimentally investigated.
- Grounding shaft is another effective way to eliminate the shaft voltage. This can be done via the usage of metal brushes or grounding rings [6.45].
- Another solution to the bearing current problems is to improve the high-frequency grounding connection from the motor to the drive and from the motor to the driven equipment.
- Establishing an alternative current path directly from rotor to stator or from rotor to frame by means of bushes can effectively reduce bearing current.
- Theoretically, using a conductive Faraday shielded between the rotor and stator would prevent the current from being induced in the shaft. However, this method is difficult to implement in practice.

6.4.10 Impact of High Temperature on Bearing Failure

The maximum permitted temperature in rolling element bearings depends on many factors, including bearing material, bearing type, lubrication type, heat treatment, manufacturing

and assembly accuracy, and bearing operation condition. Temperatures in excess of this limit can permanently cause bearing failure.

The standard stabilization temperatures are 120°C for deep-groove ball bearings and 150°C for angular contact ball bearings. Overheating bearings above their stabilization temperatures can anneal the ring and ball materials, leading to the rapid softening of the bearing steel, the reduction of load-carrying capacity, and possibly the subsequent failure.

High temperatures can lead to the decomposition, oxidation, or deterioration of some lubricates. In addition, bearing overheating also lowers viscosity of bearing lubricates and thus makes it easier for lubricates to leak off from the bearings. It was reported [6.39] that grease purge from a greased and sealed bearing occurs between the seal and the inner seal groove that rotate against each other. An increase in bearing temperature causes a pressure on grease located on the inner ring seal groove, resulting in grease purge. In order to improve the prevention of grease leakage, the cage was redesigned with optimized geometrical shape. The promising results were achieved experimentally using the improved cage.

6.4.11 Bearing Failure Associated with Motor Vibration and Overloading

Vibration can occur at anytime when a motor is in normal or abnormal operation. Vibration can worsen motor performance and reduce the bearing life due to the alternating force producing both impact force and stress reversal. An excessive level of vibration may lead to premature failure of bearings.

Motor vibration can be activated by the combination of a variety of forces, including the following: (1) mechanical, electrical, and electromagnetic unbalancing forces, which can severely reduce the bearing life; (2) misalignment forces due to shaft misalignment; (3) belt/gear driving tension forces; (4) looseness forces due to looseness of motor components such as a large radial clearance in motor bearings; (5) gravitational force of rotor; and (6) reaction forces from other devices such as gearboxes. Increasing the dynamic forces caused by unbalance, misalignment, and looseness can remarkably result in higher vibration levels and thus significantly reduce the bearing life.

The impact of increased load/force on the bearing life is pronounced. As demonstrated in Figure 6.36, doubling the load/force on bearing can reduce the bearing life by 87% for ball bearings and 90% for other rolling element bearings (e.g., cylindrical, spherical, tapered, and needle bearings) [6.46].

On the contrary, reducing the vibration level can greatly extend the bearing life. According to the data provided by Berry [6.46], by assuming the dynamic load is the major force component, and reducing the vibration level by half will extend the bearing life by 700% for ball bearings and 908% for other rolling element bearings, as shown in Figure 6.37.

As one of the leading causes of bearing failure, overloading often results in overstresses of bearing components. Overstress creates the possibility of motor component damage caused by a single extreme loading event. A common catalyst for this type of damage is improper belt tensioning. Excessive load introduced by belt can drastically reduce the expected bearing life. It has reported that a 10% increase in tension may reduce bearing life by up to 50%, depending on the system [6.47].

A tight fit between the bearing and the mating parts (i.e., shaft and bearing bore) can eliminate the radial clearance of the bearing. Under this circumstance, the bearing balls and raceways become excessively loaded, leading to rapid wear on these components and resulting in a rapid temperature rise accompanied by high torque.

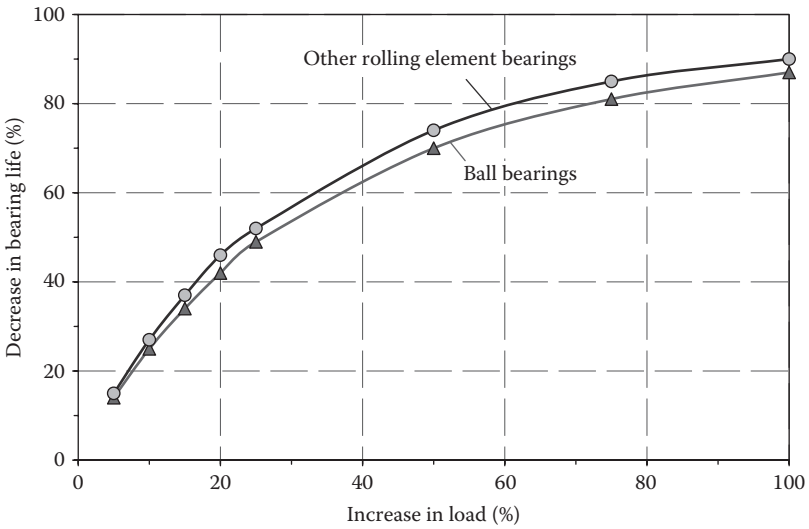

FIGURE 6.36
Impact of increased load on bearing life.

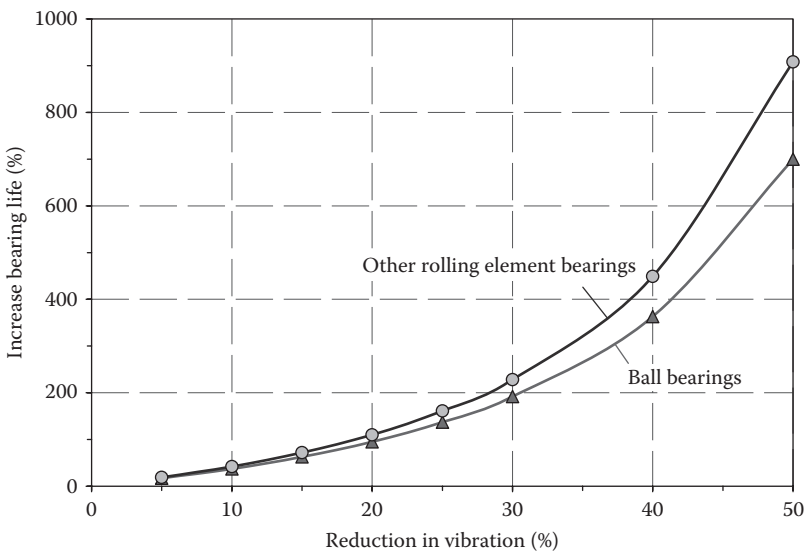

FIGURE 6.37
Impact of reduction in vibration level on bearing life.

6.4.12 Improper Bearing Installation and Bearing Misalignment

Bearing failure may be also caused by improper bearing installation. In an installation process, bearings are forced onto shafts or in bearing bores of endbells/frames. This may produce physical damage in the form of brinelling or false brinelling of the raceways, which leads to premature failure. Bearing misalignment is another common consequence

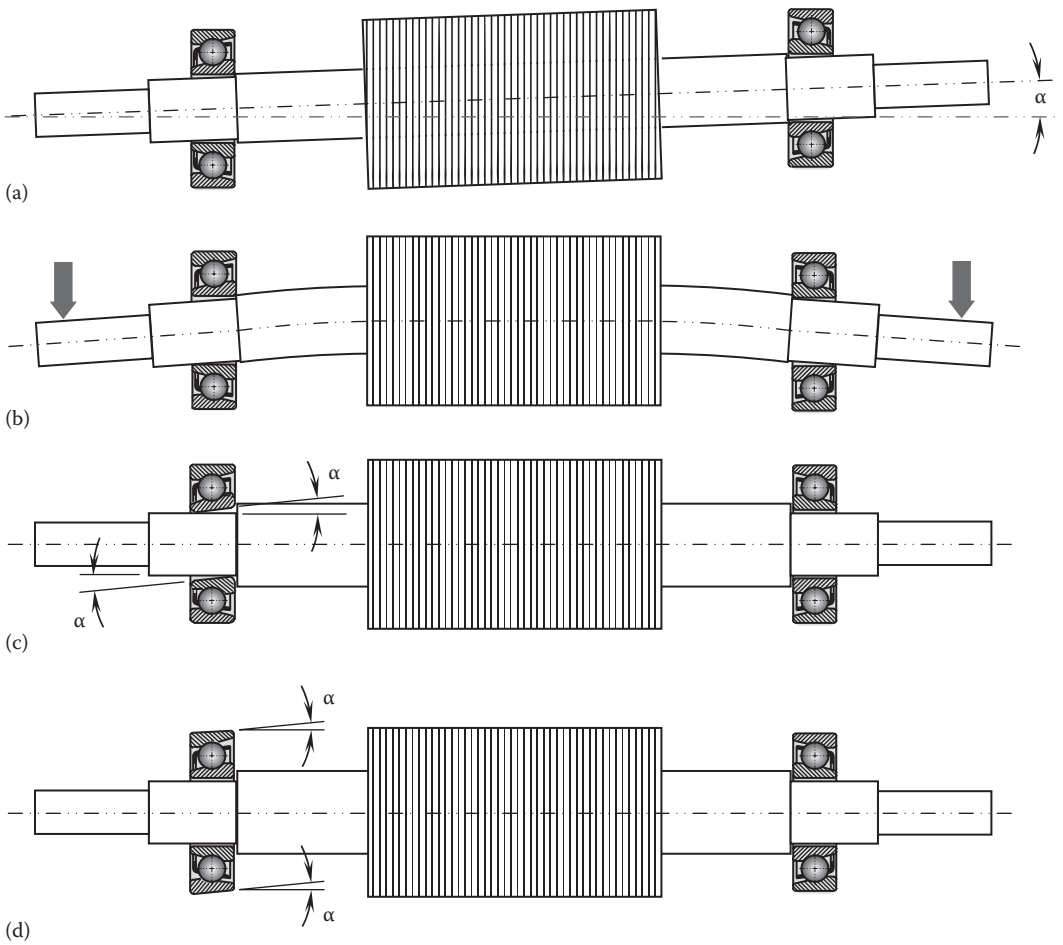

FIGURE 6.38
Four types of rolling element bearing misalignment: (a) out-off-line; (b) shaft deflection; (c) cocked or tilted inner raceway; and (d) cocked or tilted outer raceway.

of improper bearing installation. As depicted in Figure 6.38, there are four types of bearing misalignment: out-off-line, shaft deflection, cocked or tilted inner raceway, and cocked or tilted outer raceway [6.48]. Each type of misalignment can cause abnormal forces acting on the bearing that may accelerate wear of the bearing raceways, cage, and rolling elements.

6.4.13 Vertically Mounted Motor

As a motor is mounted vertically, the weight of the rotor itself as well as the possible external loads will act on the bearings in the motor axial direction. The increasing axial load can significantly change the bearing operation characteristics, for instance, resulting in larger pressure angle, pressure ellipse, and stresses on bearing rings and rolling elements.

Although many motor manufacturers claim in their motor manuals that their motors can be installed either horizontally or vertically, it must be recognized that in most cases, electric motors are primarily designed for horizontal operation. Motor bearing surveys have revealed that a considerable number of motors use deep-groove ball bearings. This type of bearing can withstand large radial loads but relatively small axial loads. For a vertically mounted motor, it may consider using tapered roller bearings or dual bearing assembles (which are similar to the front wheel bearing on a car) that have the ability to take loads in both radial and axial directions.

Lubricant retention is critical for vertically installed motor for normal operation. Due to the gravity force, vibration, and temperature effects, the lubricant in motor bearings can gradually leak out from the bearings. Therefore, the sealing capability of bearing becomes one of the key parameters in the bearing selection for reducing the risk of premature bearing failure and enhancing bearing life. In addition, better bearing sealing can prevent external contaminants from entering the bearing interior.

For a vertically mounted motor, any movement of the shaft relative to the motor bearings, as well as to the motor endbells, is not allowed, especially under vibration and high-temperature operating conditions. To avoid this problem, it is critical to use interference fit between the shaft and bearings and tight fit between the bearings and bearing bores. In addition, retaining rings or snap rings must be added to the shaft to avoid the axial movement of the bearings and shaft in any direction with respect to the motor frame. Failing to do so will cause axial movement of either the shaft or bearing relative to the motor, resulting in severe bearing damages. For any cases, the axial load on motor bearings should not exceed the maximum allowed value.

6.5 Bearing Noise

Bearing noise comes from many sources, including cage noise, race noise, seal noise, waviness noise, and lubricant noise. Some types of noise are unavoidable and acceptable, such as lubricant noise. However, some types of noise are related to the manufacturing process and can be readily avoided, such as waviness and click noise. The various types of noise in rolling bearings are grouped into four categories [6.49]: structural (cage, squeal, race, and click noise), manufacturing (waviness noise), handling (flaw and contamination noise), and others (seal and lubricant noise).

Manufacturing precision has a strong impact on bearing noise. There are a large number of parameters affecting the bearing noise level, including roundness of bearing rings and balls, shape accuracy, surface finishing, dimensional tolerance, internal clearance control, and assembly accuracy. In fact, even a slight defect in shape may cause noise and vibration. Generally, noise due to manufacturing defects can be lowered with the improved manufacturing process. For instance, waviness noise can be reduced by decreasing the waviness in the circumferential direction on the finished surfaces of the bearing raceways.

Major bearing components are heat treated to render the hardness larger than 60 HRC. Lower quenching temperatures may give bearing components lower hardness or develop soft points on them. This reduces the wear resistance of the bearing components sharply. Other defects due to improper heat treatment include quenching microstructure,

FIGURE 6.39
Bearing is cut for inspecting bearing damage and wear condition.

deformation, surface decarburization, and quenching crack. All these defects raise bearing noise levels.

Compared with ball bearings, rolling bearings are manufactured and processed according to higher precision standards, and therefore generally produce relatively low level of noise. For motors requiring particularly low-noise operation, the selection of deep-groove ball bearings or cylindrical roller bearings can provide appropriate solution.

In some motor manufacturers, bearing noise can be simply detected with modified medical stethoscopes. This has been proven to be an effective and convenient method, particularly to operators on assembly lines. In order to find root causes of bearing noise, the suspected bearing is often sliced into halves to inspect manufacturing defects, abnormal wear, and other damages (Figure 6.39). It has been found that even very tiny manufacturing defects, which cannot be identified by naked eyes, can generate significant click or waviness noise. Thus, a microscope is a necessary apparatus for the bearing inspection.

6.6 Bearing Selection

The primary factors in the bearing selection are the total system reliability during the design life and the cost-effectiveness. The selection of appropriate bearings has become crucial to the overall performance of electronic motors. The selection process must carefully consider all factors that affect bearing performance and cost, including the following:

- Radial and axial load conditions. In fact, bearing fatigue life is sensitive to the magnitude of load. Generally, if the load is doubled, the fatigue life is reduced by a factor of ten for the roller bearing and a factor of eight for the ball bearings.

- The change in the contact condition between the rolling elements and rings. When a bearing is running under loads, the forces are transmitted through the rolling elements from one ring to another. The magnitude of the load carried by an individual rolling element depends on the location of the element at any instant, the number of rolling element, and the bearing type. Due to the plastic deformation of the bearing components, the contact condition of the bearing components can alter dramatically. For instance, for a ball bearing, the contact between the balls and rings is no longer a point contact rather, it forms a contact area called contact ellipse. For a roller bearing, instead of a line contact, the contact area is a narrow rectangular.
- Rotor rotating speed range—The bearing speed has a strong impact on the selection of the bearing lubricant. Generally, the higher the bearing speed, the lower the lubricant viscosity.
- Expected bearing life and motor operation life—Usually, the life expectancy of motor can exceed 20 years. This requires an extended bearing life. However, under some harsh operation conditions, the bearing life is much shorter than expected. Hence, it is important to adjust it according to the real situation. For instance, bearings used in oscillation systems for slab caster experience high temperature, moisture, and dust level. These bearings should be replaced after 2-year service, regardless of whether the bearings are damaged or not.
- Operating temperature—The variation in operating temperature may result in the expansion or contraction of rings and rolling elements, which alters the bearing internal clearance. In some cases, the radial clearance may be eliminated due to the temperature difference between the inner and outer ring. In the bearing selection, a wide operation temperature range is highly desired.
- Sealing requirement—Under harsh environmental operating conditions, good sealing is necessary for motor bearings to prevent dust, moisture, and other foreign matters to get in the bearings, as well as the leakage of lubricant from the bearings. This is especially true for outdoor motor applications.
- Lubrication method—Bearings typically use grease or oil as lubricant. Grease lubrication is often used in applications where frequent replenishment of the lubricant is undesirable or impossible. Oil lubrication is suitable for applications that require low torque or narrow range of torque variations. There are a number of oil lubrication methods for different applications, including oil bath, circulation oil, oil jet, oil drop, and oil mist. Because bearing lubrication is one of the major causes for bearing failure, it is highly desired that bearings can be self-lubricated for extending the bearing life and reducing the maintenance cost.
- Bearing internal clearances in both radial and axial directions—For precisely controlled motion systems, bearings with small internal clearances are preferred for minimizing motor vibration and maintaining motor smooth operation. In the bearing section, it is important to take into account the variations of bearing internal clearances with the operating temperature.
- Bearing noise level—Bearing noise can be a critical factor for some applications such as medical devices. Specifically designed precision bearings generally produce very low levels of noise. However, low noise bearings are more expensive than regular bearings.
- Installation/disassembly requirements—In some harsh operating conditions, the bearing life is significantly shorter than the motor lifetime. This indicates that the

motor bearings must be changed for a certain period of time during the motor lifetime. Easy bearing installation/disassembly is the basic requirement to ensure the changes of motor bearings.

- Maintenance requirements—Low-maintenance bearing is a prime advantage for some applications such as pitch control motors in offshore wind turbines. With continuous developments in bearing material, better designs, more advanced manufacturing process, lubrication technology, precise production methods, and improved surface finishing in the bearing industry, bearing life has been greatly increased with the reduced maintenance in the last several decades. A longer maintenance cycle and lower maintenance cost mean a reduced life-cycle cost of bearing.
- Shaft and endbell/housing designs—In an electric motor, the shaft and bearings, as well as the endbell/housing, constitute a rotating system, and thus, the selection of bearing can directly affect the designs of the shaft and endbell/housing. As a consequence, it is highly desired to take into account such influences in the earlier stage of the motor design.
- Allowable misalignment of inner/outer rings—Some types of bearing have a self-aligning capability, such as self-aligning ball bearings and spherical roller bearings. Using these types of bearing can help reduce loads that resulted from the misalignment between the motor and driven machine.

However, it is very difficult to satisfy all requirements listed earlier. Each application may have its specific requirements. It is critical for motor engineers to prioritize all these factors for a specific application, make trade-offs, and identify the relatively important factors as the design factors.

6.6.1 Bearing Type Selection Based on Load

Rolling bearings are available in a variety of types, configurations, and sizes. The correct selection of bearing type is mainly determined by the direction, magnitude, and characteristics of loads acting on the bearing. Generally, a thrust ball bearing can only withstand axial loads. By contrast, needle bearings are designed to take only radial loads. In practice, motor bearings have to take both radial and axial loads.

Bearings for practical applications often need to withstand both dynamic and static loads in a variety of magnitudes and directions. Usually, many bearing manufacturers use the equivalent load to determine the bearing load ratings. When both dynamic radial loads and dynamic axial loads act on a bearing simultaneously, the dynamic equivalent radial load P_{dr} (in N) can be determined as

$$P_{dr} = X_d F_{dr} + Y_d F_{da} \tag{6.39}$$

where

F_{dr} and F_{da} are the actual dynamic radial and dynamic axial load (in N)
X_d and Y_d are dynamic radial and dynamic axial load factor, respectively.
X_d and Y_d can be found in bearing catalogs.

Similarly, the static equivalent radial load P_{sr} (in N) can be found from the following equation:

$$P_{sr} = X_s F_{sr} + Y_s F_{sa} \tag{6.40}$$

where

F_{sr} and F_{sa} are the static radial and static axial load (in N)
X_s and Y_s are static radial and static axial load factor, respectively

All values of X_d, Y_s, X_s, and Y_s are provided by manufacturers. The calculated values of P_{dr} and P_{sr} can be used to select the bearing for specific applications.

Couplings are used to connect the motor and driven machine together. The selection of flexible or rigid couplings can strongly influence bearing operation. Improper couplings may introduce additional loads to motor bearings. In addition, using belts or gears as the driving mechanism can produce the transverse force acting on the shaft, which is in turn transmitted to the motor bearings, especially on the drive end bearing. In this case, using roller bearings at the drive end is commonly recommended because of their higher load-carrying capability.

In real bearing applications, there are always some small misalignments between the motor shaft and driven machine shaft. Using flexible couplings can help accommodate the misalignments to some extent.

Different types of bearings have different load capacities. Deep-groove ball bearings can take more axial loads than ball bearings. Cylindrical roller bearings have a stable axial load-carrying capacity. This type of bearings can be safely used as long as the radial load exceeds the axial load by 2.5 times or more. In general, rolling bearings are capable of withstanding greater vibration and shock loads than ball bearings.

6.6.2 Bearing Type Selection Based on Speed

The ball bearing has relatively lower rolling resistances over a wide range of rotating speed than a roller bearing, making it perfectly suitable for medium-/high-speed and low-torque applications. Furthermore, compared with most other types of bearings, ball bearings have superior acoustic characteristics.

By contrast, a roller bearing is in line contact with the inner and outer raceways. Therefore, it can withstand much larger radial loads than the ball bearing. It is interesting to note that at very high speeds, the friction of roller bearing becomes lower than that of ball bearings.

For extremely high-speed motors, noncontact bearings such as magnetic bearings may be selected due to their extremely low friction and wear.

6.6.3 Selection of Bearing Size

Bearing size can be initially selected by the load ratings to determine the required load-carrying capacity with a given factor of safety n_s. Both dynamic and static loads must be evaluated prior to the selection. Dynamic loads are the loads related to the rotor rotation or system displacement (e.g., vehicle). Shock loads are also dynamic loads, which are frequently encountered from heavy impact to earthquake. Usually, dynamic loads are higher than static loads for motors.

In order to ensure bearing normal operation, it has been recommended [6.50] by bearing manufacturers that bearing size should be selected on the basis of static load ratings for the following conditions: (1) the bearing is stationary and is subjected to continuous or intermittent loads, (2) the bearing makes slow oscillating or alignment movements under load, (3) the bearing rotates under load at very slow speed (<10 rpm)

and only operates for short life, and (4) the bearing rotates and, in addition to the normal operating loads, has to sustain heavy shock loads.

6.7 Bearing Performance Improvement

The most recent significant advancement in bearing technology is the introduction of ceramic ball bearings. A ceramic bearing is usually made with ferrous inner and outer rings as well as ceramic balls made of silicon nitride steel, Si_3N_4. The advantages of ceramic bearings over steel bearings include lower friction, higher hardness, finer finish, lesser heat generation, and better acceleration capability. Ceramic bearings are usually used in high-speed and high-temperature (up to 500°C–800°C) applications. High-speed electric motors that require voltage isolation often utilize ceramic bearings [6.51].

Other advantages of ceramic bearings over steel bearings include the following:

- They can withstand wear and tear better compared to steel bearings.
- The modulus of elasticity of silicon nitride is 1.5 times higher than steel, indicating that ceramic balls have a smaller contact area and thus lower rolling friction and heat generation.
- The smaller mass of the ceramic balls results in less inertia and gravitational force on the bearing borne.
- Ceramic balls are less vulnerable to lubricating film breakdowns and starved lubrication conditions than steel balls. They need less lubricant and exhibit less lubrication degradation, which contribute to an increased operation lifetime.
- Rotating bearing components may experience electric charging. This leads to superfluous noise and wear out the bearings. Because ceramic bearings usually have poor electrical conductance, electric charging hardly occurs in this type of bearing.

Bearings under contaminated lubrication condition suffer often from indentations that are generated on the bearing rolling surfaces by foreign particles. During bearing operation, high stress concentrations occur in the vicinities of dents and eventually lead to cracking and surface-originating flaking. The stress concentration is expressed as

$$\frac{\sigma}{\sigma_o} \propto \left(\frac{r}{c}\right)^{-0.24} \tag{6.41}$$

where
r is the radius at the shoulder of the dent
c is the shoulder-to-shoulder half width
σ_o is the stress far away from the dent

As shown in Figure 6.40, the greater the ratio of r/c, the smaller the stress concentration and the longer the bearing life.

In order to reduce the stress concentration around surface dents, NSK [6.52] has developed super-TF bearings using the TF technology. This technology is a heat treatment process for optimizing the level of retained austenite in bearing materials [6.53]. It has been

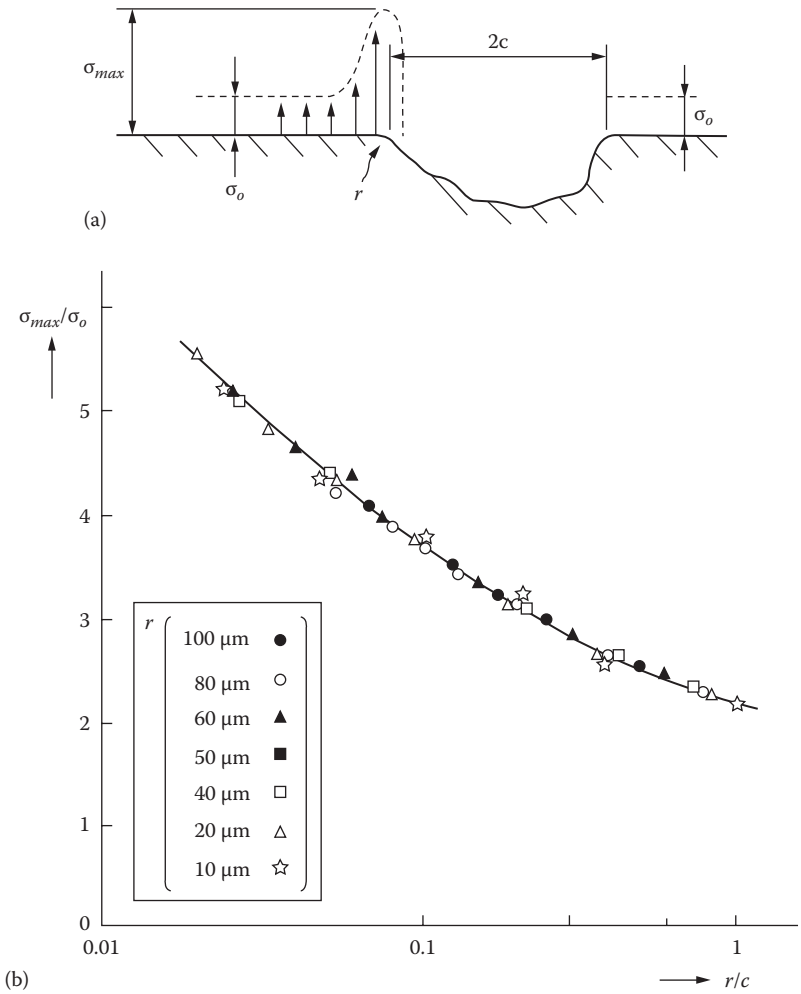

FIGURE 6.40
(a) Stress concentration around a surface dent and (b) the relationship between the stress ratio and the ration of *r/c* (U.S. Patent 4,904,094) [6.52]. (Courtesy of the U.S. Patent and Trademark Office, Alexandria, VA.)

found that the increase in the retained austenite level can significantly raise the ratio of *r/c* and thus greatly improve bearing performance and extend the bearing life.

References

[6.1] Lawrie, R. 2001. Bad bearings cause motor failure. *Electrical Construction & Maintenance (EC&M) Magazine*, February Issue. http://ecmweb.com/content/bad-bearings-cause-motor-failures.

[6.2] Stribeck, R. 1902. Die wesentlischen eigenschaften der gleit- und rollenlager (The basic properties of sliding and rolling bearings). *Zeitschrift des Vereines deutscher Ingenieure* **46**(**37**): 1341–1348 (part I), **46**(**38**): 1432–1438 (part II), and **46**(**39**): 1463–1470 (part III).

[6.3] Gu, Y. Y. 1990. *Fluid Sealing*. China Petrochemical Press, Beijing, China.
[6.4] Mayer, E. 1977. *Mechanical Seals*, 3rd edn. Newnes-Butterworth, London, U.K.
[6.5] Mendes, R. U. and Cavalca, K. L. 2014. On the instability threshold of journal bearing supported rotors. *International Journal of Rotating Machinery* **2014**: 1–17.
[6.6] Ricci, M. C. 2009. Internal loading distribution in statically loaded ball bearings, subjected to a combined radial and thrust load, including the effect of temperature and fit. *World Academy of Science, Engineering and Technology* **57**: 290–298.
[6.7] FAG. 2011. Low noise, low friction, no dust, ever: FAG generation C deep groove ball bearings. http://www.hedan.pl/download/44/low-noise-low-friction-no-dust-ever.pdf.
[6.8] New Way Precision. 2003. Air bearing application and design guide (rev D). http://www.olympic-controls.com/documents/Air Bearing Design Guide.pdf.
[6.9] Xie, X. F. 2003. Comparison of bearings: For the bearing choosing of high-speed spindle design. Technical report, Department of Mechanical Engineering, University of Utah. http://home.utah.edu/~u0324774/pdf/Comparison_of_Bearings.pdf.
[6.10] SFK. 2002. SFK sensor-bearing units—Concentrate intelligence in your motion control. Publication 5106 E. http://www.cementechnology.ir/Library/SKF.Sensor-Bearing.Units.pdf.
[6.11] Burrell, M. 2008. Bearings: Don't let them drag you down. *National Kart News*, June Issue, pp. 56–61.
[6.12] AST Bearings LLC. 2010. Technical information: Bearing materials. Document No. ENB-04-0553. http://www.astbearings.com/assets/files/Bearing-Materials-Technical-Information-Sheet_ENB-04-0553.pdf.
[6.13] Finley, W. F. and Hodowanec, M. M. 2002. Sleeve versus antifriction bearings: Selection of the optimal bearing for induction motors. *IEEE Transactions on Industry Applications* **38**(**4**): 909–920.
[6.14] GMN Bearing USA, Ltd. Deep groove radial ball bearings: Technical information. http://www.gmnbt.com/deep-groove-bearings-technical-info.htm.
[6.15] Harris, T. 2001. *Rolling Bearing Analysis*, 4th edn. John Wiley & Sons, New York.
[6.16] NIKO. Ball bearings catalogue. http://nipponkodobearings.com/English/catalogue/NIKO General Ball Bearing Catalogue.pdf.
[6.17] NTN Corporation.1999. *Ball and Roller Bearings*. Cat. No. 2202-II/E.
[6.18] Bischoff, R. F. 1982. Bearing movement preventing system. U.S. Patent 4,309,062.
[6.19] Neuhaus, B. and Watzek, M. 2013. Bearing holder. U.S. Patent Application 2013/0,169,092.
[6.20] Stribeck, R. 1907. Ball bearings for various loads. Reports from the Central Laboratory for Scientific Technical Investigation. *ASME Transaction* (**29**): 420–463.
[6.21] Palmgren, A. 1959. *Ball and Roller Bearing Engineering*, 3rd edn. SKF Industries, Philadelphia, PA.
[6.22] Oswald, F. B., Zaretsky, E. V., and Poplawski, J. V. 2012. Effect of internal clearance on load distribution and life of radially loaded ball and roller bearings. NASA/TM—2012-217115.
[6.23] Orlowski, D. 2008. Extending motor bearing life. *Pumps and System Magazine*, June Issue. http://www.pump-zone.com/topics/motors/extending-motor-bearing-life.
[6.24] The International Organization for Standardization (ISO). 2007. ISO 281:2007: Rolling bearings—Dynamic load ratings and rating life. ISO, Geneva, Switzerland.
[6.25] Harnoy, A. 2002. *Bearing Design in Machinery: Engineering Tribology and Lubrication*. CRC Press, Boca Raton, FL.
[6.26] Brake, J. T. 2011. Finding the probability distribution for failures. *Maint World* **4**: 16–21.
[6.27] Nowlan, F. S. and Heap, H. F. 1978. *Reliability-Centered Maintenance*. United Airlines Report Number AD-A066-579. Dolby Access Press, San Francisco, CA.
[6.28] Moubray, J. 1997. *RCM II Reliability-Centered Maintenance*, 2nd edn. Industrial Press Inc., New York.
[6.29] NSK. 2013. Rolling bearings. Catalog No. E1102m. http://www.jp.nsk.com/app01/en/ctrg/index.cgi?rm=pdfDown&pno=E1102.

[6.30] Mitrović, R. and Lazović, T. 2002. Influence of wear on deep groove ball bearing service life. *Facta Universitatis. Series: Mechanical Engineering* **1**(**9**): 1117–1126.
[6.31] ANSI/ABMA Standard 20-1996. 1996. Radial bearings of ball, cylindrical roller, and spherical roller types—Metric design. American Bearing Manufacturing Associate (ABMA), Washington, DC.
[6.32] Woodard, M. and Wolka, M. 2011. Bearing maintenance practices to ensure maximum life. *Proceedings of the Twenty-Seventh International Pump Users Symposium*, Houston, TX.
[6.33] Benbouzid, M. E. H. 2000. A review of induction motors signature analysis as a medium for faults detection. *IEEE Transaction on Industrial Electronics* **47**(**5**): 984–993.
[6.34] Zaretsky, E. V. 2012. How to determine bearing system life. *Machinery Lubrication*, December Issue. http://www.machinerylubrication.com/Read/29228/bearing-system-life.
[6.35] Dana Corporation. 2002. Engine bearing failure analysis guide. Form # CL77-3-402. http://www.studebaker-info.org/tech/Bearings/CL77-3-402.pdf.
[6.36] PBC Linear™. 2010. The science of self-lubrication: Debunking the myth of "lubed for life". Technical notes. http://www.pbclinear.com/Download/WhitePaper/The-Science-of-Self-Lubrication.pdf.
[6.37] Honeycutt, J. 2002. Reducing motor bearing failures. *Machinery Lubrication Magazine*. May issue. http://www.machinerylubrication.com/Read/339/motor-bearing-failure.
[6.38] McNally, W. J. 2000. Ball bearing lubrication in centrifugal pumps, in *Bill McNally's Pump and Seal Manual*. McNally Institute, Dade City, FL.
[6.39] Sato, N. and Sakaguchi, T. 2010. Improvement of grease leakage prevention for ball bearings due to geometrical change of ribbon cages. *NTN Technical Review* **78**: 98–105.
[6.40] Alger, P. L. and Samson, H. W. 1924. Shaft currents in electric machines. *Transactions of American Institute of Electrical Engineers* **43**: 235–245.
[6.41] Prashad, H. 1991. Theoretical analysis of capacitive effect of roller bearings on repeated starts and stops of a machine under the influence of shaft voltages. *ASME Journal of Tribology* **114**(**4**): 818–823.
[6.42] Schiferl, R. and Melfi, M. 2005. Bearing current problems: Causes, symptoms, and solutions. *Electrical Construction & Maintenance (EC&M)*, September Issue. http://ecmweb.com/content/bearing-current-problems-causes-symptoms-and-solutions.
[6.43] Erdman, J., Kerkman, R. J., Schlegel, D., and Skibinski, G. 1995. Effect of PWM inverters on AC motor bearing currents and shaft voltages. *IEEE APEC Conference*, Dallas, TX.
[6.44] Hoppler, R. and Errath, R. A. 2007. Motor bearings: The bearing necessities. *Global Cement Magazine*, October Issue, pp. 26–32. http://www05.abb.com/global/scot/scot393.nsf/veritydisplay/136d00b55a95de57c1257b35003072fa/$file/GC_Oct07_ABB-motor-bearings_proof_v2b.pdf.
[6.45] Oh, H. W. and Willwerth, A. 2008. Shaft grounding—A solution to motor bearing currents. *ASHRAE Transactions* **114**(**2**): 246–251.
[6.46] Berry, L. D. 1995. Vibration versus bearing life. *Reliability Magazine*, December Issue. http://www.atlan-tec.net/pdfs/Vibration.pdf.
[6.47] Davis, J. and Golden, H. 2010. The impact on bearing life of overtensioned belts. http://reliabilityweb.com/index.php/articles/the_impact_on_bearing_life_of_overtensioned_belts/.
[6.48] Schoen, R. R., Habetler, T. G., Kamran, F., and Bartfield, R. G. 1995. Motor bearing damage detection using stator current monitoring. *IEEE Transactions on Industry Applications* **31**(**6**): 1274–1279.
[6.49] Momono, T. and Noda, B. 1999. Sound and vibration in rolling bearings. *Motion & Control* **6**: 29–37.
[6.50] SKF. Selecting bearing size using the static load carrying capacity. http://www.skf.com/group/products/bearings-units-housings/ball-bearings/principles/selection-of-bearing-size/selecting-bearing-size-using-the-static-load-carrying-capacity/index.html.

[6.51] Bearing Catalogue. 2014. Learn the advantages of ceramic bearings over steel bearings. http://bearingcatalogue.com/ceramic-bearings.
[6.52] NSK. Large super-TF bearings. http://www.nskamericas.com/cps/rde/xchg/na_en/hs.xsl/download-bearings.html.
[6.53] Furumura, K., Matsumoto, Y., Murakami, Y., Nishida, S., Shiratani, T., and Takei, K. 1990. Ball-and-roller bearing system. U.S. Patent 4,904,094.

7

Motor Power Losses

Motor power losses refer to the consumption of electrical energy not converted to useful mechanical energy. Motor power losses are important in motor design for a number of reasons: (1) Power losses in electric motor can substantially increase the temperature rise in the windings and deteriorate the performance characteristics of motor. The vast majority of power losses are converted into heat energy, which must be eventually dissipated from the motor to the surrounding environment. Consequently, it is highly desired to understand the mechanisms of various power losses for providing the best suitable solution of motor cooling. (2) The motor efficiency is defined as the ratio of the power output (which equals the power input minus the power losses) to the power input. Thus, the higher the power losses, the lower the motor efficiency. From an economic standpoint, higher power losses are always associated with increased motor costs. (3) The conversion of power losses into heat energy may cause an excessive internal temperature of motor. Thus, power losses have a strong impact on the selection of cooling modes that are required to keep the motor temperature below the maximum allowed value. (4) Temperature is a major cause of degradation of insulation materials. Excessive motor temperature can accelerate the aging of winding insulations and thus reduce their lifetime. (5) High temperature can significantly reduce magnetic properties of PMs to lower the performance of PM motors. As the temperature becomes higher than the Curie temperature of the magnet, all magnetic properties are eventually lost. (6) High temperature may cause bearing grease to deteriorate, leaving motor bearings without adequate lubrication. (7) A small portion of the total power loss may be converted to sound energy, leading to high acoustic noise emitted from the motor.

In recent years, with a continuous and ever-increasing demand for high-performance and high-efficiency electric motors, a great deal of effort has been directed toward determining power losses of rotating electric machines.

The motor power losses can be briefly defined as no-load and load losses. The major no-load losses, which do not require load currents, include (1) core losses, also called magnetic losses, because alternating magnetic flux produces both hysteresis losses and eddy-current losses in the stator and rotor cores, magnets, and other motor components and (2) mechanical losses that include friction and windage losses. The primary load losses are (1) resistive losses in the stator windings, (2) resistive losses in the rotor windings, and (3) stray load losses that consist of various kinds of losses that are not mentioned previously.

Benhaddadi et al. [7.1] have provided the estimation on the contribution of each type of losses to the total power loss. Their results show that the largest contribution comes from the stator winding (35%). The following are the rotor winding and magnetic losses; each accounts for 20%. The mechanical losses are the lowest, only accounting 10%. GE [7.2] recently released the typical power loss distribution data for a four-pole motor. The largest contribution is still found from stator windings, taking 33% of the total loss. This is consistent with the value of Benhaddadi as 35%. The mechanical (14%) and stray load losses (22%) are moderately higher than but the rotor windings (15%) and magnetic losses (16%) slightly lower than the data in [7.1]. The comparison of the contribution data from these two references is presented in Figure 7.1.

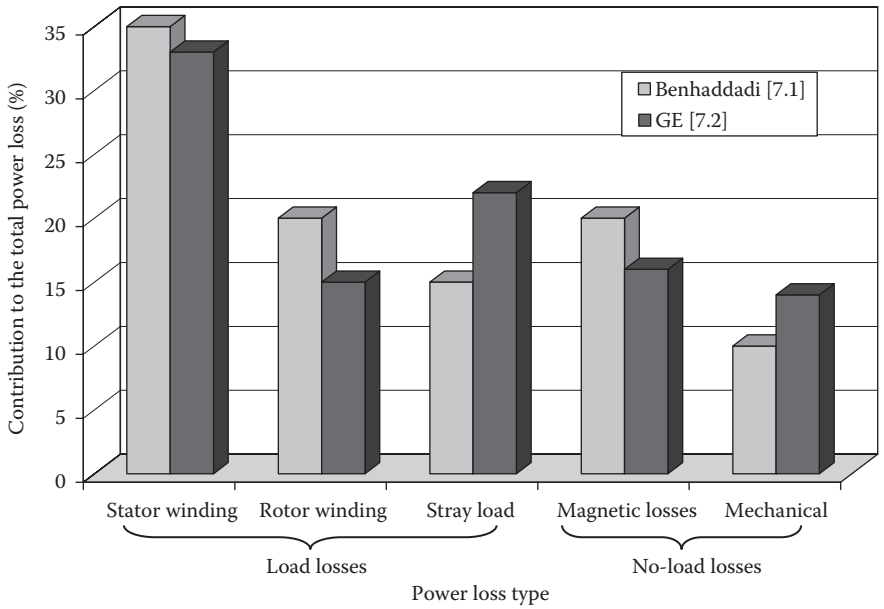

FIGURE 7.1
Comparison of power loss distributions in electric motors.

7.1 Power Losses in Windings due to Electric Resistance in Copper Wires

The most significant energy loss in a motor comes from electrical resistivity of the stator winding and either the rotor winding for a wound-rotor induction motor or the squirrel cage for a squirrel cage induction motors. For common conducting materials such as copper and aluminum, electric current is produced by the movement of electrons from one atom to another under the influence of an electric field. During this process, the migrations of free electrons cause many collisions with the captive electrons in the conducting materials. These collisions consume some energy of electrons as the basic cause of resistance.

In a DC motor, current flows uniformly across the entire cross section of the winding wires. The electrical resistance R_{DC} of a conductor is proportional to the resistivity of the material ρ (in Ω·m) and the conductor length l (in m) and inversely proportional to the cross-sectional area of the conductor A (in m^2), that is,

$$R_{DC} = \frac{\rho l}{A} \tag{7.1}$$

It must be noted that material resistivity is strongly influenced by temperature. A higher temperature typically results in more collisions between electrons, and hence, the higher resistance to electric current. For a common conducting material such as copper and aluminum, electric resistivity is approximately expressed as

$$\rho(T) = \rho(T_o)[1 + \alpha(T - T_o)] \tag{7.2}$$

where
T_o is the reference temperature
α is the temperature coefficient of resistance of the material

Thus, the resistive winding loss can be simply calculated as

$$P_r = I^2 R_{DC} = \frac{V^2}{R_{DC}} \tag{7.3}$$

where
I is the electric current flowing through the winding
V is the voltage across the winding

If there is enough space in the winding slots, the resistive winding loss can be reduced by adopting a conductor with a larger diameter.

For an AC motor, Equation 7.3 can be expressed as

$$\bar{P}_r = i_{rms}^2 R_{AC} = \frac{v_{rms}^2}{R_{AC}} \tag{7.4}$$

where
$\bar{P}_r$ is the averaged power loss
R_{AC} is the AC electrical resistance
i_{rms} and v_{rms} are the RMS current and voltage, respectively

For AC current with sine waves, i_{rms} and v_{rms} can be expressed as

$$i_{rms} = \frac{i_{peak}}{\sqrt{2}}; \quad v_{rms} = \frac{v_{peak}}{\sqrt{2}} \tag{7.5}$$

respectively. In Equation 7.5, i_{peak} and v_{peak} are the peak value of AC current and voltage, respectively.

The resistance loss in an AC motor increases with frequency due to the skin effect, which refers to the tendency of AC current to distribute in the thin layer at the conductor's outer surface. The skin depth is defined as the distance below the conductor surface where the current density has decayed to e^{-1} ($e^{-1} = 0.368$) of its value at the surface (Figure 7.2). The skin depth δ (in m) varies as the square root of the electrical resistivity and the inverse square root of frequency and relative permeability:

$$\delta = \sqrt{\frac{\rho}{\pi f \mu_r \mu_o}} \tag{7.6}$$

where
f is the frequency (Hz)
μ_r is the relative permeability
$\mu_o = 4\pi \times 10^{-7}$ (H/m) is the permeability of free space

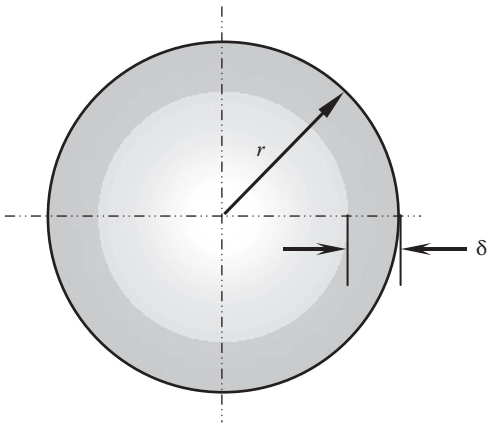

FIGURE 7.2
Skin depth of a conducting magnet wire, where $\delta < r$.

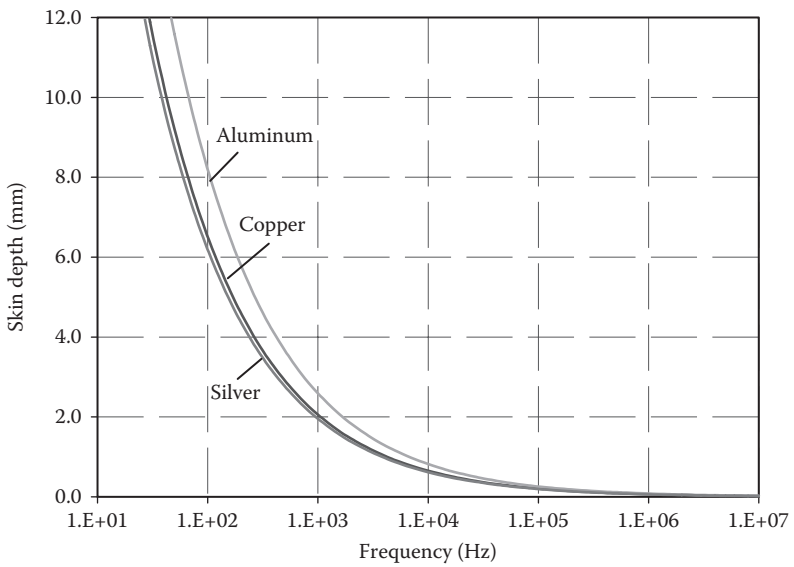

FIGURE 7.3
Variations of skin depth with frequency for different materials.

The variations of skin depth with frequency for different materials are displayed in Figure 7.3. It has shown that the skin depths for all materials reduce sharply for $f < 1$ kHz. As f becomes larger than 100 kHz, the changes in the skin depth can be ignored. For good conducting materials, skin depth varies as the inverse square root of the material conductivity. This indicates that better conducting materials have a reduced skin depth.

The ratio of AC resistance to DC resistance can be simply determined as

$$\frac{R_{AC}}{R_{DC}} = \frac{1}{2\delta/r - (\delta/r)^2} \tag{7.7}$$

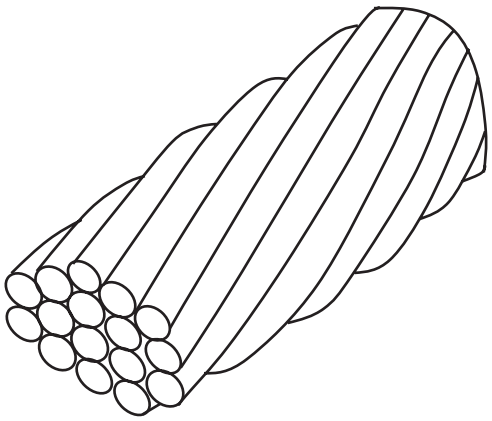

FIGURE 7.4
Litz wires used for motor windings for minimizing skin effect.

In case that $\delta \ll r$, Equation 7.7 can be simplified as

$$\frac{R_{AC}}{R_{DC}} \approx \frac{r}{2\delta} \tag{7.8}$$

This equation indicates that the smaller the skin depth, the higher the ratio of AC to DC resistance. More advanced and complete expression of the resistance ratio was derived by Ramo et al. [7.3].

The skin effect appears as the skin depth δ is smaller than the wire radius r. In order to minimize the resistance loss for high-frequency applications, the copper windings are made with multiple strands, insulated from each other and in a weaving or twisting pattern (so-called Litz wire, see Figure 7.4). It was found that the slotless structure combined with a 75-strand Litz wire in a superhigh-speed cryogenic PM motor can significantly reduce iron loss in the rotor without increase in eddy-current loss in the winding [7.4].

The resistive winding loss is the loss that is proportional to the motor load. With the increase in the motor torque, the electric current through the motor windings increases, so does the resistive winding loss. In most applications, the resistive winding loss is predominant among all losses, except motors having very high rotating speeds.

7.2 Eddy-Current and Magnetic Hysteresis Losses

7.2.1 Eddy-Current Loss

From Faraday's law of induction, when magnetic flux changes through a loop of area due to any reasons (the magnetic field change, the loop area change, or the orientation of the loop relative to the magnetic field change), an induced EMF is developed along the loop. Thus, circulating currents, that is, eddy currents, are induced in bulk conductors moving through a magnetic field.

Eddy currents are often undesirable because they consume a considerable amount of energy to internal energy without making useful work. For electric motors, eddy-current loss is caused by local circulating currents induced in conductive core components and results in the rise in temperature.

Eddy currents are affected by the electrical resistance of ferromagnetic materials in which eddy currents flow. In order to reduce eddy-current loss, both stator and rotor cores are made of a stack of laminations, which are insulated by nonconducting materials such as lacquer or metal oxide. This layered structure prevents large current loops and effectively confines eddy currents to small loops in individual layers. The sum of the individual eddy current in each piece of the laminated core is much less than that in the solid iron core. Furthermore, the addition of the silicon element into the core steel increases electrical resistance, leading to the further decrease of eddy current.

7.2.2 Magnetic Hysteresis Loss

Magnetic hysteresis phenomena occur in ferromagnetic materials. As an external alternating magnetic field is applied to a ferromagnetic material, it forces the atomic dipoles in the material to align themselves with the magnetic field. When the magnetic field suddenly changes its orientation relatively with the material, the atomic dipoles must realign themselves to accommodate such change. Because the ferromagnetic material tends to retain some degree of magnetization, known as the magnetic hysteresis, it must take a certain amount of energy to overcome such a hysteresis to adjust the atomic dipoles according to the change of the external magnetic field. In fact, hysteresis losses depend on several factors including the power frequency, the peak flux density, the material of core steel, and the orientation of the magnetic flux with respect to the grain structure of the steel.

7.2.3 Calculations of Eddy-Current and Magnetic Hysteresis Losses

Maxwell's equations, which perfectly describe classical electromagnetic phenomena, consist of four equations: Faraday's law of induction, Ampère–Maxwell's law, and Gauss's laws for the electric and magnetic fields, that is,

Faraday's law of induction

$$\nabla \times \mathbf{E} = -\frac{\partial \mathbf{B}}{\partial t} \tag{7.9}$$

Ampère–Maxwell's law

$$\nabla \times \mathbf{H} = \mathbf{J} + \frac{\partial \mathbf{D}}{\partial \mathbf{t}} \tag{7.10}$$

Gauss's law for electric field

$$\nabla \cdot \mathbf{D} = \rho_e \tag{7.11}$$

Gauss's law for magnetic field

$$\nabla \cdot \mathbf{B} = 0 \tag{7.12}$$

In Maxwell's equations, **E** and **H** are the electric and magnetic field intensities, **D** and **B** are the electric and magnetic flux densities, respectively, **J** is the electric current density, and ρ_e is the electric charge density of any external charges.

The relationships between the current density **J** and the electric field intensity **E**, electric flux density **D** and the electric field intensity **E**, and the magnetic flux density **B** and magnetic field intensity **H** are given as

$$\mathbf{J} = \sigma\mathbf{E} \tag{7.13a}$$

$$\mathbf{D} = \varepsilon\mathbf{E} \tag{7.13b}$$

$$\mathbf{B} = \mu\mathbf{H} \tag{7.13c}$$

where

σ is the electrical conductivity
ε is the electric permittivity
μ is the magnetic permeability

Using Equations 7.9 and 7.10, it can be derived that

$$\nabla\cdot(\mathbf{E}\times\mathbf{H}) = \mathbf{H}\cdot(\nabla\times\mathbf{E}) - \mathbf{E}\cdot(\nabla\times\mathbf{H}) = -\mathbf{H}\cdot\frac{\partial\mathbf{B}}{\partial t} - \mathbf{E}\cdot\left(\mathbf{J} + \frac{\partial\mathbf{D}}{\partial\mathbf{t}}\right) \tag{7.14}$$

Integrating both sides over a closed volume V surrounded by the surface S, Equation 7.14 is expressed in the integrated form,

$$\int_V \nabla\cdot(\mathbf{E}\times\mathbf{H})\,dV = -\int_V \left[\mathbf{H}\cdot\frac{\partial\mathbf{B}}{\partial t} + \mathbf{E}\cdot\left(\mathbf{J} + \frac{\partial\mathbf{D}}{\partial t}\right)\right] dV \tag{7.15}$$

Using the divergence theorem, it yields

$$\int_S (\mathbf{E}\times\mathbf{H})\,d\mathbf{S} = -\int_V \left[\mathbf{H}\cdot\frac{\partial\mathbf{B}}{\partial t} + \mathbf{E}\cdot\left(\mathbf{J} + \frac{\partial\mathbf{D}}{\partial t}\right)\right] dV \tag{7.16}$$

The left side of Equation 7.16 represents the energy flow into the volume per unit time. The first and second terms at the right-hand side represent the energy stored and dissipated per unit time, respectively. Thus, the total energy loss in the volume over a complete cycle of time becomes

$$P = \int_V \int_t \left[\mathbf{H}\cdot\frac{\partial\mathbf{B}}{\partial t} + \mathbf{E}\cdot\left(\mathbf{J} + \frac{\partial\mathbf{D}}{\partial t}\right)\right] dt\,dV \tag{7.17}$$

Since the displacement current **D** is typically relevant only at radio frequencies (in the MHz regime), the term $\partial\mathbf{D}/\partial\mathbf{t}$ can be ignored in Equation 7.17.

Using Equation 7.13a, it gives that

$$\mathbf{E}\cdot\mathbf{J} = \frac{J^2}{\sigma} \tag{7.18}$$

Equation 7.17 can be rewritten as

$$P = \int_V \left(\int_B HdB \right) dV + \int_V \left[\int_t \left(\frac{J^2}{\sigma} \right) dt \right] dV = P_h + P_e \tag{7.19}$$

where P_h and P_e are the power losses due to hysteresis and eddy current, respectively.

Using a lumped circuit approach and assumed eddy-current paths, eddy-current loss of magnetic core (in unit of W) can be derived as [7.5]

$$P_e = \frac{\pi^2}{6} V_c B^2 f^2 a^2 \sigma = K_e V_c B^2 f^2 \tag{7.20}$$

$$K_e = \frac{\pi^2 a^2 \sigma}{6} \tag{7.21}$$

where

V_c is the volume of magnetic core in unit of m^3
a is the lamination thickness in unit of m
B is the peak flux density

Equation 7.20 has shown that eddy-current loss is proportional to the square of lamination thickness a. This indicates that eddy-current loss can be greatly reduced if thinner laminations are adopted. For instance, by reducing the lamination thickness by 20%, eddy-current loss can be reduced by 36%.

Some textbooks use eddy-current loss per unit volume, in the unit of W/m^3:

$$p_e = K_e B^2 f^2 \tag{7.22}$$

Hysteresis refers to the phenomenon in which the magnetic induction of a ferromagnetic material lags behind the changing magnetic field. When a ferromagnetic material is subjected to a magnetic field, the magnetic particles in the material tend to line up with the magnetic field. As the magnetic field keeps changing its direction, the magnetic particles try to align themselves with the magnetic field. The continuous movement of the magnetic particles thus produces molecular friction, resulting in energy loss.

Hysteresis loss is strongly affected by material electromagnetic properties. The empirical formula expressing hysteresis loss per unit volume was developed by Steinmetz [7.6–7.8] as follows:

$$P_h = K_h V_c B^n f \tag{7.23}$$

where

K_h is the hysteresis coefficient
n is the Steinmetz coefficient, which has a value between 1.6 and 2.3 for most modern magnetic materials (most commonly is around 2)
f is the frequency of magnetization

The hysteresis coefficients of some materials are listed in Table 7.1 [7.9].

TABLE 7.1

Hysteresis Coefficients of Some Metallic Materials

Material	Hysteresis Coefficient K_h (J/m³) × 10⁻²
Cast iron	27.63–40.2
Sheet iron	10.05
Cast steel	7.54–30.14
Hard cast steel	63–70.34
Silicon steel (4.8% in Si)	1.91
Hard tungsten steel	145.7
Good dynamo sheet steel	5.02
Mild steel castings	7.54–22.61
Nickel	32.66–100.5
Permalloy	0.25

From Table 7.1, it can be seen that permalloy has the lowest hysteresis coefficient, and, thus, it has been extensively used in transformer laminations and magnetic recording heads with medium or high frequencies. Silicon steel is the material having the second lowest hysteresis coefficient. As a result, hysteresis loss can be mitigated by making the motor cores with silicon steel. In practice, industrial applications of silicon steel vary in quantities from the few ounces used in small relays or pulse transformers to tons used in generators, motors, and transformers.

It is apparent that eddy-current loss P_e increases with the square of the frequency ($P_e \propto f^2$), and hysteresis loss P_h increases linearly with the frequency ($P_h \propto f$). This indicates that for high frequencies, eddy-current loss P_e becomes dominant among the total energy loss P.

Magnetic hysteresis and eddy-current losses are sometimes collectively known as iron losses or core losses. This type of losses is a significant fraction of total losses of electric motors. With advanced FEA tools, the contributions of the hysteresis and eddy-current losses in motor components can be determined fairly well. As an example, Figure 7.5 plots the data from a small motor, showing the rotor's hysteresis and eddy-current losses

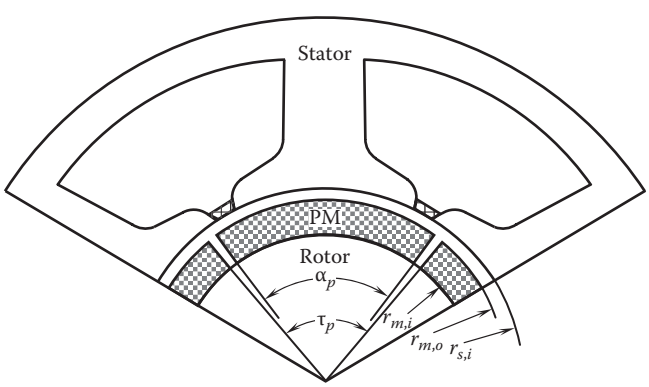

FIGURE 7.5
Eddy-current losses of PMs in PM motors having a fractional number of slots per pole.

as a function of rotor rotating speed (or equivalently frequency). The eddy-current trend shows a parabolic behavior, while the hysteresis loss follows a power law behavior as expected.

7.2.4 Losses in Stator and Rotor Iron Cores

The power losses in the stator and rotor cores consist of both hysteresis and eddy-current losses. In electric motors, the core or iron losses usually take about 20%–25% of the total power losses [7.10]. For PM motors, interior PM machines have significantly higher full-load iron losses than SPM machines.

By dividing eddy current into classical and excess eddy currents for more accurate analysis, power losses in stator and rotor iron cores can be determined as [7.11,7.12]

$$P_{core} = k_h B^2 f + K_c (Bf)^2 + K_e (Bf)^{3/2} \tag{7.24}$$

where

K_h, K_c, and K_e are the coefficients of hysteresis loss, classical eddy-current loss, and excess eddy-current loss, respectively

B is the peak flux density

The coefficients can be obtained using the curve fitting of the iron loss data from manufacturers.

There are a number of ways to reduce the core losses: (1) Utilizing a *soft* magnetic material. This is because the hysteresis loss is proportional to the shaded area enclosed by the hysteresis loop on the B–H curve. A *soft* magnetic material has a smaller shaded area within the hysteresis loop than that of a *hard* magnetic material (see Figure 7.6). (2) Using silicon grain-oriented steel. (3) Using thinner steel laminations. (4) Designing longer cores to reduce magnetic flux density.

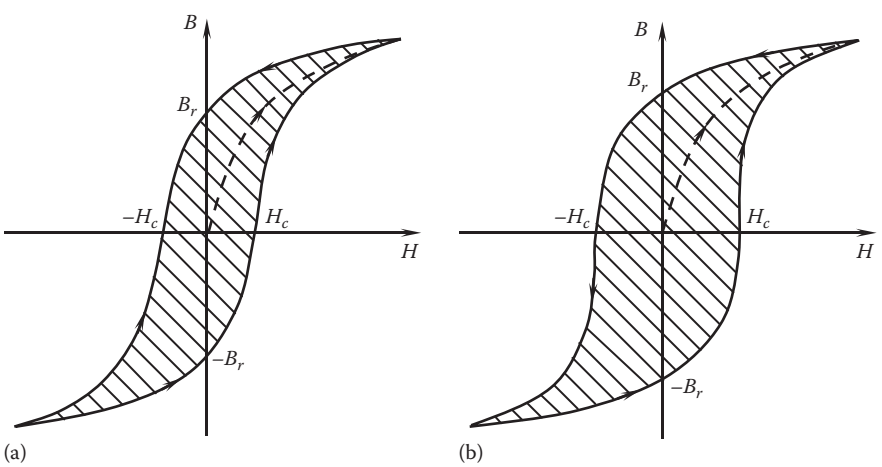

FIGURE 7.6
Magnetization hysteresis loops for different ferromagnetic materials: (a) *soft* magnetic materials with low hysteresis loss, which are desirable for motor cores to minimize power losses, and (b) *hard* magnetic materials with high hysteresis loss.

7.2.5 Losses in PMs

PM motors are extensively used in many applications for their excellent characteristics such as high power density, high efficiency, and good dynamic performance. However, eddy-current loss in PMs is often overlooked. For high-speed PM motors, eddy-current loss in PMs cannot be ignored. Eddy-current loss can be estimated as [7.13]

$$P_m \approx \frac{V_m b_m^2 B^2 f^2}{12\rho_m} \tag{7.25}$$

where
V_m is the magnet volume
b_m is the magnet width
ρ_m is the magnet resistivity ($\rho = 1/\sigma$)

Correspondingly, eddy-current loss becomes

$$P_m = K_m V_m B^2 f^2 \tag{7.26}$$

where

$$K_m = \frac{b_m^2}{12\rho_m} \tag{7.27}$$

An analytical model for predicting eddy-current losses in SPMs of PM motors was presented by Ishak et al. [7.14]. As shown in Figure 7.7, PMs are attached on the surface of the rotor that rotates at the speed of ω_r. The magnet has the inner radius $r_{m,i}$ and outer radius $r_{m,o}$.

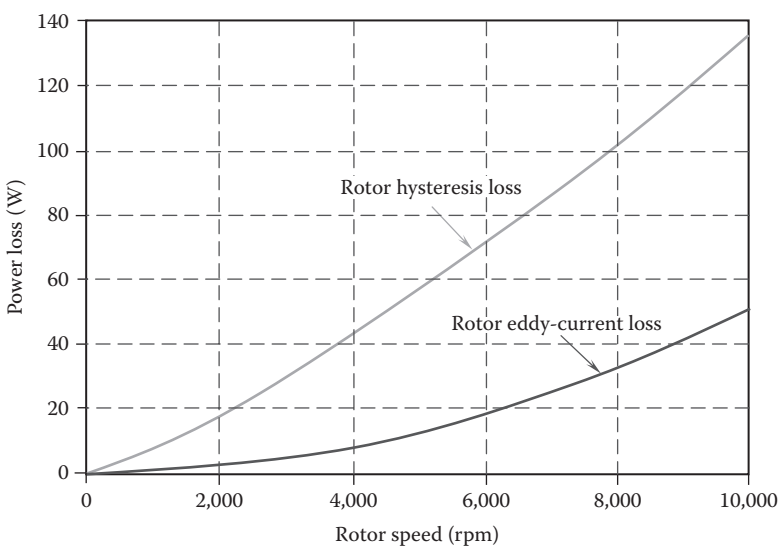

FIGURE 7.7
Rotor hysteresis and eddy-current losses as functions of rotor rotating speed from a sampler motor.

The inner stator bore radius is $r_{s,i}$. Thus, the air gap is given as the difference between $r_{s,i}$ and $r_{m,o}$. The magnet central angle corresponding to the magnet width denotes α_p.

For a PM motor with a slot number N_{slot} and pole number $2p_r$ (where p_r is the number of pole pairs), the number of slots per pole gives

$$n_{slot} = \frac{N_{slot}}{2p_r} \tag{7.28}$$

When n_{slot} is a noninteger number, the eddy-current loss per unit axial length in each magnet can be predicted as

$$P_m = 2p_r \frac{\omega_r}{2\pi} \int_0^{2\pi/\omega_r} \int_{r_{m,i}}^{r_{m,o}} \int_{-(\alpha_p/2)}^{\alpha_p/2} \rho_m J_m^2 r dr d\theta dt = \sum_u \sum_v (P_{cuv} + P_{auv}) \tag{7.29}$$

where

u is the time-harmonic order in the phase current waveform
v is the space-harmonic MMF order
ρ_m is the electrical resistivity of the magnets

The variables P_{cuv} and P_{auv} are given by

$$P_{cuv} = \frac{\mu_0^2 \alpha_p}{\rho_m} p_r \sum_u \sum_v \frac{J_{uv}^2 (up_r \pm vp_s)^2 \omega_r^2}{\left[1 - (r_{m,i}/r_{s,i})^{2vp_s}\right]^2 (vp_s)^2}$$
$$\times \left\{ \left(\frac{r_{m,o}}{r_{s,i}} \right)^{2vp_s} \frac{r_{s,i}^2 r_{m,o}^2}{2vp_s + 2} \left[1 - \left(\frac{r_{m,i}}{r_{m,o}} \right)^{2vp_s+2} \right] + \left(\frac{r_{m,i}}{r_{s,i}} \right)^{2vp_s} r_{s,i}^2 (r_{m,o}^2 - r_{m,i}^2) + \left(\frac{r_{m,i}}{r_{s,i}} \right)^{2vp_s} r_{s,i}^2 r_{m,i}^2 F_v \right\} \tag{7.30}$$

$$P_{auv} = \left[-\frac{8\mu_0^2}{\alpha_p \rho_m} p_r \sum_u \sum_v \frac{J_{uv}^2 H_v^2}{\left[1 - (r_{m,i}/r_{s,i})^{2vp_s}\right]^2 (vp_s)^4} \frac{(up_r \pm vp_s)^2 \omega_r^2}{(r_{m,o}^2 - r_{m,i}^2)} \sin^2 \left(vp_s \frac{\alpha_p}{2} \right) \right] \tag{7.31}$$

where p_s is the number of pole pairs in the stator winding MMF. In the above equations,

$$F_v = \begin{cases} \dfrac{\left(\dfrac{r_{m,o}}{r_{m,i}} \right)^{-2vp_s+2} - 1}{-2vp_s + 2} & \text{for } vp_s \neq 1 \\ \ln \left(\dfrac{r_{m,o}}{r_{m,i}} \right) & \text{for } vp_s = 1 \end{cases} \tag{7.32}$$

$$H_v = \left(\frac{r_{m,o}}{r_{s,i}} \right)^{vp_s} \frac{r_{s,i} r_{m,o}^2}{vp_s + 2} \left[1 - \left(\frac{r_{m,i}}{r_{m,o}} \right)^{vp_s+2} \right] + \left(\frac{r_{m,i}}{r_{s,i}} \right)^{vp_s} r_{s,i} r_{m,i}^2 E_v \tag{7.33}$$

where

$$E_v = \begin{cases} \dfrac{\left(\dfrac{r_{m,o}}{r_{m,i}}\right)^{-vp_s+2} - 1}{-vp_s + 2} & \text{for } vp_s \neq 2 \\ \ln\left(\dfrac{r_{m,o}}{r_{m,i}}\right) & \text{for } vp_s = 2 \end{cases} \tag{7.34}$$

This model has been validated by FEA.

7.2.6 Power Losses in Other Core Components

Eddy-current and hysteresis losses may occur in other core components such as stator end plates. In most cases, the contributions of the losses from these components to the total system power loss are relatively small and thus can be ignored in design.

7.3 Mechanical Friction Losses

Mechanical losses in an electric motor refer to the losses due to mechanical friction between two or among more motor components as they contact each other and have relative movements.

Whenever there is relative motion of two surfaces in contact, there is frictional resistance between two surfaces. The friction force opposes the relative motion of two bodies. The friction losses are independent of load and dependent on the speed of the machine. For the electric rotating machinery, a minimum of friction is highly desired.

7.3.1 Bearing Losses

Bearings are key components for rotating machinery to support rotating components with as little friction as possible. In normal operation, bearing rolling elements (balls or rollers) spin and slide between the inner and outer raceways (Figure 7.8). Therefore, the frictional resistance is produced between the rolling elements and their contact components such as the raceways, the cage, the rubbing seal (if present), and the lubricant (Figure 7.9). It has been estimated that among the total power losses of motor-driven equipment (e.g., pumps, fans, and compressors), about 20% of the loss is due to various mechanical losses, and of this, roughly 20% is attributed to bearings. This indicates that the bearing loss counts for about 4% of the total power losses [7.15].

There are a number of factors impacting on the resistance to rotation of the bearing, for instance, the bearing load, the shaft rotating speed, the bearing dimensions, the roughness of the rolling elements and raceways, the lubrication condition, and the lubricant properties.

As an important performance index, the friction torque, defined as a resistance torque when a rolling bearing rotates, has a strong impact on the bearing's working condition and lifetime. The early approach to calculate the friction torque was proposed by

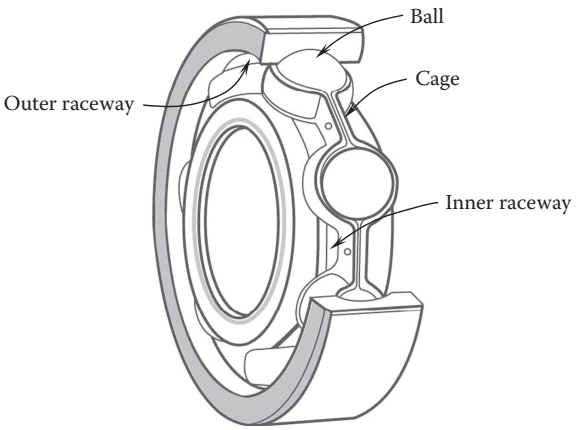

FIGURE 7.8
Ball bearing structure.

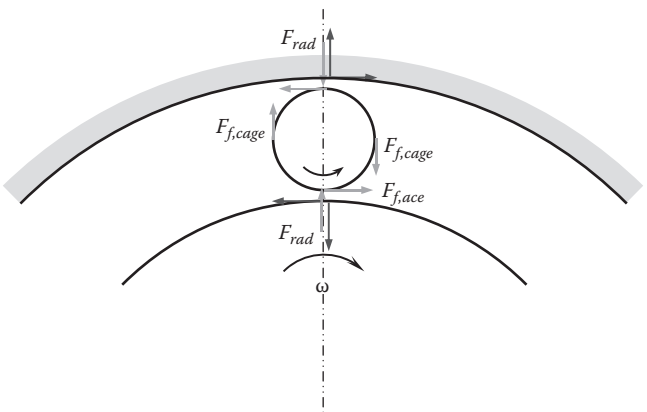

FIGURE 7.9
Bearing losses due to friction between balls and raceways, balls and the cage, and balls and the lubricant.

Palmgren [7.16,7.17]. In this approach, the total friction torque is the sum of the load friction torque T_l and the viscous friction torque T_v, that is,

$$T = T_l + T_v \tag{7.35}$$

The load friction torque is determined empirically as

$$T_l = f_1 F_\beta D_m \tag{7.36}$$

where
F_β depends on the magnitude and direction of the applied load
D_m is the bearing mean diameter, $D_m = (D_i + D_o)/2$
f_1 is a factor depending on the bearing type and bearing load expressed as

$$f_1 = z\left(\frac{F_s}{C_s}\right)^y \tag{7.37}$$

where
F_s is the static equivalent load
C_s is the basic static load rating
z and y are constants, depending on the bearing type

For radial deep-groove ball bearings, $z = 0.0004–0.0006$ and $y = 0.55$.

For bearings that operate at moderate speeds, the viscous friction torque can be estimated as

$$T_v = 10^{-7} f_o(\nu_o n)^{2/3} D_m^3 \quad \nu_o n \geq 2000 \tag{7.38}$$

$$T_v = 160 \times 10^{-7} f_o D_m^3 \quad \nu_o n < 2000 \tag{7.39}$$

where
ν_o is the kinematic viscosity of lubricant in centistokes
n is the bearing rotating speed in rpm
f_o is a factor depending on the bearing type and the lubrication method

In recent years, based on more advanced computational models, the new approach has been developed by SKF to calculate the total frictional moment (in units of N-mm) with the identified four sources of friction in every contact occurring in the bearing [7.18]:

$$M = \phi_{ish}\phi_{rs}M_{rr} + M_{sl} + M_{seal} + M_{drag} \tag{7.40}$$

where
ϕ_{ish} is the inlet shear heating reduction factor
ϕ_{rs} is the kinematic replenishment/starvation reduction factor
M_{rr} is the rolling frictional moment
M_{sl} is the sliding frictional moment
M_{seal} is the frictional moment of seal
M_{drag} is the frictional moment of drag losses, churning, splashing, etc.

The reduction factors ϕ_{ish} and ϕ_{rs} are introduced in the new friction model to account for the effects of inlet shear heating reduction and high-speed replenishment/starvation and of rolling friction, respectively.

The rolling frictional moment M_{rr} can be estimated as

$$M_{rr} = G_{rr}(vn)^{0.6} \tag{7.41}$$

where
n is the bearing rotating speed in rpm
v is the kinematic viscosity of the lubricant at the operating temperature
G_{rr} depends on the bearing type, the bearing mean diameter D_m [where $D_m = (D_i + D_o)/2$], the radial and axial loads, F_r and F_a, respectively.

TABLE 7.2

Sliding Friction Coefficient μ_{sl}

Bearing Type	Lubrication	μ_{sl}
Ball	Mineral oils	0.05
	Synthetic oils	0.04
	Transmission fluids	0.1
Cylindrical roller	—	0.02
Tapped roller	—	0.002

The sliding frictional moment M_{sl} is given as

$$M_{sl} = \mu_{sl} G_{sl} \tag{7.42}$$

where

μ_{sl} is the sliding friction coefficient (see Table 7.2)

G_{sl} depends on the bearing type, the bearing mean diameter D_m, and the radial and axial loads, F_r and F_a, respectively.

The bearing seal frictional moment M_{seal} can be estimated as

$$M_{seal} = K_1 D_s^{\alpha} + K_2 \tag{7.43}$$

where

K_1 is a constant depending on the bearing type

K_2 is a constant depending on bearing and seal type

D_s is the seal counterface diameter

α is an exponent depending on bearing and seal type

The friction torque of drag losses T_{drag} are

$$M_{drag} = V_M K_{ball} D_m^5 n^2 \quad \text{for ball bearing} \tag{7.44a}$$

$$M_{drag} = 10 V_M K_{roll} w D_m^4 n^2 \quad \text{for roller bearing} \tag{7.44b}$$

where

V_M is a function of the oil level

w is the bearing width

K_{ball} and K_{roll} are the ball- and roller-related constants, respectively,

$$K_{ball} = \frac{i_{rw} K_z (D_o + D_i)}{D_o - D_i} \times 10^{-12} \tag{7.45}$$

$$K_{roll} = \frac{K_L K_z (D_o + D_i)}{D_o - D_i} \times 10^{-12} \tag{7.46}$$

where

i_{rw} is the number of ball rows

K_z and K_L are the bearing-type and roller-bearing-type related geometry constants, respectively

The total power loss in a bearing as a result of bearing friction can be obtained using the empirical formula [7.19]

$$P_b = (1.05\times10^{-4})Mn \tag{7.47}$$

where
n is the bearing rotating speed (in rpm)
M is the total frictional moment of the bearing (in N m)

7.3.2 Sealing Losses

Some motors work under harsh environmental conditions. In order to ensure motor's normal operation, mechanical seals are installed on motor shafts to prevent foreign contamination such as dusts and wetness from the outside. When a shaft rotates, the seal tips must always exert a certain radial load on the shaft surface, resulting in friction losses at the sealing locations.

The friction force on the shaft is obtained by integrating the shear stress τ over the shaft surface:

$$F_f = R\int_0^L\int_0^{2\pi}\tau\, d\theta\, dz \tag{7.48}$$

Thus, the sealing losses are

$$P_{seal} = 2\pi RF_f\mu n = 2\pi R^2\mu n\int_0^L\int_0^{2\pi}\tau d\theta\, dz \tag{7.49}$$

where
R is the shaft radius
μ is the friction coefficient
n is the shaft rotating speed in units of rpm

7.3.3 Brush Losses

In a brushed motor such as an induction DC motor, brushes are in contact with the commutator to carry current to coils. The commutator is the rotary electrical switch, which reverses the direction of electric current periodically between the rotor and the external circuit. In general, brush losses consist of two parts. One is the electric resistance, consisting of the contact resistance occurring at the brush–commutator interface and the electric resistance through the graphite brushes. The power loss due to the contact resistance depends on the contact pressure, contact surface area, surface smoothness, and contamination condition. The I^2R power loss depends on the brush material and brush temperature. Another is the mechanical friction resistance due to the sliding contact of the brushes on the commutator, causing the friction loss. This type of power loss is proportional to the brush contact pressure p_c, kinetic friction coefficient between the brush and commutator μ_f, contact area A_c, and commutator tangential speed $r\omega$, that is,

$$P_b = \mu_f p_c A_c(r\omega) \tag{7.50}$$

where ω is the commutator rotating speed in units of rad/s.

The combination of these two effects results in heating at the brush contact interface and in the brush. Brush wear is resulted from both the mechanical friction and electrical erosion.

7.4 Windage Losses

Windage in a rotating electric machine is defined as the resisting influence of fluid (air or liquid) against not only rotating but also stationary components, creating power losses. In an electric motor, the windage power loss P_w increases exponentially as a function of the rotor rotating speed ω and the rotor radius r_r. In practice, windage losses of electric motors are very important in the motor design and optimization, primarily consisting of the following components:

- The friction loss due to the viscous shear effect in the fully developed turbulent flow. It was reported that such a loss could be up to 30% of the total windage loss.
- The dynamic loss (or rotor body loss in some references) due to driving air in the air gap. The dynamic loss depends strongly upon the thermophysical properties of air such as density and viscosity and, in turn, the air temperature in the rotor–stator air gap.
- The loss associated with the stator slots with unfilled openings. The penetration of the air flow into the slot openings and the formation of the flow recirculations in such slot openings can have complicated influence on energy loss.
- The loss associated with the roughness on rotor surfaces.
- The windage loss of some motor components such as fans.
- The ventilation path loss.

In practical engineering design, it is highly desired to minimize these losses to enhance the machine performance and efficiency.

Windage losses can be very significant for high-speed motors due to the high windage friction. There are three components of velocity in the air gap of electric motors: (1) tangential flow due the rotor rotation, (2) axial cooling flow passing through the air gap, and (3) Taylor vortices due to centrifugal forces. It is the reaction among these velocity components that determines the complex velocity field in the air gap. The importance of each velocity component depends on rotor rotating speed, cooling air flowrate, thermophysical properties of coolant (particularly density, specific heat, and thermal conductivity), rotor and stator geometries, and air-gap dimension. The velocity and pressure fields at the end-winding regions are extremely complex because of a number of factors: a large number of components, windings with irregular geometries and existing voids inside the windings, complexity in cooling flow paths, splitting and mixing of coolant, and interaction between rotor-induced flows and nonrotating flows from stationary sections [7.20]. Modern motors are often designed to small-volume, high-speed machines to increase power design and reduce overall weight. These high-speed machines may lead to a small air gap between the rotor and stator. All these factors can result in high windage loss.

Windage losses vary on a case-by-case basis, depending largely on machine type, size, rated power, coolant type, cooling methods, and many others. As an example shown in

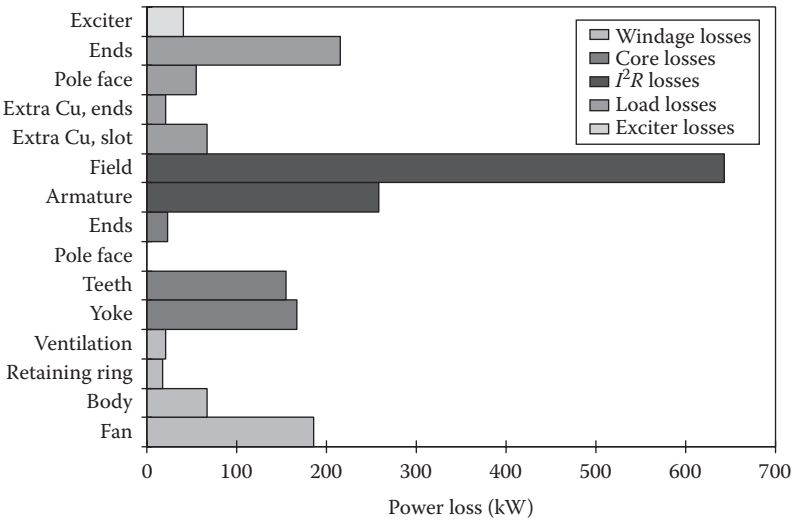

FIGURE 7.10
Various power losses for a high-power electric machine (machine *A*).

Figure 7.10 for a large-size, high-power electric machine, the overall windage loss accounts for 15.1% to the total power loss of the machine. However, for some improperly designed machines, the contribution of windage losses to the total power loss can be very large. As an example shown in Figure 7.11, the overall windage loss accounts for more than one-third, up to 37.6%. The comparison of power losses of these two machines is presented in Table 7.3.

Because of the complicated nature of the flow field inside a motor, it becomes more popular today to use CFD tools to determine the windage losses of electric motors.

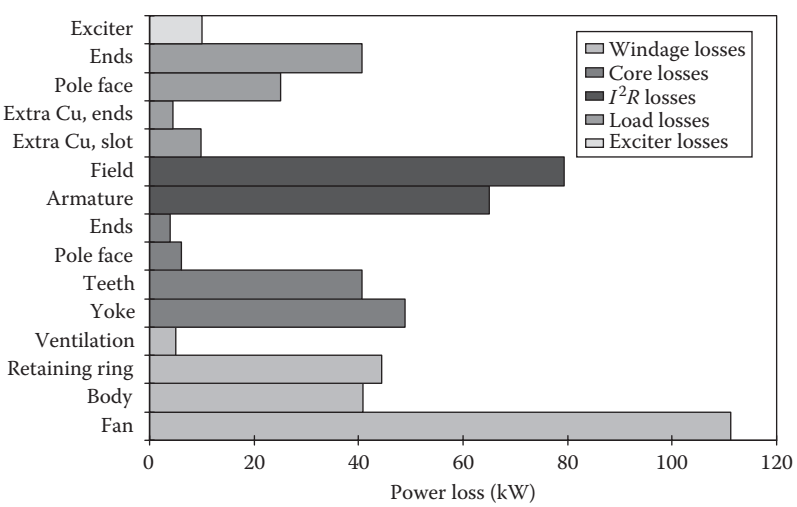

FIGURE 7.11
Various power losses for a high-power electric machine (machine *B*).

TABLE 7.3

Comparison of Power Losses in Two Large-Size, High-Power Electric Machines

Component Loss	Machine 1 Power Loss (kW)		Machine 1 Power Loss (kW)	
Fan	186 (9.6%)	Windage 291.7 (15.1%)	111.3 (20.8%)	Windage 201.5 (37.6%)
Rotor body	67.2 (3.5%)		40.8 (7.6%)	
Retaining ring	17.5 (0.9%)		44.5 (8.3%)	
Ventilation	21 (1.1%)		4.9 (0.9%)	
Yoke	167.5 (8.7%)	Iron (core) 345.4 (17.8%)	48.9 (9.1%)	Iron (core) 99.6 (18.6%)
Teeth	155.3 (8.0%)		40.6 (7.6%)	
Pole face	0 (0%)		6.1 (1.1%)	
Ends	22.6 (1.2%)		4 (0.8%)	
Armature	258 (13.3%)	Copper (I^2R)	65 (12.1%)	144.4
Field	643 (33.2%)	901 (46.5%)	79.4 (14.8%)	(27.0%)
Extra Cu, slot	66.6 (3.4%)	Load 358 (18.5%)	9.9 (1.9%)	Load 80.1 (15.0%)
Extra Cu, ends	21 (1.1%)		4.5 (0.8%)	
Pole face	54.7 (2.8%)		25.1 (4.7%)	
Ends	215.7 (11.1%)		40.6 (7.6%)	
Exciter	41 (2.1%)	Exciter (2.1%)	10 (1.9%)	Exciter (1.9%)
Total	1937.1		535.6	

7.4.1 Windage Loss due to Rotating Rotor

In a high-speed rotating system, windage loss is associated with pumping forces of the rotor in imparting energy to air at the rotor–stator annular gap. The magnitude of windage loss in electric motors varies widely from motor type, rotor geometry, rotor surface speed, air-gap depth, fluid properties, and rotor and stator surface finishes. In practice, windage loss due to rotating rotor is accounted for a large portion of the overall windage loss in the machine, and thus, it must be addressed carefully.

7.4.1.1 Taylor Vortex

Taylor [7.21–7.23] was the first who studied the flow between two coaxial smooth cylinders of which the inner is rotating. He found that when Taylor number reaches a certain value, a steady distinctive vortex structure is developed symmetrically grouped around the axis of rotation (Figure 7.12). Since then, considerable research on the Taylor vortex flow has been devoted to the investigations for better understanding of the flow phenomena and energy losses between concentric rotating cylinders [7.24–7.30]. Ustimenlo and Zmeikov [7.28] experimentally investigated the hydrodynamics of a flow in an annular channel with an inner rotating cylinder. Based on their work, the comprehensive data of shear stress, velocity, total and static pressure were presented and correlated. A theoretical analysis of the vortex flow and heat transfer was conducted by Leont'ev and Kirdyshkin [7.29]. The comparison of the theoretical formula with the experimental data on the friction coefficient has shown good agreement in the range of Taylor numbers between 4×10^3 and 10^7.

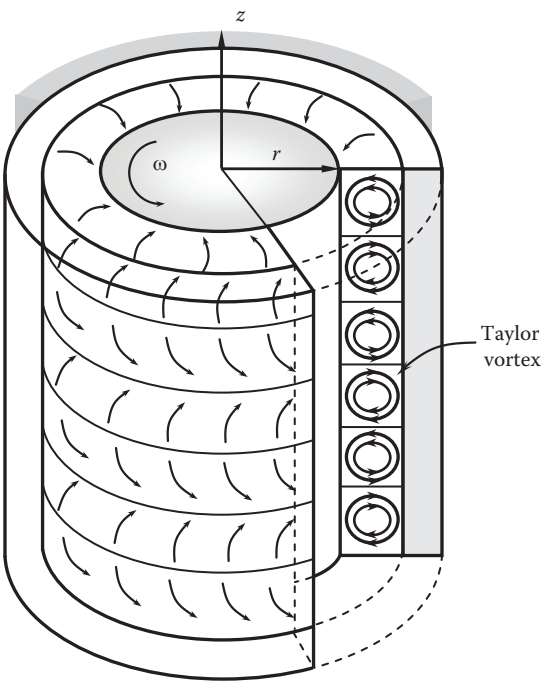

FIGURE 7.12
Flow configuration of Taylor vortices in the annular gap between two coaxial cylinders, with inner cylinder rotating and outer cylinder at rest.

As shown in Figure 7.13, radially oriented stator slots are used to mount stator windings. The stator winding in each slot is secured by a dovetail wedge, which sustains forces from the stator winding. Conventionally, the wedge is short in height, leaving the slot partially unfilled near the slot mouth with the slot opening height h_s. The stator slots distribute uniformly on the stator circumference with the slot width w_s and tooth width w_t. The air-gap depth in the radial direction is denoted by d_g. The rotor radius and stator inner radius are represented by r_r and r_s, respectively.

In fluid dynamics, Taylor number characterizes the relative importance of inertia forces to viscous force in rotating viscous fluids. As a dimensionless quantity, Taylor number is related to Couette Reynolds number Re_d as,

$$Ta = Re_d^2\left(\frac{d_g}{r_r}\right) = \frac{(\rho\omega)^2 r_r d_g^3}{\mu^2} \tag{7.51}$$

where Re_d is defined as

$$Re_d = \frac{\rho \bar{u}_\theta d_g}{\mu} \tag{7.52}$$

where

ρ and μ are the density and dynamic viscosity of air, respectively
d_g is the air-gap depth in the radial direction

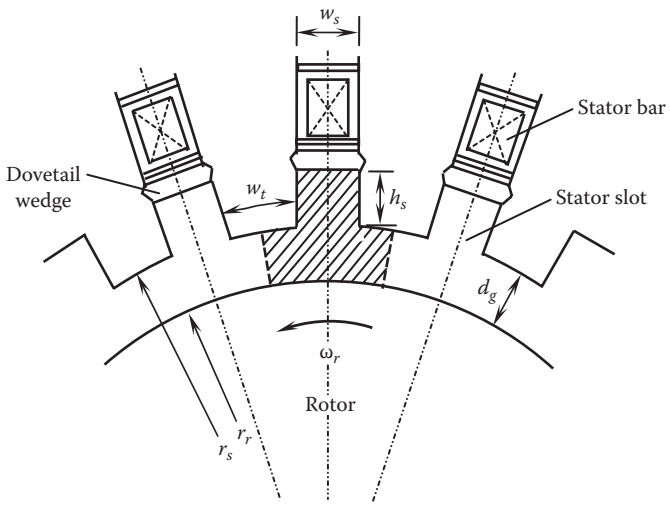

FIGURE 7.13
Geometries and configurations of air gap, state slots and teeth, dovetail wedges, and stator slot openings. The shaded area is the computational domain.

It is important to note that $\bar{u}_\theta$ is the mean swirl velocity across the stator–rotor gap, which can be obtained by integrating u_θ along the radial direction,

$$\bar{u}_\theta = \frac{1}{d_g}\int_{r_r}^{r_s} u_\theta(r)\,dr \tag{7.53}$$

The data and correlations in references [7.28] and [7.29] were combined and represented in a useful chart for friction factor for smooth rotating cylinders in a smooth coaxial enclosure without axial flow [7.30]. According to the Taylor number values, four regimes have been distinguished with a formula in each regime: laminar ($Ta \le 41$), transition ($41 < Ta \le 63$), vortex flow ($63 < Ta \le \mathrm{Ta}_{V-T}$, where Ta_{V-T} is the value at which the flow transits from the vortex-dominant flow to the turbulence-dominant flow), and turbulent ($Ta_{V-T} < Ta < \infty$).

Taylor–Couette flows between concentric rotating cylinders have been extensively studied as rotational power loss and flow instability problems. Due to the complexity of the flows in rotating machinery, a majority of the studies have assumed uniform rotor–stator gaps and smooth rotor and stator walls. In practice, windage losses and friction characteristics in electric machines are generally determined through experimental tests and numerical simulations. Analytical models that precisely predict flow fields are rather limited.

Bruckner [7.31] studied experimentally windage losses in the rotor–stator gap and gas foil bearings in electric machines. The results show an exponential rise in power loss as mean operating density is increased for both the machine windage and gas foil bearings. These losses can become increasingly significant for high-speed machines operating in high-pressure environments, especially in narrow rotor–stator gaps. Bruckner also reported that the machine windage can be nondimensionalized in terms of Taylor number and moment coefficient. Rough stator surfaces have higher torque than the smooth-walled stator.

With the CFD technique, Wild et al. [7.32] have performed experimental and computational investigations of Taylor–Couette flow. The computed flow field shows significant

variations in the axial distribution of the azimuthal shear stress due to the secondary flow associated with Taylor vortices. Three functional relations, developed by other researchers for windage torque of infinite cylinders, are found to be in good agreement with the experimental results when coupled with a correction for end wall effects. These relations are the most useful with respect to the design of rotating equipment.

It is noteworthy that rotors and stators of electric motors are not so smooth. They generally have grooves, slots, cavities, etc., on their walls. For instance, the rotor of a switch reluctance motor is shaped with several poles on the rotating cylinder. This geometry can result in a more complex mechanism of windage loss. Thus, it is important to understand and predict the effect of such structural textures on windage losses and friction characteristics.

Recently, with an increase in demands for higher performance and higher efficiency of turbomachinery and other rotary systems, a great deal of effort has been directed toward the determination of friction factors on rotating and stationary surfaces.

7.4.1.2 Friction Factor

There are two types of friction factor used in the literature: Darcy–Weisbach friction factor and Fanning friction factor. Darcy–Weisbach friction factor is commonly used in the Moody diagram for pipe friction flows, and Fanning friction factor is primarily used for rotating or swirling flows [7.33]. Obviously, for electric rotating machines, Fanning friction factor is more appropriate.

Fanning friction factor is defined as the ratio of the shear stress acting on the solid surface to the mean dynamic pressure at the same location, that is,

$$f = \frac{\tau_o}{\rho \bar{u}_\theta^2 / 2} \tag{7.54}$$

The shear stress τ_o can be evaluated from the gradient of the swirl velocity profile at the wall:

$$\tau_o = \mu \left| \frac{\partial u_\theta}{\partial r} \right|_{r=r_o} \tag{7.55}$$

The friction factor in an annular gap is a function of slot geometry, stator and rotor radii, rotational speed, and fluid properties, that is,

$$f = F(w_s, w_t, h_s, d_g, r_s, r_r, \omega, \rho, \mu) \tag{7.56}$$

To reduce the number of variables, two length ratios, the slot width-to-pitch ratio η and the slot aspect ratio A_s, are introduced as

$$\eta = \frac{w_s}{w_s + w_t} \tag{7.57}$$

$$A_s = \frac{h_s}{w_s} \tag{7.58}$$

Thus, applying Equations 7.57 and 7.58 in Equation 7.56 gives

$$f = F(\eta, A_s, Re_d) \tag{7.59}$$

7.4.1.3 Prediction of Windage Loss due to Rotating Rotor

As friction factor is determined, windage power loss P_w can be related to friction factor as

$$P_w = \pi\rho\,\bar{u}_\theta^2 r_r^2 f\omega l \tag{7.60}$$

where l is the length of the rotor.
As proposed by Saari [7.34], the windage loss of radial flux motor is associated with the resisting drag torque on the rotor:

$$P_w = k_r \pi f \rho \omega^2 r_r^4 l \tag{7.61}$$

where

k_r is the roughness coefficient (for a perfect smooth surface, $k_r = 1$; for a lamination stacked surface, $k_r = 2$–4)
f is the friction coefficient
ρ is the air density
r_r and l are the rotor radius and axial length, respectively

Equation 7.61 is essentially derived from the definition of the friction coefficient. The roughness coefficient k_r is expected to increase with the Couette Reynolds number Re_d.

Assumed that the fluid velocity varies proportionally to the distance from the air-gap midpoint with the power of 1/7, Yamada [7.35] developed an equation for the friction coefficient:

$$f = \frac{0.0152}{Re_d^{0.24}} \quad 800 < Re_d < 6\times10^4 \tag{7.62}$$

Based on their own measurements, as well as the experimental data from other investigators, Bilgen and Boulos [7.36] presented equations for the friction coefficient on smooth surfaces:

$$f = 0.515\frac{(d_g/r_r)^{0.3}}{Re_d^{0.5}} \quad 500 < Re_d < 10^4 \tag{7.63a}$$

$$f = 0.0325\frac{(d_g/r_r)^{0.3}}{Re_d^{0.2}} \quad 10^4 < Re_d \tag{7.63b}$$

The experimental friction coefficients are found to deviate less than 8.35% from the results calculated by above equations.

For the turbulent flow that $Ta >> 400$, the friction coefficient f is [7.37]

$$f = \frac{0.0095}{(Ta)^{0.2}} \tag{7.64}$$

The windage loss of axial flux motor is given by [7.38]

$$P_w = \frac{\pi\mu\omega^2(r_o^4 - r_i^4)}{2l_g} \tag{7.65}$$

where
- μ is the air viscosity
- ω is the rotor rotating speed
- l_g is the axial length of the air gap
- r_o and r_i are the shaft outer and inner radii, respectively

7.4.2 Windage Loss due to Entrance Effect of Axial Air-Gap Flow

Assuming that the air cooling flow does not have a tangential velocity component before entering the air gap, Polkowski [7.39] underlined that a rather large friction torque may be associated with the entrance effects of the axial air-gap flow. He suggested that the torque needed to accelerate the axial cooling flow into a tangential movement is presented as

$$T_a = \frac{2}{3}\pi\rho(r_s^3 - r_r^3)v_m u_m \tag{7.66}$$

where
- r_s and r_r are the radii of the stator and rotor, respectively
- v_m and u_m are the mean axial and tangential air velocities, respectively

Thus, windage losses may be associated with the cooling flow through the air gap of a high-speed motor:

$$P_a = \frac{2}{3}\pi\rho(r_s^3 - r_r^3)v_m u_m \omega \tag{7.67}$$

According to Saari [7.34], the power losses predicted by the above equations agree well with the measured results. The surface roughness caused by the stator slot openings does not significantly increase the friction losses in the air gap.

7.4.3 Windage Loss due to Stator Surface Roughness

The opposite observation to the Saari's conclusion [7.34] that the stator roughness has little effect on the rotor body windage loss was presented by Tong and Gott [7.40]. They investigated the influence of stator slot openings on the rotor windage loss in large-sized electric machines. Their results suggest that the roughness of the stator surface could significantly alter the velocity field in the air gap and thereby change windage losses.

Referring to Figure 7.10, when the rotor rotates with angular velocity ω_r, the rotor rotation-driven flow may penetrate into these unfilled slots so that the flow field in the stator–rotor air gap is distorted and leads to the variations in the friction factor on the rotor surface and correspondingly the rotor body windage loss.

Friction factor is defined as the ratio of the shear stress acting on the surface to the dynamic pressure applied on the same surface. For a rotating electric machine, friction factor is associated with the pumping action of a rotor in imparting energy to the cooling medium at the rotor–stator annular gap. An important characteristic of rotor rotation-driven flows is the tendency of fluid with high angular momentum to be flung radially outward.

With the defined unfilled aspect ratio A_s ($A_s = h_s/w_s$) and friction factor ratio f_r/f_{ro}, where f_r is the friction factor for the rotor and f_{ro} is the friction factor for the smooth stator wall (i.e., $h_s = 0$), the effect of the aspect ratio A_s on the friction factor ratio can be obtained by numerical simulations using a commercial CFD code FLUENT. As depicted in Figure 7.14, the friction factor ratio is zero as the wedge is flush with the adjacent stator surfaces. The friction factor ratio exhibits a rapid rise by increasing in A_s and then declines sharply with the further increase of A_s. When A_s approaches approximately 0.8, it reaches its local minimum. Thus, the preferred way to reduce windage loss is to redesign the wedge with either $A_s = 0$ or $A_s = 0.8$ for this specific machine. It has been found that the selection of correct A_s values can reduce rotor body windage loss by about 25% (Figure 7.15).

This may be similar to the golf ball design. As a simple, passive means of drag reduction, small dimples are made on the golf ball surface. In such a way, the dimpled surface manipulates the flow and creates vortices that can prevent or delay the boundary-layer separation on the ball surface [7.41].

When both the stator and rotor surfaces are smooth, the friction factors on the rotor and stator have shown a relative difference of about 12%, mainly resulted from the curvature effect and rotor pumping effect (Figure 7.16).

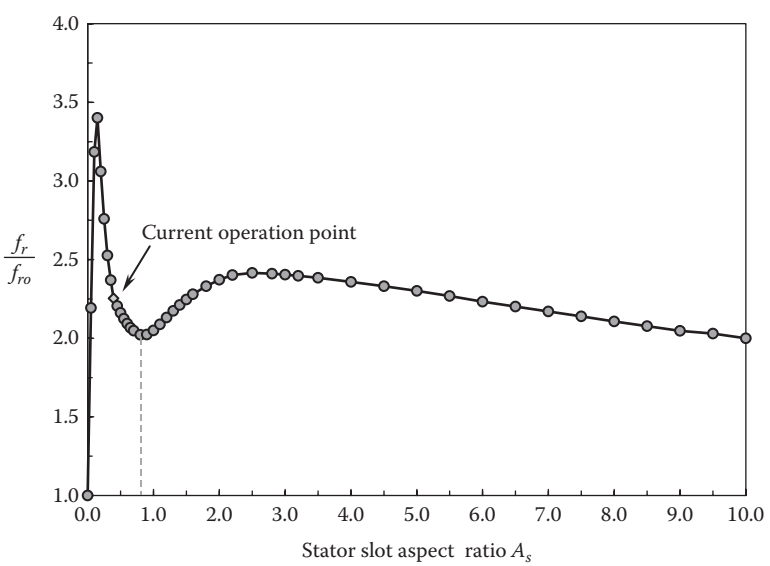

FIGURE 7.14
Effect of stator slot aspect ratio on rotor friction factor ratio.

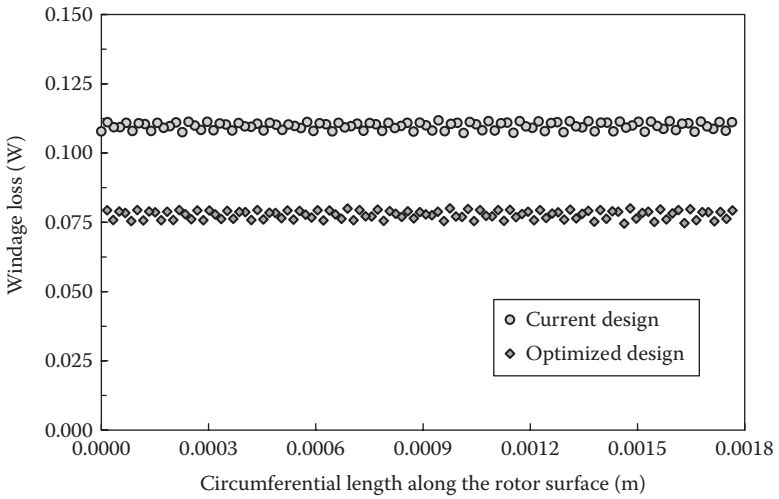

FIGURE 7.15
Comparison of rotor windage loss data between the current and optimized design.

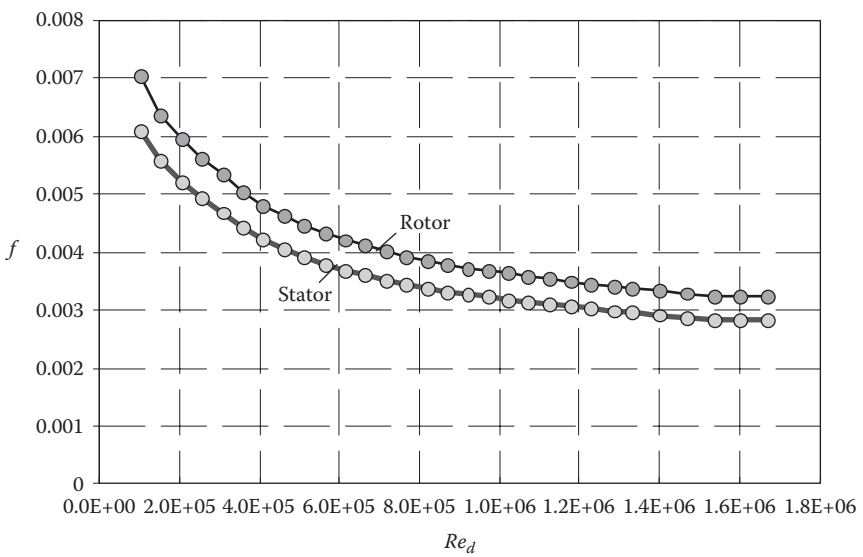

FIGURE 7.16
Comparison of friction factor on the smooth rotor and stator surfaces.

7.4.4 Fan Losses

Fans are devices that utilize electric energy to drive fan blades rotating to achieve both the air movement and the increased air total pressure. Motor cooling fans are often attached to rotor shafts at one or two ends to cool motors. As shown in Figure 7.17, a centrifugal cooling fan is mounted on one end of a rotor. When the rotor rotates, it drives the fan rotating to suck the cooling air into the machine through the ventilating slots on the endbell. Due to the centrifugal effect, the cooling air flows radially to cool the stator

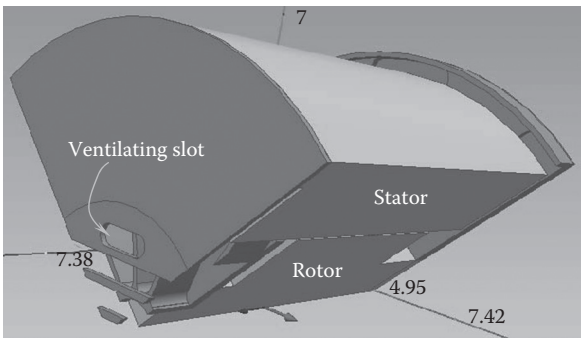

(a)

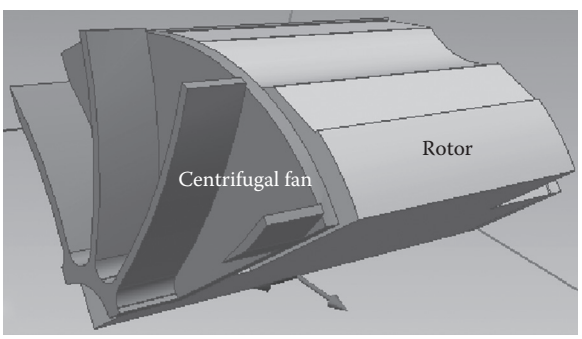

(b)

FIGURE 7.17
A centrifugal fan is mounted on one end of the rotor to suck the cooling flow into the motor: (a) the motor assembly; and (b) the centrifugal fan and rotor assembly, where the rotor with scallop-shaped structure for providing ventilation paths of axial cooling flow.

winding and then turns 180° to flow toward the rotor. Then, the cooling air turns 90° to get into the scallop-shaped cooling channels in the axial direction and finally exhausts at the other end of the machine (Figure 7.18). The exhausted air is guided by the endbell at the other end to flow over the outer surface for cooling the motor housing.

The pressure field in the machine has shown that the high static pressure zone occurs at the vicinity of the fan (Figure 7.19). A large static pressure differential is observed across the fan. In practice, the cooling fan represents a significant load on the machine, reducing available power. Generally, the fan power loss increases with the increase in the rotating speed of the fan. In addition, the fan power loss is a function of the duty cycle of the fan. As a duty cycle is larger than 50%, the fan power loss is about a constant regardless of its rotating speeds. As the duty cycle is less than 40% (i.e., the *on time* is less than 40%), the fan power loss reduces sharply in the reduction of the duty cycle [7.42].

The loss in pressure between any two points in a system is always equal to the difference between the total pressures at these points. Therefore, the total pressure loss of fan ΔP_t is the difference between the total pressure at the fan inlet $P_{t,in}$ and outlet $P_{t,out}$:

$$\Delta P_t = P_{t,in} - P_{t,out} \tag{7.68}$$

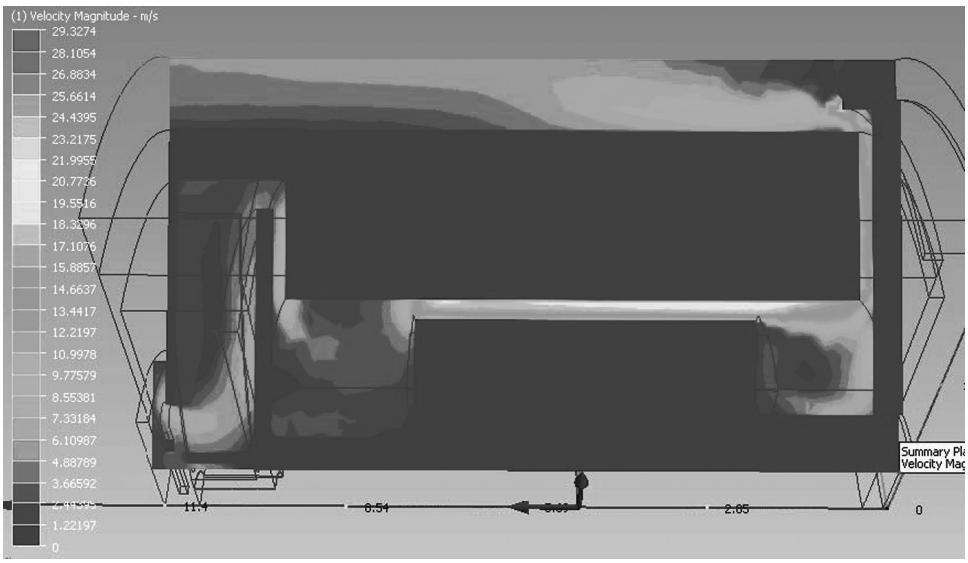

FIGURE 7.18
Velocity field through the internal cooling paths.

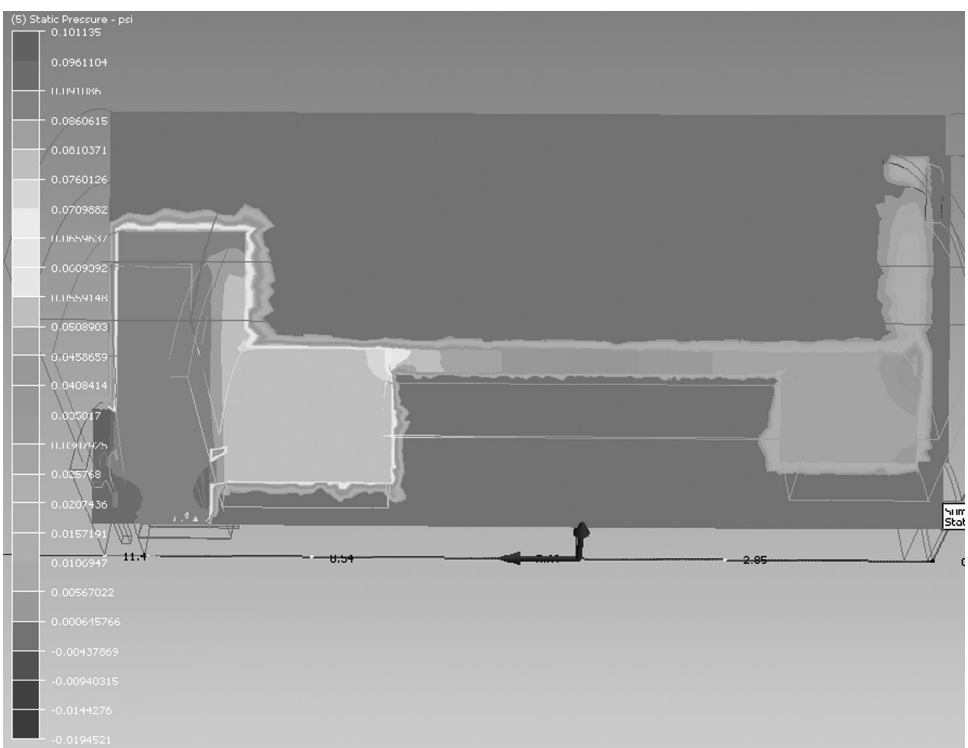

FIGURE 7.19
Pressure distribution inside the machine. The high-pressure zone is shown at the vicinity of the fan.

The total pressure at any point consists of two components: static pressure P_s and dynamic pressure P_d. Consequently,

$$P_{t,in} = P_{s,in} + P_{d,in} = P_{s,in} + \frac{1}{2}\rho V_{in}^2 \tag{7.69a}$$

$$P_{t,out} = P_{s,out} + P_{d,out} = P_{s,out} + \frac{1}{2}\rho V_{out}^2 \tag{7.69b}$$

where

$P_{s,in}$ and $P_{s,out}$ are the static pressures
$P_{d,in}$ and $P_{d,out}$ are the dynamic pressures at the fan inlet and outlet
V_{in} and V_{out} are the velocities at the fan inlet and outlet, respectively

Substituting these two equations into (7.68) yields

$$\Delta P_t = (P_{s,in} - P_{s,out}) + \frac{1}{2}\rho(V_{in}^2 - V_{out}^2) = \Delta P_s + \Delta P_d \tag{7.70}$$

All these pressures are defined in ANSI/AMCA Standard 210-07 [7.43]. The relations of these pressures and pressure differentials at the inlet and outlet of a fan are presented in Figure 7.20. With a ducted inlet and outlet, the air flow velocity along the ducted inlet is constant, and thus, the dynamic pressure remains unchanged. The static pressure decreases (relative to the pressure datum) as the air flow approaches the fan. Hence, the total pressure reaches its minimum (relative to the pressure datum) at the point of the fan inlet. Similarly, along the ducted outlet, both the air flow velocity and dynamic pressure remain constants. The static pressure decreases when the air flow leaves away from the

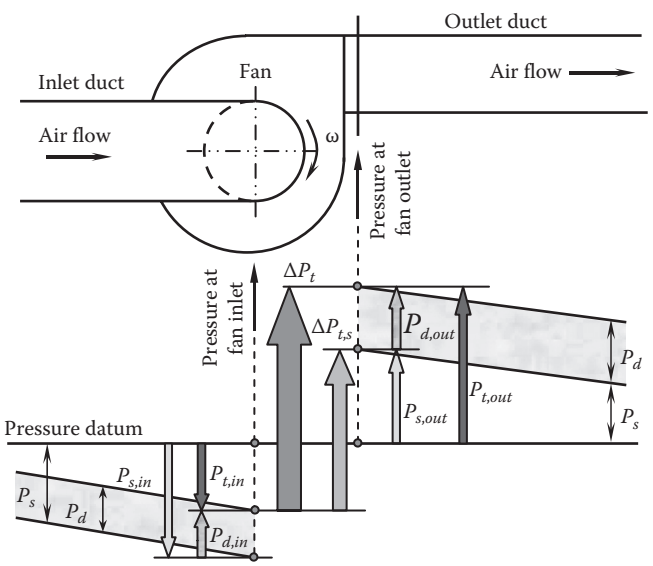

FIGURE 7.20
Relations of various pressures and pressure differentials at the inlet and outlet of a fan.

fan, causing the drop in the total pressure along the ducted outlet. It is worth to note that the total pressure of the air flow experiences a big jump when air flows from the fan inlet to the outlet due to gained mechanical energy from the fan. If the total pressure is plotted against the flow path, it can be seen that the total pressure decreases everywhere except across the fan.

Fan losses may come from (1) head loss due to the changes in flow area and direction; (2) energy lost in some components such as filters, sound attenuators, and grills; (3) friction of the duct and fan walls; (4) air flow recirculation and reentrance; and (5) windage loss of the fan itself.

7.4.5 Ventilating Path Losses

Ventilating paths inside an electric rotating machine is considerably complex due to irregular shapes, rough surfaces, and internal obstructions. Pressure losses occur at sharp turns, sudden contractions and expansions, and any torturous paths in the end-winding regions and in the gap between the rotor and stator, resulting in large ventilation windage losses [7.44].

Because ventilating paths are so complicated and vary case to case, no theoretical solutions or empirical equations are available. In order to predict the windage loss resulted from ventilating paths, it is recommended to use CFD tools.

7.4.6 Methods for Reducing Windage Losses

The increase in electric motor efficiency is extremely important for applications in modern society because any power losses ultimately imply the consumption of energy. As motor power densities decrease and output power levels increase to meet high demand of high-performance, high-speed, and cost-effective motors, power loss due to windage in some motion control systems can become significantly large. The excessive windage loss can effectively lower the machine capacity and performance. In some cases, the derating due to the total windage loss may consume over half of the available shaft power in the machine.

One effective way to reduce windage loss in a motor/generator, which is flooded with fluid, is to apply a so-called film divider [7.45]. The film divider is positioned within the air gap and freely rotatable within the gap. As the embodiment shown in Figure 7.21, the film divider is essentially a thin sleeve, which may be made of any magnetically permeable material such as fiberglass or epoxy composite. It is concentric to both the rotor and stator. During machine operation, the rotor rotates with an angular velocity of ω. As the rotor spins, the fluid in the air gap causes the film divider to spin. Ideally, the angular velocity of the film divider is ω/2. Thus, the differential vectors in each half of the gap are half of the vector flow without the film divider. Because windage loss is proportional to the 2.7 power of the velocity in the turbulent flow regime (i.e., $P_w \propto \omega^{2.7}$), the overall windage loss is lower with the film divider in place.

The comparison of windage loss in high-speed motors with and without the film divider is presented in Figure 7.22. It can be seen that the motor with the film divider has much lower windage loss than that without the film divider.

In a high-power, high-speed electric machine, windage losses are created by a large rotor body. The peripheral velocity on the rotor's surface causes significant windage losses. In order to reduce windage losses, it was proposed to optimize the rotor construction [7.46]. As shown in Figure 7.23, the rotor has a central cylindrical body provided with

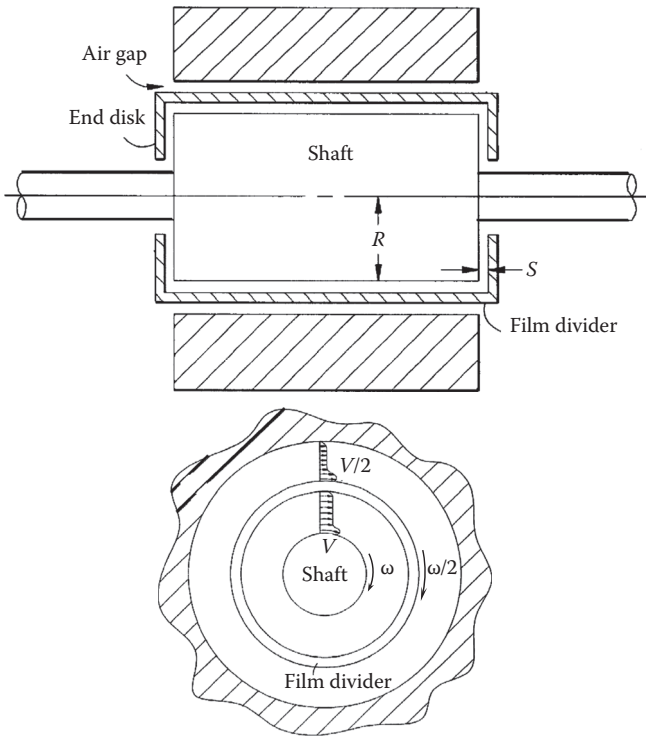

FIGURE 7.21
Using a film divider to lower windage loss in the air gap (U.S. Patent 5,828,148) [7.45]. (Courtesy of the U.S. Patent and Trademark Office, Alexandria, VA.)

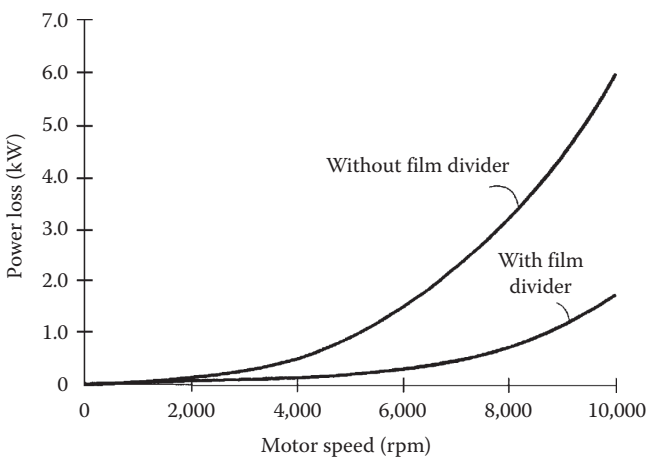

FIGURE 7.22
Comparison of windage power loss of motors with and without film divider in high-speed machine (U.S. Patent 5,828,148) [7.45]. (Courtesy of the U.S. Patent and Trademark Office, Alexandria, VA.)

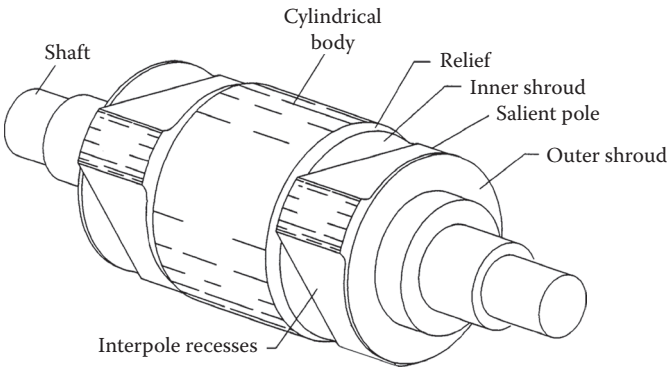

FIGURE 7.23
Optimized rotor construction for reducing windage loss (EP0489859) [7.46]. (Courtesy of European Patent Office, Munich, Germany.)

circumferentially spaced, axially extending surface recesses at the ends of the rotor, which define a desired number of salient poles at each end of the rotor. The inner and outer shrouds are provided on either side of salient poles to reduce windage losses. The outer shrouds block axial air flow into the recesses and thus reduce windage losses. Furthermore, with the reduced diameter of the central cylindrical body, the peripheral velocity of the cylindrical body is reduced, and, thereby, the windage loss is also reduced.

To further minimize windage losses, an outer cylindrical surface can be produced in the pole region of the rotor by filling interpole recesses with nonmagnetic material.

A similar idea is to use a rotor containment shell surrounding the rotor to lower windage losses [7.47]. The outer cylindrical surface of the shell is formed with a plurality of concavities in the form of annular turbulator grooves axially spaced from one another along the rotor length (Figure 7.24). These grooves will enhance the local air mixing, improve the axial heat transfer, reduce windage and friction losses, and reduce the heat penetration from the heat generated by windage into the rotor body. The optimal depth of the groove depends on a trade-off between increased resistance to tangential motion and decreased resistance to axial flow.

Smith et al. have proposed several methods for reducing power losses in motor [7.48]. One of them is to maintain constant pressure throughout the motor cavity. A pressure valve can be placed within the motor cavity to release higher-pressure air built up during operation. The maintenance of constant pressure in the cavity increases the motor efficiency due to the reduction of windage loss.

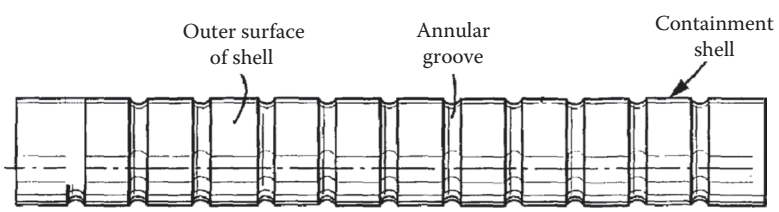

FIGURE 7.24
Rotor containment shell with a plurality of surface concavities (U.S. Patent 7,057,326) [7.47]. (Courtesy of the U.S. Patent and Trademark Office, Alexandria, VA.)

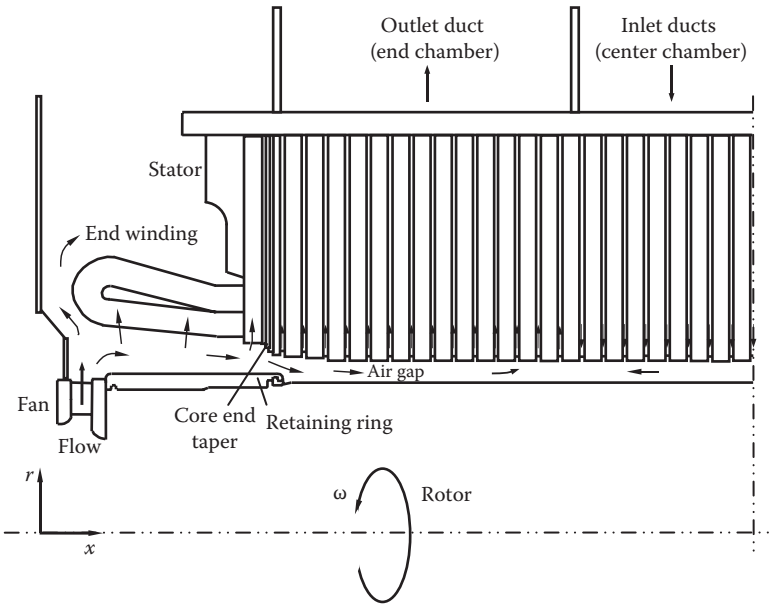

FIGURE 7.25
Schematic diagram of a ventilating cooling system in a large-size, high-power electric machine. Air flow is distributed to cool the end windings and the stator core.

One obvious way for windage loss reduction is to smooth cooling flow paths inside the motor [7.49]. All sharp edges, rapid expansions and contractions, and obstacles in flow paths should be avoided. A cooling air ventilation circuit in a large-size, high-power electric machine is presented in Figure 7.25. The inlet flow is accelerated in the radial direction by a ventilating fan, which is mounted on the end of the rotor. About one-third of the total volumetric air flowrate enters into the air gap. The remainder proceeds through and around the armature end winding. This flow allocation is thus designed and controlled to ensure sufficient air flow for the heat removal. It can be seen that at the air-gap entrance, a *bottle neck* is formed between the retaining ring inboard end and the end-core taper on the stator. As cooling gas passes through the gap entrance, the significant flow acceleration causes a large local pressure drop that is only partially recovered downstream.

By optimizing the retaining ring with the preferable spline profile and other components, the flow recirculation is eliminated, and thus, local windage loss is remarkably reduced (Figure 7.26). In addition, the enlarged air-gap entrance allows more flows to get into the air gap.

More recently, Pal [7.50] has proposed a new idea for reducing windage loss in liquid-cooled electric machines. This method uses injecting oil flow to cool the machine windings. The machine has two rotors and two stators. A number of baffles are coupled with the shaft at the center and each end of the shaft. The baffles extend radially outward from the shaft toward baffle cavities at the back iron. As the shaft rotates, oil is urged toward the baffle cavities along the baffles via centrifugal forces (Figure 7.27). The baffle directing oil to the baffle cavity substantially improves the scavenge performance. As a result, it reduces the oil level in a sump and lowers windage and friction losses.

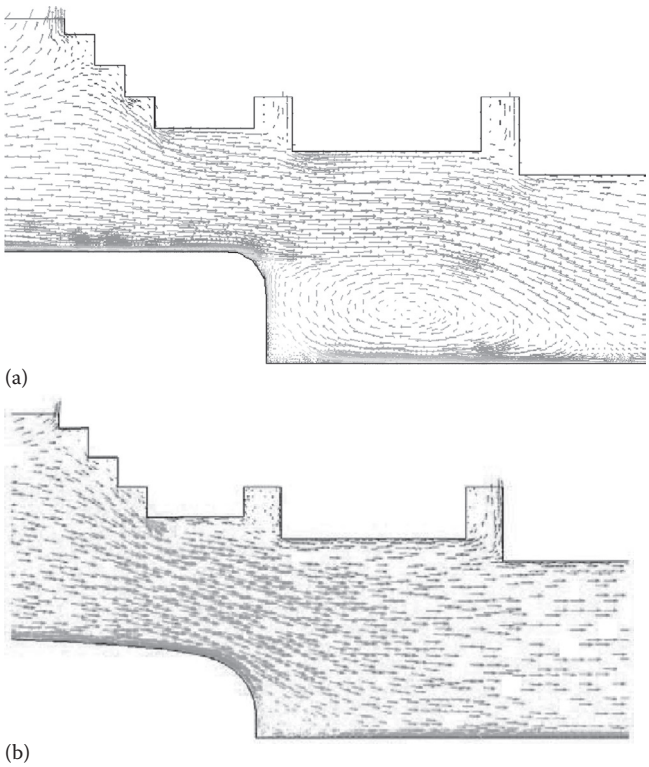

FIGURE 7.26
Reducing windage loss at the air-gap entrance by smoothing the cooling flow path: (a) original design with a large flow recirculation and (b) improved design with optimized flow path to eliminate the flow recirculation and thus reduce windage loss.

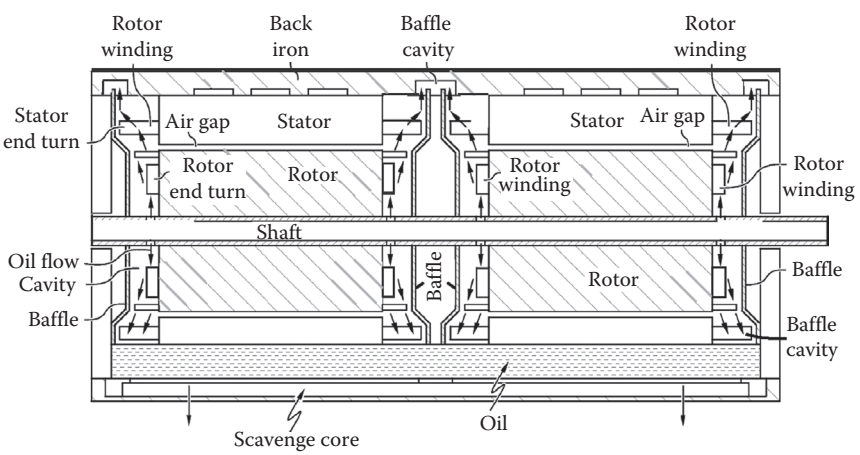

FIGURE 7.27
A liquid-cooled electric machine is cooled by injecting oil radially along a plurality of baffles via centrifugal force toward rotor and stator end windings [7.50]. (Courtesy of the U.S. Patent and Trademark Office, Alexandria, VA.)

An effective method to reduce windage losses is to use hydrogen gas to cool electric machines. The high thermal conductivity of hydrogen has proven to be a key advantage in its use as a cooling medium in electric power machines. Hydrogen has a thermal conductivity of nearly seven times higher than that of air, and its ability to transfer heat through forced convection is about 50% better than air [7.51]. At a given temperature and pressure, the density of hydrogen is only 1/14 the density of air. Due to its superior thermophysical properties, the use of hydrogen can not only reduce windage friction losses but also greatly enhance heat transfer superior properties.

Using hydrogen as coolant can be traced back to the late 1930s. Since then, this technique has been developed and successfully used in generator cooling but still not applied to electric motors.

7.5 Stray Load Losses

Stray load losses consist of a variety of minor losses not accounted previously, for instance, the losses referring to the sources such as stray flux, the cage in the slots, interbar currents, and harmonic rotor bar currents from the nonsinusoidal distribution of the slotted stator winding [7.52]. Stray load losses appear only when motors operate under load conditions and are very difficult to predict analytically and to measure accurately. The largest contribution to stray losses is harmonic energies. These energies are dissipated as currents in the copper windings, harmonic flux components in the iron parts, and leakage fluxes in the laminate core. The detailed discussions and analyses of stray losses have been provided by Aoulkadi [7.53] and Englebretson [7.54].

It is commonly accepted that the investigation of stray load losses in electric rotating machines is far from complete. Most motor engineers rely on empirical equations for the estimation of stray load losses.

Stray load losses represent a small portion of the total motor power loss. The ratio of stray load loss to motor rated power decreases with the increased motor rated power. IEEE Standard 112-2004 [7.55], GB 18613-2002 [7.56], and IEC Standard 60034-2-1 [7.57] provide assumed values of stray load losses under different power ratings. Some of them are shown in Tables 7.4 and 7.5.

TABLE 7.4

Assumed Values of Stray Losses

Machine Rating (kW)	Stray Load Loss (% of Rated Power)
1–90	1.8
91–375	1.5
376–1850	1.2
>1850	0.9

Source: IEEE Power Engineering Society, IEEE 112-2004 Standard test procedure for polyphase induction motors and generators, 2004.

TABLE 7.5

Values of Stray Losses Proposed by GB 18613-2002

Machine Rating (kW)	Stray Load Loss (% of Rated Power)
0.55–1.1	2.5
1.5	2.4
3	2.3
4	2.2
5.5–7.5	2.1
11	2.0
15–18.5	1.9
22–30	1.8
37–45	1.7
55–75	1.6
90–110	1.5
132–160	1.4
200–315	1.3

Source: Standardization Administration of China (SAC), GB 18613-2002, Limited values of energy efficiency and evaluating values of energy conservation of small and medium three-phase asynchronous motors, 2002.

For other than rated load, stray losses are assumed to be proportional to the square of the rotor current [7.55].

References

[7.1] Benhaddadi, M., Olivier, G., Ibtiouen, R., Yelle, J., and Tremblay, J.-F. 2011. Chapter 1: Premium efficiency motors. In *Electric Machines and Drives* (Ed.: Miroslav Chomat). InTech: Rijeka, Croatia. http://www.intechopen.com/download/pdf/14083.

[7.2] GE Industrial Systems. 2002. Evaluation and application of energy efficient motors. White paper publication number: e-GEA-M1019. http://www.geindustrial.com/publibrary/checkout/e-GEA-M1019?TNR=White Papers | e-GEA-M1019 | generic

[7.3] Ramo, S., Whinnery, J. R., and Van Duzer, T. 1994. *Fields and Waves in Communication Electronics*, 3rd edn. John Wiley & Sons, New York.

[7.4] Zheng, L. P., Xu, T. X., Acharya, D., Sundaram, K. B., Vaidya, J., Zhao, L. M., Zhou, L. et al. 2005. Design of a superhigh-speed cryogenic permanent magnet synchronous motor. *IEEE Transactions on Magnetics* **41**(**10**): 3823–3825.

[7.5] Zhu, Z. Q., Ng, K., and Howe, D. 1997. Design and analysis of high-speed brushless permanent magnet motors. *Eighth International Conference on Electrical Machines and Drives*, Cambridge, U.K., pp. 381–385.

[7.6] Steinmetz, C. P. 1892. On the law of hysteresis. *AIEE Transactions* **9**: 3–64.

[7.7] Mulder, S. 1995. Power ferrite loss formulas for transformer design. *Power Conversion & Intelligent Motion* **21**(**7**): 22–31.

[7.8] Hamdi, E. C. 1994. *Design of Small Electrical Machines*. John Wiley & Sons, New York.

[7.9] Rajput, R. K. 2008. *Basic Electrical Engineering*, 2nd edn. Laxmi Publications, New Delhi, India.
[7.10] Mohan, N., Undeland, T. M., and Robbins, W. P. 1991. *Power Electronic Converters. Applications and Design*, 2nd edn. John Wiley & Sons, Hoboken, NJ.
[7.11] Smith, A. C. and Edey, K. 1995. Influence of manufacturing processes on iron losses. *Proceedings of Seventh International Conference on Electrical Machines and Drives*, Durham, U.K., pp. 77–81.
[7.12] Binesti, D. and Ducreux, J. P. 1996. Core losses and efficiency of electrical motors using new magnetic materials. *IEEE Transactions on Magnetics* **32**(**5**): 4887–4889.
[7.13] Deeb, R. 2012. Prediction of eddy current losses of surface mounted permanent magnet servo motor. *20th International Conference on Electrical Machines*. Marseille, France, pp. 1797–1802.
[7.14] Ishak, D., Zhu, Z. Q., and Howe, D. 2005. Eddy-current loss in the rotor magnets of permanent-magnet brushless machines having a fractional number of slots per pole. *IEEE Transactions on Magnets* **41**(**9**): 2462–2469.
[7.15] SKF Group. 2009. SKF energy efficient bearings. Publication 6860 EN. http://www.skf.com/binary/12-31950/6860_EN.pdf.
[7.16] Palmgren, A. 1959. *Ball and Roller Bearing Engineering*, 3rd edn. SKF Industries Inc., Philadelphia, PA.
[7.17] Harris, T. A. and Kotzalas, M. N. 2007. *Rolling Bearing Analysis: Essential Concepts of Bearing Technology*, 5th edn. CRC Press, Boca Raton, FL.
[7.18] SKF Group. The SKF model for calculating the frictional moment. http://www.skf.com/group/products/bearings-units-housings/ball-bearings/principles/friction/skf-model/index.html.
[7.19] SKF Group. Power loss and bearing temperature. http://www.skf.com/group/products/bearings-units-housings/ball-bearings/principles/friction/power-loss-bearing-temperature/index.html.
[7.20] Tong, W. 2009. Numerical analysis of flow field in generator end-winding region. *International Journal of Rotating Machinery* **2008**: Article ID 692748, doi:10.1155/2008/692748.
[7.21] Taylor, G. I. 1923. Stability of viscous liquid contained between two rotating cylinders. *Philosophical Transactions of Royal Society (London)* **223**: 289–343.
[7.22] Taylor, G. I. 1935. Distribution of velocity and temperature between concentric rotating cylinders. *Proceedings of the Royal Society A* **151**: 494–512.
[7.23] Taylor, G. I. 1936. Fluid friction between rotating surfaces. *Proceedings of the Royal Society A* **157**: 546–578.
[7.24] Wendt, F. 1933. Turbulente stromungen zwischen zwei eorierenden konaxialen zylindem (Turbulent flow between two rotating coaxial cylinders). *Ingenieur-Archiv* **4**: 577–595.
[7.25] Lathrop, D. P., Fineberg, J., and Swinney, H. L. 1992. Turbulent flow between concentric rotating cylinders at large Reynolds number. *Physical Review Letters* **68**(**10**): 1515–1518.
[7.26] Okaya, T. and Hasegawa, M. 1939–1940. On the turbulent boundary layers at the surface of two rotating co-axial cylinders. *Japanese Journal of Physics* **13.2**: 29–49.
[7.27] Dou, H.-S., Khoo, B. C., and Yeo, K. S. 2007. Energy loss distribution in the plane Couette flow and the Taylor–Couette flow between concentric rotating cylinders. *International Journal of Thermal Science* **46**(**3**): 262–275.
[7.28] Ustimenko, B. P. and Zmeikov, V. N. 1964. Hydrodynamics of a flow in an annular channel with an inner rotating cylinder. *Teplofizika Vysokikh Temperatur* **1**(**2**): 220–228.
[7.29] Leont'ev, A. I. and Kirdyashkin, A. G. 1966. The theory of the convective heat transfer for the vertical flow of fluid. *Proceedings of Third International Heat Transfer Conference*, Chicago, IL, Vol. 1, pp. 216–224.
[7.30] General Electric. 1996. *Fluid Flow—Data Book*. Section 408.7: Drag-rotating cylinder enclosed. Genium Publishing, New York.
[7.31] Bruckner, R. J. 2009. Windage power loss in gas foil bearings and the rotor-stator clearance of high speed generators operating in high pressure environments. *ASME Turbo Expo 2009: Power for Land, Sea, and Air*, Orlando, FL. Paper No. GT2009-60118, pp. 263–270.
[7.32] Wild, P. M., Djilali, N., and Vickers, G. W. 1996. Experimental and computational assessment of windage losses in rotating machinery. *Journal of Fluids Engineering* **118**(**1**): 116–122.

[7.33] Black, H. 1969. Effects of hydraulic forces on annular pressure seals on the vibrations of centrifugal pump rotors. *Journal of Mechanical Engineering Science* **11**(**2**): 206–213.
[7.34] Saari, J. 1998. Thermal analysis of high-speed induction machines. PhD thesis, Helsinki University of Technology, Espoo, Finland.
[7.35] Yamada, Y. 1962. Torque resistance of a flow between rotating co-axial cylinders having axial flow. *Bulleting of JSME* **5**(**20**): 634–642.
[7.36] Bilgen, E. and Boulos, R. 1973. Functional dependence of torque coefficient of coaxial cylinders on gas width and Reynolds numbers. *ASME Journal of Fluids Engineering* **95**(**1**): 122–126.
[7.37] Awad, M. N. and Martin, W. J. 1997. Windage loss reduction study for TFTR pulse generator. *17th IEEE/NPSS Symposium on Fusion Engineering* **2**: 1125–1128.
[7.38] Dorfman, L. A. 1963. *Hydrodynamic Resistance and the Heat Loss of Rotating Solids*. Oliver & Boyd, Edinburgh, Scotland.
[7.39] Polkowski, J. W. 1984. Turbulent flow between coaxial cylinders in the inner cylinder rotating. *Transactions of ASME—Journal of Engineering for Gas Turbines and Power* **106**(**1**): 128–135.
[7.40] Tong, W. and Gott, B. E. B. 2002. Method of minimizing rotor body windage loss. U.S. Patent 6,438,820.
[7.41] Johnson, T. J. 2009. Drag measurements across patterned surfaces in a low Reynolds number couette flow facility. Master thesis, The University of Alabama, Tuscaloosa, AL.
[7.42] Hawkins, J. S., Avery, Jr., R. M., and Super, L. 2005. Method of estimating engine cooling fan power losses. U.S. Patent 6,904,352.
[7.43] American National Standards Institute (ANSI)/Air Movement and Control Association (AMCA). 2007. ANSI/AMCA Standard 320-07 Laboratory methods of testing fans for certified aerodynamic performance ration.
[7.44] Tong, W. and Vandervort, C. L. 2002. Optimization of ventilating flow path at air gap exit in reverse flow generators. U.S. Patent 6,346,755.
[7.45] Niggemann, R. E., Thomson, S. M., and Schneider, M. G. 1998. Method and apparatus for reducing windage losses in rotating equipment and electric motor/generator employing same. U.S. Patent 5,828,148.
[7.46] Brook, R. W., Grant, J. J., and Miller, H. W. 1994. Rotor with reduced windage losses. European Patent Office EP0489859.
[7.47] Ren, W.-M. and Carl, R. J. 2006. Rotor body containment shell with reduced windage losses. U.S. Patent 7,057,326.
[7.48] Smith, S. H. and Stump, D. E. 2009. System and method for reducing windage losses in compressor motors. European Patent Application EP2024691.
[7.49] Tong, W. and Vandervort, C. L. 2001. Spline retaining ring. U.S. Patent 6,285,110.
[7.50] Pal, D. 2013. Electrical machine with reduced windage loss. U.S. Patent Application 2013/0076169.
[7.51] Speranza, J. and Skoczylas, T. 2006. Increasing generator efficiency and capacity: A case study. *Electric Power 2006*, Atlanta, GA.
[7.52] Ketteler, K. H. 1984. Über den einfluss der wicklungsschaltung in induktionsmachinen auf die zusatzverluste und den einseitigen magnetischen. *Zug. ETZ-Archiv* **106**(**3**): 99–106.
[7.53] Aoulkadi, M. 2011. Experimental determination of stray load losses in cage induction machines. PhD thesis, Technische Universität Darmstadt, Darmstadt, Germany.
[7.54] Englebretson, S. C. 2009. Induction machine stray loss from inter-bar currents. PhD thesis, Massachusetts Institute of Technology, Cambridge, MA.
[7.55] IEEE Power Engineering Society. 2004. IEEE 112-2004 Standard test procedure for polyphase induction motors and generators.
[7.56] Standardization Administration of China (SAC). 2002. GB 18613-2002. Limited values of energy efficiency and evaluating values of energy conservation of small and medium three-phase asynchronous motors.
[7.57] International Electrotechnical Commission (IEC). 2007. IEC 60034-2-1 Standard on efficiency measurement methods for low voltage AC motors.

8

Motor Cooling

The power output rating of an electric motor is often limited by the ability to provide additional electric current through stator and rotor windings. However, the increase of current in the windings is constrained by temperature limitations imposed on the electric conductor insulation and PMs (for a PM motor). According to the Arrhenius equation [8.1,8.2], the failure rate of an electric/electronic device is exponentially related to the reciprocal of the operating temperature. A fairly accurate approximation of the Arrhenius equation states that an operating temperature exceeds the thermal limit by 10°C and reduces the lifetime of the device by half. Therefore, effective cooling of stator and rotor windings contributes directly to the output capability, operation reliability, and lifetime of electric motors. This is especially true in motor end-winding regions where the configuration of cooling flow paths is extremely complicated and direct forced cooling is very difficult [8.3,8.4]. In addition, the relatively poor heat dissipation from the rotor can cause the increase in rotor core losses, leading to an excessive temperature rise in the rotor and magnets. This may result in partially irreversible demagnetization of the magnets, particularly of sintered Nd–Fe–B magnets [8.5] and thus a decline in the performance of the motor.

In recent years, the development and production of high-performance, high-efficiency, and high-power-density electric motors have been accompanied by increasing heat fluxes at both the component and system levels. Over the years, significant advances have been made in the applications of air cooling and liquid cooling techniques to manage increased heat fluxes. As the prevailing market demands electric motors with better performance, lower power consumption, and smaller size, thermal management has emerged as an increasingly important aspect in motor design.

8.1 Introduction

Modern electric motors generate a large amount of heat during their normal operation as the results of various electric, electromagnetic, and mechanical losses. The great majority of motor losses are converted into heat, causing the temperature of windings, cores, magnets, etc., to rise. Excessive temperatures are generally detrimental to motor performance and reliable operation. Hot spots in a motor due to nonuniform heat fluxes and improper cooling may result in damage to winding insulation or premature bearing failure and, in turn, greatly reduce the motor lifetime. For some special applications, thermal management is critical to motor performance. For instance, a telescope tracking motor requires an extremely tight control in the temperature rise relative to the ambient temperature because any sharp and excessive temperature changes may significantly influence the telescope's tracking accuracy. Therefore, to ensure safe and reliable operation of electric motors, all heat generated in the motor must be efficiently dissipated to the ambient air.

A variety of different cooling mechanisms may be used to cool electric motors to maintain the temperatures of stator and rotor windings, as well as PMs and bearings, below the maximum allowable limit. Today, cooling of an electric motor still remains a major challenge for motor engineers and designers because of a number of factors: (1) a great number of motor parts with irregular geometries, (2) the nonuniform heat generation in different heat sources (stator and rotor windings, cores, bearings, etc.) due to various power losses, (3) the complexity in cooling flow paths, (4) cooling flow splitting and mixing, (5) interactions between the rotor-induced rotating flows and the nonrotating flows at the stationary components, (6) a variety of thermal exchange modes (conduction, convection, radiation, etc.) that are involved simultaneously, and (7) the compact and lightweight motor design, as a result of growing global demand for high-power-density motors. As a consequence, the thermal phenomena inside an electric motor are considerably complex.

Cooling of high-heat-flux heat sources can be generally divided into two steps [8.6]: (1) heat extraction, in which heat is removed from a high thermal density region (e.g., motor windings) and reformatted to a larger area, and (2) heat rejection, in which the heat is dissipated convectively to the surrounding environment.

Remarkable progresses in heat extraction and heat rejection have been made in the last several decades, including adoptions of advanced cooling techniques such as heat pipe, microchannel, heat pump, high-conductivity material, thermoelectric cooler, carbon nanotube, and recently proposed ionic wind generator in electric/electronic cooling. However, in cooling of electric motors, technologies have not yet made significant progress in past several decades. As a result of the technology stagnation, the design and development of high efficient cooling systems still remain challenges today to motor engineers and manufacturers.

8.1.1 Passive and Active Cooling Techniques

Cooling techniques are often divided into two categories: passive cooling and active cooling, depending on what the heat transfer mode would be or how cooling flows are generated. Passive cooling refers to cooling with no active mechanism such as fan or pump. Passive cooling techniques have been developed for a long time for motors that have low power losses. In a passive cooling mode, motor cooling primarily relies on heat conduction to transport the generated heat from the heat sources (e.g., stator winding) to the motor frame (e.g., motor housing and endbells) and then to dissipate the heat to the environment by natural convection and radiation. By eliminating fans or pumps, motor operation reliability is significantly increased. Compared with active cooling techniques, passive cooling techniques have lower costs, lower noise emission, and no power consumption. However, passive cooling techniques are restricted to low thermal load conditions. For large-size, heavy-duty motors, active cooling is the only choice.

In contrast, active cooling techniques require the use of external devices such as fans, blowers, and pumps to force a coolant (air or liquid) flowing through cooling channels either inside or outside, or both, of the motor. With the development of modern electric motors, which have high power density and consequently high power losses, active cooling is required to remove the waste heat produced by motor components to keep these components within permissible operating temperature limits.

The magnitude of the heat transfer coefficient is determined by a number of parameters such as heat transfer mode, geometry, flow path dimensions, coolant type, flowrate, and flow condition (laminar or turbulent). The comparison of heat transfer coefficients for different heat transfer modes is presented in Table 8.1.

TABLE 8.1

Heat Transfer Coefficients of Different Heat Transfer Modes with Different Coolants

Heat Transfer Mode	Heat Transfer Coefficient (W/m²-K)	References
Conduction	5–25	
Natural convection (air)	5–30	[8.7,8.8]
Natural convection (FC)	10–100	[8.7,8.8]
Natural convection (water)	30–300	[8.7,8.8]
Forced convection (air)	20–200	[8.7,8.8]
Forced convection (FC)	50–300	[8.7,8.8]
Forced convection (water)	300–8,000	[8.7,8.8]
Forced jet (air)	200–800	[8.7,8.8]
Forced jet (FC)	2,000–20,000	[8.7,8.8]
Forced jet (water)	8,000–50,000	[8.7,8.8]
Pool boiling (water)	2,500–3,500	[8.9]
Forced boiling (water)	5,000–100,000	[8.9]
Condensing (water)—vertical surface	4,000–11,300	[8.9]
Condensing (water)—Outside of horizontal tube	9,500–25,000	[8.9]
Radiation	5–30	

Note: Conductive heat transfer coefficient and radiative heat transfer coefficient are defined as $h_c = \frac{-\nabla(kT)}{(T_h - T_c)}$ and $h_r = \sigma\varepsilon \frac{T_h^4 - T_c^4}{T_h - T_c}$, respectively. They are estimated as the same order as natural convection.

The selection of appropriate and feasible cooling techniques depends basically on the required cooling load, cooling efficiency, cooling system operation reliability, cost of cooling system, temperature difference between the heat source and the environment, coolant thermophysical properties, geometries of heated sources, noise, and vibration. All these determining factors must be taken into account. The trade-off between these factors is highly desired in order to choose the best cooling technique for each particular application. Three liquids, namely, air, fluorocarbon (FC), and water, are chosen to compare their heat transfer coefficients for natural and forced convection and forced jet.

The results show that all cooling modes that involve a phase change can make very high heat transfer coefficients. Water is always the best coolant. However, for motor cooling applications, water has to be restricted in indirect cooling application. In all cases, air cooling has the lowest heat transfer rate, compared with FC and water.

8.1.2 Heat Transfer Enhancement Techniques

A race for increasing power density of electric motors has provided the driving force behind the scientific research and technological advancement in the field of heat transfer enhancement. It is now widely accepted that the thermal management in high-power-density motors becomes critically important. Efficient cooling plays an increasingly key role that controls the performance and stability of electric motors.

It has been recognized that the primary limitation to performance of a convective cooling system is the boundary layer of motionless air that adheres to and envelops all surfaces of the cooling system. Within this boundary layer region, diffusive transport is the dominant mechanism for heat transfer. The resulting thermal bottleneck largely determines the thermal resistance and convective heat transfer coefficient and thus cooling efficiency of the cooling system. The heat transfer enhancement can be achieved by disturbing cooling flows to lower the thickness of the boundary layer and increasing the convective contact area.

A variety of heat transfer enhancement techniques have been developed for adapting to the rapid increase in thermal load in electric and electronic devices [8.10]. For passive techniques, heat transfer enhancements are achieved by employing special surface geometries or fluid additives. Common surface geometries include coated surfaces, rough surfaces, and extended surfaces to increase the film heat transfer coefficient and to reduce the thermal resistance. Additives for liquid include solid particles or gas bubbles in single-phase flows and liquid trace additives for boiling systems.

Active techniques employ turbulators such as displaced inserts, pin fins, dimpled surfaces, surfaces with arrays of protrusions, and swirl chambers. All of these turbulators act to increase rotating/secondary flows or vortices on heat surfaces for augmenting forced convective heat transfer. These rotating/secondary flows and vortices not only increase rotating/secondary advection of heat away from surfaces but also increase 3D turbulence production by increasing shear and creating gradients of velocity over significant flow volumes.

The selection and application of heat transfer enhancement techniques are core concerns for modern motor engineers and designers. Many researchers have contributed their efforts toward better understanding of heat transfer techniques.

8.2 Conductive Heat Transfer Techniques

Heat conduction is a mechanism of heat transfer, taking place if there is a temperature gradient in a solid body or between contacted solid bodies. From the microscopic standpoint, conduction is relevant to the movement of particles (e.g., atoms or molecules) in a material. The particles vibrate randomly about fixed positions. Since the rise in temperature will result in the increase in the particle kinetic energy, the higher the temperature, the greater the particle vibration. When particles collide with their neighbors, part of the kinetic energy will be transferred from the particles that have higher energy to the particles that have lower energy until thermal equilibrium is reached. At the state of thermal equilibrium, there are an equal number of collisions resulting in an energy gain as there are collisions resulting in an energy loss. On average, there is no net energy transfer resulting from the collisions of particles.

8.2.1 Conductive Heat Flux and Energy Equations

The conductive heat flux vector $\mathbf{q}''$ is proportional to the thermal conductivity k_n and the temperature gradient:

$$\mathbf{q}'' = -\nabla(k_n T) \tag{8.1}$$

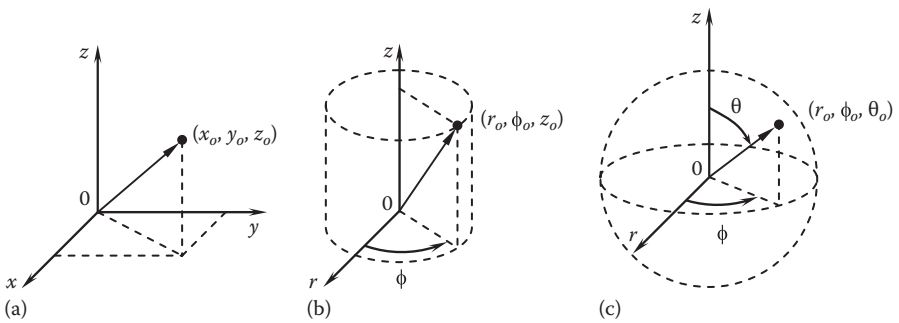

FIGURE 8.1
Coordinate systems: (a) Cartesian, (b) cylindrical, and (c) spherical.

where T is the temperature. Generally, thermal conductivity is a function of temperature. In anisotropic materials such as insulations and silicon steel laminations, thermal conductivity k_n may have different values in different directions of the material spatial orientation at a specific temperature T, that is,

$$k_n = k_n(n_1, n_2, n_3, T) \tag{8.2}$$

The negative sign in Equation 8.1 denotes that the heat flow is always from the region of high temperature to the region of low temperature. Equation 8.1 in 3D Cartesian, cylindrical, and spherical coordinate systems (see Figure 8.1) can be expressed as

$$q'' = -\left[\frac{\partial(k_x T)}{\partial x} + \frac{\partial(k_y T)}{\partial y} + \frac{\partial(k_z T)}{\partial z}\right] \tag{8.3a}$$

$$q'' = -\left[\frac{\partial(k_r T)}{\partial r} + \frac{1}{r}\frac{\partial(k_\phi T)}{\partial \phi} + \frac{\partial(k_z T)}{\partial z}\right] \tag{8.3b}$$

$$q'' = -\left[\frac{\partial(k_r T)}{\partial r} + \frac{1}{r\sin\theta}\frac{\partial(k_\phi T)}{\partial \phi} + \frac{1}{r}\frac{\partial(k_\theta T)}{\partial \theta}\right] \tag{8.3c}$$

respectively.

Energy equation governing conductive thermal energy transport in solids is based on energy conservation in a differential control volume through which energy transfer is exclusively by conduction and can be generally expressed as

$$\rho c_p \frac{\partial T}{\partial t} = \nabla^2(k_n T) + q''' \tag{8.4}$$

where
- ρ is the density
- c_p is the specific heat
- q''' is the heat generation in the control volume

Similarly, Equation 8.4 can be expressed in Cartesian, cylindrical, and spherical coordinate systems as

$$\rho c_p \frac{\partial T}{\partial t} = \frac{\partial^2 (k_x T)}{\partial x^2} + \frac{\partial^2 (k_y T)}{\partial y^2} + \frac{\partial^2 (k_z T)}{\partial z^2} + q''' \tag{8.5a}$$

$$\rho c_p \frac{\partial T}{\partial t} = \frac{1}{r}\frac{\partial}{\partial r}\left[r \frac{\partial (k_r T)}{\partial r} \right] + \frac{1}{r^2}\frac{\partial^2 (k_\phi T)}{\partial \phi^2} + \frac{\partial^2 (k_z T)}{\partial z^2} + q''' \tag{8.5b}$$

$$\rho c_p \frac{\partial T}{\partial t} = \frac{1}{r^2}\frac{\partial}{\partial r}\left[r^2 \frac{\partial (k_r T)}{\partial r} \right] + \frac{1}{r^2 \sin^2 \theta}\frac{\partial^2 (k_\phi T)}{\partial \phi^2} + \frac{1}{r^2 \sin \theta}\frac{\partial}{\partial \theta}\left[\sin \theta \frac{\partial (k_\theta T)}{\partial \theta} \right] + q''' \tag{8.5c}$$

For isotropic materials, thermal conductivity is identical in all directions (i.e., $k_x = k_y = k_z = k$, $k_r = k_\phi = k_z = k$, $k_r = k_\phi = k_\theta = k$). Taking this condition and assuming k is a constant, the aforementioned equations can be greatly simplified:

$$\frac{1}{\alpha}\frac{\partial T}{\partial t} = \left(\frac{\partial^2 T}{\partial x^2} + \frac{\partial^2 T}{\partial y^2} + \frac{\partial^2 T}{\partial z^2} \right) + \frac{q'''}{k} \tag{8.6a}$$

$$\frac{1}{\alpha}\frac{\partial T}{\partial t} = \left[\frac{1}{r}\frac{\partial}{\partial r}\left(r \frac{\partial T}{\partial r} \right) + \frac{1}{r^2}\frac{\partial^2 T}{\partial \phi^2} + \frac{\partial^2 T}{\partial z^2} \right] + \frac{q'''}{k} \tag{8.6b}$$

$$\frac{1}{\alpha}\frac{\partial T}{\partial t} = \left[\frac{1}{r^2}\frac{\partial}{\partial r}\left(r^2 \frac{\partial T}{\partial r} \right) + \frac{1}{r^2 \sin^2 \theta}\frac{\partial^2 T}{\partial \phi^2} + \frac{1}{r^2 \sin \theta}\frac{\partial}{\partial \theta}\left(\sin \theta \frac{\partial T}{\partial \theta} \right) \right] + \frac{q'''}{k} \tag{8.6c}$$

where α is the thermal diffusivity of material, $\alpha \equiv k/\rho c_p$.

8.2.2 Encapsulation and Impregnation of Electric Motor

As discussed in Chapter 4, the objectives of encapsulation and/or impregnation of electric motors are as follows:

- The encapsulation/impregnation of electric motor can remarkably enhance electrical insulation of motor windings from damage during normal operation and thus extend the motor lifetime.
- By filling voids in motor windings with epoxy resin and creating a rigid mass with optimum dielectric strength, an encapsulated and/or impregnated motor can significantly lower the thermal resistance from internal heat sources (e.g., the stator winding) to the motor housing.
- The encapsulation/impregnation increases the overall protection to motors, especially chemical and environmental protections.
- By integrating stator components (e.g., stator winding, laminations, and insulations) into a rigid mass, it increases the stator stabilization and thus reduces motor vibrations and noise levels.

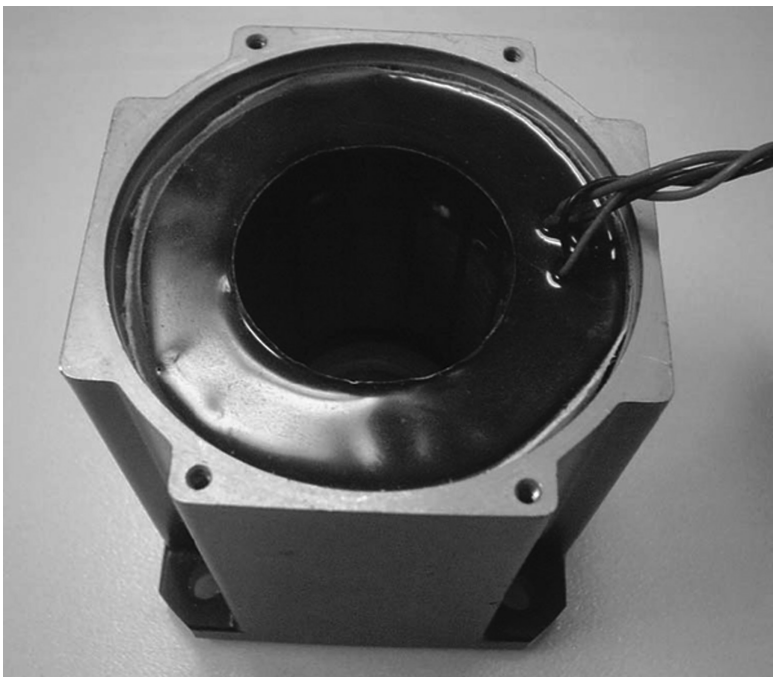

FIGURE 8.2
Encapsulation of stator winding.

Though many materials can be used in motor encapsulation/impregnation, the most popular encapsulation material is epoxy resin, used by many motor manufacturers in a wide range of applications. In the selection of encapsulation materials, thermal conductivity is one of the most important parameters. An epoxy-encapsulated stator is shown in Figure 8.2.

8.2.3 Enhanced Heat Transfer Using High-Thermal-Conductivity Material

One of the effective ways in motor winding cooling is to place high-thermal-conductivity materials between winding coils inside the winding slots and/or to interleave these materials into stacked motor laminations [8.11]. As shown in Figure 8.3a, the thermally conductive strips provide low thermal-resistant paths through which heat is transferred from internal high-temperature components (i.e., stator winding coils) to the stator laminations and housing and then dissipated to the environment. In Figure 8.3b, the thermally conductive strips are sandwiched between stacked stator laminations. In this way, heat generated inside the stator core due to the losses from eddy currents and hysteresis is conducted directly from the interior of the stator to the motor outer portions by means of these strips. Because these thermally conductive strips are directly contacted with heat sources, the cooling efficiency is considerably high. As a fact, this cooling technique can result in a significant reduction of weight and volume of motor, along with a substantial increase in the power density while operating at a moderate temperature above ambient.

There are a variety of advanced materials having exceptionally high thermal conductivities. Among them, the monolithic carbonaceous material are well known as the best

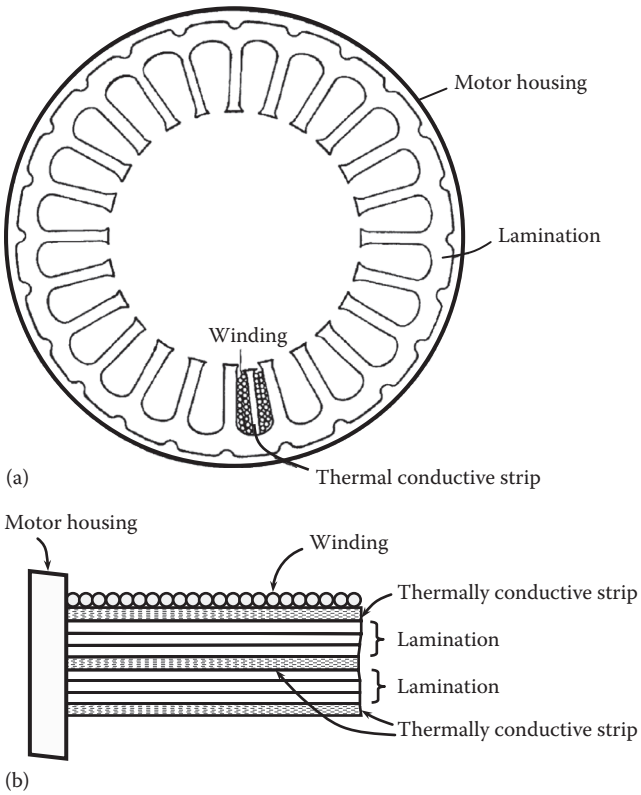

FIGURE 8.3
Using thermally conductive strips in motor cooling: (a) placed between winding coils, and (b) interleaved into stacked motor laminations (U.S. Patent 6,777,835) [8.11]. (Courtesy of the U.S. Patent and Trademark Office, Alexandria, VA.)

thermally conductive materials, such as diamonds that are made from chemical vapor deposition (CVD) at low pressures and low temperatures. One of the remarkable properties of diamond is its unsurpassed thermal conductivity. With a value of 1800 W/m-K and higher at room temperature, it exceeds that of copper (approximately 400 W/m-K at room temperature) by a factor of 4.5 [8.12]. Furthermore, diamond had been the world's hardest material until recent years [8.13].

In addition to thermal conductivity, thermal stress arising from differences in CTEs between mating parts is a key issue in motor design. In general, materials with low CTE are highly desirable for their inherent dimensional stabilities. At temperature of 300 K (26.85°C), the CTE of CVD diamond is 1×10^{-6} K^{-1}, which is much lower than that of copper (17×10^{-6} K^{-1} at 20°C) and aluminum (24×10^{-6} K^{-1} at 20°C).

The superior properties of carbon fibers such as high thermal conductivity, low thermal expansion, high strength, lightweight, and corrosion resistance have made these materials especially useful for applications where heat removal is important. Some commercial carbon fibers have nominal thermal conductivities as high as 1100 W/m-K. Experimental discontinuous fibers reportedly have thermal conductivities of 2000 W/m-K [8.14]. The development of carbon nanotubes with extremely high thermal conductivities is a major breakthrough and will be discussed in later sections.

More recently, a new advanced material called Pyriod® HT pyrolytic graphite has been developed for enhancing heat transfer in electronic cooling. With a single crystalline structure and a high purity (99.999%), the thermal conductivity of the material can be as high as 1700 W/m-K [8.15], which is about four times higher than that of copper and seven times of aluminum (205–250 W/m-K at room temperature). Moreover, this material exhibits four times the ability to sustain tensile load than natural graphite material, nearly five times the flexural load and six times Young's modulus. The material can work at extremely high temperature, up to 3300°C. Because of its superior thermal and mechanical properties, Pyriod HT can be used for thermal management applications in a variety of industries including aerospace, defense, electronic, automobile, medical device, and power generation.

8.2.4 Using Self-Adhesive Magnet Wire for Fabricating Stator Winding

The use of self-adhesive magnet wires to make stator windings has a long history in linear motor manufacturing. In a linear motor, each stator coil is produced by winding self-adhesive wire into a coil shape, subjecting the coil to rapid electric heating to activate a bounding layer on the wire and pressing the coil into its final shape. When the coil is cooled down, it forms the self-supported robust coil (Figure 8.4).

This winding technique can be easily adopted into rotating electric motors. The use of self-adhesive wires may offer advantages over conventional wires in certain winding applications: (1) As a semisolid body with minimized voids inside the coil, conductive heat transfer in the self-adhesive winding is greatly enhanced, and in turn, hot spots of the winding are mitigated or eliminated. (2) Using of self-adhesive wires allows coils to be self-supported, so that bobbins as well as coil taping are no longer necessary. (3) A stator winding made from self-adhesive wires has much smaller volume compared with a conventional winding, leading to smaller motor size and high power density.

8.3 Natural Convection Cooling with Fins

With very low heat removal capacity, natural convection cooling techniques are limited to applications with low thermal loads. Natural convection flows are induced by buoyancy forces due to density gradients caused by temperature variations in the air layer adjacent to the heated surfaces. As shown in Table 8.1, without applying heat transfer enhancement

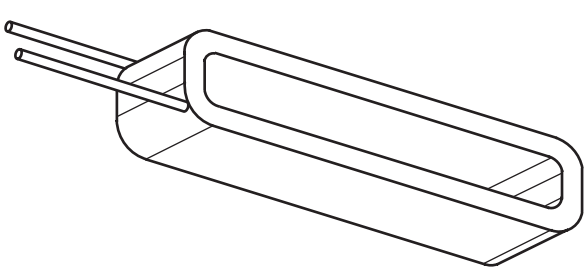

FIGURE 8.4
Stator coil made of self-adhesive magnet wire.

techniques, the heat transfer coefficient of natural air convection only ranges from 5 to 30 W/m^2-K. As a result, natural convection cooling has a limited role in motor cooling.

8.3.1 Cooling Fin

The rapid increase in power density of advanced motors and the miniaturization of motion control devices have created a need for improved cooling technologies to achieve high heat dissipation rates. Under low or moderate heat flux conditions, the most common approach in passive cooling techniques is to utilize natural convective flows that are induced and developed along hot surfaces due to density gradients in fluids (air or liquid).

In order to achieve reliability and optimal performance of motion systems, appropriate thermal management is imperative. Thus, it is desirable to increase the overall convective surface area exposed to the cooling fluid for enhancing heat transfer rates between the heat-dissipating surface and the convective cooling fluid. One of the effective methods to accomplish this objective is to directly employ various cooling fins on the external surfaces of the motor housing and endbells. Such augmentation can result in as much as an order-of-magnitude increase in the heat transfer rate without altering other motor components.

There are many techniques available to enhance heat dissipating from electric machines. Heat sinks are widely employed in electronic systems where space is limited. The use of passive natural convection–cooled longitudinal straight plate-fin heat sinks offers substantial advantages in cost and reliability but is often accompanied by relatively low heat transfer rates.

Cooling fins can be classified as either plate fins or pin fins. Plate fins are usually made of aluminum or copper by extrusion or casting processing. As shown in Figure 8.5, there are various types of plate fins, including (a) straight plate fin, (b) wavy plate fin, (c) radial–helical plate fin, (d) wavy protruding strip plate fins [8.16], (e) flared plate fin, (f) 3D radial plate fin, and (g) constructive fin [817,8.18]. The use of straight plate fins offers substantial advantages in cost and manufacturing but is often accompanied by relatively low heat transfer rates. For a plate-fin heat sink, cooling channels are formed with adjacent plate fins. When cooling flow passes through these channels, the velocity profile is identical except at the flow inlet regions. This indicates that the thickness of the flow boundary layers remains a constant both along the channel and across the channels. Bar-Cohen and Jelinek [8.19] developed guidelines and design equations for optimum plate-fin arrays.

With wavy plate fins, the cooling air flow changes its flowing direction periodically along the channel, causing the local flow separation and reattachment with the passage side surfaces. The disturbance between the cooling flow and the plate fins reduces boundary layer thickness and, as a result, increases the heat transfer coefficient. Because flared plate fins and 3D radial plate fins can effectively disturb local cooling flows, they can provide even higher heat transfer enhancement than other types of plate fins. In all designs, rough surfaces of heat sink help generate local turbulent flows that have higher heat transfer coefficient.

8.3.2 Fin Optimization

The optimization of motor cooling plate fins can be achieved by choosing appropriate values from the following design parameters: (1) fin thickness t, (2) fin spacing between adjacent fins b, (3) fin height H, (4) number of fins n, and (5) thickness of the base plate, d.

An effective way to optimize fin design is to use web-based tools. Though these tools were originally developed for the design of heat sinks, not quite the same for motor cooling

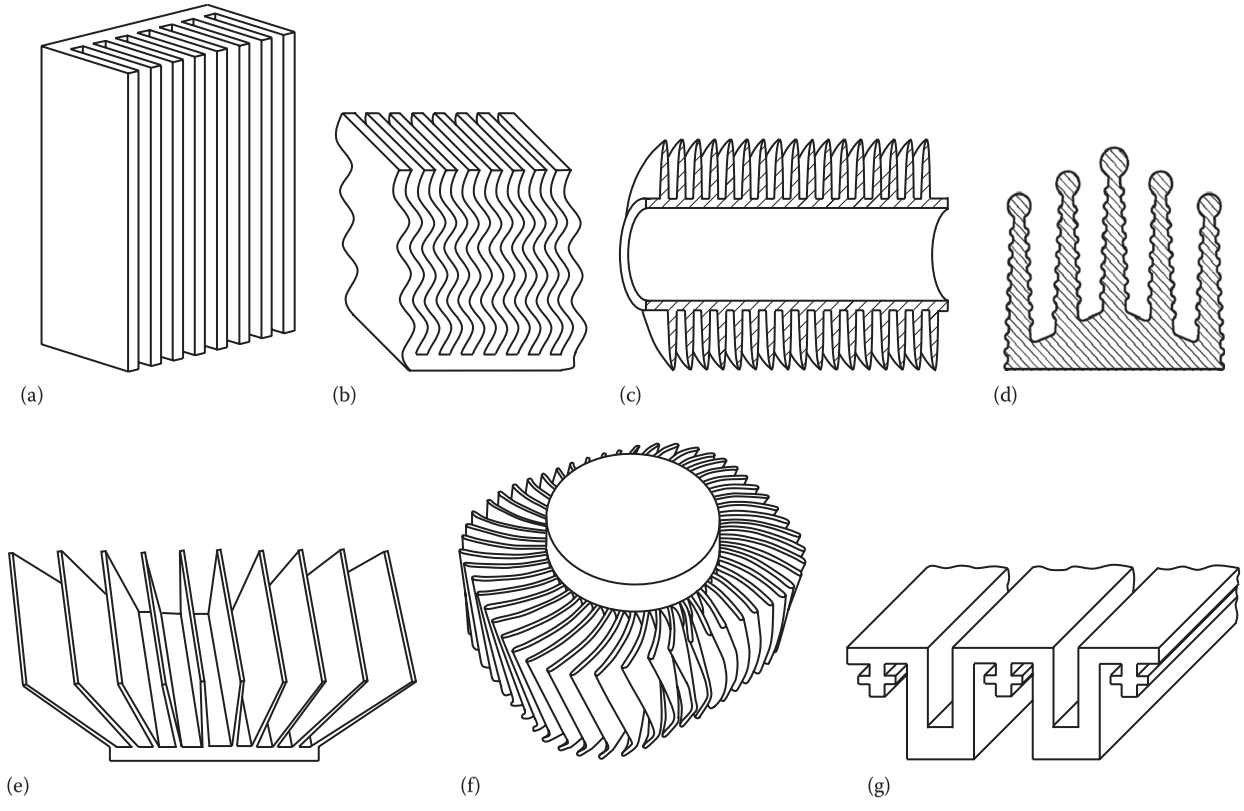

FIGURE 8.5
Types of plate fins: (a) straight plate fin, (b) wavy plate fin, (c) radial–helical plate fin, (d) wavy protruding strip plate fins, (e) flared plate fin, (f) 3D radial plate fin, and (g) constructive plate fin.

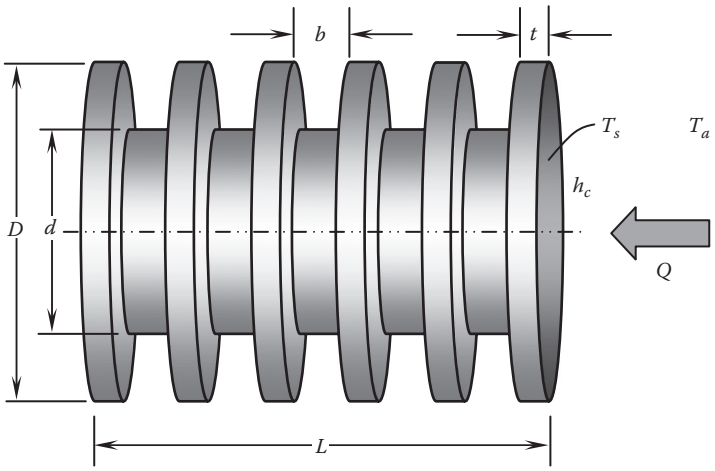

FIGURE 8.6
Thermal model of external fins on the motor's outside surface.

(e.g., the thermal load Q is generated inside the motor rather than entered at the end of the motor), it can provide a starting point for optimizing fin parameters such as fin thickness t, fin spacing b, and fin OD D, as shown in Figure 8.6. With the model in this figure, natural convection heat transfer can be calculated based on the geometry, material properties, and the boundary and ambient conditions [8.20]. Options are available to calculate both the total heat flowrate Q and the isothermal base plate temperature T_s through the independent control of the geometric parameters.

The straight plate-fin efficiency η_f is calculated as [8.21]

$$\eta_f = \frac{\tan h(mH)}{mH} \tag{8.7}$$

where
H is the fin height
m is the fin parameter, which is given as

$$m = \sqrt{\frac{2h}{k_f t}} \tag{8.8}$$

where
h is the convective heat transfer coefficient
k_f is the thermal conductivity of the fin material
t is the fin thickness

For radial plate fins, the fin height is calculated as

$$H = \frac{D - d}{2} \tag{8.9}$$

In calculating the heat transfer of heat sink, two nondimensional parameters are important, the Nusselt number Nu and the Raleigh number Ra, defined as [8.22]

$$Nu = \frac{Q}{A_t \Delta T} \frac{b}{k_a} \tag{8.10}$$

$$Ra = \frac{g\beta \Delta T b^3}{\alpha \nu} \frac{b}{D} \tag{8.11}$$

where

A_t is the total area of the outer surface exposed to air
k_a is the thermal conductivity of air
β is the thermal expansion coefficient
g is the acceleration of gravity
α is the thermal diffusivity
ν is the kinematic viscosity
$\Delta T = T_s - T_a$, the temperature differential between the heat source and the ambient

The overall motor-to-ambient thermal resistance R_{th} (in °C/W) is represented by

$$R_{th} = \frac{\Delta T}{Q} \tag{8.12}$$

To demonstrate how the web-based tools work, use the motor and fin parameters as follows: $d = 250$ mm, $t = 5$ mm, $D_1 = 340$ mm (for $H = 45$ mm), $D_2 = 330$ mm (for $H = 40$ mm), $L = 293$ mm, $Q = 1000$ W, and $T_a = 25$°C. The calculated results are displayed in Figure 8.8. It can be seen that with the increase of the fin ratio (defined as the ratio of the fin spacing b to the fin thickness t), the total thermal resistance decreases at lower fin ratios and increases at higher fin ratios. This is because that for a small fin ratio, a flow channel, which is formed between adjacent fins, is too narrow to allow enough cooling air to pass through it. Therefore, increasing the channel width (i.e., the fin ratio) will significantly improve the thermal transport between the cooling air and the fins. In contrast, as the fin ratio becomes very large, since a portion of the cooling air at the channel center region has a weak influence on the heat transport, the thermal performance will become worse for a very large fin spacing.

From Figure 8.7, it can be seen that the lowest thermal resistance occurs at the fin ratio of 1.6, regardless of the fin height. This indicates that for $t = 5$ mm, the best fin spacing is 8 mm. The corresponding fin number is 22.

Increasing the fin height will result in the decrease of the thermal resistance and in turn the increase of the heat transfer rate. As shown in Figure 8.8, when the fin height increases from 30 to 45 mm, the overall thermal resistance reduces about 22.8%. However, the fin height may be limited by several factors such as the motor's available space, manufacturing restrictions, and costs.

The calculated results can be used for estimating the improvement of a finned housing over a bald housing. The overall thermal resistance is 0.115 W/°C for the finned housing and 0.18 W/°C for the bald housing, indicating a 36% thermal improvement.

8.3.3 Applications of Various Fins in Motor Cooling

As shown in Figure 8.9, oblique plate fins are distributed oppositely on the surfaces of a totally enclosed nonventilated motor. The use of oblique plate fins can effectively reduce boundary layer thickness and improve the overall thermal performance.

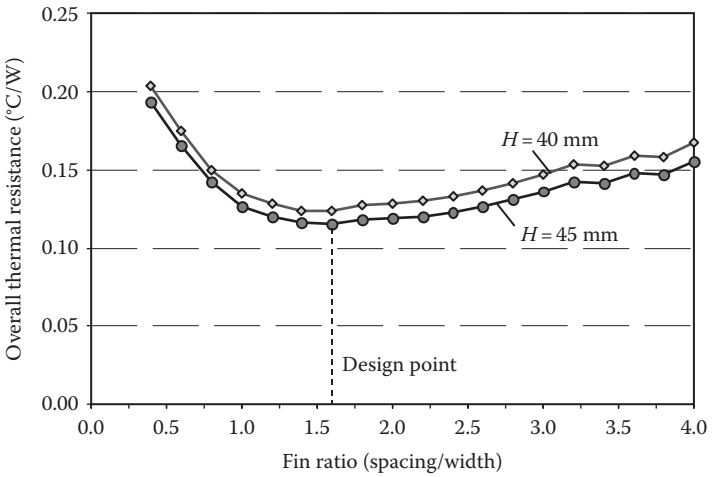

FIGURE 8.7
Effect of fin ratio on overall thermal resistance for a motor with finned housing.

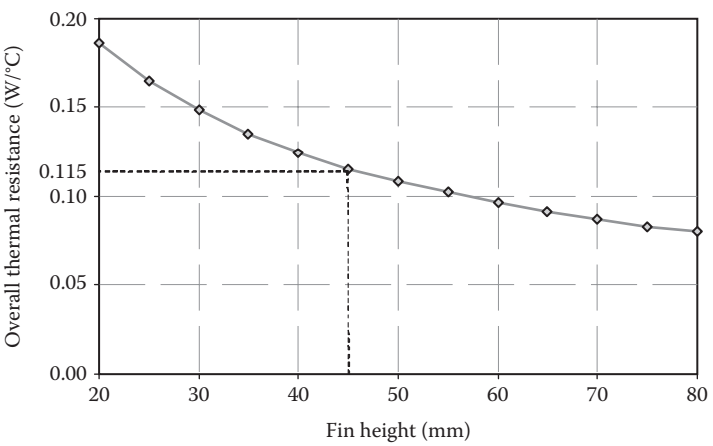

FIGURE 8.8
Effect of fin height on overall thermal resistance of a motor with finned housing.

Figure 8.10 is a perspective view of the motor frame with external and internal fins [8.23]. Because of the extended surfaces, heat generated in the motor during motor operation is dissipated into the environment at a much greater rate, thereby permitting the motor to operate under more severe load and environmental conditions without detrimental effects. This technique can be applied on totally enclosed or open externally ventilated motors. Motors that are totally enclosed and nonventilated depend entirely on the removal of heat from the frame surfaces by natural convection and radiation. Motors that have an open construction depend mainly on the moving of external cooling air into the interior of the motor and discharge the heated air out of the ventilating exits.

In order to increase the heat dissipation from the motor, cooling fins may be used at the outer surface of the endbell, as shown in Figure 8.11.

FIGURE 8.9
Oblique plate fins on the motor outer surface.

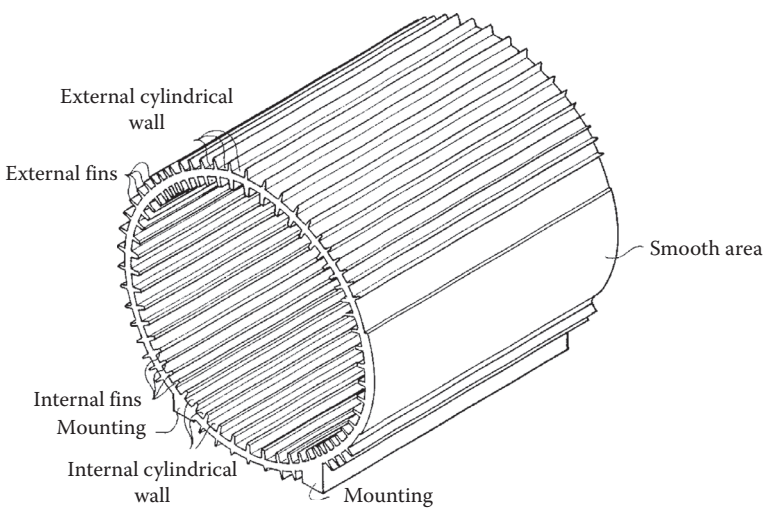

FIGURE 8.10
Outer and inner fins on the motor frame (U.S. Patent 4,839,547) [8.23]. (Courtesy of the U.S. Patent and Trademark Office, Alexandria, VA.)

For some frameless motors, the stator laminations, all of one design, are designed in irregular shapes (e.g., asymmetric rhombus or parallelogram). When these laminations are positioned relative to one another, they form radially oriented external cooling fins. In such a way, motor cooling is benefited from not only the reduction in thermal resistance due to the elimination of the housing but also the heat transfer enhancement due to the effective increase in the heat-dissipative surface area and the disturbance of the cooling air flow resulting from the fins.

Stator fins may be fabricated by prestamping a number of radial slots around the OD of the stator laminations. As the laminations are stacked together as a stator core, a plurality of plate fins are formed in the axial direction [8.24], as shown in Figure 8.12.

FIGURE 8.11
Cooling fins on a motor endbell.

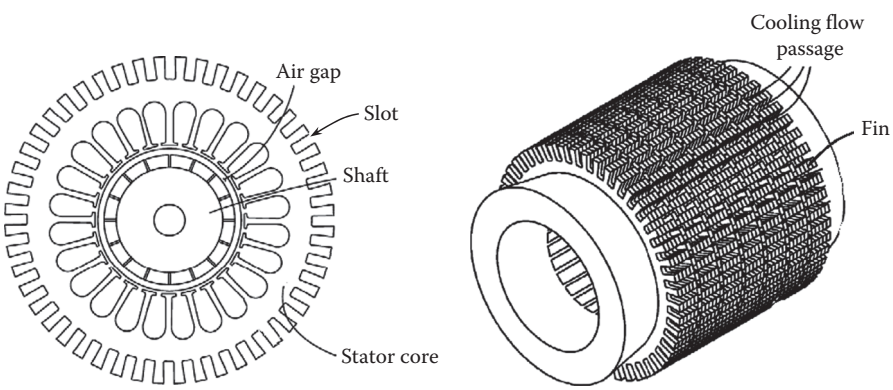

FIGURE 8.12
Stator laminations are stacked to form extending fins on the stator outer surface (U.S. Patent 8,053,938) [8.24]. (Courtesy of the U.S. Patent and Trademark Office, Alexandria, VA.)

This design can be adopted to both frame and frameless motors. For a frame motor, adjacent plate fins define a plurality of longitudinal cooling air channels that extend the entire stator. This approach requires an axial fan to drive cooling flows passing through these cooling channels. As to a frameless motor, heat dissipates directly from the fins to the environment.

A similar design of stator lamination fins is presented in Figure 8.13 [8.25]. The stator consists of a plurality of groups of juxtaposed laminations. When stacking the laminations in one group, each cooling fin portion on each lamination is aligned with a respective cooling fin portion in each lamination such that the aligned cooling fin portions form a cooling

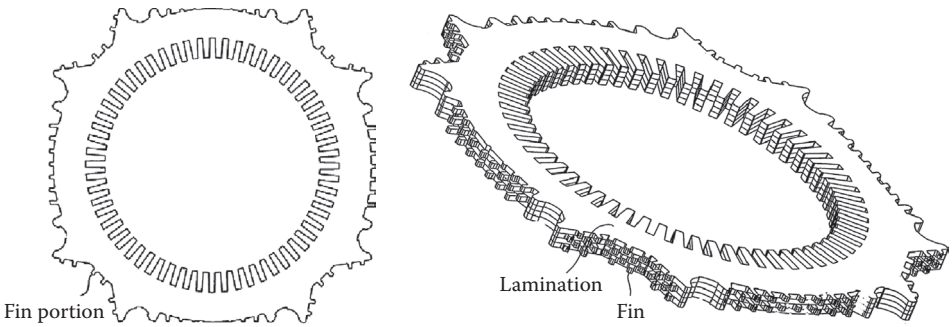

FIGURE 8.13
Fins formed from stacked stator laminations at the outer surface of the stator (WO 2005/022718) [8.25]. (Courtesy of World Intellectual Property Organization, Geneva, Switzerland.)

fin and a series of cooling fins in side-by-side arrangement are formed. Preferably, juxtaposed pairs of groups are arranged such that the cooling fins of one of the groups are staggered with respect to the cooling fins of the other group. With such shaped and arranged cooling fins, air flows between the cooling and adjacent fins are disrupted to reduce the thickness of the thermal boundary layers on the stator surfaces and hence increase conventional heat transfer coefficient.

8.3.4 Pin-Fin Heat Sink

To further improve the thermal performance of heat sinks, an array of pin fins has been used to replace longitudinal straight plate fins. Employment of such pin fins can result in better convective heat transfer characteristics because of the promotion of turbulence in the coolant passages and the increased convective heat transfer surfaces. Heat sinks using pin fins can minimize thermal resistance to improve convective cooling over traditional heat sink designs. It has been reported that with a plate–pin fin heat sink, which is the combination of plate fins and pin fins (as shown in Figure 8.14), thermal resistance can be 30% lower than the conventional plate-fin heat sinks [8.26].

Pressure drop across a pin-fin heat sink is one of the key variables that govern the thermal performance of the heat sink. In general, the total heat sink pressure drop depends on several design parameters and operation conditions, including the pin-fin geometry, pin-fin density and configuration arrangement, pin-fin size, heat sink orientation, and approach velocity (in forced convection). The design of heat sink is intended to decrease the impedance of the fluid flow through the heat sink and, thereby, reduce pressure losses.

Depending on different applications, many shapes of pin fins at the cross-sectional area can be adopted, for instance, round, square, rectangular, oval, rhombic, crescent, and raindrop shaped (Figure 8.15). Among them, the raindrop-shaped pin fins generate the lowest pressure drop across the whole heat sink by minimizing the drag force acting on fins and maintaining large exposed surface area available for heat transfer [8.27]. Square and rectangular pin fins are not preferred because they usually generate relative large flow resistances and thus high pressure drops.

Figure 8.16 depicts the flow pattern between raindrop-shaped pin fins. As cooling flow passes the pin fins, horseshoe vortices are generated in the stagnation area at the front edge of the pin fin by virtue of the staggered fin arrangement, and the flow separates

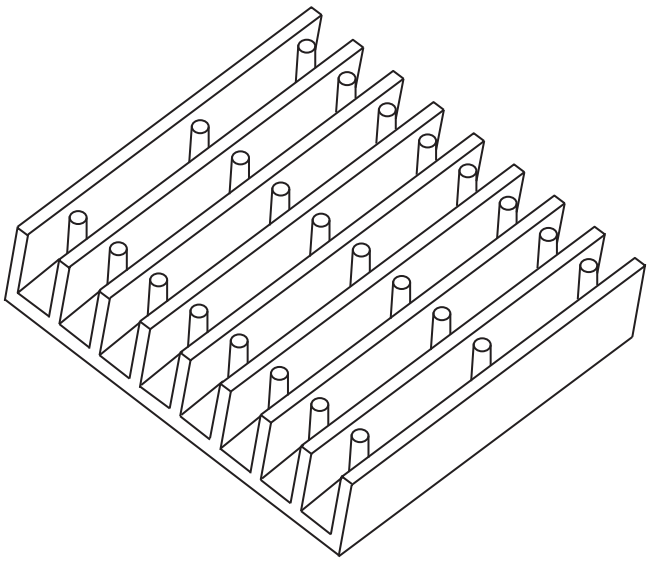

FIGURE 8.14
Plate–pin fin heat sink, which is the combination of plate fins and pin fins.

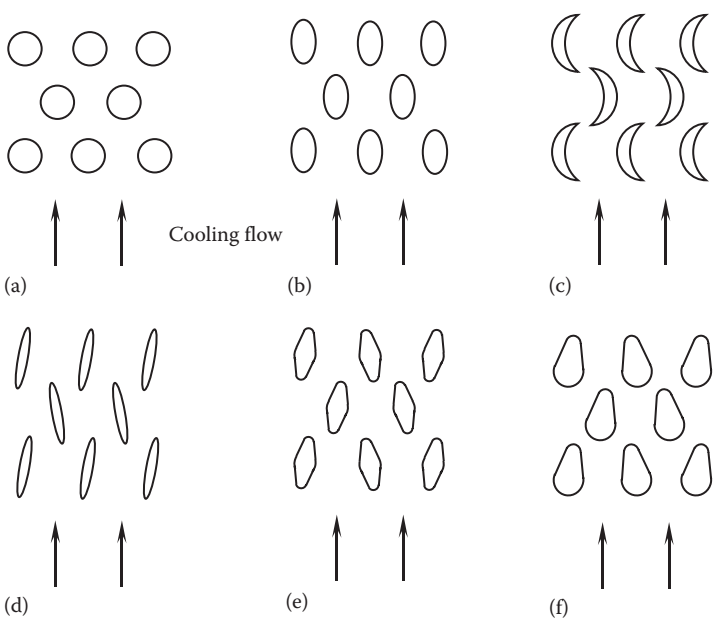

FIGURE 8.15
A variety of pin-fin shapes and arrangements: (a) round pin fins, (b) oval pin fins, (c) crescent pin fins, (d) tilted narrow oval pin fins, (e) tilted rhombic pin fins, and (f) tilted raindrop-shaped pin fins.

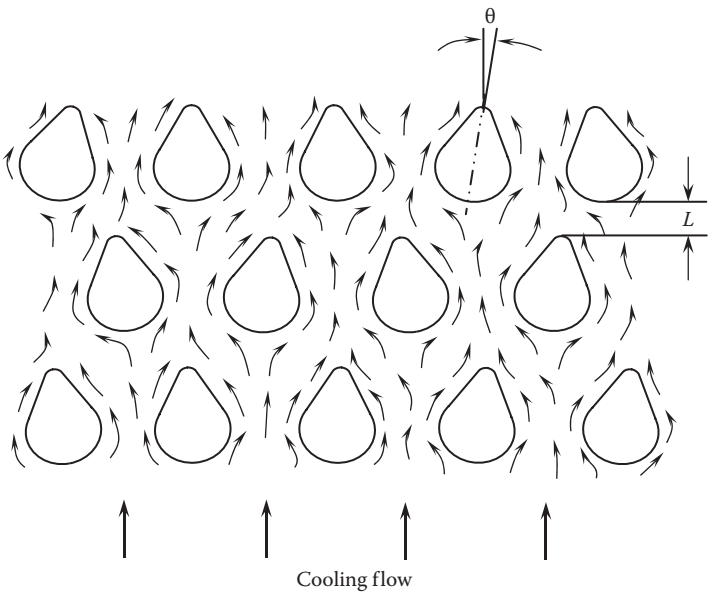

FIGURE 8.16
The flow patterns between raindrop-shaped pin fins. The horseshoe vortices generated in the stagnation areas of the pin fins and the flow separation and reattachment significantly increase the flow turbulence level and thus enhance convective heat transfer.

around the pin fins. The horseshoe vortices can essentially enhance the heat transport. The staggered and tilted arrangement of the pin fins increases the local turbulent level and reduces the size of the wakes, thus tending to reduce the local thermal boundary layer thickness and augment heat transport in these regions. As such, the pin fins serve as turbulence promoters to enhance heat transfer. The combination of the increased heat transfer coefficient and enlarged flow contact area considerably improves heat convection in the flow channel, thereby reducing or even eliminating hot spots.

The fin angle θ is defined as the angle between the fin centerline and the cooling flow direction. In Figure 8.16, a symmetry line is shown with a dash-dotted line. The angle θ of each pin fin may preferably vary between +20° and –20° for maximizing the heat transfer rate. Thus, the fin centerlines are nonparallel with respect to one another.

Another variable that can be used to maximize the heat transfer rate is the fin distance L between adjacent rows of pin fins. At the cooling flow upstream, because the temperature differential ΔT between the convective air and the heat sink is relatively large, the fin distance L can be large. As the temperature of cooling air increases along its path, ΔT becomes smaller and smaller. Thus, the fin distance L may vary accordingly for achieving higher cooling flow velocity and, in turn, higher heat dissipation rate. Regularly, the distance between adjacent rows of pin fins decreases along the cooling flow path.

There are several benefits of using raindrop-shaped pin fins. Firstly, the fins function as turbulent promoters to create local turbulence for enhancing heat transport. Secondly, the fins are designed to minimize the fin-induced wakes at the fin tails, whereby they provide the lowest resistance to the convective air flow. Thirdly, the local heat transfer can be easily controlled by varying the fin angle θ and the fin distance L. Fourthly, the local heat transfer can be alternatively controlled by changing the fin density and fin size along the cooling flow path.

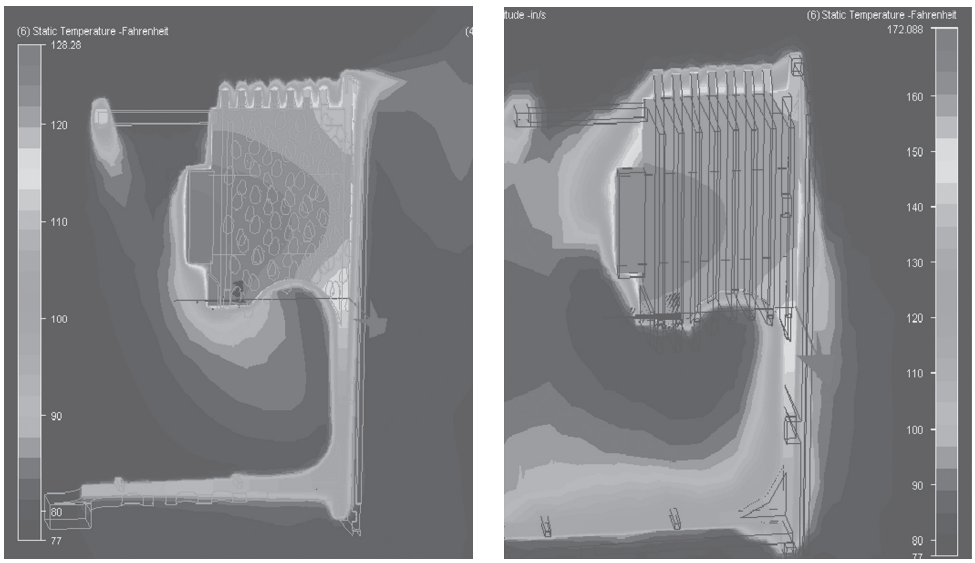

FIGURE 8.17
Numerical analysis results show that under the identical operating condition, the maximum temperature for the raindrop-shaped heat sink (a) is 53.49°C (128.28°F), which is much lower than that for the conventional heat sink with straight plate fins (b) at 77.83°C (172.09°F).

A CFD model has been carried out to compare the thermal performance between the straight plate-fin heat sink and raindrop-shaped pin-fin heat sink. As shown in Figure 8.17a, under identical thermal conditions, the straight plate-fin heat sink has the maximum temperature of 77.83°C, whereas as shown in Figure 8.17b, the raindrop-shaped pin-fin heat sink results in a maximum temperature of 53.49°C. Thus, the heat sink with raindrop-shaped pin fins can efficiently enhance the heat dissipation and improve the heat sink thermal performance by approximately 10%–30% due to not only the extended surface area in contact with the cooling fluid but also the increased local turbulence level of the fluid flow.

The pin-fin configuration can significantly affect the cooling flow pattern and consequently the thermal performance of pin fins. For example, a crescent-shaped pin fin has a concave and a convex surface. As illustrated in Figure 8.18a, crescent-shaped pin fins are configured in a concave–convex pattern at fin rows. The orientation of pin fins between the adjacent rows is opposite. This configuration forces the cooling flow to change its flow direction periodically as it makes its way through the pathway. This causes local flow separation disturbances and subsequent reattachment of flow in the fin boundary layer and correspondingly increases the flow turbulence level and thus enhances convective heat transfer. In addition, the redeveloping boundary layer from the reattachment point also contributes to heat transfer enhancement.

Referring now to the embodiment illustrated in Figure 8.18b, the crescent-shaped pin fins are configured in a concave–concave and convex–convex pattern for all fin rows. This fin arrangement forms a large number of small convergent–divergent (convex–convex pattern) and divergent–convergent (concave–concave pattern) flow channels, configured in a staggered pattern along the flow path. As a cooling flow passes convex–convex

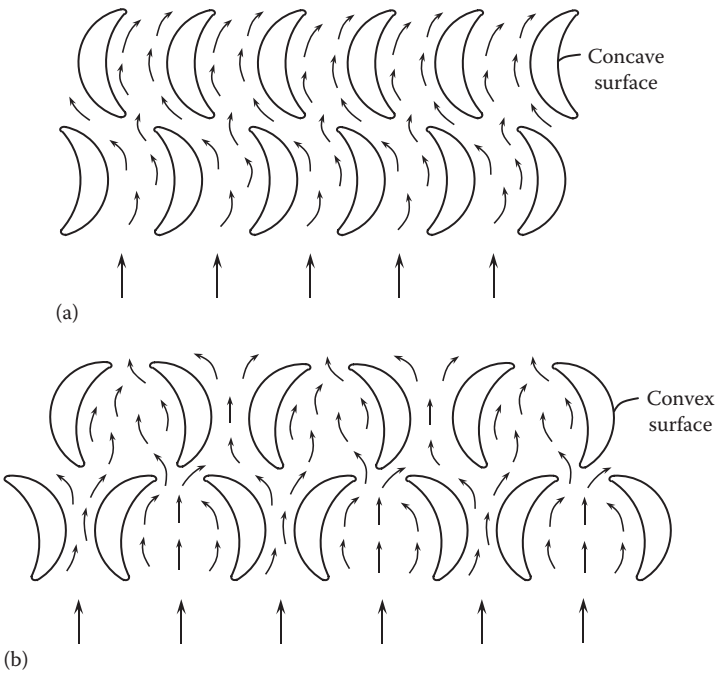

FIGURE 8.18
The flow patterns between crescent-shaped pin fins: (a) configured in a concave–convex pattern at fin rows and (b) configured in a concave–concave and convex–convex pattern for all fin rows.

fin channels, the flow is compressed at the channel entrance and expanded at the channel exit. Contrarily, as the cooling flow passes concave–concave fin channels, the flow is expanded at the channel entrance and compressed at the channel exit. Thus, the variations in the flow velocity, flow direction, and local flow pressure will increase flow reactions and turbulence level in the flow field, resulting in the high heat transfer performance between the fins and cooling flow.

Using an entropy generation minimization method, an optimal design of cylindrical pin-fin heat sinks is obtained for both the in-line and staggered arrangements [8.28,8.29].

Because of the thermally efficient structure of pin fins, motors with pin fins may provide excellent cooling solutions. Benefited from higher thermal contact areas and the promotion of turbulence in cooling flows, pin fins can provide much higher heat transfer rates than plate fins. However, pin fins have not been used in motor cooling yet, primarily due to the high cost of pin fins and some technical difficulties in fabricating pin fins.

8.3.5 Thermal Interface Materials

Thermal interface materials are extensively used in electronic cooling applications for reducing thermal resistance across a contact interface formed by any two solid bodies. Thermal contact resistance occurs due to the voids created by surface roughness effects, material defects, and misalignment of the interface. The voids on the interface are filled with air, which has very low thermal conductivity. Thus, the voids make a significant

contribution to the total thermal resistance. This is especially true for the systems with high thermal loads, a large number of contact parts, and complex surface contacts.

From the microscopic point of view, solid surfaces made by regular manufacturing processes are never perfectly smooth. Rather, the surfaces are constituted of asperities of different sizes and shapes. Therefore, when two solid surfaces are brought together, only a small portion of the matching surfaces make physical contact and the most of the matching surfaces are separated by a layer of air. The voids/gaps formed between the contacted surfaces thus result in high thermal resistance as heat is transferred across the interface. Therefore, a variety of thermal interface materials have been developed for filling voids/gaps, thus improving surface contact and heat conduction across the interface. Because thermal interface materials generally have much higher thermal conductivities than that of air, the interfacial thermal resistance can be significantly reduced.

There are several types of thermal interface materials [8.30]:

- Thermal greases typically offer the best thermal performance to serve as the most popular thermal interface materials. Thermal greases are made by dispersing thermally conductive fillers in viscous silicone or hydrocarbon oils. The use of thermal greases can effectively eliminate the interstitial air in voids or gaps and thus provide a low thermal resistance across the contacted surfaces. Thermal greases tend to wet the matching surfaces well while allowing retention of the high-thermal-conductivity asperity microcontacts. The conductivity of thermal greases is about 0.3 W/(m-K) [8.31], which is about 10 times higher than that of air.

  The characteristics of five greases were studied by Gowda et al. [8.32]. The thermal performance of these greases was measured using the laser flash thermal diffusivity method. The primary filler in these greases is spherical boron nitride (BN) with an average filler size of 60 μm. The testing results are summarized in Table 8.2. The results show that the increase in thermal conductivity is mainly due to the increase in filler loading for all five greases under different pressures. It also shows a significant reduction in thermal resistance with increasing pressure due to a combination of reduced bondline thickness and interfacial thermal resistance.
- Conductive-particle-filled silicone- or acrylic-based thermal tapes and pads offer high thermal conductivity, ranging from 0.7 to 7.3 W/(m-K), and low thermal resistance, ranging from 0.11 to 1.0°C/W, depending on the material and its thickness.
- As indicated by their name, phase-change materials can change their phase when temperature changes. At room temperature, the material is a film. As the temperature increases to a certain value, the viscosity of the materials becomes very small, allowing them to freely flow throughout the joint and fill the voids/gaps.
- Soft metal foils have been developed for years as compressible metallic shims in many applications, especially power devices. Soft metal foils are very thermally conductive, reliable, and easily adopted.
- Thermally conductive elastomers are silicone elastomer pads filled with conductive ceramic particles.
- Thermal adhesives, such as thermal adhesive pads, thermal adhesive tapes, and thermal adhesive films, provide low thermal impedance with long-term reliability.

Each type of thermal interface materials may display different levels of efficiency for reducing the thermal contact resistance, depending on the nature of the contacting

TABLE 8.2

Characteristics of Five Greases and Their Thermal Performance

					$P = 0.1$ MPa		$P = 0.2$ MPa		$P = 0.3$ MPa	
Grease	**Filler**	**Filler Loading (%)**	**Viscosity (Pa-s)**	**Density (kg/m³)**	**Bondline Thickness (μm)**	**Thermal Conductivity (W/m-K)**	**Bondline Thickness (μm)**	**Thermal Conductivity (W/m-K)**	**Bondline Thickness (μm)**	**Thermal Conductivity (W/m-K)**
A1	60 μm spherical BN	35.8	57.5	1200	56.4	4.2	51.3	4.3	48.3	4.4
A2		41.6	98	1300	71.1	5.2	67.3	5.4	59.2	5.2
A3		46.4	191	1400	92.7	5.7	74.9	7.9	69.9	8.3
B1	60 μm spherical BN + secondary filler	71.7	330	2200	50.0	6.5	47.0	7.9	43.9	8.4
B2		80.1	690	2400	57.2	7.9	51.3	9.8	51.8	10.3

Source: Tonapi, S. et al., *Electron. Cool*. November Issue, 2007.

materials, contact conditions (e.g., applied contact pressure, temperature), morphological and crystallographic characteristics of the mating surfaces (e.g., surface roughness, hardness, and wettability), and the process parameters for the thermal interface material application technique.

When the interfacial gaps are filled with a thermal interface material while the surface asperity microcontacts are allowed to form, the heat transfer between two contact bodies can take place through both the microcontacts and microgaps with filled or unfilled interface material. Thus, the overall thermal contact resistance R_c can be determined by treating the microcontact resistance R_{mc} and microgap resistance R_{mg} in parallel:

$$R_c = \frac{R_{mc}R_{mg}}{R_{mc} + R_{mg}} \tag{8.13}$$

When the thermal interface material essentially fills most microgaps, there is little direct contact between two bodies, implying $R_{mc} \gg R_{mg}$ and $R_c \approx R_{mg}$. This indicates that the thermal contact resistance is generally determined by the thermal interface material.

To improve cooling performance of electric motors, thermal interface materials can also play an important role to enhance heat transfer between contacting motor components, such as the stator core and housing, the housing and endbells, winding coils and slots, and bearings and bearing bores.

8.4 Forced Air Cooling Techniques

Forced air cooling has long been applied in motor cooling. Over recent several decades, significant advances have been made in the application of air cooling techniques to manage increased thermal loads. Today, forced air cooling techniques are extensively used for various types of motors for their simplicity, low cost, and high reliability.

Typically, a motor is constructed to have either a totally enclosed architecture or an open architecture. A totally enclosed motor is designed to prevent external contaminating particles and other foreign matter entering into the motor. Therefore, for a totally enclosed motor, there is no air ventilation between the inside and outside of the motor. In contrast, an open motor architecture permits ventilating air entering and leaving the motor freely.

8.4.1 Thermophysical Properties of Air

Air is a mixture of gases, containing approximately 78% of nitrogen and 21% of oxygen, as well as traces of water vapor, carbon dioxide, argon, and various other components. The thermophysical properties of air are functions of temperature and pressure.

Figure 8.19 displays the specific heat of air as a function of temperature. It can be seen that both constant pressure specific heat c_p and constant volume specific heat c_v increase with temperature in a nonlinear manner.

Figure 8.20 presents the thermal conductivity of air as a function of temperature. As the temperature is raised, air molecules move more vigorously, and thus, heat energy is converted into kinetic energy of air. This will lead to more collisions between air molecules per unit time and, consequently, to the increase of the thermal conductivity of air.

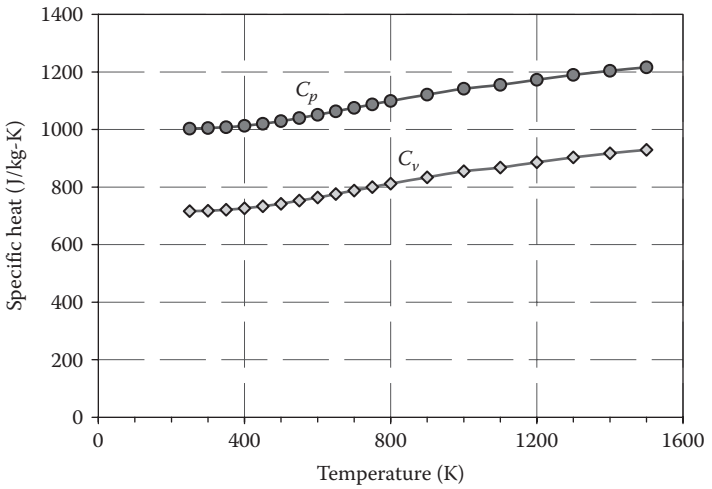

FIGURE 8.19
Specific heat of air as a function of temperature.

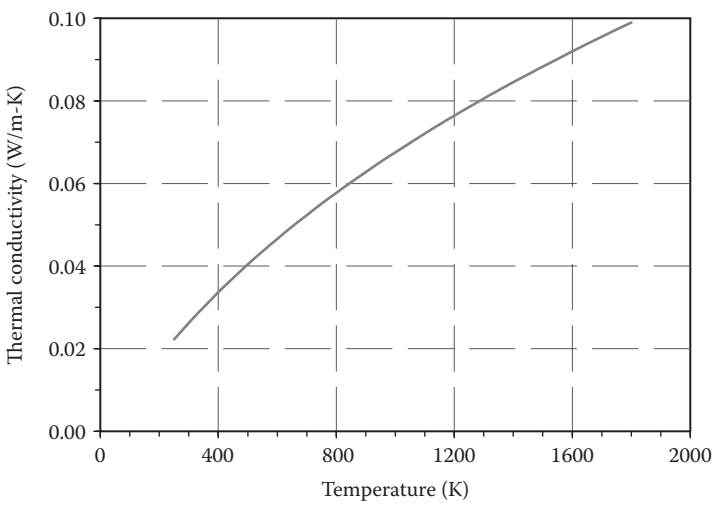

FIGURE 8.20
Thermal conductivity of air as a function of temperature.

Air density is an important parameter in determining the required mass flowrate, system pressure loss, and power. It can be seen from Figure 8.21 that air density decreases with the increase of temperature.

8.4.2 Direct Forced Air Cooling Techniques

Direct forced air cooling is the most popular cooling method for electric motors. In this cooling mode, cooling air is forced to contact directly with heat sources and exhausted out of the motor. It is to be noted that because the winding coils are always wrapped with

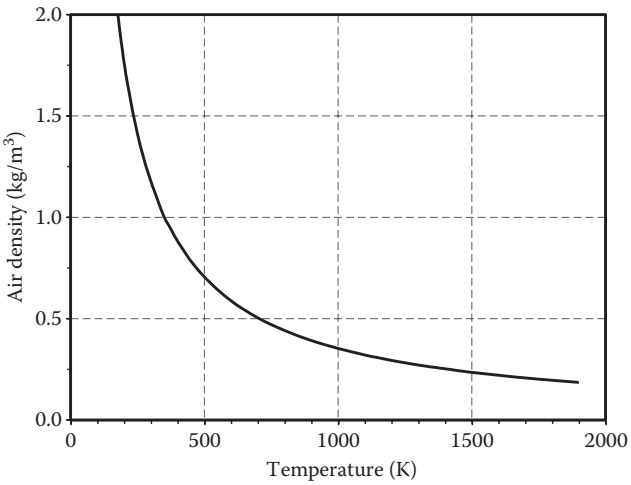

FIGURE 8.21
Air density as a function of temperature.

insulation materials that form a significant thermal barrier, the heat generated within the winding coils must first pass through the electric insulation by conduction.

8.4.2.1 Forced Air Cooling at End-Winding Regions

Hot spots may occur at the stator end-winding regions due to inappropriate cooling of end windings. This is because at the central winding region, the winding coils are in contact with the stator core. The heat generated by the windings is thus conducted through the stator core to the environment. In contrast, the heat generated at the end windings is transferred through two routes. One route travels along the copper coils to the stator core and the other route dissipates the heat to the air surrounding the end windings. Therefore, the thermal resistance of the end windings is considerably higher than that of the central winding. This is especially true for motors with a high *L/D* ratio. In practical motor design, special considerations often put on cooling at the end-winding regions.

According to the fan and cooling path arrangement, several patterns of direct air cooling systems can be identified for cooling at the end-winding regions. A simplest method is to cast a number of fan blades on the end rings during the casting process (Figure 8.22). As the rotor rotates, these blades generate turbulent swirling air flows surrounding the end windings and then force the exhaust hot air exiting the motor through the ventilation slots on the motor housing. For entirely enclosed units, because the heat carried by circulating air must be dissipated to the housing/endbells by convection with a relatively high thermal resistance, the use of this cooling mode may be only suitable for small motors with low thermal loads.

8.4.2.2 Forced Air Flowing through Internal Cooling Channels across the Motor

In this cooling mode, cooling air is introduced from one end of the motor and forced along the internal cooling channels across the motor and exhausted at another end of the motor. As shown in Figure 8.23, the internal fan is mounted at an end of the shaft and cooling air

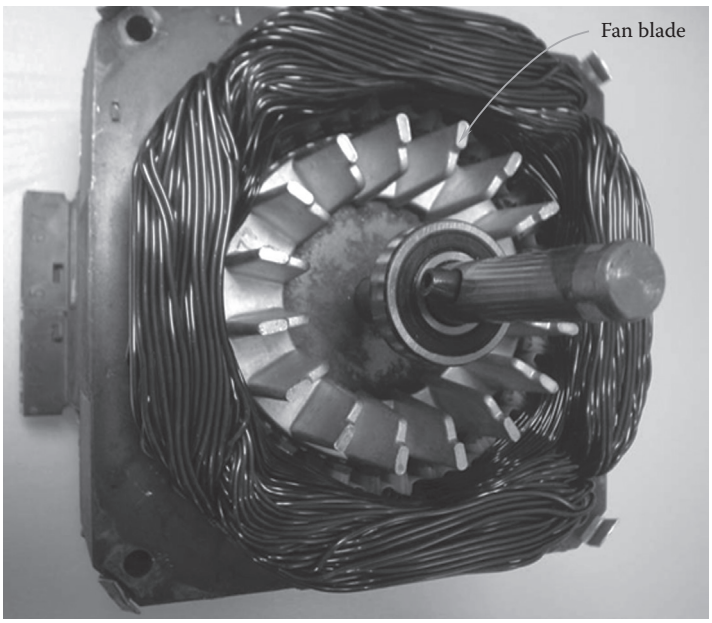

FIGURE 8.22
Rotor fan is casted together with the rotor conducting bars and end rings at each end of the rotor assembly for cooling motor windings, particularly winding end turns.

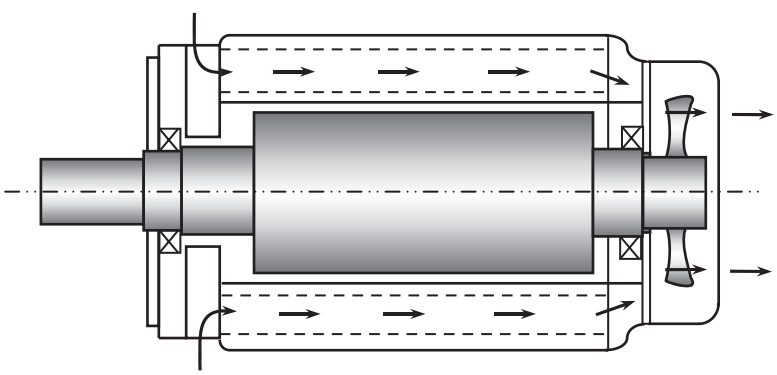

FIGURE 8.23
Open ventilating cooling system with sucked air forcing through stator cooling channels. In this design, a rotor fan is mounted at the nondrive end.

is sucked radially through the ventilating slots from the motor's outer surface and is forced to flow through the cooling channels within the stator core.

In order to provide enough cooling flows through electric motors, the arrangement of cooling channels can be rather flexible. The internal cooling channels may be formed and arranged in a variety of ways: (1) between the stator core and the motor housing (Figure 8.24), (2) through the motor housing (Figure 8.25), (3) through the stator core (Figure 8.26) [8.33], (4) between the state winding coils in the slots (Figure 8.27) [8.34], (5) within the rotor core (Figure 8.28), (6) between the rotor and stator cores (Figure 8.29) [8.35], and (7) a combination of any or all of the aforementioned (Figure 8.30).

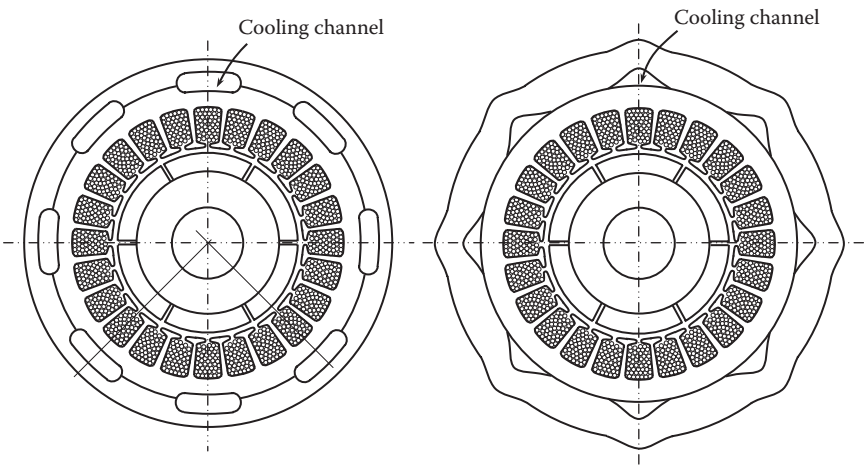

FIGURE 8.24
Arrangement of air cooling channels between the stator core and the motor housing.

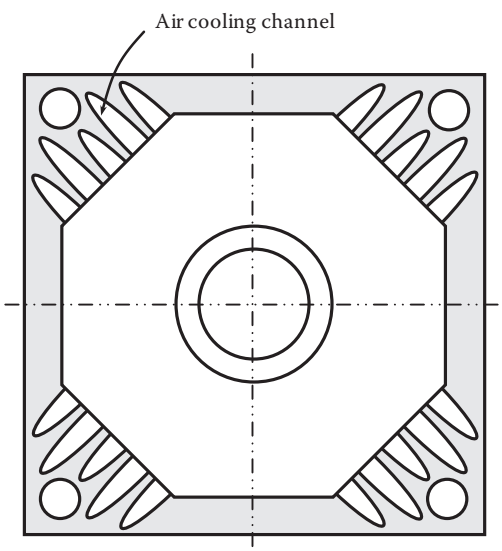

FIGURE 8.25
Air cooling channels through the motor housing.

It must be noted that as cooling air goes through the air gap or the channels through the rotor core, the cooling flow is subjected to a pumping pressure gradient in the radial direction as a consequence of the centrifugal effect, causing a complicated helical flow pattern and resulting in higher pressure drops across the flow channels but better cooling performances.

In addition, the formation of cooling channels through rotor cores or scallop-shaped channels on the rotor surface not only benefits motor cooling but also reduces the rotational inertia of the rotor for shortening the motor start time and prevents the PM between poles from magnetic leaking.

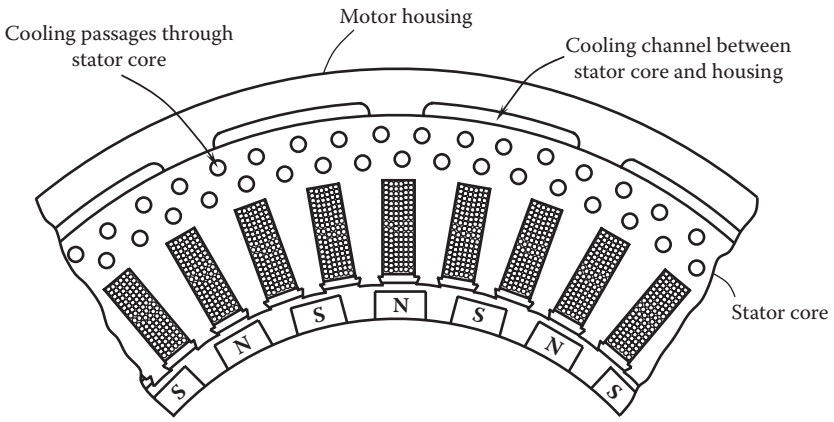

FIGURE 8.26
Cooling passages through the stator core and between the stator core and the housing (U.S. Patent 7,288,870) [8.33]. (Courtesy of the U.S. Patent and Trademark Office, Alexandria, VA.)

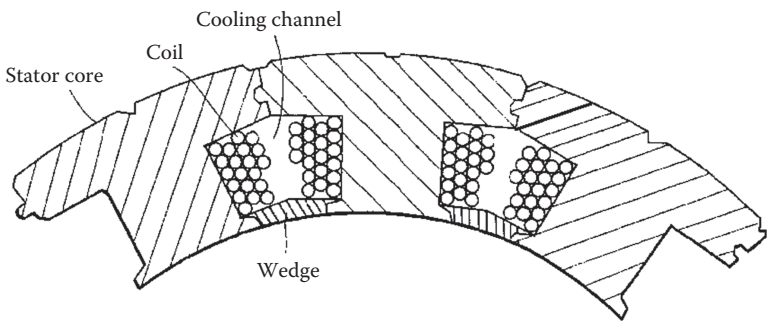

FIGURE 8.27
Cooling channels formed between stator winding coils (U.S. Patent 6,713,927) [8.34]. (Courtesy of the U.S. Patent and Trademark Office, Alexandria, VA.)

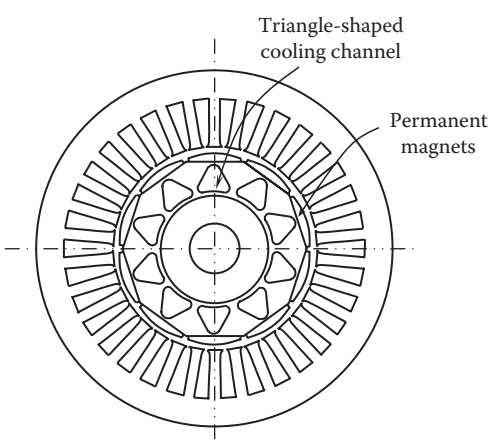

FIGURE 8.28
Triangle-shaped cooling channels through the rotor core.

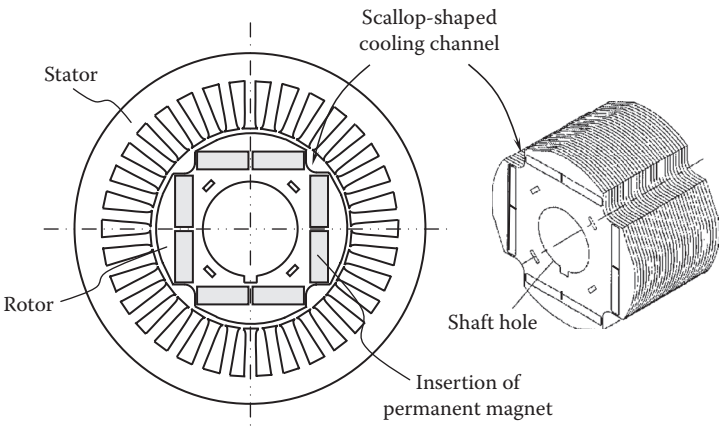

FIGURE 8.29
Scallop-shaped cooling channels between the rotor and stator (U.S. Patent 6,703,745) [8.35]. (Courtesy of the U.S. Patent and Trademark Office, Alexandria, VA.)

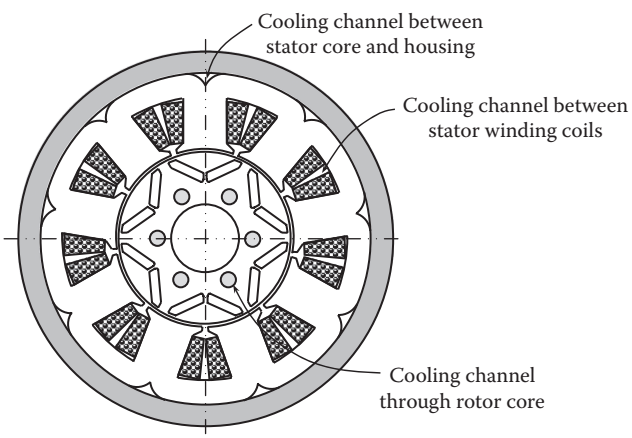

FIGURE 8.30
Combinations of different cooling channel arrangements.

8.4.2.3 Forced Air Flowing over Motor Outer Surfaces

For a totally enclosed motor, because external cooling air cannot enter into the motor, the motor may be cooled by forcing cooling air through the motor outer surface along axial plate fins (Figure 8.31). In this cooling mode, the fan is mounted on the rotor shaft outside of the motor so that the cooling air flowrate depends on the rotor rotating speed. Heat from the stator winding primarily relies on conduction from the stator to the motor housing and is dissipated to the motor surroundings by forced convection. It is noted that in this cooling mode, no internal fans are used inside the motor.

In some circumstances, mounting a cooling fan directly on the motor shaft of a totally enclosed motor is not practical. An alternative solution for motor cooling is to use an additional fan that is installed at the end of the motor. Thus, cooling air is blown over the motor

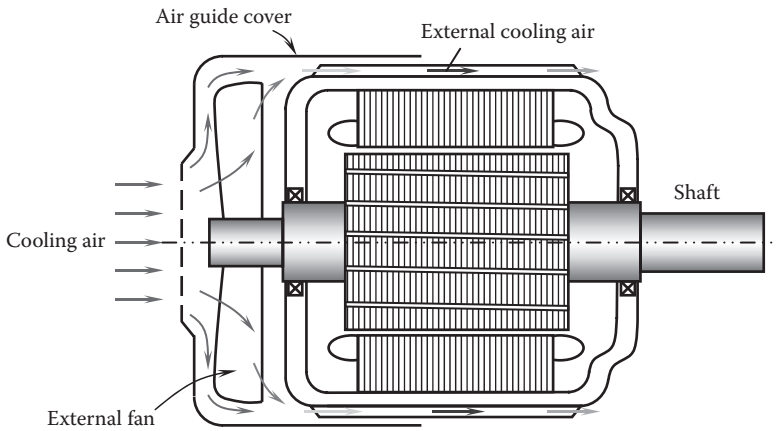

FIGURE 8.31
Cooling air is blown over the totally enclosed motor surface along axial plate fins by an external fan mounted on the shaft. No internal fan is used.

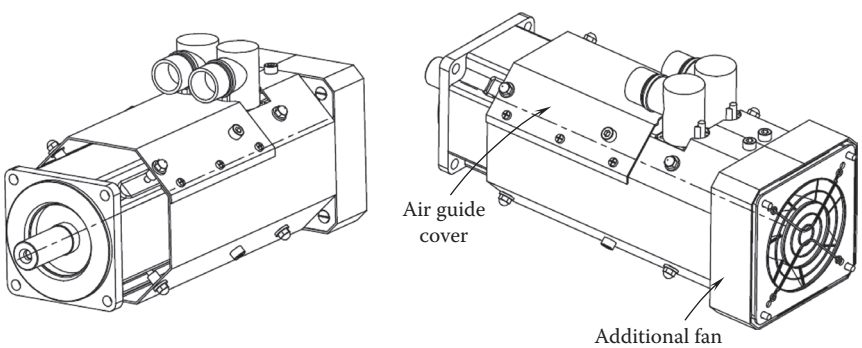

FIGURE 8.32
An additional cooling fan is mounted at the end of motor, blowing cooling air over the motor external surface. (Courtesy of Kollmorgen Corporation, Radford, VA.)

surface guided by the air guide cover (see Figure 8.32). This cooling mode can be flexibly adapted to meet different motor cooling requirements.

8.4.2.4 Forced Air Flowing through Both Motor Outer and Inner Surfaces

This cooling scheme is very similar to the one mentioned previously. To enhance heat transfer for totally enclosed motors, two sets of wafters are cast on the rotor end rings and applied to produce turbulent swirl circulating flows inside the motor. In such a way, the motor housing functions as a heat exchanger. As shown in Figure 8.33, heat generated by motor components is carried by the internal flow and is transferred to the housing wall. At the same time, cooling flow passing through the motor outer surfaces dissipates heat into the environment.

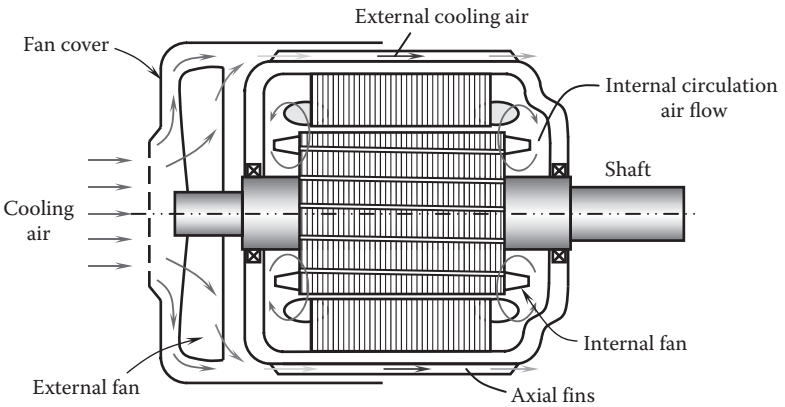

FIGURE 8.33
Motor is cooled by both external and internal air flows; the motor housing functions as a heat exchanger.

8.4.2.5 Air Jet Impingement Cooling

Jet impingement is an attractive cooling mechanism for its capability of achieving high local heat transfer rate in the region of stagnation point. This cooling technique has been extensively used in cooling of gas turbine blades. As a heat transfer enhancement technique, it has been widely used in the cooling of high-heat-flux components such as gas turbine blades and photovoltaic cells. With the increase in power output and the decrease in motor size, interest has been expressed by the motor industry in exploring this technique for cooling motor components. As shown in Figure 8.34 [8.36], the stator end windings are cooled using a jet impingement assembly, which includes a temperature-controlled fluid-generating device for bringing compressed air or other fluids onto the end windings. When the jet impinges on the end-winding surfaces, very thin hydrodynamic and thermal boundary layers form in the impingement region. Consequently, very high heat transfer

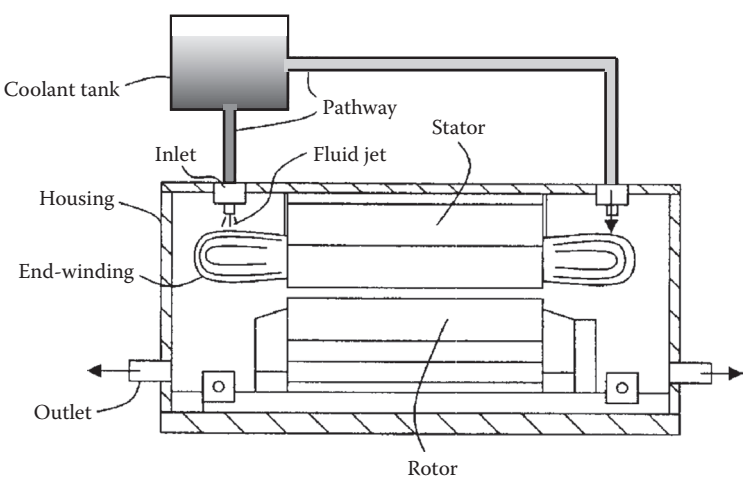

FIGURE 8.34
Cooling of end windings with an impinging jet cooling technique (U.S. Patent 6,639,334) [8.36]. (Courtesy of the U.S. Patent and Trademark Office, Alexandria, VA.)

TABLE 8.3

Cooling Efficient Improvement over Natural Convection

Cooling Technique	Cooling Efficiency Improvement (%)
Forced air	14
Impinging air jet	48
Impinging liquid jet	77

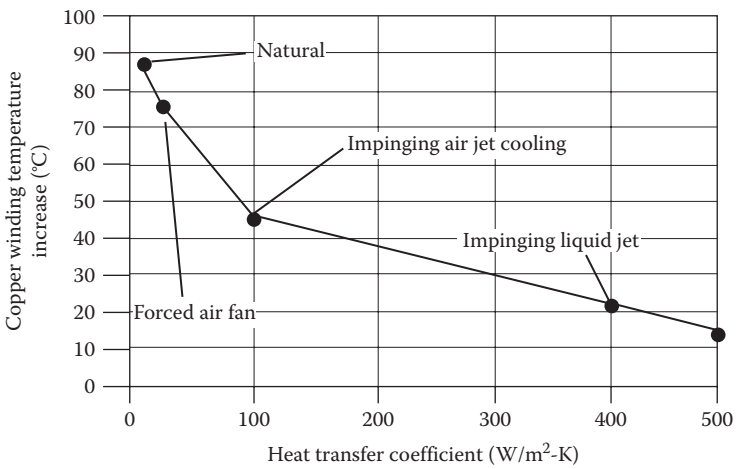

FIGURE 8.35
Temperature rise at end winding with different cooling methods (U.S. Patent 6,639,334) [8.36]. (Courtesy of the U.S. Patent and Trademark Office, Alexandria, VA.)

coefficients are obtained within a stagnation zone. The experimental results have shown that impinging jet cooling offers up to 48% higher cooling efficiency for air impinging jet and 77% for liquid impinging jet over natural convection (see Table 8.3).

Figure 8.35 displays the end-winding temperature rise over the coolant temperature for different cooling methods. Impinging jet cooling, using either air or liquid, can provide a better cooling efficiency by comparing with natural convection and forced air fan cooling. The heat transfer coefficients of jet impingement cooling are much greater than that of natural convection.

The key parameters determining the heat transfer characteristics of a single impinging jet are the Reynolds number, Prandtl number, jet diameter, and jet to target spacing [8.37]. The optimization of an impinging jet system depends on the determination of these parameters through numerical analyses and experiments.

8.4.3 Indirect Forced Air Cooling Techniques

Although forced direct air cooling of a motor can provide a higher cooling efficiency, indirect forced air cooling techniques are often encountered on large motors. For indirect air cooling, air does not directly contact with heated components; the heat generated in a motor is transferred to the ambient by means of heat-exchanging devices.

8.4.3.1 Indirect Forced Air Cooling with Heat Exchangers

Indirect forced air cooling with either air-to-air or air-to-liquid heat exchangers is generally applied to large-size, high-powered electric motors. As depicted in Figure 8.36, the motor is equipped with two axial fans at the two ends of the rotor shaft to internally circulate cooling air within an enclosed system containing the motor and the air-to-air heat exchanger. One centrifugal fan is mounted on the shaft at the outside of the motor frame to force ambient air going through the small staggered tubes of the heat exchanger. In such a way, the energy balance holds between the heat energy dissipated from the internal circulation flows Q_h and the energy carried away by the ambient cooling flow Q_c:

$$Q_h = Q_c \tag{8.14}$$

It follows that

$$\frac{\dot{m}_h}{2}\sum_{i=1}^{2}\left[c_p(T_{hi,out})T_{hi,out} - c_p(T_{h,in})T_{h,in}\right] = \dot{m}_c\left[c_p(T_{c,out})T_{c,out} - c_p(T_{c,in})T_{c,in}\right] \tag{8.15}$$

where

$\dot{m}$ is the mass flowrate

$T_{h1,out}$ and $T_{h2,out}$ are the outlet temperatures of the internal circulation flow at the motor nondrive and drive side, respectively

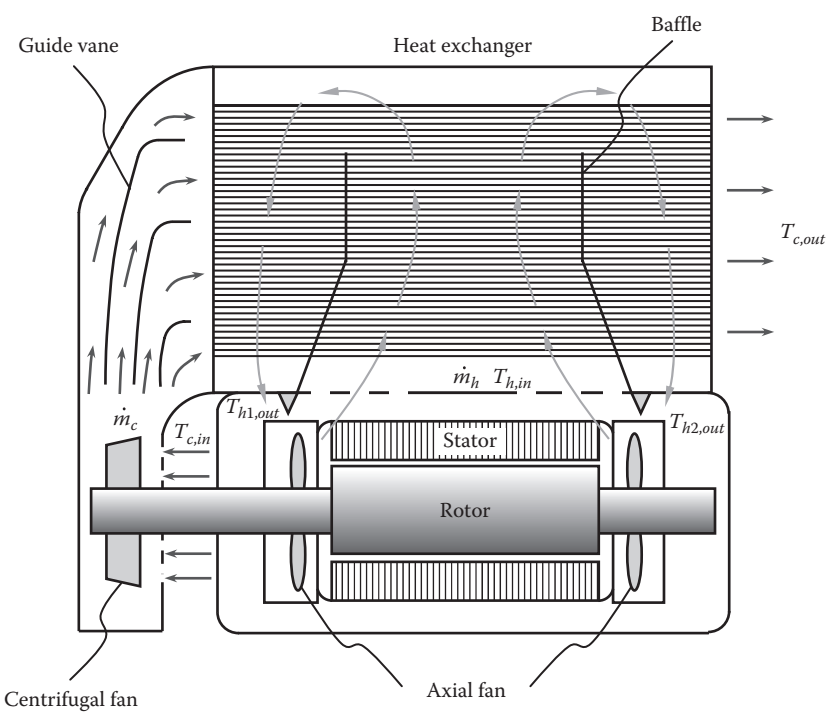

FIGURE 8.36
Forced air cooling with an air-to-air heat exchanger.

This cooling method has been successfully used for a 2350 kW totally enclosed air–air cooled motor [8.38]. With the total loss of 78.93 kW in the motor, the measured temperatures at the copper winding and the iron core are 122°C–138°C and 111°C, respectively. The measured data, including the fan performance curves and the temperature profiles of the stator and the heat exchanger, have shown good agreement with the simulated results.

8.4.3.2 Indirect Forced Air Cooling via Indirect Evaporative Air Cooler

As shown in Figure 8.37, indirect forced air cooling is achieved via an indirect evaporative cooler with the orthogonal flow configuration. The principle of heat transfer in an indirect evaporative cooler involves the use of two types of air, namely, primary air and secondary air [8.39]. The primary air is isolated from the ambient air and is circulated in a loop to cool electric motor. The secondary air is induced from the ambient into the evaporative cooler. Water is sprayed into the passage of the secondary air so that heat and mass transfer takes place. Due to the latent heat absorption during the liquid–vapor phase transition, the temperature of the secondary air reduces and thus lowers the temperature of the primary air. Assuming the same spacing is used for the primary and secondary air, it has been found that the optimum heat transfer of an indirect evaporative cooler occurs at the velocity ratio of the primary to secondary air at approximately 1.4 [8.40].

Khmamas [8.41] has proposed an indirect evaporative cooling (forced or natural) method. With this cooling method, the air cooler is modified to operate as a cooling tower to produce cooling water by the evaporation process. The cooled water is then pumped to the indoor unit passing through a radiator that is cooled by a fan. The experimental results show that the evaporation cooling effectiveness (ECE) reduces by 15% for indirect forced evaporation case and by 22% for the indirect natural case, as compared with the direct cooling case. Although it is seen that the indirect method is less effective than the direct method, some advantages can be gained such as noise reduction and low power consumption.

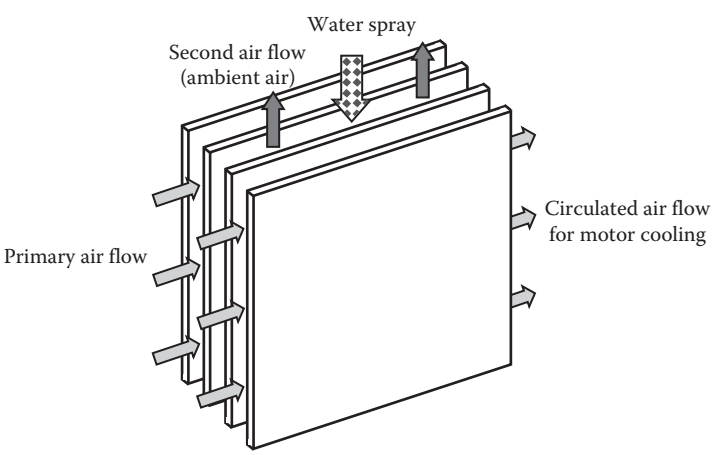

FIGURE 8.37
Forced air cooling with an indirect evaporation air cooler.

8.4.4 Fan and Blower

Fans and blowers are commonly used to provide cooling air flows to cool electric and electronic devices. They are differentiated by the method used to produce air flow and by the system pressure they must operate against. As a general rule, fans typically operate at pressures up to 13.79 kPa (2 psi) and blowers from 13.79 kPa (2 psi) to 193.1 kPa (28 psi), though some special designed fans and blowers may fall out of these ranges. In addition, blowers have much higher specific ratio (usually 1.11–1.20), which is defined as the ratio of the discharge pressure to the suction pressure, than fans (up to 1.11) [8.42].

To deal with the increasing heat loads in high-power-density motors, high-speed fans with noise, energy consumption, reliability, and weight penalties are often used.

8.4.4.1 Fan Types

Based on air flow discharge patterns, several generic fan types with varying air volume and pressure capacities can be identified such as axial fans, centrifugal fans, mixed-flow fans, and cross-flow fans. Axial fans, in which air flow is parallel to the axis of the blade rotation, are the most common type used in electric device cooling. This type of fans is the best choice for applications with high flowrates and low pressure drops. Therefore, the axial flow fans have been used in a wide variety of industrial applications, ranging from small fans for motor drive cooling to the huge fans employed in large wind tunnels. A typical axial fan used for motor cooling is shown in Figure 8.38.

A centrifugal fan has a fan wheel composed of a number of helical impellers or blades (Figure 8.39), mounted on a motor shaft. When the shaft rotates, the cooling air enters at the central part of the fan along the motor axis and then changes its flowing direction by 90° and finally is discharged in the radial direction of the impeller. During the process, the cooling air gains kinetic energy from the rotating impellers to increase its total pressure (i.e., the sum of velocity pressure and static pressure).

At a constant fan speed, a centrifugal fan can drive a constant volume of air rather than a constant mass. Centrifugal fans are the most prevalent fans used in ventilation and air conditioning applications.

A mixed-flow fan combines the high flow of an axial fan and a high pressure of a centrifugal fan. In practice, it uses a modified axial flow impeller to produce a radial component

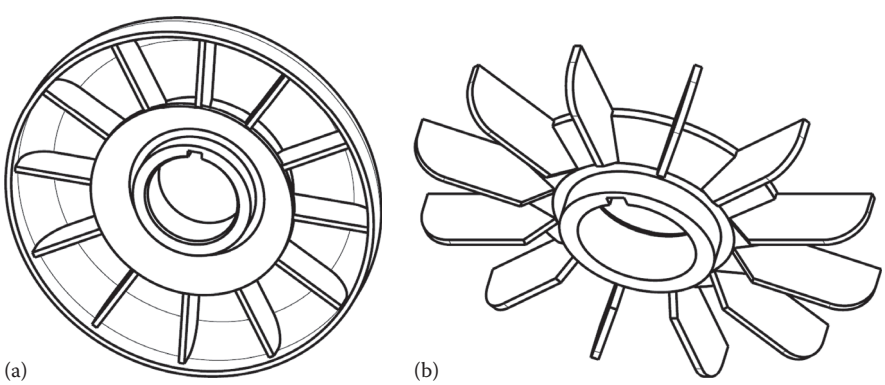

FIGURE 8.38
Casted or molded cooling fan: (a) fan structure (blades, hub, and shroud) and (b) blades on fan hub.

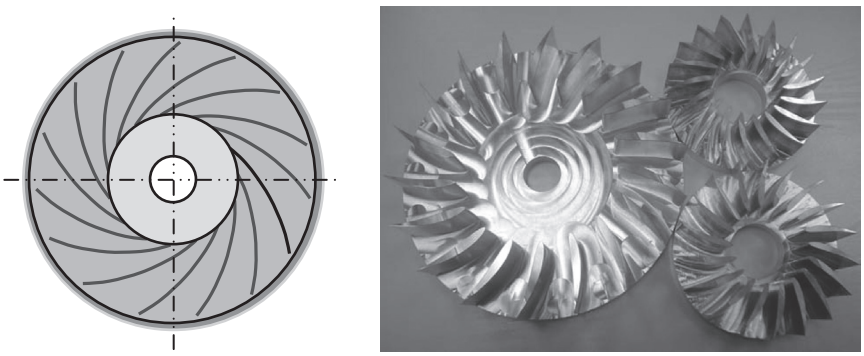

FIGURE 8.39
Helical impeller design in centrifugal fans.

of flow to add to a spiral flow. This type of fans has less outlet losses than axial fans. This provides more flexibility than with either axial or centrifugal fans in relation to fan position, fan outlet, and design of other components [8.43]. It is capable of operating throughout its performance curve without stalling. This type of fans produce less noise compared to axial fans.

Cross-flow fans, sometimes known as tangential fans or tubular fans, have been extensively used in the HVAC industry due to their silent operation and high-volume ventilating air flows at relatively low pressures. The cross-flow fan has a large *L/D* ratio and a drum-type impeller with multiple forward-curved blades. When the impeller rotates, a vortex stream is produced transversely across the impeller. By simply increasing the longitudinal axial length of the impeller, a high discharge flowrate can be achieved.

As shown in Figure 8.40, the air flows pass between the blades on one side of the impeller, through the internal space of the runner, and then through the blade passages for a second time to discharge on the other side of the impeller [8.44]. Thus, the efficiency of this type

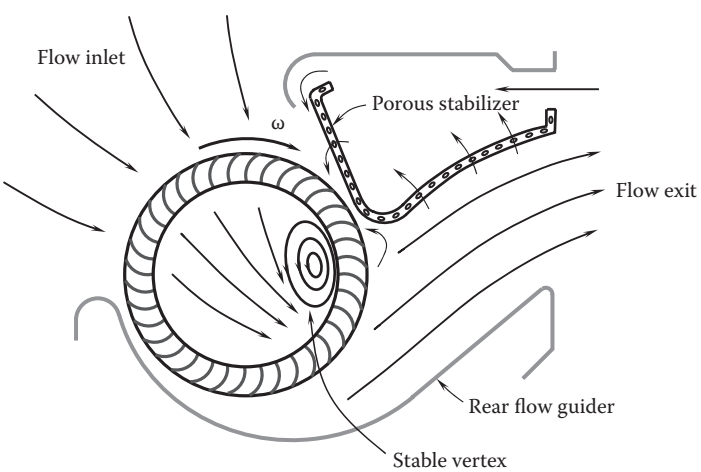

FIGURE 8.40
Cross section and flow pattern of a cross-flow fan.

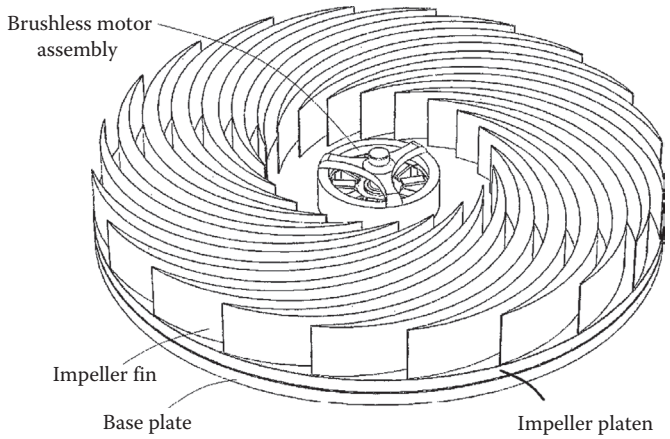

FIGURE 8.41
Combination of fan blades and heat fins as an effective cooling device (U.S. Patent 8,288,675) [8.46]. (Courtesy of the U.S. Patent and Trademark Office, Alexandria, VA.)

of fans is relatively low (<40%) due to the air passing through the blades twice. The porous structure of stabilizer is used for attenuating the fan noise. The numerical results show that the porous stabilizer does affect the emitted noise from the fan. The weak air flows moving in or out through the porous wall of the stabilizer are believed to have played an important role in uniformizing the pressure in the zone of the stabilizer and the vortex and thus are helpful for weakening the vertex flow impingement on the stabilizer wall and reducing the relevant pressure oscillations [8.45].

An innovative device architecture invented at a Sandia National Laboratory [8.46] is presented in Figure 8.41. This device, called *heat sink-impeller*, combines an impeller and rotating fins together to achieve high cooling efficiency and degradation thermal resistance. It consists of a disk-shaped heat spreader populated with helical fins on its top surface and functions like a hybrid of a conventional finned metal heat sink and an impeller. It is a cast metal impeller that floats on a hydrodynamic air bearing just a thousandth of an inch (0.03 mm) above a metal heat pipe spreader, powered by a high-efficiency brushless motor in the middle. Air is drawn in the downward direction into the central region and expelled in the radial direction through the dense array of fins.

The prototype device has shown to provide a severalfold reduction in boundary layer thickness, intrinsic immunity to heat sink fouling, and drastic reductions in noise. This type of cooler is quiet and 30 times more efficient than fan-and-heat sink solutions. It was estimated that if every conventional heat sink in the United States is replaced with this device, the country would use 7% less electricity [8.47].

Though this device was invented mainly for electronic cooling, its fundamental can be adopted for motor cooling easily.

8.4.4.2 Forward-Curved, Backward-Curved, and Straight Blades of Centrifugal Fans

For centrifugal fans, fan blades can be made forward curved, backward curved, or straight (see Figure 8.42). Forward-curved blade fans have blades with leading edges curved forward to the DIR. The fan requires a scroll housing to convert the fan kinetic energy to useful static pressure. However, the efficiency of this type of fans is rather low, about

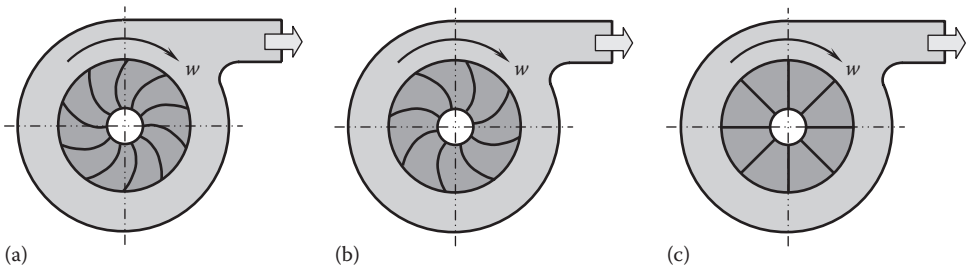

FIGURE 8.42
Three types of centrifugal fan blades: (a) forward-curved blade, (b) backward-curved blade, and (c) straight blade.

55%–65%. This type of fans requires more blades than other centrifugal fans and is best suited for applications that require high flowrates with low static pressures. Since the fans operate at relatively lower speeds, they generate relatively lower noise.

Backward-curved blade fans have blades with leading edges curved backward with respect to the rotation of the impeller. This type of fans runs faster than forward-curved type and is characterized by the most efficient fan, up to 70%–80%. The backward-curved blade fans are normally used for high air flow capacity and high static pressure applications. It should be noted that this type of fans can be designed either using or not using scroll housings, depending on the applications. For a nonscroll housing fan, the impeller can work effectively by itself.

As the simplest and least efficient centrifugal fans, straight blade radial fans have blades that extend straight from the shaft. This type of fans runs at medium speed but generates higher pressures than other types of centrifugal fans. They are often used in corrosive applications and in high-temperature environments.

8.4.4.3 Fan Performance Curve and Operation Point

Fan performance can vary widely among fan models and manufacturers. One of the most valuable pieces of information supplied by fan manufacturers is the fan performance curve, which gives the relationship between the volumetric flowrate $\dot{Q}$ delivered by the fan and the pressure difference Δp. Ventilating fans operate against pressure in their function of moving air through a motor. The fan pressure difference is normally expressed in either total pressure or static pressure (usually in the United States), and the fan volumetric flowrate is in either cubic meters per second (m^3/s) in the *SI* system or cubic feet per minute (*CFM*, ft^3/min) in the English system. Static pressure difference is defined as the difference between the fan inlet and the atmospheric pressure. The total pressure produced by a fan is the sum of the static pressure and the dynamic pressure.

When air flows through a cooling system (i.e., motor), a resistance is produced in the system against the air flow. This resistance, expressed as the sum of all static pressure losses, approximately varies as the square of the flowrate near the operation point of the fan. Thus, as the air flowrate through the system is doubled, the static pressure required to drive air flow is increased about four times. As illustrated in Figure 8.43, the operation point of the fan is determined by the intersection of the fan curve and the system resistance curve. A change in fan rotating speed and the use of the fan in different cooling systems will result in the shift in the operation point of the fan.

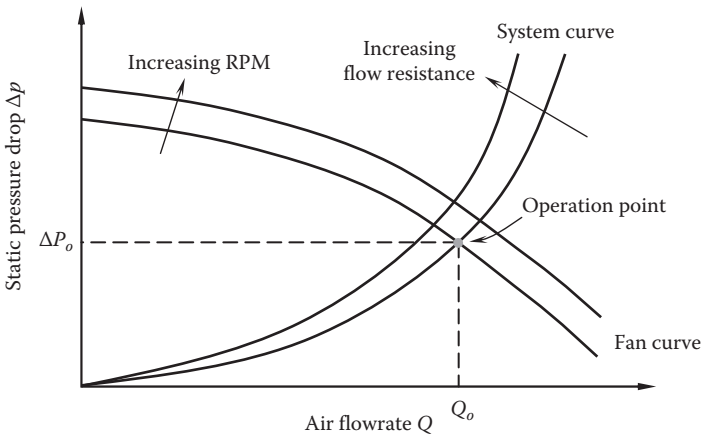

FIGURE 8.43
Fan performance characteristics.

8.4.4.4 Fan Selection

The selection of fans or blowers is critical to long-term successful operation of a motor cooling system. The factors impacting the fan or blower selection include the air flow capacity, efficiency, pressure, type of fluids, size, noise level, and cost.

As discussed previously, centrifugal fans have been frequently used in motor cooling and other high-pressure and low-flow applications. In some cases, they can be also used for low-pressure and low-flow general-purpose applications. Axial fans provide an economic solution in high flow volume and low-pressure systems (e.g., ventilation fans). The type of mixed-flow fan is a hybrid of centrifugal and axial fans, which are capable of greater air flow than centrifugal fans and higher pressures than axial fans. With more complex design, mixed-flow fans typically have higher efficiency, lower noise, and higher cost, compared with other types of fans.

The efficiency of a fan is largely determined by the design of fan blades. Specially designed airfoil blades can drive flow more efficiently and lower fan losses. Therefore, they are suitable for use in compact motors that require high cooling efficiencies with limited spaces. However, airfoil blades are specifically designed for a certain rotating direction. For motors that require bidirectional rotation (e.g., wheel-driving motors), this type of blade is no longer applicable.

8.5 Liquid Cooling Techniques

While traditional air cooling techniques have provided the lowest cost options and served small- or medium-sized electric motors well for a long time, liquid-cooled solutions have been recognized as the best means for cooling high-powered and large-sized modern electric machines. In recent years, liquid cooling is accepted as an attractive cooling method for an increasing number of applications due to higher heat transfer coefficients achieved as compared to air cooling. By moving from air cooling to liquid cooling, thermal restrictions on the design of large-size and high-power-density motors can be removed.

In fact, liquid cooling effectively increases the continuous torque rating of the motor. Application of liquid cooling may be categorized as either direct or indirect, depending upon the liquid direct or indirect contact with the heated motor components. Liquid cooling is accepted as an attractive cooling method for an increasing number of applications.

8.5.1 Thermophysical Properties of Coolants

In the selection of a suitable coolant in liquid cooling, a number of parameters must be carefully considered, including (1) thermophysical properties; (2) electrical properties (especially dielectric strength); (3) chemical compatibility of the coolant with the motor components; (4) freezing, boiling, and flash points; (5) toxicity; (6) erosion; (7) flammability; (8) impact on human health; and (9) cost. Thermophysical properties of some selected coolants including FC series coolants (which are extensively used in electronic cooling) are given in Table 8.4, compared with water. As can be seen from the table, water has the highest specific heat and the lowest viscosity. However, because water is not a dielectric liquid, it may be used for indirect cooling cases.

TABLE 8.4

Thermophysical Properties of Liquid Coolants

Coolant	Density (kg/m^3) at 1 atm	Specific Heat (J/kg-K)	Thermal Conductivity (W/m-K)	Latent Heat of Vaporization (kJ/kg)	Dynamic Viscosity (Pa-s) $\times 10^{-3}$ at 20°C	Freezing Point (°C)	Boiling Point (°C)
Aerosol	1100			216.7	0.205	−101.0	−26.1
Ammonia	609	4740	0.521	1369	0.138	−77.75	−33.34
Aromatic	860	1750	0.14		1.0	<−80	80
Dynalene HC-30	1275	3077	0.519		2.5	<−40	112
Engine oil (SAE 40)	887	1765	0.138		81.3	−12	> 310
Ethanol/water (44/56 by weight)	927	3500	0.38	1636	3.0	−26.6	
Ethylene glycol/water (50/50 by volume)	1069	3350	0.39	1.528	3.4	−37	107.2
Methanol/water (40/60 by weight)	935	3560	0.4	1.344	2.0	−38	78.9
Potassium formate/water (40/60 by weight)	1250	3200	0.53		2.2	−35	110
Propylene glycol/water (50/50 by volume)	1041	3559	0.37	1.585	5.4	−34	105.6
Silicate ester (Coolanol 25R)	910	1990	0.135		4.6	−50	
Silicone (Syltherm XLT)	852	1647	0.11	172	1.4	−111	173
FC-43	1880	1100	0.066	71	5.264	−50	174
FC-72	1680	1088	0.055	87.9	0.672	−90	56
FC-77	1780	1172	0.057	83.7	1.424	−95	97
FC-87	1650	1100	0.056	103	0.66	−115	30
R134a	1188	1420	0.013	215.9	0.209	−96.6	−26.1
Water	997	4181	0.613	2.257	1.002	0	100

For natural and forced convection, the most important parameter is the specific heat of the coolant. This is because it determines how much heat energy can be carried away by the coolant as the coolant mass flowrate $\dot{m}$ and the temperature difference ΔT are specified. A high specific heat is aimed to transfer a large amount of heat with a minimum fluid flow. A low viscosity is also desired because it helps to reduce the resistance of fluid flow. For phase-change heat transfer mechanisms such as evaporative cooling and boiling, the latent heat of vaporization is most important. Boiling and freezing points define the working range of coolants.

8.5.2 Direct Liquid Cooling Techniques

In direct liquid cooling techniques, liquid coolants are directly brought into contact with stator and rotor windings/cores. Therefore, this form of cooling offers excellent opportunities for efficiently removing heat directly from these heat sources without intervening thermal conduction resistance. As a result, direct liquid cooling has a higher cooling efficiency than other convective heat transfer modes such as air cooling and indirect liquid cooling.

The heat transfer coefficient in direct liquid cooling not only depends on the thermal physical properties of the coolant but also on the mode of convective heat transfer (i.e., natural convection, forced convection, or boiling). As shown in Figure 8.44 [8.48], due to the phase change during heat transfer processes, boiling heat transfer offers the highest heat transfer coefficient among all combinations of coolant and heat transfer mode. Though water has showed excellent heat transfer performance, it may be only used for indirect motor cooling for its poor dielectric strength.

Closed-loop systems are normally applied in direct liquid cooling (as well as in indirect liquid cooling) due to the benefits including reducing the consumption of expensive liquid coolant, reducing operation and maintenance costs, avoiding environmental issues associated with the coolant, and lowering noise levels.

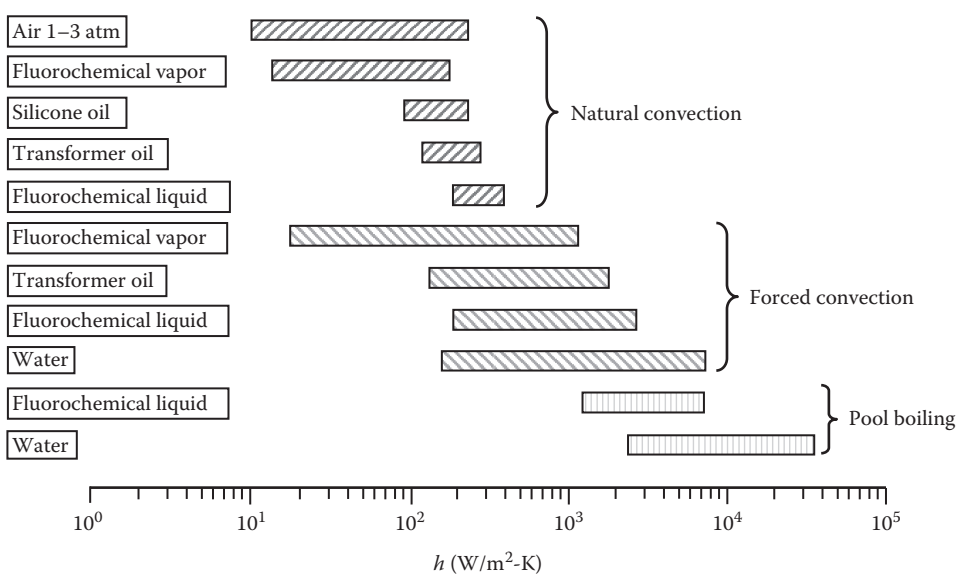

FIGURE 8.44
Relative magnitude of heat transfer coefficients for various coolants and modes of convection. (From Simons, R.E., *Electron. Cool.*, 2(2), 24, 1996.)

There are a number of direct liquid cooling techniques available in motor cooling, such as liquid spray, impinging jet, mist spray, and splash cooling. These cooling techniques are addressed in more detail in the following.

8.5.2.1 Direct Liquid Cooling of Bundled Magnet Wires

This innovative method employs shrink wraps to make magnet wires in bundles and thus liquid cooling channels are formed surrounding the magnet wires [8.49]. As shown in Figure 8.45, a plurality of magnet wires pass through each of the lamination slots. A shrink wrap is inserted into the lamination slots. The stator laminations, shrink wrap, and the magnet wires are heated to shrink the shrink wrap onto the outside of the magnet wire. Therefore, the magnet wires are secured in bundles by the shrink wrap, allowing dielectric oil to move freely inside the lamination slots surrounding the wire bundles. Since fluid can pass between and around the windings, the overall winding temperature will be normalized, essentially reducing hot spots that occur in conventional designs.

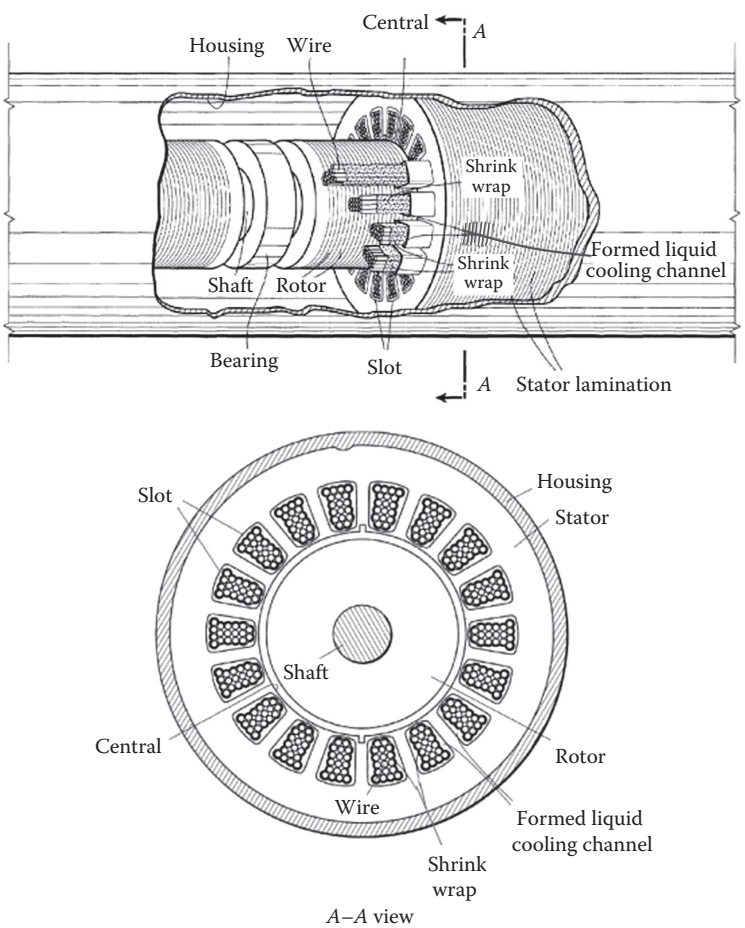

FIGURE 8.45
Enhanced heat transfer using shrink wrap surrounding magnet wires (U.S. Patent 7,679,242) [8.49]. (Courtesy of the U.S. Patent and Trademark Office, Alexandria, VA.)

8.5.2.2 Spray Cooling

Spray cooling is an efficient form of liquid cooling for applications having low to moderate thermal loads. This cooling mode offers an economical and efficient approach for extracting heat from hot surfaces through the use of latent heat of vaporization of a liquid. This approach is to spray liquid droplets onto hot surfaces to create a thin film on the surfaces. As the liquid evaporates, it absorbs heat from its surroundings and lowers the temperature on the surfaces. Hence, it has been widely used in cooling military electronics. As an efficient cooling method, this approach may be promisingly applied to motor cooling.

As demonstrated in Figure 8.46, a spray cooling system primarily consists of a liquid tank, a flow control valve, a pump, a filter, a heat exchanger, and a number of nozzles. The cooling liquid is pumped from the liquid tank and becomes droplets after passing through spray nozzles. By wetting the motor surface with liquid droplets, heat is transferred from heat sources inside the motor to the liquid film and finally dissipated to the environment via forced convection due to the liquid spray, as well as air impinging flow induced by the liquid spray, evaporation, and/or nucleation (in the case that boiling occurs). Obviously, the spray cooling process mainly relies on the phase change from liquid to vapor. Correspondingly, the exceptional cooling capacity is greatly enhanced due to the latent heat of vaporization.

It should be noted that special machining capabilities are required to manufacture spray nozzles to the precision and tolerance required. It has been revealed the variations in nozzle performance due to contamination, corrosion, and long-term wear. Placement of spray nozzles is fairly critical to assure adequate cooling.

The internal spray cooling technique has been used in motors subject to high heat fluxes. As a rotor rotates, liquid coolant such as engine oil is flung off the rotor and/or shaft surfaces in small droplets due to the centrifugal force acting on the coolant. The droplets create a fine mist and impinge on heated motor components. The droplet impingement enhances the spatial uniformity of the heat removal.

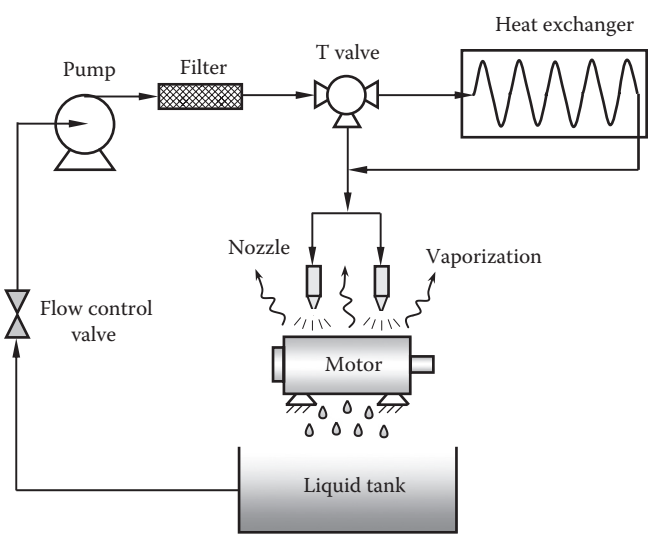

FIGURE 8.46
Spray cooling technique applied on the outer surface of a totally enclosed motor.

In a rotating machinery, an important characteristic of wall rotating–driven flows is the tendency of fluid with high angular momentum to be flung radially outward. For a motor, the rotor rotating-driven flow, usually referred to as the rotating pumping flow, plays an important role in cooling motor windings. Spray cooling occurs when liquid is forced through an array of tiny nozzles to be shattered into dispersive fine droplets. These droplets can spread on the surface and evaporate, removing large amounts of energy through the latent heat of evaporation in addition to substantial conventional effects. In a closed-loop system, the vapor is then condensed and pumped back to the nozzles. Due to its high efficiency, spray cooling can be used for high-heat-flux applications.

The heat transfer rate of spray cooling strongly depends on temperature difference between coolants and heated surfaces. At low temperature differences, heat transfer occurs primarily through single-phase convection. As the temperature difference increases, the evaporation on the liquid film surface, as well as boiling on the heated surface, can significantly augment the heat transfer rate.

Numerous spray cooling techniques have been developed and used in industrial applications. As a promising technique, the internal spray cooling technique has been proven as an effective way for electric machine cooling. The diagram of the spraying cooling system is shown in Figure 8.47. To avoid electric short circuits, dielectric liquids such as mineral oils are commonly selected as coolants. However, the selection of liquid coolant involves the trade-off between performance, functionality, cost, chemical stability, maintenance, safety, and environmental protection. The thermophysical properties of engine oil are listed in Table 8.5 as a function of temperature [8.50].

As can be seen in the figure, the cooling oil is pumped into the hollow shaft and ejected from the tiny nozzles uniformly distributed on the shaft circumference by means of the rotor centrifugal force. The droplet-like oil hits the motor end windings to carry heat away from them. The hot oil is then pumped back into the oil tank and cooled by an oil–water heat exchanger.

A CFD analysis has been carried out to predict the temperature distribution and flow field of the rotor assembly with a similar spray cooling system. An assembled view of a casted rotor assembly is shown in Figure 8.48. The rotor assembly consists of the rotor core, shaft, rotor end rings, and rear endbell. During motor operation, heat is generated in the rotor assembly due to three types of power losses: (1) mechanical power losses such as frictional loss of bearings and windage loss, (2) eddy current and hysteresis losses in the rotor core and other components, and (3) stray losses in the rotor end rings. The cooling oil enters form the rear endbell into the axial cooling duct at the shaft center, turns 90° to get into the four small radial holes near the rotor axial center, then ejects from the nozzles into the cooling ducts between the shaft and rotor core, and finally sprays from the end rings into the interior of the motor.

The mass flow field of the rotor is presented in Figure 8.49. For a one-inlet and multiple-outlet system under a steady-state condition, the inlet mass flowrate must equal to the total mass flowrate from all outlets:

$$\dot{m}_{in} = \sum_i \dot{m}_{out,i} = \sum_i \rho A_{out,i} u_{out,i} \tag{8.16}$$

where

$\dot{m}_{in}$ is the mass flowrate at the inlet

$\dot{m}_{out,i}$ is the mass flowrate at the ith outlet

$A_{out,i}$ and $u_{out,i}$ are the area and velocity at the ith outlet, respectively

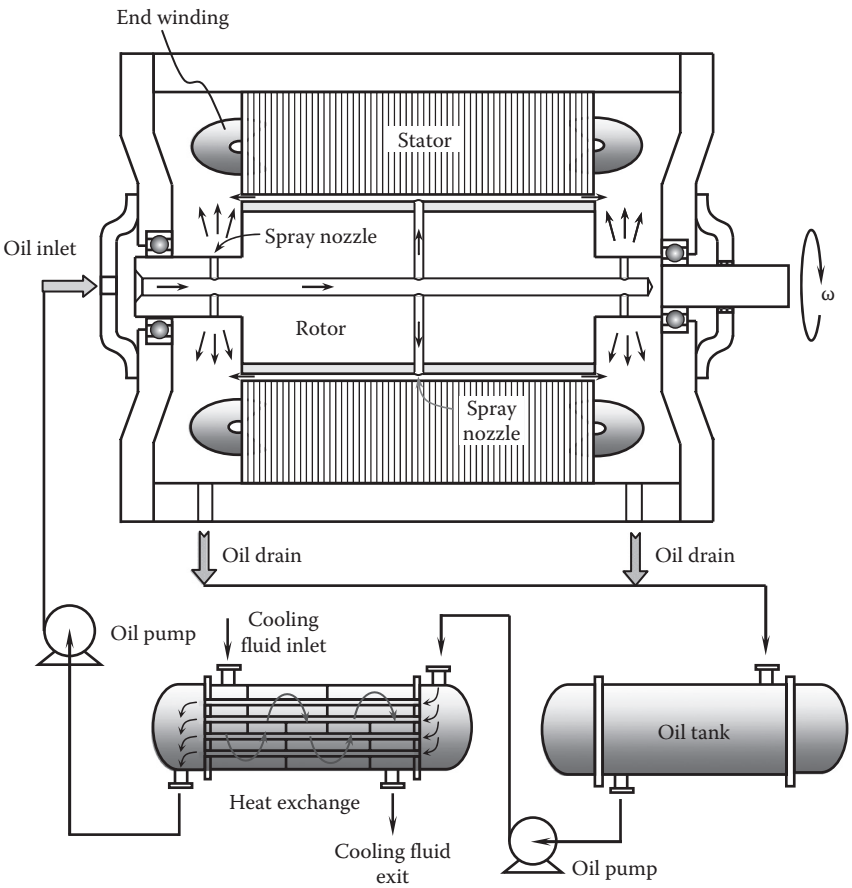

FIGURE 8.47
The internal spray cooling system by utilizing rotor centrifugal force.

TABLE 8.5

Thermophysical Properties of Engine Oil

Temperature (K)	Density (kg/m³)	Specific Heat (kJ/kg-K)	Dynamic Viscosity (Pa-s)	Thermal Conductivity (W/m-K)	Thermal Diffusivity ($m^2/s) \times 10^{-8}$	Prandtl Number	Volume Expansion Coefficient ($1/K) \times 10^{-4}$
260	908	1.76	12.23	0.149	9.324	144,500	7
280	896	1.83	2.17	0.146	8.904	27,200	7
300	884	1.91	0.486	0.144	8.529	6,450	7
320	872	1.99	0.141	0.141	8.125	1,990	7
340	860	2.08	0.053	0.139	7.771	795	7
360	848	2.16	0.025	0.137	7.479	395	7
380	836	2.25	0.014	0.136	7.230	230	7
400	824	2.34	0.009	0.134	6.950	155	7

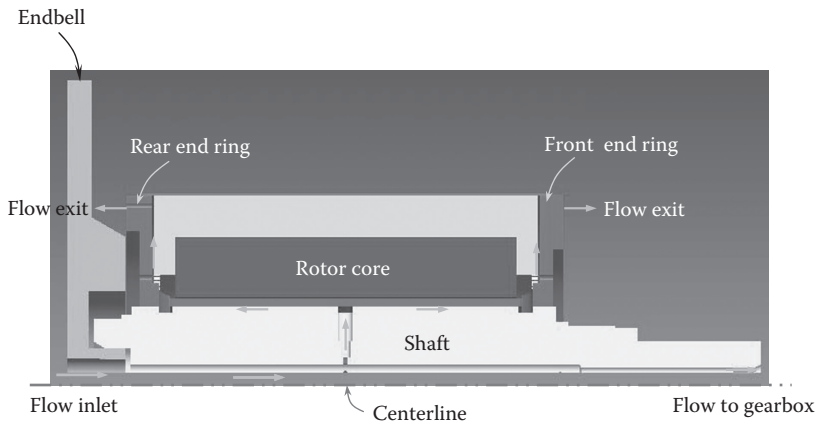

FIGURE 8.48
Cooling flow paths in the rotor assembly (only a half model shown here).

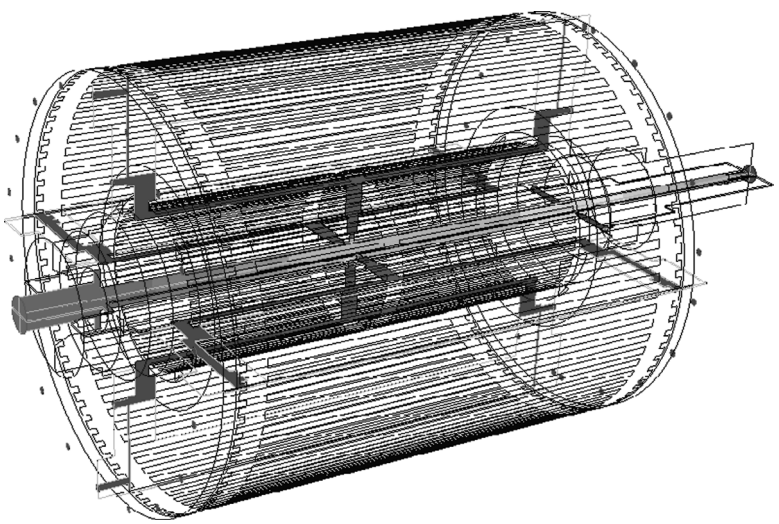

FIGURE 8.49
Cooling flow paths inside the rotor assembly.

The mass flowrate ratio at the *i*th outlet is defined as the ratio of the mass flowrate at that outlet to the total mass flowrate, that is,

$$\eta_i = \frac{\dot{m}_{out,i}}{\dot{m}_{in}} \tag{8.17}$$

Obviously, $\sum_i \eta_i = 1$.

The determination of the η value at each outlet is critical for obtaining relative uniform temperature distribution and elimination of hot spots. It requires distributing the cooling flowrate at each exit appropriately. For this purpose, the dimensions of nozzle and cooling ducts must be iteratively adjusted according to the CFD results.

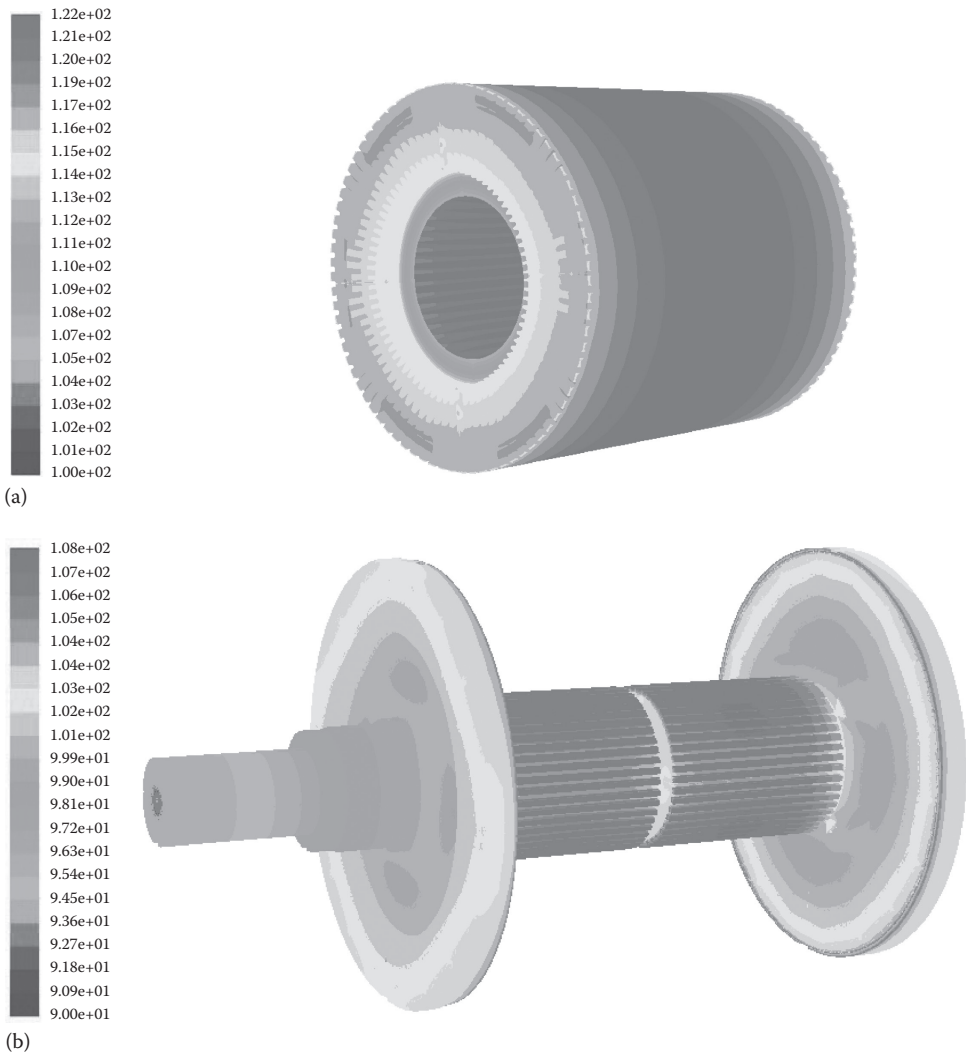

FIGURE 8.50
Temperature distributions in the rotor assembly: (a) rotor core and (b) shaft and end rings, showing the temperature generally decreasing from the center to the two rotor ends symmetrically.

The temperature distribution in the rotor assembly is demonstrated in Figure 8.50, showing that the highest temperature occurs on the outer rotor surface near the rotor axial center and the temperature generally decreases from the axial center to the rotor's two ends.

More detailed information about the temperature distribution inside the rotor assembly is given in Figure 8.51. This information can be adopted to help optimize the rotor cooling design for gaining a higher cooling efficiency and eliminating hot spots in the rotor.

8.5.2.3 Liquid Jet Impingement Cooling

Liquid jet impingement is an attractive cooling option in a number of industries over the past decades. In this cooling method, a liquid is delivered through an array of tiny nozzles

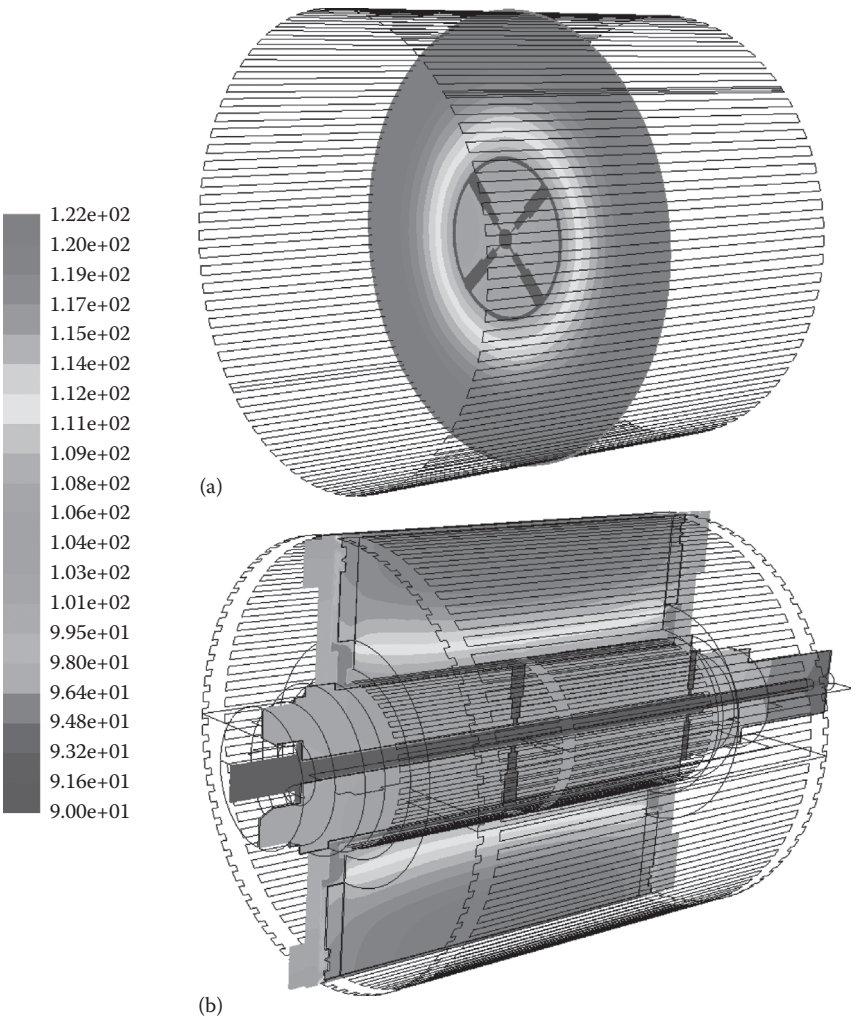

FIGURE 8.51
Temperature distributions in the rotor assembly: (a) the cross-sectional area perpendicular to the rotor axis, the highest temperature occurring at the rotor outer surface, and (b) the cross-sectional area through the rotor axial centerline.

to hit motor windings and other heat source components. For direct liquid jet impingement cooling, a dielectric liquid is required in such an approach to prevent an electrical short from the motor windings and leads unless they are properly protected. For indirect liquid cooling, water may be adopted as the best coolant due to its superior thermophysical properties. Liquid jet impingement cooling offers lower thermal resistance and improves the temperature uniformity.

8.5.3 Liquid Immersion Cooling

Liquid immersion cooling becomes very popular today in electronic cooling applications. The first computer designed to be directly cooled by a liquid was Cray-2 supercomputer,

back to 1985. Since it used a dielectric coolant that does not conduct electricity, the supercomputer could be submersed in the coolant without causing any short circuit. In addition, because the dielectric coolant has much better thermophysical properties than air, it offers the prospect of dramatically more energy-efficient cooling than those in the conventional air cooling approaches. Besides high cooling efficiency, the potential benefits of liquid immersion cooling include the high cooling capacity, temperature uniformity, reliability, and not needing to power internal fans/pumps to assist fluid cooling flows. Compared with air cooling techniques, liquid immersion cooling can help design much more dense devices without the need for flow aisles.

This cooling mode can be successfully transplanted into motor cooling. Some special dielectric coolants such as FC are particularly suitable for motor immersion cooling due to their low toxicity, stable viscosity, UV resistance, and high dielectric strength. In order to control the friction losses, this method may be limited to low rotating speed motors.

8.5.4 Indirect Liquid Cooling Techniques

In an indirect liquid cooling scheme, a liquid coolant does not come into contact with cooling components. Instead, cooling is implemented by using heat exchangers, cold plates, coolers, and other cooling products. In such cases, a good thermal conduction path is needed from heat sources (winding, core, etc.) to the coolant. Since there is no direct contact with the electric windings and connectors, water or water-based antifreezes (e.g., ethylene glycol/water, propylene glycol/water, methanol/water, and ethanol/water), even some liquid metals, can be used as the coolant, taking advantage of their superior thermophysical properties and relatively low costs. This heat transfer mode is in fact encountered in a wide spectrum of engineering systems including energy–power conversion, material procession, internal combustion, electric and electronic devices, and manufacturing process.

8.5.4.1 Indirect Liquid Cooling via Cold Plates Attached to Motor Walls

Cold plates are typically made of copper or aluminum tubes that are bonded into aluminum plates to optimize thermal conductance. Liquid-cooled cold plates may be mounted on motor external surfaces to provide very effective contact cooling for various motor applications having different thermal requirements (Figure 8.52). The dimensions of a cold plate are designed to fit the size of a motor. In practice, cold plates use either water or water-based antifreezes as a coolant. As an example, thermophysical properties of water/glycol mixtures with different mixing ratios are given in Table 8.6.

8.5.4.2 Indirect Liquid Cooling via Helical Copper Pipes Casted in Motor Housing

This cooling method uses helical copper pipes that are directly casted inside the motor housing (Figure 8.53). Water flowing through these helical copper pipes ensures more uniform cooling of the stator due to the generation of the secondary flows in these curved pipes by the centrifugal effect. The advantages of this cooling method are as follows: (1) Because the copper pipes are perfectly integrated with the housing by casting, the thermal contact resistance between the copper pipes and the housing is minimized. (2) There is no leakage from the copper pipes. However, the fabrication cost for such a cooling system is usually higher than other cooling methods, as listed in the following.

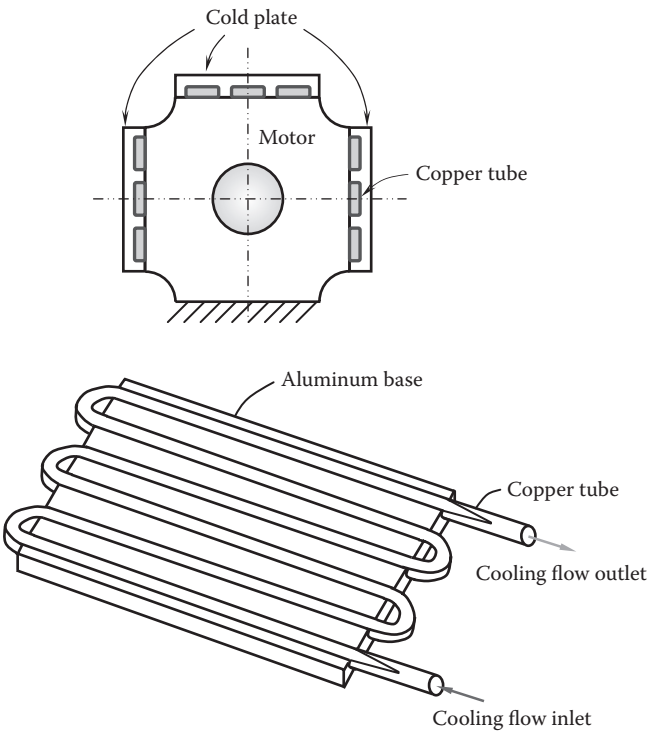

FIGURE 8.52
Cold plates used for motor cooling, mounted on the three sides of the motor.

The thermal energy dissipated to the coolant Q can be determined as

$$Q = \dot{m} C_p \Delta T \tag{8.18}$$

where $\Delta T = T_o - T_i$, the temperature difference between the outlet and inlet of the coolant.

Several correlations are available in the literature for calculating the friction factor as flows through helical pipes. Ito [8.51] proposed a model of friction factor for a turbulent flow:

$$f_c = 0.00725 + 0.076\left[Re\left(\frac{r}{0.5d} \right)^{-2} \right]^{-0.25} \left(\frac{r}{0.5d} \right)^{-0.5} \tag{8.19}$$

which is valid for

$$0.034 < Re\left(\frac{r}{0.5d} \right)^{-2} < 300$$

Srinivasan et al. [8.52] developed a model for flows in a helical pipe:

$$f_c = 0.084\left[Re\left(\frac{r}{0.5d} \right)^{-2} \right]^{-0.2} \left(\frac{r}{0.5d} \right)^{-0.5} \tag{8.20}$$

TABLE 8.6

Thermophysical Properties of Water/Glycol Mixtures with Different Mixing Ratios

Substance	Volume in Mixture (%)	Minimal Working Temperature (°C)	Temperature (°C)	Density (kg/m^3)	Specific Heat (kJ/kg-K)	Thermal Conductivity (W/m-K)	Dynamic Viscosity × 10^3 ($W\text{-}s/m^2$)	Kinematic Viscosity × 10^6 (m^2/s)
Monoethylene glycol $[C_2H_4(OH)_2]$	20	−10	−10	1038	3.85	0.498	5.19	5.0
			0	1036	3.87	0.500	3.11	3.0
			20	1030	3.90	0.512	1.65	1.6
			40	1022	3.93	0.521	1.02	1.0
			60	1014	3.96	0.531	0.71	0.7
			80	1006	3.99	0.540	0.523	0.52
			100	997	4.02	0.550	0.409	0.41
	34	−20	−20	1069	3.51	0.462	11.76	11.0
			0	1063	3.56	0.466	4.89	4.6
			20	1055	3.62	0.470	2.32	2.2
			40	1044	3.68	0.473	1.57	1.5
			60	1033	3.73	0.475	1.01	0.98
			80	1022	3.78	0.478	0.695	0.68
			100	1010	3.84	0.480	0.515	0.51
	52	−40	−40	1108	3.04	0.416	110.8	100
			−20	1100	3.11	0.409	27.5	25
			0	1092	3.19	0.405	10.37	9.5
			20	1082	3.26	0.402	4.87	4.5
			40	1069	3.34	0.398	2.57	2.4
			60	1057	3.41	0.394	1.59	1.5
			80	1045	3.49	0.390	1.05	1.0
			100	1032	3.56	0.385	0.722	0.7

1,2-Propylenglycol $[C_3H_6(OH)_2]$	25	−10	−10	1032	3.93	0.466	10.22	9.9
			0	1030	3.95	0.470	6.18	6.0
			20	1024	3.98	0.478	2.86	2.8
			40	1016	4.00	0.491	1.42	1.4
			60	1003	4.03	0.505	0.903	0.90
			80	986	4.05	0.519	0.671	0.68
			100	979	4.08	0.533	0.509	0.52
	38	−20	−20	1050	3.68	0.420	47.25	45
			0	1045	3.72	0.425	12.54	12
			20	1036	3.77	0.429	4.56	4.4
			40	1025	3.82	0.433	2.26	2.2
			60	1012	3.88	0.437	1.32	1.3
			80	997	3.94	0.441	0.897	0.9
			100	982	4.00	0.445	0.687	0.7
	47	−30	−30	1066	3.45	0.397	160	150
			−20	1062	3.49	0.396	74.3	70
			−10	1058	3.52	0.395	31.74	30
			0	1054	3.56	0.395	18.97	18
			20	1044	3.62	0.394	6.264	6
			40	1030	3.69	0.393	2.987	2.9
			60	1015	3.76	0.392	1.624	1.6
			80	999	3.82	0.391	1.10	1.1
			100	984	3.89	0.390	0.807	0.82

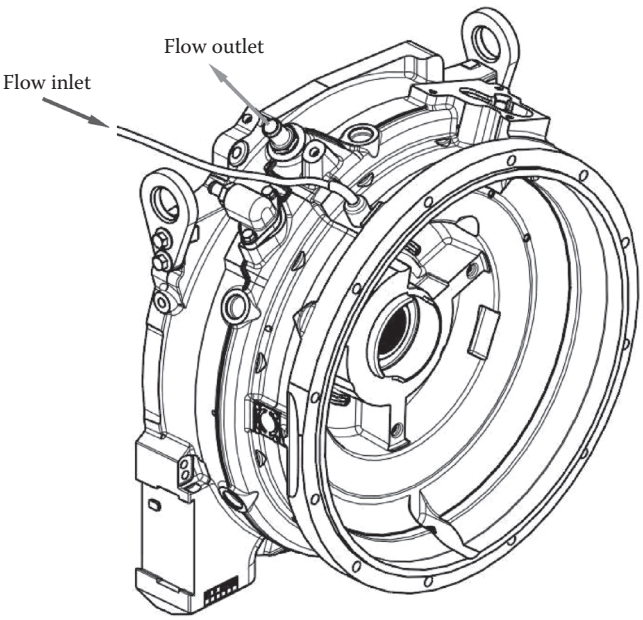

FIGURE 8.53
Assembled stator with a dual-cooling pipe casted inside the motor housing.

which is valid for

$$Re\left(\frac{r}{0.5d}\right)^{-2} < 700 \quad \text{and} \quad 7 < \frac{r}{0.5d} < 10^4$$

With the friction factor, the pressure drop across a helical pipe can be determined as

$$\Delta p = \pi d L \tau_w A \tag{8.21}$$

To reduce the pressure drop across the cooling pipe, a helical dual-cooling pipe may be adopted in the design. As shown in Figure 8.54, the adaptor is designed to distribute the coolant with an equal flowrate into the two pipes.

8.5.4.3 Indirect Liquid Cooling with Cooling Channels on Casted Motor Housing

Figure 8.55 provides another cooling scheme in which cooling water flows through sealed cooling channels. The cooling channels are formed by integrating the casted motor housing and the channel cover. Because water is distributed more uniformly into all channels, the pressure drop across the channels is much lower than that across helical copper pipes. To prevent water leakage, an interference fit (press fit or shrink fit) must be adopted between the housing and the channel cover.

8.5.4.4 Indirect Liquid Cooling via Copper Pipe in Spacer

In this cooling approach, a motor is cooled by water passing through a copper pipe in a special designed spacer near the front endbell (Figure 8.56). The stator winding is cooled by

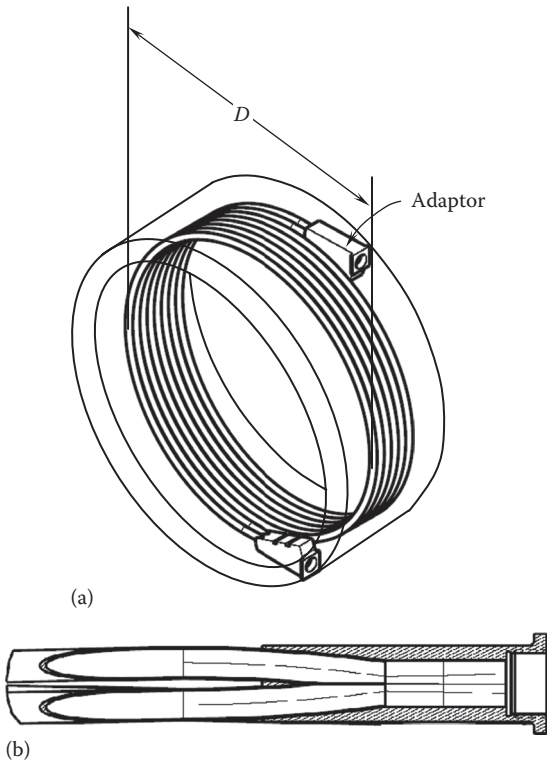

FIGURE 8.54
Components of the indirect liquid cooling system: (a) the helical dual-cooling pipe, casted directly into the motor housing for reducing thermal resistance, and (b) the adaptor at the flow inlet and outlet to connect with the helical dual-cooling pipe.

transferring heat from the winding to the motor housing and spacer, and then to cooling water. However, the present arrangement of the cooling pipe may cause nonuniform cooling on the motor, resulting in a temperature gradient along the motor axis. Furthermore, since the cooling pipe is close to the front bearing, it may shrink the outer race of the bearing to significantly reduce the bearing radial clearances, leading to the bearing lock or even failure.

8.5.4.5 Indirect Liquid Cooling through Stator Winding Slots

As discussed in Chapter 7, the biggest power loss is the resistive loss in copper windings. Therefore, in order to cool a motor more efficiently, a logical thinking is to cool these windings directly. An innovative approach was proposed by Tan et al. [8.53]. In their approach, water pipes are inserted in the stator slots (see Figure 8.57). In such a way, water flows through these intercoil pipes to carry away directly the heat generated in the winding due to the copper loss. Obviously, by this method, the thermal resistance is minimized compared with conventional cooling methods.

8.5.4.6 Indirect Liquid Cooling through Microscale Channels

With the rapid increase in power density of modern motion control systems, the traditional cooling methods such as conduction and natural/forces convection may

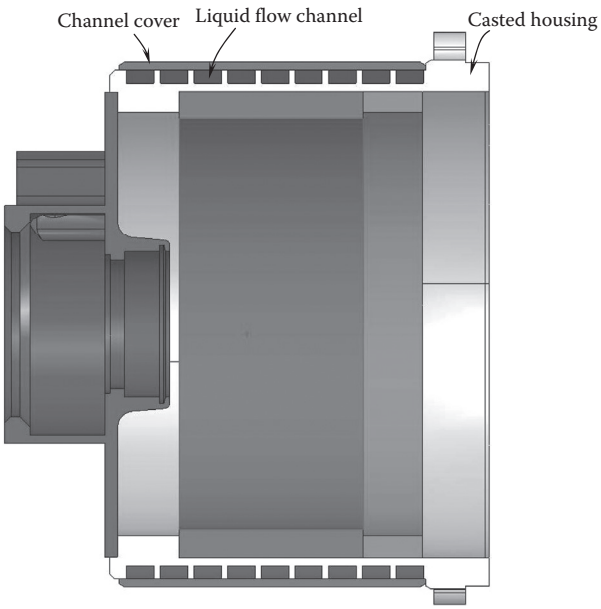

FIGURE 8.55
Liquid flow channels formed between the casted housing and the channel cover.

FIGURE 8.56
Indirect water cooling via copper pipe integrated in the spacer near the front endbell. (Courtesy of Kollmorgen Corporation.)

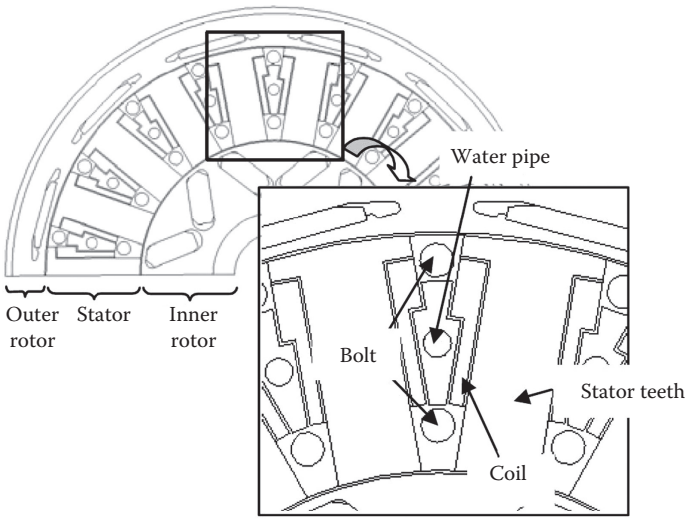

FIGURE 8.57
Water pipes inside stator slots for effectively cooling stator windings. (From Tan, N. et al., Cooling performance design for super motor and its experimental validation, *Proceedings of the 2005 International Power Electronic Conference*, pp. 1492–1488.)

be insufficient for these systems. The need for new technologies capable of dissipating high heat fluxes is of critical importance to motion industry. The use of pumped liquid through microscale channels is a promising technique in various industries for high-heat-flux applications.

As pointed out by Upadhya et al. [8.54], the performance of a liquid-cooled system depends on several factors, including (1) feature size of the microscale channel, (2) flowrate of the liquid through each channel, (3) surface area of radiator fins, and (4) air flow available for heat rejection.

8.6 Phase-Change Cooling Techniques

Phase-change cooling is an extremely effective way to cool energy systems. By accommodating large heat fluxes with relatively small driving temperature differences, heat in this approach is primarily removed through the vaporization of the working fluid utilizing the large latent heat capacity. As a consequence, the heat transfer augment is achieved and much less coolant is required as compared with single-phase cooling.

8.6.1 Cooling with Heat Pipes

Continuously increasing power densities of electric motors make using conventional conduction-based thermal management materials a problem, because heat dissipation requirements often exceed material conductivities. That makes heat pipes and other advanced thermal management materials ideal choices for direct conduction cooling.

During normal operation of an electric motor, the temperature distribution inside the motor is far from uniform. Hot spots may occur locally in some components that have higher power losses. In order to eliminate such hot spots, in addition to the overall cooling system, individual components may have their own cooling devices in place. The motor components that can be individually cooled include, but are not limited to, stator winding, bearings, electric connectors, and encoder. For the purpose of specific local cooling, the use of heat pipes may be more efficient and suitable.

Heat pipes are two-phase heat transfer devices with extremely high thermal conductivities. The world's first heat pipe was originally invented by Gaugler in 1944 and patented in 1946 [8.55]. However, it did not gain any significant attention within the heat transfer community until the space program resurrected the concept in the early 1960s [8.56]. Heat pipes rely on latent heat of evaporation of a working fluid (usually thermal refrigerant) to transmit heat from one hot point to another. Because it involves both boiling (or evaporation) and condensation, this cooling technique is generally categorized as a two-phase cooling technique. Based on its cooling mechanism, heat pipes can operate in any orientations. Furthermore, by carefully selecting coolants, heat pipes can be designed to operate over a broad range of temperatures. In motor cooling applications where it is typically desirable to maintain the motor temperature below 120°C–155°C, depending on the insulation class, copper/water heat pipes can be applied.

The thermal resistance represents the effectiveness of the heat pipe, which is defined as

$$R_{th} = \frac{T_e - T_c}{Q}$$

where

Q is the heat input

T_e and T_c are average evaporator and condenser surface temperatures, respectively

An experimental investigation of heat transfer in heat pipes with three working fluids was conducted by Mozumder et al. [8.57]. Their study reveals that the dominating parameters for heat transfer in heat pipes are average evaporator temperature T_e, saturated boiling temperature of working fluid T_{sat}, latent heat of vaporization h_{fg}, specific heat of working fluid $c_{p,l}$, and the fluid fill ratio F. The correlation for the heat transfer coefficient is given as

$$Q = hA_e(T_{sat} - T)_e = 39(Ja)^{4/5} F^{1/4} \left(\frac{T_{sat}}{T_e} \right)^5 \tag{8.22}$$

where

h is the overall heat transfer coefficient in W/(m^2-K)

A_e is the surface area at the heat pipe evaporation region in m^2

Jakob number is defined as

$$Ja = \frac{C_{p,l}(T_e - T_{sat})}{h_{fg}} \tag{8.23}$$

It must be noted that Q in Equation 8.22 has a unit of watt and the right-hand side is dimensionless.

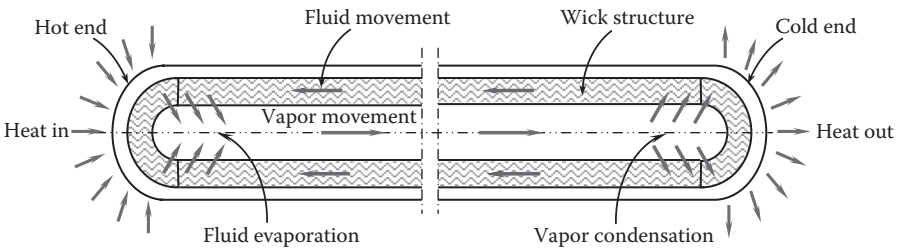

FIGURE 8.58
Performing principle of a heat pipe. It relies on both boiling (or evaporation) and condensation of working fluid.

Thus, the overall heat transfer coefficient h is given as

$$h = \frac{Q}{A_e(T_{sat} - T_e)} \tag{8.24}$$

where A_e is the surface area at the heat pipe evaporation region.

The correlation listed previously for predicting heat transfer coefficient fairly agrees with the experimental results. The investigation also shows that 85% fill ratio can be regarded as an optimum value for a heat pipe. Later, Manimaran et al. [8.58] found that the lowest thermal resistance is obtained when the heat pipe is operated at 75% fill ratio.

As illustrated in Figure 8.58, at the hot end of the heat pipe, the fluid evaporates into vapor, thereby absorbing the heat from the heat source. As the vapor migrates to the cold end through the central cavity, it condenses back into the liquid state to dissipate the heat to the environment. Then, the liquid returns to the hot end via the wick structure due to the capillary effect. With the repeat of the process, heat is continually transported from the hot end to the cold end. This indicates that heat pipes operate independently of gravity and can be effectively used in gravity-free conditions.

Since heat pipes involve the phase change of the working fluid, they have much higher effective thermal conductivity than solid materials. For instance, in some applications and orientations, heat pipes have a thermal conductivity in exceeds of 20,000 times than that of a solid copper bar of the same geometry. Also, heat pipes require no maintenance due to the lack of mechanical moving parts.

8.6.2 Cooling with Vapor Chambers

Vapor chambers can offer far superior thermal performance than traditional solid metal heat spreaders at the same thermal load and device size. With much lower thermal resistance, vapor chambers provide evenly spread temperatures on all of their surfaces, regardless of the location and thermal density of the heat source. Therefore, vapor chambers are able to deal with high-heat-flux motor components, extending the life of components and motors.

During the last several decades, boiling heat transfer techniques have been developed for cooling high-power systems, leading to the design of highly efficient vapor chambers. Since nucleate boiling attains heat flux during phase change, it has been an attractive design choice for electric motors and generators.

Although a vapor chamber looks like a heat pipe in its appearance, it has a fundamentally different cooling mechanism than that of the heat pipe. In a vapor chamber, the

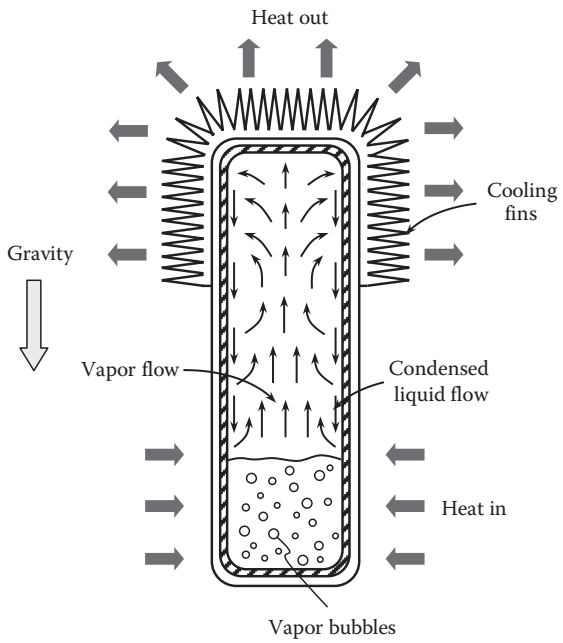

FIGURE 8.59
Boiling and condensation of coolant in a vapor chamber. The movements of vapor and liquid coolant rely on gravitational force. Fins are added on the vapor chamber at the condensation end to enhance heat dissipation.

movements of vapor and liquid coolant rely on gravitational force. This indicates that the orientation of a vapor chamber has a strong impact on its performance. To increase the cooling efficiency of vapor chamber, cooling fins may be added at the condensation end of the vapor chamber to improve the heat dissipation from it to the environment (Figure 8.59). As a result, the heat transfer enhancement can be achieved not only by increasing convective heat transfer surface area but also by creating local flow turbulence, both resulting in a higher heat convective transfer coefficient.

According to these superior thermal characteristics of heat pipes, motors with heat pipes can be made for higher power density and higher efficiency, allowing more current passing through motor windings. Heat pipes may be used to cool different motor components. As shown in Figure 8.60 [8.59], a set of heat pipes is inserted in the stator slots to directly cool the windings. Because most of the heat in an electric motor is generated in the motor winding, putting the heat pipes in close proximity to the copper winding will make the heat transfer more efficient. In addition, another set of heat pipes is incorporated into the stator core to absorb heat generated in the core due to the eddy-current losses. A perspective view of a motor with these two sets of heat pipes is provided in Figure 8.61.

Similarly, heat pipes may be also implemented in rotors to assist in dissipating heat. Referring to Figure 8.62, heat pipes can be inserted into rotor conducting bars.

8.6.3 Evaporative Cooling

A compelling evaporative cooling system has been developed to address challenges of cooling high-power devices [8.60]. This cooling system employs a noncorrosive, nonconductive

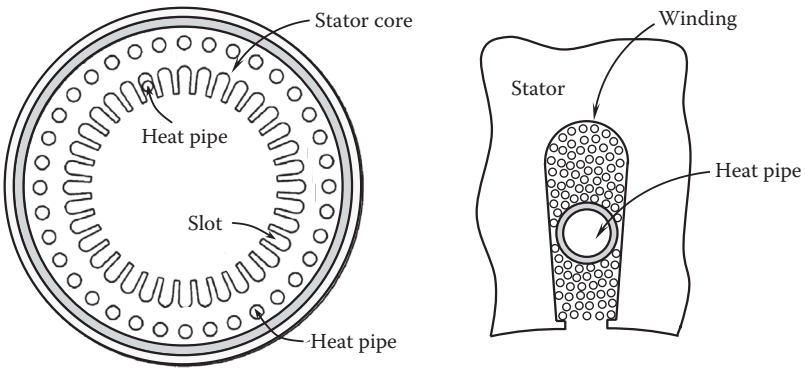

FIGURE 8.60
Heat pipes inserted in stator slots and stator core (U.S. Patent 7,569,955) [8.59]. (Courtesy of the U.S. Patent and Trademark Office, Alexandria, VA.)

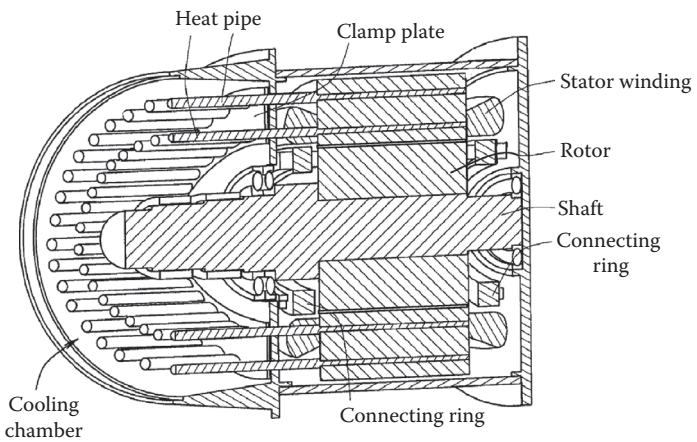

FIGURE 8.61
Cross-sectional view of motor cooling with heat pipes (U.S. Patent 7,569,955) [8.59]. (Courtesy of the U.S. Patent and Trademark Office, Alexandria, VA.)

refrigerant that evaporates on contact with hot surfaces of the high-power device, in a small, lightweight, and highly efficient closed-loop system. By taking advantage of the latent heat absorbed during phase change of the refrigerant from liquid to vapor, as well as the latent heat released during phase change from vapor to liquid, this system has a very high cooling efficiency.

As shown in Figure 8.63, the refrigerant is pumped into one or more cold plates that are optimized to acquire the heat from the device. The refrigerant vaporizes to maintain a cool uniform temperature on the device surfaces. The resulting refrigerant is then pumped to a heat exchanger where it rejects the heat to the ambient and condenses back into the liquid, completing the cycle.

The comparisons of thermal performance of the evaporative cooling system with various cold plates, as well as the air-cooled system, are plotted in Figure 8.64. It can be seen that

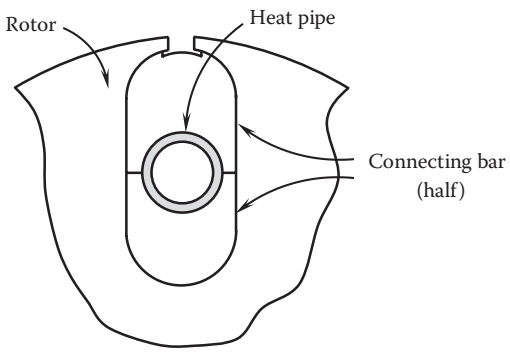

FIGURE 8.62
Heat pipe inside the rotor connection bar (U.S. Patent 7,569,955) [8.59]. (Courtesy of the U.S. Patent and Trademark Office, Alexandria, VA.)

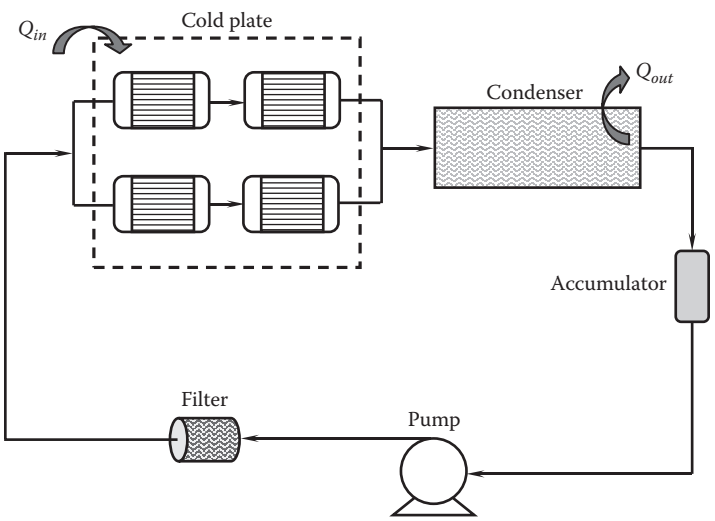

FIGURE 8.63
Evaporative cooling system.

under identical ambient conditions, the air-cooled system has the highest thermal resistance (0.094°C/W) and the evaporative cooling system (two-phase evaporative cooling) has the lowest (0.008°C/W). This indicates that by taking advantage of the highly efficient evaporation process that occurs when the liquid refrigerant changes phase to vapor, up to 11.8 times the amount of heat can be removed for the same given temperature difference by comparing with the air-cooled system. Therefore, the two-phase evaporative approach can increase the system power density (or reduce the system volume for the same power output) and improve performance reliability due to the elimination of the safety and maintenance issues associated with water cooling. In addition, the isothermal nature of the two-phase cooling system reduces thermal cycling.

By changing the material of cold plates from aluminum to copper, the thermal resistance can be lowered approximately 27%.

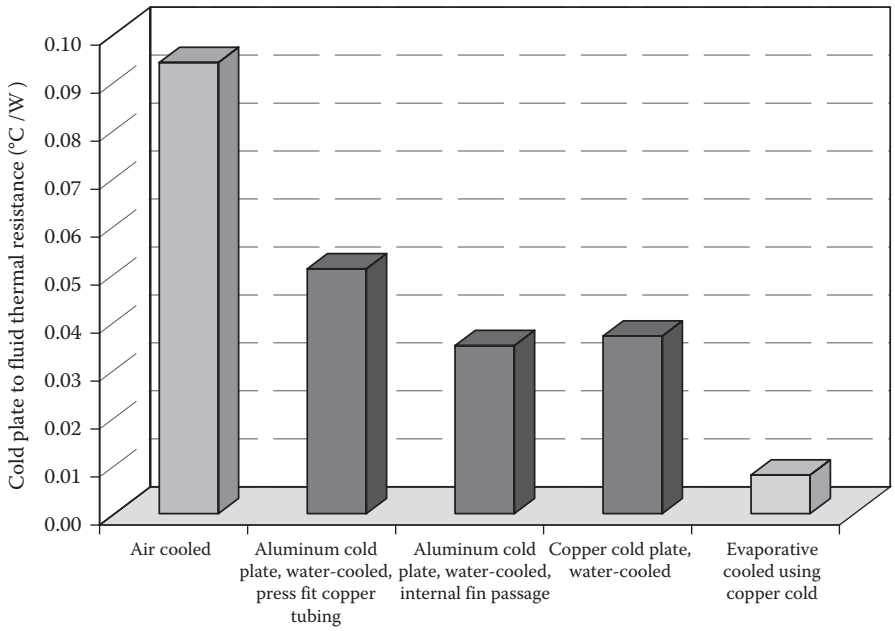

FIGURE 8.64
Comparisons of thermal performance of evaporative cooling system with various cold plates and air-cooled system.

8.6.4 Mist Cooling

Mist cooling continues to be a viable solution for a wide range of residential and industrial cooling applications for creating safer and more comfortable working environment. Mist cooling has demonstrated to remove high heat energy with relatively low coolant flowrates. In a mist cooling system, a high-pressure pump pushes water through a plurality of mist nozzles, producing microscopic droplets of water. As fine water mists hit hot air or surfaces, they evaporate to cool the surrounding space.

Totally enclosed nonventilated motors may be suitable to use the mist cooling technique. For this type of motors, all motor components are contained within a motor frame to prevent moisture, duct, and other harmful contaminates into the motor. To effectively cool this type of motors, very fine water mists are used to directly hit the outer surface of the motor. Thus, heat generated by the motor is absorbed by evaporation of water mists. Furthermore, the mixing flow of mists and air also has a favorable contribution in motor convection cooling.

8.7 Radiative Heat Transfer

Radiative heat transfer of rotating electric machines involves thermal radiation between the stator and rotor and between the stator (or rotor for the outer rotor machines) and the environment. According to the Stefan–Boltzmann law, the radiative energy E_r from a hot object at temperature T_h to its cooler surroundings at temperature T_c is given as

$$E_r = e\sigma A(T_h^4 - T_c^4) \tag{8.25}$$

where
e is the emissivity ($e = 1$ for a black body) of the object
A is the radiating area
σ is Stefan's constant ($\sigma = 5.6703 \times 10^{-8}$ W/m^2-K^4)

The impact of radiation heat transfer on electric motor cooling has been studied numerically by Chirilă et al. [8.61]. Their results show that for an internally air-cooled motor, the average temperature of the motor housing is lower when the radiation is considered for all inlet flow velocities. The maximum temperature difference obtained is about 9°C, indicating that the radiation is important for cooling the motor house at low inlet air velocities. Increase in the cooling air velocity can always significantly lower the housing temperature, from 118°C at $u = 2$ m/s to less than 80°C at $u = 8$ m/s. However, with the increase in the flow velocity, the temperature difference due to the radiation effect becomes very small, from about 9°C at $u = 2$ m/s to about 2°C at $u = 8$ m/s.

In most motor cooling schemes, a cooling system is disposed within the stator. As the result, the rotor temperatures are generally higher than those of stators. The heat generated by the rotor is thus dissipated by forced convection due to its rotation, conduction via bearings and radiation emitted to the motor housing and stationary components surrounding the rotor.

The radiation resistance between a motor and its surrounding environment depends both on the geometrical and thermal characteristics of the motor and the characteristics of the environment. This resistance is much higher than the forced convection resistance and thus is often neglected. For example, for the motors in refrigeration compressors, heat radiation is so weak that it can be neglected [8.62]. However, in some situations, particularly when totally enclosed fan-cooled (TEFC) motors are used in variable speed drives, radiation heat transfer can play a nonnegligible role at low speeds. It is also true for motors that use noncontact bearings. For these situations, radiation must be taken into account.

For outdoor electric motors, it is important in the design of a motor cooling system to consider not only the heat dissipation from the motor but also the heat from sunlight. In some circumstances, the solar loading effect could be substantial, depending on the motor size and its orientation toward the sun.

8.8 Other Advanced State-of-the-Art Cooling Methods

8.8.1 Microchannel Cooling Systems

Increasing heat densities in motion control systems cause high heat fluxes at both the component and system levels. The advancement of high-performance microchannel cooling has stimulated interest in this technique to substantially improve thermal energy removal capability. Though the microscale regime is not strictly defined, it is accepted that the characteristic length scale of microchannel ranges from a micrometer (10^{-6} m) to approximately 0.08 mm (8×10^{-5} m). Microchannels can provide a much larger contact area with the cooling fluid per unit volume and thus much higher heat transfer coefficients than conventional channels under similar thermohydraulic conditions.

According to previous studies, the microchannel cooling technique can remove heat densities up to 10 MW/m^2 [8.63].

In this technique, a cooling fluid is forced to pass through a microchannel heat sink by an external microscale pump for achieving very high heat removal rates. Because of its high heat removal capability, the researchers in Oregon Stator University are currently working with a motor manufacturer to design microchannel cooling systems in electric motors [8.64]. However, before this technique is successfully transplanted from electronic device cooling to high-power-density motor cooling, several difficulties must be overcome. Firstly, high heat-removing capability of a microchannel system is always associated with high pressure drop across the microchannels. Thus, it requires high power for driving cooling fluid through the microchannels. Secondly, due to the complex geometries of motor components, it is a challenge to achieve uniform cooling of the motor. Thirdly, heat transfer processes in microchannel are somewhat different from those in ordinary size channels. The capillarity of fluid in microchannels has a strong influence on flow patterns and heat transfer rates. This mechanism must be fully understood. Finally, it is noted that two-phase flows can be quite different from single-phase flows in microchannels. It is risky to extrapolate macroscale two-phase flow maps, flow boiling heat transfer methods, and pressure drop models to microchannels. More research is necessary to understand two-phase microchannel flows and heat transfer mechanisms.

8.8.2 Metal Foams

One of the principles of heat transfer enhancement is to extend heat dissipation surfaces. A typical example is the application of a variety of fins in heat exchangers. As the promising alternative, metal foams have been used for enhancing heat transfer in a variety of engineering applications. With a large number of open cell foams, metal foams have shown higher heat transfer enhancement than pin-fins [8.65]. Open cell foams consist of cells that are all interconnected, allowing a fluid to pass through them and thus have unique beneficial characteristics, including excellent surface-to-volume ratio (from 500 to over 10,000 m^2/m^3), high thermal conductivity, high fluid permeability and mixing, low flow resistance, low density, good thermal shock resistance, high temperature tolerance, excellent noise attenuation, corrosion resistance and other favorable properties [8.66–8.68]. It was reported that with the same pressure drop, the performance of the metal foam exchanger is superior when compared to that of conventional finned designs [8.69,8.70]. T'Joen et al. [8.71] have experimentally investigated the impacts of various parameters of metal foams on the thermohydraulic performance of a metal foam heat exchanger. Their results indicate that in all cases, heat transfer is greatly enhanced by coating metal foam on metal tubes. A good metallic bonding between the foam and the tube can significantly reduce the thermal resistance. A comparison of the performance of foam-covered tube with different foam heights has clearly showed that increasing the foam height reduces convective resistance. This technique is suitable for motor cooling by coating metal foams on the motor external surfaces, as described in Figure 8.65.

Metal foams can be fabricated from many different manufacturing processes, including investment casting, chemical vapor decomposition, electroforming, and metallic sintering, to name a few. Each fabrication process has its pros and cons and is used for certain applications. A comprehensive review of various metal foam fabrication processes was provided by Banhart [8.72].

As an indirect method, investment casting uses space-holding filler materials or melting of powder compacts that contain a blowing agent to produce cellular metal foams.

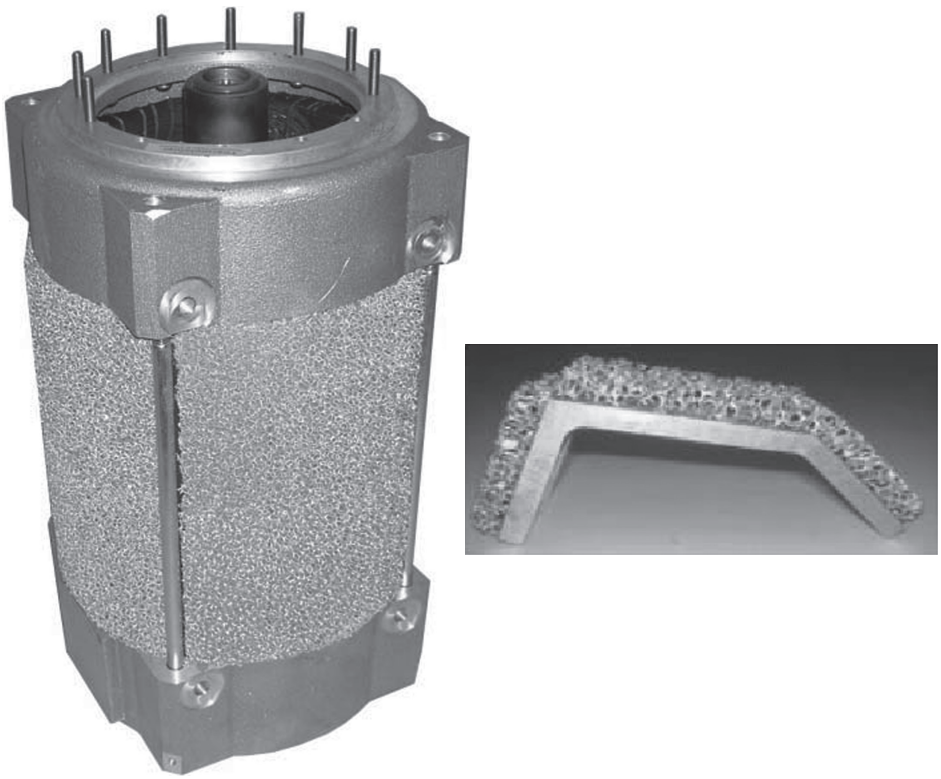

FIGURE 8.65
Enhanced motor cooling by coating metal foam with microporous structure on motor external surface. (Courtesy of Ghent University, Gent, Belgium.)

In a chemical vapor decomposition process, metal foams are made from gaseous metal. The condensed metal vapor in a vacuum chamber coats the surface of the polymer precursor to generate a film of metal foam.

Electroforming can generate a thin porous layer on a metal skin through an electrodeposition process. The metallic sintering process consists of various steps, including powder fractioning and preparation, compaction or molding, and sintering. The achievable porosity can range between 20% and 80%. In addition, using metal fibers to replace powders sheds new light on the fabrication of porous metal structures since a variety of metals can be produced as fibers.

8.8.3 Heat Transfer Enhancement with Nanotechnology

Nanotechnology deals with the control of matter at dimensions between approximately 1 and 100 nanometers (nm). The emergence and development of nanotechnology has affected/altered many aspects of engineering designs and manufacturing. It has the potential to create new materials and devices with a vast range of applications and thus has been considered as a revolutionary technology. As one of the cutting edge in innovative cooling methods, it is expected that nanotechnology can feature innovative cooling solution for electric machine in the near future.

8.8.3.1 Nanofluid

Due to the recent developments in nanotechnology, a new class of heat transfer fluid called nanofluid has attracted considerable attention from researchers and engineers. A nanofluid is a solid–liquid mixture produced by dispersing nanoparticles in a liquid (usually water, ethylene glycol, or minerals oil) to display enhanced heat transfer due to the combination of convection and conduction and additional energy transfer by particle dynamics and collision [8.73]. The studies of nanofluids with phase change have shown that the presence of nanoparticles in liquid can enhance critical heat flux (CHF) in boiling heat transfer. The mechanism of the CHF enhancement is attributed to the deposition of nanoparticles on the boiling surfaces with foamed porous layers [8.74].

The nanoparticles used in nanofluids are typically made of metals, oxides, titanate nanotubes, or carbon nanotubes with the typical particle size of less than 100 nm (or less than 50 nm in some applications). It is such tiny sizes that make the nanoparticles interact with liquids at the molecular level. Shima and Philip [8.75] have found that by varying the magnetic field strength and its orientation, the thermal properties of magnetic nanofluids (e.g., using Fe_3O_4, γ-Fe_2O_3, or Fe nanoparticles) can be tuned to vary at high values. Their results show that the nanoparticles with larger size exhibit larger thermal conductivity enhancement due to the enhanced dipolar interaction effect. Because the thermal properties of these nanofluids are perfectly reversible, these magnetic nanofluids are ideal for applications in smart devices.

8.8.3.2 Carbon Nanotube

Carbon nanotubes are well known for their outstanding thermophysical and mechanical and properties, particularly their extraordinary thermal conductivities. Measurements have shown that the thermal conductivity of single-wall carbon nanotubes (with the length of 2.6 μm and diameter of 1.7 nm) along their longitudinal axes can reach as high as 3500 W/m-K at the room temperature, which is 9.1 times higher than that of copper [8.76]. However, nanotubes exhibit a very poor thermal performance in the lateral direction. From the same test, the thermal conductivity in the lateral direction was measured as 1.52 W/m-K, which is only 0.4% of copper.

Carbon nanotubes are promising for use in various fields as a thermal material [8.77]. One potential application is to use carbon nanotubes in a layer coated onto motor surfaces for enhancing conductive heat transfer (Figure 8.66).

Another interesting property of nanotubes is that they have the highest strength-to-weight ratio of any known materials. This property may help produce lightweight motor components, for instance, combining nanotubes with other materials into composites that can be used to build lightweight fan, endbell, and housing.

8.8.3.3 NanoSpreader™ Vapor Cooler

NanoSpreader vapor coolers are patented copper-encased, two-phase vapor chambers into which pure water is vacuum sealed [8.78]. In fact, this type of vapor cooler has the same working principle as heat pipes. The heat transfer process consists of four steps: (1) At the high-temperature end, liquid evaporates to vapor by absorbing thermal energy from the heat source. (2) Vapor migrates through microperforated copper sheets toward the low-temperature end. (3) Vapor condenses back to liquid, releasing thermal energy. (4) Liquid is absorbed by a copper-mesh wick and flows back to the higher-temperature end. However,

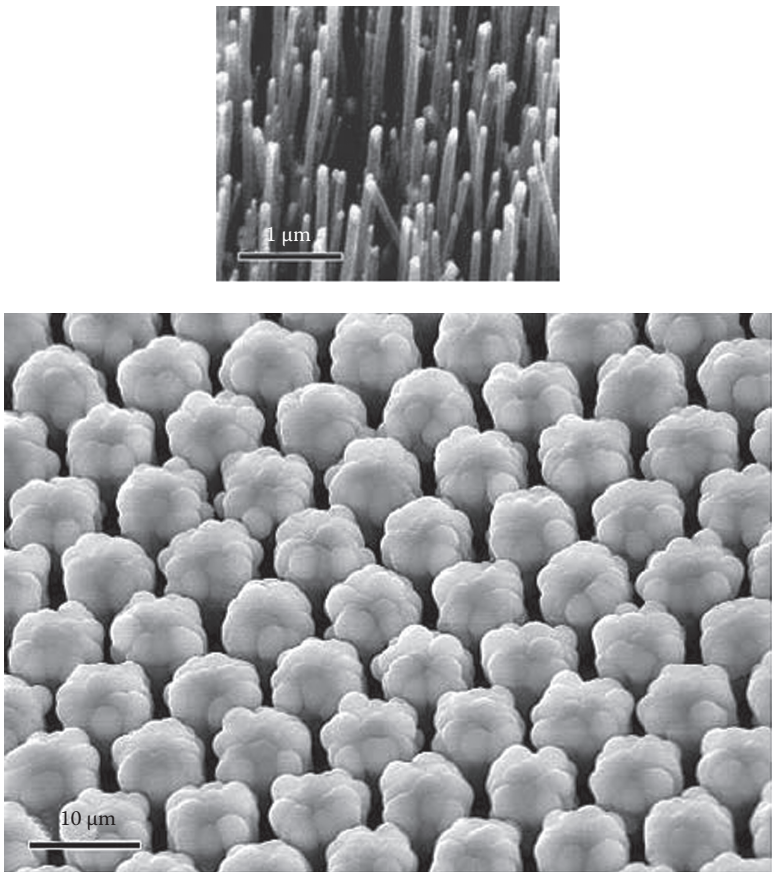

FIGURE 8.66
An array of vertically aligned carbon nanotubes. (Courtesy of NASA Ames Research Center, Moffett Field, CA.)

because of the design optimization of the NanoSpreader vapor cooler, this type of cooler has some advantages over heat pipes, including the following: (1) The reduction in thermal resistance allows to increase cooling efficiency up to 30% over the heat pipes. (2) Heat is spread in a more uniform pattern across a large thin surface area. (3) Due to the uniform heat spreading, hot spots from high-heat-flux devices are minimized/eliminated. (4) The weight can be reduced up to 30% over the heat pipes.

8.8.3.4 CarbAl™ Heat Transfer Material

CarbAl thermal material has been recognized as one of the 100 most significant product innovations in 2009 by *R&D Magazine* [8.79]. CarbAl material is a carbon-based metal nanocomposite composed of 80% carbonaceous matrix and a dispersed metal component of 20% aluminum, with a unique combination of high thermal diffusivity, high thermal conductivity, a low CTE, and low density [8.80]. As one of the passive thermal management materials, its thermal conductivity is about two times higher than that of aluminum. The speed to remove heat from a heat source (i.e., thermal diffusivity) is two and three times higher than copper and aluminum, respectively. The CTE of CarbAl material is only 29% and 41% of aluminum and copper, respectively.

8.8.3.5 Ionic Wind Generator

This innovative cooling device is known in industries as the ionic wind generator [8.81]. This type of cooling system does not use a fan or heat sink. It generates air flow based on the ionization of air molecules. A limitation of currently proposed ionic wind generator cooling systems for such devices (and for other conventional cooling devices as well) is that the generated air flow, from a first electrode toward a second electrode, is limited to a linear path that is essentially static and thus could only cool a specific region of an electronic system; particularly, only the regions that are in, or immediately adjacent, the path of the air flow could be cooled.

Because this cooling device was invented for cooling computer CPUs, with the current design, it is only able to cool limited areas within a computer. However, this type of cooling device may be good for eliminating some heat spots in electric motors.

References

[8.1] Arrhenius, S. 1889. On rates of inversion reaction in cane-sugar under the action of acids. *Zeitschrift für Physikalische Chemie* **4**: 226–248.

[8.2] Hnatek, E. R. 2003. *Practical Reliability of Electronic Equipment and Products*. Marcel Dekker, New York, NY.

[8.3] Boglietti, A., Cavagnino, A., Staton, D. A., and Popescu, M. 2009. Impact of different end region cooling arrangements on endwinding heat transfer coefficients in electric motors. *Proceedings of 35th Annual Conference of the IEEE Industrial Electronics Society*, pp. 1168–1173, Porto, Portugal.

[8.4] Tong, W. 2009. Numerical analysis of flow field in generator end-winding region. *International Journal of Rotating Machinery* **2008**: Article ID 692748. doi:10.1155/2008/692748.

[8.5] Zhu, Z. Q. 2011. Fractional slot permanent magnet brushless machines and drives for electric and hybrid propulsion systems. *International Journal for Computation and Mathematics in Electrical and Electronic Engineering* (*COMPEL*) **30**(**1**): 9–31.

[8.6] Koplow, J. P. 2010. A fundamentally new approach to air-cooled heat exchange. Technical Report Sand2010-0258. Sandia National laboratories, Albuquerque, NM. http://prod.sandia.gov/techlib/access-control.cgi/2010/100258.pdf.

[8.7] Lasance, C. 1997. Technical data. *Electronics Cooling* **3**(**1**): 11.

[8.8] Wilson, J. and Simons, R. E. 2005. Advances in high-performance cooling for electronics. *Electronics Cooling* **11**(**4**): 22–39.

[8.9] Faghri, A., Zhang, Y. W., and Howell, J. R. 2010. *Advanced Heat and Mass Transfer*. Global Digital Press, Columbia, MO.

[8.10] Webb, R. L. and Kim, N.-H. 2005. *Principles of Enhanced Heat Transfer*, 2nd edn. Taylor & Francis, New York.

[8.11] Sines, E. 2004. Electrical power cooling technique. U.S. Patent 6,777,835.

[8.12] Wild, C. and Wörner, E. 2008. The CVD diamond booklet. Diamond Materials GmbH, Freiburg, Germany. http://www.diamond-materials.com/downloads/cvd_diamond_booklet.pdf.

[8.13] Pan, Z. C., Sun, H., Zhang, Y., and Chen, C. F. 2009. Harder than diamond: Superior indentation strength of wurtzite BN and lonsdaleite. *Physical Review Letters* **102**(**5**): 05503.

[8.14] Zweben, C. 2005. Advanced electronic package materials. *Advanced Materials & Processes* **163**(**10**): 33, October Issue.

[8.15] Lemak, R. J., Moskaitis, M. J., Pickrell, D., Yocum, A. M., and Kupp. D. 2008. High performance pyrolytic graphite heat spreader: Near isotropic structures and metallization. *IMAPS Advanced Technology Workshop on Thermal Management 2008*, Palo Alto, CA.

[8.16] Meyer, IV, G. A. Sun, C.-H., Chen, C.-P., and Liu, H.-T. 2011. Heat sink for memory and memory device having heat sink. U.S. Patent 8,059,406.
[8.17] Bejan, A. and Lorente, S. 2008. *Design with Constructal Theory*. John Wiley & Sons, Hoboken, NJ.
[8.18] Lorenzini, G., Corrêa, R. L., Dos Santos, E. D., and Rocha, L. A. O. 2011. Constructal design of complex assembly of fins. *ASME Journal of Heat Transfer* **133(8)**: 081902-1–081902-7.
[8.19] Bar-Cohen, A. and Jelinek, M. 1986. Optimum arrays of longitudinal, rectangular fins in convective heat transfer. *Heat Transfer Engineering* **6(3)**: 68–78.
[8.20] Peertstra, P., Yovanovich, M. M., and Culham, J. R. 2000. Natural convection modeling of heat sinks using web-based tools. *Electronics Cooling* **6(3)**: 44–51.
[8.21] Incropera, F. P., Dewitt, D. P., Bergman, T. L., and Lavine, A. S. 2006. *Introduction to Heat Transfer*, 5th edn. John Wiley & Sons, Hoboken, NJ.
[8.22] Wang, C.-S., Yovanovich, M. M., and Cultam, J. R. 1999. Modeling natural convection from horizontal isothermal annular heat sinks. *ASME Journal of Heat Transfer* **121**: 44–49.
[8.23] Lordo, R. E. and Rudisch, W. E. 1989. Motor frame and motor with increased cooling capacity. U.S. Patent 4,839,547.
[8.24] Pal, D., Severson, M. H., and Rasmussen, R. D. 2011. Enhanced motor cooling system. U.S. Patent 8,053,938.
[8.25] Turner, W. B. and Bend, P. D. 2005. Laminated stator with cooling fins. Patent number WO 2005/022718. World Intellectual Property Organization.
[8.26] Yu, X. L, Feng, J. M., Feng, Q. K., and Wang, Q. W. 2005. Development of a plate-pin fin heat sink and its performance comparisons with a plate fin heat sink. *Applied Thermal Engineering* **25(23)**: 173–182.
[8.27] Tong, W. and Boyland, J. 2008. Heat sink. U.S. Patent Application 2008/0066888.
[8.28] Khan, W. A., Culham, J. R., and Yovanovich, M. M. 2005. Optimization of pin-fin heat sinks using entropy generation minimization method. *IEEE Transactions on Components and Packaging Technology* **28(2)**: 1–13.
[8.29] Khan, W. A., Culham, J. R., and Yovanovich, M. M. 2008. Optimization of pin-fin heat sinks in bypass flow using entropy generation minimization method. *ASME Journal of Electronic Package* **130**: 031010-1–031010-7.
[8.30] de Sorgo, M. 1996. Thermal interface materials. *Electronics Cooling* **2(3)**: 12–16, September Issue.
[8.31] Grujicic, M., Zhao, C. L., and Dusel, E. C. 2005. The effect of thermal contact resistance on heat management in the electronic packaging. *Applied Surface Science* **246(2005)**: 290–302.
[8.32] Tonapi, S., Nagarkar, K., Esler, D., and Gowda, A. 2007. Reliability testing of thermal greases. *Electronic Cooling*, November Issue.
[8.33] Mitcham, A. J. and Razzell, A. G. 2007. Stator core. U.S. Patent 7,288,870.
[8.34] Kikuchi, T., Kitada, S., Kaneko, Y., and Tsuneyoshi, T. 2004. Rotating electric machine. U.S. Patent 6,713,927.
[8.35] Chu, M. T. 2004. Rotor structure for a motor having build-in type permanent magnet. U.S. Patent 6,703,745.
[8.36] Chen, K. H., Masrur, A., Ahmed, S., and Garg, V. 2003. Jet impingement cooling of electric motor end-windings. U.S. Patent 6,639,334.
[8.37] Glynn, C. and Murray, D. B. 2005. Jet impingement cooling in microscale. *International Conference on Heat Transfer and Fluid Flow in Microscale*, Castelvecchio Pascoli, Italy.
[8.38] Chang, C.-C., Cheng, C.-H., Ke, M.-T., and Chen, S.-L. 2009. Experimental and numerical investigations of air cooling for a large-scale motor. *International Journal of Rotating Machinery* **2009**: Article ID 612723, 7pp. doi:10.1155/2009/612723.
[8.39] Kiran, T. R. and Rajput, S. P. S. 2009. Modeling of an indirect evaporative cooler (IEC) using artificial neural network (ANN) approach. *Archives of Applied Science Research* **1(2)**: 327–343.
[8.40] Erens, P. J. and Dreyer, A. A. 1993. *International Journal of Heat and Mass Transfer* **36(1)**: 17–26.
[8.41] Khmamas, F. A. 2010. Improving the environmental cooling for air-coolers by using the indirect- cooling method. *ARPN Journal of Engineering and Applied Sciences* **5(2)**: 66–73.
[8.42] Bhatia, A. 2012. HVAC—Characteristics and selection parameters of fans and blower systems. http://www.pdhcenter.com/courses/m213/m213content.pdf.

[8.43] Adnot, J., Greslou, O., Riviere, P., Spadaro, J., Kemna, R., Van Holsteun, R., Van Elburg, M. Li, W., Boorn, R. van den, Hitchin, R., and Pout, C. 2012. Final report task 5: Technical analysis ventilation systems for non residential and collective residential applications, BAT and BNAT. http://www.ecohvac.eu/downloads/Task 5 Lot 6 Ventilation Final Report.pdf.
[8.44] Kim, J.-W., Ahn, E. Y., and Oh, H. W. 2005. Performance prediction of cross-flow fans using mean streamline analysis. *International Journal of Rotating Machinery* **2005(2)**: 112–116.
[8.45] Lai, H. X., Wang, M., Yun, C. Y., and Yao, J. 2011. Attenuation of cross-flow fan noise using porous stabilizers. *International Journal of Rotating Machinery* **2011**. doi:10.1155/2011/528927.
[8.46] Koplow, J. P. 2012. Heat exchanger device and method for heat removal or transfer. U.S. Patent 8,288,675.
[8.47] Extreme Tech. 2012. The silent, dust-immune fanless heat sink to be released. *Electronic Cooling*, September Issue, p. 5.
[8.48] Simons, R. E. 1996. Direct liquid immersion cooling for higher power density microelectronics. *Electronics Cooling* **2(2)**: 24–29.
[8.49] Parmeter, L. J. and Knapp, J. M. 2010. Shrink tube encapsulated magnet wire for electrical submersible motors. U.S. Patent 7,679,242.
[8.50] Bejan, A. 2004. *Convection Heat Transfer*, 3rd edn. John Wiley & Sons, New York.
[8.51] Ito, H. 1959. Friction factor for turbulent flow in curved pipes. *Journal of Basic Engineering* **81**: 123–134.
[8.52] Srinivasan, P. S., Nandapurkar, S. S., and Holland, F. A. 1970. Friction factor for coils. *Transactions of Institute of Chemical Engineering* **48**: T156–T161.
[8.53] Tan, N., Arimitsu, M., Naruse, Y. and Watanabe, J. 2005. Cooling performance design for super motor and its experimental validation. *Proceedings of the 2005 International Power Electronic Conference*, pp. 1492–1488, Niigata, Japan.
[8.54] Upadhya, G., Munch, M., Zhou, P., Hom, J., Werner, D., and McMaster, M. 2006. Micro-scale liquid cooling system for high heat flux processor cooling applications. *IEEE 22nd Semiconductor Thermal Measurement and Management Symposium*, Dallas, TX.
[8.55] Gaugler, R. S. 1944. Heat transfer device. U.S. Patent 2,350,348.
[8.56] Grover, G. M. 1963. Evaporation, condensation heat transfer de-vice. U.S. Patent 3,229,759.
[8.57] Mozumder, A. K., Chowdhury, M. S. H., and Akon, A. F. 2011. Characteristics of heat transfer for heat pipe and its correlation. *ISRN Mechanical Engineering* **2011**: Article ID 825073.
[8.58] Manimaran1, R., Palaniradjal, K., Alagumurthil, N., and Velmurugan, K. 2012. An investigation of thermal performance of heat pipe using Di-water. *Science and Technology* **2(4)**: 77–80.
[8.59] Hassett, T. and Hodowance, M. 2009. Electric motor with heat pipe. U.S. Patent 7,569,955.
[8.60] Parker Hannifin Corporation. 2011. Two-phase evaporative precision cooling systems: For heat loads from 3 to 300kW. http://www.parker.com/literature/CIC Group/Precision Cooling/New literature/Two_Phase_Evaporative_Precision_Cooling_Systems.pdf.
[8.61] Chirilă, A.-H., Ghiţă, C., Crăciunescu, A., Deaconu, I.-D., Năvrăpescu, V., and Catrinoiu, M. 2010. Rotating electric machine thermal study. *International Conference on Renewable Energies and Power Quality*, Las Palmas de Gran Canaria, Spain.
[8.62] Boglietti, A., Cavagnino, A., Parvis, M., and Vallan, A. 2006. Evaluation of radiation thermal resistances in industrial motor. *IEEE Transactions on Industry Applications* **42(3)**: 688–693.
[8.63] Ribatski, G., Cabezas-Gómez, L., Navarro, H. A., and Saíz-Jabardo, J. M. 2007. The advantages of evaporation in micro-scale channels to cool microelectronic devices. *Engenharia Térmica (Thermal Engineering)* **6(2)**: 34–39.
[8.64] Wang, H. 2013. Microchannel cooling of electric drive motors. http://mbi-online.org/microchannel-cooling-electric-drive-motors.
[8.65] Sengstock, O. and Hooman, J. 2012. Heat transfer enhancement from a blade tip-cap using metal foams. *ASME Journal of Heat Transfer* **134**(**11**): 114505-1–114505-3.
[8.66] Mahjoob, S. and Vafai K. 2008. A synthesis of fluid and thermal transport models for metal foam heat exchanges. *International Journal of Heat and Mass Transfer* **51(15-16)**: 3701-3711.
[8.67] Tuchinskiy, L. 2005. Fabrication technology for metal foam. *Journal of Advanced Materials* **37(3)**: 60–65.

[8.68] Han, X. H., Wang, Q., Park, Y.-G., T'Joen, C., Sommers, A., and Jacobi, A. 2012. A review of metal foam and metal matrix composites for heat exchangers and heat sinks. *Heat Transfer Engineering* **33(12)**: 991–1009. doi: 10.1080/01457632.2012.659613.

[8.69] Ejlali, A., Ejlali, A., Hooman, K., and Gurgenci, H. 2009. Application of high porosity metal foams as air-cooled heat exchangers to high heat load removal systems. *International Communications in Heat and Mass Transfer* **36(7)**: 674–679.

[8.70] Hooman, K. and Gurgenci, H. 2010. Porous medium modeling of air-cooled condensers. *Transport in Porous Medium* **84(2)**: 257–273.

[8.71] T'Joen, C., De Jaeger, P., Huisseune, H., van Herzeele, S., and De Paepe, M. 2010. Thermo-hydraulic study of a single row heat exchanger consisting of metal foam covered round tubes. *International Journal of Heat Transfer* **53(15-16)**: 3262–3274.

[8.72] Banhart, J. 2001. Manufacture, characterization and application of cellular metals and metal foams. *Progress in Materials Science* **46**(**2001**): 559–632.

[8.73] Nsofor, E. C. 2008. Recent patents on nanofluids (nanoparticles in liquids) heat transfer. *Nanofluids Heat Transfer* **1(3)**: 190–197.

[8.74] Ding, Y. L., Chen, H. S., Wang, L., Yang, C.-Y., He, Y. R., Yang, W., Lee, W. P., Zhang, L. L., and Huo, R. 2007. Heat transfer intensification using nanofluids. *KONA Power and Particle Journal* **25**(**2007**): 23–38.

[8.75] Shima, P. D. and Philip, J. 2011. Tuning of thermal conductivity and rheology of nanofluids using an external stimulus. *Journal of Physical Chemistry C* **115**(**41**): 20097–20104.

[8.76] Pop, E., Mann, D., Wang, Q., Goodson, K., and Dai, H.-J. 2006. Thermal conductance of an individual single-wall carbon nanotube above room temperature. *Nano Letters* **6(1)**: 96–100.

[8.77] Gaughan, R. 2007. Cool applications for hot technologies. *Small Times Magazine*, **7**(Issue 4).

[8.78] Celsia Technologies. 2006. Nanospreader technology. http://celsiatechnologies.com/nanospreader_technology.asp.

[8.79] *R&D Magazine*. 2009. R&D 100 winners. http://www.rdmag.com/award-winners/2009/07/battle-against-damaging-heat-finds-new-hero.

[8.80] Applied Nanotech Holdings, Inc. 2013. CarbAl™ heat transfer material. http://www.appliednanotech.net/tech/CarbAl.php.

[8.81] Rosenblatt, M. N., Lee, M. M., and Gregg, J. L. 2013. Dual-purpose hardware aperture. U.S. Patent 8,571,205.

9

Motor Vibration and Acoustic Noise

Vibration refers to mechanical oscillating movements of an object from its equilibrium position. Sound to human ears is a physiological response to a physical phenomenon of periodically oscillating pressure waves in a certain range. In fact, vibration and sound are closely related to each other. Vibrating objects such as electric motor with random oscillatory movement can produce sound and it travels as acoustic waves through various mediums such as air and water. Sound waves radiate outward from the sound sources in all directions.

Often, electric rotary machines produce vibration and noise, which not only cause gradual hearing loss of operators but also deteriorate machines' operating conditions. In the present era, the use of electric rotary machinery is ubiquitous, and therefore, it is necessary to effectively control and reduce sound and vibration intensities.

Frequency is defined as the number of mechanical oscillations per unit time. Among all vibrational frequencies emitted from a vibrating object, the audible sound frequencies range approximately from 20 to 20,000 Hz. From the viewpoint of physics, noise is called an inconsistent tone that is irregularly composed of many different frequencies and sound waves. From the standpoint of physiology, noise is an unpleasant and unwanted sound.

The characteristic parameters normally used to assess vibration include natural frequency, frequency ratio, damping ratio, phase angle, dynamic displacement, velocity, acceleration, and vibration mode. Frequency is often used in studies of both vibration and sound.

9.1 Vibration and Noise in Electric Motor

When a motor is running under a full-load condition, unwanted vibration is produced due to various reasons that ultimately affect the performance of the motor. These reasons can be divided into two categories: one is dynamic and another is kinematic. The possible causes under dynamic categories are unbalanced electromagnetic reluctance forces, asymmetric air gap, bearing wear and damage, unbalanced rotor, looseness, and improper motor installation. Excessive motor vibration may damage the motor windings, develop high stress on the rotor bearings, reduce the critical speed, and deteriorate motor performance, which may lead to poor motor reliability, increased unexpected downtime, and even motor failure, while acoustic noises pollute the environment and can also harm human's health. Nonetheless, vibration and noise are important parameters for assessment of motor quality and operation reliability. Therefore, the motor design must take into account the resonance frequencies of the motor to shift the critical frequencies away from the motor's operating speed to at least ±10%. This will effectively reduce motor vibration and noise levels at motor normal operation.

It has been recognized that about one-third of motor failures are due to mechanical breakages. The largest single contributor to the mechanical breakages is high vibration, which may be attributed to defective motor designs, rough manufacturing processes, improper assemblies and installations, inadequate maintenances, and faulty operations.

The interaction between the rotor and stator is a predominant feature of vibration and noise of an electric motor. A large number of studies [9.1–9.3] have shown that the vibration model $\upsilon(t, \phi, z)$ can be expressed by three terms, each of which has a different physical origin:

$$\upsilon(t,\phi,z) = \upsilon_e(t,\phi,z) + \upsilon_m(t,\phi,z) + \upsilon_a(t,\phi,z) \tag{9.1}$$

where
t is time
ϕ is the angular position
z is the axial position on the stator frame

In Equation 9.1, $\upsilon_e(t, \phi, z)$, $\upsilon_m(t, \phi, z)$, and $\upsilon_a(t, \phi, z)$ are electromagnetic, mechanical, and aerodynamic vibrational terms, respectively. These vibrations produce forces on associate components of the motor and severely affect its performance.

Similarly, sound emitted from a motor can be expressed as the sum of these three components:

$$p(t,\phi,z) = p_e(t,\phi,z) + p_m(t,\phi,z) + p_a(t,\phi,z) \tag{9.2}$$

where $p_e(t, \phi, z)$, $p_m(t, \phi, z)$, and $p_a(t, \phi, z)$ are electromagnetic, mechanical, and aerodynamic sound pressure terms, respectively. Noise from the electromagnetic term dominates at low and medium speeds. At high speeds, the mechanical and aerodynamic noises are the most influential among the three [9.4].

The electromagnetic vibration and resulting noise resulted from various reasons such as phase imbalance, broken rotor bar, asymmetric air gap, eccentric rotor, slot openings, magnetic saturation, space/time harmonics associated with electrical and magnetic frequency, and magnetostrictive expansion of the core lamination. An electromagnetic noise is a low-frequency noise generated in the motor.

The mechanical vibration and resulting noise are associated with motor parts, which are subjected to unbalanced mechanical forces due to oscillatory motions about their equilibrium positions. The causes of mechanical vibration include unbalanced mass of rotating components, shaft misalignment, bearing deterioration, and frame distortion. The method to distinguish between an electromagnetic vibration and a mechanical vibration is to disconnect the electricity supply from the motor. In the absence of the electrical power, the electromagnetic vibration does not exist [9.5], but the mechanical vibration exists till rotary motion is sustained. Here, it should be noted that this method is applicable to IMs and not to PMMs.

As ventilating air flows through a motor, the aerodynamic vibration and noise may be generated due to the interactions of cooling air to both rotating parts (e.g., fan and rotor) and stationary parts (e.g., stator and housing). Usually, noise generated by the aerodynamic vibration is due to turbulent flow, which is proportional to the 6th to 8th power of the flow velocity (i.e., $W \propto u^{6-8}$). This indicates that a doubling of the flow velocity u can increase the sound power W by 18–24 dB, respectively [9.6]. For small-sized motors, the aerodynamic vibration and resulting noise are relatively low compared to the mechanical and electromagnetic components.

Excessive vibration can cause damages in electric motor in different ways [9.7]: (1) It can accelerate bearing failure by causing indentations on the bearing raceways at the ball or roller spacing. (2) It can loosen windings and cause mechanical damage to insulation by fracturing, flaking, or eroding of the material. (3) The excessive movement can generate high temperature, and as a result, the lead wires can become brittle. (4) It can cause brush sparking at commutators or current collector rings. As a result of these problems, motor vibration can harm motor performance, generate high noise, and even cause motor failure.

9.2 Fundamentals of Vibration

It is very important to understand vibrational phenomena such as resonance, harmonics, and damping. Thus, in order to reduce vibration and noise in electric machines, it is essential to understand the fundamentals of vibration.

Generally, vibration in rotordynamic systems can be categorized into synchronous or subsynchronous vibrations depending on the dominant frequency and source of the disturbance forces. The first type is the synchronous vibrations that have a dominant frequency component that matches the rotating speed of the rotor. This type of vibration is usually caused by the imbalance or other synchronous forces in the system. The subsynchronous vibration or whirling has a dominant frequency below the operating speed. This type of vibration is mainly caused by fluid excitation from the cross coupling stiffness [9.8].

Most of the mechanical systems in the real world are considerably very complicated. Therefore, the first step in dealing with difficult problems is to appropriately simplify problems. Generally, the fundamental equations employed in a vibration analysis of multiple-degree-of-freedom systems can be expressed in matrix notation:

$$[m]\{\ddot{x}\}+[c]\{\dot{x}\}+[k]\{x\}=\{F\} \tag{9.3}$$

where

$[m]$ is the mass matrix
$[c]$ is the damping matrix
$[k]$ is the stiffness matrix
$\{\ddot{x}\}$ is the acceleration vector
$\{\dot{x}\}$ is the velocity vector
$\{x\}$ is the displacement vector
$\{F\}$ is the acting force vector

In Equation 9.3, the physical interpretations of the terms from the left-hand side are inertial force, damping force, and spring force (or restoring force), respectively. The term on the right-hand side is external exciting or disturbing force. All these forces balance each other to maintain a dynamic equilibrium state.

9.2.1 Simple Harmonic Oscillating System

A harmonic motion refers to the oscillations that are symmetrical about a position of equilibrium. The motion may have either one frequency or amplitude, defined as simple

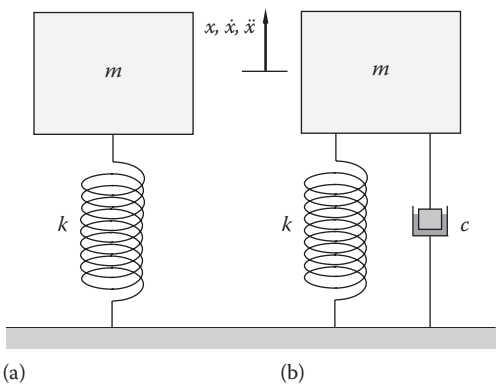

FIGURE 9.1
Oscillation systems: (a) simple harmonic oscillation system without damping and (b) damped harmonic oscillation system.

harmonic motion, or a combination of two or more components of harmonics, defined as complex harmonic motion. Simple harmonic motion oscillates with only the restoring force acting on the system. For this system, the restoring force is directly proportional to the displacement. As an example, a pendulum swings in a small arc, and in its periodic motion, the tangential component of gravity acts as the restoring force of the pendulum. It is the restoring force that interacts with the inertia property of mass (kinetic energy) to perpetuate the oscillation.

For 1D simple harmonic motion (see Figure 9.1a), the equation of motion can be obtained by means of Newton's second law and Hooke's law:

$$F = m\frac{d^2x(t)}{dt^2} = -kx(t) \tag{9.4}$$

where
F is the restoring force
m is the inertial mass of an oscillating body
$x(t)$ is the displacement from an equilibrium position as a function of time t
k is the spring constant

This equation indicates that for simple harmonic motion, the inertial force is balanced by the spring force.

Thus, applying a sinusoidal form of solution, this differential equation can be solved as

$$x(t) = A\cos(\omega t - \varphi) \tag{9.5}$$

where
A is the maximum displacement from the equilibrium position, which is also defined as the oscillating amplitude
φ is the phase angle
ω is the oscillating frequency

$$\omega = 2\pi f = \sqrt{\frac{k}{m}} \tag{9.6}$$

Accordingly, velocity and acceleration of the oscillating body can be found as

$$v = \frac{dx(t)}{dt} = -A\omega\sin(\omega t - \varphi) \tag{9.7}$$

$$a = \frac{d^2x(t)}{dt^2} = -A\omega^2\cos(\omega t - \varphi) \tag{9.8}$$

The oscillating frequency can be expressed as

$$f = \frac{1}{2\pi}\sqrt{\frac{k}{m}} \tag{9.9}$$

Since the oscillating period T is reciprocal of frequency, it follows that

$$T = \frac{2\pi}{\sqrt{k/m}} \tag{9.10}$$

The kinetic energy $E_k(t)$ and the potential energy $E_p(t)$ in an oscillating system can be described, respectively, as

$$E_k(t) = \frac{1}{2}m\left[v(t)\right]^2 = \frac{1}{2}mA^2\omega^2\sin^2(\omega t - \varphi) = \frac{1}{2}kA^2\sin^2(\omega t - \varphi) \tag{9.11a}$$

$$E_p(t) = \frac{1}{2}k[x(t)]^2 = \frac{1}{2}kA^2\cos^2(\omega t - \varphi) \tag{9.11b}$$

Therefore, the total mechanical energy E_t is the sum of the energies $E_k(t)$ and $E_p(t)$:

$$E_t = E_k + E_p = \frac{1}{2}kA^2 \tag{9.12}$$

It is worth to note that the total mechanical energy in an oscillating system is constant.

9.2.2 Damped Harmonic Oscillating System

Damping is a measure of an ability of a vibrating system to dissipate mechanical vibratory energy so that the amplitude and duration of vibration can be effectively reduced. In other words, damping creates a force that acts in the opposite direction to the object travel. It can be broadly classified into two categories: passive and active damping. Passive damping can be achieved by using mechanical properties of damping materials and/or by designing vibration-absorbing structures. In active damping, an actuator is used to generate force opposing the motion, regardless of the relative velocity across it [9.9]. Active damping employs sophisticated closed-loop control techniques to minimize the effect of

vibration. The active controllers continuously regulate the damping characteristics and require measurements of response and feedback from the vibrating system.

For a damped simple harmonic oscillating system (see Figure 9.1b), the governing equation is

$$m\frac{d^2x(t)}{dt^2}+c\frac{dx(t)}{dt}+kx(t)=0 \tag{9.13}$$

where c is the damping coefficient, given in units of N s/m or kg/s.

Introducing a dimensionless quantity called damping ratio ζ, it can be derived as

$$\zeta=\frac{c}{2\sqrt{mk}} \tag{9.14}$$

while the natural frequency of an undamped system ω_n is

$$\omega_n=\sqrt{\frac{k}{m}} \tag{9.15}$$

Equation 9.13 can be rewritten as

$$\frac{d^2x(t)}{dt^2}+2\zeta\omega_n\frac{dx(t)}{dt}+\omega_n^2x(t)=0 \tag{9.16}$$

The initial conditions are given as

$$x(t=0)=X \tag{9.17a}$$

$$\dot{x}(t=0)=V_o \tag{9.17b}$$

The solution of Equation 9.16 is in the form

$$x(t)=e^{st} \tag{9.18}$$

Substituting (9.18) into (9.16), it yields

$$s^2+2\zeta\omega_n s+\omega_n^2=0 \tag{9.19}$$

The two roots of Equation 9.19 are

$$s_{1,2}=\omega_n\left(-\zeta\pm\sqrt{\zeta^2-1}\right) \tag{9.20}$$

Thus, a general solution is given by

$$x(t)=Ae^{s_1t}+Be^{s_2t}=Ae^{\omega_nt\left(-\zeta+\sqrt{\zeta^2-1}\right)}+Be^{\omega_nt\left(-\zeta-\sqrt{\zeta^2-1}\right)} \tag{9.21}$$

where the constants A and B are determined by the initial conditions.

According to the value of damping ratio ζ, four cases can be identified as follows:

1. When $\zeta = 1$, the system is in the critical damping condition, giving the fastest return of the system to its equilibrium condition without much oscillation. For this case, the general solution can be written as

$$x(t) = (A + Bt)e^{-\omega_n t} \tag{9.22}$$

2. When $\zeta > 1$, the characteristic roots are positive, real, and distinct. Under such a circumstance, the system is overdamped. Like a critical damping, an overdamped system does not oscillate but takes a longer time to converge to its equilibrium position than a critically damped system. It is important to note that $\zeta > 1$ indicates both roots s_1 and s_2 are negative:

$$x(t) = Ae^{s_1 t} + Be^{s_2 t} \tag{9.23}$$

   Therefore, every solution in this case goes asymptotically to zero.

3. When $0 < \zeta < 1$, the term under the square root is negative and the characteristic roots are not real. Under this condition, the system is underdamped. Introducing $\omega = \omega_n\sqrt{\zeta^2 - 1}$, the characteristic roots are $(-\zeta\omega_n \pm i\omega)$, leading to the general solution as

$$x(t) = Ae^{(-\zeta\omega_n + i\omega)t} + Be^{(-\zeta\omega_n - i\omega)t} = Ae^{-\zeta\omega_n t}\cos(\omega t) + Be^{-\zeta\omega_n t}\sin(\omega t) \tag{9.24}$$

   Alternatively, Equation 9.24 can be expressed as

$$x(t) = Ce^{-\zeta\omega_n t}\cos(\omega t - \varphi) \tag{9.25}$$

   The term $\cos(\omega t - \varphi)$ in Equation 9.25 reflects the oscillating behavior of the system.

4. When $\zeta = 0$, the system is undamped, just as the simple harmonic oscillating system.

   The comparisons of four cases, critical damping, overdamped, underdamped, and undamped, with different damping ratios ζ are presented in Figure 9.2. As can be seen from the figure, for the undamped case ($\zeta = 0$), the system oscillates sustainably with a constant amplitude. Increase in the damping ratio in the range of $0 < \zeta < 1$ leads to vibration decays, accompanied with the reduction of the oscillation amplitude. The reduction in the oscillation amplitude is inversely proportional to the damping ratio ζ. When it reaches critical damping at $\zeta = 1$, the system no longer oscillates, but it monotonically reaches equilibrium in the shortest time without overshooting. For overdamped cases where $\zeta > 1$, the system experiences large damping that it does not oscillate at all. In fact, if the system is displaced from equilibrium, it takes a long time for it to return to its initial position because the damping force is so severe.

9.2.3 Forced Vibration with Damping

In many mechanical systems, it is often encountered that an external time-dependent force is applied to the system to start forced vibration. The applied exciting force may be harmonic,

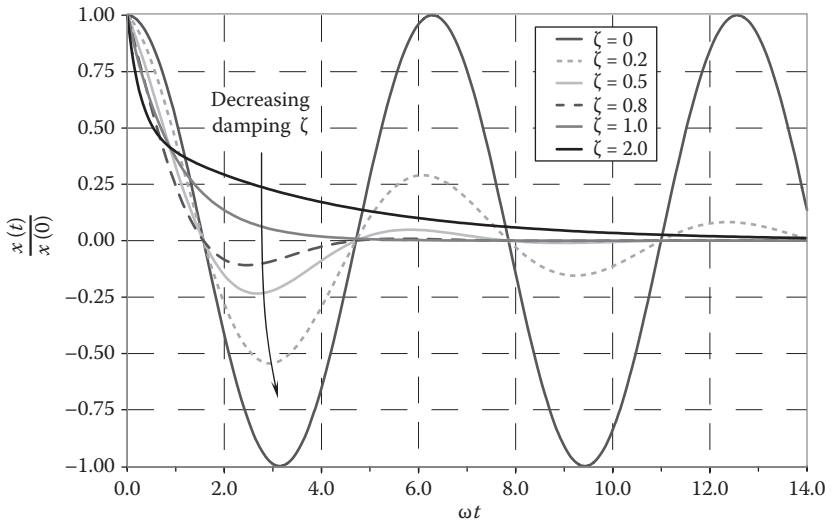

FIGURE 9.2
Comparison of damped and undamped harmonic oscillating systems with various damping ratios: (a) $\zeta = 1$, critical damping; (b) $\zeta > 1$, overdamped; (c) $0 < \zeta < 1$, underdamped; and (d) $\zeta = 0$, undamped.–

nonharmonic (periodic or nonperiodic), or random in nature. The dynamic response of a system to a suddenly applied nonperiodic excitation is called transient response.

Considering a dynamic response of a damped system to a harmonic exciting force $F(t)$ shown in Figure 9.3, this single-degree-of-freedom system has the mass m that is supported by a spring and a damper and is subject to an external exciting force in the form

$$F(t) = F_o \sin(\omega t - \varphi) \tag{9.26}$$

where
F_o is the force magnitude
ω is the excitation frequency
φ is the phase angle

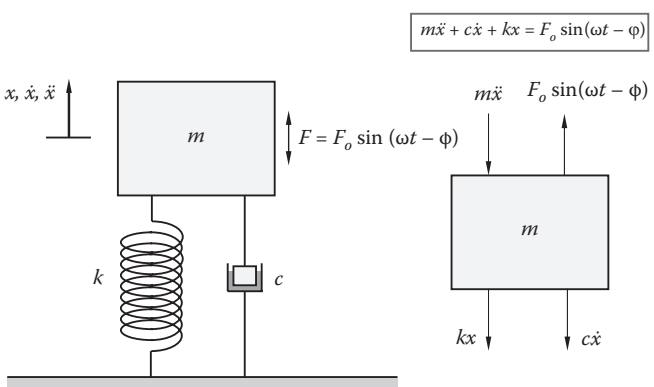

FIGURE 9.3
Forced vibration of single-degree-of-freedom system with damping.

The value of φ depends on $F(t)$ at $t = 0$. The dynamic equation of motion is given as

$$m\frac{d^2x(t)}{dt^2} + c\frac{dx(t)}{dt} + kx(t) = F_o \sin(\omega t - \varphi) \tag{9.27}$$

where
c is the viscous damping coefficient
k is the spring coefficient

The general solution of this nonhomogeneous second-order differential equation consisted of two parts: the complementary solution $x_c(t)$ and the particular solution $x_p(t)$, that is, $x(t) = x_c(t) + x_p(t)$. The complementary solution is obtained by setting the right-hand side zero:

$$m\frac{d^2x_c(t)}{dt^2} + c\frac{dx_c(t)}{dt} + kx_c(t) = 0 \tag{9.28}$$

This equation is identical to (9.13). Therefore, the general solution is given by

$$x_c(t) = Ae^{\omega_o t\left(-\zeta+\sqrt{\zeta^2-1}\right)} + Be^{\omega_o t\left(-\zeta-\sqrt{\zeta^2-1}\right)} \tag{9.29}$$

where constants A and B are determined from the specific boundary conditions and ζ values.

To obtain the particular solution $x_p(t)$, it is assumed that

$$x_p(t) = D\cos(\omega t - \varphi) + E\sin(\omega t - \varphi) \tag{9.30}$$

where D and E are constants. The associated velocity and acceleration are

$$\begin{cases} \dfrac{dx_p(t)}{dt} = -D\omega\sin(\omega t - \varphi) + E\omega\cos(\omega t - \varphi) \\ \dfrac{d^2x_p(t)}{dt^2} = -D\omega^2\cos(\omega t - \varphi) - E\omega^2\sin(\omega t - \varphi) \end{cases} \tag{9.31}$$

Substituting Equation 9.31 into 9.27, it yields

$$\cos(\omega t - \varphi)(-mD\omega^2 + cE\omega + kD) + \sin(\omega t - \varphi)(-mE\omega^2 - cD\omega + kE) = F_o\sin(\omega t - \varphi) \tag{9.32}$$

Comparing both sides of Equation 9.32, it leads to

$$D(k - m\omega^2) + cE\omega = 0 \tag{9.33a}$$

$$E(k - m\omega^2) - cD\omega = F_o \tag{9.33b}$$

Defining the frequency ratio β as the ratio of excitation frequency ω over natural frequency ω_n,

$$\beta = \frac{\omega}{\omega_n} = \frac{f}{f_n} \tag{9.34}$$

Equation 9.34 can be rewritten as

$$D(1-\beta^2)+2\zeta\beta E=0 \tag{9.35a}$$

$$-2\zeta\beta D+E(1-\beta^2)=\frac{F_o}{k} \tag{9.35b}$$

By solving Equations 9.35a and 9.35b, constants D and E can be determined as

$$D=-\frac{F_o}{k}\frac{2\zeta\beta}{(1-\beta^2)^2+(2\zeta\beta)^2} \tag{9.36a}$$

$$E=\frac{F_o}{k}\frac{1-\beta^2}{(1-\beta^2)^2+(2\zeta\beta)^2} \tag{9.36b}$$

The particular solution $x_p(t)$ becomes

$$x_p(t)=-\frac{F_o}{k}\frac{2\zeta\beta}{(1-\beta^2)^2+(2\zeta\beta)^2}\cos(\omega t-\varphi)+\frac{F_o}{k}\frac{1-\beta^2}{(1-\beta^2)^2+(2\zeta\beta)^2}\sin(\omega t-\varphi) \tag{9.37}$$

Alternatively, the particular solution $x_p(t)$ can be expressed as

$$x_p(t)=X\sin\left[(\omega t-\varphi)-\Phi\right]=X\left[\sin(\omega t-\varphi)\cos\Phi-\cos(\omega t-\varphi)\sin\Phi\right] \tag{9.38}$$

Comparing Equations 9.37 and 9.38, it follows that

$$X\cos\Phi=\frac{F_o}{k}\frac{1-\beta^2}{(1-\beta^2)^2+(2\zeta\beta)^2} \tag{9.39a}$$

$$X\sin\Phi=\frac{F_o}{k}\frac{2\zeta\beta}{(1-\beta^2)^2+(2\zeta\beta)^2} \tag{9.39b}$$

These two equations can be combined to yield the desired equation for X:

$$X=\frac{F_o}{k}\frac{1}{\sqrt{(1-\beta^2)^2+(2\zeta\beta)^2}} \tag{9.40}$$

and

$$\tan\Phi=\frac{2\zeta\beta}{1-\beta^2} \tag{9.41}$$

Thus,

$$x_p=\frac{F_o}{k}\frac{1}{\sqrt{(1-\beta^2)^2+(2\zeta\beta)^2}}\sin\left[(\omega t-\varphi)-\Phi\right] \tag{9.42}$$

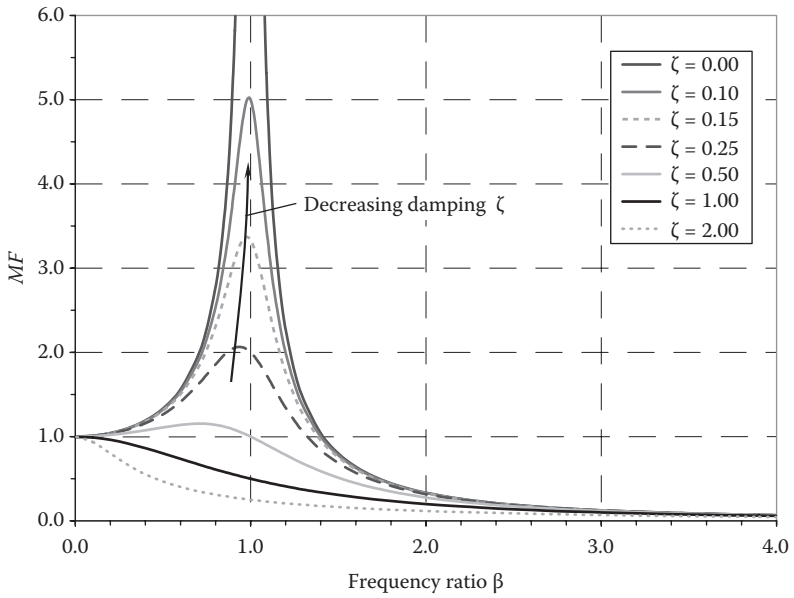

FIGURE 9.4
Variations of the *MF* with frequency ratio β and damping ratio ζ.

The ratio of the amplitude of the steady-state response to the static deflection under the action of force F_o is known as the *MF*:

$$MF = \frac{1}{\sqrt{\left(1-\beta^2\right)^2 + (2\zeta\beta)^2}} \tag{9.43}$$

Thus, the *MF* depends upon the frequency ratio β and the damping ratio ζ. The variations of the *MF* as functions of ζ and β are displayed in Figure 9.4. It can be observed that for all cases, if β is much less than 1, the *MF* approaches 1, regardless of the damping ratio. Actually, exceeding excitation frequencies cause the amplitude of forced vibration to be sufficiently small.

If β becomes large enough (i.e., $\omega \gg \omega_n$), the *MF* approaches zero for all ζ values. This is because the increase in excitation frequency always causes the increase in system inertia force, resulting in the reduction of the amplitude of forced vibration. The system exhibits resonance when $\beta = 1$, that is, the excitation frequency ω is exactly equal to the system natural frequency ω_n. At this point, the amplitude of vibration increases without bound if no damping is applied on the system.

For very small damping ratios (i.e., $\zeta \to 0$), the *MF* can go extremely high near $\beta = 1$. Theoretically, when $\zeta = 0$, the *MF* goes infinity at $\beta = 1$. Increasing ζ can reduce sharply the peak values of the *MF*, particularly at $\beta = 1$ due to the damping effect. As ζ becomes considerably large, the amplitude of the *MF* is reduced for all β values. At the critical damping where $\zeta = 1$, the *MF* decreases monotonically with the increase in the frequency ratio β. For overdamped cases that $\zeta > 1$, the *MF* approaches zero much faster than all other cases.

Figure 9.5 shows the variations of the phase angle with frequency ratio β and damping ratio ζ. At the resonance point where $\omega = \omega_n$, the phase angle is 90° for all damping ratios.

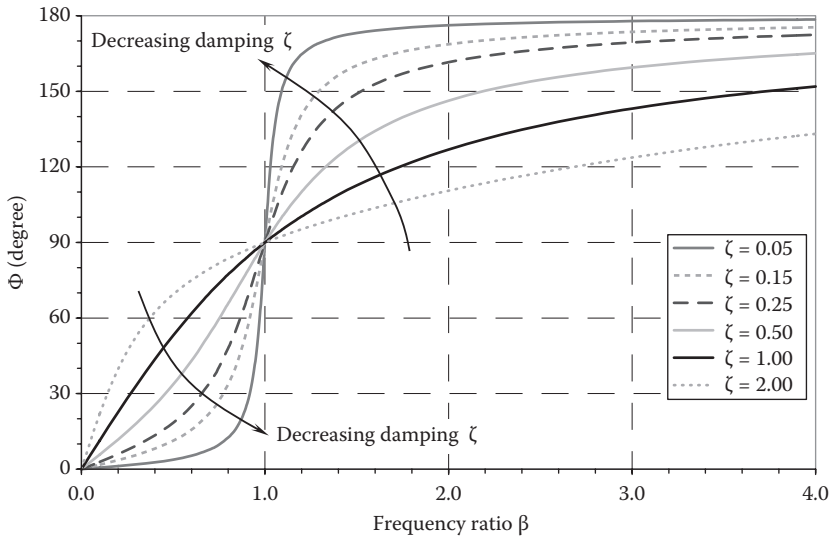

FIGURE 9.5
Variations of phase angle Φ with frequency ratio β and damping ratio ζ.

For an undamped system (where $\zeta = 0$), the phase angle $\Phi = 0°$ for $0 \leq \beta < 1$ and $\Phi = 180°$ for $\beta \geq 1$. Increasing the damping ratio ζ leads to a longer time for the phase angle to approach 180°. For $0 < \beta < 1$ and $\zeta > 0$, the response lags the excitation. Contrarily, for $\beta > 1$ and $\zeta > 0$, the response leads the excitation.

9.2.4 Forced Vibration due to Mass Unbalance

Mass unbalance is one of the most common sources of vibration excitation in rotating machinery because it develops a centrifugal force along with dynamic eccentricity. The total unbalanced force is the sum of the centrifugal force and unbalanced electromagnetic force. Rotor eccentricity increases due to this unbalanced force that tries to pull apart the rotor further away from the stator bore center, varying the air gap. This unbalanced force is proportional to the rotor rotating speed [9.10,9.11].

Although a motor is designed, manufactured, assembled, and installed with great care to ensure proper balance under working conditions, some degree of mass unbalance is always present in the motor. Under normal circumstances, slight unbalance in major rotating components with relatively low rotating speeds should not notably affect motor operation. However, if the deviation in mass symmetry about the rotating axis becomes significant or if the rotating speed of motor is considerably high, large unbalanced forces are produced to exert on the rotor, bearings, support structure, and ancillary equipment, leading to high vibration and high stresses of these components. In fact, vibration is a major cause of downtime and reliability problems for electric motors. Many sources highlight the impact of vibration on the motor performance, noise, fatigue lifetime, and failure. In a worse case, a rotor unbalance may cause the rotor and stator contact and rub each other, resulting in a severe motor failure. The vibration frequency of unbalance f_r is equal to the rotor rotating speed in the unit of revolutions per second (rps):

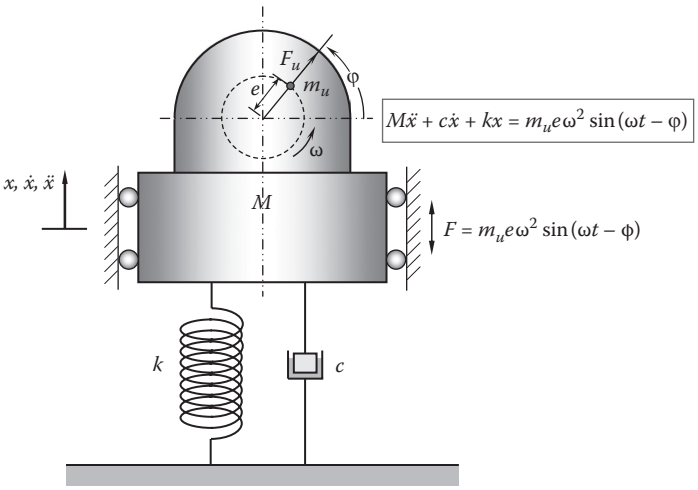

FIGURE 9.6
Forced vibration induced by unbalanced mass.

$$f_r = \frac{n}{60} = \frac{\omega}{2\pi} \tag{9.44}$$

where
the unit of rotor rotating speed n is rpm
the unit of the angular speed ω is radians per second (rad/s)

Considering the rotating system in Figure 9.6, the unbalance is represented by an unbalanced mass m_u with eccentricity e from the system rotating axis and angular velocity ω. The centrifugal force resulting from the eccentric mass is given by

$$F_u = m_u e\omega^2 \sin(\omega t - \varphi) \tag{9.45}$$

This force serves as the exciting force to induce forced vibration of the system. The total mass of the system is M. The equation of motion is

$$M\frac{d^2x(t)}{dt^2} + c\frac{dx(t)}{dt} + kx = (m_u e\omega^2)\sin(\omega t - \varphi) \tag{9.46}$$

This equation is identical to (9.27) as F_o is replaced by $(m_u e\omega^2)$. Because the complementary solution $x_c(t)$ is independent of the exciting force, it remains the same as shown in Equation 9.29. The particular solution $x_p(t)$ can be obtained by replacing F_o by $(m_u e\omega^2)$ in Equation 9.42, that is,

$$x_p = \frac{m_u e\omega^2}{k} \frac{1}{\sqrt{(1-\beta^2)^2 + (2\zeta\beta)^2}} \sin\left[(\omega t - \varphi) - \Phi\right] \tag{9.47}$$

It is noted that the damping ratio ζ in this case is based on the system mass M:

$$\zeta = \frac{c}{2\sqrt{Mk}} \tag{9.48}$$

Similarly, the system national frequency becomes

$$\omega_n = \sqrt{\frac{k}{M}} \tag{9.49}$$

The steady-state amplitude X is given by

$$X = \frac{m_u e\omega^2}{k} \frac{1}{\sqrt{(1-\beta^2)^2 + (2\zeta\beta)^2}} = \frac{m_u e}{M} \frac{\beta^2}{\sqrt{(1-\beta^2)^2 + (2\zeta\beta)^2}} \tag{9.50}$$

This equation can be alternatively rearranged as

$$\frac{MX}{m_u e} = \frac{\beta^2}{\sqrt{(1-\beta^2)^2 + (2\zeta\beta)^2}} \tag{9.51}$$

and

$$\tan\Phi = \frac{2\zeta\beta}{1-\beta^2} \tag{9.52}$$

The variations of $MX/m_u e$ are plotted in Figure 9.7 as functions of frequency ratio β and damping ratio ζ. It shows all curves start at zero amplitude. Resonances occur for various damping levels at $\beta = 1$, that is, when the excitation frequency ω is identical to the system natural frequency ω_n. At very large β values, all curves approach 1 regardless of damping.

Since the phase angle Equation 9.52 is identical to 9.41, the variation of the phase angle with β and ζ is the same as in Figure 9.5.

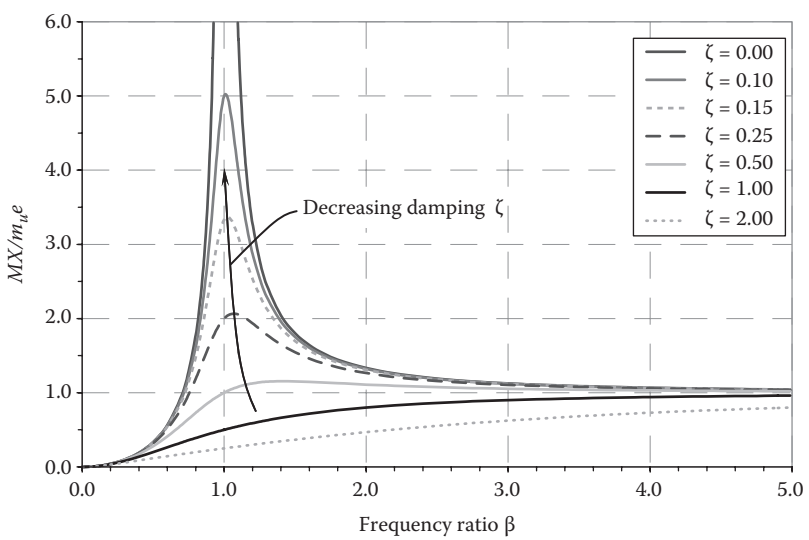

FIGURE 9.7
Variations of factor $MX/m_u e$ with frequency ratio β and damping ratio ζ.

Due to mass unbalance in rotor condition, mutual inductances between stator and rotor loops become unsymmetrical, inducing characteristic harmonics as given in the following:

$$f_{ubm} = f\left[\frac{k(1-s)}{p}+1\right], \quad k = 1, 2, 3, \ldots \tag{9.53}$$

where
p is the number of pole pairs
s is the slip
f is the supply frequency

Among all the causes of motor vibration, rotor unbalance is the most common one. In fact, unbalanced mass in a rotor creates large forces that often result in motor failure and downtime. For high-speed motors, even a very small amount of unbalance may cause a severe vibration problem. Mass unbalance in a rotor may come from manufacturing errors such as porosity in casting, improper machining process, manufacturing tolerances, and gain or loss of material during operation [9.12].

9.2.5 Vibration Induced by Support Excitation

Many motor applications involve vibrations that are induced by the excitation of motor support. A typical example is driving a vehicle on a bumpy road. The vehicle shakes due to the uneven surfaces such as broken pavement, potholes, troughs, and small stones. Vibration is transmitted through wheels to the vehicle body and other components including motors.

Another example is related to seismic waves generated by earthquakes. Earthquakes generate three types of seismic waves: primary (longitudinal) wave, secondary (shear) wave, and surface wave (mixed wave of primary and secondary waves). Due to the long wavelength and high amplitude, surface wave is the main cause of building destruction. When a building sways and oscillates during an earthquake, all objects attached to the building vibrate accordingly. This will seriously affect the safe operation of elevator motors. Therefore, it is very important to understand the excitation mechanism of motor vibration induced by support excitation because it helps design safer and more reliable elevator motors.

As demonstrated in Figure 9.8, a spring–damper system undergoes harmonic motion, where $x(t)$ denotes the displacement from the mass equilibrium position and $y(t)$ the displacement of the motor support at time t. The damping force in this case is the product of the relative velocity between the system and its support $(\dot{x}-\dot{y})$ and the damping coefficient c, that is, $c(\dot{x}-\dot{y})$, and the spring force is the product of the net spring elongation $(x - y)$ and the spring coefficient k, that is, $k(x - y)$.

The motion equation is expressed as

$$m\frac{d^2x(t)}{dt^2}+c\left(\frac{dx(t)}{dt}-\frac{dy(t)}{dt}\right)+k(x-y)=0 \tag{9.54}$$

Introducing the relative displacement $x_R = x - y$, Equation 9.54 can be rewritten as

$$m\frac{d^2x_R(t)}{dt^2}+c\frac{dx_R(t)}{dt}+kx_R(t)=-m\frac{d^2y(t)}{dt^2} \tag{9.55}$$

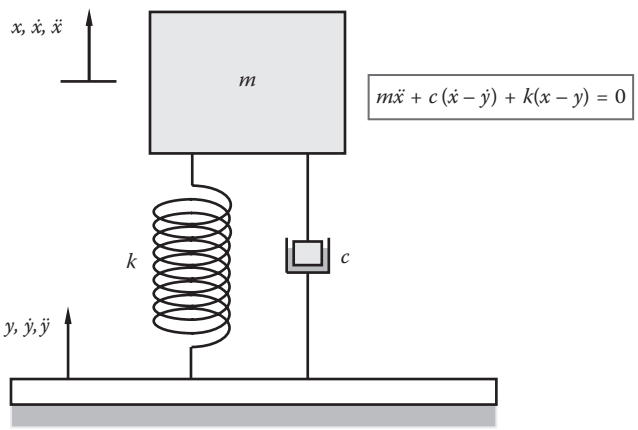

FIGURE 9.8
Vibration induced by support excitation in a two-degree-of-freedom mechanical system.

Following the same procedure as discussed previously, this equation is solved for x_R:

$$x_R(t) = \frac{\beta^2 y(t)}{\sqrt{(1-\beta^2)^2 + (2\zeta\beta)^2}} \sin(\omega t - \Phi) \tag{9.56}$$

The vector diagram shows that the relationship between three vectors is (Figure 9.9)

$$\mathbf{x} = \mathbf{x}_R + \mathbf{y} \tag{9.57}$$

It follows that

$$x^2 = x_R^2 + y^2 + 2x_R y \cos\Phi \tag{9.58}$$

The phase angle is obtained as follows:

$$\tan\Phi = \frac{2\zeta\beta}{1-\beta^2} \tag{9.59}$$

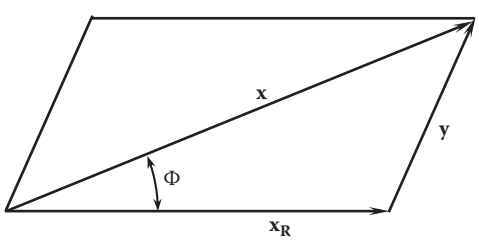

FIGURE 9.9
The relationship of three vectors given that $\mathbf{x} = \mathbf{x}_R + \mathbf{y}$. The vector $\mathbf{x}_R$ lagging behind $\mathbf{x}$ by an angle Φ.

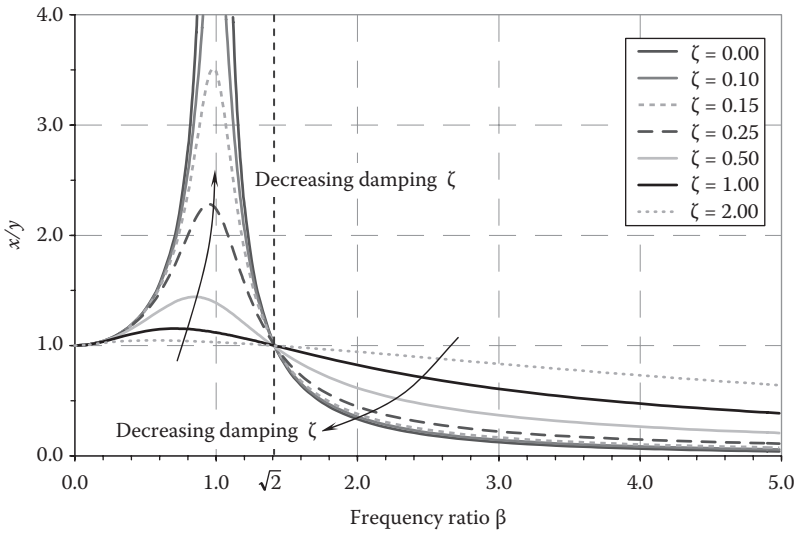

FIGURE 9.10
Variations of displacement transmissibility x/y with frequency ratio β and damping ratio ζ in a two-degree-of-freedom mechanical system where vibration is induced by the excitation of support.

The ratio of the amplitude of the response $x(t)$ to that of the support motion $y(t)$ is defined as the displacement transmissibility. Thus,

$$\frac{x(t)}{y(t)} = \frac{\sqrt{1+(2\zeta\beta)^2}}{\sqrt{(1-\beta^2)^2+(2\zeta\phi)^2}} \tag{9.60}$$

The displacement transmissibility $x(t)/y(t)$ is plotted in Figure 9.10 with various values of the damping ratio ζ and frequency ratio β. It can be seen that the value of x/y is unity for all curves at $\beta = 0$ and $\beta = \sqrt{2}$, regardless of the damping levels. At the system resonance point where $\beta = 1$, x/y becomes infinity for an undamped spring–mass system ($\zeta = 0$). Increasing the ζ value will greatly reduce the peak values of the displacement transmissibility x/y. The values of x/y are larger than 1 for $0 < \beta < \sqrt{2}$ and less than 1 for $\beta > \sqrt{2}$. Moreover, for $\beta < \sqrt{2}$, a small change in the damping ratio leads to a large change in x/y. As a contrast, for $\beta > \sqrt{2}$, the change in the damping ratio is less sensitive to the magnitude of x/y.

9.2.6 Directional Vibration

According to the direction of vibration, there are basically three types of vibration associated with the motion:

1. Radial vibration is the vibration of rotor in the radial direction. This type of vibration can be caused by several reasons: (a) Rotating magnetic field produces a traveling force wave that distorts stator and causes vibration in the stator frame and base (see Figure 9.11). (b) Any unbalance on the rotor can result in an unbalanced centrifugal force, leading to the rotor distortion. (c) Large bearing radial clearance provides free space for the rotor in the radial direction. (d) Bearing misalignment can directly lead to motor vibration.

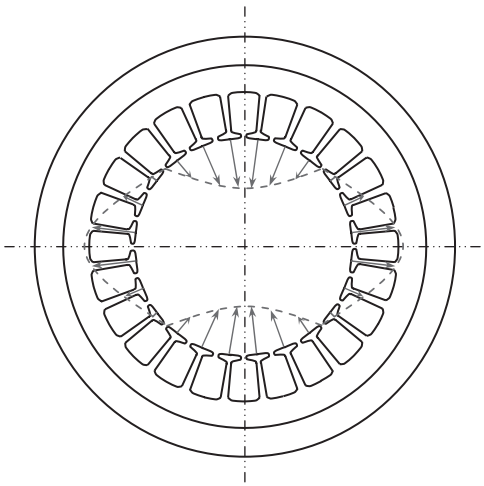

FIGURE 9.11
Stator distortion due to traveling forces as a result of rotating magnetic flux.

2. Torsional vibration is the dynamics of the rotor in the angular/rotational direction. Excessive torsional vibration and resonance lead to damaged motor components such as rotor, bearings, couplings, gears, and auxiliary equipment.
3. Axial vibration is the dynamic response of the rotor in the axial direction under external thrust forces and internal electromagnetic forces due to the misalignment of the rotor relative to the stator windings. There are indications that rotordynamic vibration and axial vibration influence each other through variations in roller bearing stiffness due to the time-dependent axial load [9.13].

In practice, a multidirectional vibration may occur to act on a motor. The interactions between different directional vibrations make the vibration problems considerably complicated.

9.3 Electromagnetic Vibrations

Magnetic field present in an air gap is the primary source for the electromagnetic vibrations due to the variation in electromagnetic forces over time. The harmonics in the electromagnetic forces induce structural vibration and acoustic noise. The following sections describe the various causes of electromagnetic vibrations.

9.3.1 Unbalanced Forces/Torques Caused by Electric Supply

Stator-related faults account for the second largest number of faults, up to 38% in IMs. Stator winding faults occur when the stator windings are shorted due to the insulation issues related to manufacturing defects, contaminations, overheating and wear, collision of the rotor and stator, and voltage stress imposed by the fast switching of inverters. The unbalanced electromagnetic flux in air gap occurs on the twice line frequency.

9.3.2 Broken Rotor Bar and Cracked End Ring

For squirrel cage IMs, broken rotor bars and cracked end rings are the commonly encountered motor faults, which may be due to manufacturing defects, pulsating loads, frequent direct online starting, and thermal and mechanical stresses from heavy-duty cycle operation [9.14]. The broken rotor bar accounts for approximately 9% of all faults of IM. Due to the bar/end ring breakages, which primarily occur at the joints between bars and end rings, the inducting current in the rotor will be redistributed, leading to overheating of the adjacent bars, torque pulsation, speed fluctuation, changes in magnetic fields, noise, and vibration.

When a broken rotor bar fault occurs in an IM, sideband frequencies f_{sb} (where $f_{sb} > 0$) will appear in stator current around the supplied current fundamental frequency f [9.15]:

$$f_{sb} = (1 \pm 2ks) f, \quad k = 1, 2, 3, \ldots \tag{9.61}$$

where s is the slip of motor.

Figure 9.12 illustrates the distribution of sideband frequencies at the sides of the fundamental line frequency. Thus, these sideband harmonics can be used to identify and detect the broken rotor bar fault.

As proposed by Thomason and Rankin [9.16], the number of broken bars n_b for full-load operation (also known as broken bar factor) can be estimated from the following equation:

$$n_b = \frac{2N_{slot}}{10^{N/20} + p} \tag{9.62}$$

where

N_{slot} is the number of rotor slots
p is the pole pair
N is the average decibel difference between upper and lower sidebands

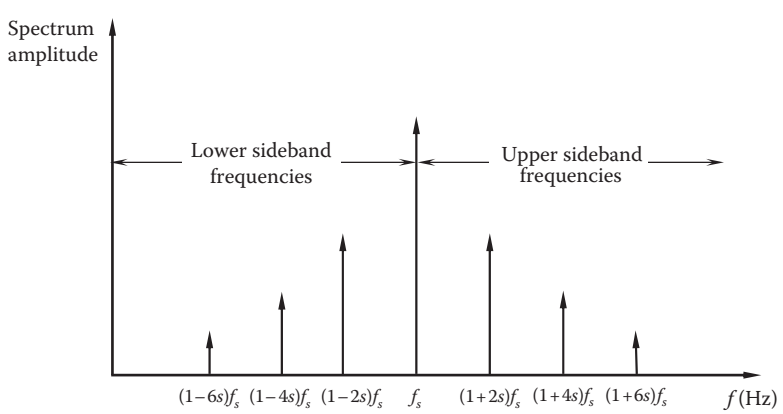

FIGURE 9.12
Sideband frequencies around the fundamental line frequency f_s.

The most important harmonics caused by the broken rotor bars f_b are as follows [9.17]:

$$f_b = (1 \pm 2ks) f, \quad k = 1, 2, 3, \ldots \tag{9.63}$$

where
s is the slip of motor
f is the supply frequency

9.3.3 Unbalanced Magnetic Pull due to Asymmetric Air Gap

As electric current flows through the stator windings, a magnetic field is generated in the air gap. The magnetic flux in the air gap thus produces an attractive force between the stator and rotor in the direction of the flux. In a system with a uniform air gap, the rotor is subjected to a uniform attraction force from all directions around it. Therefore, there is no resultant force acting on it due to symmetry. However, when an air gap asymmetry is present, a resultant traction force is produced on both the rotor and stator, occurring at the minimum air gap.

Air gap asymmetries are often encountered in almost all types of electric motors. These asymmetries distort the distribution of the magnetic flux density in the air gap and create unbalanced electromagnetic forces that act on both the rotor and stator. This phenomenon is known as UMP. The presence of UMP always tends to further increase the eccentricity magnitude, and in the worst case, the rotor may touch the stator to cause serious damage to the electric motor.

Asymmetric air gap is called eccentricity in electric motors. A general eccentricity form is cylindrical circular rotor whirling. In this form, the rotor axis always remains parallel to the stator axis and travels around it in a circular orbit with a certain radius and a certain angular velocity (or frequency). This motion is defined as the whirling motion and the corresponding orbit radius and angular velocity (or frequency) are defined as the whirling radius and whirling angular velocity (or whirling frequency), respectively. In dynamic whirling cases, the whirling velocity is equal to the rotor speed. An electric motor operated with the cylindrical circular rotor eccentricity is shown in Figure 9.13. The rotor rotates at a constant angular velocity ω_r. During the rotor rotating, its center O_r also rotates with respect to the stator center O_s at an angular velocity ω_w in a circular orbit.

There are two types of air gap eccentricity associated with electric motors: static eccentricity and dynamic eccentricity, depending on the magnitude of the rotor whirling angular velocity. In the case of a static air gap eccentricity, the positions of the maximum and minimum air gap are fixed in space, that is, the eccentric rotor displacement remains stationary with respect to the stator. This indicates that in this case, the rotor whirling angular velocity is zero (i.e., $\omega_w = 0$). In contrast, in the case of a dynamic air gap eccentricity, the positions of the maximum and minimum air gap rotate with the rotor, implying that the whirling angular velocity ω_w is the same as the mechanical angular velocity of the rotor ω_r. In either static or dynamic air gap eccentricities, the resultant force on the rotor always points to the direction of the minimum air gap, so does the resultant force on the stator but in the opposite direction.

9.3.3.1 Electromagnetic Force at Air Gap

UMP has been discussed for more than a century. Many researchers have performed intensive studies to calculate the UMP for predicting vibration characteristics of rotor

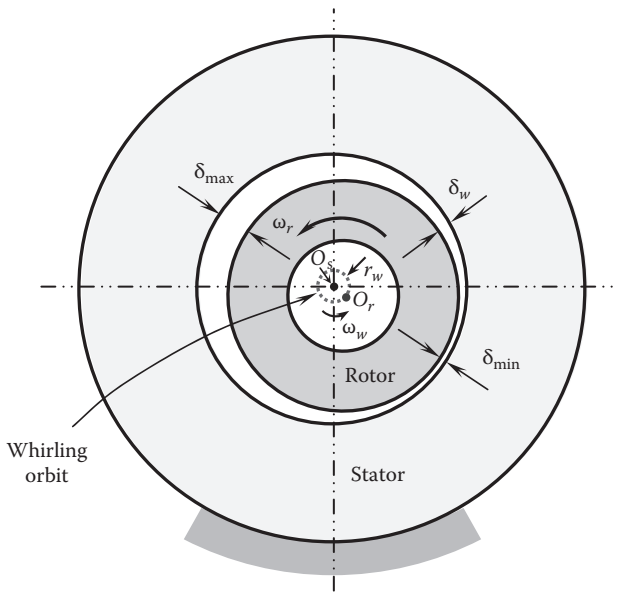

FIGURE 9.13
A general form of cylindrical circular rotor whirling.

systems due to UMP. Früchtenicht et al. [9.18] developed an analytical model for predicting the electromagnetic forces between the rotor and stator for a rotor in circular whirling motion. With their model, the stiffness and damping coefficients induced by the electromagnetic field can be determined. It was found that the electromechanical interaction can cause rotordynamic instability. Arkkio et al. [9.19] presented a simple parametric model for calculating the electromagnetic forces at the air gap field when the rotor performs cylindrical circular whirling motion with respect to the stator. They determined the model parameters of a motor by time stepping FEA including the nonlinear saturation of magnetic materials. In this study, the computed and measured forces show good agreement.

The responses due to certain deviations of shape in the rotor and the stator have been investigated numerically and analytically by Lundström and Aidanpää [9.20]. In their study, the perturbation on the rotor is considered to be of oval character, and the perturbations of the stator are considered triangular. In this case, the rotor whirling motion becomes much more complicated.

Regardless of the mechanism of air gap eccentricity, any eccentricity in the air gap results in variations of the distribution of the magnetic flux, magnetic flux density, and reluctance. The magnetic flux density B is defined as the magnetic flux Φ per unit area:

$$B = \frac{\Phi}{A} \tag{9.64}$$

Because the magnetic flux Φ is related to the total MMF F_m and the reluctance of the magnetic flux path R_m,

$$\Phi = \frac{F_m}{R_m} \tag{9.65}$$

the reluctance can be expressed as

$$R_m = \frac{\delta}{\mu A} \tag{9.66}$$

where μ is the permeability of air. Therefore, it gives that

$$\Phi = \frac{\mu A F_m}{\delta} \tag{9.67}$$

$$B = \frac{\mu F_m}{\delta} \tag{9.68}$$

This indicates that both the magnetic flux Φ and flux density B are inversely proportional to the length of the air gap.

There are two basic methods used to calculate the forces acting between the rotor and stator: the methods that are based on Maxwell's stress and the methods that are based on the principle of the virtual work. Derived from Maxwell's equations, the electromagnetic force at air gap can be expressed as

$$\mathbf{F} = \int_0^{2\pi} \left[\frac{1}{\mu_0} B_r B_\phi \mathbf{e}_\varphi + \frac{1}{2\mu_o} \left(B_r^2 - B_\phi^2 \right) \mathbf{e}_\mathbf{r} \right] r d\phi \tag{9.69}$$

where B_r and B_ϕ are the radial and tangential components of the magnetic flux density, respectively. More reliable results are obtained if the line integral in Equation 9.69 is transformed to a surface integral over the cross section of the air gap [9.21]:

$$\mathbf{F} = \frac{1}{\delta(\phi)} \int_{S_{ag}} \left[\frac{1}{\mu_0} B_r B_\phi \mathbf{e}_\varphi + \frac{1}{2\mu_o} \left(B_r^2 - B_\phi^2 \right) \mathbf{e}_\mathbf{r} \right] dS \tag{9.70}$$

where

S_{ag} is the cross-sectional area of the air gap

$\delta(\phi)$ is the air gap thickness at the angular position ϕ

$$\delta(\phi) = r_s(\phi) - r_r(\phi) \tag{9.71}$$

where $r_s(\phi)$ and $r_r(\phi)$ are the outer and inner radii of the air gap. It must be noted that this equation is valid only for small eccentricities [9.22].

It can be seen from Equation 9.70 that the electromagnetic force at the air gap is inversely proportional to the thickness of the air gap. This indicates that even a small change in air gap may result in a large change in electromagnetic force.

To better understand the effects of asymmetric air gaps on UMP, several causes of asymmetric air gap are addressed separately in the following sections.

9.3.3.2 Asymmetric Air Gap due to Nonconcentric Rotor and Stator

There are a variety of causes that can result in air gap asymmetries. As demonstrated in Figure 9.14, an asymmetric air gap resulted from the nonconcentric rotor and stator,

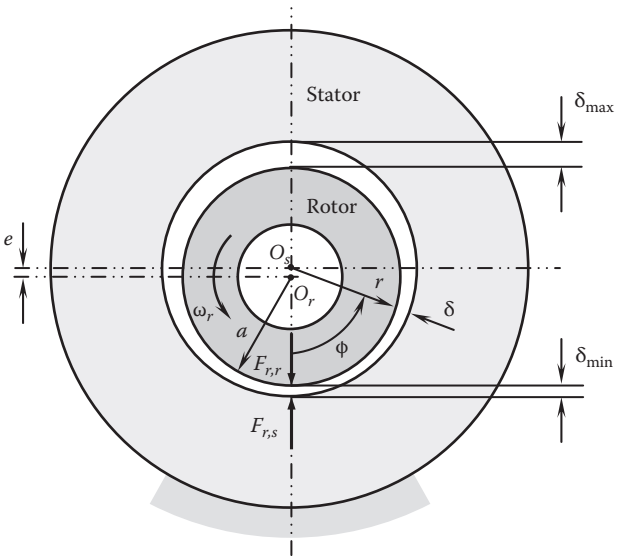

FIGURE 9.14
Asymmetrical air gap due to nonconcentric stator and rotor.

which may be due to the accumulation of tolerances during manufacturing, wear of bearings and bearing bores, poor maintenance, and many other factors. This is a special case of the general eccentricity form in Figure 9.13, with $\omega_w = 0$ and $r_w = e$. In this case, the rotor and stator axes are parallel but not coincident. The air gap profile maintains a steady state, that is, the positions of the maximum and minimum air gap are independent of the rotor rotation.

The eccentricity between the rotor and stator is defined as

$$e = \frac{1}{2}\left(\delta_{\max} - \delta_{\min}\right) \tag{9.72}$$

where δ_{max} and δ_{min} are the maximum and minimum air gaps, respectively. As the mean air gap is given as

$$\delta_m = \frac{1}{2}\left(\delta_{\max} + \delta_{\min}\right) \tag{9.73}$$

it follows that

$$e = \delta_{\max} - \delta_m = \delta_m - \delta_{\min} \tag{9.74}$$

In a polar coordinate system, the general equation of a circle with the center at (e, 0) and the radius of c can be expressed as

$$r_r^2 - \left(2e\cos\phi\right)r_r + e^2 = c^2 \tag{9.75}$$

Solving this equation, it yields

$$r_r(\phi) = e\cos\phi + \sqrt{e^2\left(\cos^2\phi - 1\right) + c^2} \tag{9.76}$$

It is easy to confirm that at $\phi = 0$, $r_r = c + e$ and at $\phi = \pi$, $r_r = c - e$.

Thus, the air gap thickness for a nonconcentric rotor–stator system can be obtained by subtracting the rotor radius from the stator radius in the polar coordinate:

$$\delta_{nc}(\phi) = r_s - r_r(\phi) \tag{9.77}$$

where the stator radius is a constant, expressed as

$$r_s = \delta_m + c \tag{9.78}$$

Therefore, the air gap for nonconcentric rotor and stator is a function of the angular spatial position and can be expressed as

$$\delta_{nc}(\phi) = \delta_m + c - e\cos\phi - \sqrt{e^2\left(\cos^2\phi - 1\right) + c^2} \tag{9.79}$$

In this case, the resultant forces acting on the rotor $F_{r,r}$ and stator $F_{r,s}$ point each other at the minimum air gap.

9.3.3.3 Asymmetric Air Gap due to Elliptic Stator

An asymmetric air gap can result from a number of manufacturing flaws, such as a noncircular stator core or a noncircular rotor.

The number of poles can significantly impact the vibration patterns. For two-pole motors, electromagnetic forces produced by fundamental flux attempt to deflect the stator into an elliptical shape. Since the stator core is mounted inside the motor housing, the restraining forces to the stator deformation primarily come from the motor housing. Unlike in the previous cases, the air gap profile is independent of the rotor rotation (Figure 9.15). The equation of the elliptic stator bore can be written as

$$\frac{r_{es}^2\cos^2\phi}{a^2} + \frac{r_{es}^2\sin^2\phi}{b^2} = 1 \tag{9.80}$$

Solving Equation 9.80 for r_{es}, it yields

$$r_{es}(\phi) = \frac{ab}{\sqrt{a^2\sin^2\phi + b^2\cos^2\phi}} \tag{9.81}$$

The rotor radius is a constant:

$$r_r = a - \delta_{\max} = b - \delta_{\min} \tag{9.82}$$

Similarly, the eccentricity of the elliptic stator is defined as

$$e_{es} = \sqrt{1 - \frac{b^2}{a^2}} \tag{9.83}$$

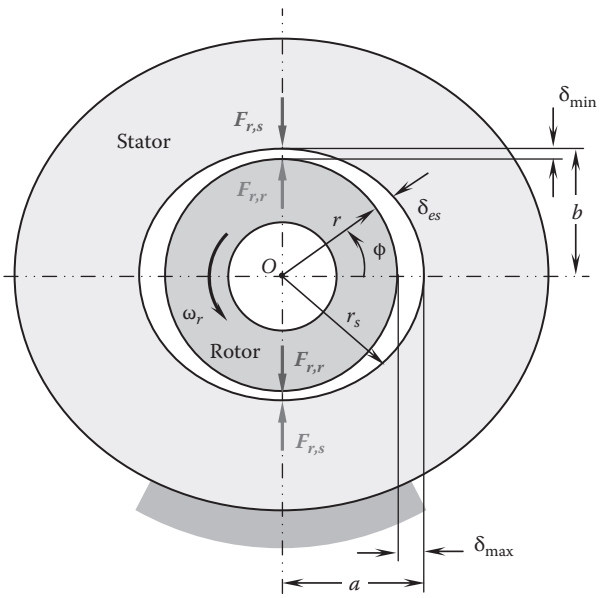

FIGURE 9.15
Asymmetrical air gap due to elliptic stator.

The difference between the maximum and minimum air gaps can be expressed as

$$\Delta\delta_{es} = \delta_{\max} - \delta_{\min} = a\left(1 - \sqrt{1 - e_{es}^2}\right) = b\left(\frac{1}{\sqrt{1 - e_{es}^2}} - 1\right) \tag{9.84}$$

Hence, the air gap is obtained by subtracting r_r from r_{es}:

$$\delta_{es}(\phi) = r_{es}(\phi) - r_r = \delta_{\max} + a\left(\frac{b}{\sqrt{a^2 \sin^2\phi + b^2 \cos^2\phi}} - 1\right) \tag{9.85}$$

For vibrations caused by unbalanced electromagnetic flux at the air gap, the frequency of vibration f equals to two times the frequency of the power source, called twice line frequency vibration:

$$f = 2f_s \tag{9.86}$$

For instance, the 60 Hz power supply shows a 120 Hz vibration at the outer surface of the stator. Finally, this twice line frequency vibration is transmitted through the motor frame to the environment.

9.3.3.4 Asymmetric Air Gap due to Elliptic Rotor

Figure 9.16 presents the asymmetric air gap due to the elliptic rotor. It is noted that the air gap profile in this case is no longer steady in the stationary coordinate system. It only maintains the steady state in the rotating frame of reference that has the same

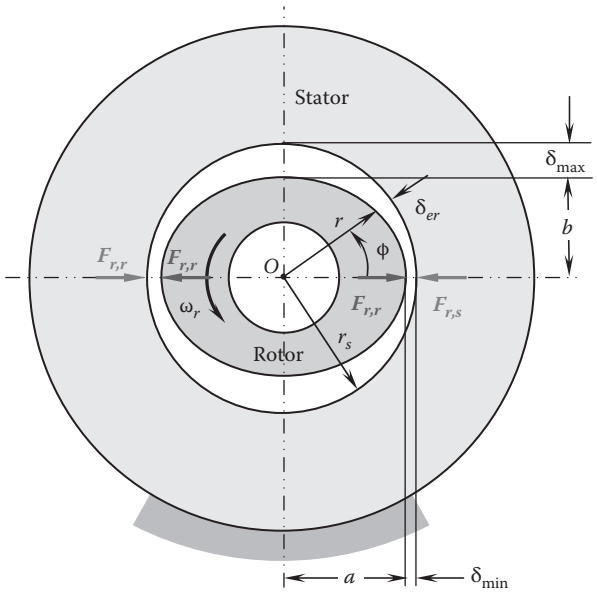

FIGURE 9.16
Asymmetrical air gap due to elliptic rotor.

rotating speed and direction of the rotor. In fact, this is a typical example of dynamic air gap eccentricity.

In the rotating frame of reference (x', y'), a rotating ellipse can be expressed as

$$\frac{x'^2}{a^2}+\frac{y'^2}{b^2}=1 \tag{9.87}$$

where a and b are the length of the semimajor axis and semiminor axis, respectively. In order to obtain the ellipse equation in the stationary frame of reference, the rotating frame of reference must be converted into a stationary frame via the conversion equation as the following:

$$\begin{bmatrix} x' \\ y' \end{bmatrix}=\begin{bmatrix} \cos(\omega_r t) & \sin(\omega_r t) \\ -\sin(\omega_r t) & \cos(\omega_r t) \end{bmatrix}\begin{bmatrix} x \\ y \end{bmatrix} \tag{9.88}$$

Thus, the rotating ellipse can be expressed in the stationary frame of reference (x, y):

$$\frac{\left[x\cos(\omega_r t)+y\sin(\omega_r t)\right]^2}{a^2}+\frac{\left[-x\sin(\omega_r t)+y\cos(\omega_r t)\right]^2}{b^2}=1 \tag{9.89}$$

The polar coordinate system uses r as the radial coordinate and ϕ as the angular coordinate. Thus, the Cartesian coordinate system (x, y) can be related to the polar coordinate system (r, ϕ) as $x=r\cos\phi$ and $y=r\sin\phi$. Consequently, the equation of the rotating elliptic rotor can be rewritten as

$$\frac{r_{es}^2\cos^2(\phi-\omega_r t)}{a^2}+\frac{r_{er}^2\sin^2(\phi-\omega_r t)}{b^2}=1 \tag{9.90}$$

The eccentricity of the elliptic rotor is defined as

$$e_{er} = \sqrt{1 - \frac{b^2}{a^2}} \tag{9.91}$$

From the equation of the elliptic rotor, it can be derived that the radius of the elliptic rotor is expressed as a function of ϕ:

$$r_{er}(\phi - \omega_r t) = \frac{ab}{\sqrt{a^2 \sin^2(\phi - \omega_r t) + b^2 \cos^2(\phi - \omega_r t)}} \tag{9.92}$$

This equation can be alternatively expressed in terms of eccentricity e [9.23]:

$$r_{er}(\phi - \omega_r t) = a\sqrt{\frac{1 - e_{er}^2}{1 - e_{wr}^2 \cos^2(\phi - \omega_r t)}} = \frac{b}{\sqrt{1 - e_{er}^2 \cos^2(\phi - \omega_r t)}} \tag{9.93}$$

The radius of the stator is a constant, expressed as

$$r_s = a + \delta_{\min} = b + \delta_{\max} \tag{9.94}$$

From this equation, the relationship of the difference between the maximum and minimum air gaps and the ellipse parameter a and b can be derived as

$$\Delta\delta_{er} = \delta_{\max} - \delta_{\min} = a - b \tag{9.95}$$

that is,

$$\Delta\delta_{er} = a\left(1 - \sqrt{1 - e_{er}^2}\right) = b\left(\frac{1}{\sqrt{1 - e_{er}^2}} - 1\right) \tag{9.96}$$

The air gap with the elliptic rotor is thus determined by subtracting the radius of the elliptic rotor from the inner radius of the stator r_s, as shown in the following three equivalent equations:

$$\delta_{er}(\phi - \omega_r t) = r_s - r_{er}(\varphi - \omega_r t) = r_s - \frac{ab}{\sqrt{a^2 \sin^2(\phi - \omega_r t) + b^2 \cos^2(\phi - \omega_r t)}} \tag{9.97a}$$

$$\delta_{er}(\phi - \omega_r t) = r_s - r_{er}(\varphi - \omega_r t) = \delta_{\min} + a\left(1 - \sqrt{\frac{1 - e^2}{1 - e^2 \cos^2(\phi - \omega_r t)}}\right) \tag{9.97b}$$

$$\delta_{er}(\phi - \omega_r t) = r_s - r_{er}(\varphi - \omega_r t) = \delta_{\max} + b\left(1 - \frac{1}{\sqrt{1 - e^2 \cos^2(\phi - \omega_r t)}}\right) \tag{9.97c}$$

For the case of dynamic air gap eccentricity, the resultant forces acting on the rotor $F_{r,r}$ and stator $F_{r,s}$, occurring at the minimum air gaps, rotate at the same rotating velocity of

the rotor. In the present situation, because of two identical minimum air gaps occurring in the system, a pair of resultant forces $F_{r,r}$ and $F_{r,s}$ acts at each of the minimum air gap, increasing the degree of the rotor eccentricity.

9.3.3.5 Asymmetric Air Gap due to Rotor Misalignment

The rotor misalignments always occur to some extent due to the need to allow some tolerances during the manufacturing process. As a misaligned rotor rotating with respect to its axis that has a small angle with the stator axis (Figure 9.17), the air gap varies along the angular position. However, these cases are more complicated than those discussed previously, usually requiring 3D analyses.

The magnetic force is inversely proportional to the air gap. For a nonuniform air gap, the smaller the air gap, the larger the magnetic force. Regardless of the causes of air gap asymmetry, an uneven air gap always results in unbalance in magnetic forces between the stator and rotor and further results in motor vibration [9.24].

9.3.3.6 Asymmetric Air Gap Resulting from Shaft Deflection

An asymmetric air gap may be induced from the rotor shaft deflection. The causes of shaft deflection may be static or dynamic in origin. The static shaft deflection is defined as the deflection that is measurable when the motor is not in operation, and the dynamic deflection is defined as the deflection that is detectable only during motor operation. A common static shaft deflection is due to the loads acting on the shaft. As a motor operates at high speeds, the centrifugal force acting on the rotor may cause the rotor shaft to bend out as a dynamic deflection (Figure 9.18).

9.3.4 Nonuniform Air Gap due to Stator Slots

The electric current that goes through the stator winding generates a rotating magnetic field and induces magnetic fluxes circulating around the air gap. However, the existence of the stator slots breaks up the uniformity of the air gap. Thus, the air gap will change periodically as the relative position of the stator and rotor changes.

As proposed by Lipo [9.25], due to the stator slot opening, the air gap variation is modeled considering the distribution of flux lines on the slots (Figure 9.19). The air gap rises linearly to the slot center in a slot and then drops up to its nominal value.

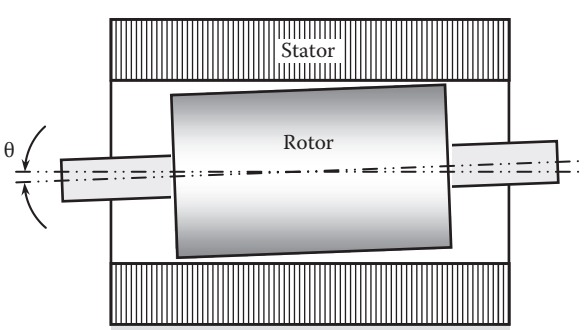

FIGURE 9.17
Asymmetric air gap resulted from the misalignment of rotor.

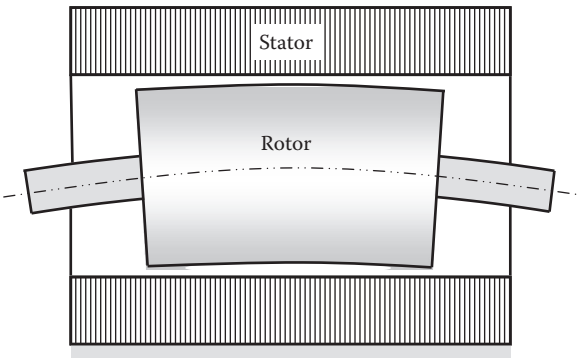

FIGURE 9.18
Asymmetric air gap resulted from the deflected motor shaft.

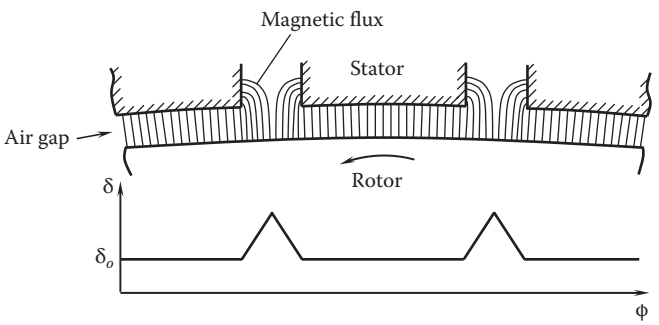

FIGURE 9.19
The impact of stator slots on magnetic flux distribution and air gap length.

The equivalent air gap of an IM is induced by replacing the actual slotted surface with an equivalent unslotted surface, which has the same cross section but with a modified *equivalent* gap. Equating the permeance of the equivalent unslotted surface to the actual permeance, the equivalent gap δ_e and the real gap δ can be related via a so-called Carter factor k_c:

$$\delta_e = \delta k_c \tag{9.98}$$

where k_c is a function of the slot geometries and the real air gap thickness. Lipo [9.25] reported that for most practical machines, δ_e is generally found to be 15%–25% larger than δ.

In practice, several situations discussed previously may occur simultaneously to cause asymmetric air gaps. For such complicated cases, FEMs may be used for predicting the unbalanced magnetic forces.

9.3.5 Mutual Action Forces between Currents of Stator and Rotor

Vibration may come from an irregular magnetic reluctance torque existing between the teeth of the stator and rotor. When the rotor rotates, the electromagnetic force on the stator varies periodically with high frequency because of the teeth structure of salient geometry. This periodic force of high frequency brings vibration and acoustic noise [9.26].

9.3.6 Vibration due to Unbalanced Voltage Operation

According to Muljadi et al. [9.27], in a weak power system network, an unbalanced load at the distribution lines can cause unbalanced voltage conditions. As an induction machine operates under unbalanced voltage conditions, it will result in unbalanced stator current, which creates torque pulsation on the shaft resulting in speed pulsation, mechanical vibration, and, consequently, audible acoustic noise and extra mechanical stress.

9.4 Mechanical Vibrations

Mechanical vibrations can be caused by a variety of factors, including but not limited to unbalanced mass in rotating parts, friction between motor components, misalignment, frame distortion, rotating speed at or near the critical speed, shocks caused by internal or external forces, looseness of parts, bearing deterioration, and various support and coupling effect problems.

9.4.1 Misaligned Shaft and Distorted Coupling

In industry, about 30% of the machines' downtime is due to the poorly aligned machine. Rotor shaft misalignment is the common problem in operation rotating machinery. It is strongly influenced by operation speed and stiffness of the coupling. Flexible couplings tend to provide less amount of vibration levels. Unlike rotor unbalance, misalignment effects on motor vibration are more complex. The vibration induced by the misalignment between a motor shaft and a driven machine shaft varies in different directions.

Misalignment is the most common cause of machine vibration. Experimental studies were performed by Hariharan et al. [9.28] on a rotordynamic test apparatus to obtain the vibration spectrum for shaft misalignment. The vibration spectra show that misalignment can be characterized primarily by second harmonics (2×) of the shaft running speed.

9.4.2 Defective Bearing

Motor bearings could be the main sources of vibration. The primary causes of bearing failures include overloads, nonuniform wear, corrosion, manufacturing errors, bearing fatigue, overheating, current flowing through bearings, high friction sintered bearing material, and improper lubrication and installation.

Most small- and middle-sized motors use rolling element bearings. A rolling element bearing basically consists of an outer and inner race, rolling balls, and a cage for holding the rolling balls. Each damaged component on a bearing can lead to vibration at specific frequencies [9.29,9.30]. Assuming that balls perform only pure rolling motions between the inner and outer races, the characteristic vibrating frequencies that are based upon the bearing dimensions can be determined for each bearing component:

$$\text{Inner race} \quad f_{inner} = \frac{N_b f_r}{2}\left(1 + \frac{d_b}{d}\cos\beta\right) \tag{9.99}$$

$$\text{Outer race} \quad f_{outer} = \frac{N_b f_r}{2}\left(1 - \frac{d_b}{d_p}\cos\beta\right) \tag{9.100}$$

$$\text{Ball} \quad f_b = \frac{d_p f_r}{d_b}\left[1 - \left(\frac{d_b}{d_p}\cos\beta\right)^2\right] \tag{9.101}$$

$$\text{Cage} \quad f_{cage} = \frac{f_r}{2}\left(1 - \frac{d_b}{d_p}\cos\beta\right) \tag{9.102}$$

where

β is the contact angle
N_b is the number of balls or rollers
f_r is the frequency of rotor rotation ($f_r = n/60$, in rps)
d_b and d_p are the diameter of ball and pitch, respectively

By omitting the clearances between rolling balls and the inner and outer raceways, the pitch diameter can be expressed as

$$d_{pitch} = d_{inner} + d_{ball} = \frac{d_{inner} + d_{outer}}{2} \tag{9.103}$$

Faults of bearing components can be detected using a cepstrum (the word is derived from spectrum by reversing the first four letters of spectrum) that reveals the periodicity of a spectrum.

9.4.3 Self-Excited Vibration

Self-excited vibration system is a system for which the exciting force is a function of the motion parameter, such as displacement, velocity, or acceleration. The motion diverges and the system becomes unstable if energy is fed into the system through self-excitation. As the motion stops, the exciting force vanishes. By contrast, in a forced vibration, the external exciting force always exists regardless of whether the motion stops or continues. Friction-induced vibration (such as motor brakes), flow-induced vibration (such as motor ventilation flows and fluid-conveying pipelines), and aerodynamically induced motion of bridge are typical examples of self-excited vibration.

A self-excited vibration can be also excited from the internal damping of the shaft material. This happens basically for the case of assembled shafts because the friction between two parts in contact is equivalent to the internal damping of the material.

For rotating electric machines, self-excitations often produce vibrations in the rotating shaft in the lateral or flexural directions, rather than in the torsional or longitudinal directions.

9.4.4 Torsional Vibration

Torsional vibration is one of the main concerns in some motor applications. Many rotating machineries such as motors, generators, compressors, and similar machines can be

modeled as two-inertia systems, connected by a shaft that functions as a torsional spring. One inertia can be taken to represent the motor's rotor and another corresponds to the driven load such as fan and pump impeller. By comparing lateral vibration, torsional failures are even more sudden and serious without obvious signs. When the system is started and approaches to steady speed, the driving and load torque can twist the shaft from its free equilibrium position by a twist angle. If both the driving and load torque are suddenly removed from the system, the twisted shaft will uncoil and drive the two-inertia system oscillating in the opposite circumferential directions with respect to the shaft [9.31]. For an undamped system, the torsional vibration continues indefinitely as the system energy converts back and forth between the kinetic and potential energy. Unlike lateral vibration, torsional natural frequencies are unaffected by machine operation speeds.

In addition, because electric motors have discrete poles, their output torques do not develop smoothly but have periodic torque pulsations or torsional vibrations. These torque variations can produce periodic velocity variations or accelerations, causing torsional vibration.

9.5 Vibration Measurements

Vibration can be primarily measured in three detection schemes for displacement, velocity, and acceleration: (1) peak-to-peak, (2) zero-to-peak, and (3) RMS. The relationship of these parameters is displayed in Figure 9.20. Generally, acceleration emphasizes high frequencies, displacement emphasizes low frequencies, and velocity gives equal emphasis to all frequencies.

The selection of proper detectors depends on the characteristics of signals. For instance, RMS detectors are typically suitable for rotating machinery such as motors, gears, and turbines. Transient signals have irregular properties and usually have wide frequency band and low energy. Thus, adopting a peak detector is a good choice.

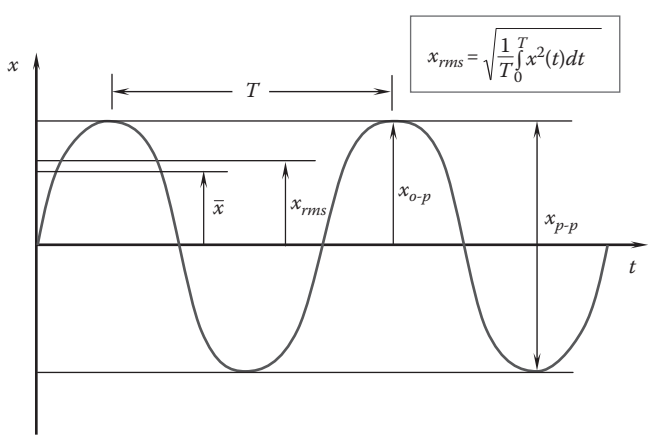

FIGURE 9.20
Comparison of average, RMS, zero-to-peak, and peak-to-peak displacements for a continuous sinusoidal signal.

Displacement is the most easily understood vibration parameter. There are several methods for measuring vibrational displacement depending upon applications. Accelerometers have long been used to measure displacement. During the measurement, the vibration levels are converted to electrical signals for data measurement by accelerometers. The benefits of using accelerometers to sense machine vibration through casing measurement include the following.

An eddy-current probe creates an alternating electromagnetic field with induced small current in the target object. Simultaneously, the eddy currents create an opposing magnetic field that resists the field being generated by the probe. The interaction of the magnetic fields is sensitive to the distance between the probe and the target object. If the distance changes, the magnetic coupling between the probe and the object is altered.

For rotating machinery, eddy-current probes are usually mounted in a casing to measure the location of the shaft relative to the casing and the amount of $1\times$ rotational vibration. Based on the measurement, it can be determined if the shaft vibration is within acceptable limits. Eddy-current probes can be also used for monitoring shaft eccentricity and thermal expansion in the axial direction. Eddy-current probes are useful for applications requiring noncontact measurements and not sensitive to environments and materials. However, this type of probes is not suitable for some conditions that require extremely high resolutions and large gap between probe and target object.

In recent years, there has been increasing interest in loop-powered vibration sensors for their simplicity and cost-effectiveness in continuous vibration monitoring. The sensor basically measures overall vibration in terms of velocity. The vibration signals taken by a loop-powered sensor are the same as an accelerometer.

Laser Doppler vibrometer (LDV) is one of the most efficient devices used in noncontact vibration measurements. This noncontact measuring technology is particularly useful for some applications where contacting vibration surfaces is difficult or even impossible. When a laser beam is directed to the measure surface from an LDV, the vibration velocity, frequency, and displacement are extracted by using the Doppler effect. For some small objects, the use of an LDV is especially desirable because there is no mass loading to the measure objects, as in other contact measurement methods.

Vibration and sound signals indicate the condition or quality of operating machines. In analyzing vibration in complicated mechanical systems, the Fourier transform is a powerful tool that takes a signal as a function of time (time domain) and decomposes it into a number of harmonic components as a function of frequency (frequency domain). This indicates that a signal can be viewed either in the time domain or in the frequency domain. The frequency domain representation is also called the spectrum of the signal, which can be used to determine the source of the vibration. Similarly, the spectrum of acoustic noise from rotating machinery can be used to design noise abatement systems. With the advanced computational techniques, the fast Fourier transform (FFT), as a digital implementation of Fourier transfer, has been developed. The FFT is the basic operation in frequency analysis, which is the most commonly used analysis method in many applications. Today, FFT-based signal-processing algorithms are widely used in signal processing.

The RMS method is often used to process vibration data. The RMS value of vibration signal is a time analysis feature that is the measure of the power content in the vibration signature. It can be very effective in detecting a major out-of-balance in rotating systems. A formula for the calculation of RMS value of a series of data is given as

$$x_{rms} = \sqrt{\frac{1}{N}\sum_{i=1}^{N} x_i^2} \tag{9.104}$$

where N is the number of data. For a continuous signal $x(t)$, RMS values can be calculated as

$$x_{rms} = \sqrt{\frac{1}{T}\int_0^T x^2(t)dt} \tag{9.105}$$

where T is the period.

9.6 Vibration Control

Vibration can be reduced by increasing either the damping capacity or the stiffness. The loss modulus is the product of these two quantities and thus can be considered a figure of merit for the vibration reduction ability [9.32].

There are many classical forms of damping, including hysteresis (structural) damping, fluid viscosity damping, Coulomb friction damping, air damping, particle damping, and magnetic and piezoelectric damping, to name a few. Each form of damping exhibits its own damping characteristics and is suitable to certain applications. In industrial applications, the most common form of damping is passive-based viscoelastic damping, used for solving a variety of noise- and vibration-related problems.

9.6.1 Damping Materials

In practice, damping can be characterized by two damping parameters: (1) loss modulus, which is defined as the product of the damping capacity and the stiffness and (2) loss tangent, which is defined as the ratio of the imaginary part to the real part of the complex shear modulus.

Damping is inherent in all resilient and viscoelastic materials. Viscoelastic materials encompass a broad range of materials, including pressure-sensitive adhesives, epoxies, rubbers, foams, thermoplastics, enamels, and mastics. The common characteristics of these materials are that their modulus is represented by a complex quantity, possessing both stored and dissipative energy components [9.33].

As presented by Chung [9.34], damping materials fall into four categories: (1) materials exhibiting high loss modulus but low loss tangent (such as cast iron and shape-memory alloys); (2) materials exhibiting low loss modulus but high loss tangent (such as rubber and other polymers); (3) materials exhibiting low values of both loss tangent and loss modulus; and (4) materials exhibiting high values of both loss tangent and loss modulus (such as graphite networks and cement-matrix composite). High damping materials must have high values of both loss tangent and loss modulus, that is, high damping capacity and high stiffness. For metallic materials, magnesium alloys have comparatively high damping capacity, up to about 3 times that of cast iron and up to about 30 times higher than that

of aluminum, and a high strength-to-density ratio. The combination of high damping, good strength, and low mass makes magnesium alloys an excellent choice for vibration damping materials [9.35].

A number of investigators have studied the vibration damping ability for a variety of materials. Based on the review of 34 reference papers, Birchak [9.36] compared specific damping capacity of 17 metals and 2 plastics, including cast iron, steel, brasses, and magnesium alloys. Schetsky [9.37] presented the values of specific damping capacity for 20 metals, from 49% of magnesium to 0.2% of aluminum, nickel, and titanium alloys. In his article, specific damping capacity is based on decay rate of strain energy.

Generally, damping is inversely proportional to temperature due to the crystallinity and viscosity in elastomers.

9.6.2 Vibration Isolation

Many devices and systems exist that incorporate features to counteract the effect of vibration on electric machines. A common approach to mitigate vibration of rotating machinery is to employ vibration isolation systems, which are used to filter out undesirable vibrations by modifying the vibration transmissibility. Good vibration isolation can be achieved by supporting the vibration source on a flexible low-frequency mounting. Thus, though exciting forces act on the system, only a small proportion of the forces can be transmitted to the support structure.

According to control schemes, vibration isolation systems can be categorized in passive, active, or semiactive type. Among them, passive isolating is extensively used in industries.

A typical example of passive isolation system is a suspension system (as the vibration isolator and shock absorber) employed in a vehicle for isolating the vehicle body from the wheel axels. Incorporating vibration isolation into motor design follows the same principles. To reduce the vibration transmitted from a motor to the ground, the motor may be directly mounted on isolators. Various isolators are available today, from isolation pads to coil spring isolators with integral vibration damping materials.

As the example shown in Figure 9.21, a vibration reduction device is revealed recently in a US patent application. This device consists of a number of O-rings as the resilient vibration dampeners and an upper and lower assembly. The removable upper and lower assemblies are coupled to one another, and the O-rings are positioned between these two assemblies to provide the capability to *tune* the device to a desired stabilization condition. This feature offers the ability to reduce or isolate vibration caused by motors [9.38].

An innovative idea is to use a multilevel magnetic system for vibration isolation [9.39]. The system includes upper and lower magnetic structures and transitions between an attract mode and a repel mode when the upper and lower magnetic structures are separated by an equilibrium separating distance. The multilevel magnetic system is placed between two objects and configured to oscillate about the equilibrium separating distance in response to a vibration from a motion source. The oscillation about the equilibrium separating distance causes the magnetic system to function as a low-pass filter that substantially attenuates vibration above the cutoff frequency, thus limiting the conduction of the vibration between the two objects.

Figure 9.22 depicts a disk-shaped repel-snap multilevel magnetic system. As shown in the figure, this system consists of upper and lower magnetic structures. Each magnetic structure has a region of coded maxels and a region of polarity. Each maxel has a code or

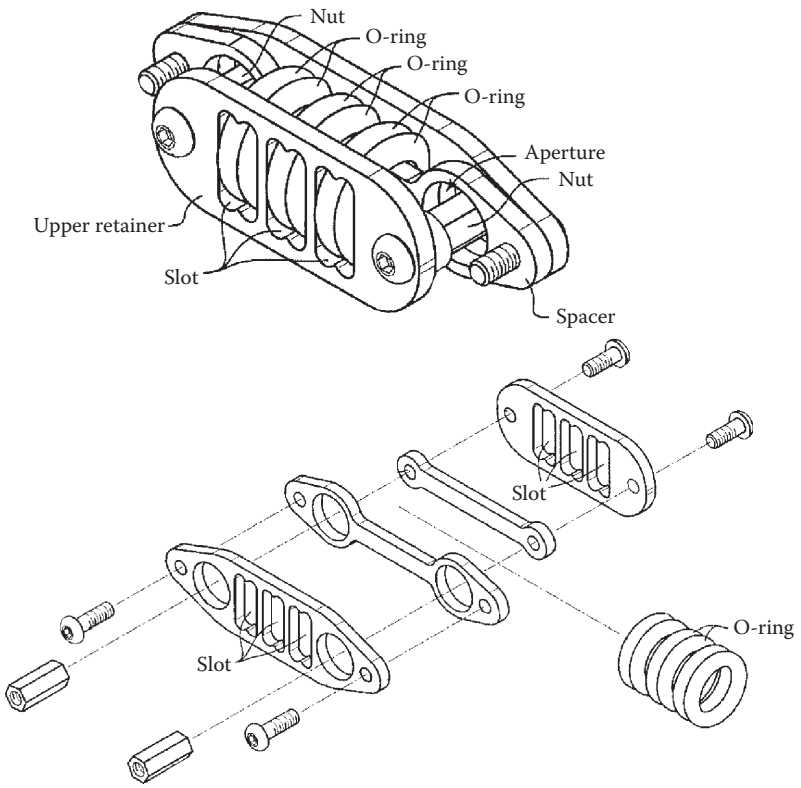

FIGURE 9.21
Vibration isolation system used to attenuate machinery vibration (U.S. Patent Application 2013/0026689) [9-38]. (Courtesy of the U.S. Patent and Trademark Office, Alexandria, VA.)

pattern of positive or negative polarity. The maxels are in seven rows for each structure, and each maxel for each row in one structure has polarity that is opposite a corresponding maxel in corresponding row in another structure. When a maxel is magnetized entirely through a magnetizable material the opposite polarities occur at the two sides of the maxel because each maxel is essentially a dipole magnetic source. Similarly, the polarity regions of the two structures have opposite polarities since they are also a dipole magnetic source. When the attractive force equals the repelling force, the system is configured to oscillate about the equilibrium separation distance in response to a vibration.

As demonstrated in Figure 9.23, a mechanical isolation system comprises four mechanical isolators comprising the contactless attachment multilevel magnetic system. These mechanical isolators are posited between the first and second objects to control mechanical impedance between the two objects.

Viscoelastic material damping pads have been designed for passive vibration damping. As shown in Figure 9.24, a laminated damping pad consists of thin viscoelastic films (0.05–0.3 mm in thickness) sandwiched between stainless steel plates (about 1.8 mm in thickness). Among various viscoelastic materials, polymers are high-energy dissipative materials that have been widely used for many years in automotive, aerospace, and electronic industries for solving complex vibration and noise problems.

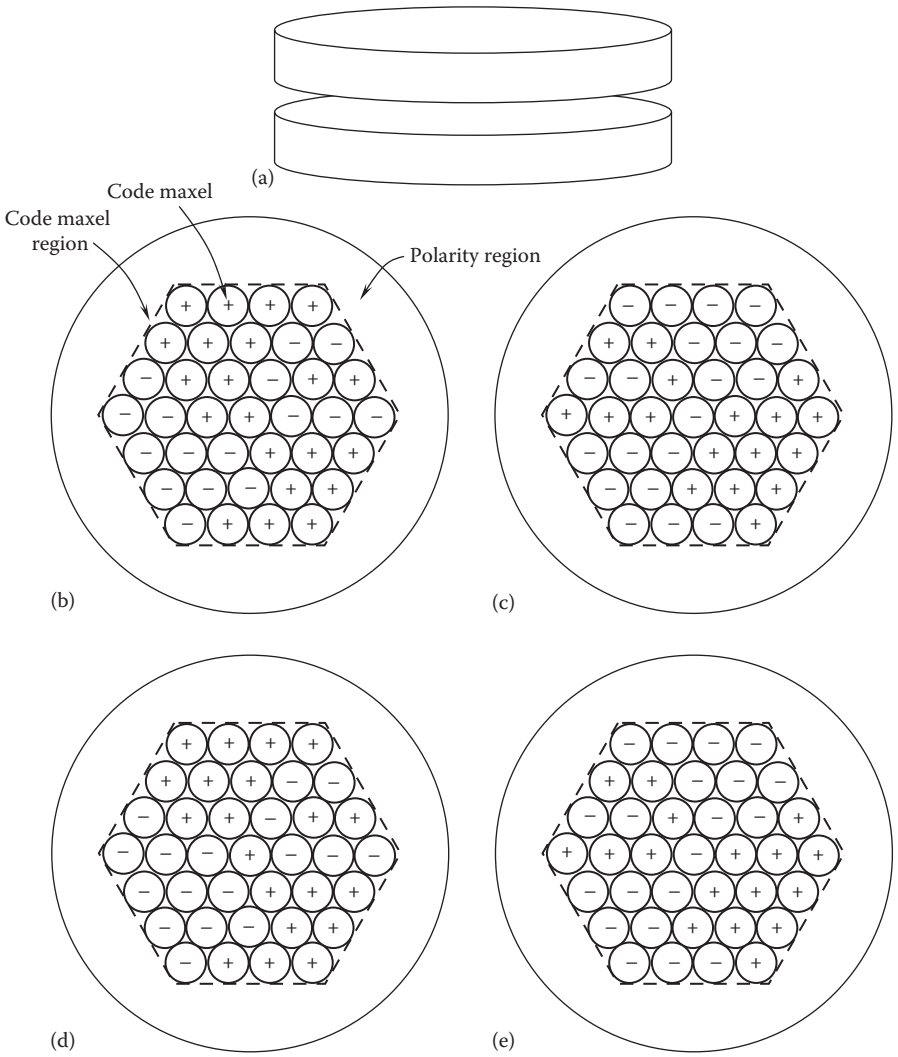

FIGURE 9.22
Multilevel magnetic system: (a) disk-shaped repel-snap magnetic system separated by an equilibrium separating distance, (b) a top view of the upper magnetic structure, (c) a bottom view of the upper magnetic structure, (d) a top view of the lower magnetic structure, and (e) a bottom view of the lower magnetic structure.

Viscoelastic materials are characterized by their shear modulus G, and loss factor η, which is defined as the ratio of vibration energy dissipated per cycle to the energy stored in all structural elements. It has been found that the performance of damping pads depends not only on the material properties (such as G and η) but also on the machine's complex interaction with the structural system to be damped. Results from Magra et al. [9.40] show that damping pads can reduce the vibration amplification factor (which is the reciprocal of η) from over 100 to 8 for an advanced photon source machine.

Molded and bonded rubber is often used as machinery mounts to absorb shock and attenuate vibration.

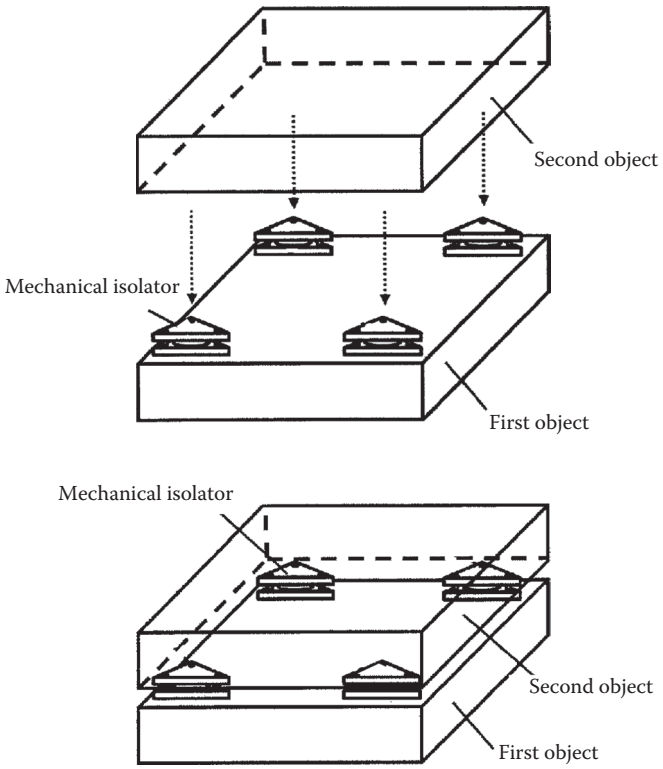

FIGURE 9.23
Mechanical isolation systems assembled into the multilayer magnetic system (U.S. Patent 8,279,031) [9.39]. (Courtesy of the U.S. Patent and Trademark Office, Alexandria, VA.)

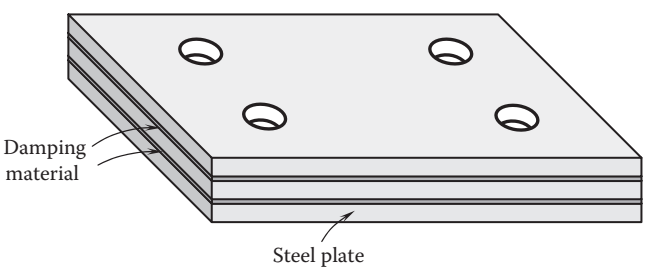

FIGURE 9.24
Laminated damping pad for providing effective damping of electric machine.

9.6.3 Tuned Mass Damper

Rotating machines such as motors and engines often incite vibration due to rotational imbalances. A tuned mass damper (TMD) is a passive damping device that utilizes the secondary mass attached to the primary structure to reduce the dynamic response of the primary structure. Figure 9.25 depicts the schematic of a two-degree-of-freedom TMD

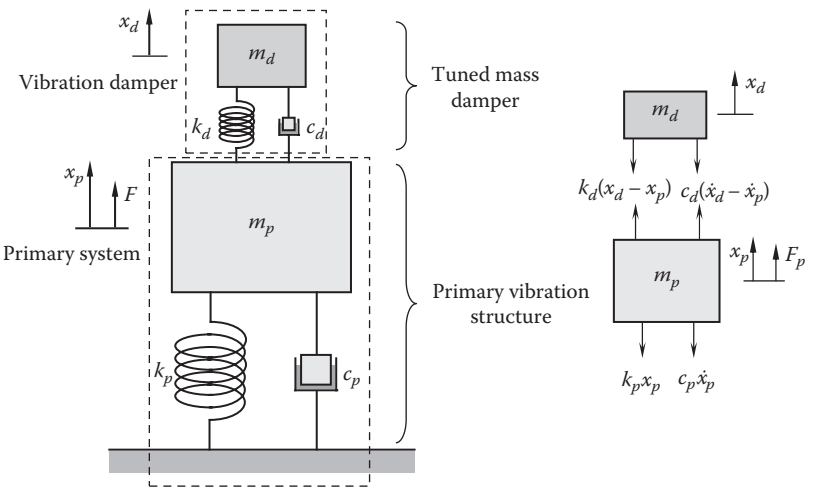

FIGURE 9.25
Two-degree-of-freedom TMD system; TMD is attached to the primary system for reducing dynamic response of the primary system.

system. It can be seen that a primary system (i.e., a motor) consists of a mass m_p, a spring (with spring coefficient k_p), and a viscous damper (with damping coefficient c_p). A TMD, or harmonic absorber, consists of a mass m_d, a spring (with the spring factor k_d), and a viscous damper (with damping coefficient c_d) and is attached to the primary system to reduce or eliminate the undesirable vibration of the primary system. Usually, m_d is chosen approximately 5%–10% of the system mass m_p. To obtain the best damping effect, TMDs set their natural frequencies substantially equal to the natural frequencies of the primary structures. It has been proven that the TMD is effective in reducing the response of structures to harmonic or wind excitations [9.41].

From the free-body diagram of the mass m_p and m_d, the equations of motion of the system can be written as

$$m_p \frac{d^2x_p(t)}{dt^2} + (c_p + c_d)\frac{dx_p(t)}{dt} - c_d \frac{dx_d(t)}{dt} + (k_p + k_d)x_p - k_d x_d = F \tag{9.106}$$

$$m_d \frac{d^2x_d(t)}{dt^2} + c_d \frac{dx_d(t)}{dt} - c_d \frac{dx_p(t)}{dt} + k_d x_d - k_d x_p = 0 \tag{9.107}$$

These two equations of motion can be expressed in the matrix form

$$\begin{bmatrix} m_p & 0 \\ 0 & m_d \end{bmatrix} \begin{Bmatrix} \ddot{x}_p \\ \ddot{x}_d \end{Bmatrix} + \begin{bmatrix} c_p + c_d & -c_d \\ -c_d & c_d \end{bmatrix} \begin{Bmatrix} \dot{x}_p \\ \dot{x}_d \end{Bmatrix} + \begin{bmatrix} k_p + k_d & -k_d \\ -k_d & k_d \end{bmatrix} \begin{Bmatrix} x_p \\ x_d \end{Bmatrix} = \begin{bmatrix} F \\ 0 \end{bmatrix} \tag{9.108}$$

It can be seen that $[m]$, $[c]$, and $[k]$ are all 2×2 matrices whose elements are the known masses, damping coefficients, and stiffnesses of the system, respectively. Because each of these matrices is symmetric, the transpose of the matrix is equal to its original matrix, that is, $[m]^T = [m]$, $[c]^T = [c]$, and $[k]^T = [k]$.

The external exciting force F is considered to vary harmonically with the frequency ω:

$$F = F_o e^{i\omega t} \tag{9.109}$$

The solutions for the equations of motion may take the form

$$\begin{cases} x_p(t) = X_p e^{i\omega t} \\ x_d(t) = X_d e^{i\omega t} \end{cases} \tag{9.110}$$

Substituting Equations 9.109 and 9.110 into the set of governing equation results in

$$\begin{bmatrix} -m_p\omega^2 + (c_p + c_d)i\omega + (k_p + k_d) & -c_d i\omega - k_d \\ -c_d i\omega - k_d & -m_a\omega^2 + c_d i\omega + k_d \end{bmatrix} \begin{Bmatrix} X_p \\ X_d \end{Bmatrix} = \begin{bmatrix} F_o \\ 0 \end{bmatrix} \tag{9.111}$$

Introducing the natural frequency ω and damping ratio ζ for the primary system and tuned mass system, respectively,

$$\omega_p = \sqrt{\frac{k_p}{m_p}} \tag{9.112}$$

$$\zeta_p = \frac{c_p}{2\sqrt{m_p k_p}} \tag{9.113}$$

$$\omega_d = \sqrt{\frac{k_d}{m_d}} \tag{9.114}$$

$$\zeta_d = \frac{c_d}{2\sqrt{m_d k_d}} \tag{9.115}$$

and defining $\bar{m}$ as the mass ratio,

$$\bar{m} = \frac{m_d}{m_p} = \frac{k_d}{k_p}\frac{\omega_p^2}{\omega_d^2} \tag{9.116}$$

the equations of motion can be rewritten in the matrix form as

$$\begin{bmatrix} -\omega^2 + 2(\zeta_p\omega_p + \zeta_d\omega_d\bar{m})i\omega + (\omega_p^2 + \omega_d^2\bar{m}) & (-2\zeta_d\omega_d i\omega - \omega_d^2)\bar{m} \\ -2\zeta_d\omega_d i\omega - \omega_d^2 & -\omega^2 + 2\zeta_d\omega_d i\omega + \omega_d^2 \end{bmatrix} \begin{Bmatrix} X_p \\ X_d \end{Bmatrix} = \begin{bmatrix} F_o/m_p \\ 0 \end{bmatrix} \tag{9.117}$$

As measured previously, in order to obtain the best damping effect, the natural frequency of the mass damper ω_d is equal to the natural frequency of the primary system ω_p:

$$\omega_p = \omega_d = \omega \tag{9.118}$$

Substituting Equation 9.118 into 9.117, it yields

$$\begin{bmatrix} 2(\zeta_p\omega^2+\zeta_d\omega^2\bar{m})i+\omega^2\bar{m} & (-2\zeta_d\omega^2 i-\omega^2)\bar{m} \\ -2\zeta_d\omega^2 i-\omega^2 & 2\zeta_d\omega^2 i \end{bmatrix} \begin{Bmatrix} X_p \\ X_d \end{Bmatrix} = \begin{bmatrix} F_o/m_p \\ 0 \end{bmatrix} \tag{9.119}$$

Hence, X_p and X_d are determined as

$$X_p = \frac{F_o}{m_p}\frac{C}{AC-B^2\bar{m}} \tag{9.120}$$

$$X_d = -\frac{F_o}{m_p}\frac{B}{AC-B^2\bar{m}} \tag{9.121}$$

where

$A = 2(\zeta_p\omega^2+\zeta_d\omega^2\bar{m})+\omega^2\bar{m}$

$B = -2\zeta_d\omega^2 i-\omega^2$

$C = 2\zeta_d\omega^2 i$

The solutions of the motion equations are thus obtained by substituting Equations 9.120 and 9.121 into 9.110.

TMDs commonly use metal coil springs and viscous dampers. They can also use other types of dampers, such as viscoelastic, air-suspended, sloshing water, and liquid column dampers. When designed, fabricated, installed, and tuned properly, TMDs can effectively absorb the vibrating energy of the structure and dissipate energy internally and hence reduce structural vibrations of machines or buildings. The 509 m (11,617 ft) supertall Taipei 101 building installed a 730 ton (0.26% of the building mass) TMD, which is the largest TMD in the world. And it is also the first ever constructed as a key architectural and visible element in the building [9.42].

TMDs can be essentially viewed as energy sinks. It was reported that with the use of the dynamic vibration absorber on a lightly damped system that have steplike trajectories or disturbances, the settling time has been greatly improved by 82% [9.43].

9.6.4 Double Mounting Isolation System

Greater attenuation of the exciting force at high frequencies can be achieved by using a double mounting, also known as two-stage mounting. In this arrangement, the machine is set on flexible mountings on an inertia block, which is supported by flexible mountings [9.44].

Figure 9.26 demonstrates the schematic of a two-degree-of-freedom double mounting system. The system consists of a primary mass m_p (machine mass) and an auxiliary mass m_a (damper mass). Dampers are placed between the primary m_p and auxiliary mass m_a and between the auxiliary mass m_a and the base. The purpose of using the system is to isolate either the base from the vibration of the machine or the machine from the vibration of the base (e.g., during an earthquake). The system is also used where there is a demand for high structure-borne noise attenuation.

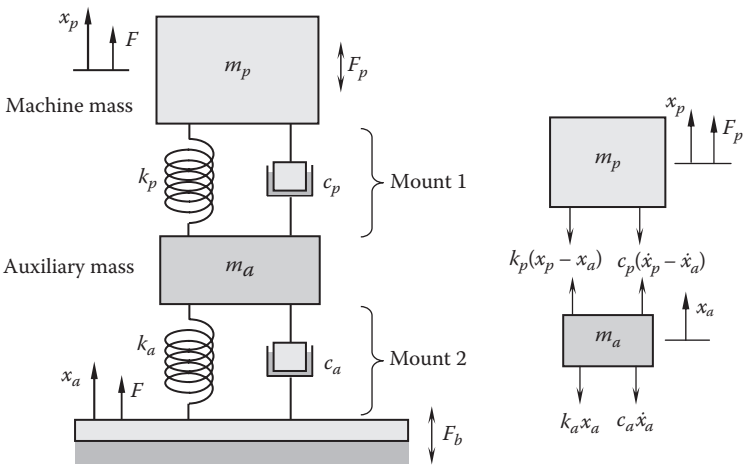

FIGURE 9.26
Two-degree-of-freedom double mounting damping system.

While the passive isolating systems are very effective in lowering the vibration transmission at high frequencies, they suffer from some drawbacks including design complexity, weight penalty, large volume, and high cost. Without any constraints, a double mounted system has totally 12 degrees of freedom, twice of the unconstrained single mounted system. Accordingly, it has 12 resonant frequencies. As a matter of fact, keeping all resonant frequencies away from forcing frequencies of a machine is a major design challenge for design engineers.

9.6.5 Viscoelastic Bearing Support

In many cases, the rotor vibratory loads are the dominant source of motor vibration. The mechanism of rotor vibration has been extensively studied and is well understood. As discussed previously, a variety of factors can impact the vibration amplitude and frequency such as rotor mass imbalance, broken rotor bar, and UMP, to name a few. Rotor structural vibration is transmitted through the bearings and then to the stator, motor housing, and finally to the motor base.

In order to interrupt the transmission path of rotor vibration, it is highly desired to design a viscoelastic bearing support that has a viscoelastic layer between the outer ring of a rolling bearing and the motor endbell [9.45], as demonstrated in Figure 9.27. In this way, vibration of the rotor is isolated from the surrounding structure. Moreover, the viscoelastic layer provides additional damping to the vibrating rotor. However, a relative soft viscoelastic bearing support can reduce the static stiffness of the machine to influence the machine operation accuracy.

9.6.6 Active Vibration Isolation and Damping

Although passive vibration isolation systems are still extensively used in industries today, they are inadequate for some applications that require high accurate control of vibration, such as optical devices, sonars, piezoelectric crystal flowmeters, medical detection devices, space structures, and other vibration-sensitive equipment.

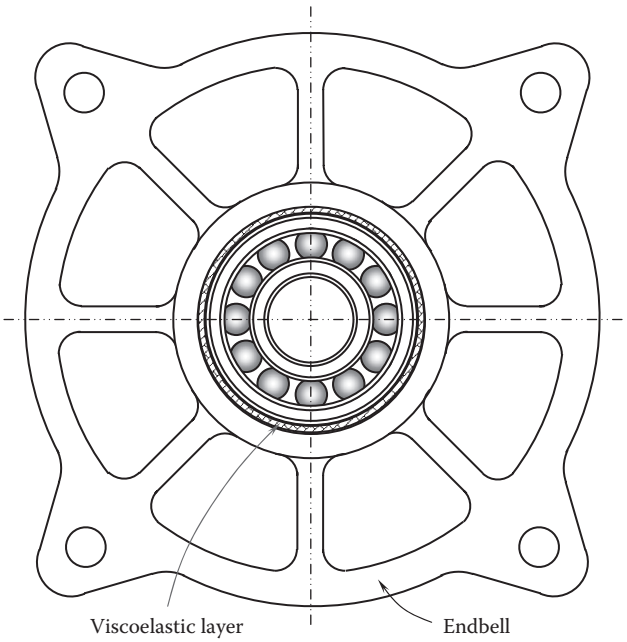

FIGURE 9.27
Viscoelastic layer positioned between the bearing outer ring and motor endbell for isolating rotor vibration from the motor and its base.

Active vibration isolation systems use external energy to directly cancel energy in systems. The system involves the use of actuators along with sensors and controllers to create actuation with the goal of reducing the transmission of vibration from the vibration source to the rest of the components in the system. Sensors are used to continuously monitor the dynamic motion of the target system and send the relevant motion data (relative displacement, velocity, acceleration, etc.) to controllers. The controllers calculate the required external forces or displacements and send the signals to actuators, which provide the desired forces or displacements to the target system, as illustrated in Figure 9.28. This method can work effectively for low vibrating frequencies. However, it is very difficult to apply it to high-frequency applications.

A semiactive vibration isolation system is presented in Figure 9.29. It combines the features of a passive and an active vibration isolation system. Unlike in an active system, the actuator in the semiactive system is treated as a passive element. The properties of the semiactive actuator such as damping ratio and stiffness can vary so that the control can be implemented without adding external energy into the system, except a small amount of energy required to change the properties of the actuator. In the semiactive system, the controller is used to determine the desired properties of the actuator, and the sensor functions the same in an active system to detect the motion of the target system [9.46].

Generally, the low-frequency isolation in the horizontal direction can be easily achieved by a passive system since it requires less concern about the horizontal static load by having a low stiffness. A vertical isolation is well implemented by an active system because it can provide a high stiffness to support static loads. Platus [9.47] has developed a passive vibration isolation system that outperforms conventional passive systems by adopting a technique called negative stiffness mechanism (NSM). The use of this system in a vertical isolation reduces the vertical stiffness and hence natural frequencies while maintaining

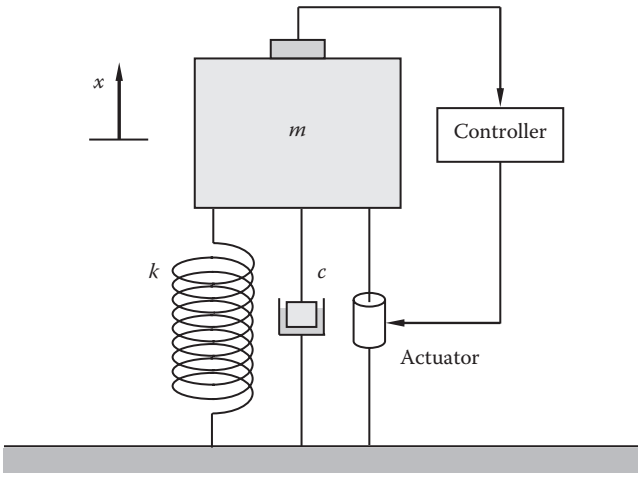

FIGURE 9.28
Active vibration isolation system.

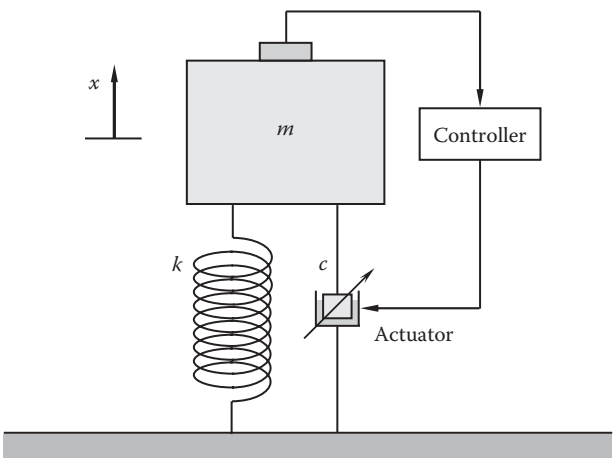

FIGURE 9.29
A semi-active vibration isolation system. The controller is used to adjust actuator damping characteristics.

static load-supporting capability. It was reported that the vertical natural frequencies can be tuned to as low as 0.2 Hz.

Active vibration damping is to actively reduce the response amplitude of the system within a limited bandwidth near the natural frequencies of the system. It offers a promise of high efficiency without the restrictions of passive methods. Active vibration control involves monitoring vibrations of a structure and utilizing the vibration signal to generate a force with the proper phase and amplitude to attenuate the vibration. An additional advantage of an active approach is the ability to supply a vibration signal that can be used independently for monitoring the vibration environment.

In some high-precision industrial applications (e.g., optical tables), vibration isolation methods are usually used for relatively low-frequency vibration problems. For high-frequency vibrations, passive damping, either broadband or tuned, provides varying levels

of structural damping performance, but both are affected by applied loads. By means of vibration sensors, actuators, and controllers, active vibration damping can be autotuned to account for varying loads [9.48], making it more attractive for industrial and medical end users.

An alternative method for active vibration isolation is to use noncontacting electromagnetic voice coil actuators (VCAs), which are used for some special applications like large telescopes and robots. In this method, electric current passing through the voice coil generates a magnetic field that interacts with the magnetic field generated by PMs to produce desired forces [9.49]:

$$F = n\pi diB \sin\theta \tag{9.122}$$

where

n is the total number of coils
d is the average diameter of the coil
i is the current through the wire
B is the magnetic field strength
θ is the angle between the magnetic flux lines and the direction of the current

Newell et al. [9.50] have used VCAs to construct an active vibration isolation system for earth-based interferometric gravitational wave detectors. This system provides vibration isolation in all 6 degrees of freedom by at least 40 dB at 0.5 Hz.

9.6.7 Measurements of Motor Vibration

A comprehensive assessment of motor vibration requires measurements of vibration acceleration in the unit of m/s^2. A typical vibration measurement system comprises a number of vibration sensors (e.g., accelerometers, velocity transducers, and proximity probes) for sensing vibration velocity or acceleration; a vibration analyzer for data acquisition, bearing condition diagnosis, and spectrum diagnosis; and a computer for processing the measurements and displaying the results. The vibration sensors are typically attached to the vibrating motor housing at different locations and on the baseplate. Since motor bearings are the load-carrying components of the mechanical drive train, the vibration sensors should be placed close to bearings to measure both motor radial and axial vibrations (Figure 9.30). The vibration sensors (used accelerometers here) produce

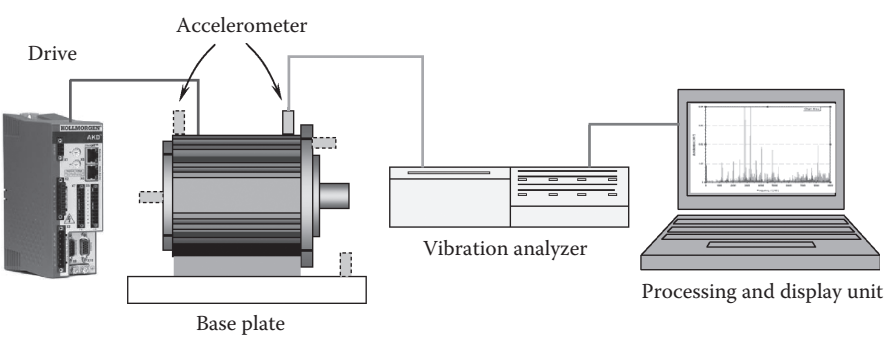

FIGURE 9.30
Motor vibration measurement using accelerometers for assessing motor vibration and diagnosing vibration root causes.

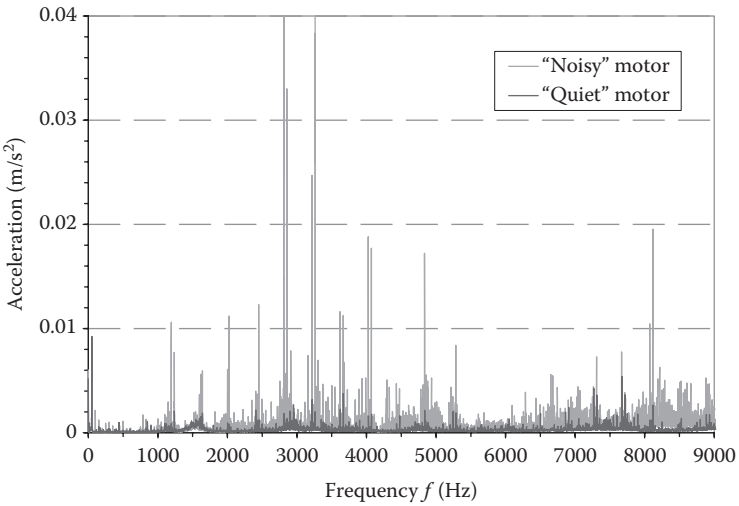

FIGURE 9.31
Comparison of measured vibration data from two PM servomotors with the same brand and same model, showing distinct differences in harmonic components of the acceleration between two motors. Courtesy of Kollmorgen Corporation.

electrical signals that are proportional to the vibrating acceleration on the measure surface. Then, the measure data are transmitted to a vibration analyzer for data processing and data recording. Finally, the measured vibration results are displayed by a computer to provide engineers for the further analysis. In such a way, mechanical and electrical defects can be identified through vibration analysis. The useful information detected from the motor vibration measurements includes bearing vibration, rotordynamic unbalance, eccentricity, and electrical faults.

As an example, the results of motor vibration for two identical servomotors are presented in Figure 9.31. For the purpose of comparison, a *noisy* motor and a *quiet* motor were selected for measuring. It can be observed that there are great differences in vibrating accelerations between the two motors for almost all frequencies, especially in the range of 1000–5000 Hz, and $f > 8000$ Hz. The root cause analysis reveals that the motor bearings and assembly quality attribute to high vibration.

A special attention must be put on keyed shafts in vibration measurements. Prior to the test, a *half key* must be placed in the shaft keyway to eliminate the influence of the unbalance that is induced from the keyway.

9.7 Fundamentals of Acoustic Noise

Noise is one of the most common occupational health hazards. In heavy industrial and manufacturing environments, permanent hearing loss is the main health concern. In the United States, growing environmental concerns and recognition that lengthy unprotected exposure to high industrial noise levels is detrimental to man have resulted in government

promulgation of noise level criteria. In many countries, especially European countries, noise reduction is an integral part of machinery safety, and law regulates the allowable noise exposure of workers. Manufacturers must make specific quantitative information on noise emitted under designed operating conditions. In recent years, the noise requirement to ensure quiet working conditions is getting even tighter.

Acoustic noise is the result of the pressure waves produced by vibration sources. Generally, a sinusoidal wave is referred to as a tone, a combination of several tones is called a sound, and an irregular vibration is referred to as noise [9.51]. Noise is defined in terms of frequency spectrum (in Hz), intensity (in dB), and time duration.

9.7.1 Tonal Noise and Broadband Noise

There are two types of noise radiation: pitched or unpitched noise. Pitched noise, also known as tonal noise, is created from vibrations of an object that occur in a fine range around one or very few distinct frequencies. Tonal noise can be extremely irritating to human hearing. An electric motor that emits tonal noise has a characteristic frequency spectrum. Unpitched noise, also known as broadband noise, has a well-distributed energy spectrum. Broadband noise is generally not irritating to human hearing and does not transmit a characteristic frequency spectrum, such as wind noise.

9.7.2 Sound Pressure Level and Sound Power Level

Sound pressure is a measure of air pressure fluctuation a noise source creates. It is usually expressed in a unit of Pascal (Pa). However, the use of Pascal as the sound pressure unit may generate a broad range of sound pressures. A convenient way to compress the scale of numbers into a manageable range is to use decibel (dB). Sound pressure converted to the decibel scale is called sound pressure level (SPL), denoted as L_p:

$$L_p = 10\log_{10}\left(\frac{p_{rms}^2}{p_o^2}\right) = 20\log_{10}\left(\frac{p_{rms}}{p_o}\right) \tag{9.123}$$

where p_{rms} is the RMS sound pressure being measured and p_o is the reference sound pressure, typically 20 μPa.

It is important to distinguish between sound power and sound pressure. Sound power is a measure of the total amount of sound energy emitted by the source over a period of time, usually expressed in watts. Sound pressure depends on the distance of observation location from the source but sound power does not. The sound power level L_w, in unit of dB, is defined by

$$L_w = 10\log_{10}\left(\frac{W}{W_o}\right) \tag{9.124}$$

where W is the sound power emitted by the source in watts and W_o is the reference power, typically 10^{-12} W. SPL L_p can be related to sound power level L_w as [9.52]

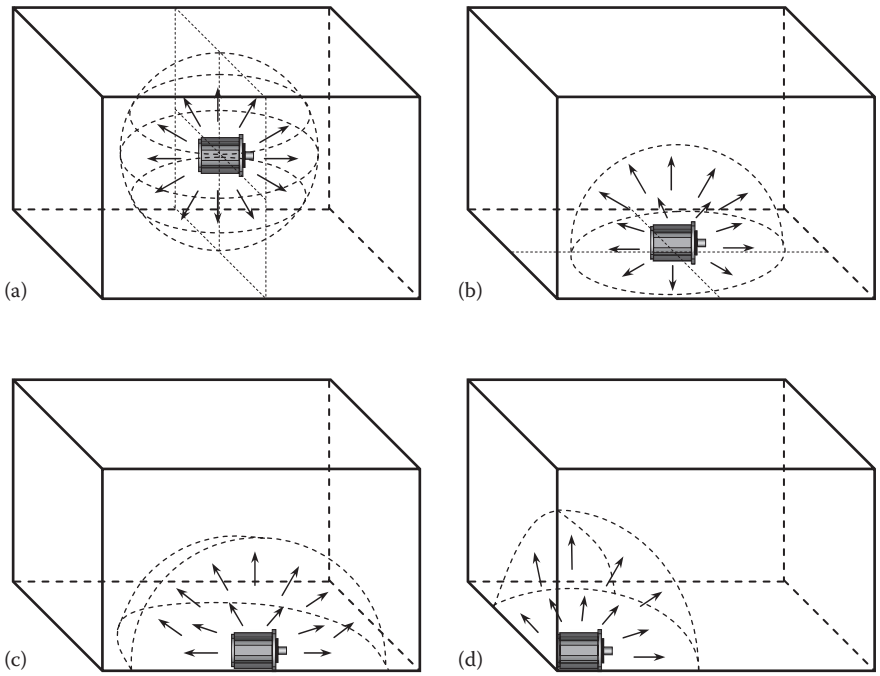

FIGURE 9.32
Directivity factor of the sound source for different source positions: (a) at room center, $Q_\theta = 1$; (b) at the center of floor, $Q_\theta = 2$; (c) at the center of floor edge, $Q_\theta = 4$; and (d) at floor corner, $Q_\theta = 8$.

$$L_p = L_w + 10\log\left(\frac{Q_\theta}{4\pi r^2} + \frac{4}{R_c}\right) \tag{9.125}$$

where

r is the distance from the source

Q_θ is the directivity factor of the source in the direction of r, which depends on the position of the sound source (see Figure 9.32)

R_c is the room constant, defined as

$$R_c = \frac{A\bar{\alpha}}{1-\bar{\alpha}} \tag{9.126}$$

where

A is the total surface area of the room

$\bar{\alpha}$ is the average sound absorption coefficient of the room

9.7.3 Octave Frequency Bands

The audible frequency range is usually divided into 10 octave bands having center frequencies at 31.5, 63, 125, 250, 500, 1,000, 2,000, 4,000, 8,000, and 16,000 Hz. The center frequency of each consecutive octave band is twice the center frequency of the previous one. In each octave band, the upper cutoff frequency is twice the lower cutoff frequency. Usually, an electric machine such as motor and generator generates and radiates noise over

the entire audible range of hearing. The amount and frequency distribution of the noise can be obtained using an octave band analyzer. This analyzer equips a set of contiguous filters, and each filter has a bandwidth of an octave. Therefore, ten such filters cover the most frequency range of interest. The measured L_p data at each octave band are very useful for determining the noise root sources.

Each octave band can be further divided into three one-third octave bands. The SPL L_p is thus determined from three measure values $L_{p,i}$ that are taken at each one-third octave band, respectively.

The comparison of full octave band and one-third octave band is presented in Table 9.1. The relationship between the upper cutoff frequency f_{n+1} and lower cutoff frequency f_n is

TABLE 9.1

Comparison of One Octave Band and One-Third Octave Band in Audible Sound Range

	One Octave			One-Third Octave		
Band	**Lower Cutoff Frequency (Hz)**	**Middle Frequency (Hz)**	**Upper Cutoff Frequency (Hz)**	**Lower Cutoff Frequency (Hz)**	**Middle Frequency (Hz)**	**Upper Cutoff Frequency (Hz)**
1	22	31.5	44	22.4	25	28.2
				28.2	31.5	35.5
				35.5	40	44.7
2	44	63	88	44.7	50	56.2
				56.2	63	70.8
				70.8	80	89.1
3	88	125	177	89.1	100	112
				112	125	141
				141	160	178
4	177	250	355	178	200	224
				224	250	282
				282	315	355
5	355	500	710	355	400	447
				447	500	562
				562	630	708
6	710	1,000	1,420	708	800	891
				891	1,000	1,122
				1,122	1,250	1,413
7	1,420	2,000	2,840	1,413	1,600	1,778
				1,778	2,000	2,239
				2,239	2,500	2,818
8	2,840	4,000	5,680	2,818	3,150	3,548
				3,548	4,000	4,467
				4,467	5,000	5,623
9	5,680	8,000	11,360	5,623	6,300	7,079
				7,079	8,000	8,913
				8,913	10,000	11,220
10	11,360	16,000	22,720	11,220	12,220	14,130
				14,130	16,000	17,780
				17,780	20,000	22,390

$$\frac{f_{n+1}}{f_n} = 2^k \tag{9.127}$$

where $k=1$ for one octave band and $k=1/3$ for one-third octave band. The middle frequency f_o in each full octave band is about $\sqrt{2}$ times the lower cutoff frequency in that band. The band width w_b of each band is given as

$$w_b = f_{n+1} - f_n = \left(2^k - 1\right) f_n \tag{9.128}$$

9.7.4 Three Sound Weighting Scales

Human hearing varies in sensitivity for different acoustic frequencies. Although the audible range of acoustic frequencies generally ranges from 20 to 20,000 Hz, humans usually are most sensitive to pure tones at frequencies between 2,000 and 6,000 Hz. Hearing sensitivity drops off above 7000 Hz and below about 200 Hz. Thus, to establish a uniform noise measurement that simulates human's perception and annoyance, several frequency weighting methods are developed to account for those frequencies most audible to the human hearing range.

Acoustic frequency weightings refer to different sensitivity scales for noise measurement. In the development of sound level meters over the years, manufacturers have built in the different response curves, that is, *A*-, *B*-, and *C*-weighting filter curves, as defined in the IEC standard 61672: 2003 [9.53] and various national standards, as shown in Figure 9.33. Among these, *A*- and *C*-weighting scales are commonly incorporated into commercially marketed sound level meters.

The *A*-weighting scale is presently the most commonly used weighting scale in measuring industrial noise, because it best predicts the damage risk of human ear. Using the decibel *A* filter, the sound level meter is less sensitive to very low and very high frequencies.

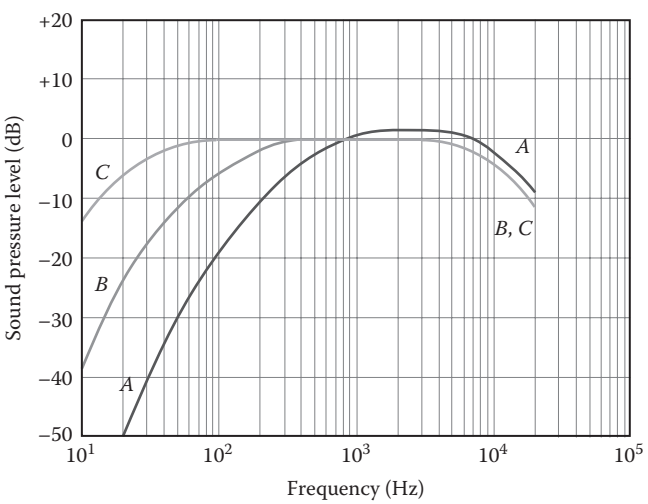

FIGURE 9.33
A-, *B*-, and *C*-weighting filter curves, defined up to 20 kHz.

Sound pressure measurements with this scale are expressed as dB(A) or simply dBA. The *A*-weighting curve in Figure 9.33 suggests that for most listeners, the noise at 100 Hz would sound about 19 dB quieter than that at 1000 Hz at the same SPL. It is worth to note that since the dBA scale is logarithmic, every increase of 10 dBA doubles the perceived loudness of hearing.

The *B*-weighting scale was used in the early time for predicting performance of loudspeakers and stereos, but today, the *B*-weighting scale is no longer in any international standard and already has very little practical use.

The *C*-weighting scale was originally designed to predict the human ear's sensitivity to tones at high noise levels. However, the ear's loudness sensitivity for tones is not the same as the ears' damage risk for noise. Much of the low-frequency noise is actually being filtered out by the ear, making it less likely to cause damage. By comparing with the *A*-weighting scale, the *C*-weighting curve is quite flat, indicating it contains much more of the low-frequency range of sounds.

9.7.5 Averaged Sound Pressure Level

The averaged SPL is the logarithm average of the measured SPL around the motor, expressed as

$$\bar{L}_p = 10\log_{10}\frac{1}{n}\left[\sum_{i=1}^{n} 10^{\left(L_{p,i}/10\right)}\right] \tag{9.129}$$

where

$L_{p,i}$ is the measured SPL at ith point
n is the total number of the points

It must be noted that $L_{p,i}$ may consist of noise produced by sources in the vicinity of the testing motor in a field test. In order to gain the SPL only produced by the motor, the background noise must be measured and subtracted from the measured noise data. This can be done by disconnecting the test motor and maintaining all other equipment operating. Then, by repeating the measurements around the motor, the background noise pressure level at ith point $L_{p,i,b}$ is obtained. As a result, the noise pressure level at ith point from the tested motor can be calculated as

$$L_{p,i,m} = 10\log_{10}\left[10^{\left(L_{p,i}/10\right)} - 10^{\left(L_{p,i,b}\right)}\right] \tag{9.130}$$

Thus, the averaged SPL only from the tested motor is obtained:

$$\bar{L}_{p,m} = 10\log_{10}\frac{1}{n}\left[\sum_{i=1}^{n} 10^{\left(L_{p,i,m}/10\right)}\right] \tag{9.131}$$

9.7.6 Types of Noise

According to the source and pattern of noise production, several types of noise can be identified; each of them has its own characteristics in noise generation and transmission.

9.7.6.1 Structure-Borne Noise

Sound waves can travel through different media such as air, water, wood, rock, soil, or metal. Depending on the media through which it travels, sound is either structure-borne or airborne. Structure-borne noise propagates through the motor structure as vibration and subsequently radiated as sound. The intensity and frequency of structure-borne noise depend on many factors such as the rotational speed of the motor, material and geometry of the vibrating components, and system structure. The structure-borne noise is a result of the action of the aerodynamically, mechanically, and electromagnetically excited forces. When the frequency of the exciting force acting on the motor, as well as the response force on the motor support, approaches to or coincides with any of the motor natural frequencies, resonance occurs accompanied with strong vibration and high noise.

9.7.6.2 Airborne Noise

Airborne noise radiates from a noise source directly into and travels through the air. As the sound waves are being carried by the atmosphere, airborne noise can directly impact human hearing. These sound waves make contact with walls, floors, or ceilings, inducing noise pollution.

Airborne sound transmission loss (STL) is a measure of the degree to which a material can effectively block or reduce transmission of airborne sound. It is usually measured at each one-third octave band frequency from 125 to 4000 Hz, in the unit of dB. While structure-borne noise is attenuated by isolation, airborne noise can be attenuated by treatment with sound-absorbing materials or through the use of barrier materials.

9.7.6.3 Aerodynamic Noise

There are two types of aerodynamic noise: rotational and nonrotational. Rotational aerodynamic noise is associated with the rotation of the rotor and fan in a motor. When a rotor rotates, the wall rotating-driven flows, also referred to as the rotating pumping flow, are generated with high angular momentum to be flung radially outward, leading to flow-induced noise. The great amount of noise from a rotating fan is caused by steady thrust and drag forces that are induced on the blades as they rotate through air, and the air turbulence produced by the cooling fan can create a great amount of noise.

Nonrotational aerodynamic noise is mainly associated with the ventilating flow inside a motor, as a result of fluctuating fluid forces in time and frequency domains. When the motor uses a fan to force cooling air flowing through the motor, the ventilating flows pass through very complicated and irregularly shaped flow passages to cool stator windings and other components. The nonuniform velocity fields, high turbulent flows, the interactions between the rotational flows and ventilation flows, and the interaction between the flows and rigid structure all contribute to the nonrotational aerodynamic noise.

9.8 Noise Types and Measurements for Rotating Electric Machines

Growing environmental sound concerns and recognition that lengthy, unprotected exposure to high industrial noise levels can be detrimental to people have resulted in increased attention to reducing industrial noise. In many countries, particularly those in Europe, the

allowable maximum noise levels that workers should be exposed to are regulated by law, through government promulgation of noise level criteria.

Increasingly strict noise regulations in the United States, European Union, Japan, and China have made the development of new electric machines with low noise emission. Specifically, the European Union has set the tightest harmonized noise limits for various industrial machines, motor vehicles, household appliances, and other noise-generating products. Because of the increased awareness of the harmful effects from high industrial noise levels and government regulations that establish acceptable noise levels in the workplace, noise reduction has become an integral part of machinery safety. Noise abatement is a concern with, for example, generator-steam and gas turbine power plants. As demands for electricity increase, the power industry faces increasing challenges to build and operate efficient and quiet power generators, for example, steam turbines, gas turbines, and electrical generators.

In an industrial environment, various machines often emit noise waves that register at high and potentially harmful decibel levels. In a power plant, noise may come from a variety of machine sources, such as generators, gas or steam turbines, fans, pumps, coolers, and other mechanical and electrical equipment, many of which may be in operation simultaneously. Individuals working in such an environment are often faced with the need to reduce the near- and far field machinery noise levels. In an environment where individuals work in close proximity to the sources of a machine noise, near field sound levels must be controlled in order to comply with noise regulation and avoid hearing damage to the workers. Where machine noise can reach areas that are near an industrial plant, it may be prudent to abate far field machine noise to acceptable levels and to avoid broadcasting neighboring communities.

Regulatory requirements for low noise from electric motors have become increasingly more stringent. Today, environmental and safety agencies throughout the world are requiring even lower noise levels. With the increased demands for high efficiency, high power, and cost-effective electric machines, the motor industry is now facing challenges to build up not only more efficient but also quieter motors.

During motor operation, noise is produced from both rotating and stationary motor components, leading to environmental problems for people nearby. Thus, to protect people's health, motor noise must fall within acceptable limits, which have been strictly regulated in North American and European countries.

Various types of acoustic noise are produced during motor operation, as addressed in the following sections.

9.8.1 Noise Types in Rotating Electric Machines

Rotating electric machines are composed of various noise sources such as stator, rotor, ventilating fan, bearings, and housing, to name a few. The mechanisms of noise generation depend on the rotation of rotor, fan, and bearings, interaction of electromagnetic fields of the rotor and stator, machine structure, geometry of ventilation paths, and operation conditions. All noise generation mechanisms contribute to the overall noise pressure level of the machine. During normal operation, the noise sources create three main types of acoustic noise: mechanical noise, electromagnetic noise, and flow-induced noise.

9.8.1.1 Mechanical Noise

Shaft misalignment in motor causes preload forces to be generated in couplings that are then transmitted to various motor components. As one of the major causes of motor vibration, shaft misalignment produces a mechanical vibration with the frequency f_s:

$$f_s = 120 n_s \tag{9.132}$$

where n_s is the rotating speed of the shaft in rpm.

Dynamically unbalanced rotor, bent shaft, eccentricity, rubbing parts, etc., produce a vibrating frequency of once per revolution or multiple of the number of revolution per cycle:

$$f_s = k n_m \quad k = 1,2,3,... \tag{9.133}$$

The magnitude of the vibration noise due to the unbalanced rotating masses depends on the degree of balancing of the rotating masses and the rotating speed.

Loose stator lamination stack results in the vibration frequency with the frequency sidebands of 1000 Hz:

$$f_{lam} = 2f \tag{9.134}$$

where f is the line frequency.

Rolling bearings are extensively used in modern electric motors. Rolling bearing generates mechanical impulses when the rolling element passes the defective groove, causing a small radial movement of the rotor. Rolling bearings produce noise with discrete frequencies corresponding to the rotating frequency of each rolling element, such as roller, cage, and inner/outer ring. The bearing noise levels depend on the speed of rotation and their manufacturing perfections. Some large-sized motors also use sleeve bearings. The noise due to sleeve bearing is generally lower than that of rolling bearings. The vibration produced by sleeve bearings depends on the roughness of sliding surfaces, lubrication, and stability and whirling of the oil film in the bearing manufacturing process and bearing assembly [9.54].

Sound power radiated from an electric machine is proportional to the vibration area S and the mean vibration velocity square $\overline{u}^2$ [9.55]:

$$W = \rho c S \overline{u}^2 \sigma_{rad} \tag{9.135}$$

where

ρ is the air density

c is the speed of sound

σ_{rad} is the radiation efficiency

This equation indicates that mechanical noise can be reduced by reducing the vibration area and/or the vibration velocity. Reducing the vibration area can be achieved by dividing a large area into a number of small areas with flexible joints between them. Reducing the vibration velocity can be achieved by using damping and vibration-absorbing materials to isolate the vibration source from other components. A reduction of the exciting forces by a factor of two can possibly lower the SPL up to 6 dB.

9.8.1.2 Electromagnetic Noise

Electromagnetic field is not uniform in the air gap and consists of various harmonics. The periodic fluctuations of the magnetic flux in the air gap cause oscillating forces on both the rotor and stator. The noise due to the fluctuating magnetic forces is called nonrotational

noise, which resulted from the asymmetry of the electric and magnetic circuit and saturation of the magnetic field.

There are many normal modes of vibration in the stator core in all directions. While the radial forces cause radial extension of the stator core and consequently vibration and structure-borne noise, the axial forces and tangential forces result in vibration of the stator core in the axial and circumferential directions.

The magnitude of rotational electromagnetic noise strongly depends on the motor rotating speed. Hence, the electromagnetic noise is characteristically tonal in character with a great number of discrete frequency tones, the most important of which are at the frequency [9.56]

$$f_{em} = N_s n \tag{9.136}$$

where

N_s is the number of stator slots
n is the motor rotating speed

Electromagnetic noise is stimulated when the electromagnetic force matches or is close to the natural frequencies of vibration of motors.

9.8.1.3 Aerodynamic Noise

Aerodynamic noise, also referred to as windage noise or flow-induced noise in some references, is generated by the interactions of turbulent ventilating air flow with rotating (e.g., rotor, fan) and stationary components (e.g., stator, endbell) inside a motor. As airborne noise, this type of noise increases with the increasing flow speed.

As discussed previously, the aerodynamic sound power generated by turbulent flows is proportional to the 6th to 8th of the flow velocity (i.e., $W \propto u^{6-8}$). Consequently, the increase in the flow velocity can result in the great increase in sound power. Thus, a logical approach to lower the aerodynamic sound power is to reduce the flow velocity and turbulence intensity. This requires that in the design of motor ventilation system, it should avoid the sudden changes in the cross-sectional areas along the flow paths and reduce the right-angle bends as much as possible.

A ventilation fan is usually a dominant noise source in a motor. The fan generates broadband aerodynamic noise as the cooling flow passes through the inlet and outlet of the fan. In practice, fan noise reduction can be achieved by the use of an absorptive silencer or by redesigning the cooling fan [9.56]. The sound power level generated by fans can be predicted in the early design stage using the Graham equation [9.57].

9.8.2 Acoustic Anechoic Chamber

Noise measurement is a necessary step to determine the SPL of an electric machine is below the allowable level. With today's technology, many types of measuring systems can be used depending on the characteristics of sound, the extent of information that is desired about the sound, and cost, from the most popular sound level meters to the professional sound-measuring systems in acoustic laboratories.

An acoustic anechoic chamber is the specially designed room that can completely absorb reflections of sound waves and insulate testing equipment from environmental sources of noise. To absorb sound waves, the interior surfaces of the acoustic anechoic chamber are covered with acoustically absorbent materials. One of the most effective types of absorbent

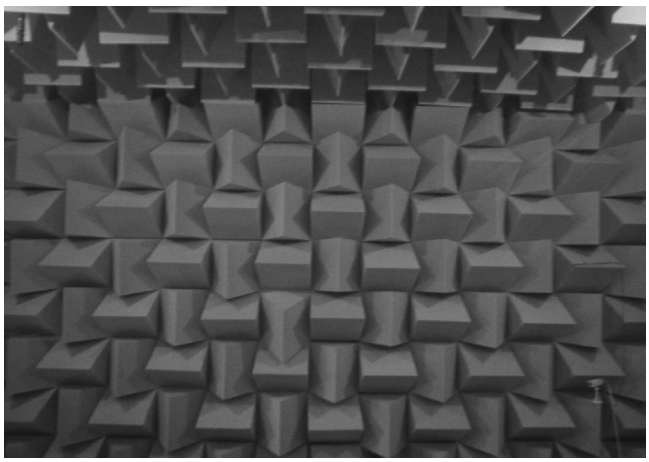

FIGURE 9.34
An anechoic chamber is specially designed to completely absorb reflections of sound waves.

materials comprises arrays of pyramid-shaped pieces, each of which is constructed from a suitably lossy material. In order to get the best results, all internal surfaces of the acoustic anechoic chamber must be entirely covered with the pyramids (Figure 9.34).

The relationship of the sound wavelength λ, phase velocity of wave v, and frequency f is given as

$$\lambda = \frac{v}{f} \tag{9.137}$$

To shield for specific range of wavelengths, the shape and size of the pyramids must be carefully designed for absorbing the range of wavelengths.

9.8.3 Measurement of Motor Noise

Typically, the anechoic chamber is used to measure the directivity of noise radiation from testing machinery or equipment and to determine the transfer function of a loudspeaker.

There are a number of elements in a sound-measuring system, including the following:

- Microphones that respond to sound pressure of a testing motor at specific locations and transform it into an electric signal. The commonly used types of microphones include piezoelectric, condenser, electret, or dynamic microphones.
- Signal amplifier boosts the amplitude of the microphone output signal to a useful level for further processing.
- Active filter that reduces high-frequency signal components, unwanted electrical interference noise, or electronic noise from the signal.
- The data storage, processing, and transportation.

Noise is measured at the rated operation conditions in the anechoic chamber by using microphones at a distance of one meter from the motor in different orientations, as shown in Figure 9.35. The noise data are taken as the test motor reaches the thermal equilibrium.

FIGURE 9.35
Measurement of acoustic noise level of electric motor by microphones in an anechoic chamber.

The spectrums of SPL from two PM servomotors are displayed in Figure 9.36. These two motors are identical in terms of brand and motor, and the testing has been conducted under the same conditions. However, their SPLs show distinct differences for almost all frequencies, especially in the range of 1000–3000 Hz.

9.8.4 Acoustic Noise Field Measurement

A field noise test was conducted in customer site at Texas. Acoustic noise data were acquired from a large-sized generator, which is installed in the open air at a height of 15 m above the ground. There are totally 15 measuring points, 5 on either side of a large-sized generator. These points were labeled from 1 to 5 going from the collector end (CE) to the turbine end (TE) of the generator, as well as along the CE (Figure 9.37). The data were acquired using a Rion®, handheld precision acoustic sound meter, interfaced with a Hewlett Packard® four-channel analyzer. The acoustic data were taken at three load levels of 17, 86, and 156 MW (156 MW is the full load).

9.9 Motor Noise Abatement Techniques

Controlling the noise level of electric motor is critical to the overall system performance. Therefore, noise abatement of motor is an important goal in motor design. The most cost-effective way to deal with the noise issue is to incorporate the reduction of noise level in an early design stage. Once a motor is manufactured, it is often expensive to modify the

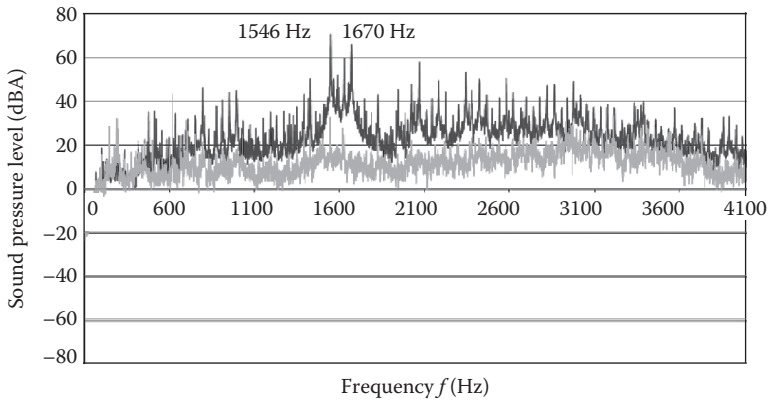

FIGURE 9.36
Comparison of SPLs for two PM servomotors with same brand and same model. Courtesy of Kollmorgen Corporation.

FIGURE 9.37
Active noise-cancelling headphones.

design for reducing noise levels. For old motors with high noise levels, an effective method to lower the motor noise exposure is to make external acoustic treatments of the motor.

A number of techniques to minimize noise level can be adopted in motor design. These techniques can be separated into two categories, passive and active.

9.9.1 Active Noise Reduction Techniques

Effective reduction in acoustic noise can be accomplished using active noise reduction techniques. One of the techniques is called noise cancellation technique. The concept of

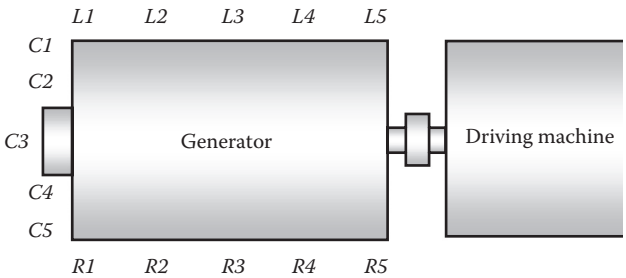

FIGURE 9.38
Measuring points around a large-sized generator.

active noise cancellation was initiated and developed in the early 1930s. Paul Lueg [9.58], a German engineer, was the first who realized the possibility of attenuating background noise by superimposing a phase flipped wave. Later, this concept was successfully confirmed by Olsen [9.59,9.60] to generate artificial sound waves that have the opposite phase to that of noise. This method is particularly useful at low frequencies because conventionally used sound absorbers do not work well at such frequencies, for which the sound wavelength is much larger than the thickness of a typical absorber.

Today, active noise reduction techniques have been successfully adopted in many commercial applications such as active mufflers, passage cars, wind tunnel testing systems, noise-cancelling headphones, and noise control in air-conditioning ducts. As a typical example, noise-cancelling headphones have been invented to eliminate any low-frequency noise from the environment. A variety of antinoise headphones is shown in Figure 9.38. These headphones involve using one or more microphones and an electronic circuitry that uses the microphone signals to generate antinoise signals, thus the generated destructive interference cancels out the ambient noise.

With today's advanced digital signal-processing techniques, it is possible to make active noise control more precisely and more efficiently. However, active damping techniques are considerably expensive because they require measurement of response and feedback control, and thus have not yet been applied to electric motors. In addition, the application of active noise cancellation on large-size electric machines is less effective due to the challenge in separating multidirectional sounds.

9.9.2 Passive Noise Reduction Techniques

Passive techniques are the simplest and least expensive means of preventing problems associated with acoustic noise. There are several conventional methods available to reduce motor noise, each has its own advantages and disadvantages for specific applications. The selection of an appropriate method depends on its effectiveness in noise attenuation and system cost.

9.9.2.1 Blocking Noise Propagation Paths and Isolating Noise Sources

Mechanical noise transmissions can be greatly reduced by blocking noise propagation paths [9.61] or isolating sources of noise. An effective and traditional way is to locate noisy machines behind purpose-built barriers. In order to achieve the maximum shielding effect, the barriers can be constructed with sound-absorbing and damping materials. For large-sized motors, noise barriers can be erected between motors and noise-sensitive

areas. Compact motors can be covered by a box with noise-absorbing and damping materials attached on its internal surfaces.

Another approach is to use mechanical dampers, such as rubber boots, reflecting enclosures, to lower the level of vibration and consequently the level of transmitted noise, as discussed in the previous sections.

9.9.2.2 Using Noise-Absorbing Materials

A common way of noise reduction is to attach sound-absorbing materials on either internal or external walls of the motor housing/endbells for absorbing sound energy. Sound-absorbing materials may come in many forms, ranging from simple foam and cellular materials to a variety of commercially made products designed specifically for the purpose. Most sound-absorbing materials contain a large number of small cavities. When sound waves pass through the air inside the cavities, certain frequencies of sound waves may result in resonance of the air inside the cavities. In such a way, sound energy is consumed and the sound pressure is reduced. The resonances depend on the size and shape of the cavities. Therefore, well-designed cavities in sound-absorbing materials can effectively reduce motor acoustic noise.

Removable and reusable blankets have been widely used for acoustical reduction applications. The benefits of using blankets include the following:

- One-time investment
- Long-term repeated use
- Without interrupting equipment normal operation
- Making equipment maintenance easier
- Providing protection for personnel

Acoustic blankets may contain single- or multifiberglass layers depending on application requirements. As an example shown in Figure 9.39, an acoustic blanket consists of two high-density layers and one low-density layer. Usually, high-density blankets are used to contact with the generator wall. Fiberglass fibers are encased within PTEE-coated (or silicone rubber-coated) fabric envelops, which are designed to withstand both chemical attack and severe mechanical abuse. Stainless steel hook-and-loop fasteners are used for jointing in blanket sections. Acoustic blankets are wrapped around the external surface of an electric machine for reducing noise levels.

In order to fit better the generator's external shape, blankets are made in a number of sections. Each section has a stainless steel identification tag that has a unique identification number corresponding to the installation drawings. Stainless steel jacketing, with a nominal thickness of 0.7 mm, is used to cover the blanket system. The jacketing normally utilizes long-reach stainless steel buckles and strikers. As with the blankets, each jacketing section has a stainless steel identification number corresponding to the installation drawings. As an alternate to separate stainless steel jacketing, integral stainless steel mesh is used. The mesh is factory-sewn to the fiberglass blanket assembly and acts to protect the blanket insulation from walk traffic and/or other abrasion damage.

A generator may be wrapped partially or completely with acoustic blankets. With an application of the generator laggings, acoustic noise at the generator bottom is blocked; only the upper half of the generator needs to be covered (Figure 9.40). The installation of the acoustic blanket on a large-sized generator is shown in Figure 9.41.

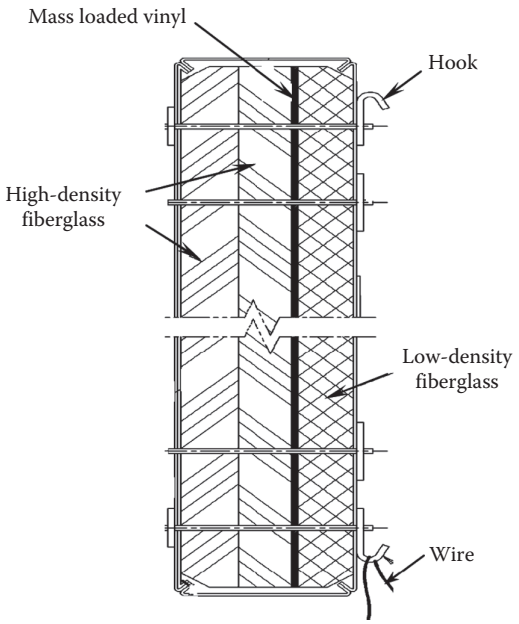

FIGURE 9.39
Acoustic blanket consisting of one low-density and two high-density fiberglass layers with a mass-loaded vinyl sandwiched between them.

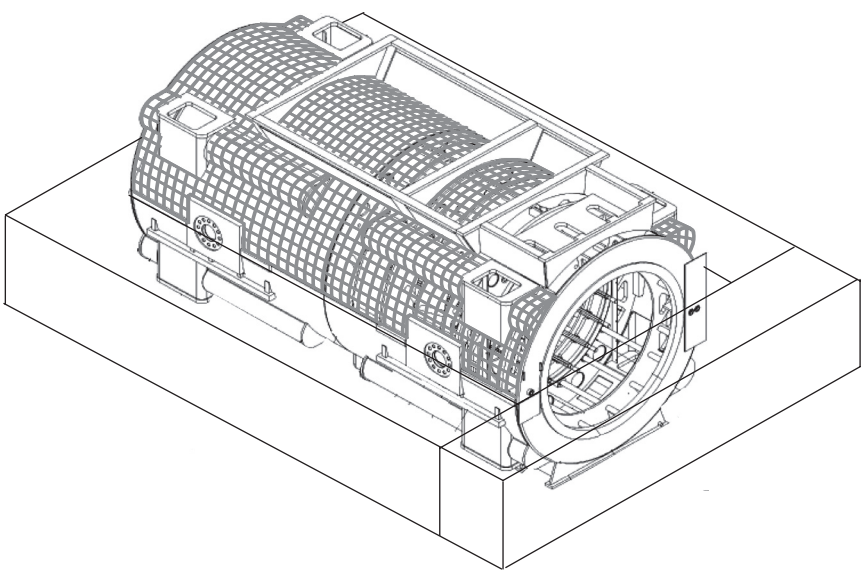

FIGURE 9.40
Covered areas by acoustic blankets on a generator.

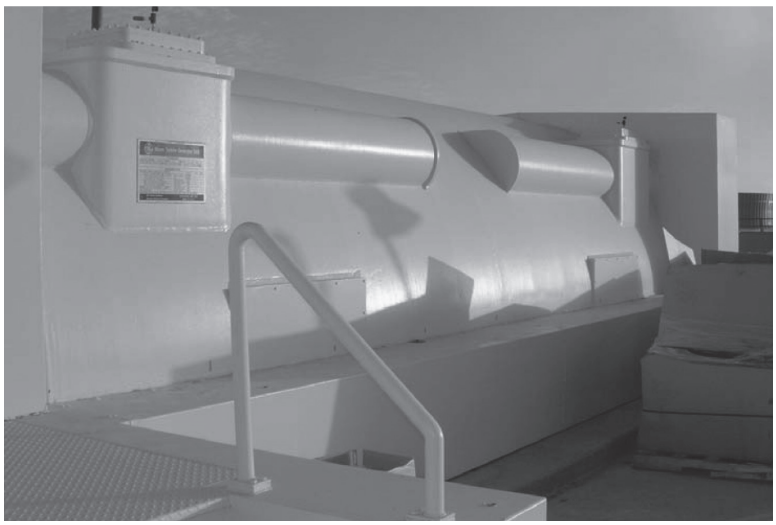

(a)

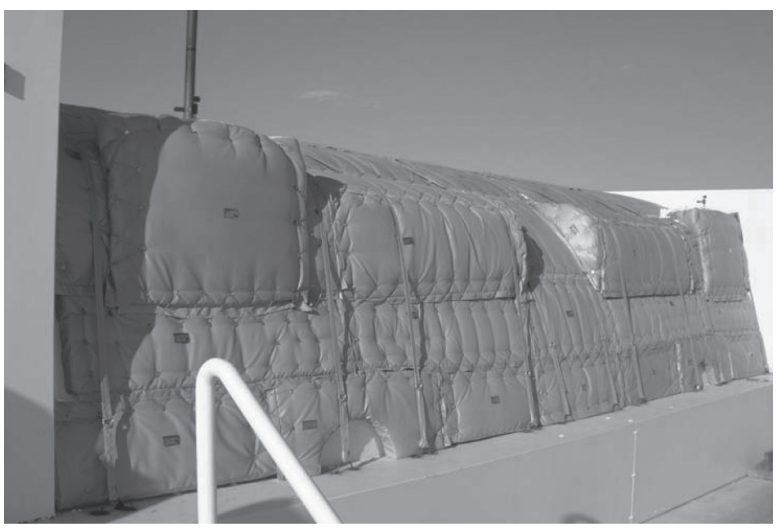

(b)

FIGURE 9.41
A large-sized generator with bared outer surfaces (a) and installed acoustic blankets for noise reduction (b).

The test data have shown that acoustic blankets have a significant impact on generator noise levels. At the generator, sides were covered with blankets; the reduction in noise levels ranges from 2 (low frequencies) to 8 dBA (Figure 9.42). It is reported that the properly used acoustic blankets on electric machines can attenuate noise pressure level by 5–10 dBA [9.62].

The spectra data at the tested generator are presented in Figure 9.43. It can be observed that blankets can reduce noise level at all frequencies. For instance, at the center of the

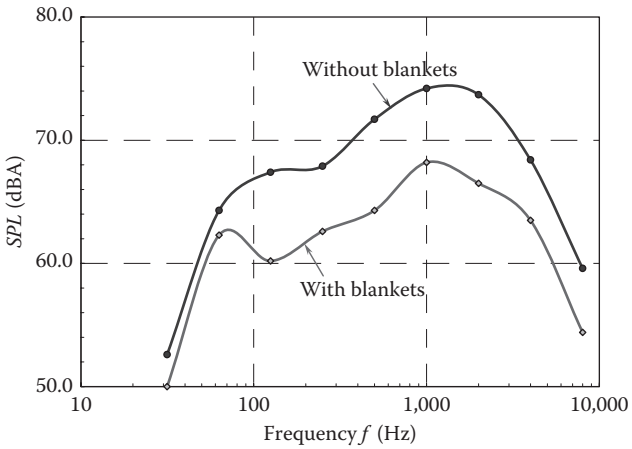

FIGURE 9.42
Effect of acoustic blanket on noise reduction for different frequencies.

generator left side, the noise level reduces from 70.8 to 66.5 dBA at $f = 60$ Hz and 72.8 to 60.5 dBA at $f = 120$ Hz.

One of most popular methods is to use some special materials to absorb sound energy. These materials such as foams or cellular materials comprise many small cavities. The drawback with these traditional noise reduction approaches is that they only work with some frequencies.

However, while the method is effective in noise reduction in some cases, it can impact the effectiveness of the heat dissipation from the housing to the ambient. In addition, this approach works for rather limited frequencies.

9.9.2.3 Motor Suspension Mounting

On undamped baseplate mountings, motor noise can be transmitted, amplified, and radiated by nonmotor structures. A motor suspension on rubber mounting or cushioned mounting can be added to the installation to reduce noise and vibration.

9.9.2.4 Noise-Attenuating Structure

Ramu [9.63] proposed a method of noise reduction for switched reluctance machines (SRMs). SRMs usually produce higher noise than other types of electric machines, making them less attractive for some commercial and industrial applications. For instance, medical devices often require quiet operation with less noise. The SRM noise is attributed to (1) the normal forces caused by various imbalances in the nonuniform air gap, (2) the discontinuous currents in the windings causing discontinuous torque that produces very high torque pulsations, and (3) the rotor functioning like an impeller to create turbulent flows in the machine, causing significant windage noise.

SRM motors have no windings or PMs on rotors. As a rotor rotates, its salient poles are like fan blades that generate turbulent air flow in the motor. The fan blade noise is

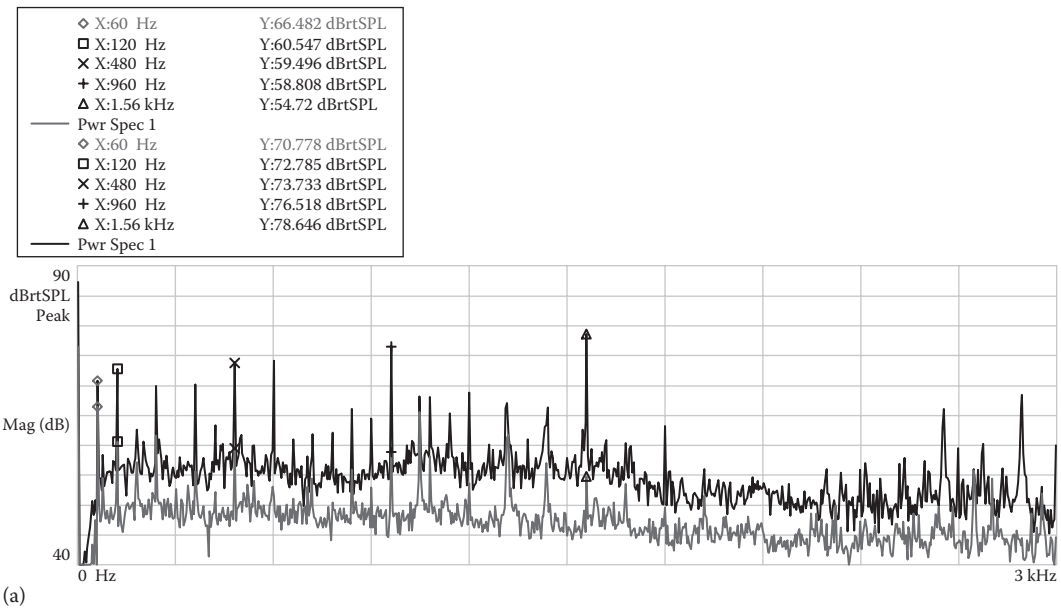

(a)

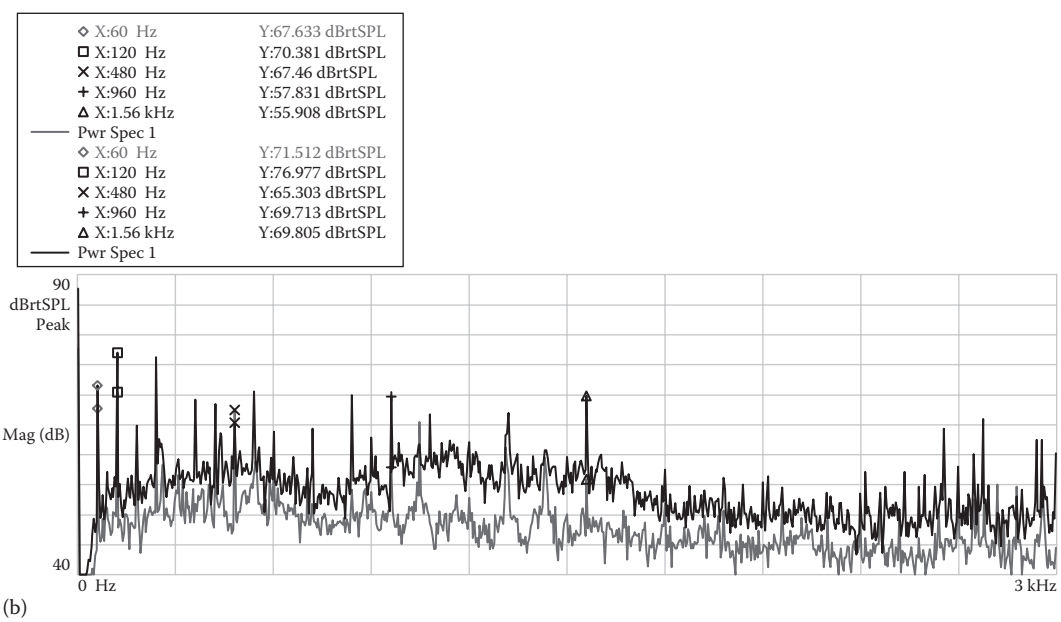

(b)

FIGURE 9.43
Spectra data at the center of generator sides: (a) left side and (b) right side; viewing from the CE. In each case, the curve with higher noise pressure levels is for uncovered acoustic blankets.

produced due to the alignment effect between the rotor and stator poles. The frequency f_{rt} of a pure tone arising from air passing through the rotor slots can be calculated by

$$f_{rt} = p_r \frac{n}{60} \tag{9.138}$$

where
p_r is the number of rotor slots
n is the rotor rotating speed (in rpm)

This tonal frequency noise has exactly the same value as the combined phase frequency of the machine.

SRM noise can be remarkably reduced by several methods, including the following:

- Encapsulating a machine's stator/rotor slots can reduce windage noise. As shown in Figure 9.44, the rotor slots are filled by epoxy to flush with the rotor outer surface and lamination end surfaces. The smooth rotor surface has much less friction than the surface with slots in which air forms recirculation flows to cause windage power loss and windage noise.
- The phase rotation of end lamination with respect to the intermediate laminations is another way to lower machine noise. It can be seen in Figure 9.45 that two end laminations are rotated oppositely about the rotational axis of the rotor to partially or fully cover the rotor slots. This creates a barrier inhibiting the air flow into and out of the slots.
- Similar to the previous discussion, the rotor/stator slots can be blocked using two end annuluses, as shown in Figure 9.46.

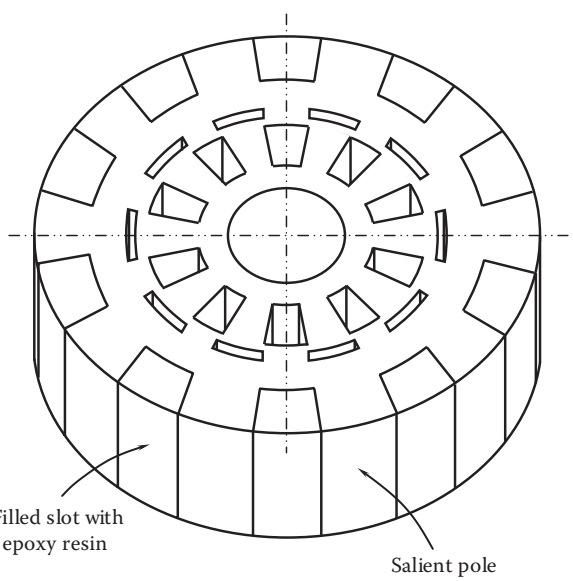

FIGURE 9.44
Rotor slots are filled with epoxy resin to reduce windage noise [9.63]. (Courtesy of the U.S. Patent and Trademark Office, Alexandria, VA.)

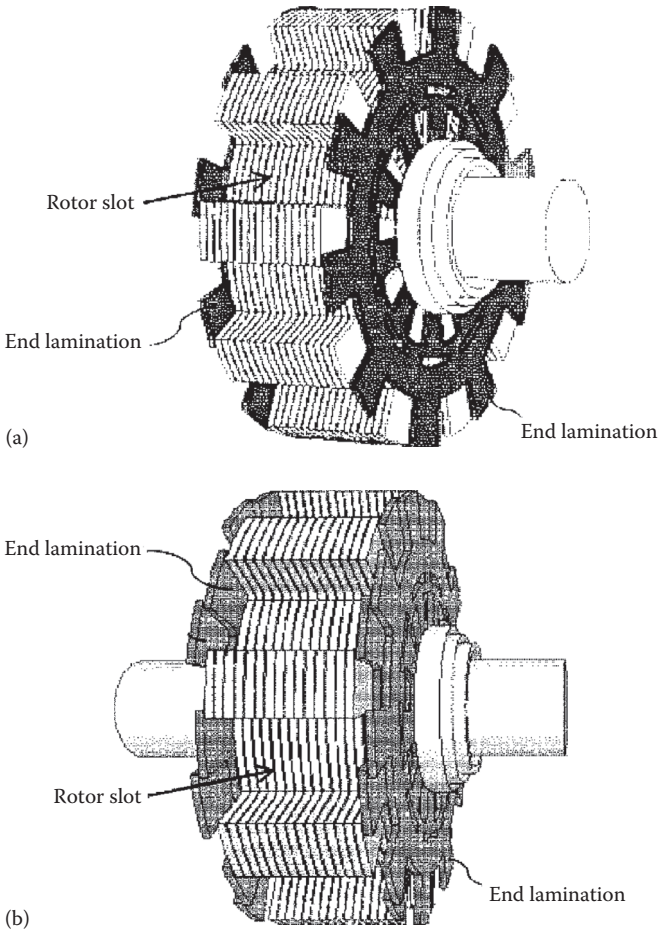

FIGURE 9.45
Phase-shifted end laminations for reducing noise: (a) shifting two end laminations in opposite directions with respect to intermediary laminations and (b) using multiple phase-shifted laminations for covering longitudinal sides of slots [9.63]. (Courtesy of the U.S. Patent and Trademark Office, Alexandria, VA.)

9.9.2.5 Smoothing Ventilation Paths

When a motor rotor runs at a high speed, it stimulates air inside the motor to form swirl flow in the air gap and at the ends. Fans attached to the rotor also generate ventilation flows primarily in the axial direction to cool motor components. As a result, the velocity field in the motor is considerably complicated. Vortex motions are associated with regions of flow discontinuity that occur at interfaces between fluids and solids in relative motion or between parallel-moving flows of different velocities. The vorticity in turbulent flows is responsible for regions of relatively intense flow mixing and activity. Briefly, noise is produced whenever vortex lines are stretched or accelerated.

Smoothing ventilation paths can reduce the flow turbulence intensity and in turn the flow-induced noise, which usually arises in applications involving turbulent flows.

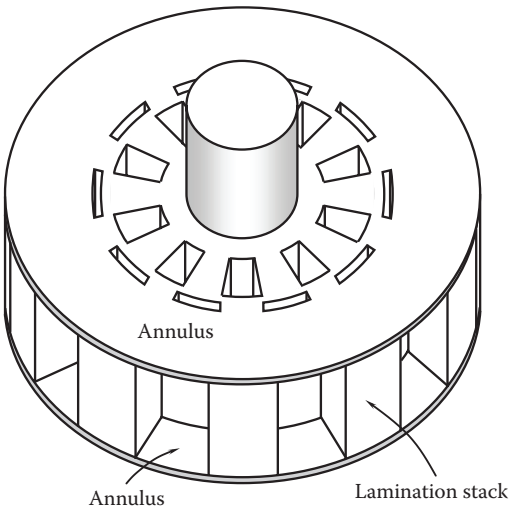

FIGURE 9.46
Adding an annulus at each end of rotor to block axial air flow paths and thus reduce acoustic noise [9.63]. (Courtesy of the U.S. Patent and Trademark Office, Alexandria, VA.)

9.9.2.6 Selecting Low Noise Bearings

During normal operation, rolling bearings make a variety of vibration and acoustic noise. As discussed in Chapter 6, the bearing noise and vibration can be briefly grouped into four categories [9.64]—structural, manufacturing, handling, and others:

- Structural noises resulted from free vibration of the bearing components, including raceway rings, rollers, seals, and cage.
- Ideally, bearing raceways are manufactured with perfect roundness and high-quality surface finish. However, because any machine has its limited machining precision, waviness usually presents on the manufactured raceway surfaces, causing waviness noise and vibration and impacting bearing frictional performance and endurance.
- Handling noise consists of flaw noise and contamination noise. Manufacturing flaws can lead to abnormal operation of bearing to produce noise. Contamination can dramatically shorten bearing life. According to failure analysis statistics, about 15% of all motor bearing failures is attributed to contamination [9.65]. Since the lubricant film thickness, which separates the mating surfaces in the rolling contact, is very thin (usually less than 1 μm), any particles in size larger than the film thickness can disturb the bearing smooth running.
- The last category of noise/vibration includes lubricant noise and seal noise. It is long recognized that oil-lubricated bearings have longer lifetime than grease-lubricated bearings because greases always contain solid particles. There are a few greases in the market that fall into the *noisy* class due to their thickener or solid additives. Typical examples are some calcium-complex greases that contain large particles of calcium salts, producing small permanent dents of raceway surfaces [9.66]. Inadequate lubrication of bearings may not only create higher motor noise but also cause higher bearing temperatures.

Most motor manufacturers randomly sample bearings for inspections. However, considering the fact that most motor failures can be attributed to premature bearing failures, it is highly recommended to conduct 100% bearing inspections, especially for some special applications under severe environmental conditions (e.g., deep sea, outer space, or desert).

Among all types of bearings, sleeve bearings make lowest noise and ball bearings generally make more noise than roller bearings [9.67].

9.9.3 Innovative Noise Abatement Methods

To address noise abatement problems, acoustic engineers presently turn to innovative methods that make new approaches to the physics of noise reduction. With the fast development of nanotechnologies in recent years, motor noise can be significantly reduced by applying nanofibers and by coating the housing and endbell internal surfaces with microsilicone paint (e.g., *Lotusan*).

The advantages of using nanotechnology in motor noise reduction include the following:

- High efficiency in noise reduction
- Taking a little space
- Low-density structure
- Reliable
- Easy to fabricate

Engineers in Georgia Tech Research Institute developed a porous metal structure that contained many cylindrical channels for attenuating aviation turbine noise [9.68]. The diameter of each channel ranges approximately from 0.1 to 0.3 mm. Later, this structure further evolved into a microscale honeycomb structure, which is composed of a large number of metallic nanotubes. This technique, unlike traditional techniques that absorb sound using a more frequency-dependent resonance, dissipates acoustic waves by wearing them down through a process called viscous shear. The reduction of sound pressure level in this approach is independent of frequencies or resonance.

References

[9.1] Timar, P. L. 1989. *Noise and Vibration of Electrical Machines*. Elsevier Science Publisher, Amsterdam, the Netherlands.

[9.2] Yang, S. J. 1981. *Low-Noise Electrical Motors*. Oxford University Press, New York.

[9.3] Granjon, P. 2005. Electromagnetic vibrations estimation of an induction motor by nonlinear optimal filtering. *Sixth IEEE International Symposium on Diagnostics for Electric Machines, Power Electronics and Drives (SDEMPED 2005)*, Vienna, Austria.

[9.4] Capitaneanu, S. L., de Fornel, B., Fadel, M., and Jadot, F. 2003. On the acoustic noise radiated by PWM A.C motor drives. *AUTOMATIKA* **44**(**3**): 137–145.

[9.5] Bate, G. H. Vibration diagnostics for industrial electric motor drives. Brüel & Kjær. Application Notes. http://www.bksv.com/doc/bo0269.pdf.

[9.6] Gerges, S. N. Y., Sehrndt, G. A., and Parthey, W. 2001. Chapter 5: Noise sources. In *Occupational Exposure to Noise: Evaluation, Prevention and Control* (Eds.: B. Goelzer, C. H. Hansen, and G. A. Sehrdt). Federal Institute for Occupational Safety and Healthy, Dortmund, Germany.

[9.7] Finley, W. R., Hodowanec, M. M., and Holter, W. G. 2000. An analytical approach to solving motor vibration problems. *IEEE Transactions on Industrial Applications* **36**(**5**): 1467–1480.
[9.8] Yoon, S. Y., Lin, Z., and Allaire, P. E. 2013. *Control of Surge in Centrifugal Compressors by Active Magnetic Bearings: Theory and Implementation*. Springer, London, U.K.
[9.9] Chikkamaranahalli, S. B., Vallance, R. R., Damazo, B. N., and Silver, R. M. 2006. Damping mechanisms for precision applications in UHV environment. *Proceedings of 2006 Spring Topical Meeting: Challenges at the Intersection of Precision Engineering and Vacuum Technology*, Pittsburgh, PA.
[9.10] Han, D. C. and Moon, H. J. 1996. Lateral vibration analysis of the rotor system with magnetic forces. *Proceedings of the 6th International Symposium on Transport Phenomena and Dynamics of Rotating Machinery*, Vol. 1, pp. 87–96, Honolulu, Hawaii.
[9.11] Ahamed, S. K., Mitra, M., Sengupta, S., and Sarkar, A. 2012. Identification of mass-unbalance in rotor of an induction motor through envelope analysis of motor starting current at no load. *Journal of Engineering Science and Technology Review* **5**(**1**): 83–89.
[9.12] Eshleman, R. and Eubanks, A. 1969. On the critical speeds of a continuous rotor. *ASME Journal of Engineering for Industry* **91**: 1180–1188.
[9.13] Evremsel, C. A., Kimmel, H. E., and Cullen, D. M. 1999. Axial rotor oscillations in cryogenic fluid machinery. *Proceedings of the Third ASME/JSME Joint Fluids Engineering Conference*, San Francisco, CA.
[9.14] Supangat, R. 2008. On-line condition monitoring and detection of stator and rotor faults in induction motor. PhD thesis, University of Adelaide, Adelaide, South Australia, Australia.
[9.15] Rashtchi, V. and Aghmasheh, R. 2010. A new method for identifying broken rotor bars in squirrel cage induction motor based on particle swarm optimization method. *World Academy of Science, Engineering and Technology* **67**(**2010**): 694–698.
[9.16] Thomson, W. T. and Rankin, D. 1987. Case histories of rotor winding fault diagnosis in induction motors. *Proceedings of Second International Conference on Condition Monitoring*. University College of Swansea, Wales, U.K.
[9.17] Faiz, J. and Ebrahimi, B. M. 2009. Locating rotor broken bars in induction motors using finite element method. *Energy Conversion and Management* **50**(**2009**): 125–131.
[9.18] Früchtenicht, J., Jordan H., and Seinsch, H. O. 1982. Exzentrizitätsfelder als ursache von laufinstabilitäten bei asynchronmaschinen. Teil I und II. *Arch. Elektrotech* **65**: 271–292.
[9.19] Arkkio, A., Antila, M., Pokki, K., Simon, A., and Lantto, E. 2000. Electromagnetic force on a whirling cage rotor. *IEEE Electric Power Applications* **147**(**5**): 353–360.
[9.20] Lundström, N. L. P. and Aidanpää, J.-O. 2011. Dynamics in large generators due to oval rotor and triangular stator shape. *Acta Mechanica Sinica* **27**(**1**): 18–27.
[9.21] Arkkio, A. 1987. Analysis of induction motors based on the numerical solution of the magnetic field and circuit equations. *Acta Polytechnica Scandinavica, Electrical Engineering Series* **59**: 1–97.
[9.22] Antila, M. 1998. Electromechanical properties of radial active magnetic bearings. *Acta Polytechnica Scandinavica, Electrical Engineering Series* **92**: 1–96.
[9.23] Clynch, J. R. and Garfield, N. 2006. Equations of an ellipse. http://www.gmat.unsw.edu.au/snap/gps/clynch_pdfs/ellipequ.pdf.
[9.24] Lee, J.-H., Lee, Y.-H., Kim, D.-H., Lee, K.-S., and Park, I.-H. 2002. Dynamic vibration analysis of switched reluctance motor using magnetic charge force density and mechanical analysis. *IEEE Transactions on Applied Superconductivity* **12**(**1**): 1511–1514.
[9.25] Lipo, T. 2004. *Introduction to AC Machine Design*. Wisconsin Power Electronics Research Center, University of Wisconsin, Madison, WI.
[9.26] Hariharan, V. and Srinivasan, P. S. S. 2010. Vibrational analysis of flexible coupling by considering unbalance. *Would Applied Science Journal* **8**(**8**): 1022–1031.
[9.27] Muljadi, E., Yildirim, D., Batan, T., and Butterfield, C. P. 1999. Understanding the unbalanced-voltage problem in wind turbine generation. *IEEE Industry Applications Society 34th IAS Annual Meeting*, Phoenix, AZ.
[9.28] Hariharan, V. and Srinivasan, P. S. S. 2011. Vibration analysis of parallel misaligned shaft with ball bearing system. *Songklanakarin Journal of Science and Technology* **33**(**1**): 61–68.

[9.29] Al-Najjar, B. 1998. Improved effectiveness of vibration monitoring of rolling bearing in paper mills. *Journal of Engineering Tribology* **212**(**2**): 111–120.
[9.30] Ozelgin, I. 2008. Analysis of magnetic flux density for airgap eccentricity and bearing faults. *International Journal of Systems Applications Engineering and Development* **2**(**4**):162–169.
[9.31] Corbo, M. A. and Malanoski, S. B. 1996. Practical design against torsional vibration. *Proceedings of the 25th Turbomachinery Symposium*, pp. 189–222, Houston, TX.
[9.32] Chung, D. D. L. 2001. Review: Materials for vibration damping. *Journal of Materials Science* **36**(**24**): 5733–5737.
[9.33] Macioce, P. 2003. Viscoelastic damping 101. *Sound and Vibration* **37**(**4**): 8–10.
[9.34] Chung, D. D. L. 2010. *Composite Materials: Science and Applications*, 2nd edn. Springer-Verlag, London, U.K.
[9.35] Kulekei, M. K. 2008. Magnesium and its alloys applications in automotive industry. *International Journal of Advanced Manufacturing Technology* **39**(**9–10**): 851–865.
[9.36] Birchak, J. R. 1977. Damping capacity of structural materials. *The Shock and Vibration Digest* **9**(**4**): 3–11.
[9.37] Schetky, L. M. and Perkins, J. 1978. The quiet alloys. *Machine Design* **50**(**8**): 202–206.
[9.38] Bloomfield, D. and Firchau, T. 2013. Vibration isolation device and system. U.S. Patent Application 2013/0026689.
[9.39] Fullerton, L. W. and Roberts, M. D. 2012. Multi-level magnetic system for isolation of vibration. U.S. Patent 8,279,031.
[9.40] Mangra, D., Sharma, S., and Jendrzejczyk, J. 1996. Passive vibration damping of the APS machine components. *Review of Scientific Instruments* **67**(**9**): 3374–3378.
[9.41] Sadek, F., Mohraz, B., Taylor, A. W., and Chung, R. M. 1997. A method of estimating the parameters of tuned mass dampers for seismic applications. *Earthquake Engineering and Structural Dynamics* **26**: 617–635.
[9.42] Kourakis, I. 2005. Structural systems and tuned mass dampers of super-tall building: Case study of Taipei 101. Master thesis, Massachusetts Institute of Technology, Cambridge, MA.
[9.43] Fortgang, J. and Singhose, W. 2005. Design of vibration absorbers for step motions and step disturbances. *ASME Journal of Mechanical Design* **127**(**1**): 160–163.
[9.44] Delcon. Double mounting. http://www.deicon.com/Double_Mounting.html.
[9.45] Tillema, H. G. 2003. Noise reduction of rotating machinery by viscoelastic bearing support. PhD thesis, University of Twente, Enschede, the Netherlands.
[9.46] Tantanawat, T., Li, Z., and Kota, S. 2004. Application of compliant mechanisms to active vibration isolation systems. *Proceedings of ASME 2004 Design Engineering Technical Conference*, Vol. 2B, pp. 1165–1172, Salt Lake City, UT.
[9.47] Platus, D. L. 1999. Negative-stiffness-mechanism vibration isolation systems. *Proceedings of the 1999 Optomechanical Engineering and Vibration Control* **3786**: 98–105.
[9.48] Coffey, V. C. 2009. Optical-table basics: From breadboards to active vibration-control systems. *Laser Focus World* **45**: 63–66.
[9.49] McBean, J. and Breazeal, C. 2004. Voice coil actuators for human-robot interaction. *Proceedings of 2004 IEEE/RSJ International Conference* **1**: 852–858.
[9.50] Newell, D. B., Richman, S. J., Nelson, P. G., Stebbins, R. T., Bender, P. L., Faller, J. E., and Mason, J. 1997. Ultra-low-noise, low-frequency, six degrees of freedom active vibration isolator. *Review of Scientific Instruments* **68**(**8**): 3211–3219.
[9.51] Yildiz, F. 2009. Potential ambient energy-harvesting sources and techniques. *The Journal of Technology* **35**(**1**): 40–48.
[9.52] Cory, W. T. W. Relationship between sound pressure and sound power levels. http://www.eurovent-certification.com/fic_bdd/pdf_fr_fichier/1137149375_Review_67-Bill_Cory.pdf.
[9.53] International Electrotechnical Commission (IEC). 2003. IEC Standard 61672 Electroacoustics—Sound level meters.
[9.54] Gieras, J. F., Wang, C., and Lai, J. C. 2006. *Noise of Polyphase Electric Motors*. CRC Press, Boca Raton, FL.

[9.55] Gerges, S. N. Y. 2000. *Ruído: Fundamentos e Controle*, 2nd edn. Universidade Federal de Santa Catarina, Florianópolis, Brazil.
[9.56] Čudina, M. and Prezelj, J. 2007. Noise generation by vacuum cleaner suction units: Part I. Noise generation mechanisms—An overview. *Applied Acoustics* **68**: 491–502.
[9.57] Graham, J. B. 1972. How to estimate fan noise. *Sound and Vibration*, May Issue, pp. 224–227.
[9.58] Lueg, P. 1934. Processing silencing sounds oscillations. U.S. Patent 2,043,416.
[9.59] Olson, H. F. and May, E. G. 1953. Electronic sound absorber. *Journal of the Acoustical Society of America* **25**: 1130–1136.
[9.60] Olson, H. F. 1956. Electronic of control of noise, vibration, and reverberation. *Journal of the Acoustical Society of America* **28**(**5**): 966–972.
[9.61] Crucq, J. 1988. Theory and practice of acoustic noise control in electrical appliances. *Philips Technical Review* **44**(**4**): 123–134.
[9.62] Tong, W., Wagner, T. A., Hughes, I. A., Gillivan, J. M., and Gibney, III, J. J. 2004. Acoustic blanket for machinery and method for attenuating sound. U.S. Patent 6,722,466.
[9.63] Ramu, K. 2012. Noise reduction structures for electrical machines. U.S. Patent Application 2012/0104879.
[9.64] Momono, T. and Noda, B. 1999. Sound and vibration in rolling bearings. *Motion & Control* **6**: 29–37.
[9.65] Hink, R. 1998. Procedures for protecting electric motor bearings. *Plant Engineering*. http://www.plantengineering.com/search/search-single-display/procedures-for-protecting-electric-motor-bearings/2459e0f67d.html.
[9.66] Bichler, M. and Roth, C. 2004. Test rig uses noise to measure grease cleanliness. *Practicing Oil Analysis*. May–June Issue.
[9.67] Hoppler, R. and Errath, R. A. 2007. Motor bearings: "the bearing necessities." *Global Cement Magazine*, October Issue, pp. 26–32.
[9.68] Nadler, J., Paun, F., Josso, P., Bacos, M.-P., and Gasser, S. 2011. Porous metal bodies used for attenuating aviation turbine noise. U.S. Patent 7,963,364.

10

Motor Testing

Safe, reliable, steady, and efficient operation of electric motors is essential for all motor applications. For example, elevator motors must have very high operating reliability and factors of safety because they are directly related to people's lives. Motor failure in a nuclear plant or in a launched rocket may cause catastrophic results, as well as tremendous economic losses and long-lasting impacts.

New motor design and development programs often incorporate prototype testing activities. Motor testing is a crucial step to ensure motor performance, efficiency, and manufacturing integrity. It can detect any potential faults, improve operation reliability, and optimize the motor design. For these purposes, a variety of tests must be conducted under different operating conditions. Testing variables may include the load (torque) level, rotating speed, voltage, current, induction, resistance, temperature distribution, and cooling flowrate.

10.1 Motor Testing Standards

There are a large number of IEEE, IEC, ANSI/NEMA, and EASA standards dealing with electric motor testing. Some of them are listed as follows:

- IEEE Standard 43-2000. Recommended practice for testing insulation resistance of rotating machines [10.1]. This document describes the recommended procedure for measuring insulation resistance of armature and field windings in rotating machines. It has addressed the general theories of insulation resistance and polarization index (PI).
- IEEE Standard 56-1977. Guide for insulation maintenance of large-current rotating machinery [10.2]. This standard provides guidelines for testing and inspection of insulation systems on motors.
- IEEE Standard 118-1978. Test code for resistance measurement [10.3]. The purpose of this code is to present methods of measuring electrical resistance that are commonly used to determine the characteristics of electric machinery and equipment.
- IEEE Standard 95-2002. Recommended practice for insulation testing of AC electric machinery (2,300 V and above) with high direct voltage [10.4]. This document provides information on the use of high direct voltage for proof tests and for periodic diagnostic tests on the ground wall insulation of stator windings in AC electric machines.
- IEEE Standard 522-2004. Guide for testing turn insulation of form-wound stator coils for alternating-current electric machines [10.5].

- IEEE 1068-1990. Recommended practice for the repair and rewinding of motors for the petroleum and chemical industry [10.6].
- ANSI/IEEE Standard 112-2004. Standard test procedure for polyphase induction motors and generators [10.7].
- ANSI/NETA MTS-2007. Standard for maintenance testing specifications for electrical distribution equipment and systems [10.8].
- ANSI/NETA ATS-2009. Acceptance testing specifications for electrical power distribution equipment and systems [10.9].
- ANSI/NETA ETT-2010. Standard for certification of electrical testing technicians [10.10].
- NEMA MG1-1993. Motors and generators [10.11]. It provides practical information concerning performance, safety, test, construction, and manufacture of AC and DC motors and generators.
- IEC 60034-1: 2010. Rotating electrical machines—Part 1: Rating and performance [10.12].
- IEC 60034-2-1: 2007. Rotating electrical machines—Part 2-1: Standard methods for determining losses and efficiency from test (excluding machines for traction vehicles) [10.13].
- IEC 60034-4: 2008. Rotating electrical machines—Part 4: Method for determining synchronous machine quantities from tests [10.14].
- IEC 60034-19: 1995. Rotating electrical machines—Part 19: Specific test methods for DC machines on conventional and rectifier-fed supplies [10.15].
- IEC 60034-29: 2008. Rotating electrical machines—Part 29: Equivalent loading and superposition techniques—indirect testing to determine temperature rise [10.16].

Because there are so many standards presently, motor manufacturers in different countries often follow different standards in their production. For instance, motor efficiency testing protocols differ from the world, and their applications on any given motor can lead to significantly different efficiency values. Therefore, it is important to unify the standards all over the world.

10.2 Testing Equipment and Measuring Instruments

There are a large variety of instruments and equipment used in motor test laboratories. The understanding of the functions and fundamental principles of these instruments and equipment, as well as correctly using them, is essential for the success of motor testing. In addition, all of the instruments must be carefully calibrated for obtaining accurate and reliable testing results. A brief introduction of the main instruments and equipment is given in the following.

10.2.1 Dynamometer

As one of the key devices in electric motor testing, dynamometers (or dynos in short) have been used extensively for measuring rotating speed, torque, power output, and force from

power sources such as motors and engines. Based on the measured operation characteristic data, motor efficiency and other useful information can be determined. Dynamometers can operate in two basic modes: (1) the absorbing or passive mode in which a dynamometer is driven by motor under test and provides a specific brake torque load to the testing unit and (2) the driving mode in which a dynamometer drives a machine to determine the torque and power required for operating such a driven machine. A dynamometer that can either drive or absorb is called a universal or active dynamometer.

Motor testing dynamometers apply braking or drag resistance to motor rotation under various operation conditions. Consequently, the absorbing dynamometer is used to absorb the power developed by the motor in motor testing. The brake power P_b, which is generated by a dynamometer and applied to the tested motor, is calculated by multiplying the torque T_{dyno} (N-m) and rotating speed ω_{dyno} (rad/s), that is,

$$P_b = T_{dyno}\omega_{dyno} \tag{10.1}$$

A variety of different dynamometers, either for absorption or drive mode or both, have been used for electric motor testing, including

- Powder brake dynamometer (absorption only)

  As its name implies, a powder brake dynamometer contains fine magnetic powder in the air gap between the rotor and stator of the brake. When current is applied to the excitation coil, a magnetic field is generated in the brake. Under the magnetic field, the magnetic powder is arranged in *magnetic chains* in accordance with magnetic flux lines, altering the powder from the free moving condition to the solid rock condition. As the brake rotates, the magnetic chains are constantly built and broken to create a great loading torque to the rotor. Thus, the loading torque can be easily adjusted by altering the excitation current. This type of dynamometer is ideal for high torque, low speed applications. It can provide full torque at zero rotating speed. Powder brake dynamometers are normally cooled with water and is not suitable for vertical operation.
- Hysteresis brake dynamometer (absorption only)

  A hysteresis brake dynamometer produces braking torque through a magnetic air gap without using magnetic particles or friction components. The hysteresis brake dynamometer usually consists of a cup-shaped rotor, a gear-shaped stator, and an excitation coil, providing precise torque loading that is independent of the shaft speed. The rotor is made of magnetic material with hysteresis characteristics. When the stator is energized, the cup-shaped rotor can spin freely. As current passes through the excitation coil, a magnetizing force is applied to the stator and the rotor is magnetically restrained, providing a braking action between the rotor and stator. This method of braking provides far superior operating characteristics such as smooth torque loading, long lifetime, high repeatability, good controllability, and less maintenance and downtime, making them the preferred choice for precise torque control in electric motor testing. Because the energy absorption through hysteresis loss is proportional to the rotating speed of the rotor, the break torque generated in the hysteresis brake dynamometer does not depend on speed. In fact, the dynamometer functions as a stable brake in the full motor ramp from the stopped state through the full rotating speed. Cooling of this type of dynamometer usually relies on either natural convection or forced convection (using

FIGURE 10.1
A motor is being tested by using hysteresis brake dynamometer.

fans or compressed air). Figure 10.1 shows a motor being tested using a hysteresis brake dynamometer.

- Eddy-current brake (absorption only)

  Eddy-current brake dynamometers produce braking torques using the principle of eddy currents induced in rotating metallic disks, which are immersed in magnetic fields. As demonstrated in Figure 10.2, when electrical current passes through coils around the disk, it generates a magnetic resistance to the rotation of the disk. The resistance load is controlled by changing the current. They are ideal for applications requiring high speeds and operating in the middle-to-high-power range. This type of dynamometer is capable of changing the load effectively at high speeds. The advantages of this type of dynamometer include low maintenance cost, precise control, simple construction, and desirable speed–torque characteristics.

- Electric motor/generator dynamometer (absorption or drive)

  Equipped with appropriate control units, electric motor/generator dynamometers can operate as either absorption or universal dynamometers, depending on applications. A motor/generator dynamometer typically uses an electric motor (either AC or DC) with its drive to simulate mechanical loads on the motor being tested. In a test, the motor under test is attached to the loading motor which acts as a generator. The main advantage of electric motor/generator dynamometers is that

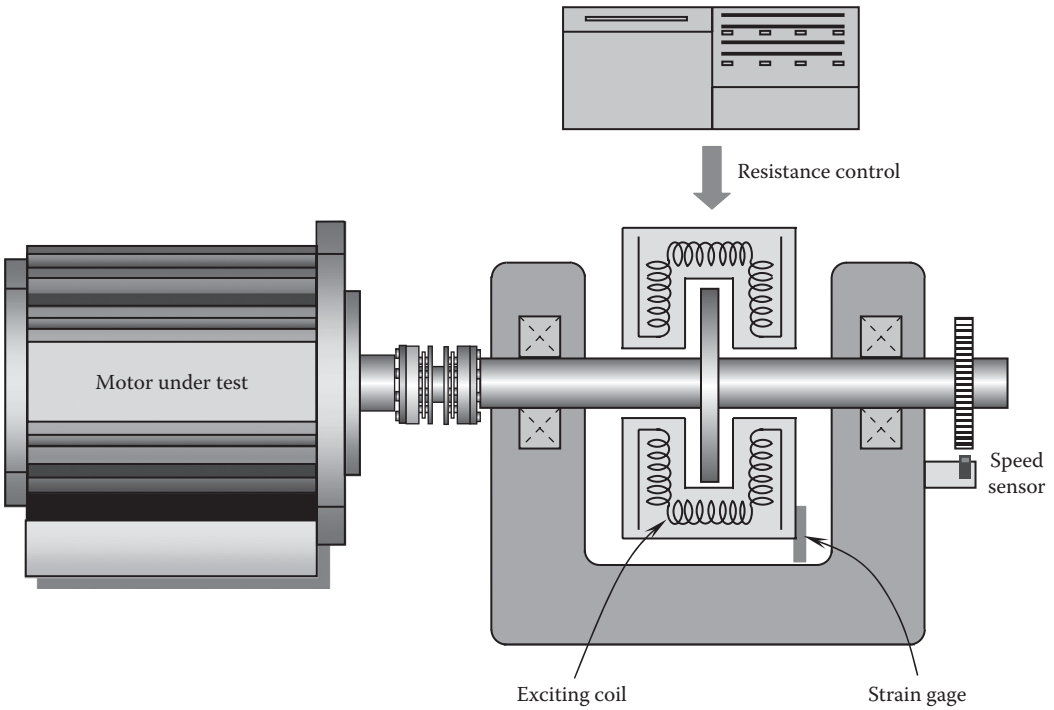

FIGURE 10.2
Eddy-current dynamometer used for motor testing, relying on eddy current generated in the rotating disk to provide resistant load to the tested motor.

they can adjust load in a large range within a very short time. However, electric motor/generator dynamometers are generally more expensive and complex than other types of dynamometers. A testing system is shown in Figure 10.3.

- Mechanical friction brake dynamometer (absorption only)

  Mechanical friction brake (Prony brake) dynamometers were invented by Gaspard de Prony in 1821. Using friction to load testing motors, this type of dynamometer is considered as one of the most simple, standard, and earliest absorbing dynamometers. Their advantages include ease of design, cost-effectiveness, simple maintenance, compactness, and high power absorption. However, due to the problems of brake torque control, as well as the rapid development in modern electronic control technologies, mechanical friction brake dynamometers are rarely used in motor labs today.

- Inertia brake dynamometer (absorption only)

  All brake types of dynamometers measure power from the torque reaction of the brake at a specific speed. An inertia brake dynamometer utilizes the test motor to accelerate a flywheel from a standing start-up through the motor speed range. This method involves measuring the change in the flywheel speed as the motor accelerates. The kinetic energy stored in the rotating flywheel is proportional to the square of the rotating speed. Thus, the flywheel has a significant amount of inertia to resist any change in speed. Today, inertia dynamometers become the standard test method for electric motors.

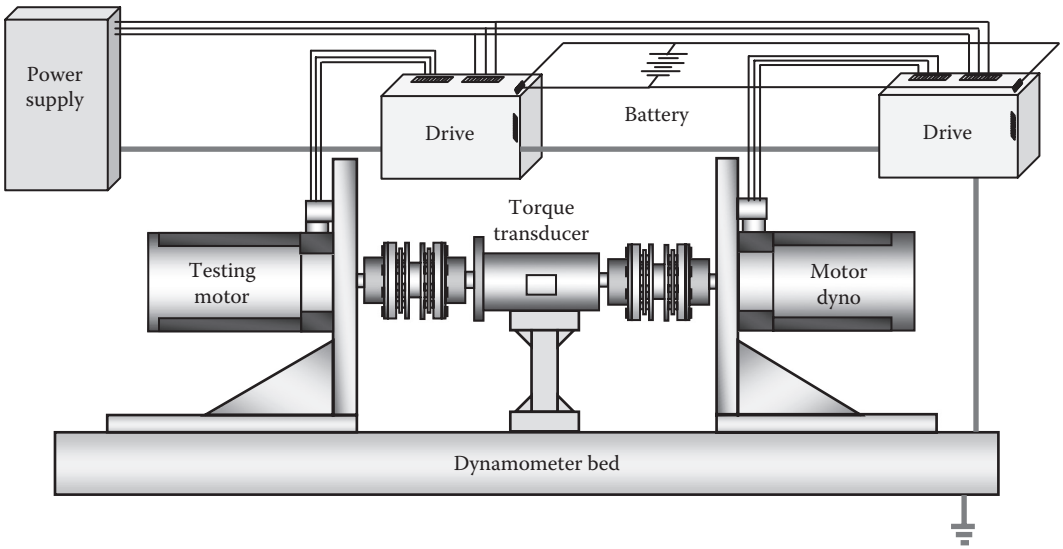

FIGURE 10.3
Motor testing system with the motor/generator dynamometer.

- Water brake dynamometer (absorption only)

  Water brake dynamometers utilize water flowing through absorbers to create loads on testing motors (Figure 10.4). This type of dynamometer is the most prevalent choice for applications that require high rotating speed, low inertia, high-power capacity and low cost. The loading on the motor being tested is dependent on the water flowrate through the brake. For their high-power capability, water brake dynamometers are commonly used in high-power, large-size motor testing. Unlike other types of dynamometer, water brake dynamometers eliminate the need for cooling and thermal overload protection systems and thus provide the most cost-effective solution for motor testing. However, using of this type of

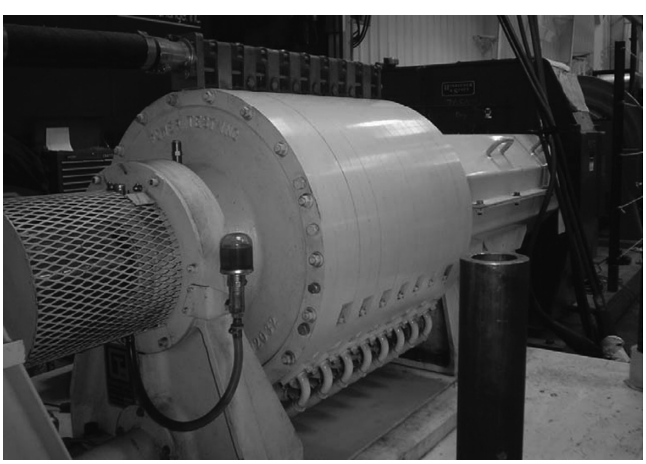

FIGURE 10.4
Water brake dynamometer for motor testing.

FIGURE 10.5
The motor being tested is driven by a water brake dynamometer.

dynamometer may take relatively long periods of time to reach the stabilized loading condition.

The testing system layout using a water brake dynamometer is shown in Figure 10.5. The motor is fixed on the test platform via steel chains and is connected with a torque transducer, which in turn is connected with the water brake dynamometer through a coupling.

- Hydraulic brake dynamometer (absorption only)

  Equipped with a hydraulic pump, a fluid reservoir, and a piping system, a hydraulic brake dynamometer provides braking drag against the motor being tested. This type of dynamometer can be used in a wide range of power. It is suitable to test extra-large motors with megawatts. Like water brake dynamometers, this type of dynamometer has no need for cooling systems.

- Chassis dynamometer (both absorption and drive)

  Chassis dynamometers are capable of very accurately measuring the speed, torque, and power. This type of dynamometer is widely used in the auto industry for performing engine tests. The typical loading modes used with a chassis dynamometer are constant force, constant speed, or a vehicle-simulation value. With the measured dynamometer shaft torque T_{dyno}, rotating speed ω_{dyno}, and the engine rotating speed ω_{eng}, the engine torque T_{eng} can be determined as [10.17]

$$T_{eng} = \frac{T_{dyno}\omega_{dyno}}{\omega_{eng}} \tag{10.2}$$

10.2.2 Thermocouples and Other Temperature Measuring Devices

Thermocouples are used to measure temperatures at different locations of the testing motor, as well as the ambient temperature. A thermal couple consists of a pair of wires, made of dissimilar thermoelectric materials. Because the two materials have different Seebeck coefficients, when the two wires are joined together at both ends, an electric potential is generated across the wire junctions. This electric potential is proportional

TABLE 10.1

Seebeck Coefficients for Various Thermocouple Types at 25°C

Thermocouple Type	Seebeck Coefficient (μV/°C)
E	61
J	52
K	41
N	27
R	9
S	6
T	41

to the temperature gradient across the wire junctions. Thus, an unknown temperature can be measured by placing one end of the wire junction (measurement junction) at the desired location and connecting the other end of the wire junction (reference junction) to a multimeter. The Seebeck coefficients for various thermocouple types are given in Table 10.1 [10.18].

For high-performance devices, the materials are typically *p*- and *n*-type semiconductors having positive and negative Seebeck coefficients, respectively. One end of the thermocouple analyzed here is connected by a metal tab. Metal tabs are also found at the other end of the thermocouple for external connections. Ceramic plates having high thermal conductivity are affixed at the ends of the thermocouple for heat spreading to ensure a uniform temperature at either end. The ceramic plates and metal interconnects are assumed to have different uniform temperatures at the top and bottom. Current density is also assumed to be constant over the areas of the junctions between different materials.

For most practical applications below 540°C, the use of resistance–temperature detectors (RTDs) is a good choice. RTDs use the principle that some materials (e.g., platinum) increase their electrical resistances with the increase of temperature. With very stable electrical properties, platinum exhibits a linear resistance–temperature relation over a wide range of temperature. This has made platinum to be the best material for RTDs. In fact, RTDs are more accurate and have better sensitivity and linearity than thermocouples. By correlating the resistance of an RTD to temperature, the RTD can be used to measure temperature precisely. However, RTDs require external power sources, have slower response time and narrower measuring range, and are more expensive compared with thermocouples.

Another alternative temperature measuring device is thermistor, which is a thermally sensitive resistor. Thermistor uses a semiconductor device to change its resistance. By comparing with thermocouples and RTDs, thermistors have the narrowest measuring range, lowest stability and linearity, highest sensitivity, and comparable accuracy and response time to thermocouples.

10.2.3 Control System

The control system in a dynamometer is one of the key elements to making stable operation of the dynamometer and getting accurate data. In motor testing, the precise control of rotating speed and torque of the dynamometer is required. This is achieved automatically through the digital dynamometer controller, which is integrated into the testing system.

An absorption dynamometer acts as a load that is driven by the prime motor that is under test. The dynamometer can be equipped with two types of control systems, that is, constant torque and constant speed, to provide different test conditions [10.19]. With a torque regulator, the dynamometer operates at a set torque, while the prime motor operates at any speed and develops the torque that has been set. Similarly, with a speed regulator, it develops whatever torque is necessary to force the prime motor to operate at the set speed.

10.2.4 Data Acquisition System

During motor testing, many parameters need to be measured and recorded, including voltage, current, power factor, rotating speed, rotating direction, torque, electrical power, mechanical power, efficiency, and switch cutout speed, to name a few. The testing facility should have the capability to deal with the majority of the requirements of the motors, and the architecture allows customized tests to be easily added.

Data acquisition systems are used to collect motor operation characteristic data in motor testing. A typical data acquisition system consists of (1) data acquisition hardware, (2) sensors (e.g., torque transducers) for measuring motor operation characteristic data, (3) signal conditioning hardware (e.g., filter), (4) control and data acquisition software, (5) analog-to-digital convertor, and (6) a computer controlling data acquisition software. Most dynamometers are equipped with a data acquisition system. In selecting a proper data acquisition system, high accuracy, fast processing speed, and high-channel-count capacity are the main factors to be considered.

10.2.5 Torque Transducer

During motor testing, motor torque can be measured by connecting the testing motor to the dynamometer through a torque transducer or torque sensor, as shown in Figure 10.6. Torque transducers fall into two categories of measurement [10.20]:

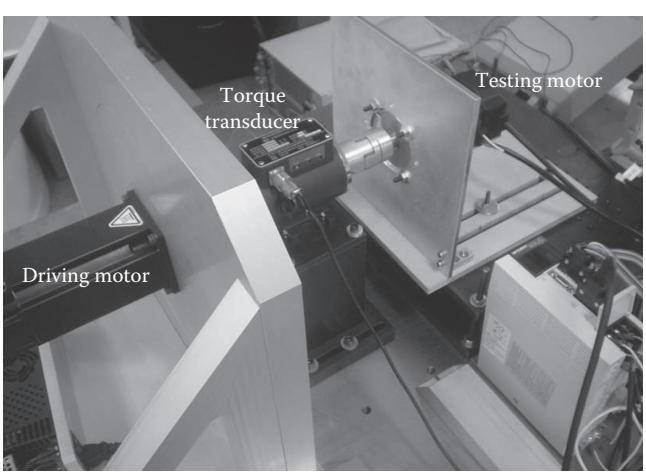

FIGURE 10.6
A torque transducer is placed between the testing motor and the driving motor.

- Reaction torque transducers. This type of transducers are nonrotating torque measuring devices and typically mounted in fixed positions. With no moving parts, reaction torque transducers offer long term reliability. They are suitable for a wide array of torque measurement applications including torsional testing machines, brake testing, bearing friction studies, and dynamometer testing.
- Rotary torque transducers. This type of transducers employs a freely rotating shaft within a fixed housing. When the shaft is torsionally stressed, a proportional change in the signal is observed. With the broad measurement range and high-precision measurement capabilities, rotary torque transducers are extensively used in motor testing, automotive engine testing, fan testing, and hydraulic pump testing. Torque-angle data obtained from motor testing are often used to draw torque-time or torque-angle plots that reveal the actual motor performance characteristics.

10.2.6 Power Supply

Power supply is a basic equipment in a motor test laboratory to provide the required power not only for the motor testing system and instruments but also for the control system for controlling the testing environment. It is widely accepted that the quality of power supply can significantly impact the motor efficiency. For instance, a phase unbalance of just 2% can increase losses by 25% [10.21]. Harmonics resulted from the voltage distortion can increase motor losses, produce vibration and noise, lower motor torque, induce torque pulsation, and result in motor overheating.

The power supply system must have a capability to provide a wide range of AC or DC voltage and current. In order to obtain accurate test results, the supply power, voltage, current, and frequency must be controlled within certain accuracies, defined by different standards (Table 10.2).

It can be seen that the requirements of IEEE Standard 112-B are significantly stricter than those of IEC 34-2. Furthermore, because harmonic distortion can increase steeply the losses of electric motors, the total harmonic distortion of the three-phase power supply should be limited within 1%. In cases that significant nonlinear loads are involved, harmonic filters may be required to reduce harmonic distortion.

10.2.7 Motor Testbed

Because testing motors come in a wide range of frame sizes, weights, loads, speeds, and power outputs, the motor testbed must be able to accommodate various testing motors,

TABLE 10.2

Accuracies of Power Supply

Item	Standard IEC 34-2 [10.13]	Standard IEEE 112 (Method B) [10.7]
Power (W)	±1.0%	±0.2%
Current (I)	±0.5%	±0.2%
Voltage (V)	±0.5%	±0.2%
Frequency (Hz)	±0.5%	±0.1%

especially large-scale motors. In order to reduce the impact of vibration on motor test, good vibrating damping materials such as cast iron are commonly used to construct motor testbeds. To firmly hold large testing motors on the testbed, T-shaped slots are usually made on the testbed. Small- and medium-sized motors can be directly installed on an L-shaped stand. During a motor testing process, a good alignment between the testing motor on the testbed and the dynamometer must be maintained.

10.3 Testing Load Level

There are a variety of methods to generate rotating torque loads to testing motors, such as the use of hysteresis brakes, eddy-current brakes, water brakes, and AC vector drives.

Motor performance test techniques generally fall into three categories: no-load, signature, and load tests. Each of these techniques contributes useful information to motor performance to a certain extent. However, each also has its limitation.

- No-load test

  As the simplest test technique, no-load test is also called *open-circuit test*, which is widely employed in the motor industry as one of the standard tests. During the testing, the rated voltage (balanced) and frequency are applied to the testing motor, and the motor shaft is uncoupled to any load. The resulting current, power, and speed are measured and compared to similar measured data made on a master motor. Therefore, this type of test requires less use of the test equipment and instrumentation. Three types of no-load test can be provided: disconnected, inferred no load, and measured no load. For no-load test, the motor torque is close to zero, and current is very small.

  According to IEEE Standard 112 [10.7], the measured input power in a no-load test is the total of the losses in the motor, including copper, friction, windage, and core losses. To determine the friction and windage losses, subtract the copper losses from the total loss (i.e., input power) at each of the test voltage points and plot the resulting power curve versus voltage, extending the curve to zero voltage. The intercept with the zero-voltage axis is the friction and windage losses. The core losses at each test voltage are obtained by subtracting the value of friction and windage losses from the input power minus copper losses.

- Load point test

  Many different load steps are programmed for motor testing, for instance, from 25% to 150% load levels. There are two test control modes: (1) speed mode in which a speed is established by the dynamometer and torque is produced based on the capability of the motor and (2) the torque mode in which a load is established by the dynamometer and speed is produced based on the capability of the motor. At each load level, the parameters that are measured include speed, torque, voltage, and current.

  In practice, the load tests are conducted at the load level of 25%, 50%, 75%, 100%, 125%, and 150%. Among these, the 100% load point is most commonly adopted. If the speed mode testing is used, the test speed is set at the rated speed. Similarly, for the load mode testing, the torque is set at the rated torque.

10.4 Testing Methods

There are a number of testing methods for electric machines. According to the testing setup, motor testing methods can be classified as [10.22]

- Mechanic differential testing method
- Back-to-back testing method
- Indirect loading testing (e.g., phantom, two-frequency, and inverse-driven) method
- Forward short-circuit testing method
- Variable inertia testing method
- Mixed-frequency testing method

Each of these testing methods has its own pros and cons. Among them, the most accurate and basic testing method is to directly load the testing motor either mechanically or electrically. Some of these testing methods are addressed in the following sections.

10.4.1 Mechanical Differential Testing Method

The mechanical differential method uses two identical motors, coupled with their main shafts through a differential cage. The two motors are connected to a common power supply in such a way that they rotate in opposite directions. As two motors rotate at the same speed, the differential cage remains stationary. If this cage is rotated, one of the motors accelerates and begins to act as a generator, while the other reduces its speed and commences to supply mechanical power to the generator through the differential gearbox. By adjusting the speed of rotation of the differential cage, it is possible to vary the loading of both motor and generator from no load to full load.

10.4.2 Back-to-Back Testing Method

This testing method also uses two motors that are not necessarily identical. This testing method has two distinct merits as the economy and the accuracy. In this method, the major part of the test power is circulated rather than dissipated, and the loss is measured as a net input rather than as the small difference between two separately measured large powers. As shown in Figure 10.7, the two motors are placed back to back each other and coupled to a floating gearbox. The two electric machines are powered from the same three-phase power supply. When they run at different speeds ω_1 and ω_2, respectively, the speed differences $(\omega_1 - \omega_2)$ can be adjusted by the floating gearbox [10.23]. A torque booster is mounted on the gearbox housing and arranged to boost the shaft rotation and to exert a reaction torque on the housing. The torque booster motor can drive either the input shaft, the output shaft, or the intermediate shafts. Thus, the power loss of the gearbox can be compensated by the torque booster to ensure that the torques on both sides of the gearbox are equal.

10.4.3 Indirect Loading Testing Method

Direct loading methods often suffer from high costs due to the complex coupling and loading mechanisms. To be able to conveniently perform heat run tests on electric motors

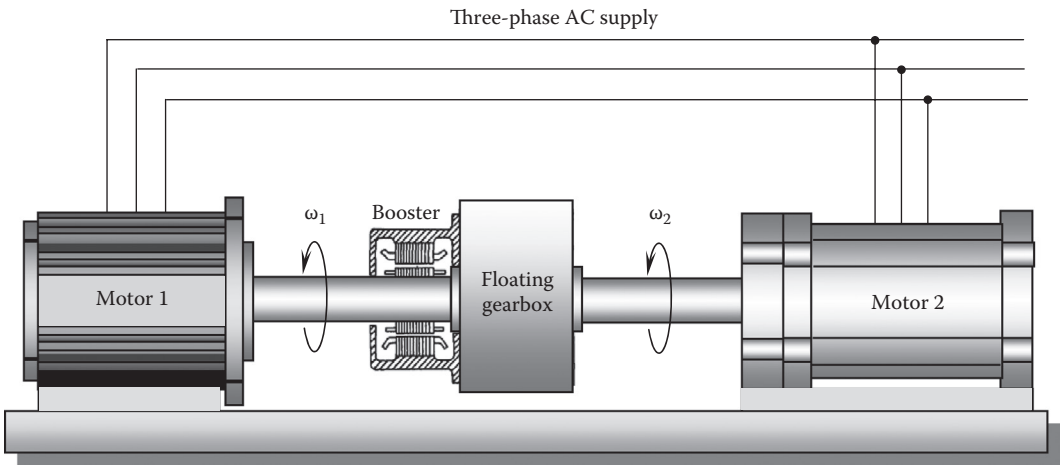

FIGURE 10.7
Back-to-back test using a floating gearbox.

with indirect loading is very important for motor manufacturers. Indirect loading schemes include phantom loading methods, two-frequency methods, and inverse-driven methods. In the phantom testing method, two identical motors are connected electrically together, with their losses supplied externally [10.24]. With indirect loading on the testing motors, no loading machine is required, nor have the test motors to be mechanically coupled. Experiments on electric machines have shown that the test simulates a true temperature run with a high degree of accuracy.

As shown in Figure 10.8, with the phantom loading method, the phase voltage of stator winding has both AC and DC components. Thus, the phase voltage of stator winding is the superimposition of DC and AC components:

$$v = \sqrt{2} v_1 \cos\left(2\pi f_1\right) + V_{DC} \tag{10.3}$$

where the magnitude of V_{DC} depends upon the connection pattern of the state winding on phantom loading.

Figure 10.8 depicts the phantom loading testing for two identical star-connected motors, without mechanical coupling between them [10.25]. Balanced three-phase voltages are applied parallelly on the star-connected stator windings of both the main and auxiliary motors. The DC current is injected into the windings in series, and a stationary DC field appears in the stator–rotor air gap. Thus, both AC and DC circuits are symmetric with respect to the AC and DC power supply, respectively. In such a configuration, the AC and DC sources can feed the two star-connected circuits at the same time. However, this configuration requires that the voltage supply is $\sqrt{3}$ times higher than the normal value if the motors are connected in delta, as often encountered in industrial applications.

Most industrial-sized IMs are connected in a delta connection, as shown in Figure 10.9 [10.26]. It can be seen from this figure how the DC loading current is injected into the windings of a delta-connected motor. The three-phase AC power supply is applied on the main motor and the auxiliary motors in a parallel manner. Three resistors R are inserted into the supply source to prevent the DC current from straying into the supply sources.

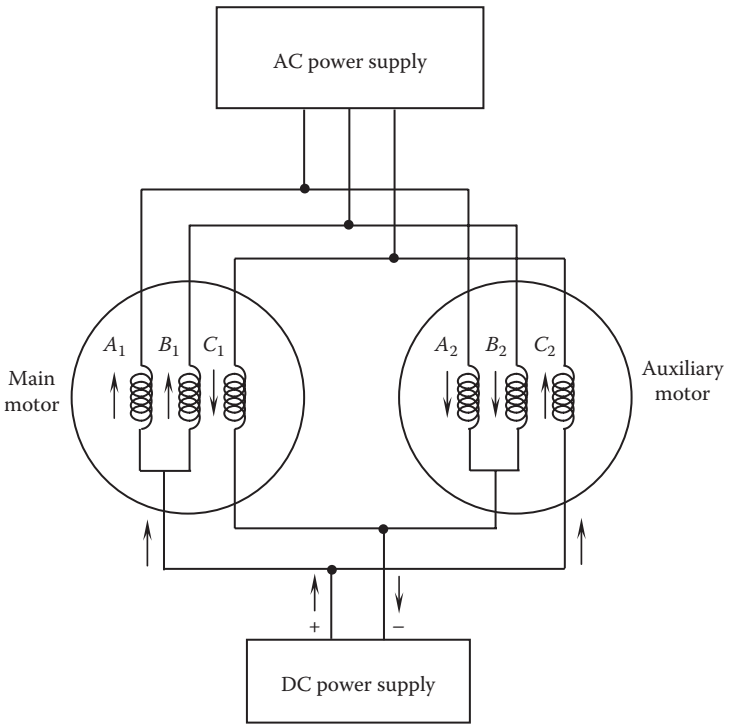

FIGURE 10.8
Phantom loading with star-connected stator windings.

The capacitor *C* is connected in parallel with the DC source to provide a path for the AC to feed into the auxiliary motor. Switch *S* should be closed during the starting process. The effective RMS values of the combined AC and DC currents flowing in each of the three-phase windings with such phantom loading method should be equal to the rated RMS currents in the motor windings [10.27].

The use of the two-frequency testing method may be traced back to the 1920s, when Ytterberg proposed a concept of connecting two voltage suppliers at different frequencies in series to produce synthetic loading of induction machine [10.28,10.29]. This method is generally known today as the two-frequency or dual-frequency method.

There are two possible loading schematics available in the two-frequency method, as presented in Figure 10.10. In each method, the main voltage v_1 has a rated frequency f_1, and the auxiliary voltage v_2 has a lower frequency f_2, where $f_2 = (0.60 - 0.95)\, f_1$. The magnitude of the auxiliary voltage v_2 is about 5%–25% of the main voltage f_1. Hence, the voltage at the stator winding becomes

$$v = \sqrt{2} v_1 \cos\left(2\pi f_1\right) + \sqrt{2} v_2 \cos\left(2\pi f_2\right) \tag{10.4}$$

Therefore, the IM draws motoring current with respect to the higher-speed field and supplies generating current with respect to the lower-speed field. The two currents beat together to form a modulated current, which is made equivalent to the normal load current for the motor [10.30].

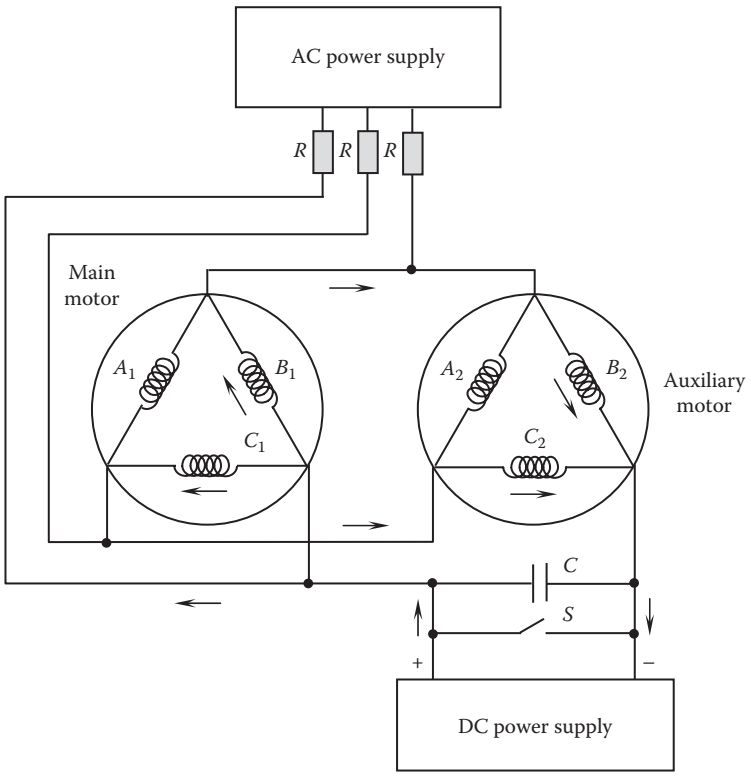

FIGURE 10.9
Phantom loading with delta-connected stator windings.

It is noted that during the testing process, the two induction machines are only coupled electrically together without mechanical shaft coupling. In this arrangement, the electromagnetic torque oscillates at the frequency of $(f_1 - f_2)$. Such oscillations may cause serious problems in vertically mounted motors [10.31]. Essentially, two induction machines operate concurrently as motors and generators.

An inverter-driven method uses a microprocessor or a digital signal processor (DSP) to generate the necessary logical control signals for PMW inverters to continually accelerate and decelerate the induction machine (Figure 10.11). The use of the power electronic inverter allows comprehensive control over all the quantities that determine the rate at which the power is dissipated inside the induction machine.

10.4.4 Forward Short-Circuit Testing Method

This testing method is an alternate loading method that manufacturers could employ with a minimum capital expenditure, especially suitable for testing ultra-large electric motors with outputs greater than 1 MW [10.32]. This conventional indirect loading method has been applied by a leading motor manufacturer for more than a half century. In this method, the motor under testing is fed with a variable frequency power supply or an alternator and is driven at the rated speed by a DC motor. The speed

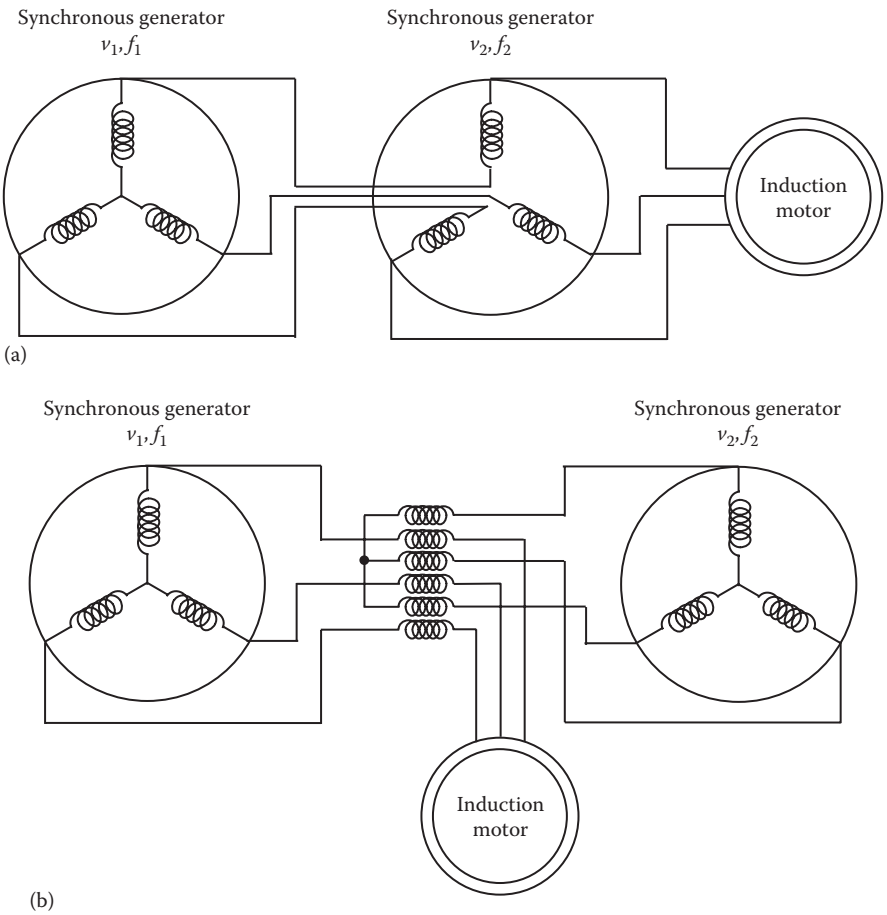

FIGURE 10.10
Two possible two-frequency loading methods.

difference between the test machine and the alternator can be correlated by adjusting the excitation of the alternator. The forward short-circuit testing method is given in Figure 10.12.

10.4.5 Variable Inertia Testing Method

Full-load temperature-rise testing of induction motors can be done by using the variable inertia testing method. This method, as a pure mechanical method in nature, is to load a test machine shaft directly with a flywheel (called "free-running inertia") and does not need to connect electrically the test machine to any other machines.

In a variable inertia testing, the testing motor is connected to the flywheel through a gearbox. This gearbox has a nonconstant speed ratio that causes the inertia referred to the motor shaft to vary smoothly with the shaft rotation angle. The inertia variation results in the change in the shaft torque and in turn the change in the rotor speed [10.33].

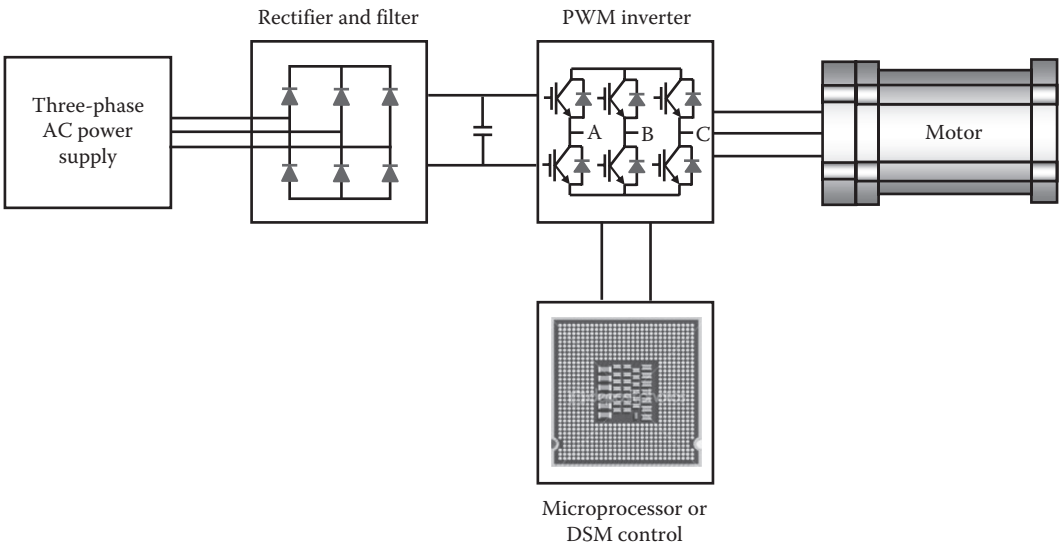

FIGURE 10.11
Block diagram of inverter-driven method.

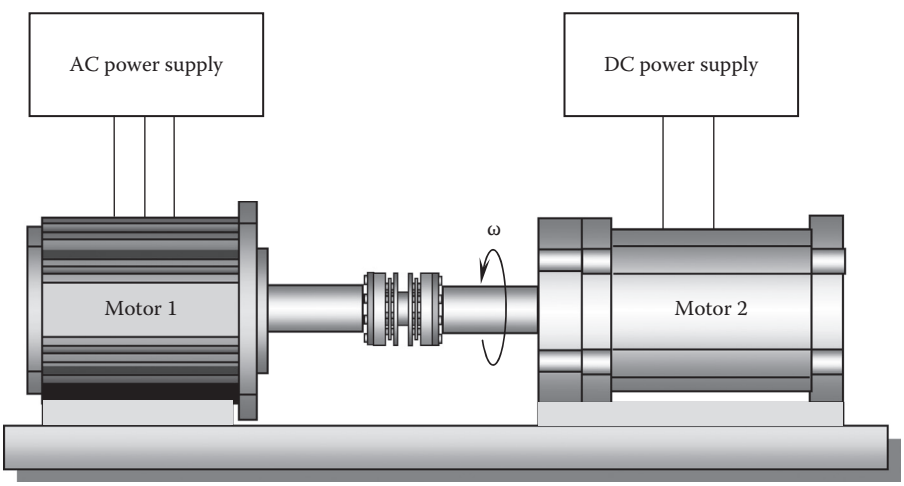

FIGURE 10.12
Forward short-circuit testing method.

10.5 Off-Line Motor Testing

Off-line testing, or static testing, is a well-known means to comprehensively test electric motors. This testing method measures the integrity of the insulation and finds stator winding faults before they become catastrophic failures. A complete set of off-line tests

include winding resistance test, megohm test, PI or dielectric absorption, step-voltage or high-potential (hipot) test, and surge test [10.34]. Off-line testing is also used as a quality assurance tool.

10.5.1 Winding Electrical Resistance Testing

Electrical resistance testing involves the measurements of individual coil resistance and phase resistance using ohmmeters. For a three-phase motor, measured phase electrical resistance data (i.e., U-V, V-W, and W-U) should be well within 5% of each other. For large-size motors, the phase resistance imbalances can be much lower. Variations between phases larger than the tolerance range for resistance are not allowed for any machine. As an example, the measured electrical resistance data of two large-size motors are shown in Table 10.3.

By taking a resistance reading of each phase, high-resistance connection can be identified. If there is a resistive imbalance exceeding a predetermined level, it can be caused by the circuit and/or the windings. In many cases, a high-resistance connection results from a solder joint between coils. Otherwise, an abnormal winding must be replaced.

10.5.2 Megohm Testing

Megohm testing, or insulation resistance testing, is to measure stator winding insulation resistance. This can help detect deteriorating insulation where the windings may potentially short to the ground. Megohm tests are usually conducted at constant DC voltages of 500–10,000 V, according to the motor's rated voltage. Readings of insulation resistance are taken after the DC voltage has been applied on the motor windings for at least 1 min. In a megohm test, the motor housing must be grounded for the safety consideration.

The insulation resistance of electric machine windings strongly depends on the insulation materials and the surface condition of the material. Generally, the insulation resistance varies proportionally with the insulation thickness and inversely with conductor surface area and temperature. Low megohm values are an indication of impending failure. However, high megohm values do not insure a good motor. Performing a PI testing can further help determine poor insulation systems. It is recommended by IEEE 43-2000 [10.1] that (1) for most machines with random-wound stator windings and form-wound windings rated below 1 kV, the minimum insulation resistance is 5 M-Ω; (2) for most DC armature and AC windings built after about 1970 (form-wound coils) it is 100 M-Ω; and (3) for most windings made before about 1970 (all field windings) it is (kV + 1) M-Ω,

TABLE 10.3

Measured Electrical Resistances from Two Large-Size Motors

Phase-to-Phase	Electrical Resistance (Ω)	Phase Resistance Unbalance (%)
U1-V1	0.02488	<0.5
V1-W1	0.02487	
W1-U1	0.02476	
U2-V2	0.02477	<0.2
V2-W2	0.02480	
W2-U2	0.02481	

where kV is the rated machine terminal-to-terminal voltage. It should be noted that all measured insulation resistances must be corrected to the temperature of 40°C. To get accurate measurements, the testing winding must be clean and free of moisture, and the winding temperature stable.

The electrical resistance R of a material is proportional to the resistivity of the material ρ (in Ω-m) and the material length l (in m) and inversely proportional to the cross-sectional area of the material A (in m^2), that is,

$$R = \frac{\rho l}{A} \tag{10.5}$$

where ρ is a function of temperature T,

$$\rho(T) = \rho_o(T_o)\left[1 + \alpha\left(T - T_o\right)\right] \tag{10.6}$$

where
α is the temperature coefficient of resistance of the material
T_o is the reference temperature

Substituting Equation 10.6 into Equation 10.5, it yields

$$R(T) = \frac{l}{A}\rho_o(T_o)\left[1 + \alpha\left(T - T_o\right)\right] = R_o(T_o)\left[1 + \alpha\left(T - T_o\right)\right] \tag{10.7}$$

Thus, a measured resistance R_m at an arbitrary measuring temperature T_m can be converted into the resistance at the reference temperature, for example, $T_o = 40°C$:

$$R\left(T = 40°C\right) = \frac{R_m(T_m)}{1 - \alpha\left(T_m - 40°C\right)} \tag{10.8}$$

This method can be useful in comparing the measured resistances of various materials at different measuring temperatures.

10.5.3 Polarization Index Testing

The purpose of polarization index (PI) testing is to determine the condition of motor insulation. In fact, the PI testing measures the time required for molecules of insulation to align (i.e., polarize) from their random orientation to resist the flow of current. According to IEEE Standard 43-2000 [10.1], the PI is normally defined as the ratio of 10 min insulation resistance to the 1 min insulation resistance. This PI ratio provides an indication of the condition of the winding. As recommended by IEEE 43-2000, the minimum value of PI is 1.5 for the thermal class A and 2.0 for the classes B, F, and H.

The winding surface condition can significantly affect the insulation resistance or PI. For instance, carbon dust or other contaminations on winding insulation surfaces may become partially conductive when exposed to moisture or oil and thus can markedly lower the insulation resistance or PI. Lower PI values indicate that the winding insulation may be damaged or influenced by contamination (e.g., dust and moisture) or/and embrittlement.

10.5.4 High-Potential Testing

The objective of the hipot testing is to verify the dielectric voltage withstand of motor insulation system. It applies a very high DC voltage to the test components (e.g., stator and motor) to measure overall insulation resistance to ground. The results provide very useful information on insulation dielectric strength. Today, this test is mandated to protect users from electric shock, fire, or smoke damage.

It is recommended by IEEE Standard 95-2002 [10.4] that the maximum test voltage is double the motor's rated voltage plus 1000 V. At the beginning of the test, the motor frame is grounded first, and a DC voltage is applied on the insulation system with slow increase in step increments until reaching the maximum test voltage. This operation avoids an electric shock on the insulation system. During the process, the leakage current data are recorded and plotted against the corresponding DC voltages on the computer monitor.

10.5.5 Surge Testing

It is reported that copper-to-copper faults are the main cause of over 80% of all winding-related failures [10.35]. During manufacturing processes, winding insulations may be damaged from bending, twining, or wrapping. The aim of winding insulation surge testing is to detect faults in turn-to-turn, coil-to-coil, and phase-to-phase insulations that cannot be discovered by other testing methods (e.g., megohm or hipot testing). Using this technique as a preventative maintenance tool, the damaged windings can be repaired or replaced to avoid motor failure in applications, as well as caused emergency outage.

Surge testing applies very short high-voltage pulses to test electric winding and their insulation. The test is performed when all windings are installed into a motor but before they are connected to each other. This test is the most effective method of insuring integrity of the copper-to-copper insulations and diagnosing actual shorted conditions between turns, coils, and phases. With an oscilloscope, some winding insulation faults, such as insulation weakness, incipient faults, and other winding problems become visible on the oscilloscope screen.

Prior to surge testing, a number of measurements must be performed on the motor with acceptable results, including winding resistance, stator winding insulation, and PI measurements.

Surge testing has been known as surge comparison testing for a long time because insulation defects have been detected by comparing the waveforms from different phases of winding. While performing a surge comparison test, each phase of stator winding is tested against the others. Because all windings are assumed to be identical, the waveforms of the windings must coincide. Otherwise, there are some insulation issues in the winding. However, with today's advanced high-speed and high-accuracy measuring devices and computer systems, surge comparison is no longer necessary. Weak insulation can be diagnosed from frequency shifts and compared to successive waveforms within one phase [10.36]. Today, surge comparison testing is still used by some motor manufacturers.

In cases that there is a turn-to-turn short, the waveforms observed during testing exhibit distinct patterns on the display of the instrument. As a coil with weak insulation undergoes a surge test, the voltage applied on the coil can jump across the weak insulation, causing the shift of the waveform, as shown in Figure 10.13.

In a motor lab test, the surge testing is conducted with the rotor removed. But in a field testing, surge testing is performed with rotor installed.

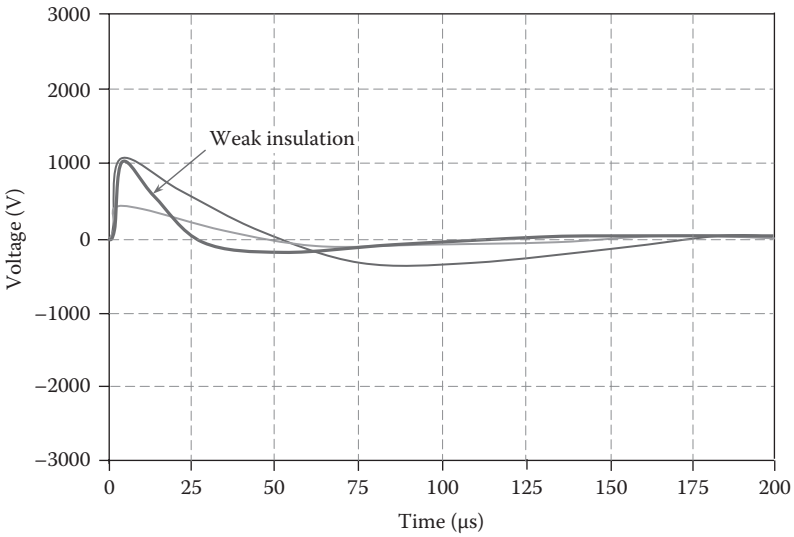

FIGURE 10.13
Surge test results. Waveform shift as an indication of weak insulation.

10.5.6 Step-Voltage Testing

Step-voltage testing is designed to provide an additional evaluation of the motor winding insulation. Usually, step-voltage testing follows a successful PI testing. Actually, it is similar to the PI test but more extensive because a number of measurements are taken at various voltage step levels. The test is necessary to ensure that the winding insulation can withstand the normal voltage spikes during operation. However, step-voltage testing is not suitable for low-capacitance machines.

As shown in Figure 10.14, as the test progresses, a DC voltage is applied to all three phases of the winding and raised slowly to a preprogrammed voltage step level and held for a period of time. Then, it is raised to the next voltage step and held for a period of time. This process continues until the desired test voltage is reached. Typically, the steps in the test are made at 1 min intervals. The voltage interval is determined by dividing the maximum voltage with the number of steps. For small or middle motors, the voltage interval can be 500 V or 1000 V.

At each voltage step level, the leakage current is monitored and plotted graphically against time. From the figure, it can be seen that for stable insulation, the leakage current exhibits nearly a linear pattern with time. A highly nonlinear behavior or abnormal increase in leakage current may be indicative of insulation issues.

10.5.7 Determination of Rotor's Moment of Inertia

There are several experimental methods to determine the rotor moment of inertia. The traditional process for estimating the rotor moment of inertia involves operating a motor through an acceleration/deceleration profile [10.37].

In a motor test, for determining the moment of inertia of the rotor and its load, three torques, that is, the motor torque T_m, the load torque T_L, and the acceleration torque T_a (or deceleration torque T_d), vary with time during acceleration (or deceleration), as demonstrated in Figure 10.15. The relationships of these torque components are given as

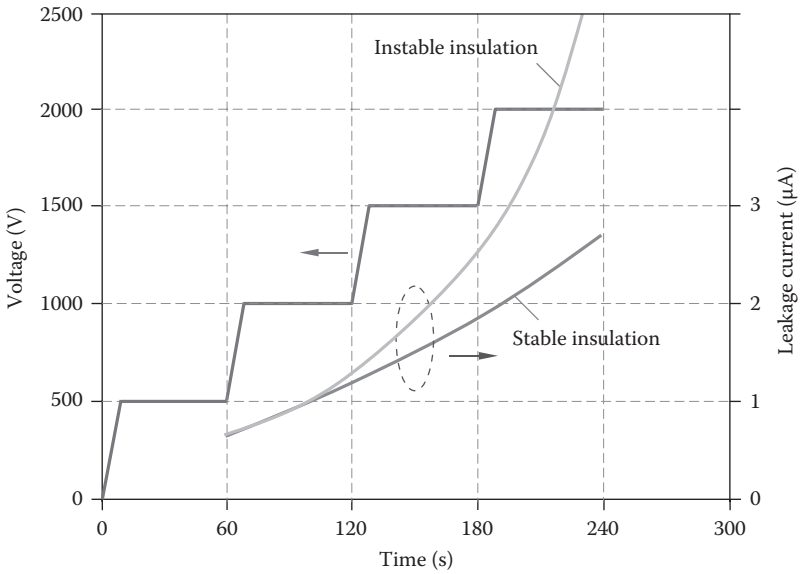

FIGURE 10.14
Step-voltage testing procedure.

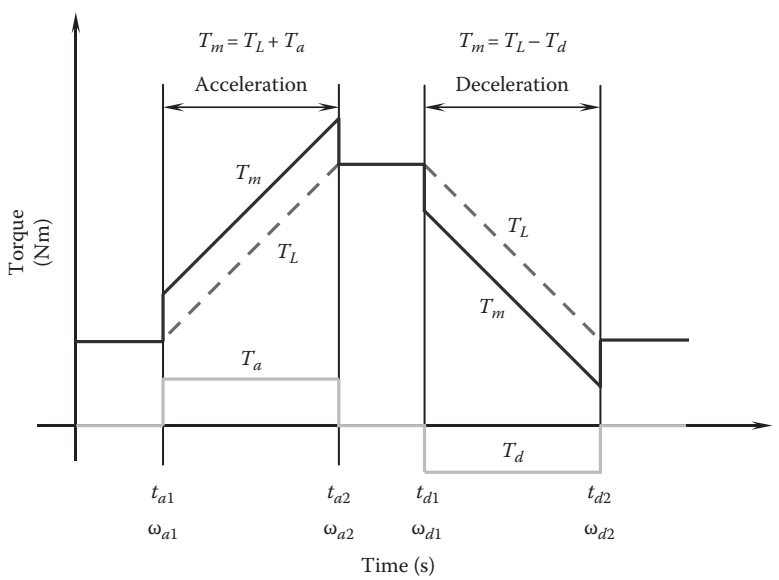

FIGURE 10.15
Relationships of motor torque, load torque, acceleration torque, and deceleration torque during the acceleration and deceleration processes in a test for determining the inertia of the test motor and load.

$$T_m = T_L + T_a \quad \text{during acceleration} \tag{10.9a}$$

$$T_m = T_L - T_d \quad \text{during deceleration} \tag{10.9b}$$

It is noted that the electric motor accelerates or decelerates in a linear manner. The acceleration torque T_a and the deceleration torque T_d are constant during the acceleration and deceleration processes. Then the rotor moment of inertia can be calculated by either of the following equations:

$$I\frac{d\omega}{dt} = T_m - T_L = T_a \quad \text{in the acceleration process} \tag{10.10a}$$

$$I\frac{d\omega}{dt} = T_m - T_L = -T_d \quad \text{in the deceleration process} \tag{10.10b}$$

Integrating both sides of the above equations corresponding to their time and angular intervals, the moment of inertia can be easily obtained. Assuming that the velocity difference in the acceleration process $\Delta\omega_a$ is equal to the velocity difference in the deceleration process $\Delta\omega_d$, that is, $|\Delta\omega_a| = |\Delta\omega_d| = \Delta\omega$, the averaged I value is given by the following equation [10.38]:

$$I = \frac{1}{2}\left[\frac{\int_{t_{a1}}^{t_{a2}} (T_m - T_L)\,dt}{\Delta\omega} + \frac{\int_{t_{d1}}^{t_{d2}} (T_m - T_L)\,dt}{-\Delta\omega}\right] \tag{10.11}$$

Rehm and Golownia [10.39] proposed a method to accelerate and decelerate a testing motor in a nonlinear manner. During acceleration and deceleration processes, the torque produced by the electric motor is sampled periodically, and the averaged torque during the acceleration/deceleration process is calculated by dividing the summation of all measure torque values with the number of torque samples. The rate of acceleration/deceleration is also determined. Therefore, the inertia (in unit of kg-m^2) of the rotor and the load connected to the motor is calculated as

$$I = \frac{\left|\frac{1}{N_a}\sum_{i=1}^{N_a} T_{a,i}\right| + \left|\frac{1}{N_d}\sum_{j=1}^{N_d} T_{d,j}\right|}{\left|\frac{\Delta\omega_a}{t_a}\right| + \left|\frac{\Delta\omega_d}{t_d}\right|} \tag{10.12}$$

where

$T_{a,i}$ is the ith torque sample acquired during the motor acceleration process
$T_{d,j}$ is jth torque sample acquired during the motor deceleration process
N_a and N_d are the numbers of torque samples corresponding to acceleration and deceleration, respectively
ω_a and ω_d are the rotating speed changes in the unit of rad/s during acceleration and deceleration, respectively
t_a and t_d are the acceleration time and deceleration time, respectively

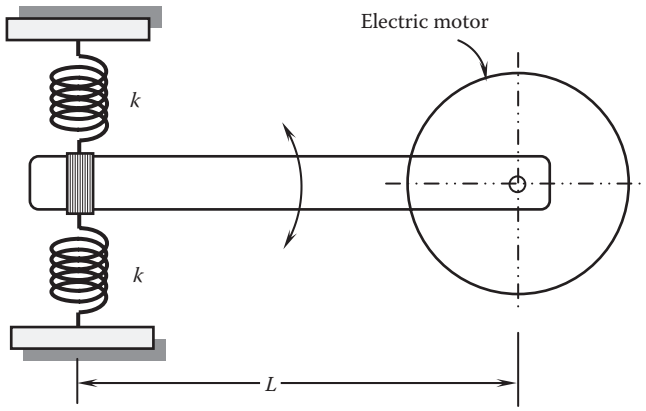

FIGURE 10.16
Oscillation test setup for measuring rotor moment of inertia.

Another effective method is called the oscillation method. To get an oscillating motion about the rotation point of the electric motor, a lever is attached to the rotor. On the end of the lever, an elastic spring with stiffness k is fixed on it. By measuring the period of time T of an oscillation, the moment of inertia can be calculated as [10.40]

$$I = \frac{kT^2}{4\pi^2}\left(1-\zeta^2\right) \tag{10.13}$$

where ζ is the damping ratio. It is noted that Equation 10.12 is valid for one spring. When two springs are used to fix on the end of the lever in opposite direction, with the distance L from the springs to the rotation point (see Figure 10.16), the equation for calculating I becomes

$$I = \frac{2kT^2L^2}{4\pi^2}\left(1-\zeta^2\right) \tag{10.14}$$

10.6 Online Motor Testing

Online testing or dynamic testing, as its name implies, is referred to the condition that power is supplied to motor for operation. Online testing is usually designed to evaluate the dynamic performance and operating characteristics of the entire motor. Therefore, online testing differs from offline testing in many aspects such as testing technologies and diagnostic methods.

10.6.1 Locked Rotor Testing

Locked rotor tests are used to determine the starting torque and current of electric motors, which are the two main indicators for assessing motor performance. In this

testing method, the testing motor is loaded to the maximum limits by applying maximum current to a hysteresis or powder brake type of dynamometer or by mechanically holding the rotor shaft from turning and energizing the stator. The voltage supplied to the stator is reduced to prevent stator winding overheating. At the rotor-locking condition, the motor operation parameters such as torque, current, and voltage are measured and displayed. Sometimes, locked rotor test is also called stalled torque test or blocked rotor test.

Locked rotor testing is very important for ensuring that the tested motor has sufficient torque to accelerate the motor when driving a specific load. If the motor cannot produce enough torque to overcome the friction in the load, the motor can be energized, but it will not drive the load. The test data can reflect the rationality of the magnetic circuit in the stator and rotor. Based on the test results, engineers can optimize the design and improve the production process.

However, this test is very hard on the motor. During testing, there is a large amount of current that flows into the motor, causing the motor to heat up rapidly. As a result, this test must be performed very quickly. With the locked rotor, a motor may draw up to six to eight times its rated current. The power supply used must be capable of regulating the motor voltage adequately during rapid changes in current to ensure the proper voltage is maintained when the data are being taken.

10.6.2 Motor Heat Run Testing

Motor heat run testing is sometimes known as motor continuous performance testing. This testing is extremely important to both motor manufacturers and end users. It was estimated that for every 10°C increase in temperature, the winding insulation life is reduced by half [10.41]. Exceeding temperatures can cause PM demagnetization and thermal aging of insulation materials.

The results of heat run tests are critical for verifying the engineering design and analysis and optimizing the motor design. More specifically, heat run tests can determine the maximum operating temperature of the tested motor and confirm that the maximum operating temperature is lower than the highest allowable temperature, which is defined by the motor insulation class based on an average 20,000 h lifetime.

A sustained heat run test is carried out at motor's full load. During the testing process, the temperature of the motor increases exponentially as various power losses are generated in the motor and converted into heat to dissipate to the environment. After a period of time, the motor reaches the thermal equilibrium condition, and the motor temperature tends to be constant. The time taken to reach equilibrium can vary widely depending on the machine size, cooling method, motor power losses, operation conditions, and ambient temperature. To obtain the temperature distribution of the motor, the temperatures of various motor components such as stator windings, bearings, PM, frame, endbells, encoder, and inlet and exit coolant, just to name a few, are measured and recorded. Temperatures on the rotating components (e.g., the shaft temperature at the shaft seal) can be conveniently measured using a thermal camera.

Ambient temperature T_a is the temperature of the air surrounding the motor. For most motor manufacturers, this temperature is defined at 40°C in their product catalogs. This does not mean the ambient temperature is set at 40°C during a heat run test. As a matter of fact, the ambient temperature in a test is controlled to maintain relatively constant at any given temperature.

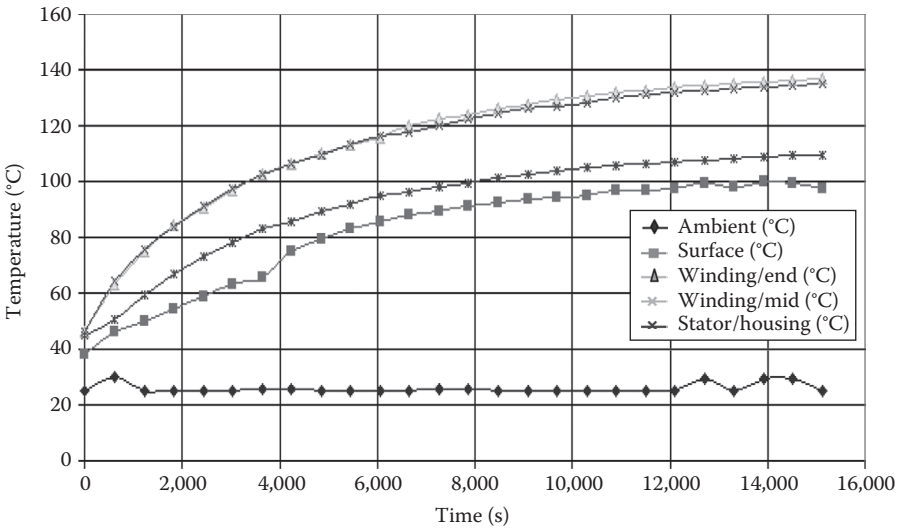

FIGURE 10.17
Results of heat run test for a servomotor at 2500 rpm and 45 N-m torque.

The temperature rise of a motor is the change in motor temperature with respect to the ambient temperature when power is applied to the motor. Obviously, the higher the ambient temperature, the lower the temperature rise of a motor. For instance, class B insulation is rated for a maximum operating temperature of 130°C. When the ambient temperature is 40°C, the allowable motor temperature rise is 90°C. As the ambient temperature becomes 50°C, the temperature rise reduces to 80°C. By considering the effect of hot spots occurring in motor windings, a 10°C hot-spot allowance is subtracted from the allowable temperature rise for the safety consideration. Thus, for $T_a = 40$°C, the allowable temperature rise for class B insulation in the earlier example becomes 80°C rather than 90°C.

As an example, the results of a heat run test for a servomotor at 2500 rpm and 45 N-m torque are provided in Figure 10.17. It shows that it takes about 4.2 h to reach thermal equilibrium. While the temperatures of stator windings at the middle and end turns approach 140°C, the temperatures of motor housing reach 110°C. The ambient temperature is controlled to maintain in the range of 25°C–30°C.

For large-size motors, the time for reaching thermal equilibrium can be very long, up to more than 10 h. For these cases, performing heat run testing continuously can save a tremendous heating time and testing resources. As shown in Figure 10.18, when the first heat run completes, the motor temperature drops sharply. As the motor temperature becomes lower than the expected thermal equilibrium temperature, the second heat run test starts immediately. It can be seen from the figure that the heating time of the second test is only one-third of the first one.

10.6.3 Motor Efficiency Testing

The aim of motor efficiency testing is to determine the motor characteristic performance. Motor efficiency is one of the most important characteristic parameters for users and manufacturers. This parameter measures how effectively electrical energy is converted

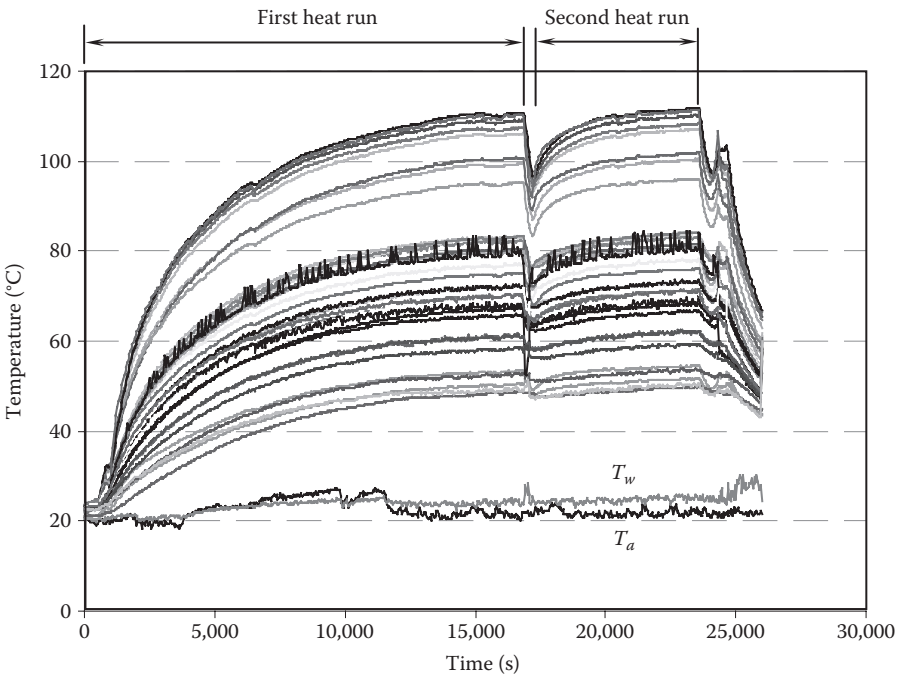

FIGURE 10.18
Thermal testing is performed at the rated speed and rated torque until thermal equilibrium is achieved. The testing data show that the successive test significantly reduces the motor heating time.

into mechanical energy by a motor. A number of factors that may affect the overall motor efficiency include power supply quality, motor size, various power losses, the transmission and mechanical components, maintenance, and mismatch of the load to motor inertia.

Motor efficiency can be measured either directly or indirectly. Usually, direct measuring methods can provide accurate results but often require high-priced instruments/equipment and long test setup time. By definition, motor efficiency is the ratio of mechanical power output P_{out} over electrical power input P_{in}:

$$\eta = \frac{P_{out}}{P_{in}} \tag{10.15}$$

As an example, the mechanical output for an IM is the production of the motor torque and rotating speed, that is,

$$P_{out} = T\omega = T\omega_s(1-s) \tag{10.16}$$

where
- s is the slip rate
- ω and ω_s are the rotating shaft speed and rotating synchronous speed in rad/s, respectively

For a PM motor, $s = 0$.

The electrical power input can be easily measured with good accuracy. The measurement of rotating speed is relatively simple and straightforward, with an achievable accuracy of ±1 rpm. The torque measurement is obtained using a highly accurate torque transducer.

The indirect way of determining the motor efficiency involves the measurement of various power losses of the motor. The motor efficiency can be alternatively expressed as

$$\eta = \frac{P_{in} - \sum P_{loss}}{P_{in}} = \frac{P_{out}}{P_{out} + \sum P_{loss}} \tag{10.17}$$

Most of these losses such as copper, core, windage, and fraction losses can be determined using no-load and load tests. However, stray load losses, which consist of miscellaneous losses except for major power losses, are hard to be directly measured. These losses may be estimated using some correlations from the literature or standards. For instance, the stray losses can be estimated using IEEE Standard 112-2004, which gives the percentage of stray losses to the rated load as 1.8% for the motor rating 1–90 kW, 1.5% for 91–375 kW, 1.2% for 376–1850 kW, and 0.9% for >1850 kW.

The test procedure is defined by the IEEE Standard 112-2004, which estimates the motor efficiency by the direct method [10.7]. As a contrast, IEC 34-2 Standard [10.13] estimates the motor efficiency using the indirect method. In fact, the indirect method has a significant degree of uncertainty, because of the instrumentation lower-accuracy specifications and the incorrect winding losses in relation to the temperature [10.42].

To avoid loading shock, the motor load maintains low levels and increases in small increments. Motor performance testing is conducted when a motor operates under normal environmental conditions.

10.6.4 Impulse Testing

Statistical data show that insulation faults are accounted for about a quarter to one-third of motor failures. The breakdown of insulating materials of motor winding can directly lead to short-circuit faults. Most stator failures often begin as turn-to-turn shorts caused by steep-fronted surges due to switching. These turn-to-turn shorts eventually develop into catastrophic copper-ground or phase–phase fault.

Impulse testing is performed by applying defined impulse voltage waveforms on the motor windings to assume lighting strike. The waveform shape, peak voltage, impedance, and application of the pulse vary and depend on the characteristics of the test motors. The purposes of the impulse test as special test are (1) to confirm the withstand of the motor's insulation against excessive voltages occurring during impulse testing and (2) to detect the weak insulation in the motor windings. In motor manufacturing, the on–off impulse voltage is normally generated by charging and discharging a capacitor in the motor windings. This steep-fronted voltage sets up a nonlinear voltage distribution that creates a turn-to-turn differential voltage and results in an oscillation between motor's inductance, capacitance, and resistance.

10.6.5 Cogging Torque Testing

Most applications of electric motors require smooth operation and constant torque. The examples include engraving machines, telescopes, nuclear magnetic resonance (NMR), and

optical instruments, just to name a few. Any pulsating torque can have a significant negative impact on the motor performance characteristics in these applications. Furthermore, cogging torque causes acoustic noise and vibration, as well as torque and speed ripples. As a result, it is highly desired to control the cogging torque to a lower level, say, less than 1% of the rated torque.

Cogging torque in a PM motor is generated from the interaction of the rotor-mounted PMs and the stator slots. Cogging measurement can be performed by either static (e.g., leverage measuring method), quasistatic, or dynamic methods. In most practical cases, the dynamic measurement method is adopted to determine cogging torque. With this method, the motor being tested has no input current and is driven by a dynamometer or motor. A torque transducer is installed between the tested motor and the dynamometer to measure the cogging torque produced with an oscilloscope. In practice, each type of motor uses different ways to measure the position of the machine being tested such as encoder, resolver, proximity sensor, and sensor bearing.

The diagram of a dynamic cogging torque measurement system is given in Figure 10.19. An electric motor is employed as the driving element. A torque transducer is placed between the motor being tested and the driving motor to detect the torque from the strain in the shaft. During the test, there is no input current to the motor being tested. The driving motor is controlled by a motor drive. In this case, the encoder is installed on the motor being tested to measure the rotor position.

It is noted that the measured torque contains the cogging torque of the driving motor. This requires that the driving motor must have very small or no-cogging torque to minimize the measuring errors. It has been proven that using a no-cogging effect, DC or hydraulic motor as the driving motor promises a very high accuracy of the measuring results. Since this setup works without any offset, the measurements are performed in a close range around the zero value.

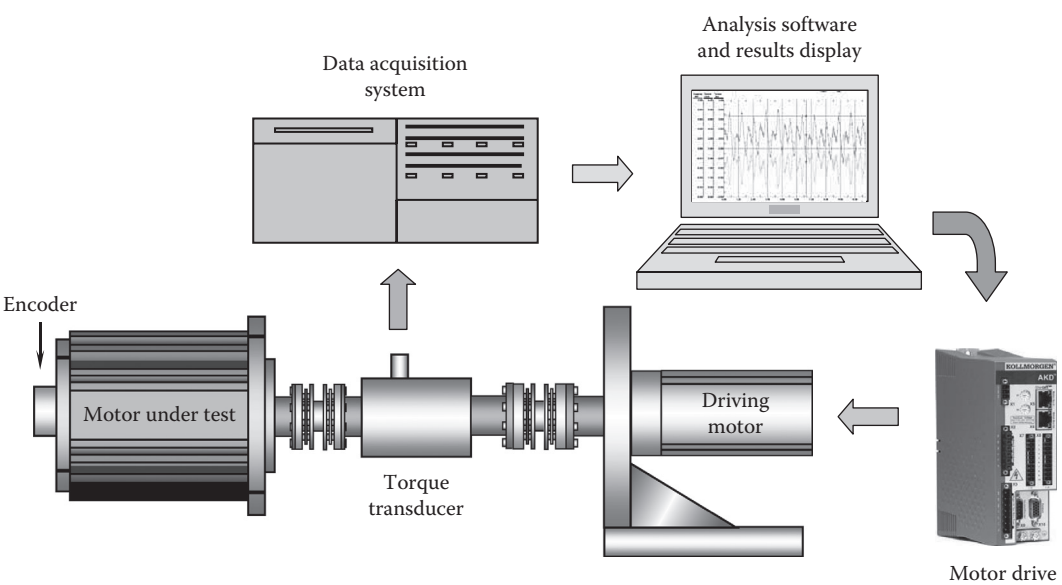

FIGURE 10.19
Dynamic cogging torque measurement employing a noncogging motor as a driving element.

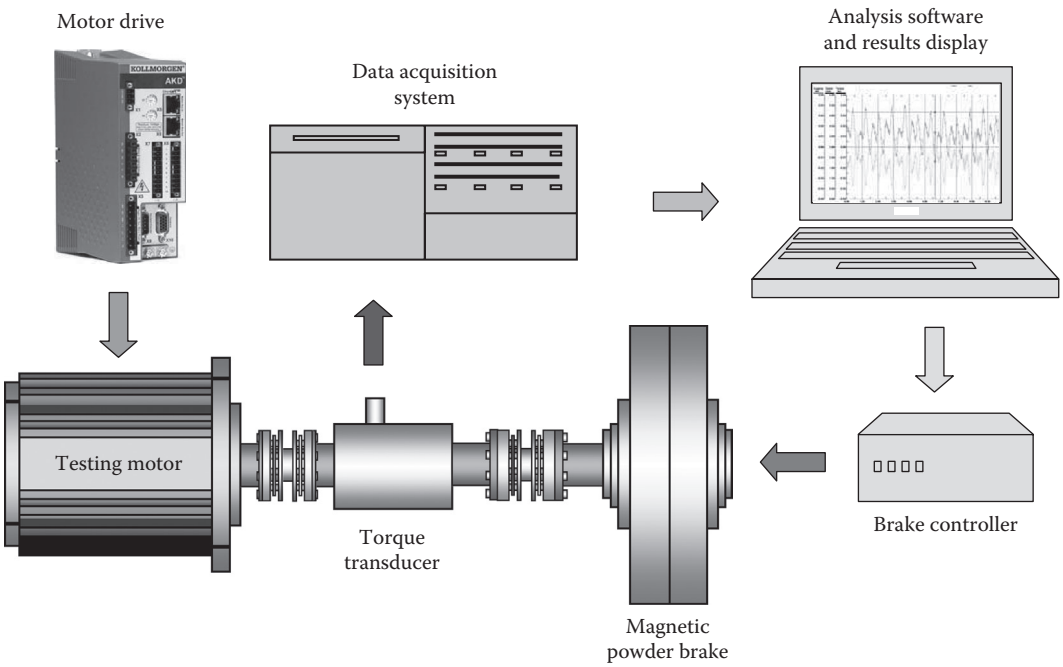

FIGURE 10.20
Alternative dynamic cogging torque measurement employing a magnetic powder brake as the driving element.

An alternative dynamic cogging torque measurement method is demonstrated in Figure 10.20. Unlike the previous testing configuration, the testing motor in this measurement method is the driving element. A magnetic powder dynamometer is used as the load device to provide the brake load to the testing motor. The resistance of the magnetic power dynamometer is controlled by the brake controller. The cogging torque of the testing motor is thus obtained from the measured torque data by the torque transducer.

A cogging torque testing system that uses a stepper motor as a driving element is shown in Figure 10.21. A harmonic gear is used to reduce the speed of the stepper motor to drive the testing motor. The high gear ratio avoids a measurable impact of the stepper motor's torque ripple to the cogging torque of the testing PM motor. The high harmonics of the stepper motor are filtered from the digital signal.

Similar to the previously addressed testing systems, a torque transducer is placed between the testing motor and stepper motor to measure the torque. The signal from the transducer is then fed into a measurement control unit. The measured torque is converted to digital values with an A/D converter and displayed on the computer monitor. As discussed by van Riesen et al. [10.43], the weight is used as an offset torque, which allows for the torque transducer to measure in its optimum scale range. The stepper motor driving the whole setup is controlled by two voltage sources. The resolution of the stepper motor can be switched from 1/1, 1/2, 1/4, to 1/8. By additionally varying the voltage from 0 to 8 V, the speed can be adjusted from 0 to 64 rpm.

The particularly prominent advantage of using the stepper motor is that it does not affect the measurement of the cogging torque of the testing motor, even though it has some cogging torque itself. In addition, because the stepper motor can determine the angular position of the testing motor, no position sensor is required.

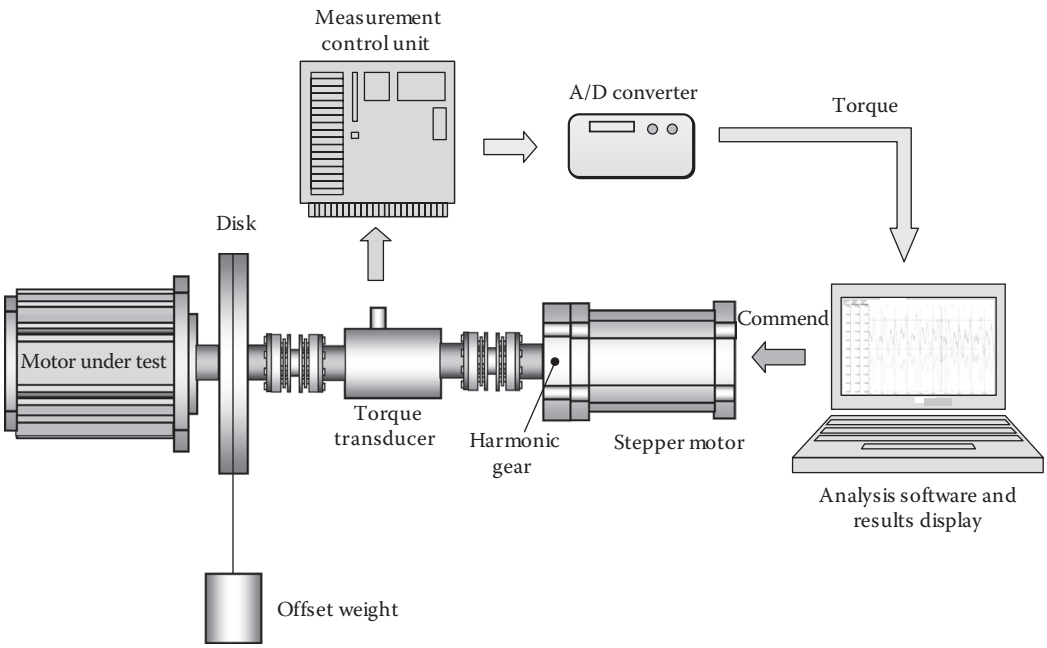

FIGURE 10.21
Dynamic cogging torque measurement using a stepper motor as the driving element.

There are primarily two different cogging torque analysis criteria: the harmonic analysis and the peak-to-peak value of the cogging torque. Many motor manufacturers often use cogging torque as a percentage of the peak-to-peak cogging torque over the motor continuous torque. The measured cogging torque from a servomotor is given in Figure 10.22, showing the peak-to-peak value of 0.04 N-m. With the measured continuous torque of 1.52 N-m from the performance test, the percentage of cogging torque is 2.63%.

10.6.6 Torque Ripple Measurement

Torque ripple of electric motors has adverse effects on the surface finishing and tolerance control in some demanding motion control applications, such as machine tool spindle drives and optical devices. In some circumstances, torque ripple may excite resonances in the mechanical portion of the drive system and produce acoustic noise. Therefore, precise torque ripple measurements are essential for identifying root causes and optimizing motor design.

The experiment setup for measuring torque ripple is depicted in Figure 10.23. The eddy-current brake is used to provide loading to the testing motor. The motor is rigidly connected to a torque transducer for measuring the maximum torque load. Isolated current and voltage transducers are used since the signals can be connected to a single common point. This is a great convenience to the data acquisition system provided that additional instrumentation errors are negligible [10.44].

Tests are conducted at different load points and different speed levels (e.g., 80% and 100% of rated speed). Accuracy of the torque load during the torque ripple test is well within the manufacturing specification of the torque transducer. Electric grounding is made on all measuring instrument such as torque box, torque transducer, and output negative signal.

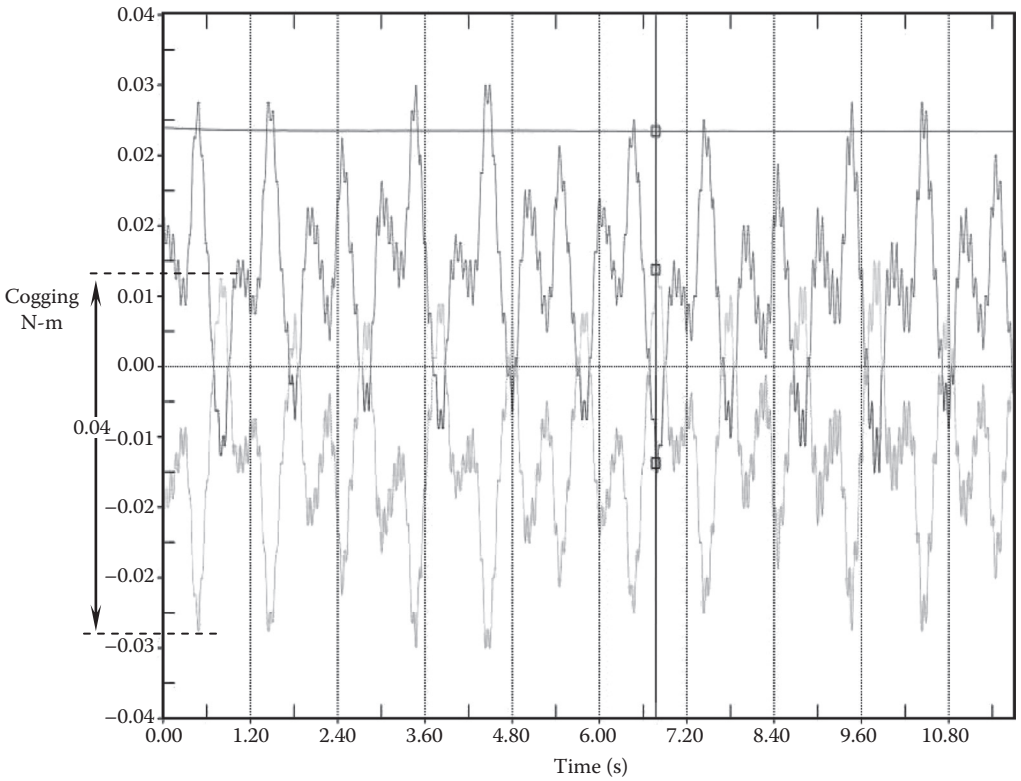

FIGURE 10.22
Measured cogging torque from a PM servomotor.

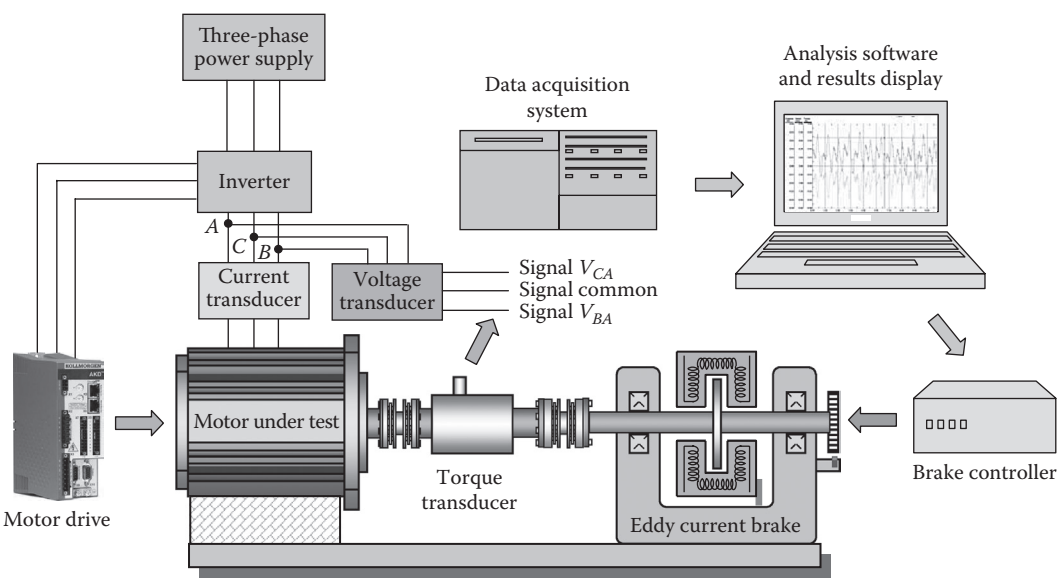

FIGURE 10.23
Experimental setup for torque ripple measurement.

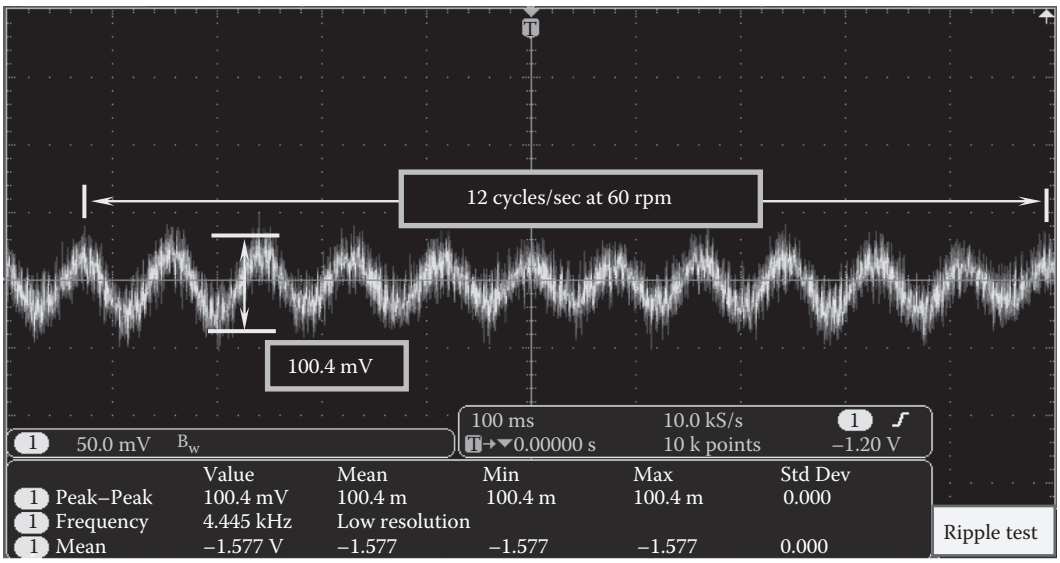

FIGURE 10.24
Results measured from a torque ripple test. The ratio of peak-to-peak torque ripple to rated torque is 5.4%.

The result obtained from a torque ripple test has shown that the peak-to-peak voltage is 100.4 mV (Figure 10.24). This value is converted into the peak-to-peak torque difference ΔT_p (where $\Delta T_p = T_{\max} - T_{\min}$). Thus, the torque ripple, which is defined as the ratio of ΔT_p to the main torque T_m, is determined to be about 5.4%.

References

[10.1] IEEE Standard 43-2000. Recommended practice for testing insulation resistance of rotating machines. Institute of Electrical and Electronics Engineers, New York.

[10.2] IEEE Standard 56-1977. Guide for insulation maintenance of large-current rotating machinery (10,000 kVA and larger). Institute of Electrical and Electronics Engineers, New York.

[10.3] IEEE Standard 118-1978. Standard test code for resistance measurements. Institute of Electrical and Electronics Engineers, New York.

[10.4] IEEE Standard 95-2002. Recommended practice for insulation testing of AC electric machinery (2,300 V and above) with high direct voltage. Institute of Electrical and Electronics Engineers, Piscataway, NJ.

[10.5] IEEE Standard 522-2004. Guide for testing turn insulation of form-wound stator coils for alternating-current electric machines. Institute of Electrical and Electronics Engineers, New York.

[10.6] IEEE Standard 1068-1990. Recommended practice for the repair and rewinding of motors for the petroleum and chemical industry. Institute of Electrical and Electronics Engineers, New York.

[10.7] ANSI/IEEE Standard 112-2004. Standard test procedure for polyphase induction motors and generators. Institute of Electrical and Electronics Engineers, New York.

[10.8] ANSI/NETA MTS-2007. Standard for maintenance testing specifications for electrical distribution equipment and systems. InterNational Electrical Testing Association (NETA), Portage, MI.

[10.9] ANSI/NETA ATS-2009. Acceptance testing specifications for electrical power distribution equipment and systems. InterNational Electrical Testing Association (NETA), Portage, MI.
[10.10] ANSI/NETA ETT-2010. Standard for certification of electrical testing technicians. InterNational Electrical Testing Association (NETA), Portage, MI.
[10.11] NEMA MG1-1993. Motors and generators. National Electrical Manufacturers Association, Rosslyn, VA.
[10.12] IEC 60034-1: 2010. Rotating electrical machines—Part 1: Rating and performance. International Electrotechnical Commissions, Geneva, Switzerland.
[10.13] IEC 60034-2-1: 2007. Rotating electrical machines—Part 2-1: Standard methods for determining losses and efficiency from test (excluding machines for traction vehicles). International Electrotechnical Commissions, Geneva, Switzerland.
[10.14] IEC 60034-4: 2008. Rotating electrical machines – Part 4: Method for determining synchronous machine quantities from tests. International Electrotechnical Commissions, Geneva, Switzerland.
[10.15] IEC 60034-19: 1995. Rotating electrical machines—Part 19: Specific test methods dc, machines on conventional and rectifier-fed supplies. International Electrotechnical Commissions, Geneva, Switzerland.
[10.16] IEC 60034-29: 2008. Rotating electrical machines—Part 29: Equivalent loading and superposition techniques—Indirect testing to determine temperature rise. International Electrotechnical Commissions, Geneva, Switzerland.
[10.17] Mustang Dynamometer. 2011. Power dyne PC operator manual. http://www.mustangdyne.com/mustangdyne/wp-ontent/uploads/downloads/2011/04/PowerDyne-PC-Users-Manual.pdf.
[10.18] Muff, M. and Towey, J. 2010. Two ways to measure temperature using thermocouples feature simplicity, accuracy, and flexibility. *Analog Dialogue* **44**(**4**): 3–8.
[10.19] Jirawattanasomkul, J. and Koetniyom, S. 2012. Design and development of road load condition for chassis dynamometer. *International Conference on Production, Materials and Automobile Engineering* (*ICPMAE'2012*), Pattaya, Thailand.
[10.20] PCB Piezotronics Inc. 2013. Torque sensors. http://www.pcb.com/linked_documents/force-torque/LT-PCBTorqueSensors_LowRes.pdf.
[10.21] De Almeida, A. T. and Ferreira, F. 1997. Efficiency testing of electric induction motors. ISR, Department of Electrical Engineering, University of Coimbra, Coimbra, Portugal.
[10.22] Çolak, I., Bal, G., and Elmas, Ç. 1996. Review of the testing methods for full-load temperature rise. *EPE Journal* **6**(**1**): 37–43.
[10.23] Morris, D. G. O. 1968. Back-to-back test for induction machines: Floating gearbox. *Proceedings of the Institution of Electrical Engineering* **115**(**4**): 536–537.
[10.24] Fong, W. 1972. New temperature test for polyphase induction motors by phantom loading. *Proceedings of the Institution of Electrical Engineering* **119**(**7**): 883–887.
[10.25] Ho, S. L. and Fu, W. N. 2001. Analysis of indirect temperature-rise tests of induction machines using time stepping finite element method. *IEEE Transactions on Energy Conversion* **16**(**1**): 55–60.
[10.26] Ho, S. L. 1992. Further development of phantom loading in induction motors. *Proceedings of International Conference on Electrical Machines* **2**: 298–302.
[10.27] Ho, S. L., Fu, W. N., and Wong, H. C. 1999. Thermal study of induction motors by phantom loading using multi-slice time stepping finite element modeling. *IEEE Transactions on Magnetics* **35**(**3**): 1606–1609.
[10.28] Ytterberg, A. 1921. Ny method for fullbelasting av electriska maskiner utan drivmotor eller avlastningsmaskin (New method for full load of electric machines without drive motor or relief machine). *S. K. Skakprov Teknisk Tidskrift* **79**: 42–46.
[10.29] Kron, A. W. 1973. Testing induction motors by means of a two frequency supply. *ETZ-A (Germany)* **94**: 77–82.

[10.30] Grantham, C. and Tabatabaei-Yazdi, H. 2000. A novel power electronic machineless dynamometer for load testing and efficiency measurement of three-phase induction motors. *Proceedings of Third International Power Electronics and Motion Control Conference* **2**: 564–569.

[10.31] Plevin, D. H., Glew, C. N., and Dymond, J. H. 1999. Equivalent load test for induction machines-the forward short circuit test. *IEEE Transactions on Energy Conversion* **14**(**3**): 419–425.

[10.32] Jordan, H. E., Cook, J. H. and Smith, R. L. 1977. Synthetic load testing of induction machines. *IEEE Transactions on Power Apparatus and Systems* **96**(**4**): 1101–1103.

[10.33] Garvey, S., Çolak, I., and Wright, M. T. 1995. The "variable inertia test" for full load temperature rise testing of induction machines. *IEE Proceedings of Electric Power Applications* **142**(**3**): 222–224.

[10.34] Thomas, T. M. 2005. On-line and off-line testing of electric motors. *IMC-2005—The 20th International Maintenance Conference*, Tampa, FL.

[10.35] Thomas, T. M. 2005. Static and dynamic motor testing as part of a predictive maintenance program. *IMC-2005—The 20th International Maintenance Conference*, Tampa, FL.

[10.36] Geiman, J. 2007. DC step-voltage and surge testing of motors. *Maintenance Technology*, March 1st. http://www.mt-online.com/march2007/dc-step-voltage-and-surge-testing-of-motors.

[10.37] Genta, G. and Delprete, C. 1994. Some considerations on the experimental determination of moments of inertia. *Meccanica* **29**(**2**): 125–141.

[10.38] Nagata, K., Okuyama, T., Fujii, H., and Okamatsu, S. 2003. Method for calculating inertia moment and driver for electric motor. U.S. Patent 6,611,125.

[10.39] Rehm, T. J. and Golownia, J. J. 2005. Method for determining inertia of an electric motor and load. U.S. Patent 6,920,800.

[10.40] Poels, P. W. 2008. Cogging torque measurement, moment of inertia determination and sensitivity analysis of an axial flux permanent magnet AC motor. Traineeship report. Charles Darwin University, Darwin, Australia.

[10.41] Crawford, D. E. 1975. A mechanism of motor failure. *Proceeding of 12th Electrical Insulation Conference*, Boston, MA. Traineeship Report DCT 3007.147.

[10.42] de Almeida, A. I., Ferreira, F. J., Busch, J. F., and Angers, P. 2002. Comparative analysis of IEEE 112-B and IEC 34-2 efficiency testing standards using stray load losses in low-voltage three-phase, cage induction motors. *IEEE Transactions on Industry Applications* **38**(**2**): 608–614.

[10.43] van Riesen, D., Schlensok, C., Schmülling, B., Schöning, M., and Hameyer, K. 2006. Cogging torque analysis on PM-machines by simulation and measurement. *Proceedings of 17th International Conference on Electrical Machine* (*ICEM*), Chania, Greece.

[10.44] Hsu, J. S., Scoggins, B. P., Scudiere, M. B., Marlino, L. D., Adams, D. J., and Pillay, P. 1995. Nature and assessments of torque ripples of permanent-magnet adjustable-speed motors. *Proceedings of IEEE Industry Application Conference* **3**: 2696–2702.

11

Modeling, Simulation, and Analysis of Electric Motors

In design and development of modern electric motors, a wide variety of engineering analyses and simulations must be carried out to ensure robust design and product optimization. These analyses may include, but not limited to, thermal analysis, CFD analysis, stress/strain analysis, resonance analysis, modal analysis, fatigue analysis, bucking analysis, burst analysis, motor mounting analysis, thermal expansion/contraction analysis, vibration and acoustic noise analysis, electromagnetic analysis, and design optimization analysis. The successful integration of these analyses into the product design cycle can significantly enhance the design quality, raise design standards, and accelerate design processes.

11.1 Computational Fluid Dynamics and Numerical Heat Transfer

As motor designs and processes grow in sophistication, motor-cooling problems become too complex to solve analytically. This forces engineers to perform numerically large simulations to gain insight into the details of fluid flow and heat transfer processes in motors. In fact, solutions generated by numerical methods can provide more insights than those by other methods in some heat transfer and fluid dynamics problems, for instance, transient fluid flow and heat transfer, 3D turbulent flows with temperature-dependent properties, multiphase flows, and compressible flows.

With the growing heat generation in modern electric motors, limited cooling capabilities may cause degradations of the motor performance and operation reliability. Today, CFD, being an integral part of the motor design for shortening the design cycle time and lowering the design cost, has played an important role to help engineers and designers gain insights of physical aspects of motor cooling. The use of CFD at the stage of the conceptual design enables motor engineers to explore alternative design options. The detailed results from a CFD simulation allow visualization of flow fields and temperature distributions in even the most inaccessible locations of a complex fluid flow and heat transfer system. A key advantage of CFD is that it provides the flexibility to readily change design parameters and determine the corresponding impacts of those changes on performance [11.1].

However, it must be noted that one of CFD issues is *garbage in, garbage out*. Despite the maturity of advanced CFD techniques, there is no guarantee that a CFD tool can automatically provide correct results. To obtain accurate simulation results, it requires thermal engineers to use their technical expertise and experiences in design and CFD work. Proper verification and validation with either experimental data or theoretical solutions are always essential parts of a CFD process.

11.1.1 Strategies in Modeling and Performing CFD Analysis

To make numerical simulations successful with available computational resources, some effective strategies may be adopted in modeling and performing CFD analysis:

- To take full advantage of geometric symmetry and periodic boundary conditions, a CFD analysis can be greatly simplified by modeling only a portion of the actual system.
- Some 3D fluid dynamics and heat transfer problems may be treated as 2D, axisymmetric problems.
- By getting rid of any unnecessary small features, which have little effect on simulation results, such as small faces, holes, edges, and fillets, it does not only simplify the problem but also make the simulation convergent. This is especially critical in cases that CFD models are converted directly from 3D CAD models, which usually contain a large amount of such small features.
- The mesh quality is the key for the success of a CFD analysis. It is highly designed to carefully select an appropriate meshing method and apply advanced meshing control techniques such as the refinement technique.
- In complex simulation problems, the iterations converge slowly and in some cases may even diverge. To ensure achieving convergence, it is suggested to run an analytical model with properly altered boundary and initial conditions. For instance, a common and effective strategy used in CFD codes for steady-state problems is to solve the unsteady form of the governing equations and then *march* the solution in time until the solution converges to a steady value. In this case, each time step is effectively an iteration, with the guess value at any time level being given by the solution at the previous time level [11.2].
- In order to facilitate convergence, the rotational speed should be initially set at a very low value and increased by small increments until reaching the normal rotating speed.
- For some large-size, complex geometry problems, a fully refined model may be too large and usually run into convergence problems. It is suggested to run the model with relatively coarse meshes first to quickly find out critical areas of interest. The critical areas are then successively refined to get the desired information in these areas.
- The addition of radiation heat transfer can significantly slow down the numerical calculation and increase the requirement of computer resources. In practice, the contribution from radiation to the overall heat transfer is generally insignificant except in a case where the temperature differences between motor components and/or between the motor and the environmental surrounding are relatively large.
- At an early design stage, some levels of approximation can be made for quickly exploring different designs.
- In dealing with heat conduction in silicon steel laminations, it is to be noted that the laminations have anisotropic thermal conductivity.

11.1.2 Rotating Flow Modeling

Rotating and swirl flows are commonly encountered in turbomachinery electric rotating machines and a variety of other applications. In an electric motor, while the stationary

parts such as the stator and housing are held statically, all parts attached to the rotor rotate at a certain velocity with respect to the rotor axis. Therefore, rotating flows are generated in the air gap between the rotor and stator and at the surroundings of fan blades, whereas interactive flows are mainly developed at the end-winding regions.

There are several approaches for modeling such rotational and interactional flows. The simplest approach is to use the single reference frame (SRF) method under the following conditions: (1) all the rotating parts rotate at the same speed with respect to a specified single axis, and (2) the problems involve moving parts and the stationary walls (as viewed from a stationary reference frame) can form surfaces of revolution with respect to the axis of rotation in the rotating reference frame [11.3]. With this approach, the entire computational domain is referred to as a single rotating reference frame. Thus, with certain restrictions, it can turn unsteady rotating flows in the stationary (inertial) reference frame into steady-state flows in the rotating (noninertial) reference frame. However, due to the restricted conditions mentioned previously, the application of this method is limited to simple problems.

When rotating parts in a system rotate about different rotating axes, or each of the rotating parts rotates about the same rotating axis but different angular speeds, or problems involve stationary components which cannot be described by surfaces of revolution, SRF is no longer applicable, and thus, the use of the multiple reference frame (MRF) method is required. With this method, the computational domain is divided into multiple domains: some are rotating and others stationary, with interfaces (which must be surfaces of revolution) separating these domains. This approach is a steady-state approximation where a rotating frame of reference is applied on the rotating domains and a stationary frame of reference is applied on the stationary domains. During the solution process, information is continually passed through the predefined interfaces between the regions. All rotating parts (e.g., a rotor) should be located inside of the rotating regions and modeled as emptiness or solid bodies. For a multiple-rotor system, the use of MRF allows individual rotors to rotate with different speeds, directions, and axes. The approaches of MRF and SRF are appropriate when the flow at the boundary between rotating and stationary regions is weakly affected by the interaction. These methods provide reasonable time-average simulation results in various applications.

The mixing plane model (MPM) is a variant of the MRF model for simulating flow through domains with one or more regions in relative motion. In this approach, each fluid region is treated as a steady-state problem. Flow field data from adjacent regions are passed as boundary conditions that are spatially averaged at the mixing plane interface.

The sliding mesh method has been developed for analyzing unsteady fluid flows. This method allows flow pattern calculations without the need of experimental data as rotor boundary conditions. As a transient approach, this method can provide the most accurate results for complex flow systems. With this method, the flow field is divided into two regions. One region, associated with the stationary components, remains stationary. Another region, associated with the rotating components, rotates relative to the stationary mesh. The two grids slide past each other in a time-dependent manner, exchanging information at the sliding interface [11.4]. At the interface, a conservative interpolation is used for both mass and momentum. The principal disadvantages for this method include the long calculation time and the required large computer resources.

The selection of appropriate model is critical for the success of computational simulation. In addition, the setup of the interface between rotating and stationary regions in MRF is also very important for the accuracy of numerical results. One example picked up here is the rotating air gap flow in a motor. As depicted in Figure 11.1, the rotor rotates counterclockwise with the rotating angular velocity ω_i, and the radii of the rotor and stator are r_i and r_o, respectively. This is a special case of the Taylor–Couette flow that has been

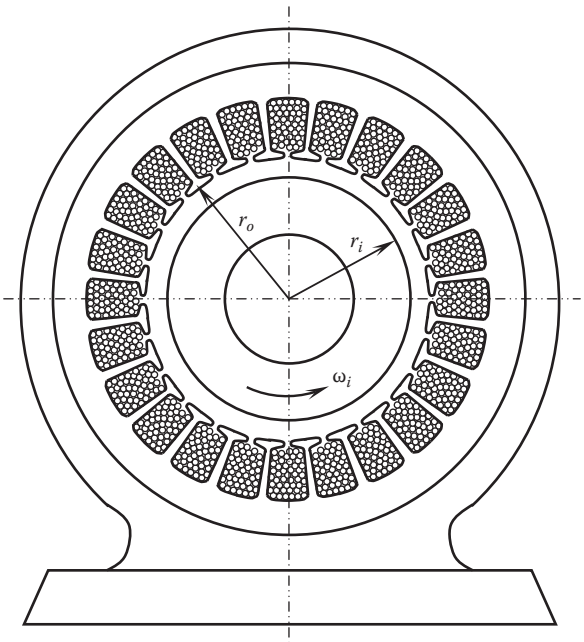

FIGURE 11.1
Schematic diagram of the formation of the air gap between the rotor and stator.

extensively studied for more than a century [11.5–11.8]. Except in the very thin boundary layers of cylinders, the tangential velocity profile of the concentric rotating flow can be theoretically derived as [11.6]

$$u_t = \frac{A}{2}r + \frac{B}{r} \tag{11.1}$$

where A and B are constants, determined from the boundary conditions at the rotor surface $u_{t,r=r_i} = r_i\omega_i$ and at the stator surface $u_{t,r=r_o} = 0$.

This problem can also be solved with a CFD model by defining multiple regions. The interface that separates the rotating and stationary regions is at $r = r_{int}$. As shown in Figure 11.2, the tangential velocity decreases in the thin boundary layer of the rotor and then increases with the radius in the rotating region until it reaches the maximum value at the interface (where $u_{t,\max} = r_{int}\omega_i$). In the stationary region, the velocity is continuous at the interface and then decreases with the radius until it vanishes at the stator surface. The comparisons between the experimental solution and the results from both the small and large rotating regions are presented in Figure 11.3. The small rotating region is set up as close as possible to the rotor but without causing difficulty in model meshing. This figure shows the significant deviations between these three cases. This may suggest that for such a problem, the use of small rotating region provides better result than the large rotating region.

11.1.3 Porous Media Modeling

In some types of electric machines, the stator winding coils are made up of bundles of strands of insulated copper wires and embedded in the slots of the stator core. At the

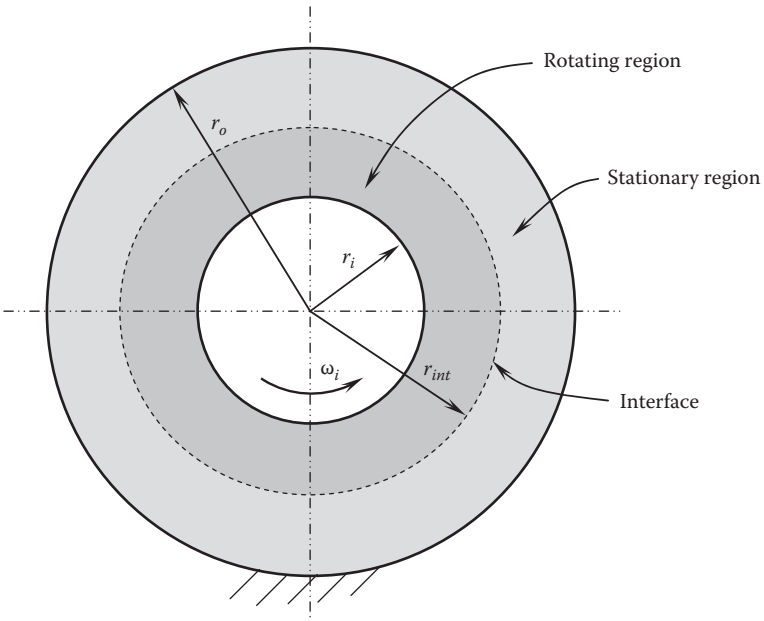

FIGURE 11.2
Defined rotating and stationary regions (as viewed from the stationary frame).

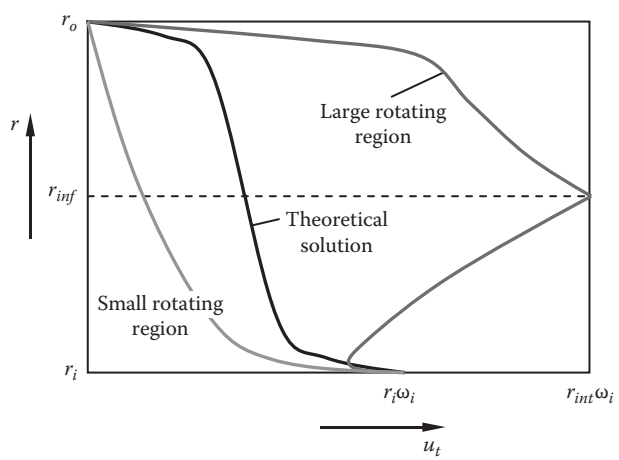

FIGURE 11.3
Comparison of theoretical solution and results from the model with multiple regions.

end-winding region, the stator coils bend to form continuous current paths. Without a resin encapsulation treatment, the stator winding contains a large number of voids in its complicated 3D structure (see Figure 4.35). Thus, to simplify the CFD analysis, the stator windings, especially at the end-winding regions, can be modeled as porous media [11.9,11.10].

Porous medium technology is defined as a utilization of specific and unique features of a highly porous medium for supporting and controlling the cooling process in electric machines. In practice, the flow velocity field and heat transportation in a 3D-structured porous medium are very complex. To overcome the difficulties, it is often required to treat the 3D structure of the porous media as a large number of hot spots homogeneously distributed throughout its volume. Moreover, the 3D model of the porous medium may be simplified into a 2D axisymmetric model.

In the porous media model, the flow passing through the stator winding with a fraction of the flow open area is equivalent to the flow passing through a porous medium with a full open area, with an identical mass flowrate and pressure drop:

$$\Delta p_a = \Delta p_p \tag{11.2}$$

$$\dot{m}_a = \dot{m}_p \tag{11.3}$$

where

Δp_a and Δp_p are pressure drops

$\dot{m}_a$ and $\dot{m}_p$ are mass flowrates from the actual and porous system, respectively

By defining the loss coefficient K,

$$K = \frac{\Delta p}{(1/2)\rho u^2} \tag{11.4}$$

Δp_a and Δp_p can be rewritten as

$$\Delta p_a = K_a\left(\frac{1}{2}\rho u_a^2\right) \tag{11.5}$$

$$\Delta p_p = K_p\left(\frac{1}{2}\rho u_p^2\right) \tag{11.6}$$

Substituting Equations 11.5 and 11.6 into 11.2 yields

$$K_a \frac{\rho u_a^2}{2} = K_p \frac{\rho u_p^2}{2} \tag{11.7}$$

That is,

$$K_p = K_a\left(\frac{u_a}{u_p}\right)^2 \tag{11.8}$$

As the most important parameter in calculating porous media flows, porosity η is introduced and defined as the ratio of the actual open area to the total flow area (i.e., 100% open):

$$\eta = \frac{A_a}{A_p} \tag{11.9}$$

Rewriting Equation 11.3,

$$\rho A_a u_a = \rho A_p u_p \tag{11.10}$$

The relationship between the velocity ratio u_a/u_p and η can be determined as

$$\frac{u_a}{u_p} = \frac{A_p}{A_a} = \frac{1}{\eta} \tag{11.11}$$

Substituting (11.11) into (11.8), it yields

$$K_p = \frac{K_a}{\eta^2} \tag{11.12}$$

Thus, the porous media inertial resistance factor ξ, defined as the pressure loss factor per unit length, can be calculated as

$$\xi = \frac{K_p}{\Delta L} \tag{11.13}$$

where ΔL is the length through the media in the flow direction.

Thus, with the equations mentioned previously, the flow characteristics can be obtained at the porous flow zone. By integrating the porous media parameters into the CFD model, the velocity and pressure fields at the end-winding region are determined.

11.1.4 Numerical Simulation of Motor Cooling

Modern electric motors have more complicated mechanical and electromagnetic structures over conventional motors for gaining better performance, higher operation reliability and efficiency, and longer lifetime. For such systems with complicated geometry, conventional analytic methods are no longer competent to provide comprehensive information of fluid flows and temperature distributions of motor in a system level. Therefore, CFD techniques have been extensively employed by motor manufacturers to help optimize motor cooling systems.

As in the example shown in Figure 11.4, a large-scale elevator motor is cooled by high volumetric air driven by a blower. Unlike most conventional motors whose rotors are on the inside of wound stators, this external rotor motor has its rotor on the motor outside to directly drive the elevator car. The advantages of the external rotor motors include increased motor torque, reduced power losses, and promoted transmission efficiency [11.11]. This type of motor is especially suitable for applications such as fans, motor-wheel driving systems [11.12,11.13], and lifting systems of forklift trucks.

Due to the symmetry of the model, only one-tenth of the motor (36°) is modeled. In order to reduce the required computing resources and accelerate the computations, the model has been simplified and defeatured without loss in accuracy. As shown in Figure 11.5, the cooling air flow enters into the stationary hollow shaft at its one end and injects into the radial cooling channels located at the central and end-winding regions. Then, the cooling air flow turns to 90° when it reaches the air gap and finally exhausts from the two endbells to the environment.

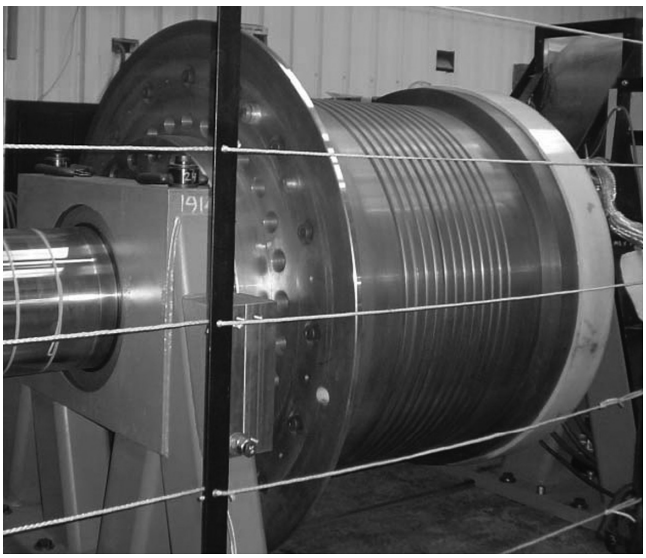

FIGURE 11.4
Large-scale elevator motor. (Courtesy of Kollmorgen Corporation, Radford, VA.)

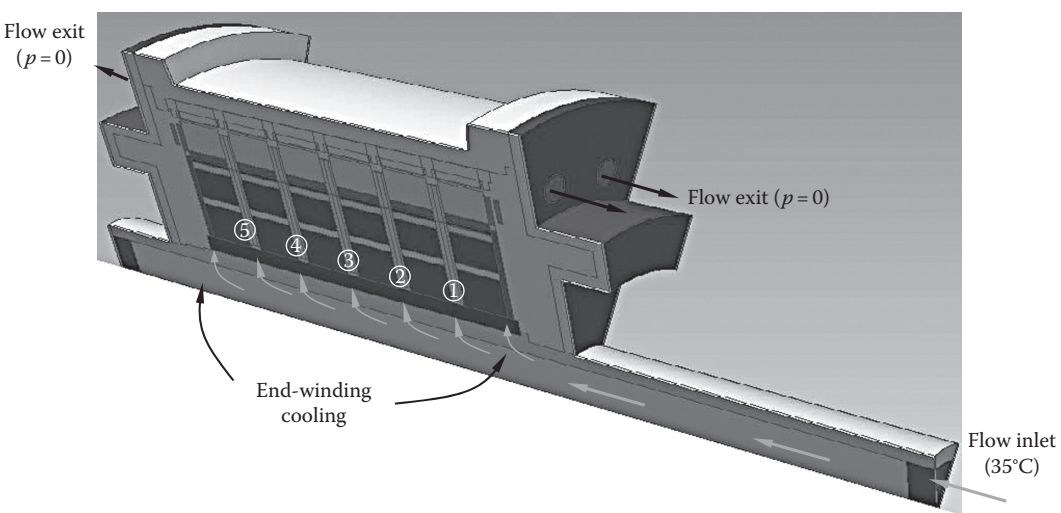

FIGURE 11.5
Forced air cooling for a large-scale elevator motor. (Courtesy of Kollmorgen Corporation.)

11.1.4.1 Mathematical Formulations

In a CFD analysis, governing equations are derived from the following fundamental laws of physics:

- Conservation of mass
- Conservation of momentum
- Conservation of energy

A time-dependent continuity equation is derived from the conservation of mass. Navier–Stokes nonlinear partial differential equations arise from applying Newton's second law to the motion of fluid. These equations consist of three time-dependent momentum equations corresponding to three coordinates. If a problem involves heat transfer, an additional time-dependent energy equation, based on the conservation of energy, has to be coupled with Navier–Stokes equations. All equations must be solved simultaneously for getting the entire flow, pressure, and temperature fields of electric motor.

The governing equation may be used with a relatively high degree of accuracy for incompressible flows if the viscosity gradient is not too large. In majority of the problems, this assumption is adequate. The temperature-dependent properties are often used in CFD analyses.

- Continuity equation

  Continuity equation is based on the conservation of mass in a fixed control volume of fluid flow and can be expressed in vector notation:

$$\frac{\partial \rho}{\partial t} + \nabla \cdot (\rho \mathbf{V}) = 0 \tag{11.14}$$

  Equation 11.14 is the continuity equation in conservation form. In this equation, the second term can be separated into two parts as priority

$$\frac{\partial \rho}{\partial t} + \mathbf{V} \cdot \nabla \rho + \rho \nabla \cdot \mathbf{V} = 0 \tag{11.15}$$

  By introducing the differential operator [11.14]

$$\frac{D(\ )}{Dt} = \frac{\partial(\ )}{\partial t} + \mathbf{V} \cdot \nabla(\ ) \tag{11.16}$$

  Equation 11.15 can be rewritten in nonconservation form:

$$\frac{D\rho}{Dt} + \rho \nabla \cdot \mathbf{V} = 0 \tag{11.17}$$

- Momentum equations

  Momentum equations are derived from the conservation of momentum, comprising three components, that is, x, y, and z momentum equations in a Cartesian coordinate system or r, θ, and z in a cylindrical system, in a general form of fluid motion equations:

$$\rho \frac{D\mathbf{V}}{Dt} = -\nabla \rho + \nabla \cdot \bar{\bar{\tau}} + \rho \mathbf{f} \tag{11.18}$$

  where

  $\mathbf{f}$ is the body force per unit mass

  $\bar{\bar{\tau}}$ is the viscous stress tensor

For Newtonian fluids, $\bar{\bar{\tau}}$ is a linear function of the velocity gradient and can be expressed as

$$\tau_{ij} = \mu\left(\frac{\partial V_i}{\partial x_j} + \frac{\partial V_j}{\partial x_i}\right) + \lambda(\nabla \cdot \mathbf{V})\delta_{ij} \tag{11.19}$$

where
- μ is the dynamic viscosity
- λ is the coefficient of bulk viscosity
- x_i and x_j denote mutually perpendicular coordinate directions

The coefficient of bulk viscosity and dynamic viscosity can be related to each other through the Stokes' hypothesis:

$$\lambda + \frac{2}{3}\mu = 0 \tag{11.20}$$

Substituting Equation 11.20 into 11.19 yields

$$\tau_{ij} = \mu\left[\frac{\partial V_i}{\partial x_j} + \frac{\partial V_j}{\partial x_i} - \frac{2}{3}(\nabla \cdot \mathbf{V})\delta_{ij}\right] \tag{11.21}$$

where δ_{ij} is the Kronecker delta operator, which is equal to 1 if $i=j$ and it is zero otherwise.

- Energy equation

  Energy equation is based on conservation of energy and expressed as

$$\rho\left[\frac{\partial h}{\partial t} + \nabla \cdot (h\mathbf{V})\right] = -\frac{\partial \rho}{\partial t} + (\mathbf{V} \cdot \nabla \rho) + \nabla \cdot (k\nabla T) + \phi \tag{11.22}$$

where
- h is the specific enthalpy that is related to specific internal energy as $h = e + p/\rho$
- T is the temperature
- ϕ is the dissipation function representing the work done against viscous forces and is expressed as

$$\phi = (\bar{\bar{\tau}} \cdot \nabla)\mathbf{V} = \tau_{ij}\frac{\partial V_i}{\partial x_j} \tag{11.23}$$

For an incompressible fluid, the energy equation can be also expressed as

$$\rho c_p\left[\frac{\partial T}{\partial t} + \mathbf{V} \cdot \nabla T\right] = \nabla \cdot (k_{eff}\nabla T) + S_h \tag{11.24}$$

where
- T is the temperature
- k_{eff} is the effective thermal conductivity ($k_{eff} = k + k_t$, where k_t is the turbulent thermal conductivity)
- S_h is the volumetric heat source

- Turbulence model

  A majority of fluid flows encountered in motor cooling are turbulent flows. There are a number of turbulence models in CFD analysis to deal with turbulent flows, such as constant eddy viscosity, standard *k*-ε, Reynolds stress, and renormalization group (RNG) *k*-ε model, just to name a few. This study employs the RNG *k*-ε turbulence model, which was derived using a rigorous statistical technique:

  k equation

$$\nabla(\rho k\mathbf{V}) = \nabla(\alpha_k \mu_{eff} \nabla k) + \mu_t \phi - \rho\varepsilon \tag{11.25}$$

  ε equation

$$\nabla(\rho\varepsilon\mathbf{V}) = \nabla(\alpha_\varepsilon \mu_{eff} \nabla\varepsilon) + C_{1\varepsilon}\mu_t \phi \frac{\varepsilon}{k} - C_{2\varepsilon}\rho\frac{\varepsilon^2}{k} - R \tag{11.26}$$

  where

  $\mu_t\phi$ represents the generation of turbulent kinetic energy

  $C_{1\varepsilon}$ and $C_{1\varepsilon}$ are constants ($C_{1\varepsilon} = 1.44$ and $C_{2\varepsilon} = 1.92$)

  α_k and α_ε are the inverse effective Prandtl numbers for *k* and ε, respectively

  In the aforementioned equations, the effect of buoyancy is ignored.

  Because turbulence always causes mixing between the fluid layers, it results in diffusion, which is treated as an increase in viscosity. As a result, μ_{eff} is introduced as the effective viscosity:

$$\mu_{eff} = \mu + \mu_t = \mu + \rho C_\mu \frac{k^2}{\varepsilon} \tag{11.27}$$

  where $C_\mu = 0.0845$.

  The *R* term in the ε equation is given by

$$R = \frac{C_\mu \rho \eta^3 (1 - \eta/\eta_o)}{1 + \beta\eta^3} \frac{\varepsilon^2}{k} \tag{11.28}$$

  where

  $\eta = Sk/\varepsilon$

  $\eta_o = 4.38$

  $\beta = 0.012$

11.1.4.2 Numerical Method

The problem approaches include setting up boundary and initial conditions and making necessary assumptions, including (1) assigning thermal physical properties to the fluid and solid components; (2) defining various power losses, which are obtained from a separate electromagnetic analysis, to the corresponding motor components as the heat sources; (3) applying the inlet boundary conditions such as volumetric flowrate (or velocity) and temperature; (4) applying the outlet boundary condition with zero static pressure; (5) assuming all outer walls as adiabatic and heat dissipation only through the cooling fluid; and (6) specifying the initial temperature to the computational domain.

The governing equations are solved on the discretized elements using commercial CFD software. All walls are treated as adiabatic and no slip. The flowrate is defined at the flow inlet, and zero pressure is specified as outlet.

The aims of performing the CFD analysis of the motor cooling include the following: (1) The main objective is to obtain the temperature distribution in the motor interior, especially around the stator windings, to avoid motor overheating. (2) The cooling flowrates and their distributions are important for the assessment of motor fan selection and performance. Insufficient cooling flows can result in hot spots occurring near the heat sources such as stator winding. Through the CFD analysis, the required air flowrate can be determined. (3) The 3D velocity field of the motor reveals fluid–solid interactions and flow patterns such as flow separation and attachment to solid body surfaces. A separated air flow may cause an increase in skin friction and impact on cooling efficiency. (4) The pressure drop data are used to evaluating motor windage losses. Attention should be focused on abnormal pressure drops at local structures for further minimizing windage losses.

The overall quality of meshes is of primary importance in predicting the temperature and velocity fields in this complex computational domain. In order to obtain accurate results, very fine meshes are set at the high-pressure gradient regions. Due to the large motor size and complicated geometries, the CFD model is meshed with more than 4 million elements: 2.27 million elements for the fluid and 2.07 million elements for the solid parts (Figure 11.6).

In order to achieve accurate numerical simulation results, the winding insulation is also taken into account in this analysis (Figure 11.7). Because the winding insulation is too thin to be meshed with a conventional method, it must be dealt with special approaches. In practice, such thin-walled objects such as shells are defined as surface parts. One effective way to deal with the meshing of thin-walled objects is to represent them only with surfaces and eliminate the thickness form of the model. In other words, the surface parts are meshed with 2D elements and are used to represent thin-walled objects. In such a way, surface parts can be used to conduct heat as well as obstruct flow. They exhibit the same heat transfer characteristics as 3D volumes.

To ensure proper convergence, residuals for mass, momentum, turbulent kinetic energy, and temperature were monitored until achieving minimum level of 10^{-4}. Furthermore,

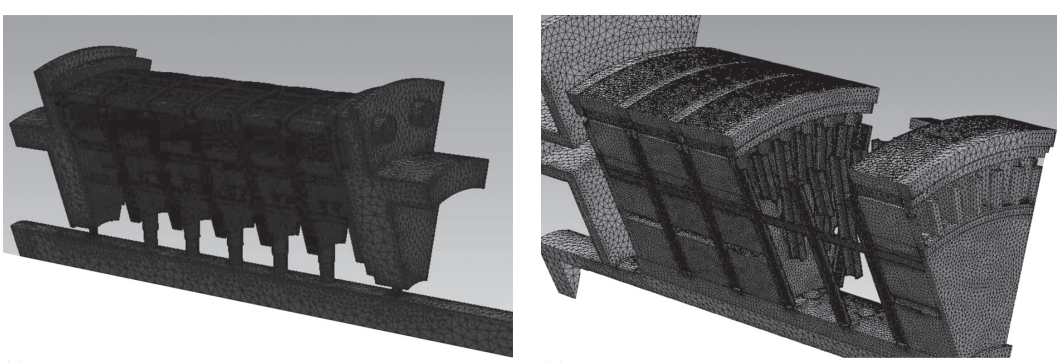

(a) (b)

FIGURE 11.6
Model meshing: (a) fluid meshing (2.27 million elements) and (b) meshing for solid parts (2.07 million elements).

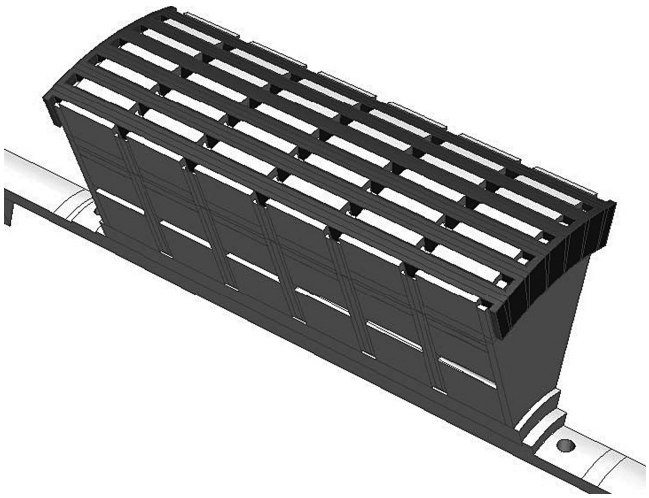

FIGURE 11.7
The thin insulation layer of stator winding is taken into account in the analytical model.

various monitoring planes at different sections of the motor fan assembly were created and monitored to achieve stable convergence for mass flow and total pressure without any undue fluctuations. In order to determine the required fan flowrate, a number of volumetric flowrates are used in this CFD analysis, including 300, 500, 700, 900, and 1200 CFM. All power losses, such as copper, core, magnet, and eddy current, are defined at the corresponding components.

To help achieve convergence, the analysis starts with pure fluid dynamics. As the flow field becomes fully developed, the heat transfer model is added to calculate the temperature distribution in the computational domain.

11.1.4.3 CFD Results

The velocity field of the motor is presented in Figure 11.8 for a flowrate of 1200 CFM. In order to clearly demonstrate the flow field, only the fluid domain is shown. High velocities occur at the radial spray nozzles on the hollow shaft. The flowrate distributions through five middle channels and two end-winding channels are displayed unevenly; the flowrate is inversely proportional to the distance from the flow inlet. This suggests that for receiving a uniform flowrate distribution, different nozzle diameters are required.

Figure 11.9 displays the velocity fields of middle cooling channels. The flow pattern at each channel is directly associated with the cooling of motor components. For example, at channel 1, the air cooling flow goes through the middle and left subchannels, and almost no flow goes through the right subchannel, resulting in a higher temperature (about 5°C) on the stator winding on the right subchannel.

The static pressure distribution inside the motor is given in Figure 11.10. It can be found that the highest pressure occurs near the nozzle where the dynamic pressure is converted into the static pressure. The pressure drop across the motor is a function of the flowrate, air viscosity, flow path geometries (e.g., air gap depth and nozzle diameter), and rotor rotating speed. The air flow travels through the nozzles, channels, air gap, and exhaust holes,

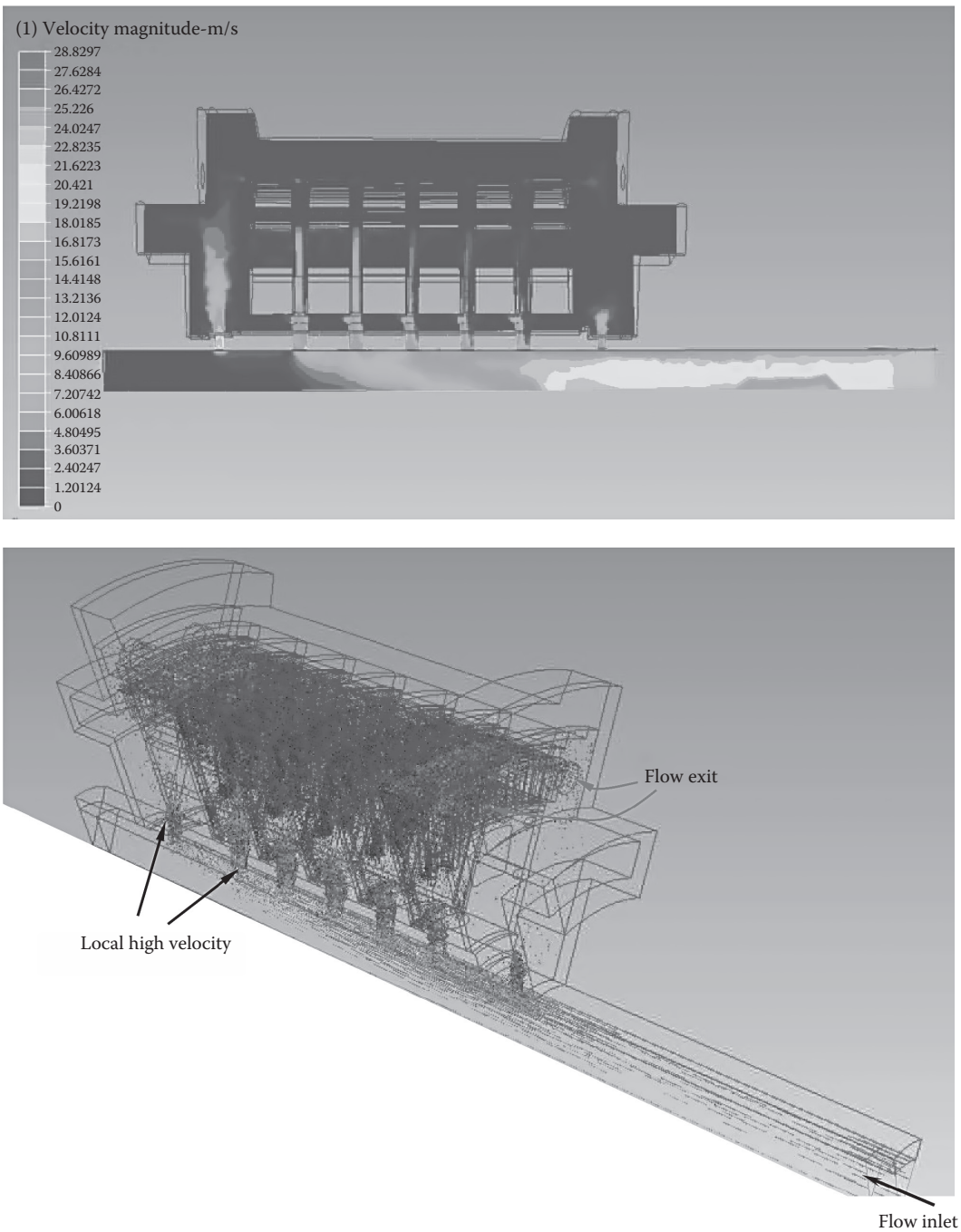

FIGURE 11.8
Velocity field through the motor interior with an intel flowrate of 1200 CFM.

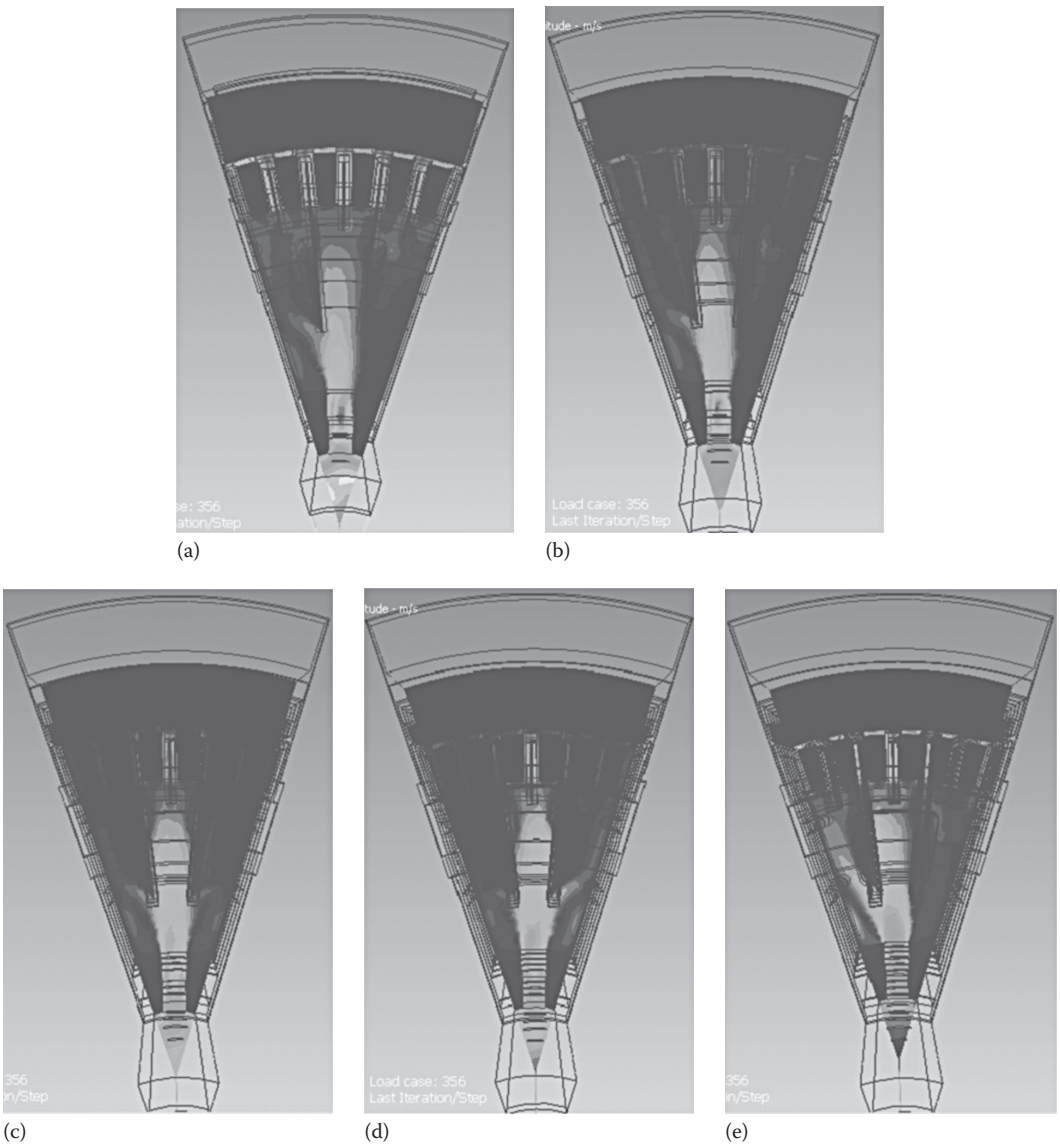

FIGURE 11.9
Velocity contours through the middle cooling channels: (a) channel 1, (b) channel 2, (c) channel 3, (d) channel 4, and (e) channel 5.

creating a pressure drop due to the restriction of flow. Based on the pressure contours in the figure, the air flow passages have been optimized for minimizing the pressure drop and reducing the windage power loss.

The temperature distribution in the motor is shown in Figure 11.11. The highest temperature for the flowrate of 1200 CFM is 93.7°C, occurring on the stator end turn near the flow inlet. This is consistent with the observation that the flowrate is inversely proportional to the distance from the flow inlet. From the calculated results, it is estimated that the temperature difference due to the nonuniform flowrate is about 10°C on the stator

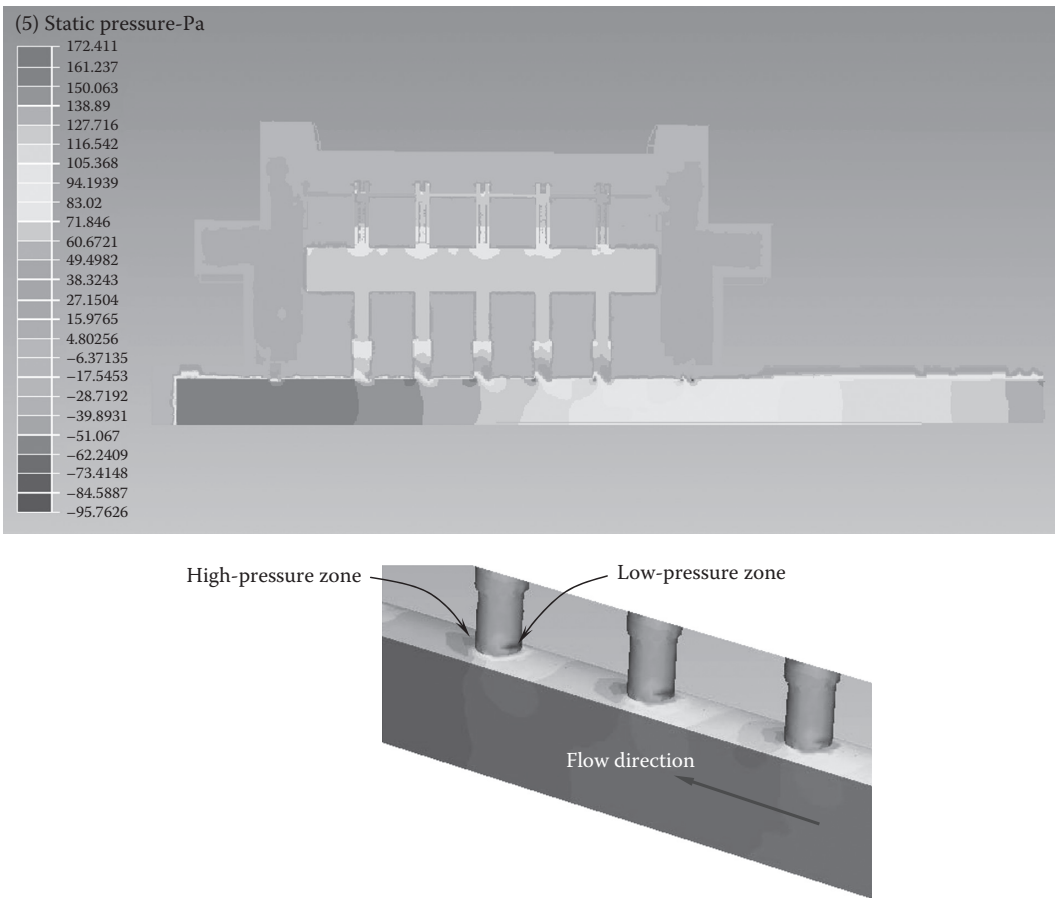

FIGURE 11.10
Pressure distribution through the motor.

winding. The temperature of magnets is shown to be 66°C. Usually, rare-earth magnets such as Nd–Fe–B are sensitive to heat. If a magnet is heated above its maximum operating temperature, it will permanently lose a fraction of its magnetic strength. If the magnet is heated about its Curie temperature, it will lose all of its magnetic properties. Therefore, it is important to always check the magnet temperatures.

Figure 11.12 shows in detail the temperature distribution in each cooling channel. It can be observed that the temperature difference on the stator winding in the same channel is usually less than 5°C.

The maximum temperature of 93.7°C indicates that the air flowrate can be further reduced, lowering not only the power consumption of the blower but also windage loss of the motor. Figure 11.13a and b presents the temperature distributions for the flowrate of 700 and 900 CFM, respectively. For the flowrate of 900 CFM, the maximum temperature is increased to 109°C (–16.3%). Continuously reducing the flowrate to 700 CFM, the maximum temperature becomes 121.7°C, which can be used for the class B insulation that has the maximum operation temperature of 130°C. For the class F insulation (maximum operation temperature of 155°C), the flowrate can be further reduced.

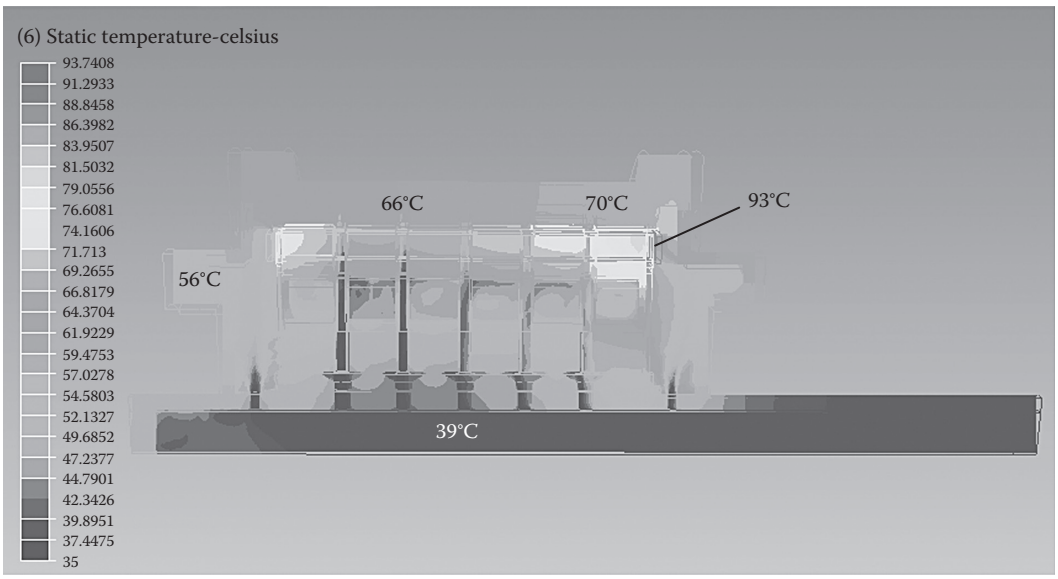

(a)

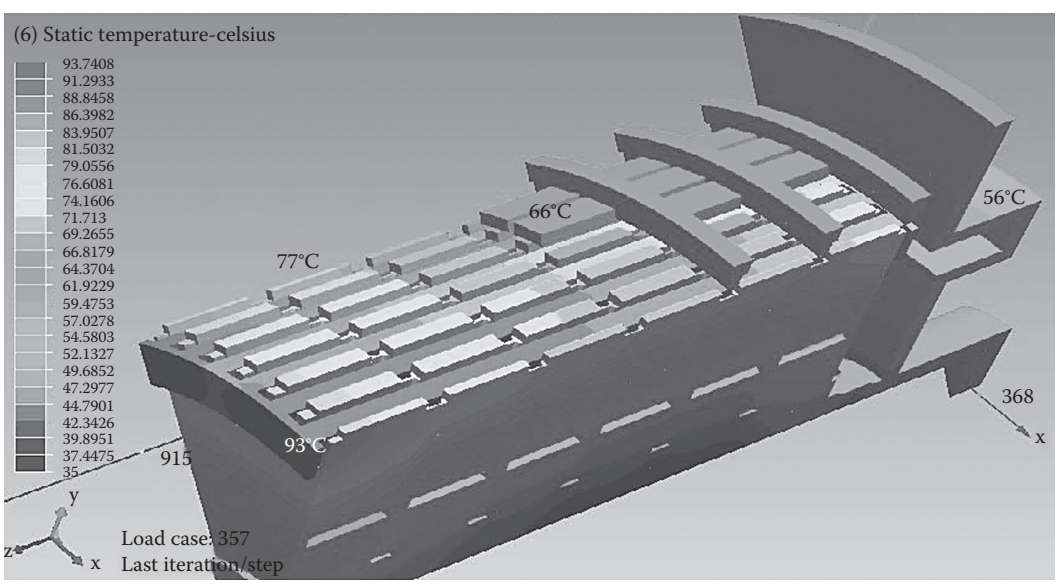

(b)

FIGURE 11.11
Temperature distribution on (a) the whole motor and (b) solid components only. The flowrate of 1200 CFM is used for the analysis.

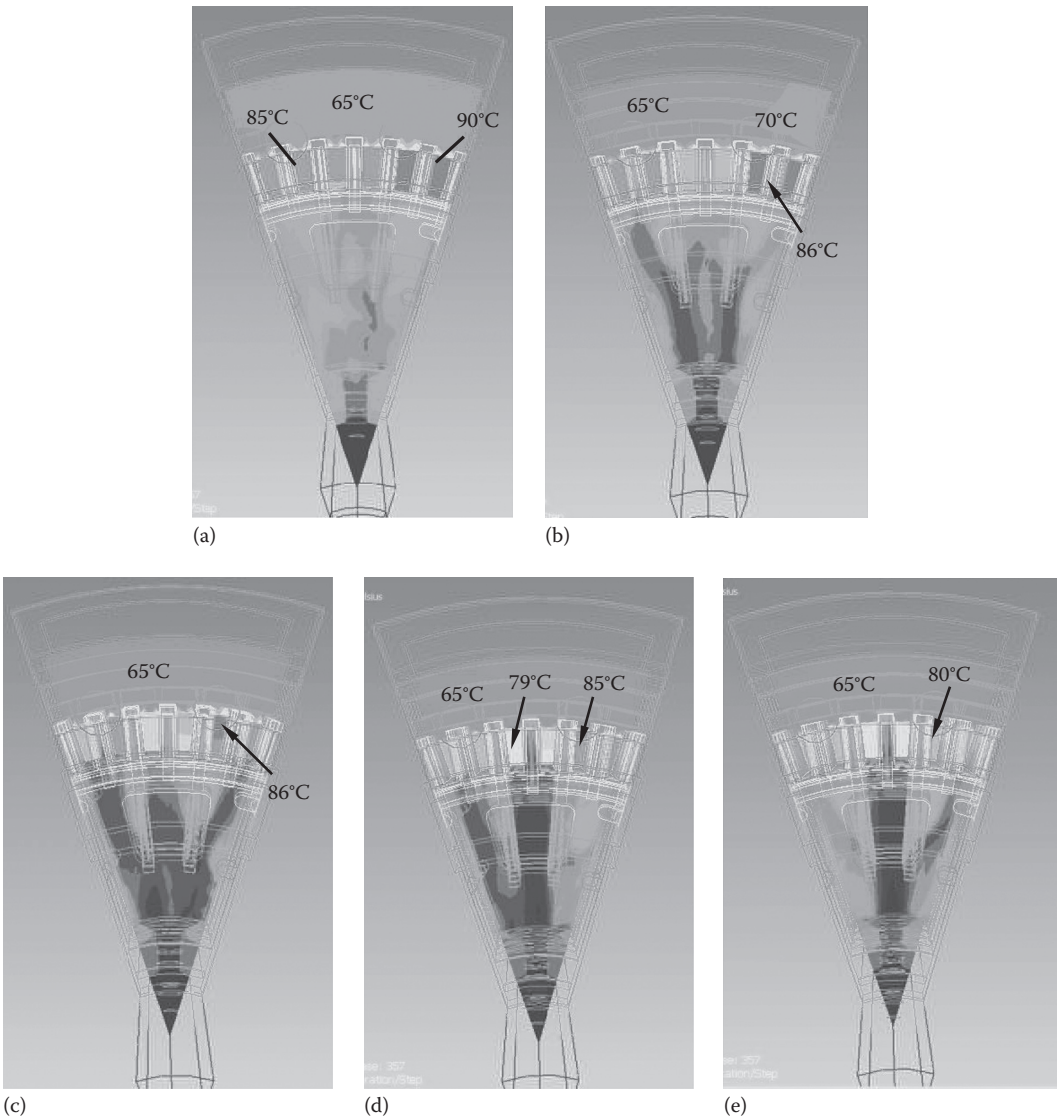

FIGURE 11.12
Temperature distributions through the cross-sectional cooling channels: (a) channel 1; (b) channel 2; (c) channel 3; (d) channel 4; and (e) channel 5.

Performing the CFD analysis with the flowrates of 300–1200 CFM (0.14–0.57 m^3/s) can provide a useful relationship between the maximum temperature and flowrate, as displayed in Figure 11.14. The results indicate that the appropriate range of the volumetric flowrate for the motor cooling is 700–900 CFM (0.33–0.42 m^3/s), with the corresponding temperatures in the range of 121°C–109°C.

Figure 11.15 presents the relationship between the flowrate and pressure at blower. This information helps select an appropriate blower/fan and determine the optimum operating points of the blower/fan.

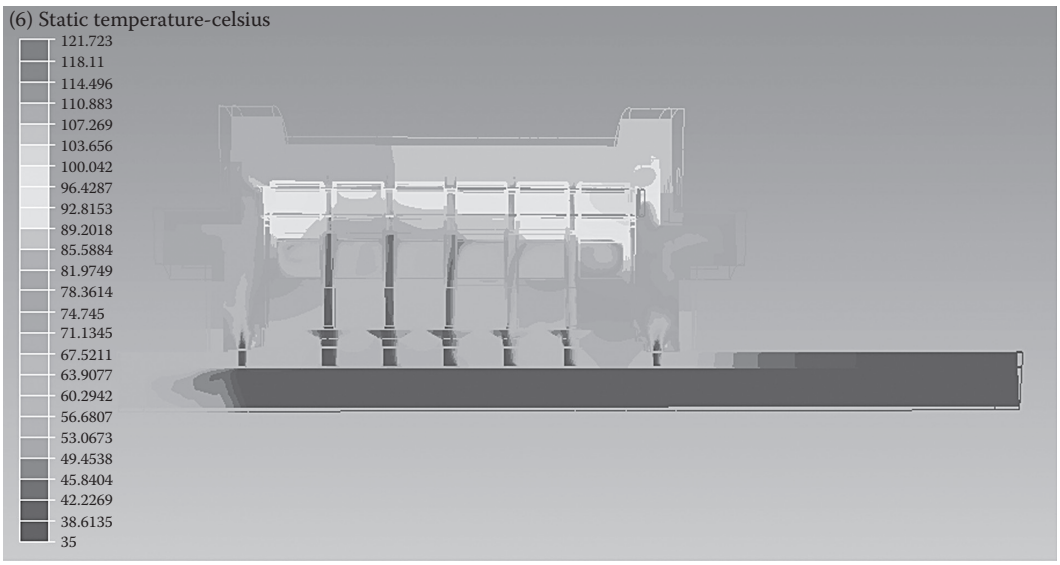

(a)

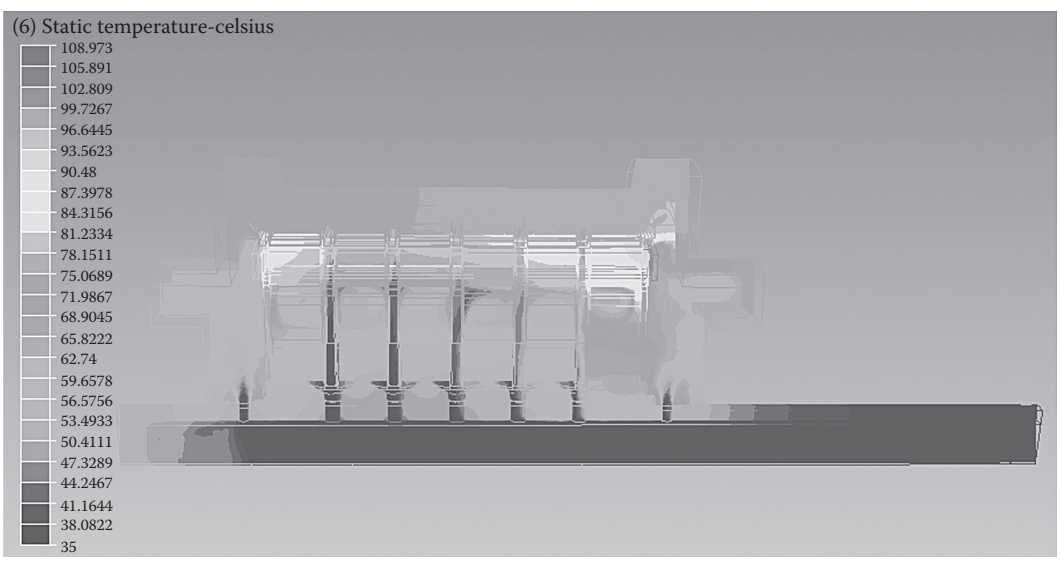

(b)

FIGURE 11.13
Temperature distributions inside the motor: (a) flowrate of 700 CFM and (b) flowrate of 900 CFM.

11.2 Thermal Simulation with Lumped-Circuit Modeling

Among various thermal analysis methods, a simple and common approach is to use lumped-circuit (or network) analogy modeling. This method is based on the analogy between electrical and thermal systems. The analogies between current I and rate of heat

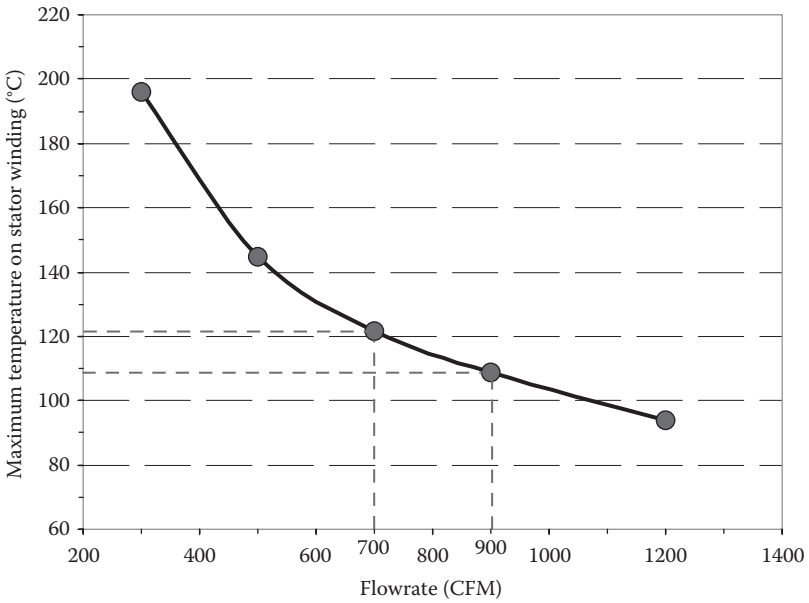

FIGURE 11.14
Maximum temperature versus flowrate. The results indicate that the required volumetric flowrate for the motor cooling is in the range of 700–900 CFM. Correspondingly, the motor maximum temperature is in the range of 109°C–122°C.

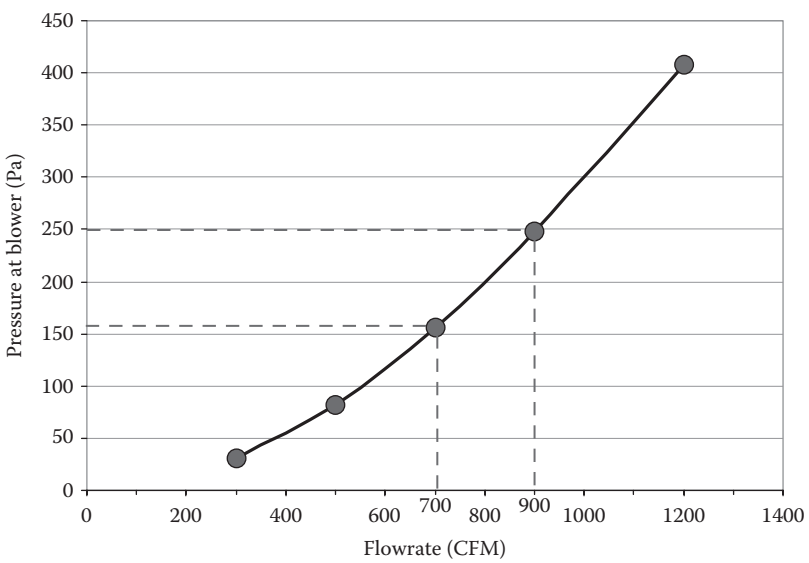

FIGURE 11.15
Blower pressure versus flowrate. The results indicate that the required volumetric flowrate for the motor cooling is in the range of 700–900 CFM.

TABLE 11.1

Analogous Parameters between Electrical and Thermal Systems

Parameter	Electrical System	Thermal System
Flow	Current I (in Ampere [A])	Heat flow q (in W)
Potential	Voltage V (in V)	Temperature differential ΔT (in °C or K)
Resistance	$R = \frac{V}{I}$ (in Ω)	$R_{th} = \frac{\Delta T}{q}$ (in°C/W)
Conductance	$S = 1/R$ (in A/V)	$G = 1/R_{th}$ (in W/°C)
Capacitance	$C = \frac{I}{dV/dt}$ (in Farad [F])	$C_{th} = \frac{q}{dT/dt}$ (in J/°C)
Ohm's law	$I = \frac{V}{R}$	$q = \frac{\Delta T}{R_{th}}$

flow q, voltage V and temperature difference between two spatial points or surfaces ΔT, etc., can be properly applied in analyzing thermal systems. In such a way, it is possible to take thermal resistances as the analog to electrical resistances. This allows thermal engineers to utilize fully developed basic laws (such as Ohm's law and Kirchhoff's law) in electrical engineering to determine heat transfer characteristics in thermal systems. The analogous parameters between the two systems are listed in Table 11.1.

In fact, this conventional approach was popular before the advanced computational techniques and CFD software have been fully developed. The lumped-circuit approach has the advantage of being very fast to calculate, but the development of the network model is time-consuming, requiring thermal engineers to spend a large amount of time in defining the circuit that accurately models all heat transfer paths and circuit elements.

By converting a complex 3D physical model into an equivalent lumped-circuit system, it greatly simplifies the problem complexity and thus reduces the simulation runtime and the memory usage. The lumped-circuit analogy method involves representation of the thermal and flow systems as a network of thermal and flow paths and components for the prediction of system-wide temperature distribution and flow field. In fact, this technique is very efficient in terms of the effort required for model definition, solution, and examination of results because it employs overall component characteristics for analyzing their systems-wide interaction. Because this technique requires much shorter time compared with CFD analysis, it is especially suitable to explore different designs at the conceptual design stage [11.15]. However, the most difficult aspect of this approach is to determine the heat transfer coefficients and the resultant thermal resistances in convective heat transfer, as well as in radiation heat transfer.

An analytical–numerical hybrid scheme for system-wide thermal modeling of electric motors has been proposed by Liu et al. [11.16]. This scheme employs finite volume method (FVM) concept to calculate heat conduction for motor components while using flow network modeling (FNM) for fluid convection calculation. This hybrid scheme not only simplifies the complicated flow simulation but also considers motor's geometry information and increases the accuracy of the simulation.

In order to develop an equivalent thermal network, it is required to subdivide the thermal system into a number of finite subvolumes called nodes. All the thermal parameters, such as temperature, thermal capacitance, and heat generation, are considered to be concentrated at the central nodal point. This point represents the mean values of the thermal

parameters in the node. The thermal models for the basic elements of electric machines have been discussed by Perez and Kassakian [11.17] in more detail.

An extended survey on the evolution and the modern approaches in thermal analysis of electrical machine has revealed that it follows the path from the lumped-parameter network, to FEA, and to today's numerical simulations using CFD techniques. It can be advantageous to use the lumped-parameter network approach for its simplicity, requirement of less computing resources, and fast calculations. FEA can be considered a convenient solution in a very complex geometry not approachable with lumped-parameter network. CFD can deal with quite complex heat transfer problems and provide very accurate results. However, it needs very knowledgeable and experienced thermal engineers to correctly set up the model and requires very high computer capabilities and powerful computing resources. As a matter of fact, each of these approaches has its advantages and disadvantages.

A comprehensive review has been made by Boglietti et al. [11.18] on the evolution and modern approaches in the thermal analysis of electrical machines. The three primary thermal analysis methods, that is, lumped-parameter thermal network, FEA, and CFD, are analyzed in depth and compared in order to highlight the qualities and defects of each. The thermal network is the most basic form to calculate conduction, convection, and radiation resistances for different parts of the motor construction. The convection heat transfer coefficient is most often based on empirical convection correlations. This is fundamentally different from CFD analysis, where the heat transfer coefficient is calculated from the CFD model itself. According to Boglietti et al., FEA can only be used to model conduction heat transfer in solid components. They expect that CFD will be more popular and widespread in thermal analysis due to the fast development in computational capability of modern computers, as well as the cost reduction of CFD software.

11.3 Thermal Analysis Using Finite Element Method

FEM has been one of the major numerical solution techniques. One of the major advantages of the FEM approach is the simplicity and ease for using FEM to solve complex geometry problems. By comparing with finite difference method (FDM) and FVM, FEM is superior in its built-in ability to handle unstructured meshes, a rich family of element choices, and natural handling of boundary conditions. As indicated by its name, FEM requires division of the solution domain into many discrete volumes or finite elements. Thus, FEM yields discretized equations that are entirely local to the elements and provides complete geometric flexibility [11.19]. Applications of FEM become more widespread for motor design engineers to analyze structural, thermal, and fluid dynamic problems and their interactions. However, it is difficult to develop computationally efficient solution methods for strongly coupled and nonequations using FEA [11.20]. In addition, FEM does not help in determining quantities such as convective heat transfer coefficients. Thus, FEM is still not comparable to professional commercial CFD codes in solving convective heat transfer and fluid dynamic problems so far.

One example of employing FEM to carry out a thermal analysis is shown in Figure 11.16. This is a frameless motor with two endbells positioned at the two sides of the stator core. The endbells are made from gray cast iron and ductile cast iron for achieving high-vibration damping and high-strength properties. The stator winding is encapsulated by epoxy resin to eliminate the voids inside the winding, improve heat transfer, and increase

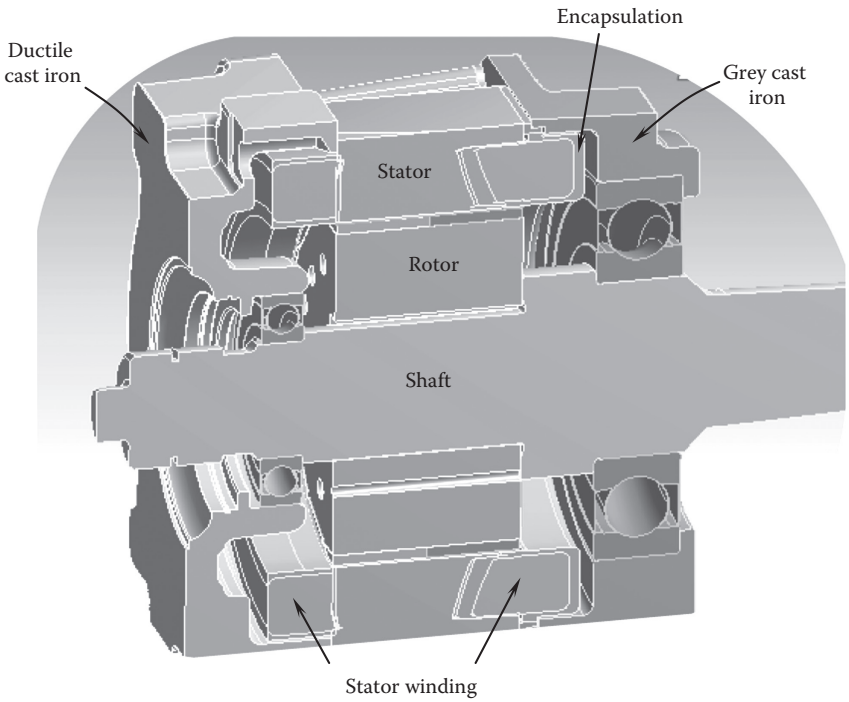

FIGURE 11.16
FEM model of an electric motor.

the winding's dynamic stiffness. The physical motor model is generated by a CAD tool and transferred into the FEM model.

This FEM analysis deals primarily with heat conduction through the motor components. The heat transfer coefficient h on the outer surfaces of the motor is obtained from the heat transfer correlations available in the literature for addressing the heat dissipation from the motor to the ambience (Figure 11.17). It shows for both horizontal and vertical surfaces, heat transfer coefficients increase exponentially with the increase in temperature. Due to the symmetry of the model, only a half of the motor is modeled. In addition to heat conduction (inside the motor) and convection (on the motor outer surfaces), the heat radiation effect is also integrated into the model. The initial temperature of the motor is set at 45°C. The thermal conductivities of copper, epoxy E88, and cast iron are functions of temperature (Figure 11.18). As can be seen from the figure, for the temperature less than 200°C, the thermal conductivity of copper decreases sharply and then becomes a linear function of temperature for $T > 200$°C. By comparison, the temperature effect on k for epoxy is rather weak; when the temperature increases from 100°C to 500°C, the thermal conductivity reduces only 8%. In addition, the increase in the silicon content of the silicon iron lamination can lead to decrease in the thermal conductivity and increase in eddy-current losses [11.21].

The power losses from the stator winding, rotor and stator cores, bearings, and others are properly defined to the corresponding components as the heat sources.

Figure 11.19 shows the meshes created for the FEM model. Relatively fine meshes are used in the vicinities of stress-concentrated regions such as sharp contact areas, entrant corners, load transfer (welds, bonded joints, reinforcing bars, etc.), abrupt changes in thickness, material properties, and cross-sectional areas. It is critical to pay attention to

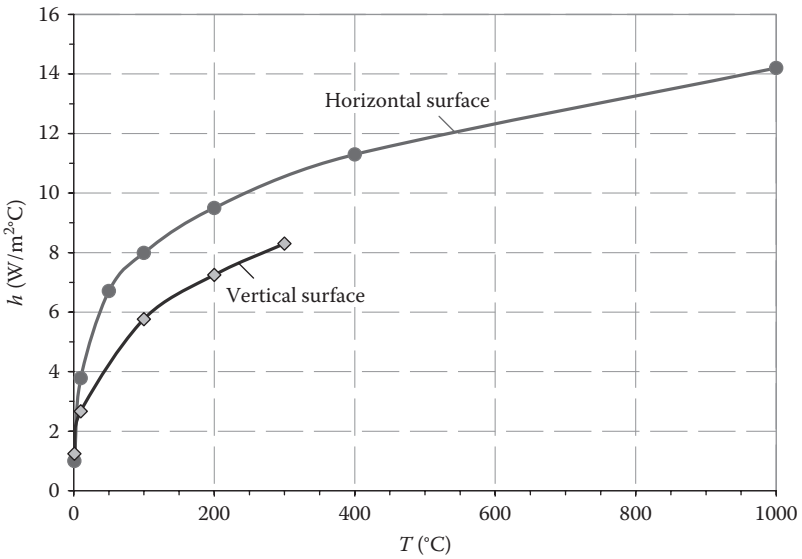

FIGURE 11.17
Hear transfer coefficients on horizontal and vertical surfaces of the motor, obtained from the thermal correlations in the literature.

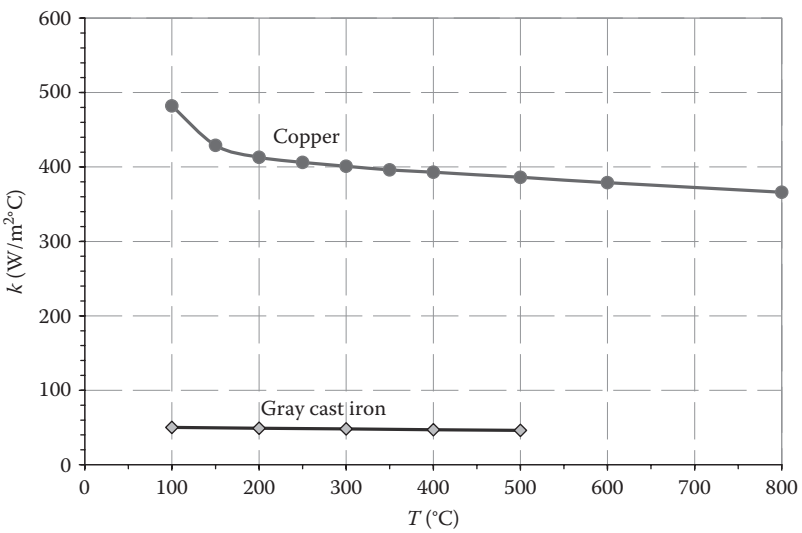

FIGURE 11.18
Thermal conductivities of copper and gray cast iron as functions of temperature.

the connections between adjacent parts and set up the same mesh pattern on them. In the mesh setting, fast transitions from small elements to large elements should always be avoided.

The calculated temperature distribution in the motor is presented in Figure 11.20. It is noted that the temperature ranges from 92.4°C to 112.7°C, with the maximum temperature occurring on the stator winding. In the rotor, temperature is quite uniform, about 95°C.

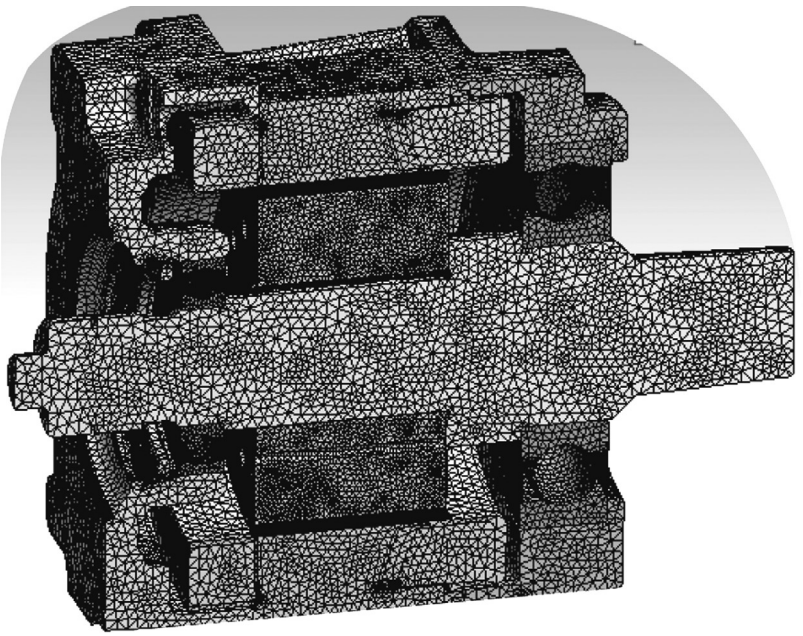

FIGURE 11.19
Meshes on the motor using FEM.

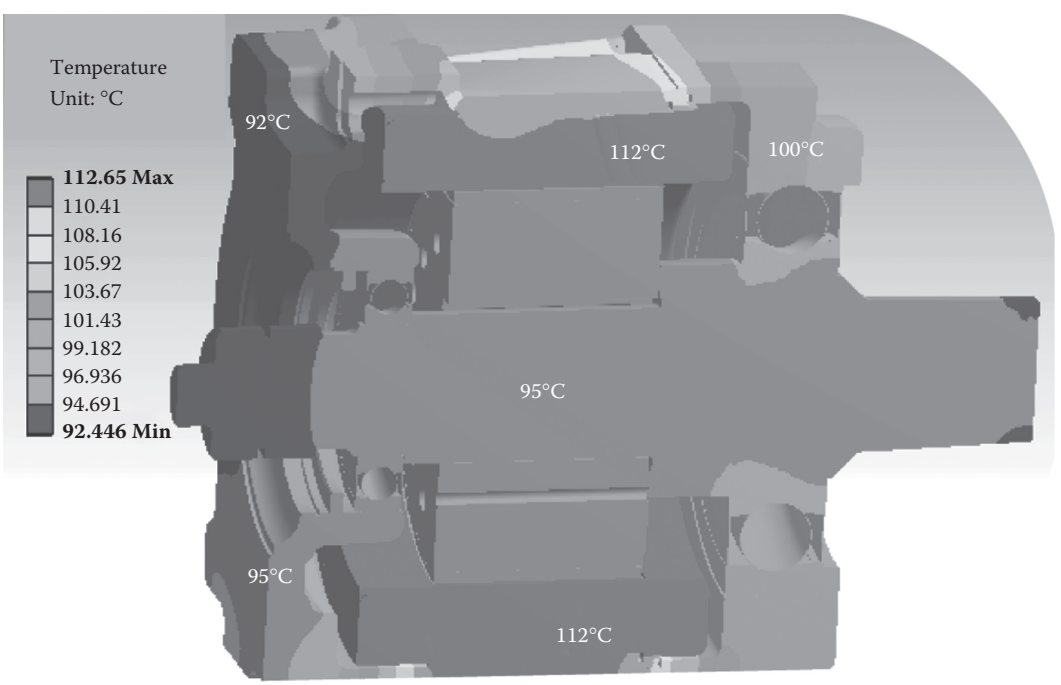

FIGURE 11.20
Temperature distribution on motor components.

The temperature at the large bearing of the drive side is about 5°C higher than that of the small bearing. Due to the gaps between the encapsulated stator winding and two endbells, the temperatures at the endbells are 10°C–18°C lower than that of the stator core. By eliminating these gaps, the temperature difference between the winding and endbells can be reduced less than 12°C.

11.4 Rotordynamic Analysis

Rotordynamic analysis is of great practical importance when designing rotating systems such as motors, generators, pumps, and compressors. It has been widely accepted that high-vibration levels of electric motors are caused by lateral critical speeds near the operating speeds. By modeling the rotating geometry and its dynamic characteristics, such as stiffness and damping, the critical speeds of rotating machinery can be predicted. As a consequence, design optimizations can be carried out to ensure that the machine operating speeds do not fall into the vicinities of its critical speeds.

The finite element rotordynamic analysis and critical-speed design sensitivity investigation are performed with a motor fan system. Results show that critical-speed separation margins of more than 30% are obtained from a rated speed of 60,000 rpm without any adverse effects from the spline shaft and that the critical-speed change rates to the support modeling of spline shaft connection points are extremely negligible. Furthermore, the critical-speed change rates to the shaft-element length changes show quantitatively that the spline shaft has some limited influence on the fourth critical speed but practically no influence on the first to third critical speeds.

11.4.1 Problem Description

Cooling fans in electric motors are typically mounted at the end of the rotor to produce high-pressure cooling air for the motor cooling. The cooling fan blows or sucks air into the motor being cooled and exhausts hot air from the interior of the motor to either an environment or a heat exchanger to be cooled before reentering the machine. A seal must be positioned between the high-pressure hot gas discharging from the fan and the low-pressure cold gas inlet to the rotor. As prevailing market trends require higher performance, high efficiency, higher reliability, lower cost, and high-power density motors, motor cooling, especially at the stator and rotor end regions, becomes a limiting factor.

Fan loss is the prime mover power transmitted through the rotor shaft to raise the static pressure of the cooling air flow through the fan. An examination of motor design data shows that fan loss could be a significant portion among the total windage losses. This loss can be effectively reduced by optimizing the fan parameters in design, including fan blade profile (for instance, 3D blade profile), number of fan blades, inlet and exit conditions, diffuser performance, and fan tip clearances.

Usually, the lack of a fan test facility causes any new fan design to rely on only numerical simulation results from CFD analysis. However, a high risk is incurred without proper validation of the numerical model through experimental investigations. The most reliable information about a physical process is given by real measurement. The motor design process can benefit from full-scale fan test data for optimizing fan performance and motor design.

With strong demands for large-size, high-power, and cost-effective electric machines, there have been growing concerns to build up the fan testing facility for optimizing machine cooling design. As the key step of a typical design process for rotating machinery, the rotordynamic analysis must be carried out prior to the construction of the fan facility.

The rotordynamic model includes the shaft–rotor assembly (shaft, couplings, and bearings), the rotor bearings, and their supports. The stiffness and mass of the bearing support play a crucial role in the calculation of the rotor critical speeds. The objective of the analysis is to determine the damped and undamped critical speeds of the fan test system with the bearing supports' stiffness, damping, and mass modeled.

11.4.2 Bearing Support's Stiffness and Damping

As demonstrated in Figure 11.21, the fan test system consists of a shaft, a forward disk and an aft disk both mounted on the shaft, journal bearings, and bearing supports. The outer ring is mounted on the disks rigidly, and fan blades are attached to the outer ring and forward disk. The system is supported with two bearings at the rotor ends with asymmetrical translational stiffness and damping values. In addition, the two bearings provide the additional damping for stabilizing the systems.

The stiffness, damping, and effective mass of the bearing supports can be determined from experimental tests. An effective approach is to use an instrumented hammer to excite the system and measure its response. Equipped with an accelerometer at one end, this hammer is used in tandem with the sensor to measure the vibration. This technique is usually called the impact input test, or impedance test, which is effective, because the impact inputs a small amount of force in the system and receives the response over a large frequency range. To properly apply this technique in this problem, it needs to select a number of locations on the bearing support for obtaining accurate results, as shown in Figure 11.22.

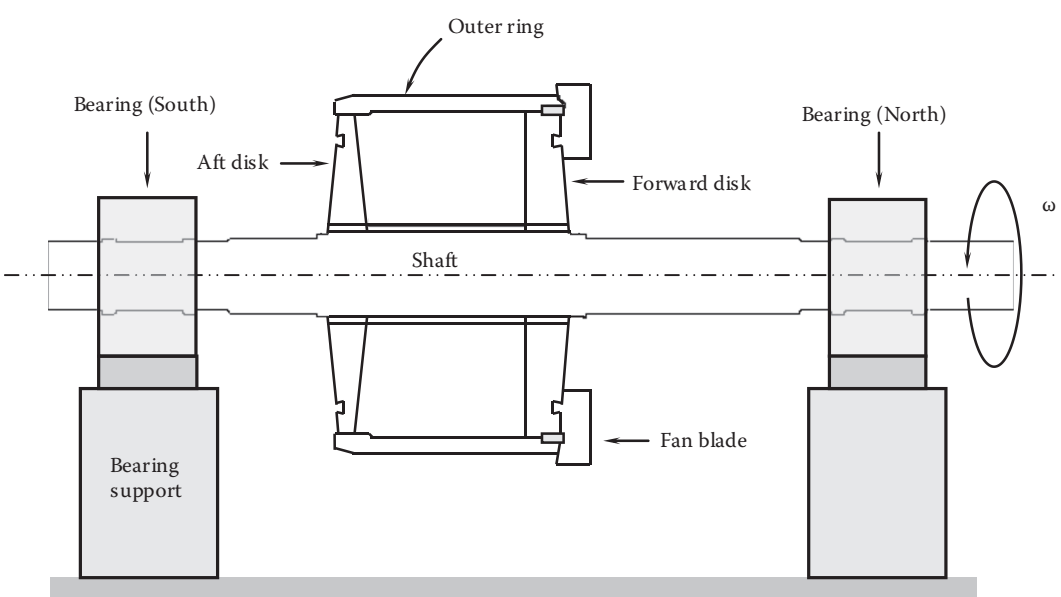

FIGURE 11.21
Configuration and components of the fan test system.

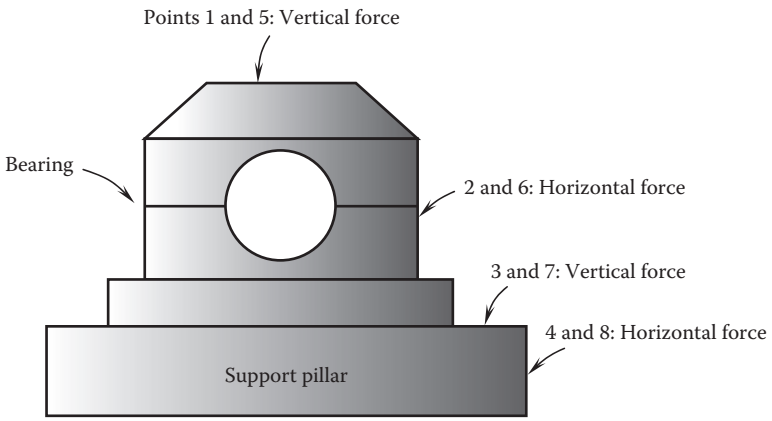

FIGURE 11.22
Using an instrumented hammer to excite the bearing support to obtain the natural frequency, damping, stiffness, and mass. Points 1 and 4 are taken on the south bearing, and points 5 and 8 are taken on the north bearing. Points 1, 3, 5, and 7 are vertical measurements, while points 2, 4, 6, and 8 are horizontal measurements.

TABLE 11.2
Bearing Support Stiffness, Damping, and Mass Data

Direction	Bearing Support	Point Location	Damping (N-s/m)	Natural Frequency		Stiffness (N/m)	Mass (kg)
				Hz	rpm		
Vertical	South	1	249,556	70	4200	5.15×10^8	2715
	North	5	340,271	82	4920	3.50×10^8	1319
Horizontal	South	2	51,837	37	2220	5.25×10^7	972
	North	6	14,010	19	1140	1.75×10^7	1228

The resulting test data as a function of frequency include force/acceleration (N-s^2/m), force/velocity (N-s/m), and force/distance (N/m). The stiffness in each direction is determined using the force/distance curve and using the value as the frequency approaches zero. The supports' damping is obtained by using the force/velocity curve and using the value at the natural frequency. The natural frequency for each bearing support direction and the resulting damping values are shown in Table 11.2.

All of the components are steel ($\rho = 7833$ kg/m^3) except for the blades that are aluminum ($\rho = 2796$ kg/m^3). The rotordynamic model of a fan test system is shown in Figure 11.23. The upper half of the cross section represents the geometry used to calculate the mass properties, and the lower half represents the geometry used to calculate the stiffness. For each of the two disks, the density and outer radius were solved for to exactly match the correct mass and mass polar moment of inertia. The forward disk includes the blade mass properties.

The disks' connections to the shaft are modeled as if they are continuous material with the shaft. The outer-ring press fit joints to the disks are modeled with a *rigid bearing* connection. This modeling technique couples the slope and displacement of the two components together.

For the undamped critical-speed analysis, only one bearing stiffness is needed. Therefore, the averaged stiffness is used in the undamped critical-speed calculation

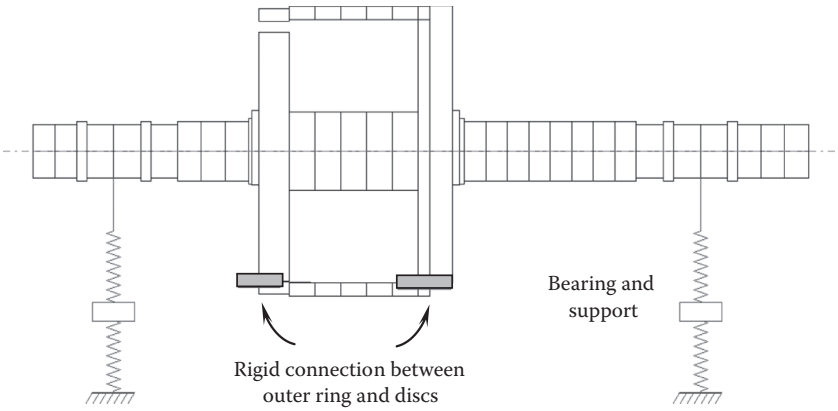

FIGURE 11.23
Rotordynamic model of fan test system.

TABLE 11.3

Translational Stiffness and Damping of the Fan Bearing Support

Translational Stiffness		**Translational Damping**	
k_{xx}, horizontal (N/m)	k_{yy}, vertical (N/m)	c_{xx}, horizontal (N-s/m)	c_{yy}, vertical (N-s/m)
1.93×10^{8}	3.85×10^{8}	4.48×10^{5}	8.50×10^{5}

(where $\bar{S}_b = 2.89\times10^{8}\,\mathrm{N/m}$). For damped critical-speed analysis, both horizontal and vertical stiffness and damping are incorporated into the model (Table 11.3).

The primary advantage in using this technique is that it can monitor phase shifts, vibration force, and coherence. When the slope of the phase–frequency curve becomes infinity, the frequency at which it occurs is the natural frequency.

The mass of the bearing support m_b is determined with the bearing support's stiffness k_b and natural frequency ω_n:

$$m_b = \frac{k_b}{\omega_n^2} \tag{11.29}$$

11.4.3 Rotordynamic Modeling

A commercial rotordynamic software has been applied for this analysis. This software is a rotordynamic program based on an FEA method and takes into account rotary inertia, shear deformation, and gyroscopic effects.

The geometry of the fan test system is shown in Figure 11.23. The mass and mass moments of inertia of the disks, outer ring, and blades are obtained from the 3D solid model. All components are made of steel except the fan blades that are made of die casting aluminum. In the rotordynamic model, the bearing spring is modeled in series with the bearing support spring.

The undamped and damped critical speeds are evaluated for synchronous forward and backward whirl. The stability of the damped critical speeds is also evaluated. The test rig design speed is 3000 and 3600 rpm with a 1.2× overspeed condition of 4320 rpm.

11.4.4 Results of Rotordynamic Analysis

The undamped and damped critical speeds are evaluated for synchronous forward and backward rotations. The stability of the damped critical speeds is also evaluated. Modern high-performance motors normally operate above the first critical speed, which is considered as the most important mode in the system, and avoid continuously operating at or near the critical speeds. The typical evaluation criterion is to maintain a critical-speed margin of ±10% between the operating speed and the nearest critical speed. Otherwise, redesign is required. The undamped critical speeds are shown in Table 11.4.

In practice, the mode shape corresponding to a critical speed is important in determining how the rotor system might vibrate when the critical speed is excited. The undamped mode shapes associated with critical speeds for the forward synchronous rotation are presented in Figure 11.24. The first mode at 2096 rpm shows that the rotor displacement at the bearings is relatively small while the vibration amplitude at the rotor center is much larger. The second mode has a conical mode shape with substantial motion at the bearings at the critical speed of 3422 rpm. This mode type is usually sensitive to rotor speed. The third mode occurring at 4847 rpm is similar to the first mode but has the larger rotor motion at the bearings. The fourth mode is similar to the second mode with a very small displacement at one rotor end.

Under the backward synchronous rotation condition, first three undamped modes keep the same shapes as the forward synchronous rotation case. The difference of the corresponding critical speeds between the two cases is less than 3%. However, the critical speed of the fourth mode becomes 4,568 rpm, which is much lower than 11,459 rpm in the previous case. Correspondingly, the mode has the second bending shape (Figure 11.25).

The evaluation of rotor stability is an important aspect of motor rotor design. Rotor system instabilities are normally associated with poor designs and inadequate selection of bearings. In practice, rotor stability is normally evaluated by the amount of damping on the first mode. The standard measure of mechanical damping is the logarithmic decrement, which is computed as the natural logarithm of the ratio between the amplitudes of two successive peaks. The relation between the mode logarithmic decrement δ and the corresponding damping ratio ζ can be found to be [11.22]

$$\delta = \frac{2\pi\zeta}{\sqrt{1-\zeta^2}} \tag{11.30}$$

TABLE 11.4

Undamped Critical Speeds

	Forward Synchronous Rotation				Backward Synchronous Rotation			
		Strain Energy (%)				Strain Energy (%)		
Mode	Critical Speed (rpm)	Rotor	Supports	Bearings	Critical Speed (rpm)	Rotor	Supports	Bearings
1	2,096	10	22	68	2081	11	22	67
2	3,422	0	38	62	3033	1	33	66
3	4,847	39	50	11	4700	41	42	17
4	11,459	9	2	89	6568	59	21	20

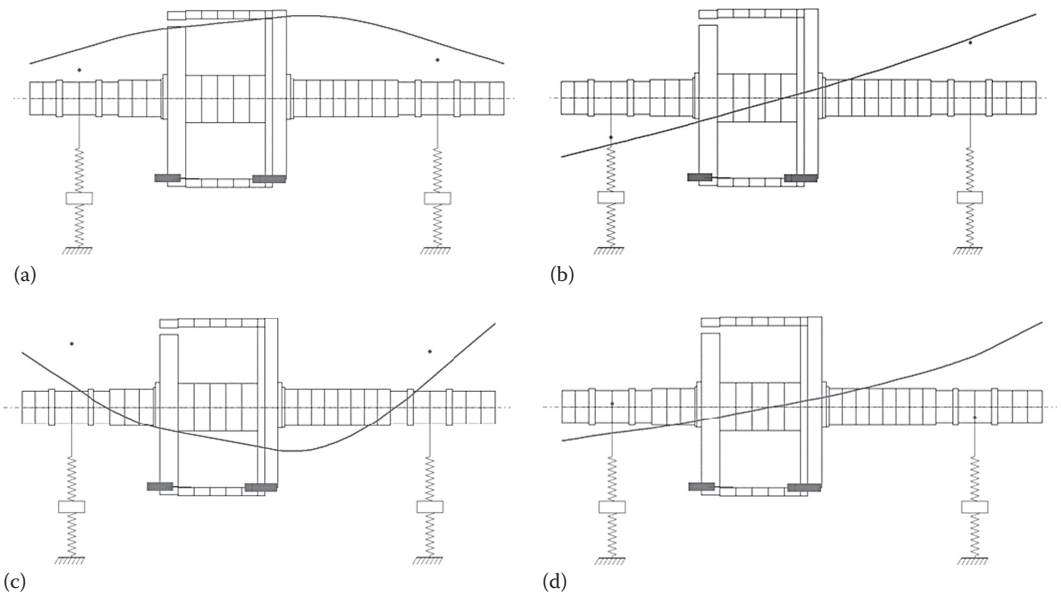

FIGURE 11.24
Undamped critical speeds and mode shapes of forward synchronous rotation: (a) mode 1: 2,096 rpm; (b) mode 2: 3,422 rpm; (c) mode 3: 4,847 rpm; (d) mode 4: 11,459 rpm.

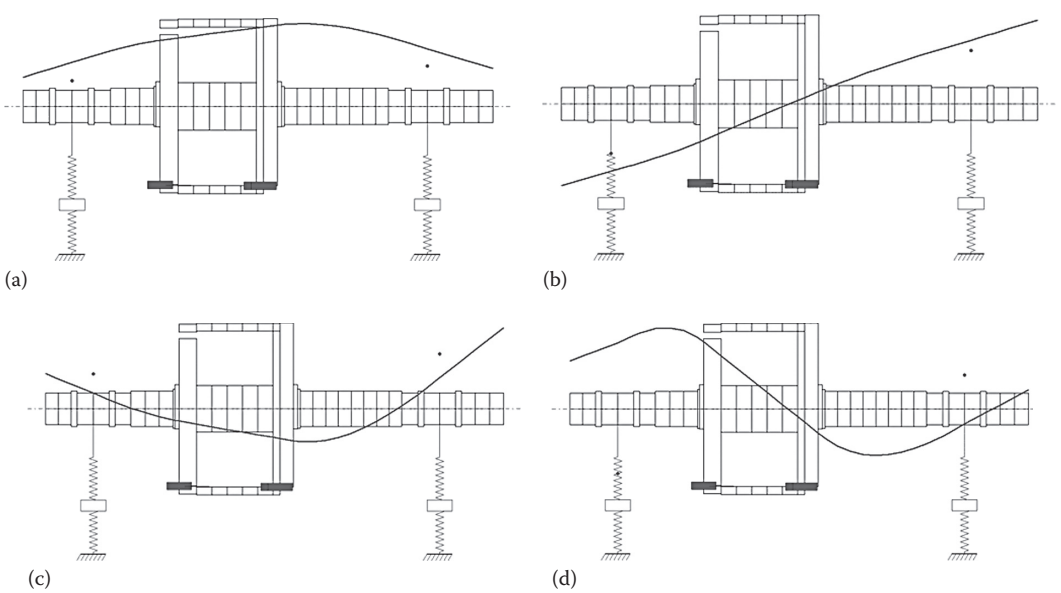

FIGURE 11.25
Undamped critical speeds and mode shapes of backward synchronous rotation: (a) mode 1: 2081 rpm; (b) mode 2: 3033 rpm; (c) mode 3: 4700 rpm; (d) mode 4: 6568 rpm.

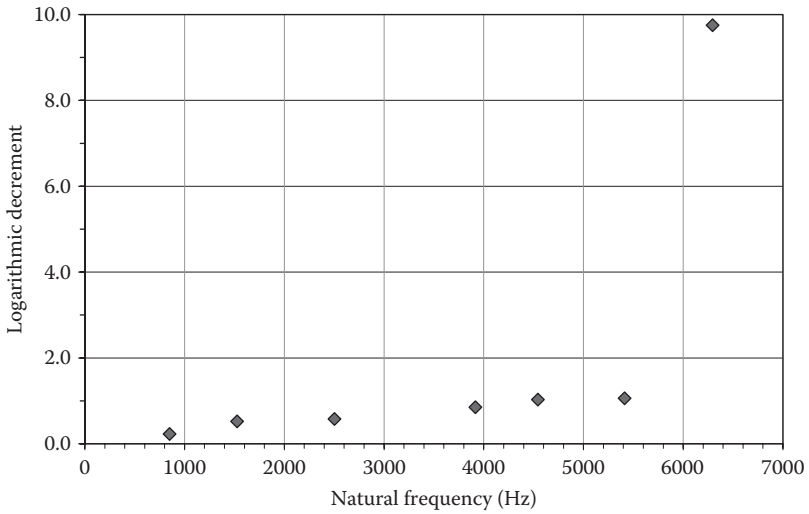

FIGURE 11.26
Damped natural frequencies versus damped ratios for determining the system stability.

TABLE 11.5
Damped Critical Speeds

Mode No.	Critical Speed (rpm)	Logarithmic Decrement at Critical Speed	Stability	% Near 3000 rpm	% Near 3600 rpm	% Near 4320 rpm
1	850	0.23	Stable	−71.7	−76.4	−80.3
2	1527	0.52	Stable	−49.1	−57.6	−64.7
3	2502	0.58	Stable	−16.0	−30.0	−41.7
4	3915	0.85	Stable	30.5	+8.8	−9.4
5	4543	1.03	Stable	51.4	+26.2	+5.2
6	5413	1.06	Stable	80.4	+50.4	+25.3
7	6295	9.75	Stable	109.8	+74.9	+45.7

Theoretically, for $\delta > 0$, the system vibration will be damped out with time, and the system is considered stable. On the contrary, for < 0, the vibration will increase with time, and the system is considered unstable. However, per API Standard 617 [11.23], for a rotor system to be stable, a minimum logarithmic decrement of 0.1 is required.

The damped natural frequencies ω_n versus logarithmic decrement δ are plotted in Figure 11.26. It can be seen from the figure that all logarithmic decrement values larger than 0.1 and thus all modes pass the stability evaluation criteria.

Table 11.5 presents the predicted damped critical speeds. The data shown in this table indicate that mode 4 fails the ±10% avoidance criteria for the 3600 rpm operating speed. Modes 4 and 5 fail the ±10% avoidance criteria for the 4320 rpm overspeed condition.

The mode shapes of damped critical speeds are plotted in Figures 11.27 and 11.28 for detail descriptions. The operating speed ranges of 50 and 60 Hz machines, as well as the overspeed range, are plotted to compare with the damped critical speeds.

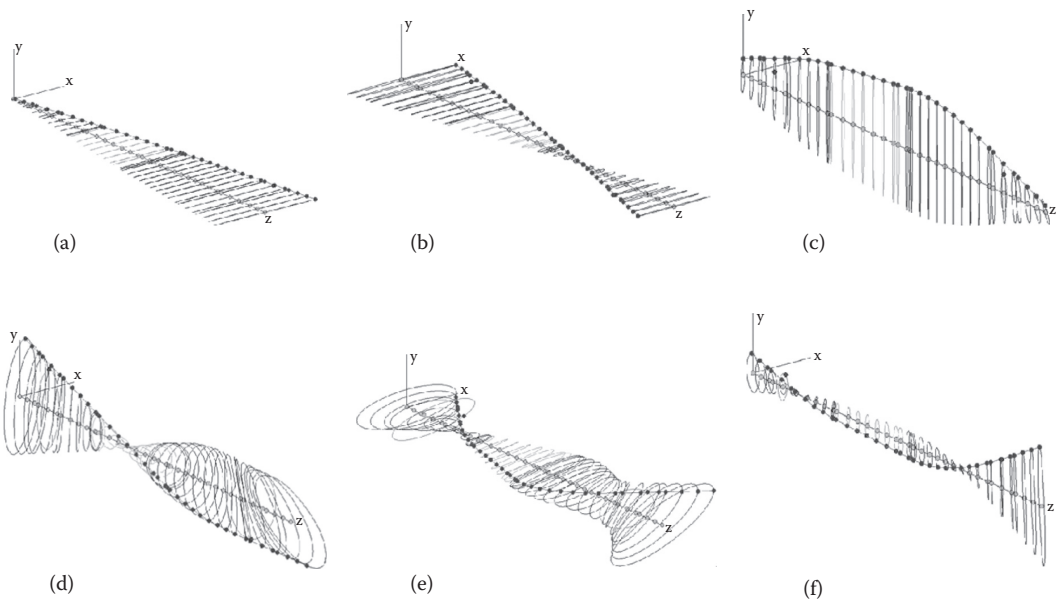

FIGURE 11.27
Damped critical-speed mode shapes: (a) mode 1 at 850 rpm; (b) mode 2 at 1527 rpm; (c) mode 3 at 2502 rpm; (d) mode 4 at 3915 rpm; (e) mode 5 at 4543 rpm; and (f) mode 6 at 5413 rpm.

11.5 Static and Dynamic Stress/Strain Analysis

In the design of electric motors, static or dynamic analysis must be performed to determine the stresses, strains, displacements, and factor of safety in motor components and structures. Stress and strain define the intensity of internal reactions of deformed solid components with the changes of dimension and shape by externally applied forces. Stresses can be further divided as tensile, compressive, or shearing stress, according to the type of loads and straining action of the loading parts. Load-deformation data obtained from tensile or compressive tests can be used to calculate the stress of the specimen:

$$\sigma = \frac{F}{A} \tag{11.31}$$

where
F is the applied force on the specimen
A is the original cross-sectional area of the specimen

Strain is a measure of the change in the specimen's length Δl to its original length l_o, defined as

$$\varepsilon = \frac{l - l_o}{l_o} = \frac{\Delta l}{l_o} \tag{11.32}$$

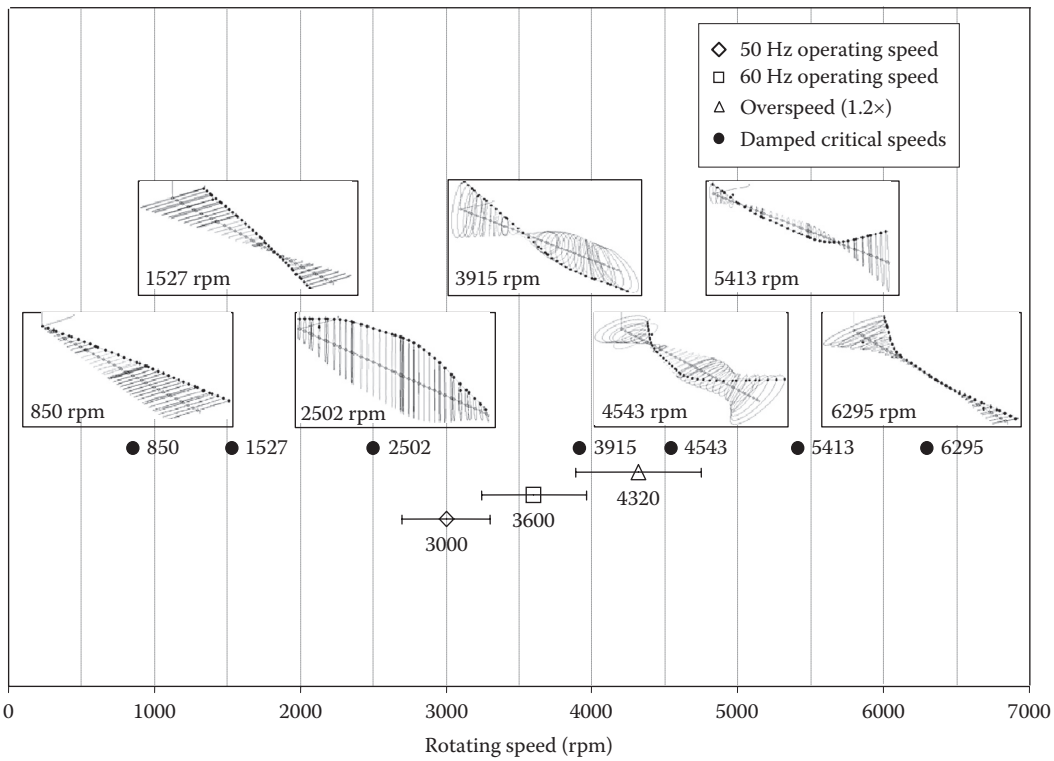

FIGURE 11.28
Predicted damped critical speeds and corresponding mode shapes.

For most solid materials, the tensile/compressive stress is directly proportional to the strain, following the Hooke's law:

$$\sigma = E\varepsilon \tag{11.33}$$

where E is the modulus of elasticity or Young's modulus. It is noted that Hooke's law describes only the initial linear portion of the stress–strain curve.

Similarly, the relationship of the shear stress τ and shear strain γ is given as

$$\tau = G\gamma \tag{11.34}$$

where G is the shear modulus of elasticity. For steel and aluminum, the shear modulus of elasticity G is approximately 40% of the modulus of elasticity E.

Unlike stress, strain is a dimensionless quantity and is often expressed in units of mm/mm or in./in. In practice, because the magnitude of measured strain is very small, it is sometimes expressed in microstrain units (e.g., μm/m).

11.5.1 Static Analysis

A static analysis is an essential part of the design process that enables the study of stress, strain, displacement, and shear and axial forces that result from static loads. The word

"static" indicates that the loads maintain invariable in their magnitudes, directions, and acting locations all the time, such as the gravitational force.

Two equilibrium equations are often used in static analysis: force balance and momentum balance with the expressions

$$\sum_i F_i = 0 \tag{11.35}$$

$$\sum_i M_i = 0 \tag{11.36}$$

11.5.2 Dynamic Analysis

A dynamic analysis determines the motor structural response based on the characteristics of the structure and the dynamic loads acting on the motor. Unlike a static loading, a dynamic loading is the forces/loads that move or change when acting on a structure. In normal operation, a rotor is subject to various loads such as electromagnetic force, external bending moment, axial force, friction force, and windage drag force. Due to the rotor rotation, these applied forces always change the directions on the rotor.

11.5.2.1 Centrifugal Force–Induced Stress on PMs

Centrifugal force refers to the force that tends to pull an object toward the axis around which it rotates and can be calculated with the formula

$$f_c = \frac{mu^2}{r} = \frac{m(r\omega)^2}{r} = mr\omega^2 \tag{11.37}$$

where
- m is the mass of the object
- r is the radius
- ω is the rotating speed

Equation 11.37 can be used to calculate the centrifugal force acting on a PM and the average stress on the magnet. Assuming that magnet mass $m = 0.0328$ kg, the magnet contact area $A = 744.5$ mm^2, and the radius $r = 62.8$ mm, the centrifugal force acting on the PM is an exponential function of the rotating speed, as shown in Figure 11.29.

With the calculated centrifugal force, the averaged tensile stress acting on the magnet is determined as

$$\sigma = \frac{f_c}{A} \tag{11.38}$$

The stress–speed curve is presented in Figure 11.30, showing that the magnet stress increases exponentially with the rotating speed.

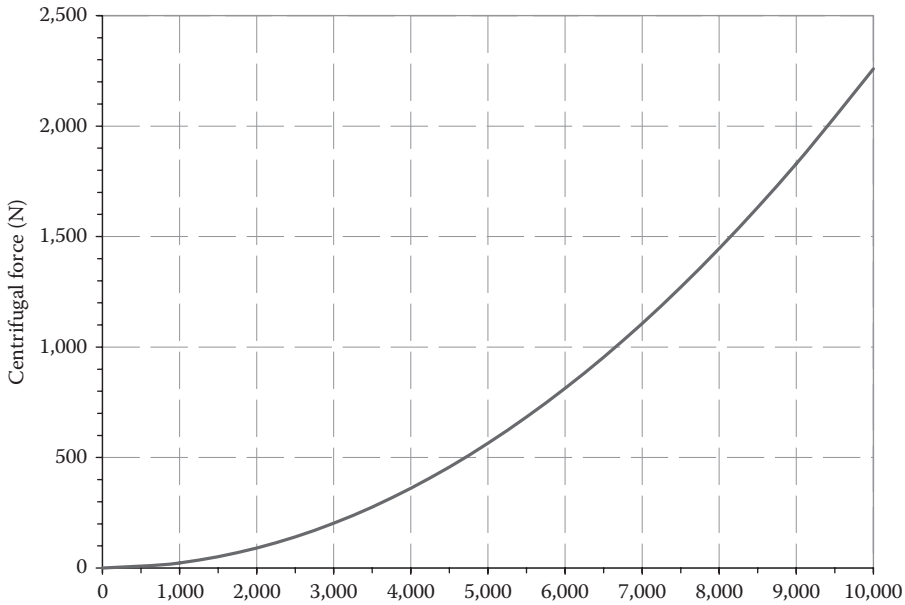

FIGURE 11.29
Centrifugal force acting on a PM under different rotating speeds.

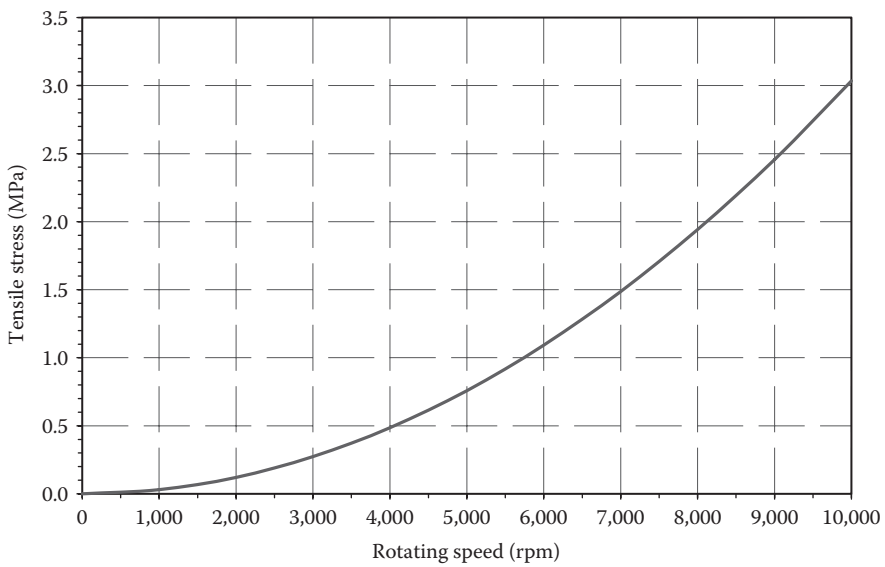

FIGURE 11.30
Average tensile stress of a PM resulted from centrifugal force under different rotating speeds.

11.5.2.2 Structural Analysis Using Finite Element Method

Analytical solutions for modern electric motors under dynamic loading conditions are unlikely to be available due to highly irregular motor geometry, complex loading condition, heterogeneous material properties, and nonlinear dynamic response of structure to a variety of loads. In practice, structural analysis is usually performed using an FEM.

Taking the fan test system as an example, due to the system symmetry, only a small portion of the system is modeled, as illustrated in Figure 11.31. For this problem, the primary consideration is the safety of the rotating system, particularly focusing on two important aspects:

- At high rotating speeds, the stress produced in each rotating component must be lower than its yield strength.
- During operation, all attached components such as blades must be held firmly against centrifugal force and other loads.

The comparison of various stresses (von Mises, radial, Hook, and axial) of the blade is graphically displayed in Figure 11.32. The stress data are well below the material yield strength, indicating that the blades can safely operate at the rotating speed of 4320 rpm.

For the safety consideration, a severe failure scenario is simulated. It assumes one blade, and its cap screws are missed from the system during operation. The aim of the analysis is to find out that under such a severe circumstance whether the whole system collapses.

A structural analysis is carried out for this scenario. The results are illustrated in Figure 11.33 for both maximum principal stress and radial displacement. These results

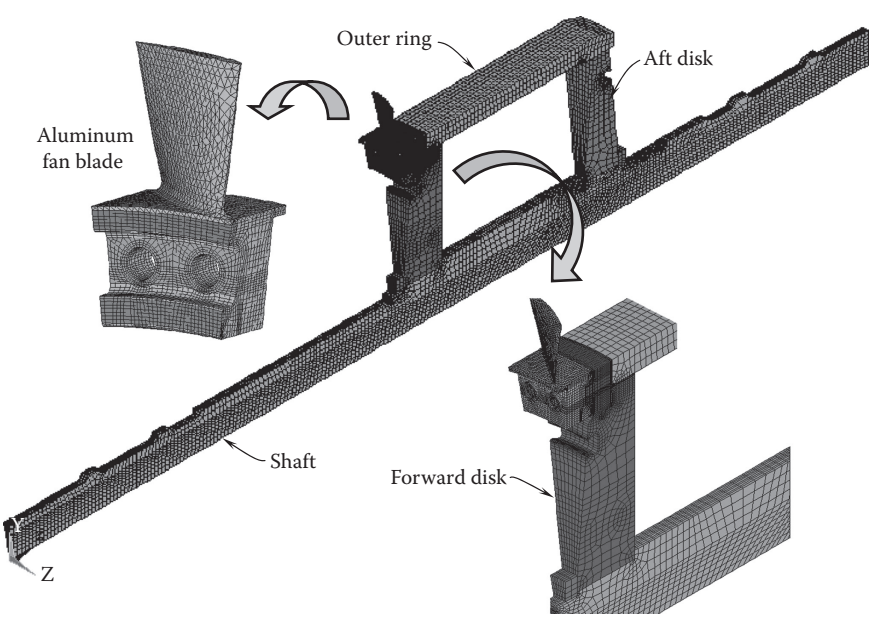

FIGURE 11.31
Mesh of the sector model for structure analysis.

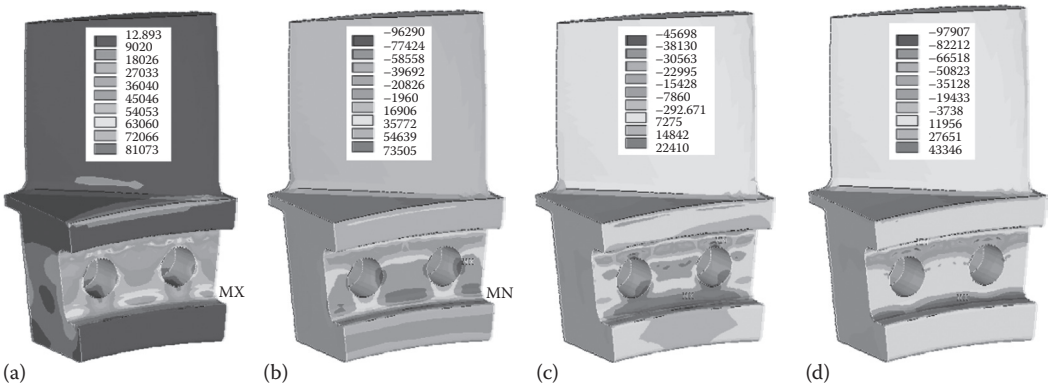

FIGURE 11.32
Comparison of various stresses of a fan blade at 4320 rpm: (a) von Mises stress, (b) radial stress, (c) hoop stress, and (d) axial stress.

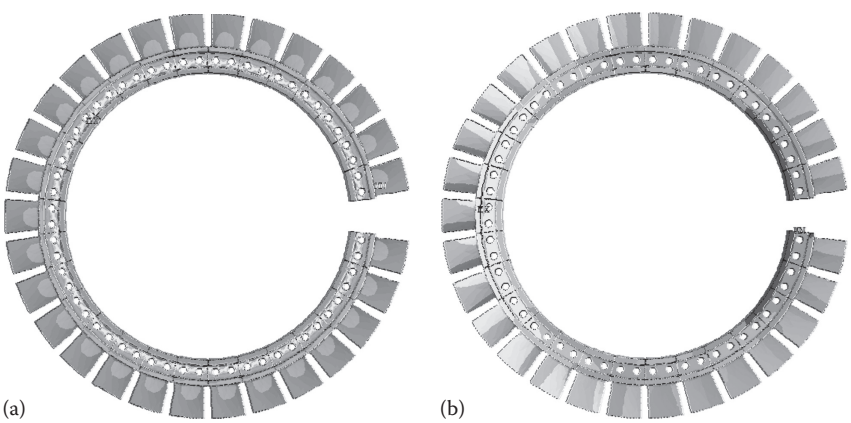

FIGURE 11.33
Results of structural analysis for missing a blade and its cap screws at 4320 rpm: (a) maximum principal stress and (b) radial displacement.

clearly show that the system unbalance due to the blade missing has a significant effect on the blade displacement. However, it does not lead to the system failure.

11.5.3 Shock Load

Electric motors may also experience shock loads caused by some accidental events such as earthquake, free fall, and sudden bump. Motors on fast moving objects (satellites, missiles, rockets, etc.) have to withstand high shock loads during acceleration and deceleration periods. According to Newton's second law, $F = ma$, the force F is proportional to the mass of the object m and the acceleration a (or deceleration if a is negative). Thus, the force F can be considerably high under high acceleration/deceleration conditions.

When shock loads occur during motor operation in a very short period of time, if the shock loads are high enough, failures of motor components can take place immediately or at late time. To prevent motor failure, a common approach to deal with shock loads at

the motor design stage is to define an artificial gravity (i.e., g value, which is a measure of acceleration) in equations at horizontal and vertical directions. For instance, 5–10 g is commonly applied for moving vehicles, and 30–100 g for missiles.

11.6 Fatigue Analysis

It is estimated that about 60% of permanent damages are caused by fatigue failure of materials and elements [11.24]. One of the main concerns in the motor design is to extend the motor's life. Factors that influence the motor fatigue life include load history, geometry, relevant materials, and manufacturing processes.

Fatigue in materials is the process of initiation and growth cracks under alternative tensile loading conditions. Fracture occurs when the effects of total stress and flaw size exceed a critical value commonly referred to as the fracture toughness. The fracture toughness depends upon a number of factors, such as microstructure and composition of the material, service temperature, loading rate, plate thickness, and fabrication processes [11.25]. However, an accurate determination of the fracture toughness is complicated.

In structural component design of electric motors, the appropriate criterion for fatigue failure should be based on consideration of failure modes of the component being designed. The fatigue damage caused by repeated dynamic loads depends on the number of cycles and the frequency of the occurrence of significant stresses. A number of motor parts are subject to cyclic loads during motor operation, leading to fatigue of materials. The material fatigue initiates from the crystalline structure and becomes visible in a later stage by plastic deformation, formation of microcracks on slip bands, coalescence of microcracks, and finally propagation of a main crack.

Several approaches are available in the fatigue analysis, from the traditional time-domain S-N analysis to the frequency-domain approach. The time-domain approach is satisfactory for periodic loading but requires large time records to accurately describe random loading processes. As a contrast, compact frequency-domain fatigue calculations can be utilized where the random loading and response are categorized using power spectral density (PSD) functions and the dynamic structure is modeled as a linear transfer function [11.26].

3D fatigue analysis can be performed using FEM. This method predicts the behavior that is otherwise difficult to find out by theoretical calculations due to the results of large number of degree of freedom involved in it. As a matter of fact, FEM is an excellent tool to calculate the fatigue life of motor components.

11.7 Torsional Resonance Analysis

Torsional resonance is one of the main causes of motor vibration that can lead to fatigue failures of the motor. As illustrated in Figure 11.34, a simple torsional resonance test facility consists of a motor and a load wheel. The motor shaft is connected directly with the load shaft. As the rotor rotates, the inertia of the load wheel provides the torsional load to the rotor, and thus, the torsional resonance of the motor can be determined.

Torsional resonance is affected on both the driving device and rotor inertias, the shaft stiffness that relies on shaft material properties, shaft size, and shaft length.

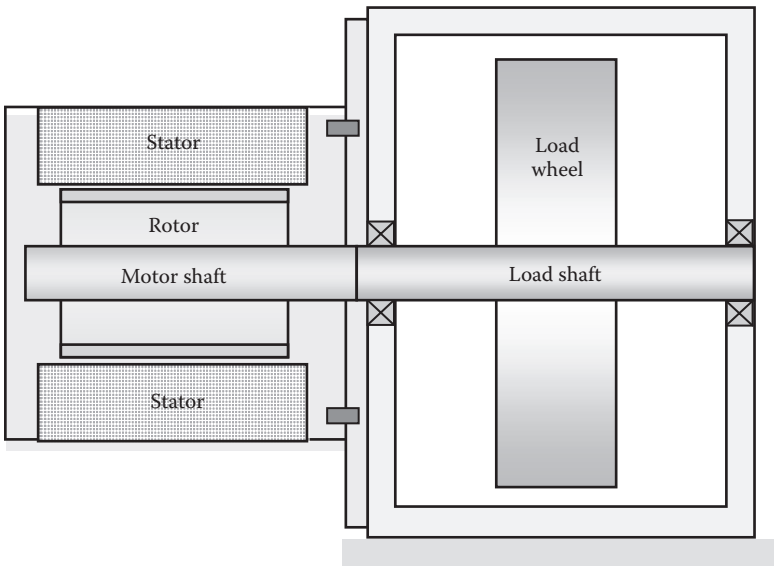

FIGURE 11.34
Torsional resonance measurement of electric motor.

The inertias of the load and motor are calculated in the following equations, respectively:

$$J_l = J_{wheel} + \sum J_{shaft} + \sum J_{i,bearing} \tag{11.39}$$

$$J_m = J_{rotor} + J_{PM} + \sum J_{shaft} \tag{11.40}$$

The torsional stiffness of each shaft segment (both load and rotor) must be determined using the formula

$$S_i = \frac{\pi\left(d_{out,i}^4 - d_{in,i}^4\right)G}{32l_i} \tag{11.41}$$

Thus, the total torsional stiffness is

$$S_t = \frac{1}{\sum\left(1/S_{i,load\,shaft}\right) + \sum\left(1/S_{i,rotor\,shaft}\right)} \tag{11.42}$$

Torsional resonant frequency (Hz) is thus calculated as

$$f_{tr} = \frac{1}{2\pi}\sqrt{S_t\left(\frac{1}{J_m} + \frac{1}{J_l}\right)} = \frac{1}{2\pi}\sqrt{\frac{S_t\left(J_m + J_l\right)}{J_m J_l}} \tag{11.43}$$

The comparison of calculated and tested torsional stiffness is presented in Figure 11.35.

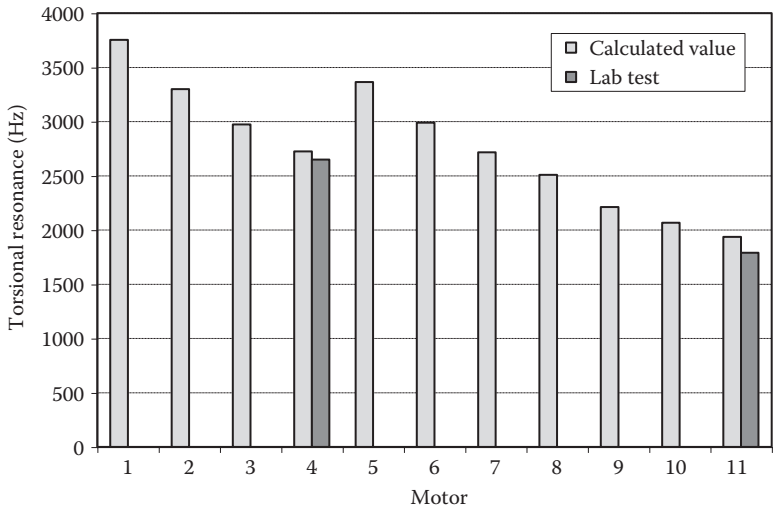

FIGURE 11.35
Comparison of calculated and tested torsional resonances for different types of motor.

11.8 Motor Noise Prediction

As a form of energy, sound is the propagation of low-amplitude pressure waves traveling with the speed of sound. In practice, noise typically refers to undesired or unpleasant sound. Acoustic noise from an electric motor may consist of a number of components: mechanical noise, which is associated with the relevant motion (e.g., rotation and vibration) between motor components; electromagnetic noise, which is activated by the fast change in the electric and magnetic field; and aerodynamic noise (or windage noise), which is introduced by flowing fluid inside the motor.

The main challenge in numerically predicting sound waves stems from the fact that sounds have much lower energy than fluid flows, typically by several orders of magnitude. This poses a great challenge to the computation of sounds in terms of difficulty of numerically resolving sound waves, especially in predicting sound propagation to the far field. Another challenge comes from the difficulty of predicting turbulent flow fields in the near field of the sound source [11.27]. In this field, the interferences between contributing waves from different parts of the source lead to the interference effect, which is greater for pure tones than for bands of noise. The prediction of motor noise level can be thus performed according to the type of noise using available commercial software.

Vibration is generally resulted from the unbalanced dynamic system. In a motor, noise is created by unequal weight distributions of the rotor assembly around its axis of rotation. In addition, noise may be generated by nonuniformly distributed rotor winding in some types of induction motors. It has been found that vacuum impregnation and/or encapsulation of stator has helped in reducing stator winding vibration and noise.

The noise reduction is always one of the design targets for motor engineers and designers. There are a number of engineering approaches available, including

- Carefully balancing the rotor to reduce motor vibration
- Increasing the thickness of motor frame wall
- Improving noise sealing by adopting acoustic blankets [11.28] or by coating/gluing a thin layer of noise-absorbing material on the motor surfaces

11.9 Buckling Analysis

In engineering practices, there are two major categories of failures in mechanical systems: material failure and structural instability. Buckling refers to a phenomenon that a part or component that is subjected to compression suddenly becomes unstable. As shown in Figure 11.36, a thin-walled sheet is subjected to compressive force F on its two ends. By increasing F until a certain value, the sheet will suddenly bend, indicating that it is no longer to withstand any loads. In this figure, δ_l and δ_o are load displacement and out-of-plane displacement, respectively. This phenomenon can also occur for other geometries such as columns, flanges, and shells. Because of its suddenness, bucking failure may cause catastrophic consequences.

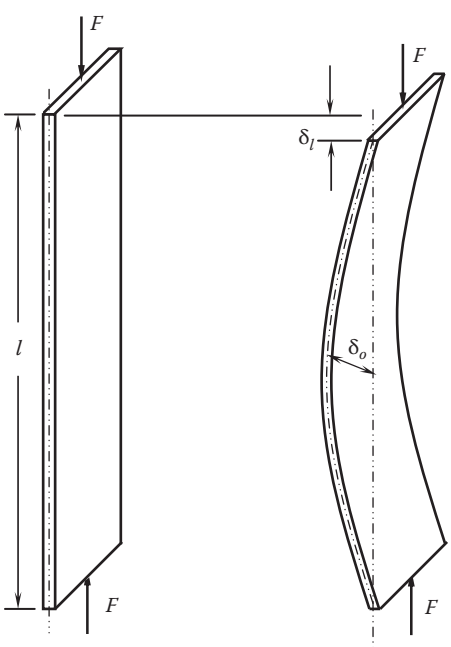

FIGURE 11.36
Buckling of a thin-walled sheet.

The key factor in bucking is the slenderness ratio of the member, defined as the ratio of the member length l and the radius of gyration k:

$$S = \frac{l}{k} = l\sqrt{\frac{A}{I}} \tag{11.44}$$

where
A is the cross-sectional area
I is the area moment of inertia

The stress at failure is called the critical buckling stress. With central loading, there are two models to cover the entire range of compression problems: Euler model and Johnson model [11.29]. The selection of an appropriate model depends on the value of slenderness ratio. The point S_1 is introduced to separate the two models:

$$S_1 = \pi\sqrt{\frac{2CE}{S_y}} \tag{11.45}$$

where
E is Young's modulus
S_y is the yield strength of the material
C is a constant depending on the column end condition

Thus, for long columns where $S > S_1$, the Euler model is used to calculate the critical buckling stress:

$$\sigma_{cr} = \frac{CE\pi^2}{S^2} \tag{11.46}$$

For intermediate-length columns where $S \le S_1$, the Johnson model is applied as

$$\sigma_{cr} = S_y - \frac{1}{CE}\left(\frac{S_y S}{2\pi}\right)^2 \tag{11.47}$$

It is noted that critical bucking stress can be well below the material yield point.

In many practical problems, loads acting on columns are often away from their centroidal axes by the eccentricity e. Correspondingly, the critical buckling stress is calculated by superposing the axial component and the bending component:

$$\sigma_c = \frac{F}{A}\left[1 + \frac{ec}{k^2}\sec\left(\frac{S}{2}\sqrt{\frac{F}{EA}}\right)\right] \tag{11.48}$$

where
F is the force
c is the distance from the neutral axis to the bending surface
ec/k^2 is defined as the eccentricity ratio

11.10 Thermally Induced Stress Analysis

Thermally induced stresses in a motor occur as some or all parts are not free to expand or contract in response to changes in temperature due to the geometric and/or external constrains. Some examples encountered in electric motors are:

- For induction motors, conductor bars and end rings are fabricated by casting aluminum or copper into rotor slots to provide the induction current paths. Due to the different thermal expansions between the casted material and silicon steel laminations, shear stresses can be developed right away at the completion of the casting process due to the different cooling rates of the two materials. This is also true during a motor heating process or motor operation at high temperatures. In fact, frequent starting often imposes thermal stresses on electric motors.
- In a shrink-fitting or press-fitting assembly, the contact pressure between two contacting members changes as the temperature changes from its original fitting temperature, resulting in the variation of contact condition and nonuniform distribution of contact pressure on the contact surface.
- For a PMM, a number of PMs are typically mounted on a rotor. Because these magnets have twice the thermal expansion coefficient over silicon steel, large shear stresses can be produced on the magnets during motor normal operation, leading to uneven axial and radial forces across the magnets and thus possibly developing micro-scale cracks on the magnets.
- When the resin is encapsulated into a stator and cured in an oven for a period of time following a certain temperature profile, the thermal stress is developed in the resin correspondingly with the change of the operation temperature.
- The shaft and housing/endbells are usually made of different materials. A fast variation in temperature may introduce thermal stress or thermal interference problems.

11.11 Thermal Expansion and Contraction Analysis

Materials change their size with the changes in temperature and pressure at different rates. All gases and most liquids and solids expand when heated and contract when cooled, referred to thermal expansion and thermal contraction, respectively. The rate of thermal expansion is characterized by the CTE β for a specific material.

CTE is the measure of how much that material will expand with the change in temperature of 1°. Three types of CTE, that is, the linear, area, and volumetric thermal expansions, are defined as

$$\beta_L = \frac{1}{L}\left(\frac{\partial L}{\partial T}\right)_p \tag{11.49a}$$

$$\beta_A = \frac{1}{A}\left(\frac{\partial A}{\partial T}\right)_p \tag{11.49b}$$

$$\beta_V = \frac{1}{V}\left(\frac{\partial V}{\partial T}\right)_p \tag{11.49c}$$

For anisotropic materials such as crystals and many composites, β_L has different values in different directions. For isotropic materials, there is only one β_L in all directions. For these materials, it is easy to find that

$$\beta_A = 2\beta_L \quad \text{and} \quad \beta_V = 3\beta_L \tag{11.50}$$

Thus, as the temperature changes from T_o to T_f, the variations in the material length, area, and volume can be calculated as

$$\Delta L = \beta_L L_o \left(T_f - T_o\right) \tag{11.51a}$$

$$\Delta A = \beta_A A_o \left(T_f - T_o\right) \tag{11.51b}$$

$$\Delta V = \beta_V V_o \left(T_f - T_o\right) \tag{11.51c}$$

where

L_o, A_o, and V_o represent the initial length, area, and volume of the material

ΔL, ΔA, and ΔV are the variations in length, area, and volume due to the thermal expansion, respectively

The linear thermal expansion coefficients of some solid materials are listed in Table 11.6.

TABLE 11.6

Linear Thermal Expansion Coefficients of Some Solid Materials

Material	Linear CTE at 20°C (μm/m-°C)	Note
ABS—glass fiber	30.4	
Aluminum 356-T6	21.4	For sand casting
Aluminum 383	21.1	For die casting
Aluminum 6061-T6	23.6	
Carbon steel 1008	12.6	
Carbon steel 1045	11.5	Cold drawn
Gray cast iron	10.8	Averaged value for the material class
Copper	16.6	
Copper casting alloy	16.9	UNS C80100
Ductile iron A536	11.6	For casting
Epoxy—cast resins and compounds, unfilled	55	
Epoxy—cast, unreinforced	100	
Epoxy/glass SMC	3.6	
Fiberglass—polyester	25	
Stainless steel 304	16.9	Averaged value for 0°C–100°C

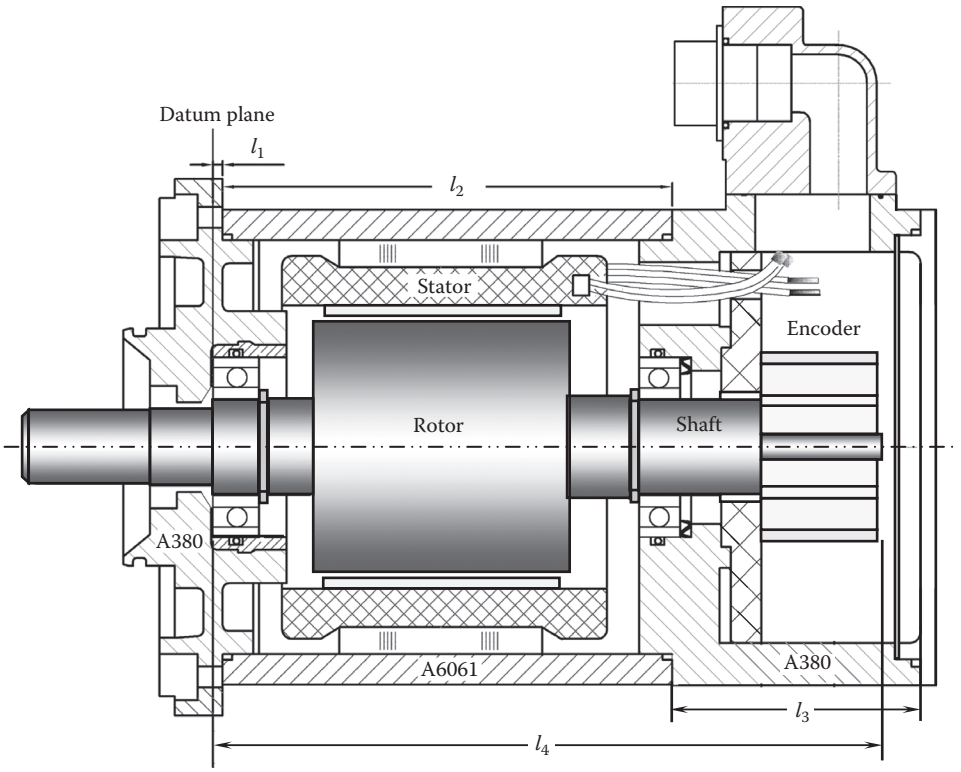

FIGURE 11.37
Calculations of displacement of the shaft and housing/endbell, respectively, for avoiding part interference during thermal expansion and contraction processes.

Thermal expansion and contraction analysis is to address the dimensional changes of motor components due to the variations in temperature during motor operation and storage processes. As a motor is heated or cooled, the dimensions of its components always vary corresponding to the temperature on them. The induced differential dimensions between these components may cause the parts to contact each other or, in more severe conditions, interferences between the parts. Therefore, to avoid undesired thermal-induced interferences, it is important to leave enough allowances for the expansion of hot components.

Figure 11.37 illustrates a regular PMM, consisting of two endbells made of die-casting aluminum A380 and a housing made from extruded aluminum A6061. The shaft is made of carbon steel AISI 1045. Because these materials have different thermal expansion rates, it is important to determine the displacements of the housing/endbell and the shaft to avoid any interference between these parts during thermal expansion.

Referring to Figure 11.37, the differential displacement of the housing and endbells Δl_h during the thermal expansion can be calculated as

$$\Delta l_h = \beta_{A380} l_1 \Delta T_1 + \beta_{A6061} l_2 \Delta T_2 + \beta_{A380} l_3 \Delta T_3 \tag{11.52}$$

where ΔT_i is the temperature difference between the part temperature T_i and the reference temperature T_{ref} (usually T_{ref}=20°C). Similarly, the differential displacement of the shaft Δl_s is

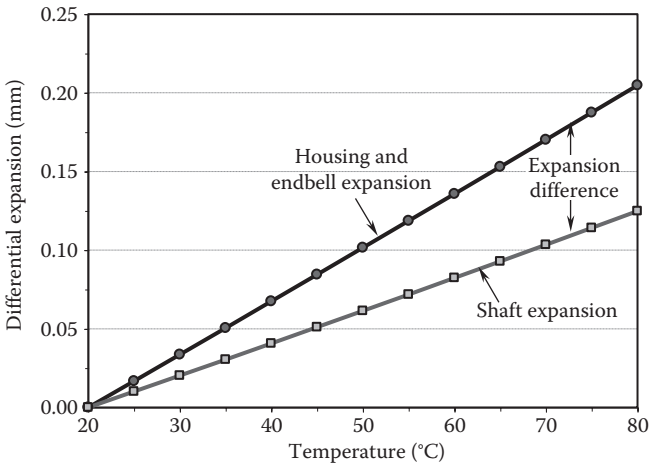

FIGURE 11.38
Comparison of thermal expansions of housing/endbell and shaft, showing that the expansion of the housing/endbell always exceeds that of the shaft.

$$\Delta l_s = \beta_{steel} l_4 \Delta T_4 \tag{11.53}$$

With the real dimensions of the motor component, the calculated results are plotted in Figure 11.38 under different temperatures. It can be observed that at the reference temperature of 20°C, $\Delta l_h = \Delta l_s = 0$. For temperatures larger than 20°C, Δl_h is always larger than Δl_s, and the difference between Δl_h and Δl_s is proportional to the temperature. The results indicate that no interference will occur during the thermal expansion process between these parts.

References

[11.1] Maksimovic, P. 2005. Next steps in CFD. *Pumps & Systems*, November Issue, pp. 44–47.

[11.2] Adair, D. 2012. Chapter 5: Incorporation of computational fluid dynamics into a fluid mechanics curriculum. In book *Advances in Modeling of Fluid Dynamics*, Chaoqun Liu (ed.). InTech, Rijeka, Croatia.

[11.3] Fluent Inc. 2006. Fluent 6.3 User's Guide, Chapter 10—Modeling flows with rotating reference frames.

[11.4] Fluent Inc. 2006. Fluent 6.3 User's Guide, Chapter 11—Modeling flows using sliding and deforming meshes.

[11.5] Couette, M. 1890. Etudes sur le frottement des liquidés. *Annales des Chimie et des Physique* **6**: 433–510.

[11.6] Taylor, G. I. 1923. Stability of a viscous liquid contained between two rotating cylinders. *Philosophical Transaction of the Royal Society of London* **A223**: 289–343.

[11.7] Wilkes, J. O. and Bike, S. G. 2005. *Fluid Mechanics for Chemical Engineers with Microfluids and CFD*, 2nd edn. Prentice Hall, Upper Saddle River, NJ.

[11.8] Dong, S. 2008. Turbulent flow between counter-rotating concentric cylinders: A direct numerical simulation study. *Journal of Fluid Mechanics* **615**: 371–399.

[11.9] Chang, C.-C., Kuo, S.-C., Huang, C.-K., and Chen, S.-L. 2009. The investigation of motor cooling performance. *International Journal of Mechanical, Industrial and Aerospace Engineering* **3**: 43–49.
[11.10] Tong, W. 2008. Numerical analysis of flow field in generator end-winding region. *International Journal of Rotating Machinery* **2008**: Article ID 692748, 10pp. doi:10.1155/2008/692748.
[11.11] Yang, T.-H. 2006. A device for externally rotary drive of offset motor. European Patent EP 1,481,887.
[11.12] Hartmann, U., Knop, C., and Mucha, J. 2011. External rotor motor with a varying armature profile. World Intellectual Property Organization (WIPO) Patent WO2011110421.
[11.13] Heinen, A. J. 2008. Wheel provided with driving means. U.S. Patent 7,347,427.
[11.14] Anderson, J., Dick, E., Degrez, G., Grundmann, R., Degroote, J., and Vierendeels, J. 2009. *Computational Fluid Dynamics: An Introduction*, 3rd edn. Springer, Berlin, Germany.
[11.15] Steinbrecher, R., Radmehr, A., Kelkar, K. M., and Patankar, S. V. 1999. Use of flow network modeling (FNM) for the design of air-cooled servers. *Proceedings of the Pacific RIM/ASME International Intersociety Electronics and Photonic Packaging Conference*, Maui, Hawaii, Vol. II, pp. 1999–2008.
[11.16] Liu, Y., Lienhard V. J. H., Booth, J. D., and Stairs, R. W. 2002. Integrated simulation toolkit for electronic controlled motor system. *Thermal Challenges in Next Generation Electronic Systems Conference*, Santa Fe, NM.
[11.17] Perez, I. J. and Kassakian, J. G. 1979. A stationary thermal model for smooth air-gap rotating electric machines. *Electric Machines and Electromechanics* **3**(**3-4**): 285–303.
[11.18] Boglietti, A., Cavagnino, A., Staton, D., Shanel, M., Mueller, M., and Mejuto, C. 2009. Evolution and modern approaches for thermal analysis of electrical machines. *Transaction on Industrial Electronics* **56**(**3**): 871–882.
[11.19] Shtrakov, S. and Stoilov, A. 2006. Finite element method for thermal analysis of concentrating solar receivers. The Computing Research Repository (CoRR), Paper No. 0607091. South-West University, Blagoevgrad, Bulgaria. http://arxiv.org/abs/cs/0607091.
[11.20] Ranade, V. V. 2002. *Computational Flow for Modeling for Chemical Reactor Engineering*. Academic Press, San Diego, CA.
[11.21] Chin, Y. K., Nordlund, E., and Staton, D. A. 2003. Thermal analysis lumped-circuit model and finite element analysis. *Sixth International Power Engineering Conference* (*IPEC*), Singapore, pp. 952–957.
[11.22] Yoon, S. Y., Lin, Z., and Allaire, P. E. 2013. *Control of Surge in Centrifugal Compressors by Active Magnetic Bearings: Theory and Implementation*. Springer, New York.
[11.23] API. 2002. API Standard 617. Axial and centrifugal compressors and expender-compressors for petroleum, chemical and gas industry services.
[11.24] Torbacki, W. 2007. Numerical strength and fatigue analysis in application the hydraulic cylinders. *Journal of Achievements in Materials and Manufacturing Engineering* **25**(**2**): 65–68.
[11.25] U.S. Department of Transportation. 2012. Steel Bridge Design Handbook: Design for Fatigue. Publication No. FHWA-IF-12-052-Vol. 12. U.S. Department of Transportation Federal Highway Administration, Washington, D.C.
[11.26] Halfpenny, A. 1999. A frequency domain approach for fatigue life estimation from finite element analysis. *International Conference on Damage Assessment of Structures*, Dublin, Ireland.
[11.27] Fluent Inc. 2006. Fluent 6.3 User's Guide, Chapter 21—Predicting aerodynamically generated noise.
[11.28] Tong, W., Wagner, T. A., Hughes, I., Gillivan, J., and Gibney J. 2004. Acoustic blanket for machinery and method for attenuation sound. U.S. Patent 6,722,466.
[11.29] Budynas, R. G. and Nisbett, J. K. 2008, *Shigley's Mechanical Engineering Design*, 8th edn. McGraw-Hill High Education, Boston, MA.

12

Innovative and Advanced Motor Design

The electric motors consume a significant amount of electricity in the industrial and tertiary sectors. In today's highly competitive global motor market, the demands for higher motor rates, higher efficiency, lower costs, and increased reliability are fueling the need for increased automation and control products with reduced energy consumption and carbon emissions. Many motor manufacturers have committed to develop their next-generation products for capturing the maximum market share and boosting profit margins. For these purposes, motor manufacturers not only fully utilize their own technical resources but also strengthen the cooperation with universities and research institutions for implementing technological breakthrough. However, there are still a variety of challenges that motor manufacturers have to face, for example, how to shorten the product development cycle time, how to apply new technologies in both existing and new products, how to differentiate their products and adapt to global markets, and how to effectively reduce the production costs. All these challenges must be appropriately considered and addressed to ensure successful outcomes.

Over the past few decades, the increasing demands for high efficiency, high torque density, low cost, and low noise electric motors have driven much R&D of innovative motor technologies. At the same time, rapid technological developments, such as 3D printing, digital technology, nanotechnology, and new composite materials, have made it possible to design and manufacture next-generation electric motors.

12.1 High-Temperature Superconducting Motor

The discovery of high-temperature superconductors (HTSs) in 1986 has strongly stimulated the R&D on superconducting materials and their industrial and military applications. In the following years, the potential economic benefits of HTS had initiated an international race among the United States, Europe, Japan, and China to develop the advanced superconductivity technology and its commercialization. Large efforts have been made to apply HTS toward power equipment such as electric motors, generators, energy storage systems, transformers, and power cables. HTS materials have much higher critical temperatures (above the liquid nitrogen temperature of 77 K or –196°C) than conventional low-temperature superconductors (LTSs) cooled with liquid helium (4.2 K or –269°C). The use of liquid nitrogen to cool HTS can lead to a reduced complexity of cryogenic system, improved system reliability and performance, and reduced total cost.

The advent of HTS has driven a quantum leap forward in advanced technologies of electric machines. Superconducting motors based on HTS are much more efficient than conventional electric motors due to zero resistance in superconducting windings. Because HTS can carry much higher currents than regular copper wires, these HTS windings are

capable of generating much more powerful magnetic fields with minimized power losses. For large synchronous superconducting motors, 50% volume and loss reduction can be achieved compared to conventional motors [12.1,12.2]. In addition, HTS motors have lower sound emissions than conventional motors. These features are especially attractive for some military customers. For instance, the US Navy is interested in applying HTS motors to its new generation of surface ships and submarines.

According to the use of HTS in motor windings, three types of HTS motors can be classified: (1) superconducting rotor type that uses HTS in the rotor winding, (2) superconducting stator type that uses HTS in the stator winding, and (3) full superconducting motor type that uses HTS in both rotor and stator windings.

Founded by the US Department of Energy (DoE), Reliance Electric Corporation demonstrated the world's first DC HTS motor in 1990 and AC synchronous HTS motor in 1993 [12.3]. The first HTS motor in Europe was made and tested at Siemens' Research Center in 2001. During experimental operation in motor and generator modes, the trial motor reached a continuous power output of 400 kW [12.4]. In 2005, IHI in Japan released the world's first full superconducting motor cooled with liquid nitrogen [12.5].

In the United States, American Superconductor has designed, built, tested, and delivered a 5 MW, 230 rpm, 6-pole HTS ship propulsion motor [12.6]. The motor uses an air core armature winding and first-generation HTS wire field winding. The aim of the project is to validate the technologies required to design and build larger HTS ship propulsion motors, as well as to develop a motor production process that streamlines development time and minimizes cost. A commercial variable frequency drive is used to power the motor. The HTS field winding uses gaseous helium as the cooling medium in a closed cycle.

The world's largest HTS ship propulsion motor of 36.5 MW (49,000 hp) was successfully tested at full power [12.7]. This motor can produce 2.9 million newton-meters of torque at a nominal rotating speed of 120 rpm. Incorporating coils of HTS wire that are able to carry 150 times the current of similar-sized copper wire, the motor is less than half the size of conventional motors and can reduce the ship weight by nearly 200 tons. With up to three times higher torque density than conventional motors, the HTS motor is more fuel-efficient. The size and weight benefits make HTS machines less expensive and easier to transport and install, as well as allow for arrangement flexibility in the ship. In addition, the absence of iron stator teeth significantly reduces the structure-borne noise.

In 2007, engineers in Sumitomo Electric designed a liquid nitrogen-cooled HTS motor of 365 kW. To simplify the cooling system and achieve high operating reliability, this motor adopts axial gap PM type. The motor armature composes of six iron-cored HTS windings and forms three phases. Heat generated by AC losses is efficiently dissipated into the liquid nitrogen through the cooling channels. This 365 kW HTS motor was successfully used to directly drive a contrarotating propeller in tandem with a 50 kW HTS motor. Due to the reduction of transmission losses, the HTS motor could provide the maximum torque of 120 N-m (at 1500 rpm) and the maximum speed of 85 km/h to electric vehicles [12.8].

A schematic diagram of an HTS motor is shown in Figure 12.1. As can be seen in the figure, while the stator winding is made of regular copper wires, the rotor winding is fabricated by HTS as superconducting magnets, which have higher energy density than PMs. The rotor winding is thermally insulated from the rest of the machine using multilayered insulation materials and cooled with a cryogenic coolant, which is introduced from the cryocooler and passes through the cooling loop in the support structure adjacent to the

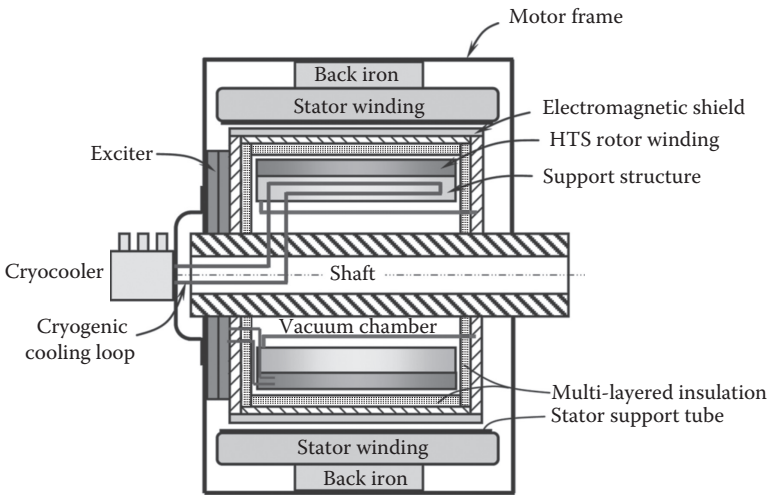

FIGURE 12.1
Schematic diagram of HTS motor.

rotor. In order to reduce radiation heat loads onto the cryogenically cooled components, the rotor winding is enclosed within a sealed vacuum chamber that rotates with the shaft. Unlike in a conventional motor, the stator winding is not housed in iron core teeth because they are saturated due to the high magnetic field imposed by the HTS windings [12.9].

Depending on the direction of the main air gap magnetic flux and the configuration of the rotor and stator against the rotating shaft, an electric motor can be classified into either RF, AF, or TF motors. Unlike the more commonly available cylinder-shaped rotor and stator in RF motors, AF motors are disk shaped, as the result of the stator and rotor being placed adjacent to each other.

The comparison of torque density of RF, AF, and TF PM motors has been performed by Pippuri et al. [12.10]. The work was carried out using a 10 kW, 200 rpm three-phase motor as the test case. The RF design is of the conventional inner rotor type. The AF design has a single-rotor, single-stator construction. The TF design has a U- and I-core stator layout with an inner rotor of two separate yokes. The magnets are mounted on the rotor surface and each of them covers 70% of the pole pitch. As shown in Table 12.1, the comparisons are made for two cases: most compact and best efficiency. In both cases, the RF topology yields the highest torque density with the given initial conditions and

TABLE 12.1

Comparison of Torque Density for Three Types of Motors

Motor Type	Torque Density for Most Compact Case (N-m/m^3)	Torque Density for Best Efficiency Case (N-m/m^3)
RF motor	16,877	14,380
AF motor	13,226	10,023
TF motor	11,504	11,504

Source: Data obtained from Pippuri, J. et al., *IEEE Trans. Magn.*, 49(5), 2339, 2013.

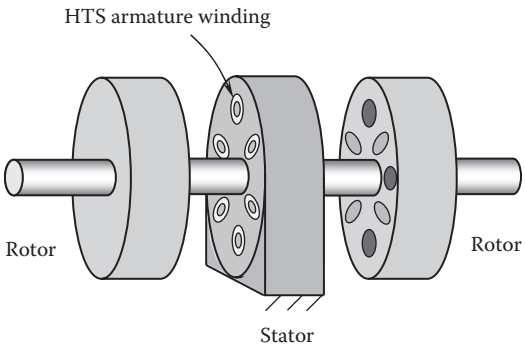

FIGURE 12.2
AF, high-temperature superconducting motor.

constraints. When comparing the AF and TF machines (TFM), the AF machine outperforms the TF design in the most compact case, and it is opposite in the best efficient case. It is interesting to note that the torque density for the TF motor remains unchanged in the two cases.

The flux of the AF motor is in the same direction with the motor shaft. Because of the large area for magnetic flux, the AF motor provides the desired performance. A schematic diagram of an AF, high-temperature superconducting motor is shown in Figure 12.2. The stator is in the middle of the motor and the two rotors are on the two sides of the stator. The stator winding is made by high-temperature superconducting materials and is cooled by a specially designed cooling system (not shown).

12.2 Radial-Flux Multirotor or Multistator Motor

RF multirotor and multistator motors have a number of distinctive advantages over conventional single-rotor and single-stator motors. By integrating multirotor or multistator into the same motor housings, the machines offer higher torque density and are usually more efficient.

12.2.1 Radial-Flux Multirotor Motor

A novel dual-rotor, toroidally wound PM motor was proposed by Qu and Lipo [12.11], as shown in Figure 12.3. There are some unique features in their design, including (1) a rotor–stator–rotor structure, (2) back-to-back windings, (3) very short end windings, (4) a high diameter-to-length ratio, (5) low air gap inductance, (6) high efficiency, (7) high torque density, (8) high overload capability, (9) balanced radial forces, (10) suitability for moderately high-speed performance, (11) low cogging torque, and (12) low material costs.

The motor illustrated in Figure 12.3a is constructed with a plurality of PMs mounted on the inner surface of the outer rotor and buried within a core of the inner rotor. The PMs buried within the inner rotor core preferably extend radially from a central opening of the inner rotor to the outer surface of the inner rotor. The inner and outer rotors

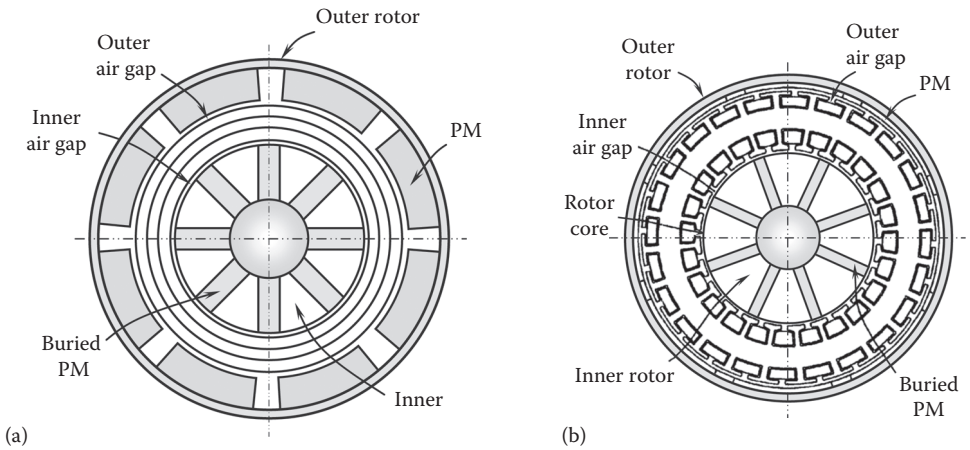

FIGURE 12.3
Structures of dual-rotor, toroidally round hybrid PM motors: (a) nonslotted machine and (b) slotted machine (U.S. Patent 6,924,574) [12.11]. (Courtesy of the US Patent and Trademark Office, Alexandria, VA.)

comprise a single integral rotor so that the inner and outer rotors rotate at the same speed. The torus-shaped stator has a hollow cylindrical shape and is preferably nested between the inner and outer rotors. A plurality of polyphase windings are toroidally wound around the stator. It is noted that the stator is nonslotted, meaning the stator does not include any radially extending teeth. A benefit of the nonslotted structure is that it avoids cogging torque. There are two air gaps in the motor. The inner air gap is formed between the inner rotor core and the stator, and the outer air gap is formed between the outer PMs and the stator.

The motor illustrated in Figure 12.3b has a similar configuration to the motor of Figure 12.3a, except for the stator structure. This motor employs a slotted stator rather than nonslotted in Figure 12.3a. In fact, the more the stator windings used in a motor, the higher the torque generated and the higher the motor efficiency. A higher torque density is thus achieved by slotting, but the slotted structure will introduce cogging torque.

The perspective view of the dual rotor and torus-shaped stator is shown in Figure 12.4. The dual rotor (Figure 12.4a) consists of an inner rotor, an outer rotor, and a closed end. The dual rotor magnetically interacts with the stator, whereby the PMs drive a magnetic field within the stator, causing a back electromagnetic force to be induced in the polyphase windings that are wound around the stator. The stator includes a plurality of *T*-shaped teeth or slots extending radially inwardly from the inner surface and outwardly from the outer surface of the stator (Figure 12.4b). The windings wound around the stator may comprise toroidally wound windings, lap windings, wave windings, or other types of windings. Since almost all of the windings on the inner, outer, and end surfaces of the stator are used for torque production, this motor creates higher efficiency and higher torque density than the conventional motors. The stator is formed by a plurality of stacked laminations that are connected together with a magnetic powdered material.

Figure 12.5 is a cutaway perspective view of the motor assembly. This figure clearly shows how the stator is nested between the inner and outer rotors. An additional gap (end air gap) is formed at the motor end, between the windings and PMs, which attached on the inner surface of the closed end (see Figure 12.4b).

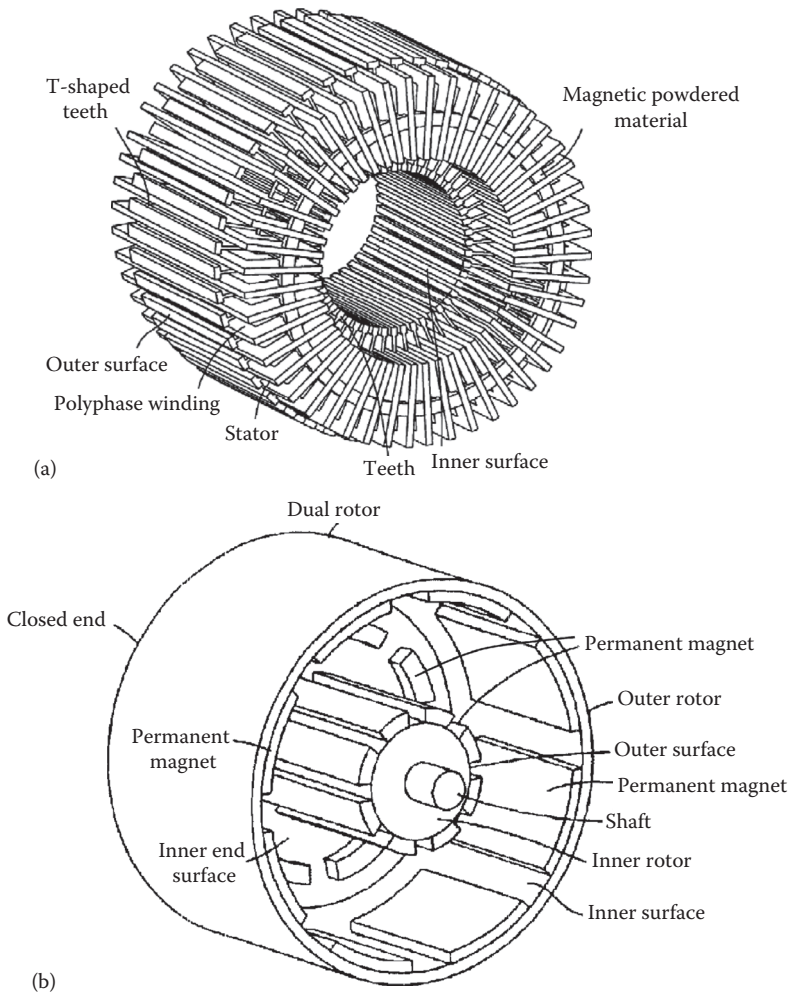

FIGURE 12.4
Dual-rotor, toroidally wound SPM motors: (a) stator and (b) dual rotor (U.S. Patent 6,924,574) [12.11]. (Courtesy of the U.S. Patent and Trademark Office, Alexandria, VA.)

12.2.2 Radial-Flux Multistator Motor

The structure of an RF dual-stator motor is presented in Figure 12.6. The motor consists of an inner stator, an outer stator, and a rotor, which inserts between the two stators via two bearings. PMs are attached to the inner and outer surfaces of the rotor. In order to achieve the concentricity of the inner and outer stators, the two stators are integrated as one part. If the two stators are made separately, an accurate position control is required. Stator windings are wound through the inner and outer slots.

An alternative design is illustrated in Figure 12.7. In this design, PMs are mounted on the surfaces of the inner and outer stators. Windings are made through the slots of the rotor. The system is supported with three bearings.

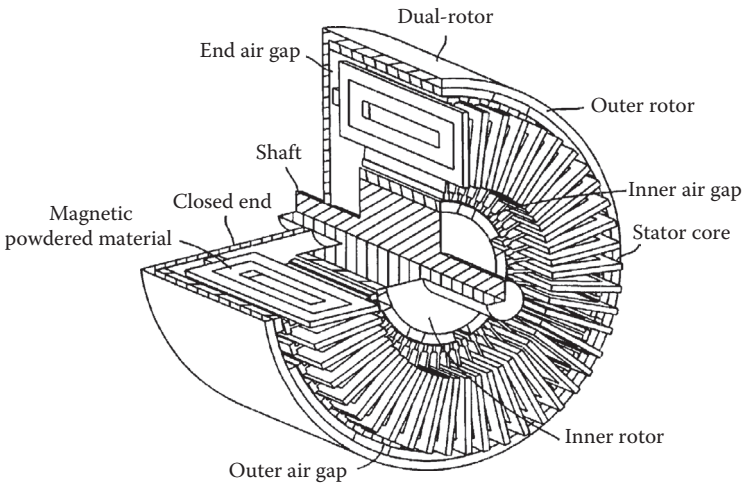

FIGURE 12.5
A cutaway perspective view of the motor assembly (U.S. Patent 6,924,574) [12.11]. (Courtesy of the U.S. Patent and Trademark Office, Alexandria, VA.)

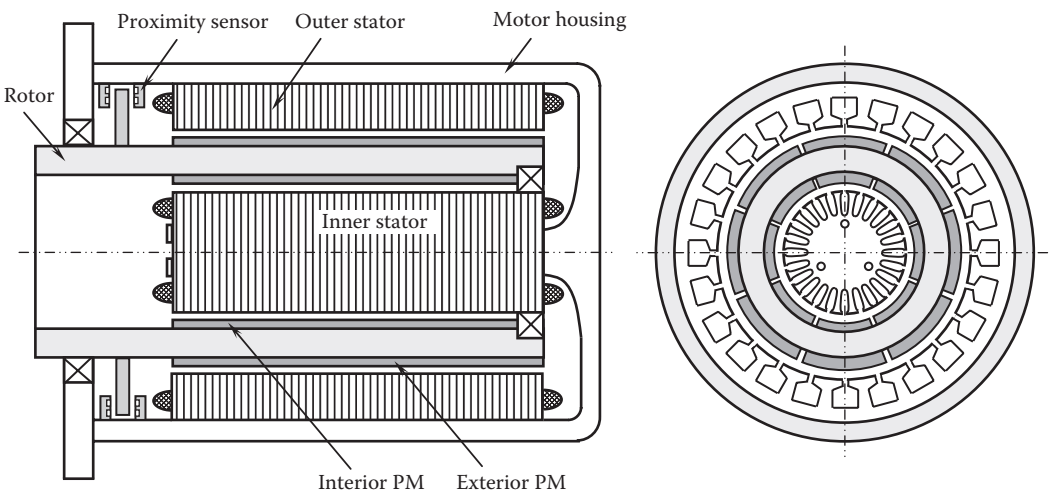

FIGURE 12.6
RF, dual-stator, PM motor with two bearings.

12.2.3 Radial-Flux Brushless Double-Rotor Machine

In recent years, a new power-split hybrid system, called compound-structure PM synchronous machine (CS-PMSM) system, has been developed for replacing the mechanical planetary gear, flywheel, clutch, starting motor, and generator used in conventional automobiles. This is a promising technology for developing future hybrid vehicles with high efficiency and reliability. As part of the efforts, a novel RF brushless double-rotor machine (BDRM) has been proposed by Zheng et al. recently [12.12].

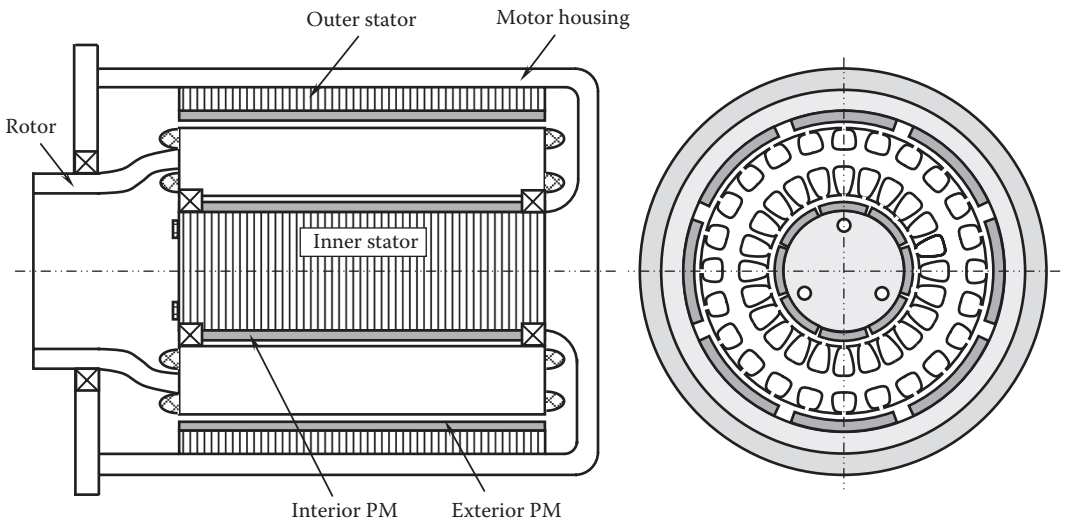

FIGURE 12.7
RF, dual-stator, PM motor with three bearings.

The CS-PMSM system is illustrated in Figure 12.8. It consists of a BDRM and a conventional machine. There are some design characteristics associated with the BDRM:

- The windings of the BDRM are mounted on the stator close to the motor case. This configuration helps dissipate generated heat from the stator windings to the environment.
- Stator phases are mutually independent with no couplings existing in-between.

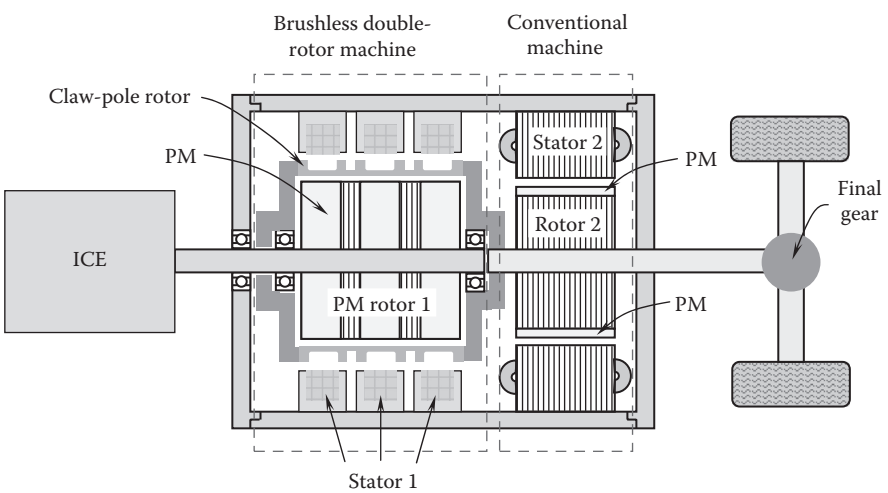

FIGURE 12.8
A CS-PMSM consisting of a BDRM and a conventional machine for driving hybrid electric vehicle.

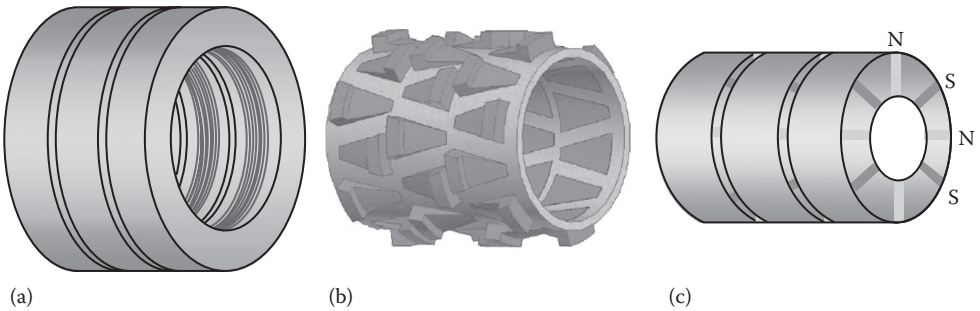

FIGURE 12.9
Perspective view of the BDRM: (a) stator, (b) claw-pole rotor, and (c) PM rotor with buried radial magnets for azimuthal magnetization.

- The BDRM is designed as a multipole machine. This is especially suitable for intermediate or high-frequency operation.
- The ring-shaped stator windings of the BDRM simplify the winding fabrication and assembly process.

The structure of the BDRM is demonstrated in Figure 12.9. The stator shown in Figure 12.9a comprises laminated iron cores and ring-shaped stator windings. Figure 12.9b shows the claw-pole rotor that has three arrays of claws mounted on a nonmagnetic bracket. While the claw-pole rotor is connected to the final gear for driving wheels, the PM rotor 1 is connected to the crank shaft of the ICE. The function of the PM rotor is to transmit the ICE torque to claw-pole rotor. The speed adjustment between the claw-pole rotor and PM rotor 1 can be achieved by energizing the stator windings with different frequencies via an inverter. The PMs are burned radially through the rotor cores with the N-S-N-S arrangement, as presented in Figure 12.9c.

The claw-pole rotor is connected to the PM rotor 2 together with the conventional machine. Thus, the total output torque of the shaft is collectively contributed by the BDRM and conventional machine.

12.2.4 Radial-Flux Double-Stator PM Machine

The structure of an RF double-stator PM machine is presented in Figure 12.10 [12.13]. The cup rotor is nested between the inner and outer stators. This machine has 24 slots wounded with three-phase windings in both the concentric outer and inner stators. The 22 pieces of PMs are mounted on the inside and outside surfaces of the rotor, where N-poles and S-poles PMs are arranged alternately along the rotor circumference. Both winding methods, that is, three-phase single-layer and three-phase double layer, can be applied to both the inner and outer stators.

This machine has the advantage that currents in both the inner and outer stators produce electromagnetic torque and both air gaps can deliver the output torque, thus improving the torque density and providing a high starting torque for hybrid electric vehicles. In addition, because of the nature of double-stator windings, the machine can flexibly change its connections, hence providing a constant output voltage for battery charging over a wide range of speed.

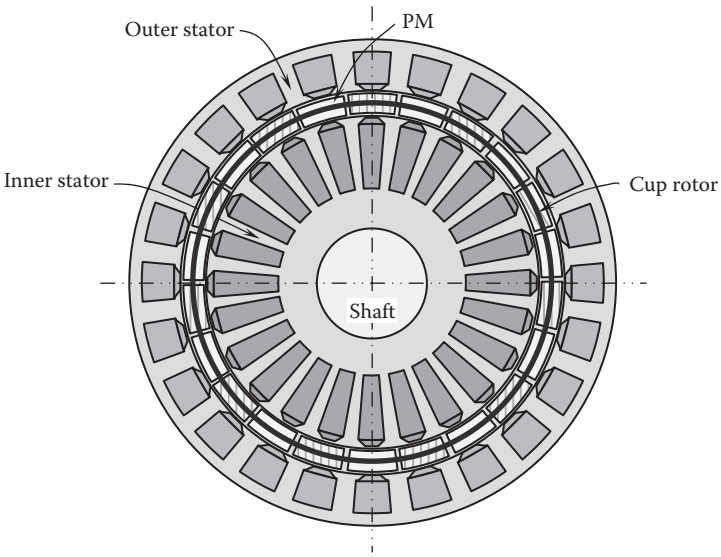

FIGURE 12.10
RF double-stator PM machine, where S-poles (shaded) and N-poles (unshaded) are arranged alternately along the rotor circumference.

12.3 Axial-Flux Multirotor or Multistator Motor

While RF motors dominate the motor market as mainstream for more than a century, AF motors have been developed in the last several decades and are attracting growing interests in recent years. AF motors may benefit from the increased efficiency, lowered axial loads acting on the rotor and bearings, and reduced motor vibration. Unlike in an RF motor in which the air gap is fixed after the rotor and stator are manufactured, the planar air gap in an AF motor is adjustable by changing the relative position of the rotor and stator.

AF motors are designed to have a higher power-to-weight ratio than RF motors, resulting in less core material and higher efficiency [12.14]. For small motors, the motor efficiency for an AF motor is about 15% higher than an RF motor with a similar size. This is attributed to the fact that the AF motor utilizes both sides of the rotor, while the RF motor utilizes only one side. Other advantages include simple cooling system, high reliability, and motor power being obtained from both ends of the spindle. Thus, the AF motors have been widely used in applications such as robots, wheel drives, hard disk drives, wind turbines, and fans.

There are many topologies of AF machines for various applications. For example, AF machines may be single-sided or double-sided, with or without slots, with or without armature core, with internal or external PM rotors, with surface-mounted or interior PM, and single stage or multistage [12.15]. Some of these topologies are addressed in the following sections.

12.3.1 Single-Sided and Double-Sided Axial-Flux Motors

A single-sided AF motor has the simplest structure with only single disk-shaped rotor and stator. In this configuration, PMs are mounted on one side of the rotor. The cross section of

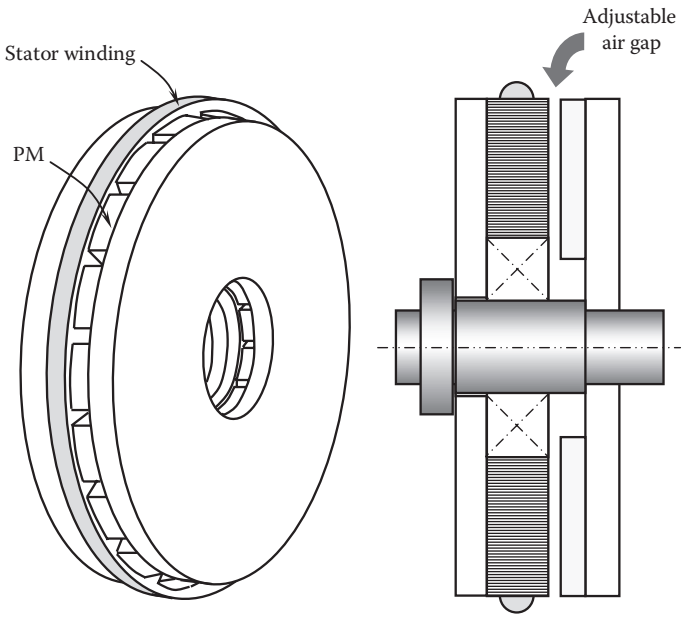

FIGURE 12.11
Single-sided AF PM motor, showing a single rotor and stator.

the rotor and stator is illustrated in Figure 12.11. The topology of AF motor allows to adjust the motor torque by adjusting the air gap, as shown in Figure 12.12.

A typical double-sided AF motor is shown in Figure 12.13. As illustrated in Figure 12.13a, the motor consists of two identical stators and one rotor, where the rotor is nested in the two stators axially. Each stator has a number of slots for receiving stator windings. The three-phase windings are uniformly distributed in the circumference of the stator and wound radially (Figure 12.13b). The PMs and iron poles are alternately embedded or glued in a disk-shaped

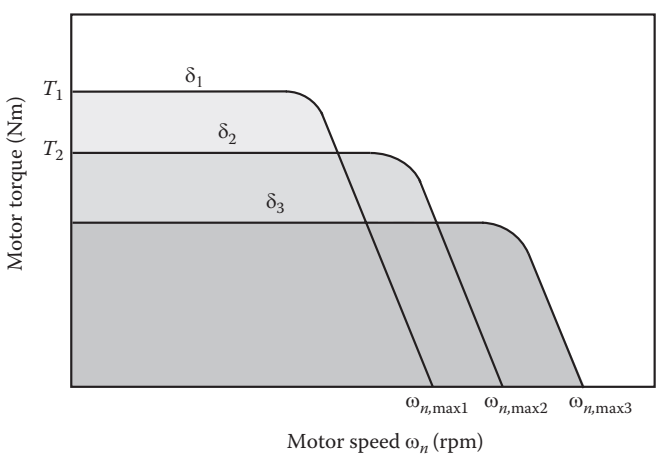

FIGURE 12.12
Adjustable motor torque by varying air gap δ in an AF motor.

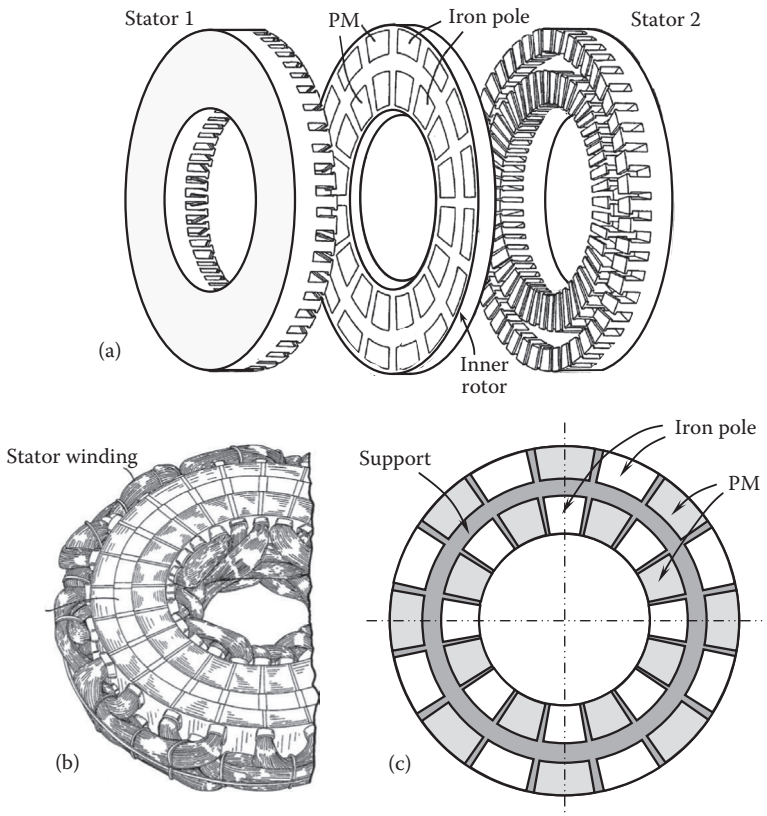

FIGURE 12.13
A stator–rotor–stator AF PM motor: (a) the motor contracture, (b) stator assembly, and (c) PM and iron pole arrangement on the rotor (U.S. Patent 7,608,965) [12.16]. (Courtesy of the U.S. Patent and Trademark Office, Alexandria, VA.)

support in two rows (Figure 12.13c). The support is made of a nonferromagnetic material such as aluminum and epoxy. [12.16]. The stators can be connected in series or parallel. A serial connection is usually preferred since it can provide equal but opposite axial forces.

The double-sided AF motors can have different configurations such as a stator–rotor–stator structure as addressed previously or a rotor–stator–rotor structure as shown in Figure 12.14. In the rotor–stator–rotor design, a single nonslotted stator is sandwiched between two rotor disks, forming axially two planar air gaps. The stator is realized by tape wound core with polyphase AC air gap windings that are wrapped around the stator core with a back-to-back connection. The active conductor portion is the radial portion of the toroidal windings facing the two-rotor structure (Figure 12.14a). Arch-shaped PMs are mounted axially on the inner surface of each rotor.

The magnetic flux path is presented in Figure 12.14b. An N-pole magnet on one rotor is placed directly opposite to its counterpart on the other rotor. It is noted that there are two identical magnetic loops. For each loop, the magnetic flux is driven by the N-pole magnet to go across the air gap into the stator core, travels circumferentially along the strip-wound stator core, returns across the air gap, and then enters the rotor core through the opposite S-pole of the PMs to complete the magnetic flux loop. Hence, it can be expected that the

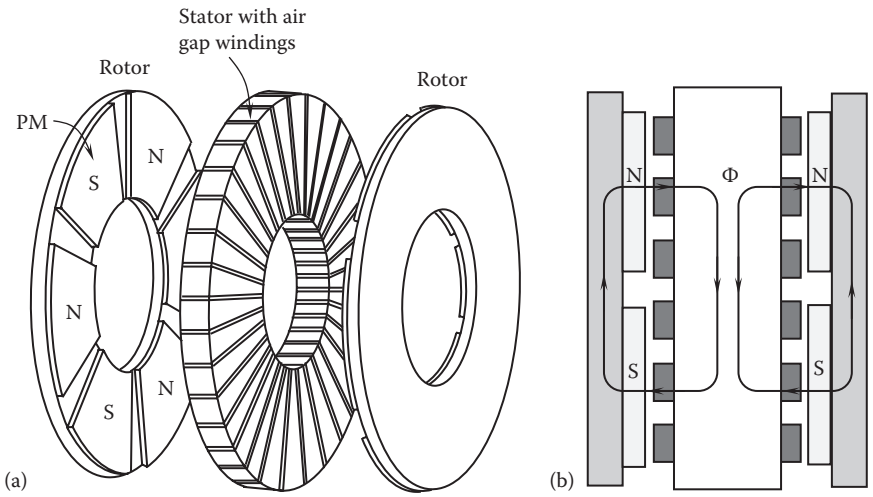

FIGURE 12.14
An AF torus-type slotless rotor–stator–rotor PM motor: (a) motor structure and (b) magnetic flux direction.

axial length of the stator core would be quite long because of the summation of the flux entering the stator from both rotors. As a matter of fact, this machine can be viewed as a combination of two independent halves due to the direction of the magnetic flux.

The slotless torus topology shown in Figure 12.14 has a high torque density and high torque-to-weight ratio. The portions between the air gap windings are assumed to be filled with epoxy resin as in all nonslotted structures in order to increase the mechanical robustness and provide better conductor heat dissipation. In addition, in the torus topology, the windings in the air gap are used for the torque production. Besides, due to the absence of stator slots, the cogging torque, magnetic flux ripple, pulsation losses in the rotor, and acoustic noise can be greatly reduced.

12.3.2 Multistage Axial-Flux Motor

For an AF motor, the torque is proportional to the OD of the motor. However, the centrifugal force acting on the rotating components significantly increases with the OD. Therefore, a common way to increase the motor torque is to design a motor with multistage arrangements. Usually, for a rotor–stator–rotor structure, a multistage machine has N stators and $N + 1$ rotors, where N is the number of stages. All rotors share the same shaft.

The double-sided AF motor in Figure 12.14 can be extended into a multiple stage machine as illustrated in Figure 12.15. The stators are formed by wrapping magnet wires radially around a nonslotted stage core. The rotors are formed by both rotor cores and axially magnetized SPM. Except for the end rotors, PMs are mounted on both sides of the rotor cores. Theoretically, there is no limit on the number of motor stage in multistage motors. This indicates that a desired high torque can be achieved by adjusting the number of motor stages.

The multistage AF machines are very competitive with respect to conventional AF and RF machines for their compact size, simple structure, and easy assembly. Because each air gap can be adjusted independently, the air gap depths in the motor can be made either identical or distinctive for obtaining the optimized motor performance for a specific application.

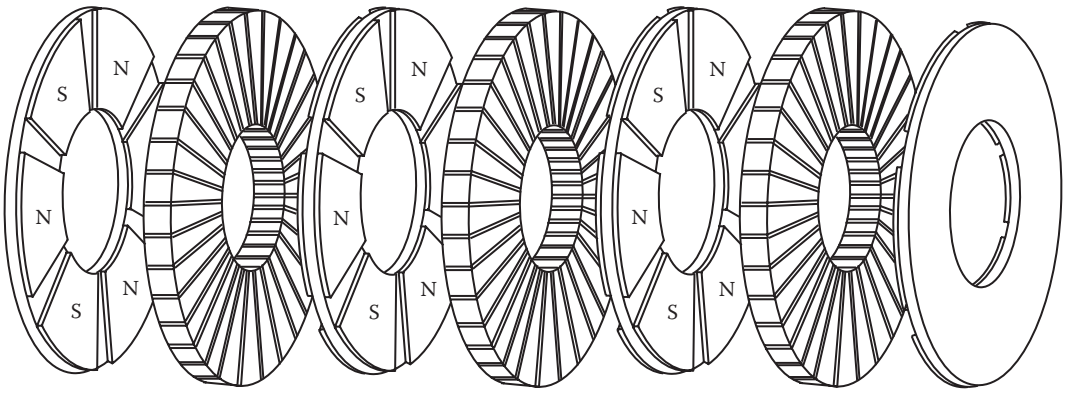

FIGURE 12.15
Perspective view of multistage of AF torus-type slotless PM motor.

12.3.3 Yokeless and Segmented Armature Motors

The yokeless and segmented armature (YASA) topology is a new type of AF motor. This type of motor has shown an improved torque density and efficiency compared to other AF motors [12.17]. The iron in the stator of the YASA motors is dramatically reduced, typically by 50%, causing an overall increase in torque density of about 20%. In fact, the elimination of yoke, elevated fill factor, and shortened end windings all contribute to the increase of torque density and efficiency of the electric machine. Therefore, this topology is highly suited for high-performance applications.

The YASA motors are primarily designed for vehicles. The segmented stator is made of powdered iron materials. The topology of a YASA motor combines two of the best-performing AF machines, the NS torus-S and the NN torus-S topologies, as shown in Figure 12.16.

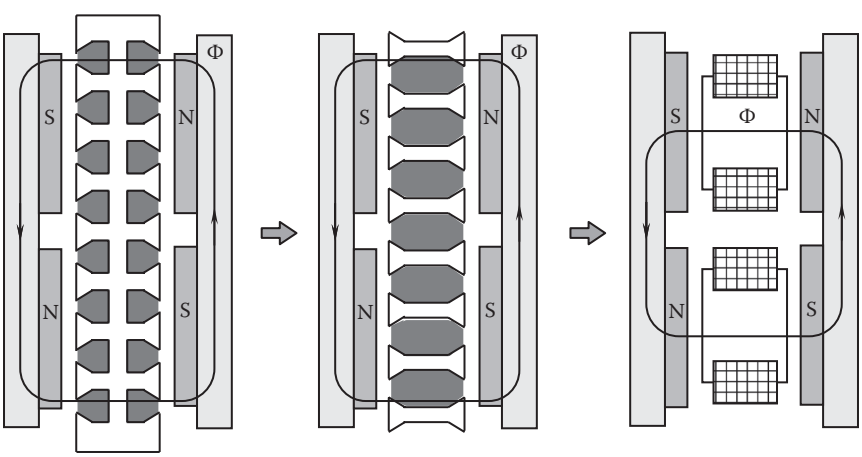

FIGURE 12.16
The topology of YASA motor, which combines two best-performing AF motors.

12.4 Hybrid Motor

A hybrid motor is the motor that combines two or more types of motor structures together so as to integrate their strengths for a better performance and operation.

12.4.1 Hybrid Excitation Synchronous Machine

Hybrid excitation synchronous machines (HESMs) have been developed in recent years for traction applications such as hybrid electric and fuel cell vehicles [12.18]. The HESMs have two excitation sources: one is the PM source that provides the air gap with constant flux and the other is the DC excitation coil source that acts as the flux regulator to adjust the air gap flux distribution. These two excitation sources can be connected either in series or in parallel.

As can be seen in Figure 12.17, a HESM consists of powdered iron cores, PMs, stator windings, and DC excitation coils. PMs are placed at the center of the rotor and the excitation coils located at the two ends of the motor. Thanks to the excitation coils, it is possible to modulate the total excitation flux in the air gap region of the machine. In addition, these additional excitation coils make it possible to improve the effectiveness of the machine in different operating regions.

12.4.2 Hybrid Hysteresis PM Synchronous Motor

A hysteresis synchronous motor (HSM) is extensively adopted in small motor applications. The combination of PMs and hysteresis materials in the rotor of an HSM has many distinct advantages over the conventional PM or hysteresis motors. The hybrid motor in which

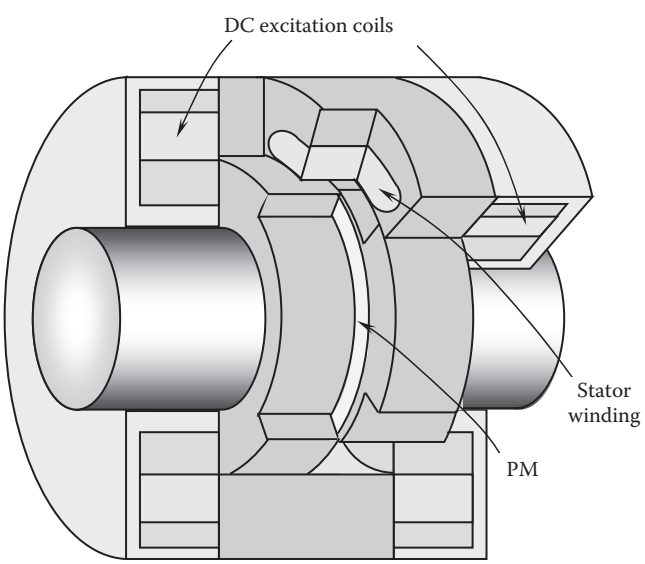

FIGURE 12.17
HESM with powdered iron core and global excitation coils.

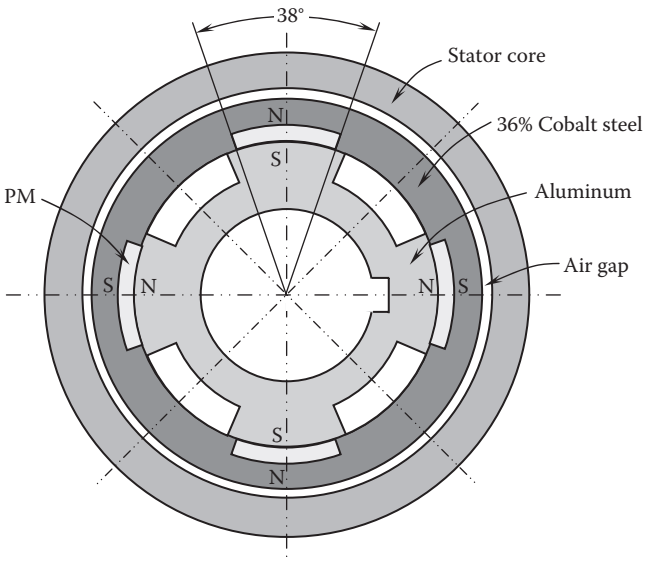

FIGURE 12.18
The structure of a hybrid PM HSM. The combination of PMs and hysteresis materials in the rotor makes the motor suitable for constant-torque and constant-speed applications.

the PMs are inserted into the slots at the inner surface of the hysteresis ring is called PM hysteresis synchronous (PMHS) motor. In fact, this type of motor combines the advantageous feature of both the hysteresis and PM motors [12.19].

Qin and Rahman [12.20] have presented a hybrid hysteresis PM synchronous motor, as illustrated in Figure 12.18. The rotor of the motor consists of a 36% cobalt–steel hysteresis alloy with rare-earth PMs to improve the overall performances of such a motor. At asynchronous speeds, the motor torque contains the hysteresis torque, eddy-current torque, and PM brake torque. At the synchronous speed, the motor torque comprises the hysteresis and PM torques. Experimental results have confirmed the validity of the motor design and shown that the hybrid motor exhibits improved speed stability over a wide range. This type of motor is especially suitable for constant torque, constant speed, and quiet applications such as gyros, time and recording equipment, and pumps.

12.4.3 Hybrid Motor Integrating Radial-Flux Motor and Axial-Flux Motor

The motor shown in Figure 12.19 integrates an RF and an AF motor together to achieve high torque density and efficiency. This motor has three sets of PMs and three stators, including one regular radial stator and two axial disk-shaped stators. The two sets of PMs are mounted on the rotor's two sides and polarized in the axial direction. Thus, the north/south polarity of the PMs alternates as the rotor rotates. The third set of PMs is mounted on the curved radial outward surface and polarized in the radial direction with alternating orientation of their N and S poles. The rotor is disposed around the shaft. Thus, the regular radial stator and the third set of PMs form a regular RF motor, and the two axial stators and the two sets of PMs mounted on the sides of the rotor form an AF motor.

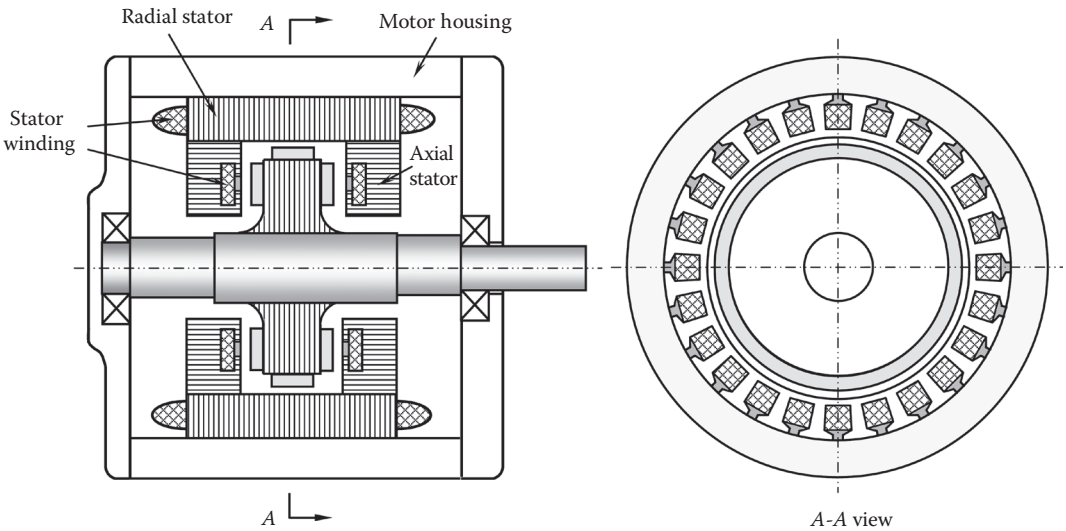

FIGURE 12.19
The new motor design that combines the RF and AF motor.

Electric currents applied to the three stators produce rotating magnetic fields that interact with the fields produced by the corresponding sets of PMs to generate a desired torque that rotates the motor shaft. For a given motor volume, this motor offers high mechanical power and torque since the entire rotor surface is used in the torque production. Typically, the motor rating can be increased one-third or greater with respect to a comparably sized RF motor [12.21].

The motor with a single-unit structure in Figure 12.19 can be expanded into a multistage form, as shown in Figure 12.20. Generally, the output power is proportional to the motor

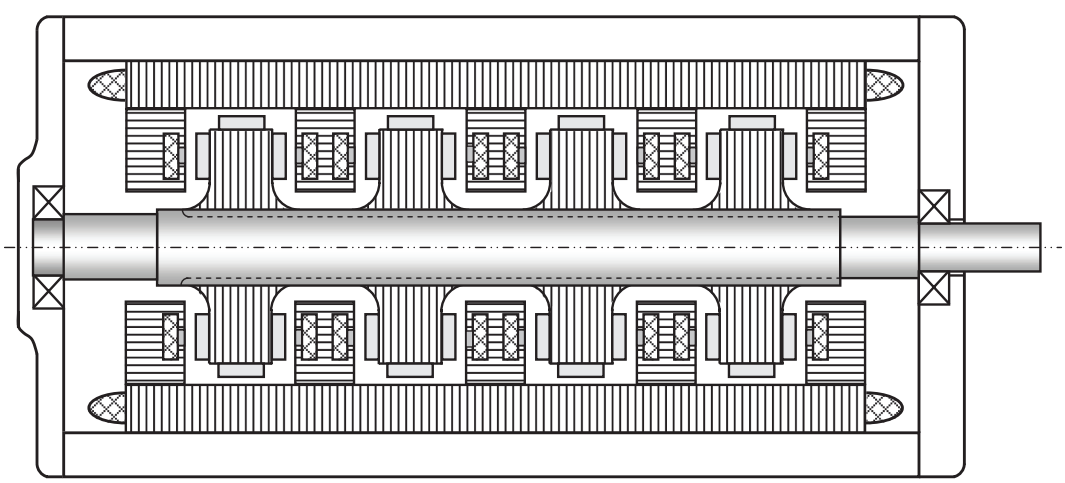

FIGURE 12.20
The motor with multistages as the integration of RF and AF motor.

OD and the stage number. Increasing the stage number can thus increase the motor torque to drive an external loading machine.

12.4.4 Hybrid-Field Flux-Controllable PM Motor

The topology of a three-phase 6/4-pole hybrid-field flux-controllable PM (FCPM) motor is presented in Figure 12.21. The main advantage of this type of motor is that the air gap flux density is directly controllable. The stator contains two types of windings, that is, the three-phase AC armature windings and the DC field windings. The key of the motor is to incorporate both PMs and DC field windings in the stator, hence offering a compact arrangement of hybrid-field excitations, while the rotor is simply composed of salient poles without winding or PMs [12.22]. PMs are closely positioned adjacent to the field windings. In such a way, the field windings serve to regulate the PM flux, offering either flux weakening or flux strengthening.

It is important to note that there is an extra air bridge in shunt with each PM. If the field winding MMF reinforces the PM MMF, the air bridge will amplify the effect of flux strengthening. On the contrary, if the field winding MMF is opposite to the PM MMF, it will increase the PM flux leakage, thus amplifying the effect of flux weakening. By choosing an appropriate width of the air bridge, a wide flux regulating range can be obtained by using a small DC field excitation.

12.4.5 Hybrid Linear Motor

Jeon et al. [12.23] proposed a novel hybrid linear motor (HLM) by both induction and synchronous operations. The motor consists of a pair of linear synchronous motors (LSMs) and a linear induction motor (LIM). The primary cores of both motors share a common ring winding, and the secondary solid conductor is arranged in both LIM and the interpole space of LSM. From the 3D FEA and experiment, the motor is verified to be effective for practical use.

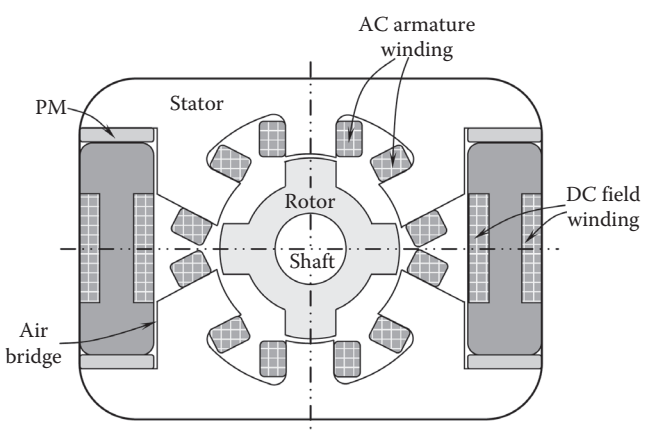

FIGURE 12.21
Topology of a three-phase 6/4-pole hybrid-field flux-controllable PM motor.

12.5 Conical Rotor Motor

In the present motor industry, almost all rotary motors are designed with a cylindrically shaped rotor and stator, so that a constant air gap is maintained in both the circumferential and axial directions. In a conical rotor motor, the rotor is in a conical shape. According to the stator shape, two groups are identified as follows:

1. The stator is in a regular shape with a constant internal diameter. Therefore, the air gap between the rotor and stator is no longer a constant; rather, it varies along the motor axial direction (Figure 12.22). It can be seen in the figure that the air gap increases linearly along the motor axis away from the bearing. This configuration may improve the motor vibrational characteristics and prevent the interference between the rotor and stator [12.24].
2. The stator is also in a conical shape, with the same conical angle as the rotor. Thus, the air gap remains a constant along the rotor axis (Figure 12.23). Sorros et al. [12.25] have designed, analyzed, and tested two micromotors, with a conventional cylindrical design and a conical design, respectively. They found that the conical motor offers comparable performance to the cylindrical motor but with a much more compact mechanical arrangement. One of the advantages of the conical design is that it eliminates the need for a long pivot bearing and hence substantially reduces the size of the motor. The high starting torque and low inertia of the conical motor have proven to be ideal for the demands of high cycle dynamic drives in various applications.

A new type of conical rotors with a variety of rotor–stator structures was proposed by Burch et al. [12.26]. As an example shown in Figure 12.24, unlike the conical rotor motors discussed previously, the rotor assembly consists of two conical rotor cores that are mounted on the motor shaft. Trapezoid magnets are attached on the conical surface of each conical core for forming the magnet field.

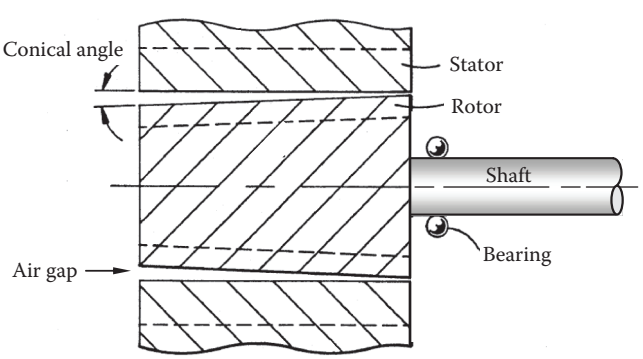

FIGURE 12.22
Conical rotor with a nonuniform air gap (U.S. Patent 5,233,254) [12.24]. (Courtesy of the U.S. Patent and Trademark Office, Alexandria, VA.)

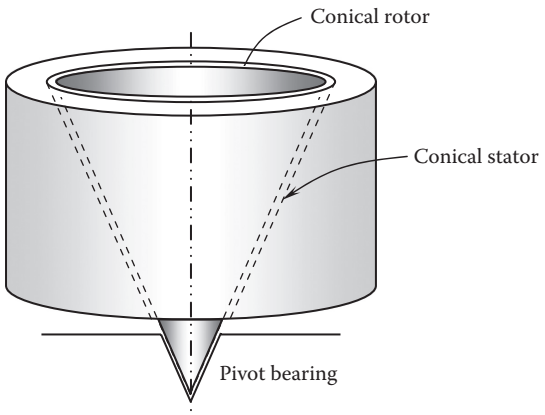

FIGURE 12.23
Conical rotor with a pivot bearing having a uniform air gap.

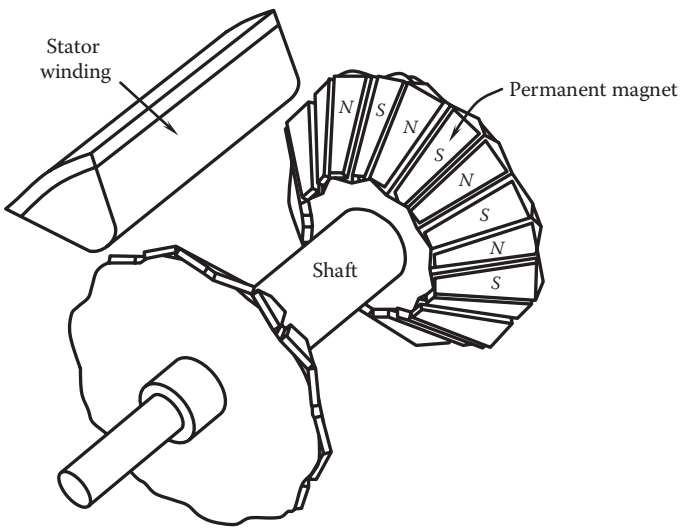

FIGURE 12.24
Conical rotor with PMs at two ends of the shaft and stator windings located between the PMs.

12.6 Transverse Flux Motor

Unlike RF or AF (TF) motors, TF motors have complex magnetic circuits. The concept of the TFM can trace back to 1895 as W. M. Morday applied for the first patent. TFMs have highest torque density, usually three to four times higher than conventional synchronous and asynchronous machines [12.27]. The use of TFMs in industrial manipulators may eliminate the conventionally required gears and build direct drive systems [12.28]. Due to their superior performing characteristics, TFMs are expected for direct drive systems, such as wheel motors of hybrid electric vehicle and wind turbines [12.29].

Usually, TFMs have a toroidal armature winding, carrying current parallel to the DIR. The stator core is salient and the rotor is equipped with PMs. The stator core often carries flux in three directions. This indicates that iron powder is a preferred core material.

However, the constructive geometry and topology of TFM are considerably complex in comparison with those of conventional RF motors, and no 2D symmetry exists. Because of the difficulty and complexity in manufacturing and thus high cost, TF motors today still stay in the R&D stage, leaving them a long way to go toward industrial production. Other disadvantages include torque ripples and normal force fluctuations [12.30].

TFM can be classified as surface PM TFM (SPM-TFM) and flux-concentrated TFM (FC-TFM). Comparing with the SPM-TFM, the FC-TFM has a higher torque density but more difficulty in manufacturing. PMs in a SPM-TFM are magnetized in the direction perpendicular to the DIR. By contrast, PMs in an FC-TFM are of parallel magnetization [12.31].

An FC-TFM of 56 poles with distributed three full phases is shown in Figure 12.25. The rotor comprises a plurality of PMs of opposite magnetization direction alternately and coaxially arranged around a rotating axis. A rotor pole is arranged between every two PMs. The stator has three phases coaxially arranged around the rotating axis and separated by the distance elements. A number of stator teeth face the rotor and the stator phases together with the distance elements.

Figure 12.26 depicts the single-stator winding and stator phase, where stator winding is formed as a multiturn saddle phase winding. As can be seen from the figure, the stator winding is formed as a closed loop and arranged between two teeth forming an angle θ.

The variations of torque components of the FC-TFM along the mechanical shift angle are depicted in Figure 12.27. The data are obtained from simulations using a FEM software. It shows the peak-to-peak cogging torque is about 0.09 N-m and the peak-to-peak reluctance torque is 0.4 N-m. Interaction torque is due to the interaction between the magnetic fields of PMs and armature current, which has a peak value of 0.55 N-m.

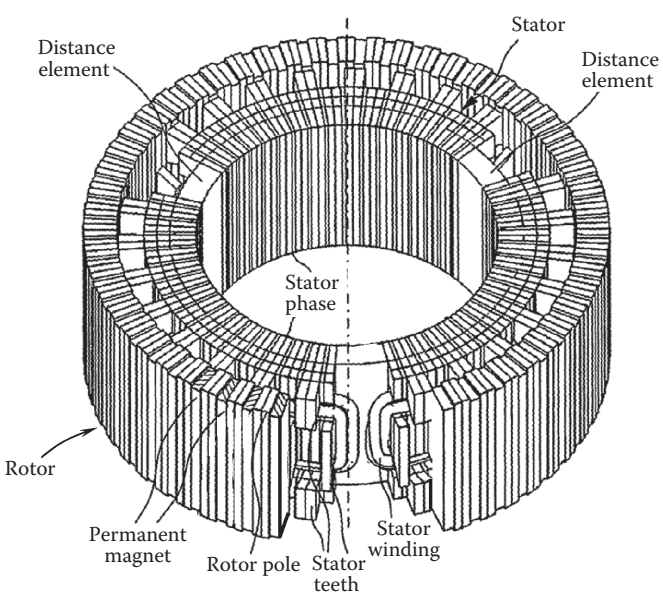

FIGURE 12.25
Perspective view of the structure of PM TF motor (European Patent 2,317,633) [12.31]. (Courtesy of the European Patent Office, Munich, Germany.)

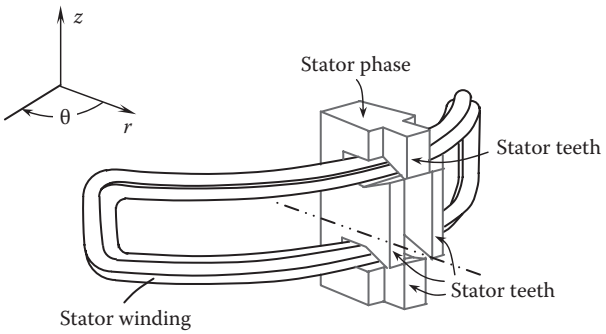

FIGURE 12.26
Single-stator winding and phase in an FC-TFM (European Patent 2,317,633) [12.31]. (Courtesy of the European Patent Office, Munich, Germany.)

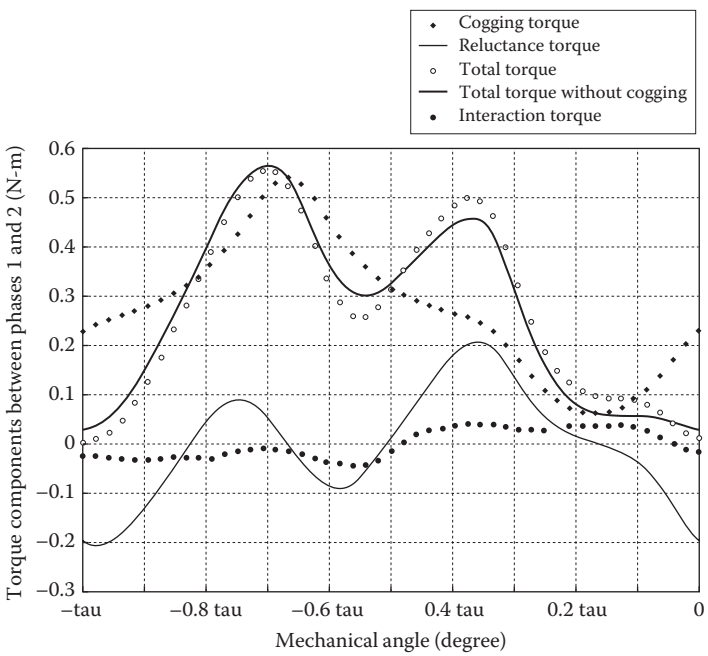

FIGURE 12.27
Torque component for the FC-TFM, obtained from simulations (European Patent 2,317,633) [12.31]. (Courtesy of the European Patent Office, Munich, Germany.)

Gieras and Rozman [12.32] have presented a TF motor as the rim-driven thruster (RDT). As illustrated in Figure 12.28, a one-phase unit consists of a rotor assembly and a stator assembly. The stator assembly includes a ring-shaped winding and a stator core, which comprises a number of U-shaped cores. The rotor assembly includes a rotor core, spacer, and a plurality of PMs. As shown in the figure, PMs with the opposite magnetic polarity are disposed alternately along forward and aft surfaces of the spacer. PMs are configured to have the magnetic pole orientations extending radially, either inward or outward. The magnetic flux induced in U-shaped cores interacts with the pole orientations of PMs to generate the force vector $\vec{F}$ in the tangential direction of the rotor.

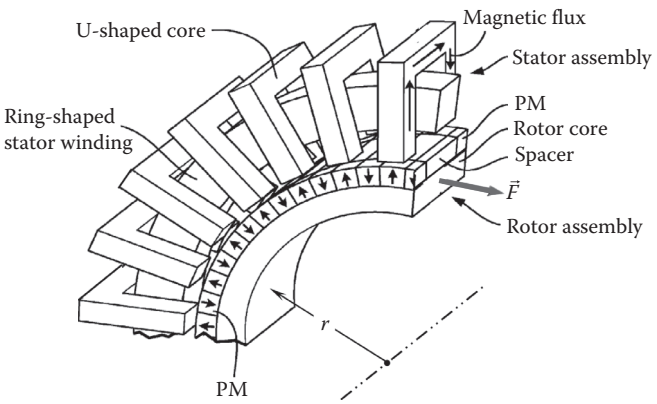

FIGURE 12.28
A partial perspective view of rotor and stator assembly of one-phase unit in a PM excited TF motor (U.S. Patent 8,299,669) [12.32]. (Courtesy of the U.S. Patent and Trademark Office, Alexandria, VA.)

Figure 12.29 depicts the structure of an RDT, which contains three identical one-phase units to form a three-phase, TF motor. The RDT includes the housing, forward and aft fairing, stator assemblies, rotor assemblies, and propulsion assembly. The propellers are connected with the rotor. The rotor shaft is supported by two bearings at its ends. While electric current within stator windings causes magnetic flux to flow through the stator cores, the oppositely oriented magnetic poles of PMs cause magnetic flux to travel through rotor assemblies. The interaction between these magnetic fluxes applies a torque to the rim. The bearings permit the rim and rotor assembly to rotate smoothly about the centerline.

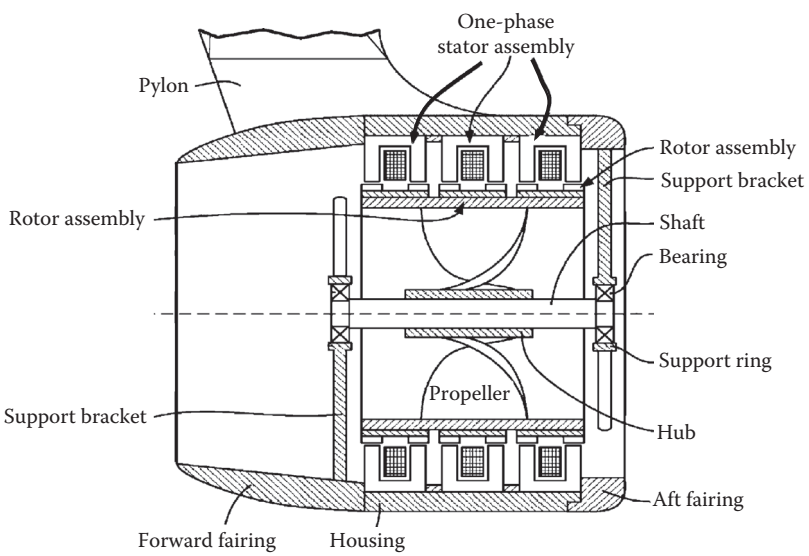

FIGURE 12.29
Structure of an RDT with a TF motor (U.S. Patent 8,299,669) [12.32]. (Courtesy of the U.S. Patent and Trademark Office, Alexandria, VA.)

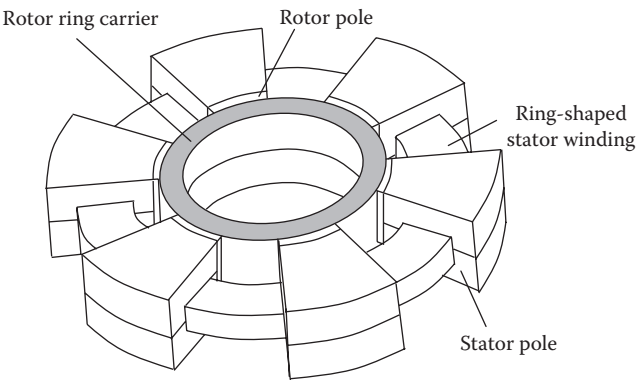

FIGURE 12.30
A 3D overview of a six-pole TF reluctance machine.

The TF reluctance (TFR) machine is a variant of the TFM with a passive rotor [12.33]. As shown in Figure 12.30, a ring-shaped toroidal stator winding is surrounded by a number of U-shaped salient poles. The main differences compared with an SRM are as follows: (1) The TFR motor has a homopolar-type stator phase winding. (2) Its phase modules are placed consecutively in the axial direction. (3) It has the same number of salient poles on the rotor and stator. (4) Each phase of the motor is an independent module. In TFM technology, it is preferable to employ a plurality of TFMs arranged in tandem for reducing torque ripples, avoiding the start-up difficulties, and obtaining continuous rotation. Generally, the motor must have three or more than three phases.

12.7 Reconfigurable Permanent Magnet Motor

The quest for high-efficiency electric motors has stimulated many novel ideas in new types of motor design. One of the latest is to push the efficiency of electric motors to above super-premium level by employing reconfigurable rotor magnets.

The reconfigurable magnet technique can stabilize the output of the machine spinning even at variable speeds. This might be especially useful for some applications. For instance, a wind turbine built with this technique can generate constant output from variable wind speeds without the use of intermediate inverters [12.34].

A reconfigurable PM motor is shown in Figure 12.31 [12.35]. Each of the four PMs is attached to a planetary gear that engages with the central gear. All the four magnets remain rotationally aligned. The motor is reconfigurable from an asynchronous mode at the start-up into a more efficient synchronous mode thereafter. The motor includes a squirrel cage for IM operation at the start-up with the PMs positioned to produce a weak magnetic field not interfering with the start-up. During the start-up, the centrifugal latching mechanism retains the PMs in the weak magnetic field position. When the motor reaches a sufficient speed, the PMs are released by the centrifugal mechanism and rotate to produce a strong magnetic field in harmony with the rotating stator magnetic field for the efficiency synchronous operation.

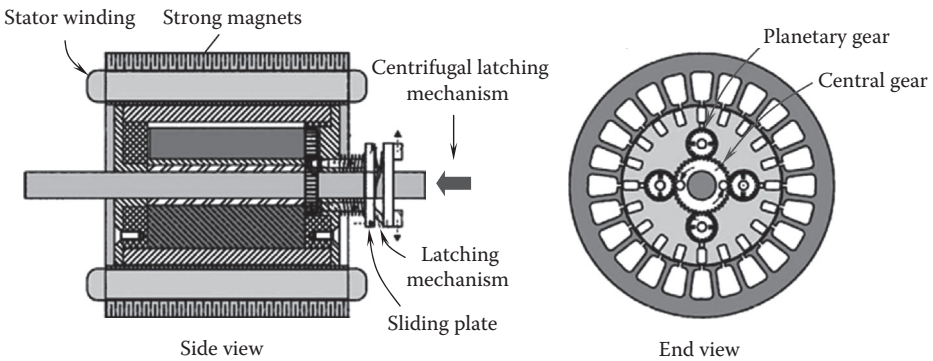

FIGURE 12.31
A cross-sectional view of reconfigurable magnet motor, revealing the details of the centrifugal clutch used to rotate the rotor magnets once the motor is reaching a certain speed (U.S. Patent 8,390,162) [12.35]. (Courtesy of the U.S. Patent and Trademark Office, Alexandria, VA.)

More detailed description of the transition between a weak magnetic field and a strong magnetic field applied to the motor is presented in Figure 12.32. The centrifugal latching mechanism includes weights, rotating plate, spring disk, sliding plate, pins, and pin seats. The weights and spring disk are designed so that when the motor is stationary, the weights remain in the inward position to the shaft and the magnets are at the weak magnetic field position. Meanwhile, the pins engage the pin seats in the central gear when the motor is at rest and the centrifugal latching mechanism holds the PMs in the weak magnetic field position. At an appropriate rotating speed, the weights move outward due to the centrifugal force, causing the spring disk to snap axially from the extended position as in Figure 12.32a to the retraced position as in Figure 12.32b. The centrifugal latching mechanism thus pulls the pins from the pin seats releasing the PMs to the strong magnetic field position. As the motor stops, the PMs are magnetically urged back to the weak field position again.

12.8 Variable Reluctance Motor

VRMs have been widely used for high-torque applications. Their inherent fault-tolerant features and other advantages have made them a prime candidate for reliability-premium applications. From the standpoint of energy conversion, VRM is unique compared to other types of motors.

According to the relationship of motion plane and flux plane, VRMs can be categorized as the transverse-flux machine (TFM) and the vernier machine (VM). As addressed previously, due to the complexity of the constructive geometry, the design and fabrication of the TFM are considerably difficult. By contrast, VMs can adopt a simple toothed-pole-stator and PM-rotor configuration. Each stator tooth is split into small teeth at the end (i.e., flux-modulation poles). Thus, a small movement of the PM rotor can cause a large movement of flux linkage in the stator armature winding [12.36].

Figure 12.33 shows an outer-rotor, flux-controllable vernier PM motor, designed for the in-wheel drive of electric vehicles. In this design, the inherent outer-rotor topology makes

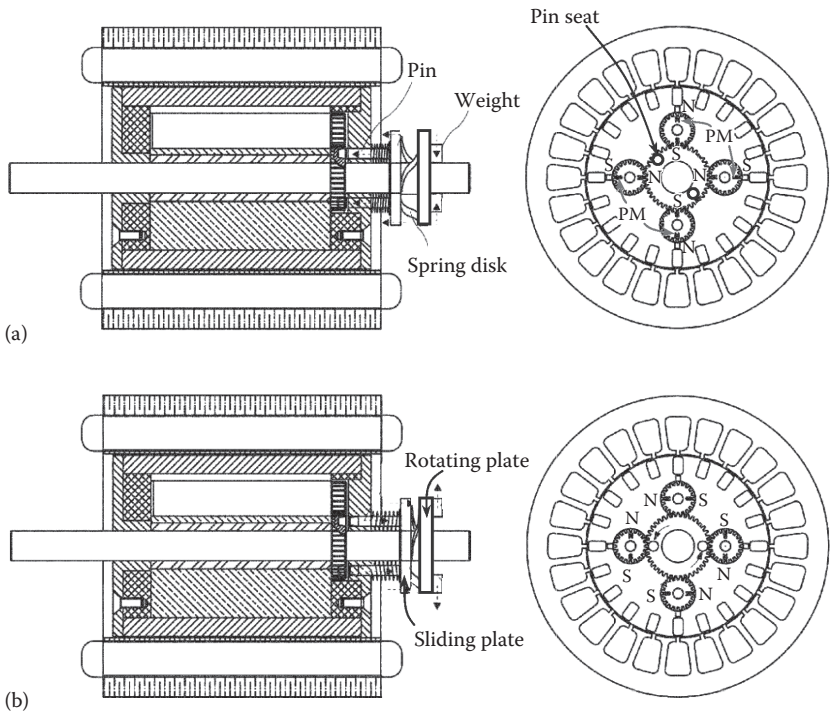

FIGURE 12.32
The side and end views of the reconfigurable electric motor with the centrifugal latching mechanism: (a) in the weak magnetic field position when the four PMs are held by the centrifugal latching mechanism and (b) in the strong magnetic field position when the four PMs are released by the centrifugal latching mechanism (U.S. Patent 8,390,162) [12.35]. (Courtesy of the U.S. Patent and Trademark Office, Alexandria, VA.)

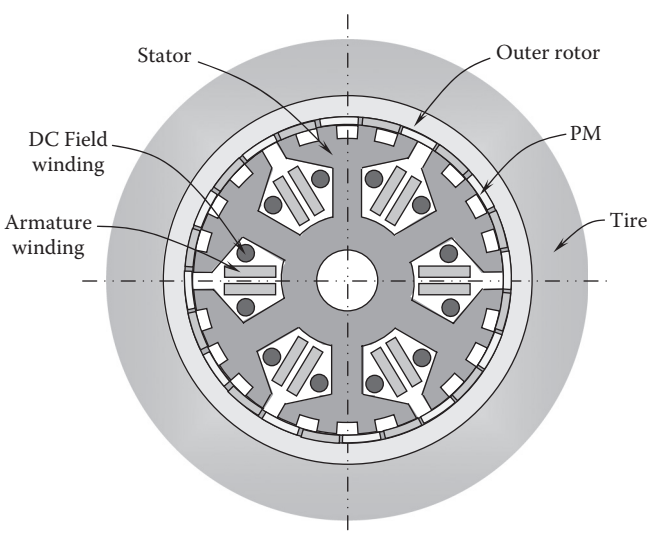

FIGURE 12.33
Configuration of vernier PM motor used as in-wheel drive.

the motor directly connect with the wheel rim and eliminates the mechanical transmission. The inner stator accommodates two sets of windings, that is, the three-phase armature windings and the DC field windings for performing the flux weakening control at high-speed operation. There are 24 salient poles, setting up in the inner stator for performing the flux modulation. Twenty-two pole pair PMs are mounted on the outer rotor. The key of the design is to use the vernier structure for obtaining the high-speed to low-speed gear effect and achieving the high output torque at low-speed operation [12.37]. This direct drive, in-wheel motor can smoothly operate within the speed range of 0–1000 rpm at different operation modes for electric vehicles.

According to excitation patterns, doubly salient motors (DSMs) can be classified into three types: PM, fielding winding, and hybrid. The VRMs deploying doubly salient structures (i.e., teeth on both the stator and rotor) have been developed for several decades with well-explored design features, torque production, and control characteristics. In recent years, doubly salient PM (DSPM) motors have gained renewed interest for some new applications, particularly in-wheel motors for electric vehicle drives.

Figure 12.34 shows the structure of a 12/8-pole (the stator pole number p_s = 12 and the rotor pole number p_r = 8) DSPM motor. Armature windings are located in the stator. Four pieces of PM are located radially at the four corners of the stator. This indicates that the leakage flux outside the stator circumference (which is generally neglected in conventional PM motors) becomes significant. Hence, to take the leakage flux into account, the design domain must be extended from the stator circumference to the surrounding space. Since the rotor consists of only silicon steel laminations, it gives motor the capability to work at very high speeds.

In order to minimize the switch frequency and hence the iron losses in poles and yokes, the number of rotor poles p_r should be selected as small as possible but must be equal to or larger than three for the capability of self-starting. As a result, the rotor poles are usually less than stator poles. In practice, p_s/p_s of 6/4, 8/6, and 12/8 are possible configurations of DSPM motors. Generally, 12/8 pole motors have less iron losses and magnetic potential drop than 6/4 pole machines [12.38].

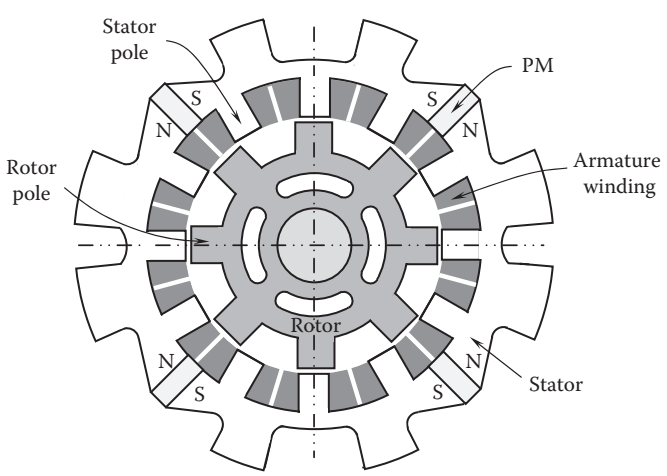

FIGURE 12.34
The cross-sectional view of a 12/8-pole DSPM.

From the investigation of DSPM motor by Cheng et al. [12.39], the following may be concluded: (1) Although the DSPM motor has salient poles in the stator and rotor, the PM torque significantly dominates the reluctance torque, exhibiting low cogging torque. (2) The air gap flux of the DSPM motor is mainly contributed by PMs, whereas the armature current contributes to the change of the flux distribution. (3) Because most of the armature flux loops through the adjacent stator poles, instead of PMs, the DSPM motor is less sensitive to demagnetization than other PM motors. (4) The inductance of the DSPM motor depends not only on the rotor position but also on the strengthening/weakening action of the armature field to the PM field. (5) The leakage flux outside the stator circumference of the DSPM motor may lead to a reduction in the effective flux of about 3%.

12.9 Permanent Magnet Memory Motor

Ostovic first proposed the innovative concepts of PM memory motors, which can be built either as variable flux memory motors (VFMMs) [12.40] or as pole-changing memory motors (PCMMs) [12.41]. Memory motors combine the flux controllability of PM motors and the employment of the flux concentration principle that enables creating air gap flux densities for high-efficiency machines.

12.9.1 Variable Flux PM Memory Motor

Unlike the conventional PM motors, the type of VFMM has the distinct ability to change the intensity of magnetization by short pulses of stator current and to memorize the flux density level in the rotor PMs. Additional advantages include high efficiency, high torque-to-weight ratio, large starting torque, full controllability of back EMF, no risk of demagnetization by the load current, zero reactive power demand on stator terminals, simple structure, and operation in a wide speed range without excessive rotor I^2R losses. In fact, VFMM is the only synchronous machine with rotor excitation that has a true speed capability without sacrificing the other machine properties. However, compared with other types of PM motors, this type of motor may have relatively low overload ability and reliability [12.42].

As shown in Figure 12.35, a four-pole VFMM consists of trapezoidal alnico PMs sandwiched by soft irons. Both the PMs and soft irons are sandwiched by triangle-shaped plates made of a nonmagnetic material. All of these components are mechanically fixed to a nonmagnetic shaft. PMs can be online magnetized or demagnetized with various magnetization levels. Tangentially magnetized PMs with red and blue represent N-poles and S-poles, respectively. The magnetic flux Φ_{max} is driven by the PMs to transit across the air gap into the stator, continuously go along the circumferential direction in the stator core, and finally come back through the air gap into the rotor for completing the loop.

VFMMs combine the advantages of a wound rotor synchronous motor (simple control of induced voltage) and a PM synchronous motor (no excitation losses), resulting in a unique synchronous machine for numerous applications.

12.9.2 Pole-Changing PM Memory Motor

Conventional PM machines have a constant number of poles, because their magnets are incorporated into rotor body in a manner that does not allow any change of machine

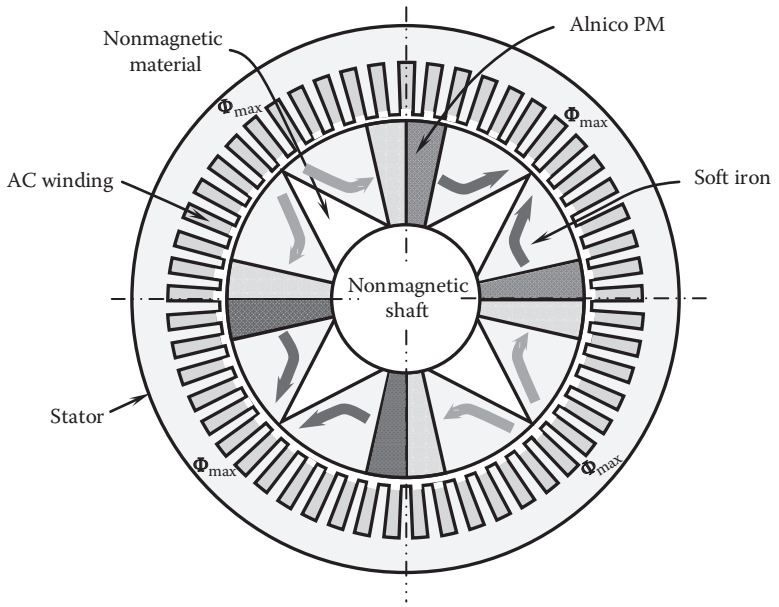

FIGURE 12.35
The cross-sectional view of a fully magnetized, PM VFMM.

topology. By comparison, a pole-changing PM memory motor has the capability to change the number of poles. This type of motor has several advantages such as high efficiency, high output power, and less thermal dissipation issue due to the lack of rotor copper losses. These make pole-changing memory motors attractive for many motor applications, among which the fan and pump applications are the most pronounced.

Figure 12.36 depicts the operational principle of an eight-pole magnetized PCMM. Due to the geometry symmetry, only a quarter of the motor is modeled. The motor contains 32 magnets positioned radially in the stator. Each pole takes a 45° sector, which contains four PMs (32/8 = 4). All of the PMs are magnetized in the tangential direction. The rotor wreath is built of PMs along with soft iron segments and is mechanically fixed to a nonmagnetic shaft.

After the stator windings are reconnected into a six-pole (a 60° sector per pole) configuration, a short pulse of stator current changes the rotor from eight-pole to six-pole magnetization (Figure 12.37). Since the number of magnets per pole is no longer an integer ($32/6 = 5.3\dot{3}$), some magnets may remain demagnetized, as shown in the figure. As a matter of fact, both flux per pole and stator current necessary to remagnetize the rotor magnets vary as a function of the number of magnets per pole. Therefore, by changing the pole number, these two important motor parameters are adjusted for optimizing motor performance.

12.9.3 Doubly Salient Memory Motor

DSPM memory motors are the combination of memory motors, namely, the online tunable flux-mnemonic PMs and DSPM motors, thus achieving effective air gap flux control. Employing the outer-rotor and double-layer-stator topology, the motor takes advantage of compact structure, low armature reaction, and direct drive capability. This type of motor can offer the unique features of pole dropping and pole reversing [12.43].

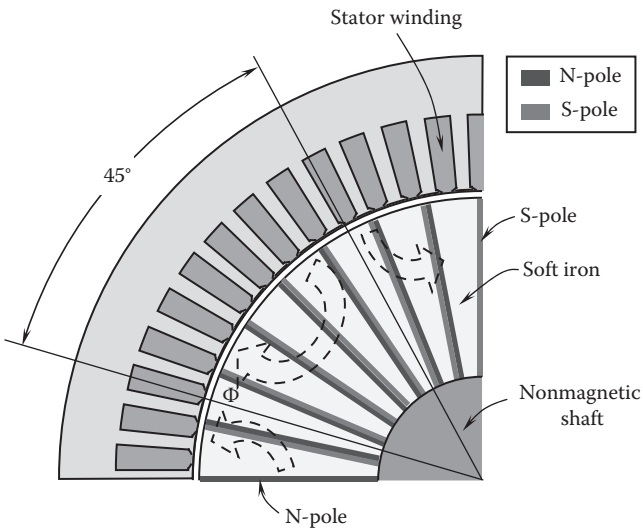

FIGURE 12.36
The cross-sectional view of an eight-pole PM magnetized PCMM.

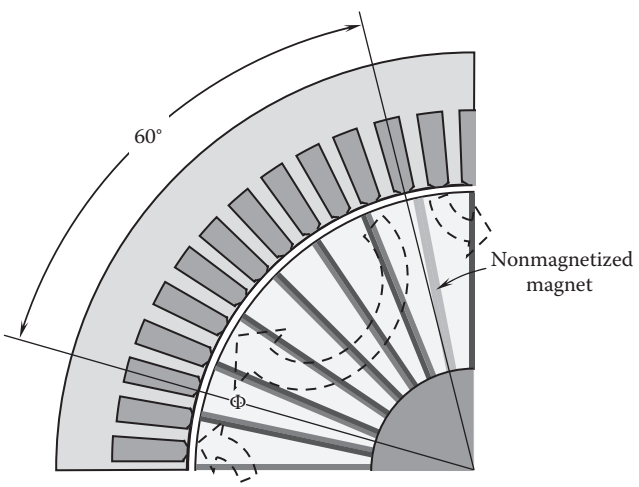

FIGURE 12.37
The cross-sectional view of a six-pole PM magnetized PCMM.

The topology of the doubly salient memory motor is depicted in Figure 12.38. It adopts an outer-rotor, an outer-layer-stator, and an inner-layer-stator structure. The motor has five-phase and 30-pole/24-pole doubly salient structure on the stator/rotor. The outer rotor only consists of lamination iron and thus offers excellent mechanical robustness. This arrangement is especially suitable for the direct drive applications such as electric vehicle in-wheel motors and wind turbines. The AC armature windings and DC magnetizing windings are located at the outer-layer stator and inner-layer stator, respectively. This effectively uses the space of the stator yoke. Alnico PMs are fixed between the inner-layer

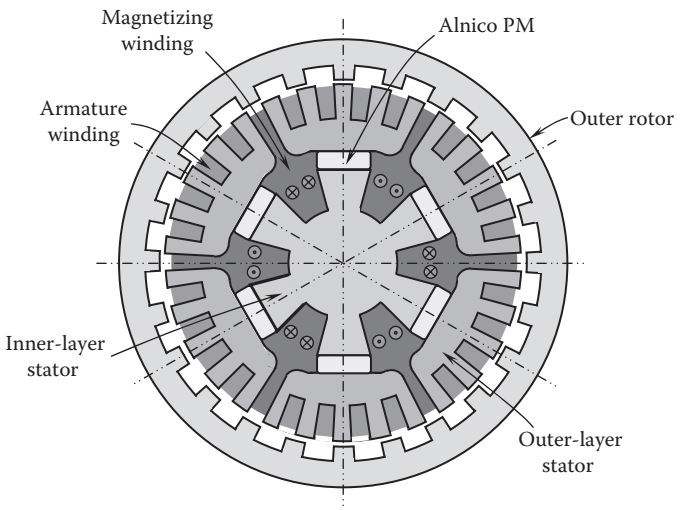

FIGURE 12.38
Topology of doubly salient PM memory motor.

stator and outer-layer stator. The using of alnico PMs can achieve a controllable air gap flux by applying temporary current pulses to the magnetizing winding to online tune the magnetization level of alnico PMs.

Compared with other types of PMs, alnico magnets exhibit good temperature stability and resistance to corrosion, high Curie temperature (approximately 840°C), but a low coercivity, which is prone to demagnetization due to shock. Furthermore, alnico magnets deliver smaller energy products than rare-earth PMs, thus degrading the machine power density. In order to address these problems, Li et al. [12.44] have presented a new flux-mnemonic dual-magnet machine that incorporates both the Nd–Fe–B and alnico PMs for providing hybrid excitation (Figure 12.39). In such a way, the proposed machine not only retains the feature of online tunable air gap flux control but also improves the machine power density.

12.10 Adjustable and Controllable Axial Rotor/Stator Alignment Motor

In a conventional RF motor, the relative position between the rotor and stator is fixed both axially and radially. In this novel PM motor, the axial alignment between a rotor and a stator is adjustable and controllable using a mechanical technique. As the PM motor is offset axially to provide axial misalignment between the rotor PM poles and the stator, the effective magnet pole strength or magnetic flux to the stator are significantly reduced, resulting in an increase in speed and a decrease in motor torque [12.45].

As shown in Figure 12.40, the stator is incorporated into the motor housing structure. PMs are mounted on the outer surface of the rotor. The rotor is connected with a hydraulic or pneumatic actuator through a pivot arm at its end. A rotor sleeve is coupled to the rotor with a plurality of parallel grooves formed on the inner surface. The grooves have

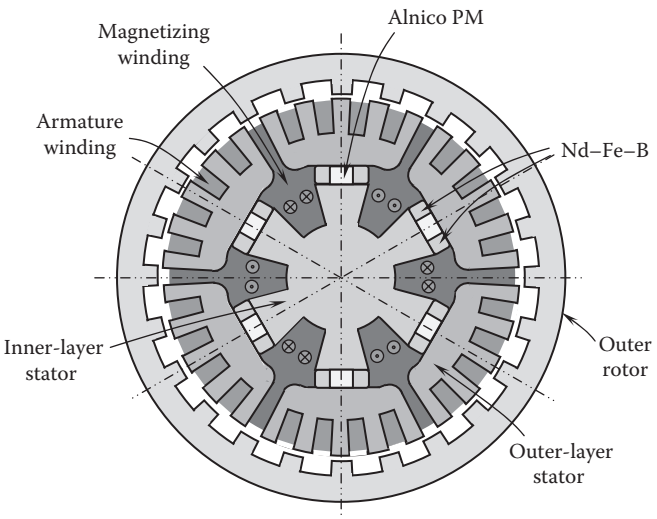

FIGURE 12.39
Doubly salient PM memory motor with dual magnet.

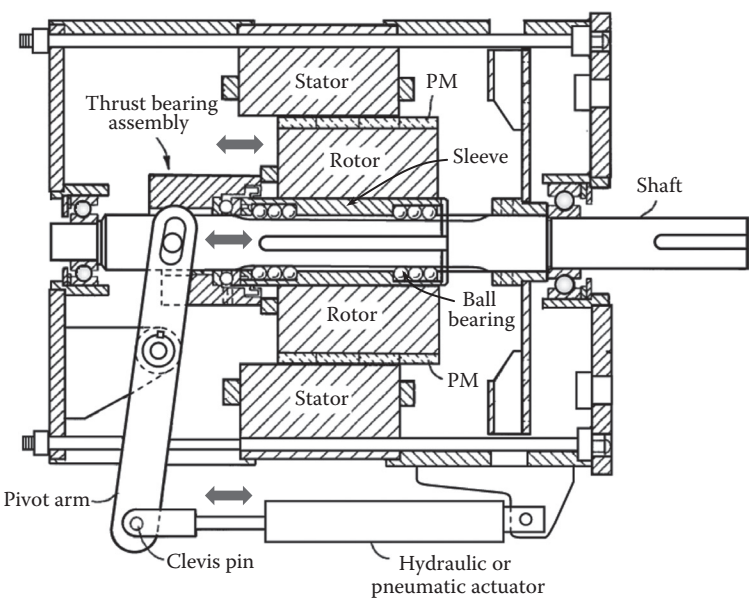

FIGURE 12.40
Structure of PM motor with adjustable axial rotor/stator alignment (U.S. Patent 6,555,941) [12.45]. (Courtesy of the U.S. Patent and Trademark Office, Alexandria, VA.)

a semicircular cross-sectional shape and are configured to receive a plurality of ball bearings. Correspondingly, the motor shaft also has a plurality of parallel grooves formed at the outer surface. The ball bearings are contained within the channel formed by both the rotor sleeve and shaft grooves. Thus, the rotor is allowed to slide axially via the ball bearings when the hydraulic or pneumatic actuator is activated.

The rotor in Figure 12.40 is about 25% disengaged with the stator. This amount of misalignment will produce an increase in speed of approximately 150% of the rated speed.

12.11 Piezoelectric Motor

Piezoelectric effect refers to the phenomenon that when a certain nonconducting material, such as quartz crystal (SiO_2) and ceramics, is subject to mechanical stress (e.g., pressure or vibration), the material generates an electric potential across it. Conversely, when an electric field is applied to the material, it undergoes mechanical distortion or vibration.

Piezoelectric motors operate based on the principle of piezoelectric effect. In a piezoelectric motor, the piezoelectric material produces high-frequency (inaudible to the human ear) acoustic vibrations on a nanometer scale to create a linear or rotary motion. Piezoelectric motors have a number of potential advantages over conventional electromagnetic motors, including the following [12.46]:

- Piezoelectric motors maintain high torque at low speed with a compact motor size. Hence, they have higher torque densities compared with conventional electromagnetic motors for the same power rating.
- This type of motor does not create electromagnetic fields, nor is affected by external electromagnetic fields. This feature is extremely important for motors used within strong magnetic field environments.
- Because of the direct drive mechanism, piezoelectric motors eliminate the need for supplementary transmissions or gear trains found in conventional electromagnetic motors. This avoids the usual backlash effects in conventional motors and thus increases the motor positioning accuracy.
- A compelling advantage of piezoelectric motors is their intrinsic steady-state autolocking capability as the driving mechanics use friction between the vibrating stator and rotor.
- With less heat generated in piezoelectric motors, cooling is no longer a critical issue in motor design.
- This type of motor has a low rotor inertia and thus provides rapid start and stop characteristics.
- With fewer mechanical components, their construction is relatively simple. Thus, piezoelectric motors are well suited for miniaturization, and their overall efficiency is relatively insensitive to size.
- In the power-off mode, the position can be maintained due to the frictional force between the contact surfaces.
- Piezoelectric motors have quiet operation.

Piezoelectric motors are generally used in low-torque and high-precision micropositioning applications, such as medical devices, robotic positioning, pharmaceuticals handling, and pick-and-place assembly.

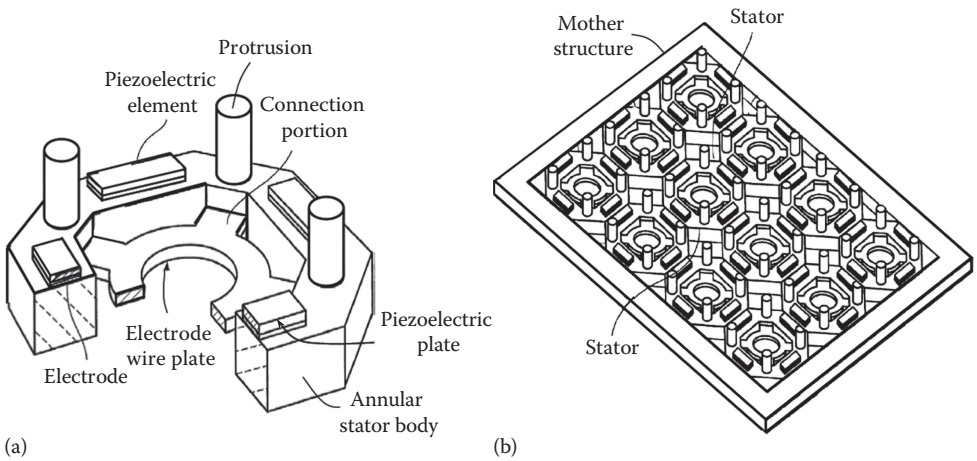

FIGURE 12.41
The structure of a piezoelectric motor: (a) a partially cross-sectional perspective view of the stator used in a piezoelectric motor and (b) the mother structure prepared obtaining the stators (U.S. Patent 8,330,326) [12.47]. (Courtesy of the U.S. Patent and Trademark Office, Alexandria, VA.)

The structure of a piezoelectric motor is presented in Figure 12.41 [12.47]. A stator includes a substantially annular stator body on which a number of piezoelectric elements are mounted. Each piezoelectric element consists of a piezoelectric plate made of ceramic, electrodes formed on the surfaces of the piezoelectric plates. A number of protrusion standings between adjacent pairs of the piezoelectric elements are in contact with the rotor for actuating the rotor (Figure 12.41a). Figure 12.41b shows the mother structure, containing 12 identical stators, each of them equipped with a plurality of piezoelectric elements. The electrodes and wiring lines may be formed by coating and backing an electroconductive paste or be formed as part of the cofiring process for making the mother structure. Then, the mother structure is cut in the thickness direction, so that each individual stator has the same structure as the stator shown in Figure 12.41a. In such a way, the stator can be assembled with a rotor for forming a piezoelectric motor.

Figure 12.42 is a schematic view illustrating the driving principle of the piezoelectric motor. Two pairs of piezoelectric elements facing each other, that is, A+ and A– and B+ and B–, are polarized in opposite thickness directions. A+ and A– constitute an A-phase, while B+ and B– constitute a B-phase. The symbols A+ and A– indicate that the piezoelectric bodies are polarized in opposite thickness directions. So does the B-phase drive.

Imaginary lines connect the center point *O* and midpoints of the short sides of the piezoelectric elements, with the length *l*. The angle between the imaginary lines E1 and E2 is about 60°. This indicates that the length of the piezoelectric element equals the length *l*. Thus, three standing waves are excited and combined to generate three progressive waves. When the central angle corresponding to the wavelength of the three progressive waves is λ_θ, the length *l* corresponds to the central angle of $\lambda_\theta/2$.

When the piezoelectric motor is driven and a progressive wave is generated in the substantially annular stator body made of an elastic member, the ends of the protrusions perform elliptical motion. Therefore, the rotor, which is in close contact with the protrusions, is rotated.

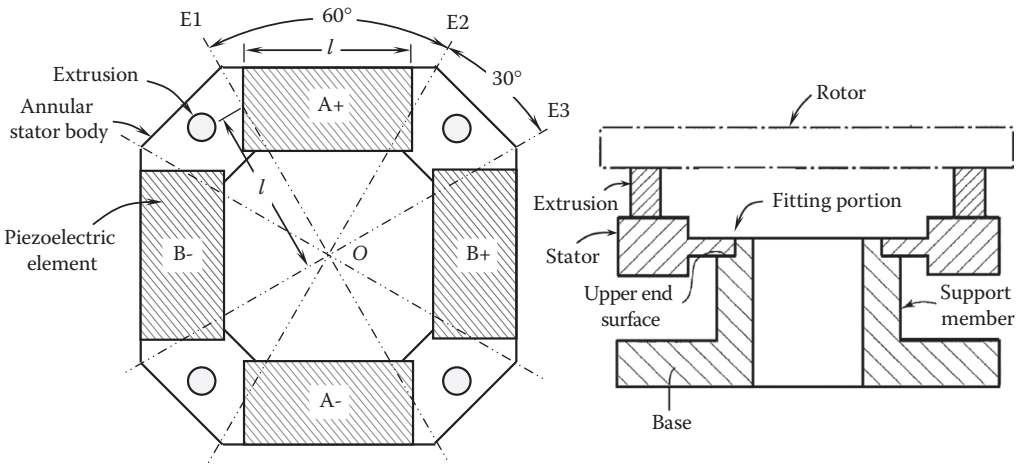

FIGURE 12.42
The driving principle of the piezoelectric motor (U.S. Patent 8,330,326) [12.47]. (Courtesy of the U.S. Patent and Trademark Office, Alexandria, VA.)

12.12 Advanced Electric Machines for Renewable Energy

As pointed by Chau et al. [12.36], the latest development of renewable energy machines is focused on three directions: the PM machine aiming to achieve high reliability and high robustness, the direct drive PM machines aiming to directly harness the renewable energy without any transmission mechanism, and the magnetless machines aiming to avoid using expensive rare-earth PMs. Among them, the magnetless machines are the most attractive to the energy industry.

In the last several years, the global price of rare-earth magnets has risen significantly, and consequently, it greatly increases the manufacturing costs of PM motors. This price soar has motivated motor engineers and material scientists to develop new types of electric machines without using magnets and to discover alternatives of rare-earth magnets.

The scientists at a US national laboratory have developed a PM-less synchronous reluctance motor [12.48]. As presented in Figure 12.43, the PM-less motor consists of a stator that generates a magnetic revolving field when sourced by an AC and an uncluttered rotor that is disposed within the magnetic revolving field and spaced apart from the stator to form an air gap. The rotor includes a plurality of rotor pole stacks having an inner periphery biased by single polarity of an N-pole field and an S-pole field, respectively. The outer periphery of each of the rotor pole stacks is biased by an alternating polarity.

Without PMs, some of these brushless synchronous machines may have a reduced size, lower weight, and less core losses. In hybrid vehicle applications, there may be little or no core losses when the system runs free without field excitations. Without a magnetic resistance, fuel efficiency may increase. In these systems, the stator fields can be cut off to enhance safety, fields can be boosted to increase or reach peak acceleration power in short time periods, power factors may be optimized (e.g., lowering the loading in inverter applications), and efficiency maps may increase due to the adjustable fields.

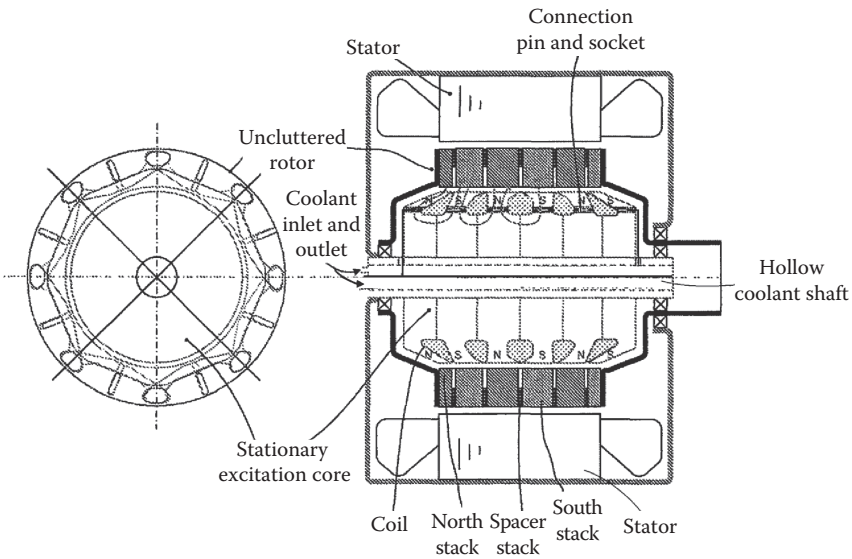

FIGURE 12.43
Cross-sectional view of the PM-less electric motor (U.S. Patent 8,264,120) [12.48]. (Courtesy of the U.S. Patent and Trademark Office, Alexandria, VA.)

Figure 12.44 illustrates in more detail the eight-pole rotor stacks that are used to form an uncluttered rotor. The stack is made of laminations. The number of magnetically isolated channels is equal to the number of poles that are equally spaced apart on the outer periphery. While the polarity along the outer peripheral surface is arranged alternately, the inner circumference of each of the north and south polarity pole stacks maintains a common polarity (Figure 12.44a and b). The inner polygonal surfaces of the spacer stacks maintain a neutral polarity (Figure 12.44c). The magnetically isolated channels in the spacer stacks are equally spaced about its annulus.

12.13 Micromotor and Nanomotor

The rapid development of microtechnology and nanotechnology has triggered vast interests and generated abundant opportunities for the development of micromotors and nanomotors.

12.13.1 Micromotor

Micromotors and microgenerators are power microelectromechanical systems (MEMS) for energy conversion between mechanical energy and electrical energy. With the continuous improvement of the MEMS technology, various types of compact, lightweight, and portable power conversion devices have been successfully designed and fabricated.

Nagle et al. [12.49] at MIT have presented the analysis, design, fabrication, and testing of a planar electrostatic induction micromotor. The structure and operating principle of this

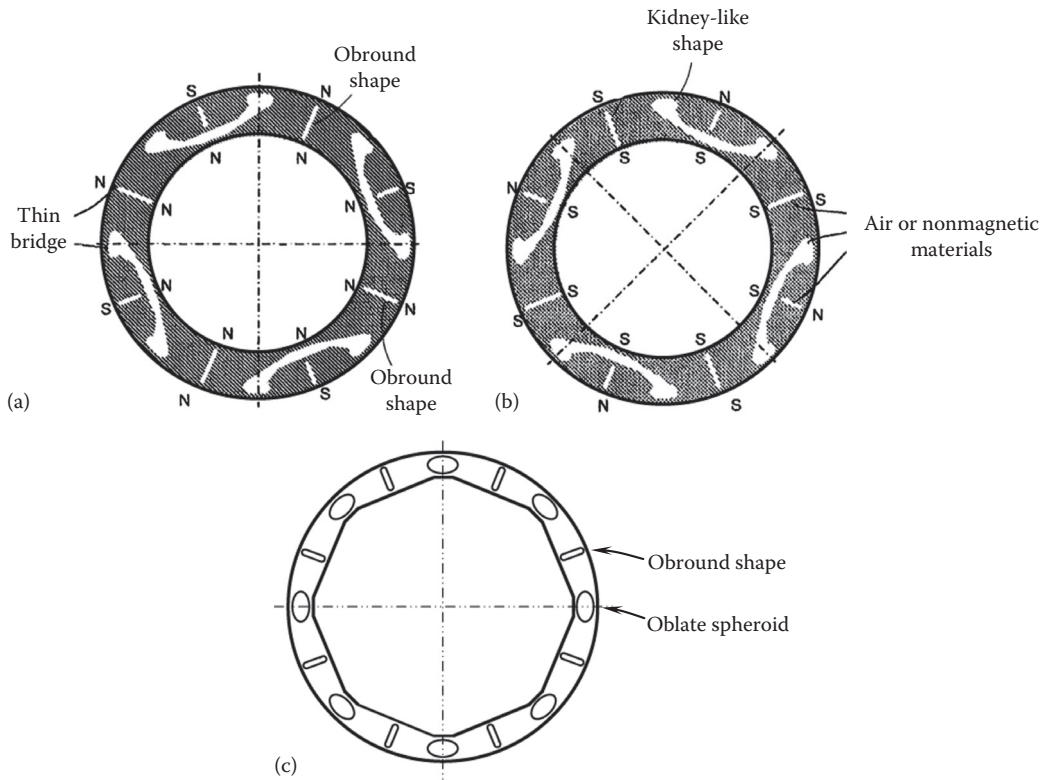

FIGURE 12.44
Eight-pole rotor stacks: (a) pole stack of north polarity, (b) pole stack of south polarity, and (c) spacer stack (U.S. Patent 8,264,120) [12.48]. (Courtesy of the U.S. Patent and Trademark Office, Alexandria, VA.)

micromotor are illustrated in Figure 12.45. This is a six-phase motor with 131 pole pairs distributed on a stator. The rotor and stator are 4 mm in diameter and separated by a gap of 3 μm. The motor produces a torque of 2 μN-m. The stator contains 768 radial electrodes, separated by a 4 μm space along their radial length. The electrodes are supported by an insulation layer. The rotor comprises a 0.5 μm sheet of moderately doped polysilicon deposited on a 10 μm thick oxide insulation layer that is deposited on a 400 μm thick silicon wafer. The rotor is tethered above the stator by eight silicon springs etched from the silicon wafer. During motor operation, external electronics excite the stator electrodes to produce a potential wave that travels circumferentially with a speed exceeding that of the rotor. The corresponding distribution of charges on the stator electrodes induces image charges on the rotor surface across the air gap.

This type of micromotors has the potential to perform Watt-level electrical–mechanical power conversion for applications ranging from portable electric suppliers to miniature pumps or blowers.

Ghalichechian et al. [12.50] reported the design, fabrication, and characterization of a six-phase, bottom-drive, variable-capacitance micromotor (VCM) rotary micromotor with a robust mechanical support provided by the microball bearings. Figure 12.46 shows the simplified 3D schematic of the micromotor, which is composed of three components: rotor (ϕ = 14 mm), stator, and stainless steel microballs (ϕ = 284.5 μm). Both the

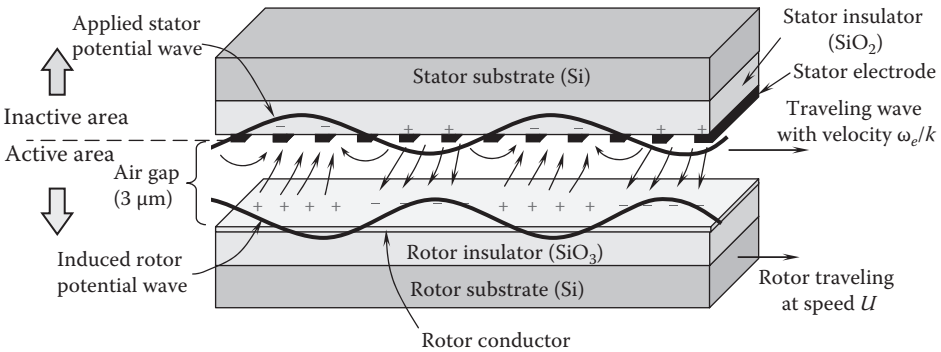

FIGURE 12.45
Operating principle of induction micromotor. Only the active area affects torque production because the electrode potential is enforced on the dividing plane.

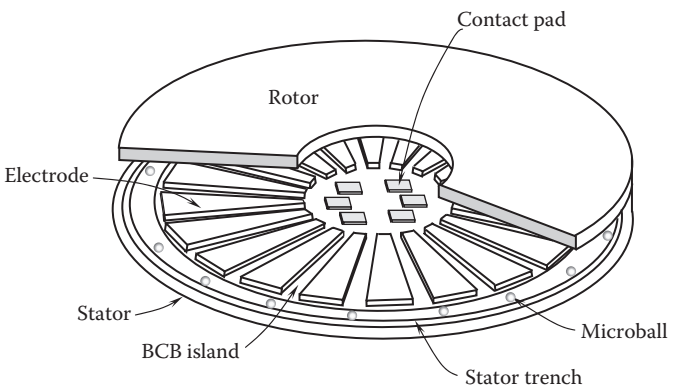

FIGURE 12.46
Simplified 3D schematic of the rotary micromotor.

stator and the rotor are fabricated separately on silicon substrates and assembled with the microballs. Electrodes attach on the stator and salient poles are made on the rotor (Figure 12.47). When a potential is applied to an electrode, image charges are induced on an adjacent salient pole, resulting in tangential and normal forces. The tangential force is the propelling force of the rotor that aligns a rotor pole to an adjacent active electrode. The normal force assists to hold the rotor on the stator. Continuous motion of the rotor is possible by sequential excitation of the electrodes with positive square pulses in a three-phase configuration.

To analyze the effect of the air gap size on the motor torque, three different air gaps (5, 10, and 15 μm) were used in the design. As expected, the motor torque increases by more than a factor of two when the air gap is decreased from 10 to 5 μm. In contrast, the torque is reduced when the air gap is increased from 10 to 15 μm. However, fabrication of a machine with a gap of 15 μm is more feasible than 5 μm. The experimental results have shown that with the estimated air gap of 10–13 μm, the measured torque is 5.62 μN-m at the voltage of 150 V.

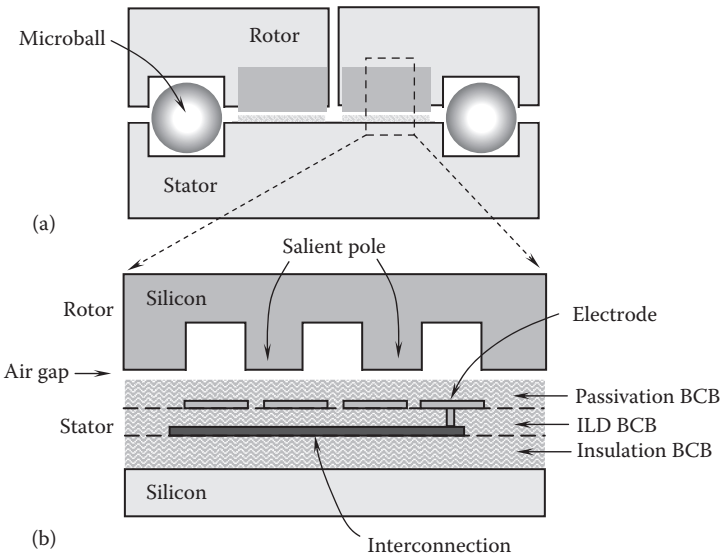

FIGURE 12.47
Schematic of (a) radial cross section of mechanical (bearing) and electric components of the micromotor and (b) azimuthal cross section of the stator and rotor active pars.

12.13.2 Nanomotor

The advent of the nanoscale electric motors has revolutionized the traditional concept of electric motors. In 2005, scientists at the Lawrence Berkeley National Laboratory unveiled a motor that operates by moving atoms between two molten droplets of metal. Completely contained within a carbon nanotube, the motor measures less than 200 nm across [12.51].

This record was broken by a research team of Tufts University in 2011 [12.52]. The team has developed the world's smallest motor with only one nanometer, made from a single molecule of butyl methyl sulfide on a copper surface. The molecular motor can be powered by electricity from a low-temperature scanning tunneling microscope or heat energy. As demonstrated in Figure 12.48, the molecule had a sulfur base. When placed on a conductive

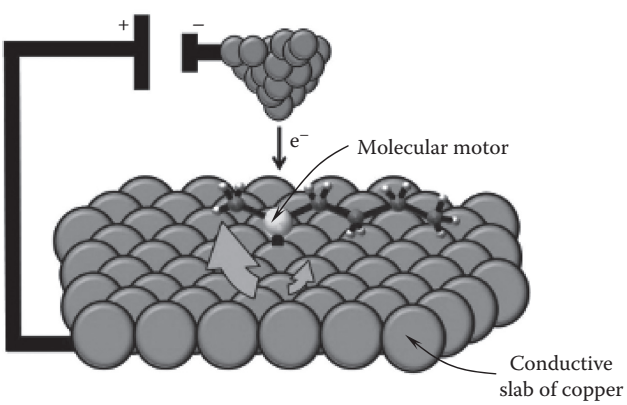

FIGURE 12.48
The working principle of the molecular motor. (Courtesy of Sykes Laboratory, Tufts University, Medford, MA.)

slab of copper, it became anchored to the surface. The sulfur-containing molecule had carbon and hydrogen atoms radiating off to form what looks like two arms (gray). These carbon chains were free to rotate around the central sulfur–copper bond.

The spinning speed of the single-molecular motor is determined by temperature. At a temperature of 100 K (–173°C), the molecular motor spins more than a million times per second. The researchers found that reducing the temperature of the molecule to 5 K (–268°C) enabled them to precisely control the direction and rotational speed of the molecular motor, lowering the molecular motor speed to about 50 rpm. This type of motor may be used in sensing and medical test devices and nanoelectromechanical systems (NEMS). However, there is still a long way to go for practical applications of the single-molecular electric motor.

References

[12.1] Papst, G., Gamble, B. B., Rodenbush, A. J., and Schöttler, R. 1997. Development of synchronous motors and generators with HTS field windings. *Superconducting Science and Technology* **10**(**12**): 924–926.

[12.2] Blaugher, R. D. 1997. Low-calorie, high-energy generators and motors. *IEEE Spectrum* **34**(**7**): 36–42.

[12.3] Schiferl, R. and Rey, C. 2006. Development of ultra efficient HTS electric motor systems. *2005 Annual Superconductivity Peer Review Meeting*, Washington, DC. http://web.ornl.gov/sci/htsc/documents/pdf/fy2006/HTSMotor-SchiferlandRey.pdf.

[12.4] TheEngineer. 2001. Siemens first in Europe with a superconductor motor. http://www.theengineer.co.uk/news/siemens-first-in-europe-with-a-superconductor-motor/269479.article.

[12.5] Takeda, T., Togawa, H., and Oota, T. 2006. Development of liquid nitrogen-cooled full superconducting motor. *IHI Engineering Review* **39**(**2**): 89–94.

[12.6] Eckels, P. W. and Snitchler, G. 2008. 5 MW high temperature superconductor ship propulsion motor design and test results. *Naval Engineers Journal* **117**(**4**): 31–36.

[12.7] American Superconductor Corporation. 2009. AMSC and Northrop Grumman announce successful load testing of 36.5 Megawatt superconductor ship propulsion motor. http://www.businesswire.com/news/home/20090113005166/en/AMSC-Northrop-Grumman-Announce-Successful-Load-Testing.

[12.8] Hayashi, K. 2008. Development of HTS motor—Present status and future prospect. Sumitomo Electric Industries, Ltd. http://www.cca08.com/pdf/presentations/1A-07-HAYASHI.pdf.

[12.9] Kalsi, S. S. 2002. Development status of superconducting rotating machines. *IEEE Power Engineering Society Winter Meeting*, Vol. 1, pp. 401–403, New York.

[12.10] Pippuri, J., Manninen, A., Keränen, J., and Tammi, K. 2013. Torque density of radial, axial and transverse flux permanent magnet machine topologies. *IEEE Transactions on Magnetics* **49**(**5**): 2339–2342.

[12.11] Qu, R. H. and Lipo, T. A. 2005. Dual-rotor, radial-flux, toroidally-wound, permanent-magnet machine. U.S. Patent 6,924,574.

[12.12] Zheng, P., Wu, Q., Bai, J. G., Tong, C. D., and Song, Z. Y. 2013. Analysis and experiment of a novel brushless double rotor machine for power-split hybrid electrical vehicle applications. *Energies* **2013**(**6**): 3209–3233.

[12.13] Niu, S. X., Chau, K. T., and Jiang, J. Z. 2008. A permanent-magnet double-stator integrated-starter-generator for hybrid electric vehicles. *IEEE Vehicle Power and Propulsion Conference*, Harbin, China.

[12.14] Aydin, M., Huang, S., and Lipo, T. A. 2004. Axial flux permanent magnet disc machines: A review. *Conference of Power Electronics, Electrical Drives and Machines* (*SPEEDAM*), Capri, Italy.
[12.15] Gieras, J. F., Wang, R., and Kamper, M. J. 2008. *Axial Flux Permanent Magnet Brushless Machines*, 2nd edn. Springer-Verlag, New York.
[12.16] Aydin, M., Lipo, A., and Huang, S. 2009. Field controlled axial flux permanent magnet electrical machine. U.S. Patent 7,608,965.
[12.17] Woolmer, T. J. and McCulloch, M. D. 2007. Analysis of the yokeless and segmented armature machine. *IEEE International Electric Machines and Drives Conference*, Vol. 2, pp. 704–708, Antalya, Turkey.
[12.18] Kosaka, T. and Matsui, N. 2008. Hybrid excitation machines with powdered iron core for electrical traction drive applications. *International Conference on Electrical Machines and Systems*, pp. 2974–2979, Wuhan, China.
[12.19] Lesani, H., Darabi, A., Gheidari, Z. N., and Tootoonchian, F. 2006. Very fast field oriented control for permanent magnet hysteresis synchronous motor. *Iranian Journal of Electrical and Electronic Engineering* **2**(**1**): 34–40.
[12.20] Qin, R. and Rahman, M. A. 2003. Magnetic equivalent circuit of PM hysteresis synchronous motor. IEEE *Transactions on Magnetics* **39**(**5**): 2998–3000.
[12.21] Hsu, J. S. and Adams, D. J. 1999. Permanent magnet energy conversion machine with magnet mounting arrangement. U.S. Patent 5,952,756.
[12.22] Zhu, X. Y., Chau, K. T., Cheng, M., and Yu, C. 2008. Design and control of a flux-control lable stator-permanent magnet brushless motor drive. *Journal of Applied Physics* **103**(**7**): 07F134-1–07F134-3.
[12.23] Jeon, W. J., Katoh, S., Iwamoto, T., Kamiya, Y., and Onuki, T. 1999. Propulsive characteristics of a novel linear hybrid motor with both induction and synchronous operations. *IEEE Transactions on Magnetics* **35**(**5**): 4025–4027.
[12.24] Fisher, E. A. and Richter, E. 1993. Conical rotor for switched reluctance machine. U.S. Patent 5,233,254.
[12.25] Sarros, T., Chew, E. C., Crase, S., Tay, B. K., and Soong, W. L. 2002. Investigation of cylindrical and conical electrostatic wobble micromotors. *Microelectronics Journal* **33**(**2002**): 129–140.
[12.26] Burch, D., Petro, J. P., and Mayer, J. F. 2011. Conical magnets and rotor-stator structures for electrodynamic machine. U.S. Patent 7,982,350.
[12.27] Weh, H. and May, H. 1986. Achievable force density for permanent magnet excited machines in new configurations. *Proceedings of First International Conference on Engineering Management: ICEM'86*, Munich, Germany.
[12.28] Beyer, S. 1997. Untersuchungen am magnetischen Kreis der permanentmagneterregten Transversalflussmaschine in Sammlerbauweise. Papierflieger: Clausthal-Zellerfeld, Germany.
[12.29] Salles, M. B. C., Cardoso, J. R., and Hameyer, K. 2011. Dynamic modeling of transverse flux permanent magnet generator for wind turbines. *Journal of Microwaves, Optoelectronics and Electromagnetic Applications* **10**(**1**): 95–105.
[12.30] Parspour, N., Babazadeh, A., and Orlik, B. 2004. Transverse flux machine design for manipulating system applications. *Proceedings of PCIM 2004 Europe* **I**: 481–485.
[12.31] Baserrah, S. 2011. Transverse flux machine. European Patent 2,317,633.
[12.32] Gieras, J. F. and Rozman, G. I. 2012. Rim driven thruster having transverse flux motor. U.S. Patent 8,299,669.
[12.33] Viorel, I.-A., Crivii, M., Löwenstein, L., Szabó, L., and Gutman, M. 2004. Direct drive systems with transverse flux reluctance motors. *ACTA Electrotehnica* **45**(**3**): 33–40.
[12.34] Teschler, L. 2013. Another way to make an energy efficient motor. *Machine Design*. Online article. http://machinedesign.com/motorsdrives/another-way-make-energy-efficient-motor.
[12.35] Finkle, L. J. and Furia, A. 2013. Reconfigurable inductive to synchronous motor. U.S. Patent 8,390,162.

[12.36] Chau, K. T., Li, W. L., and Lee, C. H. T. 2012. Challenges and opportunities of electric machines for renewable energy. *Progress in Electromagnetics Research B* **42**: 45–74.
[12.37] Liu, C. H. 2011. Design of a new outer-rotor flux-controllable vernier PM in-wheel motor drive for electric vehicle. *The 2011 International Conference on Electrical Machines and Systems*, Beijing, China.
[12.38] Cheng, M., Fan, Y., and Chau, K. T. 2005. Design and analysis of a novel stator–doubly-fed doubly salient motor for electric vehicles. *Journal of Applied Physics* **97**(**2005**): 10Q508:1–10Q508:3.
[12.39] Cheng, M., Chau, K. T., and Chan, C. C. 2001. Design and analysis of a new doubly salient permanent magnet motor. *IEEE Transaction on Magnetics* **37**(**4**): 3012–3020.
[12.40] Ostovic, V. 2003. Memory motor—A new class of controllable flux PM machines for a true wide speed operation. *IEEE Industrial Application Magazine* **9**(**1**): 52–61.
[12.41] Ostovic, V. 2002. Pole changing permanent magnet machines. *IEEE Transactions on Industry Applications* **38**(**6**): 1493–1499.
[12.42] Chau, K. T., Chan, C. C., and Liu, C. 2008. Overview of permanent-magnet brushless drives for electric and hybrid electric vehicles. *IEEE Transactions on Industrial Electronics* **55**(**6**): 2246–2257.
[12.43] Yu, C., Chau, K. T., Liu, X. H., and Jiang, J. Z. 2008. A flux-mnemonic permanent magnet brushless motor for electric vehicles. *Journal of Applied Physics* **103**(**7**): 07F103:1–07F103:3.
[12.44] Li, W. L., Chau, K. T., Gong, Y., Jiang, J. Z., and Li, F. H. 2011. A new flux-mnemonic dual-magnet brushless machine. *IEEE Transactions on Magnetics* **47**(**10**): 4223–4226.
[12.45] Zepp, L. P. and Medlin, J. W. 2003. Brushless permanent magnet motor or alternator with variable axial rotor/stator alignment to increase speed capacity. U.S. Patent 6,555,941.
[12.46] Miller, T. J. E. 2009. *Switched Reluctance Motors and Their Control*. Magna Physics Publishing and Clarendon Press, Oxford, U.K.
[12.47] Fujimoto, K. and Asano, H. 2012 Piezoelectric motor and method of manufacturing the same. U.S. Patent 8,330,326.
[12.48] Hsu, J. S. 2012. Permanent-magnet-less synchronous reluctance system. U.S. Patent 8,264,120.
[12.49] Nagle, S. F., Livermore, C., Frechette, L. G., Ghodssi, R., and Lang, J. H. 2005. An electric induction micromotor. *Journal of Microelectromechanical Systems* **14**(**5**): 1127–1143.
[12.50] Ghalichechian, N., Modafe, A., Beyaz, M. I., and Ghodssi, R. 2008. Design, fabrication, and characterization of a rotary micromotor supported on microball bearings. *Journal of Microelectromechanical Systems* **17**(**3**): 632–642.
[12.51] *Guinness World Records 2010*. 2009. Random House Publishing Group, New York.
[12.52] Tierney, H. L., Murphy, C. J., Jewell, A. D., Baber, A. E., Iski, E. V., Khodaverdian, H. Y., McGuire, A. F., Klebanov, N., and Sykes1, E. C. H. 2011. Experimental demonstration of a single-molecule electric motor. *Natural Technology* **6**: 625–629.

Index

A

Acceleration of gravity, 179, 421
Accelerometers, 513, 525, 615
AC motors, *see* Alternating current (AC) motors
Acoustic anechoic chamber, 535–536
Acoustic blankets, 540–544
Acoustic emission, 533
Acoustic noise
  acoustic anechoic chamber, 535–536
  active noise reduction, 538–539
  aerodynamic noise, 532
  airborne noise, 532
  averaged sound pressure level, 531
  A-weighting scale, 530–531
  broadband noise, 527
  B-weighting scale, 530–531
  C-weighting scale, 530–531
  electromagnetic, 482
  field noise test, 537–538
  kinematic, 481
  measurement, 536–538
  mechanical, 482
  noise abatement
    active noise reduction techniques, 538–539
    nanotechnology, 548
    passive noise reduction techniques (*see* Passive noise reduction techniques)
  nonrotational aerodynamic noise, 532
  octave frequency bands, 528–530
  rotating electric machines (*see* Rotating electric machines)
  rotational aerodynamic noise, 532
  sound power, 527–528
  sound pressure, 527
  structure-borne noise, 532
  tonal noise, 527
Active cooling, 410–411
Active noise reduction, 538–539
Active vibration damping, 524
Active vibration isolation systems, 523–524
Aerodynamic noise, 532, 535
AF motors, *see* Axial-flux (AF) motors
Airborne noise, 532
Air cooling
  direct
    end-winding regions, 434–435
    internal cooling channels, 434–438
    jet impingement, 440–441
    motor inner surfaces, 439–440
    motor outer surfaces, 438–440
  indirect
    heat exchangers, 442–443
    indirect evaporative air cooler, 443
  thermophysical properties of air
    air density, 433–434
    specific heat, 432–433
    thermal conductivity, 432–433
Air density, 433–434
Air gap, 51, 102, 108, 253, 591–592, 674
  AF motor, 646–649
  asymmetries
    cylindrical circular rotor whirling, 500–501
    eccentricity, 500
    electromagnetic force, 500–502
    elliptic rotor, 505–508
    elliptic stator, 504–505
    nonconcentric rotor and stator, 502–504
    rotor misalignment, 508
    shaft deflection, 508–509
    UMP, 500
  conical rotor motor, 655–656
  dynamic loss, 386
  end, 641
  flux density, 62, 101, 226, 664–665
  hybrid motor, 651, 654
  inner, 641
  nonuniform, 12–13, 159
    SRM noise, 543
    stator slots, 508–509
  outer, 641
  reluctance, 9
  uniform, 12–13, 115, 117
  velocity components, 386
  windage loss, 402–403
    axial flow, 393
    film divider, 399–400
Alnico magnet motors, 259
Alternating current (AC) motors
  vs. DC motors, 39
  efficiency classes, 30–32
  IM (*see* Induction motor (IM))
  motor damping, 20

PMMs, 42–43
power loss, 371
reactive power, 17
servomotor, 46
single-phase motors, 39–40
synchronous HTS motor, 638
three-phase motors, 39–40, 44, 60–61
torque–speed characteristics, 18–19
Aluminum–nickel–cobalt (Alnico), 62–63, 95–96, 664, 666–667
Ambient temperature, 35, 62–63, 124, 129, 254, 327, 409, 559, 577–578
Ampère–Maxwell's law, 374
Angular acceleration, 2, 4–5, 7
Angular contact ball bearings
back-to-back arrangement, 317
contact angle, 316
cross section, 319
face-to-face arrangement, 317
load analysis, 318
matched bearing, 317–318
performance, 317
reverse loading conditions, 316
Angular misalignment, 211
Angular speed, 6, 14, 16, 18, 45, 591
Anticorrosion
electroless plating technology, 299
electroplating, 299
electropolishing, 300–301
hydrogen embrittlement, 302–305
inorganic and organic materials, 301
inorganic coating, 300
phosphate coating, 300
protective coating, 302
PVD, 299–300
salt-spray test, 302
seals, 302
stainless steel, 302
thermally conductive paints, 301
thermal spraying process, 301
Area–moment method, 161–162
Asynchronous motors, 44–45
A-weighting scale, 530–531
Axial fan, 444
Axial-flux (AF) motors, 55–56
HTS motor, 640
hybrid motor, 652–654
torque density, 639
Axial-flux (AF) multirotor
double-sided, 647–648
magnetic flux path, 648–649
multistage machine, 649–650
rotor–stator–rotor structure, 648–649
single-sided, 646–647
slotless torus topology, 649
YASA, 650
Axial misalignment, 211
Axial rotor/stator alignment motor, 667–669
Axial vibration, 213, 330, 498, 525

B

Back EMF constant (K_e), 58, 60, 62
Background noise level, 531, 539
Backlash, 49–50, 53, 272, 669
Back-to-back testing method, 564–565
Ball bearing
angular contact ball bearings, 316–319
deep-groove ball bearings, 313–314
radial ball bearing, 315–316
Bearing
axial movement prevention, 329–331
ball
angular contact ball bearings, 316–319
deep-groove ball bearings, 313–314
radial ball bearing, 315–316
clearance, 324–327
failure mode, 36
bearing currents, 354–355
excessive load, 350
fishbone diagram, 343–345
grease leakage, 348–349
high temperature impact, 355–356
improper installation and misalignment, 357–358
improper lubrication, 347
internal radial interference condition, 351–354
lubricant contamination, 347–348
lubricant selection, 344, 346–347
motor vibration and overloading, 356–357
premature failure causes, 344, 346
seals and shields, 349–351
statistical data, 343
vertically mounted motor, 358–359
fatigue life
calculation, 335–336
determining factors, 335
failure probability distribution, 336–339
internal radial clearance, 341–343
unbalance influence, 338, 340
wear influence, 341
fitness, 328–329
journal, 309–310
load distribution, 332–334
materials, 323–324

noise, 359–360
noncontact, 320, 322
performance improvement, 364–365
preload arrangement, 331–333
radial and axial bearing load, 332
roller
cylindrical roller, 319–320
tapered roller, 320–321
thrust, 320–321
selection
based on load, 362–363
based on speed, 363
selection factors, 360–362
size, 363–364
sensor, 322–323
speed, 328
Bearing clearance, 324–327
Bearing currents, 354–355
Bearing failure mode, 36
bearing currents, 354–355
excessive load, 350
fishbone diagram, 343–345
grease leakage, 348–349
high temperature impact, 355–356
improper installation and misalignment, 357–358
improper lubrication, 347
internal radial interference condition, 351–354
lubricant contamination, 347–348
lubricant selection, 344, 346–347
motor vibration and overloading, 356–357
premature failure causes, 344, 346
seals and shields, 349–351
statistical data, 343
vertically mounted motor, 358–359
Bearing failure probability, 336–339
Bearing fatigue life
calculation, 335–336
determining factors, 335
failure probability distribution, 336–339
internal radial clearance, 341–343
unbalance influence, 338, 340
wear influence, 341
Bearing fitness, 328–329
Bearing load, 331–334
Bearing losses
ball bearing structure, 381–382
friction torque, 381–382
total frictional moment, 383–384
total power loss, 385
Bearing noise, 359–360
Bearing speed, 328
Bearing stress, 314, 328, 356, 358, 364–365
Bending moment, 165–168
Bending stress
compressive and tensional stresses, 166
single-section shaft, 165–166
stepped shaft, 167–168
Black oxide, 300, 303
Blower, 444, 448, 595, 606, 608
Bolt–nut fasteners, 290–291
Brake
eddy-current, 556–557, 583–584
hydraulic, 559
hysteresis, 555–556
inertia, 557
mechanical friction, 557
powder, 555, 582
power, 555
Prony, 557
torque, 205, 555, 652
water, 558–559
Broadband noise, 527
Broken rotor bar, 499–500
Brushed DC PM field motors, 38
Brushless DC motor, 38–39
Brushless double-rotor machine (BDRM), 643–645
Brushless motors, 53
Brush losses, 385–386
Brush motors, 53
Brush seal
flexible silicone rubber, 190
Kevlar fibers, 189–190
wire bristles, 190–191
Buckling analysis, 71, 630–631
Butterfly-base rotating fastener, 286–287
B-weighting scale, 530–531

C

Carbon equivalent (CE), 208–209
Carbon fiber, 416
Carbon steel
cold-rolled or hot-rolled carbon steel, 156–157
heat treatment process, 156
low-carbon, medium-carbon, and high-carbon steels, 156
mechanical and thermal properties, 155
Casted endbell, 277–278
Casted housing
aluminum, 261–262
casting materials properties, 263–264
die casting, 264–265

EPC, 266–268
graphite, 262–263
graphite iron, 264
gravity fed process, 264
heat treatment, 268–269
iron, 262–263
material melting temperature, 260
molten material, 260
permanent-mold casting, 265–267
pressure casting, 268
pressure fed process, 264
sand casting, 265–266
servomotor, 261–262
steel casting, 264
testing methods, 273–276
Castigliano's method, 162–163
Casting
die, 264–265
copper motors, 89
low-pressure, 88–90
endbell manufacturing, 277–278
full-mold, 266, 268
heat treatment, 114
iron *vs.* aluminum, 278
lost-foam, 266–267
material properties, 263–264
permanent-mold, 265–267
pressure, 268
sand, 265–266
squirrel cage rotor, 88–90, 113–114
steel, 264
Cast iron technique, 260
Centrifugal fan
backward-curved blade fans, 447
forward-curved blade fans, 446–447
helical impeller design, 444–445
straight blade radial fans, 447
Ceramic bearings, 364–365
CFD, *see* Computational fluid dynamics (CFD)
Chassis dynamometer, 559
Chemical vapor deposition (CVD), 299, 416
CMM, *see* Coordinate measuring machine (CMM)
CNC, *see* Computer numerical control (CNC)
Coefficient of thermal expansion (CTE), 123, 327, 416
CarbAl thermal material, 476
copper, 90
gray iron, 263
linear, area, and volumetric thermal expansions, 632–633
stainless steel, 157
Cogging torque, 222, 253
analytical methods, 9
effective driving torque, 8
nocurrent torque, 8
reduction techniques
drive current waveform modulation, 12
flux linkage, 12
magnet pole arc, 12
magnet segmentation, 12
skewed permanent magnets, 11
skewed stator teeth, 9–11
slot number per pole, 11
Soleimani's rotor structure, 12, 14
stator–rotor air gap, 12–13
step-skewed permanent magnets, 9–11
slotless stator core, 226
testing, 580–584
torque ratio, 8
vibration and acoustic noise, 8
Cold forging, 207
endbell, 279
impression-die forging, 281
phosphate coating, 300
serration fit, 131
Cold plates, 458–461
Cold rolled lamination steel, 110
Composite material, 270, 299
Compound motor, 38
Compound-structure permanent magnet synchronous machine (CS-PMSM), 643–644
Compressive strength, 262
Computational fluid dynamics (CFD), 390–391
advantages, 590
modeling and performing strategies, 590
numerical simulation, motor cooling
continuity equation, 597
energy/heat equation, 598
flowrate, 600
fluid meshing, 600
fundamental laws of physics, 596
large-scale elevator motor, 595–596
momentum equations, 597–598
pressure distribution, 601, 604
pressure drop data, 600
pressure *vs.* flowrate, 606, 608
solid meshing, 600
temperature-dependent properties, 597
temperature distribution, 600, 603–607
temperature *vs.* flowrate, 606, 608
3D velocity field, 600–603
turbulence model, 599
winding insulation, 600–601

porous media modeling, 592–595
rotating flow modeling
MPM, 591
MRF method, 591
sliding mesh method, 591
SRF method, 591
Taylor–Couette flow, 591–593
Computer numerical control (CNC), 42, 117, 193, 207, 269, 349
Concentrated winding, 243–244
Conduction, 412–413, 434, 438
direct cooling technique, 450, 465
enclosed motor, 57
FEM analysis, 611
FVM, 609
indirect cooling technique, 458
nanofluid, 475
passive cooling mode, 410
silicon steel lamination, 590
thermal network, 610
Conductive heat transfer
conductive heat flux, 412–413
encapsulation and impregnation, 414–415
energy equations, 413–414
high-thermal-conductivity materials, 415–417
self-adhesive magnet wires, 417
Conductor bar, 632
casted rotor heat treatment, 114
coil formation, 243–245
fatigue stress, 90
skin effect, 91
Conical rotors
nonuniform air gap, 655
rotor–stator structures, 655–656
uniform air gap, 655–656
Containment design
debris accumulation model, 147
debris deflection model, 147
maximum compression and shear strain energy, 148
minimum thickness, containment shell, 149
perforation energy, 148
residual energy, 149
rotor burst tests and FEMs, 147
Continuity equation, 597
Control
active, 515, 524, 539
passive, 515
Control loop
close, 45–46, 322
open, 45–47
Control system, 53–54, 322
dynamometer, 560–561
end play, 330
motion, 45–47, 58, 399, 463, 472
Coolants, 449–450
Cooling
active, 410–411
air (*see* Air cooling)
evaporative, 468–471
fin (*see* Fin cooling)
HTS motor, 638
internal channels, 434–438
liquid (*see* Liquid cooling)
liquid immersion, 457–458
microchannel, 472–473
mist, 471
passive, 410–411
phase-change (*see* Phase-change cooling)
spray (*see* Spray cooling)
Coordinate measuring machine (CMM), 180, 210–211, 322
Copper rotor, 86–87, 89–90
Core losses, *see* Eddy-current losses; Magnetic hysteresis losses
Corrosion resistance
aluminum, 157
coating protection, 108
electroless plating, 299
electroplating, 299
electropolishing, 300–301
ferrite PMs, 96
forged shafts, 207
Inconel™ alloys, 104
inorganic coating, 300
phosphate coating, 300
stainless steel, 157
Coupled rotor unbalance, 118–120
Coupling
flexible, 215–216
rigid, 213–214
Crack/cracking, 122, 156, 255
cast iron, 263
end rings, 499
fatigue, 71, 90, 627
hydrogen-induced, 209
microcracks, 350, 627
microscale, 108, 632
quenching, 360
stress concentration, 193, 265, 364
stress corrosion, 303
welding process, 260
Critical speed
damped, 617, 620–621

mechanical resonance and resonant frequency, 20
and resonance
definitions, 139
fourth-order frequency equation, 142
motion equations, 141–142
natural frequencies, 143
physical and rotordynamic analytical model, 140
Rayleigh–Ritz and Dunkerley methods, 139
two-degree-of-freedom model, 141
shaft design, 178–179
undamped, 617–619
Cross-flow fan, 445–446
CTE, *see* Coefficient of thermal expansion (CTE)
Cumulative distribution function (CDF), 337
CVD, *see* Chemical vapor deposition (CVD)
C-weighting scale, 530–531
Cylinder-base fastener, 287–289
Cylindrical roller bearings, 319–320

D

Damped harmonic oscillating system, 484–487
Damper
mechanical, 540
single-degree-of-freedom system, 488
spring–damper system, 495
TMD (*see* Tuned mass damper (TMD))
Damping
AC motors, 20
active vibration, 524
and bearing support stiffness, 615–617
forced vibration
dynamic equation of motion, 489
nonhomogeneous second-order differential equation, 489–490
phase angle variations, 491–492
single-degree-of-freedom system, 488
steady-state response, 491
transient response, 488
materials, 514–515
viscoelastic material, 516, 518
viscous, 65–66
Damping ratio, 486–488, 491–494, 497, 520, 576, 618
Darcy–Weisbach friction factor, 391–392
Data acquisition systems, 561
DC motors, *see* Direct current (DC) motors
DDR motors, *see* Direct drive rotary (DDR) motors
Deep-groove ball bearings, 313–314
Delta connection, 565
Design constant
back EMF, 58
electrical time, 63–64
mechanical time, 61–63
motor, 60–61
thermal time, 64–65
torque, 59–60
velocity, 60
Design integration, 73–74
Design process
design optimization, 72–73
flowchart, 68–71
mechanical design, 71–72
prototype motor, 73
subsystem/component approach, 68
system approach, 68
Diameter
inner, 22, 138
outer, 21–22, 138
Die casting, 264–265
Die casting copper motors, 89
Digital signal, 582
Digital signal processor (DSP), 567
Direct air cooling
end-winding regions, 434–435
internal cooling channels, 434–438
jet impingement, 440–441
motor outer and inner surfaces, 439–440
motor outer surfaces, 438–439
Direct current (DC) motors, 370
vs. AC motors, 39
brush AF motor, 56
brushless motor, 46, 53–54
brush motor, 270, 385
motor constant, 60
motor torque, 7, 9
servomotor, 46
torque–speed characteristics, 17–18
types of, 38–39
Direct drive rotary (DDR) motors, 23
cartridge DDR motors, 51–52
vs. conventional servo systems, 53
frameless DDR motors, 51–52
hollow shafts, 207
housed/frameless component, 50
Direct drive system
equivalent motor-load model, 23–24
mechanical resonance and resonant frequency, 23–24
TFM, 656
Directional vibration, 497–498
Direction of rotation (DIR), 40, 155, 446, 657

Direct liquid cooling
bundled magnet wires, 451
jet impingement, 456–457
spray cooling, 452–457
Direct loading testing, 564
Distributed winding, 243–244
Double mounting isolation system, 521–522
Doubly salient permanent magnet (DSPM) motor
PM memory motor
air gap flux control, 665
dual magnet, 667–668
good temperature, 667
topology, 666–667
VRM, 663–664
DSPM motor, *see* Doubly salient permanent magnet (DSPM) motor
Ductile iron, 157, 263–264
Duty cycle, 26, 28–29, 396, 499
Dynamic load, 42, 309, 335, 356, 363, 623, 625, 627
Dynamic rotor unbalance, 118–119
Dynamometer
brake power (P_b), 555
chassis, 559
control system, 560–561
eddy-current brake, 556–557
electric motor/generator, 556–558
hydraulic brake, 559
hysteresis brake, 555–556
inertia brake, 557
mechanical friction brake, 557
powder brake, 555
water brake, 558–559

E

Eccentricity, 309, 534, 631
asymmetrical air gap, 500–501, 503–504, 506–508
mass, 119, 493
rotor, 492
shaft, 180, 513
UMP, 500
Eddy-current brake dynamometer, 556–557
Eddy-current losses, 373–374
Ampère–Maxwell's law, 374
divergence theorem, 375
FEA tools, 377
Gauss's law, 374
lumped circuit approach, 376
Maxwell's equations, 375
in permanent magnet motors, 377, 379–381
in stator and rotor cores, 378
Eddy-current probes, 513
EDM, *see* Electrical discharge machining (EDM)
Effective thermal conductivity, 467, 598
Effective viscosity, 599
Efficiency
gearbox, 49
motor (*see* Motor efficiency)
power transmission, 25
Electrical discharge machining (EDM), 238
Electrical system, 607, 609
Electrical time constant (τ_e), 63–64
Electric motor/generator dynamometer, 556–558
Electric motors
AC motors, 39
AF motors, 55–56
brush and brushless motors, 53
characteristics
duty cycle, 26, 28–29
efficiency (*see* Motor efficiency)
insulation (*see* Motor insulation)
load-to-motor inertia ratio, 25–27
mechanical resonance and resonant frequency (*see* Mechanical resonance and resonant frequency)
operation reliability, 36
power and power factor, 16–17
speed (*see* Motor speed)
torque (*see* Motor torque)
closed loop and open loop control systems, 45–46
components, 2
DC motors, 38–39
DDR motors
cartridge DDR motors, 51–52
vs. conventional servo systems, 53
frameless DDR motors, 51–52
housed/frameless component, 50
design and operation parameters
back EMF constant (K_e), 58
electrical time constant (τ_e), 63–64
mechanical time constant (τ_m), 61–63
motor constant (K_m), 60–61
thermal time constant (τ_{th}), 64–65
torque constant (K_t), 59–60
velocity constant (K_v), 60
viscous damping (K_{vd}), 65–66
design integration, 73–74
design process
design optimization, 72–73
flowchart, 68–71
mechanical design, 71–72
prototype motor, 73

subsystem/component approach, 68
system approach, 68
enclosed motor, 57
failure modes, 74–75
gear drive motors, 49–51
history, 1–2
induction motors, 40–41
IP code, 76–78
linear motor, 56–57
mechatronics, 74
open motor, 57
PMMs, 42–43
power rating classification, 57–58
reluctance motors, 54–55
RF motors, 55
rotary motors, 36–37, 56
servomotors, 46
single-phase motors, 39–40
sizing equations, 66–67
stepper motors, 47–49
synchronous and asynchronous motors, 44–45
three-phase motors, 40
Electroless plating technology, 299
Electromagnetic force (EMF), 140, 243, 373
air gap, 500–502
axial vibration, 498
back EMF, 11, 664
constant, 58, 60, 62
sinusoidal, 39, 42, 67
trapezoidal, 13, 39
electromagnetic noise, 535
electromagnetic vibration, 498
two-pole motors, 504
unbalanced, 492, 500
vibration and acoustic noise, 509
Electromagnetic noise, 482, 533–535
Electromagnetic vibrations, 482
air gap asymmetries
cylindrical circular rotor whirling, 500–501
eccentricity, 500
electromagnetic force, 500–502
elliptic rotor, 505–508
elliptic stator, 504–505
nonconcentric rotor and stator, 502–504
rotor misalignment, 508
shaft deflection, 508–509
UMP, 500
broken rotor bars, 499–500
cracked end rings, 499
mutual action forces, 509
nonuniform air gap, 508–509
unbalanced forces/torques, 498
unbalanced voltage operation, 510
Electroplating, 299
Electropolishing, 300–301
Elliptic rotor, 505–508
Elliptic stator, 504–505
EMF, *see* Electromagnetic force (EMF)
Encapsulation, 414–415
materials, 245–247
partial and total encapsulation, 245
process, 248–249
thermoplastics, 248
thermoset plastics, 245, 248
trickle impregnation, 250
varnish dipping, 249–250
VPI
primary process, 250–252
vs. solvent varnishes, 252–253
tank, large electric motors, 250–251
Enclosed motor, 57
Encoder, 15, 45, 581
Endbell, 422, 424
casted endbell, 277–278
forged endbell, 279
iron casting *vs.* aluminum casting, 278
machined endbell, 279
stamped endbell, 277
Epoxy resins, 248–249
Evaporative air cooler, 443
Evaporative cooling, 468–471
Evaporative pattern casting (EPC), 266–268
Excitation frequency, 488–489, 491, 494
Exciting force, 141, 493, 532
attenuation, 521
harmonic, 487–488, 520
self-excited vibration system, 511
vibration isolation, 515
Exponentiated Weibull distribution, 337–338
Extra-large motors, 58
Extruded aluminum motor housing, 269–271

F

Factor of safety
bearing size, 363
crushing failure, 198
shaft design, 177
shear failure, 197
Failure
mechanism
crushing, 198
shear, 197

mode, 194
bearing (*see* Bearing failure mode)
motor, 74–75
winding failures, 36
Fan
axial fan, 444
centrifugal fan
backward-curved blade fans, 447
forward-curved blade fans, 446–447
helical impeller design, 444–445
straight blade radial fans, 447
cross-flow fan, 445–446
heat sink-impeller, 446
mixed-flow fan, 444–445
performance curve and operation point, 447–448
selection, 448
Fanning friction factor, 391–392
Fan performance curve, 443, 445, 447–448
Faraday's law of induction, 374
Fasteners
cylinder-base fastener, 287–289
forged Z-shaped fastener, 280–282
loading distribution, 298
preload, 290–291
rectangular base fastener, 289
rotary fasteners
butterfly-base rotating fastener, 286–287
square-base rotating fastener, 285–286
triangle-base rotating fastener, 283–285
thread, 290–292, 297–298
tightening process, 291–294
tightening torque, 294–297
Fast Fourier transform (FFT), 513
Fatigue analysis, 627
Fatigue failure, 205–206
FEA, *see* Finite element analysis (FEA)
FEM, *see* Finite element method (FEM)
Ferrite permanent magnets, 96
Fin cooling, 418
fin optimization
design parameters, 418
fin height *vs.* overall thermal resistance, 421–422
fin ratio *vs.* overall thermal resistance, 421–422
plate-fin efficiency, 420
thermal model, 418, 420
on motor endbell, 422, 424
motor frame with external and internal fins, 422–423
oblique plate fins, 421, 423
pin-fin heat sink (*see* Pin-fin heat sink)
plate fins, 418–419
stator lamination fins, 423–425
Finite element analysis (FEA), 22, 95, 381, 610
HLM, 654
hysteresis and eddy-current losses, 377
results, 87
rotordynamic software, 617
time stepping, 501
transient 2D, 86
Finite element method (FEM)
advantages, 610
applications, 610
frameless motor, 610–611
heat transfer coefficient, 611–612
meshes, 611–613
structural analysis, 625–626
temperature distribution, 612–614
thermal conductivity, 611–612
Fluctuating torque, 13
Fluidized-bed coating, *see* Powder coating technology
Flux concentrated transverse-flux motor (FC-TFM), 657–658
Flux-controllable permanent magnet (FCPM), 654
Forced air cooling, *see* Air cooling
Forced convection, 452
coolant heat, 450
dynamometer, 555
heat transfer coefficients, 411
hydrogen, 404
motor housing, 351, 438
resistance, 472
Forced vibration
damping
dynamic equation of motion, 489
nonhomogeneous second-order differential equation, 489–490
phase angle variations, 491–492
single-degree-of-freedom system, 488
steady-state response, 491
transient response, 488
mass unbalance, 492–495
Forged endbell, 279
Forged shaft, 207–208
Forged Z-shaped fastener, 280–282
Forward short-circuit testing method, 567–569
Fracture
mechanics, 627
toughness, 268, 627

Frame
anticorrosion (*see* Anticorrosion)
endbell manufacturing
casting process, 277–278
forging, 279
iron casting *vs.* aluminum casting, 278
machining, 279
stamping process, 277
motor assembly
fasteners (*see* Fasteners)
tapping, end surface, 279–280
tie bar, 279–280
motor housing (*see* Motor housing)
Frameless motors, 271–273
Frequency
AC supply, 44
resonance
critical speed, 20
direct drive system, 23–24
equivalent motor-load model, 20–21
load inertia, 21
three-mass system, 24–25
torsional stiffness, 22–24
total motor inertia, 21
Frequency ratio, 489, 491–492, 494, 497
Frequency spectrum, 527
Friction
bearing
ball bearing structure, 381–382
friction torque, 381–382
total frictional moment, 383–384
total power loss, 385
brush, 385–386
Friction coefficient
dynamic, 320
static, 134, 320
Friction factor, 311, 459, 462
Darcy–Weisbach, 391–392
definition, 394
Fanning, 391–392
journal bearing, 312
ratio, 394
smooth rotor *vs.* stator surfaces, 395
Full-mold casting, 266, 268
Fundamental line frequency, 499

G

Gauss's law, 374
Gearboxes, 49–51
Gear drive motors, 49–51
Gearmotor, 51
Gear ratio, 4, 6, 22, 49, 582
Geometric dimension and tolerance (GD&T), 72, 210
Glass fiber–reinforced mica tape, 234
Graphical method, 163
Gray iron, 262–264
Grease, 344, 356, 361, 547
ball bearing, 309, 313
characteristic feature, 346
improper lubrication, 347
journal bearing, 309
leakage, 348–349
thermal, 430–431
Grip length, 290

H

Hardness, 180–182
Harmonic motion, 483–484, 495
Heat conduction, 410, 412, 429–430, 590, 609, 611
Heat dissipation, 465, 468, 473, 543, 611
conductor, 649
end rings, 86
pin fin, 427–428
Heat exchangers, 442–443
Heat flux
conductive, 412–413
critical, 475
heat sources, 410
high, 440, 452–453, 465, 467, 472, 476
injection technique, 347
passive cooling techniques, 418
Heat pipes, 465–467
Heat sink, 254, 446
heat transfer, 420
microchannel, 473
pin-fin (*see* Pin-fin heat sink)
plate-fin, 418
Heatsink-impeller, 446
Heat transfer coefficient, 64, 410–412, 418, 420, 425, 427, 441, 448, 450, 466–467, 609–611
correlation, 466–467
jet impingement cooling, 441
liquid cooling, 448, 450
natural air convection, 418
passive and active cooling techniques, 410–411
Heat transfer enhancement, 411–412, 427–428, 468, 473
air jet impingement cooling, 440
cooling fin, 418
enclosed motors, 439
with nanotechnology, 474–477
Pyriod® HT pyrolytic graphite, 417

Heat treatment
carbon steel, 156
casted housing, 268–269
rotor casting, 114
and shaft hardness, 180–182
spline shaft, 201
High nitrogen steel (HNS), 324
High-potential testing, 572
High-temperature superconducting (HTS) motor
AF motor, 640
cooling system, 638
discovery, 637
potential economic benefits, 637
rotor winding, 638–639
schematic diagram, 638–639
ship propulsion motor, 638
stator winding, 638
three types, 638
torque density, 639
Hot forging, 207, 279, 281
HTS motor, *see* High-temperature superconducting (HTS) motor
Hybrid excitation synchronous machines (HESMs), 651
Hybrid-field flux-controllable PM motor, 654
Hybrid linear motor (HLM), 654
Hybrid motor
HESMs, 651
HLM, 654
HSM, 651–652
hybrid-field flux-controllable PM, 654
RF and AF motor integration, 652–654
Hybrid stepper motors, 47–49
Hydraulic brake dynamometer, 559
Hydrodynamic lubrication bearings, 310
Hydrogen embrittlement, 302–305
Hydrogen removal, 304
Hysteresis brake dynamometer, 555–556
Hysteresis synchronous motor (HSM), 651–652

I

IM, *see* Induction motor (IM)
Impregnation, 414–415
Impulse testing, 580
Indirect forced air cooling, 442–443
Indirect load testing method
inverter-driven, 567, 569
phantom, 565–567
two-frequency, 566–568
Induction motor (IM)
design types, 91–92
squirrel cage rotor
casting process, 88–90
closed slots, 85–86
conducting bars, 86–87
double-cage rotor, 87–88
open slots, 85
skin effect, 91
torque–speed characteristics, 91–92
wound rotor
advantages, 83
motor performance characteristics, 84–85
rheostats, 83
slip rings and brushes, 83–84
torque–speed characteristics, 84
Induction motors, 40–41
Inertia
coupling, 4–5, 23
gearbox, 5
load, 4–5, 18, 20–21, 47, 71
motor, 4, 18, 20–21, 23, 61, 71
Inertia brake dynamometer, 557
Inertia disk, 26–27
Inertia torque, 14
Injection molded plastic insulation, 233–235
Inorganic coating, 300
Insulation, *see* Motor insulation
Insulation resistance testing, 570–571
Interference fits
CTE, 123
definition, 122
press fit, 115
contact pressure, 125, 127
hollow shaft and rotor core dimensions, 124–125
maximum torque, 127–128
radial stress, 124
tangential strain, 126
Ringfeder® locking devices, 132–133
rotor assembly process, 116
serration fit, 131–133
shrink fit, 115–116
advantages, 128
area and volume thermal expansion coefficients, 129
elastoplastic solution, 131
heating techniques, 129–131
Lame elastic solution, 131
linear thermal expansion coefficients, 128–129
mixing technique, 129
von Mises yield criterion, 131
tolerance rings
advantages, 135
friction force, 134

pressing forces, 134–135
spring force, 132, 134
wave pitches, 132
Interior permanent magnet (IPM), 12, 14, 43, 95, 98, 378
Internal cooling channels, 434–438
Inverter, 38–39, 498, 645
intermediate, 660
inverter-driven method, 567, 569
PMW, 567
supply, 85
Involute spline, 202–203
In-wheel
drive, 661–662
motor, 663, 666
Ionic wind generator, 477
IP code, 76–78
IPM, *see* Interior permanent magnet (IPM)
Iron losses, *see* Eddy-current losses; Magnetic hysteresis losses

J

Jet impingement
air, 440–441
liquid, 456–457
Journal bearing
advantages, 310–311
convergent clearance, 309
friction factors, 312
friction regions, 311–312
hydrodynamic lubrication bearings, 310
hydrodynamic pressure, 309
lubricant film, 309–310
regular lubrication bearings, 310
self-lubricating bearings, 310
Sommerfeld number, 312
static performance characteristics, 312

K

Keyed shafts
bearing stress, 198
fitting, 198–199
material selection, 194
profile and sled runner keyseats, 195–196
shear and crushing failure, 196–197
shear stress, 197
stress concentration factors, 199–200
variables, 196
Key fitting, 198–199
Keyseat, 180, 195–196, 198–200, 202
Kinetic energy, 145–147
Kirchhoff's law, 609

L

Laminar flow, 390, 410
Lamination, *see* Rotor lamination; Stator lamination
Large motors, 58
Laser alignment, 213
Laser Doppler vibrometer (LDV), 513
Lateral deflection
bending moment, 173–174
shear force, 176–177
transverse force, 174–176
Lateral rigidity, 178
Linear induction motor (LIM), 654
Linear motor, 56–57
Linear synchronous motor (LSM), 654
Liquid cooling
direct
bundled magnet wires, 451
jet impingement, 456–457
spray cooling, 452–457
indirect
cold plates, 458–461
cooling channels, 462, 464
copper pipe in spacer, 462–464
helical copper pipes, 458–459, 462–463
microscale channels, 463, 465
stator winding slots, 463, 465
liquid immersion cooling, 457–458
thermophysical properties of coolants, 449–450
Liquid immersion cooling, 457–458
Litz wire, 231–232, 373
Load distribution, 315, 329, 332–334, 341–342
Load point test, 563
Load power loss
stray, 404–405
winding losses (*see* Winding losses)
Load-to-motor inertia ratio, 25–27
Locked rotor current (LRC), 16
Locked rotor testing, 576–577
Locked rotor torque (LRT), 7, 16
Lost-foam-casting process, 266–267
Low-pressure die casting, 88–90
Lubricant contamination, 347–348
Lubrication
hydrodynamic bearing, 310
improper bearing, 347

regular bearing, 310
tribology, 311
Lumped-circuit modeling, 607, 609–610

M

Macaulay's method, 160–161
Machinability, 89, 155–158, 263–264
Machined endbell, 279
Machined housing, 269
Machined shaft, 206–207
Magnetic flux, 8–9, 36, 40, 43, 55, 63, 102, 109, 219, 222, 253, 354–355, 369, 373–374, 498, 500–502, 509, 525, 534, 555, 639–640, 648–649, 658–659, 664, 667
Magnetic flux density, 9, 62, 95, 96, 100–101, 109, 375, 378, 500–502
Magnetic flux path, 501, 648
Magnetic hysteresis losses, 374
Ampère–Maxwell's law, 374
divergence theorem, 375
empirical formula, 376
FEA tools, 377
Gauss's law, 374
material electromagnetic properties, 376
Maxwell's equations, 375
metallic materials, 376–377
in permanent magnet motors, 377, 379–381
in stator and rotor cores, 378
Magnetic pole, 12, 43–44, 658–659
Magneto-motive force (MMF), 102, 243, 253, 380, 501, 654
Magnet wires, 451
Magnification factor (MF), 491
Mass unbalance, 139, 340, 492, 495
Materials testing, 273, 559, 563, 577
Maxwell's equations, 375
Maxwell's stress, 9, 502
Mechanical differential testing method, 564
Mechanical energy, 1, 29, 369, 399, 485, 579, 672
Mechanical friction brake dynamometer, 557
Mechanical friction losses
bearings
ball bearing structure, 381–382
friction torque, 381–382
total frictional moment, 383–384
total power loss, 385
brush, 385–386
sealing, 385
Mechanical noise, 533–534, 539, 629
Mechanical resonance and resonant frequency
critical speed, 20
direct drive system, 23–24
equivalent motor-load model, 20–21
load inertia, 21
three-mass system, 24–25
torsional stiffness, 22–24
total motor inertia, 21
Mechanical system torque, 14
Mechanical time constant (τ_m), 61–63
Mechanical vibrations, 482
defective bearing, 510–511
distorted coupling, 510
rotor shaft misalignment, 510
self-excited vibration, 511
torsional vibration, 511–512
Mechanic differential testing, 564
Mechatronics, 74, 271
Medium motors, 58
Megohm testing, 570–571
Memory permanent magnet brushless motor, *see* Permanent magnet (PM) memory motor
Metal foams, 473–474
Mica tape, 234, 243
Microchannel cooling systems, 472–473
Micromotors, 57
structure and operating principle, 672–674
tangential and normal forces, 674–675
3D schematic, 673–674
torque, 674
Watt-level electrical–mechanical power conversion, 673
Microscale channels, 463, 465
Mist cooling, 471
Mixed-flow fan, 444–445
Mixed-frequency testing, 564
Mixing plane model (MPM), 591
MMF, *see* Magneto-motive force (MMF)
Moment of inertia, 4, 61, 145–146, 163, 178, 573, 575–576, 616, 631
Momentum equation, 597
Motor assembly
fasteners (*see* Fasteners)
tapping, end surface, 279–280
tie bar, 279–280
Motor constant (K_m), 60–61
Motor efficiency
definition, 29–30
IEC standards, AC electric motors
class, testing standard, and regulation over time, 31
4 pole electric motors, 31, 33
with 50 Hz, 31–32
with 60 Hz, 31–32

IE1, IE2, and IE3, 30
IE4 standardization, 31
testing, 578–580
Motor heat run testing, 577–579
Motor housing
casted housing (*see* Casted housing)
composite materials, 270
extruded aluminum motor housing, 269–271
frameless motors, 271–273
machined housing, 269
manufacturing processes, 259
stamped housing, 269–270
3D printing technique, 270–271
wrapped housing, 259–261
Motor insulation
dielectric strength, 33–35
elements, 33
hop spot allowance, 35
material lifetime, 31, 33
standard classes, 33, 35
temperature rise, 35
thermal aging, 33, 35–36
thermal and electrical stresses, 31
Motor speed
angular and rotational speed, 14
continuous speed, 15
peak speed, 15
ripple, 15
torque–speed characteristics (*see* Torque–speed characteristics)
Motor testing
back-to-back, 564–565
data acquisition systems, 561
dynamometer
brake power (P_b), 555
chassis, 559
control system, 560–561
eddy-current brake, 556–557
electric motor/generator, 556–558
hydraulic brake, 559
hysteresis brake, 555–556
inertia brake, 557
mechanical friction brake, 557
powder brake, 555
water brake, 558–559
forward short circuit, 567–569
indirect loading (*see* Indirect load testing method)
load point test, 563
mechanical differential, 564
no-load test, 563
off-line/static testing
high-potential, 572
megohm, 570–571
polarization index, 571
rotor moment of inertia, 573–576
step-voltage, 573–574
surge, 572–573
winding electrical resistance, 570
online/dynamic testing
cogging torque, 580–584
efficiency, 578–580
impulse, 580
locked rotor, 576–577
motor heat run, 577–579
torque ripple measurement, 583–585
power supply, 562
RTDs, 560
standards, 553–554
testbed, 562–563
thermistor, 560
thermocouples, 559–560
torque transducer, 561–562
variable inertia, 568
Motor torque
cogging torque (*see* Cogging torque)
continuous torque, 6
density, 15–16
motor-load system
angular acceleration, 5
gear ratio, 4, 6
reflected load inertia, 4–5
shaft torque, 6
two-shaft gearbox, 4–5
Newton meter (N-m), 2
peak torque, 6–7
ripple, 13–14
stall torque, 7
static and dynamic
definition, 2
inertia, 4
magnitude, 3
torque vector, 3
torque–speed characteristics (*see* Torque–speed characteristics)
Multilevel magnetic system, 515, 517
Multiple reference frame (MRF) method, 591
Multi stage, 49, 646, 649–650, 653

N

Nanoelectromechanical system (NEMS), 676
Nanofluid, 475
Nanomotor, 675–676
Nanotechnology
CarbAl thermal material, 476

carbon nanotubes, 475
ionic wind generator, 477
nanofluid, 475
NanoSpreader vapor coolers, 475–476
Nanotubes, 475
National Electrical Manufacturers Association (NEMA) standard, 91–92
Natural convection, 417–418; *see also* Fin cooling
Natural frequency, 20, 139–140, 159, 207, 481, 486, 489, 491, 494, 520, 616–617, 620
Negative stiffness mechanism (NSM), 523
Noise abatement, 513, 533, 537–548
Noise attenuating structure, 543, 545
Noise prediction, 629–630
No-load power loss
eddy-current losses, 373–374
Ampère–Maxwell's law, 374
divergence theorem, 375
FEA tools, 377
Gauss's law, 374
lumped circuit approach, 376
Maxwell's equations, 375
in permanent magnet motors, 377, 379–381
in stator and rotor cores, 378
magnetic hysteresis losses, 374
Ampère–Maxwell's law, 374
divergence theorem, 375
empirical formula, 376
FEA tools, 377
Gauss's law, 374
material electromagnetic properties, 376
Maxwell's equations, 375
metallic materials, 376–377
in permanent magnet motors, 377, 379–381
in stator and rotor cores, 378
mechanical friction losses (*see* Mechanical friction losses)
windage losses (*see* Windage losses)
No-load test, 563
Nominal torque, 6
Noncontact bearing, 320, 322
Noncontact seal, 191–193
Nonferromagnetic material, 648
Nonlinear effect, 94, 275, 432, 573, 575
N-pole, 645–646, 648, 664, 671
Number of magnetic poles per phase, 44

O

Octave frequency band, 528–530
Off-line testing, 569–576
Ohm's law, 33, 609
Online testing, 576–585
Open motor, 57
Operation reliability, 36, 39, 53, 68–69, 73, 124, 341, 409–411, 481, 553, 589, 596
O-ring seal
advantages, 186
disadvantages, 188
squeezing degree, 187

P

Parallel misalignment, 212
Passive cooling, 410–411
Passive noise reduction techniques
low noise bearing selection, 547–548
motor suspension mounting, 543
noise propagation path blocking, 539
noise source isolation, 539
sound-absorbing materials, 540–544
SRM, 543, 545–547
ventilation path smoothing, 546
Passive vibration isolation system, 523
Permanent magnet (PM), 7, 10, 42, 96–98, 102–109
Permanent magnet hysteresis synchronous (PMHS), 652
Permanent magnet (PM) memory motor
DSPM
air gap flux control, 665
dual magnet, 667–668
good temperature, 667
topology, 666–667
pole-changing, 664–666
VFMM, 664–665
Permanent magnet motors (PMMs), 7–9, 42–43, 47, 62, 74, 632, 634
eddy-current losses, 377, 379–381
magnetic hysteresis losses, 377, 379–381
memory motors (*see* Permanent magnet (PM) memory motor)
rare earth (*see* Rare earth permanent magnets)
reconfigurable, 660–662
rotor (*see* Permanent magnet rotor)
stepper motor, 47–48
Permanent magnet rotor
characteristics
advantages, 94
electromagnetic properties and temperature, 95
vs. IM, 94
magnetization hysteresis loop, 94–95
corrosion protection, 107–109

demagnetization causes
external magnetic field, 101
ferrite magnet, 100
irreversible and unrecoverable losses, 100
irreversible but recoverable losses, 100
magnetic creep, 102
mechanical disturbances, 102
Nd–Fe–B magnet, 101
radiation, 102
reversible losses, 100
magnetization, 98–99
materials
alnico alloys, 95
$Fe_{16}N_2$ powder, 97
ferrite, 96
magnetic characteristics, 96
nanoalloy magnets, 97
non-rare-earth magnet, 97
rare-earth, 97
samarium–cobalt (Sm–Co) magnet, 97
maximum operation temperature, 102
mounting and retention methods
chemical retaining method, 103
glue arc magnets, 103, 104
innovative retention method, 103, 106
mechanical retaining method, 103
metallic sleeve, 104, 106–107
molded plastic cylindrical sleeve, 104, 107
permanent retaining method, 103
reinforcing fine fiber wounding, 103, 105
rotor core interior, 104–105, 108
surface-mounted PM motors, 102–103
phenomenon of magnetism, 92–93
Permanent magnet stepper motor, 47–48
Permanent-mold casting, 265–267
Permeability of air, 502
Phantom loading method, 565–567
Phantom loading testing, 565–566
Phase angle, 16, 142, 484, 488, 491–492, 494, 496
Phase-change cooling
evaporative cooling, 468–471
heat pipes, 465–467
mist cooling, 471
vapor chambers, 467–468
Phase voltage, 565
Phosphate coating, 300
Physical vapor deposition (PVD), 299–300
Piezoelectric motors
advantages, 669
driving principle, 670–671
mother structure, 670
Pin-fin heat sink
CFD model, 428
crescent-shaped pin fins, 428–429
fin distance, 427
limitations, 429
pin fin configuration, 428–429
pin-fin shapes and arrangements, 425–426
plate-pin fin heat sink, 425–426
pressure drop, 425
raindrop-shaped pin fins, 425–427
Pitch diameter, 295–296, 314, 511
Pitched noise, 527
Planetary gearbox, 49–50
Plate fins, 418
PMMs, *see* Permanent magnet motors (PMMs)
Poisson's ratio, 89, 126, 263, 326
Polarization index testing, 571
Pole-changing memory motor (PCMM), 664–666
Pole number, 44, 380, 663, 665
Powder brake dynamometer, 555
Powder coating technology, 235–236
Power
electric, 36, 39–40
mechanical, 46, 61, 453, 564, 579, 653
rated, 6, 386, 404
Power factor, 16–17, 42–43, 561, 671
Power input, 7, 17, 29–30, 369, 563, 579–580
Power loss
disadvantages, 369
eddy-current losses (*see* Eddy-current losses)
loss distributions comparison, 369–370
magnetic hysteresis losses (*see* Magnetic hysteresis losses)
mechanical friction losses (*see* Mechanical friction losses)
stray, 404–405
windage losses (*see* Windage losses)
winding losses
electrical resistance ratio, 372–373
Litz wire, 373
material resistivity, 370
resistive winding loss, 370–371
skin depth of conducting wires, 371–372
skin effect, 371, 373
Power output, 2, 16, 18, 29–30, 42, 67, 85, 89, 369, 399, 409, 440, 470, 554, 562, 579, 638, 653, 665
Power supply, 16, 38, 40, 45, 130, 505, 562, 564–565, 567, 577, 579
Prandtl number, 441, 454, 599
Preload
bearing, 331–333
bolt, 290
fastener, 290–291

Press fit, 115, 131, 135, 179–180, 462, 616, 632
  contact pressure, 125, 127
  hollow shaft and rotor core dimensions, 124–125
  maximum torque, 127–128
  radial stress, 124
  tangential strain, 126
Pressure angle, 202, 358
Pressure casting, 268
Probability density function (PDF), 337
Product design process, 589
Prony brake dynamometers, 557
PTFE seal, 191–195
Pulsating torque, 13
Pyriod® HT pyrolytic graphite, 417

R

Radial ball bearing, 315–316
Radial-flux (RF) motors, 55
  double-stator PM machine, 645–646
  multirotor
    BDRM, 643–645
    cutaway perspective view, 641, 643
    nonslotted structure, 641
    toroidally wound PM motor, 640–641
    toroidally wound SPM motors, 641–642
    unique features, 640
  multistator, 642–644
Radial vibration, 497–498
Radiation
  demagnetization of PM, 101–102
  electric motor cooling, 472
  γ-ray irradiation, 102
  heat transfer, 590, 609
  noise radiation, 527, 536
  thermal radiation, 301, 471
Radiative heat transfer, 471–472
Random winding, 243
Rare earth permanent magnets
  Nd–Fe–B, 62–63, 97, 101, 409, 604, 667
  Sm–Co, 62–63, 92, 96–97, 102
Reaction torque transducers, 562
Reconfigurable permanent magnet motor, 660–662
Rectangular base fastener, 289
Regular lubrication bearings, 310
Reliability
  bearing, 336–337, 341–342, 360
  brushed DC motors, 39, 53
  cooling fin, 418
  DDR motors, 53
  life adjust factor, 336
  motor design process, 73
  motor operation, 36
  PMM, 42
  press fit, 124
  reaction torque transducers, 562
  shrink fit, 128
  stepper motors, 47
  two-phase evaporative approach, 470
Reluctance cogging torque, 14
Reluctance motors, 54–55
Renewable energy machines, 671–673
Resistance–temperature detectors (RTDs), 560
Retaining ring, 180, 287–288, 329–330, 332, 402
Reynolds number, 389, 392, 441
RF motors, *see* Radial-flux (RF) motors
Rigid coupling, 213–214
Rim-driven thruster (RDT), 658–659
Ringfeder® locking device, 132–133
RNG k-ε turbulence model, 599
Robust design techniques, 254
Rolling bearings
  ball
    angular contact ball bearings, 316–319
    deep-groove ball bearings, 313–314
    radial ball bearing, 315–316
  roller
    cylindrical roller, 319–320
    tapered roller, 320–321
    thrust, 320–321
Root mean square (RMS), 59, 183, 371, 512–514, 527, 566
Root mean square roughness, 183
Rotary fasteners
  butterfly-base rotating fastener, 286–287
  square-base rotating fastener, 285–286
  triangle-base rotating fastener, 283–285
Rotary motor, 56
Rotary torque transducers, 562
Rotating electric machines
  aerodynamic noise, 535
  electromagnetic noise, 534–535
  mechanical noise, 533–534
Rotating speed
  accurate control, 47
  angular rotating speed, 16, 18
  bearing, 335
  dynamometers, 554–555
  measurement, 580
  retention mechanism, 90
  of rotor, asynchronous motor, 45
  stall torque, 7
  torque rotating speed, 18
  of two-shaft gearbox, 4

Rotor balancing, 109, 117, 120–121, 124
Rotor burst, 143–147
Rotor design
  assembly (*see* Interference fits)
  balancing
    ISO Standard 1940/1, 117
    machine, 120–121
    operation, 121–124
    types of unbalance, 118–120
  burst containment analysis
    burst speed, 143–145
    debris accumulation model, 147
    debris deflection model, 147
    elastic potential energy, 147
    kinetic energy, 145–147
    maximum compression and shear strain energy, 148
    minimum thickness, containment shell, 149
    perforation energy, 148
    residual energy, 149
    rotor burst tests and FEMs, 147
  casting
    heat treatment, 114
    squirrel cage rotor, 113–114
  induction motor (*see* Induction motor)
  lamination (*see* Rotor lamination)
  machining and runout measurement, 116–118
  permanent magnet rotor (*see* Permanent magnet rotor)
  rotordynamics (*see* Rotordynamics)
  stress analysis, 135–137
Rotordynamic analysis
  bearing support stiffness and damping, 615–617
  damped critical speeds, 617, 620–621
  fan loss, 614
  full-scale fan test data, 614
  motor fan system, 614
  shaft–rotor assembly, 615
  software, 617
  undamped critical speeds, 617–619
Rotordynamic instability, 501
Rotordynamics
  critical speed and resonance
    definitions, 139
    fourth-order frequency equation, 142
    motion equations, 141–142
    natural frequencies, 143
    physical and rotordynamic analytical model, 140
    Rayleigh–Ritz and Dunkerley methods, 139
    two-degree-of-freedom model, 141
  drive-side endbell mounting, 137
  rotor inertia, 137–139
  software packages, 137
Rotor lamination
  annealing, 113
  cutting, 111–112
  materials
    cobalt alloy, 110
    cold rolled lamination steel, 110
    electrical steels, 110
    manganese and aluminum, 110
    nickel alloy, 110
    selection criteria, 109
    silicon steel, 109–110
  stacking, 113–114
  surface insulation, 112
Runout, 115, 117, 118, 180

S

Safety factor, 66
Salt-spray test, 302
Sand casting, 265–266
Screw-threaded member fasteners, 290, 292
Sealing losses, 385
Seebeck coefficient, 559–560
Seismic wave, 495
Self-adhesive magnet wires, 417
  adhesive activation, 230–231
  dimensions, 231–232
  resistance heating, 231
Self-excited vibration, 511
Self-locking, 287–289, 296
Self-lubricating bearings, 310
Semiactive vibration isolation system, 523–524
Semirigid coupling, 213–214, 216
Sensor bearing, 322–323
Separately excited motor, 38
Series motor, 38
Serration fit, 131–132
Servomotors, 4, 46
Shaft design
  aluminum material, 157
  area–moment method, 161–162
  bending stress, bending moment
    compressive and tensional stresses, 166
    single-section shaft, 165–166
    stepped shaft, 167–168
  carbon steel materials
    cold-rolled or hot-rolled carbon steel, 156–157

heat treatment process, 156
low-carbon, medium-carbon, and high-carbon steels, 156
mechanical and thermal properties, 155
Castigliano's method, 162–163
cast iron material, 157
critical speed, 178–179
diametrical fit types, 193
dimensional tolerance, 179–180
dynamic shaft runout, 180
eccentricity, 180
fatigue failure, 205–206
flexible coupling, 215–216
forged shaft, 207–208
graphical method, 163
hardness, 114, 156, 158, 180–182, 186, 194, 210
heat treatment and hardness, 180–182
keyed, 22, 155, 194–200, 202
lateral deflection
bending moment, 173–174
shear force, 176–177
transverse force, 174–176
lateral rigidity, 178
loads, 159–160
Macaulay's method, 160–161
machined shaft, 206–207
material properties, 157–158
measurement, 210–211
mechanical design aspects, 177–178
misalignment
angular, 211
axial, 211
causes, 210–211
correction, 212–213
laser alignment, 213
parallel, 212
normal stress, axial force
single-section shaft, 164
stepped shaft, 165–166
tapered shaft, 164–165
rigid coupling, 213–214
rigidity, 169, 178
runout, 115, 117, 180, 189, 206
seals (*see* Shaft seals)
semirigid coupling, 213–214, 216
shaft lead, 184–185
shear strain, 168, 170
splined, 155
stainless steel materials, 157
stepped, 146, 165–167, 170–174, 179, 196, 207–208
stress concentration, 193–194
structure, 155–156
surface finishing
average peak to mean, 184
average peak-to-valley height, 184
shaft lead, 182
stainless steel and resultant surface topography, 183
surface contact area ratio, 184
surface texture, 182
tapped, 146
texture, 182
torque transmission (*see* Torque transmission)
torsional rigidity, 178
torsional shear stress and torsional deflection
single-section shaft, 168
stepped shaft, 170–172
torsional rigidity, 169
torsional stiffness, 169, 172
welded hollow shaft
direct drive and vehicle motors, 207
fabrication, 208
friction welding technology, 210
rotor lamination core, 209
weightless motor, 207
weldability, 208–209
Shaft seals
applications, 186
brush
flexible silicone rubber, 190
Kevlar fibers, 189–190
wire bristles, 190–191
noncontact seal, 191–193
O-ring
advantages, 186
disadvantages, 188
squeezing degree, 187
performance and lifetime parameters, 186
PTFE, 191–195
universal lip, 188
V-shaped spring, 189
Shear force, 176–177
Shear modulus of elasticity, 22, 163, 168, 178, 622
Shear strength, 148, 157–158, 263, 280
Shrink fit, 115–116
advantages, 128
area and volume thermal expansion coefficients, 129
elastoplastic solution, 131
heating techniques, 129–131
Lame elastic solution, 131

linear thermal expansion coefficients, 128–129
mixing technique, 129
von Mises yield criterion, 131
Shunt wound motor, 38
Simple harmonic oscillating system, 483–485
Single-phase motors, 39–40
Single reference frame (SRF) method, 591
Sizing equation, 66–67, 69
Skin depth, 371–372
Skin effect, 371, 373
Sliding bearing, *see* Journal bearing
Sliding mesh method, 591
Slinky method
advantages, 227, 229
helical stator core fabrication, 227, 229
inorganic nonconductive material insulation, 230
slotless stator design, 229
Slip, 19, 42, 45, 47, 83–85, 87, 91, 94, 129, 495, 499–500, 579
Slot liner, 232–233, 235, 241
Small motors, 58
Soft metal foil, 430
Sommerfeld number, 312
Sound power level, 527, 535
Sound pressure level (SPL), 527, 529, 531, 534–535, 537–538
Sound wave, 481, 532, 535–536, 539–540, 629
Sound weighting scale, 530–531
Specific enthalpy, 598
Specific heat of air, 432–433
Speed
continuous, 15
peak, 15
rated, 3, 18, 39, 62, 563, 567, 579, 614
ripple, 15
synchronous, 7, 19, 40, 44–45, 579, 652
SPL, *see* Sound pressure level (SPL)
Spline shafts
advantages, 201–202
heat treatment, 201
in induction motors, 200–201
involute and straight-sided splines, 202–203
stress concentration factors, 203
S-pole, 645–646, 648, 664
Spray cooling
components, 452
heat transfer rate, 453
internal spray cooling technique, 452–454
rotor assembly
CFD analysis, 453, 455
temperature distribution, 456–457
thermophysical properties of engine oil, 453–454
Spring coefficient, 489, 495, 519
Spring–damper system, 495
Square-base rotating fastener, 285–286
Squirrel cage motors, 40–41
Squirrel cage rotor
casting process, 88–90, 113–114
closed slots, 85–86
conducting bars, 86–87
double-cage rotor, 87–88
open slots, 85
skin effect, 91
Stainless steel servomotors, 302
Stamped endbell, 277
Stamped housing, 269–270
Standard
ANSI/NETA, 554
IEC, 554
IEEE, 553–554
Star connection, 565–566
Static load, 362–363, 383, 523–524, 622
Static rotor unbalance, 118–119, 121
Stator design
air gap, 253
Arrhenius equation, 254
cogging torque, 253
encapsulation (*see* Encapsulation)
insulation
glass fiber–reinforced mica tape, 234
injection molded plastic, 233–235
methods, 232
phase-to-phase, 233
powder coating technology, 235–236
slot liner, 233, 235
stator winding damage, 233
winding-to-ground, 232–233
lamination (*see* Stator lamination)
magnet wire
Litz wire, 231–232
regular, 230–231
self-adhesive, 230–232
mechanical stress, 254–255
motor cooling system, 254
robust design techniques, 254
winding
concentrated, 243–244
conductor bars, 243–245
distributed, 243–244
hand wiring, 243
motor efficiency, 243
slot fill ratio, 242

Stator lamination
annealing, 239–240
chemical etching method, 238
connected segmented lamination, 224–225
EDM, 238
fabrication process, 238–239
integration, teeth and yoke section, 225–227
laser cutting, 238
material, 219
one-piece, 219–220
silicon steel, 236–237
slinky method
advantages, 227, 229
helical stator core fabrication, 227, 229
inorganic nonconductive material insulation, 230
slotless stator design, 229
slotless stator core, 226, 228
stacking
bolting, 241
bonding with adhesive materials, 240–241
fastened by pins, 241
lamination interlocking, 241–242
riveting, 241
self-cleating, 241
slot liners, 241
thin sleeves, 241–242
welding, 240
stamping, 237–238
thickness, 237
T-shaped segmented lamination
advantages, 221
alternative large and small segmented piece, 222, 224
core losses, 221–222
grain-oriented material, 222–223
interlocking convex and concave portions, 222
patented segmented stator laminations, 222–223
two-section stator, 224–225
Steel casting, 264
Stefan–Boltzmann law, 471
Stefan's constant, 472
Stepper motors, 47–49
Step-voltage testing, 573–574
Stiffness
shaft, 21–22, 155, 273, 627
torsional, 22–25, 50, 71, 146, 169, 172, 199, 628
Stokes' hypothesis, 598
Stray load losses, 404–405
Strength property, 157, 219, 610
Stress/strain analysis
definition, 621
dynamic analysis
centrifugal force, 623–624
structural analysis, 625–626
Hooke's law, 622
load-deformation data, 621
shear stress and strain, 622
shock load, 626–627
static analysis, 622–623
tensile/compressive stress, 622
Stribeck number, 333
Structure-borne noise, 532
Support excitation, 495–496
Surface finishing
average peak to mean, 184
average peak-to-valley height, 184
shaft lead, 182
stainless steel and resultant surface topography, 183
surface contact area ratio, 184
surface texture, 182
Surface-mounted permanent magnet (SPM) motors, 43
Surface permanent magnet transverse-flux motor (SPM-TFM), 657
Surface treatment methods
electroless plating technology, 299
electroplating, 299
electropolishing, 300–301
inorganic coating, 300
phosphate coating, 300
PVD, 299–300
Surge testing, 572–573
Switched reluctance machine/motor (SRM), 54–55, 543, 545
Synchronous motors, 44–45
Synchronous reluctance motor, 54

T

Tapered roller bearing, 320–321
Tapered shafts
axial pressing force, 204
brake torque, 205
contact diameter, 203
contact force, 204–205
contact surface area, 204
traction sheave/hub, 203–204
Taylor–Couette flow, 591–593
Tensile strength, 71, 89, 109, 110, 143, 145, 156–157, 181, 262–263, 276, 290, 293, 304

Tensile testing strip material cutting, 273
Testing load, 563
Test method
  back-to-back, 564–565
  forward short circuit, 567–569
  indirect loading, 566–569
  mechanical differential, 564
  mixed-frequency, 564
  variable inertia, 568
Test platform, 559
TFM, *see* Transverse flux motor (TFM)
Thermal adhesive, 430
Thermal coefficient, 62
Thermal conductivity, 432–433, 611–612
  of air, 432–433
  materials, 415–417
Thermal contact resistance, 429
Thermal expansion and contraction analysis
  CTE, 632–633
  differential displacement, 634
  dimensional changes, 634
  of housing/endbell *vs.* shaft, 635
  linear thermal expansion coefficients, 633
Thermal interface materials
  characteristics and thermal performance, 431
  overall thermal contact resistance, 432
  surface contact *vs.* heat conduction, 429–430
  types, 430
Thermally induced stress analysis, 632
Thermal resistance, 64, 105, 250, 272, 351, 412, 421–423, 425, 429–430, 434, 446, 457, 463, 467, 470, 473, 476, 571, 609
Thermal simulation, 607, 609–610
Thermal spraying process, 301
Thermal system, 609
Thermal time constant (τ_{th}), 64–65
Thermistor, 560
Thermocouples, 559–560
Thermoplastics, 248
Thermosets, 245, 248
Thread angle, 295–296
Thread engagement, 297–298
Thread fasteners, 290–292
Thread lead angle, 295–296
Three-dimension (3D) printing technique, 270–271
Three-mass system, 24–25
Three-phase motors, 40
Thrust bearings, 320–321
Tightening factor, 297
Tightening torque, 294–297
TMD, *see* Tuned mass damper (TMD)
Tolerance, 30, 72, 74, 116, 131, 180, 186, 193–194, 199, 206, 210, 238, 253, 322, 328, 452, 503, 508, 570, 583
Tolerance rings
  advantages, 135
  friction force, 134
  pressing forces, 134–135
  spring force, 132, 134
  wave pitches, 132
Tonal noise, 527
Toroidal winding, 641, 648, 657, 660
Torque
  cogging (see Cogging torque)
  continuous, 6
  dynamic, 2–4
  instantaneous, 6
  peak, 6–7
  rated, 3, 6, 11, 18, 92, 159, 563, 579, 581
  ripple, 13–14
  stall, 7
  static, 2–4
  tightening, 294–297
Torque constant (K_t), 59–60
Torque density, 639
Torque ripple measurement, 583–585
Torque–speed characteristics
  AC IM, 18–19
  DC motor, 17–18
  servomotor, 19–20
Torque transducer, 561–562
Torque transmission
  keyed shafts
    bearing stress, 198
    fitting, 198–199
    material selection, 194
    profile and sled runner keyseats, 195–196
    shear and crushing failure, 196–197
    shear stress, 197
    stress concentration factors, 199–200
    variables, 196
  spline shafts
    advantages, 201–202
    heat treatment, 201
    in induction motors, 200–201
    involute and straight-sided splines, 202–203
    stress concentration factors, 203
  tapered shafts
    axial pressing force, 204
    brake torque, 205
    contact diameter, 203
    contact force, 204–205
    contact surface area, 204
    traction sheave/hub, 203–204

Torsional resonance analysis, 627–629
Torsional rigidity, 169, 178
Torsional stiffness, 22–24, 169, 172
Torsional vibration, 498, 511–512
Torus topology, 649
Total conformity ratio, 316
Totally enclosed fan-cooled (TEFC) motors, 472
Transverse flux motor (TFM)
  applications, 656
  classification, 657
  constructive geometry and topology, 657
  RDT structure, 659
  rim-driven thruster, 658
  rotor and stator assembly, one-phase unit, 658–659
  single-stator winding, 657–658
  six-pole TF reluctance machine, 660
  torque component, 657–658
Transverse flux reluctance (TFR), 660
Transverse force, 174–176
Triangle-base rotating fastener, 283–285
Tribology, 311
Trickle impregnation, 250
T-shaped segmented lamination
  advantages, 220–221
  core losses, 221–222
  grain-oriented material, 222–223
  interlocking convex and concave portions, 222
Tuned mass damper (TMD)
  damping ratio, 520
  free-body diagram, 519
  metal coil springs, 521
  natural frequencies, 519–520
  two-degree-of-freedom, 518–519
  viscous dampers, 521
Turbulence model, 599
Turbulent flow, 71, 386, 393, 399, 418, 459, 482, 532, 535, 543, 546, 599, 626
Turbulent kinetic energy, 599–600
Two-frequency loading method, 566–568
Two-frequency testing, 566–568
Two-phase nanofluid, 475

U

Ultimate strength, 71, 273, 293
Ultra-large motors, 58
Unbalanced magnetic pull (UMP), 500
Universal lip seal, 188
Universal motors, 38
Unpitched noise, 527

V

Vacuum pressure impregnation (VPI)
  primary process, 250–252
  vs. solvent varnishes, 252–253
  tank, large electric motors, 250–251
Vapor chambers, 467–468
Vapor cooler, 475–476
Variable flux memory motor (VFMM), 664–665
Variable inertia testing method, 568
Variable reluctance motor (VRM), 47, 54
  doubly salient motors, 663
  DSPM motor, 663–664
  high-torque applications, 661
  vernier PM motor, 661–663
Variable reluctance stepper motor, 47–48
Varnish dipping, 249–250
Velocity constant (K_v), 60
Velocity field, 71, 386, 393, 397, 532, 546, 594, 600–603
Ventilation path, 386, 396, 533, 546
Vernier machine (VM), 661
Vibration
  axial vibration, 498
  bearing failure, 483
  control
    active vibration damping, 524
    damping materials, 514–515
    double mounting isolation system, 521–522
    TMD, 518–521
    vibration isolation, 515–518, 522–525
    vibration measurement, 525–526
    viscoelastic bearing support, 522–523
  damped harmonic oscillating system, 484–487
  dynamic, 481
  electromagnetic vibrations (*see* Electromagnetic vibrations)
  forced vibration (*see* Forced vibration)
  kinematic, 481
  measurements, 512–514
  mechanical vibrations (*see* Mechanical vibrations)
  multiple-degree-of-freedom systems, 483
  radial vibration, 497–498
  simple harmonic oscillating system, 483–485
  support excitation, 495–497
  synchronous/subsynchronous vibrations, 483
  torsional vibration, 498
Vibration acceleration, 512, 525–526

Vibration isolation
active isolation systems, 523–525
active vibration damping, 524
low-frequency isolation, 523
molded and bonded rubber, 517
multilevel magnetic system, 515, 517
passive isolation system, 515, 523
semiactive vibration isolation system, 523–524
vibration reduction device, 515–516
viscoelastic material damping pads, 516, 518
Vibration velocity, 512–513, 525, 534
Viscoelastic bearing, 522
Viscoelastic material, 514, 516–517
Viscous damping (K_{vd}), 65–66
Voice coil actuators (VCA), 525
Volumetric heat generation, 598
VPI, *see* Vacuum pressure impregnation (VPI)
VRM, *see* Variable reluctance motor (VRM)
V-shaped spring seal, 189

W

Water brake dynamometer, 558–559
Waveform, 12, 14, 39, 67, 222, 243, 380, 572–573, 580
Wavelength, 495, 536, 539, 670
Weibull cumulative distribution function, 36
Weibull probability distribution, 337–338
Weldability, 156, 208–209, 301
Welded hollow shaft
direct drive and vehicle motors, 207
fabrication, 208
friction welding technology, 210
rotor lamination core, 209
weightless motor, 207
weldability, 208–209
Windage losses
axial cooling flow, 386
axial flux motor, 393
components, 386
Darcy–Weisbach friction factor, 391–392
definition, 386
entrance effect, axial air-gap flow, 393
factors of, 386
fan losses
centrifugal fan, 395–396
pressure distribution, 396–397
pressure loss, 396, 398
velocity field, 396–397
Fanning friction factor, 391–392
friction coefficient, 392–393
high-power electric machine, 386–388
radial flux motor, 392
reduction methods
film divider, 399–400
hydrogen coolant, 404
liquid-cooled electric machine, 402–403
optimized rotor construction, 399, 401
rotor containment shell, 401
ventilating cooling system, 402–403
stator surface roughness, 393–395
tangential flow, 386
Taylor vortices, 386
CFD technique, 390–391
Couette Reynolds number (Re_d), 389
flow configuration, 388–389
geometries and configurations, 389–390
Taylor number (Ta), 389–390
ventilating path, 399
Winding electrical resistance testing, 570
Winding failure mode, 36
Winding losses
electrical resistance ratio, 372–373
Litz wire, 373
material resistivity, 370
resistive winding loss, 370–371
skin depth of conducting wires, 371–372
skin effect, 371, 373
Wound rotor
advantages, 83
motor performance characteristics, 84–85
rheostats, 83
slip rings and brushes, 83–84
torque–speed characteristics, 84
Wound rotor motors, 40–41
Wrapped housing, 259–261

Y

Yokeless, 650
Yokeless and segmented armature (YASA), 650
Young's modulus, 126, 146, 160, 275, 417, 622, 631

Z

Z-shaped fastener, 280–282